SPCBIC 2021

25th – 28th October, Minna Nigeria

3RD SCHOOL OF PHYSICAL SCIENCES BIENNIAL INTERNATIONAL CONFERENCE (SPSBIC 2021)

PROCEEDINGS

THEME:
THE ROLE OF SCIENCE AND TECHNOLOGY IN THE REALIZATION OF RESEARCH AND DEVELOPMENT IN THE ERA OF GLOBAL PANDEMIC

FEDERAL UNIVERSITY OF TECHNOLOGY MINNA,
NIGER STATE, NIGERIA

PREFACE

It is a great privilege for us to present the proceedings of 3rd School of Physical Sciences Biennial International Conference (SPSBIC) 2021 devoted to the role of science and technology in the realization of research and development in the era of pandemic. We hope that authors, delegates, agencies other individuals will find this compilation very useful and inspiring.

The school of Physical Sciences 3rd Biennial International Conference is an interdisciplinary forum for the presentation of new ideas, recent developments and research findings in the field of Science and Technology. The Conference provides a platform to scholars, researchers in the academics and other establishments to meet, share and discuss on the role of science and technology in the realization of research and development in the era of pandemic. Submissions were received both nationally and internationally and severally reviewed by our international program committee. All contributions received were neither published elsewhere nor submitted for publication as asserted by contributors.

This conference brought together experts from varying fields, visions, knowledge and experience with potentials; pre-conference workshop and four keynote speakers with world class experience in varying fields of specialization in addition to over 150 scientific participants who unveiled the latest scientific evidence to boost contemporary scientific and technological research development in the era of pandemic.

The success of the conference was a function of the collective efforts of numerous individuals. Our profound gratitude goes to the Dean School of Physical Sciences Prof. Jonathan Yisa for putting the trust the in us to serves as the Local Organizing Committee (LOC). The Vice Chancellor Prof. Abdullahi Bala and the entire management team for their unflinching support that led to the success story. We are most grateful to our workshop facilitator and his team as well as our keynote speakers for accepting our invitations and travelled long distances to be with us at no cost to the University. We also acknowledge the participants themselves, without whose expert input there would have been no conference. Thank you all for your contributions.

Prof. A. Abdulkadir
Chairperson Local Organizing Committee

THEME OF THE CONFERENCE

The Role of Science and Technology in the Realization of Research and Development in the Era of Global Pandemic

SUB-THEMES OF THE CONFERENCE

- Sustainable Management of Pandemic
- Global Change, Responses and Strategies for Limiting Pandemic
- Modelling and Monitoring of Pandemic
- Science, Technology, Engineering and Mathematics as Leveraging tools for Management of Pandemic

PRE-CONFERENCE WORKSHOP TITLE

Isolation, Purification and Structural Elucidation of Compounds and Drug Testing on Animals

Local Organizing Committee Members

Prof. (Mrs) A. Abdulkadir (Chairperson)
Dr. M. I. Kimpa
Dr. U. S. Onoduku
Dr. S. Ojoye
Dr. U. Mohammed
Dr. (Mrs) L. A. Fadipe
Dr. A. A. Rafiu
Dr. A. N. Amadi
Dr. R. A. Adeyemi
Mr. A. S. Makanta
Dr. R. B. Salau
Dr. L. Adamu (Secretary)

Technical Committee

Dr. U. S. Onoduku
Dr. L. Adamu
Dr. J. O. Eichie
Dr. R. A. Adeyemi
Dr. R. B. Salau
Dr. M. I. Kimpa

Logistic Committee

Dr. S. Ojoye
Dr. A. A. Rafiu
Dr. M. I. Kimpa
Dr. A. A. Ahmed
Dr. A. N. Amadi

KEYNOTE SPEAKERS

Dr. H. A. Shaba

Dr. Halilu Ahmad Shaba was a Director, Strategic Space Applications Department (SSA), National Space Research and Development Agency (NASRDA) as well as HOD, Department of Geo-informatics & GIS Applications, Institute of Space Science and Engineering (ISSE) affiliate of Africa University of Science and Technology (AUST), Abuja.

Dr. Shaba has successfully overseen and implemented over 20 projects among which are:

- Mapping the Drivers of Deforestation and Forest Degradation in Cross River State, Nigeria (Sponsored by FAO)
- Erosion Mapping and Monitoring with Space Technology in South-East and South-South Nigeria (Sponsor by World Bank via NEWMAP).
- Monitoring deforestation and forest degradation in cross river state, Nigeria (Part of the implementation of the UN-NEDD program in Nigeria)
- National Personnel Audit Geospatial Digital Database Development: Sponsor by UBEC
- Geo-referenced Infrastructure and Demographic Data for Development (Grid3) Project in Nigeria (NASRDA, eHealth Africa, Centre for International Earth Science Information Network (CIESIN) USA and Novel T)
- Engagement for harmonization of health facilities database (Phase 1: Geospatial Tracking System (GTS): (Ministry of health, National Primary Health Care Development Agency collaborating with National Space Research & Development Agency, eHealth Africa Foundation and Novel T).
- Space Based Digital Farm Monitoring from space for 2020 dry season farming (CBN Anchor Borrower)

Dr. Shaba has also provided services to several National and International Committees/Panels throughout his tenure as director SSA, amongst are:

- Member, Nigerian Delegation to United Nations Committee on Peaceful Use of Outer Space (UN-COPUOS) from 2005 to date
- Member, Joint Expert Group 8 (JEG8) on the implementation of an integrated AU-EU Joint Strategy under the 8th Partnership on Science, Information Society and Space, 2010 to date.
- Member, Extended Coordinating Team of Global Monitoring of the Environment & Africa (GMES & Africa), 2010 to date
- Executive Committee Member & GEO Principal for Nigeria, Group on Earth Observation (GEO), Geneva, Switzerland (2013-date)

Finally, Dr. Shaba is a member of several organizations and has been conferred with the award of honorary fellow by the following prestigious bodies;

- Geo-information Society of Nigeria (GEOSON)
- Society of Professional Disaster Risk Managers of Nigeria (SOPDRIMN)
- Nigerian Cartographic Association (NCA)

Dr. M. Alkali

Dr. Muhammad Alkali is a versatile scientist, instructor, and administrator with numerous published articles in academic and scholarly journals. Before he was appointed the Group Head, SIC, Dr Alkali bagged his Ph.D. in Integrated Systems Engineering with a research bias in Spacecraft Power Systems from Kyushu Institute of Technology (KYUTECH/KIT), a prestigious University of Technology in Japan. While in Japan, he participated in the design and development of the Electrical Power System of the Arc Event Generator and Investigator Satellite (AEGIS), a scientific spacecraft also known as Horyu-IV which was successfully launched into orbit on-board the H-2A rocket in February 2016.

He received his Masters degree in Personal, Mobile & Satellite Communications from the University of Bradford, England. His tertiary education commenced with a Bachelor degree (second class- upper division) in Physics/Electronics from the Federal University of Technology Minna, Niger State. Dr. Alkali has had a colourful, impactful career spanning from Advanced Microcomputer Systems to Central Bank of Nigeria (NYSC) to SAGEM SA to the Abuja area office of the United Bank for Africa (UBA) to the National Space Research and Development Agency (NASRDA) and finally to the Nigerian Communications Satellite Limited (NIGCOMSAT) where he has served in various capacities over the years in Satellite Network Control and Applications. He was also a pivotal member of the AFRICARE-NIGERIA's project (Independent Policy Group), a think-tank for the President of Nigeria (2002-2003).

Dr. Alkali has always aimed to have an expansive international and local repertoire of knowledge while keeping abreast with industry trends. This has led to his participation in the study visit on European Union Global Navigation Satellite System in Spain, his attendance at the Indian Institute for Public Administration (IIPA) New Delhi, where he trained in Global Strategic Leadership for Growth and Sustainable Development. He attended the Advanced Visioning and Leadership Programme on Managing Human Capital and Shaping Culture organized by TL First Group/Institute of Leadership and Management of UK. He also attended a practical project management course at CCLL, Cardiff University-United Kingdom. He was among the 50 Scientists/Engineers trained at the China Academy of Space Technology/ Beijing Institute of Tracking & Telecommunications Technology for Know-how Technology Transfer training on NigComSat-1 from 2005. In 2008, he attended a Satellite networking course at PT Telkom learning Centre in Bandung, Indonesia.

Dr. Alkali is a fellow of the African Scientific Institute (FASI), a Fellow of the Institute of Corporate Administration (FCAI), a senior member of the American Institute of Aeronautics and Astronautics, Member Nigerian Institute of Physics, and a Member of the Computer Professionals Registration Council of Nigeria (MCPN). Dr. Alkali has vast interests ranging from Design thinking; energy; CT; science, technology, and innovations (STI) to spacecraft design and systems integrations (payload and bus systems).

Professor Abdul Kabir Mohammed

Professor Abdul Kabir Mohammed is currently serving as Professor and Chair of the Department of Chemistry & Biochemistry at North Carolina Central University, Durham, NC. Previously, he served as the Chair of the Department of Chemistry at Winston Salem State University, Winston-Salem, NC and prior to that appointment he was an Associate Professor at North Carolina A&T State University, Greensboro, NC.

Prof. Mohammed graduated from the University of Benin, Benin-City in 1983 with a B.Sc. (first class honors) degree in chemistry. He worked briefly in 1987 as a Graduate Assistant at Federal University of Technology, Yola (now Modibbo Adama University of Technology), before proceeding to Louisiana State University for his postgraduate education.

He received his Ph.D. in inorganic chemistry in 1982 and did postdoctoral research at Florida State University from 1982 to 1983. He was a Fulbright Scholar at Sultan Qaboos University in Oman from 2003 to 2004; and he served as a Carnegie African Diaspora Fellow at the Federal University of Technology, Minna, Nigeria in the summers of 2017 and 2019. His research interests include photophysics and photochemistry of transition metal complexes and chemical education. He teaches general, inorganic and environmental chemistry courses.

Prof. Makun Hussaini Anthony

Prof. Makun Hussaini has 29 years of experience as a university academic staff and a researcher in areas relating to food safety, environmental health monitoring, mycotoxicology and mycology. He possess a Doctorate degree in Biochemistry (Toxicology) after successful completion of a thesis entitled "Studies on mycoflora and mycotoxins contaminating guinea corn and rice in Niger State, Nigeria" This was preceded by an MSc degree in Biochemistry (thesis titled "Analysis of blood levels of trace metals, total lipids and cholesterol in Ajaokuta Steel Industry workers"). The novelty of finding *Fusarium verticillioides* in Nigerian rice during his PhD work, which is the fungi associated with oesophageal cancer (EC) in South Africa, earned him a National Research Foundation Postdoctoral Fellowship (PDF) with Food Environment and Health Research Group of the University of Johannesburg (UJ).

Being a university teaching staff for over almost three decades, Prof. Makun has taught many biochemistry and environmental toxicology related courses at both undergraduate and postgraduate levels. He has supervised and graduated over 85 B-Tech, 18 M-Tech students and 9 PhDs. The graduate students all worked on mycotoxins.

Prof. Makun has won national and international research grants to the cumulative sum of $8, 647,787. 47. He is a Fellow of Mycotoxicology Society of Nigeria (FMSN), a member of the National Agency for Food and Drug Administration and Control (NAFDAC), National Food Safety Advisory Committee of Nigeria, National Codex Committee of Nigeria, African Union Expert Committee on Contaminants in Food (2011 to date) and Joint FAO/WHO Expert Committee on Contaminants in Food (JECFA) (2012-2020). He coordinated the writing of the "discussion paper on fungi and mycotoxins in Sorghum" which was adopted as a document of the Joint FAO/WHO Experts Committee on Food Additives (JECFA) in 2012 and participated in the writing of "Proposed draft annex for "prevention and reduction of aflatoxins and ochratoxin A in sorghum" in the existing code of practice for the prevention and reduction of mycotoxin contamination in cereals (CAC/RCP 51-2003)". He wrote on the prevention and control of sterigmatocystin and diacetoxyscirpenol for the 83rd meeting of JECFA held in November, 2017 in Rome.

Prof. Makun has 72 publications, mostly on mycotoxins in peer review journals, technical papers and books. He was the immediate pass Director of Research, Innovation and Development of the Federal University of Technology Minna, Nigeria. He is currently the Lead Researcher of the Food and Toxicology Research Group and Centre Leader of the Africa Centre of Excellence for Mycotoxin and Food Safety of the Federal University of Technology Minna. Project Coordinator of the West African Food Safety Network (WAFOSAN) and Member of the African Food Safety Network. He has served as election monitor, election collation and returning officers at state and national assembly elections from 1999 to 2015). He has passion for jogging and reading. He is married to Barrister Evelyn Pambelo Hussaini and blessed with four children.

Dr. Eustace Manayi Dogo

Dr Eustace M. Dogo has over ten years of industry experience working in Russia, Europe and Nigeria. He holds a BSc and MEng degrees in Electrical Engineering from Peter the Great Saint Petersburg Polytechnic University, Saint Petersburg, Russia and PhD degree from the University of Johannesburg, South Africa. His PhD research focused on investigating imbalanced learning using Artificial Intelligence algorithms in real-world drinking-water quality detection problems, where he proposed three new dynamic selection algorithms combined with data pre-processing methods.

Among his notable contributions while at the University of Johannesburg during his postgraduate studies, Dr Eustace Dogo served as a volunteer to the 6th International Conference on Soft Computing and Machine Intelligence (ISCMI 2019) held in Johannesburg, South Africa, on November 19-20. In 2019, he served as a tutor in the first Short Learning Programme (SLP) in Computational Intelligence for Industry, organized by the Institute for Intelligence Systems in collaboration with the Department of Information Systems at the University of Johannesburg, and successfully graduated two batches of students drawn across diverse works of life (over 50 students).

Dr Eustace Dogo was recently among a panel of discussants in the University of Johannesburg's *Cloudebate* on the Fourth Industrial Revolution and Technology for People with Disabilities. Between 2018 and 2019, he co-supervised to completion 16 undergraduate students in the Department of Electrical and Electronic Engineering Science, University of Johannesburg, South Africa. He also presented a technical talk at the *POWER-GEN & DistribuTECH - GEN-X* conference and exhibition which took place in Sandton, Johannesburg in 2017.

Dr Eustace Dogo has extensive knowledge in industry, research, training and teaching. He is an active undergraduate and postgraduate degree supervisor and has authored and co-authored in reputable journals, conferences and several scholarly research books in his areas of interest. He joined the academia in 2012 and currently lectures at the Department of Computer Engineering, Federal University of Technology Minna, Nigeria. His broad research interest includes, theoretical and applied Machine Learning, Intelligent Systems, Cloud Computing and Emerging Technologies. He is married to Barrister Fatima Eustace-Dogo and blessed with three children.

CONFERENCE WORKSHOP FACILITATOR

Prof. Derek Tantoh Ndinteh

Prof. Derek Tantoh Ndinteh is an expert in areas of Natural Products Chemistry; drug discovery and drug delivery platforms. He is currently working on Natural Products Chemistry that deals with extraction, purification, isolation and characterization of chemical substances and evaluation of biological and pharmacological activities of African plants for pharmaceutical industries.

He is interested in collaborating with Federal University of Technology, Minna on the evaluation of the antidiabetic, antimicrobial, antioxidant, anticancer and anti-ulcerogenic potentials of secondary metabolites from Nigerian Medicinal Plants.

Our interaction so far with Prof. Derek Tantoh Ndinteh has been very mutual and beneficial to both Universities involved because it has potential to increase our visibility at global level based on academic activities and mainstreaming and replication of the research and teaching outcomes of this collaboration by the staff and students can be integrated into overall development of Nigeria and South Africa.

CHEMICAL/LIFE SCIENCE

MATHEMATICAL/ICT

PHYSICAL /CLIMATE SCIENCE

CHEMICAL/LIFE SCIENCE

Characterization of Hydrothermally Synthesized WO_3 nanowires and Chlorine-Calcium co – doped WO_3 Nanowire Composite

[*1]Onogwu, Udenyi Sarah, [1,2]Tijani, Jimoh Oladejo, [1,2]Bankole, Mercy Temitope
[1]Department of Chemistry, Federal University of Technology, PMB, 65, Minna, Niger State
[2]Nanotechnology Research Group, African Centre of Excellence on Food Safety and Mycotoxins, Federal University of Technology, P.M.B 65, Bosso, Minna, Niger State, Nigeria
*Corresponding author: oudenyisarah@gmail.com

Abstract

Doping WO_3 nanowires with non-metal and metal is a viable strategy to enhance its properties as compared to undoped counterpart. In this study, Response Surface Methodology optimization based on Box –Behnken design was employed for the synthesis of WO_3 nanowires via hydrothermal method where sodium-tungstate and oxalic acid were used as precursors. While sodium chloride and calcium nitrate at different mixing ratios was used as structure directing agents to prepare Cl-Ca co-doped WO_3 nanowires composites through wet impregnation- hydrothermal method. The prepared WO_3 based nanowires were characterized for their morphology, elemental composition, microstructure and mineral phase using X-ray diffraction (XRD), high resolution scanning electron microscopy HRSEM), Energy dispersive spectroscopy (EDS), high resolution transmission electron microscopy (HRTEM), Selected area electron diffraction (SAED) and. XRD/HRSEM/HRTEM analysis confirmed that the synthesized WO_3 were monoclinic, highly crystalline, compacted spherical and nanowires shaped with a diameter between 104.5 nm – 125.nm. The EDS revealed tungsten and oxygen as the dominant element irrespective of the synthesis conditions. The HRSEM/HRTEM results of the chlorine-calcium co-doped WO_3 showed morphological changes and the formation of large and narrow bundles nanowires of different length depending on the Chlorine-Calcium mixing ratio. The XRD analysis demonstrated phase changed from monoclinic to triclinic due to the presence of chlorine and calcium in the lattice layers of WO_3 nanowires composite. The EDS results for the co-doped samples revealed tungsten, oxygen as the dominant elements and calcium, chlorine in varying amounts. It was found that addition of the two dopants was responsible for the increase in the diameter of the nanowires from 178.82 to 203.50 nm compared to 125 nm obtained for pure WO_3 nanowires alone.

Keywords: Doping, hydrothermal method, nanowires, Tungsten trioxide

1. Introduction

Tungsten oxide (WO_3) also known as tungsten trioxide is an important n-type semiconductor with a band gap of 2.8eV and has attracted much interest among material scientist due to its excellent physical and chemical properties (Han *et al*., 2016). WO_3 as an excellent transition metal oxide is naturally abundant, cost effective, less toxic towards living organisms and environmentally friendly (Madare *et al*., 2019). Due to its unique properties, it has been employed in diverse applications such as gas sensing, fuel cells, water splitting, solar cells, batteries and optical devices (Han *et al*., 2016). Its intense absorption within the solar spectrum and high thermal and physiochemical stability makes WO_3 a good candidate for a visible photocatalyts compared to other metal oxides such as ZnO, CdS, SiO_2 (Han *et al*., 2016). WO_3 photocatalytic property usually in visible irradiation depends on its morphology, structure, composition, crystal phase amongst others (Guo *et al*., 2016).

WO_3 shows structural polymorphism and phase transitions at different temperature during heating or cooling (Madare *et al*., 2019). The most common phase found at room temperature is monoclinic I (γ-WO_3) formed at a temperature from 17-330^oC (Madare *et al*., 2019). However below this temperature, two other crystallographic phases exist; monoclinic II (e-WO_3) at a temperature below

43°C and triclinic (δ-WO_3) at a temperature ranging between -43°C to 17°C (Madare *et al*., 2019).. When the temperature is heated above 330°C, transformation of monoclinic phase (γ-WO_3) to orthorhombic β-WO_3 usually occurs and the material remains stable up to 740°C and at a temperature greater than 740°C, tetragonal α-WO_3 is formed(Madare *et al*., 2019).. Cubic c-WO_3 is also available as another phase of WO_3.Typical of other semiconductors, WO_3 photocatayltic activity is limited by high electron-hole recombination rates which further limit its usage in the visible light spectrum.(Han *et al*.,2016) Furthermore, the problem of fast electron – hole recombination may be responsible for the difficulty in the reduction of oxygen charge carriers separations and transfer, creation of more active sites which will improve effective redox reactions during photocatalytic process (Han *et al*., 2016), hence there is need to improve the catalytic activity of WO_3 nanowire through the incorporation of different metallic and non-metallic impurities onto its lattice layers.

Dopants tend to accelerate the surface of WO_3 nanowires. In addition, the doping of WO_3 nanowires also improve its optical properties through band gap reduction or shift in adsorption band edges (Madare *et al*., 2019). In the case of metal doping, there is usually a direct contact between the metal and the semiconductor metal oxide which lead to the formation of an electric field based on electron transfer between the two substrates according to Fermi level difference. The interaction usually results to the shifting of energy band edge and reduction of electron – hole recombination rate (Kahng *et al*., 2019). In non – metal doping, the dopants raise the maximum valence band edge of the semiconductor metal oxide and causes significant narrowing of the band gap energy.

Different methods which includes spray pyrolysis (Leng *et al*., 2019), Mechanochemical (Wang *et al*., 2003), Chemical vapor transport (Liu *et al*., 2013), solid phase reaction (Lee *et al*., 2014; Ma *et al*., 2017), Solvothermal (Guo *et al*., 2016), and Hydrothermal method (Fu *et al*., 2014; Han *et al*., 2016) have been employed in the synthesis of WO_3 nanowires. Of all these methods, the hydrothermal method is considered simple and versatile method of synthesizing nanowires from aqueous solutions because water is the most commonly used solvent. The parameters such as reaction temperature, pressure, reaction time, pH and the concentration of the precursor are usually adjusted during the synthesis (Wu *et al*., 2019; Nagyne-kovacs *et al*., 2020). In this method, the solubility of the solid which is usually the precursor increases because of the temperature and pressure generated is above the critical point of the solvent used. This method offers advantages which includes one step synthetic procedure, environmental –benign, cost effective, good dispersion in solution , in other words due to the intense conditions in the autoclave, nearly all materials can be made soluble (Wu *et al*.,2019).

More so, the hydrothermal method offers the formation of well-crystallized nanostructures. (Nagyne-kovacs *et al*., 2020). Over the years, researchers have employed conventional optimization where one factor is varied and other variable are kept constant. This approach is expensive, time consuming and often resulted to wastage of chemicals (Vakilinezhad *et al*., 2018). On the contrary, recent attention has been shifted to the optimization of synthesis procedure using statistical design of experiment (DOE) involving response surface methodology (RSM) (Lee & Abd Hamid, 2015). RSM is highly effective, safe time especially with minimum number of experiments based on the interactive effects of different process parameters (Sajad *et al*., 2015).Thus, in this study, Response Surface Methodology optimization based on Box –Behnken design was employed for the synthesis WO_3 and Cl-Ca doped WO_3 nanowires via hydrothermal method during which the interactive effects of the following parameters: Concentration, Time and Temperature were investigated. The undoped and doped prepared nanowires were characterized using different analytical techniques such as X-ray diffraction (XRD), scanning electron microscope (SEM), transmission electron microscope (TEM), Energy dispersive spectrometry (EDS), selected area electron diffraction (SAED) and UV-Vis spectroscopy.

2. Literature Review

Several researchers have employed the hydrothermal method to prepare well organized arrays of WO_3 and other semiconductor nanowires. Lu *et al*. (2018) reported the preparation of ultrathin hexagonal WO_3 nanowires (U-WO_x NW) by modified hydrothermal method and the nanowires were characterized. Also the photocatalytic performance of the nanowires with the introduction of Ag as a co-catalyst was also studied. The obtained U-WOx NW showed impressive absorption tail in the visible region and near the infrared region causing oxygen vacancies which is beneficial for photocatalysis. Pauekphong *et al*., (2019) reported the synthesis of WO_3/TiO_2 nanowires by hydrothermal method. The effect of doping dosage on crystal structure, morphology, band gap energy and the defect concentration of the synthesized sample were also studied and further characterized. Only the monoclinic phase was formed at calcination temperature of 400^oC for 2 hours. Although the doping of the TiO_2 with WO_3 did affect the lattice parameter, band gap energy, crystallite size and the effect concentration of the doped sample, but doping with 5 mol% of WO_3 into TiO_2 nanowire gave the best result for application as electrochemical sensors and ionic batteries.

Nagyne-kovacs *et al*. (2020) reported the effect of pH in the hydrothermal preparation of monoclinic tungsten oxide. Also, the importance of various additives such as ethanoic acid (CH_3COOH), sodium perchlorate ($NaClO_4$) and sodium sulphate (Na_2SO_4) on the crystal structure and morphology was investigated. From the results obtained it was found that the samples possessed nanosheets-like morphology when CH_3COOH, $NaClO_4$ were used as additives and even when none was used at a temperature of 180^oC and 200^oC. However, when Na_2SO_4 was used elongated like sheets were obtained at a temperature of 180^oC which can be attributed to the structure directing role of Na_2SO_4. In the case of effect of pH, the samples prepared at a pH of 0.1 and at a temperature of 180^oC and 200^oC were all pure monoclinic phase of WO_3.

Tehrani *et al*. (2020) reported the hydrothermal synthesis of 1D and 2D WO_3 nanostructures. The effect of time during the method was also studied to explore the structural, morphological and optical properties. Analytical techniques such as XRD, FESEM and FTIR were employed to characterize the prepared sample and the results showed that the morphological changes of the nanostructures depend strongly on the duration of time and the concentration of capping agents.

Silveira *et al*. (2020) synthesized Mo-doped WO_3 nanowires for the adsorption of methylene in wastewater. It was found that on the addition of molybdenum, the morphology of the undoped WO_3 nanowire changes from large bundles to narrow bundles with an increasing number of isolated thin nanowires. Doping with molybdenum also changed the porosity, surface area and crystalline structure of the undoped WO_3. In summary, several authors have reported hydrothermal synthesis of WO_3 nanowires; however, to the best of our knowledge, there is little or no information on the hydrothermal synthesis of chlorine-calcium co-doped WO_3 nanowires composites.

3. Methodology

3.1 Materials: Sodium tungsten dihydrate ($Na_2WO_4.2H_2O$) was purchased from sigma-Aldrich. All other chemicals (Oxalic acid $H_2C_20_4$, Hydrochloric acid HCl, Calcium nitrate $Ca(NO_3)_2$, Sodium Chloride NaCl) were analytical grade and used without further purification.

3.2 Synthesis of WO_3 Nanowires: Firstly, 16.5g of $Na_2WO_4.2H_2O$ and 0.05g of NaCl was dissolved in 50 ml of distilled water and stirred for 30 min continuously using a magnetic stirrer at 500 rpm. The pH value of the solution was adjusted to 2 using 3M HCl acid solution. Afterwards, 6.3g of $(COOH)_2.$ $2H_2O$ was added and further stirred for another 1 hour. After stirring, the suspension was transferred to a 50 ml capacity Teflon-lined stainless steel autoclave and heated to 200^oC for 1 hr 30mins in an oven and later allowed to cool to room temperature. The product was washed thoroughly with distilled water and dried at 70^oC overnight. The synthesis of WO3 nanowires was repeated using the following conditions **(**concentration of $Na_2WO_4.2H_2O$ 0.55M, 1M), reaction

temperature (140^{o}C, 200°C) at constant reaction time (2h 30 min)),The synthesis of the Cl-Ca – codoped nanocomposite was carried out as using specific quantities of NaCl and $Ca(NO_3)_2$ in percentage (1%Cl-1% Ca, 1%Cl-2%Ca, 1%Cl-4%Ca, 2%Cl-1%Ca, 4%Cl-1%Ca) and then mixed with $Na_2WO_4.2H_2O$ in distilled water. The mixture was put in a50 ml capacity Teflon-lined stainless steel autoclave and annealed for 2 hr 30mins at a temperature of 200°C to yield the Cl-Ca-codoped nanocomposite denoted as 1c-1a,1c-2a,1c-4a,2c-1a,4c-1a.(Han *et al*.,2016)

Characterization of WO_3 based nanowires

The WO_3 nanowires and Cl-Ca co-doped WO3 nanowires were characterized for their morphology, elemental composition and mineralogical phase using Zeiss Auriga High Resolution Scanning Electron Microscope (HRSEM) fitted with a secondary electron detector and an Energy Dispersive X-ray spectroscopy (EDS) option and X-ray diffractometer (XRD)-D8 bruker AXS advance, fitted with Lynxeye detector and CuKα x-ray source

4. Results and discussion

HRSEM analysis of the undoped WO_3 nanowires is presented in Plate 1.

Plate I shows the HRSEM images of the undoped WO_3 nanowires prepared at 1M, 200^{o}C and 1h 30 min; 1M, 140^{o}C and 2h 30 min, and finally 0.55 M, 200^{o}C and 2h 30 min. These images clearly indicate that products were mixture of agglomerated spherical nanoparticles and bamboo like-nanowires irrespective of the conditions. However, their size and aspect ratio are different. WO_3 nanowires synthesized at 1M, 200^{o}C and 1h 30 min had a diameter of about 125.1 nm and up to 568.3 nm in length with an aspect ratio of 4.54, while those synthesized at 1M, 140^{o}C and 2h 30 min, were approximately 247.1 nm in diameter and 1.029 µm in length with an aspect ratio of 4.16, and the ones produced at 0.55 M, 200^{o}C and 2 h 30 min were around 104.5 nm in diameter and 1.089 µm in length with an aspect ratio of 10.42, showing well-developed nanowires.

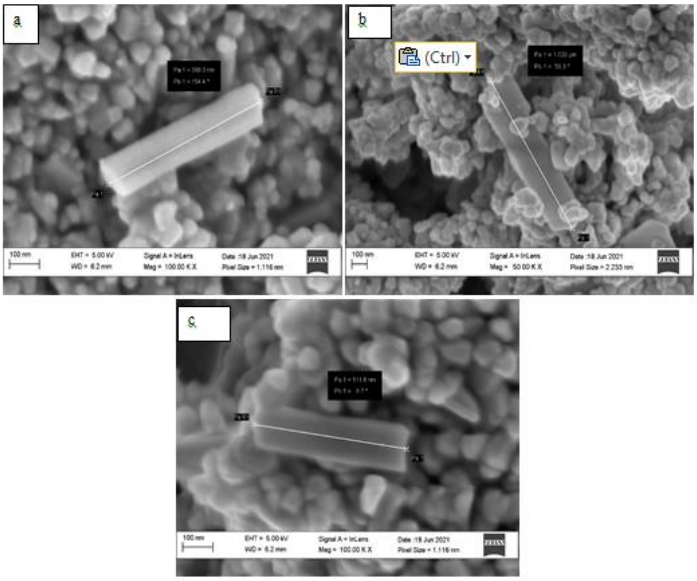

PLATE I: HRSEM Micrographs of WO_3 nanowires prepared at: (a) 1M, 200^{o}C 1h 30 min, (b) 1M, 140^{o}C and 2h 30 min, and (c) 0.55 M, 200^{o}C and 2 h 30 min

Phuruangrat *et al*. (2010) had reported that WO_3 nanowires produced by convectional hydrothermal method had lengths of 200–300 nm and a diameter of 10–15 nm (aspect ratio of 13–30), whereas hexagonal WO_3 nanowires produced from microwave assisted hydrothermal method were more than 5 mm long and less than 10 nm in diameter, with an average aspect ratio of >625. The aspect ratio of hexagonal WO_3 produced by the microwave assisted hydrothermal synthesis is higher than those in this study and can be attributed to difference in the initial precursor and the presence of surfactants such as oxalic acid in the present study.

HRSEM analysis of chlorine and calcium co-doped WO_3 nanowires

The HRSEM images of Cl and Ca doped WO_3 samples with different chlorine and calcium contents are presented on **Plate II (a-e).** The morphology of Plate II (a) reveals the formation of stacked and block bundles of nanowires with varying lengths, ranging from 645.85 nm to 1.440 μm and average bundle diameters ranging from 100 to 250 nm. In Plate II (b) with mixing ratio of chlorine to calcium (1-2), the average diameter was found to be 386.18 nm, while the average length was around 992.88 nm. In the case of Plate II (c), with the mixing ratios twice that of Plate II (b), the bundle-like nanowires had an average diameter of about 392.81 nm and a length up to 999.88 nm. Plate II (d) with the mixing ratios of chlorine and calcium (21), WO_3 nanowires had an average diameter of 367.84nm with a length measured to be about 1.527 μm and finally plate II (e) exhibited a diameter of 346.01nm and a length of 1.33 μm.

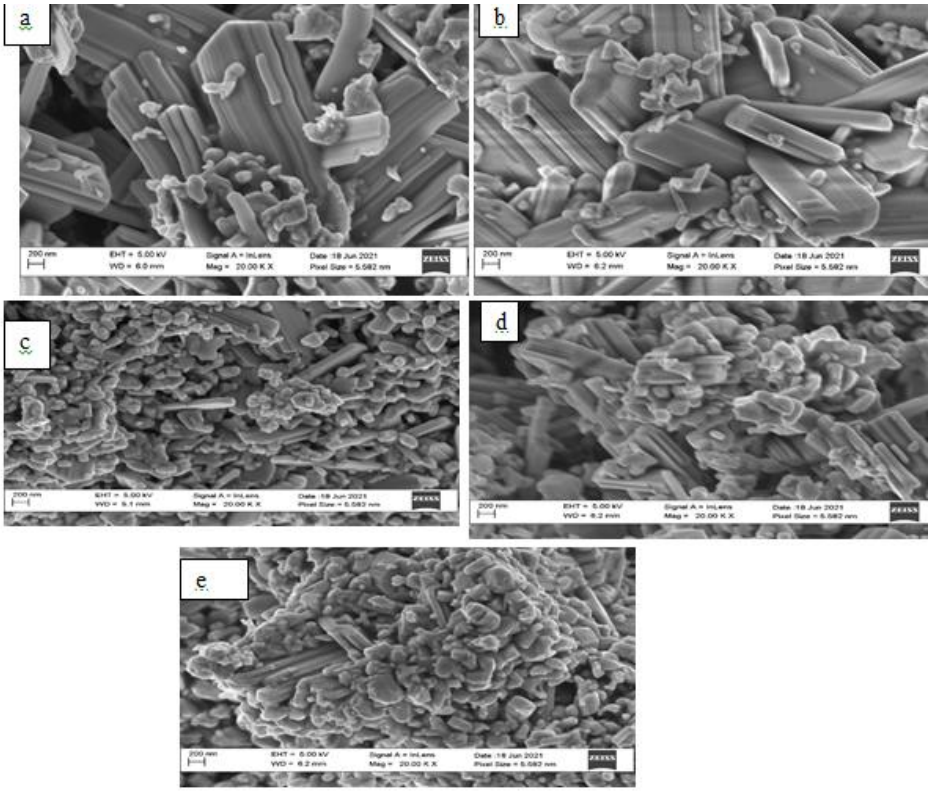

PLATE II: HRSEM Micrographs of doped WO_3 nanowires (a) 1c-1a doped WO_3 (b) 1c-2a doped WO_3 (c) 1c-4a doped WO_3 (d) 2c-1a doped WO_3 (e)4c-1a doped WO_3

In general, the formed block bundles of Cl-Ca-WO_3 nanocomposite samples were longer and wider in diameter than those of the pure WO_3 nanowires due to the addition of the two dopants. However, when the Cl and Ca-content was increased on the lattice layer of WO_3, as seen in Plate II (c) and (e), there was agglomeration of the nanowires. The increase in length and diameter observed in doped samples could be due to the large ionic radius of Ca^{2+} (0.99 Å) and Cl^- (0.81 Å) making it difficult for either Ca^{2+} or Cl^- to replace either W^{5+} or W^{6+} (which have smaller atomic radii of about 0.65 Å and 0.68 Å respectively) inside the lattice of WO_3 (Kunyapat *et al.*, 2018).Thus, both Ca^{2+} and Cl^- were deposited on the surface of WO_3 monoclinic framework, leading to an expansion of the crystal lattice as confirmed by the XRD result. Furthermore, the presence of either chloride or calcium ions in the composite could accelerate its photocatalytic activities facilitating electron transfer and oxygen mobility in the doped samples. Similar deductions have been made by Thummavichai *et al.* (2021) that synthesized Na_yWO_x bronze nanowires and found that by increasing the Na-dopant amounts to 1:12, 1:8 and 1:4, mixtures of nanorods, nanoplates and agglomerated bundled structures were observed, and the size of nanowires increased with Na-contents inside the framework.

XRD Analysis of WO_3 based nanowires

The XRD technique is commonly used to study the crystal structure and the parameters of a compound. Figure 4.1 shows the XRD diffractogram of the various WO_3 samples prepared at 1M, 200°C and 1h 30 min, (b) 1M, 140°C and 2h 30 min, and (c) 0.55 M, 200°C and 2 h 30 min represented as condition 4, 8 and 12 respectively. These showed the crystalline peaks at Bragg angle (2θ) 23.12°, 23.58°, 24.59°, 33.26°, 34.17, 36.29°, 50.73°, 55.93°, 62.42°, and 76.94° corresponding to the miller indices: (002), (020), (200), (120), (112), (022), (202), (222), (114), (420), (340), and (160). These peaks can be indexed to the WO_3 monoclinic structure for condition 4 and condition 12 and then triclinic structure for condition 8 according to Joint Committee on Powder Diffraction Standards (JCPDS) file numbers: 01-072-0677, 01-083-0950 and 01-083-0948. The mean crystalline size was calculated from the full width at half maximum (FWHM) of the XRD lines using Debye-Scherrer formula

$$d = \frac{K\lambda}{\beta cos\theta}$$

Where d is the mean crystallite size, K is the shape factor taken as 0.94, λ is the wavelength of the incident beam, β represent the full width at half maximum and θ is the Bragg angle. The average crystalline size was found to be 14.83nm, 14.93nm and 14.39nm for undoped WO_3 prepared at conditions 4, 8 and 12 respectively. This shows that crystalline size increases as the reaction time and concentration increases. Nagyne-kovacs *et al*. (2020) and Fu *et al*., (2014) reported the formation of well crystallized monoclinic WO_3 nanowires prepared hydrothermally at reaction temperature closer to the one in this study. However, to the best of the writer's knowledge the formation of triclinic phase of WO_3 nanowires using hydrothermal method has not been reported yet.

Three main diffraction peaks at 23.12°, 23.58 and 24. 24.37° can be assigned to the (002), (020) and (200) planes, respectively. The strongest intensity of the (200) plane suggests that the nanowires are preferably grown along the <200> direction, which also agrees with the HR-TEM images and SAED patterns (Figure 4.1).

XRD pattern of chlorine and calcium co-doped WO_3 nanowires composites

Figure 4.2 shows the XRD pattern of WO_3 prepared by hydrothermal approach using different mixing ratios of chlorine and calcium dopants.

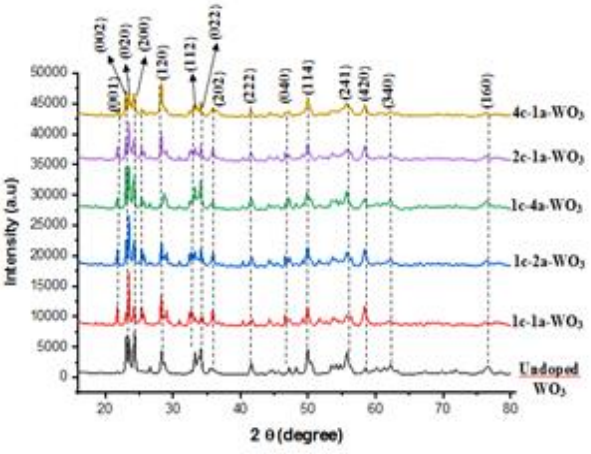

Figure 4.1 XRD pattern of undoped WO_3 prepared at different conditions

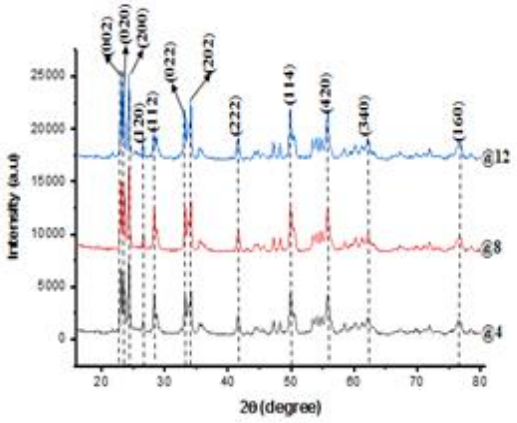

Figure 4.2. XRD patterns of Cl and-Ca doped WO_3 nanowires with different mixing ratios

The XRD patterns of WO_3 alone belongs to monoclinic phase with (JCPDS Card No: 01-72–0677, space group P21/n (14), a = 7.306 Å, b = 7.540 Å, c = 7.6892 Å) with large diffraction intensities

for (020) and (120) peaks positioned at 2 thetha values of 23.58°, 24.59° respectively. In addition, the following characteristics planes (002), (200), (112), (022), (040), (202), (222), (114), (241), (420), (340), and (160) were positioned at 2 thetha values of 23.12°, 23.58°, 33.26°, 34.17, 36.29°, 48.24°, 50.73°, 55.93°, 56.24°, 62.42°, and 76.94° respectively. This suggests the crystalline nature of monoclinic WO_3. Furthermore, the characteristics planes (001), (002), (200), (120), (112), (022), (040), (202), (222), (114), (241), (420), (340), and (160) positioned at 2 thetha values of 21.00°, 23.12°, 23.58°, 33.26°, 34.17, 36.29°, 48.24°, 50.73°, 55.93°, 56.24°, 62.42°, and 76.94° respectively, indicate the crystalline nature of monoclinic WO_3. For the doped nanocomposites (1c-1a-WO_3, 1c-2a-WO_3, 1c-4a-WO_3, 2c-1a-WO_3 and 1c-4a-WO_3),the peaks of Ca and Cl along with monoclinic WO_3 were well presented. These reveals that the pure WO_3 and co-doped composites (1c-1a-WO_3, 1c-2a-WO_3, 1c-4a-WO_3, 2c-1a-WO_3 and 4c-1a-WO_3) all belong to the same monoclinic WO_3 with JCPDS card no: 01-72–0677. This suggests that the incorporation of Cl and Ca onto the lattice framework of WO_3 did not caused changes in mineralogical phases but influenced the morphology, and their crystalline structure. Doped samples with high amount of Ca, low Cl and equal amount of Ca and Cl (1c-4a-WO_3, 1c-2a-WO_3, and 1c-1a-WO_3, respectively) caused changes in the morphology with the introduction of a new peak assigned to (100) plane while the plane at (120) was shifted from 26.55° to 25.33°.

For low Ca and high Cl-concentration (2c-1a-WO_3 and 4c-1a-WO_3), the structure of the sample remained as the crystalline feature of the as-prepared WO_3, however an extra peak assigned to planes (100) become more visible whereas the plane (112) increased in intensity as compared to the other crystallographic peaks.

A closer look at the XRD pattern of the doped-WO_3 suggests that all the peak positions were shifted to a lower diffraction angle for the calcium and chlorine doped samples. Based on Bragg's law, the observed peak shift can be related to the increase in lattice parameters, which confirms the intercalation of different Ca and Cl contents into the WO_3 layers and formed nanowires. Crystallographic growth direction of these products has been confirmed by HRTEM analysis

Similar deductions were carried out by Kong et al. (2020) who synthesized WO_3 nanoplate film was prepared by nitric acid corrosion of W foil using oxalic acid following hydrothermal method and obtained monoclinic phase.

The mean crystalline size was calculated from the full width at half maximum (FWHM) of the XRD lines using Debye-Scherrer formula

$$d = \frac{K\lambda}{\beta cos\theta}$$

Where d is the mean crystallite size, K is the shape factor taken as 0.94, λ is the wavelength of the incident beam, β represent the full width at half maximum and θ is the Bragg angle. The average crystalline size was found to be 28.48nm, 22.64nm, 17.18nm, 11.42nm, and 10.51nm for 1c:1a, 1c:2a, 2c:1a, 4c:1a and 1c:4a respectively. The incorporation of dopants (metal and non-metal) simultaneously can decrease the crystal growth of WO_3 nanowires which is quite different from the deductions of Han *et al*., (2016) who reported an increase in the crystal growth of WO_3 with the incorporation of sulphur (a non-metal dopant) alone. However, Silveira *et al*., (2020) observed that with increasing amount of Mo-doping there was a reduction in crystalline size.

EDS analysis of the undoped WO_3 nanowires

The energy dispersive spectrometric (EDS) analysis was employed to analyze the composition of the WO_3 nanowires. As shown in Table 4.1, only oxygen, tungsten and sodium elements existed in the nanowires with molar concentration, reaction time and calcination temperature. The presence of sodium originated from the precursor salt (sodium tungstate). However, no other impurity was present as similarly reported by Wanjun et al. (2016) in the fabrication of WO_3 nanowires via the

hydrothermal method in the presence of guanidine sulfate as a dispersant and Na_2WO_4 as a precursor salt.

Table 4.1: Elemental Composition of the As-synthesized Nanowires

Sample	1M, 200°C, 1h 30 min	1M, 140°C and 2h 30 min	0.55 M, 200°C and 2 h 30 min
Element	**Wt (%)**	**Wt (%)**	**Wt (%)**
O	17.08	11.95	13.17
Na	0.17	0.95	1.08
W	82.75	87.1	85.75
Total:	100	100	100

EDS analysis of the Cl and Ca doped WO_3 nanowires

Energy dispersive spectrometric (EDS) analysis for the undoped and doped samples is presented in Table 4.2. As expected, all the nanowires consisted of W, O and Na, while 1c-1a-WO_3 nanowiresincluded Ca and Cl in stoichiometric proportion. Samples 1c-2a-WO_3 and 1c-4a-WO_3 revealedthat ratio of Ca increased from 1.83% to 3.66%, while Cl remained fairly constant at 0.64%. Furthermore, in the samples 2c-1a-WO_3 and4c-1a-WO_3, Clalso increased from 1.30% to 2.58% indicating a proportionate increase when the ratio of Cl in the sample is increased from 2:4.

Table 4.2: Elemental Composition of the Undoped Ca and Cl doped WO_3 Nanowires

Sample	1M, 200°C, 1h 30 min	1c-1a-WO_3	1c-2a-WO_3	1c-4a-WO_3	2c-1a-WO_3	4c-1a-WO_3
Element	Wt (%)	Wt (%)	Wt (%)	Wt (%)	Wt (%)	Wt (%)
O	17.08	18.17	14.01	14.87	17.36	16.2
Na	0.17	0.12	0.11	0.10	0.10	0.10
Cl	-----	0.64	0.65	0.64	1.3	2.58
Ca	-----	0.92	1.83	3.66	0.91	0.91
W	82.75	80.15	83.4	80.73	80.33	80.21
Total:	100	100	100	100	100	100

HRTEM analysis of undoped, Cl-Ca doped WO_3 nanowires

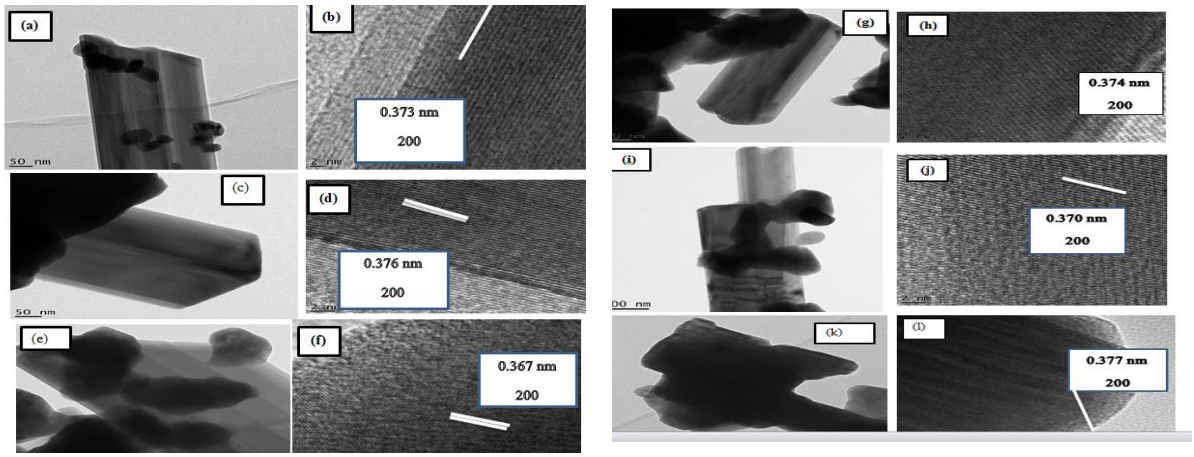

LATE III: HRTEM Micrographs of WO_3 nanowires of (a) undoped WO_3 (b) 1c-1a doped WO_3 (c) 1c-2a doped WO_3 (d) 1c-4a doped WO_3 (e) 2c-1a doped WO_3 (f)4c-1a doped WO_3

Plate III (a-l) shows the low and high magnification HRTEM images of the undoped and Ca-Cl doped nanowires, whose diameters are tens of nanometers and lengths are over several micrometres.

According to the HRTEM at low and high magnification, the undoped nanowires in Plate III (a) composed of several stacked wires approximately 1.0 ± 0.5 μm in length and 100 ± 60 nm in diameter. The high magnification micrograph in Plate III (b) revealed that the fringe interval of 0.373 nm for the undoped WO_3 agrees well with the d-spacing of (200) lattice planes perpendicular along the axis of the nanowire (reference).

For the doped sample such as 1a-1c, 1a-2c, 1a-4c, 2a-1c and 4a-1c the low and high magnification HRTEM images as shown in Plate III (c, e, g, i, k) images revealed that each nanowires of about 1.44 ± 0.5 μm long and 340 ± 87 nm wide. This increment in the length and diameter of the nanowires could be attributed to expansion of the crystal lattice during the incorporation of Ca and Cl as supported by the XRD result. The interplanar distances varied from (0.367 nm - 0.377 nm) indicating that they all grew along the [200] plane.

The HRTEM images also revealed a non-homogeneous nanowires thickness distribution, suggesting that the diameter of the nanowires strongly depended on the number of packed wire units.

SAED pattern of WO_3 based nanowires

Plate IV (a-m) reveals the selected area electron diffraction (SAED) pattern of the undoped and Cl-Ca doped WO_3 nanowires.

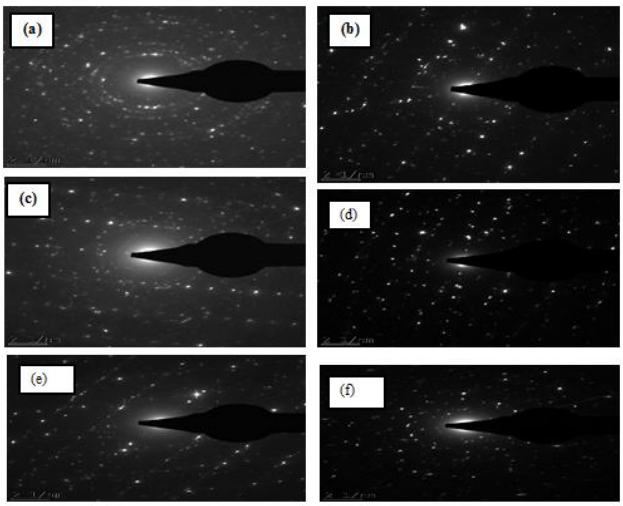

PLATE IV: SAED Micrographs of WO_3 nanowires of (a) undoped WO_3 (b) 1c-1a doped WO_3 (c) 1c-2a doped WO_3 (d) 1c-4a doped WO_3 (e) 2c-1a doped WO_3 (f)4c-1a doped WO_3

Plate IV (a-m) reveals the selected area electron diffraction (SAED) pattern of the undoped and Cl-Ca doped WO_3 nanowires. They exhibited diffraction rings, corresponding to the (002), (020), (200), (120), (112), (022), and (202) planes of monoclinic WO_3 which matches the XRD results. Previous report by Navarro *et al*. (2014), established that (020) and (002) crystal planes of WO_3 exhibited a single crystal pattern of monoclinic phase of WO_3 which is similar to this study.

According to Thummavichai *et al*., (2021) HR-TEM lattice and SAED pattern images of pure $W_{18}O_{49}$ and the 1:16 doped samples, confirmed that the lattice spacing was 0.379 nm, which matched well with the d value obtained in this study. While the SAED patterns of higher Na-doped WO_3 samples had crystal planes such as (002) and (200) spacing which matched well with the WO_3 hexagonal nanowires.

5. Conclusion

WO_3 nanowires and Cl - Ca co-doped WO_3 nanowires composites were successfully synthesized by hydrothermal method. The XRD results confirmed the formation of the nanowires to be monoclinic and triclinic phases depending on the applied conditions. The HRSEM micrographs of the as-synthesized WO_3 showed well developed nanowires at varying reaction time, concentration of tungsten salt precursor and temperature. Also, the nanowires of the Cl and Ca co-doped composite showed an increase in length and diameter compared to its undoped counterpart. The presence of Chlorine and Calcium increased the crystal lattice of WO_3 nanowires as confirmed by the XRD analysis. The characterization results addition of Cl and Ca dopant onto the WO_3 nanowires did not influenced the mineralogical phase of WO3 however affect the morphology and crystal structures.

References

Fu, L., Cai, W., Wang, A & Zheng, Y. (2014) Photocatalytic hydrogenation of nitrobenzene to aniline over tungsten oxide-silver nanowires. *Materials Letters* 142 (2015), 201–203

Guo, X., Qin, X., Xue, Z., Zhang, C., Sun, X., Hou, J & Wang, T (2016) Morphology- controlled synthesis of $WO_{2.72}$ nanostructures and their photocatalytic properties. *RSC Adv*., vol 6 48537 DOI: 10.1039/c6ra08551b

Han, F., Li, H., Fu, L., Yang, J & Liu Z (2016) Synthesis of S-doped WO_3 nanowires with enhanced photocatalytic performance towards dye degradation. *Chemical physics letters* 183-187 http://dx.doi.org/10.1016/j.cplett.2016.03.017

Kahng, S., Yoo, H. & Kim, J.H (2019) Recent advances in earth abundant photocatalyst materials for solar H_2 production. *Advanced Powder Technology*, https://doi.org/10.1016/j.apt.2019.08.035

Kong, L., Guo, X., Xu, J., Mo, Z., & Li, L. (2020) Morphology control of WO_3 nanoplate film on W foil by oxalic acid for photocatalytic gaseous acetaldehyde degradation. Journal of Photochemistry & Photobology A: Chemistry 401, 112760 https://doi.org/10.1016/j.jphotochem.2020.112760

Kunyapat, T., Xu, F., Neate, N., Wang, N., De Sanctis, A., Russo, S., Zhang, S., Xia, Y., Zhu, Y. (2018). Ce-Doped bundled ultrafine diameter tungsten oxide nanowires with enhanced electrochromic performance. *Nanoscale*, 10, 4718–4726

Lee, S., Kim, J., Lee, J., Song, H., Lee, S., Choi, K., & Shin, G. (2014). Facile fabrication of high-efficiency near-infrared absorption film with tungsten bronze nanoparticle dense layer. *Nanoscale Research Letters*,vol 9(1), 294. doi:10.1186/1556-276x-9-294

Lee, K.M., & Abd Hamid, S.B (2015) Simple Response Surface Methodology: Investigation on Advance Photocatalytic Oxidation of 4-Chlorophenoxyacetic Acid Using UV-Active ZnO Photocatalyst. *Materials* 8, 339-354 doi: 10.3390/ma8010339

Leng, J., Wang, Z., Wang, J., Wu, H-H, Li, Y-X., Guo, H., Liu, Y., Zhang, Q & Guo, Z (2019) Advances in nanostructures fabricated via spray pyrolysis and their applications in energy storage and conversion. *Chem. Soc. Rev.*, vol 48 (3015) DOI: 10.1039/c8cs00904j

Liu, G., Wang, S., Nie, Y., Sun, X., Zhang, Y., and Tang, Y. (2013).Electrostatic-induced synthesis of tungsten bronze nanostructures with excellent photo-to-thermal conversion behavior. *J. Mater. Chem*. Vol A1, pgs 10120–10129. doi: 10.1039/c3ta11479a

Lu, H., Zhu, Q., Zhang, M., Yan, Y., Liu, Y., Li, M., & Geng P (2018)Synthesis of hexagonal ultrathin Tungsten oxide nanowires with diameters below 5nm for enhanced photocatalytic performance. *Superlattices and microstructures*, 116, 17-26 Doi:10.1016/j.spmi.2018.01.032

Ma, B., Huang, E., Wu, G., Dai, W., Guan, N., & Li, L. (2017). Fabrication of $WO_{2.72}$/RGO nano-composites for enhanced photocatalysis *RSC Advances* 7(5) 2606-2614 doi:10.1039/c6ra26416f

Madare, C. C and Hassel, W. A (2019). Review on the versatility of Tungsten oxide coatings. *Physica status solidi*, 21 6, 1-16. Doi:10.1002/pssa.201900047

Nagyne-Kovacs, T., Lukacs, I.E., Szabo, A., Hernadi, K., Igricz, T., Laszlo, K., Szilagyi, I. M., Pokol, G. (2020). Effect of pH in the hydrothermal preparation of monoclinic tungsten oxide. *Journal of Solid state Chemistry*, 281, 121044 https://doi.org/10.1016/j.jssc.2019.121044

Navarro, J. R. G., Mayence, A., Andrade, J., Oleynikov, P., Parola, S., & Pawlicka, A. (2014). WO_3 nanorods created by self-assembly of highly crystalline nanowires under hydrothermal conditions, *Langmuir*, 1–6.

Pauekphong, K., Kooptarnond, K., Khangkhamano, M., Sikong, L., & Masae, M (2019) Synthesis Of WO_3/TiO_2 (B) Nanowires By Hydrothermal Method. *Digest Journal of Nanomaterials and Biostructures* Vol 4 (4) pgs 1123-1130

Phuruangrat, A., Ham, J. D., Hong, J.S., Thongtem, S & Lee, J.S. (2010) Synthesis of hexagonal WO_3 nanowires by microwave-assisted hydrothermal method and their electrocatalytic activities for hydrogen evolution reaction *J. Mater. Chem* vol 20, pgs 1683–1690

Sajad, T. Chaibakhsh, N & Moradi-Shoeli, Z (2017) Application of nanoscale ZnS/TiO2composite for optimized photocatalytic decolorization of a textile dye *Journal of Applied Research and Technology* 15, 378–385 doi.org/10.1016/j.jart.2017.03.007

Silveria, J.V., Moreas, E.C., Moura, B. V. J ., Sennna, C. A., Archango, B. S., Vascncelos, T. L., Filho A. G., Freire, P. T & Luz-lima, C. (2020). Mo-doped WO_3 nanowires for

adsorbing methylene blue dye from wastewater. *Journal of material science*, vol 55, 6429,6440. https://doi.org/10.1007/s10853-020-04472-2

Tehrani, F. S., Ahmadian, H. & Aliannezhadi, M. (2020) Hydrothermal synthesis and characterization of WO_3 nanostructures: Effect of reaction time.*Mater. Res. Express* 7 (015911) https://doi.org/10.1088/2053-1591/ab66fc

Thummavichai, K., Thi, L. A., Pung, S. Y., Ola, O., Hussain, M. Z., Chen, Y., Xu, F., Chen, W., Wang, N., & Zhu, Y. (2021). Sodium tungsten oxide bronze nanowires bundles in adsorption on of methylene blue dye under uv and visible light exposure. *Energies*, *14* (1322) pg 5 https://doi.org/10.3390/en14051322

Vakilinezhad, M.A., Tanha, S., Montaseri, H., Dinarvanda, R., Azadi., A., & Javari, H.A (2018) Application of Response Surface Method for Preparation, Optimization, and Characterization of Nicotinamide Loaded Solid Lipid Nanoparticles. *Advanced pharmaceutical bulletin* 8, 245-256 doi: 10.15171/apb.2018.029

Wang, J., Liu, G., and Du, Y. (2003). Mechanochemical synthesis of sodium tungsten bronze nanocrystalline powders. *Materials letters* vol 57 pgs 3648-3652 doi:10.1016/S0167577X(03)00142-3

Wanjun, M.U., Qianhong, Y.U., Xingliang, L.I., Hongyuan, W., Yuan, J. (2016). Hydrothermal synthesis of WO_3 nanowires in the presence of guanidine sulfate and Its photocatalytic activity. *Journal of Wuhan University of Technology-Material Science*, 31(4) 731–735.

Wu, C-M., Naseem, S., Chou, M-H., Wang, J –H & Jian, Y-Q. (2019) Recent Advances in Tungsten-Oxide-Based Materials and Their Applications. *Front. Mater*. Vol 69(49) doi: 10.3389/fmats.2019.00049.

Synthesis and Characterization of NiO Nanoparticles and B_2O_3/NiO Nanocomposite via Hydrothermal Route

Adegbola I.O[a*], Yisa J.[a], Tijani J.O[a,b], Jacob J.O [a]
[a] Department of Chemistry, Federal University of Technology, Minna, Niger State, Nigeria
[b]Nanotechnology Research Group, Africa Centre of Excellence for Mycotoxin and Food Safety, Federal University of Technology, P.M.B 65, Bosso, Minna, Niger State, Nigeria
Corresponding Author Email: ifebola4chem06@gmail.com
Phone No: 08163104049

Abstract
In this study, NiO nanoparticles and B_2O_3/NiO nanocomposites were prepared via hydrothermal route. The synthesized NiO and B_2O_3/NiO nanocomposite were characterized by high resolution scanning electron microscope (HRSEM), energy dispersive spectroscopy (EDS), X-ray diffraction (XRD) and UV-visible spectroscopy. The morphological and crystal studies of NiO and NiO/B_2O_3 nanocomposite revealed densely dispersed wire-like structure, with face-centered cubic and orthorhombic phase of crystallite size of 6.43 and 3.26 nm respectively. While the optical analysis revealed a surface plasmon resonance at 300 nm and 394 nm for NiO nanowires and 233 nm and 385 nm for B_2O_3/NiO nanowires respectively. Hence, it can be concluded that doping NiO nanowires with B_2O_3 changes its orientation with a decrease in particle size and wavelength.

Keywords: characterization, hydrothermal method, NiO nanowires, B_2O_3/NiO nanocomposites, synthesis

Introduction

There has been growing interest in the synthesis and utilisation of inorganic nanocomposites in the area of mechanical, biomedicines, catalysis, adsorption and electrochemical amongst others due to their unique sizes and structures (Wang *et al*. 2018). Metal oxide nanocomposites possess the unique features needed in addressing emerging needs in numerous sector of sciences (Fang *et al*., 2018). Moreover, metal oxides have high electrocatalytic activity and stability (Park *et al*., 2010; Iqbal and Kriek, 2018). Therefore, employing metal oxides such as iron (Fe), cobalt (Co), nickel (Ni), zinc (Zn), copper (Cu) and tin (Sn) which are environmentally friendly, cost effective and abundant in nature will aid in the availability of nano based materials for diverse applications (Manikandan *et al*., 2016; Bhaskar *et al*., 2020). Although, most metal oxides have low or poor electronic conductivity, this can be overcome by altering their microstructure or doping with other metal oxides such as strontium oxide, aluminium oxide, boron oxide and silicon oxide amongst others (Nguyen *et al*., 2018; Sk *et al*., 2016).

NiO, a p-typed semiconductor with a wide band gap of 3.6- 4.0eV, excellent optical, electrical and magnetic properties have gained great attention recently due to its use in catalysis, battery cathode, and electrochromic films (Dhas *et al*., 2020; Kaur *et al*., 2019). There are several methods in synthesising NiO-based nanocomposites of different structures such as sol-gel (Sankar *et al*., 2016), elctrospinning (Wang *et al*., 2018), chemical vapour deposition (CVD), hydrothermal (Dhas *et al*., 2020), vapour-liquid-solid (Kaur *et al*., 2016) and laser ablation. However, NiO nanoparticles possess poor electronic conductivity; low stability when compared with other metal oxide nanomaterials (Fang *et al*., 2018).Therefore doping NiO with another metal oxide like B_2O_3 will significantly enhance its active surface area, pore morphology and electronic conductivity.
In a study conducted by Yasmeen *et al*. (2016), surfactant assisted Zn-NiO nanocomposite was synthesized by homogenous precipitation method using sodium dodecyl sulphate (SDS) and hexamethylenetetramine (HMT) to alter the composition of the composite. The morphological

study revealed that ZnO-NiO nanocomposites with different composition ratios have different surface morphology and their uniformity increased on addition of different surfactant.

Igbal and Kriek (2018) also, prepared silver/nickel oxide (Ag/NiO) nanocomposites via citrate sol-gel route as electrocatalyst for oxygen evolution reaction (OER) in alkaline medium.The morphological study of NiO revealed an irregular, cotton-like surface with aggregation of particles of high surface energy. The X-ray diffraction spectrograph confirmed the formation of face-centered cubic crystalline structure similar to that described by Kaur *et al*. (2016). AgNiO on the other hand, showed a decrease in NiO intensity with peak planes indicating formation of cubic crystalline structure validating an interaction between Ag and NiO, hence confirming the formation of a nanocomposite. The crystallite size of the synthesized NiO increased as Ag to Ni concentration changes (NiO, $Ag_{0.2}NiO_{0.8}O$ and $Ag_{0.4}Ni_{0.6}O$) from 9.60 nm to 34 nm and reduced to 29 nm for $Ag_{0.8}Ni_{0.4}O$. The elemental analysis confirmed a well distribution of Ag and Ni over the scanned portion with considerable amount of oxygen distributed in the metal-associated region. In a research carried out by Dhas *et al*. (2020), NiO nanoparticles were synthesized via hydrothermal route for supercapacitor application as an efficient electrode material. The scanning electron microscopic study showed a non-uniform aggregated nanoparticles and its crystallographic study revealed a monoclinic phase of NiO with an average crystallite size of 9.3 nm.

Therefore, the physicochemical properties of NiO nanoparticles are method dependent with the exception of their crystallographic studies which shows the same structure irrespective of the method used, while NiO based nanocomposites are method and composition dependent. The sudden decrease in crystallite grain size at a higher concentration when NiO was fully saturated may be observed as revealed by Igbal and Kriel, (2018). These differences in NiO nanoparticles and its composites may alter their effectiveness in different scientific applications.

In this work, hydrothermal method was used to synthesis NiO nanoparticles and B_2O_3/NiO nanocomposite due to its simplicity in design, with no requirement of high vacuum conditions.

Materials and Methods

All reagents (ethylene glycol, 99%, H_2BO_3 99%, NaOH, 99%, $Ni(CH_3COO)_3.4H_2O$, 99% and HCl 99%) used this study are of Analytical grade AR) and were used without any further purification. The NiO nanoparticle and B_2O_3/NiO nanocomposite were synthesized using the hydrothermal method as described by Ibrahim *et al*. (2016). 50 cm^3 of 2 M $Ni(NO_3)_2.6H_2O$ was added into a solution of ethylene glycol and de-ionized (DI) water (1:1) in a 250 cm^3 beaker under continuous magnetic stirring at room temperature to disperse the Ni ions homogeneously. The mixture was transferred into the Teflon-lined stainless steel then put in a Gollenhamp muffle furnace maintained at 200 ºC for 7 hours. After the heating treatment, the product $Ni(OH)_2$was obtained. About 3% boric acid was then added to 50 cm^3l obtained $Ni(OH)_2$, stirred continuously at room temperature and allowed to age overnight. The two colloidal mixtures were separated from their respective solution by filtration; afterwards, washed several times with DI water and ethanol. The light-blue-green product was collected and dried in the oven at 120 ºC for 6 hours followed by calcination in the furnace at 400 ºC for 2 hour 30 minutes to give NiO and B_2O_3/NiO nanowires respectively as described by).

Characterization of NiO and NiO/B_2O_3 Nanowires

The nanowires were characterized using different analytical tools UV-visible spectroscopy, high resolution scanning electron microscopy (HRSEM), energy dispersive spectroscopy (EDS) and x-ray diffraction techniques (XRD).

The NiO nanoparticles and B_2O_3/NiO nanocomposite absorbance spectrum were obtained by scanning each colloidal solution using SHIMADZU UV-1800 at a scanning speed of 50 nm/min.

The samples were analysed with the aim of examining their morphology and particle shape using Zeiss Auriga scanning electron microscope at an accelerating voltage of 20 kV and a working distance of 3 - 4 mm. To take the micrograph, the surface of a high resolution cathode ray tube was photographed using polaroid positive-negative film. The elemental analysis was performed using energy dispersive spectroscopy (EDS) in the HRSEM. The X-ray diffraction patterns were obtained using Bruker D8 diffractometer with Cu-kα operated at 40 kV and 40 mA.

Results and Discussion

The UV-Visible spectroscopy is one of the analysis that reveals energy structures and optical properties of semiconducting nanomaterials. Figure (1a) shows the absorption spectrum of NiO nanoparticles observed at 300 nm and 394 nm. Figure (1b) reveals the formation of NiO/B_2O_3 nanocomposite at absorption bands of wavelengths 233 nm and 385 nm respectively. Considering these material absorption bands, both materials can be considered to be optical p-type semiconducting nanomaterials (Marouzi *et al*., 2021). It could also indicate electronic transition from valence band to the conduction band. Also, a blue shift of 233 nm and 385 nm was observed in Figure (1b). In comparison with Figure (1a) of 300 nm and 394 nm respectively, this occurrence is an evidence of the quantum confinement effect (San *et al*., 2017). This implies that the strong absorption wavelength of NiO nanoparticles becomes smaller with decrease in crystallite grain size of 6.43 nm to 3.26 nm of NiO/ B_2O_3 nanocomposite

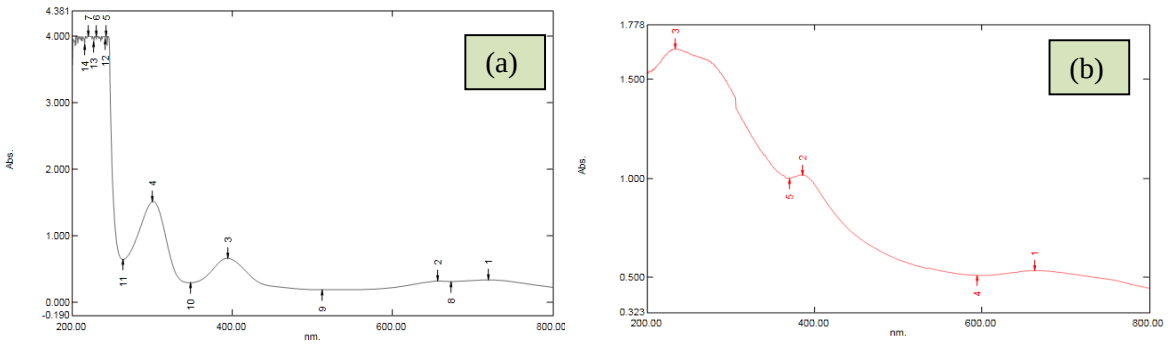

Figure 1: (a) UV absorption spectrum of NiO nanocomposite (a) UV absorption spectrum of NiO/ B_2O_3 nanocomposite

The morphological analysis of NiO nanoparticles revealed formation of densely dispersed, porous surface and a crystallite size of 6.42 nm was observed as shown in Figure 2a. While Figure 2b revealed a densely dispersed wire-like structure of B_2O_3/NiO matrix with crystallite size 3.26 nm as presented in Figure 2d. The addition of B_2O_3 influenced the size as well as the shape of NiO nanoparticles and reduced the agglomeration.

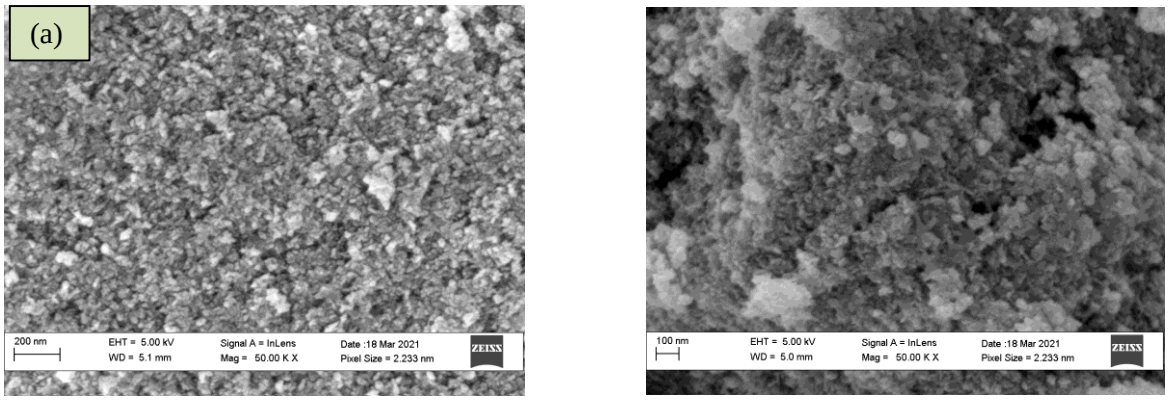

Figure 2: (a) HRSEM image of NiO nanoparticle after calcination. (b) HRSEM image of NiO/B_2O_3 nanocomposites

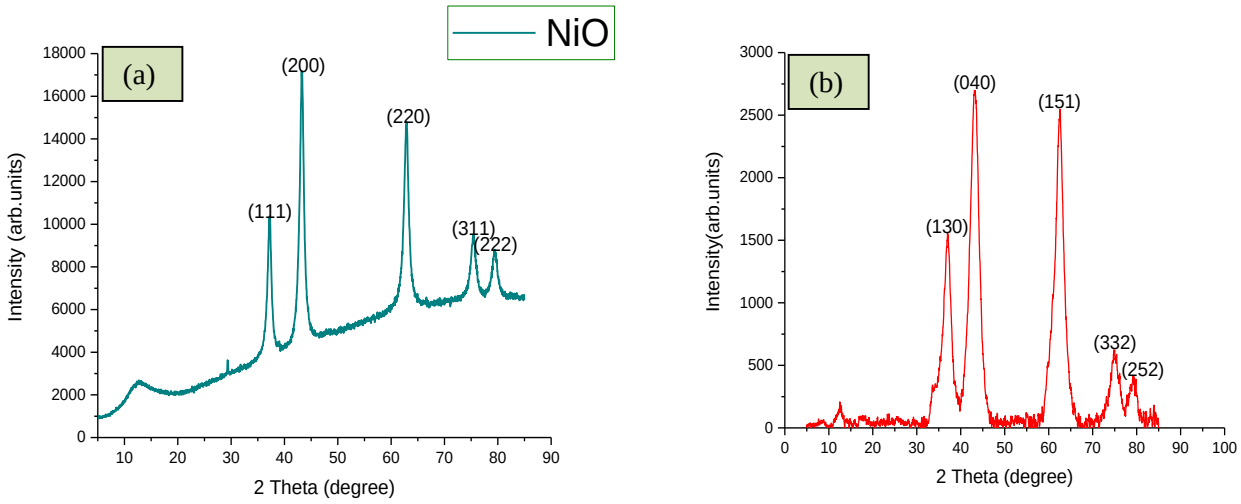

Figure 3: (a) X-ray diffraction pattern of NiO nanoparticles and (b) B_2O_3/NiO nanocomposites

The mineralogical phase and crystalline pattern of NiO nanoparticles and NiO/B_2O_3 nanocomposite were also examined using X-ray diffraction and the result is shown in Figures (3a) and (3b) respectively. Figure (3a) shows a series of diffraction pattern at (111), (200), (220), (311) and (222) planes at approximately 2Θ values of 37.25 º, 43.28 º, 62.88 º, 75.42 º and 79. 41 º respectively. All the diffraction peaks were carefully indexed to a pure face-centered cubic NiO phase (JCPDS: No 47-1049) with no impurity peaks observed (Zhiwei, 2017). Sharp and intense diffraction peaks for B_2O_3/NiO nanocomposites was observed at 2Θ values of 36.48 º, 43.60 º, 62.06 º, 76.16 º and 80.37 º with crystal planes of (130), (040), (151), (332) and (252) respectively as shown in Figure (3b). This was indexed as orthorhombic face of B_2O_3/NiO nanocomposites (JCPDS: 75- 1809). The XRD patterns imply that NiO nanowires obtained via this method consist of ultrapure phase without impurities and the starting material completely reduced to NiO. The incorporation of B_2O_3 greatly influenced the peak positions of NiO and its phase orientation from face cubic to orthorhombic.

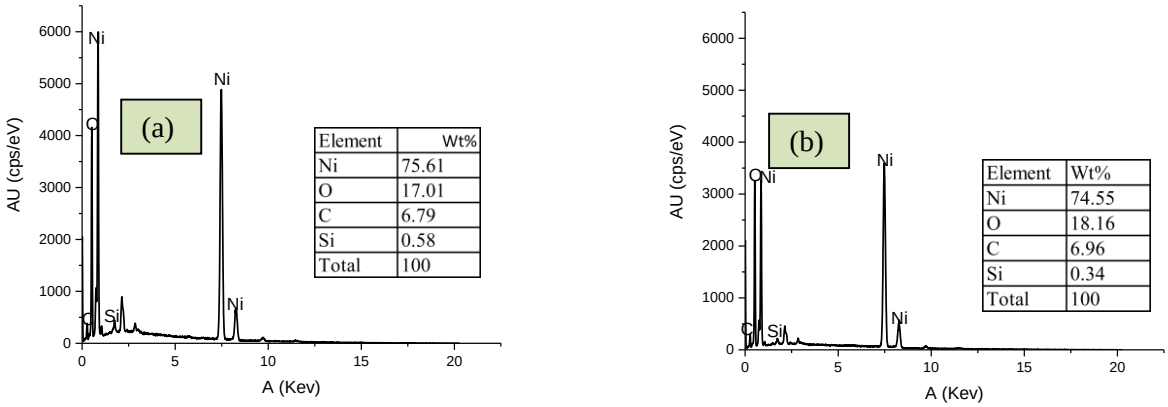

Figure 4:EDS Spectrograph of (a) NiO nanoparticles and (b) B_2O_3/NiO nanocomposite

The image of NiO and NiO/B_2O_3 as revealed by HRSEM were subjected to elemental analysis to ascertain their elemental composition. The energy dispersive spectroscopy (EDS) spectrograph as presented in Figure (4a) and (4b) revealed the presence of nickel (Ni) and oxygen (O) as the dominant element Silicon originated from the Teflon material used during the synthesis while the presence of carbon is as a result of the holey grid employed for imaging. The absence of Na

confirms that the washing procedure was also effective for the removal of unwanted ions. The absence of boron (B) in the two samples can be attributed to the fact that EDS only detects surface composition of a material. The percentage difference in weight per constituent observed in Figure (4b) could be as a result of boron present in the composition but was below EDS detection limit.

Conclusion

In summary, hydrothermal method was employed for the synthesis of NiO nanoparticles and B_2O_3/NiO nanocomposite. The XRD result confirmed the formation of a phase purity and nanocrystalline face-centered cubic and orthorhombic phase of NiO nanoparticles and NiO/B_2O_3 nanocomposite respectively.UV-Visible spectral showed the presence of B_2O_3 in the B_2O_3/ NiO with absorption bands 233 nm and 385 nm. HRSEM image revealed a spherical mesoporous structure an indication of high active surface area for capturing pollutants.It can be concluded that hydrothermal synthesis is feasible and efficient for the development of B_2O_3/NiO nanocomposites.

References

Bhaskar, V., Siddiqui1, A., Hakeem, A., Zain, A., Faheem, A., Abdullah A., Hassan, H., & Ameer, A (2020). Synthesis of mesoporous SnO2/NiO nanocomposite using modified sol–gel method and its electrochemical performance as electrode material for supercapacitors. *Springer Nature Research*. 10:11032 https://doi.org/10.1038/s41598-020-67990-8,

Dhas, S., Maldar, P., Patil, M., Nagare, A., Waikar, Sonkawade, R. & Moholkar, A. (2020). Synthesis of NiO Nanoparticles for Supercapacitor Application as an Efficient Electrode Material. *Vacuum*, 181; 109646

Fang, Z., Sajid, R., Mingze, S., Yupeng, Y., Shaowei, J. & Hong, B. (2018). Hybrid Nio–Cuo Mesoporous Nanowire Array With Abundant Oxygen Vacancies And A Hollow Structure As A High Performance Asymmetric Supercapacitor. *Journal. Material Chemistry*, 6, 21131- 21142

Gandhi, V., Ganesan, R., Syedahamed, A. & Thaiyan, M. (2014). Effect of Cobalt Doping on Structural, Optical and Magnetic Properties of ZnO nanoparticles Synthesized by Coprecipitation Method. Journal of Physical Chemistry. 118, 9717-9725.

Ibrahim S., Charinpanitkul,T., Kobatake, E., Sriyudthsak, M., (2016). Nanowires Nickel Oxide and Nanospherical Manganese Oxide Synthesized via Low Temperature Hydrothermal Technique for Hydrogen Peroxide Sensor. *Journal of Chemistry*.1-6

Iqbal, M. & Kriek, R. (2018). Silver/Nickel Oxide (Ag/NiO) Nanocomposites Produced Via a Citrate Sol-Gel Route as Electrocatalyst for the Oxygen Evolution Reaction (OER) in Alkaline Medium. Electrocatalysis. Springer Science+Business Media, LLC, part of Springer Nature. https://doi.org/10.1007/s12678-018-0455-5

Kaur, N., Comini, E., Zappa, D., Poli, N., Sberveglieri, G.(2016): Nickel oxide nanowires: vapor liquid solid synthesis and integration into a gas sensing device. *Nanotechnology*. 27, 1-10. https://doi.org/10.1088/0957-4484/27/20/20570 1

Kaur, N., Zappa, D. & Comini, E. (2019) Shelf Life Study of NiO Nanowire Sensors for NO_2 Detection. Electronic Materials Letters. https://doi.org/10.1007/s13391-019-00172-5

Manikandan**,** K., Dhanuskodi, S., Maheswari, N. & Muralidharan, G. (2016). SnO_2 nanoparticles for supercapacitor application. *AIP Conference Proceeding.* 1731, 50048

Marouzi, S., Sabouri, Z. and Darroudi, M. (2021). Greener Synthesis and Medical Applications of Metal Oxide Nanoparticles. *Ceramics International*, https://doi.org/10.1016/j.ceramint.

Nguyen, K., Hoa, N., Hung, Cc., Le, D., Duy,N. & Hieu, N. (2018). A Comparative Study on the Electrochemical Properties of Nanoporous Nickel Oxide Nanowires and Nanosheets prepared by a Hydrothermal Method. *Royal Society of Chemistry*, 8,19449-19455

Park, J., Ko, M. & Park, O. (2010). Carbon nanotube@RuO2 nanocomposite electrodes for supercapacitors. *J. Electrochem. Soc.* **150**,864–867

Sankar, S., Sharma, S., An, N., Lee, H., Kima, D., Im, Y., Cho, Y., Ganesh, R., Ponnusamy, S., Raji, P. & Purohit, L.(2016). Photocatalytic Properties of Mn-Doped NiO Spherical Nanoparticles Synthesized from Sol-Gel Method. *Optik – Int. J. Light Electron*.127, 10727–10734

San, X., Zhao, G., Wang, G., Shen, Y., Meng, D., Zhang, Y. & Meng, F. (2017). Assembly of 3D flower-like NiO Hierarchical architectures by 2D Nanosheets: Synthesis and their Sensing Properties to Formaldehyde. *Royal Society of Chemistry*. 7, 3540 - 3549

Sk, M., Yue, C., Ghosh, K. & Jena, R. (2016). Review On Advances in Porous Nanostructured Nickel Oxides and their Composite Electrodes for High-Performance Supercapacitors. *Journal of Power Sources* **308**, 121–140.

Wang, Y., Dan, L., Qianli, M., Jiao, T., Yan, S., Xue, X., Xiangting, D., Wensheng, Y., Jinxian, W. & Guixia, L.(2018). A Novel and Facile Approach to Obtain NiO Nanowire-in-Nanotube Structured Nanofibers with Enhanced Photocatalysis. *Royal Society of Chemistry*, 8, 11051

Yasmeen, S., Igbal, F., Munawar, T., Nawaz, M., AAsghar, M. & Hussain, A. (2019). Synthesis, Structural and Optical Analysis of Surfactanct Assisted ZnO-NiO Nanocomposites Prepared by Homogenous Precipitation Method. *Ceramics International*, 45, 17859-17873

Zhiwei, L. (2017). Supersensitive and superselective formaldehyde gas sensor based on NiO nanowires. *Vacuum*. Doi:10.1016/j.vacuum.2017.05.038.

Study of Mechanical and Thermal Properties of the Waste Polystyrene Foams and Chemically Modified Sweet Potatoes Starch Composites

Sallah S. Sani, Suleiman, Muhammad A. T, Stephen S. Ochigbo, Ruth A. Araga
Department of Chemistry, Federal University of Technology, Minna, Niger State, Nigeria.
Email: Sani.sallah@st.futminna.edu.ng

Abstract

Recycled polystyrene waste / chemically modified sweet potatoes starch blended composites were prepared by melt blending on the two roll to reduce the plastic wastes in the environment. The effect of the chemically modified starch contents of 0, 10, 20 and 30 wt% on the physical and mechanical properties of the composites were examined. Starch from sweet Potatoes was treated with 3.16M H_2SO_4 to reduce the particle size of the starch and increase its surface reactivity. It was observed that there was a decrease in the tensile strength (from 3.16 MPa at 10% starch content and then begin to increase rapidly), percentage elongation at break (from 3.09 % to 2.36 %), Impact strength (from 0.18 j/mm to 0.17 j/mm) and Flexural modulus (from 7.4462 MPa to 6,4107 Mpa) properties as the modified starch content increases from 0-30wt% when compared with the pure polystyrene waste. The impact strength improved at (20wt %) as modified starch content increases when compared to the pure polystyrene waste. Also there was an increase in young modulus (from 18.30 MPa to 314 MPa), density (from 1.18 g/cm^3 to 1.40 g/cm^3) and water absorption (from 10% starch content to 30% starch content) properties as chemically modified starch content increases. It can be concluded that effective blending of polystyrene waste with chemically modified sweet Potatoes starch produced plastic sheets that could be used in the household or for industrial applications.

Keywords: Plastic Waste, Chemically Modified Sweet Potatoes Starch, Biodegradability

INTRODUCTION

Synthetic polymers are the most used materials, biodegradable plastics development is considered as the best approach to solving solid waste problems, which gave rise to an interest in the development of polymers that will deteriorate or degrade into being by-products under composting environments or microorganism action (Ozcalik and Tihminlioglu, 2013). Polystyrene foam is a highly popular plastic packaging material which finds wide application in packaging of food items, electronic goods, electrical appliances, furniture. due to its excellent and protective properties. Polystyrene foam take up significant space in rubbish bins which means that bins become full more quickly and therefore needs to be emptied more often. It also causes serious problems such as blockage of sewages, clogging of water bodies which result in the death of aquatic life and release of green – house gasses when burnt. Recycling of this waste has recently received significant attention all over the world due to the changes in both regulatory and environmental issues. Increasing landfill costs and decreasing landfill space are forcing consideration of alternative options for the disposal of polystyrene materials. There are two major methods of recycling plastics, which include; mechanical recycling and chemical recycling.

On the other hand starch is one of the most studied biodegradable polymers for sheets production due to its low cost, easy processing ability, biodegradability, non – abrasive, renewable and readily available (Toral *et al*., 2002; Faria *et al*., 2012). It consists essentially of amylose and amylopectin, and their applications are determined based on the proportions of these two macromolecules, which are dependent on their concentrations in starch (Toral *et al.*, 2002). Starch granules are in microsize which can be broken down into smaller particle size using different methods: chemical, enzymatic and physical modification (Ning *et al.*, 2011; Normane *et al.*, 2018). Starch may be obtained from

various vegetable sources such as grains, roots and tubers, and also in fruits and vegetables, however, extraction of starch in a commercial level is restricted to cereals, roots and tubers (Young, 1984). Sweet potatoes starch presents a bright prospective in the area of thermoplastic starch production, because of its spherical shape, high amylose content of about 38% and high starch content (6.9% - 30.7%) (Lehmann, 2007). The use of starch in the preparation of biodegradable polymers is based on chemical, physical and functional properties of amylose to form gels and films; high amylose starch produces strong films and is therefore suitable for making thermoplastic starch material (Young, 1984).

Chemically modified starch are starch granules which are broken down to fine crystalline particles using sulfuric acid (Normane, 2018). These enable different application and benefits and demonstrate unique properties and functions due to their size effect (Suk *et al.*, 2014; David *et al.*, 2018). Chemically modified starch are usually produced to be used as filler in polymeric matrices to improve their mechanical and barrier properties. Sweet Potatoes starch is polymer made of long chains of glucose units joined together. It actually contains Amylose (a straight chain polymer made from glucose units) and Amylopectin (a branched polymer made from glucose units). The Amylose prevents the starch from becoming plastic – like, hydrochloric or sulfuric acid are used to break down the amylopectin and change the structure and properties of the polymer. According to Vieira *et al.* (2011) the hydrogen bonds between the starch and plasticizer occur as the temperature is increased, both with the crystalline regions of amylose and amylopectin as well as with the amorphous region of amylopectin. The aim of this research is to present the use of waste materials and inexpensive source of starch for polymer blend production, opted for recycled polystyrene waste and chemically modified sweet potato starch to produce composites which is available, this attempt to address the problem of non-degradability of synthetic polymer and in turn address it environmental pollution problem.

MATERIALS AND METHOD

Polystyrene foam wastes and sweet potatoes were purchased from Kure Market, Minna, Niger State. The starch was prepared from sweet potatoes. The plasticizers used include glycerol and water. Glycerol was obtained from PANLAC laboratory Minna and has the percentage purity of (98.0%)

Extraction of Starch from Sweet Potatoes

Starch was extracted from freshly purchased sweet Potatoes from Kure Market, Minna, Niger State according to the method employed by Collado and Corke (2004). Freshly harvested Sweet Potatoes were washed thoroughly, immersed in cold water for 1 hour, peeled and sliced. The slices sample were grated finely, rinsed, soaked in distilled water, washed extensively and sieved through a cheese cloth. The filtrate (starch – water mixture) was passed through a 250 µm sieve and left for 2 hours for the starch molecules to settle. The supernatant was then decanted, leaving behind the starch paste (as sediment) which was then dried in the oven at 50ºC for 5 hours. The dried starch lump was gently crushed into powder and was stored in an air tight bag for further use.

Preparation of Chemically Modified Starch

The extracted sweet Potatoes starch was subjected to acid hydrolysis as reported by Hale, (2016). 14.69 g of starch powder was mixed with 100ml of 3.16M Sulphuric acid solution at 40ºC in a 100 ml flask. The reaction mixture was stirred on a shaker maintained at 37 ± 3ºC and continuously stirred for 10 hours at 5000 rpm speed. The suspension was centrifuge for 10 minutes at 2000 rpm washed and thereafter washed with 0.5% Ammonia until neutrality was achieved. The suspension was subjected to a mechanical treatment with stirrer for 2 minutes at 1300 rpm to disperse aggregates and obtain a stable suspension. The resulting suspension was stabilized by sulfate groups present from the H_2SO_4 treatment; a few drops of chloroform was added to the suspension to avoid bacterial growth during storage.

Preparation of the composites of Polystyrene Waste/Chemically Modified Sweet Potatoes Starch

The composite of polystyrene waste and chemically modified sweet Potatoes starch (bioplastic) packaging sheets were prepared by melt mixing method on the ratio (100/0, 90/10, 80/20, 70/30, 60/40, 50/50 and 0/100 wt%). Polystyrene was melt and mixed with chemically modified sweet Potatoes starch in a two-roll mill machine in accordance with ASTM D 15 – 627 by introducing the polystyrene matrix into the heater rollers at 150^{o}C at which it melt and flows. The modified sweet Potatoes starch were then introduced to polystyrene matrix and mixed for the period of five minute (5 min), until homogenous mixture was obtained. This was then collected and subsequently placed in a metal mould 150 X 120 X 3 (mm) length, width and thickness respectively and then pressed on compression moulding machine at 150^{o}C for five minute (5 min) thereafter cold pressed at room temperature for three minutes (3 min) and pressure of 3Pa. The composites were removed from the machine and kept for further experiments. The compounding and pressing of polystyrene waste and chemically modified sweet potatoes starch were carried out in the polymer processing laboratory of the Department of Polymer Technology (Nigeria Institute of Leather Science and Technology, Zaria). Composite sheets were thereafter cut into various dimensions for characterization

Physical properties of the Composites

Density

The mass of the composites were measured using an electric weighing balance with the accuracy of 0.01gm and the volume was determined using Vernier Calliper. The density of the pure polystyrene waste, composites of polystyrene waste with chemically modified starch was calculated using the formula

$$\rho = \frac{m}{v} \quad (1)$$

where

P = density (g/cm^3)
M = Mass (g)
V = Volume (cm^3)

Water Absorption

The water absorption of composites of polystyrene waste/chemically modified sweet Potatoes starch composite sheets was determined according to ASTM D570. The specimens (70 x 30 x 3mm) were dried in an oven at 50^{o}C for 24 hours then cooled in a desiccator and immediately weighed to obtain the initial weight. After which the specimen were conditioned in a beaker containing distilled water for 1 day (24 hours) and removed from the beaker, dried at 35^{o}C until constant weight. The specimens were weighed to determine the average water absorption. This was repeated until the sample decomposes and the percentage of water absorbed was calculated using the formula (Kampeerapappun *et al.*, 2001)

$$Water\ Absorption\ (\%) = \frac{W2-W1}{W1}\ X\ 100 \quad (2)$$

Where

W_1 is Initial Mass
W_2 is Remaining Mass (After removing and cleaning at time t).

Soil Burial Degradation Test

Soil burial test of polystyrene waste/chemically modified sweet Potatoes starch was carried out at the Department of Polymer and Textile Engineering, Ahmadu Bello University, Zaria. The test was determined according to ASTM D5988. The Biodegradability of polystyrene waste/chemically modified sweet Potatoes starch composite with the specimens (70 x 30 x 3mm) was studied by weight remaining overtime in a soil environment. Samples were weighed and then buried in the soil at a depth of 10cm from the surface for 27 days (4weeks). The soil moisture was maintained

by frequent rainfall to keep the microorganisms active. The buried sample was weighed after every 3 days, and the weight loss was calculated using the formula

$$Wieght\ Loss\ (\%) = \frac{W1-W2}{W2}\ X\ 100 \quad (3)$$

Where

W_1 is Initial weight the sample

W_2 is the final weight the sample

Mechanical Properties of the Composites

Tensile Test

Tensile test was conducted according to ASTM D638 standard with a gauge length of 40mm. The samples were cut in dimension of 100 x 10 x 3mm and the test was carried out using WDW-100KN 190536 Electronic Universal Testing Machine at a cross head speed of 10mm/min. The test sample was mounted and proper gripping was observed. The tensile parameter were determined and recorded using equations 4, 5 and 6.

$$\text{Tensile Strength} = \frac{Load\ at\ break}{(original\ width)(original\ thickness)} \quad (4)$$

$$\%\ \text{Elongation} = \frac{elongation\ at\ rupture}{initial\ guage\ length}\ x\ 100 \quad (5)$$

$$\text{Young Modulus} = \frac{Load\ at\ break}{\frac{(original\ width)(original\ thickness)}{\frac{elongation\ at\ point\ on\ tangent}{initial\ guage\ length}}}\ x\ 100 \quad (6)$$

Flexural Test

The Flexural test were done on a universal testing machine. The specimens were prepared according to ASTM D790 with dimension 100mm × 20mm × 3mm in length, width and thickness respectively. The specimens were tested flatwise on a support span. The span length was 80mm apart at 0.5mm/min strain rate. The flexural strength, flexural modulus and flexural strain were determined using the equation

$$\text{Flexural Strength} = \frac{3FL}{2bd^2} \quad (7)$$

$$\text{Flexural Modulus} = \frac{FL^3}{4bd^3D} \quad (8)$$

$$\text{Flexural Strain} = \frac{6dD}{L^2} \quad (9)$$

Impact Test

The impact strength of the composite samples was carried out according to ASTM D 256 using Norwood Charpy impact testing machine (HD 96 QD Model, capacity of 15J). The specimen size was 100 x 10 x 3mm. Each sample was placed on the vice and clamped firmly. The pendulum hammer was raised to the required height and then released and strike the sample at once. Then, the impact energy absorbed by the specimen was recorded.

RESULTS AND DISCUSSION

Physical Properties

The physical properties (Density and water absorption) of pure polystyrene, chemically modified sweet Potatoes starch and composites of polystyrene waste/chemically modified sweet Potatoes starch are presented in figure 1 and 2

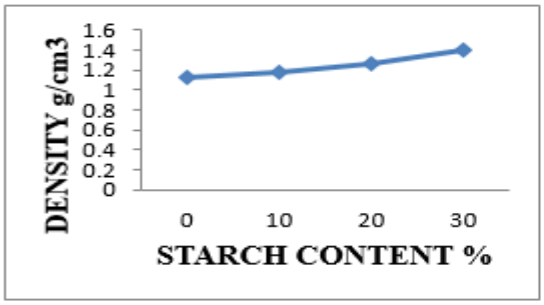

Figure 1: Effect of Starch Content on Density of the PS/ Chemically Modified Starch Composites

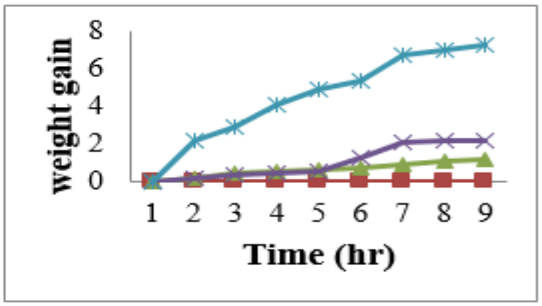

Figure 2: Effect of Starch Content on Water Absorption of the PS/ Chemically Modified Starch Composites

Figure 1 shows the density values calculated for composite material with different starch content. It was found that there is an increase in density from 1.18g/cm^3 to 1.40 g/cm^3 as the starch content increase. The highest density value recorded at 30 % starch content was 1.40 g/cm^3 and the lowest density value recorded at 10 % starch content was 1.18g.cm^{-3}. The increase in density with increase in starch loading may be due to higher density of the starch. Therefore, any increase in starch content increases the overall density of composite material. A similar trend was reported by (Srabayeeta *et al.*,2011 and Kormin *et al.*, 2017)

Starch based materials tend to absorb water because the hydroxyl group in starch can form hydrogen bond with water. Effect of chemically modified starch on water absorption of composites as a function of time is shown in Figure 2. It was observed that water absorption increased with immersion time and increasing starch content which may be due to the increased difficulty in forming polymer chain arrangements as the starch hindered the movements of the polymer segments, and also that the hydrophilic character of starch led to poor adhesion with the hydrophobic polystyrene.

Previous report shows that increase in water absorption as thermoplastic starch content increases could be due to the presence of the O-H group in the amorphous region of the starch and the O-H group increases with increase in thermoplastic starch content in the produced composite. However, compatibilisation of this material significantly decreases the water uptake (Uzochukwu *et al.*, 2020).

Mechanical properties

The Mechanical properties (Tensile Test, Impact Strength and Flexural Test) of pure polystyrene, chemically modified sweet Potatoes starch and composites of polystyrene waste/chemically modified sweet Potatoes starch are presented in figures 3, 4, 5, 6, 7 and 8

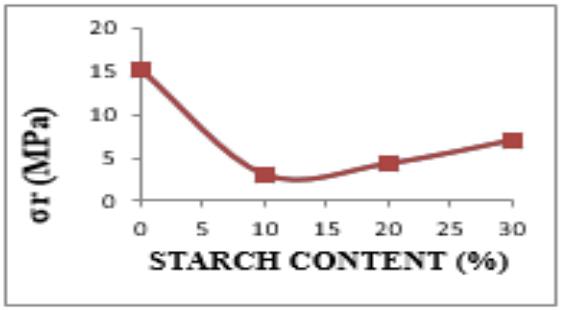

Figure 3: Effect of Starch Content on Tensile Strength of the PS/ Chemically Modified Starch Composites

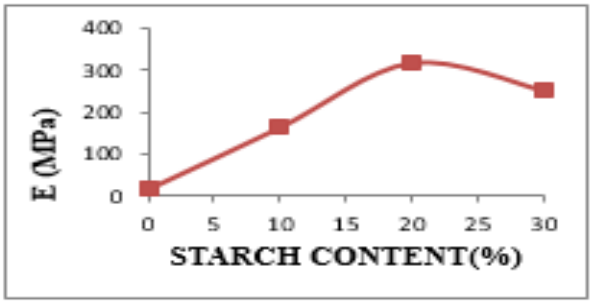

Figure 4: Effect of Starch Content on Young Modulus of the PS/ Chemically Modified Starch Composites

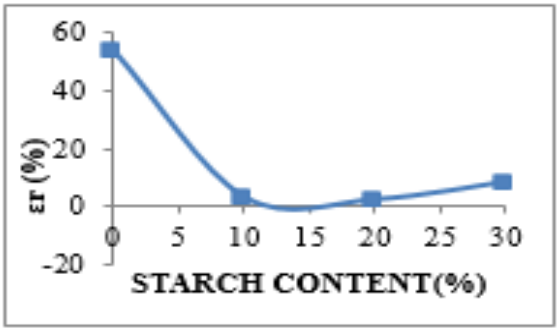

Figure 5: Effect of Starch Content on Elongation of the PS/ Chemically Modified Starch Composites

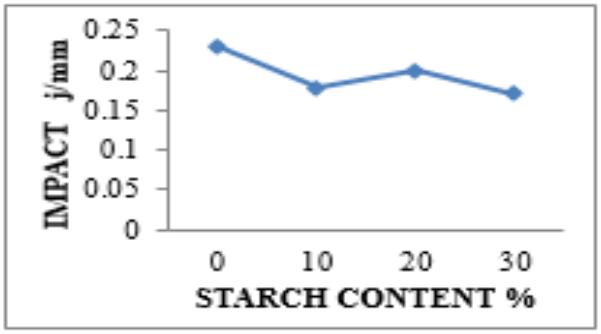

Figure 6: Effect of Starch Content on Impact of the PS/ Chemically Modified Starch Composites

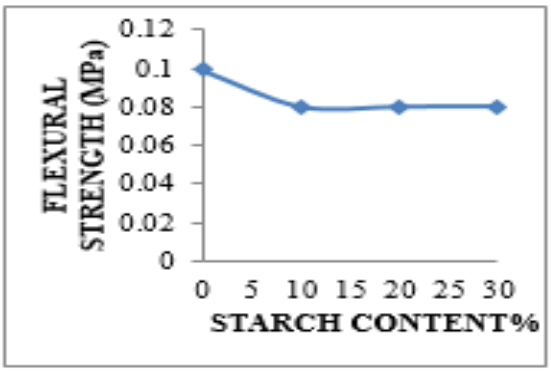

Figure 7: Effect of Starch Content on Flexural Strength of the PS/ Chemically Modified Starch Composites

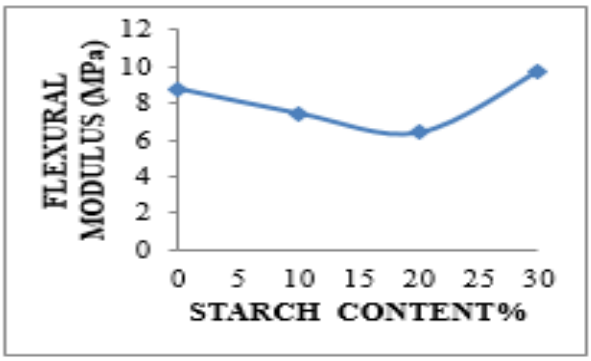

Figure 8: Effect of Starch Content on Flexural Modulus of the PS/ Chemically Modified Starch Composites

Figure 3 shows the effect of starch content on tensile strength of the composites at different filler (10, 20 and 30%) of modified sweet Potatoes starch. The result shows a decrease in tensile strength of the composite when compared with the polystyrene waste. Further increase in filler (starch content) from 10 to 30% led to an increase in tensile strength. The filler (30% starch content) had the highest tensile strength of 7.02 MPa while the 10% starch content had the lowest tensile strength of 3.16 MPa. The polystyrene waste, however, had a higher tensile strength (15.25 MPa) when compared to the composites. This observed decrease in tensile strength of the composites in comparison with the polystyrene waste might be due to improper distribution of the filler with the matrix. Previous report shows that agglomeration of starch within the polymer (polystyrene waste) matrix may also lead to this behavior and in turn lead to poor stress transfer (Yew *et al.*, 2005; Obasi *et al.*, 2014).

The effect of starch content on young modulus of the ps / chemically modified starch composites (Figure 4) at different filler (10, 20 and 30%). The young modulus was found to increase as the starch content increases from 10 to 20%. The highest Young Modulus was 314.81 MPa at 20%

starch content while the lowest Young Modulus was 3.16 MPa at 10% starch content. The composite of polystyrene and modified starch showed that Young's modulus increased from 18.30 to 314.81MPa when composites were filled with 20% of the filler. The increase in young modulus of the composite with increase in starch content could be due to the higher stiffness of the starch granules. Previous reports shows that with an increase in starch content, the filler-filler interaction becomes more pronounced than filler-matrix interaction, this leads to the agglomeration of starch granules that are inherently more rigid or stiffer than the polystyrene matrix (Balakrishna *et al.*, 2001).

The percentage elongation at break of the composite is shown in Figure 5. It was observed from the graph that elongation at break decreases as the starch content increases from 10-30% wt. The lowest elongation at break was 2.36 at 20% filler loading while the highest was 8.45 at 30% filler loading when compared with the pure polystyrene waste which was 53.65%. The decrease in elongation with an increase in starch content could be attributed to the phenomenon that the starch granule containing hydroxyl groups on its surface is highly hydrophilic, whereas polystyrene is nonpolar. Therefore, strong interfacial bond (hydrogen bond) does not form between polystyrene and starch. Chandra and Rustgi (2018) reported that the drop in elongation at break of the polymer became more prominent as the starch content increased to higher percentage. This could be due to the reason that, at higher starch contents, filler-filler interaction becomes more pronounced than filler-matrix interaction which reduces the effective cross-sectional area of the polymer sample caused by the presence of starch particles.

The effect of starch content on the Impact Strength of the composite was presented in Figure 6. The result shows a decrease in impact strength value from 0.23J/mm to 0.05J/mm as the starch content increase from 0 to 30% wt. At 20% starch content, there was a slight increase in impact strength (0.20J/mm). The decrease in impact strength with increase in starch contents may be due to crack propagation within the composite as a result of impact loading. There was also reduction in total surface area available for matrix-filler interaction which leads to increase in mobility of the matrix molecules, as a result the particle sizes that tends to accumulate and increase. This by extension result into weakening of the interfacial bond between the matrix and the filler. It is therefore expected that as the filler content and particle size increases there will be a decrease in impact strength. Kawasaki *et al*. (1998), reported that impact strength decreased by increasing filler loading due to poor interfacial bonding between the filler and the matrix, polymer causes micro-crack to occur at the point of impact, which causes the cracks to easily propagate in the composite without any compatibilizing agent. It was also reported that the decrease in impact strength may be due to agglomeration of the starch on the matrix and poor interfacial bonding which may tend to produce cracks upon impact (Kormin *et al*., 2017).

CONCLUSION

In this study, the effect of modified starch content on the polystyrene foam / sweet starch composites compatibilized with glycerol has been successfully prepared using chemical modification in order to address environmental pollution caused by this polymeric material. The results obtained has confirmed that physicomechanical properties of the blends of Polystyrene waste with modified sweet Potatoes starch were significantly affected by the amount of modified starch content in the produced composite. Within the limit of the variation presented in this study, optimum properties of the composites were obtained at sample with (20wt%) of the modified starch content mostly for Young modulus , per cent elongation at break, impact strength and flexural strength (314,81MPa, 2.36%, 0.20J/mm and 0.0801MPa). Sample with (30wt%) having the highest Tensile strength of 7.02MPa.

REFERENCES

Balakrishna, N.S., Ismail, H. & Othman, N. (2012). The Effects of Rattan Filler Loadings on Properties of Rattan Power-Filler Polypropylene Composites. *BioResources.* 7(4) 5677 – 5690.

Chandra, R.& Rustgi, R (2008). Biodegradable Polymers, *Elsevier Science Ltd*. 1273-1335.

Collado, L.S., Mabesa, R.C., & Corke, H, (2004). Bihon-type noodles from heat-moisture-treated Sweet Potatoes Starch. *Journal of food science,* 66, 604-609

David, C. A., Evzen, S., Pavel U., & Eva M, (2018). Starch Nanoparticles – Two Ways of their Preparation. *Czech Journal of Food Science,* 36.

Faria, F.O., Vercelheze, A.E.S. & Mali, S, (2012). Physical properties of biodegradable films based on cassava starch, polyvinyl alcohol and montmorillonite. *Química Nova Vol.* 35(3): 487–492.

Hale, B.Y, (2016). Thermal, Mechanical and Water Resistance Properties of LDPE/Starch Bio Based Polymer Blends for Food Packing Applications. *Jounal of the turkish chemical society article*, 3(3), 637-656.

Kawasaki, N., Billiaderis, C. G., Ogawa, H., & Arvanitoyannis, I. *Journal of Carbohydrate Polymers, 36*, 89–104.

Kormin, S., Kormin, F., M D H Beg, M B M Piah, (2017).Physical and mechanical properties of LDPE incorporated with different starch sources**,** IOP Publishing IOP Conf. Series: *Materials Science and Engineering 226* 012157 doi:10.1088/1757-899X/226/1/012157.

M.I. Uzochukwu, T.E omobolanle1, E.O Achukwu, Akawu.I (2020). Effect of Starch Content on the Physico- Mechanical Properties of Recycled Polypropylene /Sweet Potatoes Thermoplastic Starch Blend. *International Journal of Recent Engineering Science, Vol. 7,* 35-36

Ning, L.J.H., Peter, R.C., Debbie, P.A & Jiahui, Yu (2011). Preparation, Modification, and Application of Starch Nanocrystals in Nanomaterials: A review. *Journal of Nanomaterials, 573687*, 1 – 13.

Normane, M.C.D.S., Fernando, F.D.L., Rosana L.L.F., Elaine, C.D.M., Jose, I.V & Farayde M. F (2018). Production and characterization of Starch Nanoparticles.

Obasi, H. C., & Igwe, I. O, (2014). Effects of Native Cassava Starch and Compatibilizer on Biodegradable and Tensile Properties of Polypropylene, *American Journal of Engineering Research.* 3(2) 96-104

Ozcalik, O., & Tihminlioglu, F, (2013). Barrier properties of corn zein nanocomposite coated polypropylene films for food packaging applications. *Journal of Food Engineering* 114(4), 505-513.

Srabayeetab. R., Ramaraj, B., Subhas, CS, (2011). Polypropylene and Potatoes starch bicomposites: physico-mechanical properties and thermal properties, *journal of Applied polymer science* DOi:10.1002/app,33486. 120 (5) 3078-3086.

Suk, F. C., Siti, N. A. M. Y & Suh C. P, (2014). Preparation & Characterization of Starch Nanoparticles for Controlled Release of Curcumin. *International Journal of Polymer Science,* 340121, 1 – 8.

Toral, F.L.B., Furlan, A.C., Scapinello, C., Peralta, R.M & Figueiredo, D.F, (2002). Digestibility of Two Starch Sources and Enzymatic Activity of 35 and 45 Days Old Rabbits. *Revista Brasileira de Zootecnia* 31(3): 1434–1441.

Vieira, M., Da Silva, M. A., Dos Santos, L. O., & Beppu, M. M, (2011). Natural-Based plasticizers and biopolymer films: A review. *Journal European Polymer*, 47(3), 254-263.

Yew, G.H., Mohd Yusuf, A.M., Mohd Ishak, Z.A. & Ishiaku, U.S, (2005). Water absorption and enzymatic degradation of poly (lactic acid)/rice starch composites, *Polym. Degrad. Stab.* 90(3*)* 488 – 500.

Young, A. H, (1984). Fractionation of starch. In Whistler, R. L., BeMiller, J. N., & Paschall, E. F. (Eds), *Starch Chemistry and Technlogy* (pp. 249-284). San Diego: Academic Press.

Antibacterial Activity and FTIR Characterization of subfractions from Ethylacetate Fraction of *Piliostigma thonningii* against some *Salmonella species*

[1]Abdulsalami Halimat, [2]Mudi Suleiman Yusuf, [1]Daudu Oladipupo Abdulazeez Yusuf, [3] Adabara Nasiru Usman, [4]Hamza Rabiat Unekwu and [5]Abdulsalam Sa'adatu
[1,3,4]Department of Plant Biology, Federal University of Technology, Minna, Nigeria.
[2]Department of Pure and Industrial Chemistry, Bayero University, Kano, Nigeria.
[5]Department of Chemistry, Confluence University of Science and Technology Osara, Kogi State.
* E-mail of the corresponding author: halimat.abdul@futminna.edu.ng

ABSTRACT

The present study deals with the antibacterial activity and functional group analysis of Piliostigma thonningii extract, its fractions, sub-fractions and column isolates. The crude methanol extract of the plant (PT1), its partitioned-soluble fractions (PT1-01, PT1-02, PT1-03 and PT1-04), sub-fractions from VLC fractionation of ethyl acetate fraction (VLC1 –VLC7) and column sub-fractions (Et1-Et6) were screened for their antibacterial potentials using agar well diffusion technique. The crude methanol leaf extract was first partitioned with different organic solvents to afford the n-hexane-chloroform- and ethyl acetate-partitioned-soluble fractions. The antibacterial active ethyl acetate – partitioned soluble fraction was further fractionated over a vacuum liquid chromatography followed by column chromatography of the antibacterial active VLC sub-fraction (VLC5). Characterization of the antibacterial active column sub-fractions was done using Fourier transform infrared spectroscopy (FTIR). The results showed that all the fractions possess antibacterial activity on at least one of the bacteria tested, however, the ethyl acetate fraction (PT1-03) exhibited the widest zone of inhibition on the test bacteria (14-16mm) at the concentration of 100mg/ml. The zones of growth inhibition increased with increasing concentration of the extracts. The corresponding increase in concentration and growth inhibition zone was significant ($p<0.05$). The FT-IR result of the column isolate from the ethylacetate fraction revealed the presence of phenols, aldehydes, ketones, amines, amides and carboxylic acids. The spectra of the activity exhibited by the isolates signified their potency for the development of therapeutic agents against these pathogenic bacteria.

Keywords: Antibacterial activity, Column chromatography, Growth inhibition, Solvent partitioning, Spectrophotometer.

1. Introduction

The use of plants and its products has a long history that began with folk medicine and since then remarkable progress has been made in the field of medicine with the discoveries of many natural and synthetic drugs (Preethi *et al.,* 2010). Antibiotics are undeniably one of the most important therapeutic discoveries of the 20th century that had effectiveness against serious bacterial infections. However, only one third of the infectious diseases known have been treated with these synthetic products (Sharma, 2011). This is because of the emergence of resistant pathogens that are beyond doubt the consequence of years of widespread indiscriminate use, incessant and misuse of antibiotics. Antibiotic resistance has increased substantially in the recent years and is posing an ever increasing therapeutic problem (Anyanwu and Okoye, 2017). In nature, plants are bestowed with chemical compounds to help provide defense against predators. It is expected that plant extracts showing target sites other than those used by antibiotics will be active against drug resistant pathogens (Sen and Batra, 2012). Some of the secondary metabolites in plants have also been identified to act as drug precursors which may be utilized for the production of the more potent synthetic drugs. Plants natural products chemistry have played an active role in generating a significant number of candidate compounds in drug discovery programs (Pillai and Nair, 2014).

However, the climate and other ecological conditions may affect production of secondary metabolite in medicinal plants and need to be incessantly monitored to maintain the potency of the plant drugs (Chandrika *et al.*, 2013). Fingerprinting (marker compound analysis) by chemical and validated chromatographic and spectroscopic techniques are gaining importance for standardization in the herbal medicinal formulations. The evaluation of a herbal product by metabolomic fingerprinting can be accomplished by appropriate methods, including High performance liquid chromatography (HPLC) with Ultraviolet diode array detector(UV DAD), Evaporative light scattering detector (ELSD), Gas chromatography mass spectrometry (GC-MS), High performance thin layer chromatography (HPTLC), Fourier transform infrared spectroscopy (FT-IR), Near infrared (NIR), Nuclear magnetic resonance spectroscopy (NMR) or a combination of these techniques. Such techniques also provide useful information about qualitative and quantitative composition of herbal medicines and their pattern recognition by chemometry (Geethu *et al.*, 2014). The Fourier transform infrared (FTIR) spectroscopy has proven to be a valuable tool for the characterization and identification of compounds or functional groups (chemical bonds) present in an unknown mixture of plant extracts (Maobe and Nyarango, 2013). The FTIR measures predominantly the vibrations of bonds within chemical functional groups and generates a spectrum that can be regarded as a biochemical or metabolic "fingerprint" of the sample (Mariswamy *et al*., 2012). The present study therefore, evaluates the antibacterial activity, as well as; the presence or absence of various functional groups in the crude methanol leaf extract of *P. thonnigii* and its fractions using FTIR.

2. Materials and Methods

2.1 Collection and Identification of the plant

Matured leaves of *P. thonningii* were collected along Gidan kwano Road Minna, Niger State, Nigeria. The plant was identified at the herbarium unit of the Department of Biological Sciences, Ahmadu Bello University, Zaria where voucher number 171 was deposited.

2.2 Plant Preparation

The leaves were carefully washed under running water, air-dried at room temperature and then milled into fine powder. About 300 g of the powdered leaves of the plant was macerated with 1.5 liters of 70% methanol for 72 hours. The resulting mixture was filtered using a muslin cloth and subsequently concentrated using a rotary evaporator. The extract was weighed, placed in sterile sample bottles and stored in a refrigerator until required for use (Tiwari *et al*. 2011).

2.3 Solvent partitioning of crude extract

The methanol crude extract (40g) was subjected to solvent-solvent partitioning by using the methods employed by Emran *et al*. (2015). The crude extract was successively partitioned by using solvents of increasing polarity in the following order; n-hexane, chloroform and ethyl acetate in a separating funnel. The resulting fractions of the crude extract were evaporated to dryness using rotary evaporator at 40℃ to afford fractions labelled as the hexane (PT1-01), chloroform (PT1-02), ethyl acetate (PT1-03) and methanol (PT1-04) soluble fractions. All the fractions were weighed and stored in air tight containers till further analysis.

2.3.1 Reconstitution of Plant extract and Fractions

Using an analytical weighing balance one gram (1 g) of extract and each fraction were dissolved in 5 ml of 50% dimethylsulphoxide (DMSO) to make 200 mg/ml stock solution from which was serially diluted to give concentrations of 100 mg/ml, 50 mg/ml and 25 mg/ml.

2.4 Vacuum Liquid Chromatography (VLC) and Column Chromatography of Ethyl acetate Fraction of *P. thonningii*

The most antibacterial active partitioned fraction (Ethylacetate fraction of *P. thonningii*, PT1-03) was further exploited in an attempt to isolate the active principle which exhibited the antibacterial activity. The method described by Amin *et al*., (2012) was adopted for the isolation procedure. The

ethyl acetate extract was further fractionated using VLC to afford VLC sub-fractions, coded VLC1-VLC7. The most active VLC sub-fraction (VLC5) which exhibited significant activity against the test organisms were subjected to column chromatography using the method described by Dauda and Mudi (2013) with slight modification. About 250 g of silica gel (60-120 mesh size) was made into slurry of n-hexane and packed by wet method into a glass column (3.8 cm by 53 cm) in slurry of n- hexane. The sub-fraction (2g) was dissolved in methanol and then mixed with a small quantity of silica gel, dried, triturated and then loaded on top of the column already packed with silica gel. Sequential elution was carried out using stepwise gradient solvents of increasing polarity in the following order: n-hexane (100%), n-hexane - chloroform (1:1), chloroform (100%), chloroform-ethyl acetate (4:1), chloroform-ethyl acetate (1:1), chloroform-ethyl acetate (1:2), chloroform-ethyl acetate (1:4), ethyl acetate (100%), ethyl acetate-methanol (9:1), ethyl acetate-methanol (4:1), ethyl acetate-methanol (1:1), methanol (100%), methanol-water (1:1) and 100% water. The process was monitored using the thin layer chromatography. An aliquot of 20 ml of the eluates were continuously collected into test tubes from the beginning to the end of the elution, in each case the eluates having similar TLC profile were pooled together into major sub fractions which were further subjected to antibacterial activity.

2.5 Characterization of Column sub-fractions

The semi-purified sub-fractions that displayed significant antibacterial activity were identified using FTIR. The infrared spectra of the column isolates were recorded on Agilent Technologies model FTIR 4100 excoscan at the Ahmadu Bello University (ABU) Zaria, Kaduna State. The spectra were scanned in the 650 to 4000 cm^{-1} range. The spectra were obtained using transmittance method and were plotted as intensity versus wave number. The functional groups (obtained by FTIR analysis) present in each of the active column isolate was interpreted with the aid of structure correlation chart (Oyerinde and Bello, 2016).

2.6 Antibacterial assay

2.6.1 Test organisms

Clinical isolates of *Salmonella typhi*, *Salmonella paratyphi* A, *Salmonella paratyphi* B and *Salmonella paratyphi C* were obtained from the Microbiological laboratory of Aminu Kano teaching Hospital, Kano for the susceptibility tests. The organisms were used after their identity were confirmed at the Department of Microbiology, Bayero University, Kano. The stock culture was maintained on Nutrient agar slant at 4℃ in the refrigerator.

2.6.2 Antibacterial Susceptibility Test

The sensitivity of extract, fractions and sub-fraction was determined using the agar well diffusion method as described by Nas and Ali (2017) with modifications. With the aid of a sterile cotton swab the prepared bacterial suspension equivalent to 0.5 McFarland Standard (1.5×10^6 CFU) was inoculated onto sterile Mueller- Hinton agar plates. A sterile 6 mm diameter cork borer was used to bore 3 wells into the agar plates. The wells were then filled up with approximately 0.1ml of the extract solution at a concentration of 25, 50 and100 mg/ml taking care to prevent spillage onto the surface of the agar medium. The plates were allowed to stand on the laboratory bench for 1 hour to allow proper diffusion of the extract into the medium after which the plates were incubated at 37 ℃ for 24 hours, and thereafter the plates were observed for zones of inhibition and measured.

2.7 Statistical Analyses

The statistical analyses were carried out using statistical package for social sciences (SPSS-computer package). Data from the antibacterial activities of *P. thonningii* were expressed as mean ± standard error of three independent replicates and also subjected to one-way analysis of variance (ANOVA) at $p<0.05$ level of significance for comparison of the extract activities.

3.0 Results and Discussion

Plant extracts are considered to be valuable source of biological active compounds. In this study the antibacterial activity of the crude extract, fraction and fractions of *P. thonningii* were assessed against some *Salmonella species*. The crude extract and all the other fractions had good antibacterial activity against all the tested organisms except n-hexane soluble fraction (Table 3.1). This could be that the bioactive compounds present in the plant were more soluble in polar solvents as compared to the non-polar solvents. However the most active fraction was ethylacetate soluble fraction as it showed the largest zone of bacterial inhibition (11-16 mm) as such was subjected to vacuum liquid chromatography. The antibacterial activity of all the seven sub-fractions obtained from vacuum liquid chromatography of *P. thonningii* ethylacetate fraction is shown in Table 3.2. All the sub-fractions except sub-fraction seven (VLC7) showed zones of inhibition on at least one organism. However sub-fraction five (VLC5) was the most active against the bacteria strains tested, as a result of which it was further purified using column chromatography. Table 3.3 show the results of antibacterial activity of sub-fractions obtained from column chromatography of sub-fraction VLC5. The bacterial strains tested were susceptible to column sub-fraction Et1 and Et2. However Et1 indicated the strongest antibacterial activity on the test organisms at low concentration of 50 mg/ml (11-15 mm) when compared with the crude extract and previous fractions. Column sub-fractions Et3-Et6 exhibited no zone of inhibition. The present study has shown that antibacterial activity varies with fraction. The observed difference could be attributed to the variation in the distribution of active principles according to their affinity for the solvent used in fractionation. Few investigations on the antibacterial properties of *P. thonningii* have been reported. Chukwunonye *et al.*, (2017) had also reported the potency of the leaf extract and fractions of *P. thonningii* on *S. typhi* and other bacteria.

Table 3.1: Zones of growth inhibition (mm) of the crude extract and fractions of the leaves of *P. thonningii* on the test bacteria

Crude/ Fractions	Conc. (mg/ml)	*S. typhi*	*S. paratyphi A*	*S. paratyphi B*	*S. paratyphi C*
PT1	25	10± 0.33^{c}	0± 0.00^{c}	09± 0.00^{c}	0± 0.00^{c}
	50	12± 0.58^{b}	09± 0.33^{b}	11± 0.33^{b}	09± 0.33^{b}
	100	15± 0.33^{a}	12± 0.58^{a}	15± 0.33^{a}	11± 0.33^{a}
PT1-01	25	0± 0.00^{a}	0± 0.00^{a}	0± 0.00^{a}	0± 0.00^{a}
	50	0± 0.00^{a}	0± 0.00^{a}	0± 0.00^{a}	0± 0.00^{a}
	100	0± 0.00^{a}	0± 0.00^{a}	0± 0.00^{a}	0± 0.00^{a}
PT1-02	25	0± 0.00^{b}	0± 0.00^{b}	0± 0.00^{c}	0± 0.00^{c}
	50	0± 0.00^{b}	0± 0.00^{b}	11± 0.58^{b}	12± 0.33^{b}
	100	12± 0.33^{a}	8± 0.33^{a}	13± 0.33^{a}	14± 0.00^{a}
PT1-03	25	11± 0.33^{c}	0± 0.00^{c}	13± 0.33^{c}	12± 0.33^{c}
	50	12± 0.33^{b}	12± 0.00^{b}	14± 0.33^{b}	13± 0.58^{b}
	100	14± 0.33^{a}	15± 0.33^{a}	16± 0.33^{a}	15± 0.88^{a}
PT1-04	25	0± 0.00^{c}	0± 0.00^{c}	0± 0.00^{c}	0± 0.00^{c}
	50	11± 0.33^{b}	9± 0.33^{b}	9± 0.33^{b}	9± 0.33^{b}
	100	10± 0.33^{a}	12± 0.33^{a}	12± 0.33^{a}	11± 0.33^{a}

Values are presented in means ± Standard error of three replicates.
Values with the same superscript on the same column are not significantly different at P>0.05.

Keys: PT1- Methanol extract; PT1-01- n-hexane soluble fraction; PT1-02-Chloroform soluble fraction; PT1-03- Ethylacetate soluble fraction; PT1-04- Aqueous methanol soluble fraction

Table 3.2: Antibacterial activity of VLC sub-fractions obtained from Ethylacetate fraction of *P. thonningii*

Sub-fractions	Conc. (mg/ml)	*S. typhi*	*S. paratyphi A*	*S. paratyphi B*	*S. paratyphi C*
VLC1	50	11	10	11	11
	100	12	11	11	12
VLC 2	50	10	8	-	8
	100	11	10	9	8
VLC 3	50	8	-	8	-
	100	8	8	9	8
VLC 4	50	8	8	-	-
	100	8	9	-	-
VLC 5	50	13	8	12	11
	100	13	9	12	11
VLC 6	50	-	-	-	-
	100	9	-	-	-
VLC 7	50	-	-	-	-
	100	-	-	-	-

Key: - No zone of inhibition

Table 3.3: Antibacterial activity of isolates obtained from Column Chromatography (Et1-Et6) of *P. thonningii*

Fractions	Conc. (mg/ml)	*S. typhi*	*S. paratyphi A*	*S. paratyphi B*	*S. paratyphi C*
Et 1	25	13	14	12	13
	50	15	15	13	15
Et 2	25	11	-	11	-
	50	11	-	11	11
Et 3	25	-	-	-	-
	50	-	-	-	-
Et 4	25	-	-	-	-
	50	-	-	-	-
Et 5	25	-	-	-	-
	50	-	-	-	-
Et 6	25	-	-	-	-
	50	-	-	-	-

Key: - No zone of inhibition

Infra-Red spectroscopy is basically a vibrational spectrum and involves the measurement of wavelength and intensity of absorption of mid infrared light by a sample. The FTIR result for the column isolate Et1 showed that a characteristic absorption bands were exhibited at 2922.2 cm^{-1}, 2855.1 cm-1 for C-H stretching and 1692.2 cm^{-1}, 1640.0 cm^{-1} for C=C bending (Table 3.4) (Figure 1). The column isolate Et2 showed the characteristic absorption bands at 2926.0 cm-1, 2855.1 cm^{-1} for C-H stretching and 1640.0 cm^{-1} for C=C bending (Table 3.5) (Figure 2). The present FT-IR results confirmed the presence of phenols, alkanes, aldehydes, ketones, amines, amides, alkenes, carboxylic acids, and alcohols in the column isolates. Phenols are of great importance as they protect the human body from the oxidative stress, which cause many diseases including cancer, cardiovascular problems and ageing. They exhibit antimicrobial, anthelmintic, antiapoptotic and antidiarrhoeal activities (Cowan,1999). Amines and amides are the main groups of protein synthesis. Carboxylic acids are biologically very important in the formation of fat in the body and act as strong antibacterial agents (Pillai and Nair, 2014).

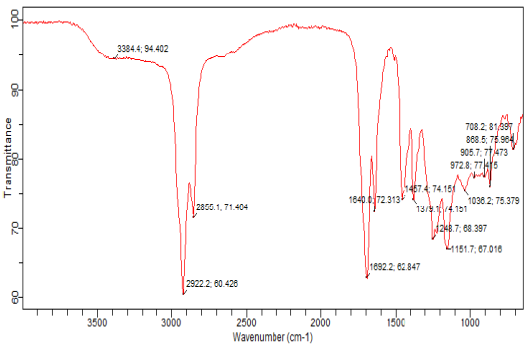

Figure 1: FTIR spectra of Column isolate Et1

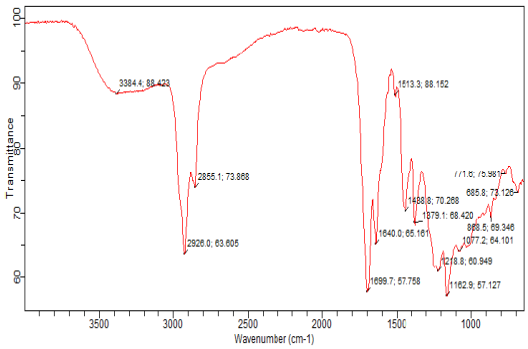

Figure 2: FTIR spectra of Column isolate Et2

Table 3.4: FTIR Interpretation of Column isolate Et1

Wave number (cm-1)	Types of vibration	Functional groups
3384.4	N-H stretch/ O – H	Amino group, hydroxyl group
2922.2, 2855.1	Asymmetrical stretching	C-H (alkanes)
1692.2,1640.0	Stretching	C=O (ester carbonyl functional group
1379.1, 1457.4	Bending and rocking	C – H (methyl or –CH3)
1036.2- 1248.7	Stretching	C-N, C-O Aliphatic amines/alcohols, carboxylic acids
708.2- 972.8	Out of plane bending	Aromatic C-H bending

Table 3.5: FTIR Interpretation of Column isolate Et2

Wave number (cm-1)	Types of vibration	Functional groups
3384.4	N-H stretch/ O – H	Amino group, hydroxyl group
2926.0, 2855.1	Asymmetrical stretching	C-H (alkanes)
1513.3-1699.7	Stretching	C=O (ester carbonyl functional group
1379.1, 1436.6	Bending and rocking	C – H (methyl or –CH3)
1077.2- 1218.8	Stretching	C-N, C-O Aliphatic amines/alcohols, carboxylic acids
685.8- 888.5	Out of plane bending	Aromatic C-H bending

4. Conclusion

The antibacterial activity of the leaves of *P. thonningii* showed that the crude extract, fractions and sub-fractions demonstrated antibacterial effect against the test organisms with higher activity in the column isolates when compared to the other fractions. The antibacterial activity of the plant parts can be attributed to the presence of some phytochemicals identified in this study. The ethyl acetate fraction of the plant extract and identified chemical isolates may therefore be a readily available source of cheap and potent antibacterial agents to be used in the therapy of infections caused by these often multi resistant organisms. These findings provided a rationale for the ethnomedicinal use of the plant in traditional medicine.

5. Acknowledgement

This study was part of a research project funded by the TETFUND Institution based research intervention (IBRI) Fund (TETFUND/FUTMINNA/2016-2017/6th BRP/18) Federal University of Technology Minna, Niger State, Nigeria.

References

Amin, N., Qadir, M.I., Khan, T.J., Abbas, G., Ahmad, B., Janbaz, K.H. & Ali, M. (2012). Antibacterial activity of vacuum liquid chromatography (VLC) isolated fractions of chloroform extracts of seeds of *Achyranthes aspera*. *Journal Chemical Society of Pakistan,* 34(3):589-592

Anyanwu, M.U. & Okoye, R.C. (2017). Antimicrobial properties of Nigerian plants. *Journal of Intercultural Ethnopharmacology,* 6 (2): 240-259

Chandrika, R., Komal, K.J., Thara, S.K.J., & Deviprasad, A.G. (2013). FTIR spectroscopic studies and antimicrobial activity in populations of *Eryngium foetidum* L. *International Journal of Pharmacy*, 3(4):813-818.

Chukwunonye, U.C.E., Ebele, O.P., Kenne, T.M. & Gaza, A.S.P. (2017). Phytochemical screening and antimicrobial activity of methanol extract and fractions of the leaf of *Piliostigma thonningii* Schum (Caesalpiniaceae). *World Applied Sciences Journal 35* (4): 621-625

Cowan, M. M. (1999). Plant products as antimicrobial agents. *Clinical Microbiology Reviews*, 12 (4): 564–582.

Dauda, U. & Mudi, S.Y. (2013). Screening and bioassay-guided isolation of antimicrobial components from *Laggera mollis. Bayero Journal of Pure and Applied Sciences,* 6(1):152 – 158.

Emran, T., Rahman A, Nasiruddin, M.N., Rahman, M., Uddin, Z., Dash, R & Layzu C. (2015). Effects of organic extracts and their different fractions of five Bangladeshi plants on *in vitro* thrombolysis. *BMC Complementary and Alternative Medicine,* 15, 128-135.

Geethu, M. G, Suchithra, P. S., Kavitha, C. H., Aswathy, J. M., Babu, D. A & Murugan, K. (2014). Fourier-transformation infrared spectroscopy analysis of different solvent extracts of Water hyacinth (*Eichhornia crassipes* mart solms.) an allelopathic approach. *World Journal of Pharmacy and Pharmaceutical Sciences,* 3 (6): 1256-1266.

Maobe, M. A. G. & Nyarango, R. M. (2013). Fourier transformation infra-red spectrophotometer analysis of *Warburgia ugandensis* medicinal herb used for the treatment of diabetes, malaria and pneumonia in Kisii Region, Southwest Kenya. *Global Journal of Pharmacology,* 7 (1): 61-68.

Mariswamy, Y., Gnanaraj, W. E. & Johnson, M. (2012). FTIR Spectroscopic studies on *Aerva lanata* (l.) Juss. ex schult. *Asian Journal of Pharmaceutical and Clinical Research*, 5 (2): 82-86.

Nas, F. S. & Ali, M. (2017). Antibacterial activity of *Boswellia dalzielii* leaves extracts against some pathogenic bacterial isolates. *Journal of Advances in Microbiology* 7(1): 1-8.

Oyerinde, A.Y. & Bello, E. I. (2016). Use of Fourier transformation infrared (FTIR) spectroscopy for analysis of functional groups in Peanut oil biodiesel and its blends. *British Journal of Applied Science & Technology,* 13(3): 1-14.

Pillai, L.S. & Nair, B.R. (2014). Functional group analysis of *Cleome viscosa* L. and *C. burmanni* W.&A. (Cleomaceae) extracts by FT-IR. *Journal of Pharmacognosy and Phytochemistry,* 2(6): 120-124.

Preethi, R., Devanathan, V.V. & Loganathan, M. (2010). Antimicrobial and antioxidant efficacy of some medicinal plants against food borne pathogens. *Advances in Biological Research* 4(2): 122-125.

Sen, A & Batra, A. (2012). Evaluation of antimicrobial activity of different solvent extracts of Medicinal plant: M*elia azedarach L. International Journal of Current Pharmaceutical Research*, 4(2): 67-73.

Sharma, A. (2011). Antibacterial activity of ethanolic extracts of some arid zone plants. *International Journal of PharmTech Research*, 3(1):283-286.

Tiwari, P., Kumar, B., Kaur, M., Kaur, G., and Kaur, H. (2011). Phytochemical screening and extraction: A review. *Internationale Pharmaceutica Sciencia,* 1(1): 98-106.

EVALUATION OF THE PHYTOCONTITUENTS, MINERAL CONTENTS, ESSENTIAL OIL COMPOSITION AND ANTIBACTERIAL ACTIVITY OF *MENTHA PIPERITA L.* LEAF EXTRACT

Liman, Ibrahim Salihu[1*], Baba Yabagi Alhaji[1*], Suleiman Alfa[2], Nimmyel NannimVincent[1*]
[1]Department of Chemical Sciences, Federal Polytechnic, Bida.
[2]Department of Biological Sciences, Federal Polytechnic, Bida.
ibrahimliman067@gmail.com, yabagibaba5180@gmail.com, cabusalman@gmail.com
nimcent@gmail.com
*Corresponding author

Abstract
There is a growing interest in the pharmaceutical industry to replace synthetic with natural products with bioactive properties such as the ones from plant sources. The aim of this study was to determine the chemical composition, mineral contents, phytoconstituents and antibacterial activity of the methanolic extract and essential oil of Mentha piperita. The essential was extracted using clevenger apparatus and the essential oil was analysed using GC/MS, result revealed (+)-menthol, menthol and neo-menthol as the main constituents, comprising 38.06, 35.64 and 6.73% of the essential oil, respectively. The preliminary phytochemical screening revealed the presence of flavonoids, saponins, alkaloids, tannins, cardiac glycosides and glycosides. while the elemental analysis of the minerals revealed K 24.020%, Na 7.780%, Ca 0.075%, Mg 0.015% and P 0.340%. Furthermore, the essential oil was tested against two gram-positive and gram-negative bacteria isolates by agar well diffusion method. Both the extract and essential oil exhibited antibacterial activities against the tested organisms. In conclusion, M. piperita can be an excellent source of nutrient and potential ethnomedicinal plant which may have minimal side effect when compared to synthetic drugs.

Keywords: antibacteria, essential oil, hydro-distillation, GC-MS, *M. piperita*

Introduction

A variety of bioactive compounds that are present in different parts of a plant has spurred a renewed interest in developing alternate therapy. The traditional herbal medical system has been practiced globally from ancient times; consequently, a great volume of literature is available on the antimicrobial activity of a variety of plant species. Multidrug resistance among the microbial pathogens has been a great concern world over. Phytochemicals from plants have shown great promise in the treatment of intractable infectious human diseases including viral infections (Cowan, 1999).

Mentha piperita L., commonly named as a peppermint, (*Mentha* x *piperita L.*), is a cross breeding of spearmint (*Mentha spicata*) and water mint (*Mentha aquatica*). *Mentha* is a variety of plants in the family Lamiaceae (mint family) in the subfamily Nepetoidae, It is assessed that 13 to 18 species exist, and the correct refinement between species remains thesame. It incorporates fragrant herbs of confounding ordered characterization, because of a high variation in morphological characters and numerous hybridisations that happen, both in wild and domisticated.

Literature Review

Fresh and dried leaves, as well as essential oils extract from aerial parts of the flowering *M piperita,* are used as fragrance as components food, cosmetic and pharmaceutical products (İşcan *et al*., 2002; Raut and Kuruppayil, 2014).

Evaluation of the nutrient composition of plant materials is of paramount importance because of the roles of this plant as a source of food and raw materials for industries; it provides both animals and man with food of different forms and ways. Plants are equally important sources of materials for our industries. Besides their use as a source of energy and in general plants are now the primary source of medicine both traditionally and scientifically (Rubatzky and Yamaguchi, 2012; Ramasamy and Kalidass, 2010).

The concentration of bioactive compounds in *Mentha* depends on species and in *M. piperita* depends on the plant variety, its maturity, geographical region, climate and processing conditions. *M. piperita* contains menthyl acetate (2%-11%), isomenthone (2%-8%), 1.2%-3.9% (v/w) essential oils composed of menthol (33%-60%), menthone (15%-32%), eucalyptol (5%-13%), menthofuran (1%-10%) and limonene (1%-7%), (Fatemi *et al.*, 2014). Moreover, *M. piperita* leaves contain 19-23% of polyphenols, which include eriocitrin and rosmarinic acid (59%-67%), luteolin 7-orutinoside (7%-12%) and hesperidin (6%-10%), (Berdowska *et al*., 2013; Kamiloglu *et al*., 2012).

A standout among the most well-known types of restorative plants predominant all through the world, in pharmaceutical, corrective, and sustenance industry, is peppermint (Marjina *et al.*, 2012). Peppermint has a carminative, antispasmodic, and antiseptic properties which make this herb popular for medicinal use for centuries (Zmora *et al.*, 2012). Aromatherapy uses essential oils, which are said to be highly concentrated substances extracted from flowers, leaves, stalks, fruits and roots (Dunning, 2013). Many essential oils are known for their antibacterial activity against gram-positive and gram-negative bacteria along with antifungal properties. They can be very good alternatives for antibiotics if properly and thoroughly studied for these effects (Babar *et al.*, 2015).

Material and Methods

Sample collection

Indigenously grown mint plants were collected from the garden of the faculty of Pharmacy garden, Usmanu Danfodiyo Univertisy, Sokoto. The identity of plant material was confirmed from the herbarium unit of the Department of Biological Sciences, Usmanu Danfodiyo Univertisy, Sokoto. The plant material was washed with clean water to remove soil and other dirt. Half of the fresh leaves of *M. piperita* was used for essential oil extraction while the other half was air dried and then ground into powder using clean pestle and mortar, sieved with a to obtain fine granules.

Extraction

Essential oils of fresh peppermint leaves were isolated by hydro-distillation (Clevenger-type apparatus) according to standard procedure described in European Pharmacopoeia (1997). The oil extract was stored in tightly closed vials at +4 ºC until analysis. The yield was calculated using the equation $RO_u=(M/B_m)x100$ where M is the mass of the extracted oil(g) and B_m is the initial leaf weight. To the fine granules, 500 g of the fine powdered sample of *M. piperita* leaves was percolated in ethanol (700 cm^3) and distilled water (300 cm^3) for three (3) days at laboratory temperature for three consecutive times and filtered. The filtrates were collected, combined and concentrated over a water bath at 35 ^{0}C. The concentrate (80.9g) collected and weighed (Halilu *et al.*, 2012).

Phytochemical analyses

The qualitative phytochemical analysis of the methanolic leaf extract was conducted to determine the presence of some secondary metabolites. The methods of Trease and Evans (1989) and Sofowora (1982) were used for the phytochemical screening of the extracts.

Mineral analysis

Mineral contents in leaves were determined using an atomic absorption spectrophotometer (Buck Scientific Model 205, East Norwalk, CT) (Anonymous, 2005). A 0.5 g amount of crushed composite sample was digested in nitric acid (Conc. HNO_3), sulphuric acid (Conc. H_2SO_4) and

perchloric acid ($HClO_4$) at 150ºC inside a fume cupboard for about 5 h to generate the digest solution. An aliquot of the digest solution was used for determination of calcium, magnesium, sodium, potassium and phosphorus contents (Gideon *et al.*, 2018).

Sodium and Potassium estimation.
Flame photometer (model FP 640) was used to obtain sodium (Na) and potassium (K). The flame photometer was set up by inserting appropriate filter usually by 768 nm for K and 589 nm wave lengths for Na respectively. This instrument was set to 100 transmittance by taking 2-10 ppm of K and Na solution. The standard curve was prepared by plotting transmittance reading against concentration of standard K and Na solution (Singh *et al*., 2012).

Calcium and Magnesium determination.
Calcium and Magnesium were determined by EDTA method. Calcium was obtained the samples by pipetting 2 ml aliquot of the sample solution into filtration flask. Three drops each KCl, NH2**,** OH and triethanolamine were added together with 0.3 g of Murexide, and it was then titrated with EDTA solution to the end point from pink to purple (Jatto *et al*., 2010).

Phosphorus determination.
Phosphorus (P) was determined using a UV-Vis spectrophotometer (model PG 1900 made in England). Digested supernatant solution 2 ml was pipette into a 50 cm^3 volumetric flask, 2 ml of the sample and 2 ml of Ammonium molybdate solution were added. After that, 1 ml of diluted stannous solutions was added, mixed again and allowed to stand for 5 minutes. The % absorbance on UV-Vis spectrophotometer at 660 nm wavelength was used to determine the concentration of phosphorus (Pytlakowska *et al*., 2012).

Gas chromatography/Mass spectrometry (GC/MS) Analysis:
The essential oils of mint samples were analysed by using a GC Clarus 600-MS Clarus 600 C (Perkin Elmer) equipped with an auto sampler. One microlitre of sample volume was injected using split method. Chromatographic separations were accomplished with a Elite 5-MS capillary column (5% Diphenyl)-Dimethylpolysiloxane, 0.25mm i.d x30 m, film thickness 0.25 m) with injections in the split mode with 20 split ratio. Analysis was carried out using helium as the carrier gas with flowrate of 1.0 ml/min. The column temperature was initially kept at 60 ºC for 3 min than gradually increased to 130 ºC at 4 ºC min^{-1} rate, held for 2 min, and finally raised to 240 ºC at 20 ºC min^{-1}. The injection port temperature was 240 ºC. The ionization voltage applied was 70 eV with mass range m/z of 20–550 amu. The separated components were identified tentatively by matching with EI-MS results of National Institute of Standards and Technology (NIST), WILEY 8th edition and NBS mass spectral library data. The quantitative determination was carried out based on peak area integration.

Collection of Bacterial Isolates

Two Gram-positive (*Staphylococcus aureus* ATCC 25923 and *Staphylococcus saprophyticus* ATCC19615), and two Gram-negative (*Escherchia coli* ATCC 25922 and *Pseudomonas aeruginosa* ATCC 27853) bacteria were obtained from Usmanu Danfodio University Teaching Hospital, Sokoto, Nigeria.

Antibacterial Screening
The antibacterial activity of the extract and essential oil determined using the agar well diffusion method. The standard inoculum of the respective bacteria were spread uniformly on four (4) sterile petri dishes labeled A, B, C and D containing the nutrient agar, two adjacent holes of 6 mm were drilled with sterile cork borer at 30 mm interval. The wells were filled with 20µl and 10µl of the

M. piperita extract and essential oil. The plates were allowed to stand for 30 minutes for pre-diffusion of the extract and then incubated at 37 ºC for 24 h. The zone of inhibition were evaluated to the nearest milliliter (mm) using tetracycline as a control. All means are in standard deviations of the triplicate result were taken. The values ≥ 9 were considered active (Rios *et al*., 1998; Alves *et al.*, 2000).

Results and Discussion

Table 1 Phytochemical screening of the *M. piperita* leave extract

Phytochemical	Test
Saponin	++
Tannin	++
Flavonoids	++
Cardiac glycosides	+
Alkaloids	+++
Glycosides	+
Volatile oil	+++

Key: +++ = present in high amount, ++ = moderately present, + = Trace amounts

Table 2 Elemental mineral components of the *M. piperita* leave extract

Mineral	% composition
Calcium	0.075
Magnesium	0.015
Sodium	7.780
Potassium	24.020
Phosphorus	0.340

Table 3 Components of the essential oil of *M. piperita*

Oil Components	*M. piperita*	RT
Pinene	0.27	5.853
Sabinen	0.20	6.975
Laevo-beta-Pinene	0.44	7.129
Beta Myrcene	0.59	7.474
Alpha phelladrene	0.10	7.797
p-Cymene	0.51`	8.611
D-Limonene	1.30	8.824
Cineole	4.62	8.882
D-isomenthone	0.61	10.142
Menthofuran	0.71	10.473
Isomenthone	0.36	10.743
Neo-menthol	6.78	11.365
(+)-menthol	38.06	11.793
Neoisomenthol	1.08	12.655
L-(-)-menthol	0.79	13.132
Isomenthol acetate	3.38	13.454
Menthol	35.64	13.865
Thymol	0.50	15.010
Beta bourbonene	0.21	15.922
Caryophyllene	0.48	17.087
Spathulenol	0.11	17.776
Caryophyllene oxide	0.76	18.065
	96.5%	

Table 4 Antibacterial activity of *Mentha piperita* against various microorganisms

Test Organism	Essential Oil		Methanolic extract		Standard	
	20µl	10µl	20µl	10µl	20µl	10µl
S. saprophyticus	13.0 ±2.3	11.3 ±2.3	10.3 ±1.5	8.3 ±0.7	16.3 ±1.2	12.3 ±0.7
S. aureus	15.0 ±1.7	14.3 ± 2.3	12.7 ± 1.4	10.6 ± 2.3	17.5 ±1.7	15.1 ±2.3
Escherichia coli	15.3 ±2.0	12.0 ±1.7	11.4 ±1.5	9.0 ±1.7	11.3 ±0.9	16.5 ±1.3
P. aeruginosa	8.3 ±0.1	-	7.6±2.1	-	10.4 ±2.4	10.4 ±1.1

(-) No zone, Zone of inhibition (mm), Mean ± SD

Discussion

The results of phytochemical screening of leaf extract of *M. piperita* revealed the presence of alkaloids, flavonoids, saponins, volatile oil, cardiac glycosides, tannin and glycosides (Table 1). The presence of these components in this species is an indication that it may have some medicinal potential. This is due to the fact that each of the components identified has one therapeutic usage or another. For instance, plants rich in saponins have immune boosting and antiinflammatory properties (Kenner and Requena, 1996). Similarly, tannins have been reported to have antibacterial potential due to their basic character that allows them to react with proteins to form stable water soluble compounds thereby killing bacteria by directly damaging its cell membrane (Ade-Ajayi *et al.*, 2011). The antibacterial activities of alkaloids and flavonoids have been reported by a number of authors (Hassan *et al.*, 2005; Aliero *et al.*, 2008; Yesmin *et al.*, 2008). They can be very good alternatives for antibiotics if properly and thoroughly studied for these effects (Babar *et al.*, 2015).

Table 2 shows the concentrations of minerals (sodium, magnesium, calcium, and potassium). The potassium content showed in the result was relatively small compared to the one reported previously (Fasuyi, 2007). The phosphorus content obtained in this study was in agreement with that obtained by previous report (Heleno *et al.*, 2013), while the values of sodium, calcium and magnesium content where higher than those reported by Erukainure *et al.* (2011). In general, the most abundant elements are potassium, calcium, sodium, magnesium and phosphorus minerals. Potassium was the most abundant element present in the sample (24.020 %), followed by sodium (7.780%) and phosphorus (0.34%). The lowest mineral content detected was calcium (0.075%). Iron was found not detected in both samples.

Table 3 the essential oil consist of complex chemical mixtures that vary widely in chemical composition. A total of 22 components, accounting for 95.59 of the total oil, was identified in the *M. piperita* essential oils. (+)-Menthol (38.06%), menthol (35.64%), neomenthol (6.78%) and cineole (4.62%) were the main components in the oil of *M. piperita* (Table 2). The chemical composition of *M. piperita* characterized by the presence of oxygenated monoterpenes such as menthol, menthone, menthyl acetate, sabinene hydrate menthofurone and 1,8 cineole (Agarwal, 2008). Aflatuni (2005) reported that menthol content in *M. piperita* origins ranged from 9.8 to 26.2%. Moreover, menthol content of different peppermint origin varies from 10% to 63% and menthone content from 12% to 76%. The results of menthol content of this study are compatible with those reported by Aflatuni (2005) and European Pharmacopoeia (1997) as 30% - 55%. Many scientific literatures revealed the antimicrobial potential of essential oils (Mimica-Dukic et al. 2003; Gulluce et al. 2007; Hussain, 2009). In view of the multiple applications of essential oils, their characterization based on their chemical profiles, is of great importance. Moreover, seasonal variation, especially harvest time, affects also significantly biological activities of oils.

It reported that peppermint oil exhibit strong activity against a wide range of human pathogenic Gramm-positive and Gramm-negative bacteria and fungal strains (Mimica-Dukic *et al.*, 2003; Gulluce *et al.*, 2007). The result from table 4 activity against all the tested bacterials except *P.*

aeruginosa which no activity at concentration of 10µl. The result of this study justifies the use of *M. piperita* in ethnomedicine for the treatment of infectious diseases caused by susceptible bacterial species.

Conclusion

This study allowed concluding that *M. piperita* hydro-distillation extract possesses very important chemical constituents as major compounds and also contains important minerals. In contrast, the essential oil showed strong antibacterial properties comparedtothe methanolic extract. In this way, *M. piperita* extracts and essential oil have a huge potential as alternatives to synthetic drug in pharmaceutical industry. Further studies should evaluate the safety and toxicity of essential oil extracted from *M. piperita* to human consumption before considering their use for medicinal purposes.

Reference

Ade-Ajayi, A. F., Hammuel, C., Ezeayanaso, C., Ogabiela, E. E., Udiba, U. U., Anyim, B. and Olabanji, O. (2011). Preliminary Phytochemical and Antymicrobial Screening of Agave sisalana Perrine juice (waste). *Journal of Environmental Chemistry and Ecotoxicological*, 3(7): 180-183

Aflatuni, A. (2005). The yield and essential oil content of mint (*Mentha* ssp.) in Northern Ostrobothnia. (http://herkules.oulu.fi/ isbn9514277465/), Oulu University Press, Finland, 52 p.

Agarwal, A.A. (2008). Chemical composition of Major Essential oil of India. Published by Swaraj Herbal Plants Ltd. Barabanki, India.

Aliero, A.A., Aliero, B.L. and Buhari, U. (2008). Preliminary Phytochemical and Antibacterial screening of *Scadoxus maltiflorus, International Journal of Pure and Applied Sciences*, **2(4):** 13-17

Babar, A., Naseer, A.A., Saiba S., Aftab, A., Shah, A.K., Firoz, A. (2015). Essential Oils Used in Aromatherapy: A systematic Review. *Asian Pacific Journal of Tropical Biomedicine* 5(8): 601-611

Berdowska, I., Zieliński, B., Fecka, I., Kulbacka, J., Saczko, J., Gamian, A. (2013). "Cytotoxic Impact of Phenolics from Lamiaceae Species on Human Breast Cancer Cells" in *Food Chemistry*, Vol. 141. No. 2 pp. 13-21.

Cowan MM (1999). Plant products as antimicrobial agents. Clin. Microbiol. Rev., 12: 564-582.

Dunning T, (2013). Aromatherapy: overview, safety and quality issues. OA Altern Med ; 1(1): 6. Pp219-219.

Erukainure, O., Oke, O., Ajiboye, A., Okafor, O. (2011). "Nutritional Qualities and Phytochemical Constituents of *Clerodendrum volubile*, A Tropical Non-Conventional Vegetable" in *International Food Research Journal*, Vol. 18. No. 4 pp.1393-1399.

European Pharmacopoeia, (1997). 3rd ed. Strasbourg, France: Council of Europe, 1298–1300.

Fasuyi, A.O. (2007). "Bio-Nutritional Evaluations of Three Tropical Leaf Vegetables (*Telfairia occidentalis, Amaranthus cruentus* and *Talinum triangulare*) as Sole Dietary Protein Sources in Rat Assay" in *Food Chemistry*, Vol. 103. No. 3 pp. 57-65.

Fatemi, F., Dini S, Rezaei, M.B., Dadkhah, A., Dabbagh, R., Naij, S. (2014). "The Effect of γ-Irradiation on the Chemical Composition and Antioxidant Activities of Peppermint Essential Oil and Extract" in *Journal of Essential Oil Research*,Vol. 26. No. 2 pp. 97-104.

Gulluce, M., F. Sahin, M. Sokmen, H. Ozer, D. Daferera, A. Sokmen, M. Polissiou, A. Adiguzel, H. Ozkan, (2007).Antimicrobial and antioxidant properties of the essential oils and methanol extract from *Mentha longifolia* L. ssp. *longifolia*. Food Chem. 103: 1449–1456.

Halilu, M. E., Abubakar, A., Garba, M. K. and Isah, A. A. (2012). Antimicrobial and Preliminary Phytochemical Studies of Methanol Extract of Root Bark of *Crossopteryx febrifuga* (*Rubiaceae*). *Journal of Applied Pharmaceutical Sciences*, 2(12), 67 – 70.

Hassan, S.W., Umar, R.A., Ebbo, A.A. and Matazu, I.K. (2005). Phytochemical, antibacterial and toxicity studies of *Parkinsonia aculeate* L. (Fabaceae), *Nigerian Journal of Biochemistry and Molecular Biology*, 20(2): 89-97.

Heleno, S.A., Stojković, D., Barros, L., Glamočlija, J., Soković, M., Martins, A. (2013). "A comparative Study of Chemical Composition, Antioxidant and Antimicrobial Properties of *Morchella esculenta* (L.) Pers. from Portugal and Serbia" in *Food Research International*, Vol. 51. No. 1 pp. 36-43.

Hussain, A.I. 2009. Characterization and Biological Activities of Essential Oils of Some Species of Lamiaceae. PhD Thesis, 257 p., Faisalabad, Pakistan.

İşcan, G., Kirimer, N., Kürkcüoğlu, M.N., Başer, H.C., Demirci, F. (2002). "Antimicrobial Screening of *Mentha piperita* Essential Oils" in *Journal of Agricultural and Food Chemistry*, Vol. 50. No. 14 pp. 43-6.

Jatto, O., Asia, I., Medjor, W. (2010). "Proximate and Mineral Composition of Different Species of Snail Shell" in *Pacific Journal of Science and Technology*, Vol 1. No.11 pp. 416-9.

Kenner, D. and Requena, Y. (1996). *Botanical medicine*: A European professional perfective. Paradign publication Brookline, Massachusetts. Pp 7-12

Khoddami, A., Wilkes, M.A., Roberts, T.H. (2013). "Techniques for Analysis of Plant Phenolic Compounds" in *Molecules*, Vol. 18. No. 2 pp. 28-75.

Kolapo, A. L., Okunade, M. B. and Ogundiya, M. O. (2009). Phytochemical Composition and Antimicrobial Activity of *Prospis africana* against Some Selected Oral Pathogens. *World Journal pf Agricultural Sciences*, 5, 90 – 93.

Marjani, A., Rahmati, R., Mansourian, A.R., Veghary, G. (2012). "Effect of Peppermint Oil on Serum Lipid Peroxidation and Hepatic Enzymes After Immobility Stress in Mice" in *The Open Biochemistry Journal*, Vol. 6. No. 51. pp. 51-55.

Mimica-Dukic, N., B. Bozin, M. Sokovic, B. Mihajlovic, M. Matavulj, (2003). Antimicrobial and antioxidant activities of three Mentha species essential oils. Planta Med. 69: 413–419.

Ramasamy, M. V., Kalidass, C. (2010) "Nutritional and Antinutritional Evaluation of Some Unconventional Wild Edible Plants" in *Tropical and Subtropical Agroecosystems*, Vol. 12. No. 3 pp 495-506.

Raut, J.S., Karuppayil, S.M. (2014). "A Status Review on the Medicinal Properties of Essential Oils" in *Industrial Crops and Products*, Vol. 62. No. 2 pp. 50-64.

Rubatzky, V.E, Yamaguchi, M. (2012). *World Vegetables: Principles, Production, and Nutritive Values*. Springer, Boston, MA.

Singh, V.K., Bikundia, D.S., Sarswat, A., Mohan, D. (2012). "Groundwater Quality Assessment in the Village of Lutfullapur Nawada, Loni, District Ghaziabad, Uttar Pradesh, India" in *Environmental Monitoring and Assessment*, Vol. 184. No. 7 pp. 73-88.

Sofowora, A. (1982). *Medicinal plants and Traditional medicine in Africa*, 2nd edition, Spectrum BookLimited, Ibadan.

Trease, G. E. and Evans W. C (1999). *Pharmacognosy* 14th edition W.B Saunders Company Limited, New York. Pp 1-34.

Yesmin, M.N., Uddin, N.S., Sanzida, M., and Muhammad A.A. (2008). Antioxidant and Antibacterial Activities of *Calotropis procera*. *American-Eurasian Journal of Agric and Environmental Science*, **4** (5): 550-553.

Zmora, P., Cieslak, A., Pers-Kamczyc, E., Nowak, A., Szczechowiak, J., Szumacher-Strabel, M. (2012). "Effect of *Mentha piperita* L. on *in vitro* Rumen Methanogenesis and Fermentation" in Acta Agriculturae Scandinavica, *Section A–Animal Science*, Vol. 62. No. 1 pp. 46-52.

Prevalence of *Escherichia coli* in Some Selected Well in Bida Metropolis, Niger State, Nigeria

*Aisha Bisola Bello, Abdullahi Idris Dabban, and Alhassan Taiwo Olutimayin
Department of Biological Sciences, Federal Polytechnic Bida, Niger State, Nigeria.
aidabban@gmail.com
alhassanolutimayin8@gmail.com
*Corresponding author: belloaisha91@gmail.com

ABSTRACT

In developing countries such as Nigeria, majority of rural dwellers depend on well water as their main source of water supply for drinking and other domestic activities. This source of water can be easily contaminated by faecal contaminants and human activities. An investigation was carried out to determine the water quality and prevalence of Escherichia coli in selected well water within Bida metropolis. Well water samples (10 closed and 5 open) were collected from selected points in Bida metropolisThe total coliform of the water sample were determined using multiple tube fermentation technique. Some physicochemical parameters such as temperature, pH and dissolved oxygen were also determined. In all the well water samples collected, a high prevalence of E.coli and coliform was observed, which ranged between 0.1 x10^2 – 0.2 x10^{2}MPN/100ml and 0.15 x10^2 - 11 x10^2 MPN/100ml which exceeds the zero MPN/100ml World Health Organisation (WHO) recommended standard. The pH of the water samples ranged from 6.0 to 6.8, which conform to the WHO standard of 6.5 to 8.5. Dissolved oxygen presented in this study ranged from 1.3 to 2.9mg/L, which is within the 1.0 to10mg/L recommended standards. This study showed a high bacteriological contamination by the presence of disease causing pathogens in well water in Bida metropolis. Management of this contamination can be achieved by treatments of the well water, educational awareness, digging deeper wells and locating wells far away from dumping sites and latrines.

Key words: Escherichia coli, Well water, Coliform, World Health Organisation.

Introduction

Water is a universal solvent, which is fundamentally important to all living things such as plants, animals and humans. It occupies about 71% of the earth crust (Mullen, 2021) and it is the major constituent of the human body weight (Williams *et al.,* 2002).Water has many strong unique properties that are so important to life on the planet. These properties includes, it is colourless; tasteless; odourless; it dissolves nearly in everything and exists as solid, liquid and gas and it is part of every living organism on the planet (Umar *et al.,* 2019). Access to safe and affordable water for drinking and domestic purposes is an essential attribute for prevention of disease outbreaks and improving quality of life (Borchard *et al.,* 2004). However, most rural areas in developing countries do not have access to potable water or treated water but rely on locally available untreated water (Umar *et al.,* 2019).

Water contamination is often as a result of sewage, waste water treatment facilities and other anthropogenic activities that can alter the physical and chemical characteristics of water. Water intended for human consumption must be free from organisms and chemical substances that may be hazardous to health. The absence of turbidity, colour, or any disagreeable taste or smell is of utmost importance in public drinking water suppliers. It a universal solvent and yet the most treacherous vehicle for transmitting diseases (Pelczar *et al.,* 2003). It harbors a variety of microorganisms such as bacteria, protozoa, virus, fungi, algae. The presence of bacteria and pathogenic (disease-causing) organisms is a concern when considering the safety of drinking water. These pathogenic organisms can cause intestinal infections, dysentery, hepatitis, typhoid fever,

cholera, salmonellosis, amoebic dysentery and other illnesses (Syed *et al.*, 2012). The inadequate supply of clean drinkable water and the frequent pollution of existing supplies has become a serious public health concern globally. Water borne diseases have been reported to be responsible for more than 5million death annually (Liew and Lepesteur, 2006; Malik *et al.*, 2012). It was also reported that water borne pathogens are infecting about 250million people annually with 10 – 20 million deaths (Dzwairo *et al.*, 2006; Malik *et al.*, 2012). In developing countries, diarrhea is a leading cause of death for children under the age of five (Ozkan *et al.*, 2007).

Total coliforms and *Escherichia coli* are indicators recommended by World Health Organization for the surveillance of water for microbial pathogens (Standridge 2008; World Health Organization 2011). The WHO also recommended that *E.coli* serves as a vital parameter for minimum water monitoring (World Health Organization 2011). *Escherichia coli*a member of the fecal coliform group, is a more specific indicator of faecal contamination than other faecal organisms (Odonkor and Ampofo 2013). Other faecal organisms include *Klebsiella* spp., *Salmonella* spp., *Citrobacter* spp. and *Enterobacter* spp. The consumption of faecal contaminated water does not always translate into infection, however the higher the faecal contaminant, the higher the microbial load present in the water. (Syed *et al* 2012).
To ensure the availability of safe and potable drinking water, multiple approach is required such as legislation and guidelines, monitoring and management, public awareness and research for innovative technological solutions (Federal-Provincial-Territorial Committee on Drinking Water and Canadian Councils of Ministers of the Environment, 2002). However, people living in rural areas are not subjected to the legislation of drinking water as they often depend on ground water such as wells, which are mostly untreated. This exposes them to greater risk of waterborne disease and outbreaks than those living in the urban or developed regions (Galanis *et al.*, 2014; Invik *et al.*, 2017). Several studies have documented the prevalence of *E. coli* in drinking water such as 45% in Gusau Nigeria (Garba *et al.*, 2009) and 60% in Zaria, Nigeria (Umar *et al.*, 2019) respectively. This study investigated the prevalence of *E. coli* in some selected well water from Bida Metropolis, North-central Nigeria.

Methodology

Sample collection

Fifteen water samples were collected asceptically from fifteen different wells using a water drawer (guga) in fifteen different locations in Bida metropolis. The samples were collected in a 200ml sterile bottle, labeled appropriately and transported in an ice pack container to the microbiology laboratory of federal polytechnic Bida, Niger state for analysis. The following physiochemical analysis (Temperature, pH, and dissolved oxygen) were taken at the point of sample collection using the standard methods (APHA, 1999)

Total coliform count

The multiple tube fermentation technique (3–3–3) was used to determine the most probable number (MPN) per 100ml of the well water samples. A volume of 10ml of water was dispensed into three test tubes of double strength lactose broth (Oxoid®, U.K), 1.0ml was inoculated into three test tubes of single strength lactose broth and 0.1 ml into three test tubes of single strength lactose broth. All the tubes were incubated and observed after 24−48 hours for production of gas which indicates positive presumptive test of coliform bacteria. This method was carried out for all samples collected.

Presumptive test

After 48 hours, the incubated test tubes where checked for change in coloration and gas production in the durham tubes. The fermentation tubes with gas production were used to carry out the confirmatory test. The total coliform count was obtained by the combination of positive tubes using the standard table of MPN from Bacteriological Analytical Manual (1998) to record the estimated bacteria count (Bacterialogical Analytical Mannual, 1998; APHA, 1999).

Confirmatory test

Brilliant green lactose bile broth (Oxoid®, U.K) was prepared in test tubes with inverted Durham's tubes inside them according to manufacturer's instruction. A loopful of inoculum from the positive tubes in presumptive test was inoculated onto the brilliant green lactose bile broth and incubated for 24- 48 hours at 35℃. The presence of gas, turbidity and color change in test tubes indicates a positive confirmed test for total coliform bacteria and tubes without gas production indicates negative results (APHA 1999).

Completed test

The positive tubes from presumptive test were inoculated into eosin methylene blue (EMB) agar and incubated for 24 hours at 35℃. Growth observed on Eosin methylene blue after 24 hours indicates the presence of faecal contaminant (*Escherichia coli*). Pure isolates were picked and transferred to nutrient agar slant, incubated for 24 hours at 35℃. The slants are refrigerated for further analysis (Gram's staining and biochemical test).

Identification of Bacteria Isolates

Gram's staining of colonies from EMB was carried out to identify the grams reaction of the isolates. Identification was done using Microscope to examine the smear with oil immersion objective lens and report bacteria as gram positive or gram negative (Chessbrough, 2000). Pure bacterial isolates from nutrient agar were identified morphologically. Biochemical test was carried out using the Microgen Biochemical Identification Kit GN-A according to the manufacturer's instructions to identify the isolates down to species level and comparing their characteristics with the known taxa as described by Oyeleke and Manga (2008).

Results

Of the 15 well water samples collected from 15 different locations in Bida metropolis in duplicate,ten (10) were from closed well and five (5) were from open well. Table 1 and Table 2 show the physiochemical parameters of the water samples for both closed well and open well respectively. For closed well, the pH ranged from 6.0-6.55 and open well ranged from 6.33-6.8. The range for dissolved oxygen in closed well was 1.3-2.90 and open well was 1.6-2.5. The maximum temperature was observed in samples B and G (28.86℃) and the minimum was in sample A (28.26℃) for closed well while for open well, the highest temperature was in sample A (29℃) and lowest in sample E (28.66℃)

Table 1: Physiochemical Parameter of close well water sample from Bida Metropolis

Parameters	Samples									
	A	B	C	D	E	F	G	H	I	J
Temperature(℃)	28.26	28.86	28.60	28.76	28.80	28.70	28.86	28.27	28.56	28.66
pH	6.25	6.44	6.34	6.55	6.0	6.49	6.5	6.36	6.27	6.33
Dissolved Oxygen (DO)	1.76	2.90	1.60	1.52	1.3	1.50	1.52	1.49	1.77	1.60

KEY: Efu-liman (A); Gbazi (B); Masaba (C); Takowasa (D); Dokoza (E); Sabongida (F); Tako-Ladzu (G); Darachita (H); Tswatamukun (I); Endazabo (J)

Table 2: Physiochemical Parameter of open well water sample from Bida Metropolis

Parameters	Samples				
	A	B	C	D	E
Temperature (℃)	29.0	28.86	28.76	28.76	28.66

pH	6.8	6.7	6.50	6.55	6.33
Dissolved Oxygen (DO)	2.0	2.5	1.7	1.6	1.6

KEY: Efu-liman (A); Masaba (B); Dokoza (C); Tako-Ladzu (D); Tswatamukun (E)

The result of the coliform count is presented in Tables 3 and 4 for close and open well water samples respectively. The coliform count ranged from 0.15 MPN/100ml to 3.5 MPN/100 ml for closed well water and 1.2 MPN/100ml to 11.0 MPN/100ml for open well water. Samples B and I had the highest coliform count of 2.4MPN/100ml for closed well water and 11MPN/100ml in samples D and E in open well water.

Table 3: Total Coliform Count for Closed Well Water Samples Using MPN Technique

	Number of Positive Test Reaction			
Water Samples	3 of 10ml	3 of 1ml	3 of 0.1ml	MPN Index per 100ml
A	2	2	2	0.35
B	3	3	0	2.4
C	3	2	0	0.93
D	3	1	1	0.75
E	3	2	1	0.15
F	3	0	2	0.64
G	3	1	1	0.75
H	2	1	0	0.15
I	3	3	0	2.4
J	2	2	1	0.28

KEY: Efu-liman (A); Gbazi (B); Masaba (C); Takowasa (D); Dokoza (E); Sabongida (F); Tako-Ladzu (G); Darachita (H); Tswatamukun (I); Endazabo (J)

Table 4: Total Coliform Count for Open Well Water Samples Using MPN Technique

	Number of Positive Test Reaction			
Water Samples	3 of 10ml	3 of 1ml	3 of 0.1ml	MPN Index per 100ml
A	3	1	2	1.2
B	3	3	0	2.4
C	3	3	1	4.6
D	3	3	2	11
E	3	3	2	11

KEY: Efu-liman (A); Masaba (B); Dokoza (C); Tako-Ladzu (D); Tswatamukun (E)

The prevalence of *E. coli* was 100% as it was present in all water samples collected. The result for the bacteriological analysis in Table 5 and Table 6 showed the presence and bacteriological count of *E. coli* of both closed and open well water samples respectively in the study area. High count of *E.coli* was observed in samples H,D,G and A (0.17-0.2 MPN/100) and low count in sample B (0.1 MPN/100) for close well water while high count was observed in samples A and E (0.14 MPN/100) and low count in sample D (0.1 MPN/100) for open well water.

Table 5: Total Bacteriological count of *E.coli* per 100ml of Close well water samples

Samples	E.coli count MPN/100ml
A	0.17

B	0.1
C	0.15
D	0.19
E	0.13
F	0.16
G	0.17
H	0.20
I	0.13
J	0.15

KEY: Efu-liman (A); Gbazi (B); Masaba (C); Takowasa (D); Dokoza (E); Sabongida (F); Tako-Ladzu (G); Darachita (H); Tswatamukun (I); Endazabo (J)

Table 6: Total Bacteriological count of *E. coli* per 100ml of Open well water samples

Samples	E.coli count MPN/100ml
A	0.14
B	0.13
C	0.12
D	0.10
E	0.14

KEY: Efu-liman (A); Masaba (B); Dokoza (C); Tako-Ladzu (D); Tswatamukun (E)

Discussion

The pH of water in this study was slightly alkaline in nature compared to the recommended standard pH for human consumption valued at 7.4 (Parker, 2013) but falls within the WHO standard pH value for water 6.5-8.5. The alkalinity of water supports the survival of coliform bacteria (Wahyun, 2015), which may be associated with increased coliform count and water borne diseases. The acidic component of a water sample attributes to the delay of cholera outbreak because it does not support the growth of *Vibrio cholera*. Charles and Angelo (2004) reported that *Vibrio cholerae* grows best under alkaline condition. Therefore, acidic environment keeps the microbial contamination low and the risk of infection or diseases low. WHO guideline recommended a controlled pH to avoid corrosion and contamination of water which may have health consequences. However, slight change in optimum temperature (25℃ -40℃) may inhibit or support the growth and survival of bacteria in water especially coliform bacteria. The temperature range recorded in this study was 28.26℃ -29℃ at the point of sampling. Optimum temperature for the growth and proliferation of enterobacteriaceae was recorded as 10℃ to 37℃ (Prescott, *et al.*, 2002). Samples in this study showed low DO with the lowest having 1.3mg/l but falls within the WHO standard of 1-10mg/l. Decrease level of dissolve oxygen indicates the presence of high level of bacteria which leads to high biological oxygen demand (BOD).

Coliform bacteria are indicators of contaminated of water posing a public health risk to the general population (CDC, 2020). The bacteria are widely used as an index of bacteriology quality of water (Ahmed *et al.*, 2005), which is attributed as the causative organism for gastroenteritis in humans. In this study, the coliform bacteria count did not match the zero (0) MPN/100ml standard for drinking water recommended by International Standard for Drinking Water, WHO and CDC (WHO, 1971; CDC, 2020). However, according to WHO (1958) standard for untreated water and the National ground water association, less than 10MPN/100ml (≤10cfu/100ml) can be acceptable for a certain period of time. Equally the high coliform count indicates the likely presence of other pathogenic organism in the water sample analyzed.

The prevalence of *E. coli* in this study indicates a possible high microbial load and pollution in the water samples. The rate of E.coli isolated in this study does not conform to the zero MPN/100ml recommended standard for drinking water (Wagner and Lanoix, 1958; WHO, 1971) and zero (0)

Maximum Contaminant Level Goal (0mg/ml) recommended by the CDC (2020). World Health Organisation (WHO, 1997) also recommended that both treated and untreated water samples should have zero *E. coli* presence. Similar studies, Garba *et al.,* (2009) and Ibrahimagic *et al.,* (2015) have also reported high prevalence of *E.coli* 45.5% and 25.4 % respectively from well water samples. Petit *et al.*, (2017) also identified a direct association between the density of *E. coli* microbes in water and the prevalence of water-related gastroenteritis. This association accounts for the use of *E. coli* as an indicator of water quality and by extension, a signal of human, domestic, and natural sources of faecal contamination (Odonkor and Ampofo, 2013; McLellan and Eren 2014; Nkansah *et al.*, 2010; Odagiri *et al.*, 2016; Pritchard *et al.*, 2016).

Conclusion

From the results obtained, it can be deduced that all the well water samples analyzed are not safe for human consumption and do not meet the required WHO standards of zero per 100ml of sample for faecal coliform. The pH and temperature were found to be suitable for high bacterial count. The presence of *Escherichia coli* in the water samples indicates a possible presence of other pathogenic disease causing microorganisms posing health risk to the public There should be a policy and regulation inplace for the construction of wells far from refuse dump, drainage systems, proper covering to minimize contamination. Simpler methods for treatment of water should also be developed and emphasized on to make well water safe for consumption.

References

Ahmed, W., Neller, R. and Katouli, M. (2005): Host Species specific metabolic finger print Database for Enterococci and Escherichia coli and its application to identify source of faecal contamination in surface waters. *Applied and Environmental Microbiology*. 71 (8): 4461-4468.

American Public Health Association (APHA) (1999). American Water Works Association. Water environment federation. American Public Health Association Inc. Washington DC. 1-46.

Borchard, M.A., Haas, N.L. and Hunt, R.J. (2004). Vulnerability of drinking water wells in La Crosse, Wisconsin, to enteric –virus contamination from surface water contributions. *Journal of Enteric and Viral Diseases*. 2: 12–27.

CDC (2020). Drinking Water Standards and Redulations. https://www.cdc.gov/healthywater/drinking/public/regulations.html Accessed 12 August, 2021.

Charles, A.K. and Angelo D. Jr. (2004). Bacteriological analysis manual. US Department of Health and Human Services FDA, US Food and Drug Administration. 3-32.

Cheesbrough M. (2000). Medical laboratory manual for tropical countries, water and sanitation decades. Bacteriological testing of water samples, 3rd edition Baltimore, and John Hopkins University press. Test kits for detection of coliforms, Escherichia coli and other indicators. *Applied and Environmental Microbiology*. 59:380-382.

Dzwairo, B., Hoko, Z., Love, D., Ghuza, E. (2006). Assessment of the impacts of pit latrines on ground water quality in rural areas: A case study from Marondera district, Zimbabwe. *Physics Chemistry of the Earth.* 31(15–16):779–788.

Federal-Provincial-Territorial Committee on Drinking Water, CCME Water Quality Task Group (2002). From source to tap: Guidance on the multi-barrier approach to safe drinking water. https://www.canada.ca/content/dam/hc-sc/migration/hc-sc/ewh-semt/alt_formats/hecs-sesc/pdf/water-eau/tap-source-robinet/tap-source-robinet-eng.pdf (accessed 19 September, 2021).

Galanis, E., Mak, S., Otterstatter, M., Taylor, M., Zubel, M.,Takaro, T. K., Kuo, M. & Michel, P. (2014). The association between campylobacteriosis, agriculture and drinking water: a case-case study in a region of British Columbia, Canada, 2005–2009. Epidemiology and Infection. 142(10); 2075–2084.

Garba, I., Tijjani, M.B., Aliyu M.S., Yakubu, S.E., Wada-Kura, A. and. Olonitola, O.S (2009). Prevalence of Escherichia Coli in Some Public Water Sources in Gusau Municipal, North -Western Nigeria. *Bayero Journal of Pure and Applied Sciences*. 2(2): 134 – 137.

Ibrahimagic A, Basic N and Idrizovic E. (2015). Prevalence of *Escherichia Coli* in Drinking Water Collected From the Local and Municipal Water Supply in Zenica-Doboj Canton, Bosnia and Herzegovina. SM Journal of Public Health and Epidemiology. 1(4):1017.

Invik, J., Barkema, H.W., Massolo, A., Neumann, N.F. and Checkley, S. (2017). Total coliform and Escherichia coli contamination in rural well water: analysis for passive surveillance. *Journal of Water and Health*. 15(15); 729-740.

Liew, K.B.and Lepesteur, M. (2006). Performance of the rural health improvement scheme in reducing the incidence of waterborne diseases in rural Sarawak, Malaysia. *Transactions of The Royal Society of Tropical Medicine and Hygiene*. 100(10):949–955.

Malik, A., Yasar, A., Tabinda, A., & Abubakar, M. (2012). Water-borne diseases, cost of illness and willingness to pay for diseases interventions in rural communities of developing countries. *Iranian Journal of Public Health*. *41*(6); 39–49.

McLellan, S.L. and Eren, A.M. (2014). Discovering new indicators of fecal pollution. *Trends in Microbiology*. 22(12); 697–706.

Mullen, K. (2021). Information on earth water. Available at https://www.ngwa.org/what-is-groundwater/About-groundwater/information-on-earths-water [access date 19 September 2021]

Nkansah, M.A., Boadi, N.O. and Badu, M. (2010). Assessment of the quality of water from hand-dug wells in Ghana. *Environmental Health Insights*. 4(2); 7–12.

Odagiri, M., Schriewer, A., Daniels, M.E., Jenkins, M.W. (2016). Human fecal and pathogen exposure pathways in rural Indian villages and the effect of increased latrine coverage. *Water Research.* 100; 232–244.

Odonkor, S.T. and Ampofo, J.K. (2013). Escherichia coli as an indicator of bacteriological quality of water: An overview. *Microbiological Research*. 4(1):5-11.

Oyeleke, S.B. and Manga, S.B. (2008). Essentials of Laboratory Practicals in Microbiology. Tobest Publisher, Minna. Nigeria. 36-75.

Ozkan, S., Tuzun, H., Gorer, N., Ceyhan, M., Aycan, S., Albayrak, S., Bumin, M.A. (2007). Water usage habits and the incidence of diarrhea in rural Ankara, Turkey. *T Roy Soc Trop Med H.* 101(11):1131–1135.

Parker, K.T. (2013). What are the benefits of drinking alkaline water?. Available: http://www.livestrong.com/article/498701-what-are-the-benefits-of-drinking-alkaline-water/.

Pelczar, M.T., Chan, E.C.S., Krieg, N.R. (2003). Water purification: Microbiology. Fifth edition, McGraw Hill, USA. 2056-2120.

Petit, F, Clermont O, Delannoy S, Servais P, Gourmelon M, Fach P, Oberlé K, Fournier M, Denamur E and Berthe T (2017). Change in the structure of *Escherichia coli* population and the pattern of virulence genes along a rural aquatic continuum. *Frontiers in Microbiology*. 8; 609.

Prescott, LM, Harley JP, Klein DA. (2002). Microbiology. 5th edition. The McGraw-Hill Companies, USA. 125-654.

Pritchard, M., Edmondson, A., Craven, T. and Mkandawire, T. (2016). Development of sustainable drinking water quality solutions for rural communities in the developing world. *Sustainable Ecological Engineering Design*. 259–277, Springer, Berlin.

Standridge, J. (2008). E. coli as a public health indicator of drinking water quality. *Journal-American Water Works Association.* 100: 65–75.

Syed, A.M., Shah Z.A., Ahmed O., Tareq A.H., and Ali F. (2012). Investigation Into The Prevalence Of Enterococci And Coliform Bacteria In Drinking Water Resources And Associated Gastroenteric Issues In Islamabad Region Pakistan. *Journal of Applied Pharmacy*. 02(04): 593-605

Umar, M., Kambai, J., Mohammed, I.B., Oko, J.O., Obafemi. A.A., Murtala, I., Ajiya, K.G., Yaya, A.A., Abdulkarim, I.M., Akafyi, D.E., Idris, S., Tashi, U.T. and Ahmed, S. (2019). Bacteriological Quality Assessment and Antibiogram Profile of Bacteria Associated with Sachet Drinking Water Sold at Zaria, Northern Nigeria. I*nternational Journal of Pathogen Research. 2(2): 1-13.*

United States. (1998). *Bacteriological analytical manual, 8th edition, 1998 and Foodborne pathogenic microorganisms and natural toxins handbook, 1998*. Gaithersburg, MD: AOAC International.

Wagner, E.G. and J.N. Lanoix, (1958). Excreta disposal for rural areas and small community World Health Organisation. Monog. No. 39 Geneva.

Wahyuni, E. A (2015). The Influence of pH Characteristics on The Occurance of Coliform Bacteria in Madura Strait. *Procedia Environmental Sciences*. 23; 130 – 135.

William, C., Sonzogoni, P., Standridge, J. and Bussen, M. (2002). Madison Preservation and Survival of *E. coli* in Well Water Sample. Wisconsin State Laboratory of Hygiene, University of Wisconsin. Submitted for routine analysis. 4-10.

World Health Organization (WHO) (1971). International Standards for Drinking water. 3rd ed. Geneva, Switzerland. Available at https://apps.who.int/iris/bitstream/handle/10665/39989/9241540249_eng.pdf;sequence=1.

World Health Organization (1997). Guideline for Drinking Water Quality. Surveliance and control of community and supplies. 3(4):96-219. Available at https://www.who.int/water_sanitation_health/dwq/gdwqvol32ed.pdf

World Health Organization (2004). Guidelines for drinking water quality. 3rd ed. Vol 1 Recommendation, Geneva, Switzerland. Available at https://www.who.int/water_sanitation_health/dwq/GDWQ2004web.pdf

World Health Organization (1958). International Guideline for Drinking Water.

World Health Organization (2011). Guidelines for Drinking-Water Quality, 4th edn. WHO, Geneva, Switzerland. http://apps.who.int/iris/bitstream/handle/10665/44584/9789241548151_eng.pdf?sequence=1 (accessed 19 September 2021).

Studies on Fungi Associated with Date Fruit (*Phoenix dactylifera* Linn) Sold in Bida, Niger State, Nigeria

*Abdullahi Asma'u Muhammad, and Alhassan Taiwo Olutimayin
Department of Biological Sciences, Federal Polytechnic Bida, Niger State, Nigeria.
abdullahiasmau7@gmail.com
alhassanolutimayin8@gmail.com
*Corresponding author

Abstract

A study was carried out on the fungi associated with healthy date fruits (Phoenix dactylifera Linn). Samples of healthy dried dates were collected from vendors of six selected retail points in Bida metropolis Niger State, Nigeria. The samples were processed by cutting into 3 mm sizes with sterilized razor blade and surface was sterilized using 1 % hypochlorite for 2 minutes. The processed samples were plated onto Potato Dextrose Agar and incubated for 5 days at 25°c. Pure fungal isolates and stock cultures were obtained on Potato Dextrose Agar plates and slants bottles using standard mycological procedures. The pure fungi isolates were characterized and identified using standard taxonomic guidelines. The most prevalent fungi obtained from this investigation was Aspergillus sp (50 %) in Big gate, 45 % in Small gate, and 41 % in Lemu and BCC road and the least prevalent fungi was Penicillium sp at 0 % in small and Big gate. Proper storage, use of suitable wrapping sheets, separation of infected from healthy dates and proper washing of dates should be encouraged to reduce the risk of infection by these organisms.

Key words: Fungi, Isolation, Phoenix datylifera Linn (date fruits).

1. Introduction

Date palm (*Phoenix dactylifera* Linn) is a species of flowering plant in the palm family *Arecacea*, cultivated for its edible sweet fruit and originated from lands around Iraq (Kiran, 2014). The species is widely cultivated and is naturalized in many tropical and sub-tropical regions worldwide. The date palm is one of the oldest fruit trees of the world and closely associated with the life of the people in the middle-east including the Kingdom of Saudi Arabia since ancient times, having religious and cultural importance. In Saudi Arabia, dates palm is the most important cash and fruit crop grown in different regions. About 900 thousand tones of the fruit is produced yearly and ranks as third largest producer in the world (FAO, 2008). Date fruits are as well being consumed in many countries of the world, Nigeria inclusive (Redmond, 2009). Dates are oval-cylindrical, 3-7cm long and 2-3cm in diameter and when ripe, range from bright red to bright yellow in colour, depending on the variety and contain a single seed (stone) about 2-5cm long 6-8cm thick (Gepts, 2002).

The date palm tree can be grown extensively and commercially in the arid region of northern Nigeria mostly the Sudan Savannah and the Sahel regions of Kaduna, Katsina, Kano, Sokoto, Kebbi, Zamfara, Jigawa, Yobe, Gombe and Bauchi state (Ikheloa *et. al*. 2002). The fruit is composed of a seed and fleshy pericarp which constitutes between 85% and 90% of date fruit weight (Hussein and Alhadrami, 1998). It has high tannin content and used medically as a cleanser and contrasting in intestinal troubles (Colman and Spencer, 2012). The fruit is consumed in many ways; as an infusion, decoction, syrup or paste, dates may be administered for sore throat, colds, bronchial catarrh and taken to relieve fever (Kiran, 2014). Date fruits are consumed directly in many forms and at all stages of the fruit development and are also utilized in many ways in modern industries (Mustapha *et al*.2003). Syrup, alcohol, vinegar and strong liquor are derived from the fruit. The sap is also used as a beverage, either fresh or fermented (Morton *et al*., 1997). The types of date fruit depend on the glucose, fructose and sucrose contents but date fruits usually contain high percentage of carbohydrate (44.88%), protein (2.3-5.6%), dietary fiber (0.4-1.5%) and fat percentage reach up to (0.2-0.5%) (Al-Kahtani *et. al*.2011).

Date palm fruit (*Phoenix dactylifera*) has been reported to be attacked by a variety of microorganism such as bacteria, yeast, and filamentous fungi (Atia, 2011). It is mostly attacked by fungal species resulting into spoilage during storage and processing (Ahmad, 2003). Although several fungal species are implicated in causing damages to date fruits, many fungal species are capable of producing mycotoxins which are secondary metabolites, highly toxic to human and animals alike (Shamsudeen and Magashi, 2005). These fungi secrete many kinds of enzymes and poisons that causes decay and loss of the nutritional value of the date and makes it unsuitable for consumption (Berbend, 2000; Ibraheem and Klaef, 2003). Fungi and other microorganisms play a significant role in deteriorating the nature and nutritive value of stored food commodities (Christensen *et al*. 2007). Open hawking of date palm fruit is a common practice especially in Northern Nigeria and Bida, Niger state is not an exception. The high patronage of this merchandize (both fresh and dried fruit) is a cause for public health concern in light of report by food and agricultural organization (FAO) of the United Nations that fungi and molds are implicated in the contamination of this fruit (Khomutov *et al*. 2011).

2. Literature Review

Various investigations have been carried out to determine fungi associated with spoilage of date fruit. Ibrahim and Rahma, (2009) carried an investigation on fungi associated with date fruits sold at Bayero University, Kano, Nigeria. Standard mycological techniques was utilized in the isolation and characterization of fungal species using a total number of 30 samples of soft date, dried date, red and yellow dates from two campuses. Cultural and microscopic identification revealed that *Rhizopus* sp.(100%)and *Mucor sp.* (100%), are the most prevalent among the isolates, followed by *Torula* sp.(40%), *Penicillium* sp. (30%), *Aspergillus* sp. (16.67%) and *Alternaria* sp. (13.33%) respectively. Provision for proper storage facilities was suggested to reduce contamination and infection by fungal spores.

Another study by Colman *et al*. (2012) isolated and identified fungal species from dried date (*Phoenix dactylifera*) fruits sold in Maiduguri metropolis in Nigeria. Mycological analysis of the fungal species was carried out with 360 dried date palm fruits which were collected from vendors within Maiduguri metropolis. The studies revealed over 90% of the fungi isolated cause serious spoilage to the fruits. Aspergillus *niger* was found to have the highest percentage of occurrence (39.17%), followed by *Aspergillus flavus, Mucor species, Aspergillus fumigatus, Trychophyton rubrum and Candida alibicans* with 17.60%, 16.67%, 12 50%, 4.16% and 0.83% respectively. To avoid mycotic infections, appropriate washing of the fruit before consumption to avoid was recommended.

Recent research by Tafinta *et al*. (2018) on fungi associated with date palm fruits isolated and characterized various fungi from three different markets (Gawon Nama Market, Old Market and New Market) within Sokoto metropolis using standard mycological procedures. Six (6) different fungal species were reported namely: *Aspergillus niger* (23.81%), *Aspergillus flavus* (15.87%), *Aspergillus fumigatus* (14.29%),*Rhizopus oryzae* (22.22%),*Mucor racemosus* (19.05%) and *Penicillium brasillianum* (4.76%).The research revealed that *Aspergillus niger* had the highest percentage of spoilage and most prevalence of all the fungi. Proper washing and storage of the fruits should be encouraged to reduce fungal spores infection and contamination. Therefore, this study investigates the possible fungi species associated with dried healthy date fruits (*Phoenix dactylifera* Linn) sold in Bida metropolis, Nigeria.

3. Materials and Methods

3.1 Sample Area/ Sample Collection

A total of 54 sample of healthy dried date fruit was collected randomly at the small gate, big gate of Federal Polytechnic Bida, Niger State; others from various spots at the old market, new market, BCC junction and Lemu road in Bida Town. All the samples were collected in clean sterile labelled

containers, and transported to Microbiology Laboratory of Science Laboratory Department of the Federal Polytechnic *Bida*, Niger State within 2 hours of collection for fungal analysis.

3.2 Isolation of fungi

The healthy dried dates samples were cut into 3mm pieces with sterile razor blade, surface-sterilized in 1% hypochlorite for 2minute, then placed on an already prepared Potato Dextrose Agar(PDA) plate containing 40ug/mL of chloramphenicol to prevent bacterial growth. The plates were incubated at room temperature for 5 days. After the incubation period, cultural characteristics of different distinct fungi colonies on the plates were observed. Pure fungi isolates of each colony was obtained by sub-culturing into sterile PDA plates and slant bottles.

3.3 Identification of Isolated Fungi

The method of James and Natalie (2001) was adopted for identification of the fungi isolates using lacto phenol cotton blue stain. The identification was achieved by transferring drops of the lacto phenol cotton blue stain on a clean grease-free glass slide. With the aid of a sterilized mounting needle a small portion of the mycelium from the fungal culture was removed and placed in the center of the stain on the slide. The mycelium was spread gently on the slide using a sterilized inoculating needle. A clean cover slip was gently placed with little pressure to avoid air bubbles. The slide was mounted and observed with x10 and x40 objective lenses respectively. The species viewed was identified by comparing with a mycological atlas (Cheesbrough, 2000).

4. Results and Discussion

The morphological characteristic of fungi isolated from healthy dried date fruits sold in Bida metropolis, Niger State is shown in the Table 1. Four fungal species from different genera were isolated which includes: *Aspergillus spp, Mucor spp, Rhizopus spp,* and *Penicillium spp. Aspergillus spp* was the most prevalent followed by *Mucor spp*. The least was the *Penicillium spp.* Figures 1 to 5 shows the distribution of fungi isolated from healthy dried date fruits from different locations in Bida town.

The findings of this study revealed some types of fungal species associated with date fruits that may cause spoilage under favorable conditions. From all the fungal isolated in this study, the most prominent was *Aspergillus* sp with the following percentage of occurrence per sample sites; Big gate (50%), small gate (45%), BCC road and Lemu road (41%), Old and New Market (39%) while the least encountered was *Penicillium sp* with 9 % percentage of occurrence in BCC Road and Lemu Road, whereas Old and New Market was 13%. Meanwhile, *Penicillium sp* was not encountered in Big and Small gates. This result shows that the date fruits were seriously contaminated with fungi and can cause serious health implications to humans after consumption. The occurrence of these fungi may be associated with exposure of the fruits to sands, dust and spores deposition on the farmlands with suitable weather conditions to triggers fungal infestation. This results are in accordance with Colman *et al*. (2012), who recorded that *Aspergillus sp* the highest prevalence of all the fungal isolated from date fruits in Maiduguri metropolis. Tafinta *et al*. (2018) also reported that date fruits spoilage is associated with filamentous fungi. However, this finding does disagrees with Ibrahim and Rahma (2009) who recorded *Rhizopus sp* and *Mucor spp* (100 %) as the most prominent among the isolates. The differences may occur due to difference in study/sampling locations, weather, nature of samples.

One of the major factors that influence fungal growth is moisture content (Hill and Waller, 1999). Since the four (4) species of fungi were isolated from healthy dried date fruits, this is an indication that healthy dried date contain potential spores that when the conditions becomes favorable triggers growth. It could also be due to increase in absorption of environmental humidity from hawking/display as the investigation was carried out during rainy season and most sellers sold dates along with other fruits such as oranges, watermelon and coconut; which has high water content,

hence, favoring the growth of fungal spores as reported by (Ahmad, 2003) that increase in humidity and temperature favors the growth of fungi. Influences from outside environment can also make date fruits encounter fungal infestation such as damage caused by insects has been known to provide entry for fungal infection and aid their spread (Dannies, 2002).

Table 1: Morphological and Microscopic Characteristics of Fungi Isolated from Dried Date Fruits

Morphology Characteristics	Microscopic Characteristic	Fungi Isolated
Compact, cluster of dark colony. Green dense velvet mycelium. Greenish-yellow hairy elevated surface	Unbranched rough conidiophores with rounded ends that bore conidia. Separate hyphae with long, smooth conidiophores. Cluster of dark walled conidia and conidia are found in chains.	*Aspergillus spp*
Whitish colonies, growing rapidly and filling the petridish with dense cottony mycelium and becoming brownish-black	Non-septate mycelia. Sporangiophores are smooth walled. Sporangia and columella are subglobose. Sporangiospores are ovoid in shape.	*Rhizopus spp*
Green and velvety	Branched conidiophores with chains of conidia looks like a brush.	*Penicillium spp*
Large white colonies which turns into black later	Erect sporangiophores are formed, Sporangiophores swells at the tip to form sporangia which are shaped. Columella is present.	*Mucor spp*

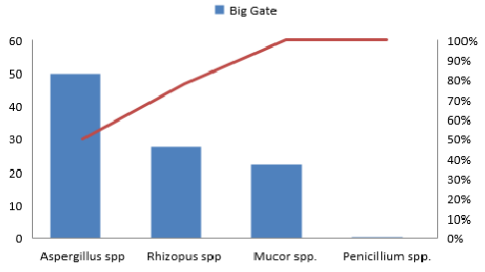

Figure 1: The percentage distribution of Fungi isolated from healthy date fruits at Big gate

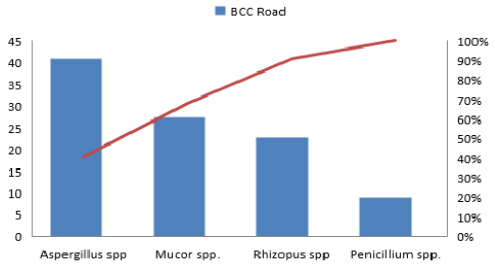

Figure 2: The percentage distribution of Fungi isolated from healthy date fruits at BCC Road.

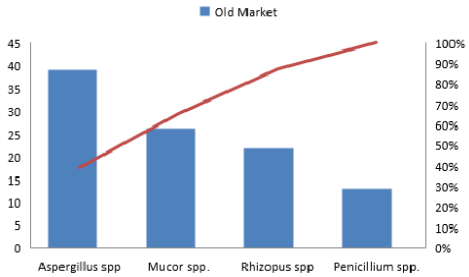

Figure 3: The percentage distribution of Fungi isolated from healthy date fruits at Old Market

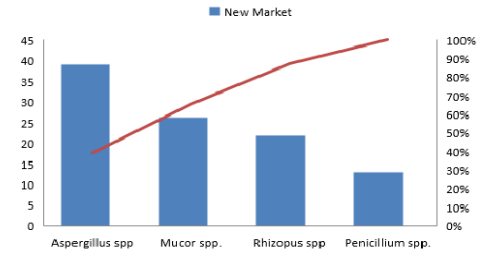

Figure 4: The percentage distribution of Fungi isolated from healthy date fruits at New Market

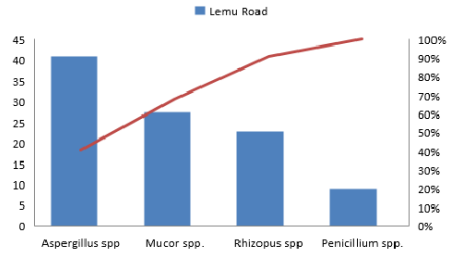

Figure 5: The percentage distribution of Fungi isolated from healthy date fruits at Lemu Road

5. Conclusion

Aspergillus spp was the most prominent fungi encountered in all the sample sites of this study. While several species of fungi cause spoilage of fruits worldwide, the presence of *Aspergillus spp* isolated from samples in this investigation shows potential danger of aflatoxins consumption which may have serious health implication. Proper storage conditions should be provided to avoid increase in moisture content and exposure to air during sales. The use of paper wraps should be encouraged. Food-borne diseases can be avoided by proper washing of the date fruits with clean water. Health orientation should also be encouraged for both vendors and consumers to reduce the prevalence of food-borne diseases.

References

Ahmad, A.A. (2003). Susceptibility of date fruits to aflatoxin production. In: The International Conference on date Palm, 16-19 September, 2003, King Saudi University, College of Agriculture, Vetinary and Medicine. Qaseem Branch. 395-407.

Al Kahtani M, El – Naggar MA, Omer SA, Eman M. Abdulkareem, M.I.A. (2011). *Effect of Toxic fusariumMonoliforme*

Atia, M.M. (2011). Efficiency of physical treatment and essential oil in controlling fungi associated with some stored date palm fruits. *Australia Journal of Basic Applied Science.* 5(6):1572

Berbendi, A. (2000). Date Palm Techniques and Application. ACSAD. Damascus Syria 286.

Cheesbrough, M. (2000). District laboratory practice in tropical countries part2, Cambridge University press, Cambridgep. 47–54.

Christensen, M. J., Folloan, R.E. and Skip, R.A (2007). Plant Pathology. *Australian Plant Pathology*. 17(2): 45-47.

Colman, S., Spencer, T.H.I., Ghamba, P.E. and Colman, E. (2012). Isolation and identification of fungal species from dried date palm (phoenix dactylitera) fruits sold in Maiduguri metropolis. *African Journal of Biotechnology*. 11(77): 12063–12066.

Dennis, S.H. (2002). Pests of Stored Products and Their Control, Belhaven Press, London.

Djerbi, M. (1983). Report on Consultancy Mission on Date Palm Pest and Diseases. FAO–Rome. Pp 28.

Food and Agricultural Organization (FAO) (2008). Date palm" In: http://faostate.fao.org/site/default

Gepts, S. (2002). The natural history of date palm *Phoenix dactylifera.* Australian Plant Pathology. 29:82-95.

Hill, D.S and Waller, J.M. (2009). Pests and Diseases of Tropical Crops, Vol.2 (ed.). Longman, Ghana. 179-182.

Hussein, A.S. and Alhadrami, G.A. (1998). The use of dates and date pits in broiler starter finisher diets. Bioresearch Technology. 66: 219-23.

Ibraheem, I.A and Klaef, M.N. (2003). Date palm culture service and production in Arab Homeland. Alis Kanjeriya Press.789.

Ibrahim, S. and Rahman, M.A. (2009). Isolation and Identification of Fungi associated with date palm fruits (*Phoenix dactylifera)* Sold at Bayero University, Bayero. *Journal of Pure and Applied Sciences.* 2:127-130.

Ikheloa M., Ugaigbe, I.M., Okoloe, C and Ench, F.K. (2002). Date production: an Asset for economic and growth and Devleopment in Nigeria.

James, G.C and Natalie, S.(2001). Microbiology, Laboratory Manual (ed.). 211-223.

Khomutov, R., Dzhavakhiya,V., Khurs, E., Ospova, T., Shcherbakova, L., Zhemchuzhina, N., Mikityul, O. and Nazarova, T. (2011). Chemical regulation of mycotoxin biosynthesis, *Doklady Biochemistry and Biophysics;* 1:25-28.

Kiran, S. (2014), "Floral Stalth on date Palm: A new Discovery" int j Resinnov Tech. 4(2). Doi:10.3329/ijarit.V412.22649.

Morton, J.F. and Mannie, F.L (1987). Date palm (*Phoenix dactylifera)* production. Fruit of worm climate. Crop Evolution. 15(3):61-67

Mustapha, A.I., Hamad, A.M, Al–kahtani. M.S. (2003). Date Varieties for Jam production in proceedings of the first university Al–Hassa; Mars publishing house: Riyadh Saudi Arabia. Pp 496–501.

Tafinta I.Y., Robert A.M., Danfulani J. S., Batagarawa U. S., Umar M. And Ocheni P. (2018). Isolation of Fungi Associated with Date Palm (*Phoenix dactylifera* Linn) fruits consumed within Sokoto Metropolis. *Journal of Microbiology and Biological Sciences.* Vol. 6(8) pp. 103-107.

Redmond, W. A.(2009).Date Palm."Microsoft Student 2009 (DVD).MicrosoftCorporation, 2008.

Shamsudeen, U. and Magashi, A. M. (2005).The effect of Dehulling on the occurrence and Distribution of *Aspergillusflavus*in Some Stored Maize Grains.*Biological and Environmental Sciences Journal for the Tropics,* BEST 1(2):26-28.

A DFT Study on the Effect of Beryllium Doping in WO_3

Ibrahim, U.[1,*] and Lawal, M.[1]
[1]*Science Laboratory Technology Department, Federal Polytechnic Kaura Namoda, Nigeria*
musalawalkt@gmail.com
[*]*Corresponding author:* uihalilu01@gmail.com / umaribrahim.slt@fedponam.edu.ng
+2348065464162

Abstract
Tungsten trioxide (WO_3), in its chemical compound contains oxygen and a transitional metal with wide range of applications such as in gas sensors and photocatalysis. Modification of oxide semiconductors including doping of transitional metals or rare earths could enhance their performance. In this work, the structural and electronic properties of pure hex-WO_3 and WO_3 doped with Beryllium (Be) [$Be_xW_{1-x}O_3$,; x= 0.25, 0.5] are calculated using generalized gradient approximation (GGA – PBE) Pseudopotentials within density functional theory (DFT) as implemented in Quantum ESPRESSO (QE) simulation package code. The results shows that the bond length of pure hex- WO_3 is 1.9371Å, but that of the Be doped WO_3 are respectively 2.0116, 2.1024Å. The result similarly shows that the pure hex-WO_3 is a semiconductor with an indirect band gap, which is in agreement with the experimental results. Doping of pure hex-WO_3 with Be of a certain percent causes disappearing of band gap and induced metallic behaviour. Density of state (DOS) and projected density of state (PDOS) of pure hex-WO_3 and doped system are similarly discussed.

Key words: WO_3, structural, electronic properties, DFT, GGA, QE

1. Introduction

Tungsten trioxide (WO_3), in its chemical compound contains oxygen and a transitional metal with wide range of applications. WO_3 in mineral form was given the name "heavy stone" by a Swedish mineralogist Cronstedt A.F in the year 1755. The WO_3 is produced by treating the tungsten with alkalis. Therefore, WO_3 has the highest melting point among other metals with 3,410ºC (6,170°F), with high electric conductivity. Chemically, WO_3 is insoluble in water and acid, but it dissolves in an alkaline solution (Cotton et al, 1999; Rollinson, 2015). WO_3 is recognized as an important photocatalytic material, this is so due to the stability in an acidic condiction and also they shear similarity in physiochemical properties with TiO_2 (Santato et al, 2001). WO_3 is an n-type semiconductor with an indirect band gap of 2.6eV and a direct band gap of 4.0eV (Likalter, 2002). It has various phases of crystallograph, such as monoclinic, cubic, triclinic, hexagonal, tetragonal and orthorhombic (Ramana et al, 2006). WO_3 is the most stable oxide, obtained as an intermediate in the recovery of tungsten from its minerals (Galatsis et al, 2002). WO_3 has wide band-gap and it was found that the band gap feature of WO_3 can be adequately varied with nitrogen doping content (Lethy et al, 2009).

In recent years, nanostructure semiconductors such as WO_3 has grabbed considerable interests due to its potential application in devices such as gas sensors and photocatalysis. It has been widely proved that modifications of these semiconductors including doping of transition metals, or rare earths, loading of noble metals and coupling of other semiconducting oxide, could enhance their properties (Xueting et al, 2011).

Density functional theory (DFT) calculations can be used to study the effect of some atomic impurities on the band gap of WO_3. It was found that the band gap reduction is often due to the formation of impurity bands and that a shift of conduction band (CB) edge can be induced by foreign atoms (Fenggong et al, 2012).

To study the effects of Beryllium doping on the structure and electronic properties of WO_3, we investigated the doping of WO_3 with Beryllium (*Be*) atoms that are substituted in place of tungsten (*W*) atom with different percentage of dopant atoms ($Be_{\varkappa}W_{1-\varkappa}O_3$; $\varkappa$ = 0.25, 0.5). In this work we investigated and analyzed our results on structural properties and band structure (BS), density of state (DOS), projected DOS (PDOS) (Electronic properties) of pure hexagonal WO_3 (hex-WO_3 MP-545665 with the *P6/mmm (191)* space group (Kristin, 2011; Jaine et al, 2011; Ong et al, 2008) and doped hex- WO_3.

2. Computational method

The calculations were performed on the standard conventional unit cell using ab-initio simulation program within density functional theory (DFT) as implemented in the Quantum ESPRESSO simulation package code. For the pure and doped WO_3, generalized gradient approximation (GGA) and Perdew-Burk-Ernzerhof (PBE) pseudopotentials are been used in approximating the exchange correlation potential (Perdew et al, 1996). Similarly, for the integrals smearing was with a Gaussian broadening of 0.05 was used to guaranty accuracy up to 0.005 Ry. Monkhorst-Pack scheme is utilized in performing the brillouin zone integration (Monkhorst, 1976) with 2×2×1 k-points grids for hex- WO_3, $Be_{\varkappa}W_{1-\varkappa}O_3$ in order to have good convergence between the computed structures and energies. The valence electrons used in this work for distinct atoms are Be 2s 2p, W 5s 6s 5p 6p 5d and O 2s 2p. A kinetic energy cut off of 40 Ry was used with a plane-wave basis set. A hexagonal unit cell of a = b =7.508 Å, c = 3.863 Å, α = β = 90°, γ = 120° and V = 188.570 $Å^3$/cell based on experimental values were used (Kristin, 2011). The super cell which was used consists of 12 atoms; 3 tungsten atoms and 9 oxygen atoms. In each calculation, all atoms were fully relaxed and geometry optimizations were obtained.

3. Results and discussion

3.1 Structural properties

From the structure of pure WO_3 figure 1, the bond length from $W - O$ is observed to be 1.9371 Angstroms (Å). As a result of introducing dopant elements, an increases in bond length was observed base on the doping concentration, it also unbond some elements of the doped compound as shown in figures 2 a & b.

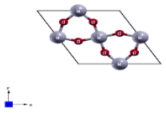

Figure 1: Schematic view of pure hex-WO_3.

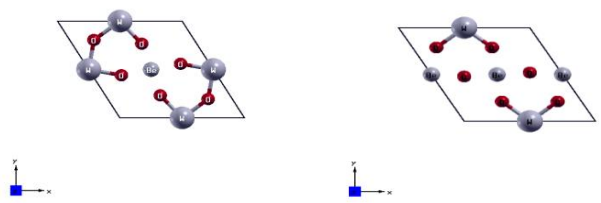

(a) (b)

Figure 2: Schematic view of hex-$Be_{0.25}W_{0.75}O_3$ (a) and $Be_{0.5}W_{0.5}O_3$ (b)

For ($Be_{0.25}W_{0.75}O_3$) Figure 2a, the bond length from $W-O$ is seen as 2.0116 Å which is 0.0745 Å greater than that of pure WO_3 and the corresponding bond length from $Be-O$ is 1.8227 Å. Similarly, figure 2a depicts 1 un-bonded atom. Figure 2b shows that, 2*Be* Doped WO_3 ($Be_{0.5}W_{0.5}O_3$) un-bonded 5 atoms of the super cell. Likewise, the bond length between *W* and *O* is 2.1024 Å, which is 0.1653 Å higher than that of pure WO_3. The bond length from $Be-O$ is 1.8820 Å, which is 0.0593 Å higher than that of $Be_{0.25}W_{0.75}O_3$. The effect of the *Be* doping is that, $Be-O$ bond lengths are shorter than the comparable $W-O$ bond lengths and to compensate for this, the range of variation in the $W-O$ is increase in all directions.

3.2. Electronic properties of pure, Be-and Mg-doped hex-WO_3

3.2.1 Pure hex-WO_3

The BS, DOS, and PDOS of pure hex-WO_3 are obtained on the basis of structural optimization using GGA. Figure 3 depicts a smaller indirect band gap. It clearly shows that the conduction band (CB) minima lie at *A* symmetry point and the maxima of the valence band (VB) is at Γ. Considering these two symmetry points, the energy band gap is E_g = 0.882eV $(\Gamma - A)$, which is in comparison with experimental measured value 1.192eV (Kristin, 2011) is underestimated as expect for DFT calculation and other computational results for other forms of hex-WO_3 whose calculated band gaps are 3.3*eV* and 2.9*eV* respectively (Chenxi et al, 2014; 2018) due to the outstanding constraints of GGA. By considering the symmetry point M for CB minima and the symmetry point Γ for VB maxima we still get another indirect (Γ - M) band gap which is 1.638eV. But the value of (Γ - M) band gap is greater than that of $(\Gamma - A)$.

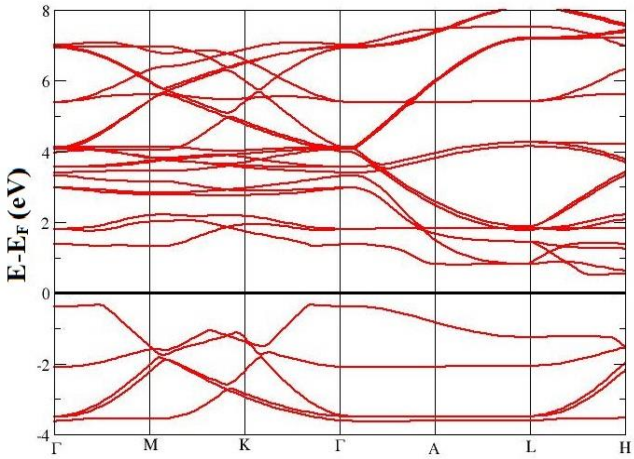

Figure 3: Band structure of pure Hex-WO_3

Figure 4 depicts the computed DOS and PDOS nearby Fermi energy level of hex-WO_3. One can see that the valence band with the range of – 38 to 0eV is mainly contributed by W 5p and O 2s, 2p states with minor contribution of W 6p, 6s and 5d states. On the other hand, the conduction band whose range is 0 to 20eV is mainly contributed by W 5d and partial contribution of W 6s, 6p and O 2p states. The DOS of hex-WO_3 below the Fermi energy level also were analyzed. It is discovered that the bonding electronic states of hex-WO_3 are – 38eV between the Fermi level and – 5.3eV. On the other hand, the partial bonding states of W 5p,W 6p, W 6s, W5d, O 2s and O 2p

states are – 38, – 16, – 16.5, – 12.5, – 16.5 and – 5 respectively. One can conclude that, the total bonding electronic states of pure hex-WO_3 are mainly contributed by W 5p then followed by W 6p and O 2s, while O 2p has the least. Consequently, from the DOS of pure hex-WO_3 it can be seen that the band gap energy is 1.1eV and this is still underestimated when compared with the experimental value.

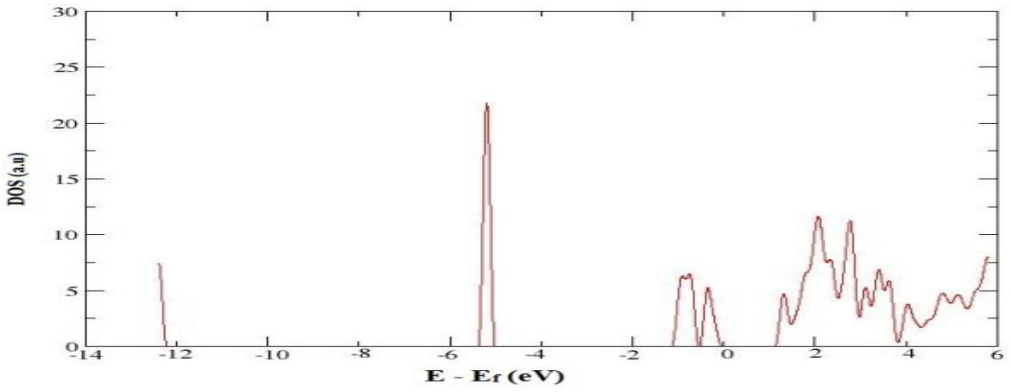

(a)

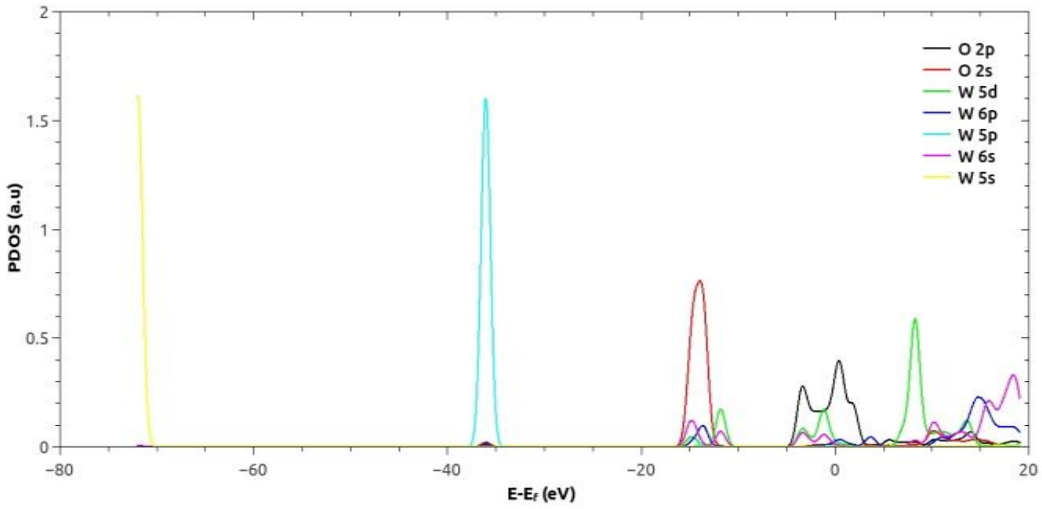

(b)

Figure 4: DOS (a) and PDOS (b) of Pure Hex-WO_3

3.2.2 Be doped WO_3

In order to explore the effect of *Be* doping on the electronic properties of hex-WO_3, BS, DOS and PDOS of $Be_{0.25}W_{0.75}O_3$ and $Be_{0.5}W_{0.5}O_3$ are shown in figure 5. It is observed that in all cases, the Fermi energy is shifted into the VB leading to the metallic-like (conductor) behavior, figure 5a. On increasing the *Be* doping, this behavior also increased, figure 5b. This observation is in line with other experimental results and some other calculations using different codes (Mansouri and Mahmoodi, 2014). Conductor behaviour of doped hex-WO_3 is the effect of substitution *Be* atoms in place of tungsten atoms, this is due to the deficit of electron in this case.

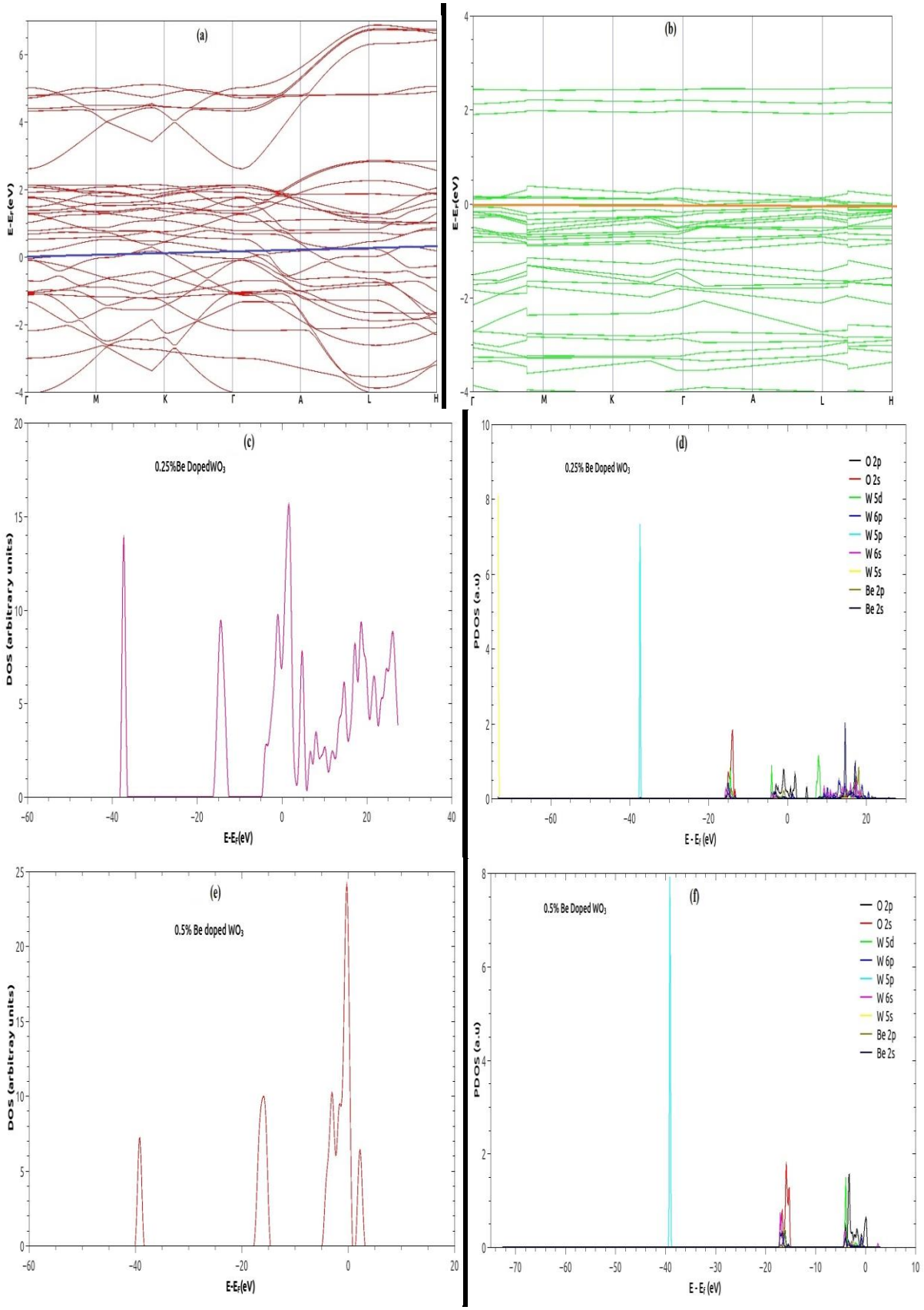

Figure 5: BS (a), DOS (c) and PDOS (d) of $Be_{0.25}W_{0.75}O_3$; BS (b), DOS (e) and PDOS (f) of $Be_{0.5}W_{0.5}O_3$.

Figures 5c and 5d show the computed DOS and PDOS nearby Fermi energy level of hex-$Be_{0.25}W_{0.75}O_3$. It is obviously that the valence band with the range of – 36 to 0eV is mainly contributed by W 5p, W 5d and O 2s, 2p states with partial contribution of W 6s, W6p and Be 2p states. On the other hand, the conduction band whose range is 0 to 20eV is mainly contributed by Be 2s, W 5d, Be 2p, and O 2p states and partial contribution of W 6p, W 6s and O 2p states. It is DOS below the Fermi energy level were also analyzed. It is observed that, the band gap energy is zero which corresponds to the result obtained in BS figure 5a.

Figures 5e and 5f illustrate the computed DOS and PDOS close to Fermi energy level of hex-$Be_{0.5}W_{0.5}O_3$. It is clearly seen that the valence band with the range of – 39 to 0eV is mainly contributed by W 5p, W 5d and O 2s, 2p states with partial contribution of W 6s, W 6p and Be 2p states. Similarly, the conduction band with the range of 0 to 10eV is slightly contributed by W 6s state. From DOS plot, the band gap energy is zero which is in line with the result obtained in BS figure 5b.

4. Conclusion

In this work, the structural and electronic properties of pure hex-WO_3 and doped WO_3 ($Be_\varkappa W_{1-\varkappa}O_3$; $\varkappa$= 0.25, 0.5) are calculated utilizing GGA – PBE within DFT as implemented in Quantum ESPRESSO simulation package code. The results shows that the bond length of pure hex- WO_3 is 1.9371Å, but that of the *Be* doped WO_3 (from W – O and Be – O for $Be_{0.25}W_{0.75}O_3$ and $Be_{0.5}W_{0.5}O_3$) are respectively 2.0116, 1.8227, 2.1024 and 1.8820Å. The DOS and PDOS graphs of pure and doped system show that the compound is ferromagnetic (magnetic) due to the hybridization on the valence band. Our results also depicts that the pure hex- WO_3 is a semiconductor with an indirect band gap, which is in agreement with experimental measurements. Moreover, doping WO_3 with *Be* as electron donor causes disappearing of band gap and induce metallic behaviour, an increase in the amount of dopant produce an increase in the valence band width.

References

Chenxi, Y., Jian-Fen, C., Xiaofei, Z., Daojian, C. and Dapeng, C. (2014). *Design of the Alkali-Metal-Doped WO_3 as a Near-Infrared Shielding Material for Smart Window*. Ind. Eng. Chem. Res. 53, 17981 – 17988, https://dx.doi.org/10.1021/ie503284xl

Chenxi, Y., Jian-Fen, C., Xiaofei, Z. and Daojian, C. (2018). *Enhanced Photochemical Performance of Hexagonal WO_3 by Metal-Assisted S – O Coupling for Solar-Driven Water Splitting*. Sci. China Mater 61(1), 91 – 100. https://doi.org/10.1007/s40843-017-9126-1

Cotton, A. F., Wilkinson, G., Bochmann, M., & Murillo, C. A. (1999). Advanced inorganic chemistry.

Fenggong, W., Cristiana, D.V. and Gianfranco, P. (2012). *Doping of WO_3 for photocatalytic water splitting*: Hints from density functional theory. *J. Phys. Chem. C 2012, 116, 8901-8909.*

Galatsis, K. Li, Y. X., Wlodarski, W., Comini, E., Sberveglieri, G., Cantalina, C., Santucci, C.and Passancantando, M. (2002). Comparison of Single and Binary Oxide of MoO_3, TiO_2 and WO_3 for Sol gel Sensors. *Sensors and Actuators* B 83:276-280.

Kristin, P. (2011). Materials project. https://www.materialsproject.org

Jaine, A., Hautier, G., Ong, S. P., Moore, C. J., Fischer, C. C., Persson, K. A., & Ceder, G. (2011). Formation enthalpies by mixing GGA and GGA+U calculations. Physical Review B, 84(4), 045115.

Lethy, K. J., Pandya, S., Beena, D., Vinodkumar, R., Sathe, V. and Pillai, V. P. M. (2009). Transparent and low resistive nanostructured laser ablated tungsten oxide thin film by nitrogen doping. *J. Phys.* D: Appl. Phys 42: 185407.

Likalter, A. A. (2002). Critical points of metals of three main groups and selected transition metals. Physical A: Statistical Mechanics and its Applications. *311*(1-2), 137-149.

Likalter A.A (2002). Impurity states and insulator-metal transition in tungsten bronzes. 252-260.

Mansouri Masoud and Mahmoodi Tahereh. (2014). *Ab-initio Probing of Electronic Structure of WO_3 Doped with Li Atoms.* 2nd International Conference on New Frontiers in Physics (ICNFP), In-stanbul, Turkey SRPioneers Publications.

Monkhorst, H, J., & Pack, J. D. (1976). Special points for Brillouin-zone integrations. Physical Review B, 13(12), 5188.

Ong, S. P., Wang, L., Kang, B., & Ceder, G. (2008). Li- Fe- P- O2 phase diagram from first principles calculations. Chemistry of Materials, 20(5), 1798-1807

Perdew, J. P., Burke, K., & Ernzerhof, M. (1996). Generalized gradient approximation made simple. Physical Review Letters, 77(18), 3865.

Ramana C. V., Utsunomiaya S., Ewing, R. C., Julie, C. M and Becker, U. (2006). *Structural Stability and phase transitions of WO_3 thin films* ' The journal of physical chemistry B 110 10430-5.

Rollinson, C. L. (2015). The Chemistry of Chromium, Molybdenum and Tungsten: Pergamon International Library of Science, Technology, Engineering and Social Studies (Vol. 21).

Santato, C., Ulmann, M, Augustynski, J. (2001). Photoelectrochemical properties of Nanostructural Tungsten Trioxide Films J phys chem *B,* 105,936.

Xueting, C., Shibin, S., Xiao, X. and Zhenjiang, L. (2011). Synthesis of transition metal-doped tungsten oxide nanostructures and their optical properties. *Materials letters 65 (2011) 1710-*1712. https://doi.org/10.1016/j.matlet.2011.02.060

First Principle Investigation on the Effect of Mg Doping on Optical Properties in WO_3

Ibrahim, U.[1,*] and Lawal, M.[1]
[1]*Science Laboratory Technology Department, Federal Polytechnic Kaura Namoda, Nigeria*
musalawalkt@gmail.com
[*]*Corresponding author:* uihalilu01@gmail.com / umaribrahim.slt@fedponam.edu.ng
+2348065464162

Abstract
Tungsten trioxide (WO_3) is a metal oxide which grabbed considerable attention because of its wide technological applications. Investigation revealed that it is widely used in gas sensor application. Modification of oxide semiconductors including doping of transitional metals or rare earths could enhance their performance. In this study, the electronic and optical properties of pure hex-WO_3 and Mg doped WO_3 ($Mg_xW_{1-x}O_3$; x= 0.25, 0.5) are calculated using generalized gradient approximation (GGA – PBE) within density functional theory (DFT) as implemented in Quantum ESPRESSO (QE) simulation package code. The result depicts that the pure hex-WO_3 is a semiconductor with an indirect band gap, which is in agreement with the experimental results. Doping of pure hex-WO_3 with Mg of a certain percent causes disappearing of band gap and induced conductor behaviour. Density of state (DOS) and projected density of state (PDOS) of pure hex-WO_3 and doped system were discussed. The complex dielectric function [$\varepsilon_{real}(\omega)$ and $\varepsilon_{im}(\omega)$] and electronic energy loss function were calculated for both pure and doped system. The relations of the complex dielectric function to inter band transitions were also discussed.

Key words: WO_3, electronic and optical properties, GGA, DFT, QE

1. Introduction

Tungsten trioxide (WO_3) is a metal oxide which grabbed considerable attention because of its wide technological applications. Investigation revealed that it is widely used in gas sensor application (Mansouri and Mahmoodi, 2016). However, WO_3 has been developed to a potential photocatalysts due to its outstanding characteristics, highly stable physicochemical and good electron transport properties, nontoxicity and no-photo-corrosion. It is also discovered that WO_3 with a band gap of 2.2 to 2.8eV, is a visible light response catalyst and this makes it substitute for the photocatalytic oxidation of organic pollutants under solar irradiation as an alternative to TiO_2. WO_3 can be synthesized using different methods which includes sol-gel, precipitation, doping (Guntapon et al, 2018) etc. Consequently, among the disadvantages of WO_3 is the possibility in occurrence of electrons-holes recombination. In order to improve the photocatalytic performance of WO_3 therefore, doping of transition metals or alkaline earth metals could either be alleviating of electrons-holes recombination process or promoting electrons to go to the conduction band easily (Xueting et al, 2011). Recent studies and developments shows that WO_3 has been doped with some transitional or alkaline earth metals such as Fe and Mo or Mg (Guntapon et al, 2018).

Density functional theory (DFT) calculations have been used to study the effect of some atomic impurities on the band gap of WO_3 (Fenggong et al, 2012). To study the effect of Magnesium (*Mg*) doping on Optical Properties of WO_3**,** we investigated the doping of WO_3 with *Mg* atoms that are substituted in place of tungsten (*W*) atom with different percentage of dopant atoms ($Mg_xW_{1-x}O_3$; x = 0.25, 0.5). In this work we investigated and analyzed our results on electronic energy loss function and dielectric function (Optical properties) of pure hexagonal WO_3 (hex-WO_3 MP-545665 with the *P6/mmm (191)* space group (Kristin, 2011; Jaine et al, 2011; Ong et al, 2008) and doped hex-WO_3.

2. Computational Procedure

The calculations were performed on the standard conventional unit cell using ab-initio simulation program within density functional theory (DFT) as implemented in the Quantum ESPRESSO simulation package code. For the pure and doped WO_3, generalized gradient approximation (GGA) and Perdew-Burk-Ernzerhof (PBE) are used in approximating the exchange correlation potential (Perdew et al, 1996). Similarly, for the integrals smearing was adopted and specifically the Maxfessel-Paxton smearing method, smearing with a Gaussian broadening of 0.05 were used to guaranty accuracy up to 0.005 Ry. Monkhorst-Pack scheme is used in performing the brillouin zone integration (Monkhorst, 1976) with 2×2×1 k-points grids for hex- WO_3 and $Mg_xW_{1-x}O_3$ in order to have good convergence between the computed structures and energies. The valence electrons used in this work for distinct atoms are Mg 2s 3s 2p, W 5s 6s 5p 6p 5d and O 2s 2p. A kinetic energy cut off of 40 Ry was used with a plane-wave basis set. A hexagonal unit cell of a = b =7.508 Å, c = 3.863 Å, α = β = 90°, γ = 120° and V = 188.570 Å^3/cell based on experimental values were used (Kristin, 2011). The super cell which was used consists of 12 atoms; 3 tungsten atoms and 9 oxygen atoms. In each calculation, all atoms were fully relaxed and geometry optimizations were obtained.

Optical properties can be computed using the complex dielectric function $\varepsilon(\omega) = \varepsilon_{real}(\omega) + i\,\varepsilon_{im}(\omega)$. Using Kramers-Krönig relations and by calculating the wave function matrix, the real and imaginary parts of the dielectric function $\varepsilon_{real}(\omega)$ and $\varepsilon_{im}(\omega)$, as well as loss function $L(\omega)$ can be derived respectively. Consequently, other optical constant such as absorption coefficient can be obtained (Gillani et al, 2019). The formulas that can be used for calculating the optical properties are given below (Duan, 2014):

$$\varepsilon_{im}(\omega) = \frac{\pi}{\varepsilon_o}\left(\frac{e}{m\omega}\right)^2 \times \sum_{V,C}\left\{ \int_{BZ} \frac{2dK}{(2\pi)^3} \left|a.M_{CV}(K)\right|^2 \times \delta\left[E_C(K) - E_V(K) - \hbar\omega\right] \right\} \quad (1)$$

$$\varepsilon_{real}(\omega) = 1 + \frac{2e}{\varepsilon_o m^2} \sum_{V,C} \int_{BZ} \frac{2dK}{(2\pi)^3} \frac{\left|a.M_{CV}(K)\right|^2}{\left[E_C(K) - E_V(K)\right]} \times \frac{\hbar^3}{\left[E_C(K) - E_V(K)\right]^2 - \hbar^2\omega^2} \quad (2)$$

$$n(\omega) = \frac{1}{\sqrt{2}}\left[\sqrt{\varepsilon_{real}(\omega)^2 + \varepsilon_{im}(\omega)^2} + \varepsilon_{real}(\omega)\right]^{\frac{1}{2}} \quad (3)$$

$$k(\omega) = n(\omega) = \frac{1}{\sqrt{2}}\left[\sqrt{\varepsilon_{real}(\omega)^2 + \varepsilon_{im}(\omega)^2} - \varepsilon_{real}(\omega)\right]^{\frac{1}{2}} \quad (4)$$

$$R(\omega) = \frac{\left[n(\omega) - 1\right]^2 + k^2(\omega)}{\left[n(\omega) - 1\right]^2 - k^2(\omega)} \quad (5)$$

$$\alpha(\omega) = \frac{2\omega k(\omega)}{c} = \frac{\varepsilon_{im}(\omega)}{n(\omega)c} \quad (6)$$

$$L(\omega) = \frac{\varepsilon_{im}(\omega)}{\varepsilon_{real}(\omega)^2 + \varepsilon_{im}(\omega)^2} \quad (7)$$

Where; C and V are the conduction and valance bands respectively. *BZ* is the first Brillouin zone, *K* is the reciprocal lattice vector, $E_C(K)$ and $E_V(K)$ represent the intrinsic energy levels of the conduction and valence bands, $\left|a.M_{CV}(K)\right|^2$ is the matrix element of momentum transition, ε_o is the vacuum permittivity, α is the unit direction vector, ω is the angular frequency, $n(\omega), k(\omega), R(\omega), \alpha(\omega)$ *and* $L(\omega)$ are the refractive index, the extinction coefficient, the reflectivity, the absorption coefficient and the energy loss function respectively.

Optical properties usually requires a dense mesh of uniformly distributed k points. Therefore we utilized BZ integration with a $10 \times 10 \times 10$ grid of Monkhorst-Pack point to the calculation.

3. Results and discussion

The electronic and optical properties of pure hex-WO_3 and the effect of doping *Mg* on pure hex-WO_3 ($Mg_xW_{1-x}O_3$; x = 0.25, 0.5) using the same super cell with 12 atoms consisting of 3 *W* and 9 *O* atoms was investigated and discussed .

3.1. Electronic properties of pure and Mg-doped hex-WO_3

3.1.1 Pure hex-WO_3

To investigate the effects of *Mg*-doping in the electronic structure of WO_3, the BS, DOS, and PDOS of hex-WO_3 are obtained on the basis of structural optimization using GGA. Figure 1 depicts a smaller indirect band gap. It clearly shows that the conduction band (CB) minima lie at *a* symmetry point and the maxima of the valence band (VB) is at Γ. Considering these two symmetry points, the energy band gap is E_g = 0.882eV $(\Gamma - A)$, which is in comparison with experimental measured value 1.192eV (Kristin, 2011) is underestimated as expect for DFT calculation and other computational results for other forms of hex-WO_3 whose calculated band gaps are 3.3*eV* and 2.9*eV* respectively (Chenxi et al, 2014; 2018) due to the outstanding constraints of GGA. By considering the symmetry point M for CB minima and the symmetry point Γ for VB maxima we still get another indirect (Γ - M) band gap which is 1.638eV. But the value of (Γ - M) band gap is greater than that of $(\Gamma - A)$.

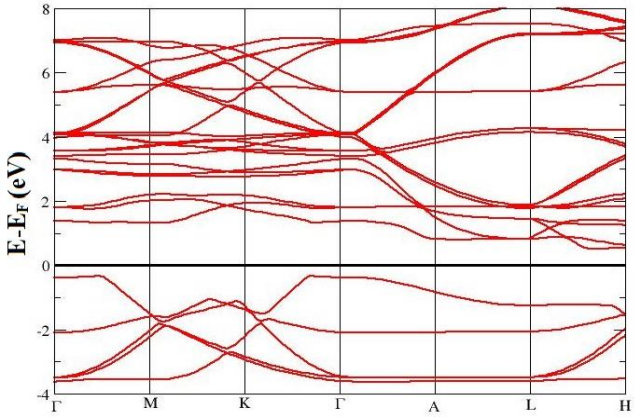

Figure 1: Band structure of pure Hex-WO_3

Figure 2 shows the computed DOS and PDOS nearby Fermi energy level of hex-WO_3. One can see that the valence band with the range of – 38 to 0eV is mainly contributed by W 5p and O 2s, 2p states with minor contribution of W 6p, 6s and 5d states. On the other hand, the conduction band whose range is 0 to 20eV is mainly contributed by W 5d and partial contribution of W 6s, 6p and O 2p states. The DOS of hex-WO_3 below the Fermi energy level also were analyzed. It is discovered that the bonding electronic states of hex-WO_3 are – 38eV between the Fermi level and – 5.3eV. On the other hand, the partial bonding states of W 5p ,W 6p, W 6s, W5d, O 2s and O 2p states are – 38, – 16, – 16.5, – 12.5, – 16.5 and – 5 respectively. We therefore conclude that, the total bonding electronic states of pure hex-WO_3 are mainly contributed by W 5p then followed by W 6p and O 2s, while O 2p has the least. Consequently, from the DOS of pure hex-WO_3 it can be seen that the band gap energy is about 1.1eV and this value is also smaller than the experimental result.

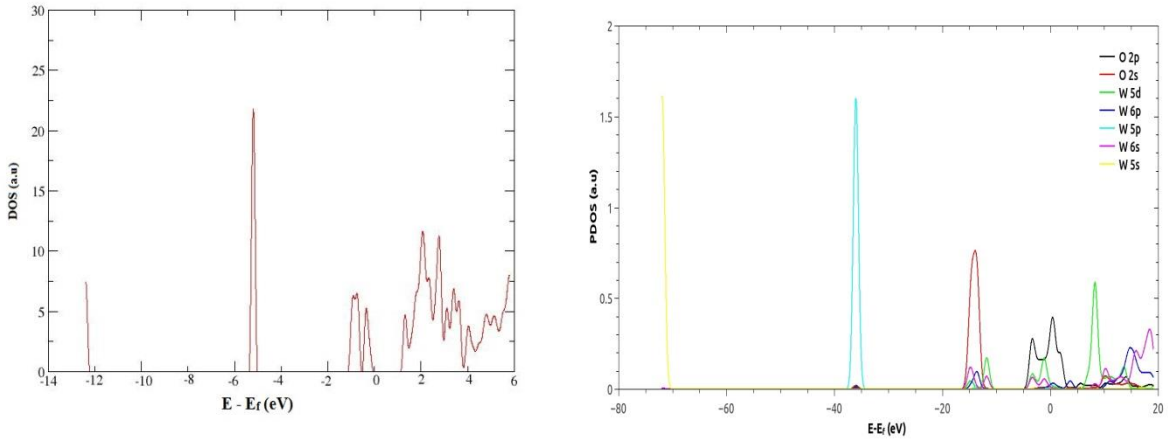

(a) (b)

Figure 2: DOS (a) and PDOS (b) of Pure Hex-WO_3

3.1.2 Mg doped WO_3

Substituting *W* with *Mg* on the electronic properties of hex-WO_3, BS, DOS and PDOS of $Mg_{0.25}W_{0.75}O_3$ and $Mg_{0.5}W_{0.5}O_3$ are discovered in figure 3. It is seen in all cases, the Fermi energy is shifted into the VB leading to the conductor behavior, figure 3a. On increasing the *Mg* doping, this behavior also increased, figure 3b. This observation is also in line with other experimental results and some other calculations using different codes (Mansouri and Mahmoodi, 2014). Conductor behaviour of doped hex-WO_3 is the effect of substitution *Mg* atoms in place of *W* atoms; this is due to the deficit of electron in this case.

Figures 3c and 3d shows the computed DOS and PDOS nearby Fermi energy level of hex-$Mg_{0.25}W_{0.75}O_3$. It is observed that the valence band with the range of – 69 to 0eV is mainly contributed by W 5s, 5d, Mg 2p and O 2s states with partial contribution of W 6s, 5d, 6p and O 2p states. The conduction band range is 0 to 10eV is mainly contributed by O 2p state and partial contribution of W 6p, and 5d states. From DOS plot, the band gap energy is zero which is in line with the result obtained in BS figure 3c.

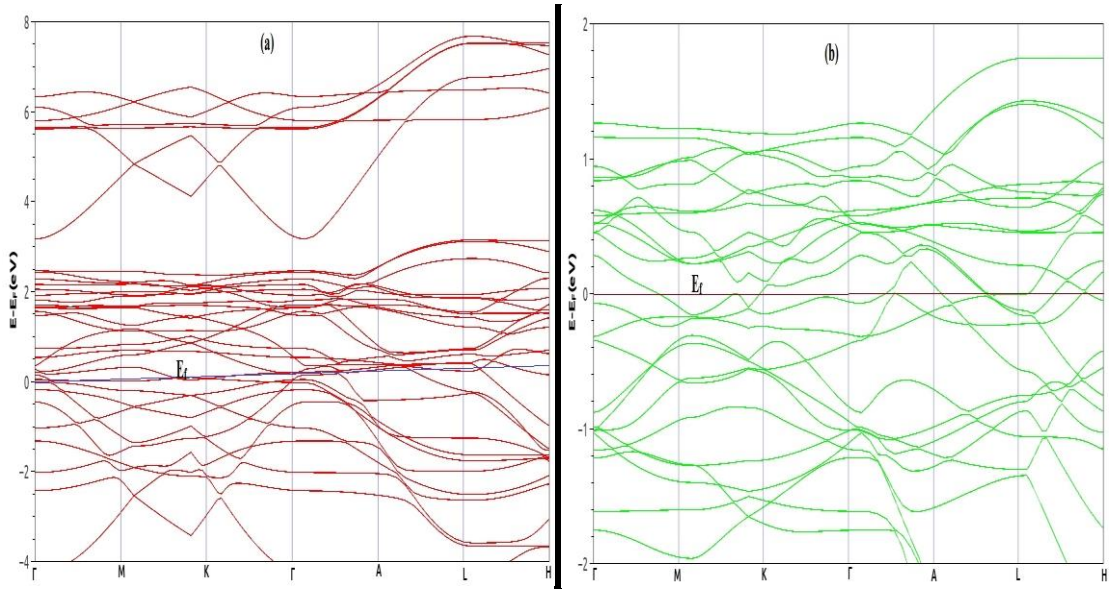

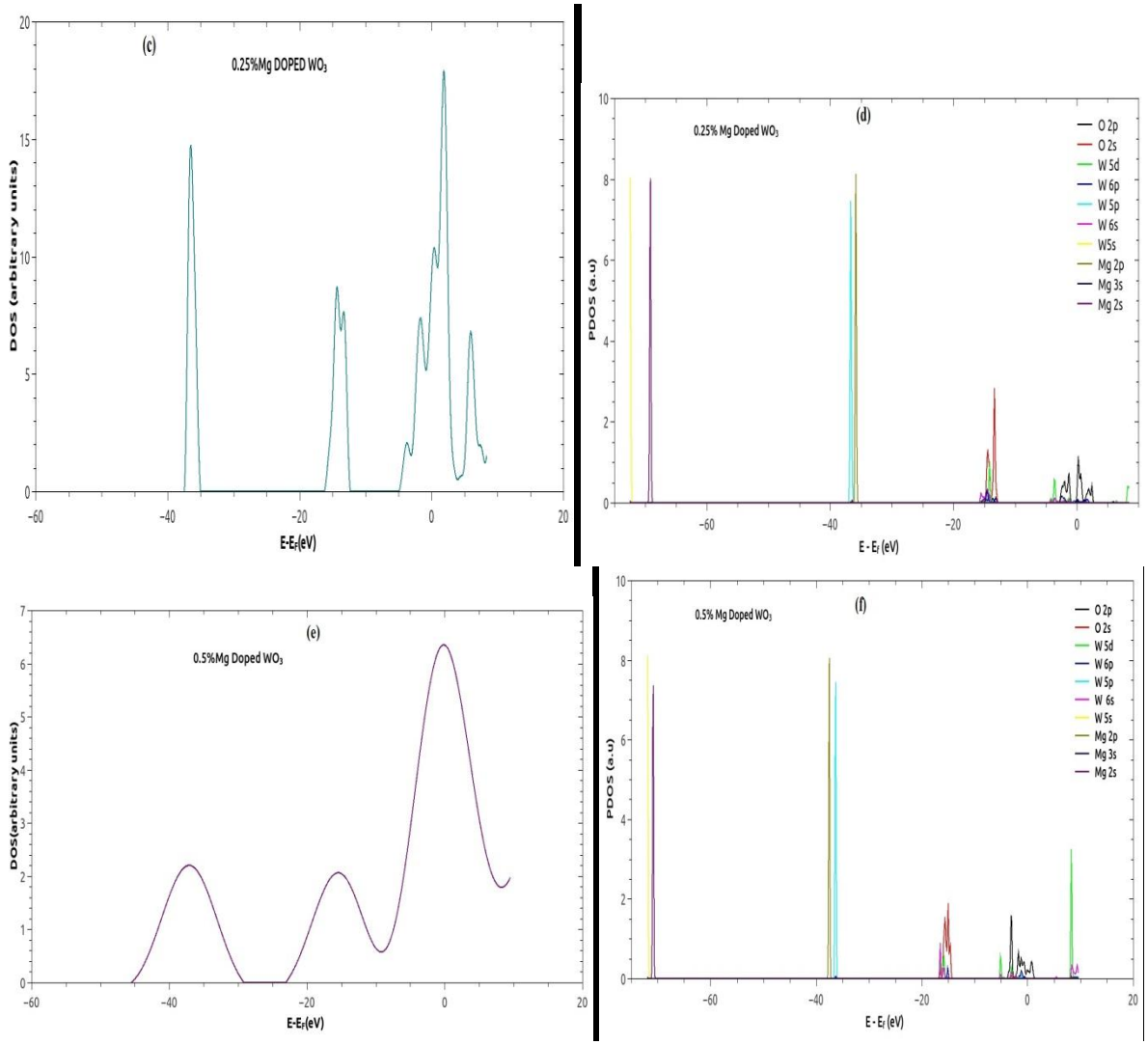

Figure 3: BS (a), DOS (c) and PDOS (d) of $Mg_{0.25}W_{0.75}O_3$; BS (b), DOS (e) and PDOS (f) of $Mg_{0.5}W_{0.5}O_3$.

Figures 3e and 3f shows the computed DOS and PDOS nearby Fermi energy level of hex-$Mg_{0.5}W_{0.5}O_3$. It is observed that the valence band with the range of – 69 to 0eV is mainly contributed by Mg 2p, W 6s and W 5p states with partial contribution of O 2s, W 5d, 6p and Mg 3s states. The conduction band range is 0 to 20eV is mainly contributed by W 5d state and partial contribution of Mg 3s, and W 6s states. From DOS plot, the band gap energy is still zero which corresponds to the result obtained in BS shown in figure 3b.

3.2. Optical properties

In order to investigate the Optical traits of Pure hex-WO_3 and $Mg_{\varkappa}W_{1-\varkappa}O_3$, the tensor components of the complex dielectric function, $\varepsilon(\omega) = \varepsilon_{real}(\omega) + i\varepsilon_{im}(\omega)$, have been computed. Figure 4 represent the calculated curves of real $\varepsilon_{real}(\omega)$ and imaginary $\varepsilon_{im.}(\omega)$ parts of dielectric function as function of the incident energy as well as electronic energy loss function for pure hex-WO_3 and $Mg_{\varkappa}W_{1-\varkappa}O_3$; $\varkappa$ = 0.25, 0.5.

The real part of the dielectric function for pure hex-WO_3 and doped system shows that, the static dielectric constant $\varepsilon_{real}(0)$ decreases systematically. Figure 4(a) depicts that $\varepsilon_{real}(\omega)$ decreases

with the increase of energy when the energy is smaller, until the energy is 0.4eV, then increases with increase in energy until it reaches the maximum with the energy of 0.75eV. When the energy is greater than 0.75eV, $\varepsilon_{real}(\omega)$ decreases expeditiously with the increasing energy and drops to the minimum with the corresponding energy of 0.9eV. $\varepsilon_{real}(\omega)$ is smaller than zero in the energy range of 0.90 – 3.20eV. Figure 4(d) depicts that $\varepsilon_{real}(\omega)$ increases with increase of energy when the energy is smaller, then reaches the maximum energy of 0.5eV. When the energy is larger than 0.5eV, $\varepsilon_{real}(\omega)$ decreases rapidly with increasing energy of 1.2eV. Similarly, Figure 4(g) shows that $\varepsilon_{real}(\omega)$ increases and decreases with increase of energy, then reaches the maximum with energy of 7.9eV. When the energy is greater than 7.9eV, $\varepsilon_{real}(\omega)$ decreases rapidly with increasing energy of 9.2eV.

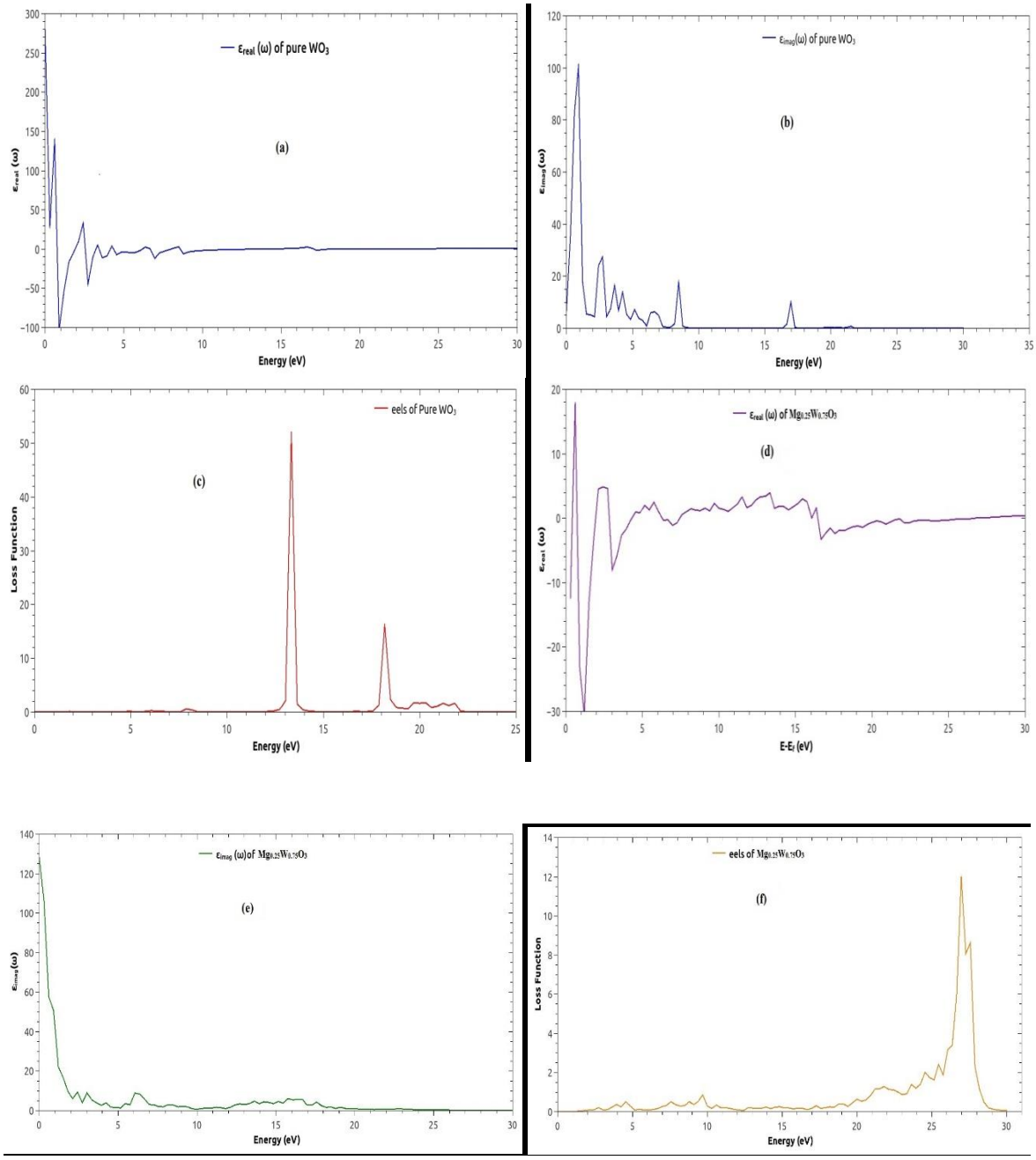

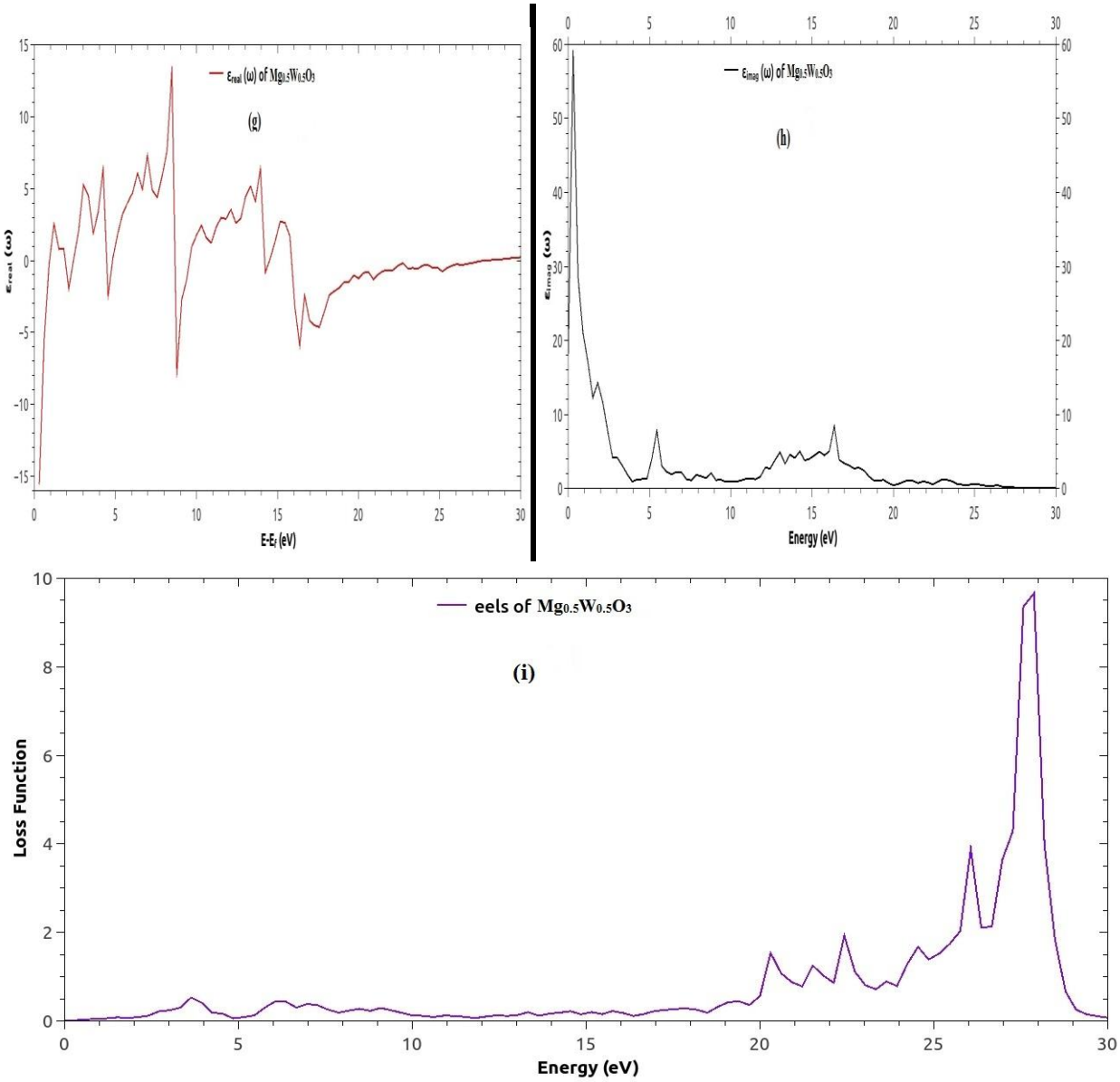

Figure 4: Real and imaginary parts of dielectric function and loss function of pure hex-WO_3 (a), (b) and (c); real and imaginary parts of dielectric function and loss function of hex- $Mg_{0.25}W_{0.75}O_3$ (d), (e) and (f); real and imaginary parts of dielectric function and loss function of hex- $Mg_{0.5}W_{0.5}O_3$ (g), (h) and (i)

On the other hand, at 0eV energy, the $\varepsilon_{im.}(\omega)$ is also zero for pure and doped $Mg_xW_{1-x}O_3$. This means that no energy is given out. We observed the main peaks in the spectra of $\varepsilon_{im.}(\omega)$ at energies of 1.0, 2.8 8.5 and 17.0eV of pure hex-WO_3 Figure 4(b); 3.0 and 6.1eV for $Mg_{0.25}W_{0.75}O_3$ Figure 4(e) and 0.2, 5.2 and 16.2eV respectively for $Mg_{0.5}W_{0.5}O_3$ Figure 4(h). $\varepsilon_{im.}(\omega)$ peaks are associated to inter-band transition from valence band (VB) to covalent band (CB) and only the following transition, 2p, 2s – O to 5d – W Figure 4(b); 2s – O to 2p – Mg, 5s, 5d – W Figure 4(e) and 2s – O to 2p – Mg , 5p, 6s – W Figure 4(h) contributed, which have angular momentum based on selection

rule (that is $\Delta l = \pm 1$). Similarly, $\varepsilon_{im.}(\omega)$ peaks cannot occur due to a single inter-band transition, since one can discover number of indirect transitions in band structure with an energy corresponding to the same peaks (Gillani et al, 2019).

From the dielectric function, the electronic energy loss function can further be described as the energy loss when electrons pass through a uniform dielectric. The corresponding oscillation frequency of the peak of loss function is described as the plasma frequency. In Figure 4(c), the maximum peak of energy loss function of pure hex-WO_3 is 13.10eV. In the range of 14.60 - 17.30eV the electronic energy loss function is zero. Figure 4(f), shows that, the maximum peak of energy loss function of $Mg_{0.25}W_{0.75}O_3$ is 26.30eV and very close to zero at 1.30eV. The maximum peak of energy loss function of $Mg_{0.5}W_{0.5}O_3$, 4(i) is 28.00eV and very close to zero at 0.70eV.

4. Conclusion

The electronic and optical properties of pure hex and doped system (WO_3 and $Mg_\varkappa W_{1-\varkappa}O_3$; $\varkappa$= 0.25, 0.5) are calculated using GGA – PBE within DFT as implemented in Quantum ESPRESSO simulation package code. Our results depicts that the pure hex- WO_3 is a semiconductor with an indirect band gap, which is in agreement with experimental measurements. Moreover, doping WO_3 with *Mg* as electron donor causes disappearing of band gap and induce conductor behaviour so increasing the amount of dopant produce an increase in the valence band width. Finally, the complex dielectric function [$\varepsilon_{real}(\omega)$ and $\varepsilon_{im}(\omega)$] and electronic energy loss function were calculated for both pure and *Mg*-doped system. The relations of the complex dielectric function to inter band transitions were similarly discussed.

References

Chenxi, Y., Jian-Fen, C., Xiaofei, Z., Daojian, C. and Dapeng, C. (2014). *Design of the Alkali-Metal-Doped WO_3 as a Near-Infrared Shielding Material for Smart Window*. Ind. Eng. Chem. Res. 53, 17981 – 17988, https://dx.doi.org/10.1021/ie503284xl

Chenxi, Y., Jian-Fen, C., Xiaofei, Z. and Daojian, C. (2018). *Enhanced Photochemical Performance of Hexagonal WO_3 by Metal-Assisted S – O Coupling for Solar-Driven Water Splitting*. Sci. China Mater 61(1), 91 – 100. https://doi.org/10.1007/s40843-017-9126-1

Duan, Y.H. and Sun, Y. (2014). *First-Principle Calculations of Optical Properties of Mg_2Pb*. Sci. China-Phys Mech Astron, 57: 233 – 238, https://doi.org/10.1007/s11433-013-5215-1

Fenggong, W., Cristiana, D.V. and Gianfranco, P. (2012). *Doping of WO_3 for photocatalytic water splitting*: Hints from density functional theory. *J. Phys. Chem. C 2012, 116, 8901-8909.*

Gillani, S.S.A., Ahmad, R., Islah-u-din, Rizwan, M., Shakil, M., M Rafique, Murtaza, G., and Jin, H.B. (2019). First-Principles Investigation of Structural, Electronic, Optical and Thermal Properties of Zinc Doped $SrTiO_3$, https://doi.org/10.1016/j.ijleo.2019.163481

Guntapon, P., Suphitchaya, S. and Mutsee, T. (2018). *Effect of doping Fe/Cu/Ti on WO_3 on furfural degradation*,MATECWeb of conferences, 192, 03048. https://doi.org/10.1051/matecconf/201819203048

Jaine, A., Hautier, G., Ong, S. P., Moore, C. J., Fischer, C. C., Persson, K. A., & Ceder, G. (2011). Formation enthalpies by mixing GGA and GGA+U calculations. Physical Review B, 84(4), 045115.

Kristin, P. (2011). Materials project. https://www.materialsproject.org

Likalter A.A (2002). Impurity states and insulator-metal transition in tungsten bronzes. 252-260.

Mansouri, M., and Mahmoodi, T. (2014). *Ab-initio Probing of Electronic Structure of WO_3 Doped with Li Atoms.* 2nd International Conference on New Frontiers in Physics (ICNFP), Instanbul, Turkey SRPioneers Publications.

Mansouri, M and Mahmoodi, T (2016). *Ab Initio Investigation on the Effect of Transition Metals Doping and Vacancies in WO_3*. Acta Physica Polonica A, 129 : 8 – 14. https://doi.org/10.12693/APhysPolA.129.8

Monkhorst, H, J., & Pack, J. D. (1976). Special points for Brillouin-zone integrations. Physical Review B, 13(12), 5188.

Ong, S. P., Wang, L., Kang, B., & Ceder, G. (2008). Li- Fe- P- O2 phase diagram from first principles calculations. Chemistry of Materials, 20(5), 1798-1807

Perdew, J. P., Burke, K., & Ernzerhof, M. (1996). Generalized gradient approximation made simple. Physical Review Letters, 77(18), 3865.

Xueting, C., Shibin, S., Xiao, X. and Zhenjiang, L. (2011). Synthesis of transition metal-doped tungsten oxide nanostructures and their optical properties. *Materials letters 65 (2011) 1710-*1712. https://doi.org/10.1016/j.matlet.2011.02.060

FUNGI SPECIES ASSOCIATED WITH POSTHARVEST SPOILAGE OF SWEET ORANGES (*Citrus sinensis*) SOLD IN BIDA METROPOLIS, NIGER STATE NIGERIA

Abdullahi Idris Dabban[1]*, Aisha Bisola Bello[2] and Alfa Suleiman[3]
[1,2,3] Department of Biological Sciences, The Federal Polytechnic Bida, Nigeria
[3]cabusalman@gmail.com
[2]belloaisha91@gmail.com
[1]aidabban@gmail.com
*Corresponding author

Abstract

An investigation was carried out on postharvest spoilage fungi associated with apparently diseased sweet oranges (Citrus sinensis) and pathological studies of these fungi on obviously healthy sweet oranges. Samples of diseased and healthy sweet oranges were collected from vendors from ten different locations in Bida metropolis, Niger State Nigeria. The samples were processed by surface sterilization using 85% ethanol, homogenized, inoculated on Potato Dextrose Agar and incubated for 7days at 30ºC. The mean viable mycological count of the samples was determined. Pure fungal isolates were obtained, identified and pathogenicity test of the pure isolates on healthy oranges were carried out using standard techniques. The study revealed over 90% of the samples were infected with one or more fungal species with mean mycological counts ranging from 1.60 X 10^2 cfu/ml to 4.60 X 10^2 cfu/ml. The highest occurring fungus encountered in this study was Aspergillus sp with 27.6% occurrence. Others include Mucor sp. (23.1%), Rhizopus sp. (15.7), Alternaria sp. (13.2%), Fusarium sp. (13.2%) and Penicillium sp. (7.4%). All the fungal isolates re-infected the healthy oranges with the exception of Fusarium sp. Good post production practices such as proper handling, transportation and storage should be encouraged. Separation and subsequent isolation of diseased oranges from healthy ones should be practiced to prevent economic loss due to these fungal pathogens.

Key words: Fungi, Postharvest, Spoilage, Sweet oranges

1. Introduction

Sweet orange (*Citrus sinensis*) is one of the most popular and widely planted fruit, grown commercially in tropical, semi-tropical and some temperate regions of the world (Onuorah *et al*., 2015). The fruit is rich in A, B and C vitamins, antioxidants as well as potassium, calcium, magnesium, iron, manganese, zinc, sodium,flavonoids, carotenoids, antioxidants, essential oils and dietary fibres, (Majo *et al*., 2005), hence it is consumed fresh or processed into juice or concentrates. The fruits and peels of oranges have been used as additives and preservatives in production of numerous desserts, jams, cookies, cakes as well as candies (Bailey and Bailey, 2006). The use of this important fruit for maintenance of good health and prevention of various health conditions such as asthma, cancer, obesity, asthma, arthritis, heart disease, kidney stones, high blood pressure and stroke have been reported (Tripoli *et al*., 2007).

Microbial attack and subsequent spoilage coupled with fairly short shelf life greatly influences the economic value of the fruit. *Citrus sinensis* contain high levels of sugars, high moisture content and low pH values which makes them predominantly desirable and susceptible to fungal spoilage (Moss, 2002; Kator, 2018). Spoilage of sweet oranges refers to any physical or chemical changes in the condition of the fruits in which they become less palatable (Onuorah *et al*., 2015). These conditions may be accompanied by alterations in taste, smell, appearance or texture due to the activities of spoilage microorganisms (Akinmusire, 2011). The spread of these conditions as a result of fungal infection in the fruits from a single infected orange to other healthy oranges during handling, bagging, storage and transportation can lead to loss of more than half of the harvested

fruit if uncontrolled (Oviasogie *et al*., 2015). The spoilage of sweet oranges is prevalent in underdeveloped and developing countries, where protection and proper handling of fresh sweet orange fruit is inadequately practiced (Liamngee *et al*., 2018).

Several fungi have been implicated in the spoilage of sweet oranges fruits. They include *Aspergillus* spp, *Rhizopus* spp, *Fusarium* spp, *Penicillium* spp, *Saccharomyces* spp, *Geotrichum* spp, *Candida* spp and *Trichosporon* spp. The fresh fruits are rendered unfit for human consumption by these organisms due to deterioration, and subsequent reduction in quality, production of off-flavour and nutrient loss (Kunta, *et al*., 2013). Keeping the above in view, the purpose of this work was to isolate and characterize filamentous fungi associated with the spoilage of post-harvest sweet oranges sold in some parts of Bida metropolis, Niger State, Nigeria.

2. Literature Review

In Nigeria, sweet oranges are usually transported to areas of high demand in open vehicles with no preservation facilities. Whereas in most markets, they are usually displayed on open trays, baskets, pans, and tables hence, expose the fruits to contamination by microorganisms including filamentous fungi (Onuorah *et al*., 2015). There have been several reports on the spoilage of sweet oranges by fungi. Bukar *et al*. (2009) carried out a mycological study in apparently diseased sweet oranges from retailers in Orange market, Kano Metropolis Nigeria. Their research revealed that up to 90% of the samples were infected with one or more fungal species. The most predominant pathogenic fungi isolated from the samples was, Aspergillus spp. (32.5%). Other fungi encountered in the study include Mucor sp. (25%), Penicillium sp (15%), Rhizopus sp (15%), Fusarium sp, (7.5%), and Alternaria sp. (5%). Proper handling from the farm, adequate storage and the separation of diseased and healthy fruits were identified as important factors in preventing spoilage and subsequent loss. The use of suitable chemical treatment of the oranges to reduce economic loss was also recommended**.**

Another research conducted by Tafinta *et al*. (2013) in Sokoto, Nigeria, fungi associated with deterioration of sweet oranges were isolated and characterized from 100 samples of fresh sweet Oranges. A total of seventy (70) samples were first collected from three selected markets in Sokoto metropolis (Central market, Kasuwar daji and Old market respectively). The oranges were allowed to deteriorate naturally for a period of two weeks under room temperature. After the incubation period, the samples were observed for spoilage. Each spoiled orange sample was cut and the liquid content inoculated on Potato Dextrose Agar (PDA) and incubated at 25ºC for 3-28. Fungi colonies obtained were identified using the slide culture technique. The study revealed that *Apergillus fumigatus* (22%), *Apergillus niger* (17%), *Aspergillus flavus* (25 %) *and Rhizopus stolonifer* (36%) were implicated in the spoilage of the sweet orange fruit. Subsequently, pathogenicity of the pure fungal isolates was determined using 30 samples of fresh sweet oranges obtained from the same markets. The research revealed *R. stolonifer* and *A. flavus* showed higher pathogenicity in the samples with rots diameter of 45 mm and 35 mm respectively, while the least pathogenic fungus was *A. niger* with 25mm rots diameter.

Onuorah *et al*. (2015) in a study isolated and identified some filamentous fungi associated with the spoilage of sweet oranges sold in major Awka Markets, Nigeria. The research revealed an average filamentous fungal count of the spoilt sweet orange fruits to be 2.0 X 10^3 cfu / ml, 1.3 X 10^3 cfu/ml, 2.1 X 10^3 cfu/ml, 1.6 X 10^3 cfu/ml and 1.8 X 10^3 cfu/ml for the samples from three different sampling sites. Fungi identified in the study consist of *Aspergillus niger*, *Aspergillus flavus*, *Rhizopus stolonifer*, *Mucor mucedo*, *Penicillium digitatum* and *Fusarium oxysporum* with percentage distribution of 27.5, 17.5, 22.5, 15.0, 10.0 and 7.5% respectively. *Aspergillus niger* was revealed to have the highest degree of spoilage. The research recommended that adequate storage facilities and good handling practices should put in place to reduce the incidence of these fungi in sweet oranges thereby minimizing their spoilage.

Liamngee *et al*. (2018) in a research isolated and identified fungi causing post harvesting spoilage of sweet orange in Buruku local government area of Benue State, Nigeria. Samples of sweet orange samples infected with rot were collected from different markets and plated on PDA using standard plating techniques. Four fungi namely *Aspergillus flavus, Aspergillus fumigatus, Rhizopus stolonifer* and *Aspergillus niger* were isolated with percentage occurrence of 11(32.4%), 10 (29.4), 8 (23.5%) and 5 (14.7%) respectively. The investigation also revealed a range of 8.8 - 35.3% distribution of fungi isolates in relation to markets. Furthermore, pathogenicity indicated 41-100% of tissue damage in the samples.

Recent investigation by Bashir *et al*. (2020) to determine fungal flora associated with post harvest spoilage of different citrus fruits (lime, lemon and sweet orange). Standard laboratory techniques were used to isolate fungi based on the morphological and microscopic characteristic. Several species of fungi were found to be associated with spoilage of the different types of citrus fruits. A total of 286 fungi were isolated where 40.56% fungi was isolated from lime, followed by lemon with 32.52% and the least was sweet lemon with 26.92%.The predominant fungi isolated were *Aspergillus niger* with (25.90%) in lime, (21.5%) in lemon and (23.38%) sweet lemon.. The pathogenicity test revealed that *Aspergillus niger* had the highest zone of spoilage, with 15.5mm, 14.5mm and 5.0mm diameter in fresh lime, fresh lemon and sweet orange respectively. The report suggested that proper postharvest handling practices should be encouraged to reduce the possibility of spoilage of citrus fruits by fungi.

3. Materials and Methods

3.1 Sample Area

The sampling sites were various vending stands at the old and new markets in Bida metropolis as well as orange vending stands at the small and big gates area of The Federal Polytechnic Bida, Niger State, North Central Nigeria.

3.2 Sample Collection

A total of 30 samples of oranges in batches of 3 were randomly selected from different locations designated A-J. Spoilt oranges were identified by observation of the physical appearance using the Method of Balali *et al*. (1995). Healthy oranges were also collected for use as controls.

3.3 Sample Processing

The orange samples were processed using the method of Balali *et al*. (1995). The apparently diseased oranges were cut from the advancing edges of lesion using a sterile knife. The cut portion of the lesion were further disinfected with 85% ethanol for 2minutes and then rinsed three times in distilled water. Each portion was then homogenized using a sterile glass rod and 4 folds serial dilution of the samples were carried out.

3.4 Isolation of Fungi

3.4.1 Preparation of Media

Potato Dextrose Agar (PDA) was prepared according to manufacturers' instruction, supplemented with chloramphenicol to prevent bacteria growth, sterilized by autoclaving at 121ºC for 15min and dispensed aseptically into sterile petri-dishes and slant bottles (Bukar *et al*., 2009; Tafinta *et al*., 2013).

3.4.2 Determination of Total Fungal Count

The PDA plates were inoculated with 0.1ml of the serially diluted samples and incubated at room temperature (27 - 30ºC) for 7 days. After the incubated period, resulting fungal colonies on the agar plates were counted and recorded in colony forming units per ml (cfu/ml) (Bukar *et al*., 2009).

3.4.3 Characterization and identification of fungal isolates

Fungal isolates obtained after the incubation period were sub-cultured to obtain pure culture. The fungal isolates were characterized and identified based on macroscopic and microscopic analysis using taxonomic guidelines and standard procedures. Macroscopic characteristics of 5-7day old fungal isolates were examined.

Microscopic examination was carried out using Lactophenol cotton blue staining as described by Fawole and Oso (1995). The pure fungal isolates were sub-cultured on SDA plates and incubated at room temperature for 2-3days. After the incubation period, a drop of sterile distilled water was transferred on a clean grease-free slide using a sterile pipette. Using a sterile inoculating needle, a pinch of the fungal mycelia was transferred aseptically from the culture plate and gently spread on the drop of water on the glass slides and then teased gently. This was followed by addition of 2-3 drops of lactophenol cotton blue stain. The slide was then covered with a clean cover-slip and examined under the microscope using x10 and x40 objective and compared with a mycological atlas.

3.5 Pathogenicity Test

Healthy oranges were surface disinfected and three 2mm holes were made using a sterile cork borer. Pure fungal isolates from the disease oranges were inoculated aseptically into the holes and the holes were sealed with candle wax. This was carried out in triplicates. The inoculated oranges were incubated in plastic containers for 7 - 14 days at ambient temperature (25- 30ºC). After the incubation period, inoculated oranges were observed for spoilage of the healthy oranges and growth of fungal colonies. These fungal colonies were matched with the colonies used as source of inoculums (Bukar *et al*., 2009; Tafinta *et al*., 2013; Bashir *et al*., 2020).

4. Results and Discussion

The mean total fungi count of the samples from the 10 sampling points ranged from 1.0 X 10^2 to 4.6 X 10^2 cfu/ml (Table 1). This is an indication that the sweet orange samples were massively infected by fungi species postharvest. Introduction of different fungi spores and subsequent spoilage of these samples could be as a result of improper postharvest practices such as handling, bagging, transportation and storage. These practices could lead to injuries of the samples and successive penetration of fungal spores, thereby leading to disease in the fruits. Bukar *et al*. (2009) reported similar findings (5.2 X 10^1 to 6.75 X 10^2 cfu/ml) in Kano, Nigeria while Onuorah *et al*. (2015) reported higher values of fungi count (1.3 X 10^3 to 2.1 x 10^3 cfu/ml) in Awka Nigeria. This variation could be due to the difference in weather and climatic conditions, as well as difference in handling, transportation and storage of the fruits.

Table 1: Mean Total Fungal Count of Sweet Orange Samples

Sampling points	Samples Collected	Infected Samples (%)	Mean Total Fungal Count (cfu/ml)
A	3	3 (100)	4.30 X 10^2
B	3	3 (100)	4.60 X 10^2
C	3	3 (100)	4.00 X 10^2
D	3	3 (100)	3.30 X 10^2
E	3	3 (100)	2.60 X 10^2
F	3	3 (100)	3.60 X 10^2
G	3	3 (100)	3.00 X 10^2
H	3	3 (100)	2.30 X 10^2
I	3	3 (100)	3.20 X 10^2
J	3	3 (100)	1.60 X 10^2
TOTAL	30	30 (100)	

Cultural and microscopic examination (Table 2) reveal *Aspergillus* sp., *Mucor* sp., *Rhizopus* sp., *Rhizopus* sp., *Fusarium* sp. and *Penicillium* sp. as the fungi isolated in this study. The frequency of occurrence of the fungi isolates (Figure 1) revealed *Aspergillus* sp. as highest occurring with 27.6% followed by *Mucor* sp. (23.1%), *Rhizopus* sp. (13.2%), *Fusarium* sp. (13.2%) and *Penicillium* sp. as the least occurring with 7.4% percentage occurrence. The occurrence of these organisms may be as a result of their ability to produce spores suspended in air, water and soil coupled with intrinsic factors such as high moisture and nutrient content and low pH of the fruit which makes an ideal environment for fungi proliferation (Bashir *et al*. 2020). Also, extrinsic factors such as temperature increase the susceptibility of the fruit to fungal attack (Bashir *et al*. 2020). This result agreed with the studies of Bukar *et al*. (2009), Onuorah *et al*. (2015) and Bashir *et al*. (2020) who isolated similar groups of organisms from citrus fruits in Kano, Anambra and Adamawa States respectively Nigeria.

Table 2: Cultural and Microscopic Characteristics of Fungi Isolated from spoilt Sweet Orange Fruits

Characteristics		Inference
Cultural (on PDA)	Microscopic	
Green colonies with white boundaries, powdery, slightly wooly, round to irregular colony shape, reverse side was pale yellow.	Unbranched rough conidiophores with rounded ends that bore conidia. Septate hyphae, simple and thick- walled. Phialides cover entire vesicle and point out in all directions.	*Aspergillus* sp
Initially white then grey cotton-like colonies, slightly spherical in shape. Covers agar surface quickly with dense growth. Reverse is yellowish.	Broad hyphae, aseptate. Long sporangiophores with round sporangia filled with spores. Absence of rhizoids.	*Mucor* sp
Grey cotton-like colonies without boundaries, dense growth that covers agar surface quickly. Reverse is whitish.	Broad scarcely septate hyphae. Long unbranched sporangiophores with a dark, round sporangium. Presence of rhizoids.	*Rhizopus* sp
White cotton-like with spherical irregular boundaries. Reverse is brownish.	Hyphae is septate. Unbranched conidiophores with oval clustered conidia. Presence of phialides with sickle shaped septate macroconidia.	*Fusarium* sp
Bluish green powdery colony with white irregular shaped border. Reverse is brown.	Septate hyphae, branched and few unbranched conidiophores with secondary branches (metulae). Flask-shape phialides are arranged on the metulae in whorls. Phialides bear unbranched chains of round conidia. Entire structure forms a brush appearance.	*Penicillium* sp.

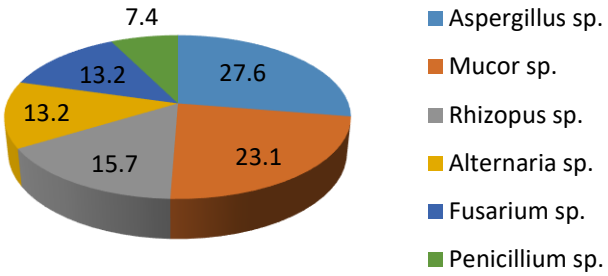

Figure 2: Percentage Frequency of Occurrence of the Fungi Isolated from Sweet Orange

The Pathogenicity test of this study (Table 2) reveals that with the exception of *Fusarium* sp. all other fungal isolates were able to re-infect the healthy oranges and produced visible disease condition. The inability of *Fusarium* sp. to cause spoilage in healthy orange samples could be because its presence on the fruit is transient or due to failure of the organism to produce necessary enzymes required to breakdown and utilize the high sugar content of the orange (Bukar *et al*., 2009; Bashir *et al*. 2020). This finding agrees with the researches of Bukar *et al*. (2009), Onuorah *et al*. (2015), who in their separate investigations reported pathogenicity of *Aspergillus* sp, *Mucor* sp, *Rhizopus* sp and *Penicillium* sp. on re-infection of the pure fungal isolates into healthy sweet oranges. Bukar *et al*. (2009) also reported the inability of *Alternaria* sp to cause spoilage in healthy sweet oranges.

Table 3: Pathogenicity Test of the Fungal Isolates on Apparently Healthy Sweet Oranges

S/No.	*Aspergillus* sp	*Mucor* sp	*Rhizopus* sp.	*Alternaria* sp	*Fusarium* sp	*Penicillium* sp
1	+	+	+	+	-	+
2	+	+	+	+	-	+
3	+	+	+	+	-	+

The presence and distribution of these fungal groups and their subsequent spoilage of sweet oranges could be due to injury and further contamination of the fruit during harvesting, transportation, packaging, storage and overall handling practices (Onuorah *et al*., 2015). The production of secondary metabolites such as aflatoxins and other mycotoxins by these organisms could pose potential health challenges to consumers of fungi-contaminated sweet oranges (Baiyewu *et al*., 2007). Furthermore, these organisms in certain conditions could cause a wide range of diseases in human and animals (Petzinger & Weidenbach, 2002; Monso, 2004).

5. Conclusion

Filamentous fungi implicated in the spoilage of sweet oranges from vendors in some part of Bida metropolis include *Aspergillus* sp., *Mucor* sp., *Rhizopus* sp., *Rhizopus* sp., *Fusarium* sp. and *Penicillium* sp. Out of these fungi isolates, *Aspergillus* sp. was the most predominant with 23.1% occurrence. Majority of the fungi isolates infected and ultimately caused spoilage of the fruit excluding *Fusarium* sp.The presence of these organisms in the fruit could pose potential health implications to consumers. For this reason, their presence in sweet oranges and other fruits should be controlled through adequate and proper washing of the harvested fruits, use of clean sterile containers for packaging, avoidance of injury in the fruit through proper handling, sufficient hygienic practices by the handlers, provision of very clean storage facilities and application of safe and food grade fungicidal substances on the sweet oranges. Lastly, orange fruits with any symptom of spoilage should be swiftly separated, properly disposed of and should not be sold or consumed.

References

Akinmusire, O. (2011). Fungal Species Associated with the Spoilage of some Edible Fruits in Maiduguri, North Eastern, Nigeria. *Advances in Environmental Biology, 5* (1), 157-161.

Baiyewu, R. A., Amusa, N. A., Ayoola, O. A., & Babalola, O. O. (2007). Survey of the postharvest diseases and aflatoxin contamination of marketed pawpaw fruit (Carica Papaya L.) in South Western Nigeria. *African Journal of Agricultural Research, 2* (4), 178-181.

Bashir, M., Hamza, F. A., & Pukuma, M. S. (2020). Postharvest Fungal Spoilage of Some Citrus Fruits. *Bioengineering and Bioscience, 7* (1), 10-14.

Bukar, A., Mukhtar, M., & Adamu, S. (2009). Isolation and Identification of Postharvest Spoilage Fungi Associated with Sweet Oranges (Citrus sinensis) Traded in Kano Metropolis. *Bayero Journal of Pure and Applied Sciences, 2* (1), 122 - 124.

Kunta, M., Sa, P., Palm, M., Rascoe, J., Timmer, K., Da Graca, J. V., et al. (2013). Sweet Orange Scab with a New Scab Disease Syndrome of Citrus in the U.S.A. Associated with Elsinoe australis. *Tropical Plant Pathology, 38* (3), 203-212.

Liamngee, K., Onah, D. O., & Jeremiah, G. (2018). Isolation and Identification of Fungi Causing Postharvest Spoilage of Sweet Orange (Citrus sinensis) in Buruku Local Government Area of Benue State. *Public Health Letters, 3* (9), 1-7.

Majo, D. D., Giammanco, M., Guardia, M. L., Tripoli, E., Giammanco, S., & Finotti, E. (2005). Flavones in citrus fruit: structure antioxidant activity relationship. *Food Research International, 38* (10), 1161-1166.

Monso, E. M. (2004). Occupational Asthma in Greenhouse Workers. *Current Opinion in Pulmonary Medicine, 10* (2), 147-150.

Moss, M. (2002). Risk Assessment of Aflatoxins in Foodstuffs. *International Biodeterioration & Biodegradation, 50*, 137-142.

Onuorah, S., Obika, I., & Okafor, U. (2015). Filamentous Fungi Associated with the Spoilage of Post-Harvest Sweet Orange Fruits (Citrus Sinensis) Sold in Awka Major Markets, Nigeria. *Bioengineering and Bioscience, 3* (3), 44-49.

Oviasogie, F., Ogofure, A., Beshiru, A., Ode, J. N., & Omeje, F. (2015). Assessment of Fungal Pathogens Associated with Orange Spoilage. *African Journal of Microbiology Research, 9*, 1758-1763.

Petzinger, E., & Weidenbach, A. (2002). Mycotoxins in the Food Chain: The role of Ochratoxins. *Livestock Production Science, 76*, 245-250.

Tafinta, I. Y., Shehu, K., Abdulganiyyu, H., Rabe, A. M., & Usman, A. (2013). Isolation and Identification of Fungi Associated with the Spoilage of Sweet Orange (Citrus sinensis) Fruits in Sokoto State. *Nigerian Journal of Basic and Applied Science, 21* (3), 193-196.

Tripoli, E., Guardia, M., Giammanco, S., Majo, D. D., & Giammanco, M. (2007). Flavonoids: Molecular Structure, Biological Activity and Nutritional Properties: A Review. *Food Chemistry, 104* (104, No.2,), 466-479.

ANTIDIARROHOEA ACTIVITY OF METHANOLIC EXTRACT OF SCOPARIA DULCIS LINN.

*OGBE AJUMA HANNAH, ABDULLAHI MANN AND LABAKE AJOKE FADIPE
Department of Chemistry, Federal University of Technology, Minna, Nigeria.
*Corresponding Author: Email: ogbehannah.ao@gmail.com

ABSTRACT

Diarrhea is a form of gastrointestinal infection caused by a variety of bacterial, viral and parasitic organisms, through contaminated food or drinking water, or from person to person as a result of poor hygienic practices. Plants have extraordinary potential uses, particularly as customary prescription and pharmacological medications. The antidiarrheal activity of the methanol extract was evaluated against castor oil induced diarrheal model, charcoal meal and enteropooling tests. The test groups received 100, 200 and 400 mg/kg of the extract. Phytochemical screening of the leaf extract showed that it contains alkaloids, tannins, saponins, glycosides, proteins and starch. The extract was evaluated for castor oil induced diarrhea. The methanol extract exhibited antidiarrheal activity in a non-dose dependent manner (P<0.05). The 200 mg/kg dose had the highest inhibition in all tested models and its activity is comparable to the standard drug (loperamide). This study demonstrates that scoparia dulcis have phytoconstituents which possess antidiarrheal activity and this validates its use in traditionally in the treatment of diarrhea.

Keywords: Antidiarrhoea activity, *Scoparia dulcis* and phytochemical screening

INTRODUCTION

Diarrhoea is a symptom of disease marked by rapid and frequent passage of semisolid or liquid faecal materials through the gastrointestinal tract (GIT) along with increased motility and secretions of GIT and decreased fluid absorption (Zayede *et al.*, 2020). Diarrhoea is a form of gastrointestinal infection caused by a variety of bacterial, viral and parasitic organisms or through contaminated food or drinking water, or from person to person as a result of poor hygienic practices (Peter and Umar, 2018). Globally, 4 – 5 million death cases of human occur annually as a result of diarrhoea. Diarrhoea is one of the leading causes of death in children below five years. Over 10% of death in children, about 800, 000 die each year as a result of diarrhoea (Nduche and Omosun, 2016). Plants have been used since time immemorial for diverse purposes in the life of mankind particularly as food, and medicines for nutrition and the treatment of diseases, respectively, in both humans and animals. They are used in all cultures of the world and have been relied upon for several millennia to support, promote and restore human health. They form a vital component of traditional medicine (TM) and their use for the maintenance of health and wellbeing is a common practice in all African societies (Mensah *et al.*, 2019)

MATERIALS AND METHODS

Collection and Preparation of Plant Material

Fresh plants of Scoparia dulcis were collected from a farm in Olowa Dekina local government area of Kogi State in the month of May, 2020. Dried plants were cut into smaller pieces and milled into fine powder by using mortar and pestle.

Extraction

Cold maceration technique was used to extract 710 kg of the plant material by soaking the powder in 2.5L methanol for 72 h with occasional agitation. The extract was filtered and the solvents

evaporated under reduced pressure with the rotary evaporator at 30 °C and the concentrate freeze-dried to obtain the crude extract (CE) which was stored at 4 °C until required for further processing.

Phytochemical Screening

Qualitative analysis were carried out on the crude methonol extract using standard procedures to identify the constituents as described by Sofowora (1983) and Trease and Evans (2002).

ANTIDIARREAL ACTIVITY

Grouping and Dosing of Animals.

For each of the three antidiarrhoeal activity test models, 20 Wister rat were used. The Wister rats were randomly divided into five groups of 4 Wister rat each for each model. In all models, the negative control groups were treated with the vehicle (distilled water, 10 ml/kg). The positive controls were treated with loperamide 3 mg/kg (in castor oil-induced diarrhoea and enter pooling models) and atropine 1 mg/kg (in gastrointestinal motility test model). The other groups (Groups 3, 4, and 5) in each model received 100, 200 and 400 mg/kg doses of the crude extract respectively.

Castor Oil Induced Diarrhea Model

Animals were fasted for 18 h and placed individually in a cage, in which the bottom floor was lined with blotting paper and was replaced every hour. Then animals received either vehicle or treatment samples as based on their fasting weight. Diarrhoea was induced by administering 0.5 mL of castor oil per oral route to each mouse just 1h after the previous treatments. The observation was continued for a period of 4h. Time of onset of diarrhoea, a total number of faecal outputs (frequency of defecation) and weight of faeces excreted by the animals were recorded. Finally, the percentage of diarrhoeal inhibition, percentage weight of wet faecal output and percentage weight of total faecal output were determined with respect to their formula (Degu *et al*., 2016; Sisay *et al*., 2017).

$$\text{Percent Inhibition} = \frac{\text{Average number of WFC} - \text{Average number of WFT}}{\text{Average number of WFC}} \times 100$$

Where, WFC=average number of wet faeces in the control group and

WFT=average number of wet faeces in the test group.

$$\text{Percentage of Wet faecal output} = \frac{\text{Mean weight of wet faces of each group}}{\text{Mean weight of wet faces of the control}} \times 100$$

$$\text{Percentage of total faecal output} = \frac{\text{Mean faecal weight of each group}}{\text{Mean weight of the control}} \times 100$$

Castor Oil Induced Charcoal Meal Test

Gastrointestinal motility test using activated charcoal was done in accordance with the method described by Sisay *et al*. (2017). Wister rat of either sex were fasted for 18 h with free access to water and treated with the vehicle, standard drug and plant extract according to their respective groups based on their fasting weight by oral gavage. After 1 hour of test/ vehicle compound administration, 0.5 mL castor oil was administered by oral gavage then 1 mL of 5% charcoal suspension was administered orally 1 hour after castor oil treatment. After 1 hour of the charcoal meal, animals were sacrificed by cervical dislocation and the small intestine was dissected out and later the total length covered by a charcoal indicator from the pylorus to cecum was measured and calculated as a percentage of the total length of the small intestine. Finally, the Peristalsis index and proportion of inhibition were calculated using the following formula:

$$\text{Peristaltic index} = \frac{\text{Mean distance travelled by charcoal meal}}{\text{Mean length of small intestine}} \times 100$$

$$\text{Percentage of inhibition} = \frac{\text{PIC} - \text{PIT}}{\text{PIC}} \times 100$$

Where, PIC=Peristaltic index of control; PIT=Peristaltic index of the test group

Castor Oil Induced Enteropooling Model

The intraluminal fluid accumulation (enteropooling) was carried out based on a method described by (Sisay *et al*., 2017). Wister rat were grouped as described earlier and fasted for 18 h prior to the experiment. Then the test compound and vehicle were given according to their grouping based on their fasting weight by oral gavage 1 hour prior to castor oil administration. After 1 hour all Wister rat were sacrificed by cervical dislocation, and then the small intestine was isolated and tied with thread at the pyloric end and the ileocaecal junction. Then the weight of filled intestine was measured and the content was drained into a graduated cylinder and volume was measured, later the weight of empty intestine was re measured again and the change in the full and empty intestine was calculated. Finally, the percentage reduction of intestinal discharge (volume) and weight of intestinal content were calculated by comparing with a negative control by the following formula.

$$\text{Mean percentage volume inhibition} = \frac{\text{MVICC} - \text{MVICT}}{\text{MVICC}} \times 100$$

Where, MVICC is the Mean volume of the intestinal content of the control group

MVICT is the Mean volume of the intestinal content of the test group.

$$\text{Mean percentage weight inhibition} = \frac{\text{MWICC} - \text{MWICT}}{\text{MWICC}} \times 100$$

Where, MWICC is the Mean weight of the intestinal content of the control group

MWICT is the Mean weight of the intestinal content of the test group.

***In-Vivo* Anti-Diarrheal Index**

The *in vivo* anti-diarrheal index (ADI) was determined by combining three parameters taken from the abovementioned models. It was then expressed according to the following formula (Zwedie *et al*., 2020).

$$\text{ADI percentage volume inhibition} = \sqrt[3]{\text{Dfreq} \times \text{Gmeq} \times \text{Pfreq}}$$

Where, Dfreq is the delay in defecation time as a percentage of negative control, Gmeq is the gut meal travel reduction as a percentage of negative control.

Pfreq is the reduction in purging frequency in the number of wet stools as a percentage of the negative control.

$$\text{D Frequency} = \frac{\text{MODTG} - \text{MODCG}}{\text{MODCG}} \times 100$$

Where, MODTG is Mean onset of diarrhoea in the test group
MODCG is Mean onset of diarrhoea in the control group

Data Analysis
Analyses were carried out using Statistical Package for the Social Sciences 20 for windows (SPSS 20). Results were expressed as Mean±SEM. Statistical significant difference were determined using ANOVA.

RESULTS AND DISCUSSION
RESULTS
Qualitative phytochemical analysis
Result of phytochemical screening (Table 1), revealed the presence of tannins, flavonoids, saponins, terpenoids, phenolic compounds, steroids and alkaloids in the methanolic extract of *Scoparia dulcis.* However, glycosides and reducing sugars were absent.

Table 1: Qualitative screenings of *Scoparia dulcis* methanolic extract (SDME)

Phytoconstituents	Presence
Flavonoids	+++
Tannins	+
Saponins	++
Phenols	+++
Glycosides	–
Steroids	++
Reducing sugars	-
Terpenoids	+++
Alkaloids	++

+++=abundance, ++= moderate, += present, (-) =absent

IN-VIVO ANTI-DIARRHEAL ACTIVITY STUDIES

Castor Oil Induced Diarrhea

The methanolic extract of *S. dulcis* significantly prolonged the time of diarrheal onset; the mean weight of faeces of rats treated with extract doses were significantly ($P<0.05$) lower than that of the negative control group. Similarly, the extract at the tested doses exhibited good antidiarreal activity against castor-oil induced diarrhea in rats. The extract inhibited diarrhea onset in a non-dose dependent manner with the 200 mg/kg dose having the highest activity, followed by 100 mg/kg and 400 mg/kg had the least activity. The percentage inhibitions of diarrhea faeces were 88, 73 and 34% respectively and were lower than that of loperamide (91%).

Table 2: Effects of *S. dulcis* methanolic extract on castor oil induced diarrhoea in rats

Treatment and dose	Mean weight of total faeces (g)	% Inhibition of total faeces (g)	Mean weight of diarrhea faeces (g)	% Inhibition of diarrhea faeces

Negative Control (2mL/kg B.W)	0.78±0.01^{d}	-	0.33±0.01	-
Loperamide (3 mg/kg B.W)	0.32±0.03^{a}	58.97	0.03±0.00	91
SDME (100 mg/kg B.W)	0.48±0.01^{b}	38.46	0.09±0.01	73
SDME (200 mg/kg B.W)	0.36±0.04^{a}	53.85	0.04±0.00	88
SDME (400 mg/kg B.W)	0.59±0.04^{c}	24.34	0.24±0.04	24

SDME= *Scoparia dulcis* methanol extract. Values are presented as mean ± standard error of mean (SEM) of three replicates. The values with different superscripts in a column are significantly different at ($P< 0.05$).

Castor Oil Induced Enteropooling

The extract (100, 200 and 400 mg/kg) non-dose dependently showed a reduction in the mean weight of intestine and mean weight of intestinal content. The activity of extract doses were significantly different ($P<0.05$) when compared to the negative control group. The percentage volume of inhibition of extract was in a non-dose dependent manner, the highest dose (400 mg/kg) had highest activity, followed by 200 and 100 mg/kg respectively. The activity of the doses were significantly ($P<0.05$) lower when compared to the standard drug, loperamide.

Table 3: Effects of *Scoparia dulcis* methanolic extract on castor oil induced enteropooling in rats.

Treatment and dose	Mean weight of intestine (g)	Mean weight of intestinal content (g)	Mean volume of inhibition (%)
Negative Control (2 mL/kg B.W)	9.90±0.24^{c}	5.82±0.59^{c}	-
Loperamide (3 mg/kg B.W)	6.83±1.00^{a}	3.24±0.35^{a}	44.33
SDME (100 mg/kg B.W)	8.50±0.74^{b}	4.33±0.39^{b}	25.60
SDME (200 mg/kg B.W)	7.03±0.67^{a}	3.96±0.37^{ab}	31.96
SDME (400 mg/kg B.W)	9.23±0.85^{bc}	4.40±0.46^{b}	34.40

SDME: *Scoparia dulcis* methanolic extract; mg/kg B.W: milligram per kilogram body weight. Values are presented as mean ± standard error of mean (SEM) of three replicates; the values with different superscripts in a column are significantly different at $p < 0.05$; n=5

Effects on Castor Oil Induced Intestinal Transit in Charcoal Meal Test

The methanolic extract of *S. dulcis* significantly ($P<0.05$) slowed down the forward motion of charcoal meal through the gastrointestinal tract at all tested doses when compare to the control group. The distance travelled by charcoal meal for 100, 200 and 400 mg/kg B.W. groups were 32.73±0.45, 29.50±1.21 and 36.81±1.14 respectively. The extract also significantly inhibited gastrointestinal transit time of charcoal meal by 58.36%, 63.80% and 53.36% at doses 100, 200 and 400 mg/k body weights respectively. The 200 mg/kg showed the highest inhibition and its activity is comparable to that of the standard drug, loperamide ($P>0.05$).

Table 4: Effect of *Scoparia dulcis* methanolic extract on intestinal motility of rats by charcoal meal

Treatment and dose	Intestinal length (cm)	Distance travelled (cm)	Peristatic Index (%)	% Inhibition
Negative Control (2 mL/kg B.W)	107.55±4.35^{a}	84.24±2.93^{d}	78.32±2.11^{e}	-
Loperamide (3 mg/kg B.W)	105.20±2.86^{a}	26.67±1.92^{a}	25.35±2.89^{a}	67.63
SDME (100 mg/kg B.W)	100.37±3.14^{a}	32.73±0.45^{b}	32.61±1.02^{c}	58.36
SDME (200 mg/kg B.W)	102.65±5.23^{a}	29.50±1.21^{a}	28.35±0.98^{a}	63.80
SDME (400 mg/kg B.W)	100.78±4.56^{a}	36.81±1.14^{c}	36.53±1.43^{d}	53.36

SDME = *Scoparia dulcis* methanol extract. Values are presented as mean ± standard error of mean (SEM) of three replicates. The values with different superscripts in a column are significantly different at $p < 0.05$.

DISCUSSION

Despite the fact that their safety and efficacy profiles have not been adequately addressed, medicinal plants have been utilized for the treatment of a variety of illnesses including diarrhea and related gastrointestinal disorders. The results from the present study revealed the presence of flavonoids, tannins, saponins, phenols, steroids, terpenoids and alkaloids in the methanolic leaf extract of *Scoparia dulcis*. The presence flavonoids, tannins, saponins, phenols, steroids, terpenoids and alkaloids have previously been reported in the leaf extract of the plant (Muhammad *et al.*, 2018).

Castor oil's usage as a diarrhea inducer is extensively documented (Shiferie and Shibeshi, 2013). It has an irritating laxative action when taken orally, which is mediated by its active metabolite,

ricinoleic acid, which is produced by intestinal lipases. Ricinoleic acid causes local irritation and inflammation of the intestinal mucosa, which leads to the generation of prostaglandins, which increase gastrointestinal motility and net water and electrolyte secretion (Gelberg, 2018).

The extract in a non-dose dependent fashion inhibited the effect of castor oil on gastrointestinal integrity of the rats in comparison to the negative control group. The methanol extract significantly ($P<0.05$) reduced the mean weight of total faeces, % inhibition of total faeces and mean weight of diarrhea faeces in experimental animals. The percentage inhibition of diarrhea faeces was observed to be highest at 200 mg/kg dose followed by 100 mg/kg and 400 mg/kg had the least inhibition.

The extract also significantly ($P<0.05$) reduced the mean weight of intestine, mean weight of intestinal content and mean volume inhibition in a non-dose dependent manner. The lower and middle doses (100 mg/kg and 200 mg/kg) had higher activities, although significantly ($P<0.05$) lower when compared to the standard drug (loperamide). One of the mechanisms through which antidiarrheal drugs work is by reducing gastrointestinal motility (Sisay *et al.*, 2018).

At all concentrations studied, the methanol extract significantly ($P<0.05$) inhibited the propulsion of the charcoal marker with highest activity observed at 200 mg/kg which is comparable to that of loperamide. This finding demonstrates that the extract has the ability to affect gut peristaltic movement, implying that it possesses antimotility properties. Certain phytochemicals such as; flavonoids, tannins and terpenoids have been reported to possess antidiarrheal activities (Jalilzadeh-Amin and Maham, 2015). Studies have found that the presence of tannins and flavonoids increases intestinal water and electrolyte reabsorption; tannins are known to increase intestinal mucosa resistance by reducing secretion, restoring abnormal water transport, and decreasing intestinal transit (Degu *et al.*, 2016).

Furthermore, flavonoids have been discovered to have a wide range of biological actions, including the inhibition of enzymes such as prostaglandin synthase, cyclooxygenase, and lipoxygenase, which may play a role in its anti-diarrheal activity (Hossain *et al.*, 2012). Terpenoids and saponins can decrease the production of autacoids such as prostaglandins and histamines (Derebe *et al.*, 2018). Saponins have also been shown to have antibacterial activity, which may be due to their capacity to form a combination with extracellular proteins, soluble proteins, and bacterial cell walls (Mummed *et al.*, 2018). Phenolic compounds and alkaloids also inhibit intestinal motility (Mishra and Sasmal, 2015).

Generally, phytochemicals exert their bioactivity either singly or in synergy with one another (Ogbeide *et al.*, 2018). This may be responsible for the displayed antidiarrheal activity of the methanol extract of *Scoparia dulcis.*

Conclusion

The methanol extract of *Scoparia dulcis* leaves is rich in phytochemicals which include; flavonoids, tannins, saponins, phenols, steroids, terpenoids and alkaloids, and has promising antidiarrheal effects, according to this study. The extract in a non-dose dependent fashion inhibited the effect of castor oil on gastrointestinal integrity in rats with 200 mg/kg dose having highest percentage inhibition of diarrhea faeces.

Similarly, the extract significantly ($P<0.05$) reduced the mean weight of intestine, mean weight of intestinal content and mean volume inhibition in a non-dose dependent manner. Furthermore, the methanol extract significantly ($P<0.05$) inhibited the propulsion of the charcoal marker with highest activity observed at 200 mg/kg which is comparable to that of loperamide. This discovery therefore lends scientific support to *Scoparia dulcis'* traditional use as an antidiarrheal medication.

References

Degu, A., Engidawork, E., Shibeshi, W. (2016). Evaluation of the anti-diarrheal activity of the leaf extract of *Croton macrostachyus* Hocsht. Ex Del. (Euphorbiaceae) in mice model. *BMC Complement. Altern. Med.,* 16, 1–11.

Derebe, D., Abdulwuhab, M., Wubetu, M. & Mohammed, F. (2018). Investigation of the Antidiarrheal and Antimicrobial Activities of 80% Methanolic Leaf Extract of *Discopodium penninervum* (Hochst.). *Evidence-Based Complement. Altern Med.,* 2018, 1–7.

Gelberg, H. (2018). Pathophysiological mechanisms of gastrointestinal toxicity. *Comprehensive Toxicology*, 139-178.

Hossain, E., Ko, S.Y. & Yang, C.J. (2012). Dietary supplementation of green tea byproducts on growth performance, meat quality, blood parameters and immunity in finishing pigs. *J. Med. Plants Res.,* 6, 2458–67.

Jalilzadeh-Amin, G. & Maham, M. (2015). The application of 1, 8-cineole, a terpenoid oxide present in medicinal plants, inhibits castor oil-induced diarrhea in rats. *Pharm. Biol.*, 53(4), 594–9.

Mensah, M.L.K., Gustav, K., Arnold D. F., Caleb, F., Alexander, K. A. & Rita, A. D. (2019). Toxicity and safety implications of herbal medicines used in Africa. DOI: 10.5772/intechopen.72437.

Mishra, C.K. & Sasmal, D. (2015). In-vivo evaluation of anti-diarrhoeal activity of ethanolic fruit and root extracts of Carissa carandas Linn. (Apocynaceae). *Int. J. Drug Dev. Res.,* 7, 216–21.

Muhammad, S. N., Samirah, I. U., Abdullahi, D. A. & Jamila, M. H. (2018). Phytochemical screening of the ethanolic leaves and root extract of *Scoparia dulcis*. *International Journal of Environmental Chemistry,* 2(2), 39-42.

Nduche, M. U. & Omosun, G. (2016). The use of medicinal plants in the treatment of diarrhoea in Nigeria: ethnomedical inventory of Abia State. *Scholars Journal of Agriculture and Veterinary Sciences,* 3(3):270-274.

Ogbeide, O.K., Dickson, V.O., Jebba, R.D., Owhiroro, D.A., Olaoluwa, M.O., Imieje, V.O., Erharuyi, O., Owolabi, B.J., Fasinu, S.P. & Falodun, A. (2018). Antiplasmodial and acute toxicity studies of fractions and cassane-type diterpenoids from the stem bark of *Caesalpinia pulcherrima* (L.) Sw. *Trop. J. Nat. Prod. Res.*, 2(4), 179-184.

Peter, A.K. & Umar, U. (2018). Combating diarrhea in Nigeria: the way forward. *J. Microbiol. Exp.*, 6(4), 191-197.

Shiferie, F. & Shibeshi, W. (2013). *In-vivo* antidiarrheal and ex-vivo spasmolytic activities of the aqueous extract of the roots of *Echinops kebericho* (Asteraceae) in rodents and isolated guinea-pig ileum. *Int. J. Pharm. Pharmacology*, 2, 110–6.

Sisay, M., Engidawork, E. & Shibeshi, W. (2020). Evaluation of the antidiarrheal activity of the leaf extracts of *Myrtus communis* Linn (Myrtaceae) in mice model. *BMC Complementary and Alternative Medicine*, 17, 1-11.

Sofowora, A. (1983). *Medicinal Plants and Traditional Medicine in Africa*. 1st ed., New York: John Wiley and Sons Ltd. 168-171.

Trease, G. E. & Evans, M.C. (2002). *Textbook of Pharmacognosy*. 12th Ed. Tindall, London. Pp. 343-38.

Zayede, D., Tafere, M. & Wubayehu, K. (2020). "Antidiarrheal activity of hydromethanolic root extract and solvent fractions of *Clutia abyssinica* Jaub. & Spach. (Euphorbiaceae) in Mice", *Evidence-Based Complementary and Alternative Medicine*, 2020, 1-9.

Chemometric Analysis of Physico-Chemical Parameters and Heavy Metals Accumulation in Bosso Dam, Minna

Corresponding Author: Unaeze, C. H.[1]
Email: chyfor1@yahoo.com
Co-Authors: Salau, R. B.[2], Jacob, J.O.[2], Ndamitso, M. M.[2], Mohammed, A. K.[3]
[1]National Biotechnology Development Agency, Abuja.
[2]Federal University of Technology, Minna.
[3]North Carolina Central University, Durham, North Carolina.

Abstract
Water quality is important the protection of humans and marine ecosystems. Over the past two decades, considerable attention has been given to heavy metals in both terrestrial and aquatic ecosystems because they can be accumulated by biota and at high concentrations are potentially toxic. Traditional biological indices or direct measurements of water quality, which are based on in situ data collection are often spatially or temporally limited. On the other hand, the complexity of information requires new analysis techniques that allow for identification of the components and possible causes of spatial and temporal variability. Bosso dam is a major source of water for both domestic and agricultural purposes in Minna metropolis. In this study, the concentration of toxic heavy metals such as Pb, Ni, Mn, Zn, Cd, Cu and Cr were determined in water from Bosso dam during wet season. One hundred water samples were collected and homogenized into ten composite samples. Water and sediment samples were digested according to the method described by Türkmen and Ciminli (2007). Techniques of Chemometrics such as Principal Component Analysis (PCA), Hierarchical Component Analysis (HCA) and Correlation Analysis (CA) were used to analyze pollution data sets from heavy metal determination and assessment of the physicochemical parameters such as pH, temperature, turbidity, Si, conductivity, NO_3^- –N, NH_4^+–N, NO^{-2} –N of water. Pb was below detection limits while Cr was detected at a value of 0.02mg/l and 0.01mg/l for Cd, Zinc, Cu, Ni, Mn in the water samples. Application of PCA and CA helped to identify the underlying pollution sources and signature at the monitoring site.

Keywords: Water quality, Heavy metals, Chemometrics, Pollution, Bosso dam

1.0 Introduction

Heavy metals refer to the, dense and metallic elements that occur in trace levels, but are very toxic and tend to accumulate, hence are commonly referred to as trace metals (Adelekan *et al.,* 2016). They are metallic elements with high atomic weight and density greater than that of water. The major anthropogenic sources of heavy metals in the environment are industrial wastes from mining sites, electroplating manufacturing and finishing plants, domestic waste-water and run off from roads. Many of these trace metals are highly toxic to humans, such as Pb, Cd, and Cr. Exposure to Pb can cause kidney and brain damage. Cd has been reported to cause damage to the adrenals and homopoietic system. Cr has also been reported to cause lung cancer (USDFFS 2018). Their presence in surface and underground water at above background concentrations is undesirable (Adelekan *et al.*, 2016).

Bosso dam is situated within Minna metropolis and is a major source of water for domestic, agricultural and industrial uses in Minna metropolis. Residents along the bank of the river often cultivate crops such as sweet potatoes, maize, tomatoes and vegetables, and use water from the river to irrigate the crops. Water from this dam is also being used for domestic and recreational (swimming) purposes and fishing. These usage expose the downstream users to some health hazards, thus the need to determine the level of heavy metals and mineral elements for the safety of the users.

Chemometric statistical analysis provides useful tools for the study of spatial uncertainty and hazard assessment. In recent times, many researchers used sample site data to model the spatial distribution of heavy metals in sediment. Also, methods of multivariate data analysis are powerful tools for the evaluation and interpretation of river pollution data. Much information is lost using only univariate graphical or statistical methods for data evaluation and interpretation. In the last decade, methods such as principal component analysis (PCA) have become accepted in the identification of temporal and spatial variation and sources of pollution in river water (Biancolillo *et al*., 2018). However, applications of different chemometrics methods to the analysis of water bodies are not common in Nigeria. Thus, the monitoring of heavy metal levels in water bodies using chemometric techniques is of great importance for protection and ensuring future sustainability of aquatic environments. However, few environmental studies on spatial distribution, identification of pollution sources, including risk assessment of trace metals in Bosso have been conducted in Nigeria (Igiri, *et al*., 2018).
Deming *et al.,* (2019) determined the spatial distribution, potential risks and sources of seven heavy metals in Yangtze River Estuary. Analyses of 55 sediment samples revealed that the distributions of metals within the river were determined by the combined effects of their sources, hydrodynamic conditions, pH and Eh. According to the geoaccumulation index (Igeo) and sediment quality guidelines, Pb, Cd and Cr were present at low levels of pollution, with Cd posing the largest ecological risk. Positive Factor Matrix (PMF) results indicated that Hg, Zn, As, Pb and Cr mainly originated from natural geological background sources, while Cu originated from anthropogenic activities and atmospheric deposition was the source of Cd. These three sources contributed to 53.0%, 32.8% and 14.2%, respectively of total heavy metal concentrations.

Yunquian *et al.,* (2019) analyzed surface sediment samples collected from 18 sites in Dongping Lake for selected heavy metals including As, Cd, Cr, Cu, Hg, Pb, and Zn to determine their spatial distribution, source, and potential ecological risks. The enrichment degree of the studied metals decreased in the order of Cd N Hg N As N Pb N Cu N Cr N Zn, and the average concentrations of Cd, Hg and As were 3.70, 3.69 and 3.37 times their background values.

With the exception of Cd, the concentrations of heavy metals decreased progressively from the southeast to the north and west within the lake. Based on the enrichment factor (EF) and the potential ecological risk index (PERI), As, Cd and Hg were the heavy metal contaminants of most concern in surface sediments. Moreover, referencing to the results of multivariate statistical analyses, it was deduced that anthropogenic As and Hg were mainly from industrial and mining sources within the Dawen River watershed, whereas, Cd originated from agricultural sources.

Although heavy metal pollution in Bosso dam has been investigated, assessing the contamination and ecological risks of heavy metals in the water using multiple approaches that are based on multivariate analytical tools is meaningful. The assessment would help characterize the contamination sources in river and surface sediments and provide a tool for effectively protecting the river environment. Thus, this study focused on the analysis of the physico-chemical quality and accumulation of selected heavy metals in water from Bosso dam, and application of chemometric techniques to the pollution data. Methods of multivariate data analysis were applied for the evaluation and interpretation of data. This analysis could be helpful for Nigerian Government to optimize the marine water monitoring plan and enhance their pollution control actions

1.1 Study Location

Bosso Dam is located at latitude 9˚ 39N and longitude 6˚ 33E in Minna, Niger state. It is a small water body with a mean depth of 6.1M (20.2FT). The dam is shaded by shrubs, trees and bushes especially in the rainy season. The main use of the dam is for water supply (portable water) for domestic and irrigation purpose. The resources in the dam are conserved and protected from poachers by making it a restricted area. Most changes in the dam were brought about by flooding

of terrestrial ecosystem with organic and inorganic materials, defecation of animals and siltation. The dominant fish species in the dam is Tilapia zilli while crocodiles also inhabit the dam.

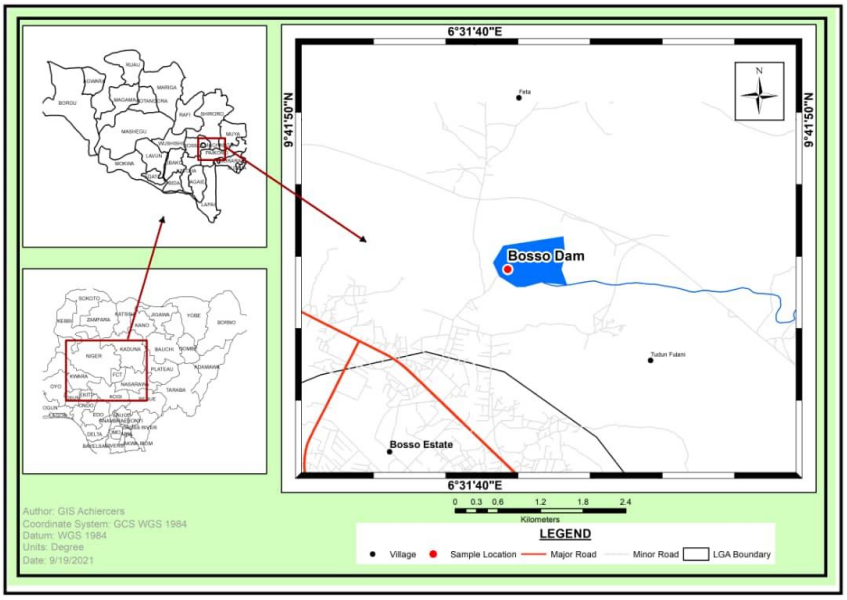

Figure 1: Map of Minna Metropolis showing location of Bosso dam in Minna

2.0 Methodology

One hundred surface water samples were collected at different points and homogenized into ten composite samples coded W1 to W10. Water samples were gently collected in clean plastic containers and were subjected to preliminarily acidification. This was done by adding 5cm^3 of nitric acid to each water sample. On-site analyses of pH, conductivity, and turbidity were carried out at the site of sample collection following the standard protocols and methods of American Public Health Organization (APHA) (APHA, 2005) and American Society for Testing and Materials (ASTM) using different calibrated standard instruments (J. DeZuane, 1997). The pH of the water samples was measured by using a pH meter. The pH meter was calibrated, with three standard solutions (pH 4.0, 7.0, and 10.0), before taking the measurements. The value of each sample was taken after submerging the pH probe in the water sample and held for a couple of minutes to achieve a stabilized reading. After the measurement of each sample, the probe will be rinsed with deionized water to avoid cross contamination among different samples.

The conductivity of the samples was measured using a conductivity meter. The probe was calibrated using a standard solution with a known conductivity. The probe was submerged in the water sample and the reading was recorded after the disappearance of stability indicator. The turbidity of the water samples was measured using a turbidity meter. Each sample was poured in the sample holder and kept inside for a few minutes before the result was recorded. Elemental analysis of water samples for Cr, Cu, Zn, Cd, Mn and Pb was carried out with Atomic Absorption Spectrometer (acetylene air), according to the ASTM standard method (ASTM, 2012) approved by APHA (2005) while the physicochemical characteristics of the water samples were carried out According to the standard methods of APHA (APHA, 2005) and Sawyer *et al.* (2005) by the filtration process. Silica was determined using the Standard Test Method for Silica in Water as described by ASTM D859-16. A test of the molybdenum-blue method was used for silica measurement.

For nitrite-nitrogen determination, the Nitrate/Nitrite-N in Water and Biosolids by Manual Colorimetry method as described by U.S. Environmental Protection Agency (2001) was used. 2cm^3 of color reagent (prepared by adding 100 cm^3 85% phosphoric acid (H_3PO_4) and 10 g sulfanilamide was added to about 800 mL reagent water and mixed to completely dissolve the sulfanilamide. 1 g

N-(1-naphthyl)-ethylenediamine dihydrochloride was added and mixed to dissolve. It was diluted to 1 L with reagent water and added to 50.0 mL of sample. It was allowed ten minutes for the color to develop, the absorbance of the sample was measure at 540 nm. Techniques of Chemometrics such as Principal Component Analysis (PCA), Hierarchical Component Analysis (HCA) and Correlation Analysis (CA) were used to analyze pollution data sets from heavy metal determination and assessment of the physicochemical parameters such as pH, temperature, turbidity, Si, conductivity, NO_3^-, NO_2–N, NH_3, NO_2^- –N of water.

3.0 Results and Discussions

3.1 Physiocochemical parameters and heavy metals in water samples from Bosso dam

The statistical result with respect to mean and standard error of mean values for Bosso dam water quality parameters and heavy metal levels are summerized in Table 1. All water samples contained Ammonia at values significantly ($P \leq 0.05$). This could be due to the increased agricultural activities in the study location during rainy season. All the nitrate levels noticed in all samples were below the World Health Organisation (WHO 2018) recommended maximum safe level (10mg/l) for human consumption. Elevated levels of nitrate and nitrite in surface waters usually result from human activities such as overuse of chemical fertilizers and improper disposal of human and animal nitrogen-containing wastes, which are converted to nitrates in the soil. Nitrogen enters waterways either from the breakdown of dead organic matter or via atmospheric nitrogen gas fixation by specially adapted plants. Excess nitrogen in rivers enhances nutrient enrichment leading to algal blooms, fish kills and weed infestation (Yahaya *et al*. 2019). High levels of dissolved forms of nitrogen (nitrate, nitrite and ammonia) can also be toxic to many aquatic organisms and can prevent the water from being used as potable supply.

Heavy metals such as Pb and Cr were below detection limit in all the water samples. However, Cd was found in water samples W1 above WHO's permissible limit with 0.008mg/l. This could be due to the direct release of effluent from Minna Water Board treatment plant located next to Bosso dam. This corroborated the suggestion by Cotman *et al.* (2019) that surface waters are used for disposal of treated effluents from wastewater treatment plants. These effluents usually contain only small amounts of various contaminants that accumulate over time in the river, especially in sediments (Cotman *et al.,* 2019). Muhammad *et al*. (2018) reported similar result and attributed such occurrence to the fact that the discharge of heavy metals into rivers by domestic and industrial activities causes their rapid association and dissociation with particulates and incorporation into bottom sediment.

Table 1: Physiocochemical parameters and heavy metals in water samples from Bosso dam

Parameters	W1	W2	W3	W4	W5	W6	W7	W8	W9	W10	WHO
pH	6.91±0.01^{b}	6.91±0.01^{a}	6.92±0.01^{a}	6.92±0.01^{a}	6.86±0.07^{a}	6.75±0.01^{a}	6.72±0.01^{a}	6.75±0.01^{a}	6.75±0.01^{a}	6.85±0.01^{a}	6.50-8.50
Temperature	27.70±0.06^{a}	27.70±0.06^{a}	27.70±0.06^{ab}	27.70±0.06^{a}	27.70±0.06^{b}	27.40±0.10^{a}	27.40±0.06^{a}	27.40±0.06^{a}	27.40±0.06^{a}	27.60±0.06^{a}	12– 25
Silica	1.90±0.06^{a}	6.60±0.06^{c}	1.70±0.06^{b}	1.70±0.06^{a}	9.40±0.06^{c}	8.60±0.06^{b}	4.80±0.06^{b}	4.70±0.06^{a}	9.60±0.06^{c}	9.10±0.06^{c}	10.00
Turbidity	18.00±0.06^{a}	18.00±0.06^{a}	14.00±0.06^{a}	14.00±0.06^{a}	12.00±0.06^{a}	21.00±0.06^{a}	19.00±0.06^{a}	34.00±0.06^{a}	30.00±0.06^{a}	61.00±0.06^{a}	5.00
Conductivity	74.00±0.06^{a}	71.00±0.06^{a}	71.00±0.06^{a}	71.00±0.06^{a}	76.00±0.06^{a}	80.00±0.06^{a}	33.00±0.06^{a}	91.00±0.06^{b}	76.00±0.06^{a}	95.00±0.06^{a}	1000
Nitrite	0.02±0.00^{b}	0.02±0.00^{c}	0.02±0.00^{a}	0.02±0.00^{a}	0.01±0.00^{a}	0.01±0.01^{a}	0.01±0.00^{a}	0.02±0.00^{a}	0.01±0.00^{a}	0.02±0.00^{a}	1.00
Nitrite as N_2	0.02±0.00^{b}	0.01±0.00^{c}	0.01±0.00^{a}	0.01±0.00^{a}	0.00±0.00^{a}	0.00±0.00^{a}	0.00±0.00^{a}	0.01±0.00^{a}	0.00±0.00^{a}	0.01±0.00^{a}	0.04
Ammonia	8.30±0.06^{c}	6.60±0.06^{c}	6.30±0.06^{c}	6.30±0.06^{c}	4.40±0.06^{b}	6.70±0.06^{c}	6.20±0.06^{b}	5.90±0.06^{b}	5.600±0.06^{c}	5.90±0.06^{c}	0.40
Copper	0.00±0.00^{b}	0.00±0.00^{b}	0.01±0.00^{c}	0.01±0.00^{c}	0.00±0.00^{a}	0.00±0.00^{b}	0.00±0.00^{a}	0.00±0.00^{a}	0.01±0.00^{c}	0.00±0.00^{ab}	0.01
Nitrate	0.70±0.06^{a}	0.44±0.01^{b}	0.38±0.01^{a}	0.38±0.01^{a}	0.500±0.06^{a}	0.60±0.06^{a}	0.13±0.01^{a}	0.11±0.01^{a}	1.60±0.06^{a}	1.44±0.01^{a}	10.00
Zinc	0.00±0.00^{a}	0.01±0.00^{b}	0.01±0.00^{a}	0.01±0.00^{a}	0.01±0.00^{b}	0.00±0.00^{a}	0.00±0.00^{a}	0.01±0.00^{c}	0.00±0.00^{b}	0.01±0.00^{c}	0.01
Manganese	0.00±0.00^{a}	0.00±0.00^{a}	0.00±0.00^{a}	0.00±0.00^{a}	0.00±0.00^{a}	0.00±0.00^{a}	0.00±0.00^{a}	0.01±0.00^{c}	0.00±0.00^{a}	0.00±0.00^{b}	0.10
Cadmium	0.01±0.00^{c}	0.01±0.00^{b}	0.00±0.00^{b}	0.00±0.00^{b}	0.00±0.00^{a}	0.00±0.00^{a}	0.00±0.00^{a}	0.00±0.00^{a}	0.00±0.00^{a}	0.00±0.00^{a}	0.00
Lead	0.00±0.00^{a}	0.00±0.00^{a}	0.00±0.00^{a}	0.00±0.00^{a}	0.00±0.00^{a}	0.00±0.00^{a}	0.00±0.00^{a}	0.00±0.00^{a}	0.00±0.00^{a}	0.00±0.00^{a}	0.01
Chromium	0.02±0.01^{c}	0.00±0.00^{a}	0.00±0.00^{a}	0.00±0.00^{a}	0.00±0.00^{a}	0.00±0.00^{a}	0.00±0.00^{a}	0.00±0.00^{a}	0.00±0.00^{a}	0.00±0.00^{aa}	0.05

Values are reported as mean ± standard error of means. Values along the rows with the different alphabetic superscripts are significantly different at $p \leq 0.05$ while values with the same alphabet are not significant at the same confidence level.

Notes: W1 to W10 represents water samples collected from ten different points

3.1.1 Chemometric Analysis

Chemometrics analysis was performed on the pollution data generated and the PCA results obtained for the elements are shown in figures 2 to 7. Two principal components having eigenvalues greater than 1 were considered. According to Liu et al. (2018), strong and moderate factor loadings range from >0.75, and <0.5 to 0.3, respectively. The first principal component (PC1) in the datasets explains 30.03% of total variance and is moderately positively loaded with Nitrate, Zn, turbidity, Silica, Conductivity, Cr, Mn and Nitrite, indicating both natural and anthropogenic sources. The dominant factor loading of Zn in the first PC1 strongly suggests that the origin of Zn could be associated to the leaching fertilizers into underground water as reported by Mmolawa *et al.* 2017). The most important anthropogenic sources zinc in soil come from discharges of smelter slags and wastes, mine tailings, coal and bottom fly ash, and the use of commercial products such as fertilizers and wood preservatives that contain zinc (Mmolawa *et al.* 2017).

The PC2 in the datasets shows 29.72 % of variance and positively loaded with Cu, Cd, Ammonia, Temperature and pH, indicating anthropogenic sources. The long-established agricultural practices near the study site can be regarded as the sources of Ammonia and Cu, while the waste water effluent can be regarded as the major source of Cd at the study site. Fertilizers can also be regarded as anthropogenic sources of ammonia and Cu.

Figure 3 shows the Hotelling T^2 plot which allows us to identify outlying samples. From the result obtained, Samples W8 and W10 were observed as the exceptional samples with unusual pollution status. The PCA scores as seen on figure 4 is about sample grouping. The plot differentiated the samples into three groups. Figure 6 represents the Biplot shows samples and variables simultaneously. The result obtained showed the different groups and their variables. HCA performed on the data reveals three major clusters (Fig. 7). Cluster 1 comprises 1, 2 and 3. The interrelated association among these samples shows similar positive loadings in PC1. Cluster 2 includes 4, 5, 6, 7, and 9. The interrelated association shows similar positive loadings in PC1. Cluster 3 contains 8 and 10, and its positive loadings are similar to PC2. HCA showed Pair 8 and 10 share similar pollution status. Their similarity is seen in their Ammonia contamination level which is the same (5.90mg/l) as well as nitrite and nitrite as nitrogen levels which are 0.02mg/l and 0.01 respectively.

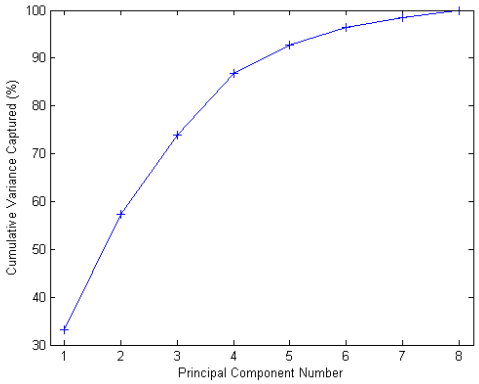

Figure 2: PCA Eigenvalue plot for water samples

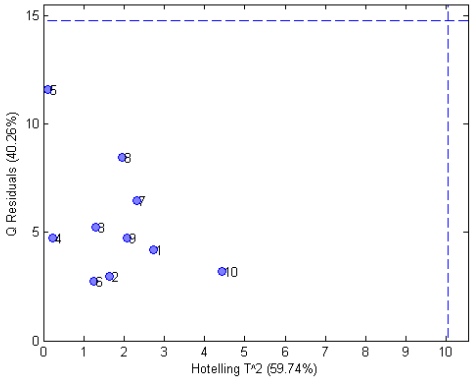

Figure 3: Hotelling T^2 plot for water samples from Bosso dam

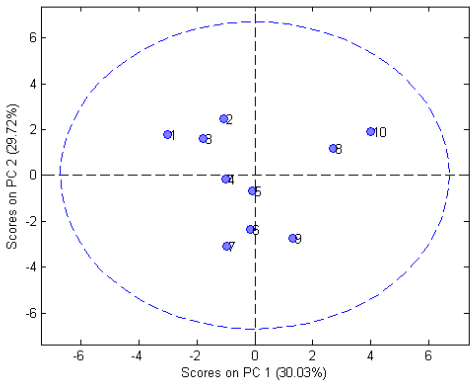

Figure 4: PCA Scores plot for water samples

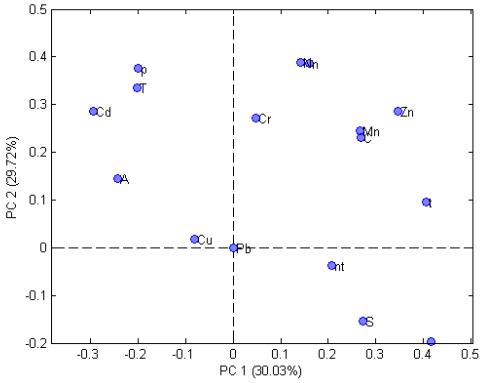

Figure 5: PCA Loadings plot for water sample

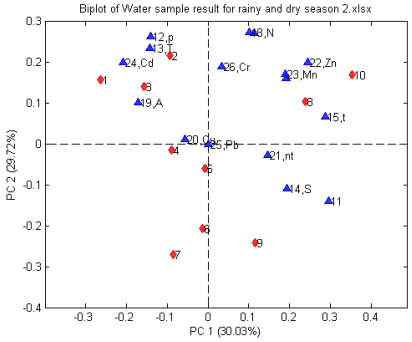

Figure 6: PCA Biplot for water samples and variables

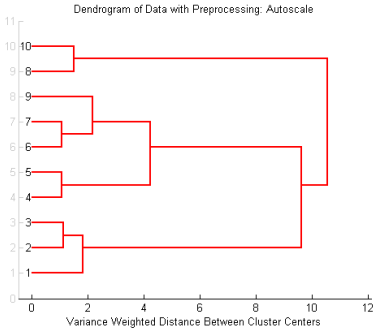

Figure 7: HCA Dendogram for water samples

3.1.2 Correlation Analysis

Correlation analysis of the data was carried out using Microsoft Excel Add-ins. The result shown in Table 2 suggests that most of the variables were negatively correlated. However, strong positive correlation was observed for Cd - NO_2^-, Cd - pH, Cd - Temperature, Pb - Cr, Cd - NH_3, NO_2^- -NH_2^--N, Zn – Mn, Cr – Zn, Cr, Mn and Cr - Pb. Cadmium concentration was strongly correlated with pH, Temperature, Nitrite, Nitrite as Nitrigen and Ammonia at 0.75, 0.66, 0.65 and 0.73 respectively, which may be due to leaching or fertilizer from irrigation water. Silica showed no positive correlation with other variables.

4.0 Conclusion

This work was undertaken to evaluate the pollution status of Bosso dam. From PCA, two principal components suggests possible anthropogenic sources. These components explain 59.79% of the total variance and high positive loading was found in samples W8 and W10. The present investigation clearly indicates that the water from Bosso dam is contaminated with some toxic heavy metals, Ammonia, Nitrite as Nitrogen. Consequently, there is a dire need to reduce/regulate the anthropogenic sources of pollution in the study area.

Table 2: Correlation among different variables

	p	T	S	t	C	n	N	A	Cu	nt	Zn	Mn	Cd	Pb	Cr
p	1														
T	**0.969159**	1													
S	-0.4093	-0.34433	1												
t	-0.62176	-0.7298	0.319241	1											
C	0.185616	0.098174	0.129887	0.334386	1										
n	0.434303	0.297305	-0.30832	0.20901	0.19927	1									
N	0.422745	0.266588	-0.29637	0.265694	0.254967	**0.993111**	1								
A	0.292907	0.142827	-0.51481	-0.01376	-0.05749	0.443681	0.462759	1							
Cu	0.382434	0.298165	-0.00985	-0.29175	0.22225	-0.20192	-0.1478	-0.0873	1						
nt	-0.07575	-0.129	0.441989	0.26257	0.231529	-0.37574	-0.28216	-0.03474	0.435493	1					
Zn	0.173931	0.176391	-0.07952	0.250258	0.557617	0.452345	0.439603	-0.43137	-0.11874	-0.35615	1				
Mn	-0.02896	-0.06036	-0.29473	0.347184	0.463693	0.49332	0.489099	-0.16762	-0.38604	-0.46655	**0.841442**	1			
Cd	**0.751012**	**0.656134**	-0.33289	-0.23578	0.032316	**0.647945**	**0.647392**	**0.732274**	0.015563	0.012771	-0.11733	-0.15297	1		
Pb	0.069012	0.5382	-1.42091	0.21682	0.33986	0.220197	0.10932	-0.83922	0.3274	0.13249	0.44271	-0.31974	0.73921	1	
Cr	0.436376	0.485238	-0.2025	-0.12227	0.471831	0.315439	0.274753	-0.35453	0.028453	-0.43992	**0.865184**	**0.573337**	0.038013	**0.82653**	1

References

Adelekan, B. & Abegunde, K. (2016). Heavy metal contamination of soil and ground water at automobile mechanic village in Ibadan, Nigeria. International Journal of the Physical Sciences. 6(5),1045-1058.

Akpoborie, I.A. (2015). Aspects of the Hydrology of the Western Niger Delta Wetlands: Groundwater conditions in the Neogene (Recent) deposits of the Ndokwa Area. Proceedings of the Environmental Management Conference: Managing Coastal and Wetland Areas of Nigeria, Sept. 12-14, Abeokuta

Raji, M.I.O., Ibrahim, Y.K.E., Tytler, B.A., & Ehinmidu, J.O. (2015). Analyses of selected heavy metals and mineral elements in pollution prone River Sokoto in Northwestern Nigeria. Journal of Pure and Applied Sciences, 3(4): 91-97.

Muhammad, H.L., R.A. Shehu, L.S. Bilbis & S.M. Dangoggo. (2014). Analyses of selected Heavy Metals and Mineral Elements in Pollution Prone Aquatic Environments of North-Western Region of Nigeria. Asian Journal of Biological Sciences, 7(6): 252-261.

Fashola, F.I., Nwankwoala, H.O & Tse, A. C. (2013). Physico-chemical Characteristics of Groundwater in Old Port Harcourt Township, Eastern Niger Delta. International Journal of Physical Sciences, 1(3), 047 – 055

Galarpe, V. R.K.R., & Parilla, R. (2014). Analysis of Heavy Metals in Cebu City Sanitary Landfill, Philippines. Journal of Environmental Science and Management 17(1), 50-59.

Hilgenkamp, K. (2006). Environmental health: ecological perspective. Toronto, Canada: Jones and Bartlett Publishers.

Igiri, B. E.,. Okoduwa, I. R,, Idoko, G.O., Akabuogu, E.P., Adeyi, A.O., & Ejiogu, I. K. (2018). Toxicity and Bioremediation of Heavy Metals Contaminated Ecosystem from Tannery Wastewater. 2568038 | 16.

Liu J, Cui B, Dong S, Zhu J, Yao W.(2018). Study on the effect of highway construction on photosynthetic rate of roadsides plant in longitudinal range-Gorge Region. Chinese Sci Bull 51(Supp):59–68

Mmolawa KM, Likuku AS, Gaboutloeloe GK. (2017). Assessment of heavy metal pollution in soils along major roadside areas in Botswana. Afr J Environ Sci Technol 5(3):186–196

World Health Organization (WHO). Guidelines for drinking-water quality, fourth edition. (2018).

Yahaya, I., Ezeh, G., Musa, Y. Mohammad, S. (2019). Analysis of heavy metals concentration in road sides soil in Yauri, Nigeria. African Journal of Pure and Applied Chemistry.

Profiling of Selected Nigerian Local Rice Varieties for their Essential Trace Elements Content

*Okoli C. J., Salau R.B., Salihu S.O., Bisiriyu M. T. and Salihu A. M.
Chemistry Department, P.M.B. 65 Federal University of Technology Minna
*corresponding author: okoli.j.chidozie@gmail.com

Abstract

Rice is a staple food crop which is widely grown across the continents. This study evaluates the essential trace element contents of some locally grown varieties of rice in Nigeria. Eighteen local variety from 14 rice producing states in Nigeria were obtained from popular markets. Samples were dried, homogenized and later digested using proportionate amount of HNO_3/H_2O_2. The concentrations of the three elements (Cu, Mn, Fe) were determined using Atomic Absorption Spectrophotometer. The method used was validated using a certified reference. The result showed the following ranges of concentrations: Cu (1.00 ± 0.02-5.00 ± 0.14), Fe (10.85 ± 0.50-38.40 ± 0.99), and Mn (1.95 ± 0.65-32.10 ± 0.24) mg/kg. The concentration of Cu, Fe and Mn in the studied local rice suggest their nutritional potentials as food for sourcing essential trace elements. The values of the essential trace elements were below the WHO permissible limit which indicates consumption safety. The rice from Idanre and Lafiagi have substantial content of Cu. Ofada and Ikirun rice are rich in Fe content. Substantial amount of Mn was found in Abakaliki and Efon-Alaaye rice. The studied local rice could play a beneficial role in management of mineral deficiency diseases.

Keywords: local rice; Nigeria; trace elements; essential; copper; manganese; iron; mineral deficiency

1.0 INTRODUCTION

Rice has been known to be very rich in carbohydrate and as well as other essential nutrients. Also, research findings have revealed that it contains an appreciable content of both beneficial and toxic heavy metals (Wong *et al.,* 2004). They are absorbed by plants through the atmosphere, fertilizers, pesticides and deposition of urban and industrial waste on the soil and the water (Duruibe *et al.,* 2007) used to irrigate the plants. So, when these food crops are consumed by humans, they are bound to absorb some of these heavy metals into their system (Jarup, 2003). Excess heavy metal accumulation in the environment is capable of having toxicological implication in humans, plants and other animals (Otitoju *et al.,* 2012).

Copper is an essential trace element that plays a vital role in the health of all living things. In humans, it is needed for the proper functioning of organs and metabolic processes. However, like all essential elements and nutrients, too much or too little nutritional ingestion of copper can result in a corresponding health effect. Daily dietary standards for copper have been set by various health agencies around the world. Some nations of the world have recommended various levels for copper intake by adults, pregnant, women, infants and children. (Scheiber *et al.,* 2013*).*

Iron is a chemical element with symbol Fe and atomic number 26. It is a member of first transition series, often refers to as the most common element on Earth and forming much of Earth's outer and inner core (Meija, 2016). Iron plays an important role in biological system, forming complexes with molecular oxygen in hemoglobin and myoglobin- major components of oxygen transport proteins in vertebrates. It also acts as an active site metal for many of the important redox enzymatic reactions dealing with cellular respiration and as well as oxidation-reduction reactions in plants and animals.

Manganese is a chemical element with symbol Mn and atomic number 25, found in a combined form either as minerals in combination with iron (Meija, 2016). Manganese (II) ions function as cofactors for a large variety of enzymes with many functions such as glucose utilization, lipid synthesis and its metabolism. It is also involved in the normal skeletal growth and activation of enzyme functions. The human system has about 10 mg of Mn which is reported to be more concentrated in the bones. Recommended dietary intake of Mn per individual with respect to age 15 is 3.3 mg/day, pregnancy is 3.0 mg/day, ages 2 - 14 (0.6 to 2.1 mg/day) while ages 19 - 50 is 2.3mg/day. Some of the side effect of high concentrations of Manganese in the body include hallucinations and nerve damage (WHO, 2001).

2. Materials and Methods

2.1 Sample collection and Pretreatment.

Eighteen different brands of locally farmed rice were sourced *from Lafiagi, Doko, Kwakuti, Kaduna, Katsina, Kano, Abakaliki, Adani, Oso-Akwa, Omor, Efon-Alaaye, Oke-Ogun, Idanre, Ofada, Ijebu Ode, Kuta, Patigi, Ikirun* in their farms. 100 grams each of the rice sample were ground using mortar and pestle. The powdered samples were sieved using 5nm mesh to remove any large debris left. The sieved samples were then kept in an air-tight container for further analysis.

2.2 Sample Pretreatment, Ashing and instrumental analysis

Large Ceramic Pestle and mortar were washed, cleaned and cleansed with concentrated Nitric Acid and then distilled water. These rice samples were homogenized thoroughly in the ceramic mortar using the pestle wide enough to accommodate the minute components of the rice mixture. The process was continued until a homogeneous blend was obtained and transferred to oven, in previously cleaned porcelain crucibles. The samples were dried and grinded into fine powder in titanium blade grinding machine. The fine powder of 100g was the average dried sample obtained. This was then kept separately in polyethylene bags, sealed, labeled and kept until further analysis.

Ground rice sample, 1g, was put in a crucible and heated on a hot plate at about 80^{o}C. The ash obtained thereafter was diluted with 2.5cm^{3}of HNO_3 and 5cm^3 hydrogen Peroxide. The digestion continued until a clear solution was obtained to signify a complete digestion. After cooling, the digested sample were filtered and diluted to 50cm^3 with distilled water into a 100cm^3 volumetric flask which was then transferred into a sample bottle for further analysis. Bulk Scientific Atomic absorption spectroscopy (AAS); *Model:* Accusys 211; *Manufacturer*: USA determined Copper, Iron and Manganese content of the samples.

2.2 Statistical Analysis

Collected data were subjected to one-way analysis of variance (ANOVA) for comparison using the SPSS software (Version 15, SPSS Inc, Chicago, USA). Results were expressed as mean ± SD and variations were considered significant when $P < 0.05$.

3. RESULTS AND DISCUSSION

The concentrations of essential trace elements in Nigerian local rice are presented in Table 1. The copper level in rice samples ranges from 1.00 ± 0.02 - 5.00 ± 0.14 while that of iron ranges from 10.85 ± 0.50 -38.40 ± 0.99 mg/kg. Manganese concentration ranges from 1.95 ± 0.65-32.10 ± 0.24 (mg/kg).

Table 1: Copper, Iron, Manganese concentration of the local rice samples

Sample	Identity	State	Cu (mg/kg)	Fe (mg/kg)	Mn (mg/kg)
S_1	Lafiagi	Kwara	4.85±0.10	19.50±0.39	2.65±0.05
S_2	Doko	Niger	2.35±0.08	13.35±0.46	3.90±0.14
S_3	kwakuti	Niger	1.80±0.01	18.85±0.11	2.85±0.02
S_4	Kaduna	Kaduna	1.30±0.01	23.60±0.27	18.79±0.06
S_5	Katsina	Katsina	4.70±0.11	26.30±0.27	16.45±0.05
S_6	Kano	Kano	1.25±0.03	16.05±0.32	1.95±0.65
S_7	abakaliki	Ebonyi	2.40±0.11	10.85±0.50	32.10±0.24
S_8	Adani	Enugu	2.20±0.10	20.25±0.82	5.25±0.13
S_9	Oso akwa	Anambra	1.80±0.10	21.95±1.14	3.60±0.19
S_{10}	Omor	Anambra	1.00±0.02	24.20±0.66	3.20±0.07
S_{11}	Efon-Alaaye	Ekiti	4.20±0.09	26.90±0.66	24.30±0.51
S_{12}	Oke-Ogun	Oyo	4.40±0.14	24.60±0.80	8.00±0.52
S_{13}	Idanre	Ondo	5.00±0.14	20.50±0.60	6.90±0.20
S_{14}	Ofada	Ogun	3.90±0.11	34.60±1.02	6.80±0.20
S_{15}	Ijebu Ode	Ogun	3.40±1.10	27.40±8.96	6.80±2.20
S_{16}	Kuta	Niger	2 .20±0.04	17.75±0.16	10.60±0.1
S_{17}	Patigi	Kwara	1.80±0.10	23.25±1.21	3.90±0.20
S_{18}	Ikirun	Osun	3.90±0.10	38.40±0.10	5.70±0.13
	RDA daily range		0.54-1.0mg	8.00-30.00mg	1.80-2.30mg
	RDA Tolerable daily Limit		10mg	45mg	11mg

Mean ±SD
**Malaysian
RDA = Recommended Dietary Allowance (µg/day), N/A = No data Dietary Guidelines available, UL = Tolerable Upper Intake Level (2010)

3.1 Copper

The rice samples from *Idanre* and Lafiagi have the highest value of copper. The concentration of *Idanre* rice (5.00±0.14) was significantly higher than all other rice samples from other locations while that of *Omor* was significantly lower than all other locations. *Katsina* was significantly higher than *Ijebu-Ode* rice but was statistically comparable to those of *Osun*, *Ofada* and *Efon-Alaaye*. This is attributed to difference in the specie of the samples under consideration; total content of soil trace elements, soil chemical and physical properties; which affect bioavailability of trace elements in plants (Cheng *et al,* 2011).

In decreasing order, the concentration of copper in the rice from the selected areas are *Idanre* > *Lafiagi* > *Katsina* > *Oke-Ogun* > *Efon-Alaaye* > *Ofada* > *Ikirun* > *Ijebu-Ode*> *Abakaliki* > *Doko* > *Kuta* > *Adani* > *Oso-Akwa* > *Kwakuti* >*Patigi* > *Kano* > *Kaduna* > *Omor*. When an individual of 60kg weight consumes about 200g of rice daily. The individual is bound to absorb 0.97 ,0.47, 0.36, 0.26, 0.94, 0.25, 0.48, 0.44, 0.36, 0.2, 0.84, 0.80, 1, 0.78, 0.68, 0.44, 0.36 and 0.78 mg/day of copper concentration of samples; S_1, S_2, S_3, S_4, S_5, S_6, S_7, S_8, S_9, S_{10}, S_{11}, S_{12}, S_{13}, S_{14}, S_{15}, S_{16}, S_{17} and S_{18} respectively. These copper concentrations (mg/day) by an individual are within the Recommended Dietary Allowance limit of (0.54-1.00) mg/day. Comparing the results of this work with similar studies, a work carried out on

locally produced rice in Thailand (Wannee *et al*, 2018) showed that the estimated daily intake of copper content of the rice samples was (0.18-0.37) mg/day and was lower than the estimated daily intake of Copper content (0.20-1.00) mg/day.

3.2 Iron

The highest amount of Iron is gotten from *Ikirun* rice and *Ofada* rice. The concentration of rice from *Ikirun* (38.40±0.99) was significantly higher than all other rice samples from other locations while that of *Abakaliki* was significantly lower (10.85±0.50) than all other locations. *Oke-Ogun* was significantly higher than *Enugu, Kaduna, Patigi, Oso-Akwa, Idanre, Adani, Lafigi, Kwakuti* rice but was statistically comparable to those of *Katsina, Ekiti, Ijebu-Ode.* This is attributed to anthropogenic activities such as the use of phosphate fertilizers, industrial activities and deposition of contaminated particles (Yuanan *et al*, 2013). In decreasing order, the concentration of Iron in the rice from the selected area was *Osun > Ofada > Ijebu Ode > Efon-Alaaye > Katsina > Oke-Ogun > Omor > Kaduna> Patigi > Oso Akwa > Idanre > Adani> Lafiagi> Kwakuti > Kuta > Kano > Doko > Abakaliki.* When an individual of 60kg weight consumes about 200g of rice daily. The individual is bound to absorb 3.9 ,2.67, 3.77, 4.72, 5.26, 3.21, 2.17, 4.05, 4.39, 4.84, 5.38, 4.92, 4.10, 6.92, 5.48, 3.55, 4.65 and 7.38 mg/day of iron concentration of samples S_1, S_2, S_3, S_4, S_5, S_6, S_7, S_8, S_9, S_{10}, S_{11}, S_{12}, S_{13}, S_{14}, S_{15}, S_{16}, S_{17} and S_{18} respectively. The Recommended Dietary Allowance of iron in this study ranges from (2.17-7.38) mg/day and it's below the Recommended Dietary Allowance (8.00-30.00) mg/day, this shows that the rice samples will be able to prevent many iron deficiencies like anemia especially in women of childbearing age, pregnant women and teenage girls because they are at greatest risk of developing iron deficiency.

3.3 Manganese

Abakaliki and Efon-Alaaye rice have the highest amount of Manganese. The concentration of manganese in the rice from *Abakaliki* (32.10±0.24) was significantly higher than all other rice samples from other locations while that of *Kano* was significantly lower (1.95±0.65) than all other locations. *Idanre* was significantly higher than *Abakaliki, Kaduna, and Doko* rice but was statistically comparable to those of *Ofada, Ijebu Ode, Idanre.* This may be due to difference in the specie of the samples under consideration; total content of soil essential elements, soil chemical and physical properties; which affect bioavailability of essential element in plants (Cheng *et al*, 2011).

In decreasing order, the concentration of Iron in the rice from the selected area was *Kano > Efon-Alaaye > Kuta > Oke-Ogun > Idanre > Ijebu- Ode > Ofada > Ikirun > Abakaliki > Kaduna > Doko > Patigi > Oso-Akwa> Omor > Adani > Kwakuti > Lafiagi> Katsina*. When an individual of 60kg weight consumes about 200g of rice daily. The individual is bound to absorb 0.53, 0.78, 0.57, 3.76, 3.29, 0.39, 6.42, 1.05, 0.72, 0.64, 4.86, 1.60, 1.38, 1.36, 1.36, 2.12, 0.78, and 1.14 mg/day of copper concentration of samples; S_1, S_2, S_3, S_4, S_5, S_6, S_7, S_8, S_9, S_{10}, S_{11}, S_{12}, S_{13}, S_{14}, S_{15}, S_{16}, S_{17} and S_{18} respectively. The manganese concentrations of S_4, S_5, S_7, S_{11}, are above RDA while S_1, S_2, S_3, S_6, S_8, S_9, S_{10}, S_{12}, S_{13}, S_{14}, S_{16}, S_{17}, S_{18} (mg/day) are below and within the limit of Recommended Dietary Allowance (1.8-2.3) mg/day. Comparing the results of this work with similar studies, a work carried out on locally produced rice in Thailand (Wannee *et al*, 2018) showed that the estimated daily intake of manganese (Mn) content of the rice samples was (2.94-3.75) mg/day and was lower than the estimated daily intake of manganese (Mn) content from the present study (1.95 ± 0.65-32.10 ± 0.24) mg/kg.

4. CONCLUSION

It is important to mention that trace elements in rice are paramount in maintaining a good healthy living, judging by the optimum level of copper, iron and manganese. This study has shown that rice samples such *Idanre, Lafiagi, Ofada, Ikirun Abakaliki, Efon-Alaaye* rice are very valuable due to their rich content in the studied elements. The concentrations of these essential trace elements are below the recommended dietary allowance which signifies that they are not toxic and are safe for consumption.

REFERENCES

Duruibe, J. O., Ogwuegbu, M. O. C. & Egwurugwu, J. N. (2007). Heavy metal pollution and human biotoxic effects. *Inter. J. Phys. Sci*., 2(5), 112-118.

Jarup, L. (2003). "Hazards of heavy metal contamination". *Brit. Med. Bull*. 68, 167–182.

Meija, J. (2016). *"Atomic weights of the elements (IUPAC Technical Report)". Pure and Applied Chemistry,* 88(3), 265-291.

Otitoju, O., Akpanabiatu, M. I., Otitoju, G. T. O., Ndem, J. I. & Uwah, A. F. (2012). "Heavy metal contamination of green leafy vegetable garden in Itam road construction site in Uyo, Nigeria". *Research Journal of Environmental and Earth Sciences* 4(4), 371-375.

Ping, L., Zhang, Y. F. (2011). "Analysis of heavy metal sources for vegetable soils from Shandong province, China". *Agricultural Sciences in China,* 10, 109-119

Scheiber, I., Dringen, R.M., & Julian, F. B. (2013). "Copper: Effects of Deficiency and Overload". In Sigel, Astrid; Sigel, Helmut; Sigel, Roland K.O. Interrelations between Essential Metal Ions and Human Diseases. *Metal Ions in Life Sciences,* 13, 359–87.

Wanne, S., Vorapot, P., & Satoshi, Y. (2018). "Heavy Metals in Sangyod Rice Samples cultivated in Phantthalung, Thailand". *Food and Applied Bioscience Journal* 6, 45-54.

WHO (2001). Essential element permissible Limit. Technical Report. 22-28.

Wong, S. S., Linm H.T., Li, G.C. (2004). "Heavy metal content of rice and shellfish in Taiwan". *Journal of Food and Drug Analysis* 12(2), 167-174.

Yuanan, H., Xueping, L., Jinmei, B., Kaimin, S., Eddy, Y. Z., Hefa, C. (2013). "Assesing heavy metal pollution in the surface soils of a regio that had undergone three decades of intense industrialization and urbanization". *Environ Sci Pollution Res* 20, 6150-6159

Green Synthesized Gold-Iodine Nanocomposite and Evaluation of its Kinetic Delivery using Dialysis Bag Method

M A Lawal[1*], M T Bankole[1], J O Tijani[1], J A, Areo[1], A S Abdulkareem[2]
[1]Chemistry Department, P.M.B. 65 Federal University of Technology Minna,
[2]Chemical Engineering Department, P.M.B. 65 Federal University of Technology Minna
*Corresponding Author Email: davydtroy06@gmail.com. 07061558721

ABSTRACT

In this research, gold nanoparticles were synthesized using green method via reduction of gold chloride using Agerantum conyzoides leaves extract. The synthesized colloidal gold nanoparticles were doped with povidone iodine using wet impregnation and ultrasonication method. The colloidal gold nanoparticle and gold-iodine nanocomposite were characterized using UV-visible spectrophotometer, HRTEM, SAED, EDX and the in-vitro release study of the gold-iodine nanocomposite on bacteria (staphylococcus aureus, E.coli and pseudomonas aereginosa) was carried out using dialysis bag method. The UV-visible spectra of the gold nanoparticle and gold-iodine nanocomposite showed a broad peak at 550 nm and 533 nm respectively. The HRTEM micrograph of the gold nanoparticle revealed that its predominantly spherical in shape with different size distribution while the gold-iodine nanocomposite was well dispersed with average particle grain size of 27.62 nm as well as different shapes (spherical and triangular). The EDX showed the elemental composition of the gold nanoparticle and gold-iodine nanocomposite, having several peaks of gold and gold-Iodine respectively. The SAED pattern of gold nanoparticle revealed sharp diffraction rings from inner to outer atomic planes with discrete spots indicating the formation of polycrystalline face centered cubic structure, while SAED of gold-iodine nanocomposite is amorphous having dull concentric rings. The gold-iodine nanocomposite has the highest release efficiency (98.58% at 180 min) on staphylococcus aureus, E.coli (81.26% at 180 min) and pseudomonas aereginosa (83.44% at 180min) compared to povidone iodine with a "burst release" of 78.4% at 20mins on the bacteria. The in-vitro release study shows a sustained release of the gold-iodine nanocomposite and follow Kosmeryer-peppas on Escherichia coli and pseudomonas aeruginosa while on Escherichia coli and staphylococcus follow first order model. The magnitude of the release exponent n indicates the release mechanism is non Fickian diffusion.

Keyword: Green, Synthesis, Gold nanocomposite, *Agerantum conyzoides*, Delivery, Dialysis bag

1 Introduction

Skin is the largest organ of the human body which offers protective capability to underlying muscles, bones, ligaments and internal organs from microbes and the elements, helps to regulate body temperature, permits the sensations of touch, heat and cold as well as an immune system to the human body (Wang *et al*., 2019). The skin is made up of three primary layers which are epidermis, dermis and hypodermis (Kim *et al*., 2019). Due to the exposure of the skin to outer environment, it is prone to several factors which could result to different type of skin damage and wound. Wounds are referred to the breakage or disruption of the skin caused by trauma or medical/physiological condition, thereby damaging the skin anatomical structure and the loss of skin physiological function occur frequently (Patra *et al*., 2018). It has been appraised that chronic wounds affect 1-2% of the population in developed countries where about 18% of diabetic patients over the age of 65 suffer from non-healing foot ulcer (Wang *et al*., 2019). Globally leg ulceration being the most prevalent type of chronic wound

is estimated at 1.51 per 1000 population (Martinengo *et* al., 2019). Wounds are generally classified into two categories: acute wounds and chronic wounds. Acute wounds usually spring from mechanical damage or exposure to extreme heat, electrical shock, irradiation or corrosive chemicals. Such wounds heal within a short period of time if correct wound management is applied (Whitney, 2015). Chronic wounds are complication of some specific diseases like diabetes, which has horrific effect on ulcer (Whitney, 2015). These wounds take longer time to heal and can boomerang at extremely high rate unless the root disease is cured (Upton *et al*., 2012). According to wound depth, wounds can be classified as three kinds: superficial wounds (only the epidermis is affected), partial thickness wounds (epidermis and deeper dermal layer are affected) and full thickness wounds (subcutaneous fat and deeper tissues are damaged) (Patil *et al*., 2020).

Wound healing is an intricate and dynamic process which involves various cells, mediators, extracellular matrix components, growth factors and proteinases (Wang *et* al., 2019). Wound healing processes are divided into three overlapping phases including hemostasis and inflammatory, proliferative and remodeling phase (Moura *et al.,* 2013). The inflammatory phase usually lasts 2 to 5 days after skin damage, while the hemostasis phase begin immediately by intravascular platelets to form a clot and stop bleeding (Moura *et al.,* 2013). The proliferative phase takes 3 days to 2 weeks after injury, new tissue formation and cell migration occur at this phase (Rasouli *et al*., 2021). Remodeling phase lasts between 3 weeks to 2 years after injury. The newly synthesized collagen III in the extracellular matrix is gradually replaced by collagen I and new born collagen fibres evolves into a more organized lattice structure augmenting tensile strength of healed skin. Remodeling phase also bring about scar formation (Rasouli *et al*., 2021).The wound healing process is often thwarted by some multi-antibiotic resistant bacteria in wound such as *Staphylococcus aureus, Pseudomonas aeruginosa* and *Escherichia coli* (Zang *et al*., 2014). These multi-antibiotic resistant bacteria have the ability to change their response to the use of medicine thereby causing deleterious infections on wounds (Zang *et al*., 2014). These infections are harder to treat, leading to higher medical cost, prolonged hospital stay and increased mortality (WHO, 2018). Hence, there is a need for novel drugs having high therapeutic efficacy against these bacteria and delivery system that will excellently control the release of drugs to their target-site for a short period of time and non-toxic to the body.

Agerantum conyzoides L commonly known as goat weed belonging to the family Asteraceae is a plant used for the treatment of several diseases since times immemorial; as purgative, febrifuge, antimicrobial, anti-ulcer, anti-inflammatory, antidysenteric, and antilithic and wound dressing (Okunade, 2002). It is also used to treat diseases associated with bleeding, particularly in the treatment of wounds and burns (Rahman *et al*., 2019).

Honey is the oldest wound-healing agent known to mankind. Experimental research illustrated more documents supporting its usage in wound healing because of its bioactivities including antibacterial, antiviral, anti-inflammatory, and antioxidant activities (Nezhad-Mokhtari *et al*., 2021). Honey induces leukocytes to release cytokines, which is what begins the tissue repair cascades (Nezhad-Mokhtari *et al*., 2021)

Iodophors are preparations that bind iodine to a solubilising agent or carrier. The water-soluble complex allows the slow release of a low concentration of free iodine when the carrier comes into contact with wound exudates (Gnanasekaran *et al*., 2019). Cutaneous injuries like chronic wounds, burns and skin infection require extreme care, thoroughness with long-term treatment of healing. Regrettably, despite earnest investigation to improve cutaneous wound care, clinical treatment of chronic wounds remains unsatisfactory in many cases. Low penetration of active agents in the open wound and local tissue reactions are some of the common problems encountered in the course of wound treatment. For example, with iodine-based agents in wound treatment, there have been concerns about allergy, ineffective penetration and toxic effects on host cells (Shing *et al*., 2021)

Several strategies including growth factor, gene delivery, cell therapy as well as micro and macroscale drug delivery has been employed in the healing of non-healing wound (Kim *et al*., 2019). In addition, the use of large sized materials as drug delivery vehicle constitute major challenges such as vivo instability, poor bioavailability, poor solubility and poor absorption in the body, issues with target-specific delivery, extent of toxicity and probable adverse effect of drugs on open wound (Patra *et al*., 2018).

Nanocarries are uprising material platform for target or specific delivery therapeutic agents (Ferrari, 2005). Over the years several delivery vehicles were designed based on different nanomaterial such as polymer, nanotubes, dendrimers, liposomes, (Patra *et al*., 2018) to mention but few. However metallic nanoparticle such as gold nanoparticles have been proven as an attractive candidate for drug delivery to their target sites (Paciotti *et al*., 2006) due to its unique properties especially in the movement and release of the therapeutic agent to the target site (Patra *et al*., 2018).

Gold nanocomposite (AuNCs) plays a significant role in advanced medicine/drug formation, targeting arena with excellent control of drug release and delivery (Patra *et al*., 2018). Gold nanocomposite has been proven to possess capability to modify active agent properties like diffusivity, immunogenicity and offer protection against proteases in wound (Kumar *et al*., 2019). Gold nano-drug delivery system are found to be non-toxic, perfectly compatible with the skin, improves drug retention (Sandhiya *et al*., 2010) and create favorable moist environment for activation and acceleration of wound healing process. It also prolongs the maintenance of effective drug concentration, reduce the period of administration and protects drug from degradation produced by proteases in wounds thereby enhancing therapeutic effectiveness (Losi *et al*., 2010).

2.0 Materials and method

2.1 Materials

Fresh *Agerantum conyzoides* plants were collected inside the farms in Minna metropolis during dry season. Thereafter, it was taken to the Department of Biological Sciences in Federal University of Technology, Minna for botanical identification. Povidone Iodine (10% v/v) was purchased from NAHSON pharmacy shop within Minna metropolis. Gold chloride ($HAuCl_4$) (99.0 %) of analytical grade was purchased from Sigma-Aldrich Chemicals, Germany.

Escherichia coli (gram negative), *Pseudomonas aeruginosa* (gram negative) and *Staphylococcus aureus* (gram positive) used were isolated from chronic wound patients were collected from the Microbiology Department of General Hospital, Minna. They were sub cultured into Nutrient Agar slants and kept in the refrigerator until they were ready for use.

2.2.1 Synthesis of Gold nanoparticle

Fresh *Agerantum conyzoides* plants were collected inside the farms in Minna metropolis during dry season. The plant was thoroughly washed with water to remove any dirt and rinsed with distilled water, the leaves were dried at room temperature away from sunlight and dust for eight weeks until a constant weight was obtained. The air dried plant parts (leaves) were grounded to powder using a blender. The extraction was carried out via aqueous extraction method as described by Shittu *et al*., (2017). The extract was prepared by measuring 2.5g of the fine powder with 100 ml sterile distilled water into a beaker and boiled at 60 ^oC for 1hr and filtered. The qualitative phytochemical analysis was carried out on the plant extract according to the methods of (Sigh *et al*., 2016) to confirm the presence of alkaloids, saponin, flavonoids, phenols and Tannis. About 1 ml of the filtrate was pipette into a beaker and 5 ml of 1 mM $HAuCl_4$ added for the reduction of Au^{3+} ions to Au^0 (equation (1), according to the method described by Sivaraman *et al*., (2010) the mixture as stirred at 180rpm for 10mins at room temperature. Color change was observed and UV–Vis spectrophotometer was used to determine the wavelength.

$$HAuCl4 + Plant\ extract \rightarrow Au° \quad (1)$$

2.2.2 Doping of Povidone Iodine on Gold Nanoparticle

Loading colloidal gold nanoparticle with clinical iodine (povidone iodine) was achieved by simply adding the required amount of iodine to the prepared gold nanoparticle in a ratio of 1:5 to allow chemisorption to take place. Doping was allowed to take place for 30 mins by sonication so as to allow more dispersion and effective doping.

2.2.3 Characterisation of AuNP and Au-INCs

Gold nanoparticle and gold-iodine nanocomposite were characterized using UV-visible spectrophotometer, HRTEM and EDS.

2.2.4 Application of Gold-iodine nanocomposite (Au-INCs)

The in-vitro drug release study of gold-iodine nanocomposite was studied by dialysis bag diffusion method. About 25 ml of Gold-iodine nanocomposite containing 10% v/v of povidone iodine was dispersed in dialysis and the dialysis bag was kept in a beaker containing 300 ml of the cultured bacteria to mimic an open wound bed, the population of bacteria introduced into the cultured media was determined using Mcfarland standard. The beaker was placed over a magnetic stirrer and the temperature of the assembly was maintained at a room temperature throughout the experiment. About 4 ml of the cultured media were withdrawn at a definite time interval and replaced with fresh equal amount of the cultured bacteria. After suitable dilutions the samples were analyzed using UV-Visible spectrophotometer at 540 nm, to determine the concentration and absorbance of the cultured bacteria. The experiment was carried out on these strains of bacteria *Staphylococcus aureus, Pseudomonas aeruginosa* and *Escherichia coli*.

2.2.5 Evaluation of drug release Kinetic

To evaluate the in-vitro drug release data several kinetics models were applied to describe the release kinetic. To understand in-vitro drug release, several mathematical models has been postulated to evaluate drug release kinetics such models include, first order model equation (1) explains the release from the system where rate of drug release is concentration dependent (Xu *et al*., 2012) and Kosmeyer-peppas model (Shen *et al*., 2011) derived a simple mathematical relationship which described the drug release from a composite system Eq. (2)

$$\log C_0 - \log C = K_1 t / 2.303 \quad (1)$$

K_1 is the first order rate equation expressed in time (hour), C_0 is the initial concentration of the drug, C is the percent of drug remaining at time t.

$$\log(Mt/M\infty) = \log K_{kp} + n \log t \quad (2)$$

Mt is the amount of drug released in time t, M∞ is the amount of drug released after time ∞,

n is the diffusion exponent or drug release exponent, K_{kp} is the Korsmeyer release rate constant.

If $n < 0.5$ then the drug release mechanism follows Fickian diffusion model (Neppas, 1985) and if $0.5 < n < 0.89$ then release mechanism follows an anomalous diffusion model. If $n = 0.5$ then the release mechanism follows Higuchi kinetic model (Rehman *et al*., 2014) and if $0.89 < n < 1$ then the release mechanism follows zero-order kinetic model (Zhai, 2012).

3 Results

3.1

Table 1 Some phytochemical composition of aqueous extract of *Agerantum conyzoide* leaf

Phytochemical constituents	Inference
Phenols	+
Flavonoids	+
Alkaloids	+
Tannins	+
Saponins	+

Keys: (+) present

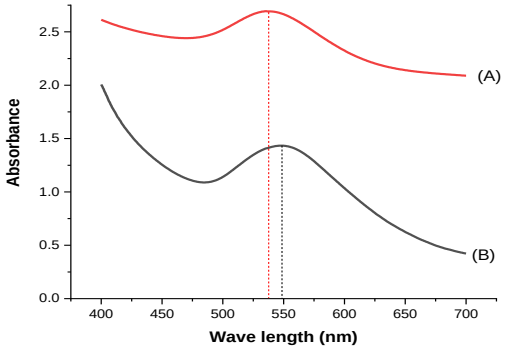

Figure 1(a & b): Absorption spectra of (A) Au-INCs and (B) AuNPs

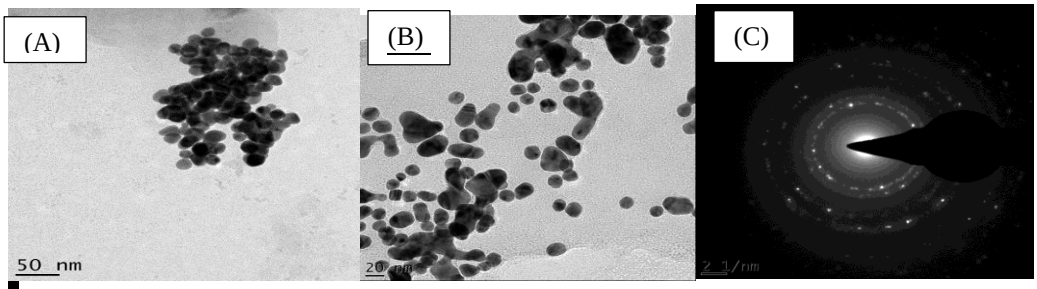

Plate I: HRTEM images of AuNPs at different scale bar(a&b) and SAED of AuNPs(c)

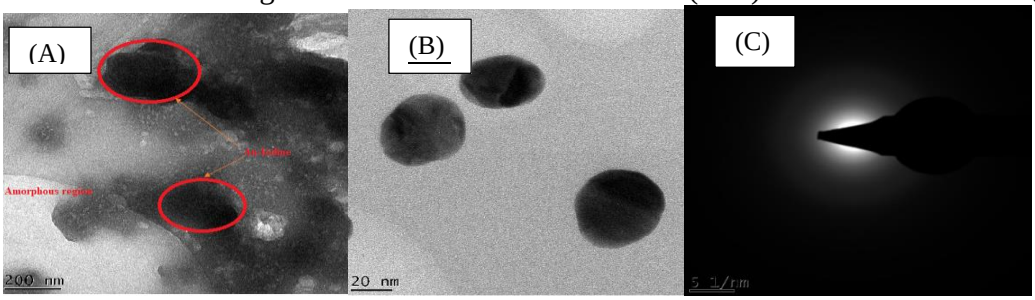

Plate II: HRTEM images of Au-INCs at different magnification (a&b) and SAED of Au-INCs

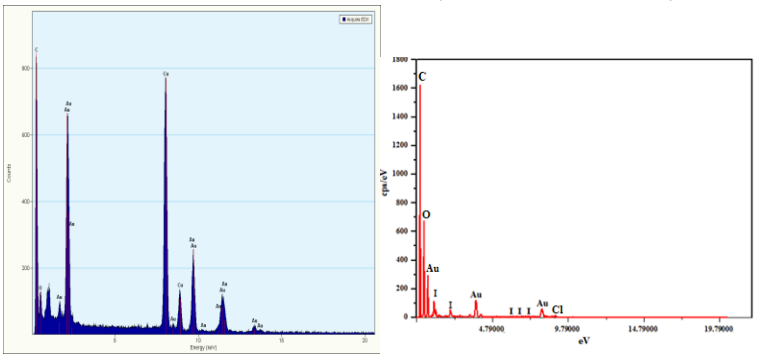

Figure 2(a&b) : EDX spectrum of AuNPs and Au-INCs

3.3 In-vitro iodine release

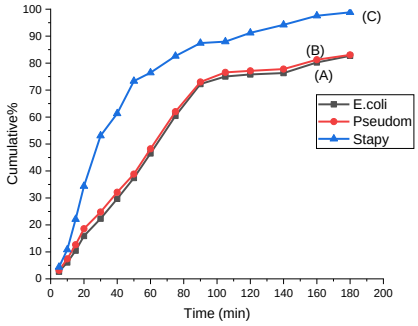

Figure 3:- In-vitro release profile of iodine from Au-INCs in different bacteria media: (a) E.coli (b) *Pseudomonas aeruginosa* (c) *Staphylococcus aureus*

3.3 Drug release Kinetic

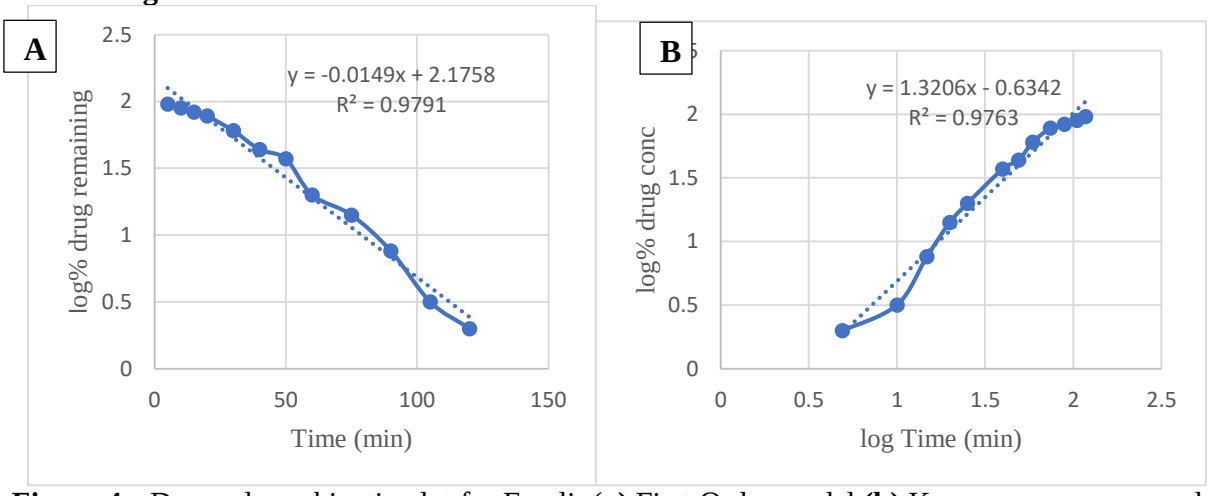

Figure 4:- Drug release kinetic plot for E.coli: (**a)** First Order model **(b)** Kosmeryer-peppas model

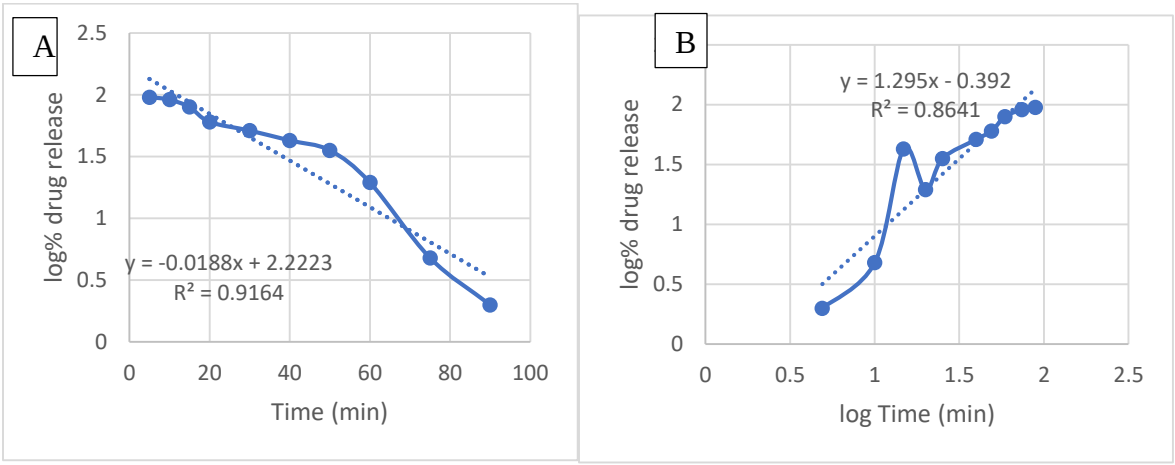

Figure 5:- Drug release kinetic plot for *Staphylococcus aureus* : (a) First Order model (b) Kosmeryer-peppas model.

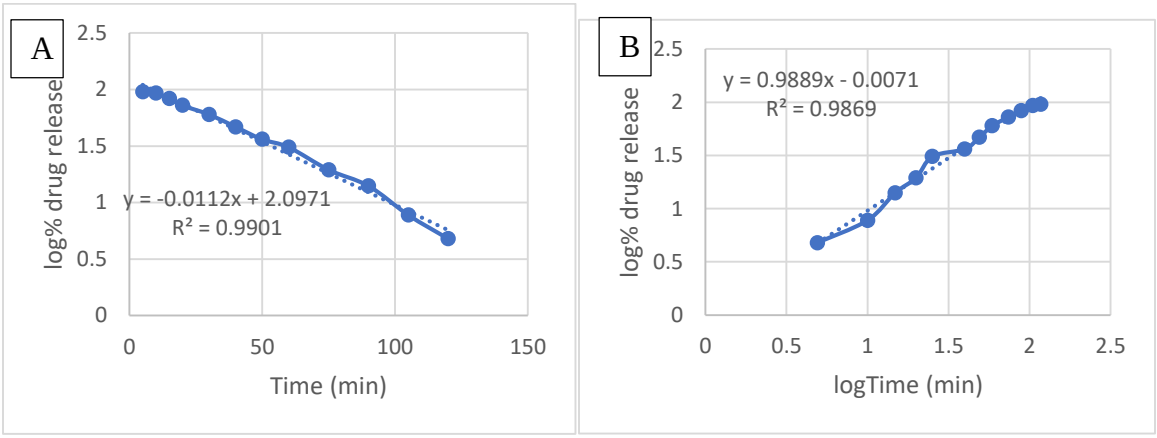

Figure 6:- Drug release kinetic plot for *Pseudomonas aeruginosa* : (a) First Order model (b) Kosmeryer-peppas model.

Table 2:- Interpretation of R-square values and rate constant of release kinetics of nanocomposite

Model	*E.coli*	*Pseudomonas aeruginosa*	*Staphylococcus aureus*
First order			
R-square	0.9791	0.8175	0.9164
K	1.49×10^{-2}	1.12×10^{-2}	1.88×10^{-2}
n	-	-	-
Kosmeryer-peppas model			
R-square	0.9763	0.9869	0.8641
K	1.885×10^{-2}	2.262×10^{-2}	6.59×10^{-2}
n	0.7794	0.7446	0.5679

4 Discussion of Result

4.1 Qualitative phytochemical constituent of *Agerantum conyzoides*

The phytochemical screening of the aqueous extract of *Agerantum conyzoides* showed the presence of tannins and flavonoids (table 1) which are examples of polyphenolic compounds that are of great importance to green synthesis of nanoparticles due to their reductive and antioxidant abilities. Tannins has been reported as reducing and stabilizing agents to synthesize silver nanoparticles on a timescale of seconds through a simple, green, room temperature protocol, and the suitability of this protocol for energy-efficient, continuous flow synthesis has been demonstrated using a simple co-axial flow reactor (Raghunandan *et al*., 2010). The flavonoids present also were found to be responsible for reduction process to produce AuNPs (Raghunandan *et al*., 2010).

4.2 UV-visible spectroscopy of AuNPs and Au-INCs

The colloidal mixture was further characterized using UV–Vis spectroscopy to detect the surface plasmon resonance (SPR) through the absorption peak of the biosynthesized gold nanoparticle as presented in figure 1b. A broad peak at 550nm was observed for AuNPs which is a peculiar plasmon band for gold nanoparticle (500 – 600nm). On compositing the AuNPs with povidone iodine the intensity increases (as well as its concentration) and a blue shift in the plasmon band. This effect may be attributed to the chelation of iodine with AuNPs thereby causing a change in the dielectric constant of the surrounding medium.

4.3 HRTEM of AuNPs

The HRTEM monograph of the AuNPs as shown in plate 1(a&b). AuNPs exhibits various size ranges and predominantly spherical shapes (Khan *et al*., 2014). The image revealed the shape to be spherical which majorly used for drug delivery, photo-thermal therapy and refractive-index sensing. The SAED in plate I(c) showed the diffraction rings from inner to outer atomic planes indicating the formation of polycrystalline gold nanoparticles having face centered cubic structure of gold nanoparticle. The narrow size distribution and the absence of agglomeration suggest that plant extract matrix prevent the agglomeration of gold nanoparticle (Fox *et al*., 2020). The elemental composition of the biosynthesized gold nanoparticle was determined by Energy Dispersion X-ray analysis (EDX). Area profiling of the biosynthesized nanoparticle in Figure 2a showed strong peak of gold confirming the formation of gold nanoparticle.

4.4 HRTEM of Au-INCs

The HRTEM monograph of gold-iodine nanocomposite as shown in plate II(a&c) reveals that gold-iodine nanocomposites are contrived of firmly packed particles that are strongly interconnected with each other with an average particle size of 27.62 nm. The strong interconnection could be attributed to iodine forming chelating ligand around the gold nanoparticles. The SAED pattern in plate II(c) revealed diffuse rings with no discrete spots which is and indicative that gold-iodine nanocomposite is amorphous. The non-crystallinity of gold-iodine nanocomposite is attributed to the complete dissolution of gold nanoparticle in iodine at ambient temperature (David and Tran, 2003) and it is also witnessed of the successful doping of iodine with gold nanoparticle.

The elemental composition in Figure 2b, showed several peaks of gold and iodine respectively. The atomic weight percent of gold and iodine are 26.53% and 15.60% respectively, while carbon has an atomic weight percent of 35.84%.

4.5 In-vitro drug release

The release profile of Au-INCs on *staphylococcus aureus* as shown in Figure 3c clearly reveals that at 120 min the release rate of iodine already achieved 91.14%. At 180 mins the release ratio of the drug achieved maximum concentration (Cmax) at 98.58%. However, over the range of 120 – 180 mins, the drug release rate was moderate. Once the composite material contacted the *staphylococcus aureus* in the first 40 mins, it started to dissolve and the release process commenced immediately. This may be due to the absorption of the small of iodine on the cell wall of *staphylococcus aureus*, therefore the release rate was higher. As the amount of iodine increases within 40 -100 mins, consequently the rate of dissolution as well as release rate was higher. But after 100 mins the iodine release gradually went along and reached stability. *Staphylococcus aureus* being a gram- positive bacteria are susceptible to antibiotic due to their larger cell wall can easily absorbed antibiotic (Breijyeh *et al*., 2020).

Figure 3 (a&b) shows the release profile of Au-INCs on *Pseudomonas aeruginosa* and *Escherichia coli* which clearly reveals that at 120 mins the release rate of iodine already achieved 73.28% and 71.45% respectively. At 180 mins the maximum concentration (Cmax) of iodine released was 83.44% and 81.26%. This prolong delay of iodine on these bacteria (gram-negative) may be due to their thin cell wall that cause reaching of antibiotic to them harder and identification of this antibiotic is easier by the bacteria and they can fight back (Zeinab *et al*., 2020).

4.6 Kinetic of Iodine release

For the kinetic study the following plots were made: log cumulative % drug remaining vs time (first order kinetic model) and log cumulative % drug release vs log time (Kosmeryer-peppas model). All plots are shown in figure 3a, 3b and 3c and the result are summarized in Table 2. On the basis of best fit with the highest correlation (R^2) value, it is concluded that *Escherichia coli* and *staphylococcus aureus* follow first order model. While *Escherichia coli* and *pseudomonas* follow Kosmeryer-peppas model. The release exponent value n of Au-INCs on the bacteria are 0.7794, 0.7446 and 0.5679. The magnitude of the release exponent n indicates the release mechanism is non Fickian diffusion.

4.7 Conclusion

Compositing povidone iodine with AuNPs was successfully achieved as shown by the TEM image in plate the distictive shape of Au-INCs which amorphous in nature as revealsed by the SAED in plate. In-vitro release of iodine on *Escherichia coli*, pseudomonas *aeruginosa* and *staphylococcus aureus* was done with Cmax and 81.26%, 83.44% and 98.58% respectively at 180 mins. The release exponent value n of Au-INCs on *Escherichia coli*, *pseudomonas aeruginosa* and *staphylococcus aureus* are 0.7794, 0.7446 and 0.5679 respectively. The magnitude of the release exponent n indicates the release mechanism is non Fickian diffusion.

REFERENCES

Breijyeh, Z., Jubeh, B., & Karaman, R. (2020). Resistance of Gram-negative bacteria to current antibacterial agents and approaches to resolve it. *Molecules*, *25*(6), 1340.

Ferrari, M. (2005). Cancer nanotechnology: opportunities and challenges. *Nature reviews cancer*, *5*(3), 161-171.

Fox, C. M., Tian, Y., & Breslin, C. B. (2020). Electrochemical formation of silver nanoparticles and their catalytic activity immobilised in a hydrogel matrix. *Colloid & Polymer Science*, *298*(6), 549-558.

Gnanasekaran, S., Rogers, S., Wickremasinghe, S., & Sandhu, S. S. (2019). The effect of diluting povidone-iodine on bacterial growth associated with speech. *BMC ophthalmology*, *19*(1), 1-5.

Kim, H.S., Sun, X., L. J. H., Kim, H. W., Fu, X., & Leong, K. W. (2019). Advanced drug delivery systems and artificial skin grafts for skin wound healing. *Advanced drug delivery reviews*, 146, 209-239.

Kumar, P.V., Kala, S.M. J. & Prakash, K. S.(2019). Green synthesis of gold nanoparticle using croton Caudatus Geisel leaf extract and their biology study. *Materials letters*, 236, 19-22.

Losi, P., Briganti, E., Magera, A., Spiller, D., Ristori, C., Battolla, B., ... & Soldani, G. (2010). Tissue response to poly (ether) urethane-polydimethylsiloxane-fibrin composite scaffolds for controlled delivery of pro-angiogenic growth factors. *Biomaterials*, *31*(20), 5336-5344.

Moura, L.I., Dias, A.M., Carvalho, E., De Sousa, H.C. (2013). Recent advances on the development of wound dressing for diabetic foot ulcer treatment. *Acta biomater*, 9(7), 93-114.

Nezhad-Mokhtari, P., Javanbakht, S., Asadi, N., Ghorbani, M., Milani, M., Hanifehpour, Y. & Akbarzadeh, A. (2021). Recent advances in honey-based hydrogels for wound healing applications: Towards natural therapeutics. *Journal of Drug Delivery Science and Technology*, 102789.

Okunade, A. L. (2002). Agerantum conyzoides L. (asteraceae). *Fitoterapis* (73), 1-16.

Paciotti, G. F., Kingston, D. G., & Tamarkin, L. (2006). Colloidal gold nanoparticles: a novel nanoparticle platform for developing multifunctional tumor-targeted drug delivery vectors. *Drug development research*, *67*(1), 47-54.

Patil, P. P., Reagan, M. R., & Bohara, R. A. (2020). Silk fibroin and silk-based biomaterial derivatives for ideal wound dressings. *International Journal of Biological Macromolecules*.

Patra, J. K., Das, G., Fraceto, L. F., Campos, E. V. R., del Pilar Rodriguez-Torres, M., Acosta-Torres, L. S. & Habtemariam, S. (2018). Nano based drug delivery systems: Recent developments and future prospects. *Journal of nanobiotechnology*, 16(1), 71.

Raghunandan, D., Bedre, M. D., Basavaraja, S., Sawle, B., Manjunath, S. Y., & Venkataraman, A. (2010). Rapid biosynthesis of irregular shaped gold nanoparticles from macerated aqueous extracellular dried clove buds (Syzygium aromaticum) solution. *Colloids and Surfaces B: Biointerfaces*, *79*(1), 235-240.

Rahman, M. S., Islam, R., Rana, M. M., Spitzhorn, L. S., Rahman, M. S., Adjaye, J., & Asaduzzaman, S. M. (2019). Characterization of burn wound healing gel prepared from human amniotic membrane and Aloe vera extract. *BMC complementary and alternative medicine*, *19*(1), 1-15.

Rasouli, M., Rahimi, A., & Soleimani, M. (2021). The interplay between extracellular matrix and progenitor/stem cells during wound healing: Opportunities and future directions. *Acta Histochemica*, *123*(7), 151785.

Sandhiya, T., & Saravanan, M. S. (2010). Rational Computation for Mining Association Rules from XML Documents. *Data Mining and Knowledge Engineering*, *2*(12).

Shing, B., Balen, M., McKerrow, J. H., & Debnath, A. (2021). Acanthamoeba Keratitis: an update on amebicidal and cysticidal drug screening methodologies and potential treatment with azole drugs. *Expert Review of Anti-infective Therapy*, 1-15.

Upton, D., Solowiej, K., Hender, C. & Woodyatt, K.Y. (2012). Stress and pain associated with dressing change in patients with chronic wounds. *Journal Wound Care*, 21, 53.

Wang, W., Lu, K. J., Yu, C. H., Huang, Q. L. & Du, Y. Z. (2019). Nano-drug delivery systems in wound treatment and skin regeneration. *Journal of Nanobiotechnology*, 17(1), 82.

Whiteny, J.A.D. (2015). Overview: acute and chronic. *Nursing Clinical North Am*, 40,191-205.

EFFECTS OF ETHYL METHANE SULPHONATE ON VEGETATIVE TRAITS OF SELECTED GENOYTPES OF GROUNDNUT (*ARACHIS HYPOGAEA* L.)

Abdullahi, A., Daudu O. A. Y., Falusi, O. A., Abubakar A. and Audu, M. A. I.
Federal University of Technology, Minna-Nigeria.
Correspondence email: Ameenahabdul495@gmail.com
Mobile: 07068130094

Abstract

Groundnut (*Arachis hypogaea* L.) is a multi-purpose legume crop widely cultivated in Sub-Saharan Africa (SSA). However, several species of groundnut suffer substantial yield losses as a result of narrow genetic base and insect-pest attack. The present study aimed to investigate the effect of EMS on morphological traits of four (4) groundnut (*Arachis hypogaea* L.) genotypes viz Samnut 24, Samnut 25, Samnut 26 and ICG4412. Field experiment was laid out in Complete Randomized Design (CRD) with three (3) replicates. The seeds of the four (4) groundnut accessions were treated with various concentration of EMS (0.0 %, 0.1 %, 0.2 %, 0.3 % and 0.4 %) for 6 hours, they were then removed and rinsed with distilled water to remove the trace of mutagen sticking to the seed coat. Data on vegetative parameters were collected following standard procedures. Results obtained showed that 0.1 % EMS concentration had the highest plant height (46.79 cm) at week 12 but was not significantly different from 0.3 % and 0.4 % concentrations (43.37 and 43.28 cm) respectively. The significantly least plant height at week 12 after planting was recorded at 0.2 % concentration (35.28 cm). No significant difference was observed among the varieties in terms of plant height. EMS concentration 0.1 % showed the significant highest number of leaves per plant at week 12 (297) while the least was recorded at 0.4 % concentration (177). Among the varieties, ICG 4412 had the significant highest number of leaves (289.20) at week 12 after planting and the least value was obtained in variety SAMNUT 26 (158.93). EMS concentration 0.1 % had the significant highest number of branches at maturity (13.25) while the least was recorded at 0.4 % EMS concentration (8.92). In terms of varietal performance, Samnut 26 had the significantly highest number of branches per plants (12.47), but was not significantly different from ICG 4412 (12.07). SAMNUT 25 was observed the have the significantly least number of branches per plant (9.13). The results obtained showed significant amount of variability in morphological parameters of the genotypes as a result of exposure to EMS which may essentially affect their productivity. This study revealed that EMS concentration 0.1 % Is the optimum concentration for inducing genetic variability in groundnut plant.

Keywords: Accessions, ethyl methyl sulfonate (EMS), genotypes, groundnut and mutagens.

1.0 INTRODUCTION

Groundnut (*Arachis hypogaea* L.), also known as earthnut, monkeynut and peanut is a native of South America belonging to the family Leguminosea (Fabaceae) genus *Arachis* (Tillman and Stalker, 2009). It is an annual or perennial plant that is distinguished from most other species by producing aerial flowers,fruiting below the soil level and it only domesticated species in the genus is *Arachis hypogaea* L. (Tillman and Stalker, 2009). Groundnut is grown in diverse environments throughout the world between 40 °N and 40 °S (Food and Agriculture Organization, 2013). Groundnut seeds are a rich source of oil (35–56%), protein (25–30%), carbohydrates (9.5–19.0%), minerals (P, Ca, Mg and K) and

vitamins (E, K and B) (Gulluoglu *et al*., 2016). The shells are also used for fuel by some local oil factories or they are sometimes spread on the field as a soil amendment (Ahmed *et al*., 2010).

2.0 Literature Review

Suradkar (2013) studied improvement of groundnut (*Arachis hypogaea* L.) through chemical mutagen Ethyl Methane Sulfonate (EMS) conducted a study to check the chemical mutagen (EMS) sensitivity on groundnut and to find out suitable concentration of EMS (0.05%, 0.10%, 0.15% and 0.20%) on two varieties of groundnuts TAG-24 and AK159. He concluded that 0.05% concentration of EMS induces good genetic variability in both varieties.

Mayor *et al*. (2018) studied induced chemical mutagenesis in groundnut (*Arachis hypogaea* L.) they treated groundnut variety (LGN-1) with EMS at different concentrations (0.2%, 0.4%, 0.6%, 0.8% and0.1 2%) to study it effect on various morphological traits when compared with control. Significant result were observed in seed germination, plant height, number of leaves and number of branches after treating the seed with the mutagen. They concluded that, lower concentration appear to be better effective treatment for inducing variability as compared with other concentrations (0.4%, to 0.12%).

It has also been found that boiled groundnuts have two and four fold increase in biochanin A, isoflavone antioxidants and genistein content, respectively (Craft *et al*., 2010).

3.0 Materials and methods

3.1 Experimental site

The study was conducted at the experimental garden of the Department of plant Biology, Federal University of Technology Minna Niger State, Nigeria. Minna is located in the north central geopolitical zone of Nigeria found within latitude 9°36′ north and longitude 6°34′ east. Minna covers a land area of 88 square kilometers with an estimated human population of 488,788 (Niger State MAAH Bulletine, 2008). Temperature ranges between 35.0 °C and 37.5 °C while relative humidity varies from 40 to 80 % (Adeboye *et al*., 2011). The area has two seasons: raining season between May to October and dry season between November and April each year. It has a low humid soil type with favourable climatic condition for planting which make it easy for groundnut crop to grow successfully and express all it traits.

3.2 Experimental material

The groundnut varieties used for the experiment were collected from the Institute for Agricultural Research (IAR), Samaru, Zaria, Kaduna State, Nigeria.

3.3 Mutagenic Treatments

Mutagenic treatment was conducted in the laboratory of the Department of plant Biology, Federal University of Technology Minna. Groundnut seeds were presoaked in distilled water for 4 hours. This allows the mutagen to diffuse more rapidly to the tissues of interest (Foster and Shu 2011). The seeds were then soaked for 4 hours at different concentrations of Ethyl Methane Sulphonate (0.0, 0.1, 0.2, 0.3, and 0.4%) (Adeeba *et al*., 2018). The treated seeds were thoroughly washed in running tap water to remove the residual effects of the mutagen if any.

3.4 Morphological Parameters

The morphological parameters were taken using the method of (Ghalmi *et al*., 2010) and (Falusi *et al*., 2012).

3.4.1 Plant height
The height of each plant were taking using meter rule from the base of the plant to the lowest leaf

3.4.2 Number of Leaves
The numbers of leave were counted manually

3.4.3 Leaf Area
The leaf area of the groundnut plants were calculated using the formular LXW (Length x width)

3.5 Statistical Analysis

The morphological data was subjected to Analysis of Variance (ANOVA) using Statistical Package for Social Sciences (SPSS 20) version 20 to determine the level of significance among the treatment. Duncan Multiple Range Test (DMRT) was used to separate the means where there are significant differences.

4.0 Results and Discussion

4.1. Effect of EMS on Plant Height of the Groundnut Genotypes

Notable variations were observed in plant height at different concentration of ethyl methane sulphonate (EMS) across different weeks. At 2 and 4 weeks after planting, the highest plant height was recorded at 0.1% concentration (19.03±1.49 cm and 26.73±1.55 cm) respectively, but was not significantly different ($p>0.05$) from plant height at 0.00% concentration (17.09±0.95 and 22.68±1.27 cm), 0.3% (17.23±1.76 cm and 22.16±1.94 cm) and 0.4% (18.20±1.69 and 24.60±1.91 cm). The significantly least plant height at week 2 and 4 were observed in 0.2% EMS concentration (12.13±1.74 and 16.86±2.26 cm respectively).

In terms of varietal performance, SAMNUT 24 had the significantly highest plant height at week 2 (19.81±0.94) cm while the least was recorded in SAMNUT 26 (13.91±1.23 cm). there is no significant difference($p>0.05$) in varietal performance of SAMNUT 25 and ICG 4412 (16.06±1.79 and 17.16±1.54) cm with that of SAMNUT 24 and SAMNUT 26 at week 2. No significant difference were observed in PH at week 4, 6, 8 10 and 12 (table 4.4.1).

Table 4.1.1: Effect of EMS on Plant Height of the Groundnut Genotypes

Parameters	PH2	PH4	PH6	PH8	PH10	PH12
0.0	17.09±0.95^{b}	22.68±1.27^{b}	28.03±1.12^{b}	31.91±1.26^{ab}	35.78±1.13^{ab}	40.16±1.34^{ab}
0.1	19.03±1.49^{b}	26.73±1.55^{b}	31.48±1.51^{b}	35.52±1.44^{b}	40.61±1.61^{b}	46.79±2.12^{c}
0.2	12.13±1.74^{a}	16.86±2.26^{a}	22.49±2.50a	27.88±2.60^{a}	31.14±2.74^{a}	35.28±2.99^{a}
0.3	17.23±1.76^{b}	22.16±1.94^{b}	27.65±2.16^{ab}	33.33±2.08^{b}	37.48±1.84^{b}	43.37±1.28^{bc}
0.4	18.20±1.69^{b}	24.60±1.91^{b}	29.57±1.54^{b}	34.20±1.34^{b}	38.30±1.01^{b}	43.28±1.05^{bc}
Varieties						
Samnut26	13.91±1.23^{a}	21.68±1.75^{a}	28.20±1.52^{a}	34.04±1.23^{a}	38.21±1.21^{a}	43.74±1.24^{a}
Samnut24	19.81±0.94^{b}	25.47±1.23^{a}	30.77±1.18^{a}	34.94±1.28^{a}	39.11±1.28^{a}	44.10±1.63^{a}
Samnut25	16.06±1.79^{ab}	21.73±2.13^{a}	26.22±2.11^{a}	30.45±2.03^{a}	34.21±2.09^{a}	38.41±2.33^{a}
ICG4412	17.16±1.54^{ab}	21.53±1.89^{a}	26.19±2.00^{a}	30.83±2.01^{a}	35.12±2.03^{a}	40.85±2.09^{a}

Means followed with same letter(s) along each column are not significantly different at 5% probability level.

PH (plant height)

4.2 Effect of EMS on Number of Leaves of the Groundnut Genotypes

For number of leaves, EMS concentration 0.1 showed the significantly highest number of leaves per plant at week 2 (20.17±1.64) but was not significantly different ($p>0.05$) from 0.3 % concentration (19.33±1.54). Statistically, concentration 0.0 % was observed to have the least number of leaves at week 2 and was significantly different from other concentrations. Although, no significant difference was observed in number of leaves per plants at week 4, concentration 0.1 % recorded the significantly highest number of leaves at week 10 and 12 (231.67±30.23 and 297.33±36.80, respectively) while the least was recorded at 0.4 % concentration (149.67±14.81 and 177.00±16.91, respectively).

In terms of varietal performance, SAMNUT 24 was observed to have the significantly highest number of leaves at week 2 (20.27±1.78) while the least was recorded in SAMNUT 25 (15.07±1.05). The significantly highest number of leaves at week 4, 6, 8, 10 and 12 were recorded in ICG 4412(56.27±2.47, 157.47±12.53, 205.07±13.72, 251.73±15.43, 289.20±17.97) respectively, while the significant least were recorded in SAMNUT 26 (26.27±0.64, 43.07±2.93, 72.27±7.08, 106.53±9.52, 158.93±16.46, respectively).

Table 4.2.1: Effect of EMS on number of leaves of the Groundnut Genotypes

Treatments	NL2	NL4	NL6	NL8	NL10	NL12
0.0	13.00±0.30^{a}	31.67±4.62^{a}	83.50±23.63^{a}	128.17±27.49^{a}	174.67±30.63^{ab}	216.08±33.11^{abc}
0.1	20.17±1.64^{c}	41.33±4.29^{a}	91.33±15.45^{a}	145.67±18.40^{a}	231.67±30.23^{b}	297.33±36.80^{c}
0.2	17.17±1.62^{bc}	36.00±3.45^{a}	86.50±15.62^{a}	121.83±16.40^{a}	167.67±21.14^{ab}	206.75±21.56^{ab}
0.3	19.33±1.54^{c}	43.17±4.65^{a}	89.50±9.21^{a}	143.33±13.01^{a}	214.33±21.40^{ab}	280.08±23.89^{bc}
0.4	14.33±0.69^{ab}	37.00±3.97^{a}	74.50±12.75^{a}	113.00±13.29^{a}	149.67±14.81^{a}	177.00±16.91^{a}
Varieties						
Samnut26	16.13±1.16^{a}	26.27±0.64^{a}	43.07±2.93^{a}	72.27±7.08^{a}	106.53±9.52^{a}	158.93±16.46^{a}
Samnut24	20.27±1.78^{b}	39.20±3.73^{b}	84.80±9.13^{b}	128.53±12.63^{b}	211.87±27.75^{bc}	262.73±35.03^{b}
Samnut25	15.07±1.05^{a}	29.60±1.24^{a}	54.93±2.37^{a}	115.73±8.10^{b}	180.27±15.15^{b}	230.93±21.61^{b}
ICG4412	15.73±0.78^{a}	56.27±2.47^{c}	157.47±12.53^{c}	205.07±13.72^{c}	251.73±15.43^{c}	289.20±17.97^{b}

Means followed with same letter(s) along each column are not significantly different at 5% probability level.

NL (number of leaves)

4.3 Effect of EMS on Leaf Area and Number of Branches at Maturity

No significant differences was observed in leaf area at week 2 across all EMS concentrations and across varieties. The significant highest leaf area was observed at 0.1 % EMS concentration at week 4, 6, 8,

10 and 12 (15.71±1.02, 17.56±0.93, 19.95±0.78, 21.76±0.83, and 24.12±0.85, respectively) while the least leaf area across the weeks was observed in SAMNUT 26.

EMS concentration at 0.1 % had the significantly highest ($p<0.05$) number of branches per plant (13.25±1.02) but was not significantly different from EMS concentration 0.3 % (13.17±1.35), concentration 0.4% was observed to have the significantly least number of branches (8.92±0.56).

In terms of varietal performance, SAMNUT 26 had the significant highest number of branches per plant (12.47±0.89) but was not significantly different from ICG 4412 (12.07±0.90) while the least was observed in SAMNUT 25 (9.13±0.87), Table (4.3.1)

Table 4.3.1: Effect of EMS on Leaf Area and Number of Branches at Maturity

Treatments	LA2	LA4	LA6	LA8	LA10	LA12	NB
0.0	5.39±0.31^{a}	10.59±0.63^{a}	13.08±0.49^{a}	15.11±0.49^{a}	17.11±0.59^{a}	19.64±0.59^{a}	10.±58±1.18^{ab}
0.1	6.14±0.39^{a}	15.71±1.02^{c}	17.56±0.93^{c}	19.95±0.78^{c}	21.76±0.83^{b}	24.12±0.85^{b}	13.25±1.02^{b}
0.2	5.05±0.59^{a}	10.92±1.12^{ab}	13.09±1.14^{a}	15.21±1.14^{a}	17.72±1.25^{a}	19.96±1.32^{a}	10.25±0.91^{ab}
0.3	6.16±0.78^{a}	13.75±0.88^{bc}	16.21±0.72^{bc}	18.69±0.64^{bc}	21.09±0.71^{b}	23.30±0.79^{b}	13.17±1.35^{b}
0.4	6.28±0.60^{a}	12.56±1.27^{ab}	14.76±1.19^{ab}	17.34±1.13^{ab}	19.67±1.08^{ab}	21.78±1.02^{ab}	8.92±0.56^{a}
Varieties							
Samnut26	6.31±0.60^{a}	9.37±0.55^{a}	12.40±0.51^{a}	15.46±0.52^{a}	17.58±0.55^{a}	19.87±0.58^{a}	12.47±0.89^{b}
Samnut24	6.05±0.51^{a}	15.68±0.75^{c}	17.55±0.78^{c}	19.60±0.77^{b}	22.07±0.83^{b}	24.68±0.84^{b}	11.27±1.17^{a}
Samnut25	5.63±0.56^{a}	13.22±1.07^{b}	14.87±1.03^{b}	16.68±1.09^{a}	18.54±1.09^{a}	20.41±1.02^{a}	9.13±0.87^{a}
ICG4412	5.23±0.25^{a}	12.57±0.86^{b}	14.94±0.86^{b}	17.29±0.86^{ab}	19.68±0.81^{a}	22.07±0.79^{a}	12.07±0.90^{b}

Means followed with same letter(s) along each column are not significantly different at 5% probability level.

LA (leaf area), NB (number of branches)

Discussion

Highly efficient mutagenesis is vital for breeding programs. The success of Ethyl methyl sulfonate (EMS) mutagenesis depend on many factors such as the treatment duration, EMS concentration and temperature. (Arisha *et al*., 2014; Gnanmurthy *et al*., 2014; Asif *et al*., 2019). Decrease in plant height observed in some mutant line due increase in EMS concentration might be due to physiological or cell damage. High concentration of EMS have also been reported to result in damage to cell constituents, molecules (Chowdhury and Tah, 2011) and growth regulators (Salim *et al*., 2009). The present result

confirm these earlier reports in groundnut (Gwnasakaran and Paradai 2015); mung bean (khan and wani 2006); soybean (pavadai *et al*., 2009).

In this study significant increase in plant height of some of the EMS concentration (0.1, 0.3 and 0.4%) over the control might be due to the effect of EMS which induces point mutation in the mutant line. This result is not in line with that of mayur *et al*. (2018), who recorded highest plant height in the control than the treatments in groundnut genotypes. This might be due to differences in EMS doses. The differences in plant height among the varieties might be attributed to differences in genotypes. Similarly, previous studies reported that sensitivity to chemical mutagens differs with genotype (Kumar *et al*., 2015; Ali *et al*., 2010).

In addition, Olorunmaiye *et al*. (2019) reported significant correlation between plant height and number of pod per plant in EMS mutant line of groundnut genotype. Therefore, plant height is a good character for selection in breeding programs. The number of leaves per plant in response to different concentrations of EMS showed that lower concentration had more effect on the plant than higher concentration over the control.

Sharma *et al*. (2005) also reported that lower doses of mutagens were more efficient than the higher doses in urdbean. However, the ability of concentration range of 0.1-0.4% EMS to induce better growth and higher biological yield compared to the 0.00% treatment showed the concentrations were able to activate optimally the phyto-hormones and growth regulators in the plant.

Number of leaves associated positively with number of pod per plant. Similar observation was made by Olorunmaiye *et al*., (2019).

The larger leaf area induced by the treatment in the present study translated to higher photosynthetic surface and ultimately better growth and higher biomass yield. Growth enhancement by application of moderate concentrations of EMS was demonstrated in *Vigna spp* (Khan *et al*., 2004) and sodium azide in groundnut on Samnut 10 and 20 (Animasaun *et al*., 2014). In terms of number of branches, some of the mutant lines showed higher number of branches (13) than the control (10), this might be due to the mutagenic effect of EMS on the mutant line.

5. Conclusion

The present work showed the utility of 0.1-0.4% concentrations of EMS to significantly improve growth performance and that 0.1 % is the optimum concentration for inducing genetic variability in the groundnut genotypes.

REFERNCES

Ahmed, S., Rafay, A., Singh, R.K. & Verma, U.K. (2010). Response of groundnut varieties to spacing. *Indian Journal of Agronomy*, 31(3),248-251

Ali, H., Shah, T.M., Iqbal, N., Atta, B.M. & Haq, M.A. (2010). Mutagenic induction of double-podding trait in different genotypes of chickpea and their characterization by STMS marker. *Plant Breeding*, *129*, 116–119.

Animasaun, D. A., Oyedeji, S., Azeez, M. A. & Onasanya, O. A. (2014). Alkylating efficiency of sodium azide on pod yield, nut size and nutrition composition of samnut 10 and samnut 20 varieties of groundnut (*Arachis hypogea* L.). *African Journal of Food, Agriculture, Nutrition and Development,* 14(7), 9498-9510.

Chowdhury, R. & Tah, J. (2011). Assessment of chemical mutagenic effects in mutation breeding programme for M1generation of carnation (*Dianthus caryophyllus*). *Research in Plant Biology*, 1(4), 23- 32.

Craft, B.D., Hargrove, J.L., Greenspan, P., Hartle, D.K., Amarowicz. R. & Pegg, R.B. (2010). Recent Advances in food and flavor chemistry. Food flavor and encapsulation, health benefits, analytical methods, and molecular biology of functional foods, Cambridge, UK: R. *Society of Chemistry* 283-296.

FAO (Food and Agriculture Organization). (2013). Groundnut Statistics. Rome: FAO: Food and Agriculture Organization of the United Nations.http://www.faostat.fao.org.

Gulluoglu, L., Basal, H., Onat, B., Kurt, C. & Arioglu, H. (2016). The effect of harvesting on some agronomic and quality characteristics of peanut grown in the Mediterranean region of Turkey. *Field Crops Resource* 21:224–232.

Gunasekaran, L. & Pavadai, P. (2015). Studies on induced physical and chemical mutagenesis in groundnut (*Arachis hypogia*) *International Letters of Natural Sciences*, 35, 25-35

Khan, S., Wani, M.R. & Parveen, K. (2004). Induced genetic variability for quantitative traits in *Vignaradiata. Pakistan Journal of Botany*, 36, 845-850

Khan, S. & Wani, M.R. (2006). MMS and SA induced genetic variability for quantitative traits in mungbean. *Indian Journal of Pulses Research*, 19(1), 50–52.

Kumar, A., Kumar, V., Lal, S.K., Jolly, M. & Sachdev, A. (2015). Influence of gamma rays and ethyl methane sulphonate (EMS) on the levels of phytic acid, raffinose family oligosaccharides and antioxidants in soybean seeds of different genotypes. *Journal Plant Biochemistry Biotechnology*, *24*,204–209.

Mayur, V., Jadhav., Rahul, K., Zote. & Amol, D. (2018). Studies on Induced Chemical Mutagenesis in Groundnut (*Arachis hypogaea* L.). *International Journal of Current Microbio logy and Applied Sciences* 7(10):

Olorunmaiye, K., Stephen, G., Joseph, G., Animasaun, D. A. & Oyedeji, S. ((2019). Mutagenic Com ponents and Dosage Effects of Ethyl Methanesulphonate *Ife Journal of Science*, 21, (2)

Pavadai, P., Girija, M. & Dhanavel, D. M. (2009). Effectiveness and efficiency and biochemical content of physical and chemical mutagens in soybean (Glycine max (L.) Merr.). *Journal of Phytology*, 1 (6), 444-447.

Salim, K., Fahad, A. & Firoz, A. (2009). Sodium azide a chemical mutag en for enhancement of agronomic trait of crops plants. *Journal of Science and Technology*, 4, 1-21

Sharma, S.K., Sood, R. & Pandey, D.P. (2005). Studies on mutagen sensitivity, effectiveness and efficiency in urdbean [*Vigna mungo* (L.) Hepper]. The *Indian Journal of Genetics & Plant Br eeding*, 65(1), 20–22.

Tillman, B. L. & Stalker, H. T. (2009). Peanut: In Johann Vollmann and Istvan Rajcan Handbook of Plant Breeding, *Oil Crops* 4: 287 – 316.

Box-Behnken Design Optimization of Process Variables for the Sol-Gel Synthesis of Zinc Tungstate Nanoparticles

[1,2]Abubakar, Hassana Ladio [1,3]Tijani, Jimoh Oladejo, [3,4]Abdulkareem, Ambali Saka and [1]Abdullahi, Mann

[1]Department of Chemistry, Federal University of Technology, Minna, Niger State
[2]Department of Chemistry, Nile University of Nigeria, Abuja, Airport Road, Jabi, Abuja, Nigeria
[3]Department of Chemical Engineering, Federal University of Technology, Minna, Nigeria
[4]Nanotechnology Research Group, African Centre of Excellence on Food Safety and Mycotoxins, Federal University of Technology, Minna, Niger State, Nigeria
***Corresponding author:** abubakarhassana25@gmail.com

Abstract

Highly crystalline Zinc Tungstate Nanoparticles ($ZnWO_4$) were successfully synthesized by a simple sol-gel technique using water and ethanol (1:1) as solvents. Effects of synthesis parameters such as reaction temperature, pH and stirring speed on the synthesized $ZnWO_4$ nanoparticles were investigated experimentally based on Box-Behnken Design. The synthesized $ZnWO_4$ at the optimum conditions was subjected to calcination at temperatures between 100°C – 900°C.The produced nanoparticles were analyzed by X-Ray diffraction (XRD), High Resolution Scanning Electron Microscopy (HRSEM) and Electron Dispersive X-ray spectroscopy (EDX). HRSEM analysis confirmed the formation of aggregated spherical shape irrespective of the synthesis conditions while EDX analysis showed Zn, W and O as the dominant elements under the applied conditions. XRD analysis demonstrated formation of highly crystalline, monoclinic phase of $ZnWO_4$ with a crystallite size of 14.51 nm at the The study showed that morphology, phase types and crystallite sizes of $ZnWO_4$ depends on the applied process variables.

Keywords: $ZnWO_4$ nanoparticles, process variables, sol-gel method

Introduction

In recent years, the sol-gel technique has been used for the production of advanced nanomaterials. The synthesis of hybrid metal oxide nanoparticles with distinct properties has been of great interest to researchers in the field of science, technology and engineering (Jaramillo-Paez *et al.*, 2021; Khan *et al.*, 2016). These nanoparticles have a wide range of applications from environmental decontamination (Ma *et al.*, 2021), humidity sensors (Arularasu *et al.*, 2016), photoluminescence (Liu *et al.*, 2020), catalysis (Geetha *et al.*, 2021) and even supercapacitors (Yesuraj *et al.*, 2019). Some important advantages of the sol-gel method include its affordability, simplicity in design and the fact that it is economical, pristine nanomaterials can be obtained at low temperatures. The general mechanism for the sol-gel process involves the formation of oxide networks through polycondensation reactions of a molecular precursor in a solvent (Jaramillo-Paez *et al.*, 2021). Sol-gel technology can be applied in many disciplines as it allows for the expansion of nanomaterials especially semiconductors for a vast array of applications. The introduction of photocatalytic technology has become a preferred method for the degradation of organic pollutants involved development of an efficient semiconductor. For decades now heterogeneous photocatalysis using semiconductors have been utilized due to factors such as low energy consumption, straightforward reaction conditions and also its simplicity (Juan and Anabel, 2019). $ZnWO_4$ has caught the attention of many researchers since $PbWO_4$ was found capable

of photocatalytically splitting H_2O, H_2 and O_2 (Tee *et al.,* 2017). With a monoclinic wolframite - type structure having the space group P2/c with oxygen ions deposited around the tungsten, $ZnWO_4$ forms an insulated [WO_6] octahedron coordination which has an asymmetric shape displaying its local atomic structures (He *et al.,* 2016), this is a very important inorganic ternary oxide material as it has been known to crystallite as a scheelite structure depending on the ionic radius of the cation (Chena *et al.,* 2017). It is a member of the tungstate family and has over the years been used for the mineralization of organic pollutants under UV (Rahmani and Sedaghat, 2019) and sunlight (Paliki *et al.,* 2016) irradiation, although the photocalytic strength of $ZnWO_4$ stand alone is not strong enough (Rahmani and Sedaghat, 2019). The enhancement of the photocatalytic activity of the semiconductor $ZnWO_4$ for practical applications has been deeply considered as the degradation of organic contaminants has been the goal of a lot of industries as well as scientists interested in environmental pollution control. A couple of approaches have been taken to further increase the quality of $ZnWO_4$ nanoparticles being synthesized, after understanding the photocatalytic mechanism of the nanoparticles. Different methods including microwave-assisted method, sol-gel, ultrasonication, photodeposition, precipitation, co-precipitation, biological, catalytic chemical vapor deposition, thermal evaporation, hydrothermal have been used for the preparation of $ZnWO_4$ nanoparticles and in some cases $ZnWO_4$ nanoparticles having controlled morphology were synthesized. Of all these, sol-gel stand out as one of the most effective method that can be utilized for the synthesis of nanoparticles with modified surfaces.

However, knowing the exact value of each parameter to be used for the optimum synthesis takes a lot of time and rounds of synthesis, as most studies that have been carried out for the sol-gel synthesis of nanoparticles required dealing with one-factor-at-a-time while holding other parameters constant, hence, more time and reagents are wasted in an attempt to predict the true optimum conditions, this will also increase the cost of synthesis. To overcome this issue, the optimization studies have been carried out using response surface methodology (RSM) based on Box-Behnken Design (Kassahun *et al.,* 2017). This is a statistical technique used for empirical model building as well as analysis of the relationship between experimental input parameters and response. The model established can precisely describe the relationship between the factor and the response values; it can pick between the different operating parameters and then give a prediction of the experimental results according to the mathematical model (Behzadi *et al.* 2020). Rahmani and Sedaghat (2019) utilized sol-gel method to prepare $ZnWO_4$ nanoparticles and found that the nanoparticles synthesized had an average crystallite size between 26 – 78 nm. Jaramillo-Paez *et al*. (2021) synthesized $ZnWO_4$ using sol-gel method and revealed the formation of monoclinic phase with the crystallite size was of 24.6 nm. SEM/TEM analysis showed that the nanocomposite material had a clear morphology with near quasi spherical/ ellipsoidal shaped particles which were highly agglomerated. Information of the sol-gel synthesis of $ZnWO_4$ nanoparticles-based Box-Behnken design is scarce in the literature. In this study, investigation and modeling of the direct and interactive effects of operating parameters on the Sol-Gel synthesis of $ZnWO_4$ nanoparticles based on Box-Behnken Design was reported. The effect of reaction temperature, pH and stirring speed on the crystallite sizes of the nanoparticles was analyzed. The synthesized $ZnWO_4$ nanoparticles were subjected to different calcination temperatures and the final products were characterized using different analytical tools.

Methodology

Materials: Analytical grade chemicals and reagents Zinc Acetate Dihydrate (99%), Sodium Tungstate hexahydrate (96%), Titanium (IV) Isopropoxide (97%), Polyethylene glycol [$HO(C_2H_4O)nH$] (98%), Boric Acid (H_3BO_3) (99.9%), Magnesium nitrate hexahydrate [$Mg(NO_3)_2.6H_2O$] (98%), Sodium Chloride (Nacl (99.5%), Ammonia (NH_3) (30%), Sodium hydroxide (NaOH) (99%), Ethanol (99.8%) and Deionized water. The chemicals/reagents were used without further purification.

Preparation of $ZnWO_4$ nanoparticles

The synthesis of $ZnWO_4$ nanoparticles was based on Box-Behnken Design. The influence of process parameters such as pH, temperature and rotations per minute (RPM) was investigated and the level of the factors considered are presented in Table 1 and the full design in Table 2, the range of level of factors considered through preliminary investigation obtained from literature.

Table 1: Box-Behnken design for experiment on $ZnWO_4$ nanoparticles synthesis

Synthesis Parameters	Range	
	Minimum	Maximum
pH	3	12
Reaction Temperature (ºC)	30	90
Agitation/Stirring Speed (rpm)	750	2000

The synthesis procedures are described as follows: 25 g of Zinc acetate dehydrate was dissolved by 250 mL of an equal mixture of distilled water and ethanol; the solution was stirred till the salt completely dissolved. The same procedure was carried out in a separate beaker but with 15g of Sodium acetate and dissolved using 250 mL of an equal mixture of distilled water and ethanol., The solution was stirred till the salt completely dissolved. 50 ml of the zinc acetate solution and 50 ml of the sodium tungstate solution were obtained in two separate beakers and poured into a 600 mL beaker at once. The pH adjustment to the desired value specified in Table 2 was done using 2 M HCl and 2 M NaOH solution, the temperature of the reaction mixture was maintained with packing ice cubes close to the beaker while it was stirred at 2000 rpm using a magnetic stirrer. The resulting solution was allowed to settle and later washed using ethanol and water in a 75:25 ratio several times to remove ionic remnants before drying at 80^{o}C for 24 hours after which the sample was taken out of the oven and pounded using a laboratory mortar and a pestle and later calcined at 300^{o}C for 2 hours.

The procedure was repeated using the experimental conditions in runs 2, 4, 6 and 13. Using data from the XRD analysis, the most suitable conditions for the preparation of $ZnWO_4$ of smallest crystallite sizes was estimated. A model of $ZnWO_4$ nanoparticles crystallite size based on the interactive effects of pH, temperature and stirring speed was developed using regression analysis and analysis of variance (ANOVA) to determine the individual and combined effects of the process parameters. The powdered $ZnWO_4$ nanoparticles (2g) each in a separate crucible were calcined at different temperatures 100^{o}C, 200^{o}C, 300^{o}C, 400^{o}C, 500^{o}C, 600^{o}C, 700^{o}C, 800^{o}C and 900^{o}C for calcination time of 3 hours.

Characterization of $ZnWO_4$ Nanocomposites

The $ZnWO_4$ nanoparticles were characterized using a powdered XRD to identify the phase of the mineral constituents of the $ZnWO_4$ nanoparticles. The $ZnWO_4$ nanoparticles was placed and also clipped on an aluminum rectangular sample holder. The diffractograms were recorded at the 2θ range of 15 º to 80º. Debye-Scherrer equation was used to calculate the crystallite size and the half height peak width was determined, the equation is as follows:

$$d = \frac{k\lambda}{\beta\cos\theta} \quad (1)$$

Here, d is the crystallite size in nm, K = 0.94, λ is the wavelength of the X-ray which is 0.1541 nm, θ is the half diffraction angle and β is the full width at half maximum in radian. The HRSEM was used

to determine the morphology of the $ZnWO_4$ nanoparticles. The EDS on the other hand was used to determine the elemental composition in the sample. 0.05 g of the sample ($ZnWO_4$ nanoparticles) was placed on aluminum stubs and then coated with gold in order to prevent charging of the sample during analysis. The sample was then examined under the microscope after being loaded into the HRSEM equipment to obtain the desired image. The peaks created in the EDS spectrum is as a result of the difference in energy,

RESULTS AND DISCUSSION

X-Ray diffraction patterns for the synthesis of $ZnWO_4$ nanoparticles

The phase structure of the sol-gel synthesized $ZnWO_4$ nanoparticles was examined using XRD technique and the spectrum obtained is shown in Figure 1

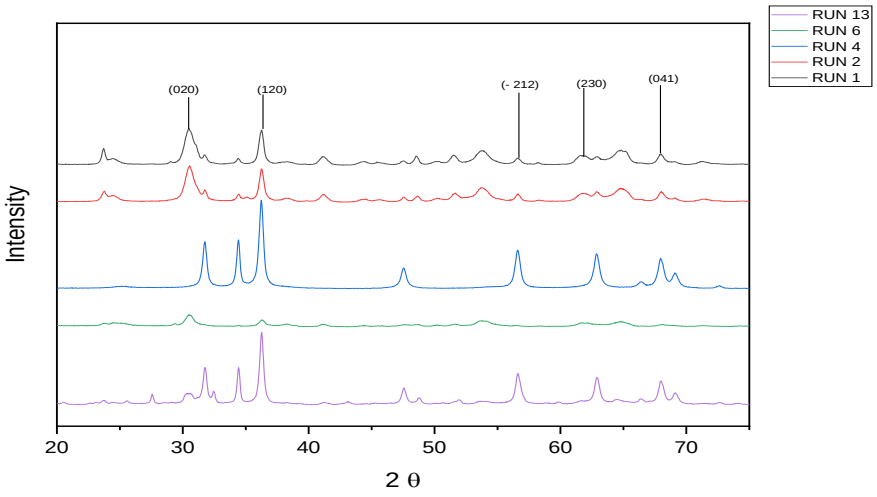

Figure 1: X-ray diffraction patterns for Run 1, 2, 4, 6 and 13

All the diffraction peaks of the synthesized $ZnWO_4$ nanoparticles can be indexed to a pure monoclinic, face-centered cubic and Anorthic (triclinic) phases respectively. For Run 1, the predominant characteristic diffraction peaks corresponding to (0 2 0) and (1 2 0) miller indices were located at 2 theta values of 31.261° and 36.774°. These observed peaks belong to a typical monoclinic phase of Zinc Tungsten Oxide ($ZnWO_4$) with JCPDS no. 15-0074 and average crystallite size of 14.51 nm. Run 2 on the other hand had predominant characteristic peaks corresponding to (0 2 0) and (1 2 0) crystal planes located at 2 theta values of 31.261° and 36.774°. This is assigned as Zinc Oxide with an average crystallite size of 11.98 nm. The sample matched well with JCPDS no. 25-1164 of zincite (ZnO) phase. Run 4 had predominant diffraction peaks at (2 2 1), (0 2 6), (2 0 6), (1 2 7), (1 1 10), (3 1 10), (0 -3 1), (0 4 2) and lastly (4 1 7) miller indices at 2 theta values of 27.16°, 32.8°, 34.4°, 36.1°, 47.5°, 56.5°, 62.9°, 67.9° and 69°, with an average crystallite size of 17.15 nm.

The prepared material was Sodium Tungsten Oxide ($Na_{2.4}Zn_{0.8}W_2O_8$) with JCPDS no. 74-2369 of face-centered cubic, In the case of Run 6, the diffraction peaks were noticed at 2 theta values of 26.00°, 29.29°, 31.76°, 31.95°, 34.43°, 36.37°, 54.60°, 62.32° and 65.35° which correspond to (1 2 1), (1 2 1), (1 0 1), (0 2 6), (1 1 2), (1 2 7), (0 4 6), (1 4 9) and (3 0 3) crystal planes, zinc tungsten oxide. This belongs to Anorthic (triclinic) with an average crystallite size of 44.51 nm. For the material prepared using Run 13 conditions, prominent diffraction peaks were observed at 2 theta values of 32.8°, 34.4°, 36.1°, 47.5°, 56.5°, 62.9°, 67.9° and 69° that matched well with the following miller indices (0 2 6), (2

0 6), (1 2 7), (1 1 10), (3 1 1), (0 -3 1), (0 4 2), and lastly (4 1 7). The average crystallite size of 19.78 nm was obtained for monoclinic phase of Sodium Zinc Tungsten Oxide ($Na_{2.4}Zn_{0.8}W_2O_8$) which is in harmony with JCPDS no. 32-1215.

Comparatively, strong diffraction peaks found in $ZnWO_4$ nanoparticles obtained from Run 1 show that it is highly crystalline and pure monoclinic phase with the smallest crystallite size at 14.51 nm. Of the five Runs, only Run 1 had the correct identity of $ZnWO_4$ nanoparticles with lattice constants a = 4.69100, b = 5.72000, c = 4.92500 and β = 90.64. The XRD patterns of the $ZnWO_4$ nanoparticles obtained in Run 1 corroborated with the findings of Rahnamaeiyan *et al.*, (2015) and Yan *et al.*, (2013) who independently reported a monoclinic phase of $ZnWO_4$ with JCPDS no. of 15-0774, and a space group of P2/c.

HRSEM analysis of $ZnWO_4$ nanoparticles

The surface morphology of the as-prepared $ZnWO_4$ nanoparticles using experiment conditions in runs 1, 2, 4, 6 and 13 were observed using the HRSEM and the corresponding micrographs is displayed in Figure 2:

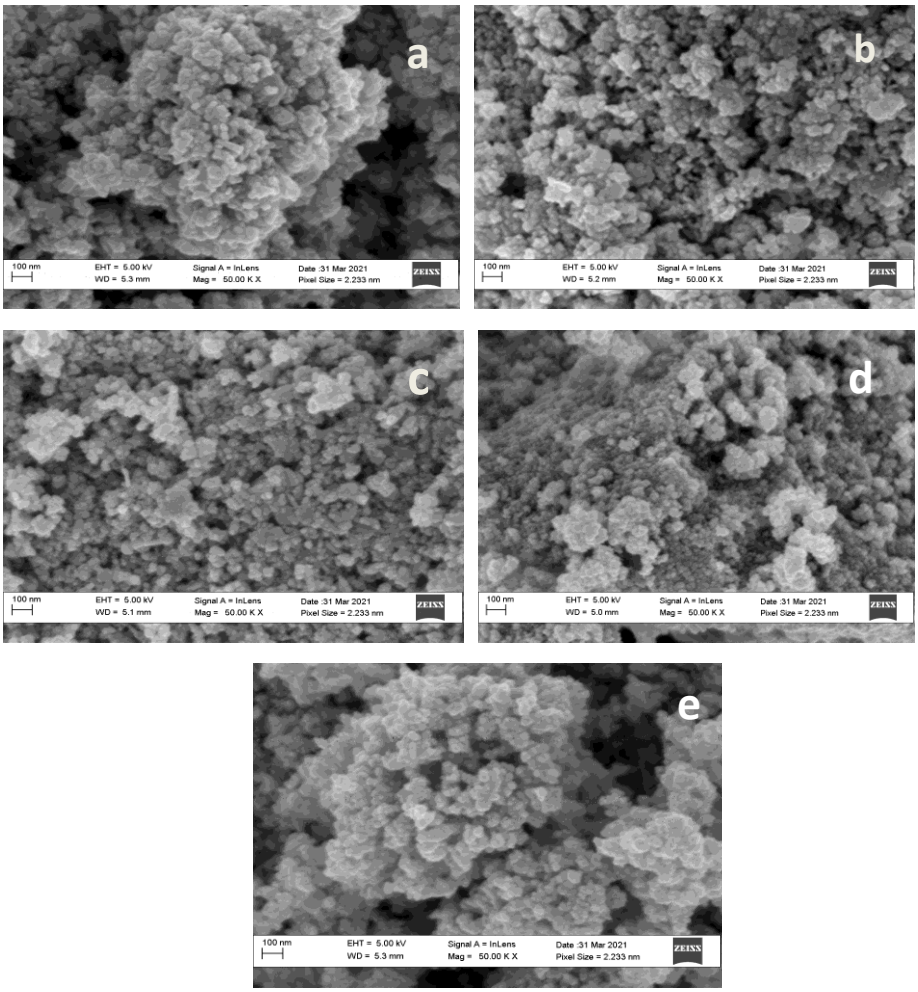

Figure 2: HRSEM of $ZnWO_4$ nanoparticles prepared at (a) Run 1, (b) Run2, (c) Run 4 (d) Run 6 and Run 13

Figure 2(a) exhibits pebble-like morphology with a jiggered surface for $ZnWO_4$ synthesized while Figure 2(b) shows a stone-like morphology of different size distribution. The nanoparticles seemed to be more clustered at Run 4 with clear agglomeration as seen in Figure 2(c). The image of $ZnWO_4$ at Run 6 (Figure 2 (d) showed nanoparticles of different sizes were clumped together. A high level of agglomeration was observed in Figure 2 (e) for Run 13. The formation of different morphological structure may be linked to the applied synthesis conditions.

EDX analysis of $ZnWO_4$ nanoparticles

The elemental composition of the $ZnWO_4$ nanoparticles synthesized at Run 1, 2, 4, 6 and 13 were measured by the EDX analysis and the results are presented in Figure 3 (a-e).

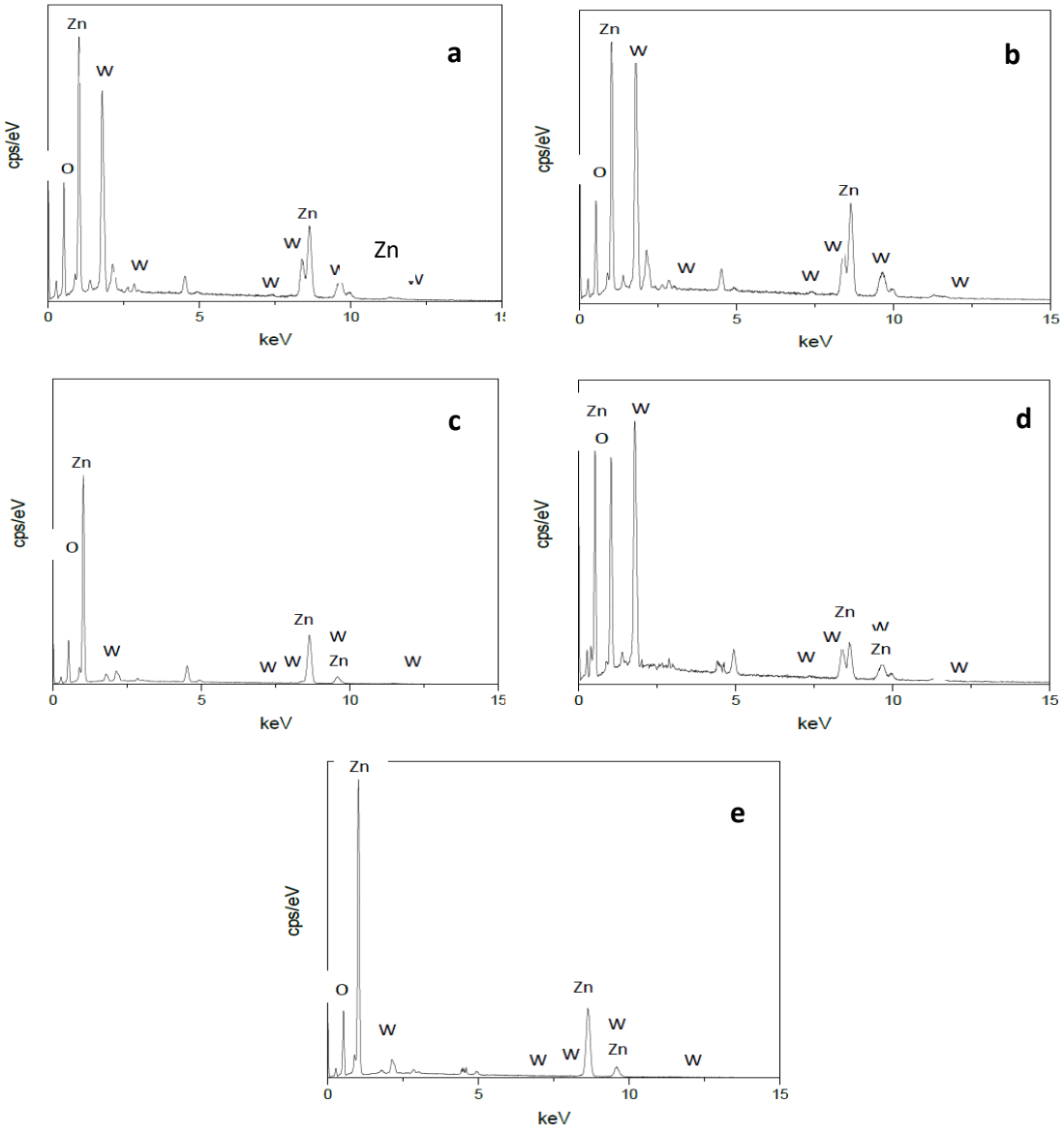

Figure 3: EDX Spectra of $ZnWO_4$ nanoparticles prepared at Run 1(a), Run 2(b), Run 4(c), Run 6(d) and Run 13(e)

EDX analysis was performed to confirm the chemical composition of $ZnWO_4$ nanoparticles obtained from Run 1, the patterns in Figure 3(a) shows the existence of Zn 23.14%, W 39.56% and O 37.3% demonstrating the successful synthesis of zinc tungstate ($ZnWO_4$) nanoparticles. The patterns in Figure 3(b) representing Run 2 shows the existence of Zn 40.21%, W 35.69% and O 24.1% demonstrating the successful synthesis of zinc tungsten oxide alongside zincite (ZnO) nanoparticles as seen from the XRD data analyzed. The patterns in Figure 3(c) representing Run 4 shows the existence of Zn 35.33%, W 36.7% and O 27.97% demonstrating the successful synthesis of zinc tungsten oxide ($ZnWO_4$) alongside sodium zinc tungsten oxide ($Na_{2.4}Zn_{0.8}W_2O_8$) nanoparticles as seen from the XRD data analyzed. Figure 3(d) representing Run 6 shows the existence of Zn 28.64%, W 23.83%, O 47.53% demonstrating the successful synthesis of zinc tungsten oxide ($ZnWO_4$) alongside sodium tungsten oxide (Na_2WO_4) nanoparticles as seen from the XRD data analyzed. At this point when the pH value is 3, the $Na_2W_4O_3$ (JCPDS no. 98-000-2045) and $Na_2W_2O_7$ (JCPDS no. 98-000-0983) phases were formed alongside that formed (Rahmani and Sedaghat, 2018).

Figure 3(e) representing Run 13 shows the existence of Zn 65.85%, O 14.26%, W 19.89%, demonstrating the successful synthesis of zinc tungsten oxide ($ZnWO_4$) alongside Sodium Zinc Tungsten Oxide ($Na_{2.4}Zn_{0.8}W_2O_8$) nanoparticles as seen from the XRD data analyzed. The results obtained from the EDX spectra of the $ZnWO_4$ nanoparticles obtained from Run 1 have supported correspondingly the results of the XRD results of zinc tungsten oxide ($ZnWO_4$) nanoparticles for Run 1.

Table 2: Full Box--Behnken design for $ZnWO_4$ nanoparticles synthesis

Experimental Run	Factor 1 A: pH	Factor 2 B: Temperature (°C)	Factor 1 C: Stirring speed (rpm)	crystallite size (nm)
1	7.5	30	2000	14.51
2	7.5	90	2000	11.98
3	12	60	750	80.05
4	12	60	2000	17.15
5	7.5	60	1375	73.50
6	3	60	2000	44.51
7	3	90	1375	65.21
8	3	30	1375	55.34
9	7.5	90	750	75.08
10	12	30	1375	85.24
11	7.5	60	1375	73.51
12	7.5	60	1375	74.79
13	12	90	1375	19.78
14	3	60	750	48.00
15	7.5	60	1375	74.45
16	7.5	30	750	40.44
17	7.5	60	1375	75.89

Statistical analysis for the process optimization of $ZnWO_4$ nanoparticles

The interaction between the pH, reaction temperature and stirring speed was checked using the Box-Behnken Design (BBD). Models such as linear, 2FI, quadratic and cubic model were tested to determine the most suitable model with the significant term. Over the years, research has shown the

utilization of standard deviation, R-squared and p-value are important in model prediction of the response (Oladipo and Gazi, 2014; Roosta *et al*., 2014; Roosta *et al*., 2015; Saleh *et al.*, 2017; Sharifpour *et al*., 2017; Vargas *et al*., 2010). A summary of the results obtained from the model analysis are presented in Table 3.

According to Table 5, it is obvious that the quadratic model possesses the lowest standard deviation value at 0.8712, a high correlation coefficient (R^2) at 0.9992, adjusted (R^2) at 0.9982 and predicted (R^2) at 0.9906. Hence, the quadratic model was found most suitable model for the estimation of crystallite size of $ZnWO_4$ nanoparticles. Also, in Table 3, the quadratic model shows an interesting correlation between the adjusted R^2 at 0.9982 and the predicted R^2 at 0.9906 which is positive. The result obtained shows a reasonable agreement between the adjusted R^2 and the predicted R^2. This again confirms that the quadratic response surface model is the most suitable for the prediction of the crystallite size of $ZnWO_4$ nanoparticles from the interaction of the variables.

Table 3: Response surface model summary for $ZnWO_4$ nanoparticles crystallite size

Source	Standard Deviation	R^2	Adjusted R^2	Predicted R^2	PRESS	
Linear	5.46	0.9423	0.9290	0.8845	775.48	
2FI	3.11	0.9856	0.9770	0.9484	346.69	
Quadratic	**0.8712**	**0.9992**	**0.9982**	**0.9906**	**63.34**	**Suggested**
Cubic	0.6124	0.9998	0.9991		*	Aliased

This finding is similar to those presented by Jafari *et al*. (2017). The variance analysis results for quadratic model of the crystallite size of $ZnWO_4$ nanoparticlesis shown in Table 4, where the quadratic model F-value of 982.48 shows the significance of the model. Marrakchi *et al*. (2017) and Sahu (2013) independently reported p-values less than 0.05 and established that the models terms were significant at 95% confidence level.

Table 4: ANOVA of quadratic model for $ZnWO_4$ nanoparticles crystallite size

Source	Sum of Squares	DF	Mean squares	F-value	P-value	Comment
Model	6710.66	9	745.63	982.48	< 0.0001	Significant
A-pH	3806.28	1	3806.28	5015.34	< 0.0001	Significant
B-Temperature	968.00	1	968.00	1275.48	< 0.0001	Significant
C-Stirring speed	1554.03	1	1554.03	2047.66	< 0.0001	Significant
AB	56.25	1	56.25	74.12	< 0.0001	Significant
AC	52.56	1	52.56	69.26	< 0.0001	Significant
BC	182.25	1	182.25	240.14	< 0.0001	Significant
A^2	49.75	1	49.75	65.56	< 0.0001	Significant
B^2	1.99	1	1.99	2.62	0.1494	Significant
C^2	36.33	1	36.33	47.87	0.0002	Significant
Residual	5.31	7	0.7589			Significant
Lack of Fit	3.81	3	1.27	3.39	0.1346	not significant
Pure Error	1.50	4	0.3750			
Cor Total	6715.97	16				

From Table 4, the pH, reaction temperature and stirring speed had significant effects on the crystallite size of $ZnWO_4$ nanoparticles because their p-values are less than 0.05. Of the three investigated factors, pH (A) with the highest F-value of 5015.34 exerted the greatest effect on the crystallite size of $ZnWO_4$ nanoparticles followed by the stirring speed (B) with an F-value of 2047.66 and lastly temperature (C) having an F-value of 1275.48. This generally means that the effect exerted by pH is greater than that of the stirring speed and the temperature as shown by the parametric coefficients. The interaction between the temperature and stirring speed (BC) had an extensive effect on the crystallite size with the highest F-value at 240.14. The pH and temperature (AB) and pH and stirring speed (AC) on the other hand had a much smaller effect on the crystallite size with F-values of 74.12 and 69.26 respectively. Furthermore, the value of quadratic function of pH was the highest on the crystallite size of $ZnWO_4$ nanoparticles with the F-value of 65.56, followed by stirring speed with the F-value of 47.87 and temperature with the F-value of 2.62. The lack of fit F-value at 3.39 shows its effect is non-significance of its effects, owing to the non-significant lack of fit of 0.1346. This further suggests that the proposed fits of the experimental data that the independent variables have considerable side effects on the crystallite size of $ZnWO_4$ nanoparticles.

For the analysis of the crystallite size of $ZnWO_4$ nanoparticles synthesized through the coefficient values presented in equation 1, pH gives a higher positive effect when compared to the other parameters. The values obtained for "Prob > F" is less than 0.05, this indicates that the model terms are significant, a lower probability value on the other hand presents a higher significance as far as the regression model I concerned. It was reported by Marrakchi *et al.* (2017) that p-values lower than 0.05 are significant, while values higher than 0.1 show that the model terms are insignificant. Here, the p-value is less than 0.0001 (Chowdhury *et al.*, 2016).

From Table 4, the values obtained for F-test shows just how the mean square of the model compares with the mean square of the residuals. F-test of the model has a value of 982.48 which means that the model is significant; this suggests that there is only a 0.1346% (from the-value for lack of fit) chance for the model F-value to occur as a result of noise (Debnath *et al*., 2017; Marrakchi *et al.*, 2017). For this model, linear term A (pH), B (Reaction Temperature), C (Stirring speed), the interactions AB, AC and BC, and the quadratic terms A^2 and C^2 were all statistically considered significant model terms.

This second order regression equation presented shows how the crystallite size of $ZnWO_4$ nanoparticles depends on pH, temperature and stirring speed during synthesis. A second order polynomial equation was used to establish the relationship between all three parameters and each response in terms of coded factors (Chowdhury *et al.*, 2016).

The final equation in the term of actual values is presented as

$$\text{Surface Area} = 74 + 21.81\,A + 11.00\,B + 13.94\,C - 3.75\,AB + 3.63\,AC - 6.75\,BC + 3.44\,A^2 - 0.6875\,B^2 + 2.94\,C^2 \quad \text{Equation 2}$$

The developed model in Equation 1 defines the relationship between the process parameters and the crystallite size of $ZnWO_4$ nanoparticles. The maximum experimental crystallite size was obtained at run 6 with the value of pH at 7.5, temperature at 90^{o}C and stirring speed at 2000 rpm, this value was also obtained at run 13 where the value of pH is 7.5, temperature at 60^{o}C and stirring speed at 1375 rpm. The minimum crystallite size was obtained at run 1 with synthesis conditions: solution pH(7.5), reaction temperature(30°C) and stirring speed (2000 rpm).

a)

A three level factorial design was used to achieve all three possible combinations capable of producing $ZnWO_4$ nanoparticles of desired crystallite size by optimizing the response within the 3-D space. The analysis of variance (ANOVA) has shown that a quadratic model is significant at p value less than 0.0001. Model reduction was done using RSM because some values were not significant. Fishe's statistical analysis proves the adequacy of the developed model as presented in Table 3 respectively (Chowdhury *et al.*, 2016).

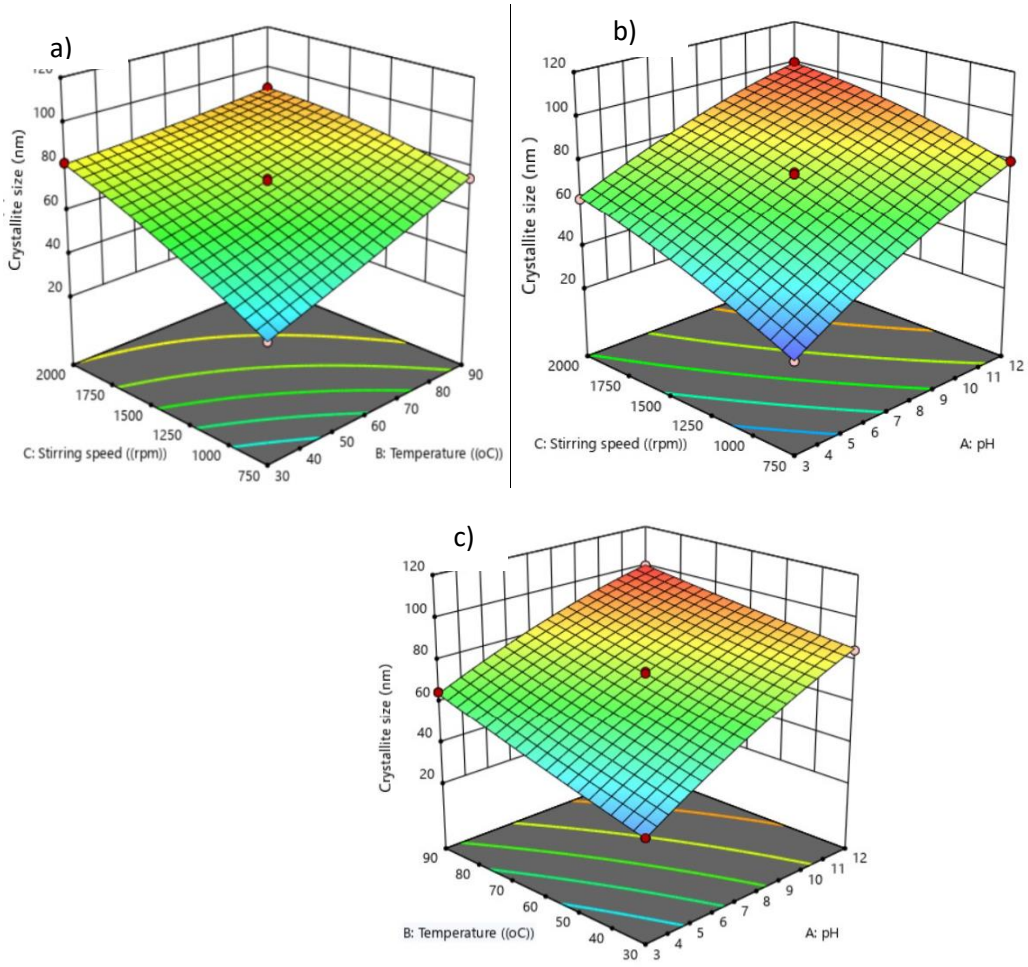

Figure 4: The three-dimensional response surfaces: (a) effect of stirring speed and temperature, (b) effect of stirring speed and pH and (c) effect of temperature and pH on the crystallite site of $ZnWO_4$ nanoparticles

The Figure 8 (a-c) show the 3-D surface interaction between the investigated parameters on the crystallite size of $ZnWO_4$ nanoparticles, Figure 4 (a) revealed the synergetic effect of stirring speed (B) and temperature (C) on the crystallite size of $ZnWO_4$ nanoparticles, Figure 4 (b) presents the effect of stirring speed (B) and pH (A) and lastly Figure 4 (c) shows the interactive effect of temperature and pH on the crystallite size of $ZnWO_4$ nanoparticles.

A 3D surface response plot is known as a graphical representation of the regression equation obtained from the model established; this is used for the study of the interaction among parameters and also to define optimum conditions for each parameter for the highest crystallite size of $ZnWO_4$ nanoparticles. These plots are based on the function of two variables while the third variable is kept at its optimum

condition. Also, these plots are based on the function of three contour plots specifying the level of significance of the interaction, an elliptical or saddle plot is obtained in a situation where there is a perfect interaction among the variables being considered. Figure 4 (a-c) represent a 3D plot of the crystallite size of $ZnWO_4$ nanoparticles using the interactions of all three variables used. It was noticed from Figure 4(a), that when both stirring speed and temperature increase, the crystallite size of $ZnWO_4$ nanoparticles also increases, this interaction has the highest F-value at 240.4 as displayed in Table 4, a high F-value suggests that the model is significant (Marrakchi *et al.*, 2017). The nature of curvature of the diagram suggests that there was optimization of stirring speed on the crystallite size of $ZnWO_4$ nanoparticles at constant reaction temperature. The surface plot shown in Figure 4(b) indicates that the synthesis conditions of obtaining higher crystallite size of $ZnWO_4$ nanoparticles depends on the stirring speed and pH, as revealed with the lowest F-value at 69.26, the crystallite size of $ZnWO_4$ nanoparticles increases as the two variables increase. At high reaction temperature conditions and pH, the crystallite size of $ZnWO_4$ nanoparticles also increase as noticed in Figure 4(c).

Model validation using residuals

Residual analysis was done in order to achieve close approximation of the real system. Residuals (*ri*) were obtained from the following regression:

$$ri = y_{i\ observed} - y_{i\ predicted} \quad \text{.....(3)}$$

where *r* is the residual response and *i* is observation. The value obtained for all observation residuals utilized in the residual plots contain the following:

- Normal plot of residuals
- Residuals vs. predicted plot
- Residuals vs. observation order plot shown in Figure 5(a-c).

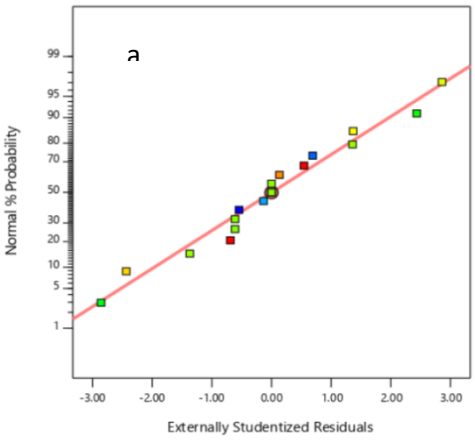

Figure 5(a): Normal plot of residuals

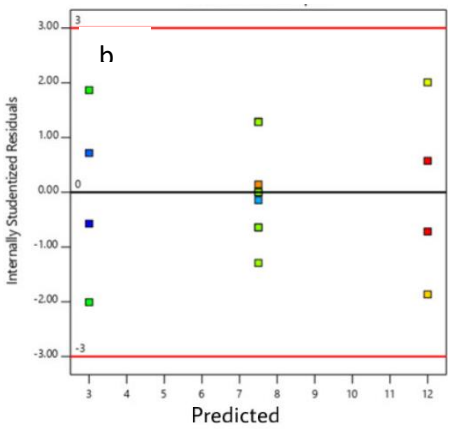

Figure 5(b): Normal probability plot of residuals vs. predicted

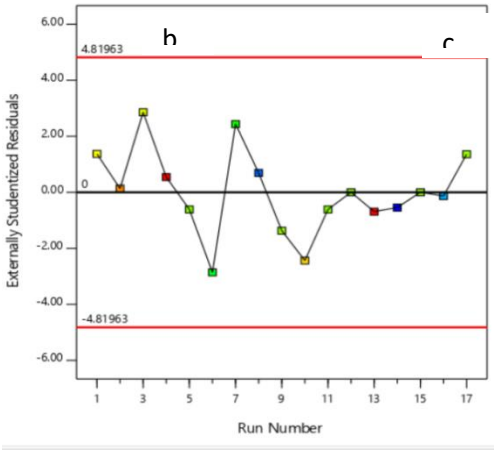

Figure 5(c): Residuals vs. observation order plot.

All three plots presented in figures 5 (a) to (c) respectively are the most important diagnostics for a model (Chowdhury *et al.*, 2016). A linear relationship proved normality in the error terms and the presented data showed no signs of problems, this indicates that the errors follow the normal distribution and support the experimental model (Draper and Smith, 2014). The residuals vs. predicted plot in Figure 5(c) displays a random scatter pattern, and it was noticed that the data were well distributed in positive and negative residuals in the range of $-2 < ri < +2$ (with *ri* being the actual residual). There is however no pattern following the residuals vs. observation order plot in Figure 5(c), this implies that all residuals correlated with each other. There is no reason to assume any violation of the hypothesis; hence the developed model is acceptable (Chowdhury *et al.*, 2016; Draper and Smith, 2014).

Experimental model validation

Figure 6 shows the relationship between the theoretical and experimental values of the crystallite size of $ZnWO_4$ nanoparticles

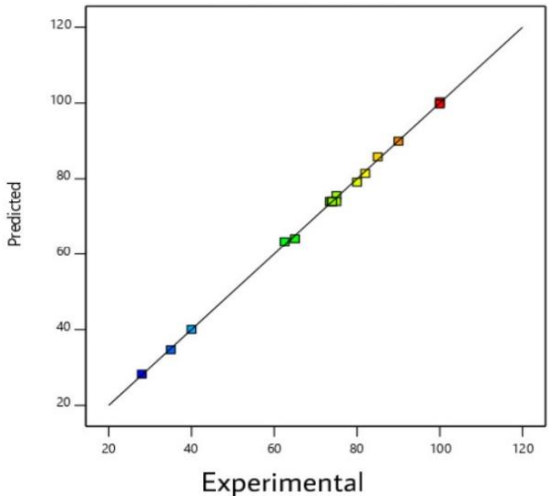

Figure 6: Relationship between predicted and experimental values of $ZnWO_4$ nanoparticles crystallite size

It can be noticed that the theoretical and experimental values of the $ZnWO_4$ nanoparticles crystallite size are very close together; this suggests that the model was developed successfully with a clear correlation between the variables of the crystallite size of $ZnWO_4$ nanoparticles.

The HRSEM images obtained when optimizing different Runs only showed a difference in the amount of clusters form as the parameters changed, however, HRSEM micrographs of nanoparticles calcined at different temperatures showed an evolution of the morphology of the nanoparticles, where it was observed that with increase in the calcination temperature, the nanoparticles went from platelet looking at lower temperatures of between 100^{o}C to 200^{o}C to spherical at temperatures between 300^{o}C and 500^{o}C and a gradual transformation into rod-like particles at higher temperatures of between 600^{o}C to 900^{o}C. The results showed how an increase in temperature can significantly affect the morphology of the synthesized nanoparticles. At the end of the analysis, the optimum conditions were gotten as reaction temperature of 30^{o}C, pH of 7.5, stirring speed of 200 rpm and a calcination temperature of 400^{o}C. finally, results from the characterizations done have been used to understand the behavior of $ZnWO_4$ nanoparticles under optimal conditions and unlike methods (Ma *et al.*, 2021, Mehdi *et al*, 2015; Yadav *et al.*, 2018).

Conclusion

In this paper, the $ZnWO_4$ nanoparticles were successfully prepared using the sol-gel method by optimization of reaction temperature, pH and stirring speed based on Box-Behnken Design. The smallest crystallite size 14.51 nm of monoclinic phase $ZnWO_4$ was obtained at the optimum conditions of pH (7.5), reaction temperature (30°C) and stirring speed (2000 rpm), this shows an attractive potential for its application in the degradation of pollutants. This study showed that optimization of process variables of simple sol-gel method without addition of catalysts, templates and surfactants is suitable for the synthesis of $ZnWO_4$ nanoparticles of desired crystallite size and morphology.

REFERENCES

Arularasu M. V., and Sundaram R. (2016). Synthesis and characterization of nanocrystalline $ZnWO_4$ -ZnO composites and their humidity sensing performance. *Sensing and Bio-Sensing Research*, 11, 20 – 25.

Behzadi S., Nonahal B., Royaee S. J. and Asadi A. A. (2020). $TiO_2/SiO_2/Fe_3O_4$ magnetic anoparticles synthesis and application in methyl orange UV photocatalytic removal. *Water Science Technology, 82(11), 2432-2445.*

Chena G., Wanga F., Yu J., Zhang H. and Zhang X. (2017). Improved red emission by codoping Li^{3+} in $ZnWO_4$:Eu^{3+} phosphors, *Journal of Molecular Structure*, 1128, 1-4.

Chowdhury S., Yusof F., Faruck M. O. and Sulaiman N. (2016). Process Optimization of Silver Nanoparticle Synthesis Using Response Surface Methodology, *Procedia Engineering*,148, 992-999.

Debnath, S., Parashar, K., & Pillay, K. (2017). Ultrasound assisted adsorptive removal of hazardous dye Safranin O from aqueous solution using crosslinked Graphene Oxide-Chitosan (GO-CH) composite and optimization by Response Surface Methodology (RSM) approach. *Carbohydrate Polymers*, 1(2), 601–628.

Draper, N.R. and H. Smith, Applied regression analysis 2014: John Wiley & Sons

Geetha G. V., Sivakumar R., Sanjeeviraja C. and Ganesh V. (2021). Photocatalytic degradation of methylene blue dye using $ZnWO_4$ catalyst prepared by a simple co- precipitation technique. *Journal of Sol-Gel Science and Technology*, 97(3), 572 – 580.

He G., Fan H., Ma L., Wang K., Ding D., Lui C. and Wang Z. (2016). Synthesis, characterization and optical properties of nanostructured $ZnWO_4$. *Materials Science in Semiconductor Processing*, 41, 404-410.

Jafari, M., Rahimi, M. R., Ghaedi, M., Javadian, H., & Asfaram, A. (2017). Fixed-bed column performances of Azure-II and Auramine-O adsorption by pinus eldarica stalks

activated carbon and its composite with zno nanoparticles: optimization by response surface methodology based on central composite design. *Journal of Colloid And Interface Science*, *6*(8), 308–385.

Jaramillo-Paez C., Navıo J. A., Puga F. and Hidalgo M. C. (2021). Sol-Gel synthesis of $ZnWO_4$-(ZnO) composite materials. Characterization and photocatalytic properties, *Journal of Photochemistry and Amp; Photobiology, A: Chemistry,* 404, 112962

Juan C. and Anabel E. L. (2019). A green road map for heterogeneous photocatalysis. *Journal of pure and applied chemistry, 92(1), 63-73.*

Kassahun S. K., Kiflie Z., Shin D. W., Park S. S., Jung W. Y. and Chung Y. R. (2017). Optimization of sol-gel synthesis parameters in the preparation of N-doped TiO_2 using surface response methodology. *Journal of Sol-gel Science and Technology, 82(2), 322- 334.*

Khan M. F., Ansari A. H., Hameedullah M., Ahmad E., Hussain F. M., Zia Q., Baig U., Zaheer M. R., Alam M. M., Khan A. M., AlOthman Z. A., Ahmad I., Ashraf G. M., Aliev G. (2016). Sol-gel synthesis of thorn-like ZnO nanoparticles endorsing mechanical stirring effect and their antimicrobial activities: Potential role as nano-antibiotics. *Scientific Reports, 6, 27689.*

Liu H., Zhao X., Shen H. Hao S. and Jian X. (2020). Enhanced photoluminescence and photocatalytic performance of a TiO_2–$ZnWO_4$ nanocomposite induced by oxygen vacancies. ***CrystEngComm***, **23(6),** 1336-1344

Marrakchi, F., Bouaziz, M., & Hameed, B. H. (2017). Activated carbon–clay composite as an effective adsorbent from the spent bleaching sorbent of olive pomace oil: Process optimization and adsorption of acid blue 29 and methylene blue. *Chemical Engineering Research and Design*, 32(16), 1–34.

Ma D., Yang L., Sheng Z. and Chen Y. (2021). Photocatalytic degradation mechanism of benzene over $ZnWO_4$: Revealing the synergistic effects of Na- doping and oxygen vacancies. *Chemical Engineering Journal, 405, 126538.*

Oladipo, A. A., & Gazi, M. (2014). Nickel removal from aqueous solutions by alginate-based composite beads: central composite design and artificial neural network modeling. *Journal of Water Process Engineering*, 72(15), 1–11.

Paliki A. K., Suresh P. and Sailja V. B. (2016). Rapid visible light photocatalytic degradation of organic pollutants using ZnWO4 nanoparticles. *International Journal of Engineering Applied Sciences and Technology*, 1(8), 183-183.

Rahmani M. and Sedaghat T, (2018). A facile synthesis of $ZnWO_4$ nanoparticles with enhanced band gap and study of its photocatalytic activity for degradation of methylene blue. *Journal of Inorganic and Organometallic Polymers and Materials*. 29, 220-228.

Rahmani M. and Sedaghat T. (2019). Nitrogen-doped $ZnWO_4$ nanophotocatalyst: synthesis, characterization and photodegradation of methylene blue under visible light. *Research on Chemical Intermediates, 45, 5111-5124.*

Rahnamaeiyan S., Nasiri M., Alborzi A., Tabatabaei M. S. (2015). Sonochemical synthesis and characterization of zinc tungstate nanoparticles and investigation of its photocatalyst application. *Journal of Materials Science: Materials in Electroncs*, 27(2).

Roosta M., Ghaedi, M., Daneshfar, A., Darafarin, S., Sahraei, R. and Purkait, M. K. (2014). Simultaneous ultrasound-assisted removal of sunset yellow and erythrosine by ZnS : Ni nanoparticles loaded on activated carbon : Optimization by central composite design. *Ultrasonics - Sonochemistry*, 21(4), 1441–1450.

Roosta M., Ghaedi, M., Sahraei, R. and Purkait, M. K. (2015). Ultrasonic assisted removal of sunset yellow from aqueous solution by zinc hydroxide nanoparticle loaded activated carbon : Optimized experimental design. *Materials Science & Engineering C*, 5(2), 82–89.

Sahu J. N. (2013). Preparation of granular activated carbon from oil palm shell by microwave-induced chemical activation: Optimisation using surface response methodology. *Chemical Engineering Research and Design*, 27(5), 1–10.

Saleh, T. A., Sari, A. and Tuzen, M. (2017). Optimization of parameters with experimental design for the adsorption of mercury using polyethylenimine modified-activated carbon. *Journal of Environmental and Chemical Engineering*, 7(9), 1–39.

Sharifpour, E., Khafri, H. Z., Ghaedi, M., Asfaram, A. and Jannesar, R. (2017). Isotherms and kinetic study of ultrasound-assisted adsorption of Malachite green carbon : experimental design optimization. *Ultrasonics - Sonochemistry*, 21(19), 1–28.

Tee S. Y., Win K. Y., Teo W. S., Koh L., Liu S., Teng C. P. and Han M. (2017). Recent progress in energy-driven water splitting. *Advanced science*, 4(5), 16000337

Trots D. M., Senyshyn A., VaslechkoL., Niewa R., Vad T., Mikhailik V. B. and Kraus H. (2009). Crystal structure of $ZnWO_4$ scintillator material in the range of 3-1423 K. *Journal of physics: Condensed Materials*, 21(32), 325402.

Vargas, A. M. M., Garcia, C. A., Reis, E. M., Lenzi, E., Costa, W. F. and Almeida, V. C. (2010). NaOH-activated carbon from flamboyant (Delonix regia) pods : Optimization of preparation conditions using central composite rotatable design. *Chemical Engineering Journal*, 162(1), 43–50.

Yadav R. S., Dhoble S. J. and Rai S. B. (2018). Enhanced photoluminescence in Tm^{3+}, Yb^{3+}, Mg^{2+} tri-doped $ZnWO_4$ phosphor: three photon upconversion, laser induced optical heating and temperature sensing. *Sensors and Actuators B: Chemical*, 273, 1425-1434.

Yan J., Shen Y., Li F. and Li T. (2013). Synthesis and Photocatalytic Properties of $ZnWO_4$ Nanocrystals via a Fast Microwave-Assisted Method. *The scientific World Journal*, 458106.

Yesuraj J. and Suthanthiraraj S. A. (2019). Bio-molecule templated hydrothermal synthesis of $ZnWO_4$ nanomaterial for high-performance supercapacitor electrode application. *Journal of Molecular Structure, 1181, 131–141.*

High Performance Liquid Chromatography-Diode Array Detection (HPLC-DAD) Profiling and *in vivo* Antimalarial Activity of Phenolic Compounds of *Combretum Glutinosum* Perr. Ex. stem bark

*Ngamwa Dumtapwa Philip and Labake Ajoke Fadipe
Department of Chemistry, Federal University of Technology, Minna, Niger State, Nigeria.
*Corresponding Author Email: dumty2016@gmail.com

ABSTRACT

Combretum glutinosum is used by traditional healers for the management of malaria. This study investigates the phenolic contents of the acetone stem bark extract as well as its antimalarial potential. The acetone stem bark extract of the plant was subjected to phytochemical screening using standard procedures. Total Phenol (TPC) and total Flavonoid content (TFC) was carried out using Folin-ciocalteus and $AlCl_3$ colorimetric method respectively. Diode array detector was used for high-performance liquid chromatography analysis (HPLC-DAD). Acute toxicity and antimalarial potential of the crude acetone extract were also evaluated. The phytochemical screening detects the presence of some selected phenolic compounds (Phenols, flavonoids, coumarins, quinones, tannins and phlobatannins). The total phenol content expressed as gallic acid equivalent (GAE) was 22.95 ±0.17 mg/g and total flavonoid content of the sample expressed as quercetin equivalent was 230.81±0.89 mg/g. The HPLC analysis revealed the presence of Phenolic acids (gallic acid, chlorogenic acid, caffeic acid), flavonoid glycoside (rutin) and flavonol (catechin) where gallic acid > rutin > chlorogenic acid, caffeic acid and catechin. The crude acetone stem bark extract revealed no sign of toxicity or mortality in mice up to 2000 mg/kg body weight (bw). In-vivo antimalarial activity of the plant extract against P. berghei using Peter 4-day suppressive test revealed that at 600 mg/kg body weight (bw), the plant extract suppressed the level of parasitemia, prolonged the mean survival time significantly ($p < 0.05$) and protected infected mice against reduction in packed cell volume, rectal temperature and body weights; all in comparison with Arthemeter at 6 mg/kg/day. This connotes that Combretum glutinosum is a potential source of phenolic compounds working either singly or in combination with other compounds which may serve as lead molecules in the development of new and effective antimalarial drugs.

Keywords: Antimalarial activity, *Combretum glutinosum,* high-performance liquid chromatography, total phenolic content and total flavonoid content.

Introduction

Plants have attracted the attention of humans since the advent of man on earth and have also found many uses in human health care. Many traditional systems have evolved in the world, which use plants to cater for the needs of humans (Oyelakin *et al*., 2020). In the traditional system of medicine, drugs are prescribed either as single plant products or a mixture of several plants depending on the disease diagnosed for treatment, and are mainly administered orally (Efthymia *et al.*, 2019). The use of plants in addressing medical challenges have been witnessed since ancient times and is regaining shape in the modern era due to their safety, effectiveness, cultural preferences, inexpensiveness, abundance, and availability (Omara *et al.*, 2020; Keita *et al.*, 2020).

Combretum glutinosum locally known as; Taramniya or Dangeera (Hausa); Ogan (Yoruba); Akwukwo Oso (Igbo); Combretum or Bush willow (English) (Onyeachusim *et al.*, 2012; Oke *et al.*, 2013;

Muhammad *et al.,* 2019). It is found in the Sahel belt parts of Senegal, Burkina Faso, Ghana, Mali, Gambia, Niger, Nigeria and in Cameroon. The plant is a bushy shrub or small tree growing up to 12 m and a deciduous species sprouting in the middle of the dry season. The trunk is usually twisted and low branched with a rounded, open crown. The lower branches typically point downwards. The bark is grey-black and may be smooth or rough with fissures on the upper surface and red to orange slash. The leaves are opposite, verticillate in threes or sometimes sub opposite, variable in shape and size, even on the same tree. *Combretum* is a very large genus, comprising about 250 species and distributed worldwide in the tropics and subtropics (*Alowanou et al.,* 2020).

Many species of *Combretum* (Combretaceae) have been used in traditional medicine for the treatment of malaria (Wimaluk *et al.,* 2015). The leaves of *C. glutinosum* is traditionally used for the treatment of malaria and other ailments (Harouna *et al.,* 2012). The root extract of the plant is reportedly rich in total phenolic compounds (Mohammed *et al* 2019). Phenolic compounds represent phytochemicals linked to antioxidant properties of plant, they have been proven to exhibit preventive and therapeutic effects against diseases (Adamu *et al*., 2016). The antiplasmodial activities of many phenolic compounds have been described in literatures. Some metabolites in this compound exert antiplasmodial effects either by elevating red blood cell oxidation or by inhibiting the parasite protein synthesis. The presence of similar phytochemicals in other plants with established antiplasmodial activity corroborates the antimalarial potential of the plant (Builders *et al.,* 2011; Builders, 2014; Builders, 2017). Therefore, the need to investigate the stem bark of the plant for its phenolic contents as well as antimalarial potentials.

Materials and Methods

Collection and preparation of plant material

Combretum glutinosum stem bark was collected within the premises of Federal University of Technology Minna, Gidan Kwano campus, Bosso, Niger state in March, 2021. The plant was authenticated by the herbarium at A.B.U Samaru, Zaria, Kaduna State (Voucher number: ABU0900120). The stem bark was air-dried and pulverized to powder.

Extraction

Exhaustive extraction of the plant sample was adopted by Nour *et al.,* (2020) with a little modification. The pulverized plant sample (400 g) was cold macerated with 70% acetone at ambient temperature of 32^0C for a week. The resulting solution was filtered with Whatmann filter paper and concentrated in vacuo and finally dried over a H_2O bath at 40^0C to yield an extract labelled as crude acetone extract of *Combretum glutinosum* (Coded Ca).

Phytochemical Screening

Phytochemical content of crude acetone extract of *Combretum glutinosum* (Ca) was evaluated using standard methods as described by Evans, (2009) and Junaid and Patil, (2020). The plant extract was screened for the presence/absence of phenolic compounds such as; phenols, flavonoids, tannins, phlobatannins, quinones and coumarins

Determination of Total Phenolic (TPC) and Total Flavonoid (TFC) Contents

Determination of total phenol content (TPC)

Total phenol content of the acetone crude extract of *C. glutinosum* (Ca) was determined using Singleton *et al*., (1999). The reaction mixture was prepared by mixing 0.5 g of the plant extract with 2.5 cm^3 of 10% Folin-Ciocalteu's reagent and 2.0 $Cm^3$of 7.5% Na_2CO_3. Blank solution containing; 0.5 cm^3 ethanol, 2.5 cm^3 of 10% Folin Ciocalteu's reagent and 2.0 cm^3 of 7.5% of Na_2CO_3 was also prepared. Samples were allowed to stand for 30 mins. The absorbance was measured using spectrophotometer at

765 nm. The same procedure was repeated for the standard solution of gallic acid. The phenolic content of the extract was determined from the calibration curve and expressed in terms of gallic acid equivalent (GAE mg/g of extract).

Determination of total flavonoid content (TFC)

The total flavonoid content was determined using $AlCl_3$ colorimetric method (Woisky and Salatino, 1998). 4 cm^3 of H_2O was added to 1g of the acetone crude extract of *C. glutinosum* (Ca) in a 10 cm^3 volumetric flask and was allowed to stand for 30 mins. 0.3 cm^3 of 5% sodium nitrite and 10% Aluminium chloride was added after 5 mins. The same procedure was repeated for the standard solution of quercetin. The absorbance was measured using spectrophotometer at 765 nm. The flavonoid content of the extract was determined from the calibration curve and expressed in terms of quercetin equivalent (QE mg/g of extract).

High Performance Liquid Chromatography Analysis

Chromatographic analysis was carried out with the aid of Shimadzu HPLC system comprising Ultra-Fast LC-20AB prominence equipped with SIL- 20AC autosampler; DGU-20A3 degasser; SPDM20A UV-diode array detector (UV-DAD); column oven CTO-20AC, system controller CBM-20Alite and Windows LC solution software (Shimadzu Corporation, Kyoto Japan); column, VP-ODS 5µm and dimensions (150 × 4.6 mm). Method reported by Okhale *et al.* (2017) was used with a little modification. The chromatographic conditions included mobile phase solvent A: HPLC grade water with 0.2% v/v formic acid and solvent B: HPLC grade acetonitrile; mode: isocratic; the flow rate is 0.6 cm^3/min; and injection volume of 1.0 µL of 10 mg/ cm^3 solution of acetone extract of the stem bark of *C. glutinosum* (Ca); detection was at UV 254 nm wavelength. Reference standards catechin hydrate, gallic acid, chlorogenic acid, rutin, quercetin, ferulic acid, caffeic acid, and luteolin were analyzed separately under the same conditions as the extract. The HPLC operating conditions were programmed to give the following: solvent B: 20% at a flow rate of 0.6 cm^3/min; and column oven temperature of 40°C. The total run time was 25 mins.

***In vivo* antimalarial studies**

Experimental animals

The LD_{50} of crude acetone extract of *C. glutinosum* (Ca) was determined using the modified limit dose test on six (6) mice of both sexes. The animals were maintained under a standard condition and fasted overnight prior to the experiment. Each mouse was given a single dose of 2000 mg/kg bw once and observed for 14 days for signs of toxicity. The behavioural changes and other changes observed in animals were recorded according to Organization for Economic Co-operation and Development (OECD) 423 guideline (OECD, 2004).

Parasite strain and inoculation

Plasmodium berghei (ANKA strain) was obtained from NIPRD. The parasites were maintained by serial passage of blood from infected mice (donor mice) to the non infected ones. Blood sample, which was taken from donor mouse with the growing parasitemia of 20-30%, was diluted using 0.9% normal saline to prepare an approximate of $5x10^7$ infected erythrocytes per milliliter of blood suspension. Each 0.2 cm^3 of blood suspension contains approximately 10^7 infected erythrocytes, which were the standard inoculums used to infect each experimental animal intraperitoneally (ip).

Four-day suppressive test

The *in-vivo* antimalarial activity of the Stem bark extract was evaluated using 4-days suppressive test on *Plasmodium berghei* infected swiss albino mice with a little modification (Peter *et al.,* 1975). 24 male and female mice of 6-8 weeks age weighing 11-34 g were infected with 0.2 cm^3 blood suspension

(about $1x10^7$ parasitized RBC) intraperitoneally and randomly divided into six groups of four mice per group with three experimental groups and three control groups (Normal control, negative control and positive control respectively) for each test sample. The extract was prepared at three different doses of 200, 400 and 600 mg/kg body weight of mice and artemisinin at 6 mg/kg bw. The extract or the standard (6 mg/kg bw) was administered as a single dose orally using oral gavage. Treatment started 3h after infection on day 0 and was then continued daily for four days (i.e. from day 0 to day 4).

On the fifth day (D4), thin smears of blood films were obtained from the tail of each mouse and smeared on microscope from the first infected mice first and then in order of their infection time. Then, the smears were fixed with absolute methanol and stained with Giemsa solution for 15 min. When dried, the film was microscopically viewed by adding a drop of immersion oil and viewing it under x100 magnification of the microscope. The parasitemia density was examined by counting the parasitized red blood cell. The chemo suppression effect of each extract was tested using the above-mentioned method (4-day suppressive test method) which was applied to test the antimalarial activity of the extract. Parasitemia level was determined by counting the number of parasitized erythrocytes out of three random fields of the microscope from each slide. Average percentage parasitemia and suppression were calculated using the following formula (Geremedhin *et al.*, 2014).

Percentage parasitemia

$$\% \text{ Parasitemia} = \frac{Number\ of\ parasitized\ RBC}{Total\ number\ of\ RBC\ count} \times 100 \quad (1)$$

Percentage suppression

$$\% \text{ suppression} = \frac{parasitaemia\ in\ negative\ control - study\ group}{parasitaemia\ in\ negative\ control} \times 100 \quad (2)$$

Determination of packed cell volume (PCV)

The PCV was determined by drawing blood from the tail of each infected mouse on day 0 and day 4 by into microhematocrit capillary tubes, sealing them with sealant, and centrifuging them at 12,000 rpm for 5 minutes. The PCV was then read using microhematocrit reader according to the formula below.

$$PCV = \frac{Volume\ of\ total\ redblood\ cells\ in\ a\ given\ volume\ of\ blood}{Total\ volume\ of\ blood} \times 100 \quad (3)$$

Changes in rectal temperature and body weights

The temperature of each infected mouse from each treatment group was determined before infection on day 0 and after treatment on day 4 using a rectal thermometer. Body weights were also determined pre and post infection using a sensitive digital weighing balance.

Determination of mean survival time (MST)

During the 4-day suppressive test against *Plasmodium berghei* infected mice, total number of mice that survived for each treatment group were monitored for a period of 14 days. The MST for each group was calculated using equation 4 below.

$$MST = \frac{Total\ number\ of\ days\ mice\ in\ a\ group\ survived}{Total\ number\ of\ mice\ in\ a\ group} \quad (4)$$

Statistical analysis

Data obtained will be analyzed using Statistical Package for the Social Sciences (SPSS) version 23 software. Results obtained will be expressed as mean ± standard error of mean (SEM). The difference in means was analysed using One Way Analysis of Variance (ANOVA). Differences between means will be regarded significant at $p < 0.05$ using Anova SPSS software followed by post hoc Duncan multiple comparison test.

Results and Discussion

Phytochemical screening (Qualitative) of crude extract of *C. glutinosum* stem bark.

The crude acetone extract *C.glutinosum* (Ca) revealed the presence of some phenolic compounds as shown in Table 1

Table 1: Qualitative screening of *Combretum glutinosum* stem bark extract

Phytochemicals	Test	Observation	Inference
Phenols	$FeCl_3$	Bluish black	+++
Flavonoids	Shinodas	Pink to crimson	+++
Tannins	Braymers	Blue-green	+++
Coumarins	NaOH	Yellow	+
Quinones	Conc. HCl	Green	++
Phlobatannins	dil. HCl	Red ppt.	+

Keys: +Present ++ Moderately Present +++ highly present

Total Phenol Content (TPC) of *C.glutinosum* stem bark extract

The total phenolic content present in the crude acetone extract of *Combretum glutinosum* (Ca) is expressed as shown in Table 2.

Table 2: Total phenol content (TPC)

	A	B	C	D	E	F	Mean
Absorbance	4.06	4.07	4.07	4.07	4.00	4.07	
Concentration (mg/g)	22.94	23.04	23.04	23.02	22.61	23.06	
							22.95±0.17 22.95±0.17

Key: TPC value is presented as Mean ± SEM of six replicate determinations (A-F). Using SPSS software.

Total Flavonoid Content of stem bark extract of *C.glutinosum*

The total flavonoid content present in the crude acetone extract of *Combretum glutinosum* (Ca) is expressed as shown in Table 3.

Table 3: Total flavonoid content (TFC) of *C.glutinosum*

	A	B	C	D	E	F	Mean
Absorbance	1.39	1.39	1.38	1.37	1.38	1.37	

Concentration (mg/g)	232.03	231.47	230.5	229.58	231.13	230.17	230.81±0.90

Key: TFC value is presented as Mean ± SEM of six replicate determinations (A-F). Using SPSS software Version.

Phenolic compounds in stem bark extract of *C.glutinosum* detected by HPLC-DAD

HPLC-DAD analysis of the extract revealed 9 peaks at 254 nm. Peaks 2, 3 and 4 showed spectra typical of phenolic acids, peak 6 showed the spectra of a flavonol while peak 8 a flavonoid glycoside. Peak 2, peak 3, peak 4, peak 6 and peak 8 were identified as gallic acid, chlorogenic acid, caffeic acid, rutin and catechin respectively, among the 9 peaks. Other compounds like 1, 5 and 9 were not recognized despite being discovered due to lack of standards.

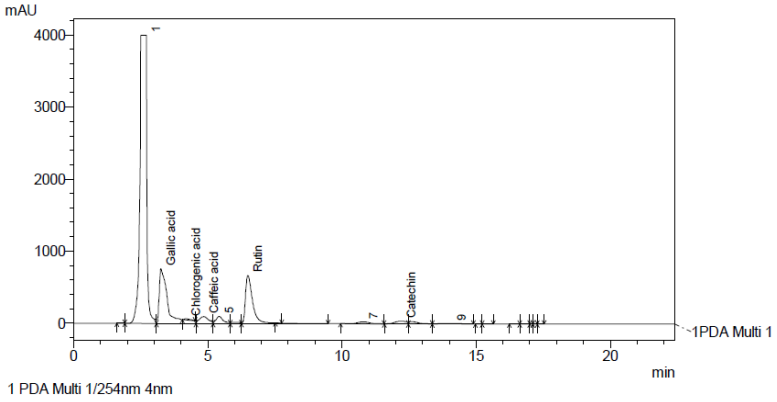

Figure 3: HPLC-DAD Chromatogram of acetone stem bark extract of *C. glutinosum* (Ca).

***In-vivo* studies**

Acute oral toxicity

In-vivo acute toxicity investigations of the crude acetone extract of *C.glutinosum* (Ca) revealed no sign of toxicity such as, rigidity, vomiting, diarrhea, depression or hair erection of mice. There was no mortality even up to the end of the 14 days observation period therefore, suggesting an LD_{50} greater than 2000 mg/kg.

Effect of extract on parasitemia and mean survival time of mice infected with *P. berghei*

The activity of the extract at 200, 400 and 600 mg/kg bw was significantly lower ($p < 0.05$) than artemether (29.50 ± 0.12%) as shown in Table 4. Extracts are considered active when % parasitemia reduction is ≥ 30%.

Table 4: Effect of extract on parasitemia and mean survival of mice infected with *P. berghei*

Doses (mg/kg b.w)	Parasitemia (at day 5)	Chemo-Suppression (%)	MST
200	56.78 ± 1.28^{d}	43.54	12 ± 1
400	48.00 ± 0.33^{c}	52.27	14 ± 0.92
600	25.34 ± 1.89^{b}	74.80	N.D
Artemether (6 mg/kg)	4.55 ± 0.78^{a}	95.48	N.D
Untreated group	100.56 ± 4.79^{e}	-	6.33 ± 1.86

Values are presented as mean ± standard error of mean (SEM). Values with different superscripts in a roll are significantly different at $p \leq 0.05$ using Anova SPSS software followed by post hoc Duncan multiple comparison test.
Key
N.D: No death detected during the observation period
MST: Mean Survival Time

Effect of extract on rectal temperature of mice infected with *P. berghei*
The results displayed no significant difference ($P > 0.05$) on rectal temperature between the treatment groups of 200, 400 and 600 mg/kg bw the positive control (arthemeter 6 mg/kg bw), the untreated group and the normal control (normal saline). This indicates the fact that rectal temperature was not affected by dose administration

Table 5: Effect of extract on rectal temperature of mice infected with *P. berghei*

Doses (mg/kg bw)	Temp. (º C)		
	Day 0	Day 4	% change in temperature (^{0}C)
200	36.57 ± 0.07^a	36.07 ± 0.62^a	-0.5 ± 0.55
400	36.87 ± 0.42^a	35.20 ± 0.12^a	-1.23 ± 0.79
600	36.95 ± 0.03^a	36.70 ± 0.12^a	0.00 ± 0.40
Artemether (6 mg/kg)	36.73 ± 0.47	36.60 ± 0.36^a	0.19 ± 0.26
Untreated group	36.77 ± 0.22^a	35.73 ± 0.73^a	0.07 ± 0.28
Normal control	36.27 ± 0.13^a	36.57 ± 0.19^a	0.30 ± 0.058

Values are presented as mean ± standard error of mean (SEM). Values with different superscripts in a roll are significantly different at $p \leq 0.05$ using Anova SPSS software followed by post hoc Duncan multiple comparison test.

Effect of extract on body weight of mice infected with *P. berghei*
The results showed an increase in body weight at 400 mg/kg bw (5.0 ± 7.42) and no significant ($P > 0.05$) difference in body weight for other dose administrations.

Table 6: Effect of extract on body weight of mice infected with *P. berghei*

Doses (mg/kg bw)	Body weight (g)		
	Day 0	Day 4	% change in weight
200	19.61 ± 2.62^a	19.10 ± 2.92^a	-0.50 ± 0.37
400	18.76 ± 5.95^a	26.21 ± 0.02^b	5.0 ± 7.42
600	29.56 ± 0.09^a	26.68 ± 0.26^a	-2.88 ± 0.60
Aremether (6 mg/kg)	23.21 ± 5.52^a	21.66 ± 5.03^a	0.64 ± 0.63
Untreated group	20.09 ± 2.18^a	20.73 ± 2.79^a	-1.55 ± 1.11
Normal control	21.65 ± 2.99^a	23.96 ± 2.88^{ab}	2.28 ± 0.17

Values are presented as mean ± standard error of mean (SEM). Values with different superscripts in a roll are significantly different at $p \leq 0.05$ using Anova SPSS software followed by post hoc Duncan multiple comparison test.

Effect of extract on PCV of mice infected with *P. berghei*

No significant difference ($p < 0.05$) was observed in the result indicating that PCV was not affected by dose administration.

Table 7: Effect of extract on PCV of mice infected with *P. berghei*

Doses (mg/kg)	PCV (%)		
	Day 0	Day 4	% change in PCV
200	38.67 ± 1.45[a]	33.33 ± 1.20[a]	-5.33 ± 0.33
400	40.00 ± 1.15[a]	32.00 ± 1.15[a]	-7.00 ± 1.00
600	38.00 ± 1.15[a]	33.0 ± 0.58[a]	-5.00 ± 0.41
Artemether (6 mg/kg)	38.00 ± 1.53[a]	36.00 ± 1.73[a]	-4.67 ± 1.20
Untreated group	41.00 ± 1.15[a]	30.33 ± 2.00[a]	-2.00 ± 0.58
Normal control	39.00 ± 1.73[a]	39.67 ± 0.88[b]	-0.67 ± 0.88

Values are presented as mean ± standard error of mean (SEM). Values with different superscripts in a roll are significantly different at $p \leq 0.05$ using Anova SPSS software followed by post hoc Duncan multiple comparison test.

Discussion

The phytochemical content of stem bark extract of *C. glutinosum* revealed in this work corroborates with similar findings reported in literatures, and it has been suggested that medicinal properties of plants are dependent on secondary metabolites such as phenolic compounds (Amako and Amupitan, 2008; Saganuwan *et al.,* 2017; Sene *et al.,* 2020).

The total flavonoid content discovered to be relatively higher than the total phenolic content is likely due to the standards used in estimating the values of TPC and TFC, a similar result was reported by Qneibi *et al.,* (2020). Literatures have reported that flavonoids from medicinal plants possess anti-*plasmodial* effectiveness in both sensitive and resistant strains of *plasmodium*. It is also attributed that flavonoids exert antimalarial action by targeting certain functional biomolecules that are essential to parasite survival (Rudrapal *et al.*,2017). Therefore, the rich flavonoid content of the extract working either singly or in combination with other phenolic compounds may have served to enrich the antimalarial potentials of the plant stem bark extract making it possess lead molecules in the development of new and effective drugs.

The presence of the phenolic acids (gallic acid, chlorogenic acid, caffeic acid), flavonol (catechin) and flavonoid glycoside (rutin) in the extract was revealed using HPLC-DAD. Phenolic acids like caffeic acid, gallic acid and chlorogenic acid in plants have been shown by previous literatures to have appreciable level of antimalarial activity (Fordjour *et al.,* 2020; Alson *et al.,* 2018). Literatures have also reported that flavonols like catechin are potent malaria inhibitors especially those with gallate moiety at C-3 (Tasdemir *et al.,* 2006; Mamede *et al.,* 2020). From literature survey it has also been shown that rutin possesses iron chelating property and antioxidant property that can help in diminishing the oxidative stress on erythrocytes induced during *plasmodium* infection through free radical scavenging and also reported for *in-vitro* anti-*plasmodial* activity too (Lue *et al.,* 2010; Shitlani *et al.,* 2016). The presence of these compounds suggests that *C. glutinosum* is a potential source of medicine.

A four-day suppressive test was carried out to assess the antimalarial tendencies of the crude acetone stem bark extract of *Combretum glutinosum* against the malaria parasite *Plasmodium berghei*. The extract suppressed malaria in a dose-dependent manner. The extract at 600 mg/kg body weight showed the highest level of suppression of parasitemia (74.80%), followed by 400 mg/kg body weight

(52.27%) and 200 mg/kg body weight (43.54%) respectively. Though the activity of the extract appeared to be lower than that of arthemeter which showed 95.48% suppression, the mean survival time of mice in the positive control (arthemeter) and at 600 mg/kg body weight showed no death during the observation period. The mean survival time of the negative control (untreated) appeared to be lower than that of the dose administrations at 400 mg/kg body weight and 200 mg/kg body weight respectively. Owing to the fact that an extract or fractions in an *in vivo* antiplasmodial activity can be classified as moderate, good or very good if it suppressed parasites by 50% or more at dose of 100, 250, or 500 mg/kg body weight per day respectively (Zeleke *et al.*, 2017). It could be said that the extract at 600 mg/kg body weight and 400 mg/kg body weight can be considered to have adequate antimalarial potentials.

Analyzing the rectal temperature of infected mice from day 0 to day 4 revealed that the extract protected the infected mice against reduction in temperature in a non-dose dependent manner. The activity of the extracts, positive control (arthemeter), untreated group and normal control group were not significantly different ($p < 0.05$). The highest protection offered by the extract on the infected mice against reduction in temperature was at 600 mg/kg body weight dose. The ability of the extract to prevent a reduction in rectal temperature is possibly due to its antimalarial efficacy (Bahtiar *et al.*, 2017).

The result on body weight changes of infected mice from day 0 to day 4 showed that by day 4, the extract offered moderate protection against the loss of body weight in a manner that was not dose dependent. There was apparently no significant difference ($p < 0.05$) between the activities of the test doses, arthemeter administration, negative control and normal control except at 400 mg/kg body weight were there was a considerable increase in body weight which is likely due to the enlargement of body organs in the body of the mice. The highest protection against body weight reduction was observed at 200 mg/kg body weight (-0.50±0.37). The prevention in body weight loss could be as a result of antimalarial tendencies of the plant extract (Nardos and Makonnen, 2017).

In protecting the infected mice against reduction in PCV on day 4, the extract displayed a non-dose dependent activity. The extract at 200 mg/kg body weight and 600 mg/kg body weight gave higher protection in comparison to 400 mg/kg body weight dose. As for the other doses the normal control showed a higher protection in comparison to the positive control (arthemeter). There was no significant difference ($p < 0.05$) between all treatments except at the normal control which showed a slight increase in PCV. The potency of the extract to inhibit reduction in PCV could be accounted for by its destructive anti-plasmodial tendencies against parasitized erythrocytes and the sustainability of available new erythrocytes (Aleheghe *et al.*, 2020).

Body weights, rectal temperature and packed cell volume are key symptoms and parameters manifested in *Plasmodium berghei* infected mice as a result increasing parasitemia from day 0 to day 4 (Mohammed *et al*, 2014). Usually a promising anti-malarial agent is expected to protect such infected mice against reduction of these symptoms and parameters (Kifle *et al.*, 2020).

The significant activity of stem bark extracts may be attributed to the rich presence of pytochemicals acting either singly or in combination synergistically at the stated doses probably accounted for the blood schizonticidal activity of fractions and therefore, antimalarial activity of plant (Ogbeide *et al.*, 2018; Ogbeide *et al.*, 2020). The discoveries in this study are in agreement with similar anti-plasmodial investigations carried out on some other plants and relates with other *in-vitro* and *in-vivo* studies conducted in antimalarial efficacy of plant parts such as leaves and barks (Mwangi *et al.*, 2015; Sadiq *et al.*, 2017; Widyawaruyanti *et al.*, 2017; Hintsa *et al.*, 2019; Kweyamba *et al.*, 2019; Fadipe *et al.*, 2020; Tali *et al.*, 2020).

Conclusion

From the findings of this study, it can be concluded that the phenolic rich acetone extract of *Combretum glutinosum* is a relatively safe plant that possess anti-malarial potentials and can be considered for the making of an anti-malarial drug.

References

Alowanou, A. G., Houehanou, T. D., Mensah, S., Alissou, K. B., Ahoyo, C. C., Akpako, R. S., Wabi, F., Houinato, R. B. M. & Hounzangbe-Adote, S. M. (2020). Status and population structures of three anthelmintic tree species along climatic gradient in Benin and the implications for conservation. Southern Forests: *Journal of Forest Science*, 2070-2639.

Alehegn, A. A., Yesufu, J. S., & Birru, E. M. (2020). Antimalarial activity of crude extract and solvent fractions of the leaves of *Bersama abyssinica Fresen*. (Melianthaceae) against *Plasmodium berghei* infection in swiss albino mice. *Evid-Based Compl Altern Med*, 9467359.

Alson, S. G., Jansen, O., Cieckiewicz, E., Rakotoarimanana, H., Rafatro, H., Degotte, G., Francotte, P., & Frederich, M. (2018). *In vitro* and *in vivo* antimalarial activity of caffeic acid and some of its derivatives. *J Pharm Pharmacol*. doi: 10.1111/jphp.12982.

Amako, N. F. & Nnaji, J. C. (2016). GC/MS Analysis and Antimicrobial Activity of pentacyclic triterpenoids isolated from *Combretum glutinosum* Perr. Ex. Dc. stem bark. *J. Chem. Soc. Nigeria*, 41(2), 164-168.

Bahtiar, A., Vichitphan, K., & Han, J. (2017). Leguminous plants in the Indonesian archipelago: Traditional uses and secondary metabolites. *Nat Prod Commun*, 12(3), 461-472.

Builders, M. I., Wannang, N. N., Ajoku, G. A., Builders, P. F., Orishadipe, A. & Aguiyi, J. C. (2011). Evaluation of antimalarial potential of *Vernonia ambigua*. *International Journal of pharmacology*, 1811, 1-10.

Builders, M.I. (2014). In Search of a Potent Antimalarial Agent: *Antiplasmodial* assessment of three herbs with folkloric antimalarial claims. *International Journal of Biomedical and Clinical Sciences*, 3(3), 40-46.

Builders, M. I. (2017). African traditional antimalarials: A review. *The pharmaceutical and chemical journal*, 4(6), 87-98.

Efthymia, E. T., Paolo, G., Effie, H., Marco, B., Vincenzo, D. F. & Laura, C. (2019). Ethnobotanical study of medicinal plants used in central Macedonia, Greece. *Hindawi Evidence-Based Complementary and Alternative Medicine*, Volume 2019, Article ID 4513792, 22 pages. https//doi.org/10.1155/2019/4513792.

Evans WC. Trease and Evans Pharmacognosy. 16th Edn. Saunders Elsevier, 2009, 135-415.

Fadipe, L. A., Ajemba, C., Lawal, B. A., Ahmadu, A.A., & Ibikunle, G. F. (2020). Phytochemical and *In-vivo* Antimalarial Investigations of *Dichrostachys cinerea* (L.) Wight & Arn. (Fabaceae) Root Bark. *Tropical Journal Natural Product Research*, 4(11), 1007-1014. Doi.org/10.26538/tjnpr/v4i11.28.

Fordjour, P. A., Adjimani, J. P., Asare, B., Duah-Quashie, N., & Quashie, N. B. (2020). Anti-malarial activity of phenolic acids is structurally related. *Research Square*, doi:10.21203/rs.3.rs-21702/v1.

Geremedhin, G., Bisrat, D. & Asres, K. (2014). Isolation, characterization and *in-vivo* antimalarial evaluation of anthrones from the leaf latex of *aloepercrassatodaro*, Journal of Natural Remedies, 14,120–125.

Harouna, S., Hilou, A., Sombie, P. A. E. D., Compaore, M., Meda, R., Millogo, J. & Nacoulma, O. G. (2012). Phytochemistry and biological activities of extracts from two Combretaceae found in

Burkina Faso: *Anogeissus leiocarpus* (DC) Guill. and Perr. and *Combretum glutinosum* Perr. Ex DC. *Universal Journal of Environmental Research and Technology*, 2(5), 383-392.

Hintsa, G., Sibhat, G. G., & Karim, A. (2019). Evaluation of antimalarial activity of the leaf latex and TLC isolates from *Aloe megalacantha Baker* in *Plasmodium berghei* infected mice. *Evid based Complement Alternat Med*, 6459498.

Junaid, R. S. & Patil, M. K. (2020). Qualitative tests for preliminary phytochemical screening: An overview. *International Journal of Chemical Studies*, 8(2), 603-608. DOI: https://doi.org/10.22271/chemi.2020.v8.i2i.8834.

Keita, J. N., Diarra, N., Kone, D., Tounkara, H., Dembele, F., Coulibaly, M. & Traore, N. (2020). Medicinal plants used against malaria by traditional therapists in malaria endemic areas of the Segou region, Mali. *Journal of Medicinal Plants Research*, 14(9), 480-487.

Kifle, Z. D., Adinew, G. M., Megistie, M. G., Gurmu, A. E., Enyew, E. F., Goshu, B. T., & Amare, G. G. (2020). Evaluation of antimalarial activity of methanolic root extract of *Myrica salicifolia* A. Rich. (Myricaceae) against *Plasmodium berghei* infected mice. *J Evid Based Integr Med*,25: 2515690X20920539.FT6T.

Kweyamba, P. A., Zofou, D., Efange, N., Assob, J. C. N., Kitau, J., & Nyindo, M. (2019). *In-vitro* and *in-vivo* studies on anti-malarial activity of *Commiphora africana* and *Dichrostachys cinerea* used by Maasai in Arusha, Tanzania. *Malar J*, 18,119.

Lue, B. M., Nielsen, N. S., Jacobsen, C., Hellgren, L., Guo, Z., & Xu, X. (2010). Antioxidant properties of modified rutin esters by DPPH, reducing power, iron chelation and human low density lipoprotein assays. *Food Chem*,123, 221-30.

Mamede, L., Ledoux, A., Jansen, O., & Frederich, M. (2020). Natural phenolic compounds and derivatives as potential antimalarial agents. *Planta Medica*, DOI: 10.1055/a-1148-9000.

Mohammed, T., Erko, B., & Giday, M. (2014). Evaluation of antimalarial activity of leaves of *Acokanthera schimperi* and *Croton macrostachyus* against *Plasmodium berghei* in swiss albino mice. *BMC Compl Altern Med*, 14,314.

Muhammad, B. Y., Shaban, N. Z., Elrashidy, F. H. & Ghareeb, D. A. (2019). Antioxidant, anti-inflammatory, antiproliferative and antimicrobial activities of *Combretum glutinosum* and *Gardenia aqualla* Extracts in vitro. *Free Radicals and Antioxidants*, 9 (2), 66-72.

Mwangi, G. G., Wagacha, J. M., Nguta, J. M., & Mbaria, J.M. (2015). Brine shrimp cytotoxicity and antimalarial activity of plants traditionally used in treatment of malaria in Msambweni district. *Pharm Biol*, 53(4), 588-593.

Nardos, A., & Makonnen, E. (2017). *In-vivo antiplasmodial* activity and toxicological assessment of hydroethanolic crude extract of *Ajuga remota*. *Malar J*, 16(25). DOI: 10.1186/s12936-017-1677-3.

Nour, E. L., Mohamed, B., Fariborz, H. & Fabian, G. (2020). Extraction processes with several solvents on total bioactive compounds in different organs of three medicinal plants. *Molecules*, 25, 4672; doi:10.3390/molecules25204672.

Ogbeide, O. K., Dickson, V. O., Jebba, R. D., Owhiroro, D. A., Olaoluwa, M. O., Imieje, V. O., Erharuyi, O., Owolabi, B. J., Fasinu, S. P., & Falodun, A. (2018). *Antiplasmodial* and acute toxicity studies of fractions and cassane-type diterpenoids from the stem bark of *Caesalpinia pulcherrima* (L.) Sw. *Trop J Nat Prod Res*, 2(4), 179-184.

Ogbeide, O. K., Okhomina, O. K., Omeregie, I. G., Unuigbe, C. A., Ighodaro, A., Akhigbe, I. U., Iheanacho, M., Akubuiro, P. C., Solomon, A., Irabor, E. E. I., Owolabi, B. J., & Falodun, A. (2020). Antimalarial, ferric reducing antioxidant power and elemental analysis of *Caesalpinia pulcherrima* leaf extract. J Chem Soc Nig, 45(4), 704-711.

Okhale, S. E., Nnachor, A. C. & Bassey, U. E. (2017). Evaluation of HPLC-UV DAD and antiproliferative characteristics of the leaf infusion of *Ximenia americana* Linn. Micro medicine 5(2):45-52.

Omara, T., Kagoya, S., Openy, A., Omute, T., Sebulime, S., Kiplagat, M. K. & Bongomin, O. (2020). Antivenin plants used for treatment of snakebites in Uganda. Ethnobotanical reports and pharmacological evidences. *Tropical Medicine and health*. https://doi.crg/10.1186/S41182-019-01870.

Onyeachusim, H. D., Ugbogu, O. A. & Ariwaodo, J. O. (2012). Vernacular names of some Nigerian plants: Igbo version. *Forestry research institute of Nigeria, Ibadan*. 1-141.

Organization for Economic Co-Operation and Development, (2004). OECD guidelines for the testing of chemicals: Acute oral toxicity up and down procedure (UDP), 1-27.

Oyelakin, A, l., Olubode, T. P. & Olawale, B. R. (2020). Ethnobotanical survey and phytochemical analysis of selected medicinal plants used in treating digestive disorder. *Journal of Medicinal Plants Studies*, 8(2), 38-42.

Peter, W., Portus, H. & Robinson. L. (1975). The four-day suppressive *in-vivo* antimalarial test. Ann Trop Med Parasit. 1975; 69:155171.

Rudrapal, M. & Chetia, D. (2017). Plant flavonoids as potential source of future antimalarial leads. *Systematic Reviews in Pharmacy*, 8(1), 13-18.

Sadiq, M. B., Tharaphan, P., Chotivanich, K., Tarning, J., & Anal, A. K. (2017). *In vitro* antioxidant and antimalarial activities of leaves, pods and bark extracts of *Acacia nilotica* (L.) Del. *Complementary and Alternative Medicine*, 17:372. DOI 10.1186/s12906-017-1878-x.

Saganuwan, A. S. (2017). Ethnoveterinary values of Nigerian medicinal plants: An Overview. *European Journal of Medicinal Plants*, 18(4), 1-35, ISSN: 2231-0894.

Sene, M., Barboza, S. F., Sarr, A., Fall, A. D., Ndione, Y. & Yoro, G. S. Y. (2020). Healing and topical anti-inflammatory activities of the total aqueous bark extract of *Combretum glutinosum* Perr. (Combretaceae). *Journal of Medicinal Plants Research*, 14(5), 215-224.

Singleton, V. L., Orthofer, R. & Lamuela-Raventos, R. M. (1999). Analysis of total phenols and other oxidation substrates and antioxidants by means of Folin-Ciocalteus reagent. Methods in enzymology 299:152-178.

Shitlani, D., Choudhary, R., Pandey, D. P., & Bodakhe, S. H. (2016). Ameliorative antimalarial effects of the combination of rutin and swertiamarin on malarial parasites. *Asian Pacific Journal of Tropical Disease*, 1808(16)61067-8.DOI: 10.1016/S2222.

Tali, M. B. T., Mbouna, C. D. J., Tchokouaha, L. R. Y., Fokou, P. V. T., Nangap, J. M. T., Keumoe, R., Mfopa, A. N., Bakarnga-via, I., Kamkumo, R. G., Boyom, & F. F. (2020). *In vivo antiplasmodial* activity of *Terminalia mantaly* stem aark Aqueous extract in mice infected by *Plasmodium berghei. Journal of Parasitology Research*, Article ID 4580526,9 pages. DOI:10.1155/2020/4580526.

Tasdemir, D., Lack, G., Brun, R., Ruedi, P., Scapozza, L., & Perozzo, R. (2006). Inhibition of *plasmodium falciparum* fatty acid biosynthesis: Evaluation of FabG, FabZ and Fabl as drug targets for flavonoids. *Journal of Medicinal Chemistry*, 49, 3345-3353.

Widyawaruyanti, A., Astrianto, D., Ilmi, H., Tumewu, L., Setyawan, D., Widiastuti, E., Dachliyati, L., Tantular, I. S., & Hafid, A. F. (2017). Antimalarial activity and survival time of *Andrographis paniculata* fraction (AS202-01) on *Plasmodium berghei* infected mice. *Research Journal of Pharmaceutical, Biological and Chemical Sciences*, 8(15), 49-54.ISSN: 0975-8585.

Wimaluk, N., Sunee, C., Somporn, P., Surapol, N., Khesorn, N., Banyong, K. & Damrong, S. (2015). Chemical Constituents and Antibacterial Activity of Volatile oils of *Combretum Latifolium*, and *C.quadrangulare kurz* leaves.Chiang Mai University *Journal of Natural Science*, 14(3), 245-256. doi:10.12982/CMUJNS.0086.

Woisky, R. & Salatino, A. (1998). Analysis of propolis: Some parameters and procedures for chemical quality control. J. Apicol Res, 37, 99–105.

Zeleke, G., Kebebe, D., Mulisa, E., & Gashe, F. (2017). *In-vivo* antimalarial activity of the solvent fractions of fruit rind and root of *Carica papaya* Linn (Caricaeae) against *Plasmodium berghei* in mice. *J Parasitol Res*. Article ID 3121050.

Effect of *Hyptis Suaveolens* Methanol Leaf Extract on *Trypanosoma brucei brucei* Infected Mice

Fatima Mohammad Madaki, Adamu Yusuf Kabiru, Emmanuel Olofu Ogbadoyi, Abdullahi Mann and Salawu Muhammad Kazir
Corresponding Author:
Address: Department of Biochemistry, School of Life Sciences, F.U.T Minna.
E-mail:nmmadaki@gmail.com

ABSTRACT

The search for new antitrypanosomal drug lead owing to the setback associated with commonly used conventional drugs is highly recommended. In the present study, trypanostatic activity of the methanol leaf extract of H. suaveolens was investigated in mice infected with Trypanosoma brucei brucei (T.b.b or T. brucei). A total of Twenty (20) mice were selected into 5 groups (A-E) of 4 mice each. Groups A to D were intra-peritoneally inoculated with 0.2 ml of blood containing approximately 10^6 cells/ml parasite. Group A, B and C mice were treated with 300 and 400 mg/kgbw leaf extract of H. suaveolens and 3.5mg/kgbw of diminazene aceturate (Berenil®) (positive control) respectively for 9 days, while group D and E served as negative (infected not treated) control and normal (0.2 ml of normal saline) control respectively. The level of parasitaemia was monitored on a daily basis. Also, effect of the extract on haematological parameters was investigated. The result revealed a dose dependent decrease in parasite in mice treated with leaf extract of H. suaveolens compared with untreated mice. The infected untreated mice also shows significant ($P<0.05$) decrease in PCV, HB and RBC and increase the WBC when compared with the control mice. However, administration of methanol leaf extract of H. suaveolens at dose of 300 and 400mg/kgbw increase the level of PCV, HB and RBC and decrease the WBC in a dose dependent fashion when compared with infected untreated mice. It is concluded that H. suavelens inhibited T.brucei parasite and ameliorated the parasites induced anemia in mice. Therefore, could be useful for management of Africa trypanosomiasis

Keywords: *Hyptis Suaveolens*, *Trypanosoma brucei brucei*, Methanol, Africa trypanosomiasis

INTRODUCTION

Trypanosomes are microscopic, unicellular parasites that causes trypanosomiasis. They belongs to five well differentiated sub genera which include all the ten less defined species of the genus trypanosome. Human African trypanosomiasis (HAT) also known as sleeping sickness is a fatal, fly-borne neuro-inflammatory disease caused by two agents (protozoa), *T. brucei gambiense* which is responsible for chronic form of HAT in West and Central Africa, and *T. brucei rhodesiense*, the etiological factor for the acute form of the disease in East Africa (Bashir *et al*., 2015; Radwanska *et al*., 2018), *T.brucei gambiense* account for over 90% of reported case. It cause chronic condition that can remain in passive stage for weeks, months or years before symptoms begin and the disease can last about 3 years before death results. *T.brucei rhodesiense* on the other hand result in acute form of infection and mortality can result within weeks and it is more virulent and rapid developing than *T.B gambiense (*Aksoy, 2011). Animal African trypanosomiasis (AAT) results from infection from other subspecies of trypanosome e.g *T. congolense, T. vivax* e. t. c. This disease are called by different name like Nagana (cattle),

Dourine (donkey, sheep, goat), Surra (camel), all of which have negative impact on the development of agriculture in Africa by causing loss and reduction in animal production. An estimated 90% of cases occur in countries enduring conflict and political/social instability, which negatively impacts on health expenditure, infrastructure, and the ability to conduct clinical trials (Musinguzi *et al*., 2016; Baker and Welburn, 2018).

Trypanosomiasis is a fatal disease that result in reproductive deficiency in man and animal. Although the parasite reside at the internal organs of infected host they are preferably localize in gonads where they cause severe deficiency in animals reproductive organs, leading to various birth complications, still birth, irregularities in female menstrual and estrogens circle, sterility, abnormal female hormone production such as Follicle stimulating hormone (FSH), Luteinizing hormone (LH) and elevated sperm morphological abnormality (Simwango *et al.,* 2017). The fight against trypanosomiasis has relied on vector control system and chemotherapies, which are faced with several challenges due to side effect of the drugs and resistance exhibited by the parasite to the drugs (Yayeh *et al*., 2018). These dilemma call for the need for continued effort to identify new chemicals principle for the treatment of Human African Trypanosomiasis (HAT).

Most of the affected populace resides in remote rural areas and commonly use traditional medicinal plants for the treatment of the disease (Mergia, 2016). Nature has presented to humanity the gift of biological diversity of natural product for healing practices (Bashir *et al*., 2015*). Hyptis suaveolens* belongs to the family *Lamiaceae* and is a rich source of medicinally important phytochemical compounds that possess antioxidant, anti-inflammatory, antispasmodic, anti-septic, anti-cancer, anti-ulcer, antimicrobial, anti-diabetic, anti-fertility, diaphoretics, anticutaneous, anticatarrhal, antirheumatic, anti-ulcer, gastroprotective, immunomodulatory, analgesic, and antiviral activity (Mishra *et al.,* 2021). *Hyptis suaveolens* contains unique terpenoid metabolites like suaveolic acid, suaveolol, methyl suaveolate, beta-sitosterol, ursolic acid, and phenolic compound like rosamarinic acid, methyl rosamarinate that have potentiality to substitute the traditional drugs as therapeutic agent against the resistant and newly emerged bacterial and viral pathogens. Pentacyclic triterpenoid, ursolic acid have been reported to have effective antiviral response against the SARS-CoV2 responsible for the present COVID-19 pandemic and HIV virus (Mishra *et al.,* 2021). This study is aimed at determining the antitrypanosomal activity of *Hyptis Suaveolens.*

MATERIALS AND METHODS

PLANT MATERIALS

The leaves of *Hyptis Suaveolens* where collected from Bosso local Government Area of Niger State Nigeria between the months of May and June, 2015. The plant specimen was identified and confirmed by a botanist at the Department of Biological sciences, Federal University of Technology Minna, Niger State. The whole studies were carried out in the Department of Biochemistry, Federal University of Technology, Minna, Nigeria.

EXPERIMENTAL ANIMALS

Albino mice, used for screening, were purchased from the Biochemistry and chemotherapy Division of the National Veterinary Research Institute (NVRI), Vom, Plateaus State Nigeria. The animals were acclimatized in the Animal Holding Unit of Department of Biochemistry laboratory, Federal University of Technology, Minna for two weeks prior to study. All experiments involving the animals were conducted in compliance with the internationally accepted principles for laboratory animal use and

care as contained in the Canadian council on Animals care guidelines on animals use protocol review (1997) and as also described by Adam *et al.* (2010).

TEST ORGANISM

Trypanosoma brucei brucei was obtained from the Vector and Parasite Unit, National Institute for Trypanosomiasis and Onchocerciasis Research, Kaduna State, Nigeria and subsequently maintained in the laboratory of the Biochemistry Department, Federal University of Technology, Minna, Niger State Nigeria, by serial passage in mice.

METHODS

PREPARATION OF PLANT EXTRACT

Fifty grams (50 g) of grounded *Hyptis Suaveolens* leaves was used for extraction. The sample was reflux for 2hr with 300 ml methanol and filtered through a whattmann's filter paper. The filtrate was concentrated to dryness as described by Mann *et al*. (2011) and modified by Madaki *et al.* (2016) at 40 degree celsius under reduced pressure on a rotatory evaporator and stored at 4 degree celsius in refrigerator until required.

PHYTOCHEMICAL SCREENING

Hyptis Suaveolens extract was qualitatively screened using standard techniques for the detection of alkaloid, flavonoids, glycosides, anthocyanins, steroids, phlobatannins, tannins and saponins (Sofowora, 1993; Edeoga, 2005; Tiwari *et al.*, 2011).

ACUTE TOXICITY TEST

Acute toxicity of the extract was determined in 2 phases according to Lorke's (1983). In Phase I, a total of 9 mice were grouped into 3 of three (3) mice each and were given a single dose of 10, 100 and 1000 mg/kg bw of the fractions respectively. A control group was also set up comprising of 3 mice and administered 2 ml/kg bw normal saline. The absence of death after 24 hours of extract administration led to the initiation of Phase II which was set up with another 3 groups of 3 mice each and were given a single dose of 1600, 2900 and 5000 mg/kg bw respectively. All doses were administered orally using esophageal cannula. The mice were observed for any adverse effect and mortality within 24 hours of treatment and after two weeks.

INFECTION OF ANIMALS

The animals were inoculated using the method described by Ogbadoyi *et al.* (2007). Blood from a highly infected mouse was obtained by cardiac puncture and collected with EDTA-coated syringe. The blood was appropriately diluted with physiological saline to serve as inoculums. Healthy mice of weight range 25-29 g were infected intraperitoneally with 0.2ml of the inoculums containing about 1×10^{6} trypanosomes. The level of parasitaemia was monitored on a daily basis. The numbers of parasite were determined using the method described by Herbert and Lumsden (1976).

ADMINISTRATION OF EXTRACT AND MONITORING THE COURSE OF PARASITEMIA

A total of Twenty (20) mice were selected into 5 groups (A-E) of 4 mice each. Groups A to D were intra-peritoneally inoculated with 0.2 ml of blood containing approximately 10^6 cells/ml parasite. Group A, B and C mice were treated with 300 and 400 mg/kgbw leaf extract of *H. suaveolens* and

3.5mg/kgbw of diminazene aceturate (Berenil®) (positive control) respectively for 9 days, while group D and E served as negative (infected not treated) control and normal (0.2 ml of normal saline) control respectively. "Rapid Matching" method of Herbert and Lumsden (1976); as described by Kabiru *et al.* (2013) was used to estimate parasite in the blood of the infected animals. The method involves a matching technique where the microscopic field in blood approximately diluted with physiological saline. A drop of blood was obtained on a slide by pinching the tip of the pre sterilized tail with a sterile needle, immediately covered with a cover slip and wet mount observed under the microscope at x40 magnification. The logarithm, from where the absolute number of trypanosomes per ml of blood was obtained (Kabiru *et al.*, 2013).

DETERMINATION OF BODY WEIGHT

Body weights of all the animals in each group were taken before the commencement of the treatment and during treatment to observe their change in body weight.

DETERMINATION OF HEMATOLOGICAL PARAMETERS

The blood samples of the mice were collected into heparinized capillary tubes with one end of the tube plasticized to determine PCV, RBC, WBC and HB and the values expressed as percentages. Hematological analysis were carried out according to standard method as described by Shittu *et al*., (2017).

RESULTS

PERCENTAGE YIELD OF *Hyptis suaveolens*

Hyptis suaveolens extract yield was 7.12% as shown in Table: 1.

Table 1: The Percentage (%) Yield of *Hyptis suaveolens* Methanol Leaf Extract

Plants	Leaf powder(g)	Extract yield (%)
Hyptis suaveolens	50.00	7.12

PHYTOCHEMICAL ANALYSIS

The qualitative phytochemical constituents of *Hyptis suaveolens* methanol leaf extract revealed the presence of tannins, alkaloids, flavonoids, phenols, saponins and glycosides while phlobatannins and, steroids were absent.

Table 2: Qualitative Constituents of *Hyptis suaveolens* Methanol Leaf Extract

Phytochemicals	*Hyptis suaveolens*
Alkaloids	+
Flavonoids	+
Saponins	+
Steroids	-
Phenols	+
Terpenoids	+
Tannins	+
Glycosides	+

Phlobatannins	-

Note: - = not dictated, += dictated

ANTITRYPANOSOMAL STUDY

ACUTE TOXICITY RESULT

Table 3: Toxicity (acute) of Aqueous Extract of *Allium sativum* (Garlic Bulb)

Group(s)	Dose (mg/kg) bw	No of animals	Mortality
Phase 1			
1	10	3	0/3
2	100	3	0/3
3	1000	3	0/3
Phase 2			
1	1600	3	0/3
2	2900	3	0/3
3	5000	3	0/3

Key: (0/2, 0/1) means 0= number of mortality recorded, 2 & 1= number of animal used

PARASITAEMIA COUNT

The results of average parasitemia count of *T.brucei* infected mice treated with *Hyptis suaveolens* methanol leaf extract is presented in figure: 1.The result showed a progressive increase in the parasite load of infected untreated group. The average daily parasitemia of infected mice treated with methanol leaf extract of *Hyptis suavelens* was significantly ($P<0.05$) reduced when compare with the negative control over the period of the experiment. The decrease in average daily parasitemia of the extract was in dose dependent pattern. However, the average daily parasitemia of infected mice treated Berenil (standard drug) was significantly ($P<0.05$) reduced when compared with extract treated group.

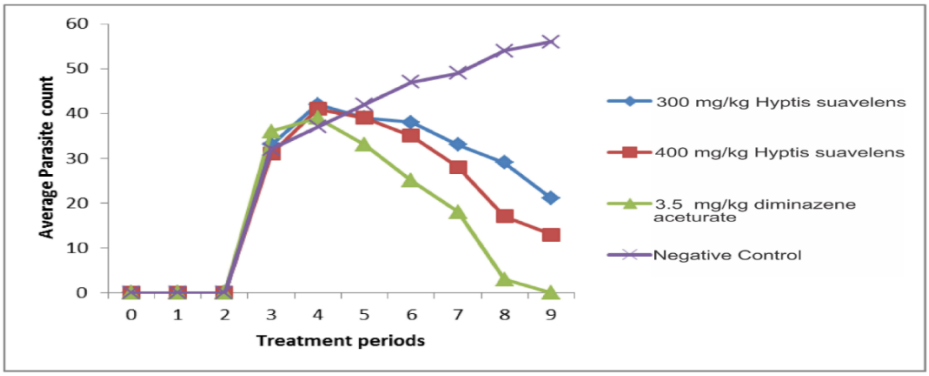

Figure 1: Average parasitemia counts of *T.brucei infected* mice treated with *Hyptis suaveolens* methanol leaf extract.

CHANGE IN BODY WEIGHT

Effect of methanol leaf extract of *Hyptis suaveolens* on body weight of *T.brucei* infected mice are shown in figure: 2. all experimental groups had decrease in body weight after 3 days of *T.brucei* infection. Although, after 9 days of treatments, the group of mice treated with 300 and 400 mg/kg of *Hyptis suaveolens* methanol leaf extract and those treated with 3.5mg/kg of diminazene aceturate (Berenil®) shows improvement in body weight compared to the untreated group which showed further decrease in body weight

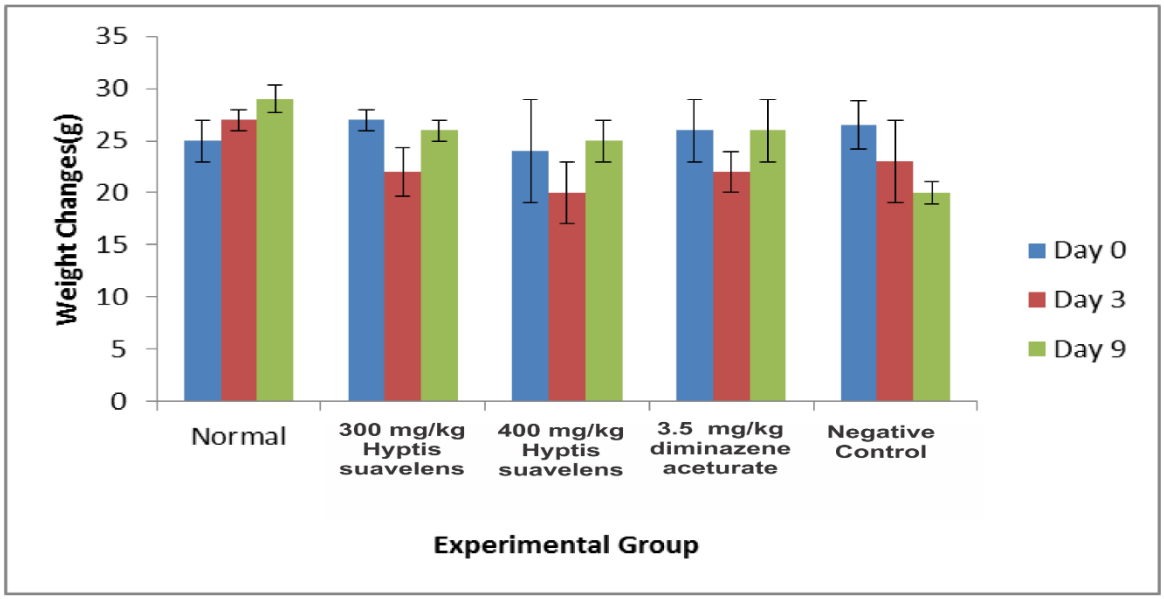

Figure 2: Effect of *Hyptis suaveolens* methanol leaf extract of on weight changes of *T.brucei* infected Mice

HEMATOLOGICAL PARAMETERS

Effect of methanol leaf extract of *H. suaveolens* on hematological parameters of *T.brucei* infected mice are shown in Table 3: *T.brucei* infected untreated mice shows a significant decrease in PCV, RBC and HB (Hb) and cause significant ($P<0.05$) increase in WBC when compared with normal mice however, treatments with methanol leaf extract of *H. suaveolens* caused a significant ($P<0.05$) increase in PCV, RBC and HB that is dose dependent but there was significant ($P<0.05$) decrease in WBC when compared to the untreated mice.

Table 3: Effect of methanol leaf extract of *Hyptis suaveolens* on hematological parameters of *T.brucei* infected Mice

	PCV (%)	RBCs ($x10^{12}$/L)	WBC ($x10^{9}$/L)	HB (g/dl)
Normal control	47.30 ± 0.97^{b}	5.52 ± 0.45^{c}	4.56 ± 0.05^{a}	15.76 ± 1.84^{b}
300mg/kg *Hyptis suavelens*	39.09 ± 0.62^{ab}	3.77 ± 0.44^{ab}	7.21 ± 0.11^{c}	13.03 ± 1.10^{b}
400mg.kg *Hyptis suavelens*	43.31 ± 1.09^{b}	4.53 ± 0.64^{b}	6.34 ± 0.28^{b}	14.43 ± 1.49^{b}

3.5mg/kg Diminazene aceturate	47.45±2.11 [b]	4.77 ± 0.19[b]	6.88±0.11[b]	15.81±1.10[b]
Negative Control	26.09±0.62 [a]	2.99 ±0.67[a]	7.33±0.45[c]	8.69±1.23[a]

DISCUSSION

Medicinal plants, for ages have been used in virtually all cultures as a source of medicine. Medicinal plant contains bioactive substances that could be used for therapeutic purposes or which are precursors for the synthesis of useful drugs (Abolaji *et al*., 2007). In the present study, several phytochemical constituents were observed and *H. suavelens* methanol leaf extract showed a significant antitrypanosomal activities which could be attributed to the presence of phytochemical compounds. According to research, natural products with trypanocidal activity belonging to a variety of phytochemical classes have been identified and have also been reported to contain alkaloids, flavonoids, phenolics and/or terpenes (Sepulveda-Boza and Cassels, 1996; Atawodi *et al*., 2003). Several alkaloids have been tested on trypanosomes *in vitro* such as in a study where isolated phytochemical compounds were tested for *in vitro* activity towards *T. b. brucei*, *T. b. rhodesiense* and *T. cruzi* together with those of the reference drugs, suramine, melarsoprol and benzonidazole (Cretton *et al*., 2015).

The acute toxicity study of *H. sauveolens* methanol extract was found to be safe at all the doses tested with no serious physiological changes and animal death recorded. An estimated LD_{50} was found to be > 5000 mg/kg bw. This result is similar to the work of Olukowade *et al*. (2021) where the minimum lethal dose (LD50) of *H. sauveolens* extracts was found to be greater than 5000 mg/kg body weight.

The antitrypanosomal activity of *H. sauveolens* demonstrated in this study could be attributed to the presence of these phytochemicals (polyphenols) in the methanol extracts. These phytochemicals may be acting singly or synergistically to bring about the trypanocidal effect observed. However, the antitrypanosomal activity demonstrated by *H. sauveolens* was lower than that of the standard drug (diaminazene aceturate) and did not completely clear the parasite from blood circulation, it only supressed parasitaemia. It has been suggested that crude plant extracts tend to have lower anti-trypanosomal effects because bioactive compounds due to the presence of impurities may require initial conversions which time lag allows for parasite proliferation (Noedl *et al*., 2003).

The negative influence of trypanosome infection on body weight of the animals has been recognized and well documented (Eghianruwa, 2012). Expectedly, the drop in PCV corresponds with the loss of body weight of infected untreated mice. The reduction in packed cell volume observed in extracts treated mice compared to diminazine aceturate treated mice could be due to acute hemolysis induced by the growing infection and increased susceptibility of red blood cell membrane to oxidative damage (Olaniyi and Ogunsami, 2001; Karori *et al*., 2008). These losses were however, significantly improved by treatment with *H. suavelens* extract particularly at high dose (400 mg/kg bw). This can best be explained by the reduced pathological effect of the parasite and enhanced physiological processes in animals during treatment with *H. suaveolens*. Also similar results obtained in other study on parasitic protozoans revealed that, methanol leaf extract *Abrus precatorius* at 25-100 mg/kg also improve weight gain of *P. berghei* infected mice (Saganuwan *et al*., 2013).

The morphological examination of cellular constituents of the blood – the red cells (erythrocytes), white cells (leucocytes), and the platelets (thrombocytes) gives the opportunity to investigate the presence of several metabolites and other constituents in the body of animals and it plays an important

role in the physiological, nutrition and pathological status of an organism (Lawal *et al*., 2015). In the present study, *T. brucei* infection caused significant decrease in PCV, RBC, HB and significant increase of WBC in experimental mice. The decreases in PCV, RBC and HB observed in *T.brucei* infected mice indicate parasite induced anemic condition which could be attributed to the destruction of the erythroblast, or, limiting their synthesis. White blood cells defend the body against infections or any foreign body. The significant increase on WBC count was recorded in *T.brucei* infected mice indicate immunological response by the animals to the parasite and this augmented the production of more WBC, to improve the health status of the animals *(Bashir et al., 2015*). However, administration of *H. suaveolens* methanol leaf extract at dose of 300 and 400mg/kg significantly ameliorated the parasite induce anemic condition by increasing the level of PCV, HB and RBC and decreasing the white blood cell count in a dose dependent fashion when compared with infected untreated mice.

CONCLUSION

In conclusion methanol extract of *Hyptis suavelens* inhibited *T.brucei* and ameliorated the parasite induced anemia in mice. Therefore, it can be suggested that *Hyptis suaveolens* could be useful agent for management of Africa sleeping sickness.

REFERENCES

Abolaji AO, Adebayo AH, and Odesanmi, OS (2007). Effects of ethanolic fruit extract of *Parinaripolyandra* (Rosaceae) on serum lipid profile and some electrolytes in pregnant rabbits. *Research Journal of Medicinal Plants* 1(4): 121-127.

Adamu, Y.K., A.S. Aderonke and E.O. Ogbadoyi, (2010). Therapeutic effects of *annona senegalensis* pers stem bark extracts in experimental African trypanosomiasis. *International Journal of Health Research*, 3(1): 45-49.

Atawodi, S. E., Bulus, T., Ibrahim, S., Ameh, D. A., Nok, A. J., Mamman, M., & Galadima, M. (2003). In vitro trypanocidal effect of methanolic extract of some Nigerian savannah plants. *African Journal of Biotechnology*, *2*(9), 317-321.

Baker, C. H., & Welburn, S. C. (2018). The Long Wait for a New Drug for Human African Trypanosomiasis. *Trends in Parasitology*, 34(10), 818-827.

Bashir L. Shittu O.K , Busari M.B, Sani S. and Aisha MI· (2015).Safety Evaluation of Giant African land Snails *(Archachatina*marginata) Haemolymph on Hematological and Biochemical Parameters of Albino Rats. *Journal of Advances in medical and Pharmaceutical Sciences*. *3(3):122-130*

Bashir, L, Shittu, O.K., Sani, S., Busari, M. B. and Adeniyi, K. A. (2015). African Natural Products with Potential Antitrypanosomal Properties: A Review. *International Journal of Biochemistry Research and Review.* 7(2): 45-79.

Cretton, S., Bréant, L., Pourrez, L., Ambuehl, C., Perozzo, R., Marcourt, L., Kaiser, M., Cuendet, M., and Christen, P. (2015)). Chemical constituents from *Waltheria indica* exert *in vitro* activity against *Trypanosoma brucei and T. cruzi*. *Fitoterapia*, 105;55–60.

Edeoga HO, Omosun G,and Uche, LC (2006). Chemical composition of *Hyptis suaveolens* and *Ocimum gratissimum* hybrids from Nigeria. *African Journal of Biotechnology*. 2006; 5(10):892-5.

Eghianruwa, K. I. (2012). The effect of supplemental antioxidants vitamin C and dimethyl sulfoxide on weight gain and survival in *T. brucei* infected and diminazene treated rats. *Veterinarski arhiv*, *82*(5), 519-529.

Herbert, W. J., & Lumsden, W. H. R. (1976). Trypanosoma brucei: a rapid "matching" method for estimating the host's parasitemia. *Experimental parasitology*, *40*(3), 427-431.

Kabiru, Y.A., Ogbadoyi, E.O., Okogun, J.I., Gbodi, T.A. and Makun, H.A. (2013). Anti-trypanosomal Potential of *Eucalyptus camaldulensis*. *British Journal of Pharmacology and Toxicology* 4(2): 25-32.

Lawal, B., Shittu, O.K., Abubakar, A. N. Haruna, GM. Sani S., Ossai, PC. (2015). Haematopoetic Effect of Methanol Extract of Nigerian Honey Bee (*Apis mellifera*) *Propolis* in Mice. *Journal of Coastal Life Medicine* 2015; 3(8): 648-651

Lorke, D. (1983). A new approach to practical acute toxicity testing. *Archives of toxicology*, *54*(4), 275-287.

Madaki, F. M., Kabiru, A. Y., Mann, A., Abdulkadir, A., Agadi, J. N., & Akinyode, A. O. (2016). Phytochemical Analysis and *In-vitro* Antitrypanosomal Activity of Selected Medicinal Plants in Niger State, Nigeria. *International Journal of Biochemistry Research & Review*, *11*(3).

Mann, A., Ifarajimi, O.R., Adewoye, A.T., Ukam, C., Udeme, E.E., Okorie, I.I., Sakpe, M.S.,Ibrahim, D,R., Yahaya, Y.A., Kabir A.Y,,Ogbadoyi, E.O.(2011) *In vivo* antitrypanosomal effects of some ethnomedicinal plants from Nupeland of North Central Nigeria. *African Journal of Traditional Complement Alternative Medicine*. 8(1):15-21.

Matovu, E., Mugasa, C. M., Waiswa, P., Kitibwa, A., Boobo, A. and Ndung'u, J. M. (2020). "Haemoparasitic infections in cattle from a *trypanosoma brucei* rhodesiense sleeping sickness endemic district of eastern Uganda," *Tropical medicine and infectious disease*, vol. 5, no. 1, p. 24.

Mergia, E., Shibeshi, W., Terefe, G., & Teklehaymanot, T. (2016). Antitrypanosomal activity of *Verbascum sinaiticum Benth*. (Scrophulariaceae) against *Trypanosoma congolense* isolates. *BMC complementary and alternative medicine*, *16*(1), 362.

Mishra P, Sohrab S, Mishra SK. (2021). A review on the phytochemical and pharmacological properties of *Hyptis suaveolens (L.) Poit*. *Future Journal Pharmaceutical Sciences*;7(1):65).

Musinguzi, S. P., Suganuma, K., Asada, M. (2016). "Full paper parasitology A PCR-based survey of animal African trypanosomosis and selected piroplasm parasites of cattle and goats in Zambia," *Journal of Veterinary Medicne*, vol. 78, no. 12, pp. 1819–1824.

Noedl, H., Wongsrichanalai, C.,and Wernsdorfer, W. H. (2003). Malaria drug sensitivity testing: new assays, new perspectives. *Trends in Parasitology*, 19, 175 – 181.

Olaniyi, M.O., aiwo, V.O. and Ogunsanmi, A.O. (2001). Haemaology and dynamics of erythrocyte membrane sialic acid concentration during experimental *Trypanosoma congolense* infection and *Trypanosoma brucei* infection in sheep. *Journal of Applied Animal Research*, 20: 57-64.

Olukowade, I. L., Elusiyan, C. A. N., Omisore, O. Adewoyin, F. B. and Adewunmi, C. O. (2021). A comparative study of the anti-protozoan activities of *Hyptis suaveolens* (L.) Poit and *Hyptis atrorubens* (L.) Poit. *World Scientific News*, 159: 71-80

Radwanska, M., Vereecke, N., Deleeuw, V., Pinto, J. and Magez, S. (2018). "Salivarian trypanosomosis: A review of parasites involved, their global distribution and their interaction with the innate and adaptive mammalian host immune system," *Frontiers in Immunology*, vol.9,

Saganuwan, S.A., & Onyeyili, P.A. (2016). The Paradox of Human Equivalent Dose Formula: A Canonical case study of *Abrus precatorius* aqueous leaf extract in monogastric animals. *Macedonian Veterinary Review*; 39(1):23–32.

Sepúlveda-Boza, S., & Cassels, B. K. (1996). Plant metabolites active against Trypanosoma cruzi. *Planta Medica*, *62*(02), 98-105.

Shittu, O. K., Lawal, B., Adeniyi, A. K., Kilani, L. T., & Saka, R. B. (2017). Effect of Methanol extract of Musca domestica larva on some Enzymes and Haematological parameters in Trypanosoma brucei brucei-infected rats. *Nigerian Journal of Basic and Applied Sciences*, *25*(2), 66-74.

Simwango, M., Ngonyoka, A., and Nnko H. J. (2017). "Molecular prevalence of trypanosome infections in cattle and tsetse flies in the Maasai Steppe, northern Tanzania," *Parasites & Vectors*, vol. 10, no. 1, p. 507.

Sofowora, A. (1993). Screening plants for bioactive agents. *Medicinal plants and traditional medicinal in Africa*, *2*, 134-156.

Tiwari, K. L., Jadhav, S. K., & Joshi, V. (2011). An updated review on medicinal herb genus Spilanthes. *Zhong xi yi jie he xue bao= Journal of Chinese integrative medicine*, *9*(11), 1170-1178.

Yayeh, M., Dagnachew, S. and Tilahun M. (2018). "Comparative experimental studies on *Trypanosoma* isolates in mice and response to diminazene aceturate and isometamidium chloride treatment," *Heliyon*, vol. 4, no. 2, article e00528.

EFFECTS OF ETHYL METHANE SULPHONATE ON VEGETATIVE TRAITS OF SELECTED GENOYTPES OF GROUNDNUT (*ARACHIS HYPOGAEA* L.)

Abdullahi, A., Daudu O. A. Y., Falusi, O. A., Abubakar A. and Audu, M. A. I.
Federal University of Technology, Minna-Nigeria.
Correspondence email: Ameenahabdul495@gmail.com
Mobile: 07068130094

ABSTRACT

Groundnut (Arachis hypogaea L.) is a multi-purpose legume crop widely cultivated in Sub-Saharan Africa (SSA). However, several species of groundnut suffer substantial yield losses as a result of narrow genetic base and insect-pest attack. The present study aimed to investigate the effect of EMS on morphological traits of four (4) groundnut (Arachis hypogaea L.) genotypes viz Samnut 24, Samnut 25, Samnut 26 and ICG4412. Field experiment was laid out in Complete Randomized Design (CRD) with three (3) replicates. The seeds of the four (4) groundnut accessions were treated with various concentration of EMS (0.0 %, 0.1 %, 0.2 %, 0.3 % and 0.4 %) for 6 hours, they were then removed and rinsed with distilled water to remove the trace of mutagen sticking to the seed coat. Data on vegetative parameters were collected following standard procedures. Results obtained showed that 0.1 % EMS concentration had the highest plant height (46.79 cm) at week 12 but was not significantly different from 0.3 % and 0.4 % concentrations (43.37 and 43.28 cm) respectively. The significantly least plant height at week 12 after planting was recorded at 0.2 % concentration (35.28 cm). No significant difference was observed among the varieties in terms of plant height. EMS concentration 0.1 % showed the significant highest number of leaves per plant at week 12 (297) while the least was recorded at 0.4 % concentration (177). Among the varieties, ICG 4412 had the significant highest number of leaves (289.20) at week 12 after planting and the least value was obtained in variety SAMNUT 26 (158.93). EMS concentration 0.1 % had the significant highest number of branches at maturity (13.25) while the least was recorded at 0.4 % EMS concentration (8.92). In terms of varietal performance, Samnut 26 had the significantly highest number of branches per plants (12.47), but was not significantly different from ICG 4412 (12.07). SAMNUT 25 was observed the have the significantly least number of branches per plant (9.13). The results obtained showed significant amount of variability in morphological parameters of the genotypes as a result of exposure to EMS which may essentially affect their productivity. This study revealed that EMS concentration 0.1 % Is the optimum concentration for inducing genetic variability in groundnut plant.

Keywords: Accessions, ethyl methyl sulfonate (EMS), genotypes, groundnut and mutagens.

2.0 INTRODUCTION

Groundnut (*Arachis hypogaea* L.), also known as earthnut, monkeynut and peanut is a native of South America belonging to the family Leguminosea (Fabaceae) genus *Arachis* (Tillman and Stalker, 2009). It is an annual or perennial plant that is distinguished from most other species by producing aerial flowers,fruiting below the soil level and it only domesticated species in the genus is *Arachis hypogaea* L. (Tillman and Stalker, 2009). Groundnut is grown in diverse environments throughout the world between 40 °N and 40 °S (Food and Agriculture Organization, 2013). Groundnut seeds are a rich source of oil (35–56%), protein (25–30%), carbohydrates (9.5–19.0%), minerals (P, Ca, Mg and K) and vitamins (E, K and B) (Gulluoglu *et al*., 2016). The shells are also used for fuel by some local oil factories or they are sometimes spread on the field as a soil amendment (Ahmed *et al*., 2010).

3.0 Literature Review

Suradkar (2013) studied improvement of groundnut (*Arachis hypogaea* L.) through chemical mutagen Ethyl Methane Sulfonate (EMS) conducted a study to check the chemical mutagen (EMS) sensitivity on groundnut and to find out suitable concentration of EMS (0.05%, 0.10%, 0.15% and 0.20%) on two varieties of groundnuts TAG-24 and AK159. He concluded that 0.05% concentration of EMS induces good genetic variability in both varieties.

Mayor *et al*. (2018) studied induced chemical mutagenesis in groundnut (*Arachis hypogaea* L.) they treated groundnut variety (LGN-1) with EMS at different concentrations (0.2%, 0.4%, 0.6%, 0.8% and0.1 2%) to study it effect on various morphological traits when compared with control. Significant result were observed in seed germination, plant height, number of leaves and number of branches after treating the seed with the mutagen. They concluded that, lower concentration appear to be better effective treatment for inducing variability as compared with other concentrations (0.4%, to 0.12%).It has also been found that boiled groundnuts have two and four fold increase in biochanin A, isoflavone antioxidants and genistein content, respectively (Craft *et al*., 2010).

3.0 Materials and methods

3.1 Experimental site

The study was conducted at the experimental garden of the Department of plant Biology, Federal University of Technology Minna Niger State, Nigeria. Minna is located in the north central geopolitical zone of Nigeria found within latitude 9°36′ north and longitude 6°34′ east. Minna covers a land area of 88 square kilometers with an estimated human population of 488,788 (Niger State MAAH Bulletine, 2008). Temperature ranges between 35.0 °C and 37.5 °C while relative humidity varies from 40 to 80 % (Adeboye *et al*., 2011). The area has two seasons: raining season between May to October and dry season between November and April each year. It has a low humid soil type with favourable climatic condition for planting which make it easy for groundnut crop to grow successfully and express all it traits.

3.2 Experimental material

The groundnut varieties used for the experiment were collected from the Institute for Agricultural Research (IAR), Samaru, Zaria, Kaduna State, Nigeria.

3.3 Mutagenic Treatments

Mutagenic treatment was conducted in the laboratory of the Department of plant Biology, Federal University of Technology Minna. Groundnut seeds were presoaked in distilled water for 4 hours. This allows the mutagen to diffuse more rapidly to the tissues of interest (Foster and Shu 2011). The seeds were then soaked for 4 hours at different concentrations of Ethyl Methane Sulphonate (0.0, 0.1, 0.2, 0.3, and 0.4%) (Adeeba *et al*., 2018). The treated seeds were thoroughly washed in running tap water to remove the residual effects of the mutagen if any.

3.4 Morphological Parameters

The morphological parameters were taken using the method of (Ghalmi *et al*., 2010) and (Falusi *et al*., 2012).

3.4.1 Plant height

The height of each plant were taking using meter rule from the base of the plant to the lowest leaf

3.4.2 Number of Leaves
The numbers of leave were counted manually.

3.4.3 Leaf Area
The leaf area of the groundnut plants were calculated using the formular LXW (Length x width).

3.5 Statistical Analysis
The morphological data was subjected to Analysis of Variance (ANOVA) using Statistical Package for Social Sciences (SPSS 20) version 20 to determine the level of significance among the treatment. Duncan Multiple Range Test (DMRT) was used to separate the means where there are significant differences.

4.0 Result and Discussion
4.1. Effect of EMS on Plant Height of the Groundnut Genotypes
Notable variations were observed in plant height at different concentration of ethyl methane sulphonate (EMS) across different weeks. At 2 and 4 weeks after planting, the highest plant height was recorded at 0.1% concentration (19.03±1.49 cm and 26.73±1.55 cm) respectively, but was not significantly different($p>0.05$) from plant height at 0.00% concentration (17.09±0.95 and 22.68±1.27 cm), 0.3% (17.23±1.76 cm and 22.16±1.94 cm) and 0.4% (18.20±1.69 and 24.60±1.91 cm). The significantly least plant height at week 2 and 4 were observed in 0.2% EMS concentration (12.13±1.74 and 16.86±2.26 cm respectively).

In terms of varietal performance, SAMNUT 24 had the significantly highest plant height at week 2 (19.81±0.94) cm while the least was recorded in SAMNUT 26 (13.91±1.23 cm). there is no significant difference($p>0.05$) in varietal performance of SAMNUT 25 and ICG 4412 (16.06±1.79 and 17.16±1.54) cm with that of SAMNUT 24 and SAMNUT 26 at week 2. No significant difference were observed in PH at week 4, 6, 8 10 and 12 (table 4.4.1).

Table 4.1.1: Effect of EMS on Plant Height of the Groundnut Genotypes

Parameters	PH2	PH4	PH6	PH8	PH10	PH12
0.0	17.09±0.95^{b}	22.68±1.27^{b}	28.03±1.12^{b}	31.91±1.26^{ab}	35.78±1.13^{ab}	40.16±1.34^{ab}
0.1	19.03±1.49^{b}	26.73±1.55^{b}	31.48±1.51^{b}	35.52±1.44^{b}	40.61±1.61^{b}	46.79±2.12^{c}
0.2	12.13±1.74^{a}	16.86±2.26^{a}	22.49±2.50a	27.88±2.60^{a}	31.14±2.74^{a}	35.28±2.99^{a}
0.3	17.23±1.76^{b}	22.16±1.94^{b}	27.65±2.16^{ab}	33.33±2.08^{b}	37.48±1.84^{b}	43.37±1.28^{bc}
0.4	18.20±1.69^{b}	24.60±1.91^{b}	29.57±1.54^{b}	34.20±1.34^{b}	38.30±1.01^{b}	43.28±1.05^{bc}
Varieties						
Samnut26	13.91±1.23^{a}	21.68±1.75^{a}	28.20±1.52^{a}	34.04±1.23^{a}	38.21±1.21^{a}	43.74±1.24^{a}
Samnut24	19.81±0.94^{b}	25.47±1.23^{a}	30.77±1.18^{a}	34.94±1.28^{a}	39.11±1.28^{a}	44.10±1.63^{a}
Samnut25	16.06±1.79^{ab}	21.73±2.13^{a}	26.22±2.11^{a}	30.45±2.03^{a}	34.21±2.09^{a}	38.41±2.33^{a}
ICG4412	17.16±1.54^{ab}	21.53±1.89^{a}	26.19±2.00^{a}	30.83±2.01^{a}	35.12±2.03^{a}	40.85±2.09^{a}

Means followed with same letter(s) along each column are not significantly different at 5% probability level.

PH (plant height)

4.2 Effect of EMS on Number of Leaves of the Groundnut Genotypes

For number of leaves, EMS concentration 0.1 showed the significantly highest number of leaves per plant at week 2 (20.17±1.64) but was not significantly different ($p>0.05$) from 0.3 % concentration (19.33±1.54). Statistically, concentration 0.0 % was observed to have the least number of leaves at week 2 and was significantly different from other concentrations. Although, no significant difference was observed in number of leaves per plants at week 4, concentration 0.1 % recorded the significantly highest number of leaves at week 10 and 12 (231.67±30.23 and 297.33±36.80, respectively) while the least was recorded at 0.4 % concentration (149.67±14.81 and 177.00±16.91, respectively).

In terms of varietal performance, SAMNUT 24 was observed to have the significantly highest number of leaves at week 2 (20.27±1.78) while the least was recorded in SAMNUT 25 (15.07±1.05). The significantly highest number of leaves at week 4, 6, 8, 10 and 12 were recorded in ICG 4412(56.27±2.47, 157.47±12.53, 205.07±13.72, 251.73±15.43, 289.20±17.97) respectively, while the significant least were recorded in SAMNUT 26 (26.27±0.64, 43.07±2.93, 72.27±7.08, 106.53±9.52, 158.93±16.46, respectively).

Table 4.2.1: Effect of EMS on number of leaves of the Groundnut Genotypes

Treatments	NL2	NL4	NL6	NL8	NL10	NL12
0.0	13.00±0.30^{a}	31.67±4.62^{a}	83.50±23.63^{a}	128.17±27.49^{a}	174.67±30.63^{ab}	216.08±33.11^{abc}
0.1	20.17±1.64^{c}	41.33±4.29^{a}	91.33±15.45^{a}	145.67±18.40^{a}	231.67±30.23^{b}	297.33±36.80^{c}
0.2	17.17±1.62^{bc}	36.00±3.45^{a}	86.50±15.62^{a}	121.83±16.40^{a}	167.67±21.14^{ab}	206.75±21.56^{ab}
0.3	19.33±1.54^{c}	43.17±4.65^{a}	89.50±9.21^{a}	143.33±13.01^{a}	214.33±21.40^{ab}	280.08±23.89^{bc}
0.4	14.33±0.69^{ab}	37.00±3.97^{a}	74.50±12.75^{a}	113.00±13.29^{a}	149.67±14.81^{a}	177.00±16.91^{a}
Varieties						
Samnut26	16.13±1.16^{a}	26.27±0.64^{a}	43.07±2.93^{a}	72.27±7.08^{a}	106.53±9.52^{a}	158.93±16.46^{a}
Samnut24	20.27±1.78^{b}	39.20±3.73^{b}	84.80±9.13^{b}	128.53±12.63^{b}	211.87±27.75^{bc}	262.73±35.03^{b}
Samnut25	15.07±1.05^{a}	29.60±1.24^{a}	54.93±2.37^{a}	115.73±8.10^{b}	180.27±15.15^{b}	230.93±21.61^{b}
ICG4412	15.73±0.78^{a}	56.27±2.47^{c}	157.47±12.53^{c}	205.07±13.72^{c}	251.73±15.43^{c}	289.20±17.97^{b}

Means followed with same letter(s) along each column are not significantly different at 5% probability level.
NL (number of leaves)

4.3 Effect of EMS on Leaf Area and Number of Branches at Maturity

No significant differences was observed in leaf area at week 2 across all EMS concentrations and across varieties. The significant highest leaf area was observed at 0.1 % EMS concentration at week 4, 6, 8, 10 and 12 (15.71±1.02, 17.56±0.93, 19.95±0.78, 21.76±0.83, and 24.12±0.85, respectively) while the least leaf area across the weeks was observed in SAMNUT 26.

EMS concentration at 0.1 % had the significantly highest ($p<0.05$) number of branches per plant (13.25±1.02) but was not significantly different from EMS concentration 0.3 % (13.17±1.35), concentration 0.4% was observed to have the significantly least number of branches (8.92±0.56). In terms of varietal performance, SAMNUT 26 had the significant highest number of branches per plant

(12.47±0.89) but was not significantly different from ICG 4412 (12.07±0.90) while the least was observed in SAMNUT 25 (9.13±0.87), Table (4.3.1)

Table 4.3.1: Effect of EMS on Leaf Area and Number of Branches at Maturity

Treatments	LA2	LA4	LA6	LA8	LA10	LA12	NB
0.0	5.39±0.31^{a}	10.59±0.63^{a}	13.08±0.49^{a}	15.11±0.49^{a}	17.11±0.59^{a}	19.64±0.59^{a}	10.±58±1.18^{ab}
0.1	6.14±0.39^{a}	15.71±1.02^{c}	17.56±0.93^{c}	19.95±0.78^{c}	21.76±0.83^{b}	24.12±0.85^{b}	13.25±1.02^{b}
0.2	5.05±0.59^{a}	10.92±1.12^{ab}	13.09±1.14^{a}	15.21±1.14^{a}	17.72±1.25^{a}	19.96±1.32^{a}	10.25±0.91^{ab}
0.3	6.16±0.78^{a}	13.75±0.88^{bc}	16.21±0.72^{bc}	18.69±0.64^{bc}	21.09±0.71^{b}	23.30±0.79^{b}	13.17±1.35^{b}
0.4	6.28±0.60^{a}	12.56±1.27^{ab}	14.76±1.19^{ab}	17.34±1.13^{ab}	19.67±1.08^{ab}	21.78±1.02^{ab}	8.92±0.56^{a}
Varieties							
Samnut26	6.31±0.60^{a}	9.37±0.55^{a}	12.40±0.51^{a}	15.46±0.52^{a}	17.58±0.55^{a}	19.87±0.58^{a}	12.47±0.89^{b}
Samnut24	6.05±0.51^{a}	15.68±0.75^{c}	17.55±0.78^{c}	19.60±0.77^{b}	22.07±0.83^{b}	24.68±0.84^{b}	11.27±1.17^{a}
Samnut25	5.63±0.56^{a}	13.22±1.07^{b}	14.87±1.03^{b}	16.68±1.09^{a}	18.54±1.09^{a}	20.41±1.02^{a}	9.13±0.87^{a}
ICG4412	5.23±0.25^{a}	12.57±0.86^{b}	14.94±0.86^{b}	17.29±0.86^{ab}	19.68±0.81^{a}	22.07±0.79^{a}	12.07±0.90^{b}

Means followed with same letter(s) along each column are not significantly different at 5% probability level.
LA (leaf area), NB (number of branches)

Discussion

Highly efficient mutagenesis is vital for breeding programs. The success of Ethyl methyl sulfonate (EMS) mutagenesis depend on many factors such as the treatment duration, EMS concentration and temperature. (Arisha *et al*., 2014; Gnanmurthy *et al*., 2014; Asif *et al*., 2019).

Decrease in plant height observed in some mutant line due increase in EMS concentration might be due to physiological or cell damage. High concentration of EMS have also been reported to result in damage to cell constituents, molecules (Chowdhury and Tah, 2011) and growth regulators (Salim *et al*., 2009). The present result confirm these earlier reports in groundnut (Gwnasakaran and Paradai 2015); mung bean (khan and wani 2006); soybean (pavadai *et al*., 2009).

In this study significant increase in plant height of some of the EMS concentration (0.1, 0.3 and 0.4%) over the control might be due to the effect of EMS which induces point mutation in the mutant line. This result is not in line with that of mayur *et al*. (2018), who recorded highest plant height in the control than the treatments in groundnut genotypes. This might be due to differences in EMS doses.

The differences in plant height among the varieties might be attributed to differences in genotypes. Similarly, previous studies reported that sensitivity to chemical mutagens differs with genotype (Kumar *et al*., 2015; Ali *et al*., 2010).

In addition, Olorunmaiye *et al*. (2019) reported significant correlation between plant height and number of pod per plant in EMS mutant line of groundnut genotype. Therefore, plant height is a good character for selection in breeding programs. The number of leaves per plant in response to different concentrations of EMS showed that lower concentration had more effect on the plant than higher

concentration over the control. Sharma *et al*. (2005) also reported that lower doses of mutagens were more efficient than the higher doses in urdbean. However, the ability of concentration range of 0.1-0.4% EMS to induce better growth and higher biological yield compared to the 0.00% treatment showed the concentrations were able to activate optimally the phyto-hormones and growth regulators in the plant. Number of leaves associated positively with number of pod per plant. Similar observation was made by Olorunmaiye *et al*., (2019).

The larger leaf area induced by the treatment in the present study translated to higher photosynthetic surface and ultimately better growth and higher biomass yield. Growth enhancement by application of moderate concentrations of EMS was demonstrated in *Vigna spp* (Khan *et al.*, 2004) and sodium azide in groundnut on Samnut 10 and 20 (Animasaun *et al*., 2014).

In terms of number of branches, some of the mutant lines showed higher number of branches (13) than the control (10), this might be due to the mutagenic effect of EMS on the mutant line.

5. Conclusion

The present work showed the utility of 0.1-0.4% concentrations of EMS to significantly improve growth performance and that 0.1 % is the optimum concentration for inducing genetic variability in the groundnut genotypes.

REFERNCES

Ahmed, S., Rafay, A., Singh, R.K. & Verma, U.K. (2010). Response of groundnut varieties to spacing. *Indian Journal of Agronomy*, 31(3),248-251

Ali, H., Shah, T.M., Iqbal, N., Atta, B.M. & Haq, M.A. (2010). Mutagenic induction of double-podding trait in different genotypes of chickpea and their characterization by STMS marker. *Plant Breeding*, *129*, 116–119.

Animasaun, D. A., Oyedeji, S., Azeez, M. A. & Onasanya, O. A. (2014). Alkylating efficiency of sodium azide on pod yield, nut size and nutrition composition of samnut 10 and samnut 20 varieties of groundnut (*Arachis hypogea* L.). *African Journal of Food, Agriculture, Nutrition and Development,* 14(7), 9498-9510.

Chowdhury, R. & Tah, J. (2011). Assessment of chemical mutagenic effects in mutation breeding programme for M1generation of carnation (*Dianthus caryophyllus*). *Research in Plant Biology,* 1(4), 23- 32.

Craft, B.D., Hargrove, J.L., Greenspan, P., Hartle, D.K., Amarowicz. R. & Pegg, R.B. (2010). Recent Advances in food and flavor chemistry. Food flavor and encapsulation, health benefits, analytical methods, and molecular biology of functional foods, Cambridge, UK: R. *Society of Chemistry* 283-296.

FAO (Food and Agriculture Organization). (2013). Groundnut Statistics. Rome: FAO: Food and Agriculture Organization of the United Nations.http://www.faostat.fao.org.

Gulluoglu, L., Basal, H., Onat, B., Kurt, C. & Arioglu, H. (2016). The effect of harvesting on some agronomic and quality characteristics of peanut grown in the Mediterranean region of Turkey. *Field Crops Resource* 21:224–232.

Gunasekaran, L. & Pavadai, P. (2015). Studies on induced physical and chemical mutagenesis in groundnut (*Arachis hypogia*) *International Letters of Natural Sciences*, 35, 25-35

Khan, S., Wani, M.R. & Parveen, K. (2004). Induced genetic variability for quantitative traits in *Vignaradiata. Pakistan Journal of Botany*, 36, 845-850

Khan, S. & Wani, M.R. (2006). MMS and SA induced genetic variability for quantitative traits in

mungbean. *Indian Journal of Pulses Research*, 19(1), 50–52.

Kumar, A., Kumar, V., Lal, S.K., Jolly, M. & Sachdev, A. (2015). Influence of gamma rays and ethyl methane sulphonate (EMS) on the levels of phytic acid, raffinose family oligosaccharides and antioxidants in soybean seeds of different genotypes. *Journal Plant Biochemistry Biotechnology, 24*,204–209.

Mayur, V., Jadhav., Rahul, K., Zote. & Amol, D. (2018). Studies on Induced Chemical Mutagenesis in Groundnut (*Arachis hypogaea* L.). *International Journal of Current Microbio logy and Applied Sciences* 7(10):

Olorunmaiye, K., Stephen, G., Joseph, G., Animasaun, D. A. & Oyedeji, S. ((2019). Mutagenic Com ponents and Dosage Effects of Ethyl Methanesulphonate *Ife Journal of Science,* 21, (2)

Pavadai, P., Girija, M. & Dhanavel, D. M. (2009). Effectiveness and efficiency and biochemical content of physical and chemical mutagens in soybean (Glycine max (L.) Merr.). *Journal of Phytology*, 1 (6), 444-447.

Salim, K., Fahad, A. & Firoz, A. (2009). Sodium azide a chemical mutag en for enhancement of agronomic trait of crops plants. *Journal of Science and Technology*, 4, 1-21

Sharma, S.K., Sood, R. & Pandey, D.P. (2005). Studies on mutagen sensitivity, effectiveness and efficiency in urdbean [*Vigna mungo* (L.) Hepper]. The *Indian Journal of Genetics & Plant Br eeding,* 65(1), 20–22.

Tillman, B. L. & Stalker, H. T. (2009). Peanut: In Johann Vollmann and Istvan Rajcan Handbook of Plant Breeding, *Oil Crops* 4: 287 – 316.

AN OVERVIEW ON THE ENVIRONMENTAL IMPACTS OF POLYETHYLENE GENERATION AND DISPOSAL IN AFRO-TROPICAL FRESHWATER ECO-SYSTEM

*Adama, B. S[1]., Ibrahim S. U[2]., Saba J. J[3]., Kinta M[1]., Samuel P. O[1].
[1]Applied Hydrobiology Unit, Department of Animal Biology, Federal University of Technology, P.M.B 65, Bosso, Minna, Niger State, Nigeria
[2] Department of Water resources, Aquaculture and Fisheries Technology, Federal University of Technology, P.M.B 65, Bosso, Minna, Niger State, Nigeria
[3] Niger State College Agriculture, Mokwa
Corresponding Author: Email: bsolomonadama@yahoo.com

Abstract
Plastics have become a modern way of life, with numerous consequences for both humans and the natural environment especially in developing and developed countries. The Nigeria fresh coastal water generally is contaminated with micro-plastic debris which floats on the surface. Plastic accumulation in our environment as a result of improper disposal or shipping splits, they are light weight, durable and are capable of travelling long distances. Soil landfill, soil leachate, unofficial recycling methods releasing chemical to the environment, burning of plastic coated wires, tyres to roast animal, nylon eating bacteria, oil and detergent containers all these contaminate are discharged into streams, river and ocean which enter into aquatic food chain causing hazardous long term carcinogenic effects to fishes, animal and human beings due to the release of diethylhexyl phythalate, lead, mercury, cadmium and as alternative materials for invasive species (barnacle, mollusc and algae , cetacean, turtle, birds) which obstruct the digestive system causing tissue damage by the toxic chemicals called polychlorinated biphenyl (PCBs). Thus, this micro-plastics waste poses various threats to public health and adversely affects flora and fauna as well as the environment especially when it is not appropriately collected and properly disposed. *However, flavo-bacterial contributes to release of methane gas from nylon break down contributing to greenhouse gas resulting into global warming.* It is concluded that aggressive campaign and enlightenment of the masses on the threats posed by polyethylene pollution should be carried out to prevent further negative environmental impact.

Keywords: *Polyethylene, Pollution; environmental; impact; micro-plastic*

1. Introduction

The use of plastics has become a modern way of life, which has many effects on both the human and natural environment. Due to the disposable culture that is present among both developing and developed nations, a lot of plastic products become litter, waste, and pollution. Plastics are process able materials based on polymers (Baner *et al*., 2007), and to make them into materials fit for purpose, they are generally processed with a range of chemical additives. These compounds are used in order to adjust the materials properties and make them suitable for their intended purpose. Effects of plastic pollution on land and aquatic environments are relatively easy to measure, as humans can readily access these places. Therefore, stereotypical images of litter along highways, plastic bottle caps in decomposing seabirds, plastic water bottles floating along a coast or river, or a variety of animals with their heads stuck in jugs are common and well known. In addition, plastic's effects on the fresh water ecosystems are somewhat known, especially when it comes to effects with mega fauna and with

microplastics entering the food webs in the upper part of the ocean, and in streams. However, there is so much more to planet Earth than just the land, rivers, shores, and ocean surface that can be seen fairly readily. **Anthropogenic Activities**: Anthropogenic activities refer to human impact on the environment or anthropogenic impact on the environment which includes impacts on biophysical environments, biodiversity, and other resources. The term anthropogenic designates an effect or object resulting from human activity. The term was first used in the technical sense by Russian geologist Alexey Pavlov, and was first used in English by British ecologist Arthur Tansley in reference to human influences on climax plant communities. The atmospheric scientist Paul Crutzen introduced the term "Anthropocene" in the mid-1970. The term is sometimes used in the context of pollution emissions that are produced as a result of human activities but applies broadly to all major human impacts on the environment. (Huesemann, 2011)

Plastics are present in the water environment in a wide variety of sizes, ranging from micrometers to meters (Van Cauwenberghe *et al*., 2015). plastic pollutants are classified mainly as primary and secondary micro-plastics (MPs). Primary MPs are polymers intentionally manufactured in a microscopic scale (the size range of 1 nm to < 5 mm) through the process of extrusion or grinding, to be used as raw materials for other products (e.g., plastic pellets and microbeads associated with industrial spillages and used in cosmetics, cleaning products or drug vectors) (Cole *et al*., 2011, Hidalgo-Ruz *et al*., 2012, Van Cauwenberghe *et al*., 2015, Alomar *et al*., 2016, Peters and Bratton 2016, Solomon and Palanisami 2016, Graca *et al*., 2017). The secondary MPs are formed during the degradation of macro plastics due to the mechanical, photolytic and/or chemical degradation of bigger plastic fragments in water environment and often result in fragmented pieces or fibers (Van Cauwenberghe *et al*., 2015, Alomar *et al*., 2016, Peters and Bratton 2016, Graca *et al*., 2017, Lambert *et al*., 2017). The smallest particles are defined as nano plastics, as the contaminants are of the size of nano-particles (< 100 nm).

Figure 1 (above): Microplastics, one of the most common plastic polluters in the ocean.

2. Literature Review

The physical and chemical properties of plastic pollutants, including particle size, shape, surface area, crystallinity, polymer type and chemical additives, determine their ecotoxicity (Lambert *et al*., 2017). There are 7 main classes of produced plastics: polyethylene (PE), polypropylene (PP), polyvinyl chloride (PVC), polystyrene (PS), Polyamide (PA), polyurethane (PUR) and polyethylene-terephthalate (PET) (Andrady 2011, Laglbauer *et al*., 2014, Avio *et al*., 2016, Solomon and Palanisami 2016). Polymer crystallinity (structure of polymer chains) affects the physical properties of plastic pollutants such as density and permeability. This property may change with the polymers' degradation

process and result in the formation of crystallites, which might differ in toxicity compared to the parent plastics (Lambert *et al*., 2017). The specific gravity of the plastics ranges from 0.91 (PE) to 1.5 (PA)g/cm3 (Andrady 2011, Avio *et al*., 2016, Solomon and Palanisami 2016). Therefore, the plastic pollutants depending on the type of material and particle size can sink to the bottom sediments or float on the water surface. Apart from the main monomer, plastics contain a variety of organic plastic additives added during their manufacturing (i.e., initiators, catalysts, solvents, antimicrobial agents, surfactants, plasticizers, flame retardants, lubricants, dispersant, antistatic agents, nano-particles, fillers, fragrances and pigments) (da Costa *et al*., 2016, Lambert *et al*., 2017, Wright and Kelly, 2017). Plastic particles have hydrophobic nature; therefore, they can adsorb other dangerous organic and inorganic contaminants such as: endocrine-disrupting compounds, pharmaceuticals, polychlorinated biphenyls (PCBs), polycyclic aromatic hydrocarbons (PAHs), polybrominated diphenyl ethers (PBDEs), personal care products and heavy metals from the surrounding water and so on (Hidalgo-Ruz *et al*., 2012, Carr *et al*., 2016, Ma *et al*., 2016, Solomon and Palanisami 2016, Graca *et al*., 2017, Pinheiro *et al*., 2017, Wright and Kelly, 2017). The degradation process of synthetic plastic pollutants is slow; therefore, the particles persist for a very long time in the water environment and become available to water organisms (Laglbauer *et al*., 2014).

Table 1: showing chemical addictives used in plastics and their effect

Toxic Additives	**Uses**	**Public health effect(S)**	**Plastic types**
Bisphenol A	Plasticizers, can liner	Mimics estrogen, Ovarian disorder	Polyvinyl chloride (PVC), Polycarbonate (PC)
Phthalates	Plasticizers, artificial fragrances	Interference with testosterone, sperm motility	Polystyrene (PS), Polyvinyl chloride (PVC).
Persistent Organic Pollutants (POPs)	Pesticides, flame retardants, etc.	Possible neurological and reproductive damage	All plastics
Dioxins	Formed during low temperature combustion of PVC	Carcinogen, interferes with testosterone	All plastics
Polycyclic aromatic hydrocarbon (PAHs)	Use in making pesticides	Developmental and reproductive toxicity	All plastics
Polychlorinated biphenyls (PCBs)	Dielectrics in electrical equipment	Interferes with thyroid hormone	All plastics
Styrene monomer	Breakdown product	Carcinogen, can form DNA adducts	Polystyrene
Nonylphenol	Anti-static, anti-fog, surfactant (in detergents)	Mimics oestrogen	PVC

Sources: (Halden, 2010)

Plastic pollutants enter the water environment from various sources. Among them can be distinguished: waste water treatment plants, cargo shipping, fisheries, human waste from beaches and urban runoff (Cole *et al*., 2011, Stolte *et al*., 2015, Peters and Bratton 2016, Alomar *et al*., 2016, Michielssen *et al*., 2016, Solomon and Palanisami 2016, Graca *et al*., 2017, Mintening *et al*., 2017, Wright and Kelly, 2017). Often, waste water treatment plants (WWTPs) are mentioned as the main sources of microplastics in aquatic environment. Micro-plastics, for example, from cosmetics and other plastic waste, end up at the municipal WWTPs (da Costa *et al*., 2016). It should be noted that most rivers with a high rate of plastic waste are located close to large urban centers. (Carr *et al*., 2016) stated, that micro-plastic particles are removed in the primary treatment zones via solids skimming and sludge settling processes and they suggested that effluent discharges from both secondary and tertiary waste water treatment facilities can contain only minimal microplastic loads discharged to the surface water.

3. EFFECTS OF PLASTIC WASTE ON THE ECOSYSTEM

Plastic waste has several impacts on the health of ecosystems and humans. Some of these are more obvious and clearly proven, for example, the entanglement of marine wildlife. Others are subtler and not well understood, such as the transport and possible concentration of contaminants by plastic waste. Again, there appears to be more monitoring of ecological and human health impacts in the marine environment than on land. Although there is little research on the specific impacts of plastic waste on land-based wildlife, there is concern that incorrectly managed landfills could lead to either the escape of plastic waste or the escape of landfill leachate containing the chemicals associated with plastic. In addition, unofficial recycling methods, particularly in developing countries, can cause the release of chemicals into the environment, for example, the burning of plastic-coated wires to extract metal. **Effects on Water:** Plastic contaminates the water bodies and oceans by storm-water runoff, flowing into watercourses or directly discharged into coastal waters. This pollution enters the food chain thereby causing hazardous long-term carcinogenic effect to fishes, animals and human beings due to the release of diethylhexyl phthalate, lead, mercury and cadmium. Nigeria's coastal water are generally contaminated from micro-plastic debris which floats on the surface. The accumulation of plastics in our environments is a result of improper disposal or shipping spills. Since they are lightweight and durable, plastics are capable of traveling long distances; ending up in terrestrial environments, along shorelines, or floating in the open ocean (Zbyszewski and Corcoran, 2011). For example, pill bottles from India along with oil and detergent containers from Russia, Korea, and China have been found on the southern parts of Hawaii (Kostigen 2008).

Figure 3 (above): Plastic bottles floating on the water.

As plastics float in the oceans, they are affecting marine wildlife. Not only do plastics end up in animals' stomachs or around their necks, but there is also growing concern that plastics are acting as a

medium for invasive species. The hard surfaces of plastics are now an alternate material for invasive species such as barnacles, mollusks, and algae to attach, compared to the natural material which previously carried invasive species for centuries (Gregory 2009). With the influx of plastics presently in our fresh waters, the accumulation of invasive species may escalate at an ever-increasing speed. **Effects on Soil:** Harmful chemicals are released by seepage in the groundwater and in the ecosystem especially in the soil from the plastics. Polymer and nylon degrading bacteria like Pseudomonas, nylon-eating bacteria and Flavobacteria contribute to the release of methane gas from the breakdown of nylon which contributes towards greenhouse gas and global warming. **Effects on Aquatic Organism**: Sea turtles are mostly affected by plastic pollution including some species of jelly fish which cause esophageal obstruction in them and also accumulate in the stomach of whales. Even small fishes also consume the tiny bits of plastic below the ocean surface. Tuna, sword fish and Lantern fish also consumes plastics by mistake which become a part of the ocean food chain. **Sea Turtles:** Numerous autopsies have shown that ingested plastic and tar are the primary culprits of stress and non-natural death for sea turtles. Debris including fishing line, ropes, nets, six pack rings, Styrofoam, and plastic bags has been extracted from turtle digestive tracts. Plastic bags floating in the water strongly resemble the shape of jellyfish, a primary food source for sea turtles, thus resulting in the ingestion of the bags (Mascarenhas *et al*., 2004). Due to anthropogenic impact, the population of leatherback sea turtles (*Dermochelys coriacea*) has steadily declined over the last two decades, placing them on the IUCN's critically endangered list (Shillinger *et al*., 2012). For the last 40 years, of the 371 autopsies conducted on leatherback turtles, 37.2 % of them had plastic in their gastrointestinal tracts (Mrosovsky *et al*., 2009). Although it is not known if the plastic ingested was the cause of death, 8.7 % of the turtles had a plastic bag presumably blocking the passage of food (Mrosovsky *et al*., 2009). Plastic has also been found to block the passage of female eggs. In a documented study, researchers removed 14 pieces of plastic from a female cloaca. This enabled the eggs to be laid, but indication of internal damage remained (Plot and Georges 2010).

Cetacean do aquatic mammals constitute the infraorder Cetacea. There are around 89 living species, which are divided into two parvorders. The first is the Odontoceti, the toothed whales, which consist of around 70 species, including the dolphin (which includes killer whales), porpoise, beluga whale, narwhal, sperm whale, and beaked whale. The second is the Mysticeti, the baleen (from Latin: balæna, lit. 'whale') whales, which have a filter-feeder system, and consist of 15 species divided into 3 families, and include the right whale, bowhead whale, rorqual, pygmy right whale, and gray whale. Most cetaceans live far from the shoreline which limits the amount of research on the ingestion of marine debris. If plastic causes unnatural death, cetaceans will most likely sink to the bottom of the ocean (Baird and Hooker 2000). Occasionally, cetaceans will wash ashore allowing for postmortem examinations. Due to cetaceans' echolocation capabilities, mistaken consumption of plastic is not probable (Secchi and Zarzur 1999). Ingestion is most likely because the debris was mixed in with the desired food. Two sperm whales (*Physeter macrocephalus*) were found off the coast of northern California in 2008 with a large amount of fishing gear in their gastrointestinal tracts (Jacobsen *et al*., 2010). One of the sperm whales had a rupture in the third compartment of the stomach caused by nylon netting; the other had netting, fishing line, and plastic bags completely blocking the stomach from the intestines (Jacobsen *et al*., 2010). **Birds:** Plastic pollution also affects the birds like Seabirds, which obstruct their digestive tract causing tissue damage by the toxic chemicals called polychlorinated biphenyls (PCBs). Marine plastic pollution can even reach birds that have never been at the sea through the food habits.

The plastic particles were found intact within the birds' gizzards and proventriculus along with the plastic debris, such as Styrofoam mixed with their feed. Small plastics such as bottle caps are often

mistaken by seabirds (*Procellariiformes spp*) for food. In several studies, it was found that diving birds that fed on fish in the water column had less plastic in their stomachs compared to those that were surface eaters (Blight and Burger 1997; Provencher *et al*., 2010). This could be because birds that maintain a diet of zooplankton may not be able to distinguish between plastics and their primary source of food due to the color or shape of the plastic pieces (Avery-Gomm *et al*., 2013). Since most adult birds regurgitate what has been ingested as a way to feed their chicks, they pass the bolus containing the plastic pieces onto their young. Birds such as the albatross and shearwater had more plastic in the first region of their stomachs and gizzards, indicating that when these plastics were regurgitated, they would be passed to their young during feeding (Moser and Lee 1992). Juvenile albatross and shearwaters were found to ingest more plastics than adults (Avery-Gomm *et al*., 2013; van Franeker *et al*., 2011). Similar to other marine life, swallowed plastic can obstruct and damage a bird's digestive system, reducing its foraging capabilities. (Ryan 1988) concluded that ingested plastics could reduce the fitness, growth rate, and food consumption of seabirds, based on the results from a study using domestic chickens (*Gallus domesticus*).

Fish: There have not been any found published studies about the effects of plastics on fish; nonetheless, there is plenty of evidence supporting that fish are consuming plastics. Many aquatic creatures use filter feeding as a passive way of feeding, and collect particles from the water that float by. This is energy efficient, which is good for such a remote area, but this also means that the microplastics that float by become a food source as well. The filter feeders at the bottom of the ocean would be primary consumers, and are vital to higher levels of the food chain. If they become disturbed by the microplastics, either due to clogging of filter feeding abilities or due to toxic effects from chemicals or pollutants in the plastics, then the deep aquatic ecosystem balance and biodiversity could be thrown off.

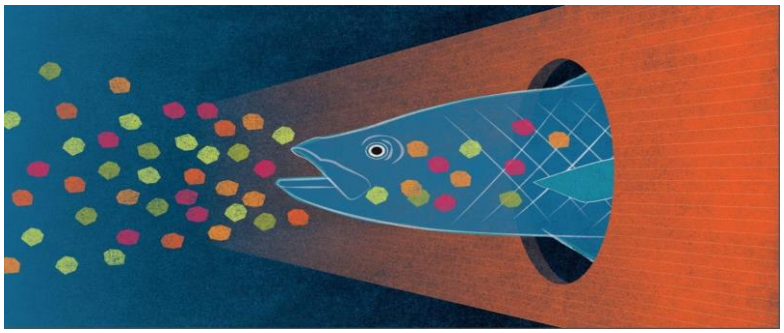

Figure 5 (above): Fish feeding on microplastic.

Microplastics present in the water makes it difficult for fish to distinguish because of their small sizes and color. Fishes tend to feed on the microplastics thereby causing damages to their digestive system.

4. Economic Importance of Plastic waste

Growing plastic consumption raises important challenges regarding environmental and health security. For what regards the environment, plastic is dangerous in a twofold way, both in its production and its disposal. At the production level most plastics are produced using petrol and natural gas, these sources, other than being non-renewable, are highly pollutant for ecosystems. Furthermore, due to the complexity and the costs of the recycling process, the great majority of the world's plastic ends up in landfills (ex. in the US 50%). Also, great quantities of plastic are dispersed into the open environment, and being plastic non-biodegradable, it can be around for a very long time. A consequence of this problem is plastic pollution in the oceans, with disastrous effects on the marine environment and its ecosystem. Furthermore, there are growing evidences connecting usage of many kinds of plastics to

some health-related issues. The two main health issues derived from plastic are the use of plastic polycarbonate, present in most food and drinks packaging and anything requiring clear and hard plastic, which has been linked to health threats such as chromosomal abnormalities, cancer and resistance to chemotherapy and the use of phthalate plasticizers, widespread softening agents (with very high quantities contained in PVC) that are considered carcinogen and dangerous for the endocrine system.

Plastic is considered a mono-use material, which is used for one purpose and immediately disposed, meaning that all its value goes immediately waste after its first use. In this regard, I will also analyze the idea of Circular Economy and how it would be possible to create a system in which non-recyclable plastic consumption is diminished, and the remaining plastic is fully recycled in a way to preserve all its value over time. Today, growing plastic production and consumption is posing serious threats, especially to developing countries, who often lack adequate facilities to dispose of such a difficult material, with tones of plastic being thrown in the open environment every year. Solving this issue is a need of primary importance in matters of environmental protection.

Method of Safe Disposal of Non-biodegradable Waste: (a) Recycling: Recycling is the process of converting waste materials into reusable objects to prevent waste. The materials from which the items are made can be reprocessed into new products. Recycling such material saves product and it also reduces the amount of manufacture to make new products. It also helps in energy saving and reducing global climate change. **(b) Incineration with energy recover**y: Most commodity plastics have gross calorific values (GCV) comparable to or higher than that of coal (Davis & Song 2006). Incineration with energy recovery is thus a potentially good option after all recyclable elements have been removed. It is argued that petrochemical carbon, which has already had one high-value use, when used again as a fuel in incineration represents a more eco-efficient option than burning the oil directly (Miller 2005). Reports by the Environment Committees of the UK Parliament (House of Commons 1993; House of Lords 1994) have supported the view that energy recovery for some types of household plastic wastes is an acceptable waste management option.

Trials conducted by the British Plastics Federation demonstrated that modern waste-energy plants were capable of burning plastic waste, even those containing chlorinated compounds such as PVC without releasing dangerous or potentially dangerous emissions of dioxins and furans (BPF 1993). **(c) Landfill:** Landfill refers the disposal of waste material by burying it. Landfills are extended storage area for non-biodegradable waste. Landfill is an area, which prevent contamination from the waste entering the area surrounding by soil and water and it also helps to reduce odour and pests. Landfills are dangerous to the environment as well as human health. Most landfills are open dumps that contaminate ground water, rivers, and lakes. When water is contaminated by landfills and consumed by animals and humans, it can lead to disease and death (Sutton & Turner, 2012). For example, a survey that was conducted in 2008 shows that 82% of landfills had openings that emit toxins into ground and surface water (Waste and Recycling Facts).

Managing the Effects of Plastics: The movement of plastics in our fresh water environments and the effects on wildlife has been researched for over 30 years. Knowledge about ocean currents gained from satellite-tracked Lagrangian drifters have been used to predict the trajectories of floating marine debris (Maximenko *et al*., 2012; Martinez *et al*., 2009). Lagrangian drifters are instruments that have been used in oceans, lakes, and rivers to measure water currents and to collect other environmental data such as temperature and salinity. Despite the ability to track waste movement, a solution to ridding our Earth's waters of plastic waste to minimize its effects on marine wildlife remains a challenge. These plastics inevitably make their way to the sea through networks of rivers and streams and then into the ocean gyres. Since the gyres are found in international waters, no country is taking responsibility for

cleaning up the oceans. Instead, several private organizations are working to solve the problem. Innovative technologies have been piloted by private companies to help identify, minimize, and eliminate plastics in our ecosystems including tracking trash through radiofrequency identification (RFID) tags and cellular transmitters, using drones or barriers to collect plastic debris, and turning plastics back into oil.

Bans: To reduce the use of plastic bags, some countries have banned plastic bags. Examples of countries and cities that have plastic-bag bans include Rwanda, Kenya, Bangladesh (ban on thinner plastic bags), Mexico City, China (ban on free plastic bags), Austin (Texas, USA), San Francisco (California, USA), and Oakland (California, USA). In 2007, San Francisco became the first U.S. city to ban the use of plastic bags (Clapp & Swanston, 2009). In Africa, Kenya and Rwanda have banned plastic bags, in 2017 and 2004, respectively. The Kenyan ban disallows producing, importing, or using plastic bags (Dunn, 2012). The ban on plastic bag in Kenya became effective in August 2017. The ban focuses on the production, importation, and uses of plastic bags. There is severe punishment for anyone who violates the rules of the ban. The first penalty is a jail time, and the second is an exorbitant fine. Violators must either pay the fine of $38,000, which is equivalent to 32,000euros, or 4-year jail sentence (BBC, 2017). Nigeria is the most populous country in Africa. It has a population of over 190 million people (UN, 2017). As such, Nigerians generate tons of waste daily, which includes single-use plastic bags. Traditional African societies, which had smaller populations, used native leaves use for wrapping items. Increase in the number of populations in Nigeria brings about the use of polyethylene in wrapping items (Akinro *et al*., 2012; Aziegbe, 2007). In Nigeria, polyethylene is used in wrappers such as table water, biscuit, salt, and ice cream. Polyethylene bags are use in all markets, restaurants, homes, and shopping centers in Nigeria. These bags are found in the entire streets and corners of the country, for example in Edo State and Ondo State in Nigeria (Akinro *et al*., 2012; Aziegbe, 2007). In Nigeria, most states and cities such as Ado-Ekiti encounter waste management problems as a result of poor management of waste (Adefemi & Awokunmi, 2009).

A study was carried out to investigate the seasonal variation of polyethylene generation and disposal in Akure City in Nigeria (Akinro *et al*., 2012). In the study, five daily markets were randomly selected and, in each market two sites were used: the processed food section and raw food section. The results of the study showed that polyethylene is generated more during dry season than rainy season. The results also showed that sachets of table water are the major contributors to polyethylene waste followed by ice cream sachets and biscuits sachets. This is because sachet water is very cheap (ranging from 5 Naira to 10 Naira); therefore, it is consumed throughout the year (Akinro *et al*., 2012). In 2017, during the 10th Global Environment Facility National Steering meeting in Abuja, Nigeria, the head of the Ministry of Environment noted the negative impacts of plastic bags and the government's wish to ban plastic bags (Sustyvibes, 2017). Although the government has not implemented this proposed ban, it would, when implemented, have widespread impacts across the country, given the reliance of millions of Nigerians on plastic bags for daily activities. The ban may be ineffective if the government does not enforce it or if the general public does not support it.

5. Recommendation

The future of aquatic ecosystem at local, national, and global scale depends on investments of individuals, communities, and governments at all political levels to ensure that our aquatic ecosystem are protected and managed in a sustainable manner, this includes not only practical solutions to the plastic waste problems, but changes in human behavior through public awareness and capacity building to better preserve the ecosystem, but various method of waste disposal should be implemented in every settlement.

6. Conclusion

Researches on worldwide production of plastics and the accompanied environmental pollution have shown that plastic wastes have constituted a major environmental issue. The effect of plastic wastes on fresh water organisms, humans and the environment at large are of public concern, and calls for the need to salvage the ecosystems and lives. Despite the fact that plastics are very useful in everyday life, the chemicals used in the production need to be thoroughly monitored so as to ensure environmental and health safety. Further research should be done on the effect of the chemicals, toxins, and invasive that can be a part of the plastic pollution and their effect on aquatic biota. The organisms which have a sessile nature and which feed opportunistically or through filter feeding have the biggest chance of being negatively affected by the plastic pollution. Further research is vital to discover even more about the effects of plastics on aquatic ecosystem, and to discover ways to mitigate certain harmful effects.

REFERENCES

Adefemi, S. O., and Awokunmi, E. E. (2009). The impact of municipal solid waste disposal in Ado-Ekiti metropolis, Ekiti-State, Nigeria. *African Journal of Environmental Science and Technology*, 3(8), 186–189.

Akinro, A. O., Ikumawoyi, O. B., Yahaya, O., and Ologunagha, N. M. (2012). Environmental impacts of polyethylene generation and disposal in Akure City, Nigeria. *Global Journal of Science Frontier Research Agriculture and Biology*, 12(3), 1–8.

Avery-Gomm, S., Provencher, J. F., Morgan, K. H., and Bertram, D. F. (2013). Plastic ingestion in marine-associated bird species from the eastern North Pacific. *Marine Pollution Bulletin*, 72(1), 257–259.

Aziegbe, F. I. (2007). Seasonality and environmental impact status of polyethylene (cellophane) generation and disposal in Benin city, Nigeria. J. Hum. Ecol,22(2), 141–147.

Baner AL, Piringer O (2007) Preservation of quality through packaging. In: Plastic packaging materials for food. Wiley-VCH Verlag GmbH, Weinheim, pp 1–8.doi:10.1002/ 9783527613281.ch01

BBC. (2017, August 28). Kenya plastic bag ban comes into force after years of delays. Retrieved from bbc.com:http://www.bbc.com/news/world- Africa 41069853

Blight, L. K., and Burger, A. E. (1997). Occurrence of plastic particles in seabirds from the eastern North Pacific. *Marine Pollution Bulletin*, 34(5), 323–325.

BPF. 1993. SELCHP trials: summary report—energy recovery from plastic waste. British Plastics.

Clapp, J., and Swanston, L. (2009). Doing away with plastic shopping bags: international patterns of norm emergence and policy implementation. *Environmental Politics*, 18(3), 315–332. Retrieved from: https://doi.org/10.1080/09644010902823717

Davis, G., Song, J. H. 2006. Biodegradable packaging based on raw materials from crops and their impact on waste management. Ind. Crop. Prod. 23, 147–161 (doi:10.1016/j.indcrop.2005.05.004).

Dunn, J. (2012). Estimating willingness to pay for continued use of plastic grocery bags and willingness to accept for switching completely to reusable bags (Unpublished Master's dissertation). Utah State University (Logan, Utah). Retrieved from: https://search.proquest.com/docview/1037089471

Gregory, M. R. (2009). Environmental implications of plastic debris in marine settings-entanglement, ingestion, smothering, hangers-on, hitch-hiking and alien invasions. Philosophical Transactions of the Royal Society, B*: Biological Sciences,* 364(1526), 2013–2025.

Halden RU (2010) Plastics and health risks. Ann Rev Pub Health 31: 179-194. House of Commons. 1993. Session 1993–94. Environment Committee, 2nd Report, Recycling,1, 470 [19].

House of Lords. 1994. The government response to the 2nd report from the House of Commons Select.
Jacobsen, J. K., Massey, L., and Gulland, F. (2010). Fatal ingestion of floating net debris by two sperm whales (Physeter macrocephalus). *Marine Pollution Bulletin,* 60(5), 765–767.
Kostigen, T. M. (2008). The world's largest dump: the great pacific garbage patch. Discover Magazine.
Martinez, E., Maamaatuaiahutapu, K., and Taillandier, V. (2009). Floating marine debris surface drift: convergence and accumulation toward the South Pacific subtropical gyre. *Marine Pollution Bulletin,* 58(9), 1347–1355
Mascarenhas, R., Santos, R., and Zeppelini, D. (2004). Plastic debris ingestion by sea turtle in Paraıba, Brazil. *Marine Pollution Bulletin,* 49(4), 354–355
Maximenko, N., Hafner, J., and Niiler, P. (2012). Pathways of marine debris derived from trajectories of Lagrangian drifters. *Marine Pollution Bulletin,* 65(1),51–62.
Miller, R. 2005. The landscape for biopolymers in packaging. Miller-Klein Associates report Summary and Full Report available from The National Non- Food Crops Centre, Heslington, York, UK:
Moser, M. L., and Lee, D. S. (1992). A fourteen-year survey of plastic ingestion by western North Atlantic seabirds. *Colonial Water birds,* 15(1), 83–94
Mrosovsky, N., Ryan, G. D., and James, M. C. (2009). Leatherback turtles: the menace of plastic. *Marine Pollution Bulletin,* 58(2), 287–289.
Provencher, J. F., Gaston, A. J., Mallory, M. L., O'hara, P. D., and Gilchrist, H. G. (2010). Ingested plastic in a diving seabird, the thick-billed murre (Uria lomvia), in the eastern Canadian Arctic. *Marine Pollution Bulletin,* 60(9), 1406–1411.
ROBBENS J., JANSSEN C.R. 2015. Microplastics in sediments: A review of techniques, occurrence and effects. *Marine Environmental Research* 111: 5-17.
Ryan, P. G. (1988). Effects of ingested plastic on seabird feeding: evidence from chickens. *Marine Pollution Bulletin,* 19(3), 125–128.
Secchi, E. R., and Zarzur, S. (1999). Plastic debris ingested by a Blainville's beaked whale, Mesoplodon densirostris, washed ashore in Brazil. *Aquatic Mammals,* 25(1), 21–24.
Shillinger, G. L., Di Lorenzo, E., Luo, H., Bograd, S. J., Hazen, E. L., Bailey, H., and Spotila, J. R. (2012). On the dispersal of leatherback turtle hatchlings from Mesoamerican nesting beaches. Proceedings of the Royal Society B:*Biological Sciences,* 279(1737), 2391–2395.
Sustyvibes. (2017, August 14). Is Nigeria considering banning plastic bags? Retrieved from: sustyvibes.com: http://sustyvibes.com/nigeria-phase-plasticbags-says-minister- nvironment/
Sutton, J., and Turner, B. (2012). Plastic Bags: Hazards and Mitigation (undergrad thesis). ollege of Liberal Arts, California polytechnic State University.
UN (United Nations). (2017) World population prospects: the 2017 revision, findings and dvance tables. *Working Paper* No.ESA/WP/248. New York, USA: Population Division, Department of Economic and Social Affairs, United Nations. Retrieved from: https://esa.un.org/unpd/wpp/Publications/Files/WPP2017_KeyFindings.pdf
van Franeker, J. A., Blaize, C., Danielsen, J., Fairclough, K., Gollan, J., Guse, N., and Turner, D. M. (2011). Monitoring plastic ingestion by the northern fulmar fulmarus glacialis in the North Sea. *Environmental Pollution,*159(10), 2609– 2615.
WRIGHT S.L., KELLY F.J. 2017. Plastic and human health: A micro issue? *Environ. Sci. Technol.* 51: 6634-6647.
Zbyszewski, M., and Corcoran, P. L. (2011). Distribution and degradation of fresh water plastic particles along the beaches of lake Huron, Canada. *Water, Air, & Soil Pollution,* 220(1), 365–372.

MOLECULAR DOCKING STUDIES OF cSrc CANCER TARGET WITH DASATINIB AND CURCUMIN AS NOVEL INHIBITOR

Akor Blessing Anthonia[1,2] and Oluwatosin Kudirat Shittu[1,2]
[1]Department of Biochemistry, Federal University of Technology, P.M.B 65, Minna, Niger State.
[2]Molecular Biology and Bioinformatics Unit, Africa Centre of Excellence for Mycotoxin and Food Safety, Federal University of Technology, P.M.B 65, Minna, Niger State.
*Corresponding Email: blessinganthonia7@gmail.com 08069805414.

Abstract

Breast cancer is one of the most common type of malignancies in women worldwide and it's a nonreceptor tyrosine kinase. Cellular Src (cSrc) is always upregulated. However current chemotherapeutics are beset with problems of undesirable side effects, poor bioavailability and lack of selectivity. In view of these limitation, there is need to search for new therapeutic of cSrc inhibitor. In this study, computer aided drug designing approach was applied to predict the suitability of docking curcumin in cSrc protein site and their interaction evaluated using auto dock vina software and lig-plot. In order to achieve the aim MSA was carried out on chain A and B of the cSrc protein sequence on NCBI database. To perform docking studies two-dimensional chemical structure of curcumin in SDF format was retrieved from PUBCHEM-NCBI database and was converted into PDB format by pymol for further analysis. The 3D crystallized chemical structure of cSrc (4ybi) with dasatinib were processed similarly as control. Automated docking software auto dock vina 4.2, chimera was used to evaluate binding affinity of ligand to the homology model of cSrc. The interaction of docked poses was evaluated using lig-plot. The MSA result indicate that chain A and chain B are homologous with E-value of zero and percent identity of 100%. Also, the binding energy of curcumin with cSrc is -9.2kcal/mol compared to dasatinib of -11.9kcal/mol.The in-silico study of curcumin in cSrc pocket region provides an alternate good inhibitor for cancer regulation.

Keywords: Breast Cancer, cSrc, Dasatinib, Curcumin, Molecular Docking, Binding Energy, E-value.

1.0 BACKGROUND OF THE STUDY

Breast cancer is a cancer that starts in the cells of the breast in women and men. Worldwide, breast cancer is the second most common type of cancer after lung cancer (10.4% of all cancer incidence, both sexes counted) and the fifth most common cause of cancer death. In 2005, breast cancer caused 502,000 deaths worldwide (7% of cancer deaths; almost 1% of all deaths) (WHO 2003). Because the breast is composed of identical tissues in males and females, breast cancer also occurs in males. Incidences of breast cancer in men are approximately 100 times less common than in women, but men with breast cancer are considered to have the same statistical survival rates as women (WHO 2006). Normal breast cells and most breast cancer cells have receptors that attach to circulating estrogen and progesterone. Estrogen and progesterone bind to the receptors and may work with growth factors (e.g., oncogenes and mutated tumor suppressor genes) to cause cancer cell growth and proliferation. Breast cancers that are estrogen and progesterone receptor positive (i.e., ER+ and PR+) are more likely to respond to hormonal therapy (e.g., tamoxifen, Raloxifene, Toremifene) and have a better prognosis than cancers that are hormone receptor negative (Cosman et al, 2003).Metastasis of cancer is developed as a result of inappropriate cell migration and invasion .Some of the most common side effects of tamoxifen are serious side effects of tamoxifen are blood clots, strokes, uterine cancer, and cataracts.

Raloxifene may infrequently cause serious blood clots to form in the legs, lungs, or eyes. Other reactions experienced include leg swelling/pain, trouble breathing, chest pain, vision changes. The side effects of these drugs make the need for the necessity of new improved drugs hence in our research study we try to find the suitable analogues with high binding affinity, which could be a possible lead molecule (Shoko et al,2008). The non-receptor tyrosine kinase c-Src, an important molecule in cell migration, adhesion, and osteoclast-mediated bone resorption
(Hiscox et al,2007) is over-expressed and activated in a large number of human malignancies, and the relationship between c-Src activation and cancer progression has been shown to be significant (Summy et al,2003).It has been previously demonstrated that active c-Src mediates tumor cell migration and promotes lung and latent breast cancer bone metastasis (Myoui et al,2003).However, the effect of c-Src on the prognosis of metastatic breast cancer patients, particularly on patients with bone metastasis, remains unclear. In the present study, c-Src expression and its effect on prognosis in metastatic breast cancer patients was evaluated. In addition, the role of c-Src in bone metastasis and visceral metastasis, respectively, was explored. Our findings revealed that c-Src expression is a significant and independent predictor for disease-specific survival (DSS) for patients with bone metastasis compared with patients with visceral metastasis. Dasatinib, a potent orally available SFK inhibitor (Lombardo et al,2004) is being studied in various solid tumors. Preclinical data suggest that dasatinib has therapeutic potential in breast cancer, including inhibition of "triple-negative" breast cancer cell lines in vitro (Finn et al,2007), inhibition of breast cancer bone metastasis in in vivo models (9, 26), and by other mechanisms. (Nautiyal et al,2009). Dasatinib as a single-agent, however, provided only limited clinical benefit in patients with ABC. In phase II trials, the disease control rate [confirmed partial response (PR) or stable disease (SD) for 16 weeks] in "triple-negative" tumors was 9.3% (Finn et al,2011) and in Her2- or hormone receptor–positive (HRþ), ABC was 13% (Mayer et al,2009). The combination of dasatinib and 5-fluorouracil was shown in vitro to produce synergistic cytotoxicity in some breast cancer cell lines (see Supplementary Fig. S1A and S1B). Oral capecitabine has shown clinical efficacy, both as monotherapy and in combination with lapatinib. The potential combination of dasatinib with a widely used oral agent provides an attractive alternative approach in ABC. Curcumin has been shown to inhibits the proliferation of various tumor cells in culture and prevents carcinogen-induced cancers in rodents. In xeno transplant or ortho transplant animal models, the growth of human tumors was inhibited by curcumin alone or in combination with chemotherapeutic agents or radiation (Kunnumakkara, et al,2008). Banerjee et al,2010 reported that curcumin induced G2/M arrest and apoptosis, inhibited cell proliferation by inhibiting the assembly dynamics of microtubules, and further activated the mitotic checkpoint in MCF-7 cells. Furthermore, cells were accumulated in the G(1) phase of the cell cycle, and curcumin suppressed the expression of zeste homolog 2 (EZH2) gene via the stimulation of three major members of the mitogen-activated protein kinase (MAPK) pathway: c-Jun NH2-terminal kinase (JNK), extracellular signal-regulated kinase (ERK), and p38 kinase (Hua et al,2010) The apoptosis is involved in the curcumin-induced inhibition of tumor cell growth. It was found that curcumin inhibited the expression of Ki-67, proliferating cell nuclear antigen (PCNA), and p53 mRNAs in breast cancer cells, and induced Bax mRNA expression with the down-regulation of p21 mRNA in the human mammary epithelial cell line. Despite the advancements in the field of cancer research, there is still an urgency to discover and develop anti-cancer therapeutics Natural products are of particular interest as chemopreventive agents because of their low toxicities and potential efficacies (Crowell et al,2009).The conventional drug discovery techniques are time consuming and expensive processes(DiMasi et al,2002)Thus, rational drug design in combination with structure based modeling and rapid screening methods offer significant potential for identifying and developing lead anticancer molecules. The use of the molecular docking method addresses deducing the ligand binding sites with a protein of known three-dimensional structure. Computational Biology and bioinformatics have the potential not only of speeding up the drug discovery process thus reducing the costs, but also of

changing the way drugs are designed. Rational Drug Design (RDD) helps to facilitate and speedup the drug designing process, which involves variety of methods to identify novel compounds. One such method is the docking of the drug molecule with the receptor (target). The site of drug action, which is ultimately responsible for the pharmaceutical effect, is a receptor. Docking is the process by which two molecules fit together in 3D. (Aberto et al,2006) One of the computational approaches, docking, helps with screening a large set of molecules based on their free binding energies and proposes structural hypotheses of how the molecules could inhibit the target. Recently, several in silico-based studies have been performed on small molecules to identify their anti-cancerous properties. Thus far, the activities of curcumin towards molecular targets such as protein kinases, proteases, and apoptosis related proteins, have poorly been explored. In this study we explored the in-silico kinase and protease inhibitor potentials of curcumin and studied the interactions cSrc.

2.0 MATERIALS AND METHODS

For our present study we used bioinformatics tools, biological databases like PubMed, Drug Bank, PDB (Protein Data Bank) and software's pymol, chimera, autodock vina and lig plot.

2.1 SEQUENCE ANALYSIS.

The Crystallized structure of cSrc Protein (PDB ID-4ybj) from gallus gallus organism were retrieved from PDB database. The complex structure is basically composed of two polypeptides of chain-A and B (286 amino acid residues). The FASTA sequence of cSrc were also retrieved for multiple sequence alignment analysis which was then inputed and blasted. (www.ncbi.nlh.gov)

2.2 PREPARATION OF LIGAND AND PROTEIN

Docking using AutoDock/Vina Intermediary steps, such as pdbqt files for protein and ligands preparation and grid box creation were completed using Graphical User Interface program AutoDock Tools (ADT). ADT assigned polar hydrogens, total gasteiger charges (-1.9975) and solvation parameters to the protein. AutoDock saved the prepared file in PDBQT format. a modified pdb format containing atomic charges, atom type definitions for ligands, and topological information. Avogadro tool was used to delete hydrogen from the ligand, energy minimization was done and then converted from lig.pdb to pdbqt. AutoGrid was used for the preparation of the grid map using a grid box. The grid size was set to 22× 22× 22 xyz points with grid spacing of 1.000Å and grid center was designated at dimensions (x, y, and z): 12.523, 4.798 and 98.644. A scoring grid is calculated from the ligand structure to minimize the computation time. AutoDock/Vina was employed for docking using protein and ligand information along with grid box properties in the configuration file.For docking, the entire receptor was enclosed inside a grid box, with a grid spacing of 1 Å, keeping the receptor rigid and the ligand as a flexible molecule. The ligand's backbone and side-chain were flexible and allowed to dock with the receptor to form all possible conformations. After defining the binding site and receptor–ligand preparation, docking runs were launched from the command prompt. The interaction energy between the ligand and the receptor was calculated for the entire binding site and expressed as affinity (kcal/mol). (Blum et al,2008)

2.3 PROTEIN–LIGAND INTERACTIONS

LigPlot was used to study protein–ligand interactions for a given pdb file encrypting the docking. The LigPlot program self-generated schematic 2D representations of the interfaces of protein–ligand complexes from standard pdb file input. The output was in the form of informative representation of the intermolecular interactions and their strengths, including hydrogen bonds, hydrophobic contacts, and atom accessibilities. Hydrogen bonds are represented by dashed lines whereas hydrophobic contacts are depicted schematically. The amino acid residues of the protein involved with the above

contacts are shown by an arc with spokes emerging towards the ligand atoms in contact and vice versa (Wallace et al,1995).

3.0 RESULT

3.1 MULTIPLE SEQUENCE ALIGNMENT (MSA)

The alignment results of MSA portrayed that the two chains of cSrc have identical amino acid sequences with E-value of zero and percent identity of 100%. Therefore, only one chain was taken for docking analysis and prediction of binding affinity between the ligand and the receptor.

3.2 Docking Studies Using AutoDock Vina

The docking process was carried out using AutoDock Vina. The docked pose with the highest affinity is represented in (Figure1) and the binding affinities of ligands are represented as kcal/mol (Table 2). The affinity value of less than or closer to 5 kcal/mol depicts negligible binding, whereas values closer to 10 kcal/mol indicate efficient binding (Table 2). The protein–Curcumin/Dasatinib docking studies are represented in Table2. Both Curcumin and Dasatinib exhibited stronger binding affinity (>5 kcal/mol for the cancer-related proteins).

3.2.1 Protein–Ligand Interactions

The protein–ligand interaction study was performed using LigPlot. The interactions of the ligands and cSrc with amino acids residues of the target proteins are shown in Figure 2. The H-bonds and hydrophobic contacts between the docked complexes are also shown.

Table 1: Representative homology model Structure comparison cSrc kinase.

Description	Scientific Name	Maximum Score	Total Score	Query Cover	E-Value	Percent Identity	Acc. Len	Accession
Type II Dasatinib Analog crystallized with cSrc.	Gallas Gallas	597	597	100%	0.0	100%	286	4YBJ

Table 2. Autodock Estimated Free Energies of Binding(G)of Compound Curcumin/Dasatinib in the Active Site cSrc Receptor.

S.No.	Receptor	Ligand	Binding Affinity(kcal/mol)	Hydrophobic Contacts	Nos of H-Bonds	Distance from best mode
1.	cSrc	Curcumin	-9.2	19	1	0.000
2.	cSrc	Dasatinib	-11.9	20	4	0.000

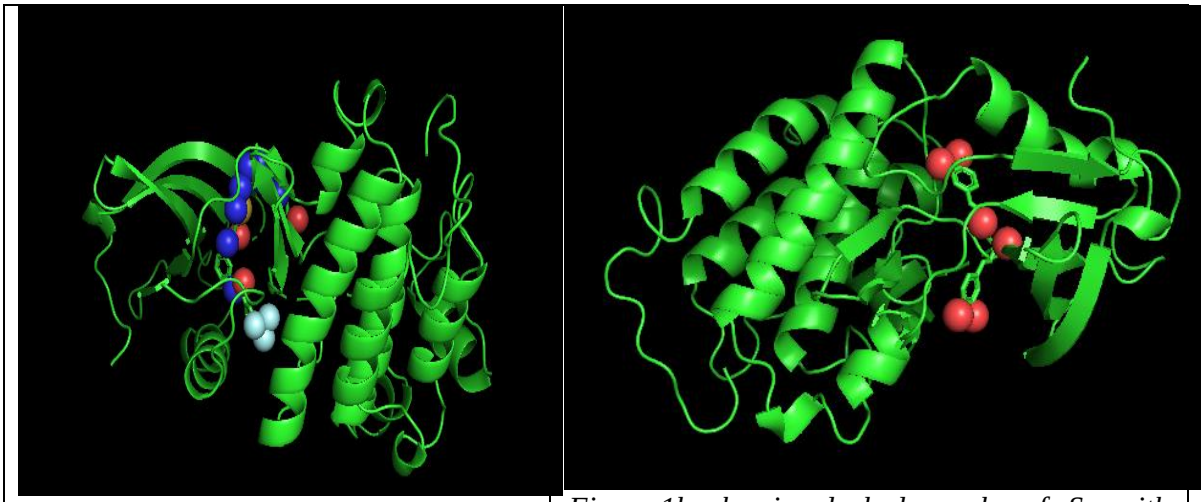

Figure 3a: showing docked complex of cSrc with Dasatinib

Figure 1b: showing docked complex of cSrc with curcumin

Figure1: showing docked complex of cSrc with Dasatinib (Fig.1a) and Curcumin (Fig.1b)

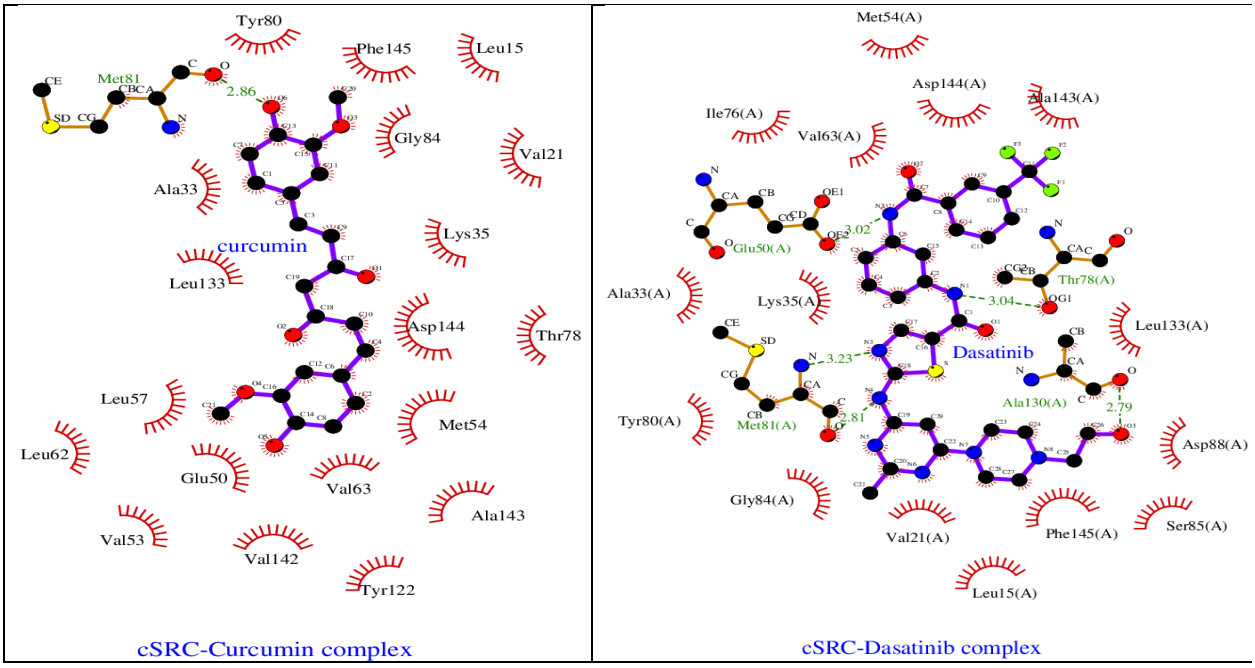

Figure 2: The interactions of the ligands and cSrc with amino acids residues of the target proteins

4.0 CONCLUSION

The present investigation sheds a new light on the potential interactions between curcumin, dasatinib to the metabolic enzyme (cSrc) indicating the involvement of multiple interactions such as H-bonds,

hydrophobic interactions and van der Waals forces, depending on the amino acid composition of binding sites and chemical properties of the docking agents and target enzymes (Fig 2). Further, this study is first of its kind to demonstrate the molecular mechanism(s) underlying the docking of a potential chemotherapeutic agent to the target enzyme, indicating the tremendous potential of this agent in catastrophing the bioenergetic machinery of malignant cells. Thus, the in-silico analyses revealed the potential of curcumin as an apoptosis inducer and a protein kinase inhibitor. Based on these studies, appropriate in vitro and in vivo experiments should be designed rationally to validate its biological activity.

REFERENCES

American Cancer Society (2007).” Cancer Facts and Figures”

Aberto, A.,and Diego B.(2006) “Computational Biology and Drug Discovery: From single – network Drugs”, Current Bioinformatics,1, 3-13.

Araujo, J.and Logothetis C. (2010) Dasatinib a potent SRC inhibitor in clinical development for the treatment of solid tumors. Cancer Treatment Review 36:492–500.

Banerjee, M., Singh, P.and Panda D.(2010) Curcumin suppresses the dynamic instability of microtubules, activates the mitotic checkpoint and induces apoptosis in MCF-7 cells. FEBS Journal 277:3437-48.

Baxter,J.(1981) Local optima avoidance in depot location. Journal of Operational Research Society 32(9):815–819.

Blum, C., Blesa, M.J.,Roli, A. and Sampels, M.(2008) Hybrid Metaheuristics: An Emerging Approach to Optimization. Studies in Computational Intelligence. Berlin Heidelberg: Springer-Verlag.114.

Berman, H.M.,Henrick, K. and Nakamura, H. (2000)Announcing the world wide Protein Data Bank. National Structural Biology.10-980.

Cosman F. (2003) “Selective estrogen-receptor modulators”, Clinical Geriatric Medicine. 19 (2):371-9.

Choi, Y.L., Bocanegra, M., Kwon,M.J., Shin,Y.K., Nam, S.J., and Yang, J.H.(2010) LYN is a mediator of epithelial-mesenchymal transition and a target of dasatinib in breast cancer. Cancer Research 70: 2296–306.

Crowell,J.A.(2005).The chemopreventive agent development research program in the Division of Cancer Prevention of the US National Cancer Institute:An overview. European Journal of Cancer 41;1889–1910.

DiMasi, J.A.,Hansen, R.W.and Grabowski, H.G.(2002) The price of innovation: New estimates of drug development costs. Journal of Health Economics 22:151–185.

David,W. Rithcie, “Evaluation of Protein Docking Predictions using Hex 3.1 in CAPRI rounds 1-2, Proteins, Structure, Fucntion and Genetics, Wiley-liss Inc.

Finn, R.S.,Dering, J.,Ginther,C.,Wilson, C.A., Glaspy,P.and Tchekmedyian,N.(2007) Dasatinib, an orally active small molecule inhibitor of both the src and abl kinases, selectively inhibits growth of basal-type/"triple negative 'breast cancer cell lines growing invitro. Breast Cancer Research Treatment.105:319–26.

Finn,R.S., Bengala, C.,Ibrahim,N.,Roche,H.,Sparano,J.and Strauss, L.C.(2011).Dasatinib as a single agent in triple-negative breast cancer: results of an open-label phase 2 study.Clinical Cancer Research 17:6905–13.

Garrett, M.M., David,S.G., Robert,S.H., Ruth,H.and William EH (1998) Automated docking using a lamarkian genetic algorithm and empirical binding free energy function. Journal of computer Chemistry 19:1639–1662

Huey,R.,Morris, G.M.,Olson,A.J. and GoodSell, D.S. (2007) A semi empirical free energy force field with charge based desolvation. Journal of computer Chemistry 28:1145–1152

Hua,W.F., Fu,Y.S., Liao,Y.J., Xia,W.J.,Chen,Y.,C.and Zeng,Y.X.(2010)Curcumin induces down-regulation of EZH2 expression through the MAPK pathway in MDA-MB-435 human breast cancer cells. European Journal of Pharmacology 637:16-21.

Hiscox, S.,Jordan,N.J., Morgan, L., Green,T.P.and Nicholson,R.I. (2007).Src kinase promotes adhesion-independent activation of FAK and enhances cellular migration in tamoxifen-resistant breast cancer cells. Clinical Experimental Metastasis 24:157–67.

Kunnumakkara,A.B.,Anand, P.and Aggarwal,B.B.(2008)Curcumin inhibits proliferation, invasion, angiogenesis and metastasis of different cancers through interaction with multiple cell signaling proteins. Cancer Letter 269:199-225.

Lombardo,L.J., Lee,F.Y., Chen, P., Norris, D.,Barrish,J.C.and Behnia,K.(2004) Discovery of N-(2-chloro-6-methyl-phenyl)-2-(6-(4-(2-hydroxyethyl) piperazin-1-yl)-2-methylpyrimidin-4-ylamino) thiazole-5-carboxamide (BMS-354825), a dual Src/Abl kinase inhibitor with potent antitumor activity in preclinical assays. Journal Medical Chemistry 47:6658–61.

Lehmann, B.D.,Bauer,J.A.,Chen, X.,Sanders,M.E.,Chakravarthy,A.B,and Shyr,Y.(2011) Identification of human triple-negative breast cancer subtypes and preclinical models for selection of targeted therapies. Journal of Clinical Investigation 121:2750–67.

Meng,X.N.,Jin,Y.,Yu,Y.,Bai,J.,Liu,G.Y.and Zhu,J,(2009) Characterization of fibronectin-mediated FAK signaling pathways in lung cancer cell migration and invasion. Breast Journal Cancer101:327–34.

Myoui,A,. Nishimura, R.,Williams,P.J., Hiraga,T., Tamura, D.and Michigami T.(2003).C-SRC tyrosine kinase activity is associated with tumor colonization in bone and lung in an animal model of human breast cancer metastasis. Cancer Research 63:5028–33.

Mayer, E., Baurain, J.F.,Sparano,J., Strauss,L.,Campone,M,and Fumoleau,P,(2009)Dasatinib in advanced HER2/neu amplified and ER/PR-positive breast cancer: phase II study CA180088. Journal of Clinical Oncology 27:43.

Nautiyal,J.,Majumder, P., Patel, B.B., Lee, F.Y. and Majumdar,A.P.(2009) Src inhibitor dasatinib inhibits growth of breast cancer cells by modulating EGFR signaling. Cancer Letter 283:143– 51.

Oleg, T. and Arthur, J.O. (2010) Auto Dock Vina: improving the speed and accuracy of docking with a new scoring function, efficient optimization, and multithreading. Journal of Computational Chemistry 31(2):455–461

Park, M.T., Kim, M.J., Kang, Y.H., Choi, S.Y., Lee, J.H. and Choi, J.A.(2005) Phytosphingosine in combination with ionizing radiation enhances apoptotic cell death in radiation-resistant cancer cells through ROS-dependent and independent AIF release. Blood 105:1724-33.

PubMed: Online Search Engine for science and biomedical articles, www.pubmedcentral.nih.gov Summy, J.M. and Gallick, G. E. (2003) Src family kinases in tumor progression and metastasis. Cancer Metastasis Review 22:337–58.

Sabbota, A.L., Kim, H.R., Zhe, X., Fridman, R.,Bonfil, R.D. and Cher, M.L.(2010).Shedding of RANKL by tumor associated MT1-MMP activates Src-dependent prostate cancer cell migration. Cancer Research 70:5558–66.

Shoko, M.,Masa-Aki,S.and Masahide, O.(2008) “Raloxifene, a selective estrogen receptor modulator, induces mitochondria-mediated apoptosis in human endometrial carcinoma cells”, 41(3):132-8.

Shoko, M., Masa-Aki, S., Masahide, O. and Yoshinori O. (2008). Raloxifene, a selective estrogen receptor modulator, induces mitochondria-mediated apoptosis in human endometrial carcinoma cells. Medical molecular morphology, 41(3):132–138.

Trott, O. and Olson, A.J. (2010) AutoDock Vina: Improving the speed and accuracy of docking with a new scoring function, efficient optimization and multithreading. Journal of Computational Chemistry 31:455–461.

Vandyke, K., Dewar, A.L., Diamond, P.,Fitter, S.,Schultz,C.G, and Sims, N.A.(2010).The tyrosine kinase inhibitor dasatinib dysregulates bone remodeling through inhibition of osteoclasts in vivo. Journal of Bone Mineral Research 25:1759–70.

Wallace, A.C.,Laskowski, R.A.and Thornton, J.M.(1995). LigPlot: A program to generate schematic diagrams of protein-ligand interactions. Protein Engineering 8:127–134.

World Health Organization International Agency for research on cancer (June 2003). "World Cancer Report".

World Health Organization t, (Feb 2006). "Fact Sheet, No 297: Cancer". Zhang, X.H., Wang, Q., Gerald, W., Hudis,C.A., Norton, L.and Smid M.(2009).Latent bone metastasis in breast cancer tied to Src-dependent survival signals. Cancer Cell.16:67–78.

EARTH SCIENCES

Geophysical Investigation of Groundwater Potentials in Selected Areas of Kaduna, Nigeria

[*1]Ahmed K. Usman, [1]Jimoh Raimi, [2]Saidat O. Abdulrasheed, [3]Quadri T. Usman
[1]Physics Department, Ahmadu Bello University, Zaria, Nigeria
[2]Chemistry Department, Ahmadu Bello University, Zaria, Nigeria
[3]Electrical Engineering Department, Ahmadu Bello University, Zaria, Nigeria
[*]Corresponding Author: Tel. +234 8164594389 Email: akusman@abu.edu.ng

ABSTRACT

Water is essential to people and the largest available source of fresh water lies underground. Increased demands for water have stimulated development of underground water resources. As a result, techniques for investing the occurrence and movement of groundwater have been improved, better equipment for extracting groundwater has been developed, and concepts of the resource management have been established. Geophysical investigation was carried out at Giwa Road, Narayi High Court and U/Pama Sabo Thasha Kaduna with the purpose of locating a suitable and high ground water potential site for drilling a productive and good water yielding borehole. Vertical Electrical Sounding (VES) method using symmetrical Schlumberger configuration with maximum current electrode separation of 200m was used in the investigation around the selected area. The VES data were collected and processed using IP2 WIN software. The processed data were interpreted to determine/recommend the suitable sites for exploitation of groundwater on the basis of thickness of aquiferous layer. From the result obtained, VES station 1 for Giwa Road, Narayi High Court was considered most suitable suitable for sinking of borehole in the area while for U/Pama Sabo Thasha VES station 1 was also considered suitable for the construction of borehole that will serve as sustainable water supply in the area.

Keywords: aquifer; borehole; low resistivity layer; terameter; vertical electrical sounding.

1.0 INTRODUCTION

Geophysics, as its name indicates, has to do with physics of the earth and its surrounding atmosphere. Its principles have been successfully used in solving ground water, mining, civil engineering and pollution problems, (Raimi, Arabi and Dewu, 2010). The role of geophysics in ground water exploration may among other reasons be attributed to fact that water is a necessity with 95% of the earth fresh water found in voids in soil and permeable geologic formation as ground water and over half of the world population relying on proper exploration of ground water for their general water supplies (Ajayi and Hassan, 1990; Raimi et al., 2010). Several geophysical methods are used for ground water exploration, some of these geophysical methods are: Electromagnetic, Ground penetrating Radar, Magnetic, seismic, Resistivity etc. Electrical resistivity method was chosen for this study because it is the quickest and most economic method especially when it comes to groundwater exploitation.

Water is essential to people and the largest available source of fresh water lies underground. Increased demands for water have stimulated development of underground water resources. As a result, techniques for investing the occurrence and movement of groundwater have been improved, better

equipment for extracting groundwater has been developed, and concepts of the resource management have been established.

Previous geologic works carried out in the area include the mapping of the general basement complex of Nigeria by various workers and works in the Northern sector of Nigeria basement complex were also carried out (Raimi, 2005). Notable amongst them are the works of Aboh (2001), Raimi (2005) and Arabi (2010).

Danladi (1985) in his hydro-geological investigation in shallow basement area of Kaduna reported groundwater in the area to occur mostly in joints, decomposed zones of basement complex and overlying alluvium. Localized geophysical explorations with similar objectives with this work have also been carried out (Ajayi and Hassan, 1990; Shemang, 1990; Olatunji, 1999; Raimi, 2005).

Pipe borne water supply is irregular and this as occasioned the construction of many wells in the study area to augment the supply. In light of this, groundwater is explored in order to determine suitable site for the construction of boreholes that will serve as sustainable water supply for the needs of the people of the study area and serve as a way of extracting the water resource in the area. This study is aimed at determining suitable sites for construction of boreholes that will serve as sustainable water supply in the study area.

2.0 MATERIALS AND METHODS

Description of the study area

The study falls within Chikun Local Government, Kaduna and is located between Latitude 10°26′10.46″ and 11°33′12.24″N and between Longitude 4°58′53.04″E and 7°31′55.776″E as shown in Figure 1.

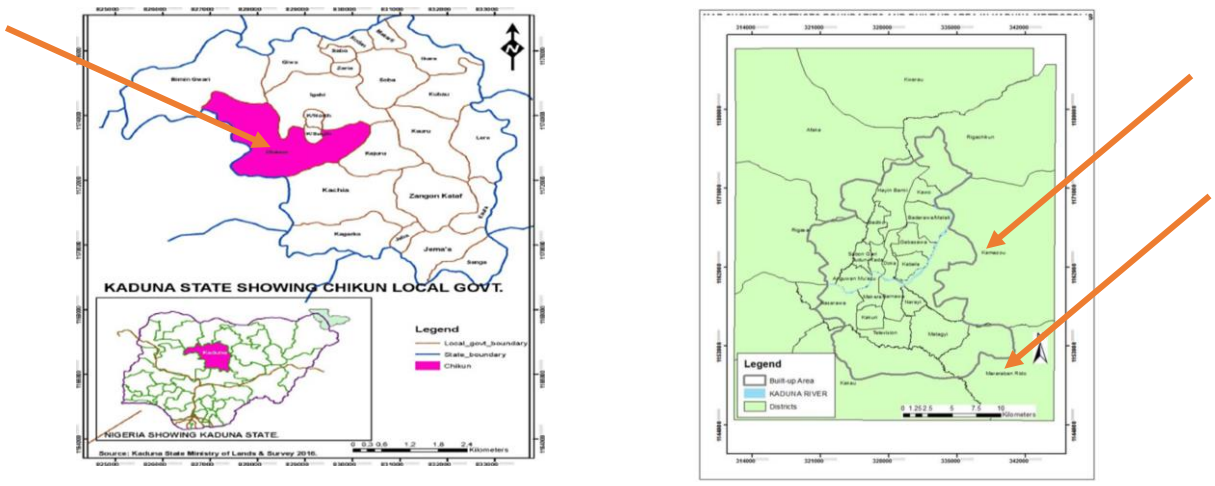

Figure 1: Study area

The study area has a tropical continental climate type characterized by wet and dry season. The tropical continental is more pronounced in the dry season particularly in December and January. The dry season is dominated by the north-east trade wind called Harmattan which prevails between November-

February. The dry season is also rainless from October to April. The wet season is dominated by the tropical maritime trade wind which starts around May to October. The area has a mean daily temperature showing a major peak in April. As such, temperatures are hot all year round except for the dry cool and dusty months of harmattan in November to February. The maximum temperature seldom falls from about 36°C as in April to about 27°C in the heart of rain season (August-October). The annual rainfall is about 1000mm (Ayoade, 1988). The natural vegetation of the study area is that of the Northern Guinea Savannah with grass dominating and scattered trees hardly higher than 4.6m with broad leaves. Meanwhile, the seasonal character of rainfall in the study area has influenced the vegetation which turns evergreen during the wet season and pale brown in the dry season respectively. The soils in the study area have been classified as tropical ferruginous soil. They are zonal soils developed under climatic regimes with appreciable but seasonal rainfall of 500-1200mm and cover nearly half of Northern Nigeria (Oguntoyinbo, Areola and Filani, 1983). The soil material consists of several feet of deposited silt sand overlaying sedimentary decomposed rock.

The soil is poorly drained because of the high percentage of fine textured materials in the upper layers, which results to water logging especially during the rainy season and tends to dry out and cracks during dry season. Alluvial soil is formed a long riverside (fadama). It is made up of several feet of grey white loamy coarse sand with layers of grey heavy molten occurring at varying depths within the profile. The alluvial soils are usually under intense cultivation of sugarcane and vegetables year-in year-out and as a result in farmers resort to using fertilizers to improve soil fertility (Ayoade, 1988). The geology of the study area is part of the basement complex geology of north central Nigeria. The region is underlain by older granitic crystalline, metamorphic rocks of Precambrian to low Paleozoic age (Oguntoyinbo, Areola and Filani, 1983). The metamorphic rocks consist of gneisses which have suffered intense weathering and have remained stable for millions of years. The prolonged weathering under tropical bioclimatic condition has produced rolling plains dotted with residuals of different origin. The study area lies on the high plains of Hausa land, with elevation ranging from 550 to 750meters above mean sea level showing a general regional slope to the south and a relative relief of 30 to 45 meters.

Techniques and procedure of Data collection and analysis

The resistivity technique used for this study is an electrical method and it uses artificial source field. In electrical methods, anomalies of a subsurface conductor depend on electrical conductivity contrast between the conductor and the host rock. Electrical method technique is simply the injection of current into the ground using a pair of electrodes which causes a potential difference in the ground which is measured by a separate pair of electrodes. There are many methods of observing these anomalies in electrical surveying. Some of these methods make use of naturally occurring fields within the earth while others require the introduction of artificially generated current into the ground (Raimi, 2005).

In the resistivity method, artificially generated electric current are driven into the ground. Any variation in subsurface resistivity (conductivity) alters the current flow patterns which in turn affect the distribution of electric potential. The resulting potential differences there established are measured at the surface. Any variations observed from the pattern of potential differences expected from uniform Earth are deviations from the uniform earth. These deviations represent the geological target of resistivity exploration.

Generally, four electrode arrays are used at the surface, one pair for introducing current into the earth and the potential difference established in the earth by the current is measured in the vicinity of current flow with the second pair. The simple method of conducting a resistivity survey measurement is as shown in figure 2 below for a homogeneous ground.

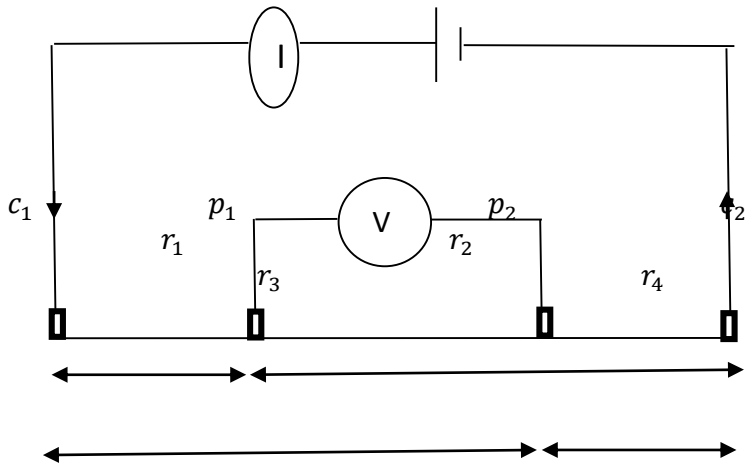

Figure 2: General four-electrode configuration from resistivity measurements

In studying the variation of resistivity with depth, as in case of layered medium, the center of the electrodes spread is often kept fixed while the electrode spacing interval is changed. This is called the Vertical Electrical Sounding (VES) (Raimi, 2005). The electrical resistivity method employed in this work is the geoelectric sounding or VES.

The electrical resistivity of a rock material limits the amount of current passing through when an electric potential is applied. If a material of resistance R has a cross-sectional area A and length L, the resistivity (ρ) can be expressed as;

$$\rho = \frac{RA}{L} \quad (1)$$

The unit of resistivity is Ohm-meter (Ωm)

Using Ohm's law;

$$V = IR \quad (2)$$

Where I = current in (A), V = potential difference in (V), R = electric resistance in (Ω)

$$\rho_a = \frac{\Delta U}{I} 2\pi\{(1/r_1 - 1/r_2) - (1/r_3 - 1/r_4)\}^{-1} \quad (3)$$

Let $K = 2\pi\{(1/r_1 - 1/r_2) - (1/r_3 - 1/r_4)\}^{-1}$

And $R = \frac{\Delta U}{I}$

Then $\rho_a = KR$ (4)

Where K is the geometric factor

ΔU is the change in potential between the electrodes

I is the current passing through the electrodes

ρ_a = apparent resistivity (Danlami, 2011).

Data Collection

The data used for this research work were collected from National Water Resources Institute Mando, Kaduna State, Nigeria. Data of two locations were used for this study. For location one (Giwa Road, Narayi High Court), three (3) VES stations were acquired while one (1) VES station was acquired for the second location (U/Pama Sabo Thasha). The data were acquired using resistivity Terameter and other accessories such as current and potential electrodes, hammer, measuring tape, cables etc

In the vertical electric sounding (VES) the potential electrode spread remains fixed but the separations of the current electrodes are progressively increased to increase the depth of investigation. Hence, choice of Schlumberger configuration is recommended which depend on the type of investigation unlike Wenner configuration which is mostly used to probe along a horizontal surface and it is more complex to use where all the four electrodes are move along the length of investigation. The Schlumberger electrode array is illustrated in Figure 3.

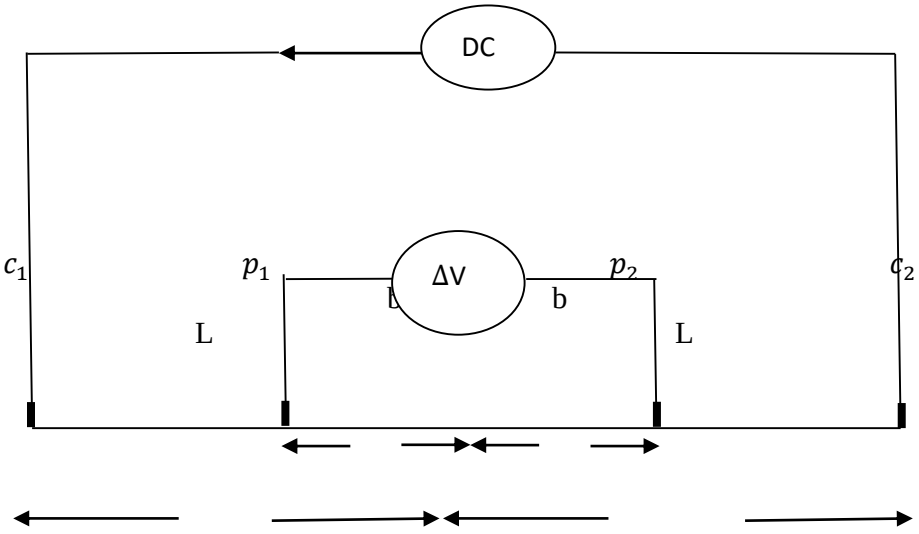

Figure 3: Generalized Schlumberger electrode configuration

Using the same procedure on the general resistivity measurement.

$$K = 2\pi\{(1/L\text{-}b - 1/L+b) - (1/L+b - 1/L\text{-}b)\}^{-1}$$

$$K = 2\pi\{(2/L\text{-}b - 2/L+b) = \pi(1/L\text{-}b - 1/L+b)\}^{-1}$$

$$K = \pi(L^2/2b - b/2) \quad (5)$$

Therefore,

$$\rho_a = \pi(L^2/2b - b/2)\frac{\Delta U}{I} \quad (6)$$

Where L is the separation between a current electrode and the centre of the configuration

b is the separation between a potential electrode at the centre of the configuration

ρ_a is the apparent resistivity of the ground for a Schlumberger array.

Therefore,

$$\rho_a = KR \quad (7)$$

where $R = \Delta U/I$

The Vertical Electrical Sounding process requires that the mid of the voltage electrode be fixed most times at the observation station, while the length of the electrical configuration be gradually increased. The increase in length of current electrode results in deeper penetration of current and also the depth of investigation. This implies that the wider the separation of current electrode the deeper the depth of investigation (Danladi, 1985; Olaniyi and Olabode, 1998; Arabi, 2010; Danlami, 2011).

Delineation of underlying geo-electric layers of each sounding stations were carried out on the principle that all point of maxima, minima and inflation on the sounding model curves processed by the software indicates existence of boundaries of different lithological composition and resistivity nature. Where values tend to infinity is an indication of fresh basement which is hard in nature and its constituents are closely packed together with little or no water present in it. This results to its rise in resistivity value (Raimi, 2005; Danlami, 2011; Idris, 2011; Martin, 2015).

The Schlumberger electrode configuration with a maximum electrode configuration of 160 m was adopted. For a sounding to the desired depth of investigation, Danlami (2011) recommended a maximum depth of penetration of the current to be 0.2L. This suggests that for a maximum value of (L) equals 160m, a depth of about 32m will be achieved which is the average depth of basement in the North Basement Complex of Nigeria (Danlami, 2011).

Data Processing

The apparent resistivity equation ρ_a = KR was used to process the acquired data and as thus; the resistance obtained for each reading was multiplied with its corresponding geometric factor and a corresponding apparent resistivity was obtained. The obtained data were processed using IP2WIN software program developed by Moscow State University. The data were plotted on a logarithm scale graph with the aid of the software that produce corresponding apparent resistivity model that reflects subsurface geology. The plots of models of the processed data are displayed in Figures 4.

3.0 RESULTS AND DISCUSSION

VES station 1 for Giwa Road, Narayi High Court (Figure 4), four geo-electric layers were delineated. The first geo-electric layer has an average resistivity value of 83.6 Ωm and a thickness of 0.74 m. The resistivity value of the second layer is 8.42Ω m and it extended from 0.74 m to 1.25 m. That is, it has thickness of about 0.513 m. The third layer has a resistivity value of 93.8 Ωm and thickness of 29.1 m and the final layer is characterized with a high resistivity value of 24764 Ωm. In VES station 2 for Giwa Road, Narayi High Court (Figure 5), the first geo-electric layer has an average resistivity value of 49.5 Ωm and a thickness of 0.75 m. The resistivity value of the second layer is 66.1 Ωm and it extended from 0.75 m to 6.02 m. That is, it has thickness of about 5.27 m. The final layer is characterized with a high resistivity value of 363 Ωm. The first geo-electric layer for VES station 3 (Figure 6) has an average resistivity value of 72.5 Ωm and a thickness of 2.53 m. The resistivity value of the second layer is 9.84 Ωm and has thickness of 4.06 m. The final layer is characterized with a high resistivity value of 7510 Ωm.

In VES station 1 (the only VES station) for U/Pama Sabo Thasha (Figure 7), the first geo-electric layer has an average resistivity value of 66.3 Ωm and a thickness of 0.75 m. The resistivity value of the second layer is 66.8 Ωm and it extended from 0.75 m to 22.4 m. That is, it has thickness of about 21.6 m. The final layer is characterized with a high resistivity value of 29579 Ωm.

Tables 1 and 2 below show the resistivity variation with thickness and depth range of all the collected VES data for Giwa Road, Narayi High Court and U/Pama Sabo Thasha respectively.

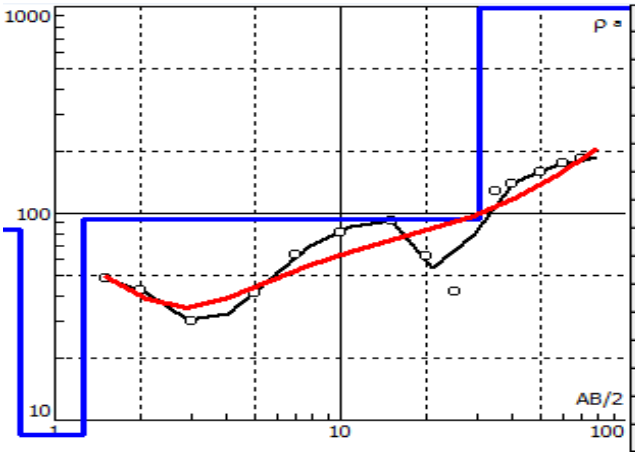

N	ρ	h	d	Alt
1	83.6	0.75	0.75	-0.75
2	8.42	0.513	1.26	-1.263
3	93.8	29.1	30.4	-30.36
4	24764			

Figure 4: The digitized model of interpreted VES station 1 for Giwa Road, Narayi High Court

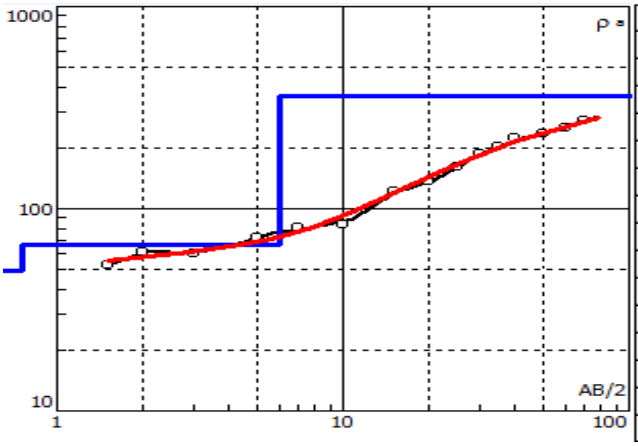

N	ρ	h	d	Alt
1	49.5	0.75	0.75	-0.75
2	66.1	5.27	6.02	-6.02
3	363			

Figure 5: The digitized model of interpreted VES station 2 for Giwa Road, Narayi High Court

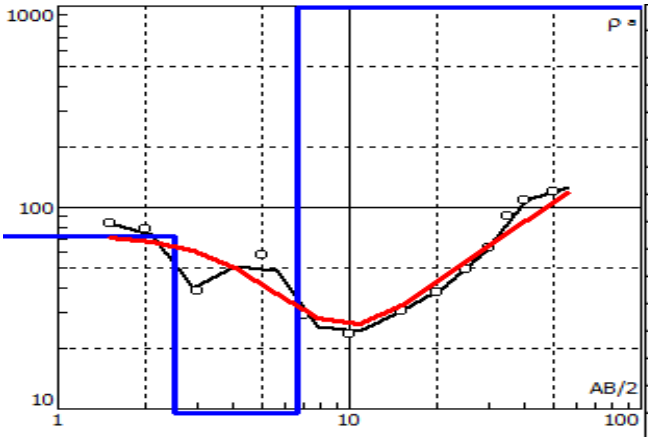

N	ρ	h	d	Alt
1	72.5	2.53	2.53	-2.53
2	9.48	4.06	6.59	-6.59
3	7510			

Figure 6: The digitized model of interpreted VES station 3 for Giwa Road, Narayi High Court

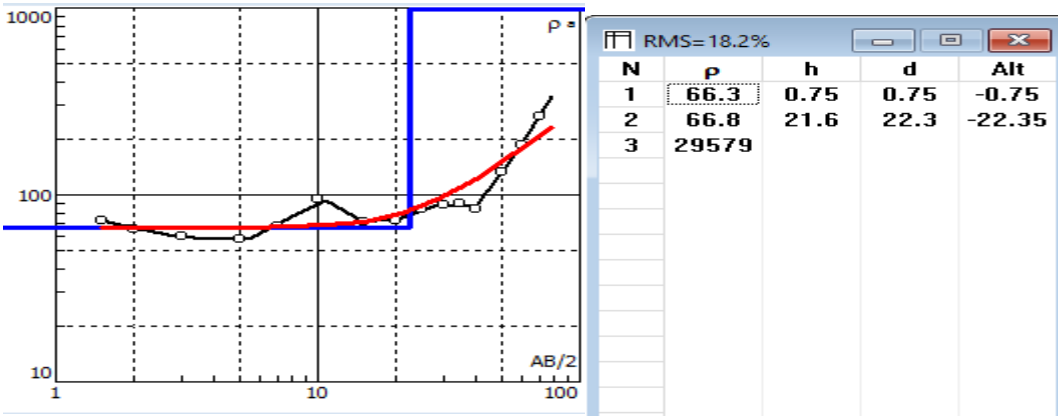

Figure 7: The digitized model of interpreted VES station 1 for U/Pama Sabo Thasha

Table 1: Summary of resistivity layers with depth and thickness of VES stations for Giwa Road, Narayi High Court

Sound No	Number of Layers	Depth (m)	Thickness (m)	App. Resistivity (Ωm)
VES 1	1	0.75	0.75	83.6
	2	1.26	0.513	8.42
	3	30.4	29.1	93.8
				24764
VES 2	1	0.75	0.75	49.5
	2	6.02	5.27	66.1
	3			363
VES 3	1	2.53	2.53	72.5
	2	6.59	4.06	9.48
	3			7510

Table 2: Summary of resistivity layers with depth and thickness of VES station for U/Pama Sabo Thasha

Sound No	Number of Layers	Depth (m)	Thickness (m)	App. Resistivity (Ωm)
VES 1	1	0.75	0.75	66.3
	2	22.4	21.6	66.8
	3			29579

VES station 1 for Giwa Road, Narayi High Court is considered suitable for groundwater exploration based on the low resistivity of the aquiferous layer bounded by high resistivity layers. VES station 1 for U/Pama Sabo Thasha is considered as most suitable site for groundwater exploration based on the low resistivity of the aquiferous layer bounded by high resistivity layers.

5.0 CONCLUSION

The layer with very low resistivity bounded above and below by high resistivity layers was considered as the aquiferous layer of the study area while the choice of suitable site for exploration of ground water was based on aquiferous layer with highest thickness. VES station 1 is recommended for Giwa

Road, Narayi High Court and VES station 1 (the only VES station) is also recommended for U/Pama Sabo Thasha and drilling should be done to the depths of 30.4 m and 22.4 m respectively based on the depths of the layers with low resistivity value bounded by high resistivity layers.

6.0 Acknowledgement
The authors appreciate National Water Resources Institute Mando, Kaduna State for providing data for this study.

References

Aboh, H.O. (2001). *Detailed Regional Geophysical Investigation of the Subsurface Terrain Structures in Kaduna Area, Kaduna State, Nigeria*. Unpublished Ph.D. Thesis, Physics Department, Ahmadu Bello University, Zaria.

Ajayi, C.O. and Hassan, M. (1990). The Delineation of the Aquifer Overlying the Basement Complex in the Western Part of Kaduna Basin of Zaria, Nigeria. *Journal of Mining and Geology,* (26), 117 – 125.

Arabi, A. S. (2010). *A Hydro Geophysical Investigation in three Locations in Kano State*. B. Sc. Project, Department of Geology, University of Maiduguri.

Ayoade, J.O. (1988). *Introduction to climatology for the tropics*. Spectrum books limited, Ibadan.

Danladi, G, (1985). *Appraisal of Hydrogeophysical Investigation in Shallow Basement Area of Zaria, Kaduna State*. Unpublished M. Sc. Thesis, Geology Department, Ahmadu Bello University, Zaria.

Danlami, B. (2011). *A Geoelectrical Delineation of Aquifer and Quantitative Estimation of its Recharge: A Case Study of Damari, Kaduna State, Nigeria*. Unpublished B. Sc. Project, Department of Physics, Ahmadu Bello University, Zaria.

Idris, A. M. (2011). *A Geoelectric Survey of Underground Water at the Ahmadu Bello University Zaria Central Mosque Using Vertical Electrical Sounding*, Unpublished B.Sc. Project, Department of Physics, Ahmadu Bello University.

Martin, N. D. (2015). *Access to Pipe-Borne Water in Kaduna South Local Government Area of Kaduna State, Nigeria.* A Published M. Sc. Thesis, Department of Geography, Ahmadu Bello University, Zaria.

Oguntoyinbo, J.S., Areola O.O. and Filani, M. (1983). *A Geography of Nigerian Development Second Edition*. Edited by Heinnemann educational books, Nig. Limited.

Olaniyi, I.O. and Olabode, T.O. (1998). Assessment of the Groundwater Potentials of a Typical Fadama Area, Kaduna state, N*igeria Journal of Engineering,* Published by C.O.E Kaduna Polytechnic, (1), (2), 86 – 92.

Olatunji, S. (1999). *Geophysical Site Investigation of the Federal College of Education, Zaria, Nigeria*. Unpublished M. Sc. Thesis, Physics Department, Ahmadu Bello University, Zaria.

Parkhomenko, E. I. (1967). Electrical properties of rocks: *New York, Plenum Press*, 314.

Raimi, J. (2005). *The Use of Vertical Electrical Sounding in the investigation of groundwater potential of Nigeria Army School of Military Police (NASMP) Zaria, Kaduna State, Nigeria*. Unpublished M.Sc. Project, Department of Physics, Ahmadu Bello University, Zaria.

Raimi, J., Arabi A.S. and Dewu B.B.M (2010). *A Geo Electric Survey for Determination of Suitable Sites for Construction of Tube-Wells for the Proposed Damari Irrigation Scheme in the North Central Basement Complex, Nigeria*. A Geophysical Report, Department of Physics, Ahmadu Bello University, Zaria.

Shemang, E.M. (1990). *Electrical Depth Soundings at Selected Well Sites within the Kubani River Basin, Zaria, Nigeria*. Unpublished M. Sc. Thesis, Physics Department, Ahmadu Bello University, Zaria.

APPLICATION OF FREQUENCY DOMAIN ELECTROMAGNETIC FOR MAPPING GOLD MINERALIZATION POTENTIAL IN IPERINDO, ILESHA SCHIST BELT, SOUTHWESTERN NIGERIA

Ahmed Kehinde Usman[1,2]*, Olawale Olakunle Osinowo[2,3], Raimi Jimoh[1], Echeche Onuh[1]
[1]Department of Physics, Ahmadu Bello University, Kaduna, Nigeria
[2]Pan African University, Earth and Life Sciences Institute, University of Ibadan, Ibadan, Nigeria
[3]Department of Geology, University of Ibadan, Ibadan, Nigeria
*Corresponding author E-mail:akusman@abu.edu.ng

ABSTRACT

Gold is a precious metal of high commercial value and great economic importance that Nigeria is endowed with. There are reports of artisanal mining (with associated ills such as banditry, communal clashes and environmental degradation) of the resource in-place of commercial exploitation which is able to contribute meaningfully towards the GDP growth of the country. This study applied Frequency Domain Electromagnetic geophysical investigation technique to evaluate the gold mineralization potential of Iperindo in Ilesha Schist Belt, southwestern Nigeria, where thriving artisanal mining of the resource have been reported and commercial exploitation capable of generating revenue and employment for the inhabitants has been challenged by lack / inadequate subsurface geological/geophysical information. The sorted and gridded electromagnetic data acquired through six (6) 336 m long E – W trending profiles, established 10 m apart from each other, delineate isolated near surface but thick (> 40 m) high conductivity zones. Some of the delineated high conductivity zones (14 – 22.12 mS/m) present vertical sharp edges, likely created by vertical faults that flank the zones on both sides. The high conductivity of these zones could be attributed to the occurrence of conductive material such as gold and associated base metals which probably exist in pegmatitic veins within the zones.

Keywords: gold mineralization; high conductivity zones, pegmatitic veins; Iperindo.

INTRODUCTION

Gold is a precious metal of high commercial value and great economic importance that Nigeria is endowed with. Gold occurrences have been reported in alluvial and eluvial placers and as primary veins from several parts of the Schist Belts in the northwest and southwest of Nigeria (Garba, 2002). Along with many of the nation's natural resource endowments, an estimate of total gold reserves in the country is unknown. This can be attributed to the mainly artisanal nature of the gold mining industry in the country and the lack of appropriate data and where the data are available; they are scanty and unreliable in nature. Gold mineralization in Nigeria has been described as orogenic, controlled by deep seated fracture system. In the Ilesha and Egbe areas, gold occurs in the amphibolites in amounts above the average primary gold content for similar rocks and it is sufficient to provide the source of some of the alluvial deposits (Elueze, 1981; Garba, 1985).

In this work, Frequency Domain Electromagnetic technique was applied to delineate possible anomalous gold concentration veins in the host rock around Iperindo in Ilesha schist belt, southwestern Nigeria. Geophysics is aspect of geology which studies the physical properties of the earth and its surrounding atmosphere. Geophysics principles have been successfully used in solving ground water,

mining, civil engineering and environmental problems, (Raimi, 2005). Electromagnetic (EM) measures the ease of flow of electric current through the earth (Reynolds, 1997). The EM techniques depends on the response of the ground to the propagating alternating field which can be generated by passing alternating current through either a small coil made up of many turns of wire or through a large loop of wire (Telford *et al*., 1990).

Electromagnetic technique measures apparent ground conductivity σ_a (equation (1)) as a function of coil separation (s), the operating frequency, f, the magnetic permeability of vacuum $\mu_0$and the ratio of the amplitudes of the secondary and primary electromagnetic fields $\frac{H_s}{H_p}$.

$$\sigma_a = \frac{4}{\omega \mu_0 s^2} \frac{H_s}{H_p} \quad (1)$$

where, $\omega = 2\pi f$. This indicates that depth of investigation depends on the frequency of the inducing field and the conductivity of the medium of propagation, the lower the frequency and the terrain conductivity the deeper the depth of penetration (Telford *et al*., 1990; Kearey *et al*., 2002).

GEOLOGY OF THE STUDY AREA

This work was carried out in Iperindo, part of Ilesha Schist Belt, southwestern Nigeria. It is located between latitude 7^o 25' N – 7^o 45' N and longitude 4^o 35' E – 4^o 55' E (Figure 1), situated within the Basement Complex of southwestern Nigeria. The Basement Complex itself has been reported by several authors to comprise largely of a metasedimentary series with associated minor metaigneous rocks that have been variably altered to migmatitic gneisses, and the Older Granites suite of both intrusive and replacement origin (Jones & Hockey, 1964: Grant, 1971; Burke *et al*., 1976). The study area is mainly underlain by granite gneiss (Figures 1 & 2) and intruded by pegmatite veins as well as quartzite and quartz schist which may be gold bearing. Other rocks in the area include migmatite, quartz feldspathic granulite, gneiss and schist. Most rocks within the study area mainly strike approximately N – S and dip between 70° - 80° W in schist and up to 80°W in quartz schist. The pegmatites and quartz veins generally intruded the host rocks as near vertical dyke with average dip of 75° having sharp to diffuse contact with the host rocks.

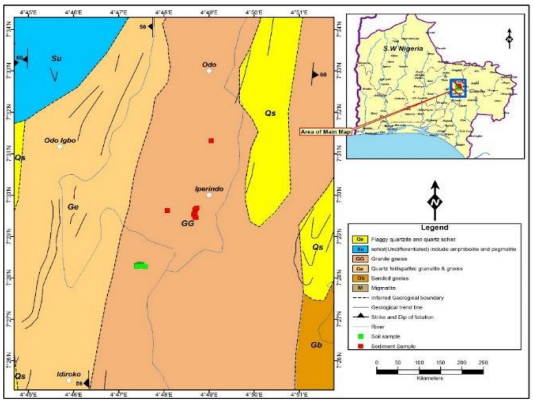

Figure 1: Geological Map of the Study Area (Adapted From NGSA, 2009).

Figure 2: Some Rock Outcrops in the Study Area.

MATERIALS AND METHODS

Data acquisition was carried out using Geonics EM34-3 Terrain Conductivity Meter (Figures 3). It is a Frequency Domain Electromagnetic (FDEM) geophysical equipment which operates on the principle of electromagnetic induction to interact with the subsurface and collect data on the electrical properties of the earth. The system consists of two coils, the transmitter and the receiver coils, each attached to separate console units through cable connections. The transmitter coil and console were used to generate the primary electromagnetic fields, while the receiver coil and console were used to analyze the secondary electromagnetic fields and take readings.

Six (6) 336 m length E –W profiles which run perpendicular to the general geological strike of the study area were established at 10 m inter profile separation (Figure 4). Station interval separation of 10 m was used to achieve a close coverage of the subsurface. Electromagnetic profiling was done using three different intercoil spacing, first with 10 m intercoil spacing, followed by that of 20 m and finally with 40 m with three different operating frequencies of 6.4, 1.6 and 0.4 KHz respectively. At each intercoil spacing, both the vertical and horizontal coplanar modes were recorded. The vertical coplanar corresponds to the horizontal dipole, while the horizontal coplanar corresponds to the vertical dipole mode. The receiver samples only the quadrature component of the secondary electromagnetic field to give direct reading of apparent conductivity in milliSiemens per metre (mS/m). Individual station points were georeferenced, using Global Positioning System (GPS) to record the longitude, latitude and elevation of each station.

Figure 3: Geophysical Crew Deploying Geonics EM34-3 Terrain Conductivity Meter

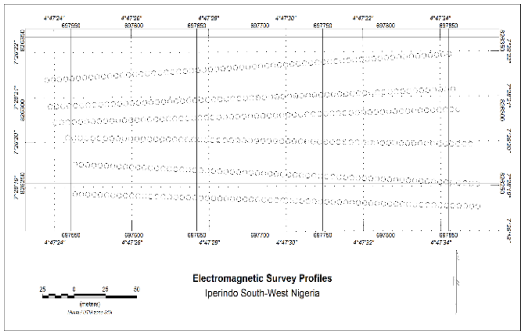

Figure 4: Electromagnetic Conductivity Survey Profiles Base Map.

DATA PROCESSING

Quality check was first performed on the data for consistency and presence of erroneous results.

The results were interpreted qualitatively by observing the spatial distribution of the conductivity values. On the field, the electromagnetic conductivity data were monitored for consistency, and stations were reoccupied in cases where spurious were obtained.

Georeferenced individual conductivity point data which have been sorted into different corresponding depths were pooled together using Oasis Montaj visualization software application. The visualization application gridded the data using Kriging gridding methods (Chiao *et al*., 2014) and generate 2D geoelectric sections, maps and 3D subsurface conductivity model. These were employed to evaluate

the gold potential of the Iperindo axis of the Ilesha Schist belt in terms of the ground conductivity distribution which is able to delineate zones of anomalous ground conductivity.

RESULTS AND DISCUSSIONS

The processed subsurface conductivity data which indicate the ground conductivity distributions are presented as 2D sections, iso depth conductivity maps, conductivity fence diagrams and 3D subsurface conductivity models which enable the evaluation of the variation in geoelectric properties of the ground in a 3D space (Osinowo *et al*., 2018). The various apparent conductivity results in milliSiemens per metre (mS/m), obtained from the study, indicate variation in subsurface electrical properties which often reflects changes in rock properties, especially properties that are associated with changes in lithology, porosity, permeability, clay content, degree of fracturing, groundwater saturation or leachate contamination (Friedman, 2005). The sorted and gridded model conductivity section of profile 1 is presented in Figure 5A. The profile which trends along E - W direction of the study area present subsurface conductivity distribution beneath the 336 m long profile station and imaged up to 60 m below the surface. The profile shows apparent conductivity distribution that range in value from 2.69 to 22.59 mS/m. The near surface, about 20 m below the surface, generally display relatively low apparent conductivity distribution which range in value from 2.69 – 11.00 mS/m. High apparent conductivity values (14.00 – 22.59 mS/m) generally characterize the deeper part of the subsurface extending up to a depth of 50 m. Low apparent conductivity values (5.00 – 11.00 mS/m) are recorded at depths of about 50 m to 60 m. The high conductivity zone displays vertical contact with the host rock and appears like a vertical fractured zone, which reveals a likely structural feature that looks like a dyke of high conductivity zone. The zone could be attributed to the presence of high density of mineralized veins between the vertical fractures. The mineralized veins could also be saturated with water or clay or a combination of all. The apparent conductivity section of profile 2 is presented in Figure 5B. The profile section indicates subsurface conductivity distribution that range in value from 4.26 to 22.16 mS/m across the profile station up to 60 m depth. This profile shows relatively low apparent conductivity values (4.26 – 11.00 mS/m) at shallow depths down to 20 m in the northeast and northwest parts. High apparent conductivity values (14.00 – 22.16 mS/m) are recorded at depths of 20 m to 60 m.

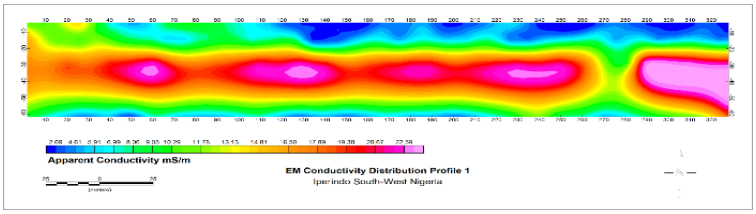

Fig. 5: A) EM Conductivity Sections for Profile 1

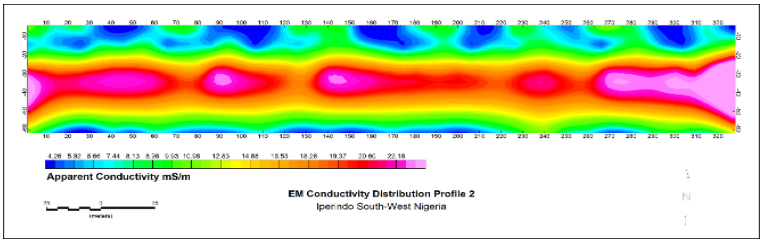

Fig. 5: B) EM Conductivity Sections for Profile 2.

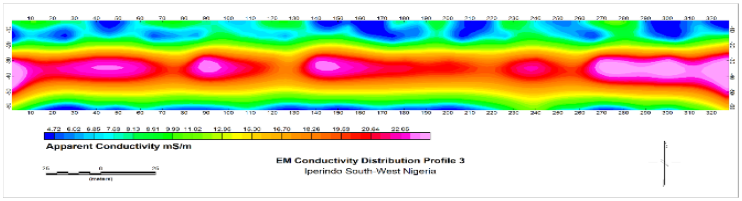

Fig. 5: C) EM Conductivity Sections for Profile 3.

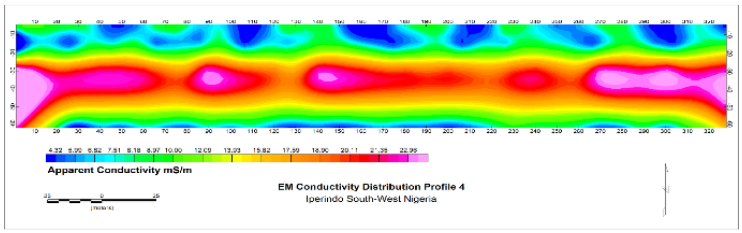

Fig. 5: D) EM Conductivity Sections for Profile 4.

In profile five (Figure 5E), apparent conductivity values range from 4.27 to 24.20mS/m up to a depth of 60 m beneath the surface. This profile shows relatively low apparent conductivity values (4.27 – 11.00 mS/m) at shallow depths of 1 m up to 20 m with isolated zones of high apparent conductivity value (15.00 mS/m) in the northeastern part. High apparent conductivity values (14.00 – 22.96 mS/m) are recorded from east to west at depths of 20 m to 60 m which decrease at depths of about 50 m to 60 m in the southern part of the profile line. Profile six (Figure 5F) shows apparent conductivity values range from less than 4.97 to 22.51mS/m up to a depth of 60 m beneath the surface. The conductivity distribution map shows relatively low apparent conductivity values (4.97 – 11.00 mS/m) at shallow depth up to 20 m and grades higher (15.00 – 22.51 mS/m) at depths of about 20 m to 50 m on the profile line.

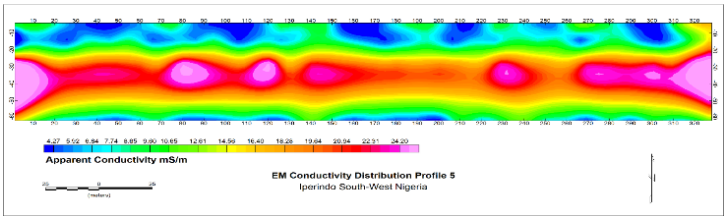

Fig. 5: E) EM Conductivity Sections for Profile 5.

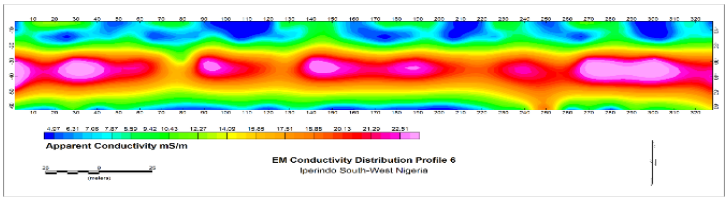

Fig. 5: F) EM Conductivity Sections for Profile 6.

The integrated individual georeferenced, filtered, gridded and depth sorted conductivity data obtained from all the occupied electrode stations along all the six (6) profiles generated 3D subsurface resistivity

distribution of the study area (Figure 6). The 40 m by 336 m by 67.5 m 3D conductivity distribution image shows conductivity variation along the x, y and z directions. The image indicates that conductivity value range from < 4.44 to 22.12 mS/m across the entire study area. The 3D resistivity image generally indicates dominantly low apparent conductivity distribution (4.44 to 11.00 mS/m **Ω**m) across the study area with isolated high apparent conductivity zones (19.00 – 23.00 mS/m) restricted to the eastern and western ends of the study area. The image also shows that the relatively high conductivity region occurs shallow and close to the surface, occurring not more than 50 m where it occurred deepest (Figure 7). The image also reveals more than 90% of the bottom section has a low apparent conductivity (3.00 – 10.00 mS/m) with some portion of high apparent conductivity (13.00 – 15.00 mS/m) corresponding to the fresh/unweathered Basement Complex of southwestern Nigeria.

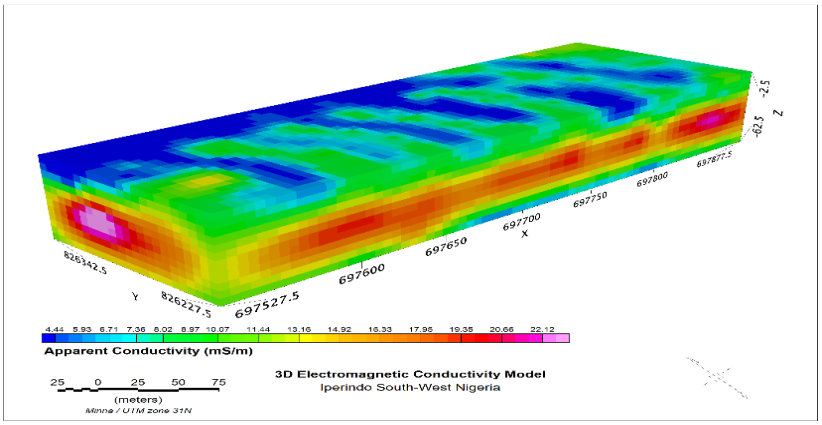

Fig. 6:3D EM Conductivity Distribution Image of the Study Area.

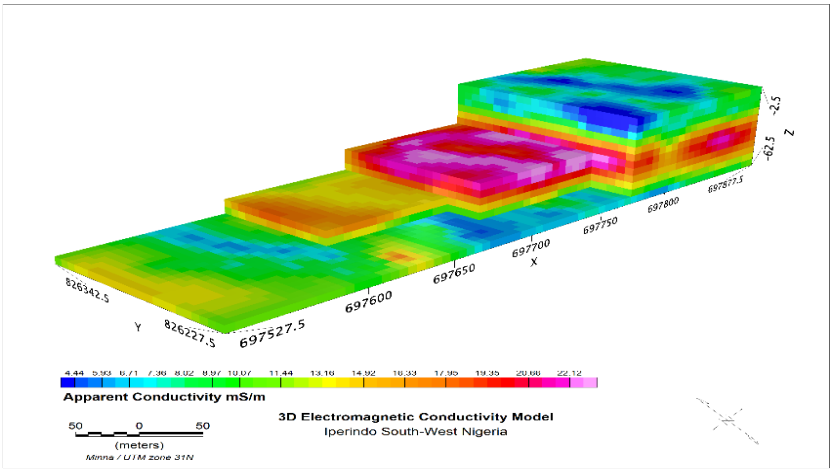

Fig. 7: Sliced EM Conductivity 3D Model to Reveal Desired Parts of the Model.

Iso depth surface conductivity distribution maps extracted from the 3D image is presented in figure 8. The figure shows seven (7) depth conductivity distribution maps extracted at 5 m, 10 m, 20 m, 30 m, 40 m, 50 m and 60 m to evaluate the variation in conductivity with depths across the study area. The iso depth conductivity distribution map at 5 m and 10 m depths display near surface conductivity distribution pattern which is dominantly low and heterogeneous (< 4.44 – 11.00 mS/m.) in nature. The iso depth conductivity maps indicate that the subsurface conductivity distribution across the study area

gradually increases with depth. At 20 m depth, the conductivity distribution varies from 11.00 to 19.00 mS/m which shows section (more than 50%) of high apparent conductivity above 15.00 mS/m. The lateral extent as well as the conductivity value of the pattern gradually increases with depth. At 50 m and 60 m below the surface, the low apparent conductivity (4.44 – 12.00 mS/m) with small portion of apparent conductivity ranging from 12.00 – 16.00 mS/m.

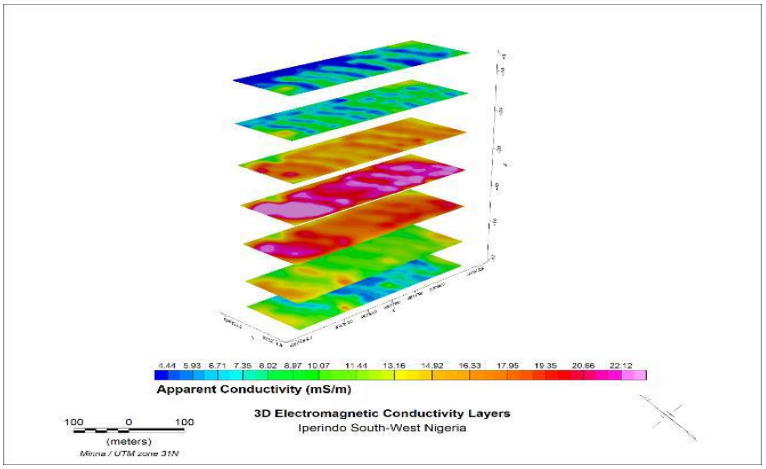

Fig. 8: Iso Depth Conductivity Map Across the Study Area.

Figure 9 presents conductivity fence diagram constructed from sets of N –S and E –W trending conductivity distribution sections which intersect themselves at right angles. The diagram, generated from the 3D conductivity model enables the evaluation of the variation of the conductivity pattern along some of the established profiles as well as across some intersecting sections. This way the pattern of conductivity distribution of the subsurface of the studied part of Iperindo situated in Ilesha Schist belt of southwestern Nigeria is appreciated. The conductivity fence presents apparent conductivity distribution that range from 4.44 to 22.12 mS/m, with some isolated zones of high conductivity values (14.00 to 22.12 mS/m) situated on some of the intersecting section walls of the fence. The zones of high conductivity as observed from the fence are restricted to the upper parts of the section walls.

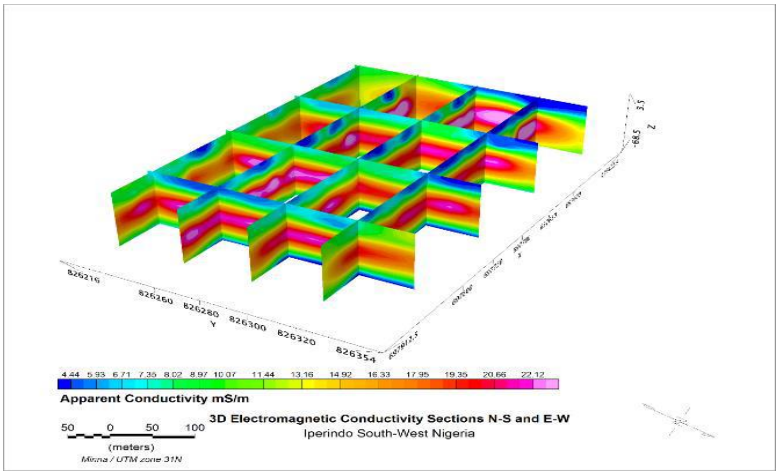

Fig. 9: Conductivity Fence Diagram from N – S and E – W Conductivity Sections.

The evaluation of electrical conductivity data generated from six (6) sets of E – W trending profiles occupied at a part of Iperindo in Ilesha Schist belt southwestern Nigeria has identified some isolated zones of conductivity distribution together with well distributed and extensive zone of low conductivity zone. The low conductivity value likely corresponds to fresh, unfractured and unweathered Basement Complex rocks of part of the Schist belt in southwestern Nigeria. On the other hand, the high conductivity zones which appeared mostly situated close to the surface are likely structurally controlled judging from the displayed linear vertical bounding edges that appeared associated with two vertical faults that flank some of the high conductivity zones on both sides. The high conductivity zones flanked by two vertical faults likely composed of several other fractures and veins situated between the two major upright vertical faults. The veins appear to be saturated with conductive materials such as base metals, gold, groundwater or clay. The conductive materials likely occur in association with pegmatitic veins which are possibly mineralized.

CONCLUSION

The imaging ability of frequency domain electromagnetic has been demonstrated in this study to evaluate gold mineralization potential of part of Iperindo in Ilesha Schist belt, southwestern Nigeria. The study identified relatively shallow high conductivity zones with possible mineralization of gold or other base metals occurring in pegmatitic veins situated within the high conductivity zones. The high conductivity zones, some of which are as deep as 60 m from the surface can be validated with geochemical drilling to quantitatively evaluate the gold mineralization potential of the area. The importance of subsurface information as such generated from geophysical investigation cannot be overemphasized, especially to generate requisite subsurface information for commercial development of gold mineralization potential of the Ilesha Schist belt. This could generate royalty tax for the government and employment for the inhabitants instead of the thriving artisanal mining activities in the area.

ACKNOWLEDGEMENT

The authors appreciate Pan African University for providing fund for this study.

REFERENCES

Burke, K.C., Freeth, S.J. and Grant, N.K. (1976). The Structure and Sequence of Geological Events in the Basement Complex of Ibadan Area, Western Nigeria, Prec. Res. Vol. 3 No. 6, 1976. https://doi.org/10.1016/0301-9268 (76)90017-6.

Chiao, L., Chen, Y., Gung, Y., 2014. Constructing empirical resolution diagnostics for kriging and minimum curvature gridding. J. Geophys. Res.: Solid Earth 119 (5), 3939e3954. https://doi.org/10.1002/2013JB010364.

Friedman, S.P., 2005. Soil properties influencing apparent electrical conductivity. Comput. Electron. Agric. 46, 45e70.https://doi.org/10.1016/j.com-pag.2004.11.001.

Garba, I. (1985). Geological and geochemical investigations of the gold occurrences north of Isanlu, Kwara State, Nigeria. *Unpublished M. Sc. Thesis, Ahmadu Bello University, Nigeria*.

Garba, I. (2002). Late Pan-African tectonics and origin of gold mineralization and rare-metal pegmatities in the Kushaka schist belt, northwestern Nigeria. *Journal of mining and geology, 38*(1), 1-12.

Grant, N.K. (1971). South Atlantic, Benue Trough and Gulf of Guinea Cretaceous Triple Junction. *Bull. geol. Soc. Am.* 82,2295-2298. https://doi.org/10.1130/0016-7606(1971)82[2295:SABTAG]2.0.CO;2.

Jones, H. A., and Hockey, R. D. (1964). The Geology of Part of Southwestern Nigeria *Geological Survey of Nigeria* (Bulletin 31), 1-101.

Kearey, P., Brooks, M., & Hill, I. (2002). An Introduction to Geophysical Exploration, ix+ 262 pp: Oxford: Blackwell Science. Price.

NGSA (2009). Nigerian Geological Survey Agency's Lineament and Geological Map of Nigeria, Scale 1:100 000.

Osinowo, O. O., Falufosi, M. O., & Omiyale, E. O. (2018). Integrated electromagnetic (EM) and Electrical Resistivity Tomography (ERT) geophysical studies of environmental impact of Awotan dumpsite in Ibadan, southwestern Nigeria. *Journal of African Earth Sciences, 140*, 42-51. https://doi.org/10.1016/j.jafrearsci.2017.12.026.

Raimi, J. (2005). *The Use of Vertical Electrical Sounding in the investigation of groundwater potential of Nigeria Army School of Military Police (NASMP) Zaria, Kaduna State, Nigeria*. M.Sc Project. Department of Physics. Ahmadu Bello University, Zaria.

Reynolds, J.M., 1997. An Introduction to Applied and Environmental Geophysics, vol.2. John Wiley and Sons Ltd., West Sussex, p. 796.

Telford, W. M., Telford, W., Geldart, L., Sheriff, R. E., & Sheriff, R. (1990). *Applied geophysics* (Vol. 1): Cambridge university press.

Palynostratigraphy, Biochronology and Paleobathymetry of a section of Awaizombe-1 Well in the Eastern Niger Delta, Nigeria

Jacinta Nkiru Chukwuma-Orji
Federal University of Technology, Department of Geology, Minna, Nigeria;
e-mail: jacinta@futminna.edu.ng

Abstract

The ditch cutting samples from a section of Awaizombe-1well located in the Northern Delta depobelt of eastern Niger Delta were analysed for palynomorphs content using acid method of sample preparation for palynormorphs recovery. The analysis recorded well-preserved and diverse assemblage of palynomorph, rich in pollen, spores and dinoflagellate cysts. The first and last occurrences of marker species, such as Racemonocolpites hians, Psilatriporites sp., Doualaidites laevigatus, Praedapollis africanus, Homotryblium oceanicum, Praedapollis flexibilies, Retitricolpites ituensis, Verrucatosporites usmensis and Retimonocolporites sp. were used for the biostratigraphic interpretation. The following interval range zones were established: Psilatriporites sp. – Racemonocolpites hians Zone, dated Early Oligocene (Rupelian age), Praedapollis africanus – Doualaidites laevigatus Zone, dated Late Eocene (Priabonian age), Doualaidites laevigatus – Praedapollis flexibilies Zone, dated Middle Eocene (Lutetian and Bartonian ages) and Verrucatosporites usmensis - Retitricolpites ituensis Zone, dated Early Eocene (Ypresian age). The first downhole occurrence of Doualaidites laevigatus at the 1482 m marks Late Eocene/Early Oligocene boundary. Paleoenvironmental and paleobathymetric interpretations using environmental/bathymetric diagnostic species revealed two environments: brackish/fluvio-marine and inner neritic to outer neritic (0 – 200 m) under relatively warm-water marine condition indicated by thermophilic dinocyst taxa, such as Lingulodinium machaerophorum, Polysphaeridium zoharyi and Homotryblium sp.

Key words: Palynostratigraphy, biochronology, paleobathymetry, Awaizombe-1 Well, Niger Delta, Nigeria

Introduction

The geographic coordinates for the Awaizombe-1 well section are latitude 5°60′ N and longitude 6°98′ E belonging to the Northern Delta Depobelt of Niger Delta Basin (Figure 1). The Northern Depobelt of Niger Delta Basin consists of paralic sequences and alluvial sands that cap the paralic sequences. The paralic sequence is of Late Eocene to Early Miocene while the alluvial sand is of Early Miocene (Doust and Omatsola, 1990). Okosun and Osterloff (2014) studied the ostracod, diatom and radiolarian biostratigraphy of the Awaizombe-1 well, Niger Delta Basin. The authors made documentary record of the ostracods, diatoms and radiolarians species recovered from the Awaizombe-1 well. However, the present work focuses on the palynostratigraphy, biochronology and paleobathymetry interpretation of a section the well (1373-1812 m depth). Palynomorphs can be very useful in the estimation of paleobathymetry due to the tiny size, high abundance in small samples, and wide distribution over terrestrial and marine environment, high taxonomic diversity, short ranges and preference for specific environmental conditions by some species. Different palynomorphs are indicators of a particular paleodepth: these depths could be terrestrial, shelf, slope, marine or abyssal.

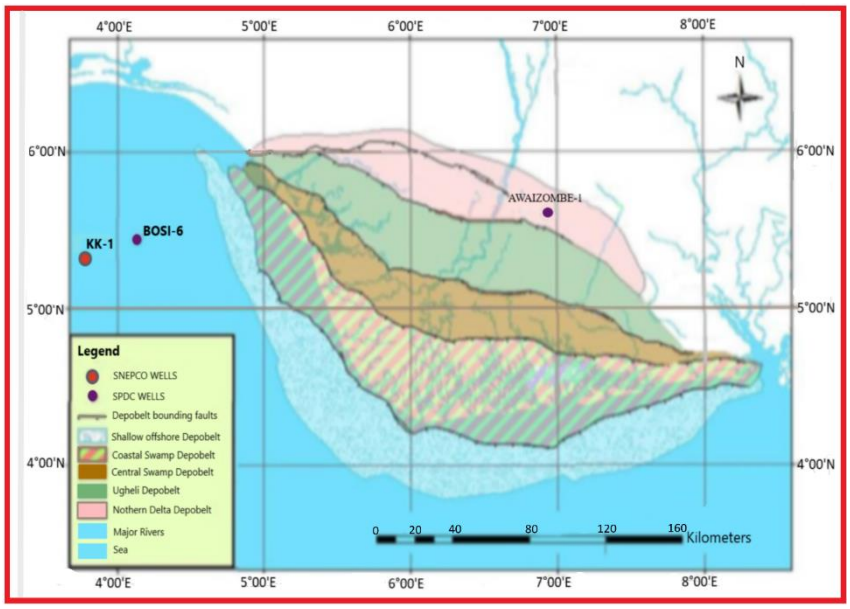

Figure 1: Location of the Awaizombe-1well (Modified after Okosun and Osterloff, 2014).

Geological Setting and Stratigraphy

The geology of the Niger Delta Basin comprises of Akata, Agbada and Benin Formations (Bankole, 2010). The Akata Formation is generally of open marine and prodelta dark grey shale with lenses of siltstone and sandstone. The age of the Akata Formation ranges from Paleocene in the proximal parts of the delta to Recent in the distal offshore. The Agbada Formation consists of cyclic coarsening-upward regressive sequences composed of shales, siltstones, and sandstones which include delta front and lower delta plain deposits ((Reijers *et al*., 1996)). The Agbada Formation ranges in age from Eocene to Holocene. The Benin Formation is the uppermost unit in Niger Delta Basin. The Benin Formation comprises a succession of Eocene to Holocene massive poorly indurated sandstones, thin shales, coals, and gravels of continental to upper delta plain origin. The Niger Delta Basin is one of the major regressive deltaic sequences in the world. The stratigraphic succession of the delta is over 12 km thick at the depocenter and occupies an area of 75,000 km^2 in the Gulf of Guinea (Ejedawe, 1981).

Materials and method

A total of 69 ditch cutting samples were prepared by the standard palynological acid maceration technique using hydrochloric (HCl) and hydrofluoric (HF) acids for carbonates and silicates removal. Fifteen grams of each sample were poured into well labeled plastic cups and arranged in a fume cupboard. Each sample was digested for 35 minutes in 40% hydrochloric acid for removal of carbonate and 24 hours in 40% hydrofluoric acid for the removal of silicate. Sieving was done using a brason sonifer to filter away any remaining inorganic matter (silicates. clay, and mud) and heavy minerals to concentrate organic matters present in the sample. Controlled oxidation was given to the sieved residue using concentrated nitric acid (HNO_3). The residue was stained with Safranin O, before being mounted on glass slides and analyzed with the aid of an Olympus Binocular light transmitted microscope.

Results and Discussion

The lithogy of the studied interval 1373 – 1812 m (439 m thick) consists of fissile grey shale and mudstone units (Figure 2). This is indicative of lower Agbada Formation (Short and Stauble, 1967).

The lower Agbada paralic units consist of thick shale unit and thin sandy units (Durugbo and Uzodimma, 2013).

The result of the analysis carried out on 69 ditch cutting samples of the studied Awaizombe-1 well consist of 89 palynomorphs specimens comprising of 58 pollen, 11 spores, 18 dinoflagellates cysts and 2 algae (Figure 2). The palynomorphs recovered are abundant, diverse, and well preserved in almost all the intervals. Photomicrographs of some of the recorded palynomorphs are presented in figure 3. The palynofloral assemblage was dominated by pollen and spores namely: *Laevigatosporites* sp., R*etimonocolpites obaensis, Psilatricolporites crassus, Zonocostites ramonae, Pachydermites diederixi, Acrostichum aureum, Verrucatosporites* sp., *Verrucatosporites usmensis.* Two algae were identified *Botryococcus braunii, Pediastrum* sp., and other notable dinoflagellate cysts include *Leiosphaeridia* sp., *Spiniferites* sp., *Polyspheridium zoharyi, Achomosphaera ramulifera, Oligosphaeridium pulcherimum, Lingulodinium machaerophorum.*

Palynostratigraphy/Palynozonation

Palynostratigraphy can be defined as the application of palynological methods to stratigraphy.
Sixty nine (69) ditch cutting samples from Awaizombe-1 well (interval 1373-1812 m) were processed for palynomorph recovery. The following flora interval zones were established using the first or last downhole occurrences (FDO or LDO) of age diagnostic palynomorphs recovered from the well (Table 1). The zones span Early Eocene (Ypresian) to early Oligocene (Rupelian). The zones were recognized based on the work of Murphy and Salvador (1999). The zones are described below from the youngest to the oldest.

Table 1: Established palynozones

Period		Epoch		Age	Age (Ma)	Palynozones (This Study)
Tertiary	Paleogene	Oligocene	Early	Rupelian	28.5 33.0	*Psilatriporites* sp – *Racemonocolpites hians*
		Eocene	Late	Priabonian	33.7	*Praedapollis africanus* – *Doualaidites laevigatus*
			Middle	Bartonian - Lutetian	49.0	*Doualaidites laevigatus* – *Praedapollis flexibilies*
			Early	Ypresian	54.8	*Verrucatosporites usmensis* – *Retitricolpites ituensis*

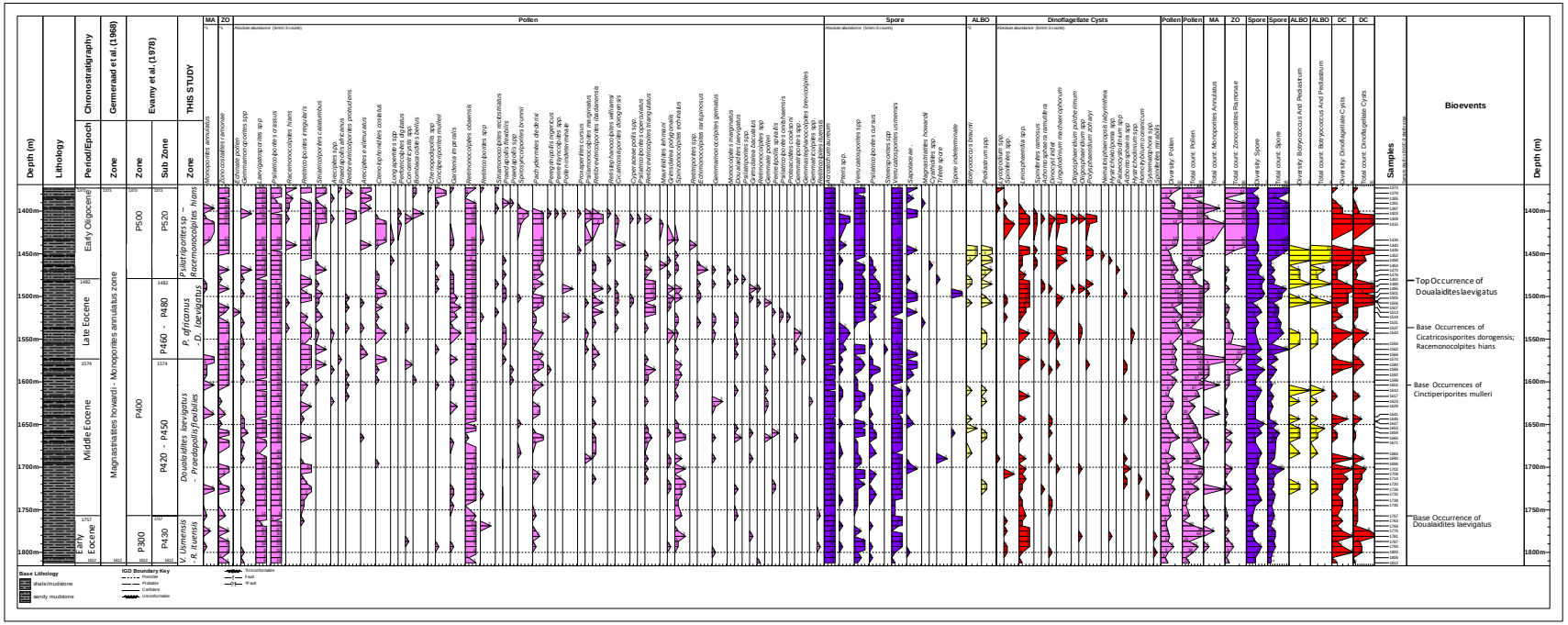

Figure 2: Palynomorph distribution chart of Awaizombe-1 well.

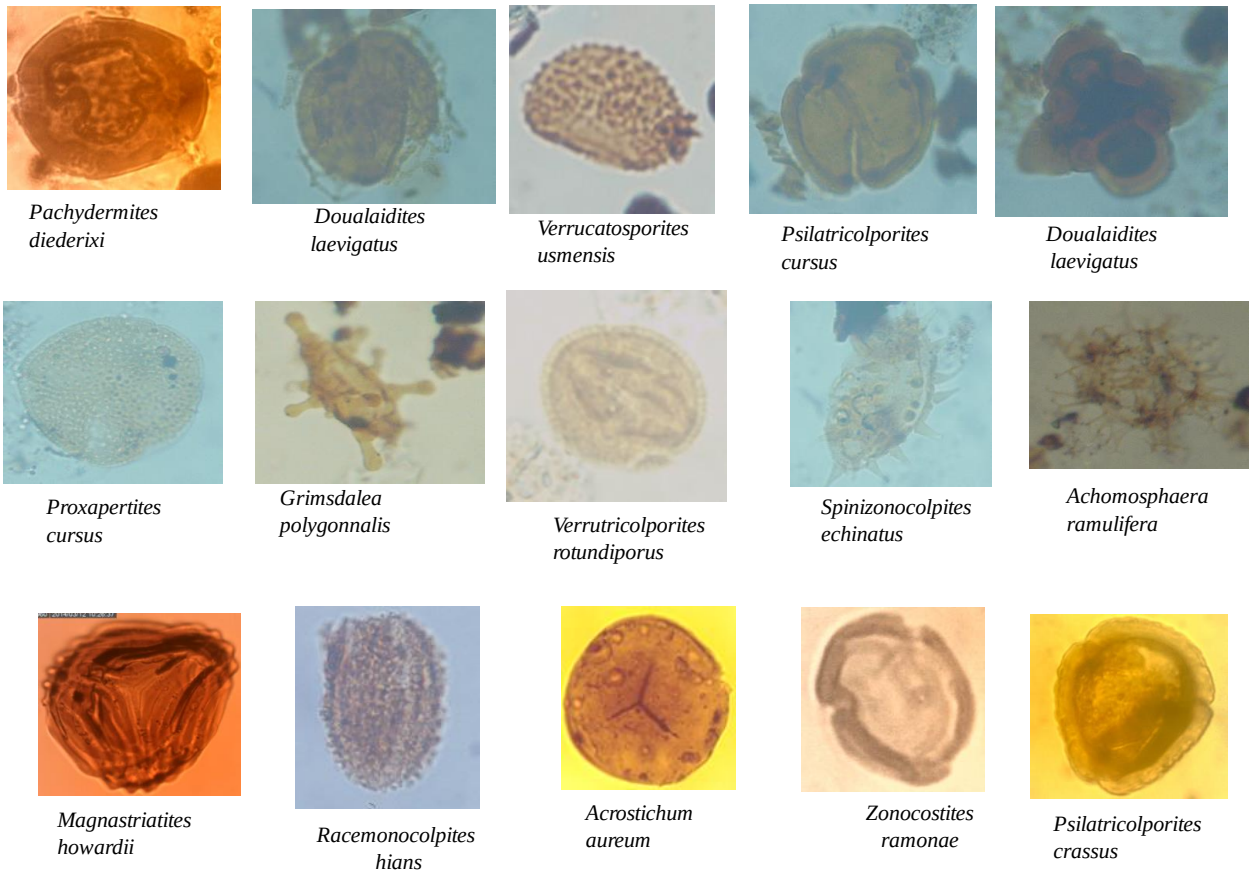

Figure 3: Micrograph of some palynomorph recovered (×400).

i. *Psilatriporites* sp – *Racemonocolpites hians* Zone (Interval range zone)

Stratigraphic interval: 1373-1482 m

Definition: The top of the zone is defined by the first downhole occurrence (FDO) *Racemonocolpites hians* while the base is marked by the first downhole occurrence (FDO) of *Psilatriporites* sp. and *Doualaidites laevigatus*. This zone is an interval range zone.

Characteristics: It is characterized by *Zonocostites ramonae, Doualaidites laevigatus*. Other characteristic palynomorphs within this zone include: *Acrostichum aureum, Pteris* sp., *Verrucatosporites* sp., *Zonocostites ramonae, Laevigatosporites* sp, *Psilatricolporites crassus* etc. This zone is also characterized by the first appearance of *Magnastriatites howardii, Monocolpites maginatus, Spinizonocolpites echinatus, Botrycoccus braunii, Pediastrum* sp., *Leiosphaeridia* sp., *Spiniferites ramosus, Spiniferites ramosus, Spiniferites* sp., *Polyspheridium zoharyi, Achomosphaera ramulifera, Nematosphaeropsis labyrinthea, Echmonocolpites gematus, Oligosphaeridium pulcherimum, Lingulodinium machaerophorum.*

Age: The zone is dated early Oligocene (Rupelian age. 33.0-28.5 Ma). This zone is equivalent to P500 zone and P520 subzone of Evamy et al. (1978). The FDO of *Doualaidites laevigatus* at the base of the zone (1482 m) is an indication of Late Eocene – Early Oligocene boundary. The FDOs of *Spinizonocolpites echinatus, Monocolpites marginatus, Oligosphaeridium pulcherimum, Oligosphaeridium* sp., *Spiniferites ramosus* and *Spiniferites* sp. within the zone are diagnostic of early Oligocene age.

ii. ***Praedapollis africanus – Doualaidites laevigatus* Zone (Interval range zone)**

Str atigraphic interval: 1482 -1574 m

Definition: The top of the zone is defined by the first downhole occurrence (FDO) of *Doualaidites laevigatus* while the base is marked by the last downhole occurrence (LDO) of *Praedapollis africanus*. This zone is an interval range zone.

Characteristics: Highly abundant and diverse palynomorphs were recovered within this zone which includes *Zonocostites ramonae, Laevigatosporites* sp., *Psilatricolporites crassus, Retimonocolporites obaensis, Leiosphaeridia* sp., *Verrucatosporites usmensis, Doualaidites laevigatus* and *Cinctiperiporites mulleri*. This abundant diversity at the upper part (1452-1604m) may have been due to the availability of light, oxygen for photosynthesis of the taxa.

Age: The zone is dated late Eocene (Priabonian age, 33.7-33.0 Ma). This zone is equivalent to P400 zone and P460-P480 subzone of Evamy et al. (1978). The LDO of *Peregrinipollis nigericus, Bombacacidites bellus* is diagnostic of late Eocene.

iii. *Doualaidites laevigatus – Praedapollis flexibilies* Zone (Interval range zone)

Stratigraphic interval: 1574 -1757 m

Definition: The top of the zone is defined by the last downhole occurrence (LDO) of *Praedapollis flexibilies* while the base is marked by the last downhole occurrence (LDO) of *Doualaidites laevigatus*. This zone is an interval range zone.

Characteristics: It is characterized by *Pachydemites diederixi, Cinctiperiporites mulleri, Doualaidites laevigatus, Zonocostites ramonae, Laevigatosporites* sp., *Acrostichum aureum* and *Psilatricolporites crassus*. The only (first and last) occurrence of *Gemmatricolporites* sp. at a depth of 1623 m was recorded within this zone.

Age: The zone is dated middle Eocene [Lutetian (49.0-41.3 Ma) - Bartonian (41.3-37.0 Ma) age]. This zone is equivalent to P400 zone and P420-P450 subzone of Evamy et al. (1978). The LDO of *Retibrevitricolporites protrudens, Ctenolophonidites costatus* are diagnostic of middle Eocene.

iv. *Verrucatosporites usmensis - Retitricolpites ituensis* Zone (Interval range zone)

Stratigraphic interval: 1757-1812 m

Definition: The top of the zone is defined by the last downhole occurrence (LDO) of *Retitricolpites ituensis* while the base is marked by the last downhole occurrence (LDO) of *Verrucatosporites usmensis*, *Retimonocolporites* sp.

Characteristics: The zone is characterized by few recoveries of palynomorph taxa, with clear absence of *Botryococcus braunii* and *Pediastrum* sp. evident at depth of 1757 m, suggesting no freshwater incursion within the interval. It is also characterized by considerably abundant recoveries of *Psilatricolporites crassus, Laevigatosporites* sp., *Retimonocolpites obaensis, Spinizonocolpites echinatus, Verrucatosporites usmensis, Verrucatosporites* sp., and *Leiosphaeridia* sp.

Age: The zone is dated Early Eocene (Ypresian age, 54.8-49.0 Ma). This zone is equivalent to P300 zone and P430 subzone of Evamy et al. (1978). The occurrence of *Monoporites annulatus, Verrucatosporites usmensis, Psilatricolporites cursus* and *Retitricolporites irregularis* are also diagnostic of early Eocene.

Paleoenvironmental/Paleobathymetric Interpretation

Paleobathymetry of Awaizombe-1 well was determined using the occurrences, co-occurrences and relative abundances of microfloral elements that are indicative of paleo-water depth. The composition and relative abundance of different types of palynomorphs are indicative of changes in paleobathymetry. Marine indicators or dwellers such as dinoflagellates are ideal for paleobathymetric/paleoenvironmental interpretations (Stover and Williams, 1982). They tend to be most abundant in rocks deposited in middle neritic to upper bathyal environments and their abundance decreases landward. Dinoflagellates used in paleoenvironmental/paleobathymetric interpretation include *Homotryblium oceanicum,* and *Polysphaeridium*

zoharyi (They proliferate inner neritic to oceanic warm and high saline water environments in subtropical to tropical regions which may have a high productivity); *Lingulodinium machaerophorum* (Inner neritic with low to normal salinity and temperate to warm water species. It is an indicator of nutrient enrichment reflecting increased productivity and may proliferate in the vicinity of the active upwelling cells or near river mouths); *Spiniferites* sp., *Spiniferites mirabilis, Achomosphaera* sp., *Hystrichosphaeropsis minimum* (Neritic to oceanic setting with stable salinity. This group can be cosmopolitan can also reach high relative abundances in high productivity areas such as upwelling regions and areas influenced by river discharge); *Nematosphaeropsis labyrinthea* (Outer neritic to bathyal species. Its occurrence indicates an increase in sea level) and *Leisphaeridia* sp. is suggestive of an outer neritic to upper bathyal (Stover et al., 1996; Chekar et al 2018). Other palynomorphs include spores, pollens, bissacate pollen and algae (Figure 4).

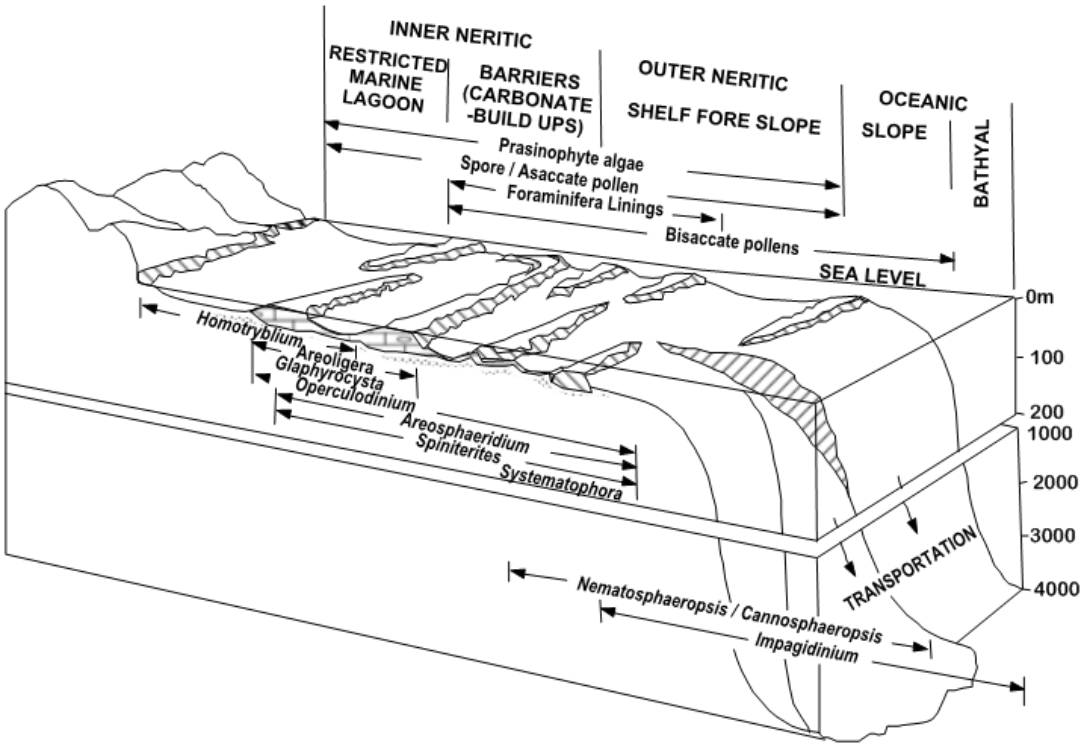

Figure 4: Palynomorphs distribution patterns from continental shelf – slope (Stover *et al*. 1996).

Relating the palynomorph distribution chart with figures 4 and 5, the paleobathymetric/paleoenvironmental interpretation of the studied well can be inferred as follows:

The interval of 1373 to 1391 m is inferred to have been deposited in brackish/fluvio-marine (terrestrial) environment, due to non-recovery of marine dinocysts indicators. Occuring within this interval are *Zonocostites ramonae, Racemonocolpites hians, Arecipites exilimuratus, Acrostichum aureum, Verrucatosporites usmensis, Retimonocolpites obaensis, Striatricolporites catatumbus, Verrucatosporites* sp., *Laevigatosporites* sp, *Psilatricolporites crassus Retitricolporites irregularis, Retbrevitricolporites protrudens* and *Cinctiperiporites mulleri*. These taxa suggest terrestrial environment.

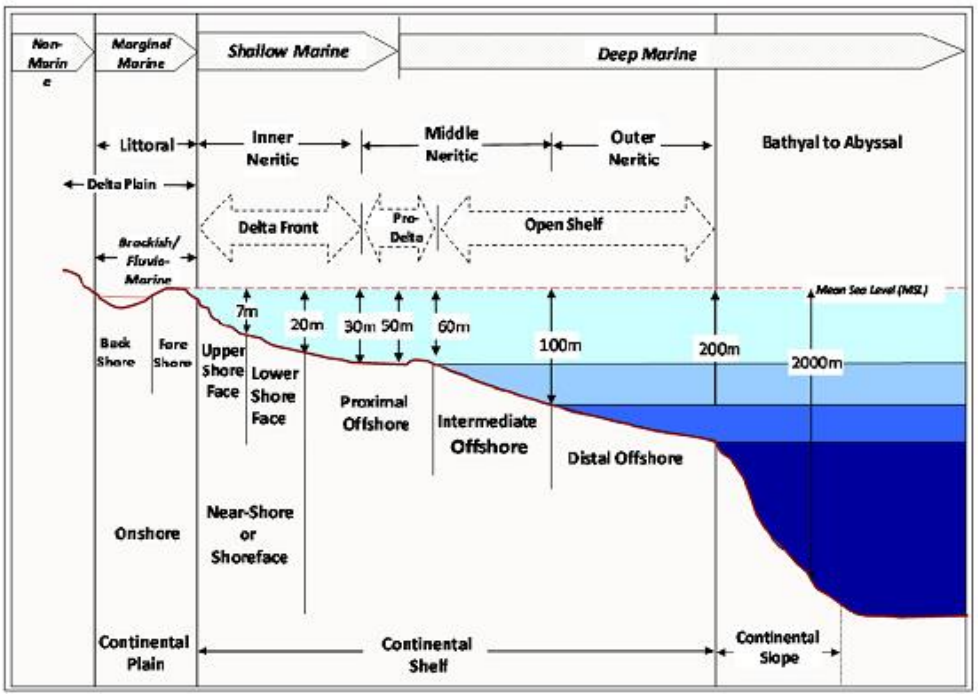

Figure 5: Depositional environments and paleobathymetric ranges used in paleoenvironmental interpretations (Ijomah *et al*., 2016).

The interval of 1391 to 1812 m is inferred to have been deposited within inner neritic to outer neritic environments (0 – 200 m). This deduction is due to the occurrences of *Leisphaeridia* sp. throughout the interval. Other dinocysts recorded within the include *Spiniferites* sp., *Spiniferites mirabilis, Spiniferites ramosus, Hystrichosphaeropsis minimum, Lingulodinium machaerophorum, Homotryblium oceanicum, Polysphaeridium zoharyi* (temperate to tropical species) and *Achomosphaera ramulifera, Achomosphaera* sp., *Nematosphaeropsis labyrinthea* (cool to temperate species) (Stover et al., 1996). The occurrence of *Botrycoccus braunii* and *Pediastrum* sp. Algae species within 1446 – 1726 m suggests fresh water incursion/influence. The thermophilic dinocyst taxa such as *Spiniferites ramosus, Spiniferites ramosus, Spiniferites* sp., *Polysphaeridium zoharyi, Lingulodinium machaerophorum,* and *Homotryblium* sp. suggest warm-water marine conditions with salinity of 7 – 10% salinity within temperate to tropical latitudes.

Conclusion

The palynological analysis of the Eocene–Oligocene succession from a section of Awaizombe-1 well in the Northern Delta depobelt of eastern Niger Delta reveals the presence of well-preserved and diverse assemblage of palynomorph, rich in pollen, spores and dinoflagellate cysts (dinocysts). The palynomorph marker events used for the biostratigraphic interpretations include the first and last occurrences of marker species, such as *Racemonocolpites hians, Psilatriporites* sp and *Doualaidites laevigatus, Praedapollis africanus Homotryblium oceanicum, Praedapollis flexibilies, Retitricolpites ituensis Verrucatosporites usmensis*, *Retimonocolporites* sp. The following interval range zones were established: *Psilatriporites* sp. – *Racemonocolpites hians* Zone, *Praedapollis africanus – Doualaidites laevigatus* Zone, *Doualaidites laevigatus – Praedapollis flexibilies* Zone and *Verrucatosporites usmensis - Retitricolpites ituensis* Zone.

The lowermost part of the Awaizombe-1 well is assigned to the Early Eocene (Ypresian age), the middle section is assigned Middle Eocene (Lutetian and Bartonian) and its upper part to the Late Eocene (Priabonian) and Early Oligocene (Rupelian). The first downhole occurrence of *Doualaidites laevigatus* at the 1482 m is an indication of Late Eocene/Early Oligocene boundary. The assigned age to the studied interval agrees with the previous work which stated that Northern Delta depobelt ranges from Eocene to Miocene (Doust and Omatsola, 1990). The established interval biozones are useful in inter and intra basin biostratigraphic

correlations. Qualitative and quantitative analyses permit paleoenvironmental and paleobathymetric interpretations. The occurrences of dinocyst groups, spores and pollen lead to the distinction, of two environments: brackish/fluvio-marine (terrestrial) and inner neritic to outer neritic (0 – 200 m) under relatively warm-water marine conditions with salinity of 7 – 10% salinity within temperate to tropical latitudes.

References

Bankole, S. I. (2010). Palynology and stratigraphy of three deep wells in the Neogene Agbada Formation, Niger Delta, Nigeria. Implications for petroleum exploration and paleoecology, PhD thesis, der Technischen Universität Berlin, 1-190.

Chekar, M; Slimani, H; Jbari, H; Guédé, K. E.; Imane Mahboub, I; Asebriy, L; and Habiba Aassoumi, H. (2018). Eocene to Oligocene dinoflagellate cysts from the Tattofte section, western External Rif, northwestern Morocco: Biostratigraphy, paleoenvironments and paleoclimate. Palaeogeography, Palaeoclimatology, Palaeoecology 507, 97–114

Doust, H. & Omatsola, E. (1990). Niger Delta divergent/passive margin basins, *American Association of Petroleum Geologists Memoir*, 48, 201-238.

Durugbo, E. U. and Uzodimma, E. (2013). Effects of lithology on palynomorph abundance in wells X1 and X2 from the Western Niger Delta, Nigeria. *International Journal of Geology, Earth and Environmental Sciences*, 3, 170 – 179.

Ejedawe, J. E. (1981). Patterns of incidence of oil reserves in Niger Delta basin. *American Association of Petroleum Geologists Bulletin*, 65, 1574 - 1585.

Evamy, B. D., Haremboure, J., Karmerling, P., Knaap, W. A., Molloy, F. A. & Rowlands, P. H. (1978). Hydrocarbon habitat of the Tertiary Niger Delta. *American Association of Petroleum Geologists Bulletin*, 62, 1-39.

Ijomah, A. K., Amajor, L. C. & Ugwueze, C. (2016). Sequence Stratigraphy and Hydrocarbon Analysis of Coastal Swamp Depobelt, Niger Delta, Nigeria. *Journal of Scientific and Engineering Research*, 3, 285 – 294.

Murphy, M. A. and Salvador, A. (1999). International Stratigraphic Guide - An abridged version, International Subcommission on Stratigraphic Classification of IUGS, International Commission on Stratigraphy, *Special Episodes*, 22, 255 – 272.

Reijers, T. J. A., Petters, S. W. & Nwajide, C. S. (1996). The Niger Delta basin, sedimentary geology and sequence stratigraphy. In T. J. A. Reijers (Ed.), *Selected chapters on geology* (pp. 100 - 117). Warri: SPDC Corporate Reprographic Services.

Short, K. C. and Stauble, A. J. (1967). Outline of the geology of Niger Delta, *American Association of Petroleum Geologists Bulletin*, 51, 761 - 779.

Stover, L. E., Brinkhuis, H., Damassa, S. P., De Verteuil, L., Herby, R. J., Monteil, E., Partridge, A. D., Powell, A. J., Riding, J. B., Smelror, M. and Williams, G. L. (1996). Mesozoic-Tertiary Dinoflagellates, Acritarchs and Prasinophytes in Jannsonius, J. and McGregor. D. C. (ed.), Palinology: Principles and Applications: American Association Stratigraphic Palynologists Foundationn Vol. 2, pp. 641-750.

Stover, L. E., and Williams, G. L. (1982). Dinoflagellates, Third North American Paleontological Convection, Proceedings, 2, 525-533

Geology and Geochemical investigation for structurally controlled gold mineralization in Mariga, North-Western Nigeria

Abdullahi S. and Ejepu J. S.
Department of Geology, Federal University of Technology, Minna, Niger State, Nigeria
Corresponding email: ejepu.jude@futminna.edu.ng +2348034065079

Abstract

Aeromagnetic and geochemical investigations were undertaken as a reconnaissance an important component in enhancing the geologic information of Mariga area as it pertains a potential for the extraction of economic gold, gemstones and associated structurally controlled mineralization. This is done with an aim of understanding the structural setting, delineating lithological contacts and possible alteration zones as well as identification of prospective zones for structurally controlled mineralization. The area is bounded between Latitude 9° 50´ to 9° 55´ and Longitude 5° 55´ to 6° 00´. The study area falls within the Schist Belt of north-western Nigeria. The lithological variations include coarse to fine grained, clastics pelitic schists, phyllites, banded iron formation and mafic metavolcanics (amphibolites). For the enhancement and general understanding of the structural geology of the area, the original TMI grid was processed, filtered and transformed to other grids using Oasis montaj software with associated extensions of the package such as MAGMAP, SPI and CET. First Vertical and Second Vertical Derivatives, Analytic Signal, Tilt Derivative and Horizontal Gradient were produced. These were done in order to extract the magnetic lineaments of the area. Density heat map was produced by employing image analysis techniques such as texture analysis and symmetric feature detection algorithms to identify the magnetic anomalies and vector analysis on their line segments to identify structural complexity. Geochemical analysis was done on soil samples and analysed for elements such as gold, silver, manganese, copper, zinc and iron. ArcGIS 10.8.1 was used for weighted overlay thematic maps such as geology, lineaments, feature orientation and geochemical anomaly. Results of aeromagnetic interpretation show that the magnetic signatures vary from -142 nT to 145 nT in the area which is quite appreciable contrasting signature for magnetic anomaly delineation. Several lineaments with major NE - SW trend was identified in the area. Also, major regional faults trending NE-SW and E-W delineated around the north-western part cross-cuts some of the lineaments and lithologic contacts. Feature intersection orientation density heat map showed areas associated contact aureoles and other deposits along with hot spot edges seem to be closely associated with structural complexity, identifiable in the aeromagnetic map. Prospective areas have been identified after the weighted overlay analysis and indicate that the north-western portion of the study area is deemed more prospective. This area recommended for further ground geophysics detailed investigations follow up.

Keywords: Aeromagnetic data, Lineaments, Lithologic contact, Feature orientation, Mineralization

1.0 Introduction

The primary sources of gold and most gemstones in Nigeria are quartz veins and the pegmatites in rocks of the Basement Complex. It can be mined either in the vein or as alluvial deposit. Most primary gold mineralization in the schist belt commonly occurs in quartz veins within several lithologies. Since most of the mineral deposits in the area are structurally controlled, these mineral occurrences are often restricted to structural elements such as faults, shear zones and lithological unconformities. Hence, knowledge of the structure interrelationship and lithologic units are essential for mineral exploration (Adebiyi *et al.,* 2021).

The area falls within the north-central zone of Nigeria which forms part of the Basement Complex intruded by pegmatites known for their economic mineralization potential. They area is also notable to host rich in metallic and industrial minerals such as lead-zinc, gold, tantalite, Niobium and gemstones.

Magnetic measurements and interpretations play important roles in understanding the variations in Earth's magnetic field that resulted from the underlying basement rocks' magnetic properties (magnetic susceptibilities), geological structures and their geometric shapes and sizes (Abdelrahman *et al.,* 2007; Abdelrahman *et al.,* 2012; Abdelrahman and Essa, 2015; Abo- Ezz and Essa, 2016; Biswas, 2016; Biswas and Acharya, 2016; Essa and Elhussein, 2017).

At short wavelengths, magnetic data reflect the susceptibility changes that could be associated with the sedimentary rocks and at long wavelengths the magnetic anomalies could reflect the susceptibility changes in the underlying basement (metamorphic and basic igneous) rocks (Telford *et al.,* 1998). Magnetic data allows for the delineation of the lateral changes in susceptibility associated with the underlying structures and by doing so information about the structural trends and its lithological changes can be inferred. To delineate the subsurface structural features from magnetic data, numerous magnetic edges enhancing techniques have been developed and used effectively by many researchers (Nabighian, 1972; Cordell and Grauch, 1985; Roest et al., 1992; Phillips, 1998; Verduzco et al., 2004; Salem et al., 2007).

Chemical analyses are usually conducted on soil samples collected on anomalous areas within the study area. It is important to note that due to high detection limit of X-ray Fluorescence (XRF), gold is usually not detected directly hence, pathfinder elements may be analysed to have a reliable information on the prospectivity of gold in the area (Steiner, 2021).

1.1 Gold Occurrence in Nigeria

In Nigeria, gold occurs both as placers (alluvial and eluvia) and primary vein deposits within the schist belts of northwest and southwestern Nigeria. Some of the most important occurrences are at Maru, Anka, Kwaga, Gurmana, Birnin-yauri, Okolum, Dogon-Daji and Iperindo areas all associated with the schist belts. It was also stressed that different types of rocks host Nigerian gold with superficially different petrographic characteristics (Fagbohun, 2021). Earlier workers stated that the Nigerian gold can be correlated with common host rocks from other parts of the world and likened their origin to that of the petrochemical characters of the host rocks. Identifying the appropriate structural patterns and hydrothermal processes necessary for gold fluid transport and deposition is important in gold exploration in Nigerian pan African basement (Garba, 1988).

It is concluded that the only controls of gold mineralisation in the Nigerian Pan African basement are essentially structural. These kind of consist of transcurrent fault systems, subsidiary faults along with other penetrative set ups together forming the overdue Pan Photography equipment conjugate fracture system (Garba, 1992). These fault systems were probably the main force that the hydrothermal gold ore essential liquids were later focused into the subsidiary fault along with other structures, along which interactions in the fluids along with suitable walls rocks or even structures induced gold depositing. Furthermore, it was observed that the regional failing structures tend to be largely not mineralized simply because they were areas of best fluid circulation and best fluid/rock quotients, whereas the actual genetically associated subsidiary set ups host the actual deposits for their decreased gold solubility as well as temperature (Darma *et al.,* 2016). The Schist belts are about the best- studied group of rocks in Nigeria because of the known mineralization such as gold, BIF, Marble, manganese and several others are associated with them (Ohioma, 2020).

2.0 Study area

The study area lies within the Akerre Sheet 162 NE of the Federal Survey of Nigeria topographical

map sheet. The area covers approximately 38.4 km^2

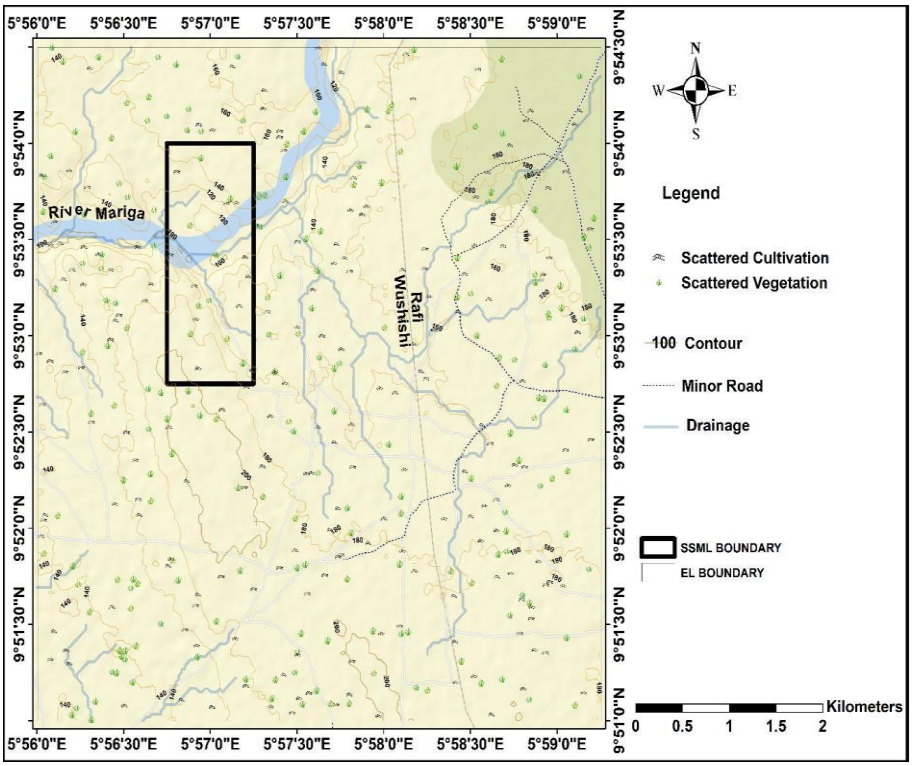

Figure 1: Location of the study area part of Akerre Sheet 162 NE. Black box represents area of geochemical sampling.

2.1 Regional Structural Setting

The schist belts are made up of many rock units such as: schists, phyllites, quartzites, banded iron formations (BIF) and amphibolites. The Older granites are mainly syn-to-late-tectonic Pan-African intrusions, ranging in size from small sub-circular cross cutting stocks to large elongate batholithic bodies emplaced into both the gneiss-migmatite-quartzite complex and supracrustal rocks during or after the main phase of Pan-African deformation (Petters, 1991).

Two major transcurrent fault systems with dextral displacements are known in the Precambrian basement. They trend in the NE-SW direction displacing earlier structures in the order of tens of kilometres. The two fault systems are known as the Anka-Yauri-Iseyin (AYI) and the Kalangai-Zungeru-Ifewara (KZI) faults and are often associated with locally developed subsidiary (NW-SE) sinistral faults (Turner, 1983). These are considered to be conjugate system of late Pan- African brittle deformation that occurred after about 530Ma on a continental scale (Ball, 1980). The close association of ultramafic and related rocks with the fault systems suggests that they might be crustal sutures. A collision-type orogeny has been suggested, involving the Pan- African region and the West African craton, in which a subduction zone dip eastward beneath the Pan-African region. Deformation and metamorphism followed the continental collision at around 660 Ma which was considered to be basement *sensu stricto*, and most radiometric ages lie in the range 600+150 Ma dating the imprints of the consequent crustal thickening in the Nigerian region. The period 650-500 Ma was characterized by extrusion of post-tectonic alkaline to calc-alkaline volcanics and brittle deformation, as the last manifestation of the Pan- African orogeny (Garba, 2002).

2.2 Data Acquisition

A high resolution airborne magnetic data of 1:100,000 Akerre Sheet 162 was used for this interpretation with other data set such as SRTM data, satellite imageries and regional geological map of Nigeria. The survey parameters of the aeromagnetic data are: Flight line spacing (500 m), Tie line spacing (2 km), Terrain clearance (80 m), Flight direction is NW-SE while the Tie line direction NE-SW. The total magnetic intensity field has been International Geomagnetic Reference Field (IGRF) (2015) corrected and super regional field of 32000 nT was deducted from the raw data. The magnetic data was further processed to investigate the presence of buried structures and lineaments that might be relevant in the mineral exploration project development.

2.3 Processing and Interpretation methodology

The original TMI grid was processed, filtered and transformed to other grids using Oasis montaj software with associated extensions of the package such as MAGMAP, SPI and CET. For the purposes of data presentation and interpretation the total field magnetic data are gridded using the minimum curvature gridding method (Briggs, 1974) with a cell size of 125 m, which represents about one quarter of the 500 m average line spacing. A 3x3 convolution filter was passed over the final grid to smooth the grid image.

This data is required for the enhancement and general understanding of the regional geology of the area. In this regard, the data can also be used to map contacts and structural features within the property. It also improves definition of the potential of known zones of mineralization, their geological settings and identifying new areas of interest. The ArcGIS software by ESRI was used to relate and overlay various layers of information, such as geology, magnetic data and extract structural features of the interpretation. The interpretation was performed on screen in the ArcMap. Aeromagnetic Data Analysis and processing was done in three major ways for simple and efficient interpretations of the subsurface structure in a qualitative and quantitative manner by implementing: Reduction to Equator (RTE), filtering and depth analysis

2.3.1 Reduced to Equator

Reduction to Equator method was implemented to position the anomalies vertically above their sources. The filtering process would serve to aid qualitative interpretation of the anomalies, while the depth analysis technique would aid the interpretation of the subsurface magnetic anomalies quantitatively. RTE was implemented on the acquired aeromagnetic data with the objective of accurately positioning anomalies directly above their causative bodies (Luo et al., 2010). The geomagnetic declination and inclination of -4.27° and -2.10° respectively at the central location of the study area was used for the RTE process.

2.3.2 First Vertical Derivative

The partial derivative of magnetic data in the vertical direction defined what is referred to as the vertical derivative. This derivative emphasis the local anomalies by enhancing the high frequency (or short-wavelength) anomalies and suppresses the low frequency (or long- wavelength) anomalies in potential field data (Dobrin and Savit, 1988). The first and second order vertical derivatives can be calculated respectively using equation 1 The equation of the wavenumber domain filter to produce nth derivative is:

$$F(\omega) = \omega^n \quad (1)$$

where: F = vertical derivative ω = wavenumber (radians/ground unit) n = order of differentiation
Note: $\omega = 2\pi k$ where k is cycles/ground unit.

2.3.3 Analytic Signal (AS)

The interpretation of magnetic field data at low magnetic latitudes is difficult because the vector nature of the magnetic field increases the complexity of anomalies from magnetic rocks. The analytic signal also known as the total gradient (Nabighian 1972, 1974 and 1984) is formed by integrating the horizontal and vertical gradients of the magnetic anomaly. The amplitude *A* of the analytic signal of the total magnetic field *T* is calculated from the three orthogonal derivatives of the field (Roest *et al.*, 1992) (Equation 2).

$$|A(x,y)| = \sqrt{\left(\frac{\partial T}{\partial x}\right)^2 + \left(\frac{\partial T}{\partial y}\right)^2 + \left(\frac{\partial T}{\partial z}\right)^2} \quad (2)$$

where A = amplitude of the analytic signal T
= total magnetic field
x, y and z = orthogonal directions

Modelled grid of analytic signal was calculated by applying finite differences to the total intensity magnetic anomaly field computed from the formulas of Singh and Sabina, (1978). Vertical derivative of the magnetic field was obtained by computation at depths of (z + Δx) and (z - Δx) dividing the difference in the depths by 2Δ*x*. The *x* and *y* derivatives are calculated in the same manner. However, contacts on analytic signal are often more discontinuous than that of its horizontal derivative.

2.3.4 Magnetic Tilt Derivative

The magnetic tilt derivative (TDR) combines all three gradients (X, Y and Z) to produce what is a called a tilt angle. The distance between the zero contour at the 45° contour is called the tilt-depth method and can give an approximation of the depth of the host body Salem et al., 2008).

The magnetic tilt derivative is calculated by the following equation:

$$\mathrm{TDR} = \tan^{-1}\left[\frac{{}^{\mathrm{dT}}/_{\mathrm{dz}}}{\sqrt{\left({}^{\mathrm{dT}}/_{\mathrm{dx}}{}^{2} + {}^{\mathrm{dT}}/_{\mathrm{dy}}{}^{2}\right)}}\right] \quad (3)$$

where dT/dx is the calculated in-line gradient, dT/dy is the measured cross-line gradient and dT/dz is the measured vertical gradient of the total magnetic field. By using measured gradients in the tilt calculation, additional details can be extracted from the data that would typically be lost in a TMI grid-based tilt calculation.

2.3.5 Source Parameter Imaging (SPI)

The SPI method (Thurston and Smith, 1997) estimates the depth from the local wavenumber of the analytic signal using the MAGMAP extension of oasis Montaj software. Thurston and Smith, (1997) and Nabighian (1972) showed that the analytic signal of the magnetic anomaly due to a 2D magnetic source can also be expressed by the complex number.

$$A_1(x,z) = \frac{\partial B_T(x,z)}{\partial x} - j\frac{\partial B_T(x,z)}{\partial z}, \quad (4)$$

Where: *B*T (*x*, *z*) is the total magnetic anomaly observation point at a distance *x* along the principal profile and a vertical distance *z* above the source

j is the imaginary number ($= \sqrt{-1}$).

The estimated depth results are interpreted in terms of the magnetic basement and shallow (intrusive) basement. could be interpreted as the depth to top of intrusions at various location. The SPI depth Grid (Figure 10) was computed in order to estimate depth to magnetic sources. The SPI depth Grid show that most magnetic sources are not deeply seated which indicate a lower cost of exploration and exploitation.

2.3.6 Shuttle Radar Topography Mission (SRTM) DEM

Hill shade Digital elevation Model (DEM). This was achieved by combining the Shuttle Radar Topography Mission (SRTM) of the area and sun shading at 45º. The DEM is then correlated with the magnetic Grids to isolate those anomalies that were suspected to be induced by the topography from the real ones. Most of the anomalies within this area of interest are not topographic anomaly; hence its worthy of further ground verification but the central portions are not influenced by the topography (USGS, 2021).

2.3.7 Magnetic Lineaments

Magnetic lineaments are linear, continuous features on a map, possibly related to deformation zones and/or lithologic contacts. In the following, the deformation zones are discussed mainly from the geophysical point of view, focusing on their magnetic properties.

In geological processes, magnetic properties of bedrock may change, depending on prevailing physical and chemical conditions and mineralogy (Airo 2005). In general, the properties of a deformation zone may vary in the following ways, when the primary magnetic mineral in bedrock is magnetite (McIntyre 1980; Henkel and Guzman 1977; Johnson and Merrill 1972).

i) Oxidizing fluid intrude into the rock material during the metamorphism.
ii) Deposition of magnetite: magnetic susceptibility increases.
iii) Reducing metamorphic fluids intrude into rock material, thus, magnetite is decomposed, thereby decreasing susceptibility.
iv) Low temperature (< 250 °C) weathering in fracture zones. This causes magnetite to be decomposed, thus, decreasing magnetic susceptibility.

It is known that increased pyrrhotite content (especially the pyrrhotite-pyrite ratio) is related to the metamorphic grade of the bedrock (Craig and Vokes 1991). Pyrrhotite in the study area is inferred to originate from the primary sedimentary protolith of the migmatitic gneisses. Geological observations suggest that pyrrhotite has been mobilized first by regional tectonic movements and subsequently by hydrothermal episodes. Accordingly, the fracture and fault zone system of the area has been one factor controlling the emplacement of pyrrhotite.

According to the discussion above, a deformation zone may induce a magnetic minimum or maximum. Brittle zones commonly carry fluids allowing different chemical and physical weathering processes to take place within the zone, resulting in decomposition of magnetite to haematite and pyrrhotite to goethite and elemental Sulphur (Steger and Desjardins, 1978). Since low-temperature weathering is supposedly the most recent chemical process in the brittle zones, it is therefore justified to assume that most linear magnetic minima represent their surface expressions. At the bedrock surface, a deformation zone may be accompanied by a topographic bedrock depression filled by soil, which may also slightly decrease the measured magnetic field. However, in some areas, a number of brittle zones are also related to high susceptibility. In addition to magnetic minima/maxima, also a sharp discontinuity or a displacement of magnetic anomalies may be an indication of a potential brittle deformation zone. A deformation zone is typically highly fractured and are characterized by concentrations of conducting minerals such as sulphides and clay.

3.0 Results and Discussion

3.1 Local geology

The study area falls within the Schist Belt of north-western Nigeria (Figure 2). The Schist Belts comprise low grade, metasediment-dominated belts trending N–S which are best developed in the western half of Nigeria. These belts are considered to be Upper Proterozoic supracrustal rocks which have been infolded into the migmatite-gneiss-quartzite complex. The lithological variations of the schist belts include coarse to fine grained, clastics pelitic schists, phyllites, banded iron formation and mafic metavolcanics (amphibolites). From the regional geological map of Nigeria, this part of Sheet 162 (Akerre) is predominantly underlain by porphyritic igneous rocks which have intruded large scale intrusions of porphyritic granites/granites/course porphyritic biotite and biotite hornblende granites are also outcropped within the Schist resulting to localised steep dips in the area. They form low strike ridges parallel to those of the schist belts. Mylonites are in contact only with rocks of the schist belts and the older granite plutons which intrude them. There are no unmylonitised basement rocks adjacent to the Mylonitic rocks. The Mylonites have a well-defined lineation or Mylonitic foliation which trends NNE-SSW, parallel to the regional structural grain. Rocks belonging to the Nupe Basin are found in the south-western portion of the map (Ako, 2014).

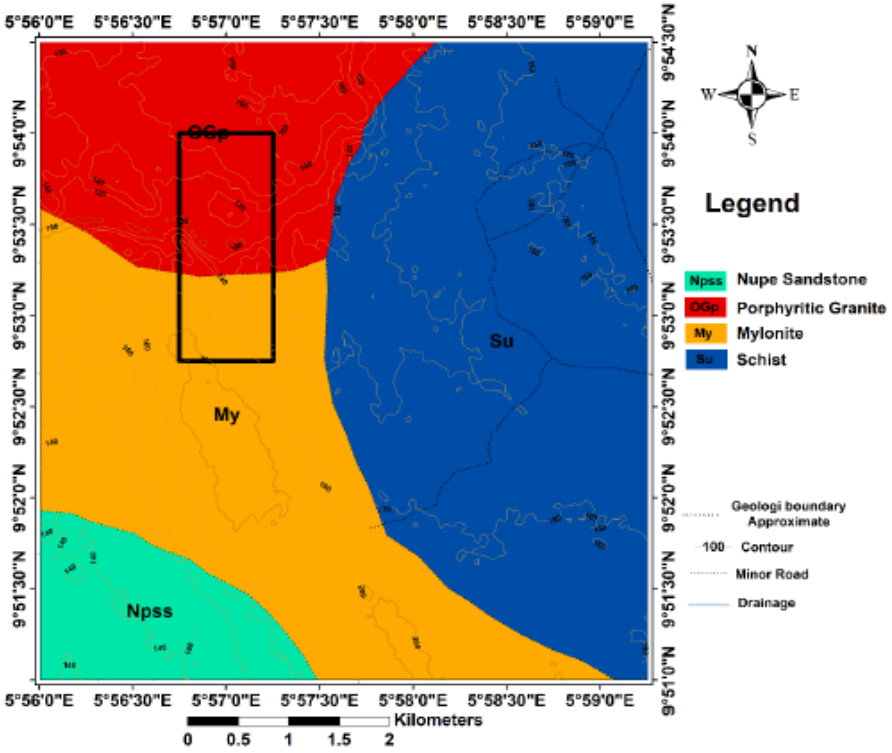

Figure 2: Geologic map of the study. Black box represents area of geochemical sampling.

3.2 Aeromagnetic data interpretation

Figure 3 shows the aeromagnetic data (RTE) for the survey area. Map shows the superposition of perturbations of distinctly different order of sizes. Large features which are visible as trends and continue smoothly over extensive distances are caused by the deeper heterogeneity of the earth's crust. These trends are called the regional trends. In contrast, small local disturbances which have primary importance but are secondary in size are called residual anomalies. These are superimposed on the regional fields and are frequently camouflaged by them. Residual anomalies may provide direct evidence of the existence of structures that are typical to reservoirs or mineral ore bodies. The high values (nT) are purple and orange and indicate appreciably magnetic rocks. The low values are the blues and greens. A gradual change in colour indicates a gradual change in the

magnetic field strength. This can be caused by either a gradual change in magnetic susceptibility of rocks near the surface, the gradual burial of a rock unit of relatively constant magnetic susceptibility, or the introduction of a new unit at depth. Conversely, an abrupt change in colour indicates an abrupt change in the magnetic susceptibility.

This is caused by juxtaposing two rock units with very different magnetic susceptibilities such as is the case with faults, volcanic dikes, or some mineralized zones. Faults can be inferred on aeromagnetic maps from linear or curvilinear features composed of discontinuous aeromagnetic highs or lows. This is also an indication that the area has undergone pronounced tectonic activities producing fractures, faults and shears. exhibits zonation and alteration probably in the form of sericite (Juliani et al., 2021). This is an indication of hydrothermal alteration which is usually associated with mineralization probably as a result of intrusion. The amplitude of the magnetic signatures varies from -142 nT to 145 nT within the exploration license which is quite appreciable contrasting signature for magnetic anomaly delineation.

In an attempt to extract meaningful lineaments from the aeromagnetic data, several derivative maps have been calculated and produced. The First vertical derivative (Figure 4) of the data was computed so as to make lineaments identification easier. This is done by observing the trends and amplitudes of the anomalies that matches the geological history of the region.

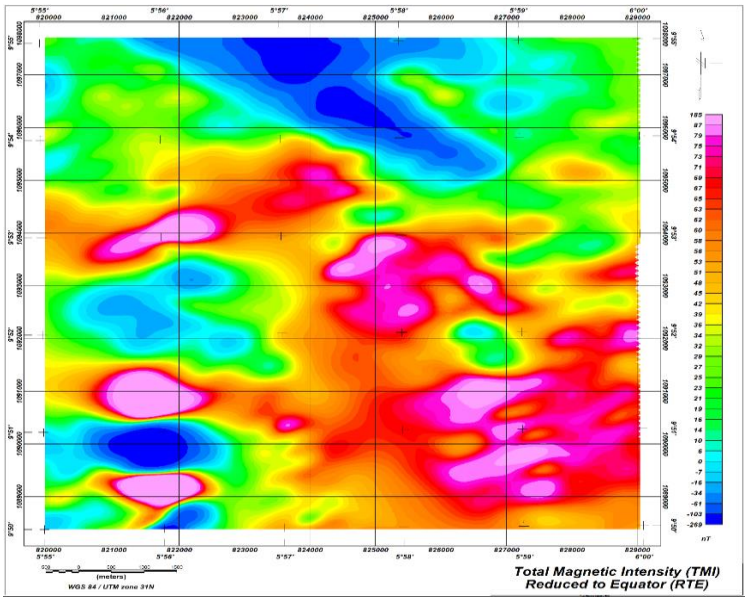

Figure 3: Total Magnetic Intensity (TMI) Reduced to Equator of the study area.

The lineaments were extracted from this map by interpreting the signatures as the edges of geological bodies and directions of structures which might have been in connection with the thermo-tectonic events. The amplitude of the signal peak of analytic signal (Figure 5) is directly proportional to the edge of magnetization. Hence source edges are easily determined. The analytic signal has a form over causative body that depends on the locations of the body (horizontal coordinate and depth) but not on its magnetization direction. This is an important feature of the analytic signal. More so, the amplitude of analytic signal is solely related to the amplitude of magnetization and this feature has been used in locating the contacts of magnetic bodies. Analytic signal is often effective at highlighting geologically meaningful subtle anomalies (Lyatsky *et al.*, 2004).

The Tilt derivative map (Figure 6) pursues the objective of extracting meaningful lineaments a bit further by highlighting very subtle, near surface structures in the dataset where the zero-contour line of the grid is said to represent geology contacts or edges of bodies. Several lineaments with different orientation were identified in the area. The lineaments can be grouped into three on the basis of their orientations. Major trend in the NE – SW direction, some trend in the NW – SE direction. Also, a major regional faults trending NE-SW was

delineated within the concession around the north-western part cross-cutting some of the lineaments and the lithological boundaries. Such structures interpreted from the aeromagnetic maps are essential channels for mineralization fluids.

The ENE-SSW trends represent the mega shear zones in Africa called the Central African Shear Zone (CASZ) which resulted from the important tectonic movements that occurred during the Pan-African orogenic cycle (Moreaus *et al.,* 1987). The ENE-SSW is also a dextral shear zone that is related to the wider mylonite belts pre-dating at the Cretaceous times, the opening of the South Atlantic Ocean (Jorgensen and Bosworth, 1989; Djomani *et al.,* 1995). The N-S lineaments are minor trends. Their formation may be associated to either the migration of the African plate over the mantle plume or shear movements along the pre-existing ENE- WSW faults in the Pan-African basement (Djomani *et al.,* 1995).

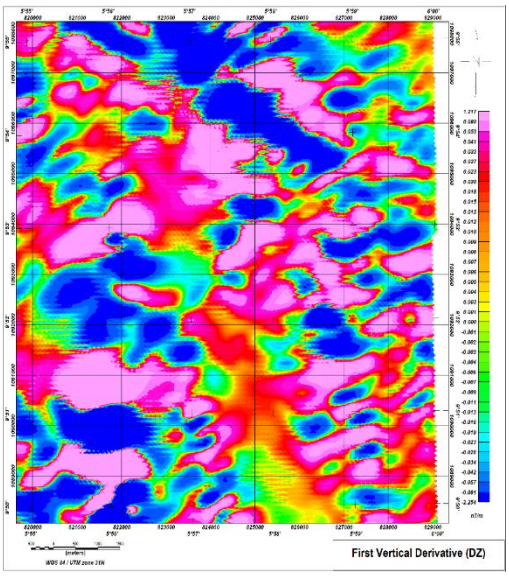

Figure 4: First Vertical Derivative map of the study area.

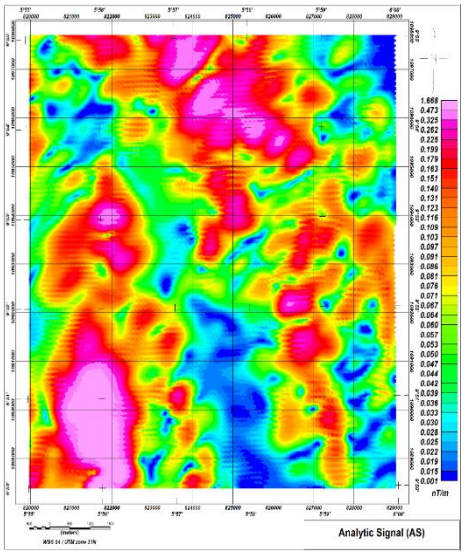

Figure 5: Analytic Signal map of the study area.

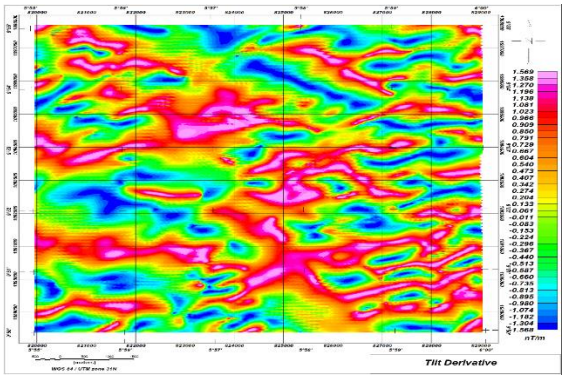

Figure 6: Tilt Derivative map of the study area.

3.3 Feature Intersection Orientation

The feature intersection orientation density heat map (Figure 7) was achieved by employing image analysis techniques such as texture analysis and symmetric feature detection algorithms to identify the magnetic anomalies and vector analysis on their line segments to identify structural complexity. This contribution presents an image processing method to generate maps that highlight regions of geological structural complexity from aeromagnetic data, efficiently and objectively.

An interesting observation is that gold deposits often are located near edges of hot spots. This is not surprising, considering that gold deposits are often located at or near hot spot edges, such as contact aureoles (e.g., Pirajno and Bagas, 2008). Researches have shown that areas associated this and other deposits along with hot spot edges seem to be closely associated with structural complexity, which can be automatically identified from the regional aeromagnetic data.

3.4 Geochemical interpretation

The concentration of gold in the soil samples ranges 0.001 - **0.0142 ppm**. These values are not very significant for an economic extraction of the resource on a scale. However, a trend as shown on the map below (Figure 8) revealed that the north-western and southern portion of the map could be promising when compared to the feature intersection orientation map. The trends and anomalies of other elements shown in the figure is correlatable to the feature intersection orientation map. These are pathfinders to gold. These anomalies are a pointer to the fact that the economic extraction of gold may be possible in the study area.

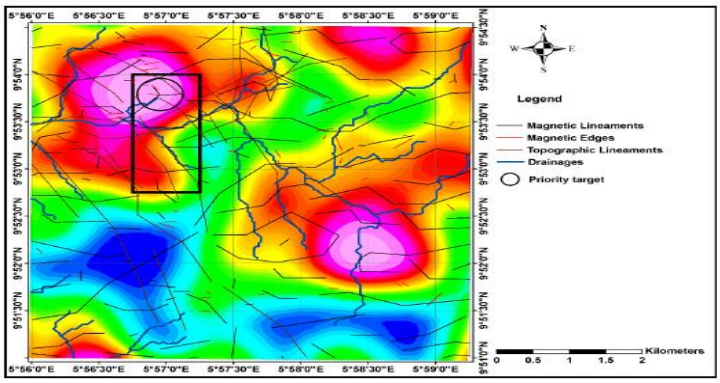

Figure 7: Structural map superimposed on the contact occurrence density heat map of the study area. Black box represents area of geochemical sampling.

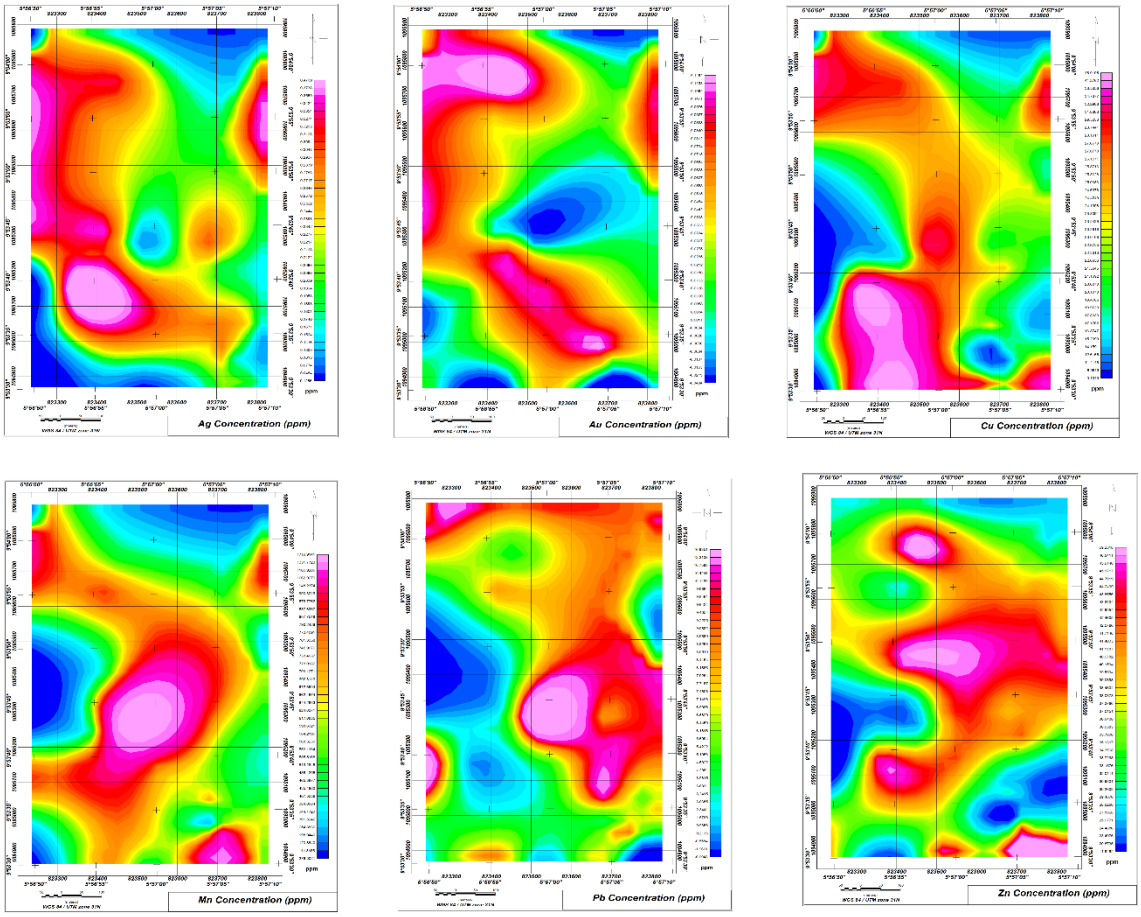

Figure 8: Distribution of Geochemical anomalies of some selected elements in the study area.

3.5 Conclusion and Recommendation

The magnetic data collected over the survey area was complex and defines features that appear related to structures such as faults, folds, and fractures. The magnetic field response varies considerably in both amplitude and character. Broad, low gradient features likely represent deeper seated bodies, whereas the sharp and high gradient responses are more likely to be related to near surface features.

The individual magnetic products have been referenced in order to better define the numerous structures throughout the area. The various gradient and derivative products fully represent the components of the magnetic field and can provide specific information not obvious in the total field data. The vertical gradient product emphasizes all subtle features in the data. In addition, the magnetic analytic signal is produced by calculating the vector sum of all three magnetic gradients to produce a grid that is independent of the effect of orientation from subsurface bodies.

Typically, the orientation of a magnetic target can produce a positive or negative response in the total magnetic field relative to its orientation. The analytic signal produces highs, which are directly over magnetic sources and are independent of the direction of the earth's magnetization vector. The feature orientation heat map allows for the identification of possible gold deposits in the tenement.

The area has undergone a pronounced tectonic activity resulting in shearing and fracturing. So, the sheared zone and fractures are potential channels for mineralization fluids. The observed zonation and likely alteration in the magnetic data are indication of hydrothermal alteration associated with

mineralization. These alteration signatures are broad and laterally extensive in the study area. From the interpreted structural map (Figure 7), zones with regional and localized aeromagnetic anomalies with associated magnetic lineaments/major faults are targets for mineralization. The intersections between linear features (faults/lineaments); sheared and fractured zones are potential traps for minerals and therefore provide a significant exploration vector. These zones extend well into this concession especially the NE-SW trending lineament almost intersecting the NW-SE trending major fault occurring around the alteration zones and the magnetic unit boundary as observed from the interpreted map. Such areas were marked with round box as priority target in (Figure 7).

Geochemical mapping carried out in the area gave credence to the viability of the area for possible gold mineralization. Encouraging pathfinders were found in the geochemical maps. However, ground-truthing, which should be followed with ground geophysical survey inform of Resistivity, Induced polarization and Electromagnetic surveys should be conducted. Results from these surveys may further agree with the results presented in this research.

REFERENCES

Abdelrahman, E.M., Abo-Ezz, E.R. and Essa, K.S. (2012). Parametric inversion of residual magnetic anomalies due to simple geometric bodies. *Exploration Geophysics*,43, 178- 189.

Abdelrahman, E.M., Abo-Ezz, E.R., Essa, K.S., El-Araby, T.M. and Soliman, K.S. (2007). Anew least-squares minimization approach to depth and shape determination from magnetic data. *Geophysical Prospection*, 55, 433-446.

Abdelrahman, E.M., and Essa, K.S. (2015). A new method for depth and shape determinations from magnetic data. *Pure and Applied Geophysics*, 172, 439-460.

Abo-Ezz, E.R. and Essa, K.S. (2016). A least-squares minimization approach for model parameters estimates by using a new magnetic formular. *Pure and Applied Geophysics*, 173, 1265-1278.

Adebiyi, L. S., Eluwole, A. B., Fajana, A. O., Salawu, N. B., Falade, S. C., Dopamu, K. O., & Alejolowo, E. A. (2021). Integrated geophysical methods for delineating crustal structures and hydrothermal alteration zones for mineral exploration projects in parts of west-central, Nigeria. Modeling Earth Systems and Environment, 1-13.

Airo, M. L. (2005). Regional interpretation of aerogeophysical data: Extracting compositional and structural features. In Airo, M. L. (Eds.), *Aerogeophysics in Finland 1972–2004: Methods, System Characteristics and Applications.* Geological Survey of Finland, Special Paper 39, 21–74.

Ako, A. T. (2014). Geology and Geochemistry of Zungeru Amphibolites, North Central Nigeria. *Universal Journal of Geosci*ences, *2*(4), 116-122.

Ball, E., 1980. An example of very consistent brittle deformation over a wide intracontinental area: the late Pan-African fracture system of Tuareg and Nigerian shield. Tectonophysics, 61: 363-379.

Biswas, A. (2016). Interpretation of gravity and magnetic anomaly over thin sheet-type structure using very fast simulated annealing global optimization technique. *Model. Earth Syst. Environ.*, 2(1), 30.

Biswas, A. and Acharya, T. (2016). A very fast simulated annealing method for inversion of magnetic anomaly over semi-infinite vertical rod-type structure. *Model. Earth Sys. Environ.*, 2(4), 198.

Briggs, I. C. (1974). Machine contouring using minimum curvature. *Geophysics*, *39*(1), 39-48.

Cordell, L. and Grauch, V.J.S., 1985. Mapping basement magnetization zone from aeromagnetic data in the San Juan Basin, New Mexico, in Hinze, William J. (ed.), The Utility of Regional Gravity and Magnetic Anomaly Maps: *Society Exploration Geophysics*, Tulsa, Oklahoma, 181-197.

Craig, J. R. & Vokes, F. M. (1991). The metamorphism of pyrite and pyritic ores. Mineralogical Society of Great Britain and Ireland winter conference on Industrial and environmental mineralogy. In.E. Bevins & P.A. Williams (Eds.), *Conference Document* p.12.

Darma, M. R., Kankara, I. A. and Shazali, N (2016): Potentials of Gold Mining and Extraction Methods in Nigeria. A paper presented at the First Umaru Musa Yar'adua National Economic Development and Poverty Eradication Conference, between 5th to 7th May, 2016.

Djomani, Y.H.P., Nnange, J.M., Diament, M., Ebinger, C.J. and Fairhead, J.D. (1995). Effective elastic thickness and crustal thickness variations in west central Africa inferred from gravity data. *Journal of Geophysics Research*, 100, 22047-22070.

Dobrin, M.B. and Savit, C.H (1998). Introduction to Geophysical Prospecting. 4th edition. McGraw-Hill.

Essa, K.S. and Elhussein, M. (2017). A new approach for the interpretation of magnetic data by a 2-D dipping dike. *Journal of Applied Geophysics*, 136, 431-443.

Essa, K.S. and Elhussein, M. (2018). PSO (Particle Swarm Optimization) for Interpretation of Magnetic Anomalies Caused by Simple Geometrical Structures. *Pure and Applied Geophysics*, 1- 15.

Fagbohun, B. J., Bamisaiye, O. A., Ayoola, F. J., Omitogun, A. A., & Adeoti, B. (2021). Identifying geochemical anomalies and spatial distribution of gold and associated elements in the Zuru Schist Belt, northwest Nigeria. *Arabian Journal of Geosciences*, *14*(6), 1-20.

Garba, I. (1988). The variety and possible origin of the Nigerian gold mineralization: Okolom, Dogondaji and Waya veins as case studies. Journal of African Earth Sciences, 7, 981-986. http://dx.doi.org/10.1016/0899-5362(88)90011-5

Garba, I. (1992). Rare earth element study of Bin Yauri gold deposit, Nigeria. Transactions of the Institution of Mining and Metallurgy (section B: Applied Earth Sciences), 101(B), 158-161.

Garba, I. (2002): Late Pan-African Tectonics and Origin of Gold mineralization and rare metal Pegmatite in the Kushaka schist belt, north-western Nigeria. *Journal of Mining and Geology*, Vol.38 (1), pp.1-12.

Henkel, H. & Guzman, M. (1977). Magnetic features of fracture zones. *Geoexploration* 15, 173–181.

International Geomagnetic Reference Field - 11th Generation (2009). https://www.ngdc.noaa.gov/metaview/page?xml=NOAA/NESDIS/NGDC/MGG/Geophysical_Models/iso/xml/IGRF-11.xml&view=getDataView&header=none.

Johnson, H. P. & Merrill, R. T. (1972). Magnetic and mineralogical changes associated with low temperature oxidation of magnetite. *Journal of Geophysical Research*. 77, 334.

Jorgensen, G.J. and Bosworth, W., 1989. Gravity modelling in the Central African Rift System, Sudan: Rift geometries and tectonic significance. *J. Afr. Earth Sci.*, 8, 283-306.

Juliani, C., Rodrigues de Assis, R., Virgínia Soares Monteiro, L., Marcello Dias Fernandes, C., Eduardo Zimmermann da Silva Martins, J., & Ricardo Costa e Costa, J. (2021). Gold in Paleoproterozoic (2.1 to 1.77 ga) continental magmatic arcs at the Tapajós and Juruena Mineral Provinces (Amazonian Craton, Brazil): A new frontier for the exploration of epithermal–porphyry and related deposits. *Minerals*, *11*(7), 714. https://doi.org/10.3390/min11070714.

LUO, Y., XUE, D.-J., & WANG, M. (2010). Reduction to the pole at the geomagnetic equator. *Chinese Journal of Geophysics*, *53*(6), 1082–1089. https://doi.org/10.1002/cjg2.1578.

Lyatsky H., Pana, D., Olson R. & Godwin L. (2004). Detection of subtle basement faults with gravity and magnetic data in the Alberta Basin, Canada. The Leading edge, 23 (12), 1282- 1288. https://doi.org/10.1190/leedff.23.1282_1.

McIntyre, J. I. (1980). Geological significance of magnetic patterns related to magnetite in sediments and metasediments – a review. *Bulletin of Australian Society of Exploration Geophysicists* 11, 19–33.

Moreaus, C., Reynoult, J.M., Deruelle, B. and Robineau, B. (1987). A new tectonic model for the Cameroon Line, Central Africa. *Tectonophysics*, 139, 317-334.

Nabighian, M. N. (1984). Toward a three-dimensional automatic interpretation of potential field data via generalized Hilbert transform: Fundamental relations. *Geophysics*, 47, 780-86.

Nabighian, M.N. (1972). The analytic signal of two-dimensional magnetic bodies with polygonal cross-section, its properties and use for automated anomaly interpretation. *Geophysics*, 37, 507-517.

Nabighian, M.N. (1974). Additional comments on the analytic signal of two-dimensional magnetic bodies

with polygonal cross-section. *Geophysics*, 39, 85-92.

NGSA (Nigerian Geological Survey Agency), 2009. Geological and Mineral Resource map of Nigeria. Authority of the Federal Republic of Nigeria.

Ohioma, O. J. (2020). Detection of Sulphide Deposit Using Uranium/Potassium Ratio Map. *Ghana Journal of Geography*, *12*(1), 145-158.

Petters, S.W. (1991) Chapter 6 Late Proterozoic-Early Palaeozoic Pan-African Mobile Belts. In: Petters S.W. (eds) Regional Geology of Africa. Lecture Notes in Earth Sciences, vol 40. Springer, Berlin, Heidelberg. https://doi.org/10.1007/BFb0020583.

Phillips, J.D. (1998). Processing and Interpretation of Aeromagnetic Data from Santa Cruz Basin-Patahonia Mountains Area, South-Central Arizona, U.S. Geological Survey Open- File Report, 2-98.

Roest, W.R., Verhoef, J. and Pilkington, M., 1992. Magnetic interpretation using the 3-D analytic signal. *Geophysics*, 57, 116-125.

Salem, A., Williams, S., Fairhead, D., Smith, R., & Ravat, D. (2008). Interpretation of magnetic data using tilt-angle derivatives. *GEOPHYSICS*, *73*(1). https://doi.org/10.1190/1.2799992.

Salem, A., Williams, S., Fairhead, J.D., Ravat, D. and Smith, R., 2007. Tilt-depth method: A simple depth estimation method using first-order magnetic derivatives. *The Lead. Edge*, 26, 1502-1505.

Steger, H.F. & Desjardins, L. E. (1978). Oxidation of sulphide minerals: Pyrite, chalcopyrite and pyrrhotite. *Chemical Geology*, 23, 225–237.

Steiner, B. (2021). Stream Sediment Geochemistry and Automated Mineralogy as Exploration Tools for LCT-Pegmatite and Granite-related Mineralisation: Case studies from the Leinster Granite (Ireland) and the Vosges Mountains (France).

Telford, W.M., Geldart, L.P. and Sheriff, R.E. (1998). Applied Geophysics (2nd Ed.), Springer, Berlin, p770.

Thurston, J.B., & Smith, R. S. 1997. Automatic conversion of magnetic data to depth, dip, susceptibility contrast using the SPITM method. *Geophysics*, 62, 807–813.

Turner, D. C. (1983). Upper Proterozoic Schist Belts in the Nigerian sector of the Pan African Province of West Africa. Precambrian Research, 21. 55-79.

USGS eros archive - digital elevation - shuttle radar topography mission (SRTM) 1 ARC-second global. (n.d.). Retrieved September 29, 2021, from https://www.usgs.gov/centers/eros/science/usgs-eros-archive-digital-elevation-shuttle-radar-topography-mission-srtm-1-arc?qt-science_center_objects=0#qt-science_center_objects.

Verduzco, B., Fairhead, J.D., Green, C.M. and Mackenzie, C. 2004. New insights into magnetic derivatives for structural mapping. *The Lead. Edge*,23, 116-119.

Aeromagnetic Investigation of the underlying Geological Structure of RafinRewa Warm Spring and its Environs, Lere, Kaduna, Northwestern Nigeria.

Ibrahim RabiuAdeiza[1]* Joseph Owolabi[1] Monday Mathew Ogwuche[2], and MomohAdavize Hameed[3]
[1]*,[1]Department of Physics, Kogi State University, Anyigba, Nigeria.
[2]Department of Physics, Ahmadu Bello University, Zaria, Nigeria.
[3]Department of Physics, Confluence University of Science and Technology,Osara, Nigeria.
[1]*odeiza21@gmail.com
[1]Josedeleowo85@gmail.com
[2]mattoogee2000@yahoo.com
[3]adavizehameed@gmail.com

Abstract

This research paper is aimed at delineating the geologic structures which could gave rise to the manifestation of the warm spring in RafinRewa, Dan Alhaji village Lere, North western Nigeria. Four High Resolution Aeromagnetic (HRAM) data of Dutsenwai (sheet 125), Ririwai (sheet 126), Bital (sheet 146) and Rahama (sheet 147) which covered the study area and beyond, were purchased from the Nigerian Geologic Survey Agency (NGSA). The study area lies between latitudes 10° N to 11° N and, longitudes 8° E to 9° E. The exact location of the warm spring manifestation is 10°25′ 35.7″ N and 8°30′ 47.0″ E with an elevation of 729m above sea level. The anomalies on the aeromagnetic map were defined by fitting a first order polynomial to the total fields, by the method of least squares to obtain the residual field data. Qualitative interpretation from second vertical derivative and analytic signal anomalies revealed the distinct pattern of the magnetic signatures. A fault trending NE-SW is observed very close to the location of the RafinRewa warm spring and can be suspected to be a conduit for heat transfer from within the earth. 3D Euler solution of the aeromagnetic data with structural index of one (SI = 1.0 for dyke) produced depth solutions and the predominant source depth range from 100 m to 1,500 m and can be observed to cluster along suspected fault zones. In conclusion the study area, could be consider for further geothermal exploration.

Key words: Aeromagnetic; Faults; RafinRewa, warm spring.

1. Introduction

Geophysics is the study of physical properties of the earth with the aids of geophysical methods. The analysis of these earth's physical properties like magnetic, electrical, electromagnetic properties reveals much about the earth, its surficial and interior contents (geological structures like voids, lineaments, faults, hydrocarbons). There are several geophysical methods involves in carrying out geophysical survey in which magnetic method is one among them.

Magnetic method has been applied severally to explore the earth's contents. It has been widely applied in so many area ranging from solid minerals exploration like gold, molybdenum, iron and many others; in oil and gas exploration, geothermal exploration and geological structural mapping. Aeromagnetic data was used to determine the hydrocarbon potential of part of sokoto basin (Ogwuche*et al.,* 2019). A buried fault was located using aeromagnetic data in south eastern Cameroun (Theophile*et al.,* 2012). Raimi*et al.,* 2014, used aeromagnetic method to investigate unexposed granitic plutons and unexposed ring complex.

It has become inherent to study the underlying geological structures for economic viability, especially for oil and gas, geothermal and other minerals that may be host in them. This is done on the basis of investigating the subsurface geology by analysing the anomalies in the earth's magnetic field. These anomalies are due to the magnetic properties of the underlying rocks, minerals, and what a few. Thus, it is

commonly possible to estimate the depth to basement and under favourable circumstances, quantitatively map basement structures, such as faults (Prieto and Morton, 2003).

1.2 Location and geological settings of the study area

The area under study lies between latitudes 10° N and 11° N and, longitudes 8° E to 9° E. The exact location of the warm spring manifestation is 10° 25′ 35.7″ N and 8° 30′ 47.0″ E with an elevation of 729m above sea level.The study area comprises of Precambrian to Lower Palaeozoic basement complex rocks into which the Jurassic Younger Granites have intruded. The geology composed of migmatite-gneiss as the oldest rocks, Pan African granites, diorite, charnockite and bauchites. The bauchite is an unusual rock of acid to intermediate composition, containing, in addition to fayalite, extremely iron rich pyroxenes (ferrohedenbergite and orthoferrosilite) (Oyawoye and Makanjuola, 1972). The area is located at the fringes of the Jos Plateau, to the SW, the centre of the Nigerian An Orogenic Younger Granite province of Jurassic age, and directly east of the near by Rishiwa ring complex (Garba*et al.*, 2012). The area is well drained by a good network of rivers (See Figure 1) most of which take their source from the nearby ring complexes of the Jos plateau. The topography of the area is more or less flat lying with the migmatites occurring as low lying exposures, while the granitic rocks stands out conspicuously thereby dotting the landscape (Garba*et.,al.2012*).

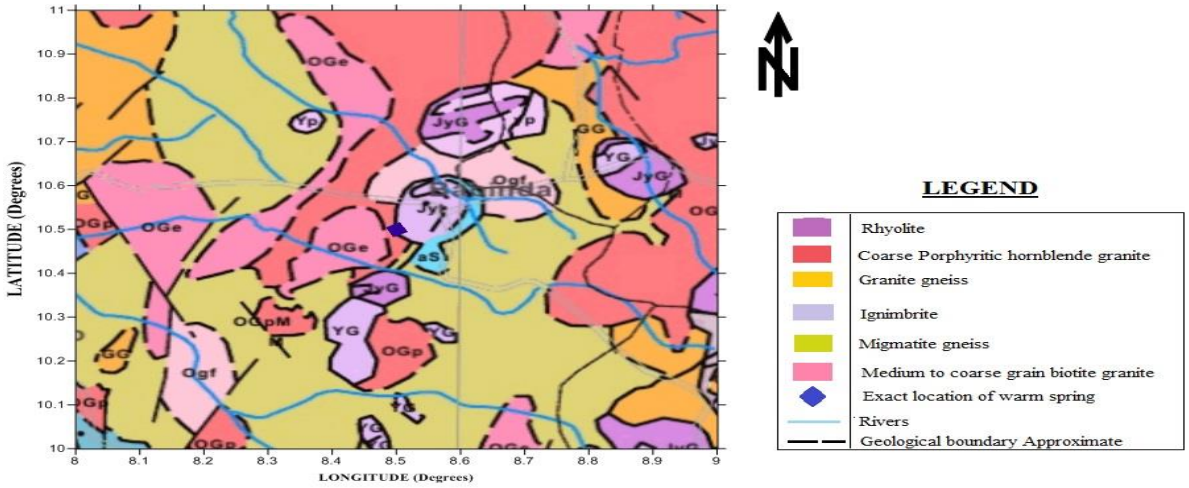

Figure (1): Geologic map of the study area (Extracted from the general geologic map of Nigeria by NGSA) 2008.

2. Materials and Method

2.1 Data acquisition

Four High Resolution Aeromagnetic (HRAM) data of Dutsenwai (sheet 125), Ririwai (sheet 126), Bital (sheet 146) and Rahama (sheet 147) between latitudes 10^0 00′ N to 11^0 00′ N and longitudes 8^0 00′E to 9^0 00′ E which covered the study area and beyond, were purchased from the Nigerian Geologic Survey Agency (NGSA).The maps, which are in half-degree sheets, was combined and a grid of the total magnetic intensity (TMI) of the study area was obtainedwhich are on a scale of 1:100,000. They were compiled from the data collected at a flight altitude of 80m, along NE-SW flight lines spaced approximately 500m apart. Figure 2 is the total magnetic field intensity (TMI) of the study area of the field strength ranging from 33041.9 to 33093.7 nT.

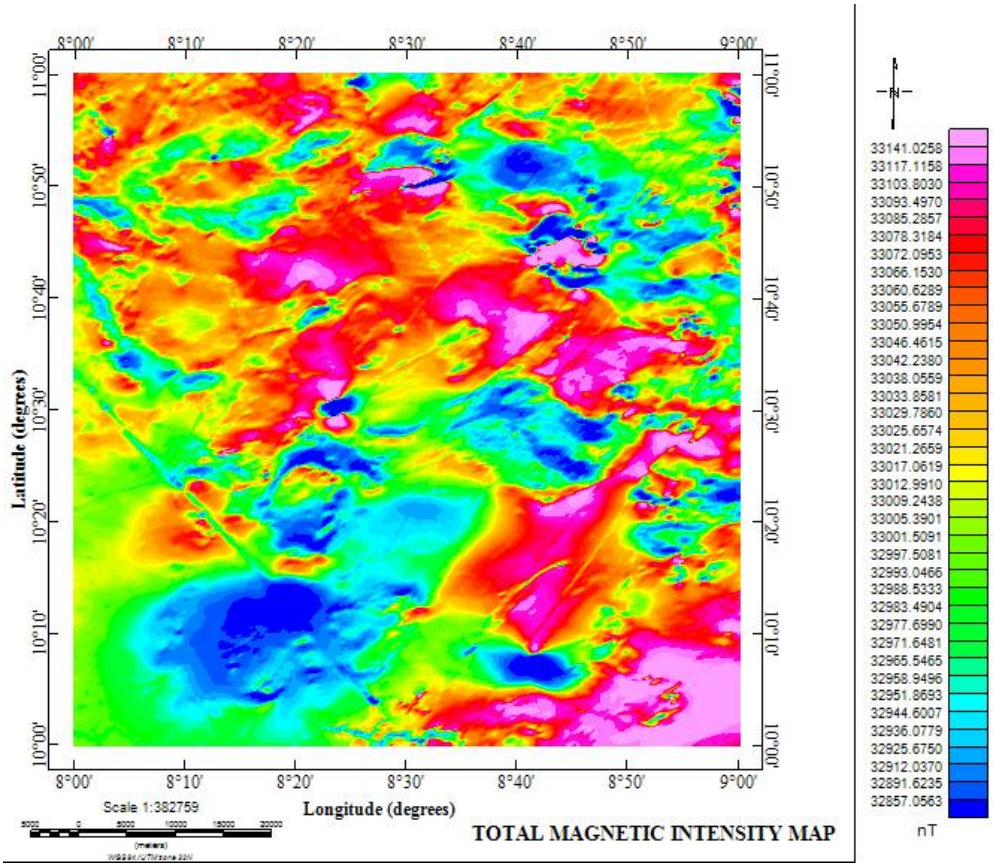

Figure (2): Total Magnetic Intensity of the Study Area

2.2 Data processing and interpretation techniques

The Total Magnetic Intensity data obtained during magnetic surveys is a combination of effect of both deep seated broader sources called regional field and shallow structures called residual field or the 'anomaly'. The regional magnetic field was separated from the residual magnetic data with the aid of SURFER 13 software. The regional field data was gridded using the 'Polynomial Regression' option on the software to produce a contour map of regional field, Figure 3. It shows a NW-SE trend of deep structures. The residual magnetic intensity map, figure 4, shows that NE-SE trend of high magnetic intensity materials but relatively average at the center around RafinRewa warm spring and it also depicts very low magnetic intensity at SW and NE.

2.3 Second Vertical Gradient

The second vertical gradient can be calculated by exploiting Laplace's equation below:

$$\frac{\partial^2 \varphi}{\partial z^2} = -\frac{\partial^2 \varphi}{\partial x^2} - \frac{\partial^2 \varphi}{\partial y^2} \qquad \text{(Blakely, 1995)} \qquad (1)$$

Second vertical derivative filters are used to enhance subtle anomalies while reducing regional trends. These filters are considered most useful for defining the edges of bodies and for amplifying fault trends. In mathematical terms, a vertical derivative can be shown to be a measure of the curvature of the potential field, while zero values (or contours) second vertical derivative contours defines the edge of the causative body. Thus, the second vertical derivative is in effect a measure of the curvature, i.e., the rate of change of

non- linear magnetic gradients. The zero magnetic contours of the second vertical derivative often coincide with the lithologic boundaries (Blakely, 1995).

2.4 Analytic Signal

The analytic signal is a complex function formed through a combination of the horizontal and vertical derivatives of the magnetic anomaly. In 3D, the analytic signal of the magnetic anomaly field T is defined as:

A(x, y, z) = 00 (2)

Where $\hat{x}$, $\hat{y}$ and $\hat{z}$ are unit vectors in the x, y and z directions, respectively $\frac{\partial T}{\partial z}$ is the vertical derivative of the magnetic anomaly field intensity, $\frac{\partial T}{\partial x}$ and $\frac{\partial T}{\partial y}$ are the horizontal derivatives of the magnetic anomaly field intensity. The above equation satisfies the basic requirement of the analytic signal, that is real and imaginary parts form a Hilbert transform pair (Blakely, 1995).

The amplitude of the analytic signal in 3D is given by:

$$|A(x,y,z)| = \sqrt{\left(\frac{\partial T}{\partial x}\right)^2 + \left(\frac{\partial T}{\partial y}\right)^2 + \left(\frac{\partial T}{\partial z}\right)^2} \quad (3)$$

Expression of the amplitude of the analytic signal gives a function that produces maxima approximately over the edges of the magnetic body source.

The distance between the inflection points of the analytic signal anomaly is directly proportional to the depth to the top of the magnetic source (Reynolds, 1997). This property is used in depths estimate.

2.5 Euler Deconvolution

Any function *f (x, y, z)* is homogeneous of degree n if

$f(tx, ty, tz) = t^n f(x, y, z)$ (4)

Where t is a real number. The plane of observation is taken at plane z = 0 and positive downward. Moreover, if *f*(*x*, *y*, *z*) is homogeneous of degree *n*, the following equation holds (Thompson, 1982)

$$x\frac{\partial f}{\partial x} + y\frac{\partial f}{\partial y} + z\frac{\partial f}{\partial z} = nf \quad (5)$$

This partial differential equation is known as Euler's homogeneity equation. Now, consider the total magnetic intensity of a point source located at the point (x_o, y_o, z_o) relative to the point of observation (*x*, *y*, *z*):

$$\Delta T(x,y) = f[(x - x_o), (y - y_o), (z - z_o)]$$

The above equation can be written as:

$$(x - x_o)\frac{\partial \Delta T}{\partial x} + (y - y_o)\frac{\partial \Delta T}{\partial y} + (z - z_o)\frac{\partial \Delta T}{\partial z} = n\Delta T \quad (6)$$

This equation expresses the magnetic field strength at any point in terms of the gradients of the total magnetic field. These gradients are related to different magnetic sources by the structural index, N. The structural index N, is a measure of the rate of change of distance of a field (Reid et al., 1990). Thompson, (1982) gives more detailed discussion on the degree of homogeneity of potential fields and structural indices of Euler deconvolution

The Euler deconvolution produces a large set of solutions. Furthermore, the Euler deconvolution is vulnerable to an incorrect choice of structural index value. In order to avoid this, the new method called Located Euler deconvolution is used. The later method begins with the calculation of the analytic signal function. It finds its peaks and then uses these locations for Euler deconvolution. This method produces far fewer solutions than the standard Euler deconvolution, estimating solutions only over recognized anomalies (Catalán et al., 2003). In both methods, the use of measured rather than calculated gradients should improve the results substantially, because both low-level noise and poor data quality in the original total field data are amplified when gradients are calculated (Reid *et al.*, 1990).

3. Result and discussion

The total magnetic field comprises of both regional and residual field (magnetic anomaly data), these are separated and shown in fig. 3 and fig. 4. Quantitative and qualitative data interpretation techniques were applied to the magnetic anomaly data with the goal of achieving the research objectives. The following were determined from the processed data; analytical signal, second vertical derivative and Euler deconvolution for depth estimation.

The analytic signal filter was applied on the residual anomaly data and areas with distinct magnetic properties were delineated. Areas with high magnetization were distinguished from areas with low magnetization and the result is presented in Figure (5). The analytic signal amplitude value varies from 0.005 nT/m to 0.293 nT/m. The result also indicates a relatively low analytic signal around the vicinity of the RafinRewa warm spring.

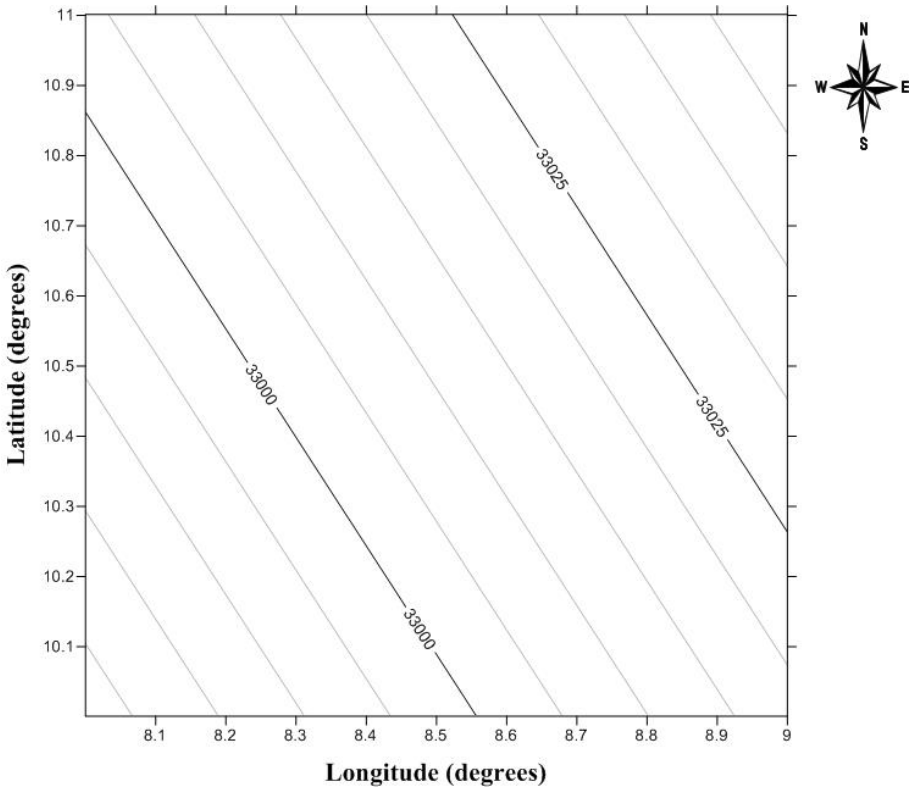

Figure (3): Regional Field Map of the Study Area

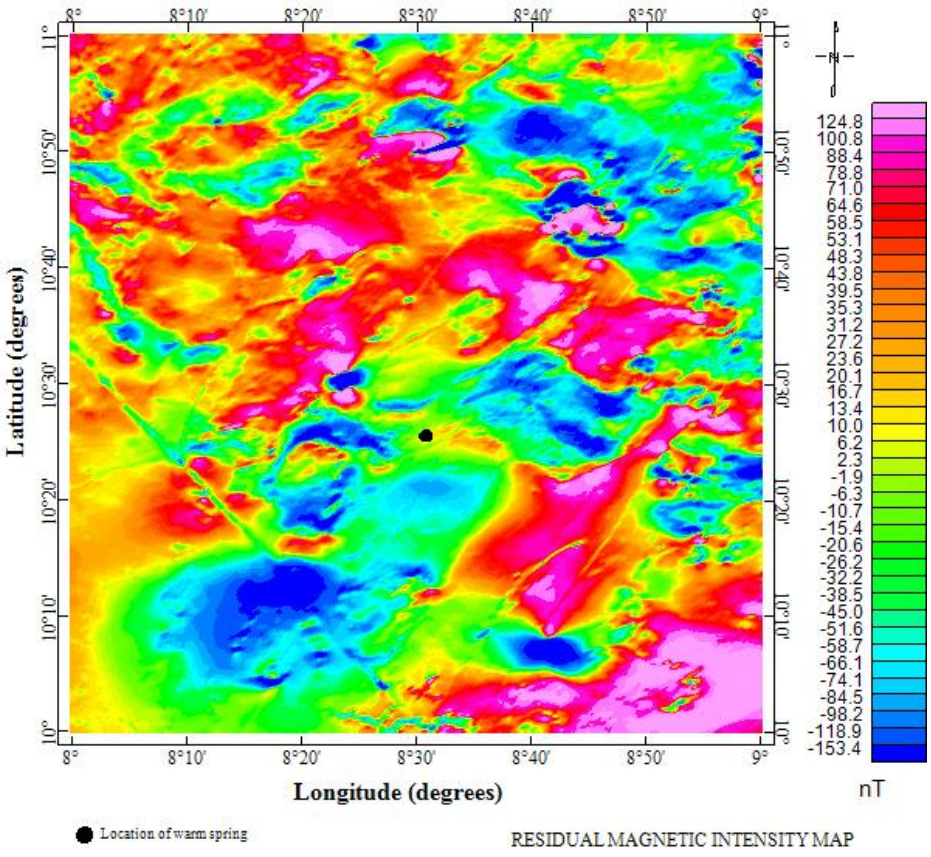

Figure (4): Residual map of magnetic intensity data of the study area

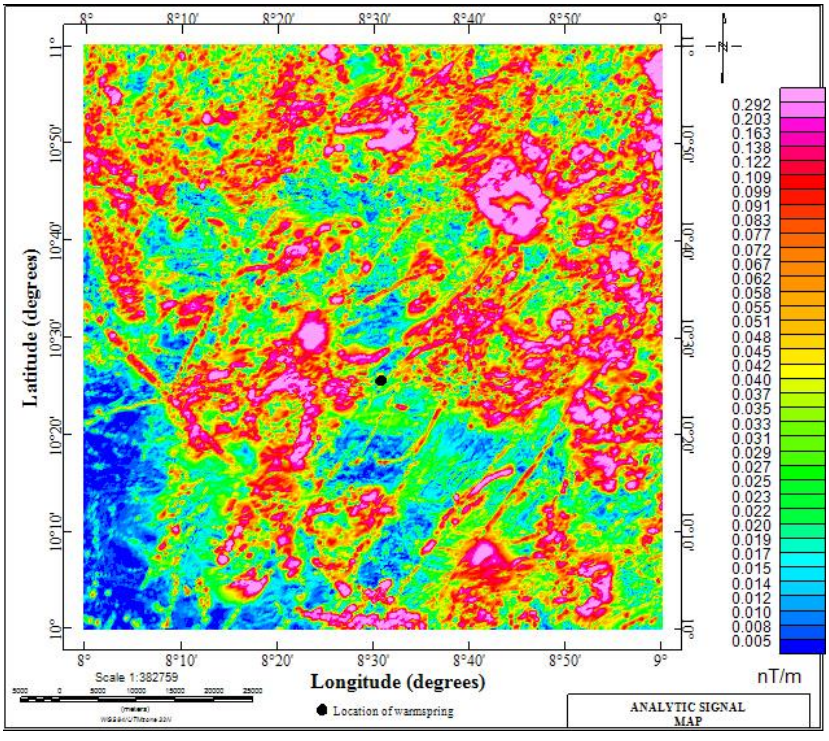

Figure (5): Analytic Signal map of the Study area

The Second vertical derivative filter, equation (1), was applied on the residual magnetic intensity data for the purpose of enhancing linear features and to indicate possible fault zones within the area of study. From the SVD map (Figure 6), the lineaments were extracted and a map produced using the PCI GEOMATICA Version 2017 software. Visual inspection of the lineament map (Figure 7) shows the distribution of faults around the study area with the dominant trend been NE-SW. A fault trending NE-SW is observed to be very close to the location of the RafinRewa warm spring and can be inferred to serve as a possible conduit for heat transfer from within the earth.

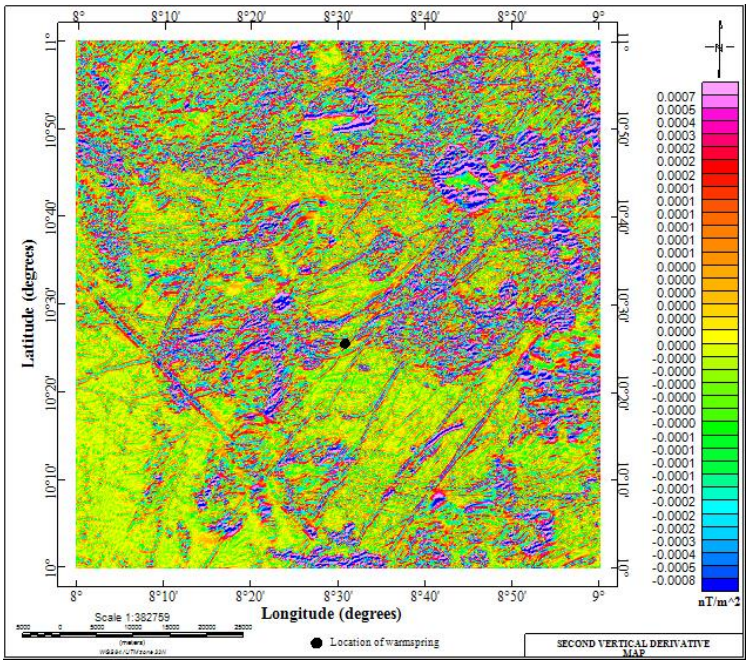

Figure (6): Second Vertical Derivative Map of the Study Area

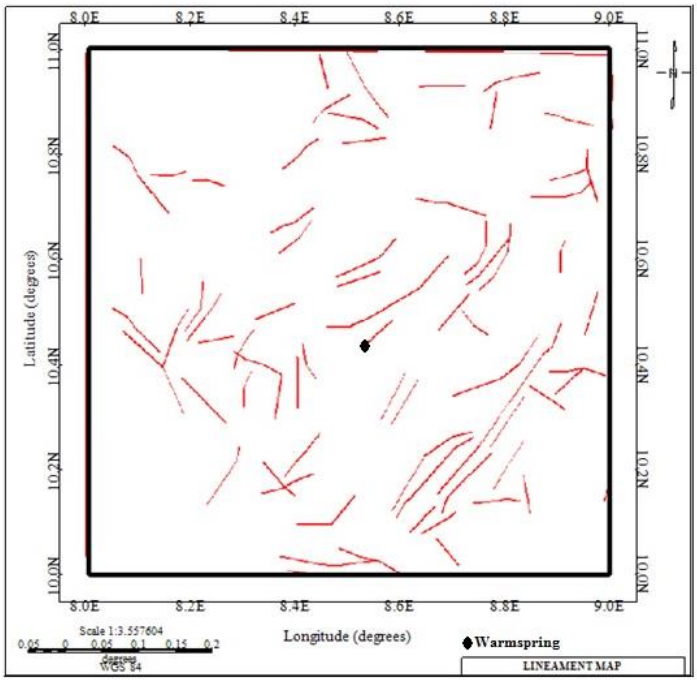

Figure (7): Lineament map of the Study Area extracted from the Second vertical derivative map

The Euler method was applied to the RMI map using a moving window of 10 km x 10 km. It was carried out using the Standard Euler 3D method of the Geosoft package software Version 6.4.2. A structural index of 1.0 was chosen due to the intrusive nature of rocks in the area. Figures (8) and (9) are respectively the plots of standard Euler depth solution and the Euler depth solution superimposed on the Lineament map of the study area, assuming a window size of 10 and maximum depth tolerance of 10 percent.
Depth to magnetic source within the study area is predominantly between 100 m to 1,500 m. However few areas with depth range between 1,500 m to 2, 500 m are distinguished within the area.

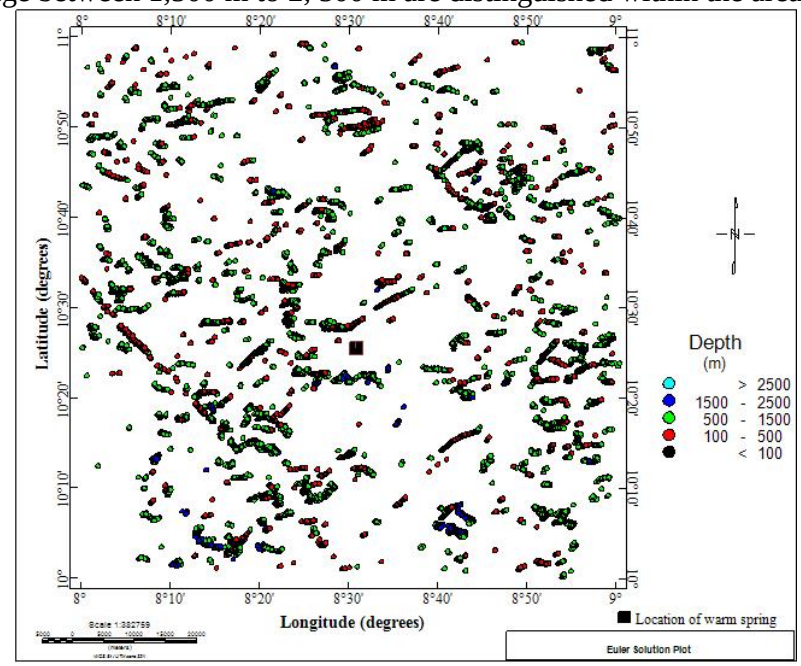

Figure (8): Euler Depth Solution of the Study Area (Structural index =1.0).

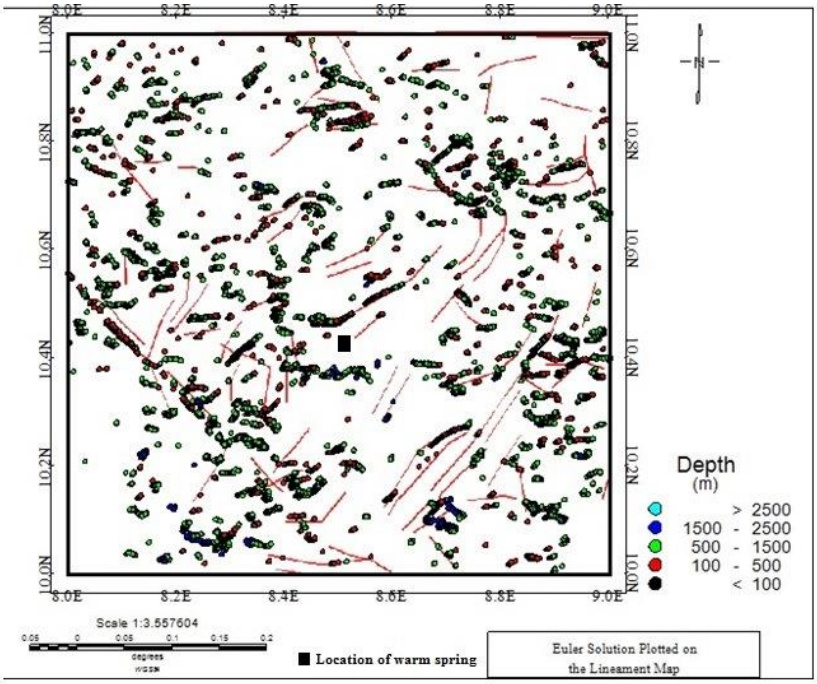

Figure (9): Euler Depth Solution Superimposed on the Lineament Map

(Structural index =1.0).

5. Conclusion and Recommendation

The interpreted aeromagnetic data in this research has helped in mapping structures underlying the RafinRewa warm springin Dan Alhaji Village Lere, Kaduna, Nigeria and its environs.Several criss-crossing lineaments and faults predominantly trending NE-SW, NNW-SSE were delineated. The RafinRewa warm spring is seen to occur at the base of a NE-SW trending lineament. These structures (lineaments) and faults might serve as host to the fluid and also as a conduits for both the fluid and thermal energy to pass to the surface. Depth to magnetic source within the study area is predominantly between 100 m to 1,500 m and were found to cluster around the suspected faults zones.

Acknowledgement

The authors are grateful to the almighty God who have make this work to come to success and also to the Nigeria Geological Survey Agency NGSA) for providing us with data sufficient for this work.

References

Blakely, R. J. (1995). Potential Theory in Gravity and Magnetic Applications, Cambridge University Press, USA.

Catálan, M., Davila, J.M. and ZEE Working Group (2003). A magnetic anomaly study offshorethe Canary Archipelago, Marine Geophysical Researches 24, 129-148.

Dawi, M.G., Tianyou, L., Hui, S., Dapeng, L., 2004. Depthestimation of 2-D magnetic anomalous sources by using Eulerdeconvolution method. Am. J. Appl. Sci. 1 (3), 209–214.

Garba M.L, E. Kurowska, K. Schoeneich, I. Abdullahi (2012). RafinRewa Warm Spring, A New Geothermal Discovery American International Journal of Contemporary Research Vol. 2 No. 9; September 2012.

Huang, L. and Guan, Z. (1998). Discussion on "Magnetic interpretation using the 3-D analytic signal" by Walter R. Roest, Jacob Verhoef, and Mark Pilkington. Geophysics 63, 667-670.

Oyawoye, M.O., Makanjuola, A.A.(1972): Bauchite: a fayalite-bearing quartz monzonite. Proc. 24th LG.C. (Montreal), Sect. 2, 251-266 (1972)

Reid, A.B., Allsop,J.M., Granser,H., Millett, A.J. and Somerton, I.W. (1990). Magnetic interpretation in three dimensions using Euler deconvolution. Geophysics, **55**, 80– 90.

Reynolds, J. M. (1997). An introduction to Applied and EnvironmentalGeophysics. John Wiley and Sons, England.

Thompson, D.T., (1982). EULDPH: A new technique for making computer-assisted depth estimates from magnetic data. Geophysics, **47**, 31–37.

Prieto, C. andMorton,G. (2003). *New insights from a 3D earth model, deepwater Gulf ofMexico:* The Leading Edge, 22(356–360).

Raimi. J., Dewu B. B. M. and Sule P. (2014). *An Interpretation of Structures from theAeromagnetic Field over a Region in the Nigerian Younger Granite Province.*International Journal of Geoscience, 5, 313-323.

Theophile N., Feumoe A. N., Eliezer M. and Fairhead J. D. (2012). *Aeromagnetic DataInterpretation to Locate Buried Faults in South East Cameroun.* Geophysica 48 (1-2), 48-63.

APPLICATIONS OF SLIDE SCAN IMAGES OF THIN-SECTIONS FOR SEDIMENTOLOGICAL STUDIES DURING LOCK-DOWN PERIODS

Isah Aliyu Goro, Abdulfatai Ibrahim Asema and Musa Suleiman Tenimu
Department of Geology, Federal University of Technology, Minna
Corresponding Author: isahgoro@futminna.edu.ng

Abstract

Several conventional and unconventional digitization tools have been used to improve viewing and acquisition of information in the field of sedimentology and sedimentary petrology, in geology and in science and technology in general. Slide scan images of sedimentary rock thin-sections provide inexpensive, very good, whole thin-section views at magnifications similar to those of the conventional microscope. This paper demonstrates how slide scan images can be obtained and how they can quickly be used to gather detailed textural, structural and compositional information of sandstones at microscopic scale. The method has been used in studying features such as grain size, grain shape, fabric, contact between grains, graded bedding, cross lamination and porosity without the need for polarizing microscope and photomicrograph. This unpopular, unconventional method is not known by most researchers even though they can be used at times of lock-down to provide vital geological information relevant to both academia and the industry. This method is also recommended to teachers in low-equipment universities and research centers where research petrological microscopes are either absent or inadequate because it utilizes simple everyday equipment such as scanners to obtain the images and personal computers, laptops, tablets and even smartphones to view the images.

Keywords: lock-down period, thin-section, slide-scan image, sedimentology, texture

1.0 Introduction

Digitization is one of the various ways to improve viewing and maximize data acquisition in the field of science and technology. Various tools have been used to digitize rock thin sections in an attempt to gather geological information at microscopic scale. Examples include petrologic microscopes, scanning electron microscopy and cathodoluminescence. These tools are very expensive, require special conditions to work and are only able to view very small portions of the thin sections. As a result, the identification and description of features such as macro-structures are usually accomplished by obtaining multiple photomicrographs. Attempts have been ongoing since the 1960s to get these information through digitization of entire thin sections for better geological information gathering especially for quantification purposes. In the last few decades, conventional photography using films were used for the digitization. More recently, researchers such as De Keyser (1999), Hansen (2000) and Tarquini and Armienti (2003) have used high resolution scanners to obtain full thin sections of rocks with high resolution pixels.

Different ways of quantifying textural parameters of sandstones based on thin section have been developed by sedimentologists over the years. For slide scan images the visual estimation and manual counting methods can easily be applied. The visual estimation method has the advantage of being relatively fast and it involves the visual estimation of such parameters as grain size, shape, sorting, percentages of components, and fabric using comparison charts (Pettijohn, 1975; Mathew *et al*., 1991).

The present paper attempts to demonstrate how slide scan images of thin sections can be used to provide vital textural and macro-structural information from sandstone samples. Specifically, attempts have been made to demonstrate how slide scan image can be obtained, how to quantify grain size parameters, how macro-structures can be deciphered from slide scan images and how porosity can be estimated. This method can be used to quickly provide these vital information for exploration and exploitation of mineral resources even during lock-down periods though many researchers do not know about it. Ill-equipped research

centres in especially developing and third world countries can also take advantage of this method because it requires only basic office equipment and laptops (or tablets/notebooks or even smartphones) for analysis.

2.0 Methods

The method for obtaining slide scan images of rock thin sections is simple. First the thin sections are produced perpendicular to the bedding of the rock samples. Four ways in which 35mm slide scan images are commonly obtained include the use of flatbed scanners, dedicated film scanners, slide duplicators and professional Photoshop. For flatbed scanner to be used, it must be the type that is able to scan negatives and slides in addition to traditional paper photos and documents. The recommended scanner must also have optical resolution of at least 2400 dpi. The scanner is connected to the computer directly and the slides are inserted on the scanner for the image which can be directly viewed in the computer via the scanner software. The image is either stored on the computer or another device for preservation or further processing. In the present work, the slide scan images of the aeolian sandstones were obtained using Polaroid Sprint Scan 35LE slide scanner.

Textural features of the rock such as grain size, morphology and fabric can easily be examined on the slide scan image by comparing with charts such as shown in Figures 1 below.

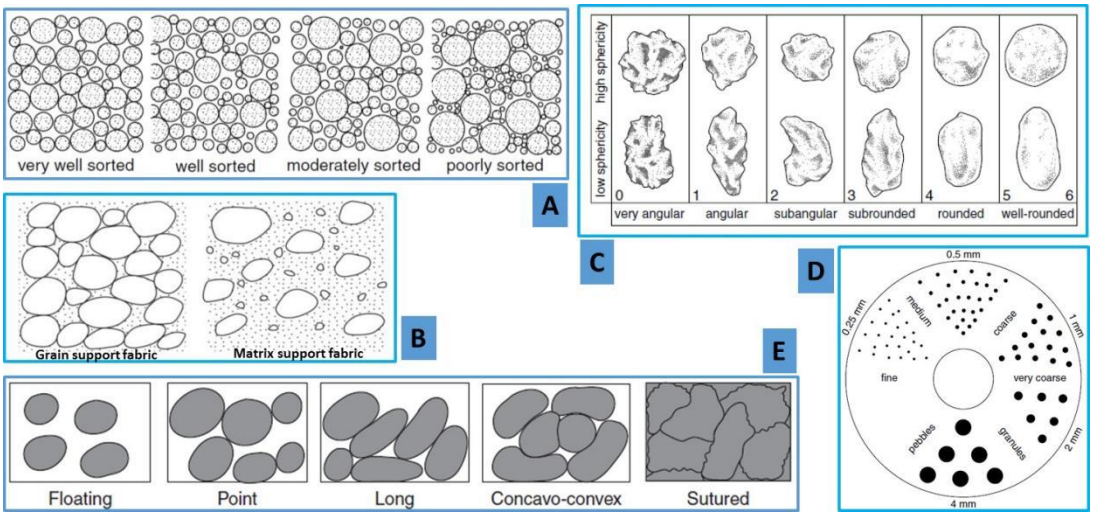

Figure 1. Charts for visual estimation of sedimentological features. **A**: Charts for visual estimation of sorting; **B**: chart illustrating fabric of sandstones; **C**: Categories of roundness for sediment grains, for each category a grain of low and high sphericity is shown; **D**: Chart for estimating grain-size of sands; **E**: Chart illustrating nature of grain contacts.

Answers to two aspects of porosity can also be obtained from slide scan images; the type and amount of porosity. Figure 2A is a sketch showing the types of porosity while Figure 2B demonstrates how porosity amount can simply be computed through gridding method. In this method, which is similar to point counting, sections of the slide scan image is enlarged and gridded. Each of the cell is now point counted for either grain or pore space. Here the grain is represented by any component that is not a pore space. At least 100 counts can be achieved for a grid of 10 by 10 cells. A table of tallies is formed from the counts which can easily be converted to frequency table from which percentages of the total pore space can be computed. In Figure 2B a total of 800 counts can be made.

3.0 Applications of thin-section slide scan images in sedimentology

In this study, the application of slide scan images in textural and macro-structural studies of sandstones will be demonstrated using slide scan images of aeolian sandstones. Attempts will be made to decipher compositional attributes from the images. These will be illustrated using the examples below.

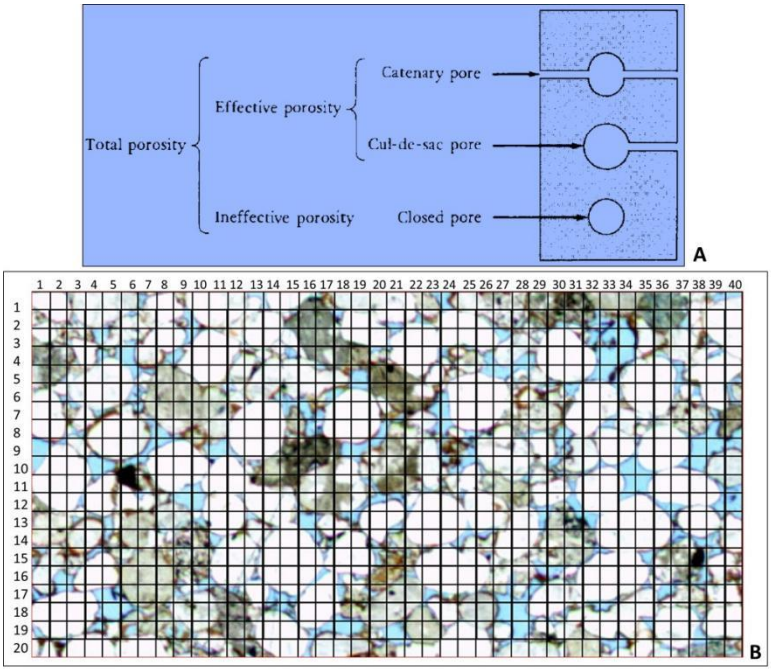

Figure 2. A: three basic types of pores; **B**: grid for porosity estimation using 800 counts.

3.1 Studies of textural characteristics of sandstones

Simple description of sedimentological attributes of sandstones can easily be done with a slide scan image. Example is shown below for the features displayed by the sample in Figure 3. The textural attributes of the sample include: 1) bimodal grain size distribution with the coarser and finer grains having good sorting individually; 2) grains are predominantly rounded with generally high sphericity; 3) grain contacts are predominantly touching with few long and concavo-convex contacts; 4) the fabric is grain-supported. Sedimentary structures observable in the sample are: 1) graded laminae showing normal grading (Fig. 3A); B: cross lamination displayed by inclined laminae (Fig. 3A). Apart from the grain contacts that indicate diagenetic phase, the observation of grain dissolution (Fig. 3B) especially at the upper left side of the sample is also indicative of diagenetic effect. Both primary and secondary (dissolution) porosity are observed (Fig. 3B). The pore spaces are better interconnected at the upper part of the slide where better permeabilities are expected. Permeability is better within the laminae coning the larger grains and lower in laminae formed by the finer grains and generally increases upwards.

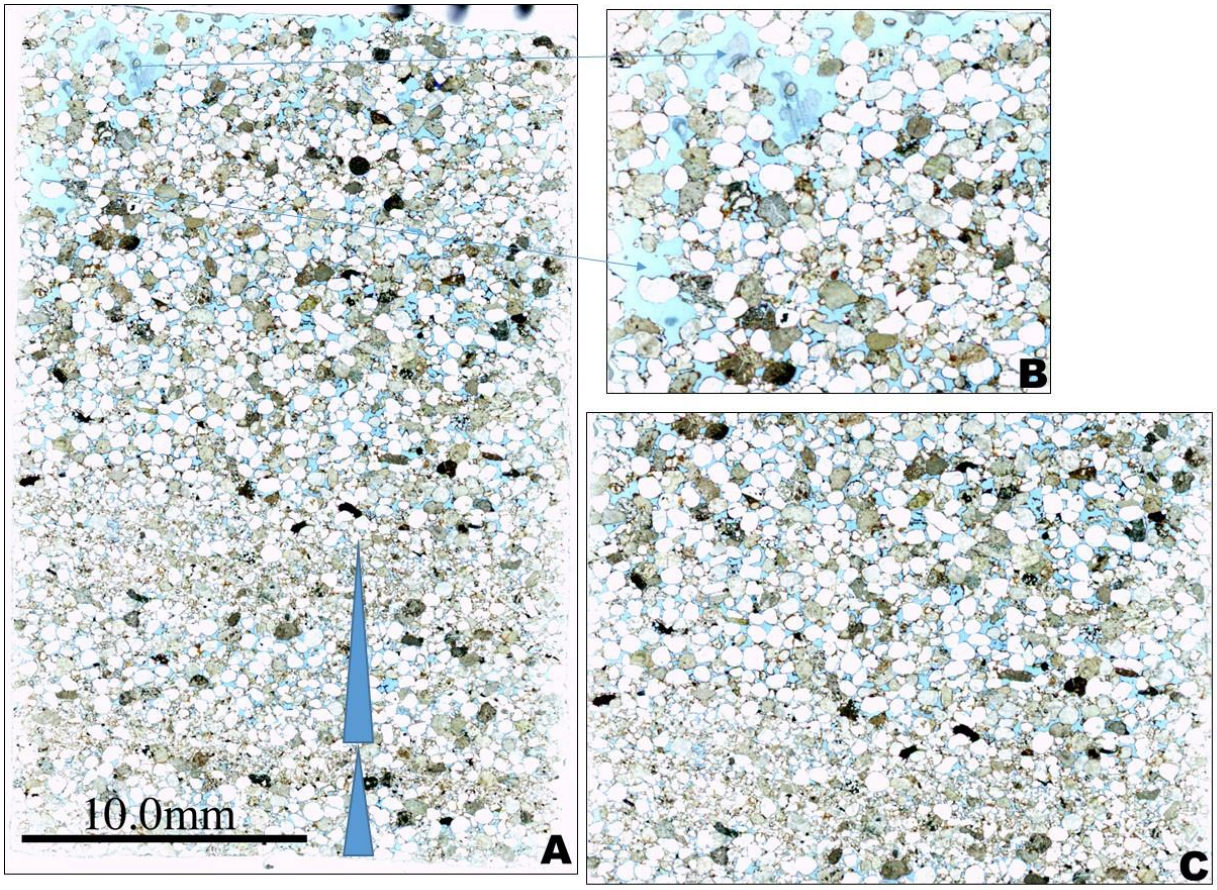

Figure 3. Slide scan image of showing whole thin section view of eolian sandstone; **A:** normal grading at the lower part of the slide; **B:** closer view of upper left side of the image showing secondary pore due to grain dissolution (arrows); **C:** alternation of fine grained lamina and coarse grained lamina indicating the bimodal grain distribution.

Figure 4 displays a closer view of the sample indicating the nature of the grain contacts. Majority of the grains do not touch each other (floating) or may just touch each other at a point (point contact). Long and concavo-convex contacts are displayed by few grains. This indicates the extent of burial.

3.2 Identification of some compositional features

Compositional features may not be well defined by slide scan images but grains such as rock fragments can be indicated when enlarged. For example, Figure 5 shows sandstone rock fragments as brown grains while the black deformed grains represent fine grained rock fragments. Grain dissolution porosities are also indicated.

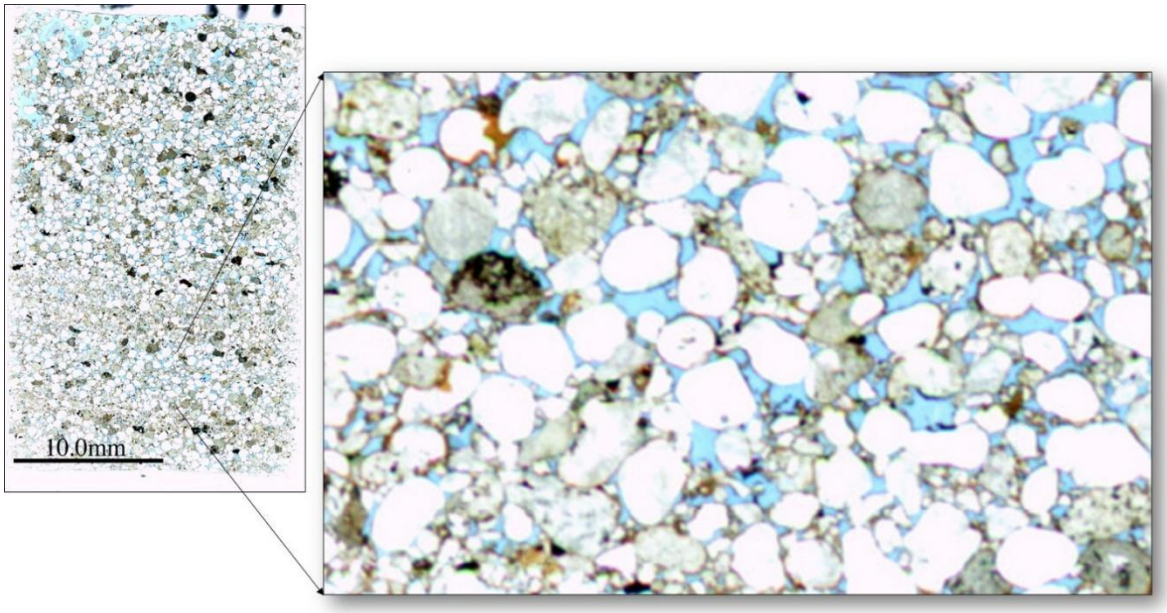

Figure 4. Close-up view to display nature of grain contacts in the sandstone

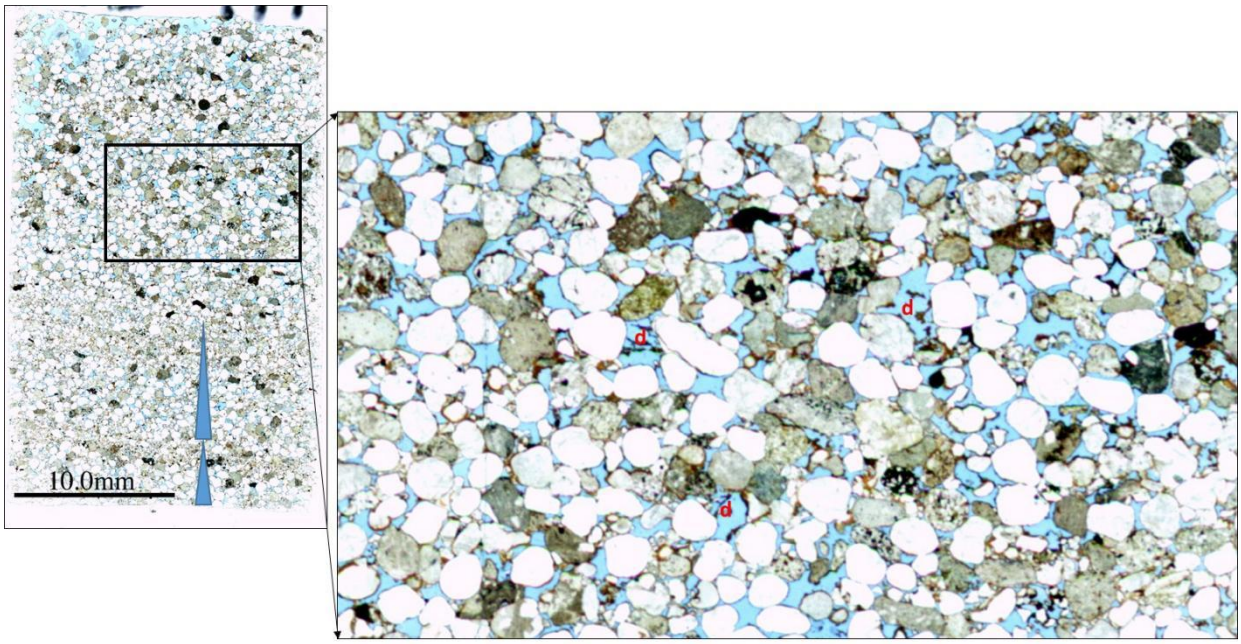

Figure 5. Close-up view showing sandstone rock fragments (brown) and fine grained rock fragments (black) as well as dissolution porosity (d).

3.3 Deciphering sedimentary structures

Deciphering macrostructures easily is one of the advantages that the slide scan images have over conventional petrologic microscopes because acquisition of several photomicrographs in order to show only one features can be avoided. Such structures include graded laminae and cross lamination. Figure 6 illustrates how these features can be discerned from slide scan images. A closer view of alternating fine

and coarse grained laminae shows that pore spaces are occluded in the finer grained laminae. This may affect vertical fluid flow in the sandstone.

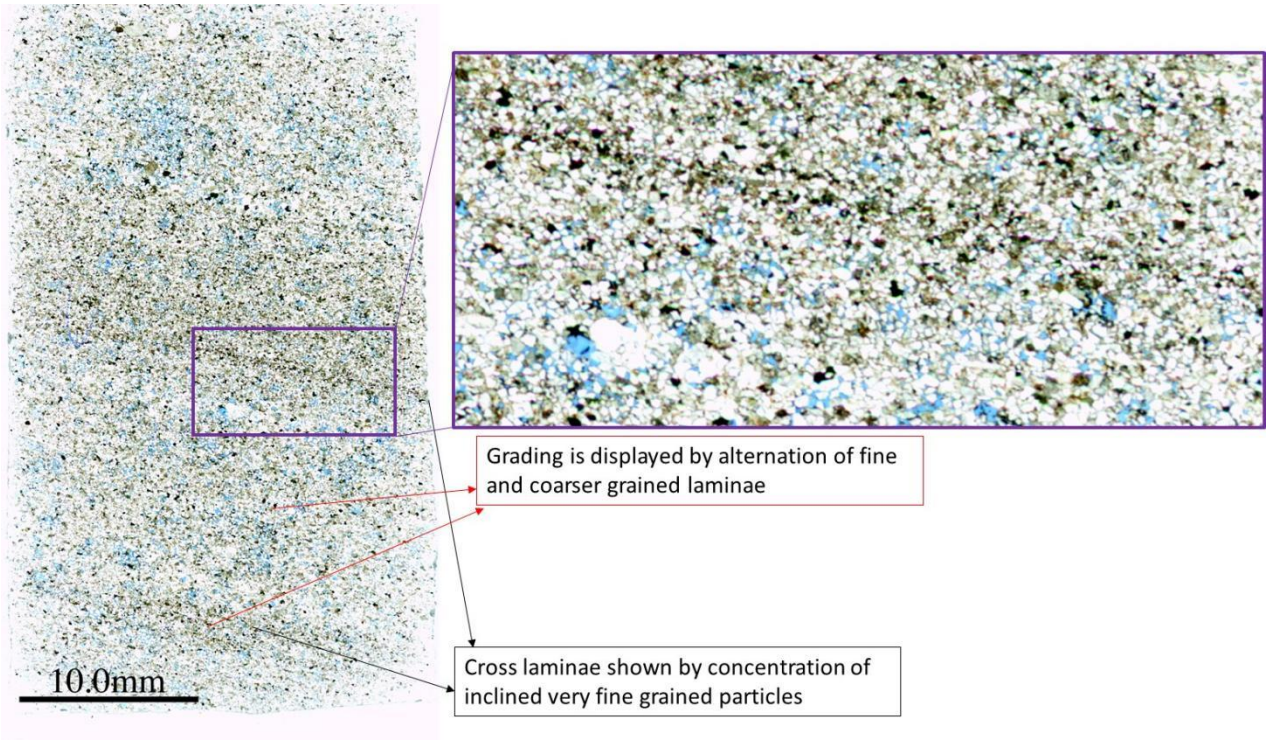

Figure 6. Grading of grain size and cross lamination.

3.4 Porosity measurement

Porosity plays relevant role in aquifers, reservoirs as well as in engineering projects that deal with rocks. The total porosity consists of the volume of voids given by all types of pore spaces either connected or not that are present in the rock and may be filled with water, air or hydrocarbon (oil or gas). Figure 7 demonstrates how quick porosity estimation can be made. Different parts of the slide scan image may be enlarged and their porosities estimated after which the average is taken. The number of cells present on Figure 7 is 800 and a total of approximately 94 cells were counted as pore spaces which gives a porosity of about 12% for the enlarged part.

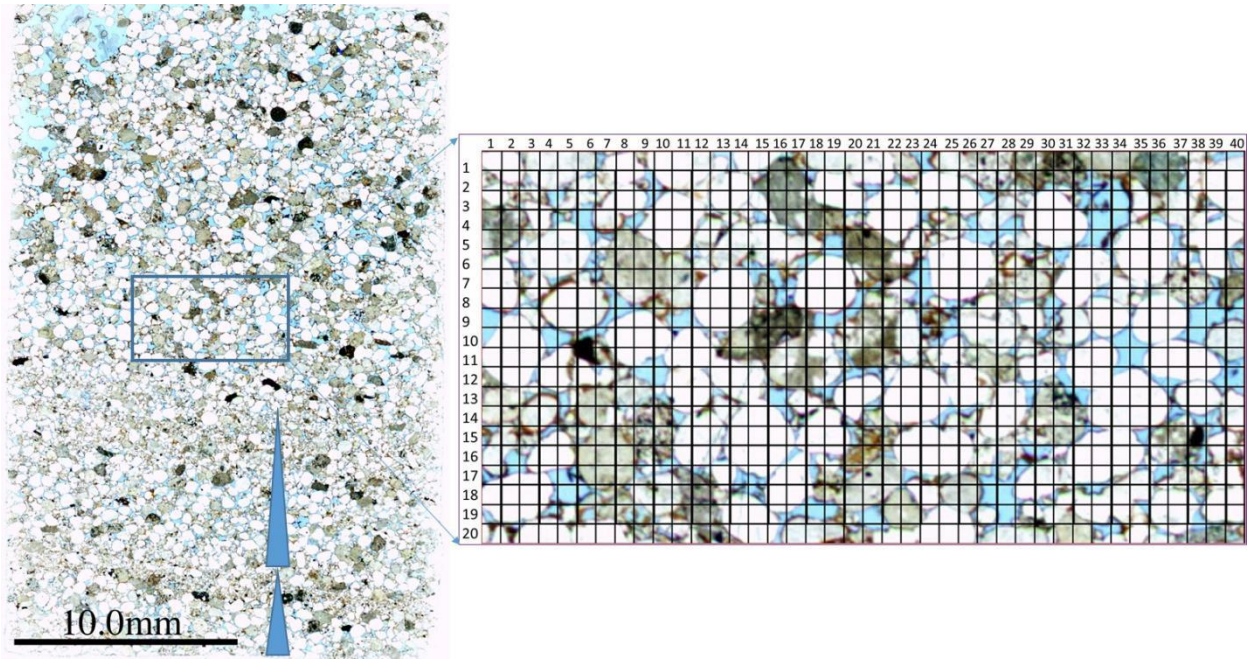

Figure 7. Porosity estimation using manual point counting (gridding method)

Fine grained, angular grains make-up the sandstone on Figure 8. The interconnectedness of the pore spaces is revealed in this sample by zooming-in the slide scan image.

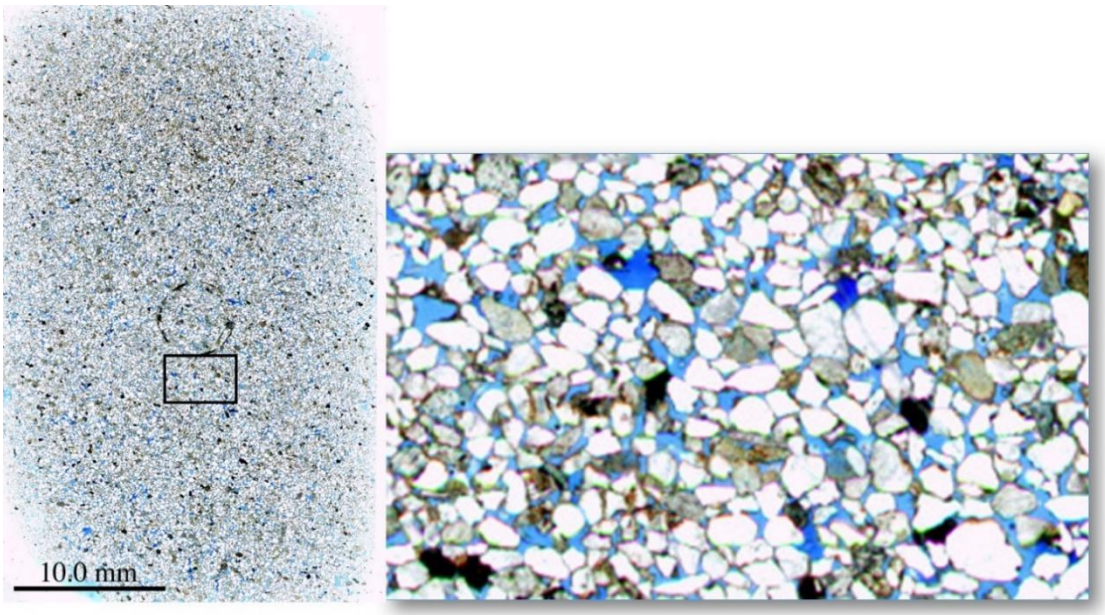

Figure 8. Interconnected pore spaces.

4.0 Discussion

Before the advent of technologies leading to direct acquisition of high resolution digital images the conventional photography was used to indirectly obtain digitized images of whole rock thick sections. This method has been practiced for decades and involves the production of negatives which were scanned and stored in CD ROMs or diskettes. The images were loaded to photography softwares and enhanced before printing digitally. However, with the arrival of more advanced digital imagery such as high resolution scanners, it is possible to obtain images at very high pixels which could be uploaded directly to personal

computers for viewing and further processing. This has led to bridging of gaps between photography (as explained above) and phomicrography obtainable from conventional petrological microscopes. More recently, slide scan images were used in solving issues pertaining the detailed description of complex textures such as reef framework in carbonate rocks at very high resolution thereby providing alternative ways in institutions where capacity for acetate peels production are lacking. This is common in laboratories that are ill equipped.

The study of slide scan images has also bridged gaps between different magnifications. In conventional microscopy, different objective lenses are inserted in order to observe features at different magnifications. Whereas if a slide scan image is directly viewed with a computer, it is easier to just crop an area in the image for further studies. Also the relationship between features of interest and the adjacent grains or features are better observed on slide scans. This means that inserting different objective lenses can be avoided.

The information gathered from the slide scan images are all vital sedimentological features that give lots of insight in to hydrodynamic conditions and processes in the environments of deposition. For example, the coarser grain sizes reflect deposition by faster flowing currents while finer grained laminae reflect deposition by slower or quieter moving currents whereas the degree roundness may reflect the transport distance and degree of reworking of the sediments. Sorting on the other hand generally reflects depositional processes; better sorting is achieved by agitation and reworking processes. For example, to-and-fro movement of current around the beach environment causes better sorting.

The fabric entails documentation of both grain orientation and packing. These information give important insights to the paleocurrent direction and mechanism of deposition of the sediments. For example, in both clastic and carbonate rocks, the recognition of grain support fabric without matrix suggests reworking by currents/wind/waves as the possible mechanism of deposition. It may also reflect deposition by turbulent flows where the suspended sediment load were separated from the coarser bedload materials that where deposited. Matrix support fabric may simply indicate deposition in low energy environments by deposition by low energy flows.

Alternation of coarse and fine grained laminae displayed by cross laminated sandstones reflects sorting of grains at the time of deposition on the foresets of sand dunes. The processes of grain flow and grain fall are two processes that causes sorting of the type displayed by the studied samples. Here, the coarser and thicker beds record avalanching of sediments on foresets while the thinner finer beds reflect suspension settling. These two processes may be the reasons for the alternation of these beds/laminae. Sedimentological interpretation discussed herein can be found in general sedimentology and stratigraphy textbooks such as Pettijohn (1978), Turcker (1994), Reading (1996) Tucker (2003), Boggs (2005), Nichols (2008), Boggs (2009), Selley (2000) and several other papers.

5.0 Conclusion

The following conclusions can be made from this paper.

1. Slide scan images can be obtained using common flatbed scanners or dedicated scanners
2. Studies of slide scan images provide quick, cheap and easy way to gather sedimentological information such as texture, macro-structures and porosity of sandstones
3. Ill equipped research institutions can take advantage of this method to provide services
4. Researchers can also take advantage of this method when access to laboratory is denied during periods of lock-down

References

De Keyser, Thomas L. (1999) Digital Scanning of Thin Sections and Peels. Research Methods Papers. *Journal of Sedimentary Research*, (69) 962-964.

Boggs, S. (2005). Principles of Sedimentology and Stratigraphy. Prentice Hall, New Jersey.

Boggs, S. Jr. (2009). Petrology of sedimentary rocks. Cambridge University Press, New York.

Hansen, Eric F. (2000) Ancient Maya Burnt-lime Technology: Cultural Implications of Technological Styles. Ph.D. dissertation, Archaeology Program, University of California, Los Angeles. University Microfilms, Ann Arbor.

Miriello, Domenico, and Gino Mirocle Crisci (2006). Image Analysis and Flatbed Scanners. A Visual Procedure in Order to Study the Macro-porosity of the Archaeological and Historical Mortars. *Journal of Cultural Heritage* (7) 186-192.

Matthew, A. J., Ann J. Woods, and C. Oliver (1991). Spots Before the Eyes: New Comparison Charts for Visual Percentage Estimation in Archaeological Material. In *Recent Developments in Ceramic Petrology*, edited by Andrew Middleton and Ian Freestone, pp. 211-263. British Museum Occasional Paper No. 81. British Museum Research Laboratory, London.

Nichol, G. (2009). Sedimentology and Stratigraphy. Wiley-Blackwell, Oxford.

Pettijohn, Francis J. (1975). Sedimentary Rocks. Harper and Row, New York.

Reading, H. G. (1996). Sedimentary Environments: processes, facies and stratigraphy. Blackwell Science, Oxford.

Tarquini, Simone, and Pietro Armienti (2003). Quick Determination of Crystal Size Distribution of Rocks by Means of a Color Scanner. *Image Analysis and Stereology*, (22) 27-34.

Selley, R. C. (2000). Applied Sedimentology. Academic Press, London.

Tucker, M. E. (1994). Sedimentary Petrology. Blackwell Scientific Publications, Oxford.

Tucker, M. E. (2003). Sedimentary Rocks in the Field. Blackwell scientific publications, Oxford.

Updates on the Geological Map of Paiko Sheet 185 on a Scale of 1:100,000, North Central, Nigeria

Abdulfatai, I. A.[1, 2], Garba, M. L.[2], Isyaku, A. A.[2] and Ikpokonte, A. E.[2]
[1]Federal University of Technology, Minna, Nigeria.
[2]Ahmadu Bello University, Zaria, Nigeria.
Corresponding author:fatai.asema@futminna.edu.ng/+2348057467043.

Abstract
Geological mapping of Paiko Sheet 185 was carried out on a scale of 1:100,000 in order to update the existing geological map of the area. Traverse as well as green line methods of mapping were employed. At each location, the lithology, colour, texture, nature of contact between lithologies and structures were noted and documented. Field observations show that the area is composed of migmatite (66.154%), coarse grained granite (14.233%), medium grained granite (13.061%), sandstone (4.177%), tonalite (2.142%), ironstone (0.092%), Talcose rock (0.089%) and marble (0.052%). The modifications made to the existing map which was produced in 2009 and colour coded in 2015 include; replacement of the alluvial lithology with the bedrock (migmatite) and renaming of talc-tremolite-actinolite schist to Talcose rock due to the absence of schistosity. Other modifications are: the removal of schist because it is actually located on the adjacent Abuja Sheet; inclusion of Sakpe Formation around Lapai as well as harmonizing the marble occurring around Kwakuti as one unit. Structures such as folds, faults, joints, unconformities, exfoliations, strain-slip cleavage, trace fossils, bedding and bedding plane were observed and recorded. The result of joint direction measurements shows that the principal joint direction is in the northwest - southeast. The economic geological resources within the sheet include, gold, lead, zinc, marble, Talcose rock, rocks, laterite, clay, sand and gravel.

Key words: Geological mapping, Paiko Sheet, lithology, structures, geological resources

1.0 Introduction

Updating of geological map at time interval is necessary to make the map more comprehensible. Some rocks and features that were not captured by earlier maps perhaps due to poor exposure might become visible as result of natural processes (such as erosion and uplift) or anthropogenic activities (such as quarrying, mining and construction). Geological mapping of Paiko Sheet 185 was carried out to update the existing map of the area. The geological map (Figure 1) of Paiko Sheet was produced by the Nigeria Geological Survey Agency (NGSA) in the 2009 on the scale of 1:100,000 with a total of 11 lithologies. The map was colour coded by Ejepu & Umar in 2015 (Figure 2). The maps show that about 85 percent of Paiko sheet is underlain by Basement Complex rocks while the remaining part is underlain by sedimentary rocks of part of Bida Basin according as suggested by the existing map. The present study was carried out using geological field mapping exercise carried out between the months of January and March, 2019 to update the existing maps.

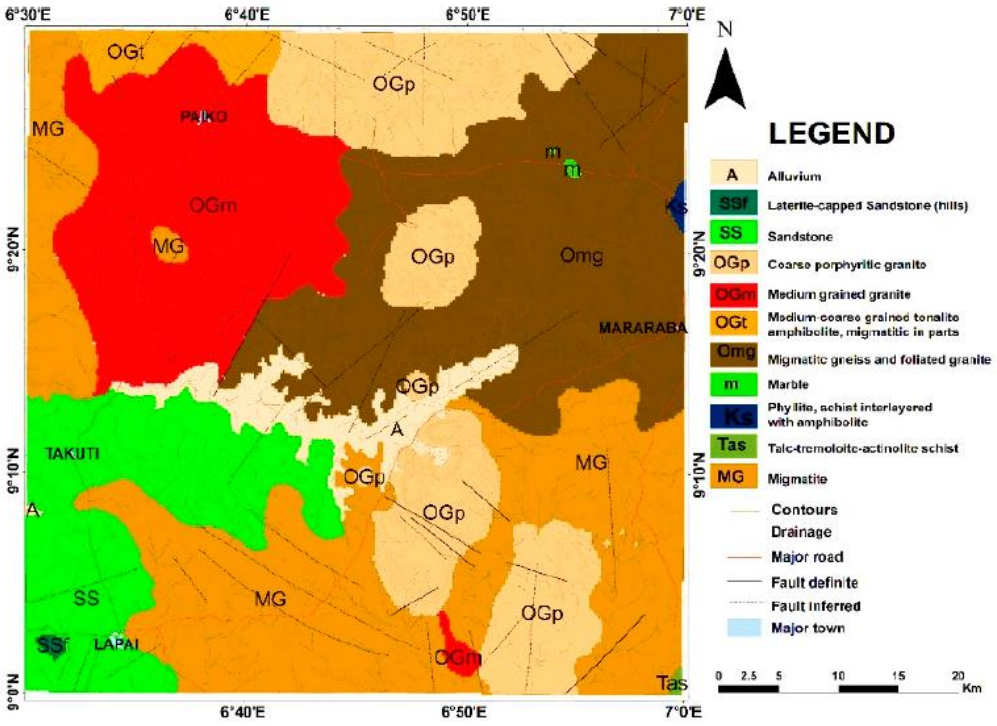

Figure 1: Geological map of Paiko Sheet 185 (NGSA, 2009)

2.0 The study area

The Paiko Sheet No 185 is located on latitude 9º00' to 9º30' and longitude 6º30' to 7º00' (Figure 3). The area covers about 3080.25 km². It is bounded to the north and south by Minna and Gulu sheets respectively and to the east and west by Abuja and Bida sheets respectively. The area is accessible by Minna – Suleja road, Lambata – Bida road, Minna – Paiko road with other secondary and minor roads as well as paths (major and minor). The inhabitant are mainly farmers but mining activities is on the increase as Paiko sheet play host to a lot of economic minerals such as gold, lead-zinc, marble among others in various locations. The major settlements include Paiko, Lapai, Pago, Lambata, Farin Doki, Kwakuti and Baban Tsauni.

The topography of Paiko Sheet 185 (Figure 3) is characterised by various landform that include ridges, inselbergs, Batholiths, earth pillar and plains. The lowest point is 130m while the highest point is 600m above sea level and are all found in southern western (east-south-east of Lapai town) and southern eastern portion of the area respectively. The summit of Kudan Batholith represents the highest point in Paiko sheet. Averagely, the eastern half has higher relief than the western half. The average relief of the north-eastern portion is the highest of all followed by south-eastern then north western potion while the least is south-western portion.

River Gurara which is located in the south-eastern part of Paiko sheet is the largest river draining the area with dozens of tributaries. The areas generally have a dendritic drainage pattern except the areas around Kudan batholith where radial drainage pattern was observed. Majority of streams take their source from the highlands within the studied area and the southern half has a better drainage system compared with the northern portion. All streams and rivers are indirect tributaries of River Niger except River Gurara that empties its content directly into it somewhere around Dere close to Koton Karfe in Kogi State.

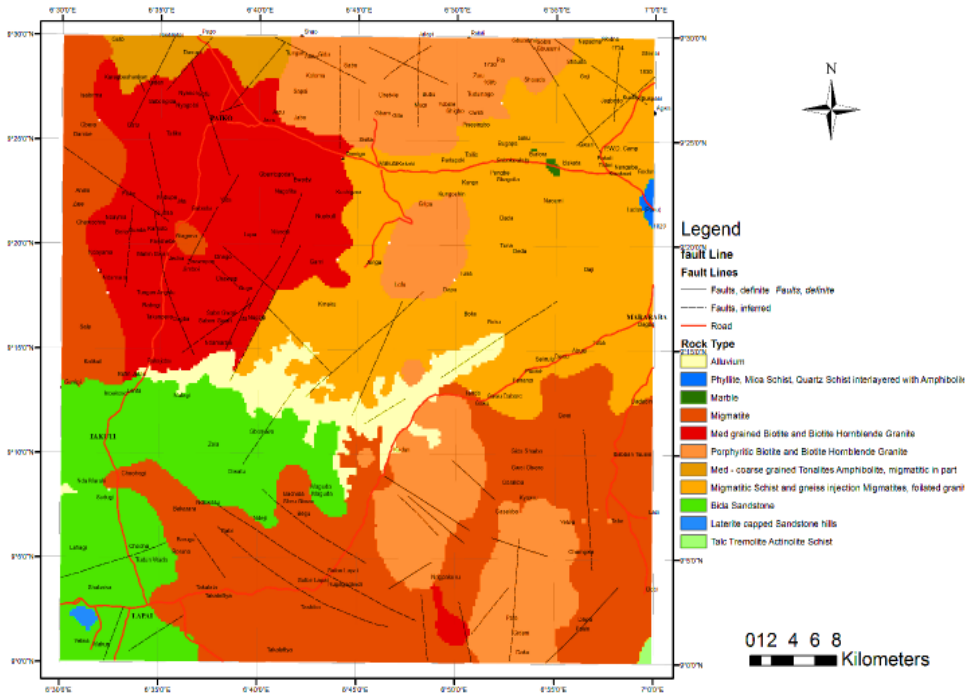

Figure 2: Colour coded Geological map of Paiko Sheet 185 (Ejepu & Umar, 2015)

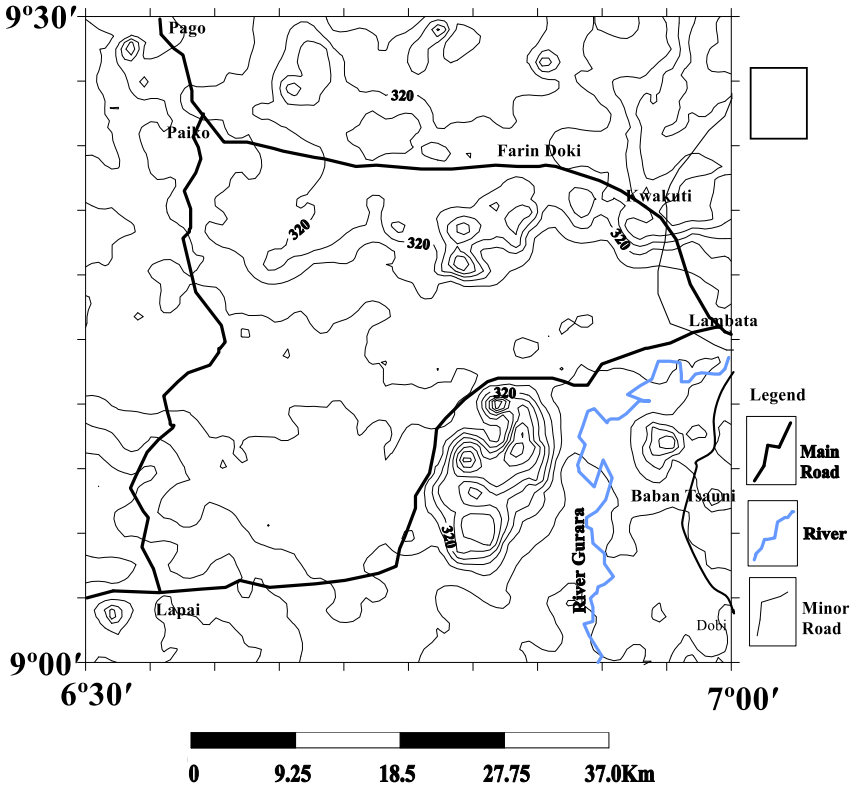

Figure 3: Topographic map of Paiko Sheet

The vegetation is of the Guinea Savannah type. The area is characterized by tropical scrubs as the major trees generally, but thicker forest exist in part of the south-western portion (Sodugi and Kpaesan). Light forest also exists in the north-western part (around Kwakuti). The climate of the area consists of two seasons (dry and rainy). The dry season usually lasted between November and April while the rainy season usually

lasted between May and October. The total annual rainfall ranges between 1270mm to 1524mm (Ejepu & Omar, 2015). The maximum daytime temperature is about 35ºC in the months of March and April, while a minimum temperature of about 24ºC is recorded in the months of December and January. The mean annual temperatures are between 32ºC to 33ºC (Njeze, 2011). The dry season is marked by the influence of harmattan which is a result of North-East trade wind that blows across the Sahara which is often laden with red dust and lasts from the month of December to the month of February (Ejepu *et al.*, 2017).

3.0 Geology of the Area

Paiko Sheet No 185 is part of the area covered by Russ (1957), and Truswell and Cope (1963) in their reconnaissance geological survey of part of Northern Nigeria. It forms part of the area studied for gold mineralization by Woakes and Bafor (1984). The geological map of the sheet was produced by NGSA in 2009 (Figure 1). The NGSA map recognized about eleven different lithologies in the area. These lithologies include Alluvium which can be found in the central part of the area; laterite capped sandstone exist in the south-western part of the area; Coarse grained porphyritic granite is found in parts of the northern, northern-eastern and southern-eastern region of the area; Medium-coarse grained tonalite and amphibolites exist in part of north-western region of the area; Migmatitic gneiss and foliated granite is found in the north-eastern part of the area; Marble exist as a small unit in part of the north-eastern part of the area; Phyllite, mica schist interlayered with amphibolites are found at the extreme end of the north-eastern part of the area; Talc-tremolite-actinolite schist can be found at the extreme end of south-eastern part; and migmatite can be found in parts of the southern and north-western part of the Paiko sheet. Migmatitic rocks dominated the area followed by granitic rocks that contain biotite and hornblende and then Sandstone Formation. The geology of the area shows that 85% of the area is occupied by basement rocks and 15% occupied by sedimentary rocks according to Ejepu and Omar (2015).

4.0 Method of Study

Traversing method was utilized mainly for the field mapping exercise along with green line mapping methods (also called exposure mapping used for mapping very large exposures). Roads (main road, minor road, main path and minor roads), road cuts and river channels were utilized to locate outcrops. Materials used include compass/clinometers that were used for measuring strikes and dips of rocks and structures, hand lens for field examination of mineral and textural composition, geological hammer for sampling, pen and field notebook for recording of field observations. Others include topographic map that was used as base map, rucksack for carrying samples, camera for taking photographs of important features and Global Positioning System (GPS) for recording coordinates.

Since the area of study cut across both Basement Complex and sedimentary terrain, the expected rock types were igneous, metamorphic and sedimentary rocks. Therefore, igneous rocks were studied using a check list proposed by Thorpe and Brown (1985) while metamorphic rocks was studied using the criteria proposed for mappable units by Fry (1984). Sedimentary rocks studies were achieved using the broad scheme developed by Tucker (1982).

Results from the geological field exercise was used to prepare geological map, cross profiles and the measurement taken for joint directions were used to prepare rosette diagram to determine the principal joint direction of the area. Appropriate map symbols were used for ease of comprehension.

5.0 Results and Discussion

5.1 Petrography

5.1.1 Migmatite-Gneiss

These are the dominant rock types in the north-eastern and southern portion of Paiko sheet. It is also exposed at the extreme end of the north-western part of the sheet. The rocks comprises of migmatites and gneisses coexisting together without any particular order. The most notable of the gneisses is exposed in the ENE (around Dagigbe) part of the sheet as shown in Plate 4d and it is located on latitude 9º21'43.1"

and longitude 6º59'55.3". The trend of the outcrop is 328ºNW. The outcrop was poorly exposed by road cut. Bandings (alternation of light and dark coloured minerals) were observed on the outcrop and boulders. The dark coloured minerals predominate as their layers are usually thicker than the light coloured minerals. It is generally hard signifying slight to no weathering. The migmatite-gneiss were intruded in part by granitic rocks. Figure 4 shows a very fine grained migmatitic rock located (latitude 9º08'37.2" and longitude 6º32'58.3") at the contact between Basement Complex and Bida Basin. The rock appeared to have been affected by shearing force due to the very fine grained nature of the grain sizes. The rock is exposed along a stream which flows southwest which appears to have taken its source around Achitupa and Kpaesan hills. They are generally low lying. Bida Sandstone unconformably overly the magmatic rock at the southern-western part of the exposure around the contact between the basement complex and sedimentary basin (Bida Basin). They are intruded in parts by granitic rocks.

Observations from hand specimens show that the migmatite – gneissic rocks from Paiko sheet 185 are generally dark in colour and composed of Biotite, quartz, plagioclase feldspar and accessory minerals. They are mostly medium to coarse grained except those that exist at Basement Complex-Bida Basin contact within south-western part of the sheet. They occupy more than 60%. It is dominated by dark coloured minerals. Majority of them appeared to have been folded ptygmatitically (Figure 7a). The antiformal closures are in north-eastern direction while synformal closures are in south-western direction.

5.1.2 Porphyritic Biotite and Biotite Hornblende Granite

This is the major rock type occupying the north-eastern part of Paiko Sheet and also form part of the rocks underlying the southern portion. The outcrops within this areas also exist in various igneous landforms. The notable igneous landforms in this area are Gbagbanpi ridge, Shaku ridge and Bodna – Sekiape ridge, Kudan ridge (the most prominent of all with a length of more than 18km, breath of more than 10km and peak of about 600m above sea level) and Dawaki hills in the south; and Pita laccoliths and Gbodna hill in the northern part of the sheet. They are porphyritc in texture and dark in appearance. It is dark coloured and the major mineral composition include biotite, quartz and feldspar. Accessory minerals are also present. Exfoliations were observed on some of the outcrops. They intruded into the Migmatite-Gneiss.

5.1.3 Medium Grained Biotite and Biotite Hornblende Granite

This rock type dominates the north-western part of Paiko sheet. A very small portion of it exist in the south-eastern part of the sheet. The outcrops within this area exist in various igneous landforms. Notable among these igneous landforms is the Paiko Laccolith. It is medium grained and consist of biotite and biotite-hornblende granite and dark in appearance. It is dark in appearance and Biotite mica is the dominant minerals followed by feldspar and quartz and then accessory minerals. Exfoliations were observed on some of these rocks. They intruded into the Migmatite-Gneiss.

5.1.4 Medium-coarse grained tonalite and amphibolites

These rocks occupies part of the extreme north-western portion of Paiko Sheet. These set of rocks were found only in this region. The tonalite which is an intermediate rock composed mainly of plagioclase feldspar with less amount of quartz and alkali feldspar with medium to coarse grained texture. It is greyish in colour. The amphibolite contain amphibole and plagioclase feldspar with some accessory minerals. It has a coarse grained texture and greenish in appearance. However the tonalite is dominant over amphibolite.

5.1.5 Talcose rock

This rock is exposed at the extreme end of south-eastern part of Paiko sheet (at an angle of 225°). It is located on latitude 9º02'11.7" and longitude 6º31'25.8". The rock is talc-rich and massive without pronounced foliation. It is poorly exposed and is overlain by lateritic soil (that shows a coarsening upward sequence) but exposed by artisanal mining activities. The artisanal miners were mining for ceramic

industries. It was weathered to varying degree ranging from slightly weathered to highly weathered rock (Plate 1). The rock is soapy to the touch. The fresh sample is greyish in colour. This type of rock is also called steatite or soap rock or talc schist (if it is foliated). It is fine-grained, massive and opaque. The outcrop cut across Paiko, Abuja, Gulu and Kuje sheets.

Plate 1: Talcose rock displaying different degree of weathering in around Dobi

5.1.6 Marble

This is exposed in the ENE part of the Paiko sheet and it is located on latitude 9º23'53.1" and longitude 6º54'46.4". The trend of the exposure is 349ºNNW. In the southern part, the deposit is overlain by thick clay which is more than 10m in some places. The clay is overlain by thicker layer of laterite deposited. In the northern part, the marble deposit is overlain by laterite directly. Two varieties of marble exist namely; the grey and coarse grained variety, and white and fine grained variety. They have interlocking texture. Artisanal mining activities by the surrounding villagers are rampant in the area. There is presence of a quarry company mining the marble deposit in additional to artisanal mining activities carried out mainly by the locals.

5.1.7 Schist

This rock types exist on latitude 9º29'38.1" and longitude 6º37'13.4" in the north-western part of Paiko sheet. The schist is poorly exposed by Shelter Clay mining activities in the area. Shelter Clay mines lateritic clay for bricks production in Pago (along Suleja-Minna road). Close to this mine are artisanal gold mining activities with a better exposure of the rock although it is highly weathered (Plate 2). It was observed that some pits were dug along a vein composed mainly of about 5m thick quartzite. Schistose structure were found preserved in part of the overlying lateritic clayey soil especially on the desiccation cracks within the Shelter Clay mine suggesting that the bed rock (schist) is the source of the soil in the area.

5.7.8 Quartzite

This rock was exposed in the north-western portion of the sheet. It was poorly exposed, low lying and occupies very little portion compared to other rocks in its surrounding. It is located on latitude 9º29'58.1" and longitude 6º37'07.2". Mining activity appeared to have taken place as lots of broken pieces were seen on and around the exposure. They also occur in the form of veins that cut across some of the artisanal gold mines nearby. They occur sporadically within this neighbourhood and appears to be the host for gold being mined in this area. They are greyish in colour and predominantly made of quartz grains with some accessory minerals.

Plate 2: Highly weathered Schist within a mining site in Pago

5.1.9 Claystone with Sandstone Intercalation

These are found in the south-western part of Paiko sheet. The outcrop is located on latitude 9º02'11.7" and longitude 6º31'25.8". The rocks are thought to be part of Bida Formation of the Bida Basin. This is because of similar features such as very high quartz content and presence of trace fossil described by Obaje (2009). The average strike/dip of beds is 104°/19° and the dip direction is 057°. This outcrop is about 190m thick above ground level. The bedding planes separating beds of these rocks are made up of ironstone. These bedding planes are usually fractured (Plate 49g) while some have ripples mark-like structures (Plate 4h).

From the lithologs shown in Figure 6, Mudstone with fine-grain Sandstones interbed directly overlain the basement rock. These (Mudstone with fine-grain Sandstones interbed) fine was in turn overlain by Conglomeritic Sandstone. Immediately above the Conglomeritic Sandstone is obscured by ironstone rubbles (they are poorly exposed). Above this point is arkosic pebbly Sandstone beds with Mudstone intercalations believed to be correlate-able to Doko Member of Bida Formation. Overlying these (arkosic pebbly Sandstone beds) is a poorly exposed bed covered by ironstone rubbles which is overlain by a very thick bed of whitish Claystone (about 60m thick) with cross laminated fine grain Sandstone interbeds (This is thought to be the lateral correlate-able to Jima Member of Bida Formation). Overlaying this is Ironstone.

5.1.10 Ironstone

This rock is underlain by claystone in the south-western part of Paiko sheet. The outcrop forms part of the *earth pillar* and located on latitude 9º02'11.7" and longitude 6º31'25.8". It comprises of oolitic ironstone and pisolitic ironstone. The oolitic ironstone overlies claystone while the oolititic ironstone was overlain by the pisolitic ironstone at the top. A lot of animal burrows (trace fossils) were observed on the ironstone but were more on the oolitic ironstone. They have a total thickness of about 20m. They were reddish brown in colour and the oolite generally has a finer texture than the pisolite. This exposure is correlate-able to Sakpe Ironstone Formation as the features observed were similar to it.

5.2 Geological Structures

Minor folds were encountered during the fieldwork exercise. They were encountered in migmatitc rocks mainly. Ptygmatitc fold (Plate 3a) were dominant on the migmatitic rocks. The antiformal closures are in north-eastern direction while synformal closures are in south-western direction. Fractures including both joints and faults were encountered during the geological field mapping exercise. Joints (Plate 3b) make larger percentage of the fracture encountered in field. Joint direction values obtained from the field were used to construct rosette diagram (Figure 5). The rosette diagram shows that the principal joint direction is in the northwest - southeast. Outcrops were highly jointed with many cross cutting one another particularly in the north-western part of Paiko sheet resulting into joint set and joint density in some cases. South-

western part the area recorded the lowest joint count. Faults mainly strike-slip faults were encountered. The amount of displacement ranges from few centimetres to several metres. Both dextral (Plate 4a) and sinistral faults were encountered. Dip-slip faults (normal faults) were observed along a stream channel close to Lefu (around the middle part of the studied area). There is existences of mini water fall at the faulted point.

Veins (Plate 4b) observed in the field are majorly made up quartz. Aplite were also noticed in some rocks. Some of these veins appear to have been either fold or emplaced in area where fractures previously existed. Some veins were found to cross-cut one another. The thickness ranges from about 1cm to about several meters. Pegmatitic veins were also noticed on some outcrops. Exfoliation which is also referred to as onion skin weathering were found mainly on the granitic rocks found within Paiko sheet. The intensity vary from one granitic rocks to another but is generally more intense in coarse grained granitic rocks with thicker blocks.

Strain-Slip Cleavage (Plate 4c) also called crenulation cleavage were observe in some tonalitic rocks of Paiko sheet. Foliation were found mainly on the migmatitic-gneiss rocks without well-defined strike/dip directions. The only exposure whose strike and dip direction is considerably clear enough was located around Dagigbe village in north-western portion of Paiko sheet (Plate 4d). The average strike/dip of the foliation is 077º ENE/69ºE while dip direction is 260ºWSW.

Trace fossils such as animal burrows and paths were observed on the sedimentary rocks (sandstones and iron stone) located in the south-western part of Paiko sheet. A lot of burrows were observed on the mottled coloured sandstone exposed by road cut between Takuti and Lapai (N09°08'32.3"; 006°32'54.5") especially in the finer grained portion of the exposure. Some of the observed burrows appeared vertical in outline. This area had magmatic rock is unconformably overlain Sandstone in one part and overlain by mudstone in other part around Achitupa village located within the southern western part of Paiko sheet (Plate 4e and 4f). This represents the contact between the basement complex-sedimentary terrains (Bida Basin). The sedimentary rocks exists in beds separated by bedding planes. The average strike and dip of beds is 104°/19° while the dip direction is 057°. The bedding planes were observed to have been fractures (Plate 4g). Ripple mark-like structures were also found on some of the beds (Plate 4h).

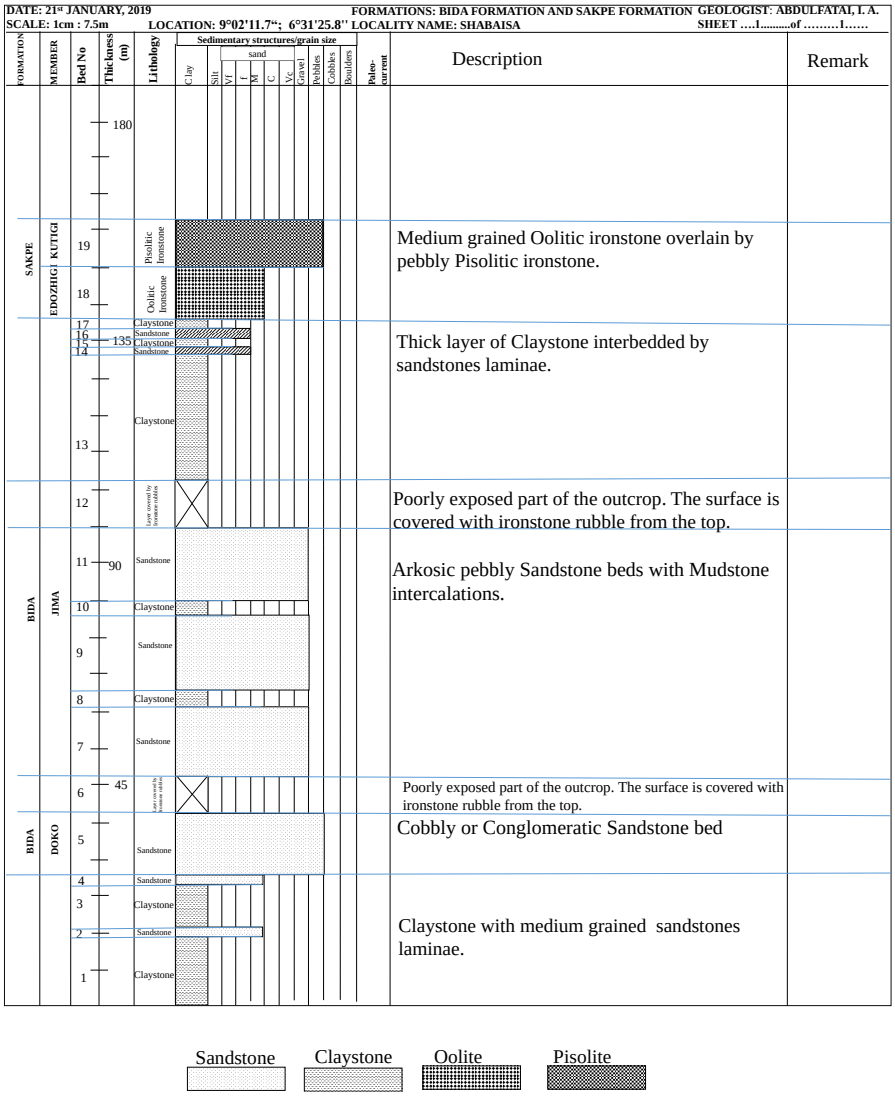

Figure 4: Lithologic section of Claystone with sandstones intercalations overlain by ironstone at Lapai (9º02'11.7"; 6º31'25.8").

a.

b.

Plate 3: Some geological structures observed in field a.) Fine-grained ptygmatitically folded migmatite around Kpaesan and Achitupa. b). Cross cutting sets of joints.

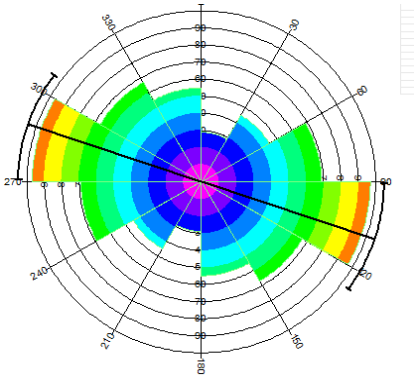

Figure 5: Rosette diagram of measured joint direction within Paiko Sheet

a.

b.

c.

d.

e.

f.

g.

h.

Plate 4: Some geological structures observed in the field. a). Dextral fault. b). Cross cutting veins. c). Strain-slip cleavage observed on an outcrop in Pago. d). Foliation observed on a gneiss around Digigbe e).

Sedimentary rock (clast supported conglomerate) overlaying basement complex. f). Mudstone overlaying a basement rock within Sedimentary-Basement contact. g). Fractured bedding plane on sedimentary exposure west of Lapai town. h). Ripple mark-like structure observed on a bedding plane on sedimentary exposure west of Lapai town

5.3 Economic Geology

Quarrying and mining activities are common in villages within Paiko Sheet. This is because these villages are rich in economic minerals or other geological resources that are economical. These activities are very common among the host communities although some companies are also involved. This has generated employments and sources of income for many people within these areas and beyond. These minerals or geological resources include Marble deposit that exists in a village called Tunga Gade although the deposit is popularly called Kwakuti Marble. Talc deposit exist in village called Gangare located after Dobi in Gwagwalada Area council, Federal Capital Territory, Abuja. The mining activity is carried out by artisanal miners from the host locality. According to the miners, they mine for ceramic industries.

Medium scale and artisanal gold mining activities are prevalent in the south-western part of the studied area particularly Dadabiri and Baban-Tsauni areas. Other areas include Pago, Ebbah and Butu in the northern half of the sheet. Sulphide ores also exist in the South-western portion of Paiko sheet especially Dadabiri and Baban-Tsauni localities. Prominent among them is galena, sphalerite, pyrite and chalcopyrite. Active mining of lead and zinc from galena and sphalerite respectively is going on in the area.

Rocks quarrying exist within the studied area. This is due to the presence of various massive intrusions that are exposed in area. They quarry these rocks into finished product such as dimension stones, chippings and dust for various construction purposes. Deposits of laterite exist in many locations within the sheet but prominent among them are Wabe, Tungan Gade and Gangare all in the north-western part of the sheet. They are exploited for subgrade in road construction and are also useful in other construction activities. Mining of sand and gravel is not restricted to any part of the sheet as it cut across the entire sheet. The mining activities are dominated by artisanal miners. Their activities are mostly restricted to areas around streams or rivers and their flood plains. These materials (sand and gravel) are mainly used for construction purposes. Lateritic clay deposit in Pago is being mined by Shelter Clay Company for the production of bricks. The southern part of Kwakuti marble deposit is overlain by approximately 10 meters thick clay although mining activity were not observed on this occurrence. The clay is overlain by lateritic soil of about 15 meters thick.

Updated Map of Paiko Sheet 185

The updated map is shown in Figure 6. The following update were made to the previous map of Paiko Sheet by the NGSA (2009):

1. Phyllite-Mica-Schist, Quartz-Schist interlayered with Amphibolite were removed from the map because they are in the Abuja Sheet which is east of Paiko Sheet. Although, the rocks were close to the boundary of Paiko sheet, it must have been included in the previous map due to lack Minna-Suleja road as construction activities have exposed the actual rock in this area which is gneiss.
2. Migmatitic Schist and Gneiss injection Migmatites, foliated granite was renamed Migmatite-gneiss because the schist in this area is not significant enough to be included in a map. And also the term foliated granite could also be termed as gneiss.

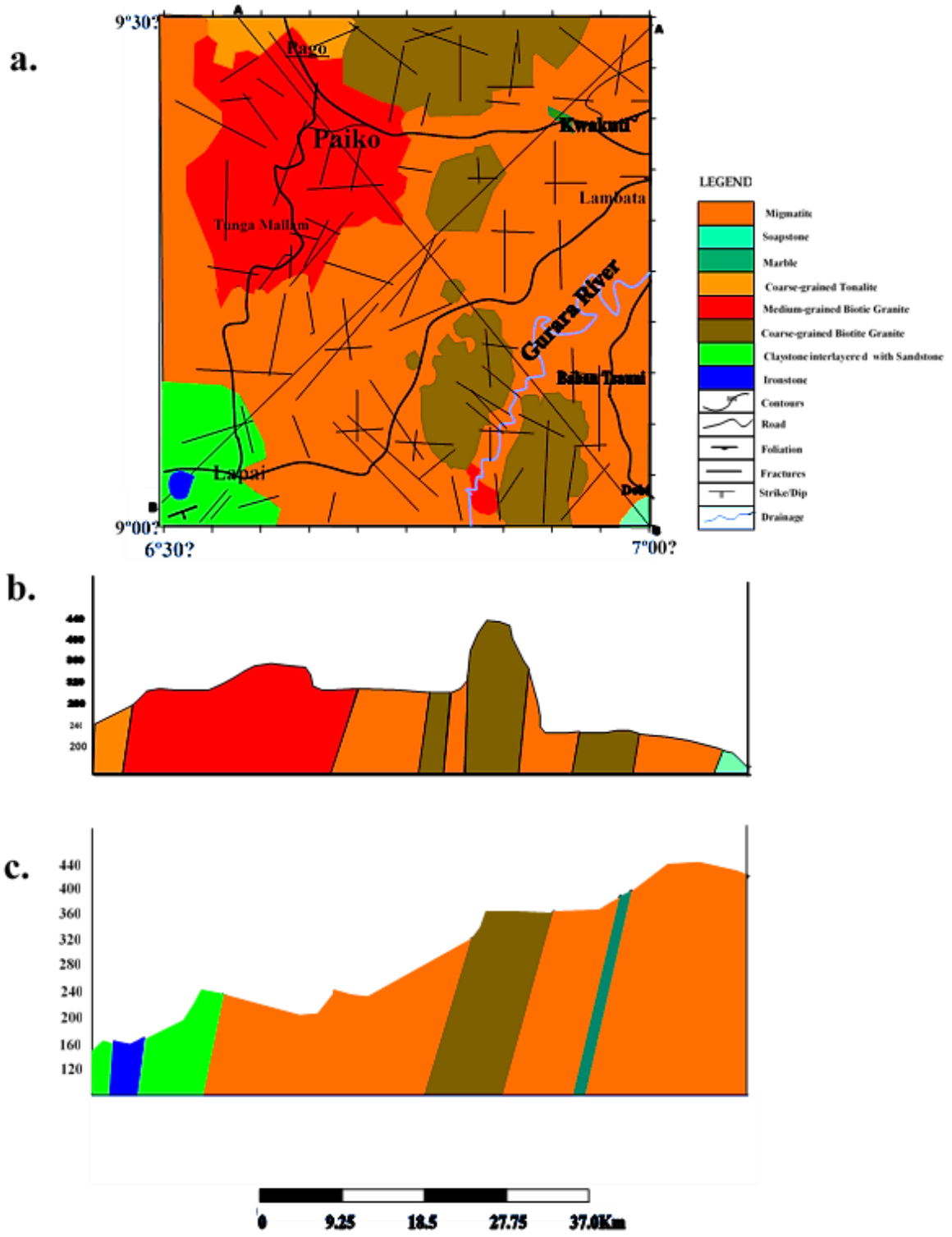

Figure 6: Updated geological map Paiko sheet 185. a.) The current geological map of Paiko sheet. b.) Cross section of progressive changes in the geology of Paiko sheet from the Northwest to the Southeast. c.) Cross section of progressive changes in the geology of Paiko sheet from the Northeast to the Southwest.

3. Migmatite was also made part of Migmatite-Gneiss. This is because of the occurrence of gneiss (though in little amount) in the part coloured migmatite.

4. Alluvial deposit part of the previous map was removed and replaced with the actual bedrock underlying this deposit which is migmatite.
5. Lateritic capped Sandstone was removed and replaced with Claystone with Sandstone intercalation which is thought to be lateral correlate-able to Bida Formation because they unconformably overlies the Basement complex. Overlying these is ironstone which is thought to be correlate-able to Sakpe Ironstone Formation because of similarity in features.
6. Talc-actinolite-Tremolite Schist was replaced with Talcose rock which is general name for talc rich deposit because schistose structure was not observed on the outcrop.
7. Harmonization of marble lithology as one unit against the two discrete units recorded in the previous maps. This is because geological contact or different lithology was not observed between two units.
8. The locality referred to as Mararaba in the earlier maps was corrected to Lambata in the updated map.

Conclusion

Paiko Sheet 185 is underlain Basement rocks (approximately 95%) and Sedimentary rocks of the Bida Basin (approximately 5%). A total of eight modification were made to the updated map comprises of seven lithological modification and one locality correction. The new map show that there are eight different major rock types underlying Paiko Sheet against 11 lithologies suggested by the earlier maps. There are however two rock types (schist and quartzite) that were not represented on the map because of their small sizes. The principal joint direction is in the North-western direction. Geological resource (such as gold, marble, lead, zinc, laterite, sand and gravel) that can be economically exploited abound within the sheet.

Recommendations

1. Petrologists especially Sedimentologists need to carry out more research to unravel the reason for the thick clay deposit within the sedimentary section of Paiko sheet as Bida Formation is popular known to be made up of mainly sandstones.
2. Petrologists and Mineralogists need to carry out more research to unravel the evolution of Kwakuti Marble. This is because the closest sedimentary basin which is the Bida Basin is about 40 kilometers away from the Marble deposit. There is need to determine the protolith to adequately understand the history of the rock.

References

Ejepu, J. S. Olasehinde, P., Okhimame, A. A. & Okunlola, I. (2017). Investigation of Hydrogeological Structures of Paiko Region, North-Central Nigeria Using Integrated Geophysical and Remote Sensing Techniques. Geosciences, 7, 122.

Ejepu, S. J. & Omar D. M. (2015). Integration of Geology, Remote Sensing and Geographic Information System in Assessing Groundwater Potential of Paiko Sheet 185 North-Central Nigeria. Journal of Information, Education, Science and Technology (JIEST) Vol. 2(1), 145-155.

Fry, N. (1984). The field description of metamorphic rocks. Milton Kaynes: Open University press, 110.

Njeze, F. A. (2011). Seasonal Rainfall Prediction. Available: http://nimet-srp.com/2011-Annual-Rainfall-Predictions.html.

Obaje, N. G. (2009). Geology and Mineral Resources of Nigeria. Springer Dordrecht Heidelberg, London, Pp5 and Pp14.

Russ, W., (1957). The geology of parts of Nigeria, Zaria and Sokoto provinces. Geological Survey of Nigeria Bulletin No. 27, 43.

Thorpe, R. & Brown, G. (1985). The field description of igneous rocks. Milton Kaynes: Open University press, 154.

Truswell, J. F. & Cope, R. N., (1963). The geology of parts of Niger and Zaria provinces. Geological Survey of Nigeria Bulletin No. 29, 53.

Tucker, M. (1982). The Field Description of Sedimentary Rocks. Milton Keynes: Open Univ. Press, 112.

Woakes, M. & Bafor, B. E., (1984). Primary Gold Mineralization in Nigeria. In Foster R.P. (Ed): Geology, Geochemistry and Genesis of Gold Deposits, 661 – 671.

Assessment of geothermal Potential in Parts of Niger Delta, Nigeria using high Resolution Aeromagnetic Data

*Osezua B. E., Salako K. A. and Alhassan U. D.
Department of Geophysics, Federal University of Technology, Minna, Nigeria
*Correspondence author: blessingosezua@gmail.com, 08142270395

Abstract

Geothermal potential in parts of Niger-Delta region of Nigeria was assessed using aeromagnetic data. The study area covers a total area of 12,100 km^2. This area is covered by four aeromagnetic data sheets, and it is bounded by latitudes 5°00′ and 6°00′N and longitudes 5°50′ and 6°50′E. The total magnetic data of the area was subjected to spectral analysis with 16 overlapping blocks. The Centroid depth and depth to top boundary obtained from the spectral analysis were used to determine the Curie point depth (CPD). The CPD obtained was then used to determine the geothermal gradient and the heat flow over the study area. The results showed that CPDs vary between 16.00 and 50.00 km. The highest CPD can be found at South-western part of Burutu. The shallowest CPD can be found at the central regions of study area corresponding to Uvwie, Udu, north of Ughelli and Isoko and extending towards the North-west (Warri) and south eastern (Patari) region. The geothermal gradient and the heat flow vary from 11.00 to 36.00 ^{o} C/km and from 28.00 and 88.00 mW/m^2 respectively; with highest heat values of 80 and 88 mW/m^2 around the central region corresponding to Udu, Uvwie and Ughelli north. It can therefore be deduced that the central part of the study area might be a probable area for geothermal energy potential with minimum CPD, maximum geothermal gradient and heat flow.

1.0 Introduction

Geothermal energy is considered as one of the most favourable expectation and dependable energy resources for Nigeria. It is renewable and sustainable source of energy from deep inside the earth that has the ability to reduce greenhouse effect, hardly affected by weather and always available to provide reliable and steady output (Dickson & Fanelli, 2004).

In Nigeria, the massive increase in population has led to the limited supply of electric power generation and the availability of other sources of energy supply. Adequate power generation is one of the vital roles for economic, financial and social growth of a country (Abraham *et al.*, 2017). Many multi-national companies as well as small and medium scale enterprises (SMEs) in the country have fold up as a result of this daunting energy challenge. In trying to provide alternative source of power to power their production plants the cost of production has increased tremendously. Many of the companies ran into deficit and had since closed down or relocate to other countries for haven leaving the area unindustrialised, open to crime rate and increased the joblessness among youths (Ikechukwu *et al.*, 2015). Future growth is expected that geothermal energy reach more than 3% of the global electricity demand by 2050 (Geothermal, 2018). If explored can reduce the prevailing challenges.

This study is focused on assessment of geothermal resources within some parts of Niger Delta area of Nigeria where majority of our multinational industries resides. The outcome of this research work will determine the amount of heat flow which is the main source of geothermal energy using acquired high resolution aeromagnetic data. This would aid in determine whether the study area is suitable for a geothermal plant.

1.2 Location and the Geological setting of the Study Area

The study area lies between latitudes 5°00′ and 6°00′N and longitudes 5°50′ and 6°50′E and covers a total area of about 12,100 square kilometers. These comprises the following areas; Burutu, Patani, Warri, Ughelli, Uvwie, Ahoada, Kwale, Isoko and Ndokwa (Figure 2). Geologically, the area falls under one of the largest sub aerial basins in Africa, situated at the intersection of the Benue Trough and the Anambra Basin (Whiteman, 1982). Marine sedimentation of the area took place in the Benue Trough and the Anambra Basin from mid-Cretaceous onwards. The earth materials falls within these area includes;

Sandstones, Ironstones, Laterites, Coarse, Phorphyritic, Schist including some Gneiss, Muscuvite, Biotite, Diorite, Migmatite and Granite (Figure 2).

The Niger Delta started to evolve in early Tertiary times when clastic river input increased and several faults were formed (Doust and Omatsola, 1989). Generally the delta prograded over the subsidizing continental-oceanic lithospheric transition zone and during the Oligocene spread onto oceanic crust of the Gulf of Guinea (Adesida *et al.*, 1997). Thickness of sediments in the Niger Delta has an average of 12 km and subsurface lithostratigraphic units of the area are the petroliferous Agbada formation which overlies the transgressive marine Akata formation which is the major hydrocarbon rock source (Chukwu *et al.*, 1991). Outcropping units of the Niger Delta include the Imo formation and Ameki Group which consists of Ameki, Nanka, Nsugbe and Ogwashi-Asaba formations. The three main subsurface litho-stratigraphic units recognized are the marine Akata Shales situated at the base of the Delta, the petroliferous parafic Agbada Formation which began in the Eocene and continued to the Paleocene and the continental Benin sands of late Eocene to recent deposit of alluvial and upper coastal plain sands that are up to 2000m thick (Thomas Otobong *et al.*, 2016).

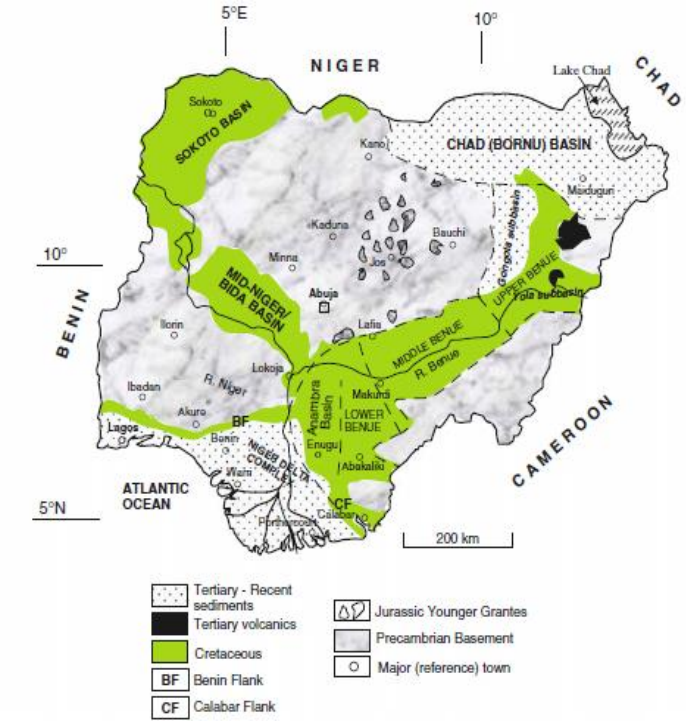

Figure 1: Geological Map of Nigeria showing the study in red outlined (Modified after Obaje, 2009).

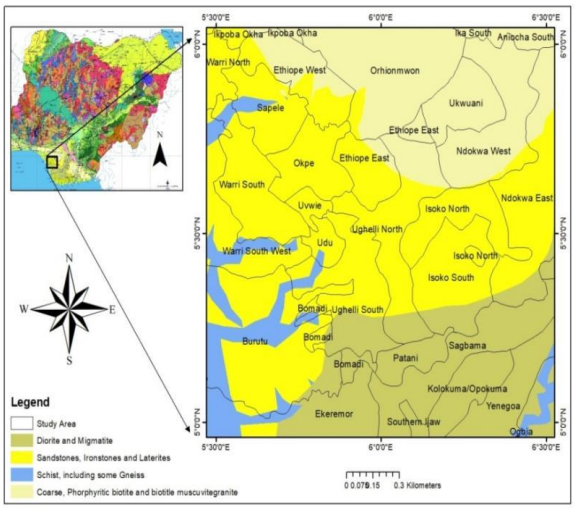

Figure 2: Location and Geological Map of the Study Area

2.0 MATERIALS AND METHOD

For this research, four aeromagnetic data sheets were obtained from the Nigerian Geological Survey Agency (NGSA), as part of the aeromagnetic survey carried out between 2003 and 2009 by Fugro Airborne Survey. The aeromagnetic sheets used were Warri (309), Kwale (310), Burutu (318) and Patari (319) which corresponds to latitudes 5° 00 and 6° 00N and longitudes 5°50′ and 6°50′E. The Survey was conducted in two phases, Phase 1 by Fugro Airborne Surveys and Phase 2 by Paterson, Grant and Watson Limited (PGW). Each grided map scaled 1:100,000 covers an area of about 3025 km^2 (i.e. $55\ km^2 \times 55\ km^2$) while the total investigated covers 12100 km^2.

2.1 Data Processing

2.1.1 Spectral Analysis method

Spectral analysis is a depth estimating method first pioneered by Bhattacharryya (1960) and later developed by Spector and Grant (1970). The method is used to determine the Curie point depth and to separate influences of the different body parameters in the observed magnetic anomaly field (Salako *et al.*, 2019). Fundamentally, the method of Spector and Grant (1970) estimates the average depth to the top boundary of the magnetized layer from the slope of the log power spectrum while the method of Bhattacharrya and Leu (1975) obtains the depth to the centroid, Z_o, (effects from the bottom) of the causative body using a single anomaly interpretation. Okubo *et al*. (1985) effectively combined and expanded both methods to propose an algorithm for regional geomagnetic interpretation oriented to the purposes of geothermal exploration. According to Spector and Grant (1970) they illustrated that the thickness depth and width of a magnetic source ensemble could affect the shape of energy spectrum. The strong term that shapes this energy spectrum is the depth factor. They demonstrated that the depth could be estimated using Equation (1)

$$E(r) = e^{-2zr} \qquad (1)$$

where, E(r) = spectral energy Normalised
r = frequency
If h is the mean depth of a layer and the depth factor for the ensemble of anomalies is

$$E(r) = e^{-2rh}$$

Therefore, a plot of the energy spectrum of a single ensemble of prism against angular frequency r would give a straight line graph whose slope is directly proportional to the average source depth, h of that ensemble (Spector and Grant, 1970). That is, the logarithm plot of the radial frequency would yield a straight line whose slope is:

$$m = -2h$$

$$h = -\frac{m}{2} \quad (2)$$

Equation (2) can be applied if the frequency unit is in radian per unit kilometer. From the slopes of the plot, the first and the second magnetic source depth was respectively estimated.

2.1.2 Curie point depth Estimation

The bottom of a magnetic source shows the thermal boundary at which magnetic mineral in the crust move from ferromagnetic state to paramagnetics as a result of the increase in temperature as depth increases down the crust (Nagata, 1961; Ross *et al*., 2006). This thermal boundary is referred to as Curie point depth and it is the outermost part of the crust that has material which develops recognisable mark in a magnetic anomaly map (Bhattacharryya and Leu, 1975). This point is assumed to be the depth for the geothermal source (magmatic chamber), where most geothermal reservoir tap their heat from a geothermal area (Eleta and Udensi, 2013). This Curie point has a temperature of 580 °C. For temperature above Curie-point, magnetic materials lose their magnetic ordering and both induced and remnant magnetisation disappear, thus for temperatures above 580°C, those materials will begin to encounter ductile deformation. The methods of Curie Point Depth determination utilize spectrum analysis techniques to separate influences of the different body parameters in the observed magnetic anomaly field. The Curie point depth is evaluated in two stages as proposed by Bhattacharyya and Leu (1975); the first stage is the estimation of depth to centroid (Z_0), of magnetic source from the slope of the longest wavelength part of the spectrum and the second stage is the estimation of the depth to the top boundary (Z_t) from the slope of the second longest wavelength part of the spectrum (Okubo *et al.*, 1985) and finally Bhattacharyya and Leu (1977) to develop the method to determine the bottom depth of magnetized bodies (Zb).

2.1.3 Depth to the Top (Z_t), Centroid (Z_0) and Bottom (Z_b) of Magnetic sources

From the first stage, the centroid depth of magnetic sources can be calculated from slope of the longest wave length part of the power spectrum (Okubo *et al*., 1985)

$$\ln\left[\frac{\sqrt{P(k)}}{|k|}\right] = \ln A - 2\pi|k|Z_o \quad (3)$$

where
P(k) is the radially averaged power spectrum of anomally,
|k| is the wave number,
A is a constant.
The second stage is the estimation of depth to the top Z_t, of the magnetic source is derived from the slope of the second longest wavelength part of the spectrum:

$$\ln\sqrt{[P(k)]} = \ln B - 2\pi|k|Z_t \quad (4)$$

Where B, is the sum of constant independent of |k|
The depth to the bottom of the magnetic source (Z_b) can subsequently be obtained from the relation (Okubo *et al*., 1985)

$$Z_b = 2Z_0 - Z_t \quad (5)$$

2.1.4 Geothermal Gradient and Heat Flow

Using the depth to the bottom of magnetic sources (Z_b), the geothermal gradient $\left(\frac{dT}{dZ}\right)$ can be estimated as:

$$\left(\frac{dT}{dZ}\right) = \left(\frac{\Theta_c}{Z_b}\right), \quad (6)$$

here Θ_c is the Curie temperature.

Next, using Z_b and $\frac{dT}{dZ}$, the heat flow (q_z) can similarly be estimated as (Okubo *et al*., 1985)

$$q_z = -\sigma\left(\frac{\Theta_c}{Z_b}\right) = -\sigma\left(\frac{dT}{dZ}\right), \quad (7)$$

where σ is thermal Conductivity. Thermal conductivity of 2.5W/m/°C as the average for igneous rocks and a Curie temperature of 580 °C (Stacey, 1977; Trifonova *et al*., 2009) are used as standard.

3.0 RESULTS AND DISCUSSION

3.1 Total Magnetic Intensity (TMI) Map and Residual Magnetic Intensity Anomaly

Figure 2 and 3 is the total magnetic intensity and residual map of the study. The total magnetic intensity map, TMI and the residual magnetic intensity map show variation of highs and lows magnetic signature. The maps were produced in aggregate colours from deep blue to light blue signifying low magnetic anomalies, the green color representing the intermediate between high and low anomalies and the red shows a high magnetic anomaly. The TMI map reveals that high magnetic anomalies could be found at Northern part of the study area with the highest magnetic signature found at north-western part of Warri. The intermediary signature found in north eastern part of kwale down towards the south western part of Burutu while the low magnetic anomalies are seen at the South Eastern part of Patari. From the residual map, high anomaly signature could be found in north eastern, central and down to the southern part of the study area. Burutu and Patari was found to have the highest anomaly while the least magnetic signature could be obtained in the western part of Burutu and the the southern part of Patari.

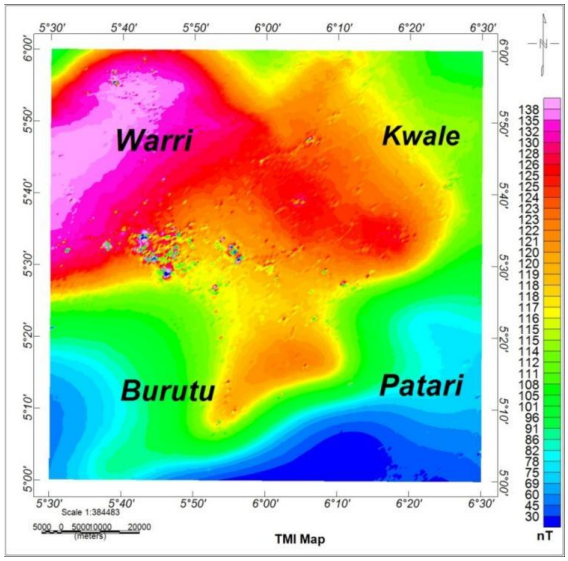

Figure 3: Total magnetic intensity map of study area (IGRF value of 33,000 nT must be added to the values in Legend)

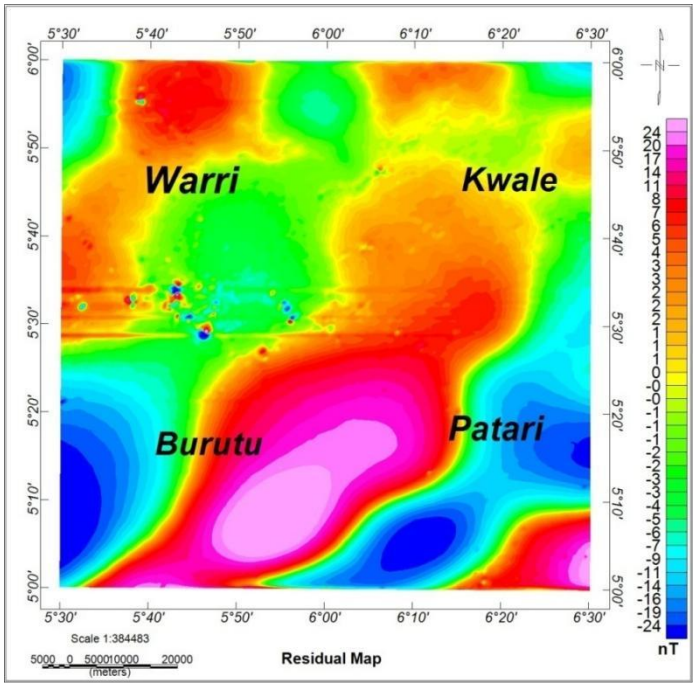

Figure 4: Residual map of study area

3.2 **Spectral Analysis**

The residual map (Fig. 3) of the study area was divided into 16 (Blocks A – P) square overlapping blocks which covered 55 km by 55 km. The divisions of residual map into spectral sections of blocks were done with Oasis Montaj. The analysis was carried out using MATLAB. Figure 4 is the Graph of logarithm of spectral energies against frequencies from block A and B. Using the determined Z_o and Z_t values in equation 2, the Curie point depths can also be determined from equation 5. The results of the determined values of Z_o, Z_t and Z_b for the sixteen blocks are shown in Table 1.

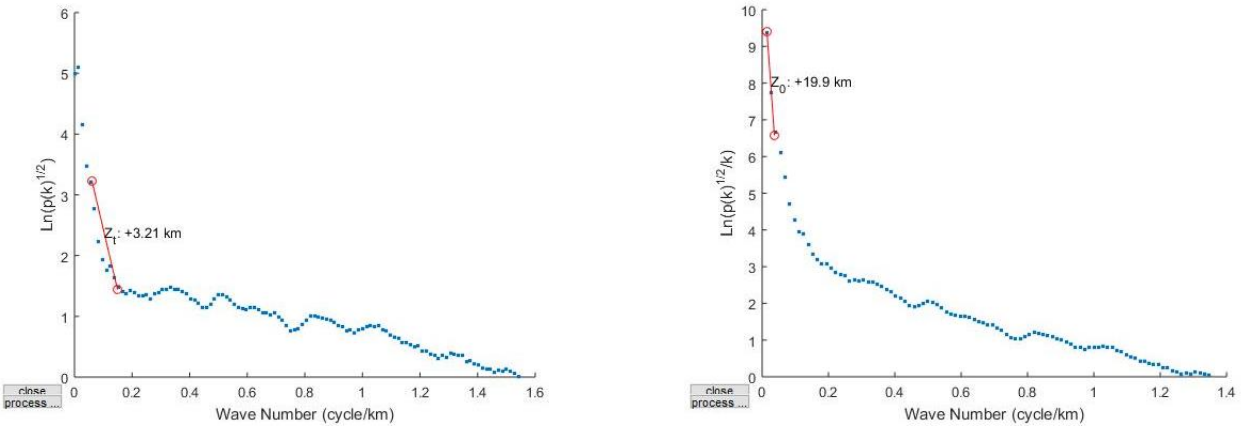

Figure 5: Sample of Graph of Energy against Wave number

Table 1: The results of the determined values of Z_o, Z_t and Z_b for the sixteen blocks

Blocks	Long (°E)	Lat (°N)	Depth to centroid, Zo (Km)	Depth to top Zt (Km)	Curie point depth, Zb (Km)	Geothermal Grad(°C/km)	Heat Flow (mWm^{-2})
A	5.75	5.75	19.9	3.21	36.59	15.85	39.78
B	5.92	5.75	21.1	9.72	32.48	17.85	44.82
C	6.08	5.75	17.7	10.5	24.9	23.29	58.46
D	6.25	5.75	18.5	8.06	28.94	20.04	50.30
E	5.75	5.58	15.2	10.2	20.2	28.71	72.06
F	5.92	5.58	14	11.7	16.3	35.58	89.31
G	6.08	5.58	20.1	11.4	28.8	20.13	50.54
H	6.25	5.58	16.9	12.4	21.4	27.10	68.02
I	5.75	5.42	19.7	13.1	26.3	22.05	55.35
J	5.92	5.42	20	12.5	27.5	21.09	52.93
K	6.08	5.42	22.6	9.2	36	16.11	40.43
L	6.25	5.42	24.2	12	36.4	15.93	39.99
M	5.75	5.25	29.5	9.76	49.24	11.77	29.56
N	5.92	5.25	19.3	7.32	31.28	18.54	46.54
O	6.08	5.25	26.1	11.6	40.6	14.28	35.85
P	6.25	5.25	22.8	8.35	37.25	15.57	39.08

3.3 **Depth to magnetic sources**

The TMI map was divided into 16 sub-sheets and each sub-sheet subjected to Fast Fourier Transform (FFT) using Oasis Montaj software, this process decomposed the magnetic data into its energy and wave number components. The energy spectrum was plotted against wave number component using a MatLab graph plotter. The graph generated gradients that were used to estimate depth to the top, Centroid and bottom of magnetic sources in accordance with equation (3) and (4) respectively.

3.5 Sedimentary Thickness

The measure of depth to the top of basement rock or magnetic sources is a representation of the extent of sedimentation. The spectral depth analysis revealed the variation of depth to top of magnetic sources to vary between 3 and 13.5 km with an average of 10.064 km.

The deepest depths in the range of 11 to 13 km could be found at the central part of the study area; this area corresponds to Uvwie, Ughelli North and Udu. The shallowest depth could be obtained at the North-western part of Warri, with depth range of 3 to 5km. Medium depth range of 8 to 10 km was found at the north eastern part of Kwale and the southern part of Burutu was recorded.

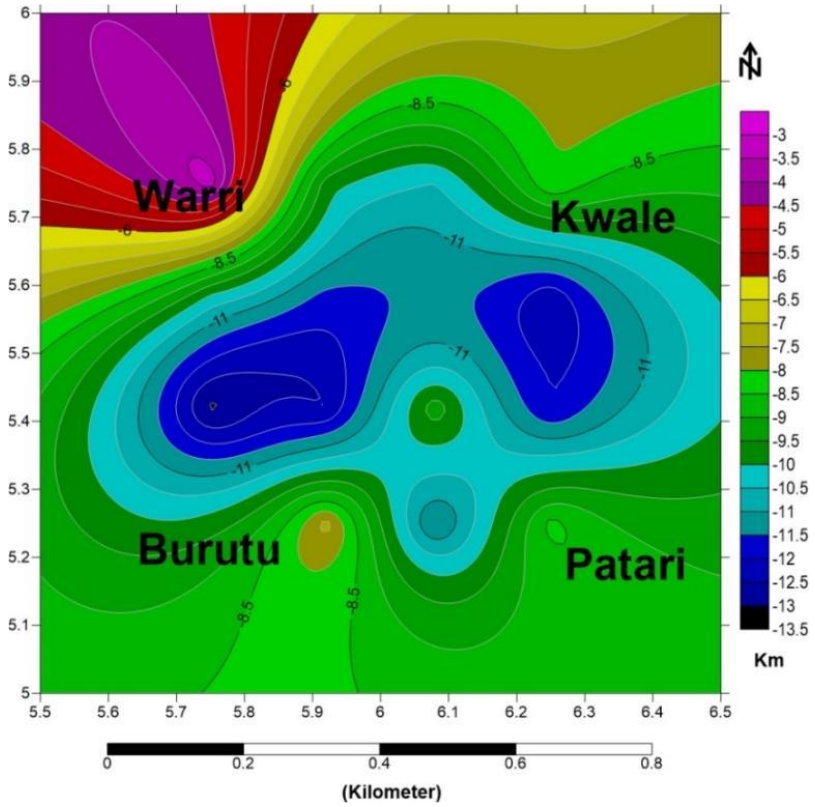

Figure 6: Contour map of sedimentary thickness

3.6 Curie point depth map

Figure 7 is the Curie point depth contour map of the study area. High values of 38 km to 50 km could be seen at the south western region with the highest values at Burutu. The lower CPD depth of 16 km to 30 km could be could be seen at the central part (Uvwie, Udu, Ughelli north and Isoko north) extending towards the North-east and the medium values at the north western and south eastern region.

3.7 Geothermal gradient map

Using a Curie temperature of 580 ℃ and the estimated Curie point depths, the geothermal gradient of study area vary between 11 to 36 °C/km. The maximum gradient values were observed at the central part below Warri, at a range of 19 to 36 °C/km. Medium and low geothermal gradient were recorded at Kwale and Burutu.

3.8 Heat flow map

The results (Table 1) show that heat flow values of the study area vary between 28 mW/m^2 and 88 mW/m^2. The heat flow contour (Figure 9) shows the highest values of 80 and 88 mW/m^2 at the central regions (Uvwie and Ughelli north). This region is found to be probable for geothermal energy exploration in accordance with Jessop *et al.* (1976).

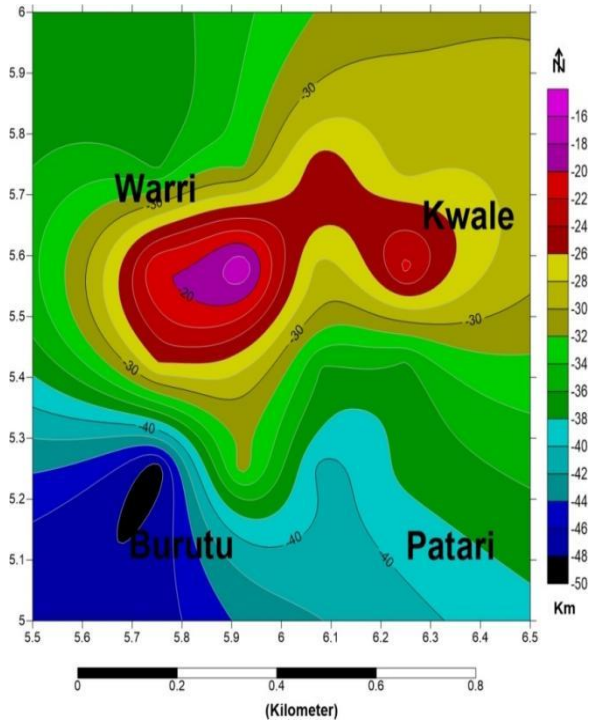

Figure 7: Curie point depth contour map of study area

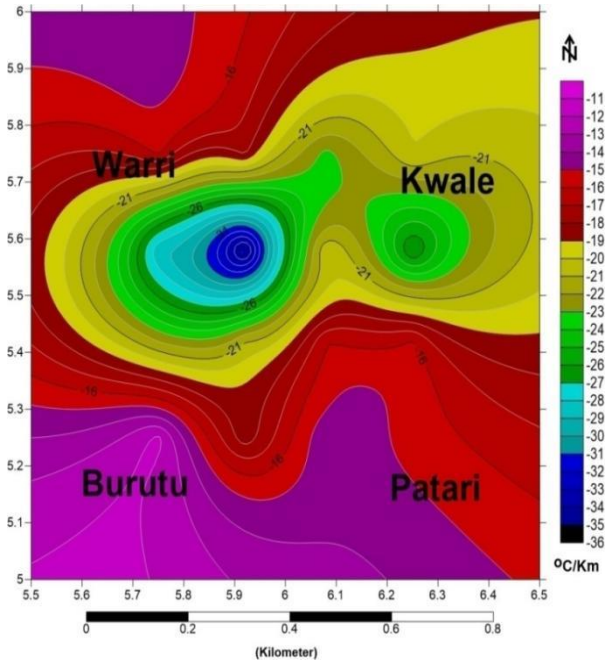

Figure 8: Geothermal gradient contour map of study.

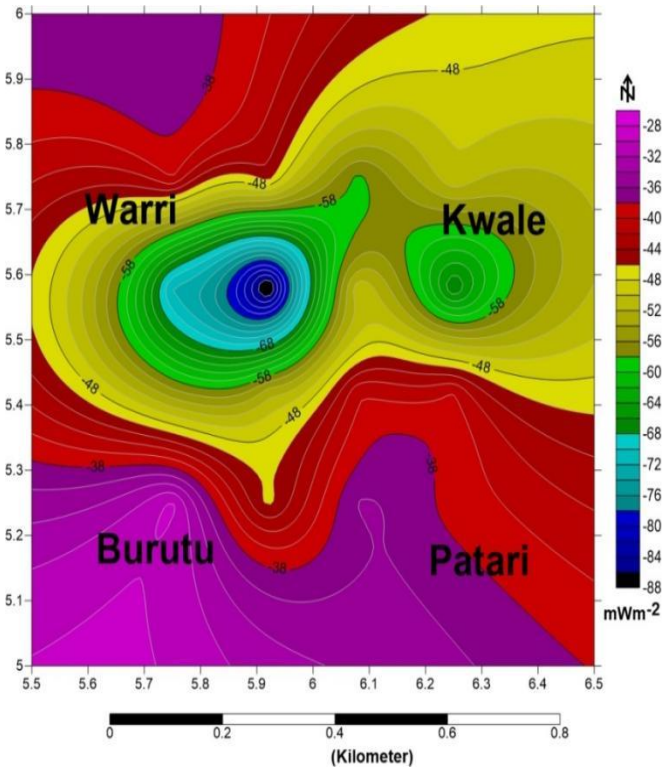

Figure 9: Heat flow contour map of study area.

4.0 CONCLUSION

The results obtained establishes the relationship between the Curie point depth and other geothermal parameters (Geothermal gradient and Heat flow) of study area. In thermally normal continental regions, the average heat flow is about 60 mWm^2. Values between 80 to 100 mWm^2 are good geothermal source, while values greater than 100 mWm^2 indicate anomalous conditions (Cull and Conley, 1983; Jessop *et al*., 1976). The shallowest Curie point depth range of 16 to 26 km was recorded at the central regions of study area. The central regions of the study area also recorded the maximum values of geothermal gradient and heat flow range of 80 to 88 mW/m^2 reveals an indication of a viable geothermal source.

REFERENCES

Abraham EM, Lawal KM, Lawal AA (2011) Interpretation of aeromagnetic data for geothermal energy investigation ofIkogosi Warm Spring, Ekiti State, South Western Nigeria. International Journal of Scientific Research 1: 103-118.25.

Abraham EM, Obande EG, Chukwu M, Chukwu CG, Onwe MR (2015) Estimating depth to the bottom of magnetic sources at Wiki warm spring region, northeastern Nigeria, using fractal distribution ofsources approac. Turkish J of Earth Sci 24.

Adedapo, JO; Kurowska, ES; Ikpokonte, AE (2013). Geothermal gradient of the Niger Delta

Adetona, A.A., and Abu, M., (2013) Estimating the Thickness of Sedimentation within Lower Benue Basin and Upper Anambra Basin, Nigeria, Using Both Spectral Depth Determination and Source Parameter Imaging. *Hindawi Publishing Corporation* ISRN Geophysics Volume Article ID 124706, pp 1-10

Aigbogun C, Olorunsola K (2018) Determination of curie point depth Anambra basin and its environs using high resolution airbornemagnetic data.

Barry Floyd (1969) landforms, Relief and associated drainage featuresin Eastern Nigerian. Springer. Pp 3-5.

Bemsen JE, Godwin OA, Kenechukwu AE, Ifeanyi CA, Ojonugwa UA, (2013) spectral analysis of aeromagnetic data over part of Southern Bida Basin, West Central Nigeria. *International Journal of Fundamental physical sciences* 3:27-31.

Bhattacharya, Bk, Leu, Lk (1977). Spectral analysis of gravity and magnetic anomalies due to rectangular prismatic bodies. Geophysics (42): 4-50.

Bhattacharyya, BK; Leu, LK (1975). Analysis ofmagnetic anomalies over Yellowstone NationalPark. Mapping the Curie-point isotherm surface for geothermal reconnaissance. J. Geo. Res. (80): 461–465.

Blackely, R.J, (1995). *Potential theory in gravity and magnetic application. Cambridge university*

Chukwu, CG; Udensi, EE; Abraham, E.M; Ekwe, AC;Selemo, AO (2017). Geothermal energy potentialfrom analysis of aeromagnetic data of part of theNiger-delta basin, southern Nigeria. *Energy*(143):846 – 853.

Dickson, M. and Fanelli, M. (2004) What is geothermal energy. Istituto di Geoscienze e Georisorse , Pisa, Italy.

E.M. Abraham, K.M. Lawal, A.C. Ekwe, O. Alile, K.A. Murana and A.A. Lawal, Spectral analysis of aeromagnetic data for geothermal energy investigation of Ikogosi Warm Spring - Ekiti State, southwestern Nigeria. Geothermal Energy (2014)

Eletta BE, Udensi EE (2012) Investigation of the Curie point isotherm from the magnetic fields of eastern sector of central Nigeria. Geosciences 2: 101-106.

Ema Michael Abraham and Elijah Edet Nkitnam (2017) Review of Geothermal Energy Research in Nigeria: The Geoscience Front. International Journal of Earth Science and Geophysics 3:015

Emujakporue GO, Ekine AS (2014) Determination of geothermal gradient in the eastern Niger delta sedimentary basin from bottom hole temperature. Journal of Earth Sciences and Geotechnical Engineering 4: 109-114.

Ewa, K; Kryrowska, S (2010). Geothermal exploration inNigeria. Proceedings, World Geothermal CongressZaria, Nigeria, (3); 1 – 59.

from recent studies. *Inter. J. of Sci. Eng.Research*2 (4): 11- 20.

Ikechukwu, I. O., Derick, C. A. and Olusola, O. B., 2015, Exploration and application of geothermal energy in Nigeria. International Journal of Scientific and Engineering Research, 6(2), 726, ISSN 2229-5518.

Jessop, AM (1990). Thermal geophysics, Elsevier, amsterdam.

Kuforijimi Olorunsola and Chibuzor G. Chukwu (2018). Analysis of Geothermal Heat flow Potentiality of Upper Bida basin Nigeria. African Journal of Environmental Science and technology.

Kuforijimi, O. and Christopher, A., 2017,Assessment of Aero-radiometric Data ofSouthernAnambra Basin for the Prospectof Radiogenic Heat Production. Journal of Applied Science and Environmental Management. 21(4), 743-748.

Lawal, TO; Nwankwo, LI (2017). Evaluation of theDepth to the bottom of magnetic sources and Heatflow from High Resolution Aeromagnetic (HRAM)Data of part of Nigeria sector of Chad basin ArabianJ. Geosciences. (10):1 – 12.

Megwara, JU; Emmanuel, EU; Peter, IO;Mohammed, AD; Kolawole, ML (2013).Geothermal and Radioactive heat studies of partof southern Bida basin, Nigeria and thesurrounding basement rocks. International Journal of Basic and Applied Sciences. pp 125-139.

Nagata, T., 1961, Rock Magnetism, 350 pp. Maruzen, Tokyo.

Nwachukwu SO (1976) Approximate geothermal gradients in Niger delta sedimentary basin. AAPG Bulletin 60: 1073-1077.

Nwankwo, CN; Ekine, AS; Nwosu, LI (2009) Estimation of the Heat Flow Variation in the Chad Basin, Nigeria. J. Appl. Sci. Environ. Manage (13).

Obaje, NG (2009). Geology and mineral resources ofNigeria. Berlin: Springer Publishers, pp. 1–203.

Obande GE, Lawal KM, Ahmed LA (2014) Spectral analysis of aeromagnetic data for geothermal investigation of wiki warm spring, north-east Nigeria. Geothermics 50: 85-90.

Olorunsola K, Aigbogun C (2017) Correlation and mapping ofgeothermal and radioactive heat production from the Anambra basin, Nigeria. African Journal of Environmental Science and Technologypages517-531.73–80.

Otobong Thomas and Onovughe Elvis (2016) Geothermal Energy: Power Potential of Hot Water from Oil Wells in Niger Delta, Nigeria. Journal of Multidisciplinary Engineering Science Studies (JMESS). Vol 2.

Reiter MA, Jessop AM (1985) Estimates of terrestrial heat flow in off shore eastern Canada. Can J Earth Sci 22: 1503–1517.

Ross, H. E., R. J. Blakely, and M. D. Zoback. "Testing the use of aeromagnetic data for the determination of Curie depth in California". Geophysics, (2006), Vol71, 10-16.

Ruth Mumba, Esther Mabedi and YankhoKalebe (2018). Aero-Magnetic Surveys for Geothermal Exploration in Malawi.Proceedings, 7th African Rift Geothermal Conference.

Rybach, L., 1976, Radioactive heat production in rocks and its relation to other Petrophysical parameters. Pure and Applied Geophysics, 114, 309-318.

Salako, K. A. and Udensi, E. E., 2013,Spectral depth analysis of parts of upperBenue Trough and Borno Basin, North-East Nigeria, using aeromagnetic data.International Journal of Science andResearch (IJSR), 2(8), 2319-7064.

Salem, A. &Fairhead, D. Geothermal reconnaissance of Gebel Duwi area, Northern Red Sea, Egypt using airborne magnetic and spectral gamma ray data. Getech (2011) pp.1–22.

Spector A, Grant FS (1970) Statistical models for interpretingaeromagnetic data. Geophysics 35: 293-302.

Tanaka, A Okubo, Y Matsubayashi, O (1999). Curie point depth based on spectrum analysis of the magnetic anomaly data in East and Southeast Asia, Tectonophysics, 306:461-470.

Trifonova, P., Zheler, Z., Petova, T. and Bojadgievak. (2009) Curie point depths of the Bulgarian territoty inferred from geomagnetic observations and its correction with regional thernal structure and seismicity. Tectono Physics. 2009; 473: 362-374.

Whiteman, A. J. (1982). Nigeria: Its petroleum geology, resources and potentials. (1) 176, (2) 238.Graham and Trotman, London, U.K.Vol.1.1, 66 ppWhiteman, A. (1982).

Zhdanov, M.S., Keller, G.V (1994). The geoelectrical methods in geophysical exploration. El series, 873p.

APPLICATION OF GEOLOGICAL AND GEOPHYSICAL DATA TO CHARACTERISE E8000 RESERVOIR IN AFENMAI FIELD OF NIGER DELTA BASIN, NIGERIA

[1] Unuevho, C.I., [2]Onuoha, K.M., [1]Amadi, A.N., [1]Ejepu, S.O. and [3]Udensi, E.E
[1]Department of Geology, Federal University of Technology, Minna, Nigeria
[2]Department of Geology, University of Nigeria, Nsukka, Nigeria
[3]Department of Geophysics, Federal University of Technology, Minna, Nigeria
***Correspondence E-mail*: c.unuevho@futminna.edu.ng**

Abstract
Afenmai Field is a partially assessed discovery within the Central Depobelt of eastern Niger Delta Basin in Nigeria. It occupies 242 km^2 surface area and presently has eight wells, giving it an average well density of one well per 31 km^2. Improved assessment of the discovery is required to upgrade the field to development drilling status. As a contribution to improving the assessment, this study characterised the E8000 sand, which bears hydrocarbon in Well 007. The data utilised comprised information on subsea vertical depth to top and base of sand and shale units, foraminifera content, geophysical logs, checkshot data, fluid contact depths, and 3D seismic volume. Sequence stratigraphic concept was employed to anlayse the sand and shale units, foraminifera content, and geophysical logs. The E8000 sand was mapped through the 3D seismic volume, and a depth- structure map was produced. The map reveals a major structure building synthetic fault in the middle of the field. The fault runs approximately east –west in the eastern part of the field and northwest- southeast in the western part. The sand is a lowstand systems tract with a roll-over anticlinal structure that forms a three-way closure with a crestal synthetic fault. The reservoir pay occupies about 4.5 km^2 areal extent, with opportunities for drilling four development wells along the east-west axis of the closure. Opportunities exist for drilling a minimum of three development wells southwards of Well 007. Approximately 4000 – 5000 root mean square amplitude value characterise hydrocarbon in the reservoir. A prospect is generated within the eastern part of the of the major structure building fault's upthrown block.

Keywords: Partially assessed discovery, roll-over anticlinal structure, development wells

INTRODUCTION

The Niger Delta Basin in Nigeria contains many unassessed discoveries (UAD) and partially assessed discoveries (PAD). Among these are Oguali Field in its Northern Depobelt (Edeki 1991), Elepo Field in Central Swamp Depobelt (Overell and Nwachukwu, 1995), and Forcardos Yokri Field in shallow offshore (Wood *et al.*, 1991). Afenmai Field is a pseudo-name adopted to preserve data confidentiality and protect economic interests of the asset operators. The field is located within the Central Swamp Depobelt in eastern Niger Delta Basin (Figure 1). It covers approximately 93.44 square miles (242 km^2). Eight wells have presently been drilled within it, and this gives it an average well density of 1 well per 11.68 square miles (1 well per 31 km^2). The field is one of the PAD in the Niger Delta Basin (Unuevho and Onuoha, 2020), with possibility of opportunities for development drilling.

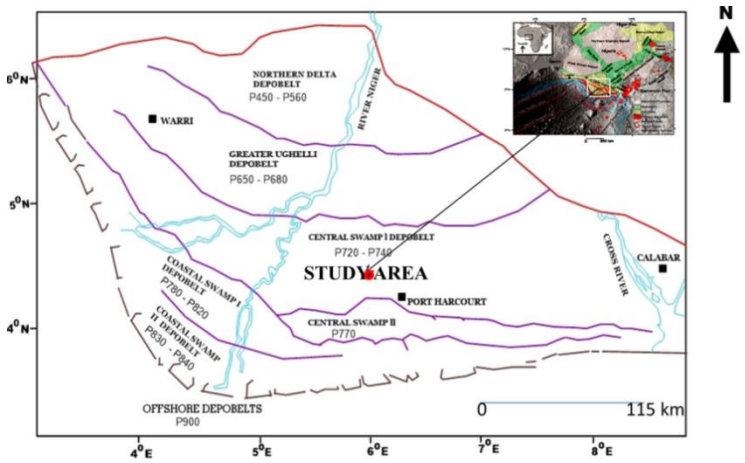

Fig.1. Study area (Unuevho and Onuoha, 2020)

Reservoir characterisation is an aspect of field appraisal upon which optimal hydrocarbon recovery hinges. Like all the UAD and PAD in the Niger Delta Basin, the Afenmai Field begs for characterisation of its reservoirs for development drilling to commence in the field. E8000 sand is among the reservoirs the asset operator found to be hydrocarbon bearing. The sand body was selected for characterization because it was penetrated by seven out of the existing eight wells in the field. The objective for characterizing this reservoir is to ascertain its spatial extent and the spatial distribution of its hydrocarbon fluids.

REGIONAL GEOLOGICAL SYNOPSIS

The origin and evolution of the Niger Delta Basin hinged on intra continental Cretaceous extensional processes. The sedimentary rock succession in the basin is Akata Formation, Agbada Formation and Benin Formation (Unuevho and Onuoha, 2021). Akata Formation is the basin's basal lithostratigraphic unit. It is dominantly a shale unit punctuated with occasional siltstones and sandstones. The formation is deposited in shelf to bathyal environments. It is overlain by the Agbada Formation comprising alternating sandstones, siltstones, mudstones and shales deposited in littoral, inner neritic, middle neritic, outer neritic and bathyal environments. It is the Agbada Formation that contains the hydrocarbon reservoirs. Hydrocarbon entrapment in the formation is structural, stratigraphic, and combined structuro-stratigraphic. The hydrocarbon source rocks are shales in the upper part of the Akata Formation, as well as shale and mudstone interbeds within the lower part of the Agbada Formation. The Benin Formation is the uppermost lithostratigraphic unit. It consists of fresh water bearing massive continental sands and gravels deposited in upper deltaic plain environment.

STUDY DATA AND METHODS

The data used in this study comprised information on subsea vertical depth to top and base of sand and shale units, foraminifera information, open-hole geophysical logs, checkshot data, and 3D seismic volume. The geophysical logs comprised gamma ray, resistivity, sonic, neutron and density log data. The foraminifera information comprise *Nonion, Cassigerinella, chiloguembelina, Uvigerina,* and *Bolivina* generic occurrence.

The project was created as Afenmai Field in a workstation with *Petrel* 2008.1.1 Geology and Geophysics interpretation software. The Imperial (British) unit system was chosen for storing

depth values, while spatial extent values were stored in metres. Minna in Nigeria Mid Belt was chosen as the Co-ordinate Reference System for the data base. The well base information, geophysical logs and 3D seismic volume were imported into the project. The lithologic data were plotted on the geophysical logs. The top and base of the lithologic units were appropriately adjusted in consonance the with respective gamma ray response. Depositional environments were reconstructed using a hybrid of the following criteria:

i. Continuity of lithologic units following Allen and Roberts (1982), Serra (1989), and Boggs (2006).
ii. Gamma ray motif following Weber (1971), Selley (1978), Larue and Lagarre (2004).
iii Foraminifera content following Okosun and Liebau (1999) on association of *Cassige*rinella *Chipolensis* with *Uvigerina* and *Bolivina,* Boersma (1980) on association of foraminifera genera with depositional environments (Figure 2), Ozumba (1995) on association of benthic foraminifera with depositional environments (Table 1), and Peters (1980) on paleo bathymetric interpretation of benthic foraminifera.

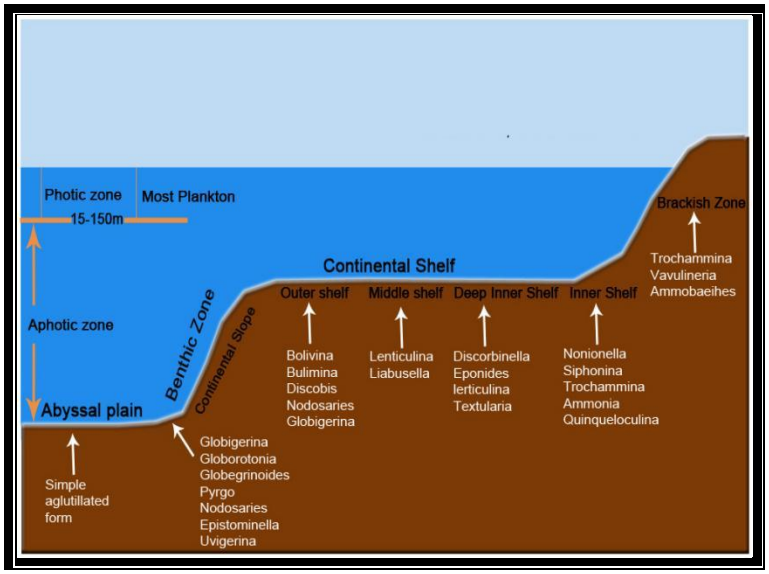

Fig. 2. Benthic foram genera association with bathymetric trend (Boersma, 1980)

Vertical juxtaposition of depositional environments was interpreted using sequence stratigraphic concepts, following Van Wagoner *et al* (1990) and Shell GLP (2011). E8000 sand was then associated with a systems tract and correlated throughout the wells.

The sonic log data was calibrated with the checkshot data in well W1000. Acoustic impedance and reflection coefficient logs were generated as products of density data and calibrated sonic log data. Synthetic seismograms were created by convolving a zero-phase synthetic wavelet with reflection coefficient log. The reservoir tops were posted to the 3D seismic volume via a well-to-seismic tie exercise. This transfers reservoirs vertical position from depth domain to time domain. A good tie was obtained with a bulk shift of 2 ms. A time depth (TDR) curve was generated from the checkshot data for well W001, which was then shared to other wells. A velocity function that describes the variation of velocity with depth was obtained from the TDR. Faults and the seismic horizon that tied with top of E8000 Sand were mapped on every tenth inline and on every tenth crossline section. The entire inlines and crosslines were gridded, and time structure map was created. Depth structure map was created from the time structure map using the velocity function. Root mean square amplitude was extracted along the mapped surface and values that characterise

the pay identified. Fluid contact information was posted onto the depth structure map to ascertain reservoir areal extent. New prospect was identified using combined analogous reservoir closure and pay characteristic RMS amplitude values.

Table 1:Benhic foraminifera association with specific depositional environment in Niger Delta (Ozumba, 1995)

BENTHONIC FORAMINIFERA	MIDDLE NERITIC	OUTER NERITIC	UPPER BATHYAL	MIDDLE BATHYAL	LOWER BATHYAL	ABYSSAL
Brizalina aenanensis						
Globocassidulina oblonga						
Sphaeroidina bulloides						
Hoeglundina elegans						
Rectuvigerina multicostata						
Cibidiodes crebbsi						
Uvigerina asperula						
Uvigerina hispida/proboscides						
Haplophragmoides narivaensis						
Siphouvigerina auberiana						

Gyroidina neosoldani

Pullenia bulloides

Bulimina alazaensis

Uvigerina subperegrjna

Bolivina scalprata retiformis

Oridosalis umbonatus

RESULTS AND DISCUSSION

Table 2 presents subsea vertical depth (SSVD) to top and base of E8000 Sand in the wells, foraminifera content in lithologic units vertically juxtaposed above and below the sand. The E8000 Sand is barren in foraminifera, indicating a high energy environment. Marine fossil in the shale directly above the E8000 Sand indicates marine transgression from top of the sand. This shows that the top of the E8000 Sand is a transgressive surface. Marine fossils in the shale directly below E8000 Sand base indicate the E8000 Sand is a regressive sand body. This makes the E8000 Sand base a regressive surface. Thus the E8000 Sand is juxtaposed between an older regression phase and a younger transgressive episode.

Table 2: Subsea vertical depth (SSVD) to top and base of E8000 Sand, foraminifera content in vertically adjacent shale units

WELL	SSVD E8000 SAND TOP (FEET)	SSVD E8000 SAND BASE (FEET)	FORAMS WITHIN E8000 SAND	FORAMS IN SHALE ABOVE E8000 SAND	FORAMS IN SHALE BELOW E8000 SAND
W001	8400	8500	BARREN	*NONION*	*BOLIVINA*
W002	9000	9200	BARREN	*UVIGEINA*	*NOT GIVEN*
W003	8700	8790	BARREN	*UVIGERINA*	*BOLIVINA*
W006	8410	8530	BARREN	*CHILOGUEMBELINA/ CASSIGERINELLA*	NOT GIVEN

W007	8300	8400	BARREN	*CHILOGUEMBELINA/ CASSIGERINELLA*	NOT GIVEN
W008	7134	7308	BARREN	NOT GIVEN	NOT GIVEN

Figure 3 shows some lithologic units vertically associated with the E8000 Sand, and the correlation of the E8000 Sand in wells W001, W002 and W003. The correlation of the sand and associated lithologic units in W006, W007 and W008 is given in Figure 4. The base of the E8000 Sand (E8000B) is sharp, showing a sharp lithofacies change from blocky (cylindrical) motif above to shale motif below. Such a sharp base represents a chronostratigraphic surface. The *uvigerina* as well as *cassigerinella* and *chiloguembelina* reflect outer shelf to upper bathyal depositional facies. The presence of *bolivina* reflect outer shelf to middle bathyal facies. The fossil barren E8000 Sand represents a marginal marine facies. The juxtaposition of marginal marine facies above outer shelf to bathyal facies indicates an unconformity. Since this unconformity is field-wide, it constitutes a sequence boundary. The juxtaposition of inner shelf facies above marginal facies indicates a transgressive surface. Thus the E8000 Sand is a lowstand systems tract.

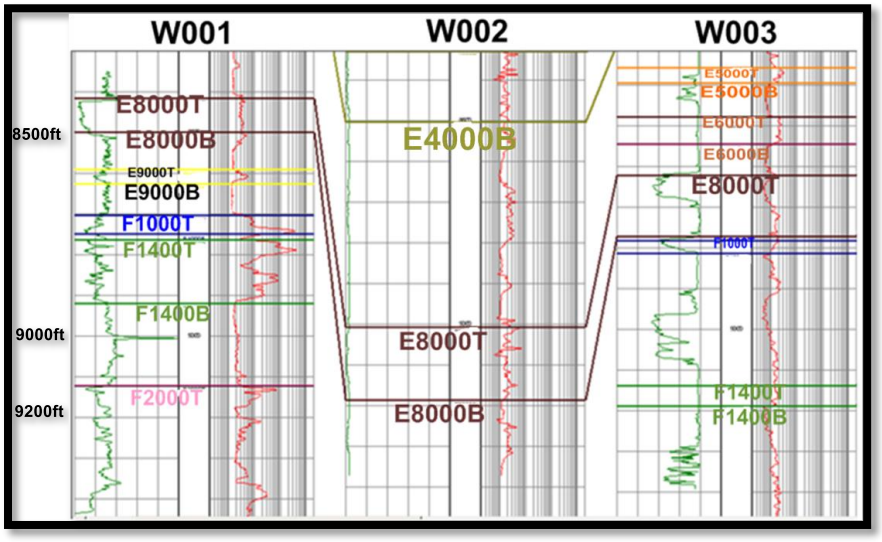

Fig. 3. Lithologic units associated with E8000 Sand, and correlation of the E8000 Sand in W001, W002, W003

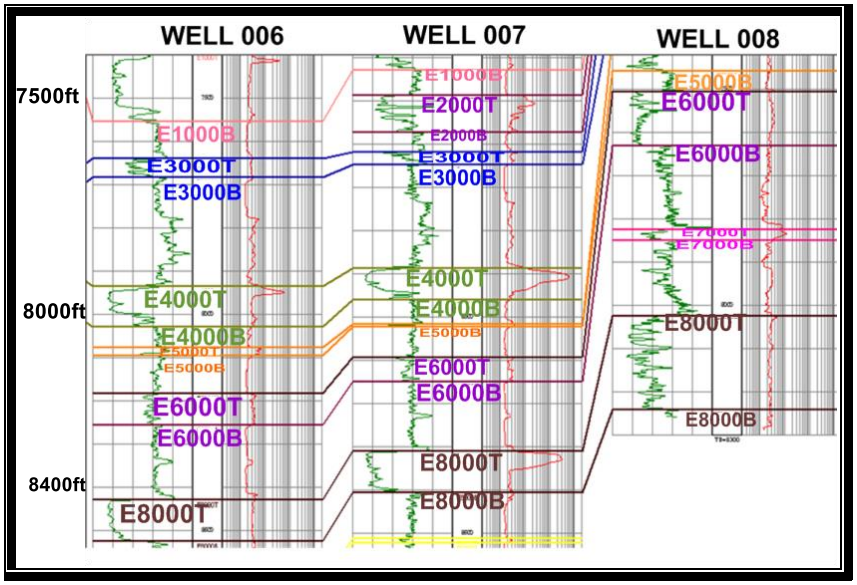

Fig. 4: lithologic units associated with E8000 Sand, and correlation of the E8000 Sand in W006, W007, W008

Figure 5 is seismic inline 11033 section. Posted on this inline section are wells 006 and 007, as well as the top of Agbada Formation, E8000 reservoirs and some other reservoirs penetrated by the wells.

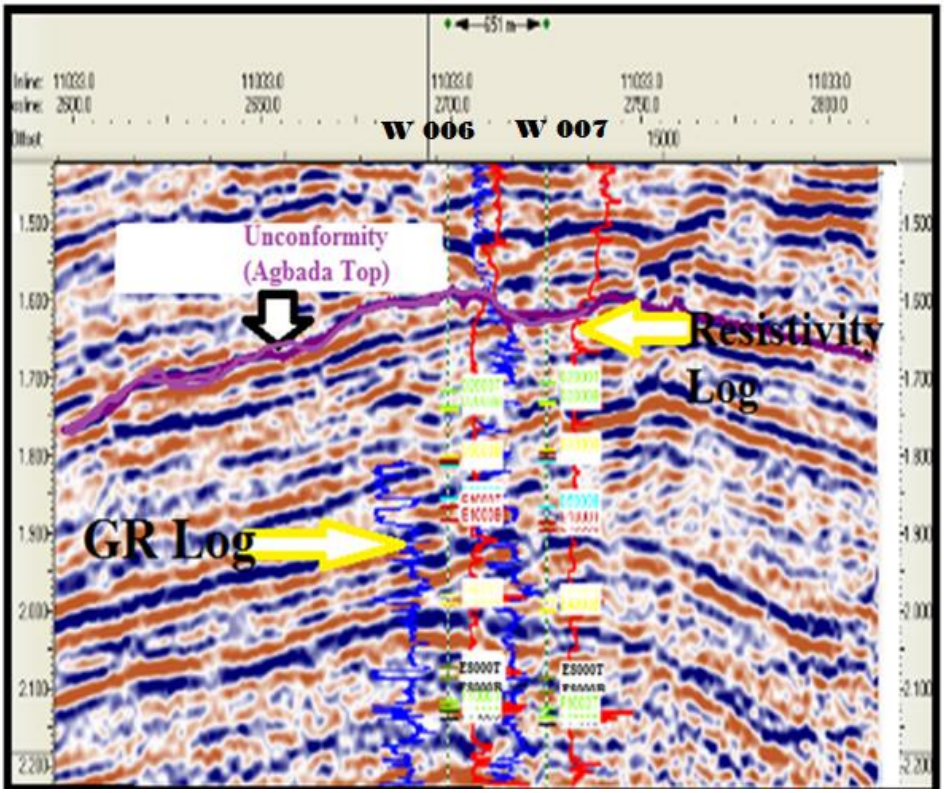

Fig. 5. Wells w006 and w007, logs and Sand tops on inline seismic section 11033

Figures 6 is a depth-structure map for the E8000 Sand. The map presents a major structure building synthetic fault that runs approximately east –westward in the eastern part of the field and northwest-

southeast in the western part. Such a major structure building synthetic fault was reported in Otigwe Field in Niger Delta Basin's Coastal Swamp Depobelt by Kurah *et al* .(2021)

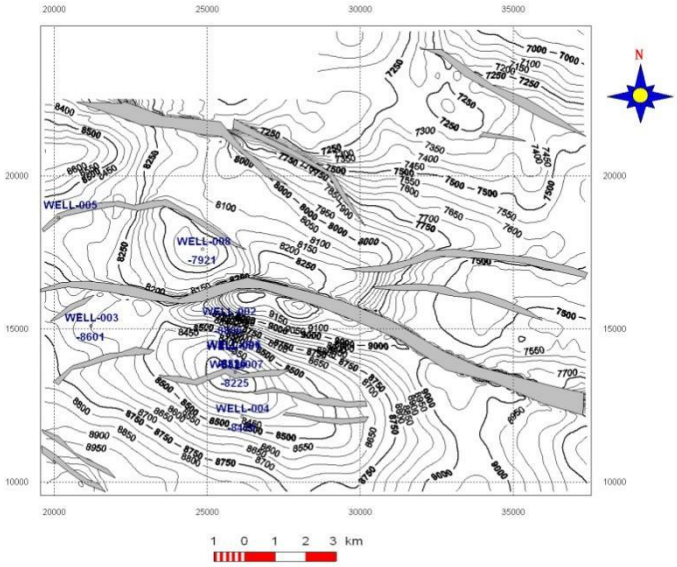

Fig.6. Depth- structure map for top of E8000 sand

Figure 7 presents spatial variation of RMS amplitude extracted along the top of the E8000 Sand. The E8000 Sand is hydrocarbon bearing only at W007. The RMS amplitude value of E8000 that characterise hydrocarbon in this well is 4000 – 5000. These are mediun RMS amplitude values. Ebere (2016) reported an association of medium – high RMS amplitude values with hydrocarbon bearing sands in deep offshore Niger Delta Basin. Onoja and Obiekezie (2019) found that similar RMS amplitude values characterise hydrocarbon reservoirs in Uzot – Field in onshore Niger Delta Basin.

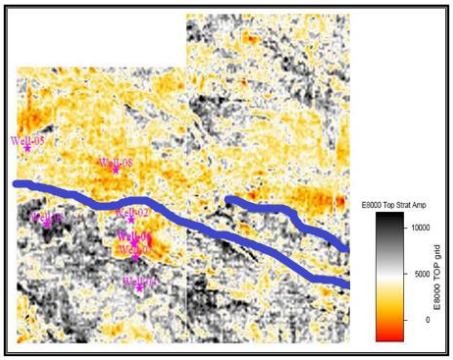

Fig. 7. RMS amplitude extracted along the top of the E8000 Sand

Figure 8 presents the the spatial extent of the reservoir pay, as well as the areal distribution of its oil and gas content. The W007 well is located on the downthrown block of the structure building synthetic fault, where it penetrated a roll-over anticline that forms a three-way closure with a crestal fault. The areal extent of this hydrocarbon filled closure is 4.5 km^2. A three – way closure is associated with a flank fault located on the eastern part of upthrown block of the structure building synthetic fault. The medium – high RMS amplitude that characterise this closure make it a hydrocarbon prospect. Hydrocarbon bearing roll-over anticlines in the form of three-way closure, as well as three-way closure prospect have been delineated in the Niger Delta Basin by Tijani *et al.* (2020) and Oloye and Olorunfemi (2021).

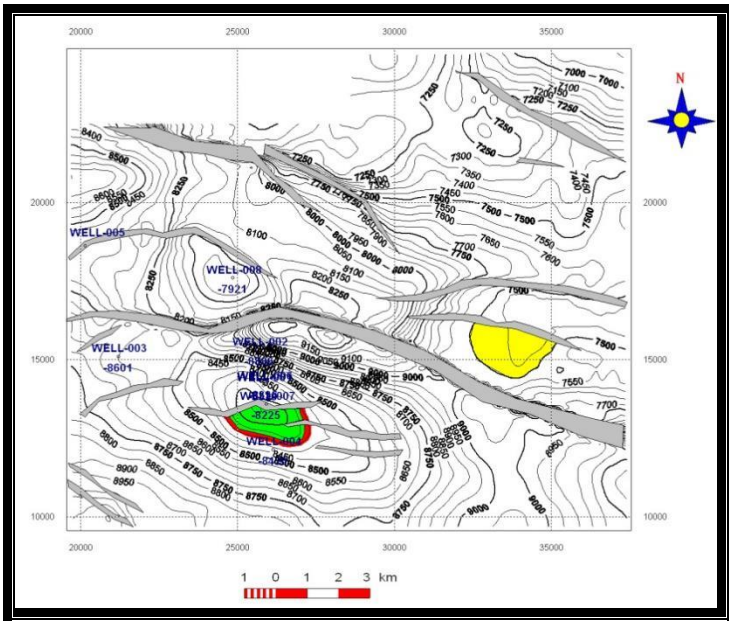

Fig.8. Areal extent of hydrocarbon accumulation and new prospect (shown in yellow) in E8000 sand

CONCLUSION AND RECOMMENDATION

Seismic structural mapping of the E8000 Sand was achieved using 3D seismic volume. The sand was delineated as a lowstand systems tract from sequence stratigraphic interpretation of combined lithologic, foraminifera and geophysical log data. The reservoir was found to be a roll-over anticline that constitutes a three-way closure with a crestal fault. Its hydrocarbon content occupies a surface area of 4.5 km^2. Only well W007 has been drilled in this closure, and opportunities for development drilling were identified southwards, eastwards and westwards of the well. RMS amplitude values of 4000 – 5000 (medium amplitude values) characterise hydrocarbon in the reservoir. A prospect was delineated on the eastern part of the upthrown block as a three-way closure with medium RMS amplitude values.

RECOMMENDATIONS

The well W007 should be re-entered and deviated southwards, eastwards and westwards in a three-phase directional drilling programme to produce E8000 optimally. The delineated prospect on the upthrown block of the structure building fault should be drilled to ascertain whether it is hydrocarbon bearing.

REFERENCES

Allen, T.O. & Roberts, A.P. (1982). *Production operations*, vol.1 (2nd ed.). Oklahoma, US: OGCI

Boersma, A.(1980). Foraminifera. In H.A. Bilal & A. Boersma (Eds.), *Introduction to Micropaleontology* (pp. 19-77). New York: Elservier.

Boggs Jr., S. (2006). *Principles of sedimentology and stratigraphy* (4th ed.). New Jersey, US: Prentice Hall

Ebere, B. (2016). *Seismic lithofacies prediction and reservoir characterization in Deep Offshore Niger Delta, Nigeria*. (Doctoral dissertation, University of Lagos, Lagos, Nigeria) Retrieved from http://ir.unilag.edu.ng:8080/xmlui/handle/123456789/3261

Edeki, A.O. (1991). Prospectivity of the northern part of the eastern Niger Delta with emphasis in deep-seated structures. *Nigerian Association of Petroleum Explorationists Bulletin*, 6(2), 47-69.

Kurah, B.K., Shariatipour, M.S. & Itiowe, K. (2021). Reservoir chracterisation and volumetric estimation of reservoir fluids using simulation and analytical methods: a case study of the Central Swamp Depobelt, Niger Delta, Basin, Nigeria. *Journal of Petroleum Exploration and Production Technology*, 11, 2347 – 2365. https://doi.org/10.1007/s13202-021-01206-1

Larue, D.K. and Legarre, H. (2004). Flow units, connectivity, and reservoir characterization in a wave dominated deltaic reservoir. Meren reservoir, Nigeria. *American Association of Petroleum Geologists Bulletin*, 88(3), 303-324.

Okosun,E.A. and Liebau, A.(1999). Foraminiferal biostratigraphy of eastern Niger Delta, Nigeria. *Nigerian Association of Petroleum Explorationists Bulletin*, 14(2), 136-154.

Oloye, o. and Olorunfemi, M.T. (2021). Seismic attributes analysis as a precursor to hydrocarbon indicators: A case study of 'OK' Field, Niger Delta. *Tanzanian Journal of Science*, 47 (1), 134 – 144.

Onoja, U.C. and Obiekezie, T.N. (2019). Application of 3D seismic attribute analyses for hydrocarbon prospectivity in Uzot-Field, onshore Niger Delta Basin, Nigeria. *International Journal of Geophysics*, 1-11. https://doi.org/10.1155/2019/1706416

Overell, J.F.S. and Nwachukwu, J.A. (1995). Marginal discoveries and prospective fields in eastern Niger Delta. *Nigerian Association of Petroleum Explorationists Bulletin*, 10(01), 12-18.

Ozumba, M.B. (1995). Late Miocene-Pliocene biostratigraphy offshore, Niger Delta. *Nigerian Association of Petroleum Explorationists Bulletin*, 10(1), pp.40-48.

Petters, S.W. (1982). Central West African Cretaceous- Tertiary benthic foraminifera and stratigraphy. *Palaeontographica*, 79, 1-104.

Serra, O. (1989). *Sedimentology Environments from Wireline Logs* (2nd ed.). Texas, US: Schlumberger educational services

Selley, R.C. (1978). *Ancient sedimentary environments and their sub-surface diagnosis* (2nd ed.). London, England: Chapman and Hall

Shell GLP (2011). *Seismic and sequence stratigraphy overview- its applications in subsurface evaluation*. Port-Harcourt, Nigeria: UIG\T\DXG

Tijani, K.A., Akaolisa, C.C.Z., Ibeneme, S.I., Opara, A.I. and Selemo, A.O.I. (2020). Structural interpretation and reservoir characterization of Ohaji Field, Niger Delta using 3D Seismic and well-log data. *British Journal of Earth Sciences Research*, 8(1), 1-16.

Unuevho, C.I. and Onuoha, K.M. (2020). Facies analysis of Afenmai Field in Eastern Niger Delta Basin of Nigeria, using combined geophysical logs, lithologic and paleontological data. *Journal of Natural and Applied Sciences*, 9 (1), 44 – 61.

Unuevho, C.I. & Onuoha, K.M. (2021). Petrophysical and reservoir rock property analyses of open-hole geophysical logs for Afenmai Field, Eastern Niger Delta Basin of Nigeria. *Journal of Mining and Geology*, 57(2), 505-512.

VanWagoner, J.C., Mitchum, R.M., Campion, K.M. & Rahmanian,V.D. (1990). *Siliciclastic sequence stratigraphy in well logs , cores and outcrops : concepts for high resolution correlation of time and facies*. AAPG Methods in exploration series(7).Tulsa, US: AAPG

Weber, K. (1971). Sedimentological Aspects of Oil Fields in the Niger Delta. *Geol Minjbouw*, 50, 209-221.

Wood, P.R. Wilson, T.P. and Subbiah, A. (1991). The impact of 3D seismic for SPDC in the Niger Delta. *Nigerian Association of Petroleum Explorationists Bulletin*, 6(2), 28-45.

GEOELECTRICAL INVESTIGATION FOR GROUNDWATER POTENTIAL AT GOVERNMENT SECONDARY SCHOOL, KWAKUTI NIGER STATE, NIGERIA

[1,2]Aliu, O.D., [1]Alhassan U.D. and [1]Salako, K.A.
[1]Department of Physics, School of Physical Sciences, Federal University of Technology, Minna
[2]Department of Geophysics, School of Physical Sciences, Federal University of Technology, Minna, Niger State.
Corresponding Author's email: aliuonotu@yahoo.com

Abstract

Vertical Electrical Sounding (VES), using Schlumberger array was carried out to investigate the subsurface layer parameters used to delineate groundwater potential of a 500 x 500 m area of land defined by latitude 9.416622 N to 9.421171 N and longitude 6.618314 E to 6.622833 E located at Government Secondary School, Kwakuti, Niger State. A total of 36 VES points at 100 m interval were sounded with a 100 m maximum half inter current electrode spacing (AB/2). Result revealed that the study area is underlain by three (3) geoelectric layers which include: the top soil with 104.5 to 2260.5 Ωm, 0.6 to 3.8 m and 0.6 to 3.8 m as its range of resistivity, depth and thicknesses respectively; the weathered/fractured layer having resistivity of 44.9 to 606.0 Ωm, depth of 4.3 to 28.6 m and thickness of 4.2 to 26.2 m was considered aquifer layer. The fresh basement has 919.4 to 3816.9 Ωm as its range of resistivity value with undefined depth and thickness. The observed curve types were 100% H. Five (5) VES stations C3, C4, D2, D5, and E4 were delineated as aquifer potentials of the study area, their resistivity, depth and thickness range from 135.2 to 227.7 Ωm, 20.6 to 28.6 m and 17.8 to 26.2 m respectively.

1.1 Introduction

Water is considered to be a basic component of life as all living things rely heavily on it for their existence. It is highly needed for domestic, agricultural and industrial use and its sources are mainly the surface and groundwater source. Presently, the use and sustainability of water is getting more complex due to population growth, urbanization and industrialization.

Groundwater is the water present in soil pore spaces beneath Earth's surface and in the fractures of rock formations. It is available in different proportions, in various rock types and at various depths on the surface layer of the earth. A unit of rock or an unconsolidated deposit that can yield a usable quantity of water is referred to as an **aquifer**. The depth at which fractures or soil pore spaces in rock becomes fully saturated with water is called the water table (Alhassan et al., 2017).

It is considered to be a less contaminable source of water which makes it suitable for drinking and agricultural purpose; though fairly dispersed all over the world, it cannot be found in good quantity everywhere, hence the need for a careful investigation/survey beforehand (Alhassan *et al*., 2015).

Various geophysical methods have been employed successfully for ground water exploration in different parts of the world over the years. Some of these methods include magnetic, electrical, electromagnetic, gravity, seismic, remote sensing etc. Of all these methods, the electrical resistivity method has been the most widely used geophysical tool for groundwater investigation because of its advantage which include simplicity in field technique and data handling procedure and it is the most effective (Anomohanran, 2013; Alhassan *et al*., 2017).

The Vertical Electrical Sounding (VES) is an electrical resistivity method that is widely used for depth sounding due to its simplicity and it is used to estimate the electrical resistivity variation of the earth subsurface vertically downward since the electrical resistivity of most rocks is dependent on the amount of water in the pore spaces within the rocks, the dissemination of these pores and the salinity of the water in the pore spaces reliability (Olawuyi and Abolarin, 2013).

In this study, vertical electrical sounding method was used to determine the depth to bedrock which constitutes the basics for geotechnical survey.

2.1 Material and Method

The material used in this study are: ABEM SAS 4000 Terrameter, handheld global positioning system (GPS), measuring tape, electrodes, cables, pegs, geologic hammer and test resistor box.

The above mentioned materials were used to investigate the parameters of the subsurface structures of the study area. The Terrameter Signal Averaging System (SAS) model 4000 and its accessories were used to carry out the vertical electrical sounding (VES) of a total of thirty six (36) points in the study area. Six traverses with 6 VES points each were made, the inter traverse and inter VES point spacing were 100 metres and the Schlumberger array pattern with half inter electrode spacing (AB/2) ranging from 1-100 meters was adopted. Through a pair of current electrodes A and B, direct current (DC) was supplied into the ground and the potential difference was measured by means of another pair of electrodes M and N called the potential electrodes.

To increase the depth of investigation, the current electrode separation was increased while the potential separation remained constant. The sensitivity of the potential electrode measurement decreases as the current electrodes spacing increases, therefore, at some point, it was necessary to increase the potential electrode spacing.

The geometric factor, K, was first calculated for all the electrode spacing using the formula:

$$K = \pi\left(\frac{\left(\frac{AB}{2}\right)^2 - \left(\frac{MN}{2}\right)^2}{MN}\right) \qquad (3.1)$$

Then the apparent resistivity (ρa) values were obtained by multiplying K by the resistance(R) values

$$\rho_a = KR \qquad (3.2)$$

Also, the apparent resistivity values obtained were plotted against AB/2 using winResist software and from the plots; the resistivity, depth and thickness of each of the subsurface layer were deduced.

3.0 Results and Discussion

3.1 Geoelectric Section

The Geoelectric section (VES curve) as shown in Figure 1.1a and 1.1b, provides information about the subsurface layer resistivity, depth and thickness as summarised in table 1.1.

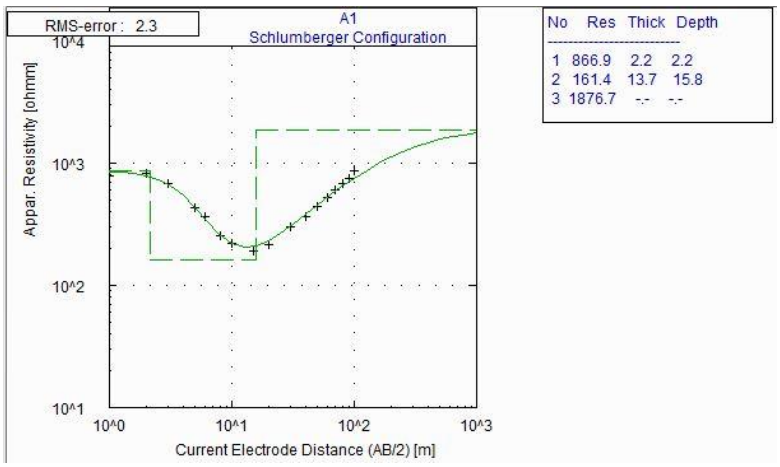

Figure 1.1a: Geoelectric section of VES point A_1

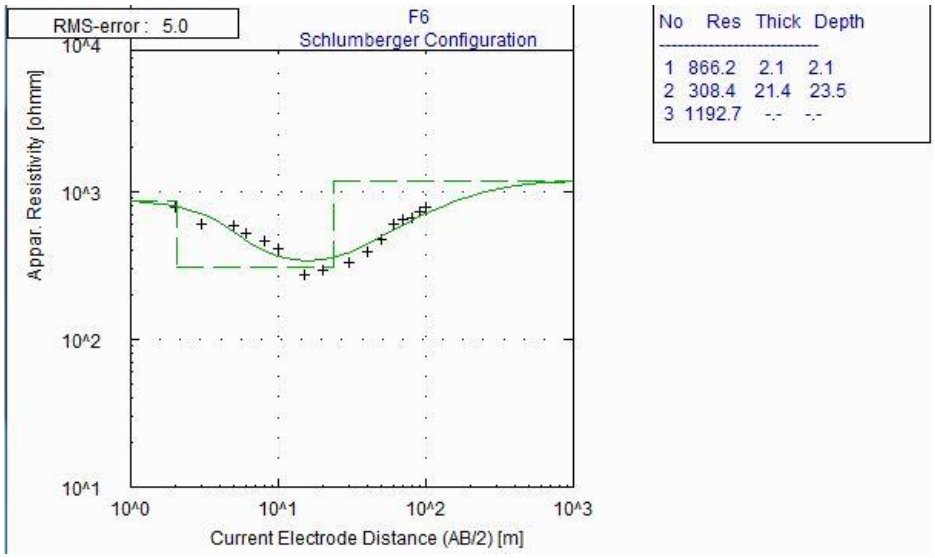

Figure 1.1b: Geoelectric section of VES point F_6

Table 1 shows the summary of results obtained from each geoelectric section across profile A to F which reveals that the study area is underlain by three (3) geoelectric subsurface layers. The first layer which is the top layer has resistivity value ranging from 104.5 – 2260.5 Ωm, its depth and thickness varies between 0.6 and 3.8 m and 0.6 and 3.8 m respectively which correspond to the geoelectrical parameters of weathered laterite and fresh laterite (table 3.1). The second layer has resistivity value of 44.9 – 606 Ωm, depth of 4.3 – 28.6 m and thickness of 3.4 – 26.2 m; this layer refers to the weathered/fractured basement. The resistivity of the third layer ranged from 919.4 – 3816.9 Ωm, its depth and thickness are undefined.

Table 1: Layer resistivity, depth, thickness and curve type

VES Stations	Latitude (°)	Longitude (°)	No. of Layers	Layer Resistivity, ρ (Ωm)			Layer Depth, d (m)			Layer Thickness, h (m)			Curve Type
				$\rho 1$	$\rho 2$	$\rho 3$	$d1$	$d2$	$d3$	$h1$	$h2$	$h3$	
A1	9.416622	6.618314	3	866.9	161.4	1876.7	2.2	15.8	∞	2.2	13.7	∞	H
A2	9.416628	6.619224	3	1081.8	239.7	2204.5	1.5	16.7	∞	1.5	15.3	∞	H
A3	9.416634	6.620134	3	1463.1	189.6	2030.3	1.9	16.7	∞	1.9	14.8	∞	H
A4	9.416640	6.621044	3	1003.7	155.5	2305.5	2.3	13.8	∞	2.3	11.5	∞	H
A5	9.416646	6.621954	3	1035.6	168.9	3528.0	1.6	12.2	∞	1.6	10.6	∞	H
A6	9.416652	6.622864	3	1073.4	281.3	3816.9	2.0	14.0	∞	2.0	12.1	∞	H
B1	9.417525	6.618308	3	1274.9	164.2	2093.7	2.3	17.2	∞	2.3	14.9	∞	H
B2	9.417531	6.619218	3	1340.7	179.2	2286.9	2.7	17.3	∞	2.7	14.6	∞	H
B3	9.417538	6.620128	3	774.2	174.4	3696.2	3.1	18.2	∞	3.1	15.2	∞	H
B4	9.417544	6.621038	3	651.0	189.4	2088.6	2.0	15.5	∞	2.0	13.5	∞	H
B5	9.417550	6.621948	3	848.8	252.5	2667.1	1.9	17.6	∞	1.9	15.7	∞	H
B6	9.417556	6.622858	3	450.6	254.6	2029.9	1.4	23.0	∞	1.4	21.6	∞	H
C1	9.418429	6.618302	3	1103.5	197.4	1906.2	2.7	21.7	∞	2.7	19.0	∞	H
C2	9.418435	6.619212	3	1114.1	186.2	3233.8	1.5	14.1	∞	1.5	12.6	∞	H
C3	9.418441	6.620122	3	1190.8	135.2	1991.3	2.2	23.0	∞	2.2	20.8	∞	H
C4	9.418447	6.621032	3	657.4	135.3	982.4	2.4	28.6	∞	2.4	26.2	∞	H
C5	9.418454	6.621942	3	104.5	44.9	3131.8	0.8	4.3	∞	0.8	3.4	∞	H
C6	9.418460	6.622852	3	1070.3	163.9	1834.9	0.6	4.8	∞	0.6	4.2	∞	H
D1	9.419333	6.618295	3	666.8	606.0	2746.8	1.0	7.2	∞	1.0	6.1	∞	H
D2	9.419339	6.619205	3	1019.7	159.7	1172.5	2.8	20.6	∞	2.8	17.8	∞	H
D3	9.419345	6.620115	3	1859.6	135.8	1252.2	1.8	18.7	∞	1.8	16.9	∞	H
D4	9.419351	6.621026	3	1443.1	200.2	1024.0	1.5	20.1	∞	1.5	18.5	∞	H
D5	9.419357	6.621936	3	1480.7	227.7	1468.5	1.6	25.7	∞	1.6	24.1	∞	H
D6	9.419363	6.622846	3	537.3	192.4	1452.3	2.1	20.5	∞	2.1	18.4	∞	H
E1	9.420236	6.618289	3	1656.5	85.9	946.1	1.5	24.0	∞	1.5	22.4	∞	H
E2	9.420242	6.619199	3	2260.5	102.8	919.4	1.5	16.7	∞	1.5	15.2	∞	H
E3	9.420249	6.620109	3	1076.3	136.5	1612.5	3.3	20.2	∞	3.3	16.9	∞	H
E4	9.420255	6.621019	3	889.3	186.6	1369.5	2.5	26.0	∞	2.5	23.5	∞	H
E5	9.420261	6.621929	3	834.2	230.7	1604.5	1.3	25.4	∞	1.3	24.1	∞	H
E6	9.420267	6.622840	3	532.4	231.4	1432.2	1.1	23.2	∞	1.1	22.1	∞	H
F1	9.421140	6.618283	3	1426.9	97.3	1299.4	1.4	9.4	∞	1.4	8.0	∞	H
F2	9.421146	6.619193	3	888.7	112.4	1457.2	3.8	19.9	∞	3.8	16.2	∞	H
F3	9.421152	6.620103	3	2203.2	130.2	1504.9	3.3	21.1	∞	3.3	17.8	∞	H
F4	9.421158	6.621013	3	1048.4	172.4	1492.5	3.3	21.2	∞	3.3	17.9	∞	H
F5	9.421165	6.621923	3	1455.5	193.4	1799.5	2.8	20.2	∞	2.8	17.4	∞	H
F6	9.421171	6.622833	3	866.2	308.4	1192.7	2.1	23.5	∞	2.1	21.4	∞	H

3.2 Geologic sections of the study area

Figure 2.1 to 2.6 reveals the vertical geologic section through profile A – F showing the layers of the subsurface structure, their depth and thickness.

3.2.1 Geologic Section of Profile A

The geologic section through profile A (Figure 2.1) reveals that the profile is characterised by three layers. The first layer is the top soil which spreads through the entire profile; its resistivity, depth and thickness range from 866.9 – 1463.1 Ωm, 1.5 – 2.3 m and 1.5 – 2.3 m respectively.

The second layer is a weathered/fractured layer, its resistivity, depth and thickness varies between 155.5 and 281.3 Ωm, 12.2 and 16.7 m and 10.6 and 15.3 m respectively; it spreads across the entire profile. The third layer underlies the second layer, it is the fractured/fresh basement, it has a resistivity range of 1876.7 – 3816.9 Ωm and undefined depth and thickness.

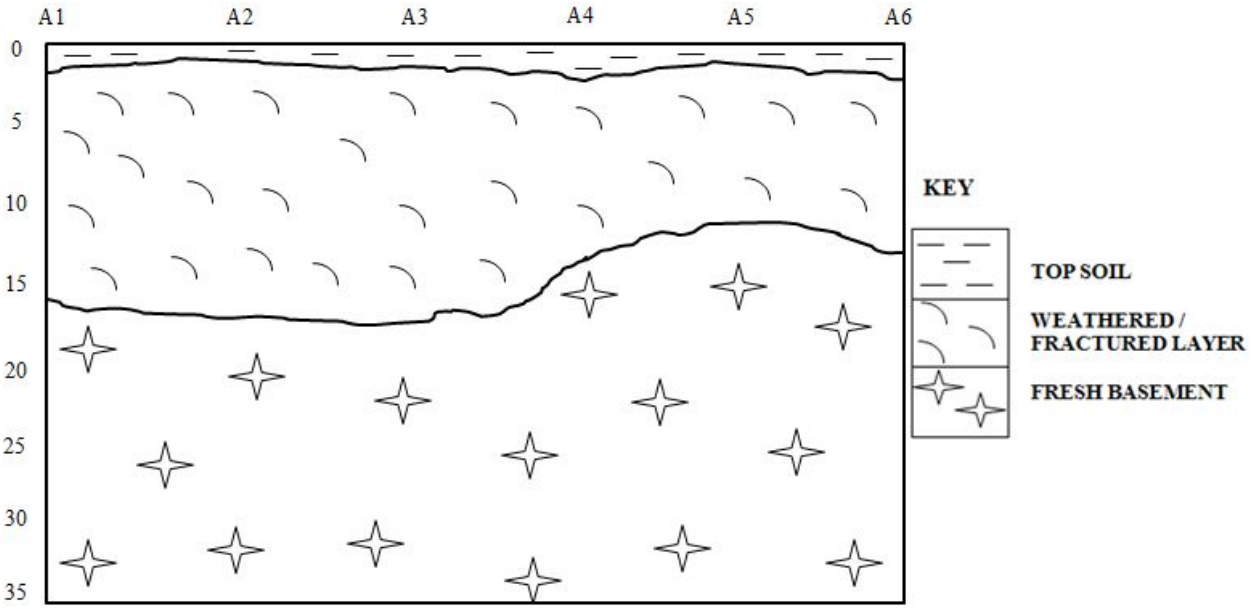

Figure 2.1: Vertical geologic section through profile A

3.2.2 Geologic Section of Profile B

Figure 2.2 represents the geologic section through profile B, it reveals that the profile is characterised by three geoelectric layers. The first layer which is the top soil spreads through the entire profile; its resistivity, depth and thickness range from 450.6 – 1340.7 Ωm, 1.4 – 3.1 m and 1.4 – 3.1 m respectively. The second layer refers to the weathered/fractured layer, its resistivity, depth and thickness varies between 164.2 – 254.6 Ωm, 15.5 – 23.0 m and 13.5 – 21.6 m respectively; it spreads across the entire profile. The second layer is underlain by the third layer which is the fresh basement, it has a resistivity value of 2029.9 – 3696.2 Ωm and undefined depth and thickness.

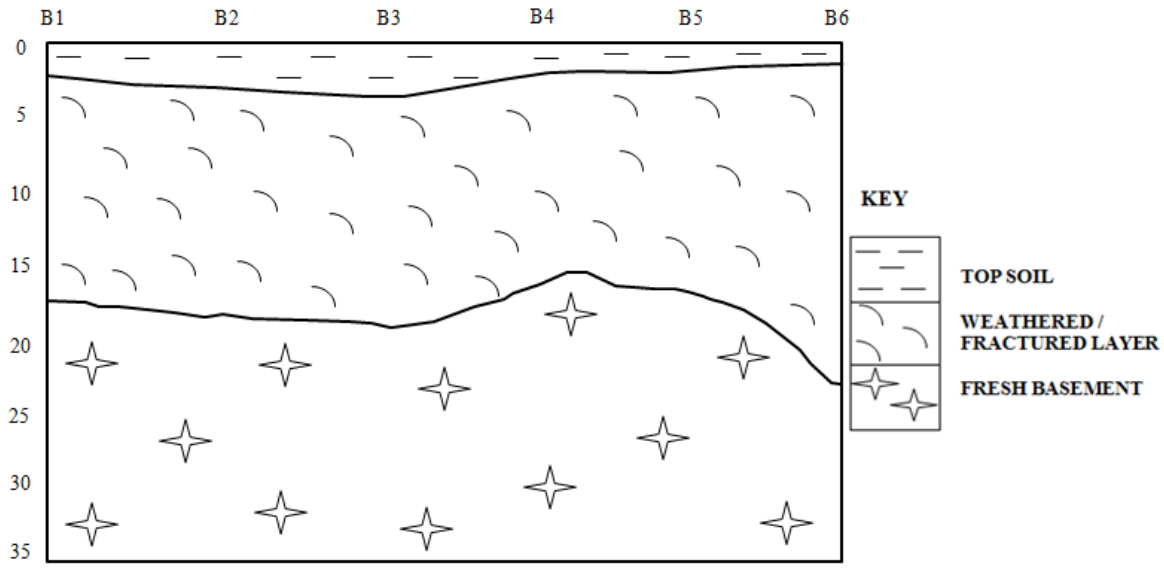

Figure 2.2: Vertical geologic section through profile B

3.2.3 Geologic Section of Profile C

The geologic section through profile C (Figure 2.3) reveals that three distinct layers exist therein. The first layer is the top soil spreading through the entire profile; its resistivity, depth and thickness ranges from 104.5 – 1190.8 Ωm, 0.6 – 2.7 m and 0.6 – 2.7 m respectively. The second layer is a weathered/fractured layer which also spreads across the entire profile, its resistivity, depth and thickness varies between 44.9 – 197.4 Ωm, 4.3 – 28.6 m and 3.4 – 26.2 m respectively. The third layer which is the fresh basement underlies the second layer, it has a resistivity range of 982.4 – 3233.8 Ωm and undefined depth and thickness. There is a reservoir effect spreading from VES C_3 to C_4 which makes these points favourable for groundwater development.

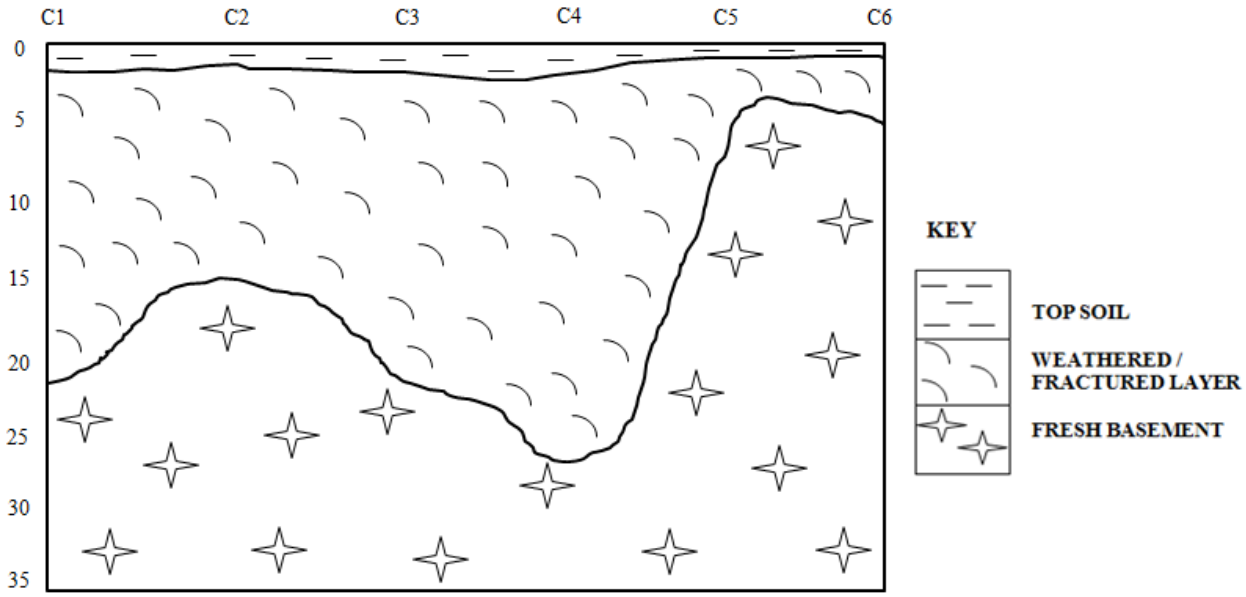

Figure 2.3: Vertical geologic section through profile C

3.2.4 Geologic Section of Profile D

Three geoelectric layers exist within profile D as clearly revealed by its geologic section (Figure 2.4). The first layer which is the top soil spreads through the entire profile; its resistivity, depth and thickness range from 537.3 – 1859.6 Ωm, 1.0 – 2.8 m and 1.0 – 2.8 m respectively. The second layer which is the weathered/fractured layer has resistivity, depth and thickness of 135.8 – 606.0 Ωm, 7.2 – 25.7 m and 6.1– 24.1 m respectively; it spreads across the entire profile. The fresh basement which is the third layer underlies the second layer, it has a resistivity range of 1024.0 – 2746.8 Ωm with depth and thickness undefined. VES point D2 and D5 are good points for groundwater exploitation.

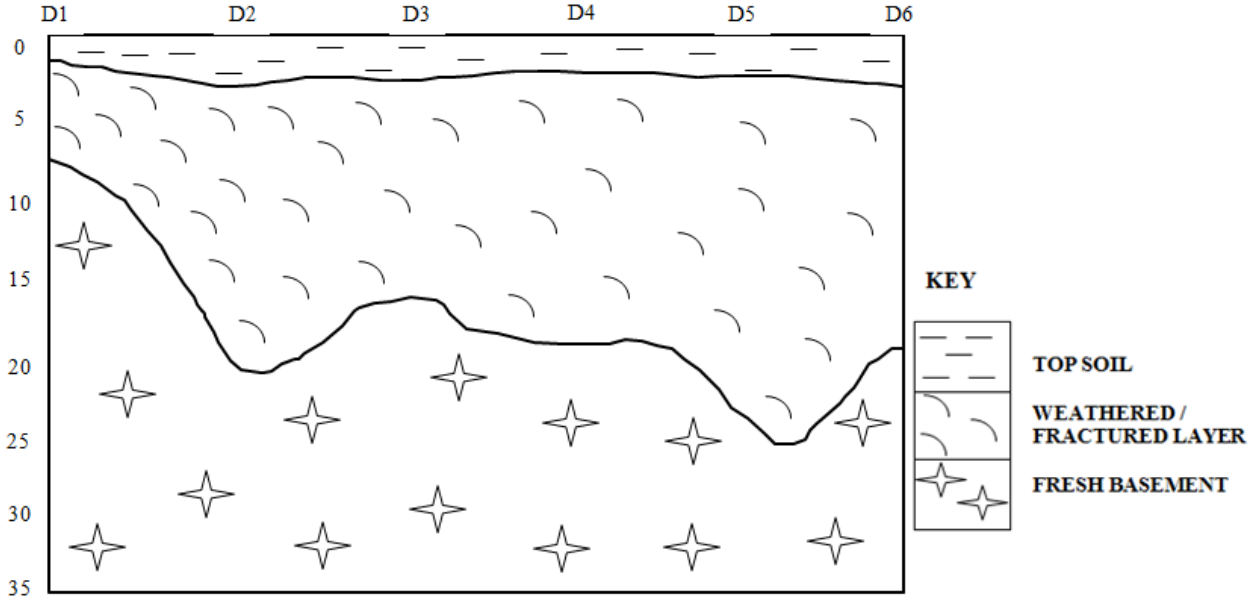

Figure 2.4: Vertical geologic section through profile D

3.2.5 Geologic Section of Profile E

Figure 2.5 shows the geologic section through profile E, it reveals that three distinct layers exist therein. The first layer is the top soil which spreads through the entire profile; its resistivity, depth and thickness range from 532.4 – 2260.5 Ωm, 1.1 – 3.3 m and 1.1 – 3.3 m respectively. The second layer is a weathered/fractured layer which also spreads across the entire profile, its resistivity, depth and thickness varies between 85.9 – 231.4 Ωm, 16.7 – 26.0 m and 15.2 – 24.1 m respectively. The third layer which is the fresh basement has a resistivity range of 919.4 – 1612.5 Ωm with an undefined depth and thickness. VES point E_4 will be suitable for groundwater development.

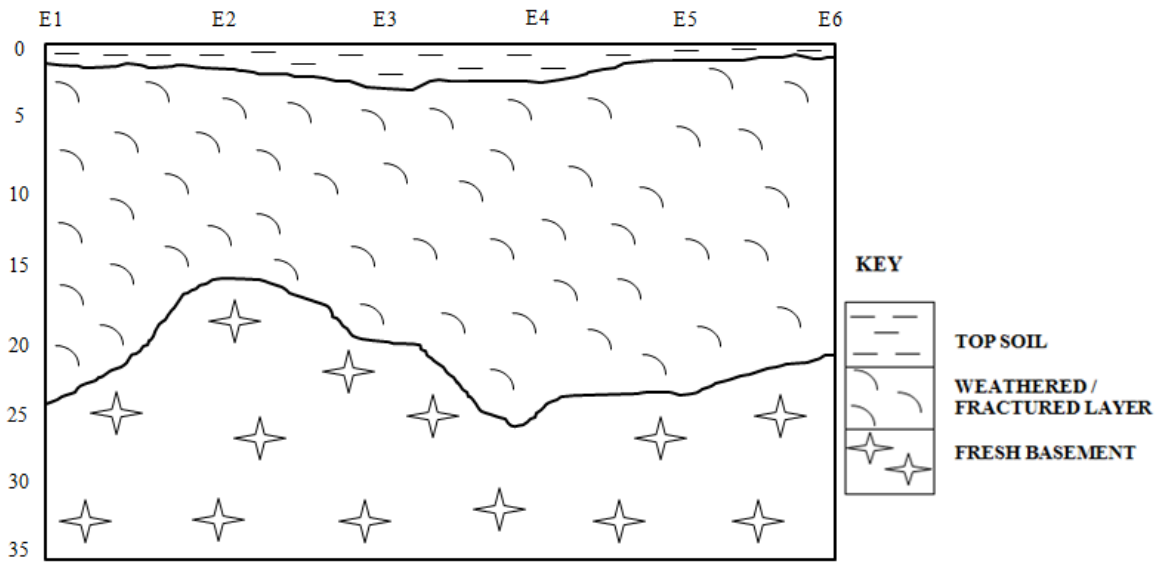

Figure 2.5: Vertical geologic section through profile E

3.2.6 Geologic Section of Profile F

The geologic section through profile F (Figure 2.6) reveals that the subsurface is made up of three geoelectric layers. The first layer is the top soil which spreads through the entire profile; its resistivity, depth and thickness range from 866.2 – 2203.2 Ωm, 1.4 – 3.8 m and 1.4 – 3.8 m respectively. The second layer is a weathered/fractured layer which also spreads across the entire profile, its resistivity, depth and thickness varies between 97.3 – 308.4 Ωm, 9.4 – 23.5 m and 8.0 – 21.4 m respectively. The third layer which is the fresh basement has a resistivity range of 1192.7 – 1799.5 Ωm with an undefined depth and thickness.

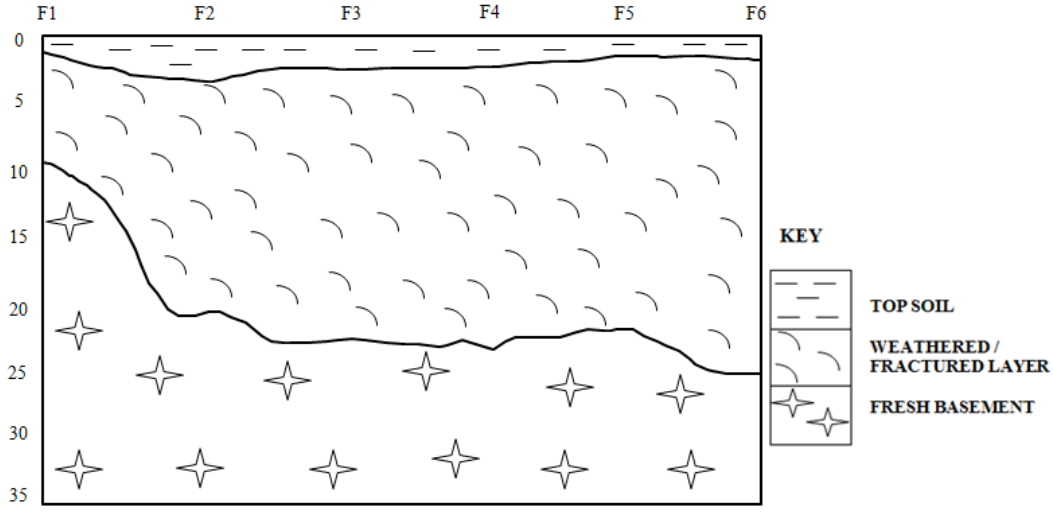

Figure 2.6: Vertical geologic section through profile F

3.3 Delineated aquifer potentials of the study area

Table 2 contains the VES points delineated as aquifer potential of the study area, the range of resistivity, depth and thickness of these aquifers are 135.2 to 227.7 Ωm, 20.6 to 28.6 m and 17.8 to 26.2 m respectively.

Table.2 Delineated aquifer potentials of the study area

VES Stations	Latitude (°)	Longitude (°)	No. of Layers	Layer Resistivity ρ (Ωm)			Layer Depth (m)			Layer Thickness (m)			Curve Type
				ρ1	ρ2	ρ3	d1	d2	d3	h1	h2	h3	
C_3	9.418441	6.620122	3	1190.8	135.2	1991.3	2.2	23.0	∞	2.2	20.8	∞	H
C_4	9.418447	6.621032	3	657.4	135.3	982.4	2.4	28.6	∞	2.4	26.2	∞	H
D_2	9.419339	6.619205	3	1019.7	159.7	1172.5	2.8	20.6	∞	2.8	17.8	∞	H
D_5	9.419357	6.621936	3	1480.7	227.7	1468.5	1.6	25.7	∞	1.6	24.1	∞	H
E_4	9.420255	6.621019	3	889.3	186.6	1369.5	2.5	26.0	∞	2.5	23.5	∞	H

4.0 Conclusion

Electrical resistivity method has been shown to be a suitable and very efficient tool in investigating groundwater potential by the results obtained from the analysis of the data acquired in field of survey. The resistivity of the top layer, weathered/fractured layer and fresh basement layer varies from 104.5 to 2260.5 Ωm, 44.9 to 606.0 Ωm and 919.4 to 3816.9 Ωm respectively across the entire study area; the depth of the top layer ranges from 0.6 to 3.8 m, that of the weathered/fractured layer varies from 4.3 to 28.6 m while that of the fresh basement layer is undefined across the six(6) profiles investigated; also, the study area has 0.6 to 3.8 m and 4.2 to 26.2 m as the thickness of its the top layer and weathered/fractured layer respectively, the fresh basement layer has an undefined thickness.

References

Alhassan, U. D., Obiora, D. N., Okeke, F. N. (2015). The Assessment of Aquifer Potential and Aquifer Vulnerability of Southern Paiko, North Central Nigeria, Using Geoelectric Method. *Global Journal of Pure and Applied Sciences*. 21: 51-70.

Alhassan, U. D., Obiora, D. N., Okeke, F. N. (2017). Geoelectrical Investigation of Groundwater Potentials of Northern Paiko, Niger State, North Central Nigeria. *Journal of Earth Science*. 28(1). Available: http://en.earth-science.net.

Anomohanran, O. (2013). Geophysical Investigation of Groundwater Potential in Ukelegbe, Nigeria. *Journal of Applied Sciences*. 13(1): 119-125.

Olawuyi, A. K.; Abolarin, S. B. (2013)Evaluation of Vertical Electrical Sounding Method for Groundwater Development in Basement Complex Terrain of West-Central Nigeria. *Nigerian Journal of Technological Development*. 10 (2): 22-28.

Hydrochemical and Bacteriological Evaluation of Surface and Groundwater Sources in Mpape Area of Abuja, North Central Nigeria

Oguntade, A. S[1*] and Idris-Nda, A[1]
[1]Department of Geology, Federal University of Technology, Minna, Nigeria
[1]oguntade.adebayo@gmail.com
[1]idrisnda@futminna.edu.ng
* Corresponding author

Abstract

Access to potable water is a major concern confronting most developing nations particularly with the overwhelming health burden posed by polluted water and its sources. A total of fifteen water samples were collected and analyzed for their chemical and bacteriological parameters to evaluate quality status of surface water and groundwater sources in Mpape Area of Federal Capital Territory, North Central Nigeria. The results of the physical parameters measured on site were within the recommended limits while other parameters were analyzed using equipment in accordance with American Public Health Association Standard in a standard laboratory. The result of the laboratory analyses of the water samples showed that the mean concentration of some of the physicochemical parameters such as sodium, calcium, magnesium, potassium, sulphates, chlorides, nitrates, fluorides and phosphates were within the permissible limit recommended by both World Health Organization (WHO) and Nigerian Standard for Drinking Water Quality (NSDWQ). However, the mean concentration of iron, manganese, turbidity, total suspended solids, lead, cadmium, nickel and chromium were found to be higher than their respective recommended limits. Water Quality Index (WQI) based assessment revealed that over 85% of the samples were contaminated by Escherichia coli and total coliform with the highest values recorded in surface water and this inferred anthropogenic contamination in almost all the water samples and these bacteria could cause water borne diseases.

Keywords: Hydro-chemical, Bacteriological, Evaluation, Contamination, Water quality index

1. Introduction

Water is a universal solvent and natural resource tapped by all living organisms to meet their need on earth. It is an essential ingredient for sustainability and survival of every life form on earth. According to the World Health Organization (2014), about 1.1 billion people do not have access to potable water supply while about 2.0 million persons die every year due to water-borne or water related diseases. Also, the World Resource Institute (2018) reported that the World's water systems face formidable and alarming threats due to contamination arising from anthropogenic interference. The present study area is Mpape which is one of the main suburbs of Abuja. The total area covered was around 30.80 km^2 lies within the latitude: 9°7'0" N, 9°10'0"N and longitude 7°28'0"E, 7°31'0"E (Figure 1). It is a large, densely populated district in Bwari Area Council within the Federal Capital Territory, Abuja and it is about 10 minutes' drive from the centre of Abuja. It is a hilly area located opposite Maitama, across the expressway linking Asokoro and Kubwa. Rock blasting and stone crushing industry in Nigeria especially around Mpape District in Abuja has been growing rapidly due to increasing demand of construction industries such as Julius Berger, Arab contractors, Bulet Construction, Dantata and Sawoe Construction among others. The rock formation in the area is predominantly granitic (Figure 2). All major open cast mining and stone crushing operations release particulate emissions that do not only deteriorate water quality but also cause serious health problems. Stone crushing and allied activities generally have a considerable impact on the water bodies as well as socio-economic setting of local population. The various human activities domiciled in the area constitute point sources of water pollution.

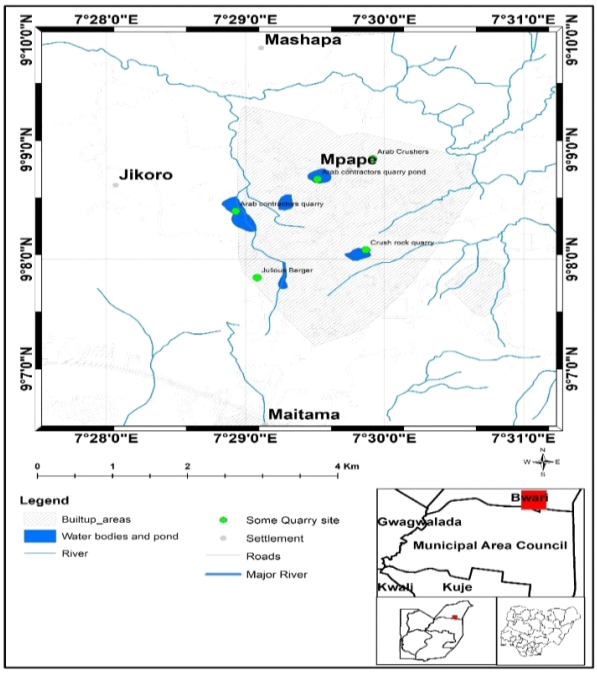

Figure 1: The topographical map of the study area.

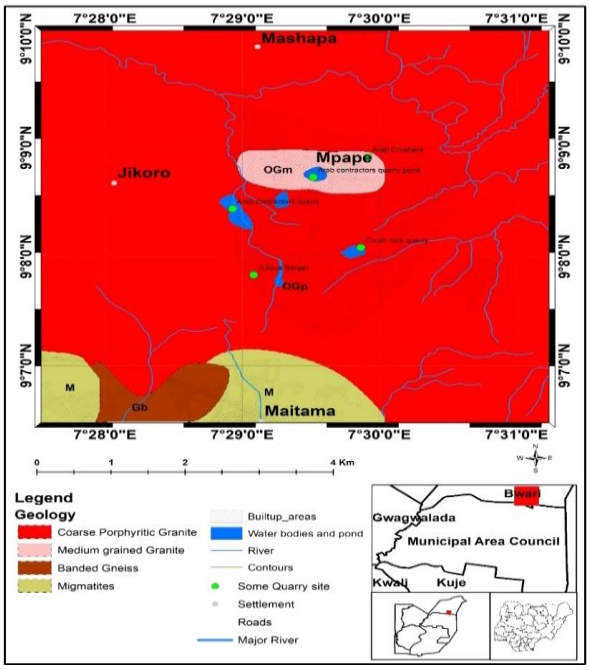

Figure 2: The geological map of the study area.

2. Literature Review

Increase in demand for water resources globally occurs essentially due to population growth and modern developments. Thus the welfare of every society is tied to the sustainable exploitation of water resources (Bear, 2000). The surface water resources cannot adequately satisfy the astronomical increasing demand for portable water in both developing and developed countries. Therefore, surface and groundwater serve as the main sources of water for domestic and industrial use but groundwater accounts for about 98% of the world's fresh water and it is fairly well distributed throughout the world (Buchanan, 1983). Both surface and groundwater continue to serve as reliable sources of water supply in most rural and urban communities in Nigeria and are susceptible to quality degradation from poor effluent management anthropogenic activities. They are renewable resources and their availability and use of which are influenced by many factors such as the lithology of the area, climatic patterns and water quality (Anornu *et al.*, 2009). However, human activities and seepage of hazardous materials into groundwater have affected its quality (Olasehinde, 1998; Ajibade *et al.*, 1987).

3. Methodology

A total of fifteen (15) surface and groundwater water samples were collected at different points in the study area. Sample containers used were rinsed with water thrice to avoid cross contamination. Proper labelling including the sample numbering and location were done. The geographical location of each sample was determined with a hand held Global Positioning System (GPS). The measurement of the following physical parameters such as $_{P}H$, temperature, electrical conductivity and total dissolved solids of both surface and ground water samples were determined on site using Multi-Meter device following the standard protocols and methods of American Public Health Organization (APHA) and American Society for Testing and Materials (ASTM). For laboratory analysis of chemical and bacteriological parameters, glass and plastic containers were used to collect sample in each location. Two drops of concentration HNO_3 were added to the water samples in the plastic container. The water samples in the plastic containers were used for the determination of major cations and heavy metals while the samples in the glass container are for the determination of anion.

4. Results and Discussion

The statistical summary of the whole parameters is presented in Table 4.1 while the mean results of the measured parameters were compared with guidelines values of World Health Organization (2012) and the

Nigerian Standard for Drinking Water Quality (NSDWQ, 2015) to determine the suitability of water sources within the study area.

Table 4.1: Statistical summary of results of physico-chemical and bacteriological analyses of surface and groundwater water samples in Mpape Area.

Parameters (mg/L)	Minimum	Maximum	Mean	WHO	NSDWQ
pH	5.5	8.7	6.42	6.5-8.5	6.5-8.5
Temp (°C)	20.8	38.3	28.65	Ambient	Ambient
EC (µs/CM)	70	766	326.4	1000.0	1000.0
TDS	30	370	155	500.0	500.0
Turbidity (NTU)	0.20	88.30	7.80	5.0	5.0
TSS	2.20	530.50	48.25	30.0	-
Na	2.10	14.10	5.08	200.0	200.0
Ca	2.02	18.68	7.40	75.0	-
Mg	2.00	7.20	4.23	30.0	20.0
K	3.71	9.58	5.92	12.0	-
Fe	0.0411	2.5340	0.36	0.3	0.3
Mn	0.01	0.69	0.27	0.2	0.2
Cu	0.001	0.030	0.0048	1.0	1.0
Zn	0.031	0.788	0.366	1.0	3.0
Pb	0.001	0.6333	0.114	0.05	0.01
Cd	0.0001	0.0300	0.0025	0.001	0.003
Ni	0.001	0.245	0.0414	0.02	0.02
Cr	0.001	0.333	0.0725	0.05	0.05
Co	0.0005	0.0620	0.0171	-	-
SO_4^{2-}	11.60	19.00	13.107	250.0	100.0
Cl^-	13.00	45.70	24.053	200.0	250.0
HCO_3^-	3.00	14.50	7.62	-	-
CO_3^{2-}	0.50	7.10	3.58	-	-
NO_3^-	2.50	24.40	13.593	50.0	50.0
F^-	0.08	0.78	0.339	1.5	1.5
PO_4^{3-}	0.04	1.98	1.113	5.0	-
E.coli (cfu/100ml)	0.0	60.0	16.80	0.0	0.0
Total Coliform (cfu/100ml)	6.0	60.0	23.47	10.0	10.0

4.1 Hydrochemical Characterization

The result obtained for the physical parameters revealed that the mean values of pH 6.42, temperature 28.65°C, electrical conductivity 326.4 µs/CM and total dissolved solids 155 mg/l were within the allowable limits while those of turbidity 7.80 NTU and total suspended solids 48.25 mg/l were above the allowable limit (Figure 3).

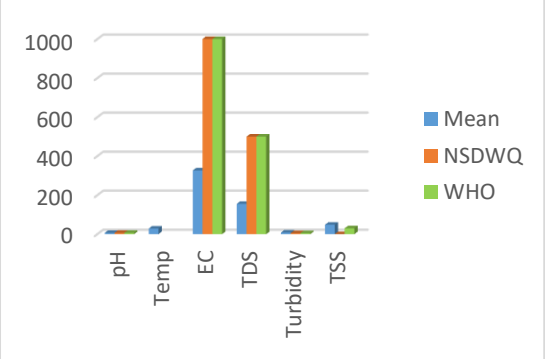

Figure 3: Mean result of the physical parameters compared with NSDWQ (2015) and WHO (2012) standards.

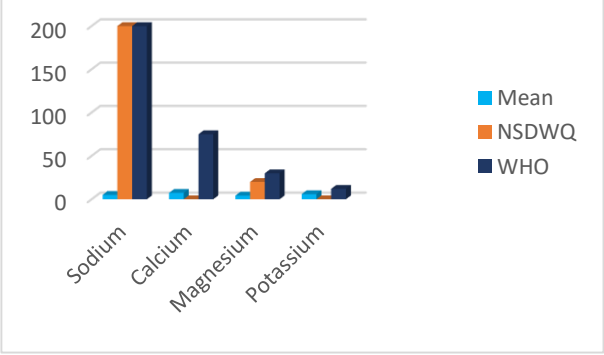

Figure 4: Mean result of the cations compared with NSDWQ (2015) and WHO (2012) standards.

The average concentrations of the four major cations analyzed such as sodium 5.08 mg/l, potassium 5.92 mg/l, calcium 7.40 mg/l and magnesium 4.23 mg/l were within the recommended acceptable limit of 200.00 mg/l, 12.00 mg/l, 75.00 mg/l, and 30.00 mg/l respectively (Figure 4). The average concentrations of analyzed anions such as chloride 24.05 mg/l, sulphates 13.12 mg/l, nitrates 13.59 mg/l, fluorides 0.34 mg/l and phosphates 1.113 mg/l were observed to be lower than their respective maximum acceptable limit of 200.00 mg/l, 250.00 mg/l, 50.00 mg/l, 1.50 mg/l and 5.00 mg/l respectively (NSDWQ, 2015; Figure 5) thereby indicate no serious pollution. Though their presence may be as result of poor sanitation, leachate from dumpsite, industrial effluent and fertilizer application or geogenically induced via chemical weathering and bedrock dissolution. (Dan-Hassan et al., 2012; Amadi and Nwankwoala, 2013; Unuevho et al., 2016; Akpah and Ezeigbo, 2010; Isiaku and Ezeigbo, 2010; Nwankwor and Etche, 1990).

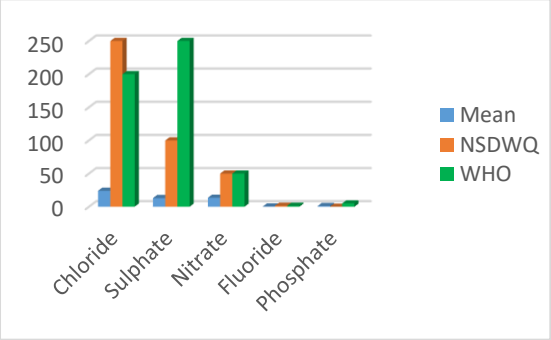

Figure 5: Mean result of the anions compared with NSDWQ (2015) and WHO (2012) standards.

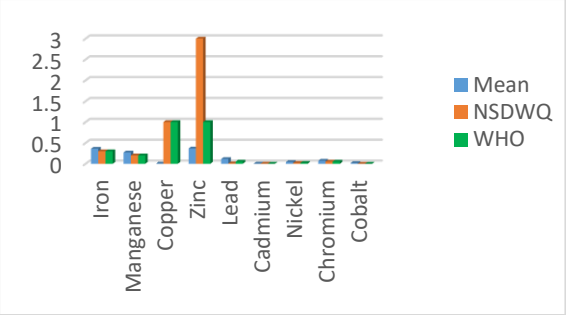

Figure 6: Mean result of the trace metals compared with NSDWQ (2015) and WHO (2012) Standards.

Some of the heavy metals analyzed in this present study included iron (Fe), manganese (Mn), copper (Cu), zinc (Zn), lead (Pb), cadmium (Cd), nitrate (Ni), chromium (Cr) and cobalt (Co). The average concentration of these trace elements analyzed such as iron 0.36 mg/l, manganese 0.27 mg/l, lead 0.114 mg/l, cadmium 0.0025 mg/l, nickel 0.0414mg/l and chromium 0.073 were found to be above the permissible limit of 0.3 mg/l, 0.2 mg/l, 0.05 mg/l, 0.001 mg/l, 0.02 mg/l and 0.05 mg/l but the average concentration of copper 0.0048 and zinc 0.366 were found to be within the permissible limit of 1.00 mg/l and 3.0 mg/l (Figure 6).

4.2 Bacteriological Parameters of the Water Samples

The bacteriological quality of most water resources within the study area was very poor mainly due to surficial contamination. During rainfalls E.coli from human and animal wastes (Figures 7 and 8) especially via open defecation were transported into the surface water sources or infiltrated into the groundwater aquifers and contaminated the water sources.

Figures 7: Open defecation along the water drainage by a man in Mpape.

Figures 8: Drinking of contaminated water by cows in Mpape.

The practice of open defecation along stream channels as currently practiced in the area reveals poor sanitation in the area and this practice favours bacteria contamination of water. A correlation of the highest concentration of total coliform and Escherichia coli as shown in Figure 9 further confirmed the fact that both

water sources were poor bacteriologically and their presence could cause cholera and other water borne diseases.

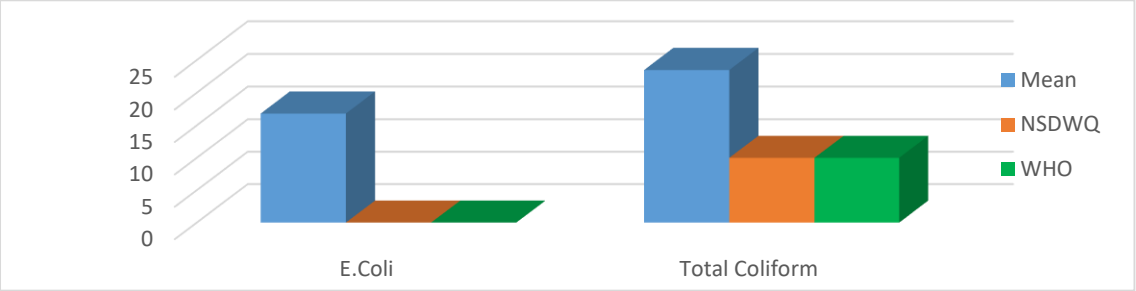

Figure 9: Mean concentration of E.coli and total coliform Compared with NSDQW (2015) and WHO (2012) standards.

4.3 Water Quality Index Determination

Water quality Index (WQI) is one of the most effective tools to communicate information on the quality of water to the concerned stakeholders. WQI scale which helps to estimate an overall quality of water based on the values of water quality parameters. The objective of WQI is to turn complex water quality data into information that is understandable and usable by the public. In this study, the WQI for drinking purpose was considered and permissible WQI for the drinking water was taken from the overall WQI given as:

$$\text{Overall WQI} = \frac{\sum qiwi}{\sum wi}$$

Table 4.2 showed the five groups of WQI ranging from excellent water to water unsuitable for drinking while the water quality (WQI) of all the water samples was calculated and presented in Table 4.3.

Table 4.2: Water quality classification based on WQI value.

WQI Value	Water Quality
<50	Excellent
50-100	Good water
100-200	Poor water
200-300	Very poor water
>300	Unsuitable for drinking

Table 4.3: Summary of computed WQ1 values for the groundwater in the area.

Parameters (mg/L)	**C**	**S**	**q_i**	**w_i**	**q_iw_i**
pH	6.42	6.5-8.5	85.60	0.133	11.385
Temp (°C)	28.65	Ambient	-	-	-
EC (µs/CM)	326.4	1000.0	32.64	0.001	0.033
TDS	155	500.0	31.00	0.002	0.062
Turbidity (NTU)	7.80	5.0	156.00	0.200	31.200
TSS	48.25	30.0	160.08	0.033	5.280
Na	5.08	200.0	2.54	0.005	0.013
Ca	7.40	75.0	9.87	0.013	0.128
Mg	4.23	30.0	14.10	0.033	0.465
K	5.92	12.0	49.33	0.083	4.094
Fe	0.36	0.3	120.00	3.333	399.960
Mn	0.27	0.2	135.00	5.000	675.000
Cu	0.0048	1.0	0.48	0.010	0.005
Zn	0.366	1.0	36.60	0.010	0.366
Pb	0.114	0.05	228.00	20.00	4560.000
Cd	0.0025	0.001	250.00	1000.00	250000.000
Ni	0.0414	0.02	207.00	50.00	10350.000
Cr	0.0725	0.05	145.00	20.00	2900.000
Co	0.0171	-	-	-	-

SO_4^{2-}	13.107	250.0	5.24	0.004	1310.000
Cl^-	24.053	200.0	12.03	0.005	2406.000
HCO_3^-	7.62	-	-	-	-
CO_3^{2-}	3.58	-	-	-	-
NO_3^-	13.593	50.0	27.19	0.020	0.544
F^-	0.339	1.5	22.60	0.667	15.074
PO_4^{3-}	1.113	5.0	22.26	0.050	1.113
E.coli (cfu/100ml)	16.80	0.0	1680.00	0.000	0.000
Total Coliform (cfu/100ml)	23.47	10.0	234.70	0.100	23.470

The computed WQI values for the study area were contained in (Table 4.3) while the overall water quality index (WQI) was calculated by aggregating the quality rating (q_i) with unit weight (w_i) linearly and the result shows below.

$$\text{Overall WQI} = \frac{\sum qiwi}{\sum wi} = \frac{272694.192}{1099.702} = 247.971$$

The computed overall WQI was 247.971 belonging to the very poor water category. The high value of the WQI obtained may be due to the impact of faecal contamination and leachate from the dumpsite on the water sources as well as infiltration arising from fertilizer application and unlined soak-away within the vicinity. It may also be as a result of high concentration of turbidity, total suspended solids, iron, manganese, lead, cadmium, nickel and chromium in the water samples which can be attributed to natural sources such as bedrock dissolution and chemical weathering.

5. Conclusion

The quality status of surface water and groundwater sources from Mpape area of Federal Capital Territory, North-Central Nigeria was investigated in the present study using physico-chemical and bacteriological indices. The significant presence of some of the parameters analyzed was attributed to rock-water interaction leading to bedrock dissolution, chemical weathering and dilution effect of the leachate from nearby dumpsite. The bacteriological result showed that water samples were poor due to the significant presence of E.coli and total coliform. Finally, Water Quality Index (WQI) based assessment revealed that over 85% of the samples were contaminated by E. coli and total coliform with the highest values recorded in surface water and this inferred anthropogenic contamination in almost all the water samples.

References

Ajibade, A.C. (1987). The origin of the Older Granites of Nigeria: some evidence from Zungeru region. *Nigeria Journal of Mining and Geology*, 19(1), 223-230.

Anornu, G.K., Kortatsi., and Saeed, Z.M (2009). Evaluation of Groundwater Resources Potential in the Ejisu-Juaben District of Ghana. *African Journal of Environmental Sciences and Technology*.

Bear, J., Cheng, A.H.D., Sorek, S., Quazar, D., and Herrera, I. (2000). Seawater intrusion in coastal Aquifers-Concept, Methods and Practices. *Journal of Hydrology*, 118.

Buchanan, T.J. (1983). Artificial research of groundwater, International Water Technology Conference and Exposition (AUGA EXPO, 83) Acapulco, Mexico. 8-14.

NSDWQ, (2015). Nigerian Standard for Drinking Water Quality. Nigeria Industrial Standard, NIS-554-2015.

Olasehinde, P.I., and Amadi, A.N. (2009). Assessment of Groundwater Vulnerability in Owerri and Its Environs, Southern Nigeria. *Nigerian Journal of Technological Research*, 4(1), 27-40.

World Health Organization/UNICEF. (2015). Progress on Drinking Water and Sanitation: 2015 Update. Geneva, Switzerland: World Health Organization.

Estimation of Depth to Structures Associated with Gold Mineralisation Potential over Southern Part of Kebbi State using Aeromagnetic Data

[*1]Augie A.I., [2]Salako K.A., [2]Rafiu A.A. and [3]Jimoh M.O.
[1]Department of Applied Geophysics, Federal University Birnin Kebbi, Nigeria.
[2]Department of Geophysics, Federal University of Science and Technology Minna, Nigeria.
[3]Department of Geology, Federal University of Technology Minna, Nigeria.
[*]Corresponding Author: email; ai.augie@fubk.edu.ng, Phone; +2348137330559

Abstract
In this study, magnetic signatures together with the geological settings of the area were employed in estimating the depth to structures that may host gold mineral over southern part of Kebbi State and its environs. Acquired aeromagnetic grids data covering the study area was processed, analyzed and interpreted using the following techniques; IGRF computation, Reduction to Equator (RTE), First Vertical Derivatives (FVD) and Euler Deconvolution. Results from these techniques have revealed the alteration zones and depth to the structures that could be host to gold mineralisation. These regions were corresponded to the following areas; Fakai, SE parts of Yauri and Shanga, Ngaski, Zuru, Magama, Rijau, Eastern part of Wasagu/Danko and Bukkuyum. FVD technique revealed the spatial and structural resolution in imagery thereby showing major structures which normally play an important role in determining the gold mineral. The structures found within the aforementioned areas are the architecture of a mineralized body as compared with the geology of the area, which falls under the following earth materials; quarzt-mica schist, granite, biotite, gneiss, diorite, medium coarse grained and biotite homblende granite. Estimated depth to magnetic sources (anomalies)/ or structures that could be host to gold mineralisation was found to be from 81.616 m to 181.171 m using algorithms Euler Deconvolution.

Keyword: Depth to structures, Gold mineralization, Yauri-Zuru schist belt, First vertical derivative and Euler deconvolution.

INTRODUCTION

Structures in the Nigerian basement complex usually control the mineralisation and may be deep-seated and therefore require a geophysical approach that will delineate the possible pathways for gold exploration and exploitation (Ejepu *et al.,* 2018). The gold mineralisation is found through structurally controlled and spatially associated with shear zones and hydrothermal veins formed in response to the regional stress field (Sani *et al.,* 2017).

Structures such as fractures in gold mineralisation act as conduits for the mineralisation solution and second, as loci of deposition of mineralisation fluid (Adetona *et al.,* 2018). Faults and shear zones are potential pathways of fluids (Sani *et al.,* 2019) and thus, knowledge of the structural architecture of a mineralised area, the distribution and orientation of faults and shear zones, their formation and possible reactivation during the structural evolution and the tectonic conditions is a key to understand the formation, origin and location of mineral deposits as well as for exploration and findings of new targets as suggested in Adewumi and Salako (2018).

Historically, recorded gold production in Nigeria started by 1913 and peaked in the period of 1933 (Garba, 2000 & 2003). The gold production declined during the Second World War period and never recovered as mines were abandoned by mostly colonial companies (Danbatta, 2005). In Northern Nigeria, the most prominent occurrences are found at Maru, Anka, Malele, Tsohon-Birnin Gwari, Kwaga and Gurmana (Danbatta, 2008).

The discovery of petroleum led to a subsequent shift of the Nigerian economy, leading to a lack of attention to gold exploration, despite the widespread potentials. This development has prompted a need to map out regional structural features as well as its depth which might serve as conduits for the mineralizing fluids in areas where such mines were abandoned (Augie & Sani, 2020).

In this study, acquired aeromagnetic data was used with the view to determine the depth to the structures that could be host to gold mineralisation using the algorithms Euler deconvolution method. The method makes use of a structural index in addition to producing depth estimates. In combination, the structural index (SI) and the depth estimates have the potential to identify and calculate depth estimates for a variety of geologic structures such as faults, magnetic contacts, dikes, sills, etc (Daniel *et al.*, 2019).

LOCATION AND GEOLOGICAL SETTINGS OF THE STUDY AREA

The study area lies within the southern part of Kebbi state and, some part of Zamfara and Niger States between latitudes 10°30′0″N and 12°0′0″N, and longitudes 4°0′0″E and 5°30′0″E. The area covers the following local government areas (LGAs); Yauri, Zuru, Ngaski, Shanga, Fakai, Danko/Wasagu, Sakaba, Koko Besse, Maiyama, Bagudo and Suru in Kebbi State, Kebbe, Gummi and Bukkuyum LGAs in Zamfara State and, Rijau, Agwara, Borgu and Magama LGAs of Niger State (Figure 1).

Geologically, the study area falls under the Basement Complex rocks and some part of sedimentary basin. These comprise of; granite, rhyolite, biotite-granite, meta-conglomerate, quartz-mica schist, migmatite, varieties of schists, sandstones, ironstones and laterites (Figure 1). The metasediments in these areas also comprise of quartzites, schists and phyllites; whereas the Older Granites consist of granodiorites/ or diorites. Furthermore, dacites/rhyolites are overlain and intrude the basement gneisses, metasediments and granitic rocks of the southern (Anka-Yauri schist) part Kebbi (Bashar *et al.*, 2017).

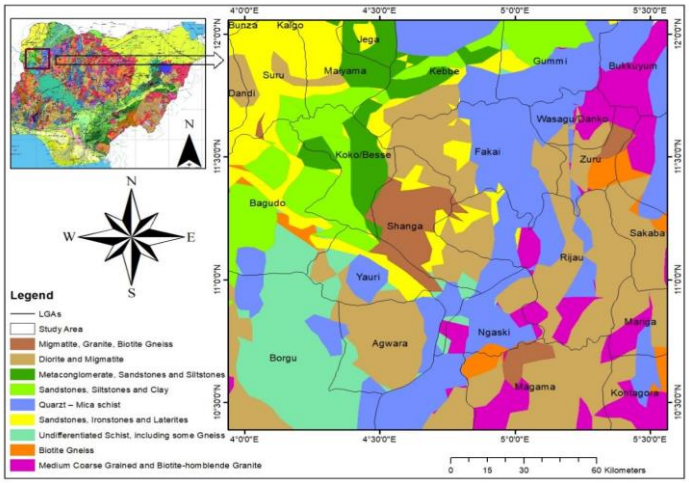

Figure 1: Location and Geological Map of the Study (Olugbenga & Augie, 2020).

METHODOLOGY

Aeromagnetic surveys over parts of the country were carried out by Fugro airborne surveys between 2005 and 2010 on behalf of the Federal Government of Nigeria. The data are under the custody of the Nigeria Geological Survey Agency (NGSA). In this study, nine (9) aeromagnetic data were used covering southern part of Kebbi and its environs of Basement Complex of northern Nigeria. These aeromagnetic datasets consist of sheets; 72 Giru, 73 Eokku, 74 Donko, 95 Kaoje, 96 Shanga, 97 Zuru, 117 Konkwesso, 118 Yelwa and 119 Chifu. The data were established under

the following high-resolution survey conditions; Flight line spacing (500 m), Terrain clearance (80 m), Tie line spacing (2000 m), Flight direction is NW-SE and the Tie line direction is NE-SW.

The acquired data were corrected by removing geomagnetic gradient using the main/core field (International Geomagnetic Reference Field, IGRF). The data was collected in grid form which was further converted it in digitized form (X, Y and Z). The X and Y represents longitude and latitude respectively measured in metres (m), and Z represent the magnetic intensity measured in nano Tesla (nT). The acquired corrected aeromagnetic dataset was subjected to the minimum curvature gridding method to produce the Total Magnetic Intensity (TMI) map.

DATA PROCESSING

In this study, different processing techniques were employed to processed, enhanced, and interpreted magnetic data with aid of Geosoft (Oasis Montaj) and Surfer software. These techniques include: reduction of magnetic equator (RTE), first vertical derivative (FVD) and Euler Deconvolution. The Total Magnetic Field Intensity (TMI) value acquired from NGSA which was short-up 33,000 nT for the convenience of contouring or imaging. For these reasons, the value (33,000 nT) must be added back to give the TMI grids for the area (Augie & Ologe, 2020; Augie & Ridwan, 2021). The generated core fields (DGRF for the epoch period) are subtracted from the grid values (TMI) to give the magnetic anomaly (TMI anomaly) as shown in Fig. 2.

(a) Reduction to Magnetic Equator (RTE) Technique

The study area falls within magnetic equatorial zones of low inclination (low latitudes) where reduction to pole technique cannot be applied; because the North to South bodies have no detectable induced magnetic anomaly at zero geomagnetic inclination. This technique can make the data easier to interpret without losing any geophysical meaning. At low latitudes, a separate amplitude correction is usually required so as to prevent North-South signal in the data from dominating the results. As a result, reduced to the pole data may present a less 'honest' view of the data.

RTE techniques usually has an amplitude component [*sin(I)*] and a phase component [*i.cos(I) cos(D-θ)*]. The field strength is only required for apparent susceptibility calculation, but is re-calculated along with the inclination and declination in the other controls, so the values are always synchronized (Reid *et al*, 1990), as given in equation (1).

$$L(\theta) = \frac{[\sin(I) - i.\cos(D-\theta)]^2 \times (-cos^2(D-\theta)}{[sin^2(Ia) + cos^2(Ia).cos^2(D-\theta] \times [sin^2(I) + cos^2(D-\theta)]}, if\ (Ia| < I), Ia = I \quad (1)$$

where,

I is Geomagnetic inclination in ^{o}, D is Geomagnetic declination in ^{o} azimuth and Ia is inclination for amplitude correction (never less than I).

(b) First Vertical Derivatives (FVD) Technique

FVD was applied to TMI anomaly (RTE) in order to quantify the spatial rate of change of the magnetic field in horizontal, or vertical directions. Derivatives essentially enhance high frequency anomalies (that is shallow features) relative to low frequencies anomalies (that is deep features) and sharpen the edges of anomalies (Adewumi & Salako, 2018).

Vertical derivatives are a measure of curvature, and large curvatures are associated with shallow anomalies. Thus, it enhances near-surface features at the expense of deeper anomalies. The anomaly in FVD is considerably narrow and more closely reflects the width of the magnetic rock body causing it and the derivatives are given in equation (2):

$$\mathbf{FVD} = \frac{\partial M}{\partial z} \quad (2)$$

(a) Euler Deconvolution Technique

Euler deconvolution is a useful tool for providing initial estimates of the locations and depths of magnetic sources (Adetona *et al.*, 2018). Euler deconvolution is a method to estimate the depth of subsurface magnetic anomalies and can be applied to any homogeneous field, such as the analytical

signal of magnetic data. It is particularly good at delineating the subsurface contacts (Ajala *et al*, 2021). It is based on the fact that the potential field produced by many simple sources obeys Euler's homogeneity equation (Holden *et al.*, 2008). If a given component of the magnetic anomalous field ΔT (x, y, z) satisfies the following equation:

$$\Delta T(x, y, z) = tn\Delta T(x, y, z) \tag{3}$$

where n is the degree of homogeneity, then differentiating Equation 3 with respect to t gives Equation 4:

$$X\frac{\partial \Delta T}{\partial x} + X\frac{\partial \Delta T}{\partial y} + X\frac{\partial \Delta T}{\partial z} = n\Delta T \tag{4}$$

where x, y, and z are the coordinates of the field observation points and assumed to be at the origin.

According to Thompson, (1982), considering the potential field data, Euler's deconvolution equation can be expressed as

$$(x - x_0)\frac{\partial \Delta T}{\partial x} + (y - y_0)\frac{\partial \Delta T}{\partial y} + (z - z_0)\frac{\partial \Delta T}{\partial z} = N(B - T) \tag{5}$$

where (x_0, y_0, z_0) is the position of a magnetic source whose total magnetic field T is measured at (x, y, z). The total field has a regional value B, and N is the degree of homogeneity (structural index), which is equivalent to n in Equation (5). The unknown coordinates (x_0, y_0, z_0) are estimated by solving a determined system of linear equations using a prescribed value for N with the least squares method.

RESULTS AND DISCUSSION

TMI and RTE Maps

Figure 2 is the colour image of the IGRF corrected total magnetic intensity (TMI). The map gives the vector sum of all components of the magnetic field. It primarily used in this study to reveal the magnetic characteristic of the various lithological units in the area. The magnetic signatures range from a low of 32951.0 nT (minimum) along NW region of the study area, to a high of 33114.0 nT (maximum) in the SE parts of the region.

TMI anomalies were further reduced to magnetic equator in order to produce anomalies which depend on the inclination and declination of magnetized body, the local earth's field and orientation of the body with respect to the magnetic north. With application of reduced to the equator (RTE), the regional magnetic field align horizontally and most of the source magnetizations are horizontal. The resultant composite color depicting reduced-to-equator magnetic anomalies are given in Figure 3. The distinct pattern in Figure 3 of highs and lows and, the steep gradients between them at places that describe prominent magnetic linears are attributable to the complex assemblage of features of varied dimensions and direction.

The high magnetic trend lies under the following areas; Bagudo, Koko/Besse, Suru, Shanga, Northern part of Zuru, Yauri, Southern part of Ngaski, Wasagu/Danko, Northern part Borgu and Magama. While the areas of low magnetic anomalies are; Southern part of Zuru, Sakaba, Northern part of Ngaski, Rijau, Mariga and Northern parts of Gummi & Bukkuyum. The areas with moderate magnetic trend are; Fakai, Kebbe, Southern part of Gummi, Agwaru and Northern part of Borgu (see Figure 3).

Thus, lows and high regions were characterized in difference rock formations that lead to difference in the magnetic susceptibility of the rocks within the area and usually the susceptible rocks occur at depths shallower than the curie points isotherm.

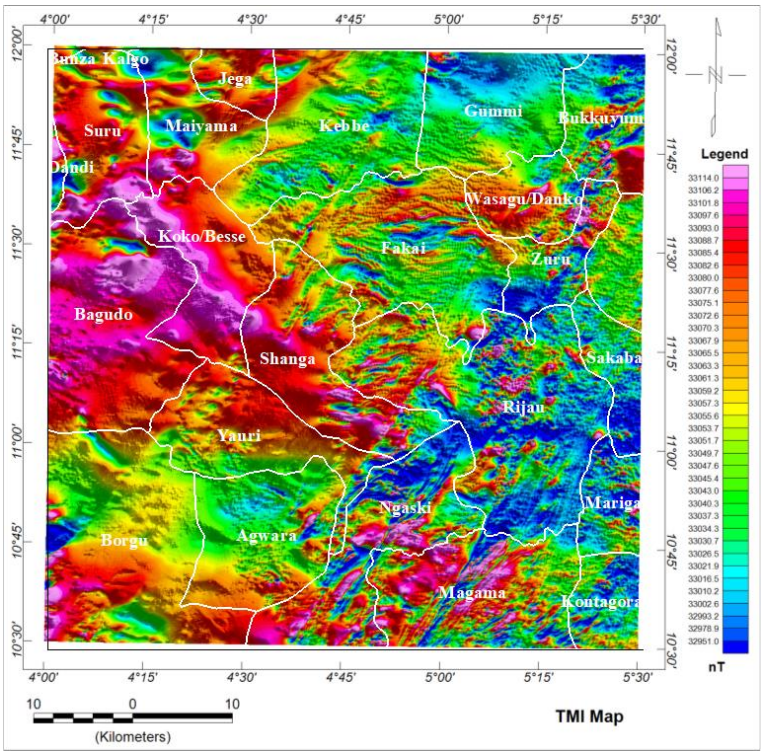

Figure 2: Total Magnetic Intensity (TMI) Map of the Study

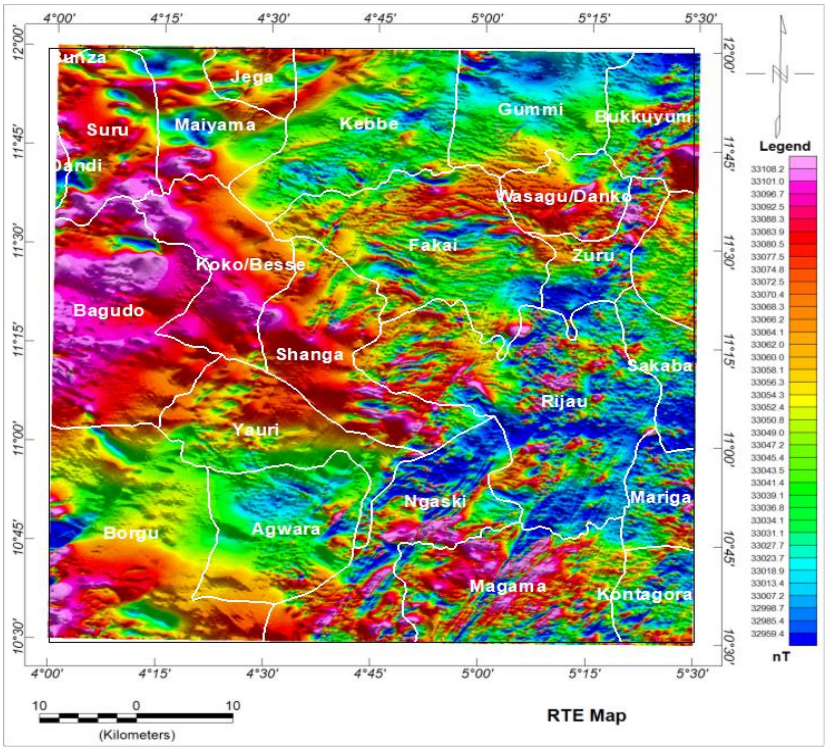

Figure 3: Reduction to Magnetic Equator (RTE) Map of the Study Area

FVD Map

FVD map (Figure 4) enhanced the spatial and structural resolution in imagery thereby showing major structural and lithological detail which were not previous appear in TMI and RTE maps (Figures 2 & 3). Looking at Figure 4 carefully, most of the structures delineated are found within

SE and NE part of the study area. These areas were corresponding to; Fakai, SE parts of Yauri and Shanga, Ngaski, Zuru, Magama, Eastern part of Wasagu/Danko and Bukkuyum.
These structures found within the aforementioned areas are the architecture of a mineralized body and, according to the geological setting (see Figure 1) of the area, the regions comprise of the following rock materials; quarzt-mica schist, granite, biotite, gneiss, diorite, medium coarse grained and biotite homblende granite. Most of these structures found in the area has underlain on basement complex as compared with the geological map of the study area (Figure 1).

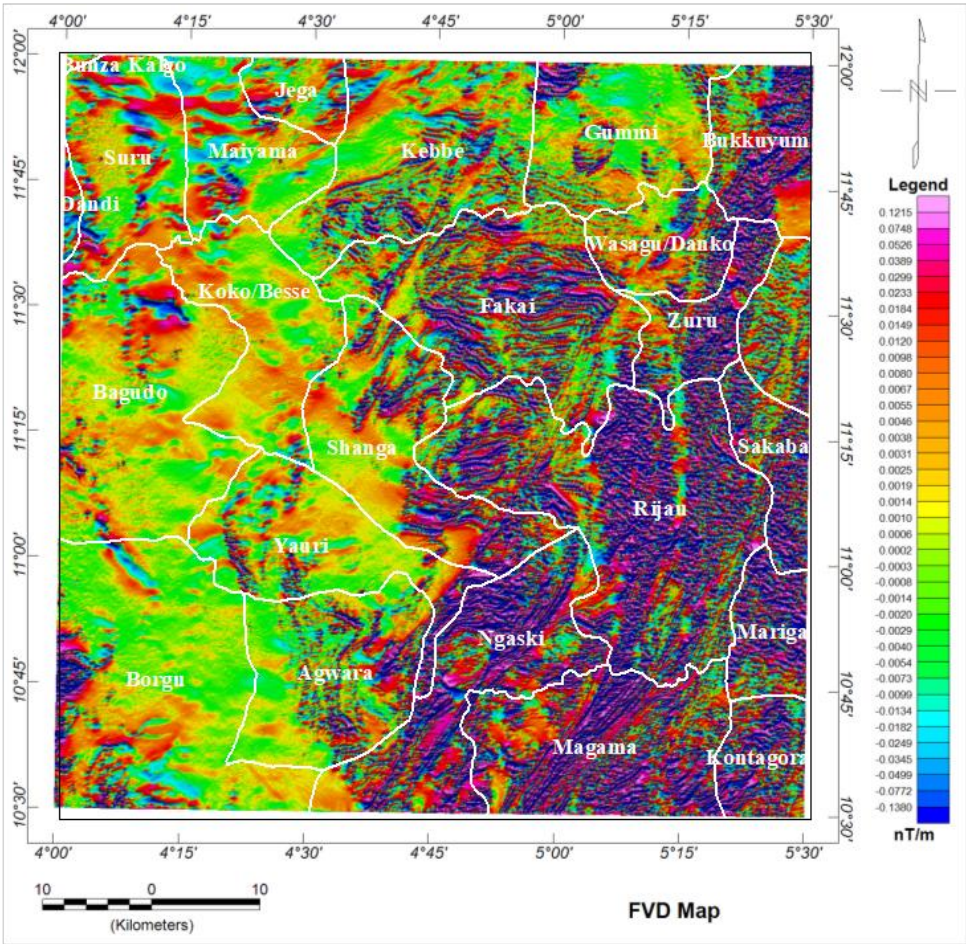

Figure 4: First Vertical Derivative (FVD) Map of the Study Area

Euler Deconvolution Map

Figure 5 presents the result of the Euler deconvolution map produced from the study area. The Euler Depth map shows that the depth to magnetic sources (anomalies)/ or structures that could be host to gold mineralisation. Shallow and deeper depths were obtained from these results which were ranges from 81.616 m to 544.740 m. shallow depths ranging from 81.616 m to 181.171 m at the areas corresponds to; Fakai, SE parts of Yauri and Shanga, Ngaski, Zuru, Magama, Eastern part of Wasagu/Danko and Bukkuyum. These regions have falls under Nigerian basement complex which usually control the mineralisation as compared with the results from FVD map and the geological setting of the area (Figure 1).

The regions of deeper depths on the Euler depth map corresponds to the regions of thick sediments on the Figure 5. These zones have lies under the following areas; Bunza, Bagudo, Dandi, Jega, Suru, Koko/Besse, Western parts of Yauri and Shanga, and Southern parts of Borgu. The maximum depth of 544.744 m was obtained and this may be sufficient for hydrocarbon as compared with the geology of the area.

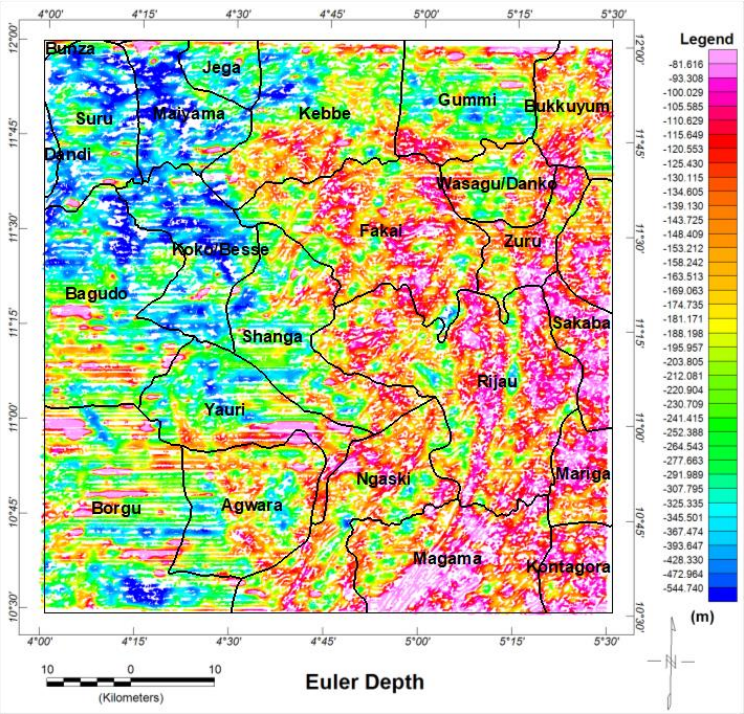

Figure 5: Euler Deconvolution Map of the Study Area

CONCLUSION

The acquired aeromagnetic data of southern parts of Kebbi State and its environs has been analysed and interpreted qualitative and quantitatively using three processing techniques; Reduction to Magnetic Equator (RTE), First Vertical Derivatives (FVD) and Euler deconvolution. The result obtained from these techniques have revealed the structures and also depth to that structures that may host gold mineral. These areas were corresponding to; Fakai, SE parts of Yauri and Shanga, Ngaski, Zuru, Magama, Eastern part of Wasagu/Danko and Bukkuyum. The depth to magnetic sources (anomalies)/ or structures that could be host to gold mineralisation was found to be from 81.616 m to 181.171 m.

REFERENCES

Adetona, A. A., Salako, K. A. and Rafiu, A. A. (2018). Delineating the Lineaments Within the Major Structures around Eastern Part of lower Benue Trough from 2009 Aeromagnetic Data, FUW Trends in Science & Technology Journal, Vol. 3 No. 1, pp. 175–179 e-ISSN: 24085162; p-ISSN: 20485170.

Adewumi, T. and Salako, K.A. (2018). Delineation of Mineral Potential Zone using High Resolution Aeromagnetic Data over Part of Nasarawa State, North Central, Nigeria, Egyptian Journal of Petroleum, https://doi.org/10.1016/j.ejpe.2017.11.002

Ajala, S.A. Salako, K. A. Rafiu, A. A, Alahassan, U. D. Adewumi, T. and Sanusi, Y.A. (2021). Estimation of Sedimentary Thickness for Hydrocarbon Potential over Part of Adamawa Trough, Nigeria Using Magnetic Method, Earth Sciences Pakistan (ESP), 5(1), 07-11, DOI: http://doi.org/10.26480/esp.01.2021.07.11

Augie, A.I. and Ologe, O. (2020). Analysis of Aeromagnetic Data for Coal Deposit Potential over Birnin Kebbi and its Environs Northwestern Nigeria, Nigerian Journal of Science and Environment, Vol.18 (1), pp. 145 – 153.

Augie, A.I. and Ridwan, M.M. (2021). Delineation of Potential Mineral Zones from Aeromagnetic

Data over Eastern Part of Zamfara, Savanna Journal of Basic and Applied Sciences, Vol. 3(1), pp. 60-66.

Augie, A.I. and Sani A.A. (2020). Interpretation of Aeromagnetic Data for Gold Mineralisation Potential over Kabo and its Environs NW Nigeria, Savanna Journal of Basic and Applied Sciences, Volume 2, No. 2, pp. 116-123.

Bashar, M. G. Sanusi, Y. A. and Udensi, E. E. (2017). Interpretation of Aeromagnetic Data Over Birnin-Kebbi and Its Adjoining Areas Using First Vertical Derivative and Local Wavenumber Methods, IOSR Journal of Applied Geology and Geophysics, Vol. 5(5), pp. 44-53.

Danbatta, U. A. (2005). Precambrian Crustal Development of The Northwestern Part of Zuru Schist Belt, NW Nigeria. A paper presented at the 41st Annual Conference of Nigerian Mining, and Geos. Soc. (NMGS).

Danbatta, U.A. Abubakar, Y. I. and Ibrahim A. A. (2008). Geochemistry of Gold Deposits in Anka Schist Belt, Northwestern, Nigeria, Nigerian Journal of Chemical Research, Volume 13, pp. 19-29.

Daniel, E. Jimoh, R and Lawal, K. (2019). Delineation of Gold Mineral Potential Zone Using High Resolution Aeromagnetic Data Over Part of Kano State, Nigeria, Journal of Geology Geophysics 8:464. 10.35248/2381-8719.464

Daniel, E. Jimoh, R and Lawal, K. (2019). Delineation of Gold Mineral Potential Zone Using High Resolution Aeromagnetic Data Over Part of Kano State, Nigeria, Journal of Geology Geophysics 8:464. 10.35248/2381-8719.464

Ejepu J. S. Unuevho, C. I. Ako, T. A. & Abdullahi S. (2018). Integrated Geosciences Prospecting for Gold Mineralization in Kwakuti, North-Central Nigeria, Journal of Geology and Mining, Vol. 10(7), pp. 81-94, DOI: 10.5897/JGMR2018.0296.

Holden, E.J., Dentith, M., and Kavesi, P. (2008). Towords the Automatic Analysis of Regional Aeromagnetic Data to Identify Regions Prospectives for Gold Deposits, Computer Geosciences, 34, 1505 – 1513

Olugbenga, T. T. and Augie, A. I. (2020). Estimation of Crustal Thickness within the Sokoto Basin North-Western Nigeria Using Bouguer Gravity Anomaly Data, WASET, International Journal of Geological and Environmental Engineering, Vol. 14, No. 9, pp. 247–252.

Reid, A.B. Allsop, J.M. Granser H, Millet A.J. & Somerton, I.W. (1990). Magnetic interpretation in three dimensions using Euler deconvolution. Geophysics, Vol.55, pp.80-91

Sani, A.A. Augie, A.I. and Aku, M.O. (2019): Analysis of Gold Mineral Potentials in Anka Schist Belt North Western Nigeria using Aeromagnetic Data Interpretation, Journal of the Nigerian Association of Mathematical Physics, Volume 52, pp 291-298.

Sani, M.A. Raimi, J. Elatikpo, S.M. and Lawal, K.M. (2017). Magnetic Interpretation of Structures Associated with Gold Mineralisation Around Kundila and Ginzo Area, Northwestern Nigeria, Nigerian Journal of Scientific Research, 16(2): 240 – 246. njsr.abu.edu.ng

Thompson, D.T. (1982). A New Technique for Making Computer-Assisted Depth Estimates from Magnetic Data, Geophysics, Vol.47, pp.31–37.

IMPACT OF WASTE DISPOSAL SITE ON GROUNDWATER QUALITY AT RAFIN-TOFA SOLID WASTE DUMPSITE, KAMPALA, NIGER STATE, NIGERIA

Atabo, S.I., Alhassan, U. D. and Rafiu, A. A.
Department of Geophysics, Federal University of Technology, Minna, Nigeria

Abstract
A massive solid waste dumpsite at the outskirt of Minna metropolis was investigated using 2D electrical resistivity imaging (ERI), with the aims of determining the impact of the dumpsite on groundwater quality. By visual observation of solid waste dumpsite, it is found that it consists of various constituents such as paper, organic matter, metals, glass, ceramics, plastics, textiles, dirt, and wood among others. Resistivity data were collected from parallel survey profile lines using a Wenner-Alpha array configuration. Inversion of the data was carried out using 2D regularized least-squares optimization methods with robust (L1-norm) model constraints. Potential zone of leachate infiltration into the subsurface from the dumpsite was identified from the electrical imaging. A synthetic resistivity inverse model was used to discuss and validate the field results. The 2D ERI sections of the model resolve clearly the subsurface lithological variations. Interpretation of the field data showed that 2D ERI technique was effective in delineating groundwater contaminated zones. The vertical and horizontal sensitivity of the 2D Wenner-Alpha array for sub- surface resistivity variations made it possible to determine the position and extent of leachate infiltration into groundwater. The current work demonstrates the usefulness of the ERI technique as a complementary tool for environmental site investigation.

Keywords: 2D, waste, dumpsite, resistivity, leachate, infiltration, Wenner-Alpha, groundwater

Introduction

The Earth's surface which is the troposphere, sits at the interfaces of the solid lithosphere, the gaseous atmosphere, and the watery hydrosphere. Gases, liquids, and solids are exchanged between these spheres in three grand cycles. These cycles include the water or hydrological cycle, the rock cycle and the biogeochemical cycle. The Earth crust is also constantly being altered by geogenic and anthropogenic processes at extremely slow rates in human terms.

Geophysical principles have been used to unravel the dynamic nature of the earth (Rein hard, 2006). Various geophysical exploration methods have been and are used on land surface and beyond to solve a variety of subsurface detection problems (Ameh *et al.*, 2020). Each of these methods measures properties that are related to subsurface lithology and their geologic configurations (Gadallah & Fisher, 2009). The subsurface properties of the earth vary in diverse ways. These include; density, propagation velocity, magnetic susceptibility, electromagnetic wave reflectivity and transmissivity, self-potential, resistivity and induced polarization. These properties are measured using diverse formats. There are three basic ways in which the electrical current can be conducted within the earth, these includes Electrolytic, Ohmic and Dielectric conductions (Lowrie, 2007). In the electrolytic conduction (ionic conduction), the electrical current is propagated through the pores of the rocks or soil saturated with water, containing ions of minerals and dissolved salts. In the Ohmic conduction (electronic conduction), the electrical current is propagated via the crystalline structure of some materials in the rocks, mainly metals. Dielectric conduction has to do with the existence of an alternating electrical field which can cause ions in the structure of insulating materials to have a cyclic change in their positions. Geoelectrical properties are utilized in geophysics to exploit for materials in the subsurface which may be located by their anomalous electrical conductivities (Slater *et al*., 2010). Resistivity method involves the introduction of

electrical current into the ground and the resultant measured potential differences at the surface give an indirect indication of the subsurface resistivity distribution.

Any material that is discarded after its primary use is termed waste. Society produces different types of waste; domestic waste, industrial wastes, mining wastes and radioactive wastes (Ranke, 2001). Liquid or solid wastes, hazardous or non-hazardous wastes infiltrating into groundwater can cause some chemical reactions which may produce substances dangerous to environment & health (Ige, 2013). In the last decade the study area has witness a major increase in waste disposal on uncontrolled disposal sites. Waste disposal is an expensive urban environmental problem. The degradation of water quality is undesirable irrespective of whether it results directly from leachate escaping from the landfill or from geogenic processes (Rowe, 2011; Amadi *et al*.,2017). Leachate is formed when rainwater and runoff percolate through solid waste, leaching out soluble salts and biodegraded organic products. Due to downward Darcy velocity and diffusion, contaminants will migrate from the landfill through soil into the groundwater system (Franz, 1993).

Study Description

This study site is located on the SE of Zungeru sheet 163 which is NW of Minna metropolis (Figure 1.5). It lies within latitude 9°40′22.0″North and 9°41′01.9″North and longitude 6°26′6.7″East and 6°25′53.2″East, it occupies a total area of about 5.3 km^2. The site is located along Maikunkele-Zungeru road. A portion of this site is already been utilized for engineered open waste dumpsites serving the Southwestern part of Minna city. On a general note, all the sites under study are at the outskirt of Minna metropolis with good road network which allow for easy access to the sites.

Topographically the dumpsite area is mostly flat lying, with moderately undulating ridges within the vicinity of Maikunkele urban sprawls of Minna (Figure 1.1). The altitude of the area is about 280 meters above sea level. All streams around the area drain into the River Chanchaga catchment basin. Most tributaries of the River Chanchaga are ephemeral and dry up during the zenith of dry season. The drainage system of the study area is structurally controlled. The drainage pattern of the study area is characterized as dendritic in nature.

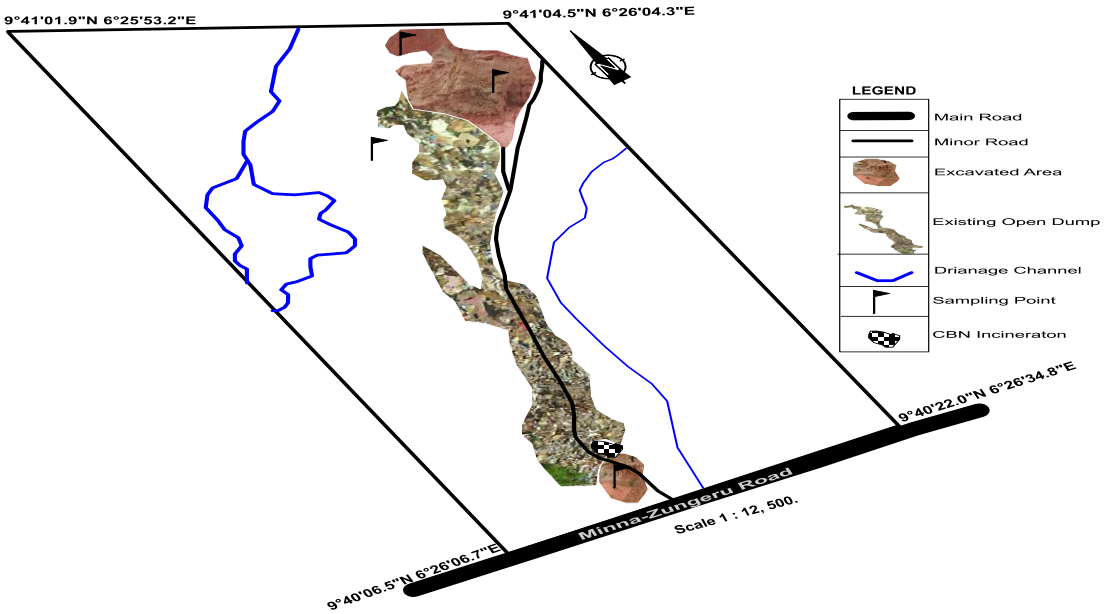

Figure 1.1: Study Area Location

Materials and Method

2D Electrical Resistivity Imaging (ERI) survey using a Wenner-Alpha array as outlined by Loke (1999) was conducted along six parallel profiles within the vicinity of the dumpsite. The selection

of the ERI locations was dependent on the availability of areas free of heap of waste as an obstacle. When the conditions to enable the electrodes penetrate the natural soil was allowed, the roll-along technique was applied for getting continuous profile. The apparent resistivity measurements were acquired using ABEM SAS 4000 Terameter equipment. A pre-defined sequence of combinations of four stainless steel electrodes with current electrodes ($C_1 and\ C_2$) and potential electrodes ($P_1 and\ P_2$) for different electrode spacing (a) and data acquisition levels (n) was adopted.

The profile length (L) of the electrical cable spread was restricted 100m with a total of 21 electrodes on a profile line. At the initial series of measurement transverse the spacing in the middle of nearby electrodes (a) at 1a was set at 5m. For the initial measurement, electrodes numerals 1, 2, 3 and 4 represents C_1, P_1, P_2 and C_2. For the following measurement, numbers electrodes 2, 3, 4, and 5 represents C_1, P_1, P_2 and C_2 in that order. This arrangement was sustained till electrodes numbers 18, 19, 20 and 21 represents C_1, P_1, P_2 and C_2 in turn. Eighteen mid-points were established for the first measurement sequence. The entire measurement technique was replicated for 2a, 3a, 4a, 5a, 6a etcetera. Beginning at the first series of measurement 1a, a total number of 18 mid-points were established, and the mid-point decreases by three in successively sequences measured. For a profile of 100m, at 2a, mid-points =15, at 3a=12, 4a =9, 5a=6 and 6a=3 (Figure 1.2). The subsurface resistivity values acquired are arranged in apparent resistivity pseudo-sections which give a qualitative approximation of the subsurface resistivity distribution. An inversion procedure using the RES2DINV software ver. 3.71 (Loke, 2012) was used to generate 2D ERI sections from the apparent resistivity data. RES2DINV uses finite difference method based on the regularized least squares optimization procedure to produce a true 2D synthetic resistivity model is designed to discuss and validate the interpretation of the field data. The software iteratively determines the model blocks (Figure 1.3) resistivity that will closely produce the measured apparent resistivity data (Loke, 1997).

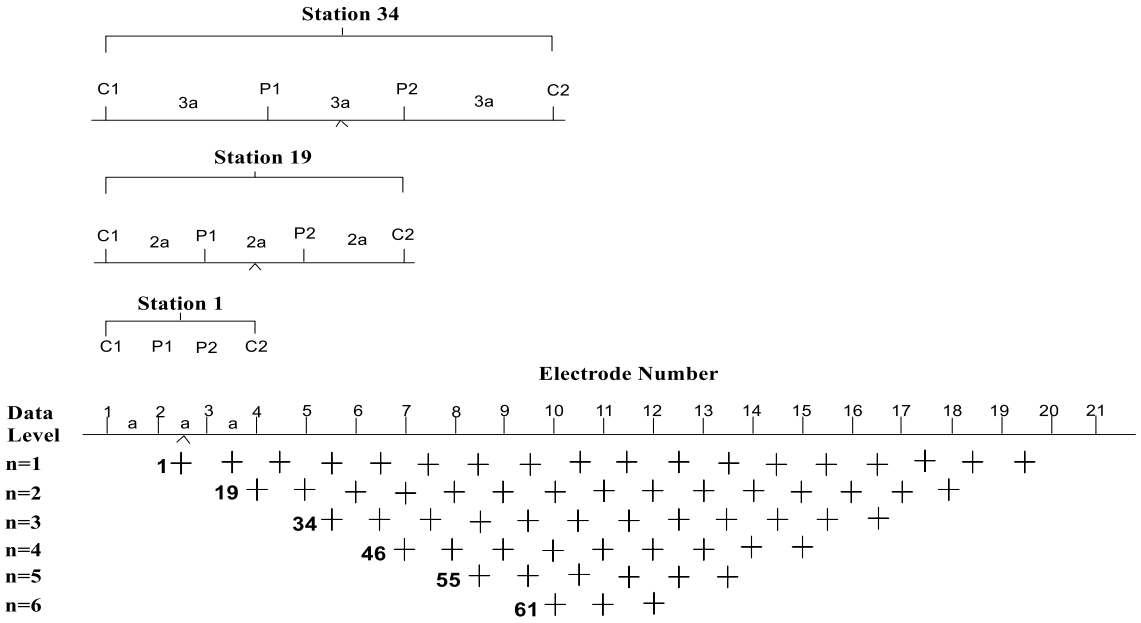

Figure 1.2 Sequence of 2D Wenner resistivity measurement to build a pseudosection (After Loke, 1999).

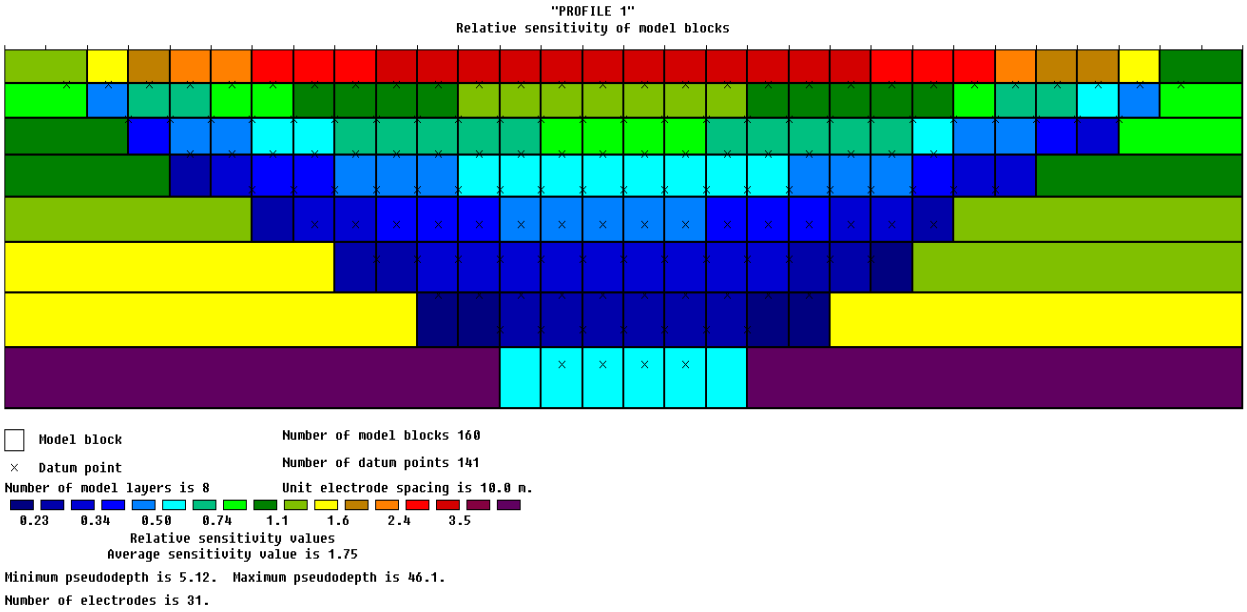

Figure 1.3: Relative sensitivity of the apparent resistivity model block

Results and Discussion

The 2D Earth resistivity imaging obtained along profile 01 is shown in Figure 1.4. The inverse model of this profile shows a clear disparity between low, moderate and large conductive zone within the subsurface. From the surface to about 6 m depth on the profile, the resistivity response is of a moderate range between 13 ohm-m to 41 ohm-m. This is interpreted as unpolluted lateritic soil with a minimal leachate contamination zone observed at 65 m to 70 m on the surface profile distance to the depth of about 6 m. From 0.0 m to 40.0 m distance on the surface profile line, the profile is characterized by low resistivity value range of 2 ohm-m to about 8 ohm-m. This is interpreted as possible polluted zone due to leachate infiltration from the dumpsite. From about 45 m to 100 m on the profile, from the depth of 12.0 m to 19.8 m, the profile is characterized with high resistivity value range of about 70 ohm-m to above 131 ohm-m. This zone is interpreted as unsaturated and unpolluted fresh basement rock.

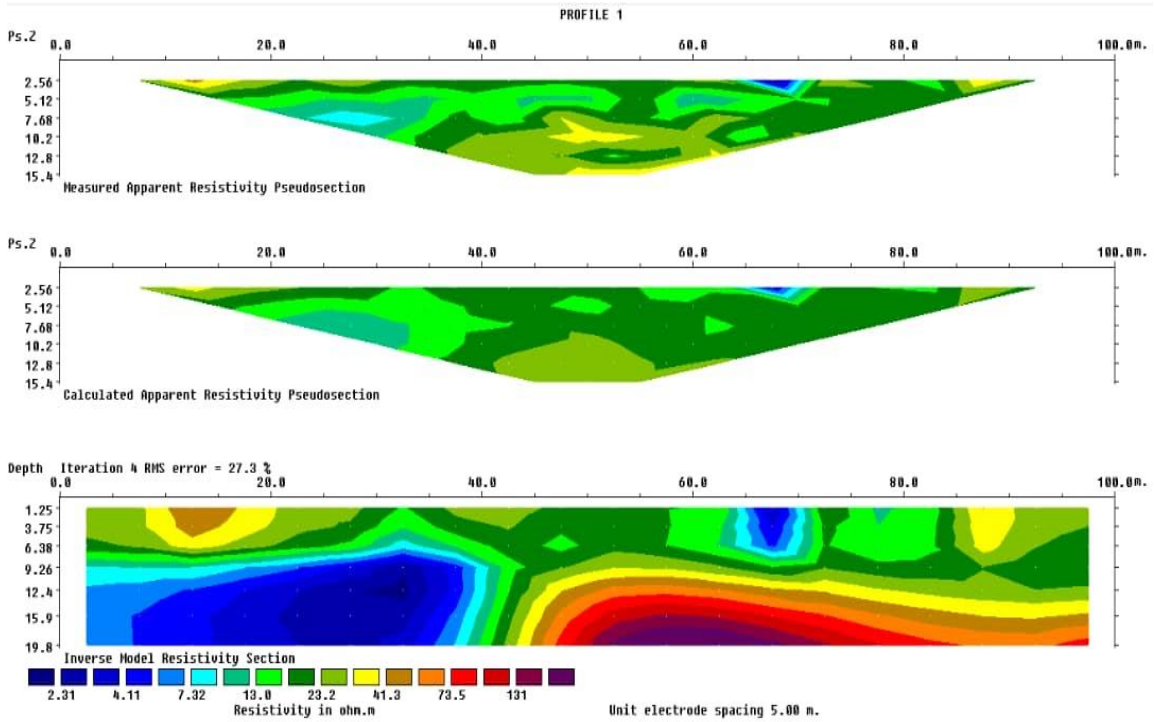

Figure 1.4: 2D Inverse ERI Plot for Profile 01

A more resistive zone representing the fresh basement rock zone with unsaturated waste underlain a much conductive leachate saturated top layer (Figure 1.5). Unfractured basement rock are often less infiltrated due to the competent nature of the materials that defined the rock. Irrespective of the disposal of a range of waste types with differing resistivity were at the site, the 2D ERT model shows relatively little variation within the area of the landfill. It is likely that this may be due to mixing of leachate within the landfill, which has led to the homogenization of saturated waste resistivity.

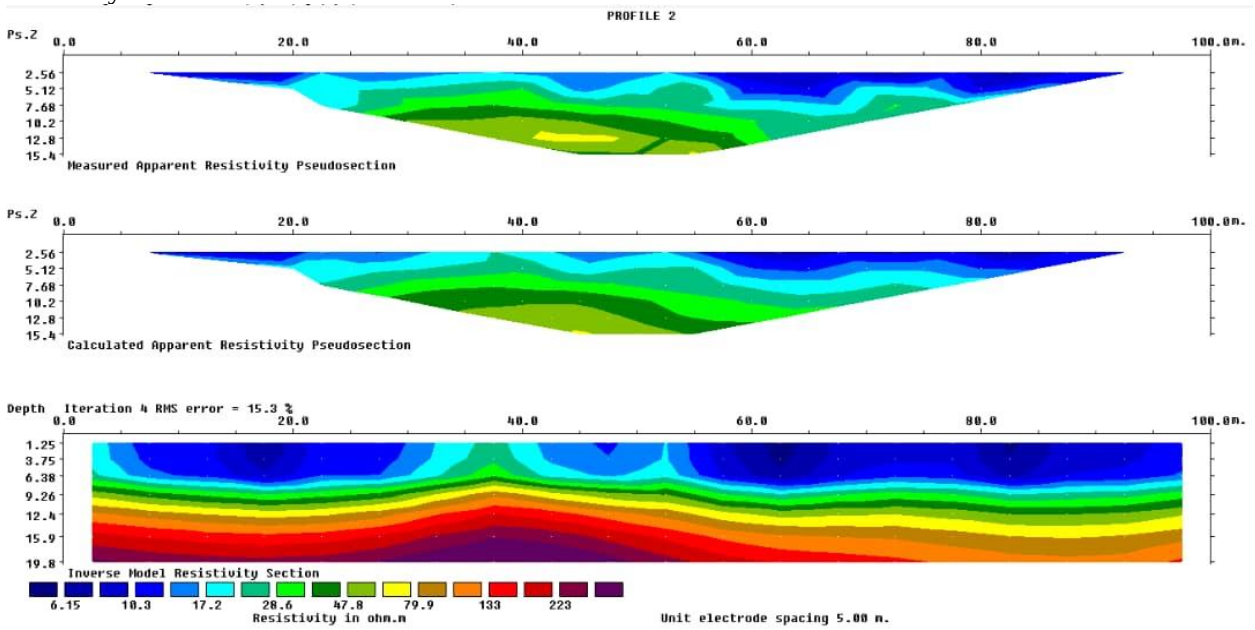

Figure 1.5: 2D Inverse ERI Plot for Profile 02

The model reveals homogenous low electrical resistive zone (< 8.0 Ohm-m to 17.8 Ohm-m) at depth ranging from 1.25-19.8 m across the model (Figure 1.6). This reflects a leachate infested

shallow subsurface. From the depth of 12.4 m - 19.8 m across the profile the moderately high resistivity response (87.9 Ohm-m to >131.0 Ohm-m) of this zone on the profile is observed reflects an unsaturated subsurface lithology. It is evident that this area is free from leachate contaminations.

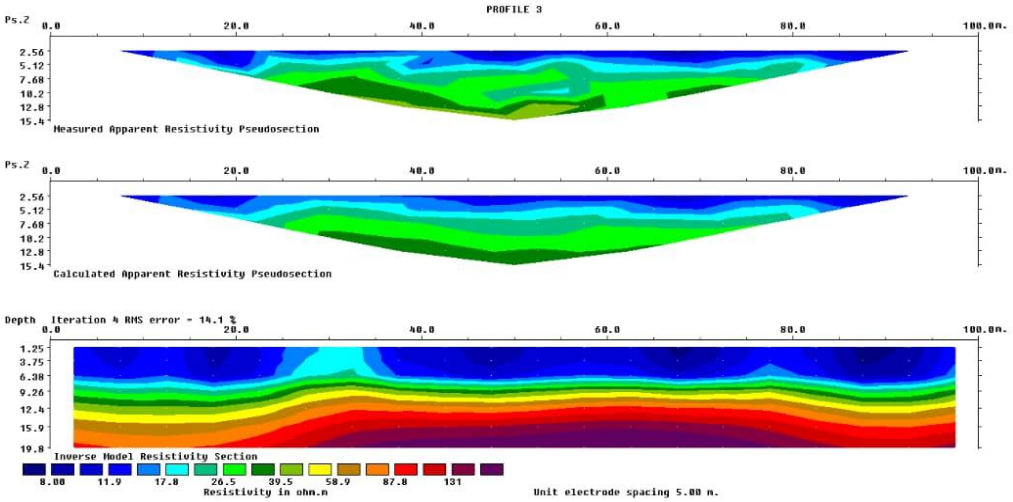

Figure 1.6: 2D Inverse ERI Plot for Profile 03

The ERI generally shows lower resistivity zones from about 6 m to 16 m depth of the profile (Figure 1.7). This area on the profile is characterized with low resistivity value range of less than 4 ohm-m to about 15 ohm-m indicating that this zone is highly conductive. The zones of low resistivity as expressed in the middle layer extend to both end sections of the profile; this zone is identified as anomalous zone with the greatest potential for association with leachate infiltration. The shallowest exposed bedrock is found around 25 m to 40 m, 50 m to 55 m and 85 m to 90 m on the surface of the profile, with resistivity values ranging between 88 ohm-m to above 204 ohm-m. This layer represents weathered to moderately weathered basement rock, as observed on the surface.

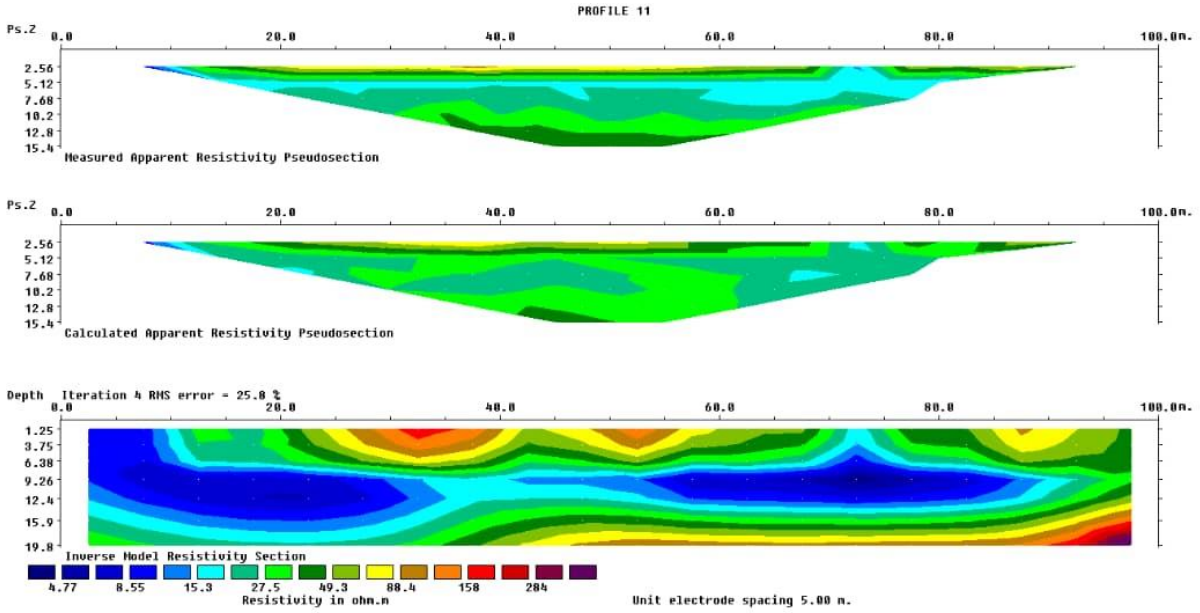

Figure 1.7: 2D Inverse ERI Plot for Profile 04

Conclusion

Electrical resistivity imaging surveys have been undertaken at an un-engineered waste dumpsite. Data from these surveys have been modeled using 2D inversion algorithms. By visual observation of the solid waste dumpsite, it is found that it consists of various constituents such as paper, organic matter, metals, glass, ceramics, plastics, textiles, dirt, and wood among others. The ERI results provide 2D subsurface images with good spatial resolution along the survey profile. From the interpretation of the 2D inverse models, it was established that low resistivity zones below the waste dumpsite are indicative of leachate migration into the groundwater that is contained in the bedrock. The disposal of waste on the dumpsite is a potential threat to the contamination and pollution of groundwater resources within the vicinity of the dumpsite and beyond.

Reference

Amadi, A. N., Olasehinde, P. I., Obaje, N.O., Unuevho, C.I., Yunusa, M.B., Keke, U., & Ameh, I. M. (2017). Investigating the Quality of Groundwater from Hand-dug Wells in Lapai, Niger State, North-central Nigeria using Physico-chemical and Bacteriological Parameters. *Minna Journal of Geoscience*, 1(1), 77 – 92.

Ameh, I. M. Amadi, A. N. Unuevho, C. I. and Ejepu, J. S. (2020). Hydrogeophysical Investigation of Groundwater Systems in Otukpo, Benue State, North-Central Nigeria. J. Chem. Soc. Nigeria, Vol. 45, No.5, pp 897 – 905.

Franz, T. (1993). Hydrogeological computer model used in evaluating contaminant transport. Geotechnical News, 11(4), pp. 50-52

Gadallah, M.R. and Fisher, R. (2009). *Exploration Geophysics*. Springer-Verlag Berlin Heidelberg.

Ige, O. O. (2013). Geological and Geotechnical Evaluation of an Open Landfill for Sanitary Landfill Construction in Ilorin, South-western Nigeria. *Journal of Environment and Earth Science*, 3 (3), 9-17.

Loke, M. H. (1997). Res2DINV software user's manual. *University Sains Malaysia, Penang*.

Loke, M. H. (1999). Electrical imaging survey for environmental and engineering studies. (A practical guide to 2-D and 3-D surveys). Retrieved from http://www.abem.se/files/res/2dnotes.pdf.

Loke, M. H. (2012). Res2dinv ver. 3.71: Rapid 2-d resistivity & ip inversion using the least-squares method. geotomo software.

Lowrie, W. (2007). Fundamentals of Geophysics (Second Edition). Cambridge University Press, New York.

Ranke, H. G. (2001). Appropriate Design and Operation of Sanitary Landfill in Sustainable Economic Development and Sound Resource Management in Central Asia. Proceedings of an International Conference, Nottingham, United Kingdom.

Rein hard, K. (2006). *Groundwater Geophysics*. Springer-Verlag Berlin Heidelberg Press London, 92.

Slater, L. D., Ntarlagiannis, D., Day-Lewis, F. D., Mwakanyamale, K.., Versteeg, R. J., Ward, A., Strickland, C., Johnson, C. D., & Lane Jr., J.W. (2010). Use of electrical imaging and distributed temperature sensing methods to characterize surface water-groundwater exchange regulating uranium transport at the Hanford 300 Area, Washington: *Water Resources Research*, 46 (10).

MATHEMATICS/ICT

An Intelligent Model for Detecting the Sensitivity Sentiments in Learners' Profile on Learning Management System

Muhammad Kudu Muhammad[1], Ishaq OyebisiOyefolahan[2], Olayemi Mikail Olaniyi[3] & Ojeniyi Joseph Adebayo[4]
[1,2,3&4]Federal University of Technology, Minna, Nigeria
{muhammad_kudu, o.ishaq, mikail.olaniyi, ojeniyia}@futminna.edu.ng

Abstract
*Mobile learning is enhanced through learner information analytics. Electronic learning systems are capable of offering personalized learning experiences with regards to learners' distinct attributes including knowledge, skills, and competencies required in evolving effective learning and teaching. User profiles on the Learning Management System (LMS) networks is evolving area of research by utilising social networks plugins in order to harvest data for sentiment analysis. Recently, a high-level sentiment analysis is adopted for the purpose of understanding the opinions of learners concerning a specific product or trends from reviews or tweets. Therefore, sentiment analysis is useful in improving the understanding of learners/user opinion, and also extracting trends about privacy and security of profile information on the LMS. The automated schemes are trained with hidden patterns in the comments or reports, then assign diverse sentiments to different reports indicating the severity and sensitivity regarding privacy of attributes in the learner profile information supplied to the LMS during the registration. The existing approaches require manual prioritization and partitioning, which is complex and time-inefficient. The first phase is the design of an opened questionnaire to be adopted during voluntary interview sessions with selected learners on different LMS such as Centre for Open Distance and eLearning (CODeL), National Open University of Nigeria (NOUN), and other LMSs for the purpose of generating learners profile information. In the second phase, **20** attributed were identified as most relevant for inclusion in mobile learner's profile information in which (**12**) attributes were considered to be most-sensitive, more-sensitive (**2**), less-sensitive (**3**), nominal (**3**), and non-sensitive (**0**) respectively. In this regard, the paper proposes deep learning networks techniques such as convolutional neural network (CNN), LSTM- based for the purpose automatically discovering sensitive attributes requiring privacy and protection from the public access or exploitation. The outcomes were better when compared to the manual-based thematic approach previously utilised in terms of effectiveness and accuracy.*

Keywords: Intelligent, Attributes, Sensitivity, Profile, Learner, Privacy, Security, LMS.

1.0 Introduction

The procedures and ways of learning changed tremendously in the area of education as a result of computer systems and internets. Today hi-tech names replaces the old names; for instance, Life in to e-life, learning in to e-learning, Education becomes e-Education, Money

into e-Money, Governance into e-Governance to mention but few (Jaiswal, 2012 and Mallya and Srinivasan, 2019).

The Learning Management System (LMS) enable students and academics to utilize e-learning or web-based and online teaching resources to assist in a self-spaced information collection, collaborative, and problem-solving related actions. Specifically, higher level of education (such as universities) has adopted the LMS in order to improve the practice of educators and learners, and provides learning management functionalities for these institutions. Again, LMS adoption improves the learning and teaching activities and administration, but, it is yet to have lasting positive impact on pedagogy (Singh and Miah, 2018). One concern is featured prominently, which is the protection of the privacy of users. The problems of security (or privacy) continue to attract the attention of users and developers. In fact, attackers can easily determine actions, transaction consummated, traffic data, and location information of users for potential security and privacy compromises (Yaru Wang *et al.*, 2019).

Learners are the target of mobile learning system (Mallya and Srinivasan, 2019). Mobile learning systems provides direct communication and connections to the participants that are learning under the distance learning system. Learners in Mobile learning have the strength to extend and improve their learning system above the classroom learners known as formal educational system (Yong, 2011).

Learners enrolled into m-learning system and immediately assigned to them the identities using they own digital mobile devices facilities for distance learning with the aids of portable devices to register their personal information profile inform of Learners Profile Form. However, learners are having more interest in distance learning education particularly mobile learning system regardless to location using these portable devices to achieve e-learning events and activities, there is a critical concern on the security and privacy (private information) from the level of management and technology perspective (Yong, 2011, Asuquo *et al.,* 2018, Caviglione and Coccoli (2020) and Atasoy *et al.* 2020).

The contributions of this articles include:

1. Precise summary of learner (s) profile and privacy preservation issues in learning management systems;
2. Related works and research gaps to mobile learning system privacy open issues are established;
3. Conceptual intelligent model to detect a sensitive attributes in mobile learner(s) profiles for learning management system is developed;
4. Validation is done on both attributes selection and determination which yield a very positive results;
5. Recommendations for further work on the design of an intelligent model using convolutional neural network (CNN) to detect the sensitivity of learner(s) attributes in mobile learning environments.

The remaining sections include: Section **2,** the related works and research gaps, Section **3** is the conceptual intelligent model, Section **4** are results and discussion of the study. Section **5** are the concluding part of the study and future work.

2.0 Related works

M-learning is the notion that allowed a learner to learn from any place at any time using portable learning devices such as hi-tech devices (Almaiah and Al Mulhem, 2019). According

to (Jaiswal, 2012), mobile learning declines restraint of learning location through the mobility of portable device which contain complementary features of both traditional learning and e-learning. Also Basak and Wotto, 2018, described M-learning as suitable, because learners and learning materials are available and accessible nearly anywhere, everywhere at any location "just in time" (Uther, 2019) but have problem of data protection.

Almaiah and Al Mulhem, (2019), mentioned that learners of mobile learning are able to learn from the existed different foundations of learning activities across globe at convenient period with another form of e-learning which is instigated through mobile technologies which cause linkage of data. The advantages of mobile learning over other online learning are; Learning can happen anytime and anywhere, learning happen after class hours, provision of better interface between learners-to-lecturers and learners-to-learners even while moving, appraisal/evaluation of learning content as when due, and weaker learners can be improved by lecturers during their learning processes. However, mobile learning has some issues that can be drawbacks its activities. These limitations are network challenges, how to use some of these mobility technology devices, physical interface between the lecturer and the learner is a problem and above all the security and privacy issues to protect the learners' profiles (Mallya and Srinivasan, 2019).

Kambourakis and Damopoulos (2013) and Peng., *et al*. (2016), appraises that, as part of learners' requirements, they should be able to establish some information in the lecture room, perceive among themselves and not necessarily everything that can be exposed to third party. When moving to the next level, learners should feel free, satisfied and comfortable to access to their information and details autonomously without fear of biased. Liu *et al.* (2018) established that, mobile learning originally is to communicate high level educational learning contents, principally for learners using mobile hi-tech devices. In this context, each learner experience is unique and standard base on the mobility of technology and learning criteria.

Again according to Almaiah and Al Mulhem (2019) data privacy of learners' in m-learning is very important (private information) sensitive attributes. However, in the context of this study, data privacy issue of sensitive and non-sensitive will be clearly stated through selection of attributes for learners' that uses mobile learning applications as their tools learning mechanism. The research work will have features selection instrument of sensitive information of learners' by hiding, use privacy criteria and requirements to safe and protects their data from third parties. There will be a kind of privacy policy and preservation that can enforces network not to disclose any learners' information, until learner (s) consent has been granted.

2.1 Research Gap

Above all, it is argued that privacy issues are not adequately considered in current m-learning platforms and especially within collaborative m-learning (Kambourakis, 2012). Mobile learning is a developing inclination which is subjected to respond to the issues of particular educational contexts, improve formal learning, enhance learning assistance for learners across ages and revenue spectrums to support learning opportunities mainly in an environments where educational chances are narrow or small. However, use of mobile technologies for m-learning initiate loss of privacy and attacks on learner and distance learning centre security. Mobile learning system supplies learners with exceptional mobile tools lead them attractive to thieves and create mobile device related issues. These issues are

related with the safeguarding of data stored on mobile tools and learners personal data on their learning curve and assessments.

The most critical concerns about the use of mobile devices in learning are privacy preservation of the learners' profile, the security risks and vulnerability attack issues on learning content. Since mobile learning devices such as smartphones and tablets have higher portability and very prone to digital and physical attacks as a results of widespread usage (Shonola and Joy, 2014). The concern about privacy issues in the m-learning realm appears to be recorded high among distance learning programme most especially in a developing country such as Nigeria where there is a large amount of cybercrime and internet security threat are on the increase (Shonola and Joy, 2014). These challenges penetrate and hinder the progress of mobile based distance educational system, particularly in the area of privacy and security. Main privacy issues/challenges in mobile learning systems are illustrated in the Figure **2.1**.

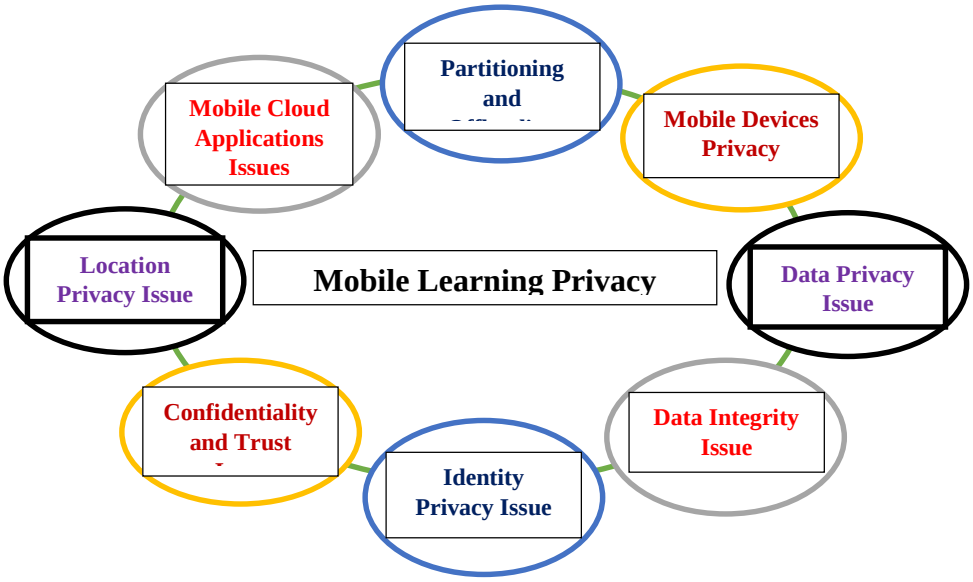

Figure 2.1: Mobile Learning System Privacy Issues

Online Distance Learning (ODL) in particular m-learning supposed to have the state-of-the-art data privacy preservation against adversaries. Data and identity privacy are the most problematic among the highlighted/mentioned mobile learning system privacy issues (Chamikara *et al.*, 2019). For instance, how to sufficiently outline adversarial background knowledge for anonymization? What are the learners' sensitive data that need to be private? And learner' shared their information among themselves and their lecturers. This days learners share their location data, share each other's' posts and information on social media platforms. Are they mindful of the privacy inferences of these relationships? Most of mobile learning institutions' consider application of learners' data privacy as nothing, since they themselves are not aware of their privacy. Hence, this research work will put into consideration issue by identifying some of learners sensitive data with technical solution to address privacy for learners' profile.

Sensitive learner profile attributes that can be used for privacy preservation in the field of mobile learning would be determined from the personal characteristics, learner(s) course (s), assignment and assessments, course evaluation, learner(s) support staff/ academic adviser, lecture materials, mobile devices and disciplinary acts. Each of this data type has parameters and sensitive attributes that need privacy. For this research study and to answer the first research question rose: What types of sensitive information need for learner(s) privacy in mobile learning? They are need to collect information from learner(s) information record(s). The types of information needed can be illustrated in Table 2.**1**.

From Table **2.1**, Personal information data type have three sensitive attributes indicating (SA) such as Grade Point Aggregates (GPA) and lettering grade, Location, Medical records and Family circumstance. The nature of infringements/violations and the punishment are both sensitive attributes requirement for disciplinary acts. The learner(s) course(s) have four requirements while only letter grade is the sensitive attribute. Assignment and assessments, mobile devices and courses evaluations contain grade (s), cost/price and accommodation as sensitive attributes respectively. Learner(s) support staff or Academics adviser(s) and lecture materials do not have sensitive attribute but Quasi-identifier attributes that also need privacy.

Table 2.1. Learners' information and their requirements.

Category/Data type	Requirements
Personal information	Name, Registration Number, Age, Programme, CGPA (SA), Location (SA), and Family circumstances (SA), Medical records (SA) & Department.
	Course title (LS), Course code (LS) and Letter Grade (SA), GPA (SA).
Assignment and assessments	Assessment type (LS), Assessment ID (NS) and Grade (SA)
Course evaluation	
Learner's support staff	Name of Lecturer (N), ID Number (N) & Accommodation (SA)
Disciplinary Acts	Support staff name (NS), Academic adviser's name (SA)
	Nature of infringement (LS) and Punishment (SA)

Key: SA – Sensitive Attributes, NS-Non-sensitive, LS-Less sensitive and N-normal

Therefore, looking at these types of information, sensitive attributes (private information) is the concern for study. In this context these criteria parameters will be an instrumental tool to check all the factors during and after data collections (Pre-processing, processing and post-processing). Hence, these mentioned parameters/criteria will denied breach of privacy violations, leakage of information, inferences and even stalking. After having all the necessaries and required type of information (sensitive/non-sensitive attributes), entities and fields, these now form student data records which in this study called Learner(s) Profiles in mobile learning system.

3.0 Materials and Method

3.1 Conceptual model

The proposed conceptual intelligent model of learner's profile sensitive attributes in mobile learning managing system for preserving privacy is mainly subdivided into three layers including registration layer, sentiment layer, learning layer adopted from (Caviglione and Coccoli, 2020) as illustrated in Figure **3.1**.

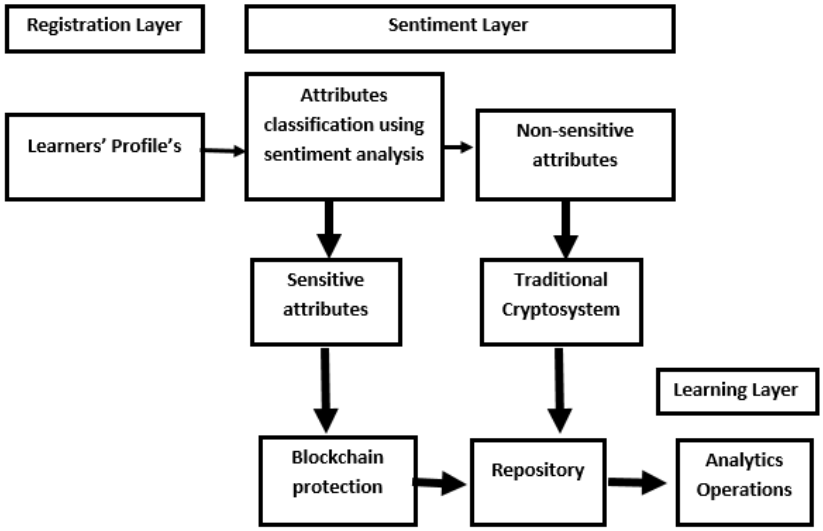

Figure 3.1: The proposed Intelligent model.

From Figure **3.1**, the **registration layer** is composed of diverse smart devices powered by software and hardware, which serve as user devices, servers, mobile agent and cloud infrastructure to register their profile/details. It is responsible for collecting diverse information concerning the mobile learner comprising of multifacated attributes and data elements. The process of obtaining relevant information learner in the mobile learning management system can be performed with mixed technological, wireless, wired and other devices.

The **sentiment layer** is the most central of the proposed model because it performs the distinct functionalities concerning mobile learner information profiled in the previous layer including creation, collection, processing and respository, on the general context. In particular, the privacy of learner profile is taken into account by partitioning the original learner profiled data using attributes classification sentiment analysis powered by convolutional neural network (CNN) a LSTM-based into sensitive and non-sensitive attributes. The sensitive attributes are safeguarded with Block chain, while the non-sensitive attributes of learner profiled data are secured with Advanced Encryption standard (AES) as traditional cryptosystem both before resposing on the server.

The **learning layer** makes use of different learning approaches using the mobile setting. The third party access to the repository is regulated in order to enforce security and privacy of sensitive attributes of learner's data using smart contracts of Blockchain and cryptosystem keys. This layer enables informed consent for privacy and autonomy (Jones, 2019) during learning analytics of mobile learning in learning management systems. The vulnerability of data layer to attacks on the profile of learners such as exploiting location, health records,

academic records, and other personal information considered sensitive to the learner can be protected adequately through appropriate permissioned access schemes.

3.2 Collection and Analysis of Data

The study adopted the face-to-face interview with **11**-point questions to be answered by participants for the purpose of collecting information on the sensitivity of profile data attributes. The participants were drawn from learners of Centre for Open Distance and eLearning (CODeL, Federal University of Technology, Minna, Nigeria, NOUN and other Universities through **volunteer sampling technique** in order to garner the responses of self-selected learners on relative sensitivity of profile information elements supplied to the LMS. The interview instrument was designed using open-ended questions that require participants to supply unique responses to the questions posed by the interviewers.

During analysis, the first step is to convert the original interview audio transcripts into MS Word documents using version 2016 or earlier. This can be achieved by creating a single document to represent the participants, interviewer and interview activities. Again, the data entities are simplified by separating the interviews are separated into distinct participants and name the files as participant **1**, participant **2**, to the end, which are saved into a folder.

The second step is to conduct content and thematic analysis on the semi-structured interviews using MS Excel 2016 tool on available themes in the different interview transcripts. The different files were combined and analysed accordingly. The nodes and cases are coded under distinct topics and subjects or themes. Thereafter, the relationships between interview participants' responses are summed up and presented in order of magnitude in the next session.

4.0 Results and Discussion

4.1 Demographic information of interview participants

The distribution of gender of participants that participated in the interview sessions are presented in Figure **4.1**. From the Figure **4.1**, there were as twice as many male participants as female participant during interview session, which represented **60.0**% to 40.0% respectively.

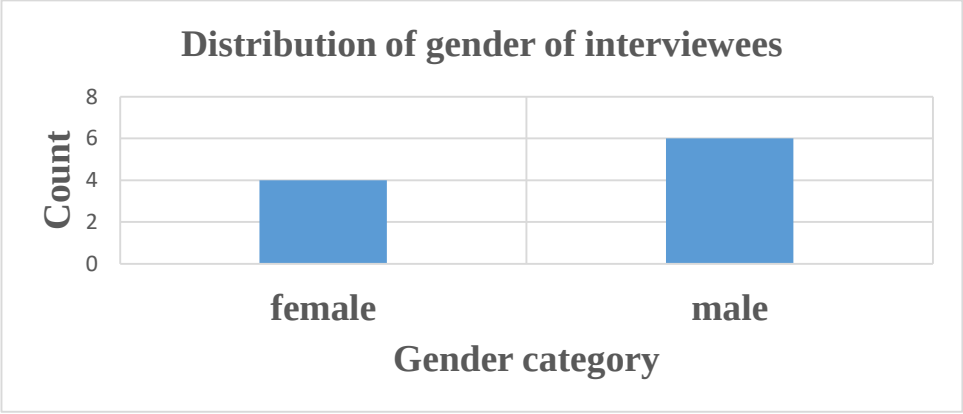

Figure 4.1: Gender distribution of interviewees.

The distribution of age of interview participants are presented in Figure **4.2**. This reveals that the oldest participant is the **5**th interviewee which is **24** years. Whereas, the youngest participant is **19** years old. This is indicative of the affinity of participants to technology and

reliability of responses provided during the interview session relating to the use of technology and issues of privacy in case of generation Z. Also, the largest number of participants during the interview were **20** years old, and followed by **21** years old.

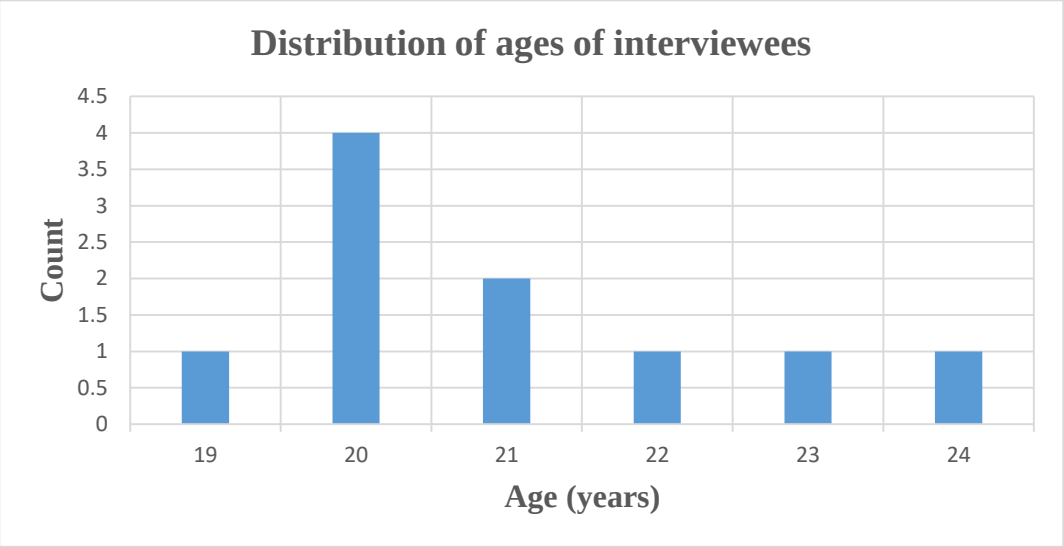

Figure 4.2: Distribution of ages of interviewees.

4.2 Attributes selection

The purpose of determing the attributes to be included in the proposed class partition model, the selected learners on the LMS were interviewed whose responses and counts for the attributes are presented in Table **4.1**.

Table 4.1: The learner profile information attributes sensitivity.

Learner Profile Attribute	Interview Participant	Response Count
name of learner	p3, p6,	2
Age	p1, p2, p8, p10	4
residential address	p1, p3, p5, p8, p10	5
permanent home address	p5	1
date of birth	p1, p2, p6, p9	4
medical history	p2	1
state of origin	Non-applicable	0
LGA	Non-applicable	0
previous academic record (CGPA)	p4, p7	2
current academic record (GPA)	p4, p7	2
Gender	p8, p9	2
marital status	p6, p10	2
sponsorship details	Non-applicable	0

guardian/parents	p1, p8	2
Courses	p3, p6	2
Hobbies	Non-applicable	0
blood group	p6, p10	2
Genotype	p4, p7, p9	3
contact information	p1, p2, p3, p4, p5	5
IP Address	p3	1

From Table **4.1**, after a survey of 10participants, the most sensitive attributes in learners profile information include: residential address, age, date of birth, medical history, blood group, and genotype information. While, non-sensitive attributes include: name of learner, state of origin, contact information, permanent home address, state of origin, local government of origin, previous academic records, current academic records, gender, marital status, sponsorship details, sponsorship details, guardian/parents details, course of study, hobbies, and IP address.

4.2 Attributes Determination

The preliminary results from the initial model validation utilised standard students' profile dataset collected from UCI Open University Data of students' assessments. The partitioning operations of the proposed scheme using deep learning approach, which classify learner's attributes into sensitive, normal, and non-sensitve text data elements or partitions are shown in Figure **4.3**.

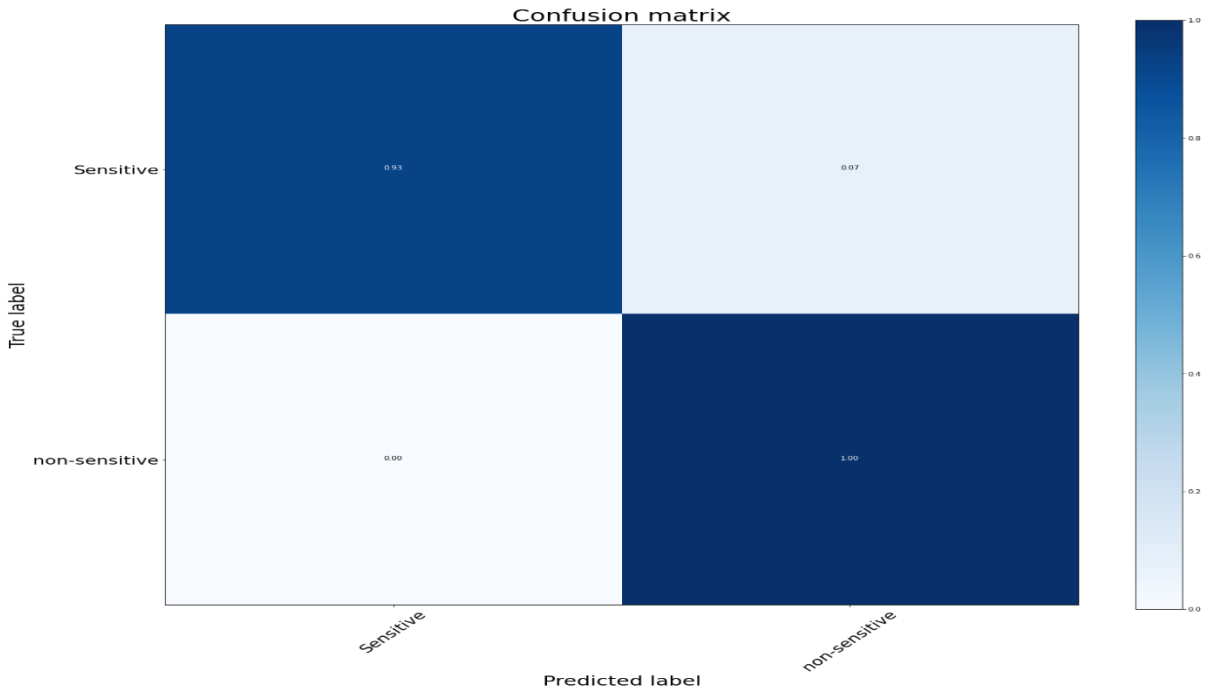

Figure. 4.3: Confusion matrix of the text classification.

From figure **4.3**, its show that confusion matrix is **2**x**2** that is sensitive and non-sensitive attributes that reflect four possible conditions; Sensitive attributes, true positive (TP) with result of **0.91**, false positive (FP) that is a Type I error with **0.07** result, false negative (FN) which is type II error (non-sensitive) with **0.00** result and true negative (TN) is the total sensitivity outcome of **1.00**. When compared the learners' responses in table **4.1** with the true label in figure **4.3** it show that many participants interviewed agreed that their attributes are very sensitive to them, which is significant by giving **91**% of the research study. While looking at the predicted label in the same figure **4.3**, it shows that the number of learners'/participants or attributes selected to be non-sensitive are very few, that is not significant (**09**%) from the same table **4.1**.

5.0 Conclusion

The automated schemes are trained with hidden patterns in the comments or reports, then assign diverse sentiments to different reports indicating the severity and sensitivity regarding privacy of attributes in the learner profile information supplied to the LMS during the registration. The study have identified the relevance of learning analytics to educators and education regulatory agents in modifying the practice and process of sharing knowledge and skill across the mobile based learning platforms.

However, the learning analytics is one potent tool required to be built into the LMS in order to continue to advance the experience of the learners, content of learning, and learning situation, which require certain attributes of the learners to be accessed and analyzed over-time. Consequently, the existing approaches require manual prioritization and partitioning, which is complex and time-inefficient. In this regard, the paper proposes deep learning networks techniques such as convolutional neural network (CNN), LSTM- based recurrent neural network (RNN) techniques for the purpose automatically discovering sensitive attributes requiring privacy and protection from the public access or exploitation. The outcomes were better when compared to the manual-based thematic approach previously utilised in terms of effectiveness and accuracy. In this way, the privacy of the learner is preserved during learning analytics operations of educators or education service providers. It is recommended, the future work needs to establish performance evaluation using more datasets while generating strong security of the sensitive data items in the learner's profile.

Reference

Almaiah, M. A., & Al Mulhem, A. (2019). Analysis of the essential factors affecting of intention to use of mobile learning applications: A comparison between universities adopters and non-adopters. *Education and Information Technologies*, *24*(2), 1433–1468. https://doi.org/10.1007/s10639-018-9840-1

Asuquo, P., Cruickshank, H., Morley, J., Ogah, C. P. A., & Lei, A. (2018). *Security and Privacy in Location-Based Services for Vehicular and Mobile Communications : An Overview , Challenges and Countermeasures*. *XX*(Xx), 1–25.

Atasoy, E., Bozna, H., & Abdulvahap, S. (2020). *Active learning analytics in mobile : Active visions from PhD students*. *15*(2), 145–166. https://doi.org/10.1108/AAOUJ-11-2019-0055

Basak, S. K., & Wotto, M. (2018). *D-learning : Conceptual definition and*. (July). https://doi.org/10.1177/2042753018785180

Caviglione, L., & Coccoli, M. (2020). *A Holistic Model for Security of Learning Applications in Smart Cities*. *16*(01), 1–10.

Chamikara, M. A. P., Bertok, P., Liu, D., Camtepe, S., & Khalil, I. (2019). Efficient privacy preservation of big data for accurate data mining. *Information Sciences*, (xxxx). https://doi.org/10.1016/j.ins.2019.05.053

Gursoy, M. E., Inan, A., Nergiz, M. E., & Saygin, Y. (2016). *Privacy-Preserving Learning Analytics : Challenges and Techniques*. *1382*(114), 1–14. https://doi.org/10.1109/TLT.2016.2607747

Gursoy, M. E., Inan, A., Nergiz, M. E., & Saygin, Y. (2018). Privacy-Preserving Learning Analytics: Challenges and Techniques. *IEEE Transactions on Learning Technologies*, *114*, 1–14.

Jaiswal, D. (2012). *NEW APPROACHES IN LEARNING : E-LEARNING , M-LEARNING AND U-LEARNING*. *I*(Ii), 197–203.

Jones, K. M. L. (2019). Learning analytics and higher education: a proposed model for establishing informed consent mechanisms to promote student privacy and autonomy. *International Journal of Educational Technology in Higher Education*, *16*(24), 1–22.

Kambourakis, G. (2012). *Security and Privacy in E-Commerce*. *6*(3), 366–402. https://doi.org/10.4018/978-1-4666-1800-8.ch010

Kambourakis, G., & Damopoulos, D. (2013). A competent post-authentication and non-repudiation biometric-based scheme for M-learning. *IASTED Multiconferences - Proceedings of the IASTED International Conference on Web-Based Education, WBE 2013*, 821–827. https://doi.org/10.2316/P.2013.792-005

Liu, Q., Li, T., Yu, Y., Cai, Z., & Zhou, T. (2018). Data Security and Privacy Preserving Techniques for Wearable Devices: A Survey. *Jisuanji Yanjiu Yu Fazhan/Computer Research and Development*, Vol. 55, pp. 14–29. https://doi.org/10.7544/issn1000-1239.2018.20160765

Mallya, R., & Srinivasan, B. (2019). Article ID: IJMET_10_03_063 Cite this Article Ramananda Mallya K and Dr. B Srinivasan, Effect of Cloud Based Mobile Learning on Engineering Education. *International Journal of Mechanical Engineering and Technology (IJMET)*, *10*(3), 614–621.

Shonola, S. A., & Joy, M. (2014). Mobile learning security issues from lecturers' perspectives (nigerian universities case study). *EDULEARN14 Proceedings*, (July), 7081–7088.

Singh, H., & Miah, S. J. (2018). Design of a mobile-based learning management system for incorporating employment demands : Case context of an Australian University. *Education and Information Technologies*. https://doi.org/https://doi.org/10.1007/s10639-018-9816-1

Uther, M. (2019). *Mobile Learning — Trends and Practices*. 10–12. https://doi.org/10.3390/educsci9010033

Wang, Yaru, Zheng, N., Xu, M., Qiao, T., Zhang, Q., & Yan, F. (2019). Hierarchical Identifier: Application to User Privacy Eavesdropping on Mobile Payment App. *Sensors*, *19*(3052), 1–19. https://doi.org/10.3390/s19143052

Yong, J. (2011). Security and privacy preservation for mobile e-learning via digital identity attributes. *Journal of Universal Computer Science*, *17*(2), 296–310. https://doi.org/10.3217/jucs-017-02-0296

MODELLING AND FORECASTING VOLATILITY IN NIGERIA: EVIDENCE FROM THE STOCK MARKET

Zubair, A. U; and Usman, A.
Department of Statistics,
Federal University of Technology, Minna, Nigeria
Corresponding Author: zubairsland@yahoo.co.uk

Abstract

Trades in stock market anywhere in the world is faced with intense volatility due to stocks prices instability in real time that is mostly driven by information and other market dynamics. This research examines two volatility models with two different error distributions innovations in modelling and forecasting the continuous compounded return series (CCRS) of Nigeria All Share Index (NGX-ASI) spot prices spanning the period of January 30, 2012 to June 30, 2021. The Generalized Autoregressive Conditional Heteroscedastic (GARCH) and Asymmetric Power Autoregressive Conditional Heteroscedastic ARCH (APARCH) volatility models under Student-t Distribution (S^tD) and Generalized Error Distribution (GED) error innovations are utilized. The best-fitted model is determined using Akaike's Information Criterion (AIC) while Mean Square Error (MSE) is used to evaluate forecasts performance of the fitted volatility models. The results from the analysis showed that amongst competing models, APARCH (1,1)-GED was selected to be the best fitted volatility model with better forecasting power for the CCRS-NGX-ASI spot prices. This is because it produces the smallest AIC and MSE values.

Keywords: GARCH models; Error distributions; Volatility; Forecasting; Stock market

1. Introduction

It is a well-known fact that the monetary markets are highly unstable and replete with uncertainties. In financial time series, modelling and forecasting volatility is a pertinent task in stock markets due to the significant role it plays in a nation's economy. Over the years, a number of researchers have devoted their time to examining and analysing the importance of volatility in risk management. Owing to this, exact and precise estimation of asset returns volatility is crucial in evaluating the risk involved in an investment. Having an idea about the volatility future stock returns boosts investor confidence in deciding whether to hold an asset or not (Bentes and Menezes, 2012). The volatility of asset returns is a proportion of how much the returns change around its normal. Also, volatility is the most perfect proportion of hazard in financial markets and by this, it has turned into the normal cost of vulnerability. A decent volatility model and conjecture assist with affecting the public certainty fundamentally and likewise on the more extensive worldwide economy. Return volatility is a key concern in investment decisions, portfolio allocation, risk management, option pricing, microeconomic policymaking. volatility predictions in this context can play the role as a trigger factor for the financial markets and the economy (Poon and Granger, 2003). Therefore, to model and represent appropriately the structures of financial time series, models such as the Autoregressive Conditional Heteroscedasticity (ARCH) and Generalized ARCH

(GARCH) models have been suggested to knob the structures of financial time series (Lawrance, 2013). These models and its various extensions can be used in estimation and prediction of the volatility in assets returns series, asset risk management, security pricing, foreign exchange rate movement analysis and interest rate long term and short-term relationships (Caiado, 2004).

Over the years, limited studies have explored the possibility of modelling and forecasting the volatility in Nigeria stock market. A study of note is that of Kolade (2013) where the underlying characteristics of the Nigeria stock market was examined using the NSE all-share index as proxy for modelling the volatility in the stock market. The GARCH (1, 1), GARCH-in-mean (1, 1), TGARCH (1, 1), and EGARCH (1, 1) model were estimated with the result indicating high obstinate volatility for NSE return series. Most studies in Nigeria have either focused on individual stocks, normal error distributions or limited by weekly or monthly dataset which is not a good representation of all the securities traded in the capital market and in this era of big data analytics (Emenike and Aleke (2012), Ibrahim, (2017), and Iwada and Omoyeni (2018)). In this regard, this research attempts to expand on the existing literature by carrying out a comprehensive study of the Nigeria stock utilizing not just individual stocks but daily closing prices of Nigeria Exchange All Share Index ((NGX-ASI)) prices as proxy for evaluation. This study also fills a gap by incorporating NGX-ASI prices spanning the period we were battling with the novel Covid-19 virus to enable us assess its impact on the Nigeria stock market. Hence, it is the drive of this research to probe the ability of the GARCH and APARCH models in predicting the volatility in Nigeria stock market using the Student-*t* distribution (S^tD) and Generalized Error Distribution (GED) as error innovations. An important question to be answered in this research is which of the models can be regarded as the best in estimating training and test data for the daily closing prices of NGX-ASI.

2. Methodology

In this section, the data used for the research is described and the methodology frame work in achieving the research objective is presented.

2.1 Data Description

The NGX-ASI data utilized for the research was obtained from https://app.datawarehousepro.com/go/cbnstatistics on the 30th June, 2021. This research utilized daily NGX-ASI spanning the period of January 30, 2012 to June 30, 2021. All the sample was partitioned into the training/in-sample and testing/out-sample period. The training set utilised for estimating parameters of the models constituted 2215 observations spanning January 30, 2012, to January 11, 2021. The testing set used for evaluating the forecasting framework consisted of 115 observations from January 12, 2021, to June 30, 2021. This generates a total of 2331 observations of spot prices, which we then converted into logarithmic return series because of the statistical properties it possesses.
Let:

$$y_t = \log\left(\frac{NGX_t}{NGX_{t-1}}\right) \tag{1}$$

where NGX_t and NGX_{t-1} represent the present NGX-ASI price at time *t* and previous NGX-ASI price at time *t*-1. y_t as shown in equation (1) is the continuously compounded return series which this study uses in assessing volatility.

2.2 Test for Stationarity

Most time series variables are usually not stationary in their pure form. This is why it is suitable to transform them to achieve stability in the series. Here, a stationarity test on the NGX-ASI returns is performed utilizing the Augmented Dickey-Fuller (ADF) test. The goal is to study the null hypothesis that ϕ =1 in (2) alongside the alternative ϕ <1.

$$w_t = \phi w_{t-1} + z_t \tag{2}$$

Where phi [ϕ] is real-valued constant with differing values of (0,0.8,1), W_t is the dependent variable at time t and Z_t the random error generated at time t.
Therefore, the formulated hypothesis of concern is H_0: *series is not stationary* versus H_1: *series is stationary*.

2.3 Testing for ARCH Effect

In modelling volatility, it is important to affirm the relevance of estimating GARCH-type models by testing the existence of ARCH effects in the residuals (a phenomenon called Heteroscedasticity). Two tests can be adopted to test for ARCH effect on the residuals and they are Ljung-Box statistics Q (m) and Lagrange multiplier (LM) test. In this research, the Q(m) and LM test are adopted. For simplicity, let it be assumed that $\varepsilon_t = y_t - \mu_t$ is the residuals from a mean equation. After getting the residual ε_t, the squared residual is regressed on a constant and its q lags.

$$\varepsilon_t^2 = \tau_0 + \tau_1\varepsilon_{t-1}^2 + ... + \tau_q\varepsilon_{t-q}^2 + D_t, \quad t = q+1,...,T \tag{3}$$

where, D_t is the error term, q is a pre-identified positive integer, and T is the sample size.
The H_0 prescribes no ARCH effect of order q defined as:

$$H_0\text{: (ARCH) } \tau_1 = \ldots = \tau_q = 0$$

Against

$$H_1\text{: (ARCH) } \tau_1 \neq \ldots \neq \tau_q \neq 0$$

Now let the Sum of Square Residual, $SSR_0 = \sum_{t=q+1}^{T}(\varepsilon_t^2 - \bar{\omega})^2$, where $\bar{\omega} = (1/T)\sum_{t=1}^{T}\varepsilon_t^2$ is the sample mean of ε_t^2 and $SSR_1 = \sum_{t=q+1}^{T}\hat{D}_t^2$, where $\hat{D}_t$ is the least square residuals of the prior linear regression. Hence an F-test is obtained as follows:

$$F = \frac{(SSR_0 - SSR_1)/q}{SSR_1/(T-2q-1)} \ . \tag{4}$$

Equation (4) follows an F-distribution with q degrees of freedom and $T - 2q - 1$ under H_0. When T is sufficiently large, F can be used as the test statistic, which has a $\chi_q^2(\tau)$ distribution with q degrees of freedom under the H_0. The decision rule is to reject the H_0 if $mF > \chi_q^2(\tau)$, where $\chi_q^2(\tau)$ is the upper 100(1 - τ)th percentile of $\chi_q^2(\tau)$ or the p-value of mF < τ , for a Type I error.

2.4 Model specification

In this research, two conditional heteroscedastic volatility models are used; they are GARCH and APARCH models. Each of the models are fitted based on two error innovation

distributions which are Student-t Distribution (S^tD) and the Generalized error Distribution (GED). These models and the respective error innovations are given in the following subsections.

2.4.1 GARCH Model

The GARCH (*p*, *q*) model **(**Bollerslev, 1986 and Bollerslev *et al*., 1992) where *p* represents the GARCH component and *q* represents the ARCH component can be generally expressed as:

$$\sigma_t^2 = \omega + \sum_{i=1}^{p} \alpha_i z_{t-i}^2 + \sum_{j=1}^{q} \beta_j \sigma_{t-j}^2 \tag{5}$$

Where ω is the mean of unconditional variance (long-run average variance)
α_i is ARCH parameter at lag (i) and β_j is the GARCH parameter at lag (j)

where $\omega > 0$, $\alpha_i > 0$, $\beta_j > 0$ for $i = 1,\ldots, p$ and $j = 1, \ldots, q$. Also, *p*, *q* are the order of the ARCH terms z_t^2 and GARCH terms σ^2 respectively. σ_t^2 is the conditional variance with z_t^2 being the disturbance term. If $p = q = 1$ in equation (5), the most basic parsimonious GARCH (1, 1) is obtained and model is defined as:

$$\sigma_t^2 = \omega + \alpha_1 z_{t-1}^2 + \beta_1 \sigma_{t-1}^2 \tag{6}$$

where ω, α_1, and β_1 represent constant, ARCH and GARCH component of the model respectively and if $\alpha_1 + \beta_1$ represents the change in response function of shocks to volatility persistence and a value greater than 1 implies that response function of volatility increases with time and a value less than 1 implies that shock decay with time. Also, if the parameters ω, α_1, and $\beta_1 > 0$ and $\alpha_1 + \beta_1 < 1$ then the series is said to be stationarity. The unconditional variance of z_t in GARCH (*p*, *q*) is given as:

$$\mathrm{Var}(z_t) = \omega \left[1 - \left(\sum_{i=1}^{p} \alpha_i + \sum_{j=1}^{q} \beta_j \right) \right]^{-1} \tag{7}$$

2.4.2 Asymmetric Power ARCH Model

Ding *et al*. (1993) developed the Asymmetric power (APARCH) as an elongation of the traditional GARCH model to allow for asymmetry in the conditional variance. The specification of the APARCH (*p*, *q*) model is mathematically presented as:

$$\sigma_t^{\delta} = \omega + \sum_{i=1}^{q} \left(\alpha_i | \varepsilon_{t-1} | - \gamma_i \varepsilon_{t-1} \right)^{\delta} + \sum_{j=1}^{p} \beta_j \sigma_{t-j}^{\delta} \tag{8}$$

Where ω, is constant, α_i is ARCH parameter at lag (i)and β_j is the GARCH parameter at lag (j)
Where δЄŔ, $\alpha_i \geq 0$ and $-1 < \gamma_i < 1$ γ_i is coefficient of the leverage effect. The APARCH models transforms to the GARCH-family models when parameters are as follows:

- If $\delta = 2$, $\gamma_i = 0$, $\beta_j = 0$ for ($i = 1, ..., q$ and $j = 1, \ldots, p$) Engle (1982) ARCH model is obtained.

- If $\delta = 2$, $\gamma_i = 0$, for ($i = 1, \ldots, p$) Bollerslev (1986) GARCH model is obtained.
- If $\delta = 2$, Glosten *et al*. (1993) GJR-GARCH model is obtained.
- If $\delta = 1$, Zakoian (1994) TARCH model is obtained.
- If $\delta = 1$, $\gamma_i = 0$, for ($i = 1, \ldots, P$) Engle (1982) ARCH model is obtained.

2.5 Distributional Assumptions of GARCH Models

The two error innovation distributions used in this research, that is, Student-*t* Distribution (S^tD) and Generalized error Distribution (GED) are given below.

2.5.1 Student-*t* Distribution (S^tD)

The S^tD is given as

$$f(d;h) = \frac{\Gamma\left(\frac{h+1}{2}\right)}{\sqrt{h\pi}\,\Gamma\left(\frac{h}{2}\right)}\left(1+\frac{d^2}{h}\right)^{\frac{-h+1}{2}} \tag{9}$$

where h is the number of degrees of freedom, d variable is a real number, and Γ is the Gamma function.

2.5.2 Generalized Error Distribution (GED)

The generalized error distribution proposed by Nelson (1991) is given by

$$f(h) = \frac{d \times \exp\left[-0.5\left|\frac{h}{\lambda}\right|^d\right]}{\lambda \times 2^{\left(1+\frac{1}{d}\right)}\Gamma\left(\frac{1}{d}\right)}, \text{ where } \lambda = \left[2^{\frac{-2}{d}}\,\frac{\Gamma\left(\frac{1}{d}\right)}{\Gamma\left(\frac{3}{d}\right)}\right]^{\frac{1}{2}} \tag{10}$$

For $-\infty < h < \infty$ and $0 < d < \infty$ where $\Gamma(.)$ is the Gamma function and k is the tail fatness parameter. Note that if $d = 2$, then h behaves like a standard normal distribution.

2.6 Model Selection and Performance Evaluation of Volatility Models

An assessment of the fitness and forecasting performance of the competing models is carried out using goodness of fit statistics, which is Akaike's Information Criterion [AIC]. Model with the smallest AIC values is best amongst the competing models. Their respective statistic is defined as

$$AIC = 2f(\hat{\theta}) + 2\text{k} \tag{11}$$

Here $f(\theta)$ is the log-likelihood function, and k is the number of parameters.

In this study, we are employed loss function often times utilized to assess the forecast performance of GARCH models. The loss function is given as follows.

$$MSE = c^{-1}\sum_{t=1}^{c}(\hat{\sigma}_t - \sigma_t)^2 \tag{12}$$

where c, σ_t, and $\hat{\sigma}_t$ are the out-of-sample observation, actual volatility and forecast volatility at time t respectively.

3. Results and Discussion

Preliminary investigations were conducted to give us an insight into some commonly held stylized fact about financial time series variable. Occasioned by this, a descriptive analysis of the NGX All Share Index Price (NGX-ASIP) and NGX All Share Index Returns (NGX-ASIR) was carried out as displayed in Table 1 below. Some statistical properties of NGX-ASIP and NGX-ASIR are presented. The NGX-ASIP reported skewness, standard deviation, mean, and kurtosis amongst others of daily NGX All Share Index Price to be 0.1491, 6129.82, 31724.16,
-1.1039 respectively.

Table 1: Descriptive Statistics of NGX ASI Price and Returns Series

Statistics	NGX All Share Index Price	NGX All Share Index Returns
Mean	31724.16	0.0003
Median	30819.1000	-0.0001
Maximum	45092.83	0.0798
Minimum	20123.51	-0.0503
Variance	37574763.33	0.0001
Std Dev	6129.82	0.0100
Kurtosis	-1.1039	5.4355
Skewness	0.1491	0.3329
Jarque-Bera	126.98	2911.3
Probability	0.0000	0.0000
Observation	2331.00	2330.00

The plot in Figure A presents the volatility pattern of NGX-ASIP series. From the series, it can be visually observed that the Nigeria Exchange Market experienced a sharp downturn in 2012, 2016 and 2020. This could be attributed to the recovery from the universal financial crisis in 2008, recession the Nigerian economy slipped into 2016 and the novel COVID-19 pandemic effect in 2020.

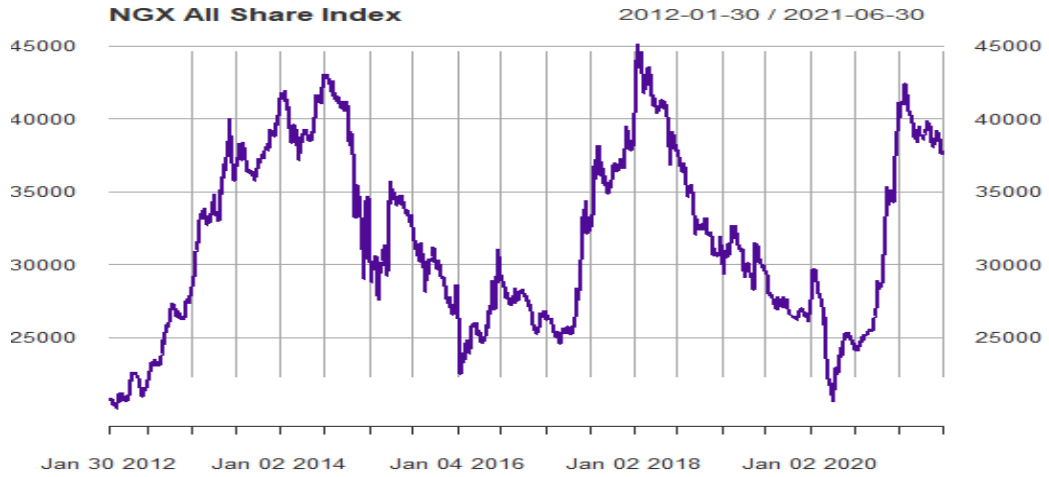

Figure A: Daily NGX All Share Index Price movement (January 30, 2012, to June 30, 2021)

It can also be observed that the series fluctuates from a low to high and high to low

movements during the period of study. This is largely due to the volatility exhibited by financial variables and by extension, depicts that the series is non-stationary. NGX-ASIR yields a positive mean daily return of 0.0003 with a variance of 0.0001 and standard deviation of 0.0100.

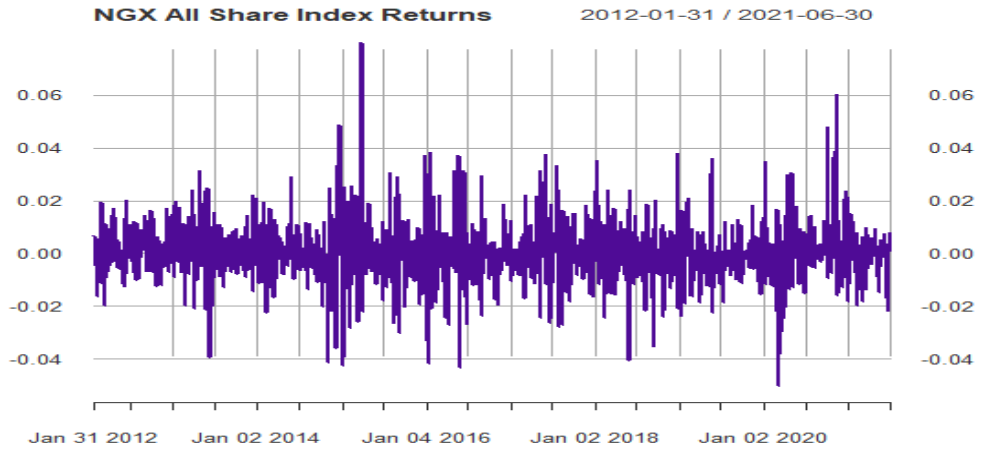

Figure B: Daily NGX All Share Index Returns movement (January 30, 2012, to June 30, 2021)

The maximum for NGX-ASIR is reported to be 0.0798 with a corresponding minimum value of -0.0503. NGX-ASIR series skewness is 0.3329, signifying left-tail and kurtosis of 5.3235, which is greater than 3 to be distributed normally. In essence, this means that Nigeria Exchange All Share Index Return series is peaked around its mean value and is termed leptokurtic (that is, it possesses a fat tail). The Jarque-Bera test indicates that NGX-ASIR is not from the normal distribution, as a result of the rejection of the H_0 that the returns are normally distributed at 0.05 significance level. Table 2 presents the unit root test (URT) using ADF test to check for stationarity. The result shows that the Tau statistic value is significant at 0.05 level of significance. This implies that the H_0 of no stationarity is not accepted and it can be established that the NGX-ASIR series is stationary.

Table 2: URT using ADF for NGX-ASIR

	ADF statistics	P-value	Comment
NGX-ASIR	-12.169*	0.01	Stationary

**Signify 5% significance level*

Next is the test for ARCH effect. Table 3 presents the results of *Q* (*m*) and *LM* tests. It can be observed that both tests produced a *p*-value of $2.2\times 10^{-16} < 0.05$ which is of high significance. Hence, at 5% significance level, the H_0 of no ARCH effect is not accepted. This implies that NGX-ASIR exhibit the effect of ARCH.

Table 3: Test for ARCH Effect

NGX-ASIR	F-statistic	P-value	Comment
Q (*m*)	533.6	2.2e-16*	ARCH present
LM	307.98	2.2e-16*	ARCH present

** Signify 5% significance level*

3.1 Parameter Estimation of GARCH-type Models

After affirming the existence of ARCH effect in the NGX-ASIR series, results for all the GARCH models stated in the methodology are presented with their corresponding error distributions in Table 4a and Table 4b. The estimated models are GARCH (1, 1), GARCH (1, 2), GARCH (2, 1), GARCH (2, 2), and APARCH (1, 1) volatility models following error distributions, that is, S^{t}D and GED.

Table 4a: Results of the Parameter estimation of GARCH-type models

Model	Error	ω	α_1	α_2	β_1	β_2	Skew	Shape
GARCH (1, 1)	S^{t}D	0.00014*	0.36226	-	0.58614*	-	-	3.72644*
		(0.0000)	(0.0000)	-	(0.0000)	-	-	(0.0000)
	GED	0.00013*	0.30485	-	0.59298*	-	-	1.09527*
		(0.0000)	(0.0002)	-	(0.00000)	-	-	(0.0000)
GARCH (1, 2)	S^{t}D	0.00015*	0.40569	-	0.33319*	0.20371*	-	3.77631*
		(0.00156)	(0.0000)	-	(0.00413)	(0.00000)	-	(0.0000)
	GED	0.00014*	0.35038	-	0.27543**	0.25981*	-	1.10349*
		(0.0000)	(0.0000)	-	(0.01802)	(0.00085)	-	(0.0000)
GARCH (2, 1)	S^{t}D	0.00014*	0.36336	0.00342	0.58596*	-	-	3.71717*
		(0.0000)	(0.0000)	(0.99734)	(0.00000)	-		(0.0000)
	GED	0.00013*	0.30515	0.00101	0.59284*	-	-	1.09488*
		(0.0000)	(0.0000)	(0.98100)	(0.00000)	-	-	(0.0000)
GARCH (2, 2)	S^{t}D	0.00015*	0.40567	0.00365	0.33308**	0.20390*	-	3.77669*
		(0.0000)	(0.0000)	(0.99996)	(0.02848)	(0.00005)	-	(0.0000)
	GED	0.00014*	0.35009	0.00211	0.27587	0.25975**	-	1.10354*
		(0.0000)	(0.0000)	(0.88979)	(0.09231)	(0.02929)	-	(0.0000)

*Note: In parenthesis are p-values, * and ** signify significance at 1%, and 5% level respectively*

Table 4b: Results of the Parameter estimation of GARCH-type models

Model	Error	ω	α_1	β_1	γ_1	δ	Skew	Shape
APARCH (1,1)	S^{t}D	0.00041	0.22274	0.40266	-0.03928	3.08332	-	4.60805
		(0.04483)	(0.0000)	(0.0000)	(0.03763)	(0.0000)	-	(0.0000)
	GED	0.00032	0.19585	0.44237	-0.02091	3.23285	-	1.15152
		(0.06116)	(0.0000)	(0.0000)	(0.04324)	(0.00135)	-	(0.0000)

*Note: In parenthesis are p-values, *, ** and *** signify significance at 1%, 5% and 10% level respectively*

The outcome from Table 4a and 4b show that the often-held stylized characteristics of NGX-ASIR volatility were captured by almost all the models owing to the significant statistical coefficients recorded at α = 0.01%, 0.05% and 0.1% significance level. The ARCH and GARCH term coefficients in the models were positive and significant, implying that the previous NGX-ASIR can impact the current NGX-ASIR. The sum of ARCH and GARCH (that is, $\alpha_1 + \beta_1$) which serves as measure of volatility persistence were found to be high even

though it did not exceed one ($\alpha_1 + \beta_1 < 1$). What this implies is that the Nigeria Exchange Market volatility shock is very persistent. It also indicates that such models are stationary and stable. The leverage effect γ which is a measure of the influence of bad and good news to the NGX-ASIR volatility was captured by the APARCH model to be significant, statistically. Negative coefficients in APARCH signifies that bad news surges volatility than good news. The presence of leverage effect in the Nigeria Exchange Market for this period of study is in tandem with research carried out by (Okpara 2011).

Table 5: Model Selection Criteria of the GARCH-type models

Model	Log-likelihood	AIC	BIC
GARCH (1,1)			
Student-t	7426.583	-6.7042	-6.6914
GED	7428.728	-6.7062	-6.6933
GARCH (1,2)			
Student-t	7428.233	-6.7048	-6.6894
GED	7431.013	-6.7073	-6.6919
GARCH (2,1)			
Student-t	7426.473	-6.7032	-6.6878
GED	7428.605	-6.7052	-6.6897
GARCH (2,2)			
Student-t	7428.233	-6.7039	-6.6859
GED	7431.013	-6.7064	-6.6884
EGARCH (1,1)			
Student-t	7429.143	-6.7056	-6.6902
GED	7432.196	-6.7084	-6.6929
APARCH (1,1)			
Student-t	7408.307	-6.6859	-6.6679
GED	7424.292	-6.7094	-6.6991

Values in Bold signify the largest Log-likelihood and the least AIC and BIC

In Table 5 above, the model selection criteria and log-likelihood of the fitted GARCH-type model is presented. The performance is evaluated for each model with its corresponding error distributions. From the results obtained, it is observed that for the GARCH-type models the Generalized Error Distribution performed best because it reported the largest log likelihood values and the least AIC values across the models in comparison with the student-t distribution. This result is in tandem with those obtained in the research carried out by (Ekong & Onye, 2017).

Table 6: Forecast Performance Evaluation of the Models

Model	MSE	MAE
GARCH (1, 1)		
Student-*t*	0.000137131	0.00429223
GED	**0.000137117**	**0.004291467**
GARCH (1, 2)		
Student-*t*	0.000137128	0.004292156
GED	**0.000137116**	**0.004291438**
GARCH (2, 1)		
Student-*t*	0.00013713	0.004292215
GED	**0.000137117**	**0.004291462**
GARCH (2, 2)		
Student-*t*	0.000137128	0.004292155

GED	**0.000137116**	**0.004291449**
EGARCH (1, 1)		
Student-*t*	0.000137141	0.004292535
GED	**0.000137116**	**0.004291761**
APARCH (1,1)		
Student-*t*	0.000137192	0.004293818
GED	**0.000137115**	**0.004291434**

Values in Bold signify the least MSE and MAE loss functions

In this research, the MSE loss functions empirical results in Table 6 shows that in GARCH (1,1), GARCH (1,2) GARCH (2,1), GARCH (2,2), and APARCH (1,1), the Generalized Error distribution performed better across the model in the evaluation of the forecasting performance, since it returns the least MSE values. Generally, the APARCH (1, 1)-GED is the best fitting and forecasting model for the NGX-ASIR series which served as the proxy for the Nigeria Exchange Market owing to smallest MSE values it reported when compared to the other models. This is consistent with the outcome of AL-Najjar (2016) which stated that the model with the best fit is the best for forecasting.

4. Conclusion

In the study, attempts have been made to model the volatility of the Nigeria Stock Market proxy by the Nigeria All Share Index using the Generalized Autoregressive Conditional Heteroscedastic (GARCH) models under two error distributions. On the basis of the results obtained from the analysis on the NGX-ASIR data, it observed that most of the coefficients were statistically significant. The GARCH (1, 1), GARCH (1, 2) GARCH (2, 1) GARCH (2, 2) and APARCH (1, 1) performed relatively well in capturing some of common features of volatility. The study reported that NGX-ASIR series show volatility clustering and high persistence. This high persistence entails that a shock like the novel COVID-19 virus which increases volatility would have a long-lasting effect on the Nigeria Stock Market. From the empirical result obtained, it was demonstrated utilizing AIC criterion that the best fitting model was the APARCH (1, 1) with Generalized Error Distribution (GED). Also, the forecasting performance evaluation using MSE show that the APARCH (1, 1)-GED provides a better forecast performance for the Nigeria Stock Market amongst the competing models. This study has shown that the best fitting model also provides the best volatility forecasting performance.

Reference

Bentes, Sónia R. and Rui Menezes (2012), Entropy: A new measure of stock market volatility? Journal of Physics – Conference Series 394, 012033.

Bollerslev T. (1986). Generalised Autoregressive Conditional Heteroskedasticity. *Journal of Econometrics* 31, 307-327.

Caiado, J. (2004). Modelling and forecasting the volatility of the portuguese stock index PSI-20. *Estudos de Gestão*, *9*(1), 3-22.

Ding, Z., Granger, C. W., & Engle, R. F. (1993). A long memory property of stock market returns and a new model. *Journal of empirical finance*, *1*(1), 83-106.

Emenike, K. O., & Aleke, S. F. (2012). Modeling Asymmetric Volatility in the Nigerian Stock Exchange. European Journal of Business and Management, 4(12), 52-59.

Ekong, Christopher N. & Onye, Kenneth U., 2017. "Application of Garch Models to Estimate and Predict Financial Volatility of Daily Stock Returns in Nigeria," MPRA Paper 88309, University Library of Munich, Germany.

Engle, R. F. (1982). Autoregressive conditional heteroscedasticity with estimates of the variance of United Kingdom inflation. *Econometrica: Journal of the econometric society*, 987-1007.

Ibrahim, S. O. (2017). Forecasting the volatilities of the Nigeria stock market prices. *CBN Journal of Applied Statistics*, *8*(2), 23-45.

Iwada, E. M., Omoyeni, O. T., & Temitope, A. (2018). Modeling Volatility in Selected Nigerian Stock Market. *International Journal of Economics and Financial Management*, *3*(1), 30-43.

Lawrance, A. J. (2013). Exploratory graphics for financial time series volatility. *Journal of the Royal Statistical Society: Series C (Applied Statistics)*, *62*(5), 669-686.

Nelson, D. B. (1990). Stationarity and persistence in the GARCH (1, 1) model. *Econometric theory*, *6*(3), 318-334.

Okpara, G. C. (2011). Volatility modeling and the Nigerian stock return relationship in EGARCH-in-mean framework. *International Journal of Current Research*, *3*(8), 176-185.

Poon, S. H., & Granger, C. W. 2003), Forecasting volatility in financial markets: a review. In *Journal of Economic Literature, 41(2), 478–539.*

DISCRIMINANT ANALYSIS WITH LOGISTIC REGRESSION METHODS IN PREDICTION OF BABY'S WEIGHT AT BIRTH IN NIGER STATE, NIGERIA.

Gana, Y; and Usman, A.
Department of Statistics
Federal University of technology Minna, Nigeria
Corresponding Email: yahayagana963@gmail.com ; abu.usman@futminna.edu.ng

Abstract:
The study compares two statistical methods: Discriminantt analysis with Logistic regression model inpredicting birth weight of an expectant mother. Normal birth weight and Low birth weight. 240 cases of (infants) was observed with the following measurements considered maternal height (x_1), maternal weight (x_2), maternal age (x_3), baby's weight (x_4), baby's sex (x_5), gestational age (x_6) and parity (x_7) of an expectant mother, Discriminant Analysis classified the Normal birth weight correctly (64.6%) while it recorded (64.7%) success rate in classifying the Low birth weight. In the case of the Logistic regression, it recorded (76.8%) and (52.9%) success rate in classifying the Normal birth weight and Low birth weight respectively. The overall predictive performance of the two models was high with the Logistic regression having the highest value (65.8%) Among the seven characteristics examined, Maternal height, maternal age, Baby's weight, sex, gestational age and parity were not significant variables for identifying Birth weight by both methods while Mothers weight is important identifying variable for both except Mothers age which was significant in the Discriminant analysis. The study shows that both techniques estimated almost the same statistical significant coefficient and that the overall classification rate for both was good while either can be helpful in selection of birth weight however, given the failure rate to meet the underlying assumptions of Discriminant Analysis, Logistic Regression is preferable.

Keywords: Logistic Regression, Classification, Birth Weight, Discriminant Analysis.

Introduction

Birth weight is an important indicator for assessing future growth patterns of children and investigating direct health risks and in adulthood. It is a key variable in any longitudinal study of child health.

It is the weight of the child at birth and be defined as the baby's first weight gain in the first 60 minutes after birth. High birth weight refers to babies weighing more than 4kg, full-size or normal babies weighing between 2.5 kg and 4 kg, low birth weight (LBW) means babies weighing less than 2.5 kg, and low weight at birth (i.e less than 2.5 kg) increases prenatal death rates, causes range from premature birth to placental insufficiency. During pregnancy, the baby's birth weight can be estimated in different ways and the height of the fundus (the top of the mother's uterus) can be measured from the public bone. This measurement in centimetres generally corresponds to the number of weeks pregnant after week 20. The clinical manifestations of babies at birth vary, because many factors affect the size of the baby at birth. To determine if there is convergence between the two analytical methods of analysis classifiying birth weight into one of two populations (low birth weight and the normal birth weight).

Yarnold *et. al* (1994) stress that logistic regression and linear discriminant analyses are multivariate statistical methods and are two of the most popular methodologies for solving classification problems involving dichotomous class variable. Furthermore, view logistic regression as a tool to predict the probability of group membership in relation to several variables independent of their distribution, based on calculating the odds of having the outcome divided by the probability of not having it. It is an on-parametric and assumed a distribution free sample. The Discriminant analysis on the other hand is used to determine which set of variables discriminates between two or more naturally occurring groups and to classify an observation into these known groups. It is a parametric method and assumes that the sample comes from a normally distributed population and that the covariance matrices of the independent variables are the same for all groups.

Halperin *et. al.* (1971): compared the two methods and noted only small differences in the classification ability between the analytical procedures. Dattalo (1995) found that both methods performed well as classification technique but concluded that the logistic was more parsimonious and easier to interpret. Hyunjoon *et. al.* (2010) also found that the two models are equally effective in predicting restaurant bankruptcy, but concluded that the logit model is preferred for restaurant bankruptcy prediction because of its theoretical soundness. Antonogeorgos *et. al.* (2009) in evaluating factors associated with asthma prevalence among 10-12 years old children concluded that the two methods resulted in similar result while

Edokpayi *et. al.* (2013) compared the two methods in classifying and assessing the relative importance of the fruit form characteristics, but concluded that the two methods were of nearly equal value but logistic regression would be preferable whenever the normality assumption are violated.

Balogun *et. al.* (2014) compared the two methods in classifying and assessing drug offender characteristics, but concluded that the two methods gives closely value but logistic regression would be preferable whenever the normality assumption are violated.

Low birth weight is a major public health problem in developing countries including Nigeria. Epidemiological observations have shown that infants weighing less than 2,500 grams are approximately 20 times more likely to die than infants heavier, closely related to fetal morbidity and mortality and Infant. In India, 3.035% of babies are born with low birth weight and more than half of them are full-term. Low weight loss is an important contributor to the Millennium Development Goals (MDGs) to reduce child mortality. Actions to achieve the MDGs will need to ensure children have a good start in life by ensuring that women start their pregnancies healthy, are well nourished, and get through pregnancy and childbirth safely. Understanding the prevalence and factors contributing to and perpetuating this problem will help address this important cause of infant mortality in order to reduce and achieve the Millennium Development Goals. Identifying the factors that cause the still high rate of low birth weight and putting in place remedial measures to combat this problem should be seen as a major public health challenge. In this context, the present study was carried out to find out the prevalence of low birth weight in term infants and to discover maternal risk factors associated with low birth weight infants.

The objectives of the study are to: Estimate the probability of correct classifications and misclassifications respectively and determine which variables appear significant in classifying the dependent variable by inspection of the coefficient.

Material and Methods

The data for the study consist of seven maternal characteristics Maternal height (x_1), Maternal weight (x_2), Maternal age (x_3), Baby's weight (x_4), Baby's sex (x_5), Gestational age (x_6) and Parity (x_7) as the independent variables, and birth weight as the dependent variable.

Sample and Sampling Techniques

The study adopts a simple random sample (srs) techniques and the study uses data from Jumai Babangida Aliyu Maternal and Neonatal Hospital Minna, Niger State. It is based on information of 240 live births in the hospital from June to September, 2020. The data were collected by measuring the infant's birth weights, infant's gender of 240 deliveries and selected maternal variables.

Discriminant Analysis

Given a set of p independent variables X_1, X_2,...,X_p, (Maternal characteristics in this case), the technique attempt to derive a linear combination of these variables (Maternal characteristics) which best separate or discriminates the two groups (low birth weight and normal birth weight). The functions are generated from a sample of cases for which group membership is known; the functions can then be applied to new cases with measurements for the predictor variables, but unknown group membership.

In general form, The Discriminant function for this study is expressed in the form

$$Z = W_0 + W_1X_1 + W_2X_2 + \cdots + W_kW_k \quad (1)$$

where: Z = discriminant score; W_0 = discriminant constant; W_k= discriminant weight or coefficients; X_k = an independent variable or predictive variables.

The procedure automatically chooses a first function that will separate the groups as much as possible, it then chooses the second function that is both uncorrelated with the first function and provides as much further separation as possible. The procedure continues adding functions in this way until reaching the maximum number of functions as determined by the number of predictors and groups in the dependent variable. In two group discriminant function, there is only one discriminant function. The discriminant score obtained from the discriminant function shall classify the birth weight into one of the two groups.

In testing the classification performances of the discriminant function, use the overall hit ratio which is the same thing as percentage of the original group cases whichcorrectly classified, the dependent variables using the standardized discriminant coefficients. The greater the magnitude of the coefficients, the greater the impact of the variable as an identifying variable. However, to test the significance of the discriminant function as a whole we shall use the Wilks' Lambda. The analysis of variance (ANOVA) table for the discriminant function score is another overall test of the discriminant analysis model. If the probability value (p-value) is less than 0.05 (level of significance) means the model differentiates between the groups significantly better than chance.

Classification Rule

The classification rule is that;

$if \quad \hat{Y} \geq \hat{M} \quad classified\ as\ group\ one\ (\pi_1)andif \quad \hat{Y} < \hat{M} \quad classified\ as\ group\ two\ (\pi_2)$

where $\hat{Y}$ denote the Discriminant function, and $\hat{M}$ denote the mean Euclidean distance for Normal birth and Low birth weight groups

Logistic Regression

We shall let Y denote the drug data which is categorical and can take one of the two possible values, denoted 1 and 2 (Y_1= Low birth weight, Y_2=Normal birth weight).

Let $X = (x_1, x_2, \dots, x_6)$be the explanatory variables. This method uses the predicted probabilities to assign cases into the categories of the dependent variable and then compares the results with their actual categories. It can also be used to explain the effects of the explanatory on the dependent variables (Birth weight).

The logistic regression model can be defined mathematically as:

$$\pi(x) = \frac{e^{\beta_0+\beta_1 x_1+\cdots+\beta_n x_n}}{1+e^{\beta_0+\beta_1 x_1+\cdots+\beta_n x_n}} \quad (2)$$

Where π is the probability of the event occurring (i.e the probability of selecting a particular drug offenders). $X_1 + X_2 + \cdots + X_7$ are the independent or predictor variables and $\beta_1, \beta_2 \dots \beta_7$ are the coefficients representing the effects of the predictor variables and β_0 is the intercept (the value of the equation when all the X's are zero

Evaluation of the logistic regression model

In assessing the logistic regression model involves an overall evaluation of the model, the statistical significance of the individual regression coefficients, the goodness of fit statistics and the validation of predicted probabilities. A logistic model is said to provide a better fit if it demonstrates an improvement over the intercept only model. An improvement over this baseline is examined by using three inferential statistical tests: the likelihood ratio, score and Wald tests. The statistical significance of individual regression coefficients (i.e, β) is tested using the Wald test statistic The Hosmer-Lemeshow (H - L) is the inferential goodness of fit test used to assess the fit of a logistic model against actual outcome. The H – L statistic is a Pearson Chi-square statistic.

A test of assumption of multivariate normality and equal covariance matrices of the discriminant analysis

In order to decide which method to use, we consider the assumptions for the application of each one. In the case of discriminant evaluation a everyday distribution of the data and equal covariance matrices and that the violation of this assumption will render unreliable or invalid interpretation and inference of the result analysis

Normality Assumption

The simplest method of assessing normality is by producing a histogram. The normal plot, P – P or Q – Q plot can also be used to assess the normality of a distribution. It is also possible to use Kolmogorov-Smirnov test if a sample size is greater than 50 or Shapiro-Wilk test if sample size is smaller than 50. In the study analysis, since the sample size shall be greater than 50 the Kolmogorov-Smirnov test can use. The convention is that a significant value greater than 0.05 indicates normality of the distribution

Results and Discussion

The discriminant analysis and logistic model are analyzed using SPSS version 23.

Table 1: Independent variable

Variablecode	Description
X_1	Maternal height
X_2	Maternal weight
X_3	Maternal age
X_4	Baby's weight
X_5	Baby's sex
X_6	Gestational age
X_7	Parity

Table 2: Classification of data by Logistic Regression and Discriminant Function Methods

		PredictedGroupMembership			
ActualGroup	**No.ofcases**	**DiscriminantAnalysis**		**LogisticRegression**	
		1	2	1	2
1	83	64(64.6%)	35(35.4%)	76(76.8%)	23(23.2%)
2	157	30(35.3%)	55(64.7%)	40(47.1%)	45(52.9%)
Overall%correctlyclassified		64.7%		65.8%	

From the table 2 above, the classification performances of the two methods. There are 157 cases of normal birth and 83 cases of the low birth weight, discriminant analysis predicted correctly 64(64.6%) and misclassified 35(35.4%), while the logistic regression classified correctly 76(76.8%) and misclassified 23 (23.2%). The discriminant analysis classified correctly 55(64.7%) of the cases and misclassified 30(35.3%) while the logistic regression 45(52.9%) cases were correctly classified and misclassified 40(47.1%) of the cases. The overall percentage correct classification of the birth weight was 64.7% and 65.8% for the discriminant analysis and the logistic regression method respectively. The results have therefore shown that the overall classification rate for both methods was good and either can be helpful in predicting the possibility of detecting or selecting birth weight.

Table 3: Hosmer-Lemeshow

Step	Chi-square	Df	Sig
1	6.667	8	0.573

From table 3 above suggests that the model is a good fit to the data since $p = 0.573 > 0.05$. However, the chi-square statistic shows that the weight depend on the categorical data

Table 4: Variables and Coefficients for the Discriminant Analysis and the Logistic Regression models

DiscriminantAnalysis				LogisticRegression		
Independent Variables	**Wilk's Lambda**	**Canonical coefficient**	**p-values**	**Wald test**	**coefficient**	**p-values**
Constant	-	8.089	-	10.037	0.021	0.002
Maternal height	0.990	-0.074	0.180	0.029	0.012	0.864
Maternal weight	0.974	0.047	0.028	0.000	0.032	0.996
Baby's weight	0.977	0.083	0.142	15.475	0.289	0.000
Sex	1.000	-0.199	0.940	0.458	0.310	0.498
Gestational age	0.992	-0.789	0.226	0.832	3.570	0.362
Parity	0.865	0.723	0.007	1.278	0.776	0.028
Maternal age	0.765	0.004	0.044	1.679	0.543	0.015

From table 4 above, the Wilks' lambda was used to test which independent variables contributes significantly to the discriminant function. The F test of the Wilks' lambda shows that, two of the independent variables Maternal height, Baby's weight and sex were not significant ($p>0.05$), while the remaining variables Maternal weight, parity and maternal age is highly significant at ($p<0.05$). For logistic regression the coefficient for the classification equation and is used to assess the relative classifying importance of the dependent variable (Birth weight). The Wald statistic is used to test the null hypothesis that the coefficients of independent variables in the model are zero. From the table, only one of the mothers characteristics Mothers weight is significant with an associated $p<0.05$. However, the four other variables Mothers Height, Age, Babies weight and sex were not significant.

However in comparison, both methods identified almost the same variable. Mothers Weight is significant for both methods, while Mothers height, Baby's weight and sex were equally not significant for the two methods. Both methods however differ in the estimation of Mothers age. The direction of relationship was the same, but there were some extreme differences in the magnitude of the coefficients.

According to Andrew et. al, (1986), for purposes of parameter estimation, logistic regression is more robust than discriminant analysis. But as observed by Press et. al. (1978), if the populations are normal with identical covariance matrices, discriminant analysis estimators are preferred to logistic regression estimators.

Table 5: Test of Normality and equal covariance matrices

	Kolmogorov-Smirnov			Shapiro-Wilk		
	Statistic	**d.f.**	**Sig**	**Statistic**	**d.f.**	**Sig**
Maternal height	0.091	99	0.040	0.980	99	0.146
Maternal weight	0.154	99	0.000	0.847	99	0.000
Baby's weight	0.121	99	0.001	0.911	99	0.000
sex	0.092	99	0.037	0.984	99	0.264
Gestational age	0.353	99	0.000	0.635	99	0.000
Parity	0.232	99	0.342	0.123	99	0.022
Maternal age	0.332	99	0.443	0.231	99	0.432

From table 5 above, the result of the test of normality is presented. When the assumption for normality and equal covariance matrices were tested using the Kolmogorov-Smirnov test and Shapiro-wilk test respectively. The significant value of some of the classification variables were less than 0.05 while others were greater than 0.05, indicating that some of the variables were not normally distributed.

Conclusion and Recommendations

The study has compared empirically the logistic regression with linear discriminant analysis, both methods were of nearly equal value (64.7% and 65.8%), and almost selected the same set of The F test of the Wilks' lambda shows that, two of the independent variables Maternal height, Baby's weight and sex were not significant ($p>0.05$), while the remaining variables Maternal weight, parity and maternal age is highly significant at ($p<0.05$). For logistic regression the coefficient for the classification equation and is used to assess the relative classifying importance of the dependent variable (Birth weight). The Wald statistic is used to test the null hypothesis that the coefficients of independent variables in the model are zero. From the result of the study only one of the mother's characteristics i.e mother's weight is significant with an associated $p<0.05$. However, the four other variables mother's height, Age, Babies weight and sex were not significant.

The finding agrees with Montgomery *et. al.* (1987) and George Antonogeorgos *etal* (2009) that the two methods result in similar results. A test of assumptions of multivariate normality and equal covariance matrices of the discriminant analysis were not satisfied. We thus agree with the conclusion of Press *et. al,* (1978) that the use of logistic regression would be preferable whenever practical in situations where the normality assumptions are violated.

Reference

Balogun, O.S., Balogun, M.A., Abdulkadir, S.S. and Jibasen, D. (2014), A Comparison of the performance of Discriminant Analysis and the Logistic Regression methods in Classification of Drug Offenders in Kwara State. International Journal of Advanced Research, Vol.2, Issue10, page 280-286.

Dattalo, P. (1995), A Comparison of Discriminant Analysis and Logistic regression: Journal of Social Services Research, Volume19,Issue 3-4,pages121-144.

Edokpayi, A.A., Agho, C., Ezomo, J.E., Edosomwan, O.S. and Ogiugo, O.G. (2013). A Comparison of the Classification Performance of Discriminant Analysis and the Logistic Regression Methods in Identification of Oil Palm fruit Forms. A Paper Presented at the Annual Conference of Nigerian Statistical Association. 11-13th, September, 2013, pp20-26.

George Antonogeorgos, Demosthenes. B. Panagiotakos, Kostas. N. Priftis and AnastasiaTzonou (2009), Logistic Regression and Discriminant Analysis in evaluating factors associated With Asthma Prevalence among 10-12 year old children: Divergence and Similarity of the two Statistical Methods: International Journal Pediatrics.Volume2009, pp1-7.

Halperin, M.Blackwelder, Weverter, J.I. (1971): Estimationofthe Multivariate Logistic risk function: A Comparison of the discriminant function and Maximum Likelihood Approaches. J. Cnron. Dis. 24.125-158.

Hyunjoon Kim and ZhengGu (2010), Predicting Restaurant bankruptcy: A Logit model in Comparison with Discriminant Model; Tourism and Hospitality Research Journal, Vol.10, Pp171-187.

Kleinbaum, .D.G, Kupper, .L.L, Muller, .K.E., and Morgens-Tern, H. (1982), Epidemiologic Research: Principles and Quantitative Methods. Van Nostr and Reinhold Company, New York, p. 281-417.

Montgomery, N.E., White, M.E. and Martin, S.W. (1987), A Comparison of Discriminant analysis and Logistic Regression for the prediction of Coliform Mastitisin dairy Cows: Canadian Journal of Veterinary Research 51 (4) Pp 495-498.

Yarnold, P.R., Hart, L.A., and Soltysik, R.C. (1994), Optimizing the Classification Performance of Logistic Regression and Fisher's Discriminant Analysis: Journal of Educational and Psychological Measurement, 54,73-85

Multivariate Analysis of Dynamic Transmission of Coronavirus Disease with Control Measures in Nigeria.

Sheshi, M. M; and Usman, A.
Department of Statistics,
Federal University of Technology, Minna, Nigeria
Corresponding Author: sheshimm01@gmail.com

Abstract

Severe Acute Respiratory Syndrome (SARS Cov-2), COVID-19 (Coronavirus) emerged in Wuhan in early Dec ember 2019 and then spread exponentially across the globe. Although, a series of prevention strategies such as (lockdown, social-distancing, Hand Washing) have been enforced to control this pandemic. Based on the data issued by March 30, 2020 daily report, the epidemic of SARS-CoV-2 so far has caused 693224 cases and resulted in 33106 deaths in more than 200 countries. Referring to the data reported, World Health Organization declared the outbreak a pandemic. In this context, the purpose of the study is to analyse the dynamic transmission of coronavirus disease measures in Nigeria. Regression Analysis, General MANOVA and Principal Component Analysis (PCA) were utilized. After applying regression analysis, the regression analysis gives a standard trend for both control and transmission dynamics. From the General MANOVA, we observe that all the test statistic signify that there is no significant influence of the vaccine on the Geopolitical zones since there values are greater than the p-values. Also from the Principal Component Analysis on Confirmed, Recovered, Death, Active Cases, Testing, First dose, Second dose and Population, we observed that the eigenvalue for the components Confirmed cases of COVID-19 have the largest eigenvalue thus, it implies that the 86% of the variable accounts for the total variation of the data set. It is also clear from the PCA we conclude that the recovery rates for all the states in Nigeria are significantly higher than the mortality rate. Hence, this also implies that the vaccine plays a vital rule in reducing the spread of the disease in addition to the preventive measures based on the data obtain from NCDC COVID-19 website | covid19.ncdc.gov.ng

Keywords: Regression Analysis, General MANOVA and Principal Component.

1. Introduction

World Health Organization (WHO's) official definition state that COVID-19 is a viral disease caused by a new coronavirus. It was first reported on the 31st of December 2019 in the Wuhan Province of China. First recognized in the mid-1960s, COVID-19 belongs to a larger family of respiratory viruses called *Coronaviridae* and affects both humans and animals (Demeco et al., 2020) and are also known to cause severe respiratory infections such as severe acute respiratory syndrome (SARS-CoV), middle east respiratory syndrome (MERS-CoV), and now globally famous novel coronavirus severe acute respiratory syndrome (SARS-Cov-2) and the disease is named as COVID-19 by WHO. The disease infects the upper respiratory and gastrointestinal tract of birds and mammals. Owing to its slow mutation, the virus poses a treatment and control challenge. It manifests anywhere between 2 and 14 days of infection with the virus prevailing even after 27 days in some cases (Ali & Alharbi, 2020) and has an

average incubation period of 5.2 days (Li et al., 2020). The disease has average mortality duration of 6-24 days depending on prevailing clinical conditions of patients, their health, and age as well. Common infection symptoms include respiratory complications, high fever, dry cough, sore throat, sneezing, muscle pain, and fatigue. According to the WHO, COVID-19 can be transmitted from an infected person to one who is not infected upon contact, cough droplets, and sneezing where the virus enters the body through eyes, nose, or mouth (Centre for Disease Control (CDC), 2020). COVID-19 droplets can land at a distance of up to 1.8M and survive upwards of 2 hours to two days. Traces of the virus have also been found on infected people's stool but no infection through stool has been confirmed yet. The virus can be prevented and controlled through a variety of measures against daily routines, with the most effective one being the avoidance of touching one's mouth, nose, and eyes (NCDC, 2020). Other measures include avoiding close contact with infected people, remaining at home if infected, regularly cleaning and disinfecting surfaces, maintaining proper hygiene practices especially when coughing or sneezing, using facial covering equipment like face masks and face shields when in crowded places and regularly washing your hands with soap and plenty of water or hand sanitizers. Treatment for COVID-19 remains in the realm of uncertainties and the only care that patients of the virus have been getting is supportive. Experts for example argue that perhaps the best approach to treat COVID-19 is through proper prevention and management measures (Ali & Alharbi, 2020). However, scientists from all over the world have been working very hard towards finding a treatment for the disease or even better, a vaccine. It is in this spirit that numerous research laboratories from every corner of the world have invested so much in resources towards developing and manufacturing a vaccine that will hopefully help flatten the COVID-19 curve for all humanity's sake.

Two Arab nations Bahrain and United Arab Emirate (UAE) were among the first to conduct phase three clinical trials of the vaccine. Interim results from the vaccine's phase 3 trials in the UAE and Bahrain found the vaccine to have an 86% efficacy rate (Reuters, 2020). The UAE Ministry of Health also reported the vaccine to be 100% effective in the prevention of mild and severe COVID-19 cases (Reuters, 2020). Official phase 3 results were however not out at the time of writing this paper. The National Health Regulatory Authority (NHRA) on 13th of December released an official statement granting the vaccine's full approval based on data from trials conducted across several countries. Recently, China has also approved this vaccine and they claimed that the efficacy of this vaccine is 79%, although we do not have any published data available for this. The vaccine has been approved in various countries like the UAE and Bahrain where phase 3 trials were conducted as well as China where the vaccine is approved for general use. UAE had administered over 2 million doses of the vaccine while Bahrain had administered 97,000 doses as of mid-January.

2. Methodology

In this section, the data used for the research is described and the methodology frame work in achieving the research objective is presented.

2.1 Data Description

Regression Analysis, General MANOVA and Principal Component Analysis were utilized on NCDC COVID-19 data from the website | covid19.ncdc.gov.ng and *Demographic Statistics Bulletin 2017 (https://nigerianstat.gov.ng/download/775)* using SPSS IBM (26) and Minitab EXE.

2.1 Multiple Regression

The multiple regression model is given by:

$$\hat{y} = \beta_o + \beta_1 X_1 + \beta_2 X_2 + \beta_3 X_3 + \cdots + \beta_n X_n$$

Where $x_i = (x_{i\,1}, x_{i2}, \ldots, x_{in})$, for $i = 1, 2, 3, \ldots, n$ is called the independent variable e_i is the error term: $\underline{Y} = \underline{X}\underline{\beta}$, and

$$\beta = \begin{bmatrix} \beta_o \\ \beta_1 \\ \beta_2 \\ \beta_3 \\ \beta_4 \\ \vdots \\ \beta_n \end{bmatrix}, \text{ and } \quad \underline{X} = \begin{bmatrix} X_{11} & X_{12} & X_{13} & & X_{1n} \\ X_{21} & X_{22} & X_{23} & \cdots & X_{2n} \\ X_{31} & X_{32} & X_{33} & & X_{3n} \\ & \vdots & & \ddots & \vdots \\ X_{n1} & X_{n2} & X_{n3} & \cdots & X_{nn} \end{bmatrix}$$

Therefore $\beta = (X'X)^{-1} \times (X'Y)$

$SST = Y'Y - \mu$; $SST = Y'Y - \frac{(\sum Y)^2}{n}$; $\mu = \frac{(\sum Y)^2}{n} = \sum Y^2 - n\bar{Y}^2$ and $\bar{Y} = \frac{\sum Y}{n}$,

SSβ $= \beta' (X'Y)$ which impliesSSE $= TSS - SS\beta$.

2.3 General MANOVA

We have four basic test statistic for MANOVA
This include

1. Pillias Trace
2. Wilk's Lambda
3. Hottelling-Lawley Trace (T^2)
4. Roy's Maximum Root

Using the Characteristics Equation

$|BW^{-I} - \lambda I| = 0$

$$\text{Wilks Lambda} = \Lambda = \prod_{i=1}^{p} \frac{1}{1+\lambda_i}$$

$$Pillias\ Trace = \vee = \sum_{i=1}^{p} \frac{\lambda_i}{1+\lambda_i}$$

$$Hotelling = T^2 = \sum_{i=1}^{p} \lambda_i$$

$$Roy's\ Maximum\ Root = \theta = \frac{\lambda_{Largest}}{1+\lambda_{Laegest}}$$

2.4 Principal Components Analysis (PCA).

The main goal of PCA is to reduce the dimensionality in a set of correlated attributes into a smaller set of uncorrelated attributes that explain the majority of the variation in the original attributes. The sample data matrix of *n* number of samples that are resulted to *k* number of characterization methods can be represented by matrix X, where

$$X = \begin{bmatrix} x_{11} & x_{12} & x_{13} & & x_{1k} \\ x_{21} & x_{22} & x_{23} & \cdots & x_{2k} \\ x_{31} & x_{32} & x_{33} & & x_{3k} \\ & \vdots & & \ddots & \vdots \\ x_{n1} & x_{n2} & x_{n3} & \cdots & x_{nk} \end{bmatrix}$$

A deviate matrix D is constructed by mean-centreing the data of the matrix X. This is done by subtracting the mean of the data from each data point. Mean-centreing removes the arbitrary bias from measurements.

$$D = \begin{bmatrix} x_{11} - \bar{X}_1 & x_{12} - \bar{X}_2 & x_{13} - \bar{X}_3 & \cdots & x_{1k} - \bar{X}_k \\ x_{21} - \bar{X}_1 & x_{22} - \bar{X}_2 & x_{23} - \bar{X}_3 & & x_{2k} - \bar{X}_k \\ & \vdots & & \ddots & \vdots \\ x_{n1} - \bar{X}_1 & x_{n2} - \bar{X}_2 & x_{n3} - \bar{X}_3 & \cdots & x_{nk} - \bar{X}_k \end{bmatrix}$$

The covariance matrix of the data set S, is constructed by,

$$S = \frac{D.D^T}{n}$$

Resulting to;

$$S = \begin{bmatrix} c_{11} & c_{12} & c_{13} & & c_{1k} \\ c_{21} & c_{22} & c_{23} & \cdots & c_{2k} \\ c_{31} & c_{32} & c_{33} & & c_{3k} \\ & \vdots & & \ddots & \vdots \\ c_{n1} & c_{n2} & c_{n3} & \cdots & c_{nk} \end{bmatrix}$$

where,

$$Cij = 1/n\{(xi - \bar{X}i)(xj - \bar{X}j)\}(i,j = 1,2,\dots,k)$$

To avoid the scale-dependency of the covariance matrix it is useful to normalize the data by dividing each matrix element by its standard deviation.

Normalized matrix element C_{ij},

Correlation matrix is symmetric due to the fact, $C_{ij} = C_{ij}$ and it is always real and positive definite.

3 Result and Discussion

3.1 Regression Analysis: Geopolitical Zones versus First Dose, Second Dose

Table 1 indicate the regression trend for the control measure under consideration (AstraZeneca).

Table 1:

Predictor	*Coef*	*SE Coef*	*T*	*P*	*VIF*
Constant	2.7247	0.4363	6.25	0.000	
First Dose	0.4611	0.2648	1.74	0.091	35.7
Second Dose	−0.6526	0.4331	−1.51	0.141	35.7

S = 1.69488 R-Sq = 11.9% R-Sq(adj) = 6.8%

The regression equation is

Geopolitical Region $= 2.72 + 0.461\ First\ Dose - 0.653\ Second\ Dose$
The result from table 2 shows the contribution of the vaccine.

Table 2: Analysis of Variance

Source	*DF*	*SS*	*MSS*	*F*	*P*
Regression	2	13.250	6.625	2.31	0.115
Residual Error	34	97.669	2.873		
Total	36	110.919			

From the table p-value (significant value) = 0.115 which is greater than 0.05. Thus it implies that there is no significant influence of the vaccine on the Geopolitical regions. Figure 1 shows the residual plot for test of Normality of the variables.

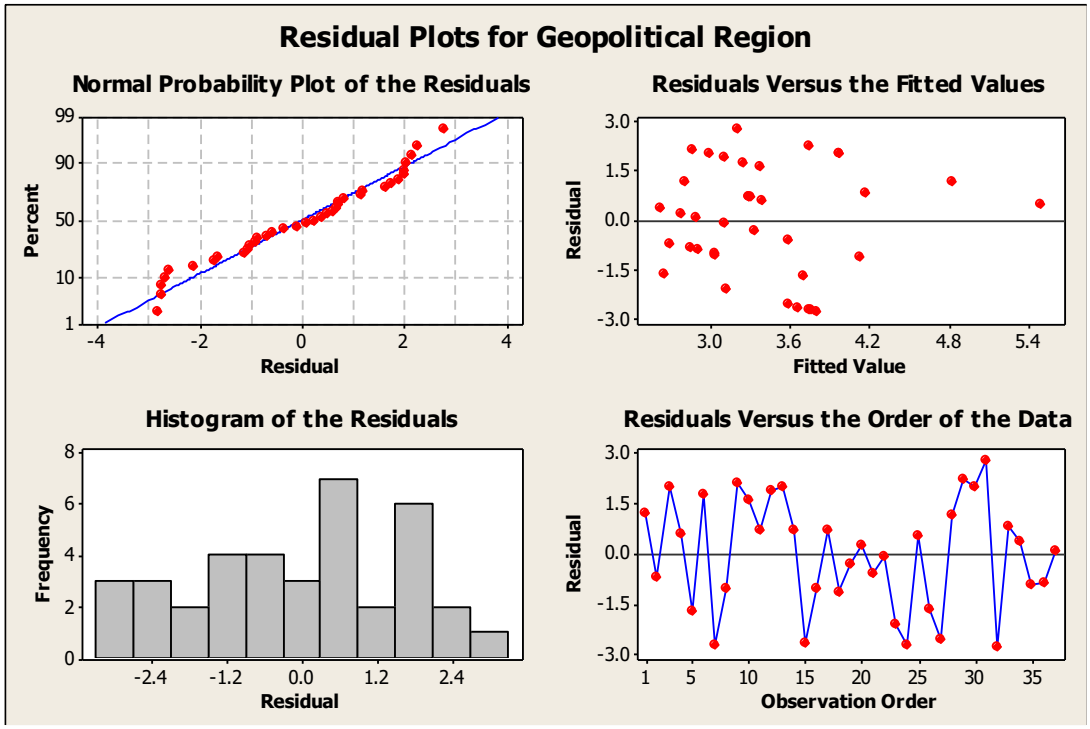

Fig 1: Residual Plot for Control Measures

From the graph we observed that the normal probability plot shows that the data is normally distributed since the data points revolve along around the straight line. Base on the residual versus the fitted value it is also shown that the variables are normally distributed since data points that falls below and above the marginal line are approximately equal. Base on the histogram plot we observed that the data points are normally distributed. Finally from the residual versus the order of the data, we observed that there exist no outliers in the data points.

3.2 Regression Analysis: Geopolitical Zones versus Confirmed, Recovered, Death

Table 3 shows the regression trend of the transmission dynamic. The regression equation is
Geopolitical Zones = 3.00 + 0.00273 Confirmed - 0.00300 Recovered + 0.0193 Death

Table 3: Regression trend of the transmission dynamic

Predictor	*Coef*	*SE Coef*	*T*	*P*	*VIF*
Constant	3.0044	0.3857	7.79	0.000	
Confirmed	0.002731	0.001400	1.95	0.060	2945.7
Recovered	-0.002995	0.00148	-2.02	0.051	2952.6
Death	0.019264	0.009389	2.05	0.048	7.8

S = 1.60929 R-Sq = 22.9% R-Sq(adj) = 15.9%
The result from table 4 shows the effect of the transmission dynamics.

Table 4: Analysis of Variance

Source	*DF*	*SS*	*MSS*	*F*	*P*
Regression	3	25.455	8.485	3.28	0.033
Residual Error	33	85.464	2.590		
Total	36	110.919			

From the table p-value (significant value) = 0.03 which is less than 0.05. Thus it implies that there is significant influence of the effect of the transmission dynamics on the Geopolitical regions. Figure 2 shows the residual plot for test of Normality of the variables.

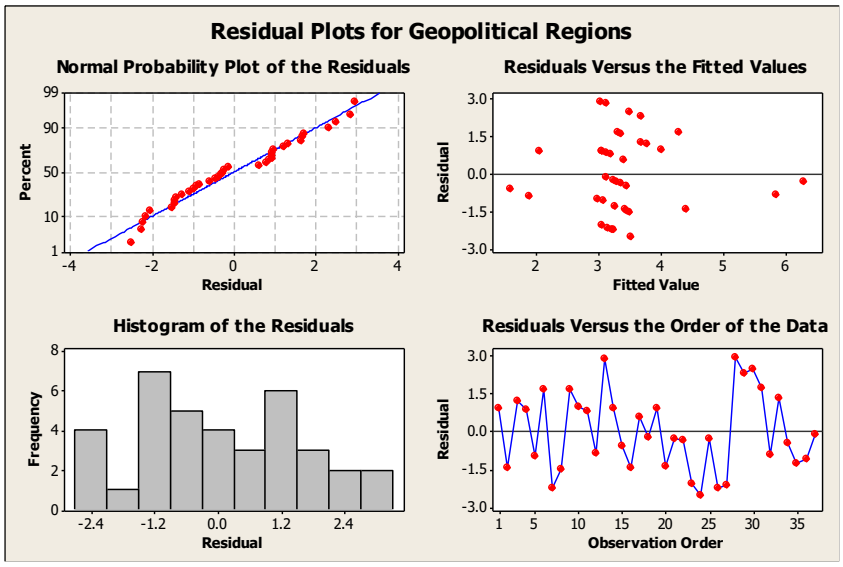

Fig. 2: Residual Plot for Transmission Dynamics

From the graph we observed that the normal probability plot shows that the data is normally distributed since the data points revolve along around the straight line. Base on the residual versus the fitted value it is also shown that the variables are normally distributed since data points that falls below and above the marginal line are approximately equal. Base on the histogram plot we observed that the data points are normally distributed. Finally from the residual versus the order of the data, we observed that there exist no outliers in the data points.

3.3 Compare Mean: First Dose versus Second Dose

Table 5:

Report

Geopolitical Zones		First Dose	Second Dose
North Central	Mean	7.103657	3.871700
	N	7	7
	Std. Deviation	3.9950374	2.5641360
	Std. Error of Mean	1.5099822	.9691523
North East	Mean	4.419833	2.644267
	N	6	6
	Std. Deviation	1.3349524	.5771159
	Std. Error of Mean	.5449920	.2356066
North West	Mean	6.461300	3.828314
	N	7	7
	Std. Deviation	3.2400625	2.3188587
	Std. Error of Mean	1.2246285	.8764462
South East	Mean	3.782000	1.922620
	N	5	5
	Std. Deviation	.5533170	.3929127
	Std. Error of Mean	.2474509	.1757159
South South	Mean	5.017283	2.680383
	N	6	6
	Std. Deviation	1.9525646	1.0460287
	Std. Error of Mean	.7971312	.4270394
South West	Mean	13.822183	7.502150
	N	6	6
	Std. Deviation	13.2616186	8.3892323
	Std. Error of Mean	5.4140331	3.4248898
Total	Mean	6.849203	3.796595
	N	37	37
	Std. Deviation	6.3751401	3.8972790
	Std. Error of Mean	1.0480666	.6407087

From Table 5 it is observed the First and Second dose those not have equal mean across all the geopolitical zones. Similarly Southwest have the highest Standard Error in the first dose (5.414) and second dose (3.424).

3.4 General Linear Model: First Dose, Second Dose versus Geopolitical Region

MANOVA for Geopolitical Region
s = 2 m = 1.0 n = 14.0

Table 6:

Criterion	*Test Statistic*	*F*	*Num*	*Denom*	*P*
Wilks'	0.57589	1.906	10	60	0.062
Lawley – Hotelling	0.70761	2.052	10	58	0.044
Pillai's	0.44073	1.752	10	62	0.089
Roy's	0.66418				

In table 6 we observe that all the test statistic signify that there is no significant influence of the vaccine on the Geopolitical zones since there values are greater than the p-values.

Table 7: SSCP Matrix (adjusted) for Geopolitical Region

	First Dose	*Second Dose*
First Dose	395.8	212.9
Second Dose	212.9	115.4

Table 8: SSCP Matrix (adjusted) for Error

	First Dose	*Second Dose*
First Dose	1067.3	668.9
Second Dose	668.9	431.4

Table 9: Partial Correlations for the Error SSCP Matrix

	First Dose	*Second Dose*
First Dose	1.00000	0.98589
Second Dose	0.98589	1.00000

Table 10: EIGEN Analysis for Geopolitical Region

Eigenvalue	0.6642	0.04343
Proportion	0.9386	0.06137
Cumulative	0.9386	1.00000

Table 10 above indicates that first dose accounts for 94% of the variation while second dose accounts for only 6% of the variation.

3.5 Principal Components Analysis (PCA).

Table 11 indicates KMO and Bartlett's test of sampling adequacy.

Table 11: KMO and Bartlett's Test

Kaiser-Meyer-Olkin Measure of Sampling Adequacy.		.838
Bartlett's Test of Sphericity	Approx. Chi-Square	543.475
	Df	10
	Sig.	.000

This measure varies between 0 and 1, and value closer to 1 are better. This test provide minimum standard which should be passed before principal component analysis. Thus the 5 variables pass KMO test since 0.838 is greater than 0.5. We start by implementing a Principal Component (PC) on all 36 States, for variables: (1) Confirmed (2) Recovered (3) Death (4) Active Cases (5) Testing (6) First dose (7) Second dose and (8) Population**.**

Table 12: Principal Component Analysis: Confirmed, Recovered, Death, Active Cases, Testing Eigen analysis of the Correlation Matrix

Factors	1	2	3	4	5	6	7	8
Eigenvalue	6.8893	0.7161	0.1804	0.1143	0.0690	0.0179	0.0130	0.0000
Proportion	0.861	0.090	0.023	0.014	0.009	0.002	0.002	0.000
Cumulative	0.861	0.951	0.973	0.988	0.996	0.998	1.000	1.000

From Table 12 we observed that the eigenvalue for the components Confirmed cases of COVID-19 have the largest eigenvalue thus, it implies that the 86% of the variable accounts for the total variation of the data set while, 14% is due to error.

Table 13: Component Analysis

Variable	PC1	PC2
Confirmed	-0.376	0.176
Recovered	-0.375	0.178
Death	-0.361	0.055
Active Cases	-0.353	0.149
Testing	-0.365	0.092
Population	-0.226	-0.949
First Dose	-0.373	-0.019
Second Dose	-0.374	-0.047

The table 13 is the component analysis derived from table 12, it also indicates that first dose, second dose and death are statistically significant since PC2 show there value are less or equal to 0.05.

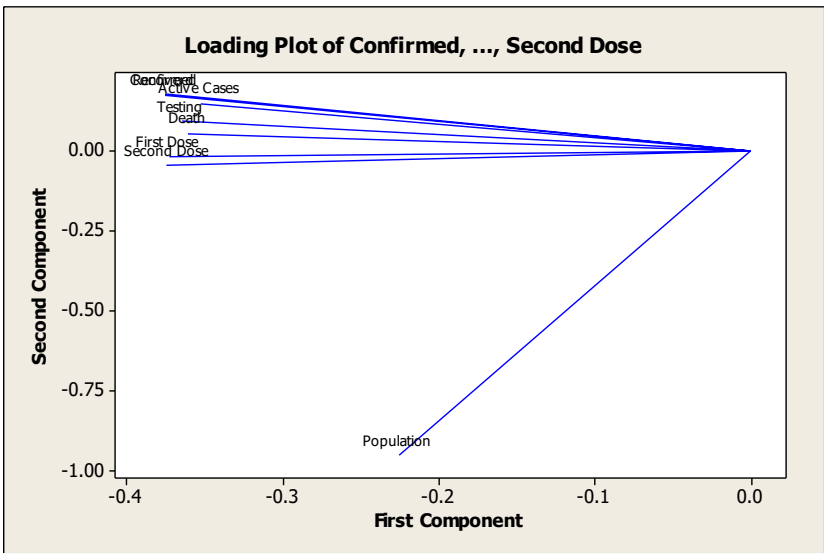

Fig. 3: Factor Loading Plot

Figure 3 shows the loading plot of Confirmed, Recovered, Death, Active Cases, Testing, First dose, Second dose and Population. From the graph we observed that Confirmed, Recovered, Death, Active Cases, Testing, First dose, Second dose are positively and highly correlated while Population have a negative correlation.

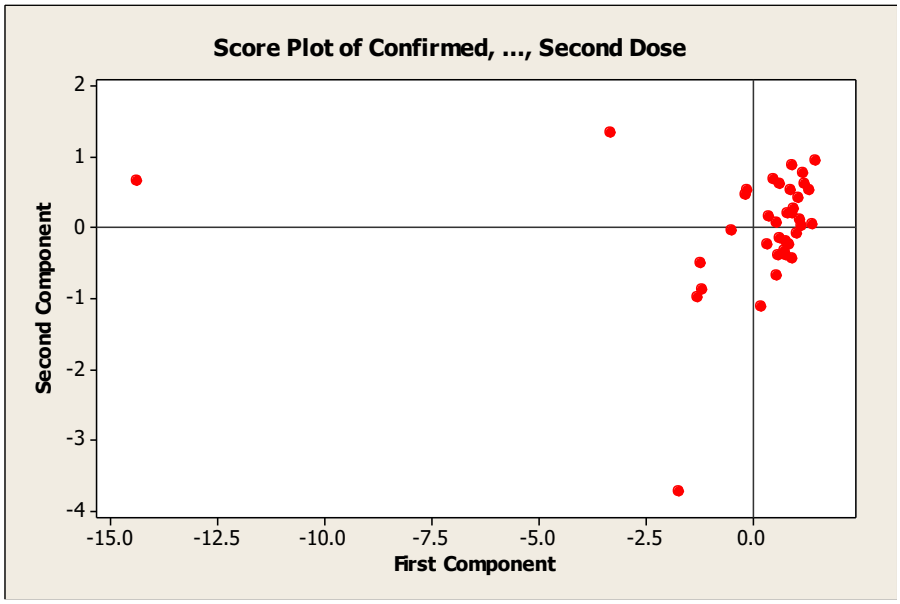

Fig. 4: Score Plot

Figure 4. Shows how the State with the lowest levels of vaccination cluster to the left of the Origin $(0,0)$, *and* those with the largest levels have high scores for their First Component.

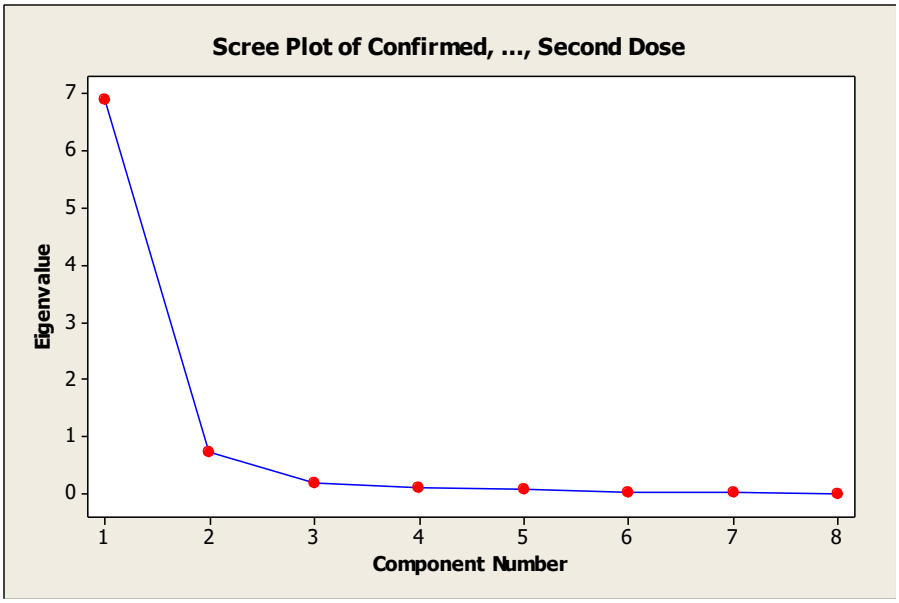

Fig 5: Scree plot

Figure 3 shows a rough bar plot of the eigenvalues. The scree plot shows that the first factor is indeed the largest and we have the impression that this factor will adequately approximate this data and account for 86% of the variation. The eigenvalues and the cumulative proportions of the explained variance are displayed in Table 3 and Table 4 considering the eigenvalue as criterion for retaining a variable in Scree plot in figure 3, it would be reasonable to retain the first PCs. A commonly accepted rule says that it suffices to keep only PCs with eigenvalues larger than 1. However, the second eigenvalues is approximately close to 1; so that the first 2 PCs can be retain to explain 86% of the total variability.

4. Conclusion

Based on the finding of the study using the given information, the principal component analysis of Confirmed, Recovered, Death, Active Cases, Testing, First dose, Second dose and Population, we observed that the eigenvalue for the components Confirmed cases of COVID-19 have the largest eigenvalue thus, it implies that the 86% of the variable accounts for the total variation of the data set. It is also clear from the PCA that the recovery rates for all the states in Nigeria are significantly higher than the mortality rate, this also implies that the vaccine (AstraZeneca) plays a vital rule in reducing the spread of the disease. The regression analysis gives a standard trend for both control and transmission dynamics. And the regression model is given by:

$$Geopolitical\ Zones_{Control} = 2.72 + 0.461\ First\ Dose - 0.653\ Second\ Dose$$

and

$Geopolitical\ Zones_{Transmission}$ = 3.00 + 0.00273 Confirmed - 0.00300 Recovered + 0.0193 Death.

It was also observed from the General MANOVA that all the test statistic signify that there is no significant influence of the vaccine on the Geopolitical zones since there values are greater than the p-values. It is obvious that the first and second dose of the vaccine have significant influence on some of the Geopolitical Zones, hence we can say that the vaccine plays important role in the fight against COVID-19 in addition to the preventive measure.

References

Ali, I., & Alharbi, O. M. L. (2020). COVID-19: Disease, management, treatment, and social impact. Science of the Total Environment, 728, 138861, doi:10.1016/j.scitotenv.2020.138861.

Centre for Disease Control (CDC). (2020). COVID-19 overview and infection prevention and control priorities in non-US healthcare settings. Retrieved from https://www.cdc.gov/coronavirus/2019-ncov/hcp/non-us-settings/overview/index.html.

Clinical Trials. (2020). Clinical trials [Online]. Retrieved from https://www.clinicaltrialsarena.com/comment/COVID-19-vaccine-efficacy-approval/

Demographic Statistics Bulletin (2017) *(https://nigerianstat.gov.ng/download/775)*

Demeco, A., Marotta, N., Barletta, M., Pino, I., Marinaro, C., Petraroli, A., Moggio, L. and Ammendolia, A., (2020). Rehabilitation of patients post-COVID-19 infection: a literature review. Journal of International Medical Research, 48(8).

Li, Q., Guan, X., Wu, P., Wang, X., Zhou, L., Tong, Y., Feng, Z. (2020). Early transmission dynamics in Wuhan, China, of novel coronavirus-infected pneumonia. TheNew England Journal of Medicine, 382(13), 1199–1207. doi:10.1056/NEJMoa2001316

Population by State *(https://web.archive.org/web/20110519235026/http://www.population.gov.ng/files/nationafinal.pdf)*. *population.gov.ng*

Reuters. (2020). Reuters.com. [Online]. Retrieved from https://www.reuters.com/article/health-coronavirusemirates/uae-says-sinopharm-vaccine-has-86-efficacyagainst-covid-19 idUKKBN28J0G4

A NOTE ON COMBUSTIBLE FOREST MATERIAL (CFM) OF WILDLAND FIRE SPREAD

Zhiri, A. B. [1*]; Olayiwola, R. O.[2] and Somma, S. A.[3]
[1,2,3]Department of Mathematics
Federal University of Technology, Minna, Nigeria.
[*1]a.zhiri@futminna.edu.ng
[2]olayiwola.rasaq@futminna.edu.ng
[3]sam.abu@futminna.edu.ng

Abstract:
In this paper, a mathematical model for combustible forest material of a wildland fire is presented. The equations describing the fractional components of forest fire were carefully studied. The reaction before a forest can burn or before fire can spread must involves fuel, heat and oxygen. The coupled dimensionless equations describing the phenomenon have been decoupled using perturbation method and solved analytically using eigen function expansion technique. The results obtained were graphically discussed and analysed. The study revealed that varying Radiation number and Peclet energy number enhances volume fractions of dry organic substance and moisture while they reduced volume fraction of coke.

Keywords& Phrases : Combustion, eigen function expansion, fire, fuel, ignition

1. Introduction

Fire is a natural disturbance that occurs in most terrestrial ecosystems around the world. It is also a tool that has been used by humans to manage a wide range of natural ecosystems worldwide. As such, it can produce a spectrum of effects on Combustible Forest Material (CFM) (dry organic substance, moisture and coke). CFM are part of the key factors to determine whether forest fire will escalate or not. Fons (1946) was the first to attempt to describe fire spread using a mathematical model. He focused his attention on the head of the fire where the fine fuels carry the fire and where there is ample oxygen to support combustion. He further, pointed out that sufficient heat is needed to bring the adjoining fuel to ignition temperature at the fire front. Therefore, he reasoned that fire spread in a fuel bed can be visualized as proceeding by a series of successive ignition and that its rate is controlled primarily by the ignition time and the distance between particles. Finney *et al.* (2013) reported that most studies on the effect of Fuel Moisture Content (FMC) have focused on dead fuel moisture (Md); thus, understanding on the mechanisms of fire spread in live vegetation is minimal.

Rossa *et al.* (2016) investigate live fuel complexes which are usually tall and have high fuel loads, so are difficult to reproduce in the laboratory. On the other hand, in field fires, live and dead fuels are usually combined in variable proportions and there is a lack of control over ambient parameters, which complicates the detection and isolation of FMC effects on fire be haviour. However, vegetation types dominated by live fuel (such as shrub lands) contribute

to a significant fraction of fire activity worldwide. Schaaf*et al.* (2007) examined that theoretical formulations of fire spread applied to shrub fuels or crown fires usually predict a strong spread ratedecrease with increased fuel moisture.

Perminov (2018) worked on mathematical modelling of wildland fires initiation and spread using a coupled atmosphere-forest fire setting, he stated that mathematical model gives an opportunity to describe the different conditions of the crown forest fires spread taking account different weather conditions, state of combustible forest materials, which allows applying the given model for prediction and preventing fires. It overestimates the rate of crown forest fire spread that depends on crown properties: bulk density, moisture content of forest fuel, wind velocity and the influence of boundary layer of atmosphere.

The purpose of this paper is to investigate the resultant effects of the dimensionless parameters as involved in the system in relation to CFM. We established an analytical solution using eigen function expansion technique.

2. Materials and Method

Model Formulations

Here we extend the work of (Perminov, 2018) in regards to wildfire spread model. We assume that the gas phase is made up of only oxygen, there is thermal equilibrium between the gas and solid phases, pressure and wind velocity of the forest canopy are constant, ash is neglected and the forest environment consist of five-phase porous medium which are dry organic substance (Matter), water in liquid state (Moisture), solid pyrolysis product (coke), ash and gas phase. Under these assumptions, the equations that describes wildland fire propagation are:

$$\left.\begin{aligned}\rho_g\left(\frac{\partial C_{ox}}{\partial t}+v\frac{\partial C_{ox}}{\partial x}\right)=\frac{\partial}{\partial x}\left(\rho_g D_T\frac{\partial C_{ox}}{\partial x}\right)-\frac{\alpha}{C_{pg}\Delta h}\left(C_{ox}-C_{ox_\infty}\right)-\\ \left(1-\alpha_c\right)k_1\rho_s\varphi_s C_{ox}e^{-\frac{E_1}{RT}}-k_2\rho_m T^{\frac{1}{2}}\varphi_m C_{ox}e^{\frac{-E_2}{RT}}-k_3 S_\sigma\rho_g\left(1+\frac{M_c}{M_1}C_{ox}\right)\varphi_c C_{ox}e^{\frac{-E_3}{RT}}\end{aligned}\right\} \quad (1)$$

$$\left.\begin{aligned}\left(\phi\rho_g C_{pg}+\left(1-\phi\right)\sum_{i=1}^{s+m+c}\rho_i C_{pi}\varphi_i\right)\frac{\partial T}{\partial t}+\rho_g C_{pg}v\frac{\partial T}{\partial x}=\frac{\partial}{\partial x}\left(\lambda_T\frac{\partial T}{\partial x}\right)-\frac{\alpha}{\Delta h}\left(T-T_\infty\right)\\ -4K_R\sigma T^4-k_2\rho_m q_2 T^{\frac{1}{2}}\varphi_m e^{\frac{-E_2}{RT}}+k_3 S_\sigma\rho_g q_3\varphi_c C_{ox}e^{\frac{-E_3}{RT}}\end{aligned}\right\} \quad (2)$$

$$\rho_s\frac{\partial\varphi_s}{\partial t}=-R_s,\ \rho_m\frac{\partial\varphi_m}{\partial t}=-R_m,\ \rho_c\frac{\partial\varphi_c}{\partial t}=-\alpha R_s-\frac{M_c}{M_1}R_c \quad (3)$$

$$\left.\begin{aligned}\varphi_s\left(x,0\right)=\varphi_{so},\ \varphi_m\left(x,0\right)=\varphi_{mo},\ \varphi_c\left(x,0\right)=\varphi_{co},\ C_{ox}\left(x,0\right)=C_{ox_o},\ C_{ox}\left(0,t\right)=C_{ox_\infty}\\ C_{ox}\left(\mathrm{L},t\right)=C_{ox_\infty},\ T\left(x,0\right)=T_o,\ T\left(0,t\right)=T_\infty,\ T\left(\mathrm{L},t\right)=T_\infty\end{aligned}\right\}$$

(4)

Such that;

$$\left.\begin{aligned} R_s &= k_1\varphi_s\rho_s \exp\left(-\frac{E_1}{RT}\right) \\ R_m &= k_2\varphi_m T^{\frac{1}{2}}\rho_m \exp\left(-\frac{E_2}{RT}\right) \\ R_c &= k_3 S_\sigma \rho_g \varphi_c C_{ox} \exp\left(-\frac{E_3}{RT}\right) \end{aligned}\right\} \quad (5)$$

where;

$(\varphi_s, \varphi_m, \varphi_c)$ define volume fractions of the multiphase reactive medium, that is φ_s corresponds to dry organic substance, φ_m is the moisture in liquid drop state combined with CFM, φ_c is coke(condensed pyrolysis product), C_{ox} is the concentration of oxygen, T is the temperature (in Kelvin), t is the time, x is a coordinate in the system of coordinates connected with the centre of an initial fire (distance), T_∞ is the unperturbed ambient temperature, $k_j, j = 1,2,3$ are the pre- exponential factors of chemical reactions, $E_j, j = 1,2,3$ are the activation energy of chemical reactions, C is the concentration, R is the universal gas constant, S_σ is the specific surface of the condensed product of pyrolysis (coke), v is the equilibrium wind velocity vector, U is the reference velocity, λ_T is the turbulent thermal conductivity, C_{ox_∞} is the unperturbed density of concentration of oxygen, $P_i, i = (s,m,c)$ is the i^{-th} phase density, that is ρ_s is the density of dry organic substance, ρ_m is the density of moisture, ρ_c is the density of coke, ρ_g is the density of gas phase (a mix of gases), Δh is the crown height, M_c is the molecular mass of carbon, M_1 is the mass of combustible forest material (CFM), C_{pg} is the thermal capacity of a gas phase, $q_j, j = 2,3$ defines heat effects of processes of evaporation of burning, D_T is the diffusion coefficient, α is the coefficient of heat exchange between the atmosphere and a forest canopy, R_s, R_m, R_c are mass rates of reactions of dry CFM pyrolysis (chemical decomposition of substance by heating with allocation of combustible gases), of moisture evaporation from CFM (drying), coke burning, α_c is the coke number of combustible forest material (CFM), σ is the Stefan-BoltzMann constant, K_R is the integrated absorptance, $C_{p_i}, i = (s,m,c)$ is the i^{-th} phase of thermal capacity, s is the dry organic substance, m is the moisture, c is the coke, ox is the oxygen (O_2).

Our mathematical modelabove consists of equations (1)—(3) such that (1) and (2) corresponds to mass concentration of oxygen and energy balance respectively, (3) describes the volume fractions of the multiphase reactive medium (dry organic substance, moisture and coke respectively), (4) is the initial and boundary conditions and (5) is the mass rate of chemical reaction that describes the speed of CFM.

3. Method of Solution

3.1 Non-dimensionalisation

We make the variables in equation (1) – (4) dimensionless by introducing the following dimensionless variables:

$$\left.\begin{aligned} x' = \frac{x}{L},\ t' = \frac{Ut}{L},\ v' = \frac{v}{U},\ \psi_1 = \frac{\varphi_s}{\varphi_{so}},\ \psi_2 = \frac{\varphi_m}{\varphi_{mo}},\ \psi_3 = \frac{\varphi_c}{\varphi_{co}},\ \phi = \frac{C_{ox} - C_{ox_\infty}}{C_{ox_o} - C_{ox_\infty}} \\ \in = \frac{RT_0}{E},\ \theta = \frac{E\left(T - T_o\right)}{RT_o^{\,2}},\ f = \frac{E_1}{E_3},\ r = \frac{E_2}{E_3} \end{aligned}\right\} \quad (6)$$

Then equation (1)—(4) (after dropping prime) becomes;

$$\left.\begin{aligned} \frac{\partial \phi}{\partial t} + v\frac{\partial \phi}{\partial x} = \frac{\partial}{\partial x}\left(D_1 \frac{\partial \phi}{\partial x}\right) - \beta_1 \phi - \beta_2 \psi_1 \left(\phi + q\right) e^{\frac{f\theta}{1+\in\theta}} \\ -\beta_3 \left(1+\in\theta\right)^{\frac{1}{2}} \psi_2 \left(\phi + q\right) e^{\frac{r\theta}{1+\in\theta}} - \beta_4 \psi_3 \left(\phi + p\right)\left(\phi + q\right) e^{\frac{\theta}{1+\in\theta}} \end{aligned}\right\} \quad (7)$$

$$\left.\begin{aligned} \frac{\partial \theta}{\partial t} + v\frac{\partial \theta}{\partial x} = \frac{\partial}{\partial x}\left(\lambda_1 \frac{\partial \theta}{\partial x}\right) - \alpha_1 \left(\theta + \gamma_1\right) - R_a \left(1 + 4 \in \theta\right) - \delta \psi_2 \left(1+\in\theta\right)^{\frac{1}{2}} e^{\frac{r\theta}{1+\in\theta}} \\ +\delta_1 \psi_3 \left(\phi + q\right) e^{\frac{\theta}{1+\in\theta}} \end{aligned}\right\} \quad (8)$$

$$\left.\begin{aligned} \frac{\partial \psi_1}{\partial t} = -a\psi_1 e^{\frac{f\theta}{1+\in\theta}};\ \frac{\partial \psi_2}{\partial t} = -b\psi_2 \left(1+\in\theta\right)^{\frac{1}{2}} e^{\frac{r\theta}{1+\in\theta}};\ \\ \frac{\partial \psi_3}{\partial t} = \beta\psi_1 e^{\frac{f\theta}{1+\in\theta}} - \gamma\left(\phi + q\right)\psi_3 e^{\frac{\theta}{1+\in\theta}} \end{aligned}\right\} \quad (9)$$

$$\left.\begin{aligned} \psi_1\left(x,0\right) = 1,\ \ \psi_2\left(x,0\right) = 1,\ \ \psi_3\left(x,0\right) = 1 \\ \phi\left(x,0\right) = 1,\ \ \ \phi\left(0,t\right) = 0,\ \ \ \phi\left(1,t\right) = 0 \\ \theta\left(x,0\right) = 0,\ \ \ \theta\left(0,t\right) = \sigma_1,\ \ \ \theta\left(1,t\right) = \sigma_1 \end{aligned}\right\} \quad (10)$$

where;

$$
\left.
\begin{aligned}
&a=\frac{k_1 L e^{\frac{-fE_1}{RT_o}}}{U},\quad b=\frac{k_2 T_o^{\frac{1}{2}} L e^{\frac{-rE_3}{RT_0}}}{U},\quad \beta=\frac{\alpha_c k_1 \rho_s \varphi_{so} L e^{\frac{-fE_3}{RT_o}}}{U\rho_c \varphi_{co}},\ \gamma=\frac{M_c k_3 S_\sigma \rho_g L}{M_1 U \rho_c}\left(C_{ox_o}-C_{ox_\infty}\right)e^{\frac{-E_3}{RT_o}},\\
&q=\frac{C_{ox_\infty}}{C_{ox_o}-C_{ox_\infty}},\quad D_1=\frac{D_T}{LU}=\frac{1}{P_{em}},\ \beta_1=\frac{\alpha L}{C_{pg}\Delta h U},\ \beta_2=\frac{(1-\alpha_c)k_1\rho_s\varphi_{so}L}{\rho_g U}e^{\frac{-fE_3}{RT_o}},\\
&\beta_3=\frac{k_2\rho_m T_o^{\frac{1}{2}}\varphi_{mo}Le^{\frac{-rE_3}{RT_o}}}{\rho_g U},\ \beta_4=\frac{k_3 S_\sigma \rho_g \frac{M_c}{M_1}\left[C_{ox_o}-C_{ox_\infty}\right]L\varphi_{co}e^{\frac{-E_3}{RT_o}}}{\rho_g U},\ p=\frac{\frac{M_1}{M_c}+C_{ox_\infty}}{C_{ox_o}-C_{ox_\infty}},\\
&\lambda_1=\frac{\lambda_T}{L\rho_g C_{pg}U}=\frac{1}{P_e},\quad \alpha_1=\frac{\alpha L}{\rho_g C_{pg}U},\ R_a=\frac{4K_R\sigma L T_o^{\,3}}{\rho_g C_{pg}\in U},\ \delta=\frac{k_2\rho_m q_2 T_o^{\frac{1}{2}}L\varphi_{mo}e^{\frac{-rE_3}{RT_o}}}{\rho_g C_{pg}\in T_o U},\\
&\delta_1=\frac{k_3 S_\sigma \rho_g q_3 \varphi_{co} L\left(C_{ox_o}-C_{ox_\infty}\right)}{\rho_g C_{pg}\in T_o U}e^{\frac{-E_3}{RT_o}},\ \gamma_1=\frac{T_o-T_\infty}{\in T_o},\quad \sigma_1=\frac{T_\infty-T_o}{\in T_o}
\end{aligned}
\right\}
$$

(11)

3.2 Approximate Analytical Solution

After Applying perturbation method to decouple equations (7)—(10), we then use direct integration and eigenfunction expansion technique, to obtain the approximate analytical solution of equations (7)—(10) as follows:

$$\phi(x,t)=\sum_{n=1}^{\infty}Ae^{-c_1t}\sin n\pi x+v\left(\sum_{n=1}^{\infty}\left(\begin{array}{l}-2A_{49}\sum_{n=1}^{\infty}Ate^{-c_1t}-2A_{50}\sum_{n=1}^{\infty}\left[\frac{A_1}{c_1}+A_{53}e^{-c_2t}-A_{54}e^{-c_1t}\right]\\ -A_{56}\left[1-e^{-c_1t}\right]-2A_{51}\sum_{n=1}^{\infty}\sum_{n=1}^{\infty}A_{52}\left[\begin{array}{l}AA_1te^{-c_1t}-A_{55}e^{-(c_1+c_2)t}\\ +A_{55}e^{-c_1t}\end{array}\right]\\ -2A_{42}\sum_{n=1}^{\infty}\sum_{n=1}^{\infty}A_{52}\left[\begin{array}{l}\frac{A_1^{\,2}}{c_1}+A_{57}e^{-c_2t}+A_{58}e^{-2c_2t}-\frac{A_1^{\,2}}{c_1}e^{-c_1t}\\ -A_{57}e^{-c_1t}-A_{58}e^{-c_1t}\end{array}\right]\\ -2A_{43}\sum_{n=1}^{\infty}\sum_{n=1}^{\infty}\sum_{n=1}^{\infty}\left[\begin{array}{l}AA^2{}_1te^{-c_1t}-A_{59}e^{-(c_1+c_2)t}\\ -A_{59}e^{-(c_1+c_2)t}-A_{60}e^{-(c_1+2c_2)t}\\ +A_{59}e^{-c_1t}+A_{59}e^{-c_1t}+A_{60}e^{-c_1t}\end{array}\right]\\ +2A_{44}\sum_{n=1}^{3}\sum_{n=1}^{3}A_{61}\left[1-e^{-c_1t}\right]-2A_{45}\sum_{n=1}^{\infty}\sum_{n=1}^{\infty}A_{52}\left[\begin{array}{l}AA_1te^{-c_1t}\\ -A_{55}e^{-(c_1+c_2)t}\\ +A_{55}e^{-c_1t}\end{array}\right]\\ +2A_{46}\sum_{n=1}^{\infty}\sum_{n=1}^{\infty}\sum_{n=1}^{\infty}\left[A_{62}e^{-2c_1t}+A_{63}e^{-(2c_1+c_2)t}-A_{62}e^{-c_1t}-A_{63}e^{-c_1t}\right]\end{array}\right)\sin n\pi x \qquad (12)$$

$$\theta(x,t)=\left(\sigma_1+\sum_{n=1}^{\infty}\left(A_1+\left(b_n-A_1\right)e^{-c_2t}\right)\sin n\pi x\right)+ v\left(\sum_{n=1}^{\infty}\left(\begin{array}{l}-2\frac{A_{72}}{c_2}\left[1-e^{-c_2t}\right]-2A_{73}\sum_{n=1}^{\infty}\left[\frac{A_1}{c_2}+\left(b_n-A_1\right)te^{-c_2t}-\frac{A_1}{c_2}e^{-c_2t}\right]\\ -2A_{68}\sum_{n=1}^{\infty}\sum_{n=1}^{\infty}A_{52}\left[\begin{array}{l}\left[1-e^{-c_2t}\right]\frac{A_1^{\,2}}{c_2}+2A_1\left(b_n-A_1\right)te^{-c_2t}\\ +\left[e^{-c_2t}-1\right]\frac{\left(b_n-A_1\right)^2}{c_2}\end{array}\right]\\ +2A_{69}\sum_{n=1}^{\infty}\frac{A}{\left(c_2-c_1\right)}\left[e^{-c_1t}-e^{-c_2t}\right]+2A_{70}\sum_{n=1}^{\infty}\sum_{n=1}^{\infty}A_{52}\left[\begin{array}{l}\frac{AA_1}{\left(c_2-c_1\right)}e^{-c_1t}-\frac{A\left(b_n-A_1\right)}{c_1}e^{-(c_2+c_1)t}\\ -\frac{AA_1}{\left(c_2-c_1\right)}e^{-c_2t}+\frac{A\left(b_n-A_1\right)}{c_1}e^{-c_2t}\end{array}\right]\end{array}\right)\sin n\pi x\right) \qquad (13)$$

$$\psi_1(x,t)=1+v\left(-A_3\sum_{n=1}^{\infty}A_2\sin n\pi x-a_6\left(t+\left(\left(\sigma_1t+\sum_{n=1}^{\infty}\left(A_1t-A_2e^{-c_2t}\right)\sin n\pi x\right)\right)\right)\right) \qquad (14)$$

$$\psi_2(x,t)=1+v\left(-a_7\left(\begin{array}{l} t+r(e-2)\left(\sigma_1 t+\sum_{n=1}^{\infty}\left(A_1 t-A_2 e^{-c_2 t}\right)\sin n\pi x\right)+ \\ \frac{1}{2}\in\left(\sigma_1 t+\sum_{n=1}^{\infty}\left(A_1 t-A_2 e^{-c_2 t}\right)\sin n\pi x\right)+ \\ \frac{1}{2}\in\left(r(e-2)\right)\left(\begin{array}{l}\sigma^2{}_1 t+2\sigma_1\left(\sum_{n=1}^{\infty}\left(A_1 t-A_2 e^{-c_2 t}\right)\sin n\pi x\right) \\ +\sum_{n=1}^{\infty}\sum_{n=1}^{\infty}\left(\begin{array}{l}A_1{}^2 t-\frac{2A_1}{c_2}(b_n-A_1)e^{-c_2 t} \\ -\frac{(b_n-A_1)^2}{2c_2}e^{-2c_2 t}\end{array}\right)\sin^2 n\pi x\end{array}\right) \\ -a_7\left(A_7+\sum_{n=1}^{\infty}B_1\sin n\pi x\right)\sum_{n=1}^{\infty}A_2\sin n\pi x\end{array}\right)\right) \quad (15)$$

$$\psi_3(x,t)=1+v\left(\begin{array}{l} a_9\left(A_8 t+A_9\sum_{n=1}^{\infty}\left(A_1 t-A_2 e^{-c_2 t}\right)\sin n\pi x\right) \\ +a_8\left(\begin{array}{l}A_{10}\sum_{n=1}^{\infty}\frac{A}{c_1}e^{-c_1 t}\sin n\pi x+A_{11}\sum_{n=1}^{\infty}\sum_{n=1}^{\infty}\left(B_2 e^{-c_1 t}+B_3 e^{-(c_1+c_2)t}\right)\sin^2 n\pi x \\ -A_{12}t-A_{13}\sum_{n=1}^{\infty}\left(A_1 t-A_2 e^{-c_2 t}\right)\sin n\pi x\end{array}\right) \\ +a_9 A_9\sum_{n=1}^{\infty}A_2\sin n\pi x-a_8\left(\begin{array}{l}A_{10}\sum_{n=1}^{\infty}\frac{A}{c_1}\sin n\pi x+A_{11}\sum_{n=1}^{\infty}\sum_{n=1}^{\infty}(B_4)\sin^2 n\pi x \\ +A_{13}\sum_{n=1}^{\infty}A_2\sin n\pi x\end{array}\right)\end{array}\right) \quad (16)$$

where;

$$c_1=\left(\beta_1+D_1(n\pi)^2\right),\ A=\frac{2\left[1-(-1)^n\right]}{n\pi},\ b_1=\left(4R_a\in+\alpha_1\right),\ b_2=\left(\sigma_1\left(4R_a\in+\alpha_1\right)+\left(R_a+\alpha_1\gamma_1\right)\right),$$

$$c_2=\left(b_1+\lambda_1(n\pi)^2\right),\ A_1=\frac{2b_2\left[(-1)^n-1\right]}{n\pi c_2},\ A_2=\left(\frac{b_n-A_1}{c_2}\right),\ A_3=a_6 f(e-2),\ A_4=r(e-2),$$

$$A_5=\frac{1}{2}\in,\ A_6=\in\left(r(e-2)\right)\sigma_1,\ B=\frac{b_n-A_1}{2},\ B_1=(2A_1+B),\ A_7=\left(A_4+A_5+A_6\right),\ b_n=\frac{2\sigma_1}{n\pi}\left[(-1)^n-1\right]$$

$$A_8=\left(1+f(e-2)\sigma_1\right),\ A_9=f(e-2),\ A_{10}=\left(1+(e-2)\sigma_1\right),\ A_{11}=(e-2),\ B_2=\frac{AA_1}{c_1},$$

$$B_3=\frac{A(b_n-A_1)_1}{c_1+c_2},\ A_{12}=\left(1+(e-2)\sigma_1\right)q,\ A_{13}=(e-2)q,\ B_4=\left(B_2+B_3\right),\ A_{14}=\left(1+f(e-2)\sigma_1\right)q,$$

$$A_{15}=f(e-2)q,\ A_{16}=\left(1+r(e-2)\sigma_1\right),\ A_{17}=r(e-2),\ A_{18}=\left(1+r(e-2)\sigma_1\right)q,A_{19}=r(e-2)q,$$

$$A_{20}=\frac{1}{2}\in\left(\left(1+r(e-2)\sigma_1\right)\sigma_1\right),\ A_{21}=\frac{1}{2}\in r(e-2)\sigma_1,\ A_{22}=\frac{1}{2}\in\left(\left(1+r(e-2)\sigma_1\right)\sigma_1 q\right),$$

$$A_{23}=\frac{1}{2}\in r(e-2)\sigma_1 q,\ A_{24}=\frac{1}{2}\in\left(1+r(e-2)\sigma_1\right),\ A_{25}=\frac{1}{2}\in r(e-2),\ A_{26}=\frac{1}{2}\in\left(1+r(e-2)\sigma_1\right)q,$$

$$A_{27}=\frac{1}{2}\in r(e-2)q,\ A_{28}=(p+q)\left(1+(e-2)\sigma_1\right),\ A_{29}=(p+q)(e-2),\ A_{30}=(pq)\left(1+(e-2)\sigma_1\right),$$

$$A_{31}=(pq)(e-2),A_{32}=\left(a_1A_{14}+a_2A_{18}+a_2A_{22}+a_3A_{30}\right),\ A_{33}=\left(a_1A_{16}+a_2A_{20}\right),\ A_{34}=\left(a_2A_{19}+a_2A_{23}+a_2A_{26}\right),$$

$$A_{35}=\left(a_2A_{17}+a_2A_{21}+a_2A_{22}+a_2A_{24}\right),\ A_{36}=\frac{1}{2}a_1A_8,\ A_{37}=\frac{1}{2}a_1A_{15},\ A_{38}=\frac{2}{3}a_1A_9,\ A_{39}=\frac{1}{2}A_{33},\ A_{40}=\frac{1}{2}A_{34},$$

$$A_{41}=\frac{2}{3}A_{35},\ A_{42}=\frac{2}{3}a_2A_{27},\ A_{43}=\frac{3}{8}a_2A_{25},\ A_{44}=\frac{2}{3}a_3A_{10},\ A_{45}=\frac{2}{3}a_3A_{29},\ A_{46}=\frac{3}{8}a_3A_{11},\ A_{47}=\frac{1}{2}a_3A_{38},$$

$$A_{48}=\frac{1}{2}a_3A_{31},\ A_{49}=\left(A_{36}+A_{39}+A_{47}\right),\ A_{50}=\left(A_{37}+A_{40}+A_{48}\right),\ A_{51}=\left(A_{38}+A_{41}\right),\ A_{52}=\left[\frac{1-(-1)^n}{n\pi}\right],$$

$$A_{53}=\frac{b_n-A_1}{c_1-c_2},\ A_{54}=\frac{A_1(c_1-c_2)+c_1(b_n-A_1)}{c_1(c_1-c_2)},\ A_{55}=\frac{A(b_n-A_1)}{c_2},\ A_{56}=2\frac{A_{32}A_{52}}{c_1},\ A_{57}=\frac{2A_1(b_n-A_1)}{c_1-c_2},$$

$$A_{58}=\frac{(b_n-A_1)^2}{(c_1-2c_2)},\ A_{59}=\frac{AA_1(b_n-A_1)}{c_2},\ A_{60}=\frac{A(b_n-A_1)^2}{2c_2},\ A_{61}=\frac{A_{52}A^2}{c_1},\ A_{62}=\frac{A^2A_1}{c_1},\ A_{63}=\frac{A^2(b_n-A_1)}{(c_1+c_2)},$$

$$A_{64}=\left(a_4A_{16}+a_4A_{20}-a_5A_{12}\right),\ A_{65}=\frac{a_4A_{17}}{2},\ A_{66}=\frac{a_4A_{21}}{2},\ A_{67}=\frac{a_4A_{24}}{2},\ A_{68}=\frac{2a_4A_{25}}{3},\ A_{69}=\frac{a_5A_{10}}{2},$$

$$A_{70}=\frac{2a_5A_{11}}{3},\ A_{71}=\frac{a_5A_{13}}{2},\ A_{72}=\left(A_{64}A_{52}\right),\ A_{73}=\left(A_{65}+A_{66}+A_{67}-A_{71}\right)$$

The computation were done using computer symbolic algebraic package MAPLE to generate the graphs.

4. Results and Discussion

We solve the systems of partial differential equations describing the fractional components of forest fire. We decoupled the equations using perturbation method. The effectof Radiation number (R_a) and Pecletenergy number (P_e) on Volume fractions of dry organic substance $\psi_1(x,t)$, moisture $\psi_2(x,t)$ and coke $\psi_3(x,t)$ were vividly discussed and analysed. Analytical solution given by equations (12)—(16), is computed using computer symbolic algebraic package MAPLE 17 to generate the graphs. The numerical results obtained from the method are then shown in Figures1, 2, 3, 4, 5 and 6.

Figure 1adisplays the graph of volume fraction of dry organic substance $\psi_1(x,t)$ against time t for different values of Radiation number (R_a). It is observed that the volume fraction of dry organic substance decreases with time and increases as the Radiation number increases.

Figure 1bdepicts the graph of volume fraction of dry organic substance $\psi_1(x,t)$ against distance x for different values of Radiation number (R_a). It is observed that the volume fraction of dry organic substance increases but later decreases along the distance and maximum volume fraction of dry organic substance increases as the Radiation number increases.

Figure 2adepicts the graph of volume fraction of moisture $\psi_2(x,t)$ against time t for different values of Radiation number (R_a). It is observed that the volume fraction of moisture decreases with time and increases as the Radiation number increases.

Figure 2b displays the graph of volume fraction of moisture $\psi_2(x,t)$ against distance x for different values of Radiation number (R_a). It is observed that the volume fraction of moisture increases but later decreases along the distance and maximum volume fraction of moisture increases as the Radiation number increases.

Figure 3a displays the graph of volume fraction of coke $\psi_3(x,t)$ against time t for different values of Radiation number (R_a). It is observed that the of volume fraction of coke increases with time and decreases as the Radiation number increases.

Figure 3b depicts the graph of volume fraction of moisture $\psi_2(x,t)$ against distance x for different values of Radiation number (R_a). It is observed that the volume fraction of coke

decreases but later increases along the distance and minimum volume fraction of coke decreases as the Radiation number increases.

Figure 4a depicts the graph of volume fraction of dry organic substance $\psi_1(x,t)$ against time t for different values of Peclet energy number (P_e). It is observed that the volume fraction of dry organic substance decreases with time and increases as Peclet energy number increases.

Figure 4b displays the graph of volume fraction of dry organic substance $\psi_1(x,t)$ against distance x for different values of Peclet energy number (P_e). It is observed that the volume fraction of dry organic substance increases but later decreases along the distance and maximum volume fraction of dry organic substance increases as the Peclet energy number increases.

Figure 5a depicts the graph of volume fraction of moisture $\psi_2(x,t)$ against time t for different values of Peclet energy number (P_e). It is observed that the of volume fraction of moisture decreases with time and increases as the Peclet energy number increases.

Figure 5b depicts the graph of volume fraction of moisture $\psi_2(x,t)$ against distance x for different values of Peclet energy number (P_e). It is observed that the volume fraction of moisture increases but later decreases along the distance and maximum volume fraction of moisture increases as the of Peclet energy number increases.

Figure 6a displays the graph of volume fraction of coke $\psi_3(x,t)$ against time t for different values of Peclet energy number (P_e). It is observed that the of volume fraction of coke increases with time and decreases as the Peclet energy number increases.

Figure 6b depicts the graph of volume fraction of coke $\psi_3(x,t)$ against distance x for different values of Peclet energy number (P_e). It is observed that the volume fraction of coke decreases but later increases along the distance and decreases as Peclet energy number increases.

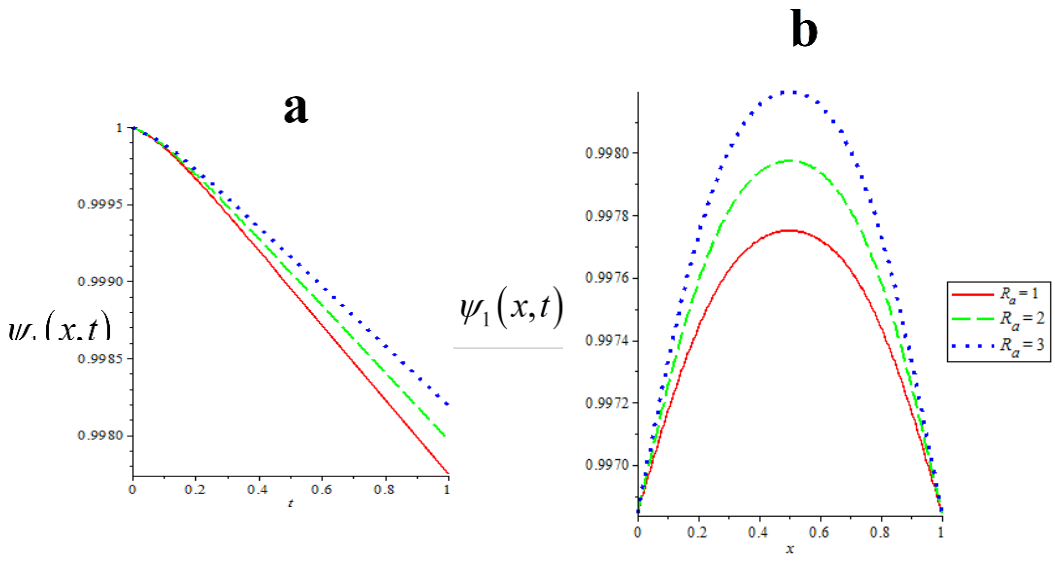

Figure 1: Effect of Radiation number (R_a) on volume fraction of dry organic substance.

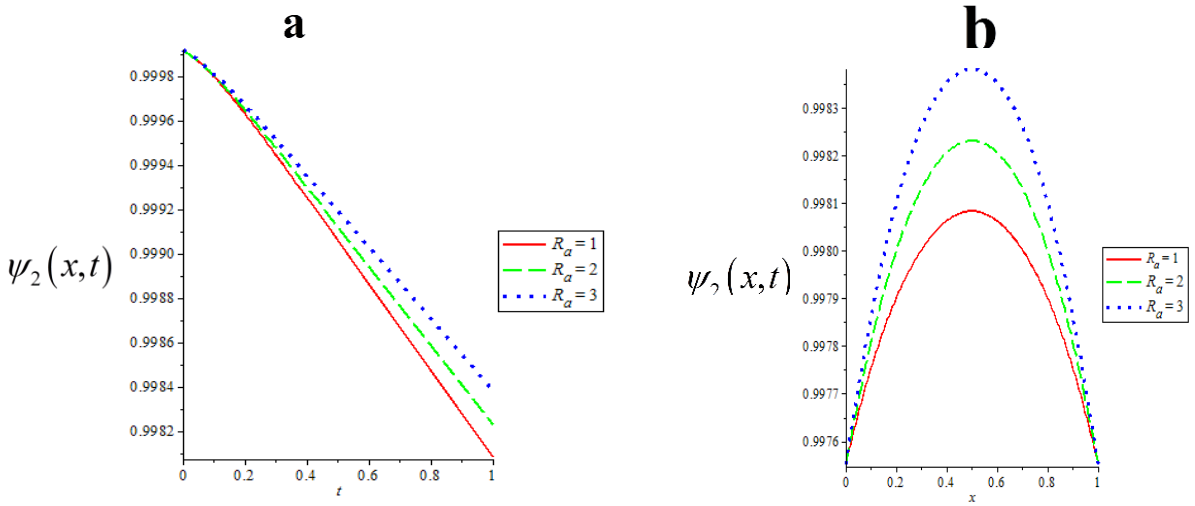

Figure 2: Effect of Radiation number (R_a) on volume fraction of moisture.

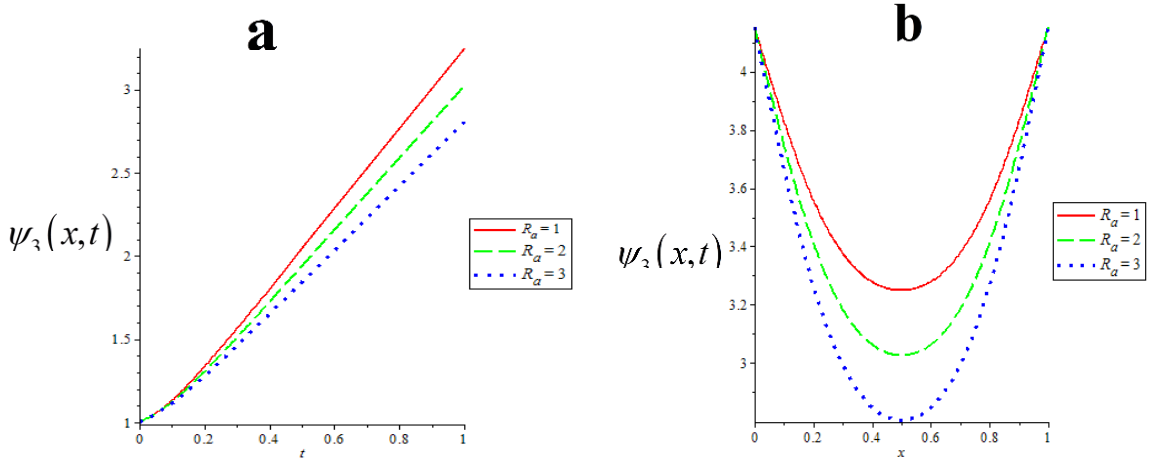

Figure 3: Effect of Radiation number (R_a) on volume fraction of coke.

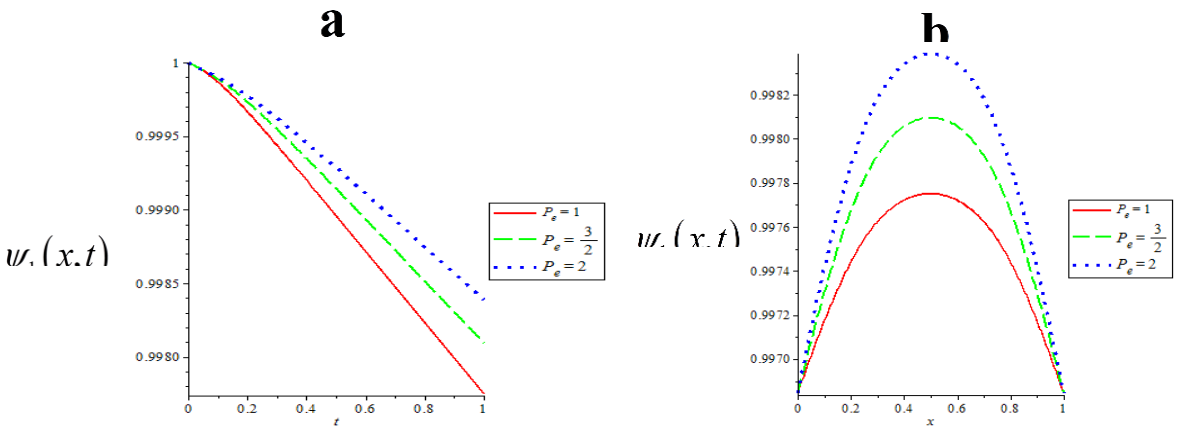

Figure 4: Effect of Peclet energy number (P_e) on volume fraction of dry organic substance.

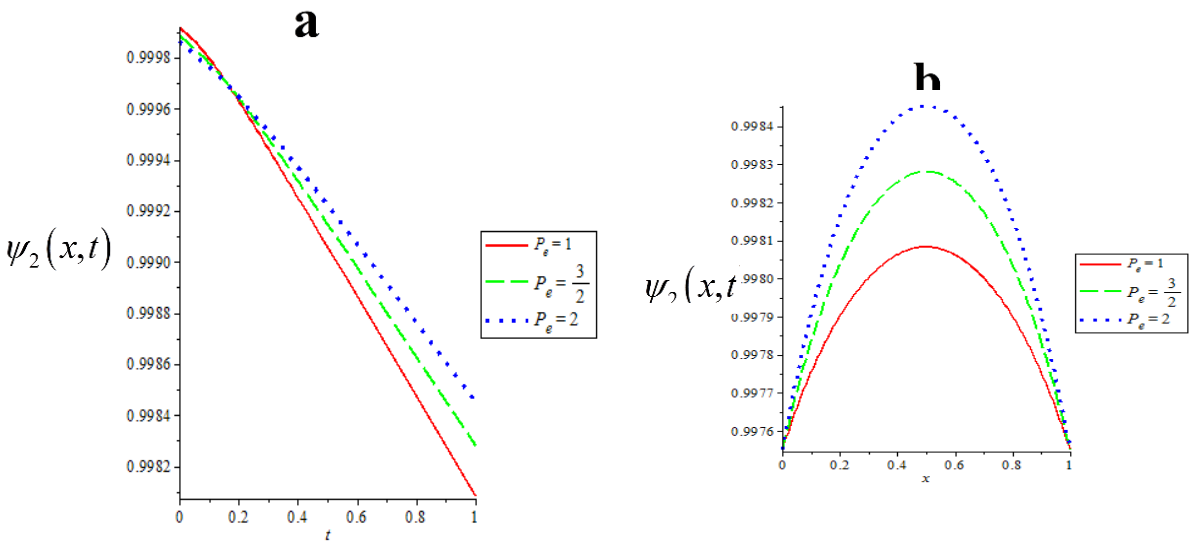

Figure 5: Effect of Peclet energy number (P_e) on volume fraction of moisture.

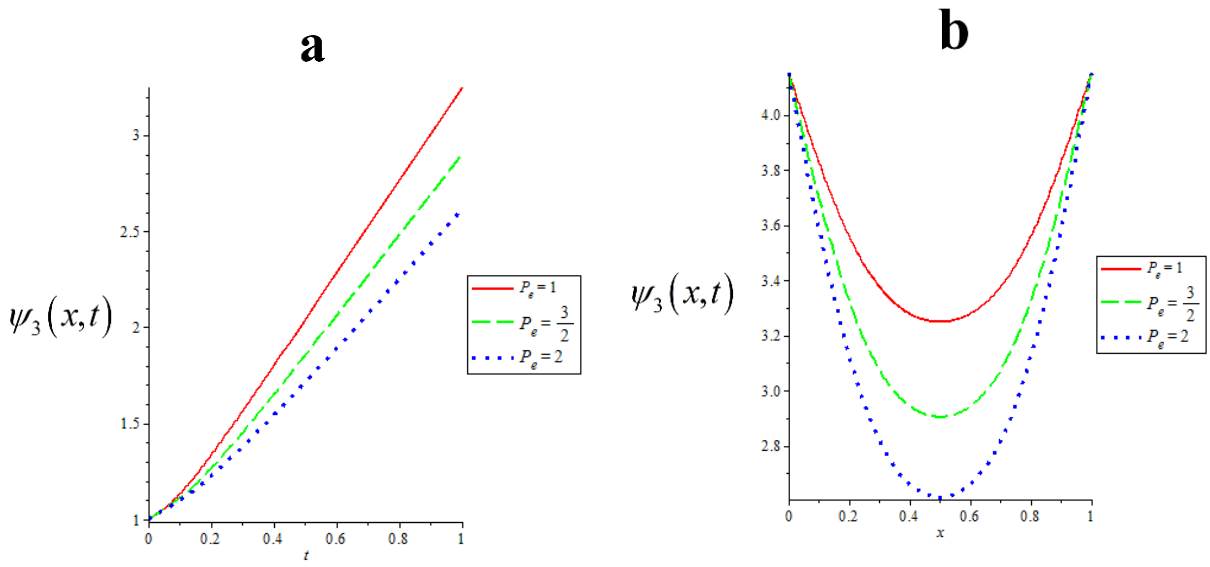

Figure 6: Effect of Peclet energy number (P_e) on volume fraction of coke

5. Conclusion

From the results of our studies we conclude that radiation number and peclect energy number enhance the volume fractions of dry organic substance and moisture and decrease volume fraction of coke. These occur as a result of varying the dimensionless parameters as demonstrated in Figures 1, 2, 3, 4, 5, and 6 respectively. The inference drawn from this study is that an increase in Radiation number and Peclet energy number reduces the burning rate of dry organic substance and dehydration of moisture. With continuous removal of heat from a burning scene, the CFM are better preserved. Based on this knowledge, the fire fighters or combaters are better equipped to manage CFM.

References

Finney, M. A., Cohen, J. D., McAllister, S. S. & Jolly, W. M. (2013) On the need for a theory of wildland fire spread. *International Journal of Wildland Fire* **22**(1), 25–36. doi:10.1071/WF11117

Fons, W. (1946). Analysis of fire spread in light forest fuels. *J. Agr. Res.* 72(3):93-121, illus.

Perminov, V. A. (2018). Mathematical modelling of wildland fires initiation and spread using a coupled atmospheric-forest fire setting, *The Italian Association of Chemical Engineering, 70, 1747-1752* doi: 10.3303/CET1870292 ISBN978-88-95608-67-9; ISSN 2283-9216

Rossa, C. G., Veloso, R. &Fernandes, P. M. (2016). A laboratory-based quantification of the ffect of live fuel moisture content on fire spread rate. *International Journal of Wildland Fire* **25**(5), 569–573. doi:10.1071/WF15114.

Schaaf, M. D., Sandberg, D. V., Schreuder, M. D. &Riccardi, C. L. (2007). A conceptual framework for ranking crown fire potential in wildland fuelbeds. *Canadian Journal of Forest Research* **37**, 2464–2478. doi:10.1139/X07-102.

BINARY LOGISTIC REGRESSION MODELING OF IMPACT OF AGRICULTURAL CREDIT FINANCE AND FARMERS' SOCIO-ECONOMIC CHARACTERISTICS ON SMALL SCALE FARMING IN NIGER STATE
(Case study of MINNA Branch, Niger state, Nigeria)

JIYA, Jibril Edda, (jibya2005@gmail.com)
YAKUBU Yisa (yisa.yakub@futminna.edu.ng.com
Department of Statistics, Federal University of Technology, Minna, Nigeria

ABSTRACT
Inadequate support for farmers from government-owned financial institutions in terms of agricultural credit facilities has been identified as one of the major problems affecting farming operation, particularly that of the small scale farmers, in Nigeria. This work investigates and models the impact of agricultural credit facilities as well as that of socio-economic characteristics of farmers on small scale farming in Niger state using Chanchaga and Bosso Local Government areas of the state as a case study. The research design employed the use of data from Bank of Agriculture, Minna Branch office in order to achieve an accurate representation of the population under study. Binary Logistic Regression modeling approach was used on the collected data so as to get an idea of a prospective customer defaulting on payment. It was observed that the amount of loan granted to the farmer, the farmer's age and gender contributed significantly to the performance of the loan at 0.05 level of significance. Credit facilities therefore play crucial role in the operation of small scale farming.

Keywords: Agriculture, Credit facility, Socio-economic characteristics, Bank of agriculture

Introduction

Agriculture contribute immensely to the Nigeria economy in various ways, namely, in the provision of food for the increasing population, create employment, generation of foreign exchange earnings and provide market for finished industrial products. Globally, agriculture has been identified as a major component in the achievement of the second millennium development goals- to eradicate extreme poverty and hunger (Kerten et al, 2017; United Nations, 2015), and such government has placed so much focus development of agriculture across the world. If the focus of world is to eradicate poverty using agriculture as a medium, new investment in agricultural research, and perhaps, technological developments directed towards enhanced agricultural farming is required (Jones &Ejeta, 2016). About three- quarter of the world's poor live in rural areas that are majorly involved in agricultural activities (Marris, 2018; World Bank, 2014).Agricultural development is a process that involves adoption by farmers (particularly small farmers) of new and better (Garba, 1987; Crebiyi, 1999). This is due to the fact that the most of the new practices have to be purchased but few farmers have the financial resources to finance it.

NACB (Bank of Agriculture) was established in November, 1972 to grant loans for sources has neither supplied the amount of credit needed, nor has it provided credit on the term required by farmers to modernize their farming method. According to CBN (1986), other farm credit schemes include;

1. The establishment of rural branches of commercial banks throughout the country following a mandatory Federal Government policy Directive in 1976.

2. The creation of the River Basin Authorities in 1979 throughout the country.
3. The establishment of both enhanced and state-wide Agricultural Development Projects throughout the country between 1972 and 1980 to facilitate among other things the provision of agricultural credit to farmers.
4. The development of state ministry operated and other Government sponsored Agricultural credit programmes in the half of the 1970's
5. The development of technical support and agro service establishments that facilitate the supply of credit to farmers throughout the country between 1976 and 1980.

However, the persistent failure of the above institutions and conventional banks to adequately finance agricultural activities in mid 1970's was a clear evidence that the country was in need of further financial and institutions reforms that would revitalize the sector by encouraging the flow of institutional credit into it. Also the unpredictable and risky nature of agriculture production, the importance of agriculture to our national economy, the urge to provide additional incentives to further enhance the development of agriculture to solve the problem of food insecurity, and the increasing demand by lending institutions for appropriate risk aversion measures in agricultural lending provided justifications for the establishment of the Nigeria in 1977 (Mafimisebi et al, 2009).

A smallholding or smallholder is a small farm operating under a small-scale agriculture model. Definitions vary widely for what constitutes a smallholder or small-scale farm, including factors such as size, food production technique or technology, involvement of family in labour and economic impact. When small-scale farmers earn more, they inject their incomes directly into the rural economy, creating growth and diversification. Almost every example of large-scale national poverty reduction was kick-started by rising incomes among small-scale farmers. Smallholder farming systems are perceived to share certain characteristics which differentiate them from large-scale, profit-driven enterprises. These include limited access to land, financial capital and inputs, high levels of vulnerability and low market participation (Gilbert, 2020).

In the 25 years since Clayton Christensen coined the term "disruptive innovation," much has been written about the benefits of shaking up established business practices. Even before the current pandemic, there was a growing recognition that our food systems, too, needed to be remained. Today's food systems must feed 7.8 billion people without compromising future productivity or the health of our planet. Yet they must also fairly reward and recognize the work of the millions of people at their base, in particular small-scale producers. Financial policies and programmes are therefore directed providing cheap credit to our farmers as means of increasing their investment opportunities which assist in reduction of poverty levels (Orji, 2017).

In this regards Nigeria government put various agriculture financing schemes, institutions and programmes that could provide micro, small, median and large scale producers, processors and marketers. Some of this organization includes National Accelerated production (NAP), 1972. Agricultural Development programmes (ADP), 1975.Nigeria Agricultural and Co-operative Bank (NACB), 1978. Rural Banking programmes (1977 - 1991) Peoples Bank of Nigeria(1988), River Basin Development Authority (RBDA), 1977 to date, Nigeria Agricultural Insurance Corporation, (NAIC), Agricultural Credit Guarantee scheme Fund (ACGSF), 1978 till date, Bank of Agriculture (BOA, a merger of NACB and

PBN), 2010,Small and Median Enterprises Equity Investment Scheme (LASACS), 2009, among others.

Before the introduction of credit schemes to farmers in Nigeria, commercial banks were often sceptical to give credit to farmers. This is because small scale farmers lack acceptable collateral security whereas bankers are interested in collateral securities which are highly liquid and which possess "money value'' certainty. It was in recognition of this fact that federal government in various periods put in place credit policies and established credit institutions and schemes that could facilitate the flow of agricultural credit to farmers (Adegeye and Dittoh, 1985).Bank of Agriculture is Nigeria's premier agricultural and rural development financial institution. It is wholly owned by the Federal government of Nigeria (Central Bank of Nigerian (CBN) 40% and Federal Ministry of Finance incorporated 60%) and Federal Ministry of Agriculture takes supervision (Bank of Agriculture, 2010).The Bank was incorporated as Nigerian Agricultural Bank (NAB) in 1973 and in 1978 was renamed Nigeria Agricultural and Co-operative Bank (NACB), The Nigeria Agricultural, Co-operative and Rural Development Bank (NACRDB) limited was incorporated in 2000 following the merger of the defunct Nigerian Agricultural and Cooperative Bank (NACB), People's Bank of Nigeria (PBN), and risk assets of the Family Economic Advancement Programme (FEAP).

The birth of the Nigeria Agricultural, Co-operative and Rural Development Bank (NACRDB) limited which later become Bank of Agriculture was one of the efforts of the Federal Government of Nigeria aimed at boosting the delivery of agricultural, Macro and Micro credit, to improve agricultural development and thereby alleviate poverty especially among the rural and urban poor Nigerians (BOA Staff Employee Handbook) reversed Edition.

2. Methodology

Data Collection

The research population comprises of small scale farmers whose major farming activities covers both the production of cash and food crop which their data will be sourced in order to establish the impact of credit facilities and its significant effect on their farming operations. Data were collected on 300 small scale farmers in Niger State from the Credit department of Minna branch office of Bank of Agriculture (BOA) using the simple random sampling technique.

The six variables identified in the code sheet in Table 1 were studied in this work. These variables have been recognized to be associated with cash loan performance of the customers. Respondent's age was measured in years with five levels and coded as shown in the code sheet. Gender was classified into two levels as shown; income was categorized into two levels; educational qualification was and loan amount borrowed by the customer were each categorized into four levels while respondent's household size was classified into three levels as given in the code sheet in Table 1. The dependent variable Loan Performance was categorized into two levels, coded as 0 for poor performance and 1 for good performance.

Table 1: Code Sheet for Loan Performance Data

variable	description	Codes/values

1	Age	1=21 - 30 years 2=31-40 years 3=41-50 years 4=51-60 years 5=61-70 years
2	Gender	1 = Male 2 = Female
3	Yearly income(#'000)	1 = 1 - 250 2 = >250
4	Level of education	0 = Nonformal 1 = Primary 2 = Post-pry 3 = Post-sec
5	Loan amount(#'000)	1 = 80 - 120 2 = 121 - 160 3 = 161 – 200
6	Household size	1 = 1-4 2 = 5-8 3 = 9-12
7	Loan performance	0 = Poor 1 = Good

Data on each of these variables were carefully collected from the Credit department of Minna branch office of Bank of Agriculture (BOA) using the simple random sampling technique.

The goal of this study was to investigate the impact of these variables on small scale farming in Niger state.

Model Fitting

If Y denotes the customer's loan performance, with values "1" for good performance and "0" for poor performance, then, for every sampled customer, the probability that his/her loan performs as expected (i.e., a success) is $\pi(x) = P(y = 1\ /x\ )$, and the corresponding probability that the loan performs poorly (i.e., a failure) is $1 - \pi(x) = P(y = 0\ /x)$.Let the vector$\boldsymbol{x'} = (\boldsymbol{x_1}, \dots, \boldsymbol{x_2})$denote the set of the p predictor variables in Table1, which may be categorical or continuous. The multiple logistic regression model, which relates the probability of a customer's loan performance status to the predictor variables x is given by:

$$\hat{\pi}(x) = \frac{e^{\beta_0+\beta_1 x_2+\beta_2 x_2+\beta_3 x_3+\beta_4 x_4+\beta_5 x_5+\beta_6 x_6}}{1+e^{\beta_0+\beta_1 x_2+\beta_2 x_2+\beta_3 x_3+\beta_4 x_4+\beta_5 x_5+\beta_6 x_6}} \qquad (1)$$

Where $\pi(x)$ is the predicted probability for the ith infant atx_i; x_i $(i = 1, \dots, 6)$denote, respectively, respondent's age, gender, annual income, level of education, loan amount, and

household size. $\hat{\beta}_0$ denotes the estimated intercept while $\hat{\beta}_j$, $j = 1,2,\dots,p$ denotes the estimated logistic regression coefficient for the *i*th predictor variable.

Since model (1) is nonlinear, the logit transformation on $\pi(x)$ yields the multiple linear logistic regression model

$$\hat{g}(x) = logit\big(\hat{\pi}(x)\big) = ln\left[\frac{\hat{\pi}(x)}{1-\hat{\pi}(x)}\right] = \beta_0 + \beta_1 x_2 + \beta_2 x_2 + \beta_3 x_3 + \beta_4 x_4 + \beta_5 x_5 + \beta_6 x_6 \quad (2)$$

where all the terms are as defined above. This model was fitted to the collected data and the parameters $\hat{\beta}_0, \hat{\beta}_1, \dots, \hat{\beta}_6$ were estimated via maximum likelihood (MLE) method with the aid of a statistical package (SPSS version 22).Equation (2) is the natural log odds of a customer (a small scale farmer) whose loan performs well.

The fitted model was then checked for goodness so as to know if it accurately explains the data or if it incorrectly classify cases as often as it correctly classifies them. The fitted model was assessed using a test, which is based on the deviance statistic (D), where D is given as -2log Likelihood statistic, with the log-likelihood function as given in equation (3). The deviance statistic is basically a measure of how much unexplained variation there is in our fitted logistic regression model – the higher the value the less accurate the model (Hosmer et al, 2013). This statistic compares the difference in probability between the predicted outcome and the actual outcome for each case and sums these differences together to provide a measure of the total error in the model.

Now, for n independent observations $(x_1, y_1), (x_2, y_2), \dots, (x_n, y_n)$, the likelihood function (Hosmer et al, 2013) is given by

$$l(\boldsymbol{\beta}) = \prod_{i=1}^{n} \pi(x_i)^{y_i}[1 - \pi(x_i)]^{1-y_i} \quad (3)$$

and the log-likelihood function is:

$$\ln l(\boldsymbol{\beta}) = \sum_{i=1}^{n} \{y_i ln[\pi(x_i)] + (1 - y_i) ln[1 - \pi(x_i)]\}$$

$$= \sum_{i=1}^{n} \left\{y_i ln\left[\frac{\pi(x_i)}{1-\pi(x_i)}\right] + ln[1 - \pi(x_i)]\right\} \quad (4)$$

Estimating the value of$\boldsymbol{\beta}$, the vector of parameters that maximizes $\boldsymbol{ln\, l(\beta)}$ requires differentiating (4) with respect to β and this is done using logistic regression software like SPSS.

3. Results and Discussion

The code sheet in Table1 shows all the six categorical predictor variables and one dependent variable for this study each with the respective categories. Table2 reveals that the first category of each of these predictors was used as the reference category in this work. Next the baseline (or constant-only) model was fitted to the data and the model is given in Table3. The value of the deviance statistic (-2Log Likelihood) for this model is given at the bottom of the table as −2LL = 585.023.From this table we observed that this

baseline model is a significant predictor of the outcome (< 0.001). We then consider the accuracy of classifying the observations of the customer's loan performance status by this model, as given in Table4. From this table we observed a 100% correct classification of the poor loan performance (i.e.,$y_i = 0$) group and 0.0% correct classification of the good loan performance ($y_i = 1$) group with 75.3% overall percentage of correct classification. This indicates that the fitted baseline model's approach to prediction is only accurate 75.3% of the time.

The multiple logistic regression model given in Equation (2) was then fitted to the data as given in Table 5. From this Table, we observed that the logistic regression coefficients for the small scale farmers in the 31 – 40 and 41 – 50 years age group were negative (-1.321 and -1.157 respectively) and significant (P<0.05) while that of those aged 51 – 60, and 61 – 70 years were also negative (-0.275 and -0.734 respectively) but not significant (P>0.05). Since the 21 – 30 years age group is our reference category as given in Table 2, each of these coefficients is the log of the ratio of odds of the corresponding age group to the odds of the 21 – 30 years age group. That is, each of the coefficients -1.321 and -1.157 is the log of the ratio of odds of the farmers within 31 – 40 and 41 – 50 years age group, respectively, to the odds of the farmers in the 21 – 30 years group. The corresponding odds ratios (0.267, 0.315, 0.760, and 0.480) indicate that farmers in the 31-40, 41 – 50, 51 – 60, and 61 – 70 years age group, respectively, are 73.3%, 68.5%, 24.0%, and 52.0%less likely to experience poor loan performance than their colleagues in the 21 – 30 years age group, even after controlling for the other variables in each case.

The coefficients for the farmers with household size of 5 -8 and 9 -12 were both negative (-0.136 and -0.044 respectively) and not significant (P>0.05). Since the small scale farmers with household size of 1- 4 is the reference category, each of these coefficients is the log of the ratio of odds of the farmers with 5 – 8 and 9 – 12 household size, respectively, to the odds of those with household size of between 1 and 4.The corresponding odds ratios (0.873 and 0.957) indicate that farmers with 5 - 8 and 9 – 12 household size, respectively, are 12.7% and 4.3% less likely to experience poor loan performance than their colleagues whose household size is between 1 and 4 even after controlling for other variables.

The coefficient for the farmers' gender (SEX) was positive (0.860) and significant, as the p-value is less than 0.05. Since the male group is our reference category, this coefficient is the log of the ratio of odds for the female group to the odds for the male group. The corresponding odds ratio (2.363) indicates that the female farmers are 136.3% more likely to experience poor loan performance than their male counterparts even after controlling for the other variables.

The coefficient for the farmers' annual income was negative (- 0.221) and not significant (P>0.05). Since from Table 2, the farmers with annual income within #100,000 - #250,000 group is our reference category, this coefficient is the log of the ratio of odds for the farmers with annual income above #250,000 to the odds for those farmers whose annual income falls within #100,000 - #250,000 group. The corresponding odds ratio (0.801) indicates that the farmers in the group of annual income above #250,000 are 19.9% less likely to experience poor loan performance than their colleagues with annual income of between #100,000 and #250,000 even after controlling for the other variables.

The coefficients for the small scale farmers whose levels of education falls within the *primary school*, *post-primary school*, and *post-secondary school* group were each negative

(-0.057, - 0.198, and – 0.544, respectively) and non-significant (*P*>0.05). From Table 2, the *non-formal* level of education group of these farmers is our reference category, thus these coefficients are, respectively, the log of the ratio of odds of the farmers whose level of education falls within *primary school, post-primary school*, and *post-secondary school* groups to the odds of the farmers in the *non-formal* level of education group. Each of the corresponding odds ratios (0.944, 0.821, and 0.580) respectively indicate that farmers with *primary school, post-primary school*, and *post-secondary school* groups as highest level of education are 5.6%, 17.9%, and 42%less likely to experience poor loan performance than their colleagues in the *non-formal* group of level of education, even after controlling for the other variables in each case.

The coefficient for the farmers whose cash loan amount falls within #121,000 - #160,000 group was negative (-1.536) and significant (*P*<0.05) while that of those in #161,000 - #200,000 group was also negative (-19.980) but non-significant (P>0.05).Since the small scale farmers within #80,000 - #120,000 cash loan group is the reference category, the coefficient (-1.536)is the log of the ratio of odds of the farmers with cash loan within #121,000 - #160,000 group to the odds of their colleagues with cash loan within #80,000-#120,000 group. The corresponding odds ratio of 0.215 indicates that farmers with cash loan within #121,000-#160,000 group are 78.5% less likely to experience poor loan performance than their colleagues whose cash loan falls within #80,000-#120,000, even after controlling for other variables. The coefficient (-19.980) is the log of the ratio of odds of the farmers with cash loan within #161,000 - #200,000 group to the odds of their colleagues with cash loan within #80,000-#120,000 group. The corresponding odds ratio of 0.000 indicates that farmers with cash loan within #161,000-#200,000 group are 100% less likely to experience poor loan performance than their colleagues whose cash loan falls within #80,000-#120,000, even after controlling for other variables.

The estimated logit is

$$\hat{g}(x) = logit\big(\hat{\pi}(x)\big) = ln\left[\frac{\hat{\pi}(x)}{1-\hat{\pi}(x)}\right] = 0.004 - 1.321\alpha_1 - 1.157\alpha_2 - 0.275\alpha_3 - 0.734\alpha_4 - 0.136\beta_1 - 0.044\beta_2 + 0.860\gamma - 0.221\lambda - 0.057\varphi_1 - 0.198\varphi_2 - 0.544\varphi_3 - 1.536\omega_1 - 19.980\omega_2 \text{e} \quad (5)$$

The associated estimated logistic probabilities can be obtained by

$$\hat{\pi}(x) = \frac{e^{0.004-1.321\alpha_1-1.157\alpha_2-0.275\alpha_3-0.734\alpha_4-0.136\beta_1-0.044\beta_2+0.860\gamma-0.221\lambda-0.057\varphi_1-0.198\varphi_2-0.544\varphi_3-1.536\omega_1-19.980\omega_2}}{1+e^{0.004-1.321\alpha_1-1.157\alpha_2-0.275\alpha_3-0.734\alpha_4-0.136\beta_1-0.044\beta_2+0.860\gamma-0.221\lambda-0.057\varphi_1-0.198\varphi_2-0.544\varphi_3-1.536\omega_1-19.980\omega_2}} \quad (6)$$

Table 2: Categorical Variables coding

			Parameter coding			
		Frequency	(1)	(2)	(3)	(4)
new age	21-30	60	0.000	0.000	0.000	0.000
	31-40	115	1.000	0.000	0.000	0.000
	41-50	95	0.000	1.000	0.000	0.000
	51-60	24	0.000	0.000	1.000	0.000
	61-70	6	0.000	0.000	0.000	1.000
Level of education	non formal education	48	0.000	0.000	0.000	
	primary edu	26	1.000	0.000	0.000	
	post primary edu	185	0.000	1.000	0.000	
	post secondary edu	41	0.000	0.000	1.000	
size of household	1-4	64	0.000	0.000		
	5-8	125	1.000	0.000		
	9-12	111	0.000	1.000		
amount of cash loan borrowed	80000-120000	250	0.000	0.000		
	121000-160000	41	1.000	0.000		
	161000-200000	9	0.000	1.000		
respondent's yearly income	100000-250000	228	0.000			
	>250000	72	1.000			
Respondent's gender	male	219	0.000			
	female	81	1.000			

Table 3:Baseline Model Coefficient

		B	S.E.	Wald	df	Sig.	Exp(B)
Step 0	Constant	-1.116	.134	69.489	1	.000	.327

-2LL = 585.023

Table 4: Classification Table for the baseline model

		Predicted		
		Performance of the accessed loan		Percentage Correct
		0-49	>50	
Performance of the accessed loan	0-49	226	0	100.0
	>50	74	0	0.0
Overall Percentage				75.3

Table5: Coefficient Table

	B	S.E.	Wald	df	Sig.	Exp(B)
age2			14.931	4	.005	
age2(1)	-1.321	.386	11.718	1	.001	.267
age2(2)	-1.157	.388	8.864	1	.003	.315
age2(3)	-.275	.523	.276	1	.599	.760
age2(4)	-.734	.943	.607	1	.436	.480
hhs2			.147	2	.929	
hhs2(1)	-.136	.381	.126	1	.722	.873
hhs2(2)	-.044	.389	.013	1	.910	.957
sex(1)	.860	.337	6.494	1	.011	2.363
yearly_income4(1)	-.221	.348	.405	1	.525	.801
educational_qualif			1.072	3	.784	
educational_qualif(1)	-.057	.626	.008	1	.927	.944
educational_qualif(2)	-.198	.385	.263	1	.608	.821
educational_qualif(3)	-.544	.545	.997	1	.318	.580
loan_amnt4			7.584	2	.023	
loan_amnt4(1)	-1.536	.558	7.584	1	.006	.215
loan_amnt4(2)	-19.980	12910.306	.000	1	.999	.000
Constant	.004	.480	.000	1	.993	1.004

-2LL = 300.481

Table 6: Classification Table

			Predicted		
			Performance of the accessed loan		Percentage Correct
Observed			0-49	>50	
Step 1	Performance of the accessed loan	0-49	216	10	95.6
		>50	62	12	16.2
	Overall Percentage				76.0

CONCLUSION

This study has unveiled the impact of financial credit facilities and socio-economic characteristics of farmers on small scale farming in Niger State. It was observed that these facilities and characteristics play a crucial role in the operation of small scale farmers, The agricultural development policies will therefore be more ensured, if the investment on research and human development are given a proper attention in form of improved educational standard of the people to be able to design an appropriate research and in return formulate a sustainable policy programme. Increase in farming operations particularly that of

small scale farmers is a related venture of the government, the various financial institutions, private enterprise and group of individuals.

References

Adetunji, O. (1999) 'Microfinance Market in Nigeria'. ***Microfinance Update***. 1 (1) Pp 5-6

Aiyedun, J.O. (1996) *Impact of Agricultural Development Project on Farmers'Income and Productivity. A Case Study of Five Local Government Areas*. Unpublished M.Sc. Dissertation. Zaria: Department of Agricultural Economics and Rural Sociology, Ahmadu Bello University.

Ajakaiye, M.B. (1986) 'Credit as an Instrument for Livestock Development In Nigeria'. Paper Delivered at the National Seminar on the 2nd Livestock Development Project, 9th – 10th December, 1986

Auchan, (1986)*An Empirical Study of the Impact of Agricultural Credit at Farm Level in Funtua Local Government Area of Kaduna State, Nigeria*. Unpublished M.Sc. Dissertation. Zaria: Department of Agricultural Economics and Rural Sociology, Ahmadu Bello University.

Baker, C.B., Barghava, V.K. (1974) 'Financing Small Farm Development'*India Australian Journal of Agricultural Economics*. 18, (2) Pp 101 - 117

Blasé, M.G. (1971) *Role of Institutions in Agricultural Development. Institution for Agricultural Development*. (Blasé M.G. ed.). Pp169. Iowa. Iowa University Press, Ames.

Brenner, (1971) *Agriculture and the Economic Development of Low Income Countries*. Netherlands Institution of Social Studies, The Hague. Monton And Company Paperback Series. No.2 Pp 40 – 43

Edordu, C.C.(1981) 'The Role of Farmers' Co-operatives Under the Agricultural Guarantee Scheme', in *Agricultural Credit and Finance in Nigeria. Problems and Prospects*, Proceedings of Seminar Organised by Central Bank of Nigeria.

Egwuatu, B.S.C. (2004) 'Voices of Microfinance'. *Microfinance Matters*. A publication of UNCDF. Issue 1 January - February 2004.

Fabiyi, Y.L. and Ositimenhin, K.O.(1984) 'An Analysis of the Impact of Credit on Rice Production: A Case Study of Ondo and Oyo States of Nigeria'. *Savings and Development*, 4, (6), Pp. 353 – 360

FAO (2000) Micro credit: Effects on Rural Poverty and the Environment. In *The State of Food and Agriculture*. Publication of the Economic and Social Development, FAO

Galbraith, J.K. (1952) 'The Supply of Capital for Underdeveloped Areas'. (Banes, E. K ed.), Proceedings of the International Conference on Agricultural Cooperative Credit. Berkely, Carlifornia, August 4th- October 2nd, 1952

Idah, M.L. (1996) *An Evaluation of the Impact of NACBs Direct Investment Loan Scheme*. Unpublished M.Sc. Dissertation. Zaria: Department of Agricultural Economics, Ahmadu Bello University.

Agricultural production to individual farmers, groups of farmers as well as state and selected Government agencies, (Bank of Agriculture Hand Book April 2013)

Yakubu et al, Binary logistic Regression Methods for Modeling Broncho – pneumonia status in infants from Tertiary Health Institutions in North Central Nigeria.

Ijere, M.O. (1998) 'Agricultural and Economic Development'. In *Readings in Agricultural Finance*' (Ijere, M.O. and Okorie, A. eds.) Longman Nig. Plc.

Ilebanmi, B.C. (1983) *Impact of Credit on Small Scale Food Producing Farmers of Akoko South and Akoko North*. Unpublished M.Sc. Dissertation. Zaria: Department of Agricultural Economics, Ahmadu Bello University.

Effects of Exchange Rate on import and export of oil and non-oil products in Nigeria: A multivariate GARCH modelling Approach

Okemmiri Hillary U (hillaryjim81@gmail.com) and Yisa Yakubu

ABSTRACT:

An exchange rate is the value of a Nation's currency in terms of the currency of another nation or economic zone. The study aimed to determine the effect of Exchange Ratevolatility on import and export of oil and non-oil products in Nigeria using yearly data from 1981 to 2020.The research employs Constant Conditional Correlation(CCC) and Diagonal Vector Error Correction Heteroskedasticity(DVECH) components of Multivariate GeneralizedAutoregressive Conditional Heteroskedasticity(GARCH) models.We observedthat the distribution is positively skewed which is an indication of a non-symmetric series, meaning that there is an asymmetric effects (not normally distributed) in the data. The result of DVECH and CCC exhibit similar behavior showing significant influence ofExchange Rate on importation and exportation of oil and non-oil products.The result from the summary statistics reveals that the money spent by Nigeria government to import non-oil product N3937.533 Billion is on higher rate as compared to what is realized to export our non-oil products N618.4662 Billion, this could put the country at deficit. Conclusively, based on Log likelihood, the DVECH model is found to be the best model.

KEYWORDS: MULTIVARIATE *GARCH, Exchange rate, Volatility*

I. INTRODUCTION

Export is a catalyst necessary for the overall development of an economy (Abou-Strait, 2005). It was also noted that foreign trade creates an avenue for foreign capital to flow into a country (Akinwunmi and Adekoya, 2016). This increases the earnings of the country thereby creating an avenue for growth by raising the national Income. Successive Nigerian governments on their part have shown efforts over the years to grow the non-oil export trade by establishing supportive policies. Some of these policies with varying degrees of successes include but not restricted to: protectionism policy in the mode of import substitution policy of industrialization in the 1960s; trade liberalization policy (this took the form of Structural Adjustment Programme) of the mid-1980s and export promotion policy o1990s which was executed through intensified policy support to Small and Medium Scale Enterprises (SMEs) to enhance productivity and subsequently, export of local products. Income of the country also increases the level of employment in the economy as higher demand for exports will require more production which will, in turn, lead to the employment of more people (Adenugba and Dipo, 2013). Exportation by a country also helps attain a favourable balance of trade and balance of payment position for the exporting country provided its exports reasonably exceed its imports. Exportation is required by any economy to enhance revenue and usher in economic growth and development. It is therefore crucial for economic progress and this has informed the idea of export-led growth.

Exchange Rate in Nigeria

Any exchange rate policy's goal is to determine an optimal rate of exchange while also preserving its stability. Over the years, efforts have been made to fulfil these goals and establish efficiency in the foreign currency market by employing a variety of ways.
Exchange rate arrangements in Nigeria have evolved from a fixed exchange rate regime in the 1960s to a pegged exchange rate regime in the 1970s and 1980s, and finally to various forms of the floating exchange rate regime adopted in 1986 following the adoption of the Structural Adjustment Program (Dada & Oyeranti, 2012).
Nigeria is yet to attain the ranks of a developed economy due to a lack of structural change, among other factors. Also, it was observed that a factor crucial to this lack of economic progress is the lack of economic diversification which has caused the economy to rely heavily on the crude oil sector for revenues and as the major export commodity in the economy (Osuntogun, 2007). Before the 1970s, Nigeria's exports were predominantly non-oil commodities with agricultural commodities accounting for the high contribution. However, in the 1970s, when the price of crude oil in the international market sky rocketed, the contribution of non-oil exports began falling and has remained low ever since. This is majorly due to the money-spinning nature of oil exports which makes it more profitable to export oil and less profitable to export non-oil commodities.
Oil is the most important non-renewable energy resource in the world. It is used as an intermediate good in textile, defence and transportation industries as well as a raw material in the world economy. Therefore, oil price changes are quite relevant to the world economy.

Oil price changes especially affect the oil-dependent countries (Alagözet.al., 2017: 144). Oil price changes effect oil exporting and importing countries very differently. These effects can be either on the supply and demand sides and they can be direct or indirect.

2. LITERATURE REVIEW

According to Richard (2018), goods and services sold and rendered in international business must be paid for, and payments for these goods and services are usually made in different currencies. As a result, both the seller and the buyer must agree on a basis of conversion. For the currencies involved, this is known as the exchange rate. The method by which one currency is converted into another is referred to as an exchange rate. Ceteris paribus, this rate also reflects the strength of the economy of that country.

Any currency that isn't a country's native currency is referred to as foreign. It is the mathematical representation of the international medium of exchange, which is a method of settling foreign accounts or debts arising from international economic activities. The price per unit of a country's currency quoted in terms of another currency is also referred to as the exchange rate.

It is the quantitative representation of a country's currency in terms of another country's currency. The price of one unit of a currency in terms of another currency is commonly used to define an exchange rate. It's also known as the value of a foreign currency in terms of a domestic currency, i.e. how much one currency is worth in terms of another.

Empirical Review

Adelowokan et al. (2015) used the ADF test for stationarity and the error correction technique to investigate the impact of exchange rate fluctuation on economic growth and investment in Nigeria from 1986 to 2014. GDP, investment, exchange rate, interest rate, and inflation are among the variables used. The findings revealed a negative association between exchange rate volatility and investment and economic growth, as well as a positive relationship between inflation, interest rates, and exchange rate. They advised that Nigeria implement a sound exchange rate management system to help the country thrive economically.

Ali et al. (2015) looked at the influence of the naira's actual exchange rate mismatch on Nigeria's economic growth. They used data from quarterly surveys from 2000 to 2014. The departure of the real exchange rate from a sustainable equilibrium path, estimated using the behavioral equilibrium exchange rate technique, was used to calculate the estimate of the real exchange rate misalignment. The analysis found that the actual exchange rate misalignment has a detrimental influence on Nigeria's economic growth. They advised that a market-based exchange rate arrangement be used indefinitely to ensure that the Naira's exchange rate follows a path of long-term stability.

Amassoma and Odeniyi (2016) also looked into the relationship between Nigerian economic growth and currency rate fluctuations. In order to investigate this nexus, researchers used the Johansen test for co-integration and the error correction model technique. In both the short and long run, the results demonstrated a positive but insignificant link between exchange rate variations and economic growth in Nigeria.

In a recent study, Richard (2018) looked at the relationship between the foreign exchange rate and the Nigerian economy from 1986 to 2018. His main goal was to figure out how the Nigerian economy and the foreign exchange rate are linked. In order to determine this link, he used a theoretical framework. Interest rates, external reserves, oil output, foreign direct investment, oil price index, inflation rate, terms of trade, diaspora remittances, purchasing managers' index, and foreign public debts all have a direct impact on the rate of exchange in Nigeria, according to him. According to his findings, there is a link between Nigeria's macroeconomic indicators and the foreign exchange rate. The monetary authorities should pursue a stable foreign exchange rate policy, he suggested. Furthermore, both the monetary and fiscal authorities should be encouraged to collaborate and ensure that leakages from the external reserves account are prevented, as well as that the determinants of exchange rate that have a positive relationship with some macroeconomic variables are closely monitored.

For the period 1985 to 2016, Akindele (2018) investigated the efficacy of the Nigerian foreign exchange market. He used secondary time series data and analysed it with two equations, while estimating it with the fully modified OLS technique. His research found that GDP, oil prices, interest rates, and inflation rates all have a significant and positive relationship with the Nigerian exchange rate, whereas broad money supply has a negative relationship with the Nigerian exchange rate. He came to the conclusion that Nigeria's foreign exchange rate market was inefficient, and that the country's monetary authorities should ensure transparency in determining exchange rates in order to reduce the risks associated with exchange rate fluctuations.

Umeora (2013) looked into the impact of accumulating external reserves on Nigeria's exchange rate and inflation. He based his findings on secondary data from the CBN statistical bulletins. To determine the effect of external reserves accumulation on inflation and exchange

rates, he used a simple linear regression model. The regression results showed a negative relationship between external reserves accumulation and the exchange rate in Nigeria, but a positive relationship between inflation and external reserves accumulation in Nigeria. He also noted that the money supply in Nigeria was a factor in the country's inflation.

He suggested that the government ensure the best possible use and management of the country's foreign reserves.

3. MATERIALS AND METHODS

Central Bank of Nigeria data on exchange rate of different country currencies in the world to Nigeria Naira and data on import, export of oil and non-oil products will be used for the analysis. The study employs data collected from Central Bank of Nigeria Statistical Bulletin, 2019. The sample period is from 1981 to 2019. In analysing the data collected from secondary sources, Multivariate Generalized Autoregressive Conditional Heteroskedasticity (GARCH) models will be employed to measure the effect of exchange rates on some micro economic variables like import and export of oil and non-oil products in Nigeria and its effect on inflation rate in the country.

Multivariate GARCH Representations

The Diagonal Vector Error Correction Heteroskedasticity (DVECH) Representation: Let's have a quick glance at the Diagonal Vector Error Correction Heteroskedasticity (DVECH) representation before diagonal VECH for crystal clear. Applying the VECH operator to a symmetric matrix stacks the lower triangular elements into a column. Since $\boldsymbol{H_t}$is a symmetric matrix, in specifying the multivariate GARCH model we can employ the VECH transformation of $\boldsymbol{H}t$. consider the following specification:

$$\boldsymbol{Vech(H_t) = Vech\ (A_0) + \sum_{i=1}^{q} A_i Vech(\varepsilon_{t=i}\ \varepsilon'_{t=i}) + \sum_{i=1}^{p} B_i Vech\ (H_{t=i})} \ldots..(2)$$

where $\varepsilon_t = (\varepsilon_{1t}, \varepsilon_{2t}, \ldots . \varepsilon_{nt})'$Are the error terms associated with the conditional mean equations forY_{1t}toY_{1t}, A is an (N x N)positive definite matrix of parameters and A_i and $B_i$are [N(N + *1*) / 2 * (N + 1) / 2] matrices of parameters. In the case two variables (N=2) and p=q=1the multivariate GARCH representation given by (2) can be written out in full as:

$$\begin{bmatrix} h_{11,t} \\ h_{12,t} \\ h_{22,t} \end{bmatrix} = \begin{bmatrix} a_{11}^0 \\ a_{12}^0 \\ a_{22}^0 \end{bmatrix} + \begin{bmatrix} a_{11} & a_{12} & a_{13} \\ a_{21} & a_{22} & a_{23} \\ a_{31} & a_{32} & a_{33} \end{bmatrix} \begin{bmatrix} \varepsilon_{1,t-1}^2 \\ \varepsilon_{1,t-1}\varepsilon_{2,t-1} \\ \varepsilon_{2,t-1}^2 \end{bmatrix} + \begin{bmatrix} b_{11} & b_{12} & b_{13} \\ b_{21} & b_{22} & b_{23} \\ b_{31} & b_{32} & b_{33} \end{bmatrix} \begin{bmatrix} h_{11,t-1} \\ h_{12,t-1} \\ h_{22,t-1} \end{bmatrix} \ldots\ldots\ldots \quad (3)$$

where $h_{11,t}$ the conditional variance of the error associated with $y_{1t}, h_{22,t}$ is the conditional variance of the error associated with $y_{2t}$and $h_{12,t}$ is the conditional covariance between the errors.

In the diagonal representation (due to Bollerslev, Engle and Woodridge. 1988) $A_i$and$B_i$in (2) are diagonalmatrices. This assumption forces the individual conditional variances to have GARCH (p, q) form and thecovariances to have a GARCH (p, q) form. As an example, consider the diagonal representation of VECH (H_t) inthe case of two variables (N = 2) and p = q = 1:

$$\begin{bmatrix} \boldsymbol{h_{11,t}} \\ \boldsymbol{h_{12,t}} \\ \boldsymbol{h_{22,t}} \end{bmatrix} = \begin{bmatrix} \boldsymbol{a_{11}^0} \\ \boldsymbol{a_{12}^0} \\ \boldsymbol{a_{22}^0} \end{bmatrix} + \begin{bmatrix} \boldsymbol{a_{11}} & \boldsymbol{0} & \boldsymbol{0} \\ \boldsymbol{0} & \boldsymbol{a_{22}} & \boldsymbol{0} \\ \boldsymbol{0} & \boldsymbol{0} & \boldsymbol{a_{33}} \end{bmatrix} \begin{bmatrix} \boldsymbol{\varepsilon_{1,t-1}^2} \\ \boldsymbol{\varepsilon_{1,t-1}\varepsilon_{2,t-1}} \\ \boldsymbol{\varepsilon_{2,t-1}^2} \end{bmatrix} + \begin{bmatrix} \boldsymbol{b_{11}} & \boldsymbol{0} & \boldsymbol{0} \\ \boldsymbol{0} & \boldsymbol{b_{22}} & \boldsymbol{0} \\ \boldsymbol{0} & \boldsymbol{0} & \boldsymbol{b_{33}} \end{bmatrix} \begin{bmatrix} \boldsymbol{h_{11,t-1}} \\ \boldsymbol{h_{12,t-1}} \\ \boldsymbol{h_{22,t-1}} \end{bmatrix}$$

The Constant Conditional Correlation Representation In the past years, a new class of multivariate GARCH models has been developed. They focus on the parameterization of the conditional correlation matrix. Such models have the flexibility of univariate GARCH models with respect to the conditional variances. They need simple conditions to ensure the positive definiteness of H_t and the estimation is much easier than the usual Multivariate generalized autoregressive conditional heteroscedasticity (MGARCH) models. The constant conditional correlation (CCC) model of Bollerslev (1990) is a fruitful endeavour to explore the MGARCH model indirectly in the correlation direction instead of modelling the variance covariance matrix H_t directly. CCC model has several advantages mentioned above. Now we define the structure of the constant conditional correlation matrix R and the variance covariance matrix H_t as follows

$$R = \begin{bmatrix} 1 & \cdots & 1 \\ \vdots & \ddots & \vdots \\ 1 & \cdots & 1 \end{bmatrix}$$

Where,ρ_{ij} is the correlation coefficient measuring the correlation of variable *i*with variable *j*. He then defines the conditional variance matrix $H_t$as: $H_t = D_t R D_t'$

Where

$$D_t = diag(\sigma_{1t}, \sigma_{2t}, \ldots . \sigma_{Nt})$$

The basic idea is that every variance–covariance matrix can be decomposed in the above way. Therefore, we can characterize the dynamics in the following way.

$$H_t = \begin{bmatrix} {\sigma^2}_{1t} & \sigma_{12,t} & \cdots & \sigma_{1N,t} \\ \sigma_{12,t} & {\sigma^2}_{2t} \cdots & & \sigma_{2Nt} \\ \vdots & & \ddots & \vdots \\ \sigma_{1N,t} & \sigma_{2Nt} \cdots & & {\sigma^2}_{Nt} \end{bmatrix}$$

$${\sigma^2}_{1t} = W_i + \sum_{j=1}^{q} \alpha_{i,j} {\varepsilon^2}_{i,t-j} + \sum_{j=1}^{p} \beta_{i,j} {\sigma^2}_{i,t-j} \qquad i - 1, \ldots, n$$

$$\sigma_{ij,t} = \rho_{ij}\sigma_{it}\sigma_{jt} \qquad i, j = 1, \ldots, n, i \neq j$$

The usual conditions to ensure the positivity of the variances and the stationarity hold:

$$W_i = 0, \alpha_{i,j} > 0, \beta_{i,j} > 0 \; and \sum_{j=1}^{q} \alpha_{i,j} + \sum_{j=1}^{p} \beta_{i,j} < 1$$

The total number of parameters is$(p + q + 1)N + \frac{N(N-1)}{2}$, when p = q = 1 parameters need to be estimated, which is not so many but still lack parsimony. Positive definiteness of the

variance covariance matrix is controlled by the correlation matrix, while only the usual requirements of positivity constraints for GARCH model suffice. In order to obtain the parameters, maximum likelihood estimation method can be used (Xiaojun Song, 2009).

4.0 DATA ANALYSIS:

Here, we shall focus on the analysis of data and econometric interpretation which is typically the case in financial application. The aim is to examine the volatility spill over of exchange rate on import and export of oil and non-oil products and inflation rate on exchange rate in Nigeria via MGARCH models.

Table 4.1 Summary Statistics

Average Annual Exchange Rates of US dollar, Pound sterling, Deutschemark, Japanese yen, CFA franc, French franc, Swiss franc, Dutch guilder to Nigeria Naira; and import of oil, import of non-oil, export of oil, export of nonoil and inflation rate.

Variable	Obs	Mean(B)	Std.Dev.	Min	Max
US dollar	39	73.44756	63.48489	0.6369	197
Pound sterling	39	132.0397	97.22627	0.6962	291.9343
deutschemark	39	16.4239	18.25571	0.256766	58.8307
Japanese yen	39	0.696185	0.644818	0.002852	2.0259
CFA franc	39	0.13851	0.117899	0.001685	0.325624
French franc	39	3.085142	4.782266	0.084268	17.0935
Swiss franc	39	63.85763	62.00558	0.312689	198.229
Dutch guilder	39	11.85012	13.60142	0.227722	52.5115
Import of oil	39	862.9722	1151.108	0.0518	3686.892
Import of nonoil	39	2920.915	3937.533	5.0697	16914.4
Export of oil	39	4843.723	5665.524	7.2012	17282.25
Export of non-oil	39	348.6404	618.4662	0.2032	3207.017
Inflation rate	39	19.23629	17.02732	5.382224	72.8355

Table 4.1 shows the summary statistics of the annual average yearly exchange rates of different country currencies to Nigeria Currency for 39 years from 1981 to 2019. A summary statistics of some economic activities that might be affected by the volatile nature of the exchange rate fluctuations is shown in the table. are Export and Import of oil and non-oil products. The table also shows the Inflation Rate in the country. From the table, the result reveals that Pound sterling has highest exchange rate to Nigeria naira; followed by US dollar. It was observed that an average of N862.9722 Billion was spent in import of oil products in the country while the average of N4843.723 Billion spent on the export of oil products. The country spent larger amount of N2920.915 Billion on an average to import non-oil products and a lesser amount of N348.6404 Billion on an average to export same, non-oil products. It was revealed in the result that the inflation rate in the country is at N19.23629 on an average.

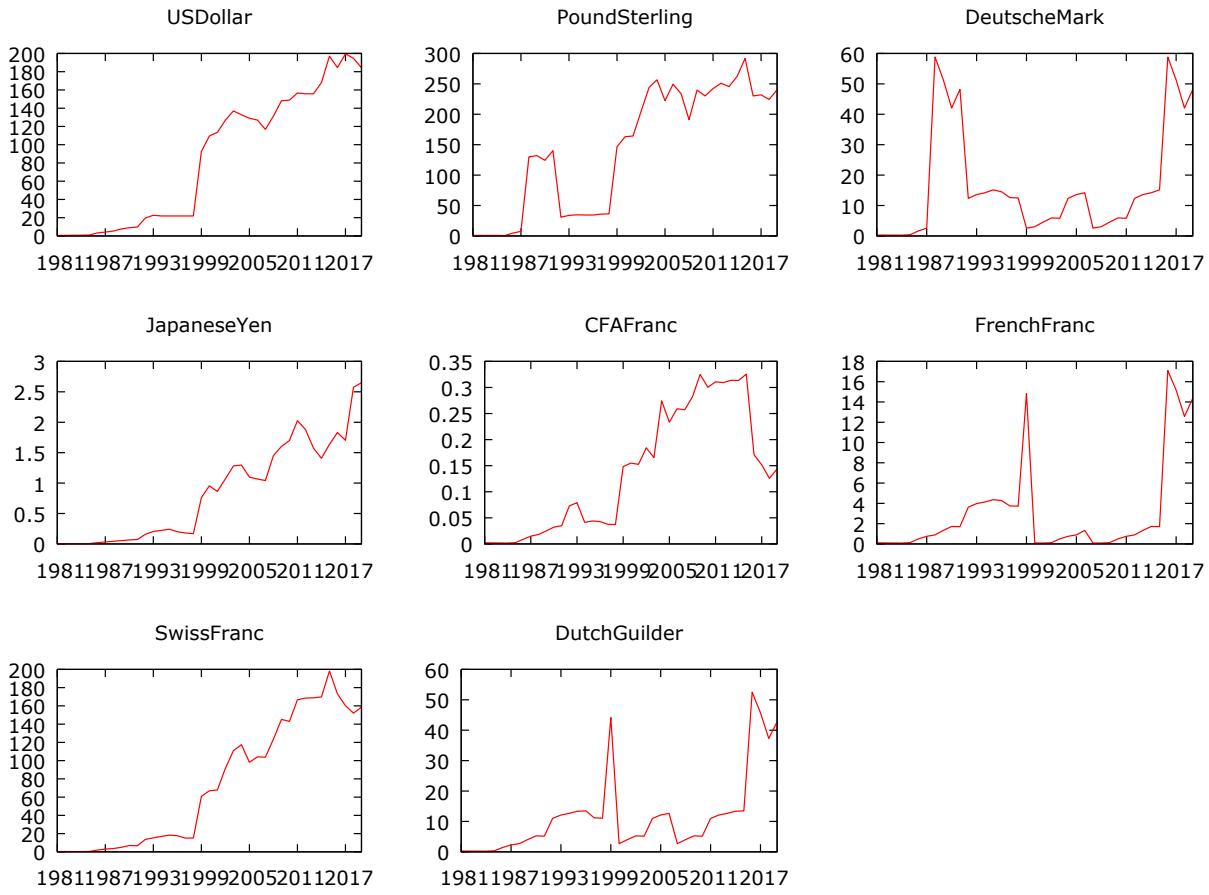

Fig 4.1: Graphical Representation of Exchange Rates to Nigerian naira of some country currencies.

Figure 4.1 indicates that all the series are not stationary as they contain a trend components which should be remove before modelling. These trend components have been taken care of, as explained above which can be seen in figure 4.2. From the graph values at the y-axis stands for the average exchange rate in Billion while on the x-axis represent the year studied. The pattern reviles an upward trend in the exchange rates to Nigeria currency.

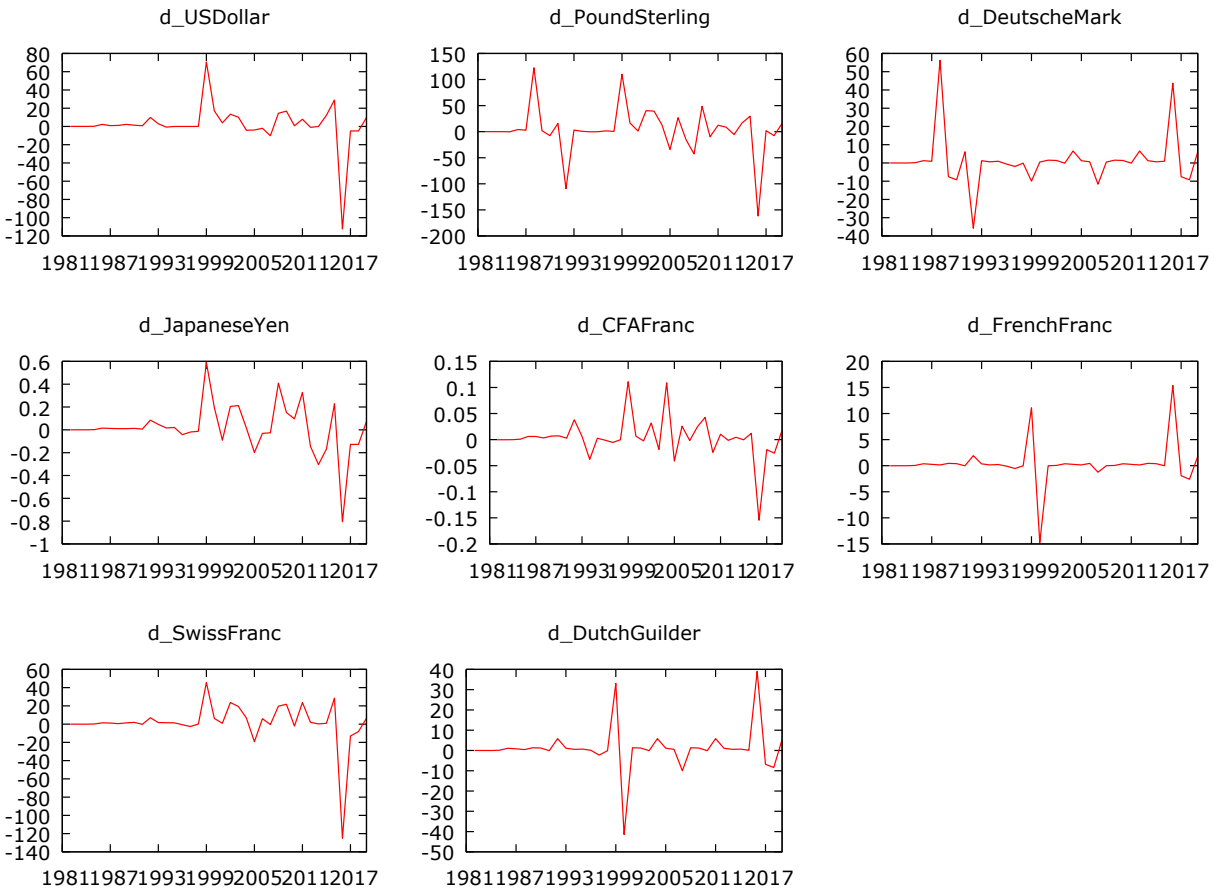

Fig 4.2: Graphical Representations of the first Difference of the Logarithms of Exchange Rates, to Nigerian naira of some country currencies:

From figure 4.2 we can observe a constant (stationary) mean and variance in the fluctuations of the exchange rate.

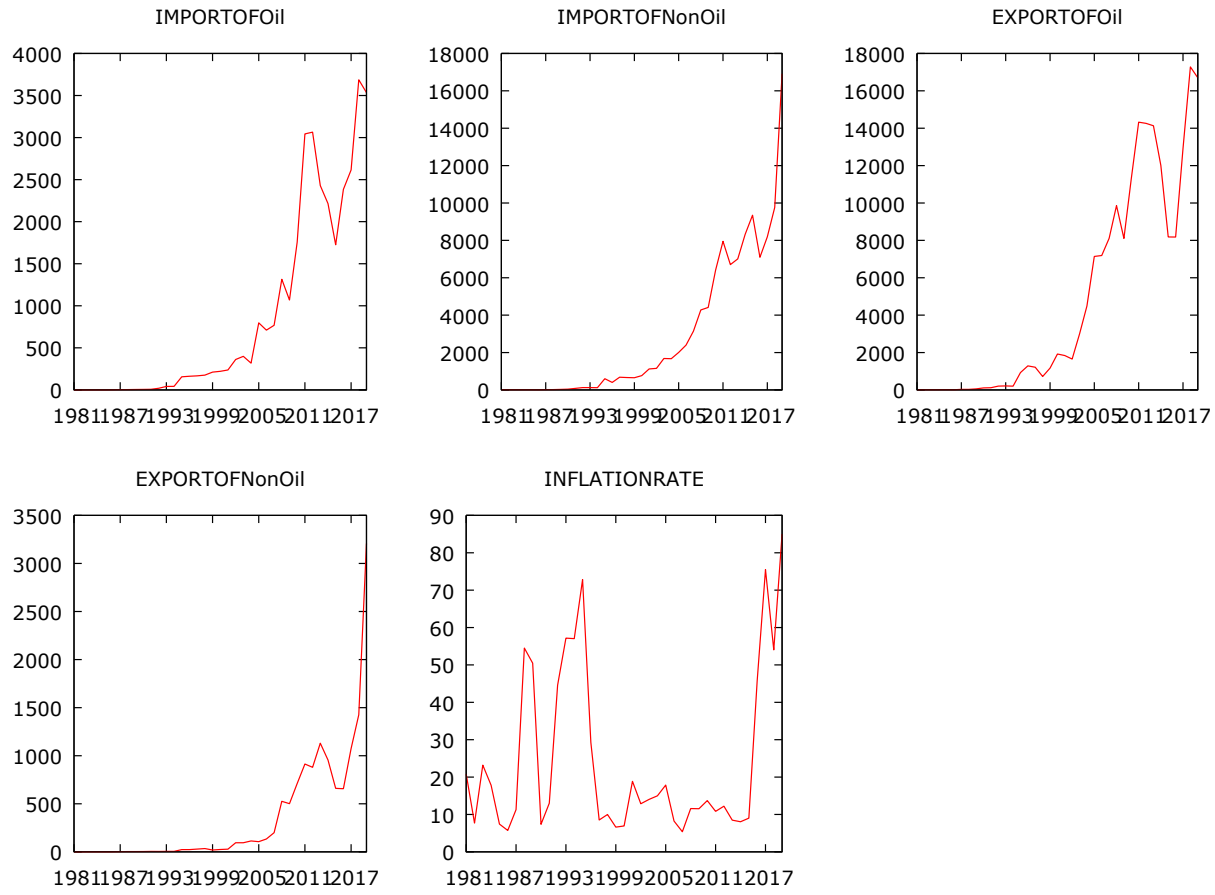

Fig 4.3: Graphical Representation of Endogenous Econometric variables used

Figure 4.3 also indicates that all the series are not stationary as they contain a trend components which should be removed before modelling. These trend components have been taken care of, as explained by first difference shown in figure 4.4. From the graph values at the y-axis stands for the average import of oil and non-oil products from the specific graph, and the inflation rate in Billion. While the x-axis represent the years studied. The graph depicts an upward trend in the activities of import of oil and non-oil products and as well on inflation rate.

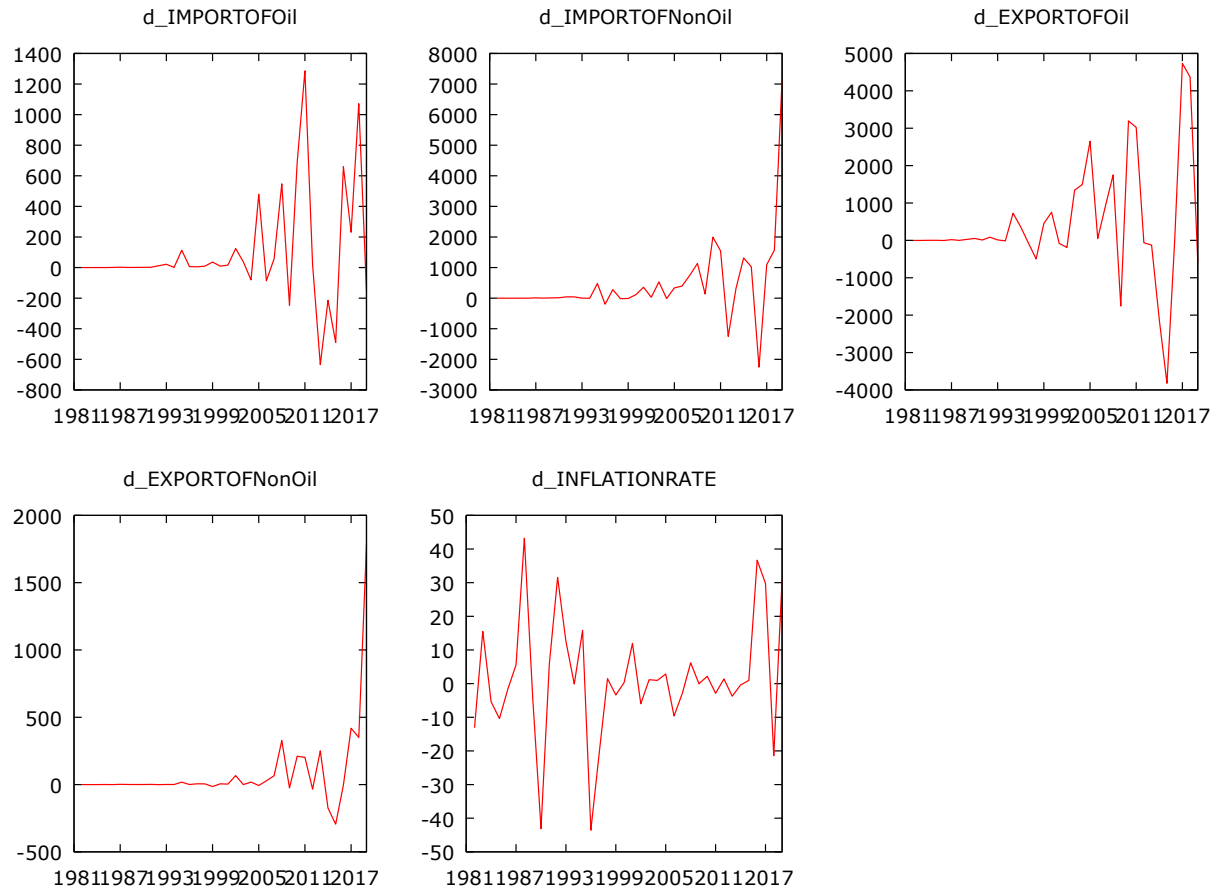

Fig 4.4: Graphical Representation of the first Difference of the Logarithms of the Endogenous Econometric variables used

From figure4.4 we can observe a constant (stationary) mean and variance in the fluctuations of export and imports of oil and non-oil products and as well inflation rate.

4.2: Normality Test for the Dependent Variable GDP

To achieve the overall objective of the research, we examine the characteristics of the unconditional distribution of the exchange rate. This will enable us to explore and explain some stylized facts embedded in the financial time series. JarqueBera, Doornik-Hansen test, Shapiro-Wilk W and Lilliefors normality test is used to demonstrate this and the results are given in the table below: Note that these tests is a goodness–of–fit measure of departure from normality, based on the sample kurtosis and skewness. Under the null hypothesis of normality, the statistic JB has an asymptotic chi-square distribution with two degrees of freedom.

Table 4.2: Normality Test for the Dependent Variable GDP

Exchangerate		
Test Statistic	**Test Statistic Value**	**p-value**
Doornik-Hansen test	8.74511	0.0126189
Shapiro-Wilk W	0.849562	0.00010563
Lilliefors test	0.257088	0.0000
Jarque-Bera test	5.22849	0.032232
Imports of Oil		
Doornik-Hansen test	35.6828	1.78475e-008
Shapiro-Wilk W	0.756518	1.19748e-006
Lilliefors test	0.27196	0.0000
Jarque-Bera test	9.1944	0.01008
Imports of Non-Oil Products		
Doornik-Hansen test	23.022	1.00195e-005
Shapiro-Wilk W	0.756947	1.21947e-006
Lilliefors test	0.238934	0.0000
Jarque-Bera test	23.9882	6.18056e-006
Exports and Re-Exports of Oil		
Doornik-Hansen test	21.6066	2.03319e-005
Shapiro-Wilk W	0.806013	1.12075e-005
Lilliefors test	0.261139	0.0000
Jarque-Bera test	5.40005	0.0672037
ExportsRe-Exports of Non-Oil		
Doornik-Hansen test	58.1854	2.31847e-013
Shapiro-Wilk W	0.614229	6.58445e-009
Lilliefors test	0.302637	0.0000
Jarque-Bera test	209.025	4.08208e-046
Inflationrate		
Doornik-Hansen test	59.7106	1.08148e-013
Shapiro-Wilk W	0.713062	2.07506e-007
Lilliefors test	0.279363	0.0000
Jarque-Bera test	26.6914	1.59966e-006

Null Hypothesis: residuals are multivariate normal

Table 4.2 indicated the test of Normality of the econometric variables used in this research.This will enable us to explore and explain some stylized facts embedded in the financial time series. The listed test statistic shown in the table is some statistic used to check the normality of variables. From the table, the result reviles that all p-values of the test statistic (JarqueBera, Doornik-Hansen test,Shapiro-Wilk W andLilliefors)are all less than 5% error level. Thus,it's denote that the distributionisskewedwhich is an indication of a non-symmetric series (not normally distributed), meaning that there is an asymmetric effects in these models (i.e. volatility is higher in a falling market than in a rising market) which is another stylize fact of financial time series.

Table 4.3 System Residual Portmanteau Tests for Autocorrelations. Lagrange-multiplier test

Null Hypothesis: no residual autocorrelations up to lag h

lag	chi2	df	Prob
1	56.201	25	0.00034
2	43.4258	25	0.01256

H0: no autocorrelation at lag order

The result from the Table 4.3 reveals that the error term of exchange rate variables are serially correlated and the null hypothesis of no autocorrelation can be rejected since the p-value is less than 0.05. Hence, it is concluded that there are strong autocorrelations in the residuals of the exchange rate return. The proposed Multivariate Generalized Autoregressive Conditional Heteroskedasticity (GARCH) models accounts for the presence of serial correlation that occur in the series.

Modeling of DVEC and CCC models in Multivariate version Table 4.4 contains the number coefficients, log-likelihood and information criteria for multivariate DVECH and CCC models. And the table is given below:

Table 4.4 Diagonal VECH MGARCH model

Sample: 1981 - 2019	Number of obs	=39
Distribution: Gaussian	Wald chi2(5)	=577.66
Log likelihood = -495.1441	Prob> chi2	=0.000

The result from table 4.4 reviles that exchange rate of US Dollar to Nigeria naira have significant influence on the economic activity of import and export of oil and non-oil products in the country with their p-values less than 0.05, except for import oil products and inflation rate with p-value greater than 0.05.It is observed that exchange rate of Pound sterlingto Nigeria naira have significant influence on import and export of oil and non-oil products in the country with their p-values less than 0.05, except for inflation rate whichis non-significant with p-value = 0.895 greater than 0.05.Exchange rate of Deutschemark to Nigeria naira have no significant influence on import and export of oil and non-oil products in the country with their p-values greater than 0.05, except for inflation rate with p-value = 0.000 less than 0.05 have significant influence. And exchange rate of Japanese yen to Nigeria naira have significant influence on the economic activity of import non-oil products and export of oil and non-oil products in the country with their p-values less than 0.05, and not significant to import oil and inflation rate with p-value greater than 0.05. From the table sigma0 denote the variance covariance matrix coefficients. The significance of each variance and covariance is shown by their p-value.

Table 4.5 Diagonal VECH MGARCH model

Sample: 1981 - 2019	Number of obs	=39

	Coef.	Std. Err.	Z	P>z	[95%	Conf.
US dollar						
Distribution: Gaussian	Wald chi2		= 59.50			
Log likelihood = -252.6489	Prob> chi2		=0.000			
Importofoil	-0.02802	0.012857	-2.18	0.029	-0.05321	-0.00283
Importofnon-oil	-0.02802	0.012857	-2.18	0.135	-0.06473	0.008691
Exportofoil	0.025147	0.005649	4.45	0.000	0.014075	0.036218
Exportofnon-oil	0.010796	0.003373	3.2	0.001	0.004185	0.017407
Inflationrate	-0.11098	0.026679	-4.16	0.000	-0.16327	-0.05869
_cons	0.05439	0.252938	0.22	0.83	-0.44136	0.550139
	20.532	9.316583	2.2	0.028	2.271837	38.79217
Pound sterling						
Importofoil	-0.08468	0.034278	-2.47	0.013	-0.15186	-0.0175
Importofnonoil	0.034859	0.010338	3.37	0.001	0.014596	0.055122
Exportofoil	0.022703	0.006173	3.68	0.000	0.010603	0.034802
Exportofnonoil	-0.15758	0.048828	-3.23	0.001	-0.25328	-0.06188
Inflationrate	-0.06134	0.462924	-0.13	0.895	-0.96865	0.845978
_cons	60.01975	17.05108	3.52	0.000	26.60024	93.43926
Deutschemark						
Importofoil	0.012638	0.008786	1.44	0.15	-0.00458	0.029858
Importofnonoil	0.001169	0.00265	0.44	0.659	-0.00402	0.006363
Exportofoil	-0.00221	0.001582	-1.39	0.163	-0.00531	0.000895
Exportofnonoil	-0.00595	0.012515	-0.48	0.634	-0.03048	0.018579
Inflationrate	0.425463	0.118653	3.59	0.000	0.192907	0.658019
_cons	4.499281	4.370415	1.03	0.303	-4.06657	13.06514
Japanese yen						
Importofoil	-5.8E-05	0.000175	-0.33	0.743	-0.0004	0.000286
Importednonoil	0.000132	5.28E-05	2.5	0.013	2.84E-05	0.000236
Exportofoil	9.72E-05	3.15E-05	3.08	0.002	3.54E-05	0.000159
Exportofnonoil	-0.00042	0.00025	-1.67	0.095	-0.00091	7.25E-05
Inflationrate	-4.52E-06	0.002366	0	0.998	-0.00464	0.004632
_cons	0.188824	0.087131	2.17	0.03	0.01805	0.359598
Sigma0						
1_1	824.8661	186.7954	4.42	0.000	458.7539	1190.978
2_1	1069.852	296.2869	3.61	0.000	489.14	1650.563
3_1	1.174377	61.96109	0.02	0.985	-120.267	122.6159
4_1	6.813416	1.648106	4.13	0.000	3.583188	10.04364
2_2	2762.957	625.6865	4.42	0.000	1536.634	3989.28
3_2	379.2514	128.6371	2.95	0.003	127.1273	631.3755
4_2	9.085527	2.688459	3.38	0.001	3.816245	14.35481
3_3	181.5162	41.10531	4.42	0.000	100.9513	262.0811
4_3	-0.27808	0.581181	-0.48	0.632	-1.41718	0.861014
4_4	0.072147	0.016338	4.42	0.000	0.040125	0.104168

	Coef.	**Std. Err.**	**Z**	**P>z**	**[95%**	**Conf.**
CFA franc						

Importofoil	-0.00013	2.96E-05	-4.35	0.000	-0.00019	-7.1E-05
Importofnonoil	3.89E-05	8.94E-06	4.36	0.000	2.14E-05	5.64E-05
Exportofoil	3.51E-05	5.34E-06	6.57	0.000	2.46E-05	4.55E-05
Exportofnonoil	-0.0002	4.22E-05	-4.83	0.000	-0.00029	-0.00012
Inflationrate	-0.00076	0.0004	-1.91	0.056	-0.00155	2.03E-05
_cons	0.055833	0.014741	3.79	0.000	0.026942	0.084725
French franc						
Importofoil	0.004981	0.002103	2.37	0.018	0.00086	0.009103
Importofnonoil	0.000361	0.000634	0.57	0.569	-0.00088	0.001604
Exportofoil	-0.00091	0.000379	-2.39	0.017	-0.00165	-0.00016
Exportofnonoil	-0.00061	0.002995	-0.2	0.839	-0.00648	0.005262
Inflationrate	0.084507	0.028397	2.98	0.003	0.028849	0.140164
_cons	0.271224	1.04597	0.26	0.795	-1.77884	2.321289
Swiss franc						
Importedoil	-0.01735	0.012826	-1.35	0.176	-0.04248	0.007792
Importofnonoil	0.024247	0.003868	6.27	0.000	0.016665	0.031828
Exportofoil	0.008867	0.00231	3.84	0.000	0.00434	0.013395
Exportofnonoil	-0.10819	0.01827	-5.92	0.000	-0.14399	-0.07238
Inflationrate	-0.13673	0.173209	-0.79	0.43	-0.47621	0.202756
_cons	16.35879	6.379872	2.56	0.01	3.854474	28.86311
Dutch guilder						
Importofoil	0.012379	0.005848	2.12	0.034	0.000918	0.023839
Importofnonoil	0.001829	0.001764	1.04	0.3	-0.00163	0.005285
Exportofoil	-0.00184	0.001053	-1.75	0.08	-0.00391	0.000221
Exportofnonoil	-0.00726	0.00833	-0.87	0.383	-0.02359	0.009061
Inflationrate	0.213114	0.078971	2.7	0.007	0.058334	0.367893
_cons	2.095623	2.908761	0.72	0.471	-3.60544	7.796691
Sigma0						
1_1	0.002065	0.000468	4.42	0.000	0.001149	0.002982
2_1	-0.01274	0.023552	-0.54	0.589	-0.0589	0.03342
3_1	0.713961	0.18317	3.9	0.000	0.354954	1.072967
4_1	0.025376	0.065375	0.39	0.698	-0.10276	0.153509
2_2	10.39702	2.354461	4.42	0	5.782363	15.01168
3_2	10.70207	10.29833	1.04	0.299	-9.48229	30.88644
4_2	28.22745	6.470381	4.36	0	15.54574	40.90917
3_3	386.8068	87.59448	4.42	0	215.1247	558.4888
4_3	52.29119	29.45479	1.78	0.076	-5.43913	110.0215
4_4	80.40561	18.20828	4.42	0	44.71803	116.0932

Table 4.5 indicated that exchange rate of CFA franc to Nigeria naira have significant influence on the economic activity of import and export of oil and non-oil products in the

country with their p-values less than 0.05, except for inflation rate with p-value greater than 0.05.It is observed that exchange rate of French franc to Nigeria naira have significant influence on import and export of oil products and on inflation rate in the country with their p-values less than 0.05, except for import and export of non-oil products which are non-significant with p-value greater than 0.05.Exchange rate of Swiss franc to Nigeria naira have no significant influence on import oil products and on inflation rate in the country with their p-values greater than 0.05, while it significantly influence export of oil products, import and export of non-oil product with p-value = 0.000 less than 0.05. And exchange rate of Dutch guilder to Nigeria naira have significant influence on import of oil products and on inflation rate in the country with their p-values less than 0.05, and not significant to import of non-oil, export of oil and non-oil products with p-value greater than 0.05. From the table sigma0 denote the variance covariance matrix coefficients. The significance of each variance and covariance is shown by their p-value.

Table 4.6 Constant conditional correlation MGARCH model

Sample: 1981 - 2019	Number of obs	=39
Distribution: Gaussian	Wald chi2(5)	=342.94
Log likelihood = -522.7784	Prob> chi2	=0.000

	Coef.	Std. Err.	z	P>z	[95%	Conf.
US dollar						
Importofoil	-0.02802	0.018729	-1.5	0.135	-0.06473	0.008691
Import ofnonoil	0.025147	0.005649	4.45	0.000	0.014075	0.036218
Exportofoil	0.010796	0.003373	3.2	0.001	0.004185	0.017407
Exportofnonoil	-0.11098	0.026679	-4.16	0.000	-0.16327	-0.05869
Inflationrate	0.05439	0.252938	0.22	0.83	-0.44136	0.550139
_cons	20.532	9.316582	2.2	0.028	2.271839	38.79217
ARCH_USdollar						
_cons	824.8661	186.7967	4.42	0.000	458.7514	1190.981
Pound sterling						
Importofoil	-0.08468	0.034278	-2.47	0.013	-0.15186	-0.0175
Importofnonoil	0.034859	0.010338	3.37	0.001	0.014596	0.055122
Exportofoil	0.022703	0.006173	3.68	0.000	0.010603	0.034802
Exportofnonoil	-0.15758	0.048828	-3.23	0.001	-0.25328	-0.06188
Inflationrate	-0.06134	0.462924	-0.13	0.895	-0.96865	0.845978
_cons	60.01975	17.05108	3.52	0.000	26.60024	93.43926
ARCH_poundsterling						
_cons	2762.957	625.6753	4.42	0.000	1536.656	3989.259
Deutschemark						
Importofoil	0.012638	0.008786	1.44	0.15	-0.00458	0.029858
Importofnonoil	0.001169	0.00265	0.44	0.659	-0.00402	0.006363
Exportofoil	-0.00221	0.001582	-1.39	0.163	-0.00531	0.000895

Exportofnonoil	-0.00595	0.012515	-0.48	0.634	-0.03048	0.018579
Inflationrate	0.425463	0.118653	3.59	0.000	0.192907	0.658019
_cons	4.499281	4.370414	1.03	0.303	-4.06657	13.06514
ARCH_DeutscheMark						
_cons	181.5163	41.10558	4.42	0.000	100.9508	262.0817
corr(USdollar,poundsterling)	0.708671	0.07971	8.89	0.000	0.552443	0.864899
corr(usdollar,deutschemark)	0.003035	0.160123	0.02	0.985	-0.3108	0.31687
corr(poundsterling,deutschemark)	0.535528	0.114206	4.69	0.000	0.31169	0.759367

Table 4.6 shows the result from CCCMGARCH model. The result indicate that exchange rate of US dollar to Nigeria naira have significant influence on some economic activity of import non-oil and export of oil and non-oil products in the country with their p-values less than 0.05, except for import of oil products and inflation rate with p-value greater than 0.05.It is observed from same model that exchange rate of Pound sterling to Nigeria naira have significant influence on import and export of oil products and not significant to inflation rate in the country with the p-values = 0.895 which is greater than 0.05.Exchange rate of Deutschemark to Nigeria naira has no significant influence on import and exports of oil and non-oil products. It is only significant to inflation rate in the country with the p-values less than 0.05. From the table the correlation between each currency is measured by the model. The result reveal that p-value = 0.000 indicate that there is significant relationship between exchange rate of US dollar, pound sterling to Nigeria naira is correlated likewise pound sterling, deutschemark.

Table 4.7 Constant conditional correlation MGARCH model

Sample: 1981 - 2019	Number of obs	=39
Distribution: Gaussian	Wald chi2(5)	= 424.20
Log likelihood = -29.6692	Prob> chi2	=0.000

	Coef.	**Std. Err.**	**z**	**P>z**	**[95%**	**Conf.**
Japanese yen						
Importofoil	-5.8E-05	0.000175	-0.33	0.743	-0.0004	0.000286
Import ofnonoil	0.000132	5.28E-05	2.5	0.013	2.84E-05	0.000236
Exportofoil	9.72E-05	3.15E-05	3.08	0.002	3.54E-05	0.000159
Exportofnonoil	-0.00042	0.00025	-1.67	0.095	-0.00091	7.25E-05
Inflationrate	-4.52E-06	0.002366	0	0.998	-0.00464	0.004632
_cons	0.188824	0.087131	2.17	0.03	0.01805	0.359597
ARCH_Japaneseyen						
cons	0.072147	0.016338	4.42	0.000	0.040125	0.104168
CFA franc						
Importofoil	-0.00013	2.96E-05	-4.35	0.000	-0.00019	-7.1E-05
Import ofnonoil	3.89E-05	8.94E-06	4.36	0.000	2.14E-05	5.64E-05
Exportofoil	3.51E-05	5.34E-06	6.57	0.000	2.46E-05	4.55E-05

Exportofnonoil	-0.0002	4.22E-05	-4.83	0.000	-0.00029	-0.00012
Inflationrate	-0.00076	0.0004	-1.91	0.056	-0.00155	2.03E-05
_cons	0.055833	0.014741	3.79	0.000	0.026942	0.084725
ARCH_CFAfranc						
_cons	0.002065	0.000468	4.42	0.000	0.001149	0.002982
French franc						
Importofoil	0.004981	0.002103	2.37	0.018	0.00086	0.009103
Import ofnonoil	0.000361	0.000634	0.57	0.569	-0.00088	0.001604
Exportofoil	-0.00091	0.000379	-2.39	0.017	-0.00165	-0.00016
Exportofnonoil	-0.00061	0.002995	-0.2	0.839	-0.00648	0.005262
Inflationrate	0.084507	0.028397	2.98	0.003	0.028849	0.140164
_cons	0.271224	1.04597	0.26	0.795	-1.77884	2.321289
ARCH_ French franc						
_cons	10.39703	2.354462	4.42	0.000	5.782364	15.01169
corr(Japaneseyen,CFAfranc)	0.561852	0.109579	5.13	0.000	0.34708	0.776623
corr(Japanese yen, French franc)	0.24407	0.150589	1.62	0.105	-0.05108	0.53922
corr(CFAfranc, French franc)	-0.08694	0.158918	-0.55	0.584	-0.39842	0.224528

Table 4.7 indicate that exchange rate of Japanese yen to Nigeria naira have significant influence on import non-oil and export of oil products only in the country with their p-values less than 0.05, while it is not significant on import of oil export of non-oil products and inflation rate with p-value greater than 0.05.It is observed from same model that exchange rate of CFA franc to Nigeria naira have significant influence on import and export of oil and non-oil products and not significant to inflation rate in the country with the p-values = 0.056 which is greater than 0.05.Exchange rate of French franc to Nigeria naira has no significant influence on import and exports of non-oil products. It is only significant to import and export of oil products and on inflation rate in the country with the p-values less than 0.05. The result reveal that p-value = 0.000 indicate that there is significant relationship between exchange rate of Japanese yen and CFA franc to Nigeria naira.

Table 4.8 Constant conditional correlation MGARCH model

Sample: 1981 - 2019	Number of obs	=39
Distribution: Gaussian	Wald chi2(5)	= 463.36
Log likelihood = -310.6104	Prob> chi2	=0.000

	Coef.	**Std. Err.**	**z**	**P>z**	**[95%**	**Conf.**
Swiss franc						
Importofoil	-0.01735	0.012826	-1.35	0.176	-0.04248	0.007792
Import ofnonoil	0.024247	0.003868	6.27	0.000	0.016665	0.031828
Exportofoil	0.008867	0.00231	3.84	0.000	0.00434	0.013395
Exportofnonoil	-0.10819	0.01827	-5.92	0.000	-0.14399	-0.07238
Inflationrate	-0.13673	0.173209	-0.79	0.43	-0.47621	0.202756

_cons	16.35879	6.379872	2.56	0.01	3.854475	28.86311
ARCH_SWISSfranc						
_cons	386.8068	87.59442	4.42	0.000	215.1249	558.4887
Dutch guilder						
Importofoil	0.012379	0.005848	2.12	0.034	0.000918	0.023839
Import ofnonoil	0.001829	0.001764	1.04	0.3	-0.00163	0.005285
Exportofoil	-0.00184	0.001053	-1.75	0.08	-0.00391	0.000221
Exportofnonoil	-0.00726	0.00833	-0.87	0.383	-0.02359	0.009061
Inflationrate	0.213114	0.078971	2.7	0.007	0.058334	0.367893
_cons	2.095623	2.908762	0.72	0.471	-3.60545	7.796692
ARCH_dutchguilder						
_cons	80.40563	18.20827	4.42	0.000	44.71807	116.0932
corr(swissfranc,dutchguilder)	0.296509	0.14605	2.03	0.042	0.010257	0.582762

Table 4.8 indicatethat exchange rate of Swiss franc to Nigeria naira have significant influence on import non-oil, export of oil and export of nonoil products only in the country with their p-values less than 0.05, while it is not significant on import of oil products and inflation rate with p-value greater than 0.05.It is observed from same model that exchange rate of Dutch guilder to Nigeria naira have significant influence on import oil and inflation rate only not significant to import of nonoil, export of oil and non-oil in the country with the p-values greater than 0.05. The result reveal that p-value = 0.042 indicate that there is significant relationship between exchange rate of SWISS Franc and Dutch guilder to Nigeria naira.

5.0 SUMMARY AND CONCLUSION

The result from the summary statistics reveals that the money spent by Nigeria government to import non-oil product #3937.533 Billion is on higher rate as compared to what is realized to export our non-oil products #618.4662 Billion, this could put the country at deficit. Result based on normality revels that the exchange rate of the country currencies studied is not normally distributed. It infers that the exchange rate to Nigeria naira is skewed and has presence of kurtosis meaning that there is an asymmetric effects in these models (i.e. volatility is higher in a falling market than in a rising market) which is another stylize fact of financial time series. The results from the Multivariate Generalized Autoregressive Conditional Heteroskedasticity (MGARCH) reveal the influence of some of the currency exchange rate to Nigeria naira on the economic activities studied in this work. We employed two multivariate volatility models (i.e. DVECH and CCC), the results indicated that the models from DVECH and CCC exhibit similar behaviour for exchange rate volatility of each countries on the economic activity of Nigeria. We further observe that the Log likelihood from both models, DVECH = -747.793 and CCC= -863.058. it infers that the CCC model performs better than DVECH model.

REFERENCES

Adelowokan, O. a. (2015). Exchange rate volatility on investment and growth in Nigeria: an empirical analysis. Global journal of management and business research, 21-30

Akindele, O. O. (2018). Foreign Exchange Market Efficiency in Nigeria (The Past and Current Exchange Rate Returns). Sumerianz Journal of Economics and Finance, 1 (1), 14-21.

Ali, A. I. (2015). Real exchange misalignment and growth in Nigeria. CBN Journal of Applied Statistics, Vol. 6, No. 2.

Amassoma, D. a. (2016). The nexus between exchange rate variation and economic growth. Singaporean Journal of Business Economics and Management Studies, Vol. 4, No. 12, pp 7 – 28

Bassey, K. J. (2019). On economic growth - reserves accumulation nexus in Nigeria: a nonlinear asymmetric co-integration estimation. West African Journal of Monetary and Economic Integration, Vol. 19, No. 1

Bayat, T. M. (2014). Exchange rates and foreign exchange reserves in Turkey: nonlinear and frequency domain causality aproach. Theoretical and Applied Economics, Vol XXI, No. 11(600(, pp. 27-42

Dada, E. A. (2012). Exchange Rate and Macroeconomic Aggregates in Nigeria. Journal of Economics and Sustainable Development, Vol.3, No.2.

Danladi, J. (2009). External Reserves and Macroeconomic Performance. Ibadan: Unpublished Masters Thesis. University of Ibadan. Ibadan.

Elijah, A. O. (2020). Ardl-Bound Testing Approach to the Connection Between External Reserve And Economic Growth In Nigeria. *Journal of Academic Research in Economics*, *12*(2).

10) Folorunsho, M., Ajisafe, R. A. & Olofin, O. P. (2019). Capital controls, entrepreneurship and economic growth in selected developing countries. Asian Economic and Financial Review, 9(2):191-212.

Igbanugo, I. C. & Eze, E. A. (2017). Empirical Analysis of Exchange Rate Regime and External Reserves Accumulation in Nigeria (1970-2015) . , International Journal of Research in Management, Economics and Commerce, Volume 07 Issue 07, Page 69-79

IMF. (2009). International Monetary Fund, Annual Report. Retrieved from www.imf.org/external/pubs/ft/ar/2009/eng/pdf/a1.pdf

International Monetary Fund. (2014). BPM6 Compiltion Guide. Washington DC, USA: International Monetary Fund, Publication Services

Kalu, E. U., Ugwu, O. E., Ndubuaku, V. C. & Ifeanyi, O. P. (2019). Exchange Rate and Foreign Reserves Interface: Empirical Evidence from Nigeria. The Economics and Finance Letters , Vol. 6, No. 1, pp. 1-8 .

Nwachukwu, N. E., Ali, A. I., Abdullahi, I. S., Shetimma, M. A., Zirra, S. S., Falade, B. S. & Alenyi, M. J. (2016). Exchange Rate and External Reserves in Nigeria: A Threshold Cointegration Analysis . CBN Journal of Applied Statistics, Vol. 7 No

Nwosa Philip. (2017). External reserves and economic growth in Nigeria. Journal of Entrepreneurship, Business and Economics, 110-126

Nwosa Philip. (2017). External reserves and economic growth in Nigeria. Journal of Entrepreneurship, Business and Economics, 110-126

Onwuka, M. E. (2014). Impact of External Reserve and Foreign Debt on Naira Exchange Rate. *Journal of International Academic Research for Multidisciplinary*, Volume 2, Issue 6

Osuka, B. a. (2008). Foreign Exchange Fluctuations and the Nigeria Fledging Economy. The Nigerian Banker.

Raju, J. V. & Gokhale, M. S. (2013). Causality between Exchange Rate and Foreign Exchange Reserves in the Indian Context. Global Journal of Management and Business Research Finance , Vol.13, Issue 7 Version 1.0 .

Richard, C. O. (2018). Foreign Exchange Rate Nexus and the Nigeria Economy: A Theoretical Perspective, 1986 – 2018. *European Journal of Accounting, Finance and Investment*, Vol. 4, No. 12

Umeora, C. E. (2013). Accumulation of External Reserves and Effects on Exchange Rates and Inflation in Nigeria. International Business and Management, Vol. 6, No. 2, 2013, pp. 105-114

AN APPLICATION OF ANALYSIS OF COVARIANCE (ANCOVA) TECHNIQUE IN ELIMINATING THE EFFECT OF CONCOMITANT VARIABLES ON SALES OF GRAND CEREALS OIL.

DANIEL Bitrus Dajel, Yisa YAKUBU
Department of Statistics, Federal University of Technology, Minna
kyenretdang@gmail.com, yisa.yakubu@futminna.edu.ng

ABSTRACT

Analysis of covariance (ANCOVA) is an extension of analysis of variance (ANOVA) that allows modelling and adjustment for input variables that are measured but not randomized or controlled in the experiment. ANCOVA tests whether factors have an effect after removing the variance due to covariates. Data for this work are on sales of grand cereals oil being produced by Grand Cereals and Oil Mills Limited Company located in Jos, Plateau State, Nigeria. Effects of sales managers' age and gender on the recorded sales of this product were first examined using the ANOVA technique. Then the ANCOVA technique was employed to investigate whether sales differ by the sales managers' age and gender and whether there is significant interaction effect between these variables (age and gender) in terms of the average sales after adjusting/controlling for the sales volume. The ANOVA result shows that gender and age have a statistically significant effect on sales ($p< 0.001$) and that the fitted model accounted for 49.8% of variation in the data, with a mean squared error (MSE) of 70.782. The effect of age after adjusting for the covariate was observed to be significant ($p< 0.001$). The fitted ANCOVA model accounted for about 80.5% of the total variation in the sales data with a MSE of 27.028, which is a substantial reduction, indicating a sharp increase in the power of the test to detect the significant effects. We then conclude that, the middle age group has a significant effect on the volume of sales than the young and old considering their work experience and their strength.

Keywords: Analysis of Covariance, Eliminating effects of concomitant variable, Analysis of sales

INTRODUCTION

Most companies in the wake of the 21st century are confronted with diverse challenges especially in a developing country like Nigeria with series of diversity in their marketing and sales. The Grand Cereals and Oil Mills Limited Company has made remarkable success as one of the earliest milling Companies that penetrated the heart of the most populous black African nation in within the West African region. One of the guiding principles of any business organization is to maximize profit and any other reason is added. Thus, for any business to be carried out the firm would undergo a strong business research to determine the strategies that will be employed to run a successful business in a given society in order to improve its volume of sales. In addition, it is generally known that several organizations adopt different marketing strategies such as promotion and experimental design to boost its influences and to survive the market competition. Generally speaking, in a designed experiment, any variables that should theoretically correlate with the dependent variable on

similar types of subjects should be considered as possible covariates (Stevens, 1992). There have been several attempts by different scholars in trying to reduce the variability of the mean square error using the analysis of variance technique especially when there is a covariate (especially in market research). This trend has grossly affected the sales of products produced by manufacturers in various parts of the country and therefore constitutes a problem. Therefore, this work employs the ANCOVA technique to eliminate the effect of the concomitant variables in market research.

1.1 Experimental Design

Experimental Design as a branch of statistics, mainly involves the arrangement and procedures adopted in an experimental study. This has to do with how participants are allocated to the different groups in an experiment. The research is being carried out in objective and controlled fashion so that precision is maximized and specific conclusions can be drawn regarding the hypothesis. Generally, the purpose is to establish the effect that a factor or independent variable has on a dependent variable. The principles of experimental design play an important role in research that does not follow the strict tenets of hypothesis testing. However, this research focused on planning research that will utilize experimental design in order to test and validate the relationship between and among experimental variables. Experimental design as a subset of scientific investigation is a popular and widely used research approach. The essence of experimental design and perhaps the most important reason researchers choose to design and conduct experiments is the precision with which one can analyse the relationship between and among variables and to make that analysis as objective as possible. To look at it from another perspective, experimental design minimizes ambiguity and attempts to eliminate confusion. A true experimental design relies on testing the relationships between and among variables; generally speaking, one variable, the independent variable, is controlled in order to measure its effect on other, dependent, variables. A central concern of any researcher using experimental design must be control; in experiments, the researcher chooses an intervention, associated with the independent variable, and controls how that intervention is applied, or introduced, into the research setting. If the experimental design is applied correctly, then a causal relationship can be established between the independent variable and dependent variable(s).

1.2 Analysis of variance

Analysis of variance is also considered one of the basic tools that will be used in this research. Analysis of variance (ANOVA) involves comparing random samples from several populations. The sample sizes for the treatment groups are possibly different, say, Ni and we assume that the samples are all independent. Moreover, we assume that each population has the same variance and is normally distributed. What analysis of variance does is, to tests the relationship between a categorical and a numeric variable by testing the differences between two or more means. This test produces a p-value to determine whether the relationship is significant or not. ANOVA also can be thought of in terms of a model plus error. Here, the dependent variable scores constitute the data, the experimental conditions constitute the model and the component of the data not accommodated by the model, again, is represented by the error term. Although the dependent variable in ANOVA is most likely to be measured on a quantitative scale, the statistical comparison is drawn between the groups of subjects receiving different experimental conditions and is categorical in nature, even when the

experimental conditions differ along a quantitative scale. Therefore, it is a particular type of regression analysis that employs quantitative predictors to act as categorical predictors.

1.3 Regression

Regression analysis attempts to explain data in terms of a set of independent variables or predictors and a residual component (error). Typically, regression deals with predicting a quantitative dependent variable from one or more quantitative independent variables, and in determining the relative contribution of each independent variable to the prediction: there is interest in what proportion of the variation in the dependent variable can be attributed to variation in the independent variable(s). Regression also may employ categorical (also known as nominal or qualitative) predictors: the use of independent variables such as sex, marital status and type of teaching method is common. Moreover, regression is the elementary form of GLM, it is possible to construct regression GLMs equivalent to any ANOVA and ANCOVA GLMs by selecting and organizing quantitative variables to act as categorical variables.

1.4 Analysis of covariance

In some experiments where we use ANOVA some of the unexplained variability (i.e. the error) is due to some additional variable (called a covariate) which is not part of the experiment. If we can somehow remove the effect of this variable, we could reduce the error variance thus enabling us to get a more accurate picture of the true effect of the independent variable. This is the main goal of **Analysis of Covariance (ANCOVA).**

Regression and analysis of variance are probably the most frequently applied of all statistical analyses. One reason for the frequent use of regression and analysis of variance (ANOVA) applications is their suitability for many different types of research design. Both regression and ANOVA procedures are applicable to experimental, quasi-experimental and non-experimental data. Regression allows examination of the relationships between an unlimited number of predictor variables and a response or dependent variable, and enables values on one variable to be predicted from the values recorded on one or more other variables. Similarly, ANOVA places no restriction on the number of groups or conditions that may be compared, while factorial ANOVA allows examination of two or more independent variables or factors on a dependent variable. ANCOVA has been applied to a number of different statistical operations (Cox & McCullagh, 1982), it is most frequently used to refer to the statistical technique that combines regression and ANOVA. As the combination of these two techniques, ANCOVA calculations are more involved and time consuming than either technique alone. Fisher (1932; 1935) originally developed ANCOVA to increase the precision of experimental analysis. Today, it is applied most frequently in quasi-experimental research, where, unlike experimental research, the topics investigated are most likely to involve variables that, for practical or ethical reasons, cannot be controlled directly. In these situations, the statistical control provided by ANCOVA has particular value. Nevertheless, in line with Fisher's original conception, many experiments can benefit from the application of ANCOVA. This arrangement has an analysis of covariance as a method used to boost the precision of an experiment in special cases.

ANCOVA usually features and become vital to adopt when an experiment originally with response variable Y has an explanatory variable say X, where the variable Y is linearly related to the independent variable X but not wholly dependent on it. If a variable can only be observed along with Y but cannot be subjected to the experimenter’s control, then such a

variable is called a covariate or concomitant variable. Therefore, ANCOVA basically encapsulates the adjustment of the observed response variable in order to account for the uncontrollable variables that may arise during experimentation. In most experiments where such adjustment is required but it is ignored, the concomitant variable could inflate the error mean square and make the true differences in the response of the treatment hard to detect thereby limiting the possibilities of rejecting the null hypothesis. Put loosely, ANCOVA is a method of adjusting the observed response variable *(Y)* for the effect of an uncontrollable nuisance variance (covariate).

In the light of the above, one can say that there are several factors that may affect sales of certain products of a company. Some of these factors may result to poor sales and bankruptcy of a firm. The basic idea is to augment the analysis of variance model containing the factor effects with one or more additional quantitative variables that are related to the response variable. This augmentation is intended to reduce the variance of the error terms in the model. Thus, covariance models are just a special type of regression model. In other words**,** the analysis of covariance is a statistical tool which can be used to identify in a variable of interest, say Y, the amount of variation which is a result of variation in another variable, say X, upon which Y is dependent. Analysis of covariance can then be applied to remove this variation from the variable of interest. The related variables are referred to as concomitant variables.

This study apply the ANCOVA technique in eliminating the effect of concomitant variables in sales of grand cereals oil. This aim will be achieved through the following objectives:

(i) To test for the significance of the difference among the various independent variables in terms of sales using ANOVA technique.
(ii) To employ ANCOVA technique to examine the effect of the covariate on the sales.
(iii) To examine the significance of interaction between the covariate and other independent variables.

2. METHODOLOGY

Data collection

Data for this work were on sales of Grand Cereals Oil being produced by Grand Cereals and Oil Mill limited, Jos, Plateau State in Nigeria. The data set consists of sales of Grand Cereals Oil for thirty years (1991-2020) by male and female sales managers from three different age groups randomly selected from the company. There are two independent variables namely, Age, with three levels as 20 - 28 years, 29 – 37 years, and 38 – 46 years; Gender with two levels, male and female. The dependent variable is the yearly volume of sales while the covariate is the yearly average sales for thirty years.

2.1 THE MODEL AND NOTATIONS

We can apply one-way (one-factor) analysis of variance to test the hypothesis that the volume of sales means from the three age groups are equal. The analysis of variance model would be

$$Y_{ij} = \mu + \alpha_i + \varepsilon_{ij} \ldots (1)$$

where Y represents the volume of sales on the ijth factors, μ is the overall mean, α_i is the treatment, and $\varepsilon_{ij}$is the random error term for the analysis of variance model.

If we make the assumptions necessary Y_{ij} random variables with true means, additivity, and the ε_{ij} are independently and normally distributed with mean zero and common variance δ^2, an analysis of variance can be performed validly.

Since for each volume of sales that will be measured, it is possible to measure the effect of the age on the volume of sales as well as the effect of the gender on the volume of sales. It is now possible using a regression analysis to determine how the volume of sales Y, varies as a result of gender and differences in age (i.e. X_1 and X_2) respectively. A (linear) regression model would be

$$Y = \beta_o + \beta 1_{x1} + \beta 2_{x2} + \varepsilon_{ij} \text{ ….. (2)}$$

where Y is the volume of sales,β_0 is the overall mean of the volume of sales, while X_1 and X_2 are the two independent variables (age and gender) respectively. $\varepsilon_{ij}$is the random error term whereas β_1 and β_2 are the coefficient for the regression model between Y and X_1, X_2.
To determine just exactly how to remove from estimates of variance the variation due to the covariate X, the regression model must be rearranged. Recall that the ANCOVA model can be written as,

$$Y_{ij} = \mu + \alpha_j + \beta z_{ij} + \varepsilon_{ij} \quad (1)$$

Y_{ij} is the i_{th} score in the j_{th} treatment, μ is a constant common to all Y scores,α_j is the effect of the J_{th}treatment level and the error termε_{ij}, reflects random variation due to any uncontrolled source? The new term βz_{ij} represents the influence of the covariate on the dependent variable. It comprises the regression coefficient parameter β, which represents the degree of linear relationshipbetween the covariate and the dependent variable and Z_{ij}, the particular covariatescore corresponding to the Y_{ij}.
the slope of the regression line employed in the ANCOVA GLM, which is given by

$$\hat{\beta} = \frac{\sum_{j=1}^{p}\sum_{i=1}^{N}(Z_{ij}-\bar{Z}_J)(Y_{ij}-\bar{Y}_J)}{\sum_{j=1}^{p}\sum_{i=1}^{N}(Z_{ij}-\bar{Z}_J)^2} \quad (2)$$

$\hat{\beta}$may also be calculated from

$$\hat{\beta} = \frac{\sum_{i=1}^{N}(Z_{i1}-\bar{Z}_1)^2\, b1+\sum_{i=1}^{N}(Z_{i2}-\bar{Z}_2)^2\, b2+\sum_{i=1}^{N}(Z_{i3}-\bar{Z}_3)^2\, b3}{\sum_{i=1}^{N}(Z_{i1}-\bar{Z}_1)^2+\sum_{i=1}^{N}(Z_{i2}-\bar{Z}_2)^2+\sum_{i=1}^{N}(Z_{i3}-\bar{Z}_3)^2} \quad (3)$$

Equation (3) reveals$\hat{\beta}$ as the weighted average of the separate (within group) regression lines, b1, b2 and b3, where each experimental condition regression coefficient (b1, b2 and b3) is weighted by the variation of the covariate scores in that experimental condition. Consequently, $\hat{\beta}$may be called the within groups regression coefficient ($\hat{\beta}$ =bw). An important point to appreciate is that equations (2) and (3) provide a regression coefficient which is free of the influence exerted on the dependent variable scores by the experimental conditions. A little algebra applied to equation (1) reveals

$$Y_{faij} = Y_{ij} - \beta z_{ij} = \mu + \alpha_j + \varepsilon_{ij} \quad (4)$$

where Y_{faij} is the fundamental adjusted dependent variable score observed if all influence of the covariate is removed from the dependent variable score. The Y_{faij} correspond to the points on the dependent variable axis intersected by eachof the experimental condition regression lines. This is where the value of the covariate equals zero. Traditionally in ANCOVA however, the dependent variable scores are not adjusted to remove all influence of the covariate. Instead, adjustment is made as though all subjects had obtained a covariate score equal to the general covariate mean.

Now, replacingβz_{ij} in equation (1) with $\beta(Z_{ij} - Z_G)$ provides the single factor independent measures experimental design GLM for traditional ANCOVA with one covariate,

$$Y_{ij} = \mu + \alpha_j + \beta(Z_{ij} - Z_G) + \varepsilon_{ij} \ldots (5)$$

Applying the same algebra to equation (5) as was applied to equation (1)
Provides

$$Y_{aij} = Y_{ij} - \beta(Z_{ij} - Z_G) = \mu + \alpha_j + \varepsilon_{ij} \ldots (6)$$

where Y_{aij} is the adjusted dependent variable score based on the differencebetween the recorded covariate score and the general covariate mean scaled by the regression coefficient that will be estimated from the data. The experimental condition means of the Y_{aij} scores correspond to the points on the dependent variable axiswhere the separate experimental condition regression lines intersect the line representing Z_G.
Although the GLMs described by equations (1) and (5) employ the same regression coefficient, obviously the adjustments provided by βz_{ij} and$\beta(Z_{ij} - Z_G)$ do not provide identical adjusted dependent variable scores.

2.2 REGRESSION SLOPES USED IN ADJUSTMENT

Looking at the application of the covariance analysis, three different regressions of Y on X can be seen:

1 - The overall regression of all Y's on all X's.

2 - The within treatment regressions (assumed to be the same regression in each treatment, by setting each equal to the average).

3 - The regression of the Y group means on the X group means. The "average within-treatment" regression slope is found by

$$b=\frac{\sum XY}{\sum XX}$$

In adjusting the error sum of squares by this slope, and the total (treatment + error) sum of squares by the "overall" regression slope, given by

$$b = \frac{\sum XY}{\sum X^2}$$

we assume the two are approximately equal, that is, that the "pooled" or "average" within treatment regression slope is the same as the overall regression slope. The third regression, means on means, is not used.

Now that it is known how to adjust total variance to remove that amount which is "an inflation" caused by variation in the concomitant variables upon which the variable of interest is dependent, multiple covariance can be used in the analysis of covariance. Although the computations become more involved, the objective remains identical to that in simple covariance. That is, to determine the regression relationship between Y and the independent X, adjust the observations of Y by means of this relationship to some standard values of the X, and then examine the adjusted values of Y by the analysis of variance. In the multiple covariance case, the "adjustment" is a little more involved, but the objectives are the same.

In simple covariance, a two-factor experiment (assuming there is an interaction effect) would have the model:

$$Y_{ijk}=\mu + \alpha_i+\beta_j+(\alpha\beta)_{ij}+\gamma(X_{ij}-\bar{X}\ldots) +\varepsilon_{ijk}$$

where μ is the grand true mean of the Y_{ijk}

$\alpha_I$is the treatment effect (first factor i.e factor A)

β_j is the block effect (second factor i.e factor B)
$(\alpha\beta)_{ij}$ is the interaction effect between the two factors A and B,
$\gamma(X_{ij}-\bar{X}\ldots)$ is the regression relation which adjusts Y forvariation in X, and ε_{ijk} is the error associated with Y_{ijk}.

For the multiple covariance case in which there are m covariates. This approach is not computationally feasible time-wise, however, this method remains essentially unchanged regardless of the number of factors or the experimental design as given above.

RESULTS AND DISCUSSION

The generated results are presented and fully discussed in this section.

Table 1: Descriptive statistics (**dependent variable: Sales**)

Age	gender	Mean	Std. Deviation	N
20-28 years	Male	20.2667	6.72070	30
	Female	22.2667	6.72070	30
	Total	21.2667	6.73938	60
29-37 years	Male	25.3333	3.27302	30
	Female	44.1333	15.11276	30
	Total	34.7333	14.40088	60
38-46 years	Male	30.2667	6.72070	30
	Female	35.7000	7.07667	30
	Total	32.9833	7.37033	60
Total	Male	25.2889	7.05555	90
	Female	34.0333	13.69118	90
	Total	29.6611	11.71217	180

Table 1 above presents the mean, standard deviation and sample size for each combination of groups of the two independent variables (age and gender). From the table, we can see that group sizes were equal with 30 sales points in each group (n = 30 for each group) and that mean sales was higher for female in the three age groups compared to that of the male.

However, the means of the groups are **not** adjusted for the covariate (sales volume i.e., they are **unadjusted means).**

Table 2: Test of between subjects effects (**dependent variable: Sales**)

Source	Type III Sum of Squares	df	Mean Square	F	Sig.
Corrected Model	12238.294[a]	5	2447.659	34.580	.000
Intercept	158360.672	1	158360.672	2237.308	.000
Age	6433.878	2	3216.939	45.449	.000
Gender	3440.939	1	3440.939	48.613	.000

age * gender	2363.478	2	1181.739	16.696	.000
Error	12316.033	174	70.782		
Total	182915.000	180			
Corrected Total	24554.328	179			

The above reveals that age, gender and the interaction between age and gender are statistically significant at 0.01 level of significance that there is an effect on the sales.

Table 3: Model summary

GgModel	R	R Square	Adjusted R Square	Std. Error of the Estimate
	.706[a]	.498	.484	8.41319

a. Predictors: (Constant), gender dummy code by age grp2 dummy code interaction, gender dummy code by age grp1 dummy code interaction, age1, age2, gender1
The table above reveals that 50% of the data fit the regression model.

Table 4: ANOVA

Model		Sum of Squares	df	Mean Square	F	Sig.
1	Regression	12238.294	5	2447.659	34.580	.000[b]
	Residual	12316.033	174	70.782		
	Total	24554.328	179			

a. Dependent Variable: sales
b. Predictors: (Constant), gender dummy code by age grp2 dummy code interaction, gender dummy code by age grp1 dummy code interaction, age1, age2, gender1

Table 5: Coefficients

		Unstandardized Coefficients		Standardized Coefficients		
Model		B	Std. Error	Beta	T	Sig.
1	(Constant)	35.700	1.536		23.242	.000
	age1	-13.433	2.172	-.542	-6.184	.000
	age2	8.433	2.172	.340	3.882	.000
	gender1	-5.433	2.172	-.233	-2.501	.013
	Int	3.433	3.072	.110	1.118	.265
	int2	-13.367	3.072	-.427	-4.351	.000

a. Dependent Variable: sales

Table 6: Adjusted means

Age	Gender	Mean	Std. Deviation	Adjusted mean
	Male	20.267	6.7207	13.546
20-28 years	Female	22.267	6.7207	15.546
	Total	21.267	6.73938	14.52732
	Male	25.333	3.27302	22.06028
29-37 years	Female	44.133	15.11276	29.02054
	Total	34.733	14.40088	20.33242
	Male	30.267	6.7207	23.546
38-46 years	Female	35.7	7.07667	28.62333
	Total	32.983	7.37033	25.61297
	Male	25.289	7.05555	18.23335
Total	Female	34.033	13.69118	20.34212
	Total	29.661	11.71217	17.94893

The table above shows the adjusted mean from the original mean.

Table 7: the mean, standard error and confidence interval of age

Age	gender	Mean	Std. Error	95% Confidence Interval	
				Lower Bound	Upper Bound
20-28 years	Male	27.644	1.058	25.554	29.733
	Female	28.079	1.022	26.062	30.097
29-37 years	Male	20.553	1.002	18.575	22.531
	Female	32.795	1.18	30.466	35.124
38-46 years	Male	29.821	0.96	27.926	31.716
	Female	39.075	0.981	37.138	41.011

The table 6 above, shows a two-way ANCOVA, where the mean values of the groups of the two independent variables have been adjusted by the covariate (sales volume). This is important because the statistical significance of the two independent variables is based on the adjusted means and **not** the unadjusted means. If we ignore these adjusted means, it would be as though the two-way ANCOVA was never run. Therefore, the **Estimates** table above presents the adjusted mean. Table 3 and 4 reveals the standard error and 95% confidence interval of the adjusted mean for the dependent variable for each combination of groups of the two independent variables. **Descriptive statistics** and **estimates** in table 1 above, which reflects sales managers who belong to the young group of age and are also male, shows that the **unadjusted mean** sales for this group were 20.2667 (in naira), whereas when adjusted for the continuous covariate the **adjusted mean** sales were 13.546 (in naira). In other words,

the sales for this group were **lower** when the initial volume of sales was taken into account. Considering the managers who are male and are middle aged, the **unadjusted mean** sales for this group were 25.3333 whereas when adjusted for the continuous covariate, the **adjusted mean** sales were 22.06028 (in naira). In other words, the sales for this group were higher when the initial volume of sales was taken into account.

However, to determine whether there is an **interaction effect** between the two independent variables (age and gender) in terms of dependent variable (sales), after controlling for the covariate (sales volume), let's consider the table below.

Table 8: ANOVA TABLE

Source	Type III Sum of Squares	df	Mean Square	F	Sig.	Partial Eta Squared
Corrected Model	19774.762[a]	6	3295.794	119.294	.000	.805
Intercept	537.307	1	537.307	19.448	.000	.101
sales_vol	7536.468	1	7536.468	272.788	.000	.612
Age	2010.672	2	1005.336	36.389	.000	.296
Gender	2375.670	1	2375.670	85.989	.000	.332
age * gender	1125.013	2	562.506	20.360	.000	.191
Error	4779.566	173	27.628			
Total	182915.000	180				
Corrected Total	24554.328	179				

The table above shows that all the variables are significant after adjusting for covariates in the response variable.

Table 9: Mode summary

Model	R	R Square	Adjusted R Square	Std. Error of the Estimate
1	.897[a]	.805	.799	5.25619

a. Predictors: (Constant), sales_vol, gender1, age1, int2, int, age2

The table above reveals that 80% of the data fit the regression model after adjusting for the covariate.

Table 10: Mode summary

Model		Sum of Squares	Df	Mean Square	F	Sig.
1	Regression	19774.762	6	3295.794	119.294	.000[b]

	Residual	4779.566	173	27.628
	Total	24554.328	179	

a. Dependent Variable: sales

b. Predictors: (Constant), sales_vol, gender1, age1, int2, int, age2

Table 11: Coefficients

Model		Unstandardized Coefficients		Standardized Coefficients		
		B	Std. Error	Beta	t	Sig.
1	(Constant)	15.851	1.538		10.306	.000
	age1	-10.995	1.365	-.444	-8.054	.000
	age2	-6.279	1.623	-.253	-3.868	.000
	gender1	-9.253	1.377	-.396	-6.721	.000
	Int	8.818	1.947	.281	4.529	.000
	int2	-2.989	2.020	-.095	-1.480	.141
	sales_vol	.196	.012	.783	16.516	.000

a. Dependent Variable: sales

Table 8 above revealed that, the *p*-value for this interaction effect is **.0001** (i.e., $p = .0001$). Since .0001 is **less than** .05 (i.e., it satisfies $p < .05$), this means that there **is** a statistically significant two-way interaction effect. It indicates that we were correct in thinking that the **effect** of age on sales (after controlling for volume of sales) **depends** on gender or, equivalently, the **effect** of gender on sales (after controlling for sales volume) **depends** on whether the gender is accompanied by age.

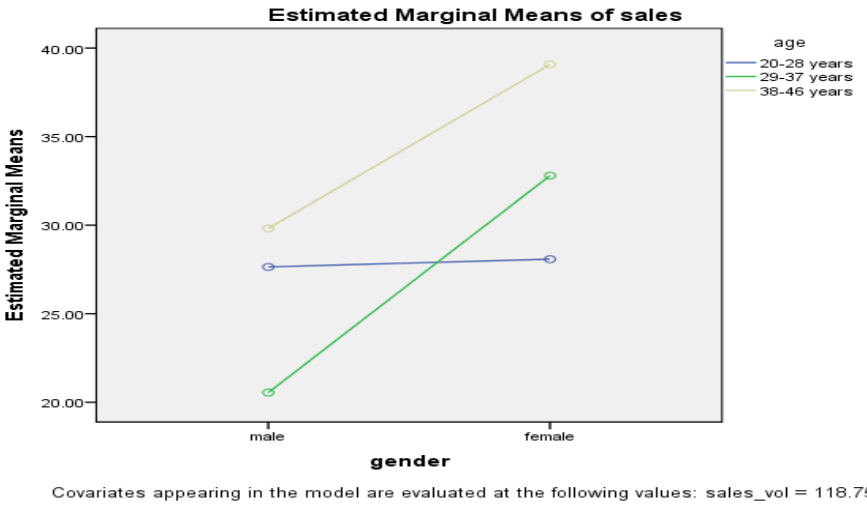

Figure 1: a plot showing the interaction effect of gender and sales mean.

In a two-way ANCOVA, the mean values of the groups of the two independent variables have been adjusted by the covariate (sales volume). This is important because the statistical significance of the two independent variables is based on the adjusted means and **not** the unadjusted means. If we ignore these adjusted means, it would be as though the two-way ANCOVA was never run. Therefore, the **Estimates** table above presents the adjusted mean, standard error and 95% confidence interval of the adjusted mean for the dependent variable for each combination of groups of the two independent variables.

Overall, it would appear that gender has a similar impact on sales when undertaken in addition to young and middle age, but has a much larger impact when combined with an elderly age group. Main effect gender: A statistically significant main effect of gender indicates that there is a difference in the effect of gender on sales (after controlling for sales volume) when keeping fixed (averaging over) the levels of age (i.e., taking age into account as a whole, but ignoring whether a manager was in the "young", "middle" or "elderly" age group). In other words, there is a difference in sales (after adjusting for sales volume) between managers who are male and female when ignoring which age group, a manager belongs and vice versa.

Conclusion

The data collected from grand cereal and oil mills limited was used to apply the analysis of covariance technique to eliminate the effect of concomitant variable in the sales. The estimates of the adjusted mean were obtained alongside the reduced error mean square which was obtained to be 27.267 which is relatively small. This means that analysis from this ANCOVA technique or model can be considered reliable to a large extend. Also, the estimates were seen to be close to the corresponding actual values which were lying between plus or minus the standard errors of the estimates. Thus, the selected model is considered to be useful for eliminating the effect of covariate in the analysis of volume of sales.

In the same vein, the researcher was also able to found that when using ANOVA technique to eliminate the effect of the covariate, the error mean square always turns out to high. Ignoring the covariate will lead to a skewed or bias data.

REFERENCES

Roger W. Ferguson (2011). Challenges of Financial Innovation. A journal of innovation policy and economy. Vol. 12(1), pg.5. Published by the university of Chicago Press.

Cox and McCullagh (2011), Analysis of covariance in agronomy and crop research. A Canadian journal of plant science,, pg 4.

Christopher (2018). Analysis of covariance with heterogeneity of regression and random covariate. A Ph.D. thesis submitted to the department of Psychology University of Mexico, pg. 25.

Stevens (2002), Applied multivariate statistics for social sciences (4th edition, pg. 16). Published by Lawrence associates' publishers.

Gullick and Bugg (1992), A concept analysis of self-monitoring. A journal of advance nursing/vol.57(3), pg.339.

Moore 1983; An analysis of the financial management techniques. A journal of business finance and accounting/vol.10, issue 4/p.623-645

Munro's Statistical method for health care research. 6th edition by Stacey and Elizabeth.

EVALUATING STUDENTS' ACADEMIC PERFORMANCE USING CLUSTERING TECHNIQUES (A CASE STUDY OF SCHOOL OF ENGINEERING, FEDERAL POLYTECHNIC, BIDA)

[1]ALKALI Y. I. (alkaliyandagi@gmail.com)
[2]Yisa YAKUBU (*yisa.yakubu@futminna.edu.ng*)
[1]Department of Statistics, the Federal Polytechnic, Bida
[2]Department of Statistics, Federal University of Technology Minna

ABSTRACT

Predicting students' performance becomes more challenging due to large volume of data in educational databases. Data Clustering is the task of grouping a set of objects in such a way that objects in the same group are more similar to each other than to those in other groups. Clustering categorizes data into groups such that objects are grouped in the same cluster when they are similar according to specific metrics. It is one of the methods in data mining to analyse the massive volume of data. With clustering, interesting patterns and structures can be found directly from very large data sets with little or no background knowledge. This work evaluates students' academic performance using clustering techniques. Data on examination raw scores of final year Higher National Diploma (HND) students from five departments of School of Engineering, The Federal Polytechnic, Bida, were collected from the Examination and Records Unit of the Polytechnic. For each department, three clustering algorithms (namely, the k-Means, k-Medoids, and Fuzzy C Means (FCM)) were used to organize the collected data (the students' examination raw scores) into three clusters based on similarity. These clusters define the students' academic ability (performance) and they include average, good and excellent performance. The clustering algorithms were then compared based on Cluster Size, Cluster membership, and number of iterations taken to reach convergence. Recommendations for further studies were made at the end of the work.

Keywords: Clustering techniques, Students' academic performance, K-means, K-mediods, Fuzzy C-mean

1. Introduction

Clustering is the unsupervised classification of patterns (observations, data items, or feature vectors) into groups called clusters. The clustering problem has been addressed in many contexts and by researchers in many disciplines; this reflects its broad appeal and usefulness as one of the steps in exploratory data analysis. Data analysis underlies many computing applications either in a design phase or as part of their online operations. Data analysis procedures can be dichotomized as either exploratory or confirmatory based on the availability of appropriate models for the data source, but a key element in both types of procedures (whether for hypothesis formation or decision-making) is the grouping or classification of measurements based on either (i) goodness-of-fit to a postulated model or (ii) natural groupings (clustering) revealed through analysis. Cluster analysis is the organization of a collection of patterns (usually represented as a vector of measurements or a

point in a multidimensional space) into clusters based on similarity. Intuitively patterns within a valid cluster are more similar to each other than they are to a pattern belonging to a different cluster.

Clustering is useful in several exploratory pattern analysis, grouping, decision making and machine learning situations including data mining, document retrieval, image segmentation and pattern classification. However, in many such problems there is little prior information (e.g., statistical models) available about the data and the decision maker must make as few assumptions about the data as possible. It is under these restrictions that clustering methodology is particularly appropriate for the exploration of interrelationships among the data points to make an assessment (perhaps preliminary) of their structure.

One of the common problem that exist in the academic environment today is applicants with different academic abilities. It is therefore imperative for the administrators to streamline students according to their academic abilities that will help place applicants properly in where they belong. This grouped students based on their academic ability (Grouws & Cebulla, 2000). In institutions of higher learning in Nigeria today, students' academic performance has come under analysis so as to ease placement in admission, class, place of primary assignment during their National Youth Service Corps (NYSC) year etc. There are numbers of factors that affect academic performance of students one of which is their family socio-economic status.

Unlike the classification algorithm, clustering belongs to the unsupervised type of algorithms. It is the most widely used technique in data mining. Clustering techniques are used in this work to partition groups according to their academic abilities.

Data mining is a process of extracting and discovering patterns in large data sets involving methods at the intersection of machine learning, statistics, and database systems. Educational Data Mining (EDM) is the field of study concerned with mining educational data to find out interesting patterns and knowledge in educational organizations (Sreenivasarao *et al*, 2012). A lot of work have been done in educational data mining to predict students' academic performance using different data mining techniques such as classification and clustering techniques.

Saa and Abu (2016) study and explores multiple factors theoretically assumed to affect students' performance in higher education, and finds a qualitative model which best classifies and predicts the students' performance based on related personal and social factors. Durairaj and Vijitha (2014) propose Educational Data mining model for Predicting Students' Performance using Clustering Algorithms. They predicted the students' performance, used WEKA data mining through clustering, which paved way to strategic management tool.

Saxena *et al* (2014) examined the clustering analysis in data mining that analyzes the use of k-means algorithm in improving students' academic performance in higher education and presents k-means clustering algorithm as a simple and efficient tool to monitor the progression of students' performance. Rana *et al* (2016) proposed a work to evaluate the performance of students of Digital Electronics of university institute of engineering and technology. The researcher had applied unsupervised learning algorithms such as K-means and Hierarchical clustering using WEKA tool as an open source.

Sivaram *et al* (2010) surveyed the applicability of clustering and classification algorithms for recruitment data mining techniques that fit the problems which are determined. Veeramuthu *et al*. (2014) designed a model to present as a guideline for higher educational system to improve their decision making processes. The authors aim to analyse how different factors affect a student learning behaviour and performance using K-means clustering algorithm. Govindasamy et al (2018) analysed students' academic performance using clustering techniques. The authors compared four clustering algorithms- k-Means, k-Medoids, Fuzzy C Means (FCM) and Expectation Maximization (EM), based on Purity, Normalized mutual information (NMI) and time taken to form clusters.

This work evaluates students' academic performance using three clustering algorithms namely, the k-Means, k-Medoids, and Fuzzy C Means (FCM), and compares these algorithms based on Cluster Size, Cluster membership, and number of iterations taken to reach convergence.

2. Methodology

2.1 Data collection

The data set used for this work consists of examination raw scores of final year Higher National Diploma (HND) students from five departments of School of Engineering, The Federal Polytechnic, Bida. These data were collected from the Examination and Records Unit of the Polytechnic. The departments include Electrical Engineering, Chemical Engineering, Agricultural Engineering, Mechanical Engineering, and Civil Engineering departments. Because of the differences in peculiarity of courses within each of the Schools in the polytechnic, each department was treated separately and the three clustering algorithms (namely, the k-Means, k-Medoids, and Fuzzy C Means (FCM)) were used to organize the collected data (the students' examination raw scores) into three clusters based on similarity. Five courses were randomly selected from each of the departments to serve as the data set variables. These are given in Table 1 below.

Table 1: Sampled Departmental Courses

Department	Variables (Sampled Courses)				
	X1	X2	X3	X4	X5
Agric. Eng.	ABP441	ABP442	ABP443	ABP445	ABP446
Chem. Eng.	CHE421	CHE422	CHE423	CHE424	CHE425
Civil Eng.	CEC420	CEC421	CEC423	CEC424	CEC426
Mec. Eng.	MEC401	MEC441	MEC445	MEC447	MEM441
Elect. Eng.	MTH313	EEP444	EEP446	EEP447	EEC447

2.2 Similarity Measures

Since similarity is fundamental to the definition of a cluster, a measure of the similarity between two patterns drawn from the same feature space is essential to most clustering procedures. It is most common to calculate the dissimilarity between two patterns using a distance measure defined on the feature space. The well-known distance measure and the most popular metric used for patterns whose features are all continuous is the Euclidean distance. This is given by

$$d(x_i, x_j) = \left(\sum_{i=1}^{n}\left(x_{i,k} - x_{j,k}\right)^2\right)^{1/2} = ||x_i - x_j||^2, \;\; i = 1, \ldots, n, j = 1, \ldots, n \quad (1)$$

The Euclidean distance has an intuitive appeal as it is commonly used to evaluate the proximity of objects in two or three dimensional space. Thus it is used in this work to calculate the squared distance between all data points to the chosen centroids.

2.3 Clustering Algorithms

Cluster analysis is a technique for identifying homogeneous groups of objects. It is commonly used in multivariate analysis for procedures that seek to separate the component data into groups. This technique can be used as an exploratory data analysis tool to organize the observed data into meaningful groups or clusters based on similar characteristics.

The primary purpose of cluster analysis is to group or cluster objects or items based on their characteristics and similarity. This means that cluster analysis can define the structure of the data by placing the most similar object into groups or clusters. Therefore, clustering of objects will result in high internal homogeneity (within a cluster) and high external heterogeneity (between clusters). Cluster analysis is concerned with exploring data sets to assess whether or not they can be summarized meaningfully in terms of a relatively small number of groups or clusters of objects which resemble each other and are different in some respect from the objects in other cluster. The closeness or dissimilarity of the cluster is dependent on the distance measure of the cluster. The distance determines the similarities and are computed between pair of objects across the variables (Dillon & Goldstein, 1984).

2.4 K-Means Clustering

One of the famous technique in cluster analysis is K-Means clustering. The clustering technique seeks an optimal partition of the data by minimizing the sum of squared error criterion with an iterative optimization procedure. Given D, a data set of n objects, and k, the number of clusters to form, a partitioning algorithm organizes the objects into k partitions (k ≤n), where each partition represents a cluster. The clusters are formed to optimize an objective partitioning criterion, such as a dissimilarity function based on distance. The algorithm is composed of the following steps:

1: Place k points into the space represented by the objects that are being clustered. These point are present initial group centroids.

2: Assign each object to the group that has the closest centroid.

3: When all objects have been assigned, recalculate the positions of the k centroids.

4: Repeat steps 2 and 3 until the centroids no longer move. This produces a separation of the objects into groups from which the metric to be minimized can be calculated.

2.5 The k-Medoids Algorithm

The k-Medoids algorithm is related to the k-Means algorithm and the medoid shift algorithm. Both the k-Means and k-Medoids algorithms are partition (breaking the dataset up into groups). k-Means attempts to minimize the total squared error, while k-medoids minimizes the sum of dissimilarities between points labeled to be in a cluster and a point designated as the centre of that cluster. In contrast to the k-Means algorithm, k-Medoids chooses data points

as centres (medoids or exemplars).k-Medoids is also a partitioning technique of clustering that clusters the data set of n objects into k clusters with k known a priori.The algorithm is composed of the following steps:

1. Using Euclidean distance measure in equation (1), compute the distance between every pair of all objects and the corresponding medoids.

2: Calculate *Pij* to make an initial guess at the centres of the clusters where

$$p_{ij} = \frac{d_{ij}}{\sum_{i=1}^{n} d_{ij}} \quad i = 1...n, \quad j = 1...n$$

(2)

3: Calculate $\sum_{i=1}^{n} p_{ij} \left(j = 1...n \right)$ at each objects and sort them in ascending order.

Select *k* objects having the minimum value as initial group Medoids.

4: Assign each object to the nearest Medoids.

5: Calculate the current optimal value, the sum of distance from all objects to their Medoids.

6: Replace the current Medoid in each cluster by the object which minimizes the total distance

to other objects in its cluster.

7: Assign each object to the nearest new Medoid.

8: Calculate new optimal value, the sum of distance from all objects to their new medoids. If

the optimal value is equal to the previous one, then stop the algorithm. Otherwise, go back to the step 6.

2.6 The FCM Algorithm

Fuzzy C-Means (FCM) is a method of clustering which allows one piece of data to belong to two or more clusters. This method is frequently used in pattern recognition. FCM algorithm works by assigning membership to each data point corresponding to each cluster centre on the basis of distance between the cluster centre and the data point. More data is near to the cluster centre and its membership towards the particular cluster centre. Clearly, summation of membership of each data point should be equal to one. After each iteration membership and cluster centres are updated according to the formula:

Algorithm for Fuzzy C Means

Let $X = (x_1, x_2, x_3, ...x_n)$ be the data points and $V = (v_1, v_2, v_3, ...v_c)$

1. Select randomly c cluster centres.
2. Calculate the fuzzy membership using the following relation:

$$\mu_{ij} = \frac{1}{\sum_{k-1}^{c}\left(\frac{d_{ij}}{d_{ik}}\right)^{(2ml-1)}} \qquad (3)$$

3. Compute the fuzzy centres V_j using

$$V_j = \frac{\left(\sum_{i=1}^{n}\mu_{ij}\right)^{m} x_i}{\sum_{i=1}^{n}\left(\mu_{ij}\right)^{m}} \quad \forall_j = 1,2,...,c \qquad (4)$$

4. Repeat 2 & 3 until the membership U value is achieved or $U^{k-1} - U^{k} < \beta$
   Where K is the iteration step, β is the termination centre between [0,1].
   U is the fuzzy membership metrics, n is the fuzzy index, c represents the number of clusters centres, μ_{ij} represent the membership of i^{th} data to j^{th} cluster, d_{ij} represents the Euclidean distance of i^{th} and j^{th} cluster.

3. Results and Discussion

The data for the analysis was done through the use of R software and the following results were generated.

Table 1a Agricultural Engineering

Algorithm Type	Dept. size	No of clusters	Cluster size	Cluster membership ID	Iterations
K-means	15	3	6, 4,5	1(1,4,5,10,11,14) 2(8,9,12,15) 3(2,3,6,7,13)	3
K-mediods	15	3	6,4,5		8
Fuzzy C-means	15	3	3,6,6		75

From table 1a, department size is 15, the number of clusters is 3, cluster sizes are 6,4 and 5 number of iterations reached before convergence is 3 for K-means. K-mediod has 6,4 and 5 cluster size and 8 iterations and lastly for Fuzzy C-means, it has 3,6 and 6 cluster size and 75 iterations.

Table 1b Chemical Engineering

Algorithm Type	Dept. size	No of clusters	Cluster size	Cluster membership ID	Iterations
K-means	31	3	16, 6,9	1(1,4,8,11,12,13,14,15,17,19,20,22,23,25,26,28) 2(2,3,5,6,10,21) 3(7,9,16,18,24,27,29,30,31)	3
K-mediods	31	3	12,9,10		9

Fuzzy C-means	31	3	14,7,10		75

From table 1b, department size is 31, the number of clusters is 3, cluster size is 16, 6 and 9 number of iterations reached before convergence is 3 for K-means. K-mediod has 12, 9 and 10 cluster size and 9 iterations and lastly for Fuzzy C-means, it has 14,7 and 10 cluster size and 75 iterations.

Table 1c Civil Engineering Department

Algorithm Type	Dept. size	No of clusters	Cluster size	Cluster membership ID	Iterations
K-means	48	3	13,13,22	1(8,21,23,24,27,31,33,34 .35,38,40,4245) 2(6,10,11,14,17,18,19,22 ,29,30,32,44,46) 3(1,2,3,4,5,7,9,12,13,15, 16,20,,25,26,,28,36,37,3 9,41,43,47,48)	3
K-mediods	48	3	21,14,13		11
Fuzzy C-means	48	3	11,22,15		75

From table 1c, department size is 48, the number of clusters is 3, cluster size is 13,13 and 22 number of iterations reached before convergence is 3 for K-means. K-mediod has 21,14 and 13 cluster size and 11 iterations and lastly for Fuzzy C-means, it has 11,22 and 15 cluster size and 75 iterations.

Table 1d Mechanical Engineering

Algorithm Type	Dept. size	No of clusters	Cluster size	Cluster membership ID	Iterations
K-means	29	3	8, 12,9	1(1,2,3,4,5,7.9,16) 2(11,12,13,14,15,17,18,2 4,26,27,28,29) 3(6,8,10,19,20,21,23,25)	3
K-mediods	29	3	8,8,13		18
Fuzzy C-means	29	3	9,8,12		75

From table 1d, department size is 29, the number of clusters is 3, cluster size is 8,12 and 9 number of iterations reached before convergence is 3 for K-means. K-mediod has 8,8 and 13 cluster size and 18 iterations and lastly for Fuzzy C-means, it has 9,8 and 12 cluster size and 75 iterations.

Table 1e Electrical Engineering

Algorithm Type	Dept. size	No of Clusters	Cluster size	Cluster membership ID	Iteratio ns
K-means	54	3	19, 14,21	1(2,810,12,14,15,16,20, 22,24,25,28,32,33,36,3 7,50,53,54) 2(3,5,6,9,13,18,23,26,2 9,30,35,38,40,46) 3(1,4,7.11,17,19,21,27, 31,34,3941,42,43,44,45 ,47,48,49,51,52)	3
K-mediods	54	3	23,21, 10		25
Fuzzy C-means	54	3	16,21,17		75

From table 1e, department size is 54, the number of clusters is 3, cluster size is 19,14 and 21 number of iterations reached before convergence is 3 for K-means. K-mediod hass 23,21 and 10 cluster size and 25 iterations and lastly for Fuzzy C-means,it has 16,21 and 17 cluster size and 75 iterations.

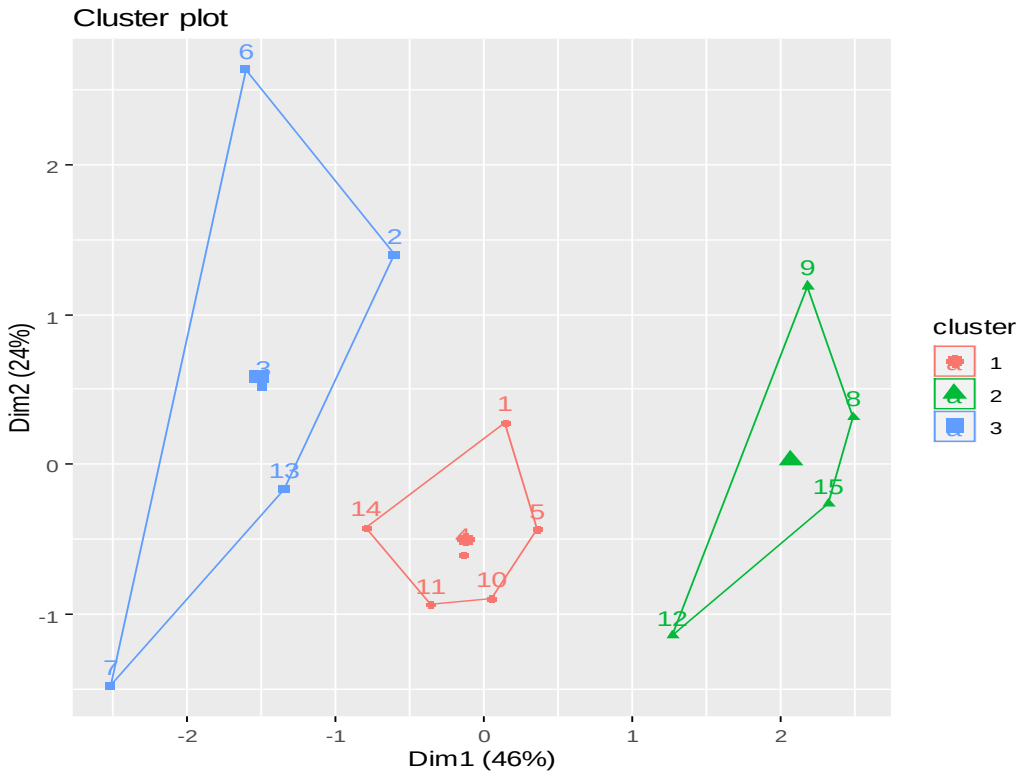

Fig1 cluster plot of Agricultural Engineering Department

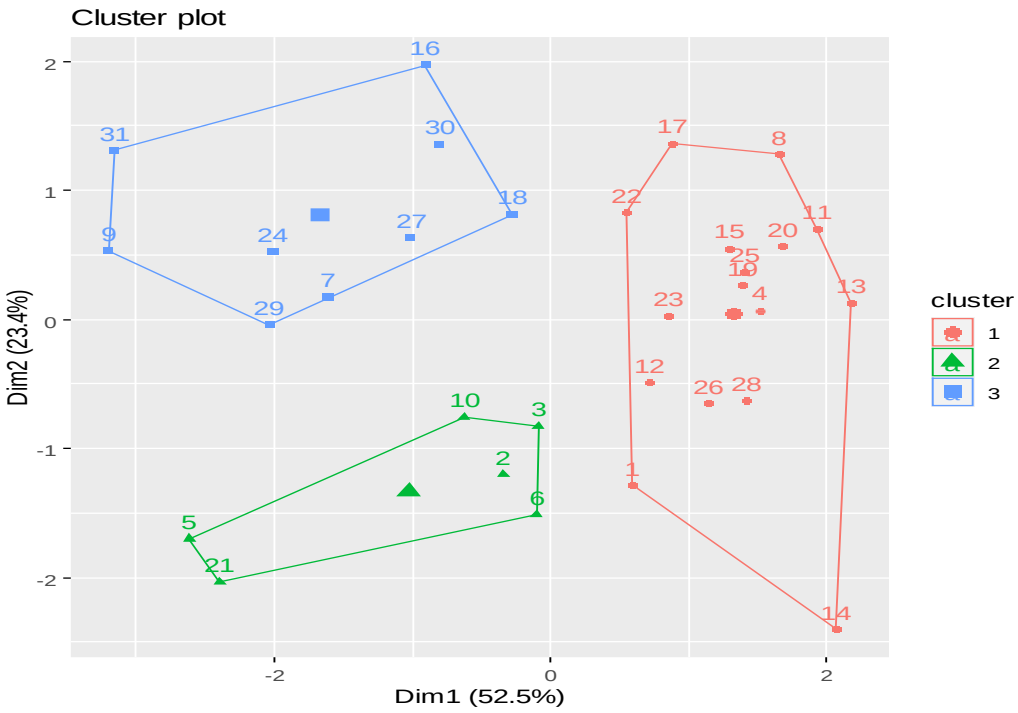

Fig2 cluster plot of Chemical Engineering Department

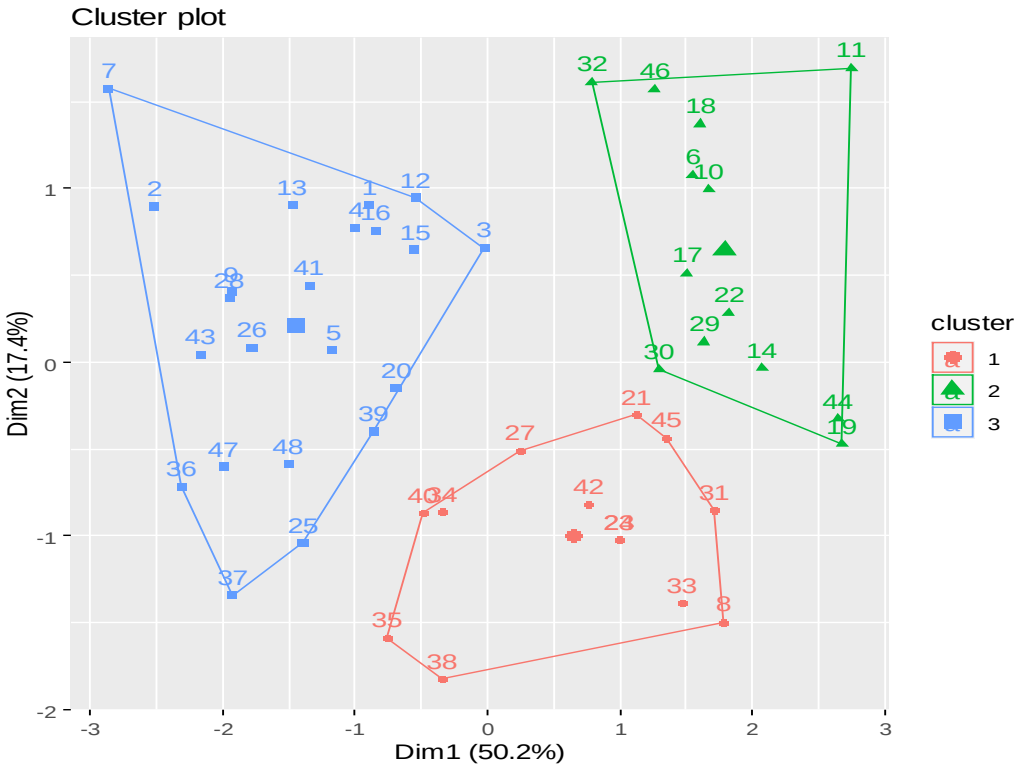

Fig3 cluster plot of Civil Engineering Department

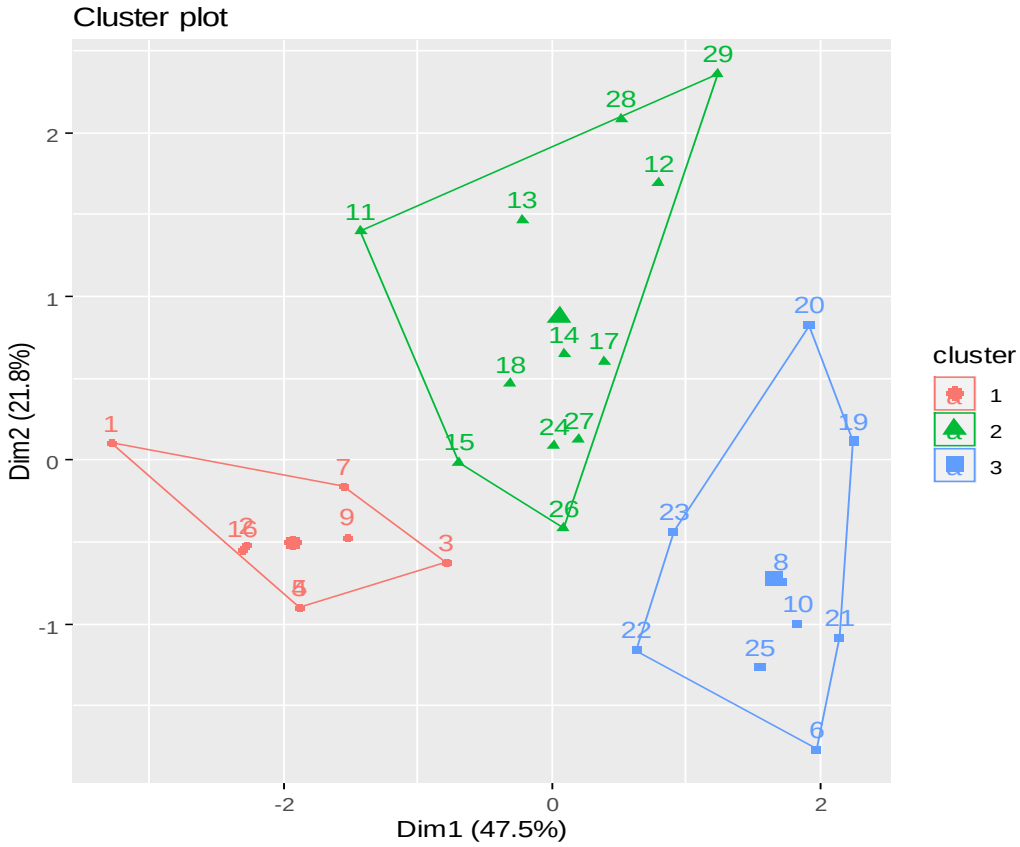

Fig4 cluster plot of Mechanical Engineering Department

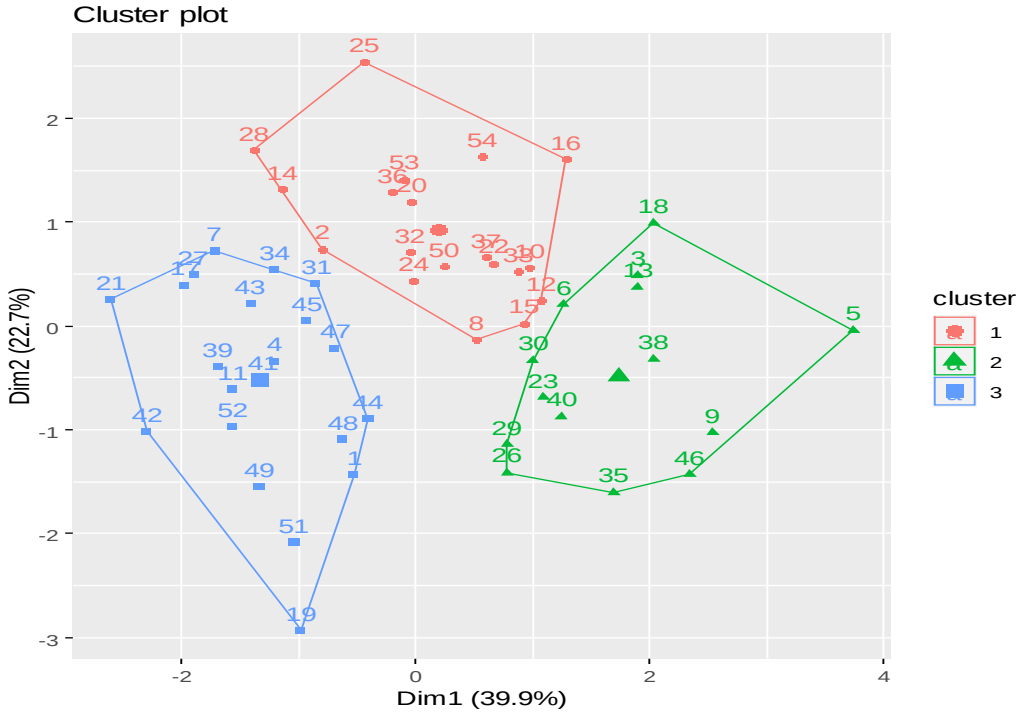

Fig4 cluster plot of Electrical Engineering Department

3.2 Performance of clustering Algorithm

The cluster quality is evaluated using the number of clusters, cluster size and membership of the clusters. The total number of clusters is three (Average Good, and Excellent). The above table shows the total number of requirement that are distributed when K-Means algorithm is applied.

Conclusion

The research work has shown interest in revealing that the clustering techniques serve as powerful tool in educational data mining. Here three different clustering algorithm are discussed using the student raw score data on final semester grade of School of Engineering, Federal Polytechnic, Bida. Clustering Algorithms: K-Means, K-Mediods and FCM were examined and compared based on based on performance using the student data set. The number of clusters, size of the cluster and cluster membership. The result shows that FCM and K-mediods perform better than K-means clustering

References

Aldenderfer., M.S, & Blashfield, H.K. (1984) *Cluster Analysis*. United States SAGE Dillion, W.R & Goldstein, M.(1984) *Multivariate Analysis*. Canada: John Willey & Sons Inc.

Durairaj, M., and C. Vijitha(2014)., "Educational Data mining for Prediction of Student PerformanceUsing Clustering Algorithms." , *International Journal of Computer Science and InformationTechnologies* , 2014, Vol. 5(4), pp. 5987-5991.

Grouws, D.A., & Cebulla, K.J. (2000), *Improving student Achievement in Mathematics.*
Brussel: International Academy of Education (IEA), Brussels, Belgium.

Rana, Shiwani, and Roopali Garg(2016)., "Evaluation of student‟s performance of an institute usingclustering algorithms.", *International Journal of Applied Engineering Research*, 2016,Vol.11(5), pp. 3605-3609.

Saa, Amjad Abu (2016). "Educational Data Mining & Students‟ Performance Prediction.",*International Journal of Advanced Computer Science and Applications*, 2016, Vol. 7(5), pp.212-220.

Saxena, Prashant Sahai, and M. C. Govil(2014)., "Prediction of Student‟s Academic Performanceusing Clustering.", Special Conference Issue: National Conference on Cloud Computing & Big Data., 2014,

Sreenivasarao, Vuda, and Capt Genetu Yohannes (2012). "Improving academic performance of students of defence university based on data warehousing and data mining" Global Journal of Computer Science and Technology. Vol. 12(2), pp 29-36.

Sivaram, N., and K. Ramar(2010)., "Applicability of clustering and classification algorithms forrecruitment data mining." , *International Journal of Computer Applications, 2010,* Vol. 4,No. 5, pp. 23-28

Veeramuthu, P., Dr R. Periyasamy, and V. Sugasini(2014)., "Analysis of Student Result UsingClustering Techniques." *IJCSIT), International Journal of Computer Science and InformationTechnologies,* 2014, Vol. 5, No. 4, pp. 5092-5094.

.Velmurugan. T and T. Santhanam(2010), "*Computational Complexity between K-means and Kmedoids clustering algorithms for normal and uniform distributions of data points*", Journal ofComputer Science, Vol. 6, Issue 3, 2010, pp.363-368.

Xu,R., & Wunsch, D.C. (2007*). Clustering*, New Jessey: John Wiley & Sons, Inc

Building Density and Housing Submarket: A Historico-geographic Approach on Urban Morphology

Mohammed J. K.[1*], Aliyu A. A.[2] and Saidu U. A.[3]
[1&3]Department of Estate Management and Valuation, The Federal Polytechnic, Bida, Nigeria
[2]Department of Urban and Regional Planning, The Federal Polytechnic, Bida, Nigeria
[1]muhammad.jibrinkatun@fedpolybida.edu.ng
[2]aliyuabdul777@gmail.com
[3]saidumadakikamala@gmail.com
* Corresponding author

Abstract

An increase in building density as a result of urban densification has become a global trend as it changes the urban forms of many cities of the developing world. This study investigates spatial changes in the building density of housing submarkets of Bida, Nigeria from 2008 to 2018. Data collected for the study includes satellite images and base map of demarcated areas, which were georeferenced and the buildings were digitised using point features and vector approach in ArcGIS environment to achieve the area coverage, number of buildings, and buildings per hectare (ha) in the housing submarkets. The finding of the study reveals that from 2008 – 2018 the Town housing submarket had the highest number of buildings per area coverage with >10 building units/ha. The study further reveals that in the year 2018, the Gbazhi housing submarket had its highest number of buildings per area coverage with >10 building units/ha. It was concluded that the housing submarkets had a high number of buildings in the total area coverage which indicates that larger parts of the area coverage of these submarkets have already been exhausted. It was therefore recommended that there is the need for rational densification (planned densification) for urban development in order to check the increasing uncontrolled building density.

Keywords: Building density, housing submarket, urban morphology, urban densification

1. Introduction

Urban densification is the increase in urbanisation level of a limited area, which could have an adverse effect on the biodiversity of its green spaces by destroying the habitats and soil temperature increase or pollutions (Vergnes et al., 2014). Urban densification causes a lot of challenges to cities ranging from decline in housing affordability, pressure on infrastructure and difficulties of city management. Urban densification has a consequential effect on affordable housing and may cause change in the housing market. As a result of change in the housing market the entire city or national economy would experience shift either negatively or positively (Gulyani et al., 2018).

The housing market is very imperative because of the place it holds in the economy (Seo, 2008). Housing construction easily contributes to gross domestic product and its market has a direct impact on the national economy (Hu et al., 2013). Housing is a special kind of commodity which is fixed (Renigier-Biłozor et al., 2017). Consequently, the location of the house is very imperative, since this feature is unchangeable (Cichociński & Dąbrowski, 2013). Housing has demonstrated its importance to the broader economy during the global financial crisis of 2007 – 2011, which has its roots in the United States housing market as its contribution to the national GDP fall during the period. Information on trends in housing prices is therefore essential to the governments, market participants and central banks (Hill & Scholz, 2017).

However, there is a large body of literature on housing market (Leung, 2004;Wu et al., 2014;Muehlenbachs et al., 2015;Yang et al., 2017;Tupenaite et al., 2017;Zhou, 2018;Cameron, 2018;Cheung et al., 2018;Wang et al., 2018). For example, Xiao (2012) studied urban morphology and housing market with emphasis on street network pattern, where street pattern is a fundamental determinant of house prices and street network pattern influences accessibility. Wang et al. (2018) analyses the spatial patterns and driving forces of Chinese housing prices where various theoretical dimensions on housing supply, demand and market, are viewed as determinants of a housing price model to examine the effect of prices of land on housing prices. These authors did not consider housing submarket in their respective studies.

Available literature on housing submarket (for example, Royuela & Vargas, 2007;Park, 2013;Manganelli et al., 2014), very little is written on delineation of housing market (for example, Wu & Sharma, 2012;Manganelli et al., 2014). Studies on urban densification of housing submarkets is rare in the literature (Mohammed et al., 2021). Bida is experiencing urban densification which has attracted people from different parts of the country which has consequently led to an increase in housing demand. The intensity of housing demand in the city has also resulted in increased house rents.

Therefore, this study examines the pattern of spatial changes in the building density of housing submarkets of Bida, Nigeria from 2008 to 2018.

2. Literature Review

2.1. Housing Submarket

Housing submarkets are typically defined as geographic areas where the price per unit of housing quantity (defined using some index of housing characteristics) is constant (Goodman & Thibodeau, 1998). Although as an urban economic, land use and residential location model – the residential location theory (Alonso, Muth, Mills) is also applicable to housing market segmentation. Even without certain factors, segmentation of an urban area can still be carried out, if there is disparity in households' preferences and/or income with respect to accessibility and space (Kauko *et al*., 2002).

Although, there is agreement by several researchers on using locational and structure features to define a submarket, identifying a submarket and approach to be adopted have little consensus (Xiao, 2012). Usually, spatial and non-spatial specifications for housing submarket are the main two methods(Islam & Asami, 2009; Xiao, 2017).

2.2.Spatial Approach to Housing Submarket

Peopele's housing choice of homogenous preferences based on geographic predefined areas are enphasised by spatial specifications which is the main index (e.g. political districts, north/south, inner/outer city, and postcode districts) (Xiao, 2012).

Hitherto, several studies has formed housing segmentation based on spatial specification For example, McCluskey & Borst (2011) used Geographically Weighted Regression (GWR), a geostatistical modeling methods to identify and demarcate the housing submarkets. The procedure effectiveness was established by improving the accuracy of the predictive model for housing market segmentation as compared to standard universal unsegmented model for the study areas. Goodman & Thibodeau (1998) described housing submarkets as a geographical area where housing price per service unit is constant and characteristics of individual housing are available for purchase. They argue that hierarchical models offer a suitable framework for housing submarkets delineation. Wu & Sharma (2012) developed a methodology for submarket classification based on spatially constrained data-driven to achieve spatially integrated housing market segments. Precisely, a data driven model on cluster analysis and principal component analysis was built for housing submarkets delineation. Their findings show that spatially contiguous submarkets can be obtained without compromising housing hedonic model accuracy and attribute homogeneity.

Park (2013) proposes spatial housing submarkets division basis in enhancing the housing market understanding. The division's theoretical background is built upon the nexus between the structure house prices and commuting patterns. An assessment of the process of 'expansion-overiap-merging' between residential spheres, defined as a unit containing of a centre of employment and the surrounding residential area, provides an overview of a probable form of merged residential spheres in big cities. An empirical study of the Seoul spatial housing submarkets were identified on the basis of the hierarchies between the local authorities from commuting patterns. Manganelli *et al*. (2014) adopted Geographically Weighted Regression (GWR) in housing market analysis, in homogeneous areas identification and defining a single location marginal contribution to the property's value at the housing market. Their results of territory zone the housing market into homogeneous market areas, they concludes that the findings has useful implications in terms of taxation, programming territorial transformations, and checking ongoing or post planning decisions.

2.3. Criticisms of Spatial Approach

Both spatial and non-spatial approaches to housing market segmentation have received wide range criticism. Spatial-based determinations have been reprimanded for their error. Because of fast urbanization and the rise of polycentricity, the urban framework has turned out to be more intricate and thus the social spatial structure is changing and social spatial isolation has been upgraded. The main spatial models adopted to characterise the preferences spatial divisions appears to be less effective in peoples preference reflection and each characteristic choice in these type of cities. The traditional approaches risk is that it underestimates the amount in the submarkets. More so, the spatial based specification often looks like an *ad hoc* reason be that the use of geographical boundaries that are pre-identified. The requirements also include a prior acknowledgement of the local context and consequently make scientific research complex and not simply replicated (Xiao, 2012).

As being arbitrary is the criticism of the spatial approach, the criticism of the non-spatial specification being unstable over time. For being a non-spatial nature is another criticism of the approach and its ambiguities in presentation for interventions of policy (Xiao, 2017).

This indicates that both spatial and non-spatial approaches of housing submarket delineation cannot effectively represent true nature of the submarket. However, the spatial approach to housing submarket was proven to be better in terms physical policy and assessment. It is therefore better to employ spatial method in delineating housing submarket. It is on this background that this study intends to adopt spatial approaches to delineate housing submarket.

2.4. Urban Morphology, Density and Densification

There are three basic concepts used by the built environment experts to address the issue of how density affects people's lives; density, perceived density and crowding (Alexander, 1993). Density described relationship between a given physical area and the number of objects in that area (Medayese *et al*., 2015). Density has an intrinsic relationship with urban morphology; it plays an important role in the shaping of urban forms. One of the pioneer planners Ebenezer Howard pointed out that countryside have less density and greener environment compared to the growing industrial city (Medayese *et al*., 2015). Alonso suggest that moving closer to the city centre the density increases and distance away from the city centre causes decrease in density (Alonso, 1964). Density refers to by the two authors is both population density and housing density which result from rapid urbanisation.

More recently, studies shows that compact development provides solutions to many urban problems such as reducing urban sprawl and infrastructure provision (Broitman & Koomen, 2015; Chhipi-Shrestha *et al*., 2017; Vergnes *et al*., 2014). However, considering Howard's and Alonso's thought and the recent compact development that changes urban morphology, urban densification can be referred to as planned urban densification (deliberate) and unplanned urban densification (not deliberate). Therefore urban densification can be divided into two categories; planned urban densification and unplanned urban densification (Mohammed et al., 2021).

Amer *et al*. (2017) examines urban densification through roof stacking where three consecutive levels (urban, social and engineering) systematic approach was considered. Chandrabose (2019) conducted a study on urban densification and 12-year changes in cardiovascular risk markers. In a different perspectives, Delmelle *et al*. (2014) assesses urban densification without growth management where it focused on local land development and housing trends in Charlotte, North Carolina, USA. Ghadami and Newman (2019) investigate the effect of the urban densification policies made after the Islamic Revolution on the urban spatial structure of Tehran as the most important metropolis in Iran. Urban densification is conceived as urban regeneration method. For example, Treija *et al*. (2018) examines the existing approaches focused on densification in large housing estates in order to define the typical challenges of this process, the examples of infill developments in large housing area Imanta in Riga was analysed. Vuckovic *et al*. (2019) investigates urban densification potential in the effects of heat island mitigation and outdoor thermal conditions improvement in Vienna, Austria.

Measuring urban density has been a problem of many researchers (Ståhle *et al*., 2008). Broitman and Koomen (2015) measured residential densification using a high level of detail spatial data that covers the whole of Netherland. They describe land use by employing 100 metre resolution rasterised data, residential density and local explanatory variables of wide range. Wang et. al. (2019) generate a land use transition of 2001 to 2011 matrix using land use maps with the aid of ArcGIS and examines the spatial and temporal urban density changes. In contrast, Jiao (2015)acquired high quality Landsat TM/ETM+ images, where the

images classified using the Maximum Likelihood Classification method in ENVI 4.5. The results from image classification processed using a non-linear least squares method to fit the pro-posed urban land density functions in order to fit a nonlinear function to the observed data by refining the parameters in successive iterations. They employed Trust-region algorithm in their study. They fit the urban land density functions with Matlab. Urban densification was also measured using microclimate simulations with different models. The results are compared, and uncertainty ranges are documented by testing the impact of urban fabric on current climate (Loibl, 2019). Shahtahmassebi (2016) developed framework for measuring urban densification using time series of impervious surface fractions (ISFs) derived from remotely sensed imagery.

3. Methodology

3.1 Study Area

Bida town in the north central geopolitical region of Nigeria is the study area which is an ancient and typical traditional settlement located on latitude 9.083N and longitude 6.017E (see Figure 1). The town is the headquarter of Nupe ethnic group in Nigeria with mostly traditional buildings and a total built up area of 67.45km2. According to the last national population census, the town have about 255,008 inhabitants (Mohammed & Sulyman, 2019).

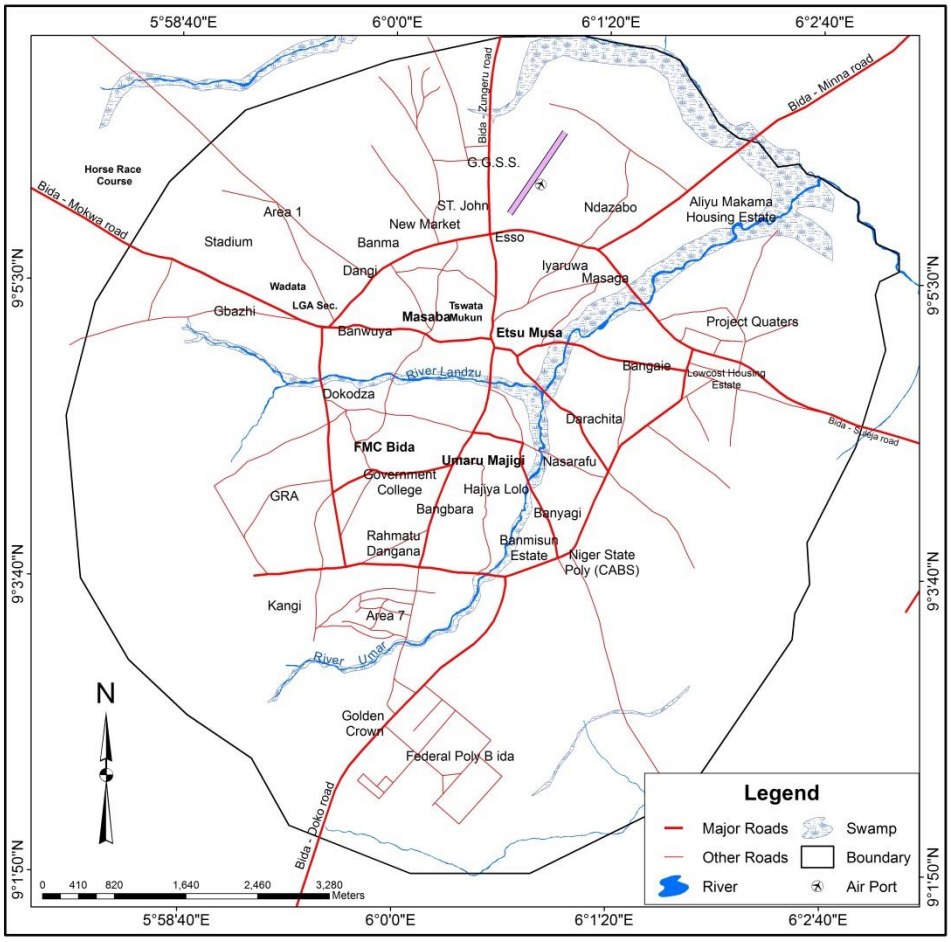

Figure 1. Bida, the Study Area

3.2 Data and Analysis

Satellite imageries were captured for the housing submarkets using the area demarcations. For each demarcated area, three satellite imageries were capture for three different periods, i.e. 2008, 2013 and 2018 using maximum resolutions on the Google Earth application. Images captured using area demarcation gives better resolution. The choice of Google Earth is due to its user friendly and historical images available.

Satellite images captured based on the demarcated areas were georeferenced where vector approach was adopted in digitising all the buildings using point features in ArcGIS environment. The entire buildings for each year under study were represented by points.This research adopted residential density measurements by Niger State Urban Development Board (2015). Using this, residential density is measured using occupancy rates of building and number of buildings in a given location to give level of density.Cartographic approach is employed in presenting residential density level across the housing submarkets and study period in the study area.

4. Results and Discussion

It was found out in Table 1 that in the year 2008, the Town housing submarket being the largest submarket had the highest number of buildings with a total of 25,945. This is followed by Wadata with 1,020 buildings, Poly area with 787 and GRA with 773. The study shows that Rahmatu Dangana being the smallest housing submarket also recorded lowest number of buildings in that year. The result also shows that the Town with largest area coverage and highest number of building units had the highest number of buildings to area ratio with 21.35 this is followed by Rahmatu Dangana with 5.72, Wadata 2.56 and Gbazhi 2.27. The lowest buildings to area ratio is recorded for Eyagi with 0.23.

In the year 2013 Town housing submarket had highest number of building units with 34,242. This is followed by Gbazhi with 2,077, Ndazabo 1,758, Wadata 1,707 building units respectively. During this period, the study shows that Rahmatu Dangana had smallest number of building units. The result also shows that Town submarket recorded highest number of building to area ratio with 28.18, followed by Gbazhi with 9.62, Rahmatu Dangana 9.10 and Wadata 4.28 respectively. The lowest building to area ratio is recorded for Eyagi with 0.42.

Consequently, this result shows a tremendous transition in the housing submarket of the study area where all the housing submarkets had the number of their housing units increased at different rates. The results also implies that Gbazhi had very high residential development where the number housing units recorded for the year 2008 was 489 with building to area ratio of 2.27 and increases to 2,077 with building to area ratio of 9.62 in the year 2013.

In the year 2018 Town submarket had highest number of buildings with 29,985 followed by Poly Area with 2,450, Ndazabo 2,346, Gbazhi 2,331, Wadata 2,300 and Kangi 2,134 building units respectively. The lowest number of building units recorded was in Rahmatu Dangana with 124. The Table also revealed that Town submarket had highest building to area ratio with 24.68. This is followed by Gbazhi with 10.80 and Rahmatu Dangana 8.55. The lowest building to area ratio was recorded for Eyagi with 0.54 (Table 1).

Table 1: Building Units Per Hectares by Housing Submarkets 2008 - 2018

Submarket	Year 2008				Year 2013				Year 2018			
	Area Coverage (Ha)	Building Units	Ratio	Building Units/Ha	Area Coverage (Ha)	Building Units	Ratio	Building Units/Ha	Area Coverage (Ha)	Building Units	Ratio	Building Units/Ha
Kangi	457.52	661	1.44	<2	457.52	1103	2.41	2-4	457.52	2134	4.66	2-4
Rahmatu	14.5	83	5.72	5-6	14.5	132	9.10	9-10	14.5	124	8.55	7-8
Dangana Town	1214.97	25945	21.35	>10	1214.97	34242	28.18	>10	1214.97	29985	24.68	>10
Poly Area	823.13	787	0.96	<2	823.13	1648	2.00	2-4	823.13	2450	2.98	2-4
Eyagi	725.34	165	0.23	<2	725.34	304	0.42	<2	725.34	393	0.54	<2
Gbazhi	215.81	489	2.27	2-4	215.81	2077	9.62	9-10	215.81	2331	10.80	>10
Wadata	398.51	1020	2.56	2-4	398.51	1707	4.28	2-4	398.51	2300	5.77	5-6
Avenue	417.08	524	1.26	<2	417.08	1283	3.08	2-4	417.08	1976	4.74	2-4
Ndazabo	692.99	605	0.87	<2	692.99	1758	2.54	2-4	692.99	2346	3.39	2-4
Project Qtrs	984.31	358	0.36	<2	984.31	793	0.81	<2	984.31	1466	1.49	<2
GRA	800.08	773	0.97	<2	800.08	1442	1.80	<2	800.08	1889	2.36	2-4

In an attempt to explain variation in densification in housing submarkets of the study area in terms of number of buildings per hectares as presented in Figure 2, 3 and 4. The study attempts to explain densification based on number of buildings per hectares, but it does not directly highlight the factors responsible for the high or low number of buildings in the housing submarket.

The study shows in Figure 2 that in the year 2008, Town housing submarket had highest number of buildings per area coverage with >10 building units/ha. This is followed by Rahmatu Dangana with 5-6 number of building units/ha, Gbazhi and Wadata had 2-4 number of building units/ha each. All other submarkets had <2 building units/ha in that year.

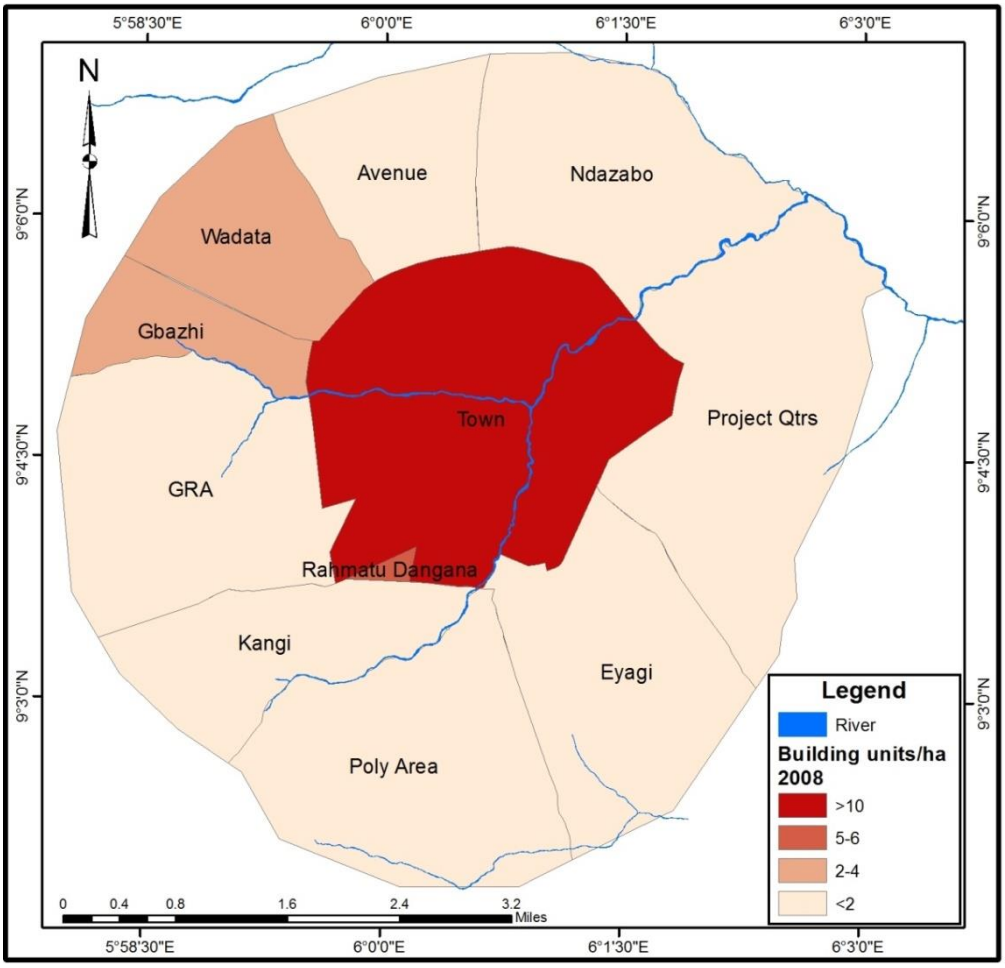

Figure 2: Number of Building Units/Ha by Housing Submarkets in the Year 2008

This implies that Town submarket with largest area coverage and highest number of buildings also had highest number of buildings per area coverage. The consequences of this is that density in Town submarket cannot easily be controlled as the residential density has reached a level that if there is any disaster such as fire outbreak or epidemics, it will hardly be curtailed due to the pattern of residential development. The result also implies that during this years it is only Gbazhi and Wadata that had more than two number of building units/ha among submarkets in the urban fringe.

Residential density within the urban area of Bida considering the number of building units in the housing submarket is presented in Figure 3. Findings of the study in this section shows that Town housing submarket has the highest with >10 number of building units/ha in the year 2013. This is followed by Rahmatu Dangana and Gbazhi with 9-10 number of building units/ha, and Kangi, Poly Area, Wadata, Avenue and Ndazabo had 2-4 number of building units/ha. Housing submarkets that recorded the lowest number of buildings per area coverage are Eyagi, Project Quarters and GRA with <2 number of building units/ha.

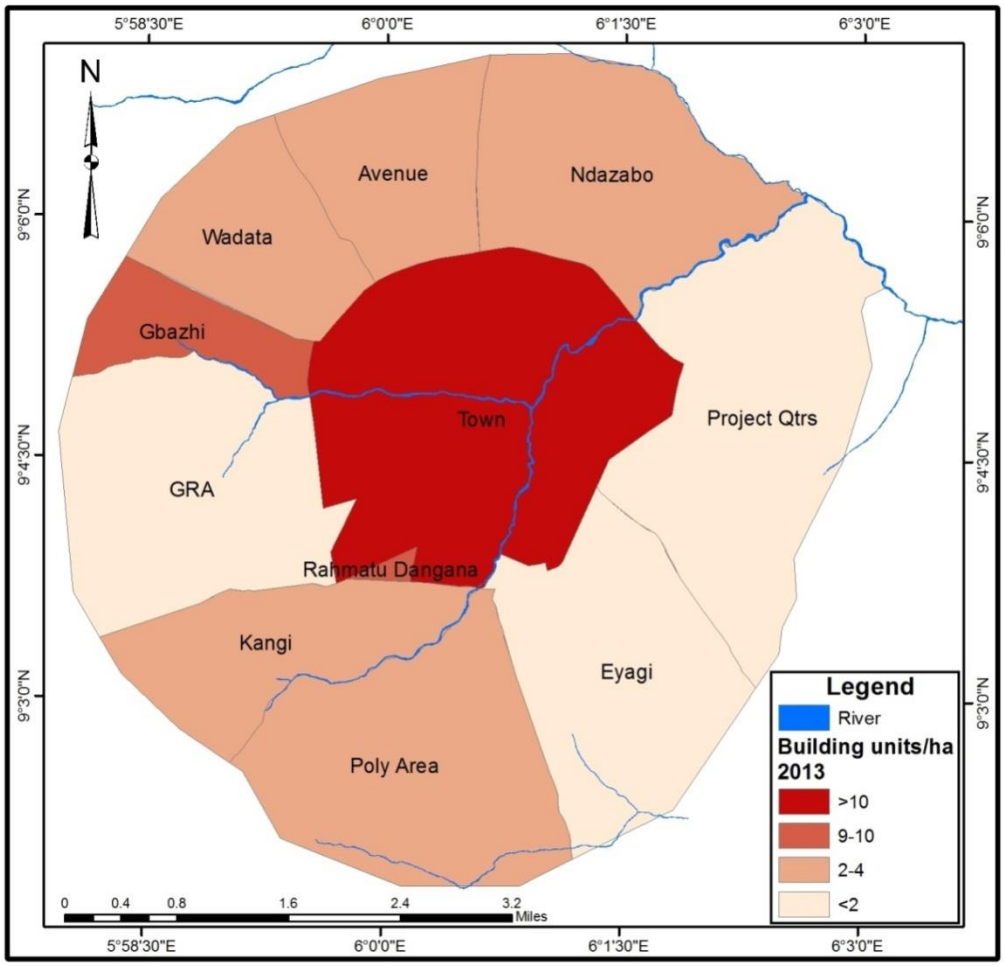

Figure 3: Number of Building Units/Ha by Housing Submarkets in the Year 2013

The implication of this result is that large amount of variation and tremendous transition in housing development in the housing submarket occurred during this period. The research therefore observed that there was high level of urban morphological transformation resulting from the increasing level of urbanisation that leads to high number of housing units in the housing market, which contributed to how the urban area looks like and shapes the future of urban development and the overall image of the town. This could one way or the other have impact on a number of housing economics such as housing affordability, housing supply, housing demand and the housing market which includes the rental value of residential apartments.

Urban densification in Bida proceeds in an unstructured manner in the year 2018. The study shows in Figure 4 that the Town and Gbazhi housing submarkets records highest number of buildings per area coverage with >10 building units/ha each. The study also reveals that Rahmatu Dangana and Wadata had 7-8 and 5-6 number of building units/ha each respectively in that year, and by implication made us to understand that Eyagi and Project Quarters had lowest number of buildings per area coverage with <2 building units/ha each.

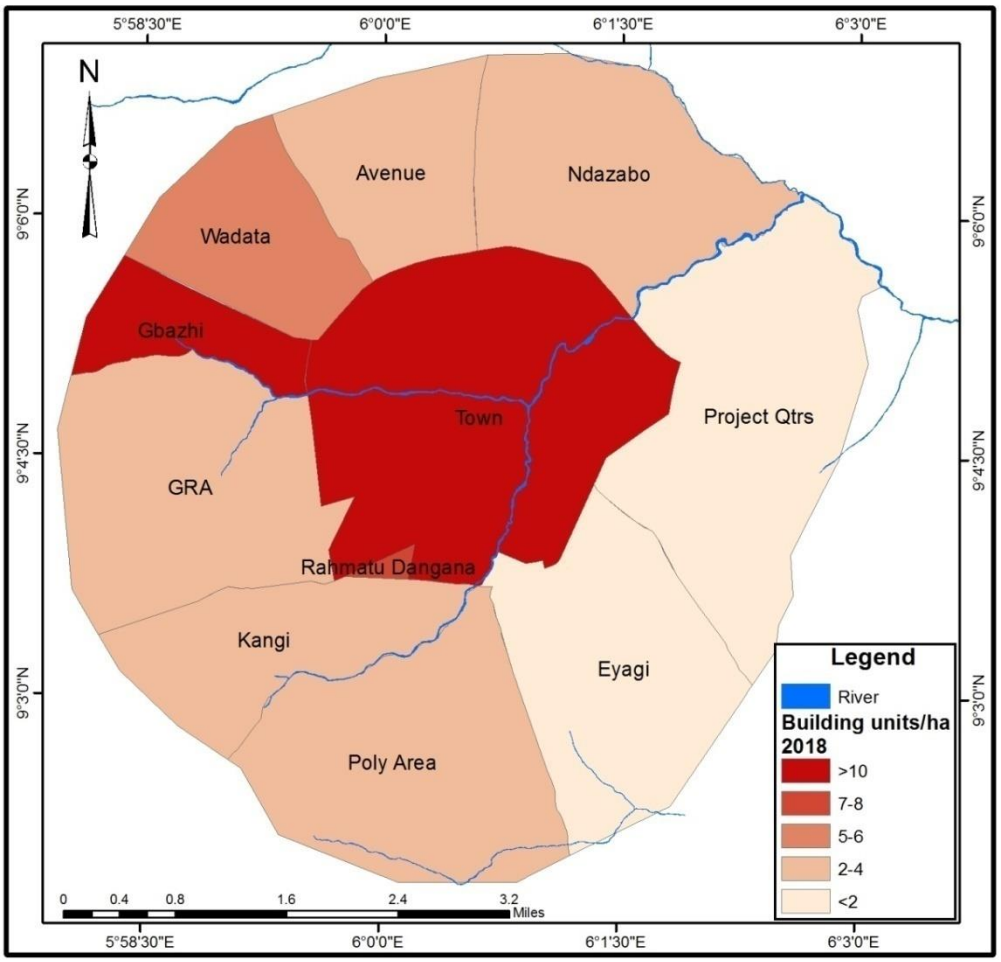

Figure 4: Number of Building Units/Ha by Housing Submarkets in the Year 2018

The pattern of residential development demonstrates urbanisation level that could make it difficult for any urban upgrading that may be needed later or increases the level of informality in the urban fabric. This result indicates that the housing submarkets had high number of buildings in the total area coverage which indicates that larger parts of the area coverage of these submarkets have already been exhausted.

The resultsin this study revealed that Rahmatu Dangana with smallest area coverage is highly developed in the year 2013. The implication of this result is that transition in the urban morphology experienced tremendous changes where number of buildings in the Town submarket reduced from 34,242 in the year 2013 to 29,985 in the year 2018. This could be attributed to Bida old market razed by fire in early 2018. The result also implies that there

were high residential development in Poly Area, Ndazabo and Gbazhi submarkets during this period which may have occasioned the sudden reduction.This confirms Broitman and Koomen (2015) findings where wide variation in residential density among neighbourhoods was observed. The implication of the above is that this pattern would one way or the other has impacts on the rental value of residential apartments in the study area.

5. Conclusion

The study revealed an increasing residential density in the housing submarkets of Bida. It can be concluded that the inner part of the city has a higher number of buildings throughout the study period and it is the region where commercial and cultural activities are carried out. The city centre maintains a consistently high number of buildings units/ha and high residential density through the years under review. The structure of the town shows that areas around the Central Business District (CBD) are of high density while locations within the urban fringe tend to have lower residential densities. The study will help urban planners and urban managers differentiate between economic and social classes and respond to affordable housing. It will also help urban planners and authorities to efficiently solve the problem of spatial growth and management and assisting in the assessment of housing values to evaluate planning regulations and urban land-use policies. The study, therefore, recommends planned densification in order to achieve sustainable residential density control. GIS application should be given priority in the assessment of residential density and housing market issues, particularly, the housing submarkets.

References

Alexander, E. R. (1993). Density Measures: A Review and Analysis. *Journal of Architectural and Planning Research*, *10*(3), 181–202.

Alonso, W. (1964). *Location and land use: Toward a general theory of land rent. Publication of the Joint Center for Urban Studies*. Harvard University Press.

Amer, M., Mustafa, A., Teller, J., Attia, S., & Reiter, S. (2017). A methodology to determine the potential of urban densification through roof stacking. *Sustainable Cities and Society*, *35*, 677–691. https://doi.org/10.1016/j.scs.2017.09.021

Broitman, D., & Koomen, E. (2015). Residential density change: Densification and urban expansion. *Computers, Environment and Urban Systems*, *54*, 32–46. https://doi.org/10.1016/j.compenvurbsys.2015.05.006

Cameron, T. (2018). *The House Rules: Housing Market Responses to Oil Price Shocks in Canada* [Masters Dissertation]. University of Ottawa.

Chandrabose, M., Owen, N., Giles-Corti, B., Turrell, G., Carver, A., & Sugiyama, T. (2019). Urban Densification and 12-Year Changes in Cardiovascular Risk Markers. *Journal of the American Heart Association*, *8*(15). https://doi.org/10.1161/JAHA.119.013199

Cheung, R., Wetherell, D., & Whitaker, S. (2018). Induced earthquakes and housing markets: Evidence from Oklahoma. *Regional Science and Urban Economics*, *69*, 153–166. https://doi.org/10.1016/j.regsciurbeco.2018.01.004

Chhipi-Shrestha, G., Hewage, K., & Sadiq, R. (2017). Impacts of neighborhood densification on water-energy-carbon nexus: Investigating water distribution and residential landscaping system. *Journal of Cleaner Production*, *156*, 786–795. https://doi.org/10.1016/j.jclepro.2017.04.113

Cichociński, P., & Dąbrowski, J. (2013). Spatio-Temporal Analysis of the Real Estate Market Using Geographic Information Systems. *Real Estate Management and Valuation*, *21*(2), 73–82. https://doi.org/10.2478/remav-2013-0019

Delmelle, E., Zhou, Y., & Thill, J.-C. (2014). Densification without Growth Management? Evidence from Local Land Development and Housing Trends in Charlotte, North Carolina, USA. *Sustainability*, *6*(6), 3975–3990. https://doi.org/10.3390/su6063975

Ghadami, M., & Newman, P. (2019). Spatial consequences of urban densification policy: Floor-to-area ratio policy in Tehran, Iran. *Environment and Planning B: Urban Analytics and City Science*, *46*(4), 626–647. https://doi.org/10.1177/2399808317722168

Goodman, A. C., & Thibodeau, T. G. (1998). Housing market segmentation. *Journal of Housing Economics*, *7*(2), 121–143.

Gulyani, S., Talukdar, D., & Bassett, E. M. (2018). A sharing economy? Unpacking demand and living conditions in the urban housing market in Kenya. *World Development*, *109*, 57–72. https://doi.org/10.1016/j.worlddev.2018.04.007

Hill, R. J., & Scholz, M. (2017). Can Geospatial Data Improve House Price Indexes? A Hedonic Imputation Approach with Splines. *Review of Income and Wealth*. https://doi.org/10.1111/roiw.12303

Hu, S., Cheng, Q., Wang, L., & Xu, D. (2013). Modeling land price distribution using multifractal IDW interpolation and fractal filtering method. *Landscape and Urban Planning*, *110*, 25–35. https://doi.org/10.1016/j.landurbplan.2012.09.008

Islam, K. S., & Asami, Y. (2009). HOUSING MARKET SEGMENTATION: A REVIEW. *Review of Urban & Regional Development Studies*, *21*(2–3), 93–109. https://doi.org/10.1111/j.1467-940X.2009.00161.x

Jiao, L. (2015). Urban land density function: A new method to characterize urban expansion. *Landscape and Urban Planning*, *139*, 26–39. http://dx.doi.org/10.1016/j.landurbplan.2015.02.017

Kauko, T., Hooimeijer, P., & Hakfoort, J. (2002). Capturing Housing Market Segmentation: An Alternative Approach based on Neural Network Modelling. *Housing Studies*, *17*(6), 875–894. https://doi.org/10.1080/02673030215999

Leung, C. (2004). Macroeconomics and housing: A review of the literature. *Journal of Housing Economics*, *13*(4), 249–267. https://doi.org/10.1016/j.jhe.2004.09.002

Manganelli, B., Pontrandolfi, P., Azzato, A., & Murgante, B. (2014). Using geographically weighted regression for housing market segmentation. *International Journal of Business Intelligence and Data Mining 13*, *9*(2), 161–177.

McCluskey, W. J., & Borst, R. A. (2011). Detecting and validating residential housing submarkets: A geostatistical approach for use in mass appraisal. *International Journal of Housing Markets and Analysis*, *4*(3), 290–318. https://doi.org/10.1108/17538271111153040

Medayese, M., Martins, V. E., & Abdrazack, N. T. (2015). Density. In L. Egunjobi (Ed.), *Contemporary Concepts in Physical Planning* (First Edition, Vol. 1, pp. 263–290). University of Ibadan.

Mohammed, J. K., & Sulyman, A. O. (2019). Spatio-temporal Analysis of Bida Housing Market using Geographic Information System. In L. T. Ajibade, N. B. Tanimowo, G. Amuda-Yusuf, & N. A. Bello (Eds.), *The Proceedings of International Conference of Environmental Sciences* (pp. 306–316).

Mohammed, J. K., Sulyman, A. O., & Alhaji, A. A. (2021). Spatial Pattern of Residential Densification in Housing Submarket of a Traditional Urban Area. *Baltic Surveying*, *14*, 25–33. https://doi.org/10.22616/j.balticsurveying.2021.14.003

Muehlenbachs, L., Spiller, E., & Timmins, C. (2015). The housing market impacts of shale gas development. *The American Economic Review*, *105*(12), 3633–3659.

Park, J. (2013). The Division of Spatial Housing Submarkets: A Theory and the Case of Seoul. *Environment and Planning A*, *45*(3), 668–690. https://doi.org/10.1068/a45337

Renigier-Biłozor, M., Biłozor, A., & Wisniewski, R. (2017). Rating engineering of real estate markets as the condition of urban areas assessment. *Land Use Policy*, *61*, 511–525. https://doi.org/10.1016/j.landusepol.2016.11.040

Royuela, V., & Vargas, M. (2007). Defining housing market areas using commuting and migration algorithms. Catalonia (Spain) as an applied case study. *IREA–Working Papers, 2007, IR07/07*.

Seo, W. (2008). *Spatial impacts of micro neighborhood environments on residential real estate resale values: The importance of physical disorder* [The Ohio State University]. http://rave.ohiolink.edu/etdc/view?acc_num=osu1228281862

Ståhle, A. (2008). *Compact sprawl: Exploring public open space and contradictions in urban density*. School of Architecture, KTH.

Treija, S., Bratuškins, U., & Koroļova, A. (2018). Urban Densification of Large Housing Estates in the Context of Privatisation of Public Open Space: The Case of Imanta, Riga. *Architecture and Urban Planning*, *14*(1), 105–110. https://doi.org/10.2478/aup-2018-0014

Tupenaite, L., Kanapeckiene, L., & Naimaviciene, J. (2017). Determinants of Housing Market Fluctuations: Case Study of Lithuania. *Procedia Engineering*, *172*, 1169–1175. https://doi.org/10.1016/j.proeng.2017.02.136

Vergnes, A., Pellissier, V., Lemperiere, G., Rollard, C., & Clergeau, P. (2014). Urban densification causes the decline of ground-dwelling arthropods. *Biodiversity and Conservation*, *23*(8), 1859–1877. https://doi.org/10.1007/s10531-014-0689-3

Vuckovic, Loibl, Tötzer, & Stollnberger. (2019). Potential of Urban Densification to Mitigate the Effects of Heat Island in Vienna, Austria. *Environments*, *6*(7), 82. https://doi.org/10.3390/environments6070082

Wang, L., Omrani, H., Zhao, Z., Francomano, D., Li, K., & Pijanowski, B. (2019). Analysis on urban densification dynamics and future modes in southeastern Wisconsin, USA. *PLOS ONE*, *14*(3), 1–22. https://doi.org/10.1371/journal.pone.0211964

Wang, S., Wang, J., & Wang, Y. (2018). Effect of land prices on the spatial differentiation of housing prices: Evidence from cross-county analyses in China. *Journal of Geographical Sciences*, *28*(6), 725–740. https://doi.org/10.1007/s11442-018-1501-1

Wu, C., & Sharma, R. (2012). Housing submarket classification: The role of spatial contiguity. *Applied Geography*, *32*(2), 746–756. https://doi.org/10.1016/j.apgeog.2011.08.011

Wu, J., Deng, Y., & Liu, H. (2014). House price index construction in the nascent housing market: The case of China. *The Journal of Real Estate Finance and Economics*, *48*(3), 522–545.

Xiao, Y. (2012). *Urban morphology and housing market* [PhD Thesis]. Cardiff University.

Xiao, Y. (2017). *Urban Morphology and Housing Market*. Springer Singapore. https://doi.org/10.1007/978-981-10-2762-8

Yang, S., Hu, S., Li, W., Zhang, C., & Torres, J. (2017). Spatiotemporal Effects of Main Impact Factors on Residential Land Price in Major Cities of China. *Sustainability*, *9*(11), 2050. https://doi.org/10.3390/su9112050

Zhou, Z. (2018). Housing market sentiment and intervention effectiveness: Evidence from China. *Emerging Markets Review*. https://doi.org/10.1016/j.ememar.2017.12.005

EFFECTS OF ONE MISSING OBSERVATION ON ESTIMATES OF MODEL PARAMETERS AND THEIR STANDARD ERRORS IN CENTRAL COMPOSITE DESIGNS (CCDs)

Hajara SOKODABO (2017sokodabohajara@gmail.com)
Yisa YAKUBU (yisa.yakubu@futmnna.edu.ng)
Department of statistics, Federal University of Technology, Minna

Abstract

We may be confronted with a situation in which some observations are lost or unavailable due to some accident or cost constraints and their absence has a very bad impact on the estimates of the regression coefficients. This work investigates the effect of one missing observation of different types of design points on the estimated model for the candidate central composite designs considered. Three different Central Composite Designs (CCD) were studied in this work, which include the 2-factor, 3-factor and the 4-factor CCDs. The regression coefficients and their standard errors were first studied for the full designs and then, similar results were investigated separately for one factorial point missing, one axial point missing and one centre point missing for each of the designs considered. It was observed that missing observations of each of the design points have adverse effect on the regression estimates and standard errors of the model parameters of each of the designs considered. For the 2-factor CCD, the quadratic effect (x_1^2) *for factor one was observed to be the largest but negative on the yield for the full design* $(\hat{\beta} = -0.806)$*, while that of factor two* (x_2^2) *was the smallest on the yield* $(\hat{\beta} = 0.069)$ *after the cross-product* (x_1x_2) *effect* $(\hat{\beta} = 0.150)$*. The standard errors of each of these two quadratic effects are the highest* $(SE\ coef = 0.505)$ *after that of the cross-product effect* $(SE\ coef = 0.639)$*.For the 3-factor CCD, it was observed that the linear effects of* x_1*and* x_3 *are the most significant linear effects while the quadratic effects of* x_2 *and* x_3 *are the most significant quadratic effects in the case of the full design. When a factorial run is missing, the estimated effect of each of the model parameters remain almost unchanged, indicating that the factorial point looks less influential for the regression estimates for this design. However, the standard error of each of these effects become higher with the linear, quadratic, and cross-product effects behaving similarly for the missing factorial run in this design.*

Keywords: Missing observations, Estimates of model parameters, Standard errors, Central composite design

1.0 Introduction

Statistically designed experiment is an indispensable technique in the design stage of a product or a process for investigating the effects of several factors on a quality characteristic of interest. These experiments play a key role in the design of new products, improvement of existing ones as well as the design and development of manufacturing processes to produce

them, which are the crucial activities in most industrial organizations today. In most industries today, for instance, biotechnology and pharmaceuticals, medical devices, electronics and chemical industries etc., experimental design methodology has resulted in shorter design and development time for new products as well as products that are easier to manufacture, products with higher reliability and enhanced field performance, products that meet or even exceed customer requirements. The tools required for adequate selection of a design and the subsequent fitting and evaluation of the hypothesized model, using the data generated by the design, have been developed in an area of experimental design known as response surface methodology **(**RSM**)**.

1.1 Response Surface Methodology

Response Surface Methodology is an area of experimental design which consists of a group of mathematical and statistical techniques used in the development of an adequate functional relationship between a response of interest, y, and a number of associated control (or input) variables denoted by $x_1, x_2, \ldots, x_k$ (Myers and Montgomery, 2009).

The most extensive applications of RSM are in the industrial world, particularly in situations where potential influence of several process variables on some quality characteristic of the process is being investigated. RSM is widely used to explore and to optimize response surfaces in these experiments. RSM is sequential in nature and so the experimenter begins with a screening experiment to identify important factors. Follow-up experiments then seek to improve the performance of the response. This process allows the experimenter to learn about the process or system under study as the investigation proceeds. For example, suppose the growth of a plant is affected by certain amount of water, sunshine, and other variables. These variables can vary continuously and when treatments are from a continuous range of values, then a Response Surface Methodology is useful for developing, improving, and optimizing the response variable.

1.1.1 First-Order Response Surface Designs

In practice, the form of the relationship between the response variable *y* and the *k* input variables is usually unknown and it is therefore approximated, within the experimental region, by a low-order polynomial model such as a first-order model:

$$y_u = \beta_0 + \beta_1 x_{1u} + \beta_2 x_{2u} + \cdots + \beta_k x_{ku} + e_u \qquad (1.0)$$

where $y_u (u = 1, 2, \ldots, n)$ is the *u*th response value obtained as a result of applying the *u*th treatment combination; x_{iu} is the level of the *i*th factor in the *u*th treatment combination, $i = 1, 2, \ldots, k$; β_i is the unknown coefficient associated with the *i*th factor, e_u is the random error associated with the *u*th observation, and is assumed to be independently and normally distributed with mean zero and common variance σ^2. Over n observations model (1.0) can be expressed in matrix form as

$$y = X\beta + e \qquad (1.1)$$

where $\mathbf{y} = (y_1, y_2, ..., y_n)'$ is an n x 1 vector of responses, **X**is an *n* x*p*(*p = k +1*) matrix of input variable observations, with column of ones, $\mathbf{1_n}$, as its first column; $\boldsymbol{\beta} = (\beta_0, \beta_1, ..., \beta_k)'$ is a *p* x *1* vector of unknown parameters to be estimated, and $\mathbf{e} = (e_1, e_2, ..., e_n)'$ is an*n* x *1* vector of random errors distributed as $\mathbf{N(0, \sigma^2 I_n)}$. The ordinary least squares estimator of $\boldsymbol{\beta}$ is

$$\hat{\beta} = (X'X)^{-1}X'y \qquad (1.2)$$

First-order model is used to describe the flat surfaces that may or may not be tilted. This model is not suitable for analysing maximum, minimum, and ridge lines. The first-order model approximation of the function *f* is reasonable when *f* is not too curved in that region and the region is not too big. Examples of first-order designs include the 2^k factorial designs and their fractional replicates in which the main effects are not aliased with each other, the simplex designs and the Plackett-Burman (1946) designs.

The variables in response surface designs are usually coded. The use of coded variables in place of the input variables facilitates the construction of experimental designs. Coding removes the units of measurements of the input variables and as such, distances measured along the axes of the coded variables in a *k* –dimensional space are standardized, i.e., defined in the same metric (Khuri and Cornell, 1996).

A convenient coding formula for transforming the system of input variables (X_i) to a unitless system in the coded variables (x_i) is,

$$x_i = \frac{2X_i - (X_{il} + X_{ih})}{X_{ih} - X_{il}}, \quad i = 1,2, \dots, k \qquad (1.3)$$

Where $X_{il}$and X_{ih} are, respectively, the low and high levels of X_i. The use of coded variables in place of the original input variables when fitting polynomial models ensures computational ease and increased precision of model coefficient estimates. For instance, the model matrix for a first-order (2^3 $factorial$) design with its variables coded is given in Table 1.1.

Table1.1. Model Matrix for a first-order 2^3 $factorial$ design with coded variables

x_0	x_1	x_2	x_3
1	-1	-1	-1
1	1	-1	-1
1	-1	1	-1
1	1	1	-1
1	-1	-1	1
1	1	-1	1

1	-1	1	1
1	1	1	1

Interest is always centred on **orthogonal** first-order designs since they have a diagonal information matrix that leads to uncorrelated estimates of the model parameters. That is, the property of orthogonality gives a measure of a design's ability in providing minimum-variance estimation of model parameters. A design is said to be orthogonal if

$\sum_{u=1}^{N} X_{ui}X_{uj} = 0$, for all $i \neq j$ and also 1'x_i = 0, for $i = 1,2,\ldots,k$, which implies that $Var(\hat{\beta}_j)$is minimal$(1 \leq j \leq p)$.

1.2.2 Second-Order Response Surface Designs

At a point on the response surface that is remote from the optimum, there is little curvature in the system and it is usually assumed that a first-order model is an adequate approximation to the true surface in a small region of the *x*'s. In this situation a procedure for moving sequentially in the direction of the maximum increase in the response (i.e. along the path of *steepest ascent*) is used. Experiments are conducted along this path until no further increase in response is observed. Then a new first-order model may be fit, a new path determined, and the procedure continued. Eventually, the experimenter will arrive in the vicinity of the optimum. This is usually indicated by **lack- of-fit** of a first-order model. At that time, axial runs are added to allow the quadratic terms to be incorporated into the model to give a second–order model. The resulting second-order experiments are then conducted to obtain a more precise estimate of the optimum.

The eventual objective of RSM is to determine the optimum operating conditions for the system or to determine a region of the factor space in which operating specifications are satisfied. Hence, RSM is a set of techniques that encompasses and such a set includes:

a. Setting up a series of experiments that will yield adequate and reliable measurements of the response of interest.
b. Determining a model that best fits the data collected from the design chosen by conducting appropriate tests of hypotheses concerning the model's parameters.
c. Determining the optimal settings of the experimental factors that produce the maximum (or minimum) value of the response.

1.3 Missing Observations in Designed Experiments

In an experimental work, situations often arise where some observations are lost or unavailable due to some accidents or cost constraints. Missing observations can occur as a result of many causes during the conduct of an experiment.

(i) Animals can invade and destroy some experimental units.
(ii) Floods or fires can occur and damage a part of the experiment.
(iii) On some occasions workers have been known to unintentionally leave out some of the experimental units when setting up the experiment.

Missing observations can create a big problem by making the results of a response surface experiment quite misleading, thereby adversely affecting the inference. Thus the estimates of the parameters will be misleading. Besides, unavailability of some observations destroys the useful properties of the design, such as **orthogonality**, **rotatability** and **optimality**. The design may break down as a result of missing observations. Herzberg and Andrews (1976) Cited but in the reference and Andrews and Herzberg (1979) define the situation when a design's information matrix is 'singular' as the breakdown of the experimental design. In this situation, estimation of the parameter effects becomes impossible. The problem of missing observations becomes more serious when experimental runs are very costly, and especially when some factors are hard to change.

The data with missing observations may be handled by dropping the corresponding rows of the model matrix $\boldsymbol{X}$(i.e., the rows in the model matrix corresponding to the missing observations in the data) and then proceed with the analysis of the remaining data using least squares procedure. However, dropping the rows of $\boldsymbol{X}$ amounts to changing the design structure and this adversely affects the useful design properties stated above (Herzberg and Andrews (1976)).

Otherwise, the remaining data may be handled by obtaining estimates for the missing observations using the techniques provided by some authors (e.g., Allan and Wishart (1930a), Yates (1933), Anderson (1946), Cochran and Cox (1957) etc.), for computing missing plot values, substitute these estimates in to the data and then proceed with the analysis. For instance, an expression derived by Yates (1933) for obtaining an estimate for a single missing observation **x**in a randomized blocks design (RCBD) is given by

$$\boldsymbol{y_i} = \frac{(\boldsymbol{bB+tT-G})}{(\boldsymbol{b-1})(\boldsymbol{t-1})} \qquad 1.4$$

Where b is the number of blocks, t is the number of treatments in the experiment, B is the total of the remaining observations in the block with the missing unit, T is the total of the remaining observations for the treatment with the missing unit, and G is the grand total with the missing unit. In the case of more than one missing observations, the above expression is used by means of iteration. The estimated value is then substituted into the data and the analysis is carried out on the complete data but with the error degrees of freedom reduced by 1.

All these techniques only make the analysis of the remaining observations as simple as possible, but do not guard against the losses involved. Besides, in the analysis of classical experimental designs such as the randomized blocks, Latin squares, split-plots etc., interest is more on comparison of factor effects than model prediction. However, in response surface designs, the term 'response surface' implies that interest in these studies is more on predictive capability of the designs than the comparison of treatment effects since the points on the fitted surface are predicted responses. Thus, in these designs, if too many observations are missing the whole experiment is lost since the resulting information matrix will be 'singular'.

To minimize the effects of missing observations, we require designs which guard against (or are insensitive to) the effect of the missing observations. Such response surface designs are said to be **robust** to the missing observations in terms of a given criterion.

Box-Behnken Design

The Box-Behnken designs (BBDs) are alternate choice for fitting quadratic models that requires 3 levels of each factor and are rotatable (or "nearly" rotatable). This class of designs involves combining two-level factorial designs with balanced incomplete block designs (BIBD) in a particular manner. In a Box-Behnken design, the treatment combinations are at the midpoints of edges of the process space and at the centre. These designs may be used when performing non-sequential experiments. That is, when the plan is to perform the experiment once. BBDs have fewer design points, thus they are less expensive to run than central composite designs with the same number of factors. The designs allow efficient estimation of the first- and second-order coefficients. However, BBDs have limited capability for orthogonal blocking compared to the central composite designs. The geometric view and design matrix of the completely randomized 3-factor BBD with 3 centre points are given respectively in Figure 1.2 and Table 1.3.

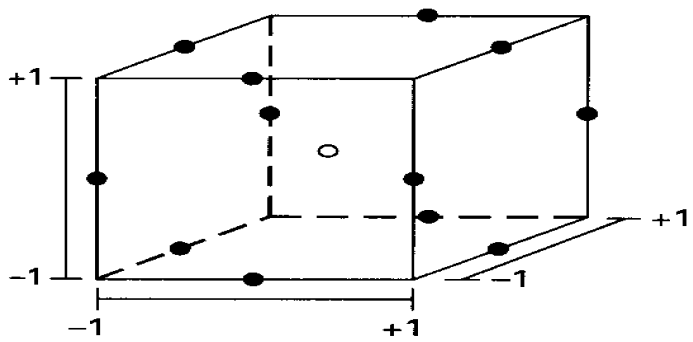

Fig. 1.2. Geometric view of a completely randomized 3-factor BBD (source: Box and Behnken (1960))

Table 1.3. Design matrix for the completely randomized 3-variable BBD (source: Box and Behnken (1960))

Run	x_1	x_2	x_3	points
1	-1	-1	0	
2	1	-1	0	factorial
3	-1	1	0	
4	1	1	0	
5	-1	0	-1	
6	1	0	-1	factorial
7	-1	0	1	
8	1	0	1	
9	0	-1	-1	
10	0	1	-1	factorial
11	0	-1	1	

12	0	1	1	
13	0	0	0	
14	0	0	0	centres
15	0	0	0	

The CCD is the most popular among the second-order designs. The distance of the axial runs from the centre of the design is denoted by α, the choice of which is crucial to the performance of the design. Box and Hunter (1957) discuss extensively on the choice of α for the CCD. The authors developed the notion of **design rotatability**, where, a design is said to be rotatable when it's scaled prediction variance ($v(x) = NVar[\hat{y}(\mathrm{x})]/\sigma^2$) is constant for all points that are equidistant from the design centre. That is, rotatability ensures that the quality of prediction at a point **x** in the design space is a function of the distance, ρ, of the point from the design centre and therefore, equally-good predicted values will be obtained for all points that are of the same distance from the centre of the design. The purpose of the idea of design rotatability was, in part, to impose a type of stability on $v(x)$, since a reasonably stable scaled prediction variance provides insurance that the quality of the predicted value, **($\hat{\boldsymbol{y}}$(x)),** is similar throughout the region of interest. Rotatability provides some useful guidelines for the choice of design parameters – for instance, the choice of α and n_c in the CCD.

2.0 Methodology

2.1 Candidate Designs

Three different central composite designs were considered in this work. These designs are given in the table below, where k is the number of design variables, n_f is the number of factorial points, n_α is the number of axial points, n_0 is the number of centre points, and N is the total number of design points. These designs are given in the Table below.

Table 1: Candidate CCDs considered

k	n_f	n_α	n_0	N
2	4	4	4	12
3	8	6	6	20
4	16	8	7	31

The central composite design (CCD) consists of factors with five levels that involve three components. They are:

i. a complete (or a fraction of) 2^k factorial design with factor levels coded as -1, 1 (called the factorial portion),
ii. an axial portion consisting of $2k$ points arranged so that two points are chosen on the coordinate axis of each control variable at a distance of α from the design centre,
iii. n_0 centre points.

Thus the total number of points in a CCD is $n = 2^k + 2k + n_0$. These three components of the design play important and somewhat different roles.

i. The factorial portion consists of n_f equally-spaced points that contribute to the estimation of linear terms and are the only points that contribute to the estimation of the interaction terms in the model.

ii. The axial portion consists of points lying on the axis of each input variable, and in this portion of the design, the factors are not varying simultaneously but rather in a one-factor-at- a-time array. Thus no information regarding the interaction effect is provided by this portion of the design. However, the axial portion allows for efficient estimation of pure quadratic terms in the model, and without these points, only the sum of the quadratic terms, i.e., $\sum_{i=1}^{k} \beta_{ii}$, can be estimated.

iii. The centre runs provide an internal estimate of error (i.e., the pure error), and efficiently provide information about the existence of curvature in the system. If curvature is found in the system, the addition of axial points allows for efficient estimation of the pure quadratic terms.

The geometric view and design matrix of a 2-factor CCD are given respectively in Figure 1 and Table 2.

Table 2: Design matrix for a completely randomized 2 –factor CCD with 3 centre points (source: Box and Wilson (1951))

Run	x_1	x_2	points
1	-1	-1	
2	1	-1	factorial
3	-1	1	
4	1	1	
5	$-\alpha$	0	axials
6	$+\alpha$	0	
7	0	$-\alpha$	
8	0	$+\alpha$	
9	0	0	centres
10	0	0	
11	0	0	

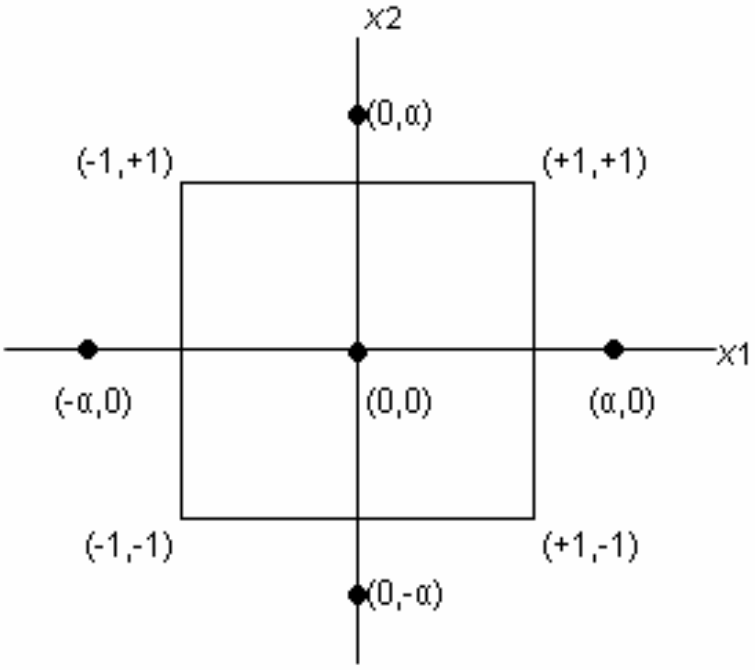

Fig. 1.. Geometric view of a completely randomized 2-factor CCD (source: Box and Wilson (1951))

2.2Model and Notation

The second-order model includes all the terms in the first-order model, plus all quadratic terms like $\beta_{11}x_{1i}^2$ and all cross product terms like $\beta_{13}x_{1i}x_{3j}$

It is usually expressed as

$$y_u = \beta_0 + \sum_{i=1}^{k}\beta_i x_{iu} + \sum_{i=1}^{k}\beta_{ii}x_{iu}^2 + \sum_{i=1}^{k-1}\sum_{j=i+1}^{k}\beta_{ij}x_{iu}x_{ju} + e_u \qquad (1.5)$$

In matrix form, this model can be expressed as

$$\mathbf{y} = \boldsymbol{\beta}_0 + \mathbf{x}'\mathbf{b} + \mathbf{x}'\mathbf{B}\mathbf{x} + \mathbf{e}, \qquad (1.6)$$

where $\mathbf{b}$ is a *kx1* vector of the first order regression coefficients and $\mathbf{B}$ is a *k*x*k* symmetric matrix whose main diagonal elements are the pure quadratic coefficients (β_{ii}) and whose off-diagonal elements are one-half the mixed quadratic coefficients($\beta_{ij}, i \neq j$) (Montgomery, 2005). Examples of the 2nd –order designs include

(i) the 3^k factorial designs and their fractional replicates,
(ii) the central composite designs (CCD) introduced by Box and Wilson (1951),

the Box-Behnken designs (BBD) introduced by Box and Behnken (1960), etc.

3.0 Results and Discussion

(1) Two- Factor CCD ($k = 2, n_f = 4, n_\alpha = 4, n_0 = 4; N = 12$)

Table 2 shows the effects of missing different types of design points on the estimates of regression coefficients and their standard errors in a two-factor CCD with the given parameters. In the first column of the Table, the regression coefficients and their standard errors are presented for the full design and in the other columns, similar results are presented separately for one factorial point missing, one axial point missing, and one centre point missing.

It can be observed from this Table, that the quadratic effect(x_1^2)for factor one was the largest but negative on the yield for the full design ($\hat{\beta} = -0.806$) while that of factor two (x_2^2) was the smallest on the yield ($\hat{\beta} = 0.069$) after the cross-product (x_1x_2) effect($\hat{\beta} = 0.150$).The standard errors of each of these two quadratic effects are the highest ($SE\ coef = 0.505$) after that of the cross-product effect($SE\ coef = 0.639$). When a factorial point is missing, the estimated effect of each of the terms is almost doubled except for the x_1 term. The estimated effect for the cross-product (x_1x_2)term becomes about six times larger under one missing factorial point($\hat{\beta} = 0.959$) and its standard error also becomes higher ($SE\ coef = 0.699$) under this scenario.

For the estimates of the other terms in the model, the factorial point looks less influential. When an axial point is missing from the full design, the estimated effects of x_1 and the cross-product (x_1x_2) terms were not affected but their standard errors become higher. The same is the case for a missing centre run. It can be observed that both the linear and quadratic effects ofx_2 were highly affected by a missing axial run as each of these effects recorded the highest standard errors when this run is missing compared to other missing runs. However, the highest standard errors were observed for the linear and quadratic effects of x_1 when a centre run was missing.

Table2: Estimated Regression Coefficients and Standard errors for a 2-factor CCD

	Missing Point							
	None		Factorial		Axial		Centre	
Terms	Coef	SE coef	Coef	SE coef	Coef	SE coef	Coef	SE coef
Constant	8.125	0.639	8.125	0.542	8.125	0.669	8.033	0.804
x_1	0.313	0.452	-0.091	0.442	0.313	0.473	0.313	0.492
x_2	0.564	0.452	0.968	0.442	0.828	0.611	0.564	0.492
x_1^2	-0.806	0.505	-1.008	0.442	-0.900	0.546	-0.76	0.586

x_2^2	0.069	0.505	-0.133	0.442	0.349	0.669	0.115	0.586
x_1x_2	0.150	0.639	0.959	0.699	0.150	0.669	0.150	0.696

(2) Three- Factor CCD ($k = 3, n_f = 8, n_\alpha = 6, n_0 = 6; N = 20$)

Table 3 shows the effects of missing different types of design points on the estimates of regression coefficients and their standard errors in a three-factor CCD. In the first column of the Table, the regression coefficients and their standard errors are presented for the full design and in the other columns, similar results are presented separately for one factorial point missing, one axial point missing, and one centre point missing.

From this Table it can be observed that the linear effects of $x_1$and x_3 are the most significant linear effects while the quadratic effects of x_2 and x_3 are the most significant quadratic effects in the case of the full design. When a factorial run is missing, the estimated effect of each of the model parameters remain almost unchanged, indicating that the factorial point looks less influential for the regression estimates for this design. However, the standard error of each of these effects become higher with the linear, quadratic, and cross-product effects behaving similarly for the missing factorial run in this design. When an axial run is missing, the estimated effect of each of the interaction terms remain unchanged. When a centre run is missing, the change in the estimated effect of each of the model parameters was not significant and thus the axial point seems less influential for the estimates for this design and in terms of the standard errors, the linear and quadratic effects are similar, while the cross-product terms are also similar.

Table3: Estimated Regression Coefficients and Standard errors for a 3-factor CCD

	Missing Point							
	None		Factorial		Axial		Centre	
Terms	Coef	SE coef	Coef	SE coef	Coef	SE coef	Coef	SE coef
Constant	10.165	0.444	10.164	0.468	10.18	0.408	10.257	0.507
x_1	-1.104	0.295	-1.115	0.343	-1.104	0.27	-1.104	0.307
x_2	0.087	0.295	0.076	0.343	0.421	0.334	0.087	0.307
x_3	1.020	0.295	1.032	0.343	1.02	0.27	1.02	0.307
x_1^2	-0.760	0.287	-0.756	0.307	-0.861	0.27	-0.791	0.307
x_2^2	-1.042	0.287	-1.038	0.307	-0.665	0.345	-1.074	0.307
x_3^2	-1.149	0.287	-1.144	0.307	-1.249	0.27	-1.18	0.307
x_1x_2	-0.350	0.385	-0.331	0.476	-0.35	0.353	-0.35	0.401

x_1x_3	-0.500	0.385	-0.519	0.476	-0.5	0.353	-0.5	0.401
x_2x_3	0.150	0.385	0.131	0.476	0.15	0.353	0.15	0.401

(3) Four- Factor CCD ($k = 4, n_f = 16, n_\alpha = 8, n_0 = 7; N = 31$)

Table 4 shows the effects of missing different types of design points on the estimates of regression coefficients and their standard errors in a four-factor CCD. In the first column of the Table, the regression coefficients and their standard errors are presented for the full design and in the other columns, similar results are presented separately for one factorial point missing, one axial point missing, and one centre point missing.

From this Table it can be observed that, in the case of the full design, the linear effects of $x_1$and x_3 are the most significant linear effects; the quadratic effects of x_1, x_3, and x_4 are the most significant quadratic effects while all the interaction effects were significant except that between x_2 and x_4. The linear, quadratic and the cross-product effects exhibit similar behavior in their standard errors. When a factorial run is missing, only a slight change were observed in the estimated effects of the model parameters, indicating that the factorial point seems less influential for the regression estimates for this design. Similarly, the corresponding standard errors were only observed to change slightly with similar behavior in the linear, quadratic and the cross-product effects.

When an axial run was missing, the estimated regression effects almost remain unchanged, indicating that the axial point seems less influential for the regression estimates for this design. A significant change was observed in the standard errors of the linear and quadratic effects of x_1, and in the quadratic effects of x_2, x_3, and x_4, while the interaction or cross-product effects exhibit similar behavior in their standard errors for this missing axial run.

When a centre run was missing, the estimated regression effects remain unchanged while the standard errors of the linear and quadratic effects were similar with that of the missing axial runs.

Table4: Estimated Regression Coefficients and Standard errors for a 4-factor CCD

	Missing Point							
	None		Factorial		Axial		Centre	
Terms	Coef	SE coef	Coef	SE coef	Coef	SE coef	Coef	SE coef
Constant	6544.2	53.1	6547.3	52.1	6541.8	57.2	6543.6	57.4
x_1	92.2	42.2	113.8	44.6	90.2	45.8	92.2	43.6
x_2	-76.7	42.2	-55.1	44.6	-76.7	43.6	-76.7	43.6
x_3	-305.6	42.2	-327.1	44.6	-305.6	43.6	-305.6	43.6

x_4	-38.9	42.2	-60.4	44.6	-38.9	43.6	-38.9	43.6
x_1^2	-446	111	-452	109	-459	147	-446	115
x_2^2	-86	111	-92	109	-81	120	-86	115
x_3^2	-526	111	-532	109	-521	120	-526	115
x_4^2	-216	111	-222	109	-211	120	-216	115
x_1x_2	753.7	44.8	729.5	47.7	753.7	46.2	753.7	46.2
x_1x_3	-526.2	44.8	-502	47.7	-526.2	46.2	-526.3	46.2
x_1x_4	-175	44.8	-150.8	47.7	-175	46.2	-175	46.2
x_2x_3	-628.7	44.8	-604.5	47.7	-628.8	46.2	-628.7	46.2
x_2x_4	30	44.8	54.2	47.7	30	46.2	30	46.2
x_3x_4	-277.5	44.8	-301.7	47.7	-277.5	46.2	-277.5	46.2

4. Conclusion

This study has shown that missing a single observation of any of the three different categories of points in a central composite design (factorial, axial, and centre points) adversely affects the estimates of effects of the model parameters as well as their precision. The tables of the parameter effects estimates and their corresponding standard errors for each design show the behaviour of the intercept, linear, quadratic, and interaction effects due to these missing points. It was observed that the extent of the effect depends on the type of the missing point. Therefore, the practitioner should always endeavour to investigate the effect of missing observations on CCDs when faced with the challenges of the design choice. Knowledge of this will alert the practitioner prior to data collection as to where in the design region he/she should expect the worst prediction and where to collect more data if the need arise.

References

Allan, F. E. and Wishart, J. 1930. A Method of Estimating the Yield of a Missing Plot in field Experimental Work. *Journal of Agric. Science* 20.3: 399-406.

Anderson, R. L. 1946. Missing –Plot Techniques. *Biometrics Bulletin* 2.4:41-47.

Andrews, D. F. and Herzberg, A. M. 1979. The robustness and optimality of response surface designs. *Journal of Statistical Planning and Inference* 3:249-257.

Box, G. E. P. and Wilson, K.B. 1951, On the Experimental Attainment of Optimum Conditions (with discussions). Journalof the Royal Statistical Society Series B 13(1):1-45.

Cochran, W. G. and Cox, G. M. 1957. *Experimental Designs*. 2nd ed. New York: John Wiley and Sons Inc.

Myers, R. H., Montgomery, D. C. and Christine, M. A. (2009): Response Surface Methodology: Process and Product Optimization Using Designed Experiments, 3rd Ed., John Wiley and Sons inc.

Box, G.E.P; Behnken, D.W. (1960). Some New Three Level Designs for the Study of Quantitative Variables. Technometrics. 2: 455-475.

Herzberg, A. M. and Andrews, D. F. 1976. Some considerations in the optimal design of experiments in non-optimal situations. *Journal of Royal Statistical Society* 38:284-289.

Khuri, A. I. and Cornell, J. A. 1996. *Response Surfaces: Design and Analysis*, New York: Marcel Dekker.

Yates, F. 1933. The Analysis of Replicated Experiments when the field Results are incomplete. *Empirical Journal of Experimental Agriculture* 1:129-142.

Vector Autoregressive and Autoregressive Integrated Moving Average Modelling of inflation Rate in Nigeria: time series estimates dynamic causal effects and correlation over time.

[(1)]Okemmiri Hillary Uche (*hillaryjim81@gmail.com*),
[(2)]Yisa Yakubu (yisa.yakubu@futminna.edu.ng) and [(3)]Mohammed Makama G.
Statistics Department Federal University of Technology Minna.

ABSTRACT

Inflation is an important indicator of economic activity often used by decision makers to plan economic policies and remains a subject of utmost concern and interest to policy makers. This work models inflation over the period 1990-2018, using autoregressive integrated moving average (ARIMA) and Vector Auto regression (VAR) modeling techniques. ARIMA model is used to fit Nigerian historical consumer price index (CPI) time series expressed in terms of past values of itself plus current and lagged values of error term. Data for the last six months were used to evaluate the performance of the prediction. VAR model is used to investigate the effect of money supply, Nigeria oil prices and exchange rate on inflation rate over the same period. Unit root test (Augmented Dickey- Fuller test) was used to check the integration order of the variables. A cointegration analysis with the four variables was then employed. Both the trace test and max Eigen value statistics revealed that individual variables are cointegrated with inflation at 5% significant level. A Vector Error Correction Model (VECM) was then estimated. It was observed that there is no long run causality running from the independent variables to inflation. In addition, money supply and exchange rate has no short run causality to inflation. The result ARIMA model shows that ARIMA (1,1,0) was the best model out of the fitted ARIMA models.

KEY WORDS: ARIMA model, VAR model, Inflation

1.0 INTRODUCTION

Inflation is the time value of money. It is defined as the persistent increase in the level of general prices of goods and services and fall in the purchasing value of money over a given period of time. Prices of goods and services may increase when people have more money than the goods and services available so that the prices of goods and services are put under pressure to rise. Also, the cost of producing goods and services may increase due to increases in the cost of raw materials, bad weather, increase in the wages, increase in government taxation, increase in international oil prices or other factors that affect the supply and production of goods and services. This increases the prices of final goods and services produced.

There are many measures of inflation although all seek to show the price change in living costs. They include;

- Consumer Price Index (CPI); this is the most common index and measures the changes in prices of essential household basket from a consumer perspective.

- Price Producer Index (PPI); the index measures the changes in prices from a producers' perspective.
- Employment Cost Index (EPI); this index tracks changes in the labor market cost hence measuring inflation of wages, and employer-paid benefits.
- Gross Domestic Product Deflator (GDP-Deflator); measures the change in level of prices of all new domestically produced, final goods and services in an economy.
- International Price Program (IPP); tracks price changes in the foreign trade sector.

Given that $\boldsymbol{I}_t$ is the index at time t, $\boldsymbol{P}_{ti}$ is the price of the i^{th} commodity at time$t$, $\boldsymbol{P}_{oi}$ is the base period and $\boldsymbol{W}_i$ is its weight. The $\boldsymbol{i}_{th}$ commodity weight at the base period is expressed as;

$$W_{0i} = \left[\frac{p_{0i}q_{0i}}{\sum_{i=1}^{n} p_{0i}q_{0i}}\right]$$

This implies that the index at a time t is given by:

$$I_t = \sum_{i=1}^{n} W_{0i} * \left[\frac{p_{ti}}{p_{0i}}\right].$$ This is the Laspeyres formula.

High inflation reduces the value of money and thereby loss of purchasing power. This makes future prices less predictable. Sensible spending and saving plans are harder to make since inflation causes changes in price and discourages saving if the rate of return does not reflect the increase in level of prices. In terms of investment, businesses do not venture into long term productive investments as they are not sure whether the prices will continue rising or will drop at a future date. This causes misallocation of resources by encouraging speculative rather than productive investments. Inflated prices makes domestic goods and services expensive in the world markets worsening the country's terms of trade.

Inflation creates winners and losers though it harms more than helps. Borrowers benefit from a general increase in prices or a reduction in purchasing power. In addition, producers experience higher profits when consumer prices increases in the short run. This occurs when consumer prices rise while wages paid to employees remain relatively stable allowing producers to benefit for a time until wages adjust to reflect the higher prices consumers are paying. Lenders and savers earn interest rates that assume some rate of inflation, and when the actual rate exceeds the expected rate, they both lose. Inflation is seen as a regressive form of taxation with the most vulnerable being the poor and fixed income earners.

Inflation has been a problem facing many countries of the world especially unindustrialized countries. It started during the early 60s, which results to the incorporation of economic policies as measures to reduce the effect of inflation in the societies. Most of these measures taken by developing countries to check the problem of inflation are in the form of the use of central bank instruments of credit control. This is aimed at reducing the volume of money in circulation and sustaining it to ensure low cost of living. Nigeria as a developing country is also faced with the problem of inflation. In Nigeria inflation is a problem for policy makers since 1990s, and ever since then till date the rate of inflation is on the increase. Inflation is neither new to the Nigerian economy system of Nigeria nor the world at large. Evidence has shown that inflation persist both in the advanced countries and unindustrialized countries, with difference in magnitude or rates. The rates of inflation in developing countries are more than those in the developed countries. Inflation may be defined as process of continuous

increase in price of goods and services as result of: large volume of money in circulation used in the exchange of few goods and services. High price of imported goods arising from increase in foreign price and instability of international exchange rate, sub-charge from port congestion, storage facilities, marketing arrangements plus the distribution network. There has been an increase in the price of oil since the removal of subsidy and this led to increase in price of most items, and increase in transportation fare is a living example at hared Dewett and Navalur (2010).

2.0 LITERATURE REVIEW

2.1 Introduction

The chapter gives the empirical and conceptual literatures of past works on ARIMA, SARIM and VAR models used as univariate models for making forecast.

Okafor & Shaibu (2013) empirically developed a univariate autoregressive moving average model for Nigerian inflation and analyzed their forecasting performance for data between 1982- 2010. The study showed that ARIMA (2,2,3) tracked the actual inflation appropriately. The conclusion drawn was that Nigerian inflation is largely expectations-driven. In addition it showed that ARIMA models can explain Nigeria inflation dynamics successfully and help to predict future prices.

In a study to forecast Bangladesh's inflation, Faisal (2001) applied a Box Jenkins ARIMA time series model. One year forecasting was done for consumer price index of Bangladesh using a structure for ARIMA forecasting model where a time series was expressed in terms of past values of itself plus current and lagged values of a 'white noise' error term were drawn up. Validity of the model was tested using standard statistical techniques and the best model was proposed on the basis of various diagnostic and selection & evaluation criteria. The study found many disadvantages of ARIMA model as it neglected the inclusion of explanatory variables and conducted the forecasts only on past values of the dependent variable in combination with present and past moving average terms. So incorporating the judgmental elements with the selected ARIMA model can enhance the predictability of model for forecasting consumer price index of Nigeria and better assist the policymakers.

Various inflation forecasting models have been applied in forecasting inflation rates in apex banks of developed and developing countries. In Bank of Japan, Fujiwara and Koga (2002) presented a statistical forecasting method (SFM) that related many economic and financial time series data without making structural assumptions other than setting up the underlying variables. The SFM was built on many VAR models from combinations of the underlying variables. The data considered were the CPI, domestic wholesale price index, import price, industrial production index, investment, unemployment rate, monetary aggregate, government bond yield and effective exchange rate. The result showed that SFM could provide reliable forecasts information that cannot be extracted when a single structural-type estimation is used. Bruneau et al. (2003) assessed the usefulness of dynamic factor models of Bank of France for generating headline and harmonized index of consumer prices (HICP) inflation forecast for the Euro area. The authors applied Stock and Watson's (1999) out-of-sample methodology and estimated within the sample period January 1988 and March 2002 for inflation, with balanced and unbalanced panels. The total HICP, as well as its five main sub-components (manufacturing, services, processed food, unprocessed food and energy were used. Their results showed evidence to support the improvement of factor/or combined factors in modelling than using the simple AR model for forecasting HICP core inflation and total inflation, and the overall results were found to be robust to potential datasnooping.

Conceptual Literature

Omekara, Ekpenyong and Ekerete (2013) were of the view that inflation in Nigeria is periodic in nature. They used Periodogram and Fourier series analysis from 2003 to 2011 to model Nigerian monthly inflation rates. They attributed the periodicity of inflation rate to variations in government administration. The forecasts generated were found to be accurate for Nigeria. Using monthly CPI data from 2003 through 2011, Amadi, Gideon and Nnoka (2013) proposed SARIMA (1,1,0) x (1, 1, 1) to be the most reliable model for monthly inflation rate of Nigeria. In their study on modelling and forecasting inflation for Nigeria, Otu et al. (2014) explored ARIMA in line with Box and Jenkins using monthly data covering the period October 2003 to November 2013. The out-of-sample forecast was between November 2013 and November, 2014. They reported ARIMA (1,1,1)(0,0,1) as adequate for Nigeria. The study attributed the volatility of inflation in Nigeria to money supply, exchange rate depreciation, petroleum prices and low level of agricultural production. Kelikume and Salami (2014) adopted a univariate model of the form of Box-Jenkins model and a multivariate model in the form of vector autoregression to forecast inflation for Nigeria using monthly data on changes in CPI and broad money supply from January 2003 to December 2012. The result, according to the authors reported the VAR model as the most adequate for forecasting inflation in Nigeria because it returned smaller RMSE. Adams et al. (2014) modelled the Nigerian CPI using ARIMA model in line with Box-Jenkins approach.

They used CPI data between the period 1980 and 2010, and forecast for five years ahead (i.e. 2011 to 2015). The result favoured ARIMA (1, 2, 1) as the most suitable for Nigeria. Yemitan and Shittu (2015) employed Kalman filter technique to implement a state space model to forecast inflation for Nigeria using monthly data from January 1995 to December 2014. The authors introduced structural breaks to capture major political, monetary and macroeconomic events in the country. They concluded that Kalman filter technique is relatively more efficient than Box-Jenkins. They attributed the efficiency of Kalman filtration to availability of built-in which allows information update. To test the efficacy of artificial neural networks (ANN) in inflation forecasting, Onimode et al. (2015) applied ANN and AR (1) on Nigeria monthly CPI data from November 2011 to October 2012 and submitted that neural network is more efficient than univariate autoregressive models in forecasting inflation up to four quarters ahead. Duncan and Martinez- Garcia (2015) using seasonally adjusted quarterly data on CPI from 1980Q1 to 2016Q4 of fourteen (14) Emerging Market Economies (EMEs) including Nigeria, adopted both Frequentist and Bayesian techniques to forecast inflation for Nigeria. The variable considered in the models include: exchange rate, commodity prices/index, global inflation and industrial production index. The findings support the adequacy of Random Walk based on Atkeson and Ohanian (RW-AO) as it produces the lowest RMSPEs. The authors therefore suggested that RW-AO should be used by the EMEs for inflation forecasting. Employing a Univariate Autoregressive Integrated Moving Average (ARIMA) modelling in line with Box-Jenkins technique, Kuhe and Egemba (2016) forecasted inflation for Nigeria using annual CPI data from 1950 to 2014. They found ARIMA (3, 1, 0) to be the best fit for Nigerian CPI data. The out-of-sample forecast (i.e. 2015 to 2020) reveals a continuous rise in inflation throughout the period. In a comparative study to determine the more efficient model between ARIMA-Fourier and Wavelet models, Iwok and Udoh (2016) who obtained ARIMA-Fourier model by combining both the linear and sinusoidal components of the CPI utilized MSE, MAE, and MAPE of the two models to determine their adequacy and concluded that Wavelet model outperformed the ARIMA-Fourier model. They

attributed the performance of Wavelet model to its flexibility in handling non-stationary data as well as the possibility of simultaneous utilization of information in both time-domain and the frequency domain. John and Patrick (2016) forecasted monthly inflation rate for Nigeria using data from January 2000 to June 2015 and found ARIMA (0,1,0) x (0,1,1) to be adequate because the insample forecast obtained was tightly close to the original series.

A recent paper by Lee (2012) looked at the predictive performance of the univariate time series model, Phillips curve and the naive model in forecasting inflation for countries that have adopted inflation targeting. The study found that the univariate time series model yields superior forecast than the Phillips curve and the naive model. A wide number of literature Hafer and Hein (1990), Ang, Bekaert and Wei (2007) have also shown that the univariate time-series model (ARIMA) model tends to outperform and/or equally perform the same as the interest rate model or Phillips curve in forecasting inflation in the USA.

Forecasting of macroeconomic variables with nonparametric methods mainly use Artificial Neural Networks (ANNs). Moshiri and Cameron (2000), Kamruzzaman and Sarker (2003), Binner et al. (2005) and Duzgun (2010) compared ANNs to ARIMA models in forecasting inflation. This strand of research finds that the sophisticated ANNs model tends to outperform ARIMA model and performs equally as the ARIMA model in some other cases. However, He et al. (2012) show that ARIMA model are suitable for forecasting inflation in the USA and that ANNs model sometimes cannot improve the forecasting results.

METHODOLOGY

3.1 Empirical analysis

Different sources can cause inflation simultaneously. Previous studies on inflation in Nigeria have shown that some key factors that affect the rate of inflation are money growth, supply shocks and exchange rate movements. To derive the inflation equation we analyze the impact of the relevant explanatory factors in this study.

Price of goods is assumed to be determined by money market equilibrium. Money supply is increased by velocity of circulation- changes in the way people hold money and the government has tried to control this through tightening and loosening of the monetary policy. Money supply is generally expected to grow at the same rate as the real output so as to maintain the price level. If money supply grows faster than real output it causes inflation, this is in the case where aggregate demand increases while aggregate supply remains static. In the period under review periods where money supply has grown are characterized with high pricing index leading to the assumption that an increase in money supply will result to increase inflation.

Oil prices account for the influence of supply shocks since it is a major input in the economy. Oil is used from the production level to transportation of goods hence has effect on the cost of the end products. Inflation is assumed to follow the same direction as the changes in oil prices and can help in elaborating short term movements in inflation. During the period under review, for instance in 2008 and 2011 oil prices were trending high which corresponded with high inflation rate.

Exchange rate, another variable in this study is assumed to influence inflation through its effect on net exports. Nigeria embraces the free floating exchange rate system where demand and supply forces of market determine the daily value of one currency against another. The exchange rate affects the prices of directly imported goods as well as and indirectly through the local goods that are under competitive pressure from imported goods. As illustrated by our data, exchange rate in mid-2011 hit highs of Kes 105 in turn skyrocketing general prices of goods and services.

In this study we use a combination of these theories based on the assumptions discussed above and develop a model for inflation such that;

$$\underset{+}{\Pi_t} = f(\underset{+}{M2_t}, \underset{+}{P_t}, \underset{+}{E_t})$$

where an increase in Money supply($M2$), Murban oil prices (P) and Exchange rate (E) leads to an increase in inflation(Π) in period t.

3.2 ARIMA Models

The Box-Jenkins (ARIMA) model is in theory the most general class of models for forecasting time series and was first popularized by Box and Jenkins (1970). $ARIMA\ (p, d, q)$ completely ignores independent variables and assumes that past values of the series plus previous error terms contain information for the purposes of forecasting. The integers refer to the Autoregressive (AR), Integrated (I) and Moving Average (MA) parts of the data set respectively. The models are applied in some cases on data which show evidence of non-stationarity which can be stationarized by transformations such as differencing and logging. The model takes into account historical data and decomposes it into AR process, where there is a memory of past events; an integrated process, which accounts for stationarity, making it easier to forecast; and a MA of the forecast errors, such that the longer the historical data, the more accurate the forecasts will be, as it learns over time. The ARIMA models are applicable only to a stationary data series, where the mean, the variance, and the autocorrelation function remain constant through time.

Autoregressive process AR expresses a dependent variable as a function of past values of the dependent variable. A p_{th}-order process is of the form:

$$y_t = \alpha + \emptyset_1 y_{t-1} + \emptyset_2 y_{t-2} + \cdots\cdots\cdots\cdots\cdots\cdots\cdots + \emptyset_p y_{t-p} + \varepsilon_t$$

Where;$Y_t$is the stationary depended variable being forecasted at time t. $y_{t-1}, y_{t-2}, \cdots\cdots, y_{t-p}$is the response variable at time lags $t-1, t-2 \ldots\ldots t-$ $p$respectively.$\alpha = \mu(1 - \emptyset_1 - \cdots\cdots - \emptyset_p)$. $\emptyset_1, \emptyset_2, \ldots\ldots\ldots \emptyset_p$ are the coefficients to be estimated. ε_t is the error term at time t with mean zero and a constant variance. Using the backshift operator we can write the $AR(p)$ model as;

$$(1 - \emptyset_1 B - \emptyset_2 B^2 - \cdots\cdots - \emptyset_2 B^2) y_t = \emptyset(B) y_t = \varepsilon_t$$

The moving average model of order $MA(q)$ is defined as;

$$y_t = \varepsilon_t + \theta_1 \varepsilon_{t-1} + \theta_2 \varepsilon_{t-2} + \cdots\cdots + \theta_q \varepsilon_{t-q}$$

Where;q is the number of lags in the moving average and $\theta_1, \theta_2, \ldots\ldots\theta_q$ are parameters to be estimated. The moving average operator is given by;

$$\theta(B) = \theta_1 B + \theta_2 B^2 + \cdots\cdots + \theta_q B^q$$

To create an ARMA model, we begin with an econometric equation with no independent variables $Y_t = \beta_0 + \varepsilon_t$ and add to it both the AR process and the MA process.

$$y_t = \beta_0 + \emptyset_1 y_{t-1} + \emptyset_2 y_{t-2} + \cdots\cdots + \emptyset_p y_{t-p} + \varepsilon_t + \theta_1 \varepsilon_{t-1} + \theta_2 \varepsilon_{t-2} + \cdots\cdots + \theta_q \varepsilon_{t-q}$$

$\beta_0 + \emptyset_1 y_{t-1} + \emptyset_2 y_{t-2} + \cdots\cdots + \emptyset_p y_{t-p}$ is the AR(p), and $\theta_1 \varepsilon_{t-1} + \theta_2 \varepsilon_{t-2} + \cdots\cdots + \theta_q \varepsilon_{t-q}$ is the MA(q) process. Where the $\emptyset_s$ and θ_s are the coefficients of the autoregressive and moving average processes respectively.

The integrated ARMA or ARIMA model is a broadening class of ARMA model which includes a differencing term. A process is said to be $ARIMA\ (p, d, q)$ if

$$\nabla^d y_t = (1 - \mathrm{B})^d y_t$$

is an $ARMA\ (p, q)$. The is generally written as;

$$\emptyset(B)(1 - \mathrm{B})^d y_t = \theta(1 - \mathrm{B})\varepsilon_t$$

A first- differenced inflation series is of the form:

$$CPI_t = (\nabla CPI_t) = CPI_t - CPI_{t-1} = \Delta CPI_t - \Delta CPI_{t-1}$$

Thus the $ARIMA\ (p, 1, q)$model may be specified as:

$$CPI_t = \beta_0 + \emptyset_1 CPI_{t-1} + \emptyset_2 CPI_{t-2} + \cdots\cdots + \emptyset_p CPI_{t-p} + \varepsilon_t + \theta_1 \varepsilon_{t-1} + \theta_2 \varepsilon_{t-2} + \cdots\cdots + \theta_q \varepsilon_{t-q}$$

Where CPI_t, is the differenced inflation series of order 1 , and $\emptyset, \beta, and\ \theta$ are the parameters to be estimated.

Test stationarity of the time series data

To model the series we check the structure of the data in order to obtain some preliminary knowledge about the stationarity of the series; whether there exist a trend or a seasonal pattern. A time series is said to a stationary if both the mean and the variance are constant over time. A time plot of the data is suggested to determine whether any differencing is needed before performing formal tests. If the data is non-stationary, we do a logarithm transformation or take the first (or higher) order difference of the data series which may lead to a stationary time series. This process will be repeated until the data exhibit no apparent deviations from stationarity. The times of differencing of the data is indicated by the parameter *d* in the ARIMA (*p,d,q)* model.
Then an Augmented Dickey-Fuller Test (ADF Test) is used to determine the stationarity of the data.

Augmented Dickey-Fuller Test (ADF Test)

The ADF test is used to test for unit root. The testing procedure for the ADF test is the same as for the Dickey–Fuller test but it is applied to the model. A random walk with drift and trend is represented as;

$$\Delta y_t = \alpha + \beta_t + \gamma y_{t-1} + \delta_1 \Delta y_{t-1} + \cdots\cdots + \delta_{p-1} \Delta y_{t-p+1} + \varepsilon_t$$

whereα is a constant, $\beta$the coefficient on a time trend and p the lag order of the autoregressive process. Imposing the constraints$\alpha = 0$ and $\beta = 0$corresponds to modeling a random walk and using the constraint $\beta = 0$ corresponds to modelling a random walk with a drift.

The test statistics , value is calculated as follows:

$$\tau = \frac{\hat{\gamma}}{\sigma_{\hat{\gamma}}}$$

Where:$\hat{\gamma}$ is the estimated coefficient and $\sigma_{\hat{\gamma}}$ is the standard error in the coefficient estimate

The null-hypothesis for an ADF test: $H_0 : \gamma = 0$ vs $H_1 : \gamma < 0$

Where H_0: is the null hypothesis (has unit root) and H_1: Does not have unit root. The test statistics value τ is compared to the relevant critical value for the Dickey Fuller Test. If the test statistic is less than the critical value, we reject the null hypothesis and conclude that no unit-root is present. The ADF Test does not directly test for stationarity, but indirectly through the existence (or absence) of a unit-root.

Maximum likelihood estimation

The maximum likelihood estimation (MLE) will be used to estimate the ARIMA model. This technique finds the values of the parameters which maximize the probability of obtaining the data that we have observed. For ARIMA models, MLE is very similar to the least square estimates. In a standard Gaussian, the likelihood function is;

$$logL = -\frac{T}{2} log(2\pi) - \frac{T}{2} log\delta^2 - \frac{1}{2\delta^2} \sum_{t=1}^{T} {\varepsilon_t}^2$$

Where is T is the time $t = 1, \ldots, T$of the historical data, ε_t and δ is the error and constant variance respectively. The log likelihood reports the logarithm of the probability of the observed data coming from the estimated model. We choose the model where the log likelihood is maximal.

3.2.1 Parameter Estimation

To estimate the parameters, we run the selected model(s) as guided by the log likelihood, standard error and AICc values. The result will provide the estimate of each element of the model. The parameters with the least standard error in Root Mean Square Error (RMSE),

Root Mean Square Percent Error (RMSPE), and Mean Absolute Error (MAE) will be selected. The full model equation will be indicated.

3.2.2 Model diagnostic checking

Estimated model(s) will be considered most appropriate if it typically simulate historical behaviour as well as constitute white-noise innovations. Historical behaviour will be tested by ACF and PACF of estimated series and choose the one which best describes the temporal dependence in the inflation series i.e., the model(s) whose residuals show no significant lags. White-noise innovations will be tested by a battery of diagnostic tests based on estimated residuals as well as by over-fitting. The Ljung-Box test will also be used to verify whether the autocorrelation of a time series are different from zero. If the result rejects the hypothesis, this means the data is independent and uncorrelated; otherwise, there still remains serial correlation in the series and the model needs modification.

The Ljung Box Test

The standard portmanteau test for checking that the data is a realization of a strong white noise is that of Ljung and Box (1978). It involves computing the statistic

$$Q(m) := n(n+2)\sum_{j=1}^{m} \hat{\rho}_j^{\,2} \Big/ (n-j)$$

and rejecting the strong white noise hypothesis if $Q(m)$ is greater than the $(1-\alpha)$quantile of ${x^2}_m$. n is the sample size, $\hat{\rho}_j$ is the sample auto correlation at lag j and m is the lag order that needs to be specified. This is one-side (i.e. one-tail) test, so the computed p-value should be compared with the whole significance level(α). In practice, the selection of m may affect the performance of the $Q(m)$statistic. Several values of m are often used. Simulation studies suggest that the choice of $m \approx ln(T)$ provides better power performance.

3.3 VAR Model

The Vector Autoregression (VAR) model, proposed by Sims (1980), is one of the most successful, flexible, and easy to use models for analysis of multivariate time series. It is applied to grasp the mutual influence among multiple time series. VAR models extend the univariate autoregressive (AR) model to dynamic multivariate time series by allowing for more than one evolving variable. All variables in a VAR model are treated symmetrically in a structural sense; each variable has an equation explaining its evolution based on its own lags and the lags of the other model variables (Enders, 2003).

Let $Y_t = (y_{it}, y_{2t}, \cdots\cdots, y_{nt})'$ denote an $(n \times 1)$ vestor of time series variable (inflation, money supply, oil prices and exchange rate). A VAR model with p lags can be expressed as follows;

$$Y_t = c + \Psi_1 Y_{t-1} + \Psi_2 Y_{t-2} + \cdots\cdots + \Psi_p Y_{t-p} + \epsilon_{t,} \qquad t = 1, \cdots\cdots, T$$

Where Ψ_i is a $(n \times n)$ coeeficient matrix,$\epsilon_{t,}$ is an $(n \times 1)$ unobservable zero mean white noise vector process, and c is an $(n \times 1)$ vector of constants (intercept).

Estimates $\Psi_i$of contain information on short run adjustments while c contain information on long run adjustments in changes in Y_t

3.3.1 Data Validation

We first check for stationarity for all the data sets. If the data is stationary, then we have an unrestricted VAR, if it's not stationary then the data needs to be modified to allow consistency

in estimation of the relationships among the series. This can be done through log or differencing which then prompts for a cointegration test to check relationships among the variables. If the results show that there is cointegration then we have to use Vector Error Correction Model (VECM). VEC model is a special case of VAR for variables that are stationary in their differences. If there is no cointegration then we use unrestricted VAR. Before estimating VAR/VECM we determine the VAR/VECM model. We should also conduct the impulse function and variance decomposition to analyze the dynamic property of the model before conducting stability test on the model.

3.3.2 Cointegration

Macroeconomic time series are typically non-stationary, as established by Nelson & Plosser, (1982). When traditional regression analysis is used on two non-stationary time series, a spurious regression may result Granger & Newbold (1974). Testing for cointegration is necessary step to check if you are modeling empirically meaningful relationships. If variables have different trends processes, they cannot stay in fixed long-run relation to each other, implying that you cannot model the long-run, and there is usually no valid base for inference based on standard distributions. If you do not find cointegration it is necessary to continue to work with variables in differences instead. In a nutshell, cointegration assumes a common stochastic non-stationary (i.e. I ((1)) process underlying two or more processes X and Y.

$$X_t = \gamma_0 + \gamma_1 Z_t + \varepsilon_t \sim I(1), \qquad Y_t = \delta_0 + \delta_1 Z_t + \eta_t \sim I(1)\,, \qquad Z_t \sim I(0)\,, \varepsilon_t . \eta_t \sim I(0)$$

η, ε are stationary process $I(0)$ with zero mean, but they can be serially correlated.
Although X_t and Y_t are both non-stationary$I(1)$, there exists a linear combination of them, which is stationary; $\delta_1 X \sim \gamma_1 Y_t(0)$. In other words, the regression of Y and X yields stationary residuals $\{\varepsilon\}$.

In general, given a set of non-stationary (of type I(1)) time series variables $,\{X_{1,t}, X_{2,t} \cdots\cdots, X_{k,t}\}$ there exists a linear combination consisting of all variables with a vector β, such that:

$$\beta_1 X_{1,t} + \beta_2 X_{2,t} + \cdots\cdots + \beta_k X_{k,t} \sim I(0)$$

Where$\beta_j \neq 0, j = 1,2, \cdots\cdots, k$ .If this is the case, then the X's are cointegrated to the order of . $C, I(1,1)$. The Johansen test has two forms: the trace test and the maximum Eigen value test. Both forms/tests address the cointegration presence hypothesis, but each asks very different questions.

Table 1.1

Descriptive Statistics showing monthly CPI and annual Investment Rate, MONEY Supply, Exchange rate, Foreign exchange reserves and International Trade in Nigeria

Variable	Mean	Std. Dev.	Min	Max
CPI	20176.38	21781.8	90	72940
Investment	4641.129	6892.673	14.47	21607.68
MONEY Supply	4641.129	6892.673	14.47	21607.68

Exchange rate (Naira)	32013.00	32301.92	222.65	113547.9
International Trade	2060874	1438398	1298.997	7111444

The result from this Table shows the descriptive statistics of exchange rate fluctuations, CPI, Investment, Money Supply, Exchange rate and International Trade in Nigeria. From the table we observed that International Trade has higher average with mean of 2060874 in millions followed by Exchange rate with mean 32013 in millions and CPI has mean of 20176.38. The minimum and maximum outcome of the macroeconomic variables is given in the table.

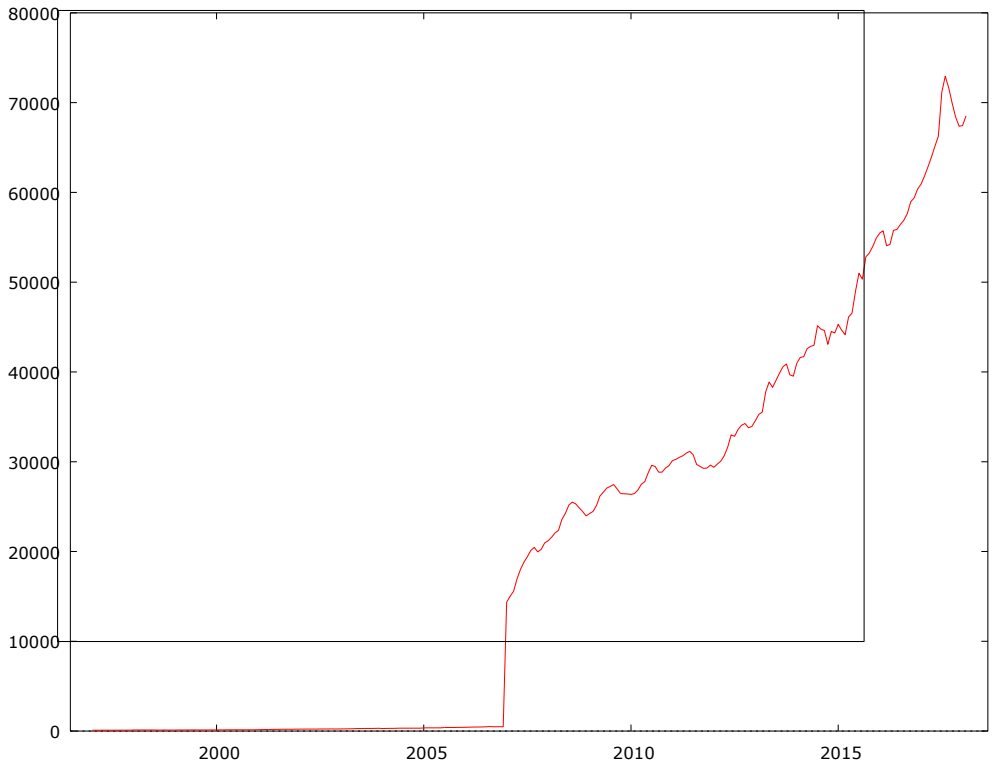

Fig 2 Time Series plot of Nigeria CPI 1995 - 2019

The result from the time series plot show the variation of consumer price index (CPI). From the graph it is shown that the first ten years 1991 to 2008 have low CPI. The data is not stationary since it does not display a particular state of statistical equilibrium evidencing that the variance changes with time. A slight increase (upward trend) was observed in the trend after 2008. It increases continuously till 2019.

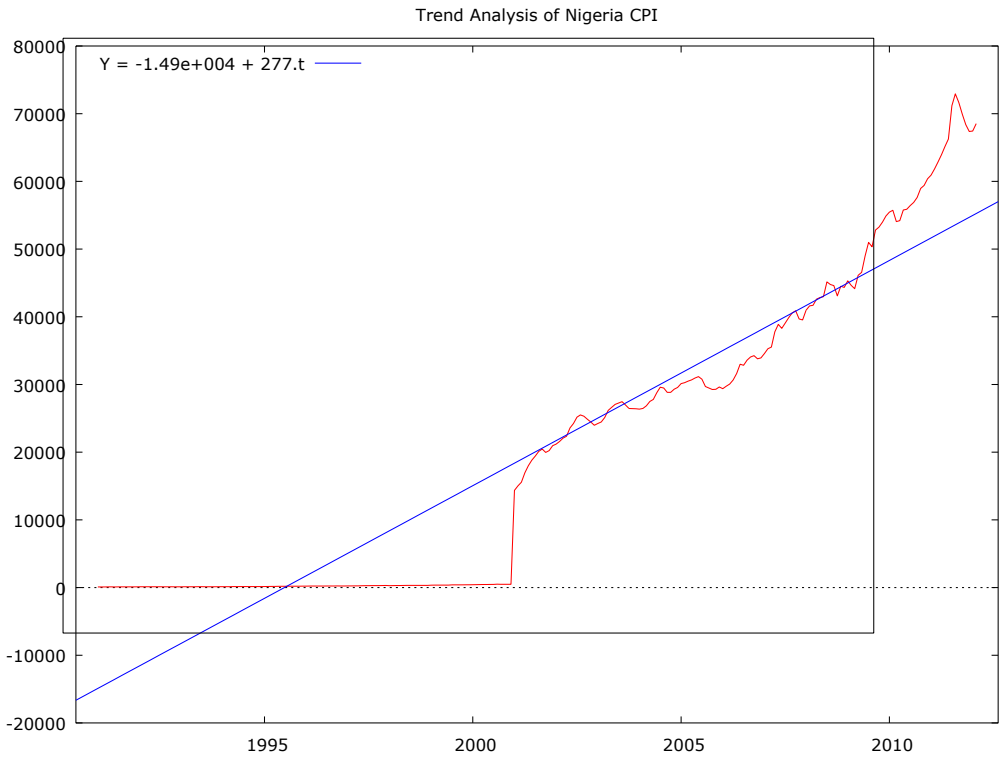

Fig 2: Trend Analysis of Stock price

The result from figure 2 shows the trend analysis of consumer price index (CPI). The result shows that the consumer price index (CPI) have an upward trend. It infers that consumer price index (CPI) rise over the period of time studied in this work.

4.2 AUTOCORRELATION AND PARTIAL AUTOCORRELATION FUNCTIONS

Running the autocorrelation and partial autocorrelation functions will also tell us about the type of transformation requires. Below are the ACF and PACF for the CPI data before differencing is performed. The graph below shows the ACF and PACF the ACF decaying slowly suggesting non stationarity behaviour. The autocorrelations are significant for a large number of lags but perhaps the autocorrelations at lags 2 and above are merely due to the propagation of the autocorrelation at lag 1.

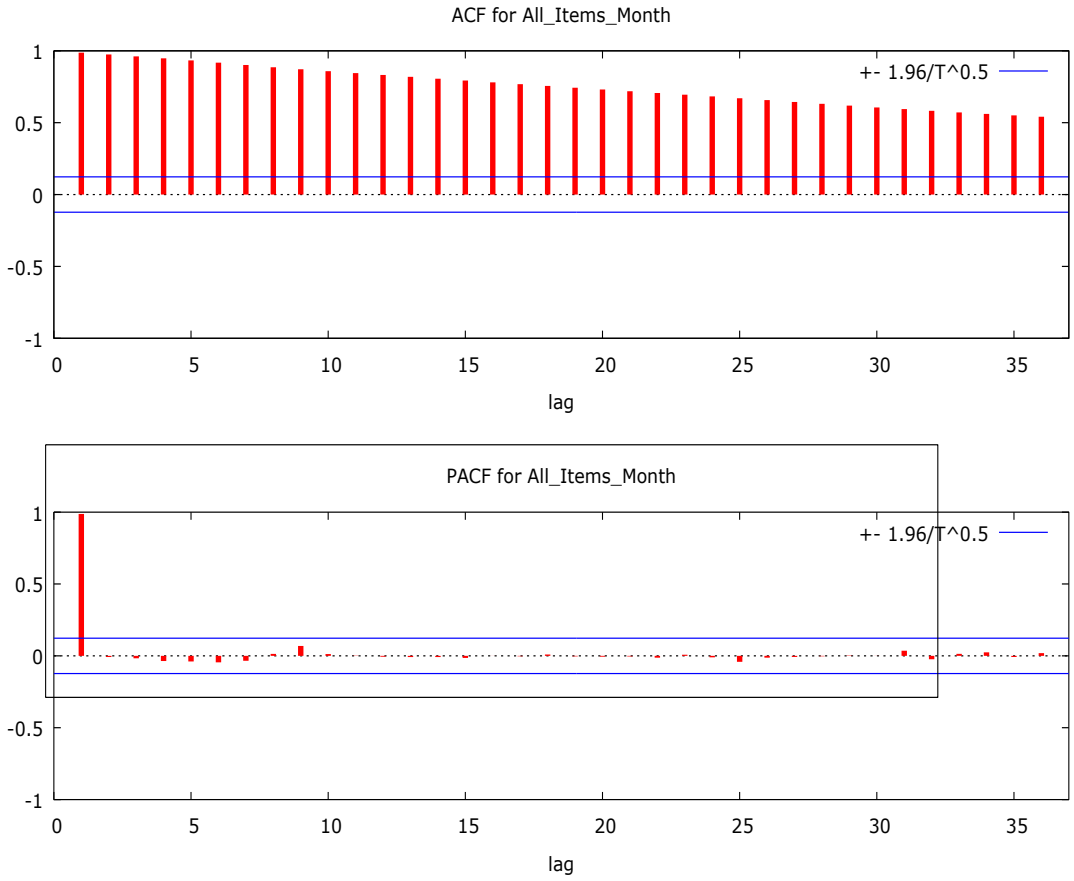

Figure 1: ACF and PACF for inflation series

The corresponding PACF plot has a significant spike only at lag 1 and then cuts off, meaning that all the higher-order autocorrelations are effectively explained by the lag-1 autocorrelation. The non-stationarity is of the order one as only the first-lagged bar is significantly higher than the cut-off line i.e. the first lag PACF is above the critical limit. This indicates the presence of non-stationarity and suggests first order differencing as the remedy. If a time series is stationary then its autocorrelogram should decay quite rapidly from its initial value of unity at zero lag.

Table 1.2 Unit Root Test for CPI Series

Test for unity we use the Augmented Dickey-Fuller (ADF) test for unit test hypothesis;
H_o: the CPI has unit root (non-stationary) Vs H_1: CPI data has no unit root (stationary)

	Test Statistic	**1% Critical**	**5% Critical Value**	**10% Critical Value**	**MacKinnon approximate p-value for Z(t)**
Z(t)	-1.777	-3.675	-2.969	-2.617	0.3917

The test produces a Dickey-Fuller test statistics = -1.777 greater than the critical value at all levels 1%, 5% and 10%; the p-value = 0.3917 is greater than 0.05 hence we fail to reject the

null hypothesis and conclude the data is non-stationary. Thus, the monthly CPI need to be differenced before modeling.

Table 1.3
Model 1 (1,1,1): ARIMA, using observations 1997:02-2018:02 (T = 253)
Dependent variable: (1-L) Monthly CPI
Standard errors based on Hessian

	Coefficient	*Std. Error*	*z*	*p-value*		**RMSE**
const	269.966	87.0608	3.1009	0.00193	***	1070.9
phi_1	0.613431	0.339795	1.8053	0.07103	*	
theta_1	-0.499122	0.37424	-1.3337	0.18230		

Modified Box-Pierce (Ljung-Box) Chi-Square statistic

Lag	***12***	***24***	***36***	***48***
Chi-Square	3.4	4.6	8.5	14.1
DF	9	21	33	45
P-Value	0.945	1.0000	1.0000	1.0000
Log-likelihood	-2123.999		Akaike criterion	4255.998

Table 1.3 shows the result of ARIMA (1,1,1) from the table we observed that AR(1) is significant at a level with p-value = 0.0710 and the Ljung-Box statistic shows that the model ARIMA (1,1,1) has good fit since the p-values of Ljung-Box statistic at different lag 12, 24, 36 and 48 are all greater than 0.05. infers that the error term in the model is not serially correlated.

Table 1.4
Model 2 (1,1,0): ARIMA, using observations 1997:02-2018:02 (T = 253)
Dependent variable: (1-L) _Monthly CPI
Standard errors based on Hessian

	Coefficient	*Std. Error*	*z*	*p-value*		**RMSE**
const	270.838	77.5132	3.4941	0.00048	***	1072.9
phi_1	0.130213	0.0623045	2.0899	0.03662	**	

Modified Box-Pierce (Ljung-Box) Chi-Square statistic

Lag	***12***	***24***	***36***	***48***
Chi-Square	4.4	5.9	9.5	14.5
DF	10	22	34	46
P-Value	0.928	1.0000	1.0000	1.0000
Log-likelihood	-2124.472		Akaike criterion	4254.944

Table 4.4 shows the result of ARIMA (1,1,0) from the table we observed that AR(1) is significant at a level with p-value = 0.03662 and the Ljung-Box statistic shows that the model ARIMA (1,1,0) has good fit since the p-values of Ljung-Box statistic at different lag 12, 24, 36 and 48 are all greater than 0.05. infers that the error term in the model is not serially correlated.

Equation	Parms	RMSE	R-sq	Chi2	P>chi2
CPI	9	6.12068	0.7781	122.6954	0.0000
MONEY SUPPLY	9	540.618	0.9954	7634.172	0.0000
EXCHANGE RATE	9	6483.58	0.9691	1099.509	0.0000
EXTERNALDEPTH	9	679.853	0.8574	210.3676	0.0000

Table 1.7 ARIMA Models comparison Using AIC and Standard Error

Variable	ARIMA(1,1,0)	ARIMA(1,1,1)	ARIMA(1,1,2)	ARIMA(2,1,1)
S.E phi_1	0.0623045	0.339795	0.103455	0.137632
S.E theta_1		0.37424	0.122347	0.120442
Log likelihood	-2124.472	-2123.999	-2123.778	-2123.753
AIC	4254.944	4255.998	4257.556	4257.505

From the tabulation above, ARIMA (1, 1, 0) has the smallest AIC value of 241.1. Evaluating the set errors, the same model has the smallest error (S.E phi_1 = 0.0623045). We therefore conclude that ARIMA (1,1,0,) is the best model from the combination.

4.1.1 Test for Cointegration

To avoid spurious regression, testing for cointegration is a necessary step to check if we are modeling empirically meaningful relationships. We run a cointegration test with the null hypothesis being no cointegration. The number of lags in the VAR is based on the evidence provided by AIC. The cointegration test amongst inflation, Money supply, Oil prices, and Exchange rate include four lags in the VAR.

Table 1: Cointegration Test Johansen test:

Rank	Eigenvalue	Trace test	p-value	Lmax test	p-value
0	0.85079	90.077	0.0000	68.487	0.0000
1	0.37026	21.590	0.1056	16.648	0.0725
2	0.089718	4.9415	0.5727	3.3840	0.7248
3	0.042341	1.5575	0.2486	1.5575	0.2479

The results above indicates that there exists one cointegrating equation for both the Trace and Maximum Eigen value tests hence we reject the null hypothesis. This implies that there exists a long run relationship between inflation and the independent variables. This is the long run cointegrated model. The coefficients for the variables are long run coefficients. The coefficients show that when Money supply (M) and Exchange rate(E) goes down inflation goes up and vice versa and while oil prices (P)go up, inflation goes up and vice versa. The normalized cointegrating relation assuming one cointegrating relation r = 1

Table 9. Vector Autoregressive Model

Log likelihood	=-975.038	AIC	=57.77362
FPE	=1.52E+20	HQIC	=58.32587

The result from this table shows that all the parameters from the equation CPI, Money supply, exchange rate and external depth are significant since their p-value are less than 0.05 level of significance.

4.2 Model comparison

Finally we compare the ARIMA and VAR model prediction accuracy, the model with the smallest errors has the better forecasting ability. In this case VAR model has the least error of 0.23% mean absolute percentage hence the better model in forecasting inflation.

Table 10: Comparison of ARIMA and VAR models

Variable	ARIMA(1,1,0)	VAR
RMSE	1072.9	6.12068
MAE	473.48	0.34123
MAPE	62.456	0.239519

Finally we compare the ARIMA and VAR model prediction accuracy, the model with the smallest errors has the better forecasting ability. The result from table 4.12 shows that VAR model have minimum value of RAME, MAE and MAPE. Thus it infers that VAR model is more appropriate to forecast the Nigeria CPI than ARIMA (1,1,0)

5.0 CONCLUSION AND RECOMMENDATION

This study analyses the determinants of inflation in Nigeria using ARIMA and VAR model where the forecasting power of historical inflation data and the determinants of inflation are investigated.

In ARIMA model we use historical consumer pricing data to model inflation for the period of January 2005 –June 2018. ARIMA model (1, 1, 0) resulted as the best model. The study shows that despite the exclusion of explanatory variables there is evidence of substantial inflation inertia concurring with Durevall & Sjo (2012) findings. This is also evidence by the hypothesis that if the level of inflation is determined by inertia then the parameters on lagged inflation should sum to unity. Parameters of the selected lagged parsimonious model in this study sum approximately to unity.

In the vector autoregressive model we examine effects of money supply, oil prices and exchange rate, on consumer price inflation using a vector error correction model. We used the VEC model because the time series are all stationary after first differencing and are cointegrated. A cointegration framework exhibit a long run relationship where a gain in money supply and exchange rate result to a drop in inflation and a gain in oil prices result to a gain in inflation rate. Change in exchange rate and money supply affect inflation negatively while change in oil prices have positive effect on inflation.

There is no long run equilibrium between the independent variables and inflation. The absence of relation over a long span of time between supply shocks factors i.e. exchange rate and oil prices is because the prices are determined by factors that affect demand and supply of the foreign exchange and oil. These findings are consistent with evidence presented by of Durevall & Ndungu (2001).

Testing for causality shows that there is no long run causality running from money supply, oil prices and exchange rate variables to inflation. However, short run causality was established from oil prices to inflation. In our model oil prices are likely to be an efficient nominal anchor since it affects the level of prices in the short run. Reasonably, oil prices solely accounts for the largest share in Nigeria imported good at about 25% and is key to production of goods and services thus it can capture the influence of supply shocks. It is therefore seen that imported inflation influences domestic inflation. Money supply also failed to show long run effect on inflation implying that money growth does not determine prices as often perceived.

In the VAR model, lagged values of inflation are seen to be significant with a large coefficient confirming the results of the ARIMA model that inflation inertia substantially exist.

Recommendation

The selected models can enhance the predictability of model for forecasting consumer price index of Nigeria and better assist the policymakers. Further analysis using additional specifications of inflation expectations such as output gap, real GDP, employment rate data which are more current in Nigeria would be useful.

References

AfDB (2011) 'Inflation Dynamics in selected East African countries: Ethiopia, Kenya,Tanzania and Uganda'.

Andrle, M., Berg, A., Morales, R.A., Portillo, R. and Vlcek, J. (2013) 'Forecasting and Monetary Policy Analysis in Low-Income Countries: Food and non-Food Inflation in Kenya', *IMF Working Paper WP/13/61*.

Durevall, D. and Ndungu, S.N. (2001) 'A Dynamic Model of Inflation for Kenya 1974-1996', *Journal of African Economies*, vol. vol.10, no. Issue 1, pp. 92-125.

Durevall, D. and Sjo, B. (2012) 'The Dynamics of Infaltion in Ethiopia and Kenya'.

Enders, W. (2003) *Applied Econometric Time Series*, 2nd edition.

Faisal, F. (2001) 'Forecasting Bangladesh's Inflation Using Time Series ARIMA Models'.

Granger, C.W.J. and Newbold, P. (1974) 'Spurious Regressions in Economics', *Journal of Econometrics 2*, pp. 111-120.

Kennedy, A. and Bernard, B. (2012) 'Determinant of Inflation in Ghana- An Economic Analysis'.

Loungani, P. and Swagel, P. (2001) 'Sources of Inflation in Developing Countries'.

Mohanty, M.S. and Marc, K. (2011) 'What determines inflation in emerging market economies?', *BIS Paper No 8*.

Nelson and Plosser (1982) 'Trends and random walks in macroeconmic time series: Some evidence and implications', *Journal of Monetary Economics*, vol. 10, no. 2, pp. 139-162.

Okafor, C. and Shaibu, I. (2013) 'Application of ARIMA Models to Nigerian Inflation Dynamics', *Research Journal of Finance and Accounting*, vol. 4, no. 3.

Shumnay, R.H. and Stoffer, D.S. (2011) *Time Series Analysis and its Application*, SpringerScience + Business Media.

Sims, C.A. (1980) 'Macroeconomics and Reality', *Econometrica*, vol. 48, January.

Sim, C.A., Stock, J.H. and Watson, M.W. (1990) 'Inference in Linear Time Series Models with Same Unit Roots', *Econometrica*, pp. 113-144.

Sumaila, U.R. and Laryea, S.A. (2001) 'Determinants of Infaltion in Tanzania', *CMI Working Paper*.

Adams, S.O., Awujola, A. and Alumgudu, A.I. (2014). Modelling Nigeria's Consumer Price Index using ARIMA Model. *International Journal of Development and Economic Sustainability*, 2(2), 37 – 47.

Amadi, I. U., Gideon, W. O. & Nnoka, L. C. (2013). Time Series Models on Nigerian Monthly Inflation Rate Series. *International Journal of Physical, Chemical and Mathematical Sciences*, 2(2), 124-128.

Altug, S. and Cakmakli, C. (2015). Forecasting inflation using survey expectations and target inflation: Evidence for Brazil and Turkey. University of Amsterdam Working paper No IAAE2015-580.

Ang, A., Bekaert, G. and Wei, M. (2007). Do Macro Variables, Asset Markets, or Surveys Forecast Inflation Better? *Journal of Monetary Economics*, 54, 1163-1212.

Atkeson, A. and Ohanian, L.E. (2001). Are Phillips curves useful for forecasting inflation? *Quarterly Federal Reserve Bank of Minneapolis*, Winter 2001: pp. 1-12.

Bank of England (2015). Evaluating forecast performance. Independent Evaluation Office, Bank of England.

Bjornland, H.C., Gerdrup, K., Jore, A.S., Smith, C. and Thorsrud, L.A. (2009). Does forecast combination improve Norges Bank inflation forecasts? Working paper, Economics Department, Norges Bank, Norway.

Blinder A.S. (1997). Is there a core of practical macroeconomics that we should all believe? *American Economic Review*, 87, 240-250.

The MLE-Distributions fitting for detecting extreme points, and possible repetitions of sudden breaking points in data

Bello A.O. [1*], Abdullahi U. [2], Adetutu O. M. [3], Onotu I.S. [4], Oguntolu F.A. [5]
Department of Statistics, Federal University of Technology, Minna, Nigeria[1; 2,3,4]
Department of Mathematics, Federal University of Technology, Minna, Nigeria[5]
oyedelebello2@futminna.edu.ng[1*]

Abstract
This work reports on how to use the probability graphical method via the maximum likelihood estimation (MLE) approach to obtain the various pivoting model's parameters that gives the highest estimate value among the class of unbiased estimates. The probability distribution fitting was implemented via the graphical method. This helps to detect various outliers, intervals and the possible repetitions of sudden breaking points. The fitting was also obtained to predict and help in assessments during breakdowns in economic activities. Self-written R code and the Easyfit software were used to fit the household income data to suggest the possible probability distribution(s) for the data. The distributions were taken as the functional form of the income's (X as an r.v) probability distribution and they were empirically solved using the MLE method. The estimate that is most consistent with the sample data was solved computationally based on the distribution function(s).

Keywords: Extreme points, batching effect, probability graphical plots, normalization, panel data, sudden breakdown, Maximum likelihood estimation

1.0 Introduction

The presence of extreme values, repeated values and breaking points in data, often regarded as the sudden breakdown in a system affects data analysis outcome and the subsequently predictions. The batch effects cannot be overlooked when we are to obtain true parameter estimates from data for fitting distributions in a graphical technique. The accuracy of fitting the head and tails of each plot depends heavily on the precisions of the pivoting parameter's estimates. To accurately fit the probability distribution for a household income, it is vital for the measuring of the location parameter of each household income's potential, for a given geographical region. This is important for economic or developmental planning. It is possible that different distributions may be suitable for different household incomes in different geographical areas. Household income is often used as an economic indicator. Fitting the accurate distribution will ensure an accurate estimation of parameters which will eventually aid correct economic decisions. In basic economy theory there are several factors that could be responsibility for extreme income records. Detection of extreme household income may not necessarily be as a result of enrichment through corrupt means.

Household income refers not only to the salaries and benefits received but also to receipts from any personal business, investments, dividends and other income (Onotu *et al*., 2017). Furthermore, household members do not need to be related to be part of a household, rather incomes of all the members of a household who are 15 years and older are required. The search for a method of fitting a continuous probability distribution to data and their parameterization is quite trickish and volatile. Karian and et al. (2012) suggested the need to first decide on what type (or family) of distributions to consider, secondly to decide on what fitting method to use either method of moments, maximum likelihood, least squares or

Bayesian approach etc. and conclusively the need to develop a specific computational scheme to estimate the parameters associated with the fit. This was also supported by Vito Ricci (2005) noting that ''The first step in fitting distributions consists, choosing the mathematical model or function to represent data in the better way''. The choice of method of estimation, such as the Bayesian and MLE is a matter of computational power availability (See Mehrotra *et al*. 2000; Abdulrahim *et al*., 2020; Bello *et al*., 2016).

1.1 **The Lognormal Distribution**

The probability distribution function(pdf) of the lognormal with parameters μ and σ, with both non-negative, makes pdf more preferable to -∞<x> +∞ of the popular normal distribution, because we hope not to have negative income values. Therefore, the function's range x>0;

$$f(x)=\begin{cases}\dfrac{1}{x\delta\sqrt{2\Pi}}\exp\left[-\dfrac{(\ln(x)-\mu)^2}{2\delta^2}\right] & \text{if } x>0\\ 0, & \text{otherwise}\end{cases} \tag{1}$$

The moments of the lognormal distribution can be obtained using the Bayesian analysis of a generalized form of the lognormal distribution (see Martín and et al., 2014), Also by using moment matching estimation (MME), analogic, and maximum likelihood estimation (MLE). The moment's standard characteristic functions of log-normal function are;

$$\left.\begin{aligned}\alpha_1 &= e^{\mu+\delta^2/2}\\ \alpha_2 &= (e^{\delta^2}-1)e^{2\mu+\delta^2}\\ \alpha_3 &= \sqrt{e^{4\delta^2}-1}(e^{\delta^2}+2)\end{aligned}\right\} \tag{2}$$

The parameters of the log-normal distribution μ and σ represent the mean and variance supporting $x\in(0,+\infty)$ with entropy $\log(\delta e^{\mu+\frac{1}{2}\sqrt{2\Pi}})$ and the fisher information $\begin{pmatrix}1/\delta^2 & 0\\ 0 & 2/\delta^2\end{pmatrix}$.

The most frequent occurrence being a point of global maximum of a density function is obtainable by $\mathrm{mod}e[X]=e^{\mu-\delta^2}$; and median; $med[X]=e^{\mu}$. The log-normal parameters are derived by arithmetic of mean and of the variance.

$$\mu=\ln(E\mid X\mid)-\frac{1}{2}\ln(1+\frac{Var[X]}{(E[X])^2})=\ln(E[X])-\frac{1}{2}\delta^2 \tag{3}$$

and

$$\delta^2=\ln(1+\frac{Var[X]}{(E[X])^2}) \tag{4}$$

However, to avoid local maximum approximation, when dealing with extreme points or outliers in a dataset. The global maximum estimate is best achieved for the location and scale parameters of a log-normal distribution by using geometric mean and geometric standard

deviation respectively compared to the arithmetic approach. The cumulative distribution for the log-normal distribution is given by

$$F(x)=\frac{1}{\delta\sqrt{2\prod}}\int_0^x\frac{1}{t}e^{-\frac{1}{2}(\frac{\ln t-\mu}{\delta})^2dt=}\frac{1}{\delta\sqrt{2\prod}}\int_0^{\ln x}e^{-\frac{1}{2}(\frac{x-\mu}{\delta})^2dx} \quad (5)$$

$$\text{CDF}=\frac{1}{2}+\frac{1}{2}erf\left[\frac{\ln x-\mu}{\sqrt{2\delta}}\right] \quad (6)$$

Random number generation for log-normal computations is usually achieved initially from a normal distribution with mean μ and standard deviation δ and construct $r=e^{\mu}$. Knowing that normal distribution may not be suitable for a variable that is inherently non-negative such as we have in household income which is likely to be strongly skewed due to the possible presence of outliers. Many natural phenomena are well described by lognormal function. Some previous works have used the function to fit hydrology points such as for hydrology research to analyse extreme values of variables such as the maximum value of daily rainfall and rivers rising. Also, the social-economic research of Clement and et al. (2005) where it was noted that seventy per cent of the population's income is most likely to follow a lognormal distribution. The thirty per cent omitted when lognormal is used may be spurious to population income modelling if the thirty per cent consist the outlier's values or the turning point values that can control the eighty per cent of the total income of the population, as suggested by Pareto principle. This work thereby seeks to include Pareto distribution and Extreme value function computationally with the lognormal function to fit the income's panel data and its synthetic data.

1.2 The Pareto Distribution

The power-law distribution is also named Pareto distribution, it was originally implemented to study the allocation of wealth among individuals. It proposed that a larger share of the wealth of any society (approximately 80%) is owned by a smaller fraction (about 20%) of the people in the society. The distribution of higher-income individuals follows a Pareto distribution (Wataru, 2002). This is similar to the presence of some extreme income in our case of consideration. The Pareto has been widely used in many applications such as in economics, actuarial science, survival analysis, hydrology, and many others See (Geerolf, 2014; Charles, 2014 and Phillip, 2020)

$$f(x)=\begin{cases}\dfrac{\beta\lambda^{\beta}}{x^{\beta+1}}, & \text{if } x>\lambda\\ 0 & \text{otherwise}\end{cases} \quad \textbf{(7)}$$

The Pareto distribution supports $x\in(\lambda+\infty)$; $\lambda>0$ and $\beta>0$. The Pareto distribution is characterized by cumulative density function; $1-(\frac{\lambda_m}{x})^{\alpha}$ for $x\geq\lambda_m$. The root of the equation

is unstable with allows the shape and scale parameters to be of two roots. This gives appropriate intervals and conditions for possible extreme observations around the parameter estimate.

$$\mu = \begin{cases} \infty & \text{for } \beta \le 1 \\ \dfrac{\beta\lambda_m}{\beta - 1} & \text{for } \beta > 1 \end{cases} \qquad \textbf{(8)}$$

and

$$\delta^2 = \begin{cases} \infty & \text{for } \beta \in \\ \dfrac{\lambda_m^2 \beta}{(\beta-1)(\beta-2)} & \text{for } \beta > 2 \end{cases} \qquad \textbf{(9)}$$

The mode λ_m, median $\lambda_m \sqrt[\beta]{2}$ and fisher information; $\begin{pmatrix} \frac{\alpha}{x_m^2} & -\frac{1}{x_m} \\ \frac{1}{-x_m} & \frac{1}{\delta^2} \end{pmatrix}$

1.3 The Extreme Value Distribution

This distribution is an example of application of Weibull's idea around 1951 reported that the strength of a certain material follows an extreme value distribution. The extreme value distribution is also used in life and failure data analysis. The Largest extreme value distribution will be more appropriate with its parameters μ and δ> 0 having the pdf;

$$f(x) = \frac{1}{\delta} \exp - [x-\mu] \big/ \delta \ \exp[-e \frac{-(x-\mu)}{\delta}] \qquad \textbf{(10)}$$

The cumulative distribution of extreme value distribution $F(x) = \int_{-\infty}^{x} f(u)du = \int_{-\infty}^{\pm\frac{x-\mu}{\delta}} g(z)dz = G(\pm\frac{x-\mu}{\delta})$ where G(z) is the cumulative function of g(z) which is given by $G(z) = \int_{-\infty}^{z} e^{-\mu - e^{-\mu}}\, du = \int_{e^{-z}}^{\infty} e^{-y} dy = e^{-e^{-z}}$ where we have made the substitution y = e−u in simplifying the integral.

The Moment Method for the Extreme Value Distribution

Algebraic moments of order r are defined as the expectation value

$$\alpha_r^{'} = E(x^r) = \int_{-\infty}^{+\infty} x^r f(x)dx \qquad \textbf{(11)}$$

For $\alpha_0^{'}$ =1 and $\alpha_1^{'}$ is the mean value of the distribution, α_2 as the variance of the model with α_3 and α_4 for the kurtosis and skewness respectively. Central moments of order r are defined as $\alpha_r = E((K - E(k))^r)$.

Errors of Moments

Consider a sample with n observations $x_1, x_2, ..., x_n$ we define the moment-statistics for the algebraic and central moments α_r' and α_r as $\alpha_r' = 1/n\sum_{r=0}^{n} x^r$ and $\alpha_r' = 1/n\sum_{r=0}^{n}(x^r - m_1^r)^r$.

The covariance between an algebraic and a central moment is

$$Cov(\alpha_q, \alpha_r) = 1/n(\mu_{q+r} - \mu_q\mu_r + rq\mu_2\mu_{r-1}\mu_{q-1} - r\mu_{r-1}\mu_{q+1} - q\mu_{r+1}\mu_{q-1}) \quad \textbf{(12)}$$

2.0 Maximum Likelihood Method

Having notable extreme values in any real-life data can be worrisome. Outliers raised the possible question of sudden system error (non-random error) or observational error. In cases where we desired to obtain reliable estimate(s) for further estimation in an iterative process, or to present point estimates for predictions, budgeting and planning purposes. The MLE-estimation is a good procedure for exploring data with extreme values.

2.1 MLE-Log-normal

$$f(x) = \frac{1}{\sqrt{2\prod}\delta x}\exp - \frac{[\log(x) - \mu)^2]}{2\delta^2} \qquad \textbf{(13)}$$

The likelihood function for n-observation household income $x_1, x_2, ..., x_n$, with parameters μ and δ^2

$$L(\mu, \delta^2) = \frac{1}{\sqrt{2\prod}\delta x_1}\exp - \frac{[\log(x_1) - \mu)^2]}{2\delta^2} + \frac{1}{\sqrt{2\prod}\delta x_2}\exp - \frac{[\log(x_2) - \mu)^2]}{2\delta^2} + ... + \frac{1}{\sqrt{2\prod}\delta x_n}\exp - \frac{[\log(x_n) - \mu)^2]}{2\delta^2}$$

$$L(\mu, \delta^2) = \prod_{i=1}^{n}\frac{1}{\sqrt{2\prod}\delta x_i}\exp - \frac{[\log(x_i) - \mu)^2]}{2\delta^2} \qquad \textbf{(14)}$$

$$L(\mu, \delta^2) = \frac{1}{(\sqrt{2\prod}\delta^2 x_i)^{\frac{n}{2}}}\exp - \frac{1}{2\delta^2}\sum_{i=1}^{n}[\log(x_i) - \mu)^2] \qquad \textbf{(15)}$$

The value of μ and δ that maximize the likelihood function are maximum likelihood estimator (MLE) is denoted by $\hat{\mu}$ and $\hat{\delta}$. The parameters were obtained by partial derivation of the log-likelihood function with respect to μ and δ respectively.

$$\log L(\mu, \delta) = \frac{-n}{2}\log_e 2\prod - \frac{n}{2}\log_e \delta^2 - \frac{1}{2\delta^2}\sum_{i=1}^{n}[\ln(x) - \mu] \quad \textbf{(16)}$$

$$\partial \log L(\mu, \delta)/\partial\mu = \frac{1}{2\delta^2}\sum_{i=1}^{n}[ln(x) - \mu]$$

$$\partial \log L(\mu, \delta)/\partial\mu = 0$$

$$\frac{1}{2\delta^2}\sum_{i=1}^{n}[ln(x)-\mu]=0$$

$$\sum_{i=1}^{n}(log(x)-\mu)=0$$

$$log\sum x=n\mu$$

$$\hat{\mu}=log\sum x/_n \quad \textbf{(17)}$$

Partial differentiation of equation (16) w.r.t. δ^2 yielded $\delta^2=\sum_{i=1}^{n}(log(x_i)-\mu)$

2.2 MLE-Pareto Distribution

$$f(x)=\frac{\beta\lambda_m^{\beta}}{x_i^{\beta+1}} \quad \textbf{(18)}$$

The likelihood functions for n-observation household income $x_1, x_2, ..., x_n$, considering Pareto pdf;

$$L(\beta,\lambda)=\frac{\beta\lambda_{m_1}^{\beta}}{x_1^{\beta+1}}+\frac{\beta\lambda_{m_2}^{\beta}}{x_2^{\beta+1}}+...+\frac{\beta\lambda_{mn}^{\beta}}{x_n^{\beta+1}} \quad \textbf{(19)}$$

$$L(\beta,\lambda)=\beta^n\lambda_m^{n\beta}\prod_{i=1}^{n}\frac{1}{x_i^{\beta+1}}$$

$$log_e L(\beta,\lambda)=n\,ln\,\beta+n\beta\lambda_m-(\beta+1)\sum_{i=1}^{n}ln\,x_i \quad \textbf{(20)}$$

The partial derivation of the Pareto logarithm likelihood function w.r.t. each parameter yielded $\hat{\beta}=\frac{n}{\sum_i(ln\,x_i-ln\,\lambda_m)}$ with s. e$(\hat{\beta})=\hat{\beta}/_n$

2.3 MLE-Extreme Largest Distribution

$$L(\mu,\delta)=\frac{1}{\delta}e^{(x_1-\mu)\delta}\,exp[-e^{(x_1-\mu)\delta}]+\frac{1}{\delta}e^{(x_2-\mu)\delta}\,exp[-e^{(x_2-\mu)\delta}]+...+\frac{1}{\delta}e^{(x_n-\mu)\delta}\,exp[-e^{(x_n-\mu)\delta}] \quad \textbf{(21)}$$

$$L(\mu,\delta)=\prod_{i=1}^{n}\frac{1}{\delta}e^{(x_i-\mu)}\exp[-e^{(x_i-\mu)\delta}]$$

$$L(\mu,\delta)=\frac{n}{\delta}e^{\Sigma(x-\mu)\delta}\,exp[-e^{\Sigma(x-\mu)\delta}]$$

$$log_e L(\mu,\delta)=n\,log\,\delta+\sum(x-\mu)\delta-e^{\Sigma(x-\mu)\delta} \quad \textbf{(22)}$$

The parameters of the extreme distribution of any type can be obtained by the partial differential $\log_e L(\mu,\delta)$ with respect to the parameter of interest.

3.0 Graphical Evaluations

To make appropriate graphical evaluations, it is vital to construct theoretical and empirical distributions approximations for the datasets in the form of probability distribution functions (p.d.f.) suspected. The graphical method will be evaluated under a curve that is non-negative, the area under the whole curve is 1. The areas under the curve between values will give the probability of that range of values as prescribed by Karian and Dudewicz, (2000). In cases of the distributions under consideration, the empirical distribution parameters are unspecified and their values are to be estimated from the data. At the initial graphical evaluation, histogram is plotted for the data under evaluation in comparison to distributions under suspicion. The p.d.f.s under consideration will be compare with the empirical probability function (e.d.f.) of the data and will also be compared using their cumulative distribution function (CDF).

It will be necessary to set a baseline distribution for easy caparison. This will help us to answer the following questions appropriately from graphical evaluations; Is the distribution function (d.f) well-matched visually for the main body of the e.d.f.? Also, where the tails of the d.f.s well-matched visually to the tails of the e.d.f.? Subsequently, we employed the Quantile-Quantile (Q-Q) plots, which are scattered plots comparing the fitted from the data with the theoretical distributions in terms of the standard parameters' values. In the plots, for the y-axis, we have empirical quantiles and, on the x-axis, we have the curves obtained from the theoretical model. The probability curve on histograms can be graphically compared to the standard shapes associated with the suspected probability distributions. Graphical tools can suggest the kind of pdf to use to fit the model (Marie Laure et al., 2014). A well schemed graphical technique will provide insights on skewness, behaviour in the tails, presence of multi-modal behaviour, and outliers

3.1 Goodness-of-Fit (GOF)

To know how good is a data fit to the distribution(s) it required a pragmatic approach. If only descriptive statistical information is available, then a simple visual comparison will be sufficient if and only if the data is free of many extreme values. A further check after the parameter estimation process will be more reasonable. The goodness of fit tests relevant to determining the most suitable statistical distribution for the data is Kolmogorov-Smirnov (KS), Akaike's Information Criterion (AIC) and Bayesian Information Criterion (BIC). Akaike's Information Criteria (AIC) is a tool used for model selection. The AIC offers a relative measure of the information lost when a given model is used to describe reality. The AIC selects the model with the minimum AIC value as the best fit model (See Matt, 2019 for further reading).

3.12 The dangers of classical averaging on batch data with extreme values

When data is large in number of cases and number of variables or number of times of observation in a multiple response permutation procedure (MRPP) of panel data, where the secondary data collected do not give detailed information. The users of data are left with lump total average values(Y) of x panel members across the periods(t) of collections.

$x_{i;}$ - panel menbers per household; y_{it} is classical mean income over time - t

1	x_1	$\xrightarrow{lump\ \text{Averaging}}$	y_{11}	y_{12}	.	..	y_{1t}
2	x_2	"	y_{21}	y_{11}	.	..	y_{2t}
$n-household$	.	"	.	.	.	..	.
.	.	"	.	.	.	..	.
.	.	"	.	.	.	..	.
n	x_n	"	y_{n1}	y_{n2}	.	..	y_{nt}

Y is average of all y_{it} in m - batches

It is impossible to have physical inspection in order to probe any sudden extreme values or sudden dropped in income value for give time t and i[th] panel members.

Given certain values $Y_1, Y_2, \ldots, Y_n$ as members of the same class or system, to arrive at a value that best represents the class value (Y_i) of the system considering effect of actions with respect to constraints; select a certain hypothesis (h_0) if and only if $Y_i < Co$ otherwise select the alternative hypothesis if $Y_i > Co$. The appropriate line of action will only be a guaranteed if only if $y_{it} \ldots, y_{nt}$ or any of x_i does not contain extreme values, then, the simple estimator $\frac{\sum_i^n Yi}{n}$ would have been sufficient. Otherwise, using trimmed mean approach to trim off the weights of the extreme values will be considered. Also estimating the percentiles range may be helpful to have the correct line of action. However, the case is not computationally straightforward when dealing with of with extreme values in a batch data. The constraints to the line of decision, based on position of Co within Y_1 to Y_n, necessitated a form of interval measures. The interval measure with heavy heads and tails usually patterns data with extreme values at the highest and lowest measuring lines. To obtain a sufficient Y_i for a delicate system with two end measures is a highly sensitive computation and must not be trivialized. Say, you are supposed to recommend certain household among clusters of households for social funding if their average income representation is less than 100 dollars and to recommend for taxes if greater than 870 dollars. The income for certain households is found to be 56, 30, 99, 2000, 1500, 80, and 2100 dollars respectively. The traditional averaging estimation gives 837 dollars as the average income of the area. This average income of 837 dollars is a wrong representation for more than two-thirds of the population's income. This could be more deadly with medical data analysis.

4.0 Computational Procedure

Fitting the most adequate distribution for real-life data begins with engaging the exploratory data analysis (EDA) which can suggest the kind of pdf to fit the data. Easyfit and R function (Cullen d Frey) graph were used in this paper. We initially selected only the distributions that both packages suggested for the data. The panel data on household income's location and scale parameters were estimated respectively. We also realized that the use of central density obtained from the summation of the product of each value and their frequency per sum of all their frequency is a misleading average value for a certain given population, because of the

presence of extreme values in the scatter plot of the data. To reduce the effect of extreme values and the batching effect from the averaging of household's income over the years and across households in a data, we estimated for other central density measures; trimmed mean, mode, and median. Each parameter from this different central density was separately used to generate larger samples using their log form of mean, trimmed mean, mode and median. The values of parameters estimated were used directly in the cases of Pareto and extreme value distributions. For mle-lognormal computation, we use the mu(meanlog) and sigma(sdlog), that is, the logarithm of income across the original surveyed data, and we generated the log-transformed sample N=100, 200 and 500 batches of data using r code "-rlnorm (1: N, m=meanlog, sd=sdlog)". The generated sample was used to evaluate the performance of MLE and MME, before the estimates for the pdf's parameters were iteratively coded into the graphical plots. The MLE and MME performance is compared with the baseline theoretical CDF. This was done under varying sample sizes. To obtain the suitable location parameter that will help to normalize the batch effect on data with extreme values and breaking points, the MLE was used to select the suitable location parameter by finding the likelihood function for each sample point under the four location estimators considered (see table 3). The product of each estimator likelihood function was obtained. The EDF, CDF-baseline graphs for evaluations were then constructed.

5.0 Results and Discussions

Cullen d Frey graph provided by the descdist function in R and the Easyfit software both agreed on the significant fit of normal, log-normal, Weibull, Pareto, gamma and beta distributions.

However, the underlying theoretical properties of lognormal, Pareto and Extreme value distributions relating to the household income data at hand guided our choice of using them.

5.1 MLE Method and MME Evaluation

Goodness-of-fit statistics

Location Parameter Estimates for lognormal	Matching Moments Method	MLE
Mean	11.328105	11.44235452
Standard Deviation	1.996814	0.9834032
Kolmogorov-Smirnov statistic	0.3300693	0.2327564
Cramer-von Mises statistic	15.6761084	4.5059558
Anderson-Darling statistic	81.9090422	29.5680999
Akaike's Information Criterion	13179.75	12848.56
Bayesian Information Criterion	13188.18	12856.99

Goodness-of-fit criteria

Table 1

From Table 1; the matching moment method (MME) and maximum likelihood method (MLE) produced 11.328105 and 11.44235 logarithm arithmetic mean with standard deviation of 1.996814 and 0.9834032 respectively. AIC values put the MLE at 12848.56 less than 13188.18 for the MME. Therefore, we continue to consider only the MLE method and its estimates for further computations and graphical evaluation constructions.

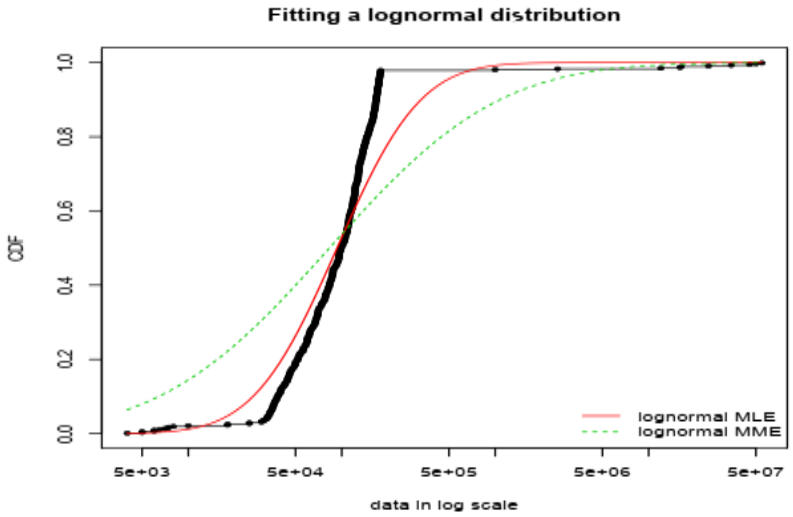

Figure 1(Black lines are the baseline)

The method of maximum likelihood was used to estimate the parameters for the three distributions under consideration and the parameters for each model were used to randomly generate 100 samples, 200 samples and 500 samples for the respective distributions.

5.12 Evaluating Lognormal and Pareto Empirical Probability Distributions

From Fig 1, the result is the graphical comparison of the empirical and theoretical CDF of lognormal using the maximum likelihood estimation and the matching method of the moment. Table 1, showed the AIC and the standard error of the estimate of the location parameter. The lowest AIC and standard error are achieved with MLE on lognormal distribution. This confirmed log-normal to be suitable for our income data fitting.

Table 2 Log-Normal and Pareto Distributions Fit Evaluation-Table II

	100 Samples		**200 Samples**		**500 sample**	
Distribution	**Log-normal**	**Pareto**	**Log-normal**	**Pareto**	**Log-normal**	**Pareto**
$L(\theta)$	0.0004186823	5.9932e-05	0.00087468	0.0001100977	0.0008037468	0.000260585
AIC	12178.70	16171.75	13179.75	17179.75	14179.75	23179.00

The likelihood value L(Θ) of the parameters for each distribution was estimated and presented in Table 2 above. The l(θ) value of the log-normal distribution is larger at 100 samples, 200 samples and 500 samples respectively. This implied that the log-normal function is consistent with the sample data compared to the Pareto distribution. (Also see the blue line in Fig2)

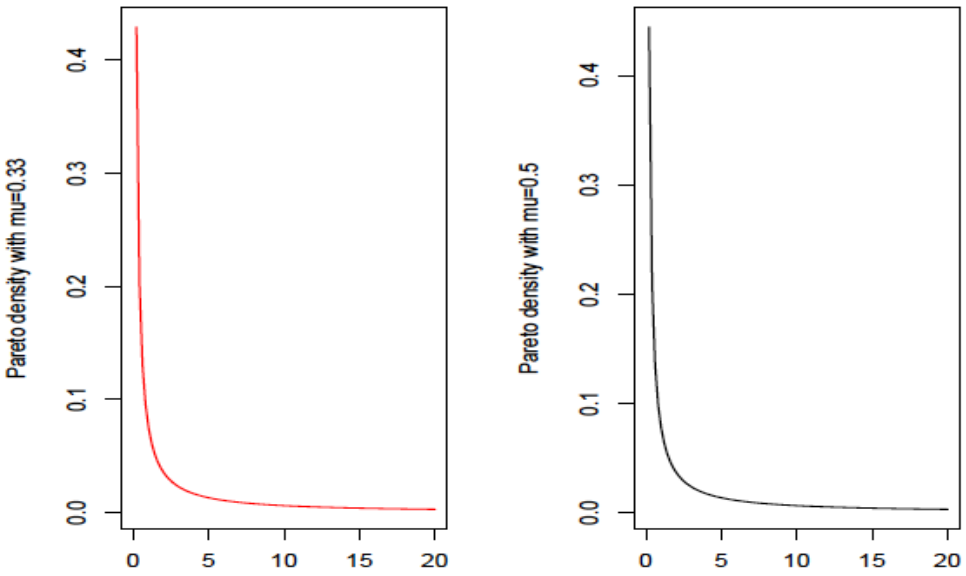

Fig 1.5 plot of varying λ the shape parameter

The root of the partially differentiated log-likelihood function of Pareto distribution (type I and II) with respect to the shape and location parameters yielded (0.33, 0.5) and (0.082402, 0.07967) respectively. The plots of the fitted distribution with the two different roots show little deviation (fig 1.5 and 2). The extreme value distribution breaks down at the verge of estimation. Figure 2 confirmed log-normal to be more suitable in comparison to the Pareto, because the blue line(lognormal) is the most consistent with the movement of the data-line represented by the black-dots, compared to the red line and the dotted green line representing pareto of type I and II respectively.

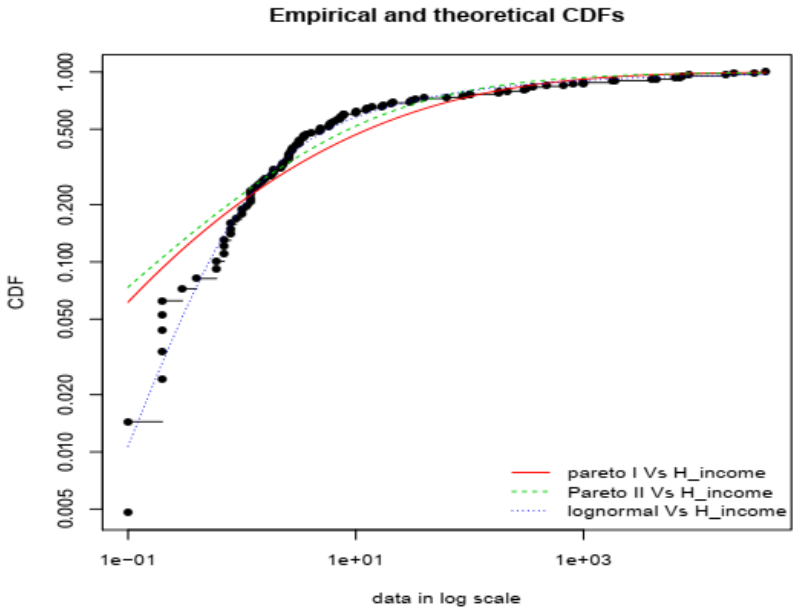

Figure 2-The graphical comparison for Pareto 1 & II and Log-normal distributions

5.20 Log-normal Parameters turning

Location Parameter	Log (Mean)	Log(mode)	Log(median)	Trimmed Mean
$f(x_1)$	2.375297e-06	6.667624e-09	2.441384e-06	2.442240e-06
$f(x_2)$	6.775384e-06	6.523536e-07	6.488569-06	6.484578e-06
.	.	.	.	.
.	.	.	.	.
.	.	.	.	.
$f(x_n)$	6.509270e-06	4.435462e-07	6.276967e-06	6.273698e-06
	0.0007769066	0.0003445284	0.0007566447	0.0007563607

Table 3-Empirical distribution parameters tuning

Fig 3 shows the points on the P-P plot falling approximately on and along the baseline, suggesting the compatibility of the log-normal distribution to the empirical household income data. The Q-Q plot does not show any great departure from the baseline (no lack-of-fit), only for some pockets of extreme data points that are not well captured by the lognormal distribution function. The empirical and theoretical cumulative density function shows the adequacy of the log-normal distribution to the data fit (see Fig 3).

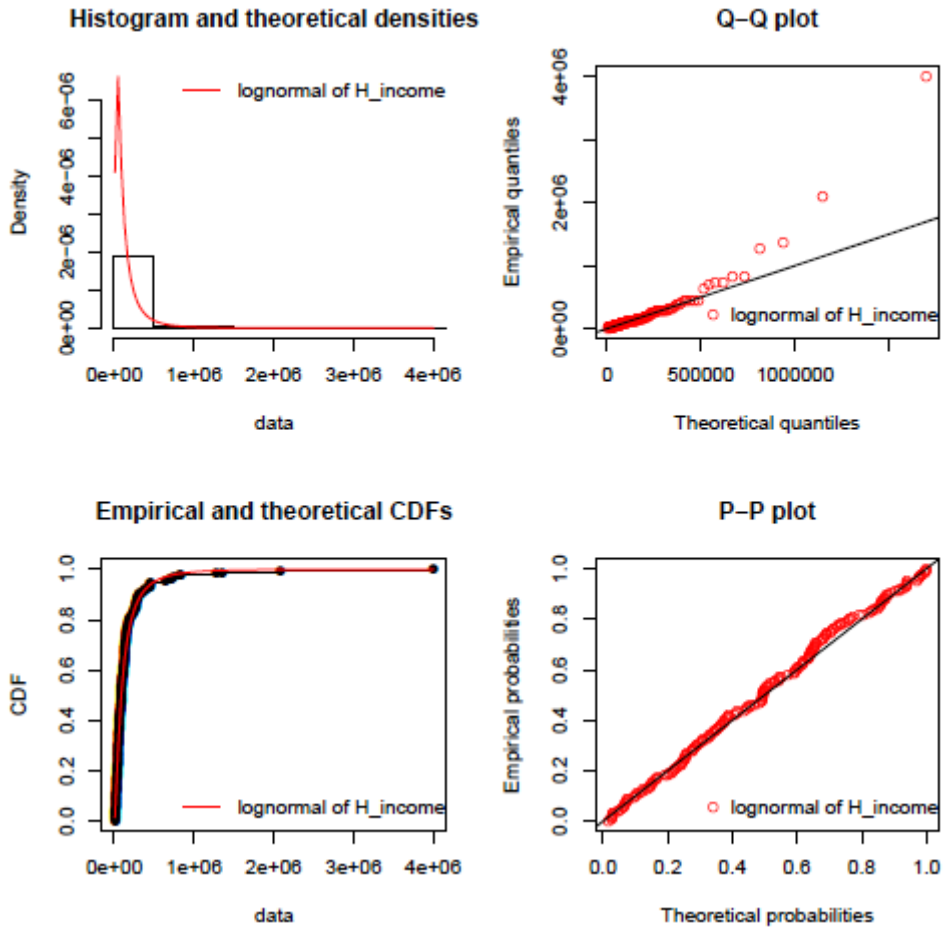

Figure 3-The income data empirical distribution and the log-normal theoretical cumulative density function plots

Regardless of the above outcomes, log-normal shows little inadequacy as it is not able to capture few pockets of outliers in the data which was uncovered by the Q-Q plot and not by any other graphical assessment (See Fig 3). Further work of joining parameters of Pareto distribution and lognormal distribution catered for the pockets of extreme values not captured by lognormal distribution (See Fig 4).

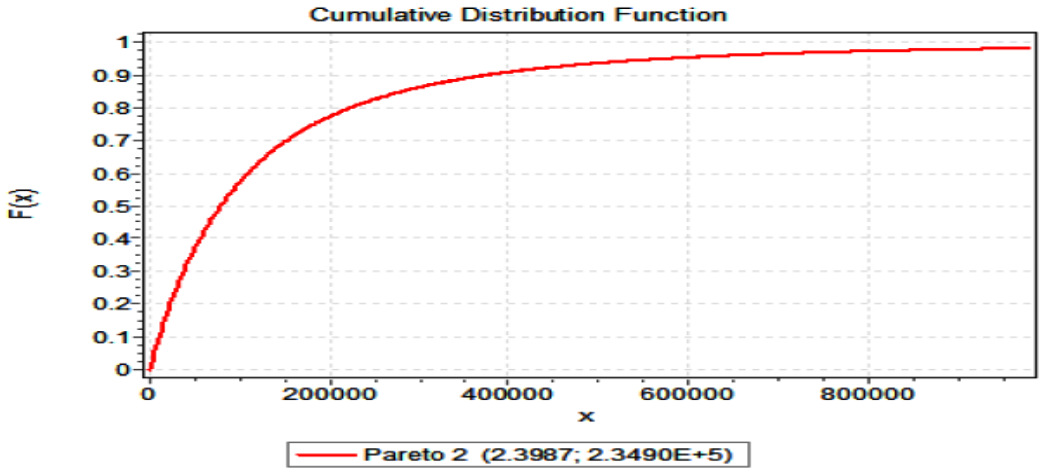

Fig 4

6.0 Conclusion

Summarily, the MLE approach and Log-normal function are more preferred, easier and suitable for fitting income datasets with turning points, extreme values and batch effects. The normalization approach that is reliable for a household's income dataset with turning points, extreme values and batch effects is the use of log-normal function on the data points. This is also used in the bioinformatics approach for dealing with extremely large datasets. The breaking points detection is now possible by fitting new data to be compared with the obtained empirical fit as the new baseline. The points not captured by the baseline indicates there are breaking points, extreme values, and the various loosed data points which are off the baseline reveals the levels and quantities of turning points and extreme values present.

7.0 Reference

Abdulrahim Louzaoui and Mohamed El Arrouchi (2020) "On the Maximum Likelihood Estimation of Extreme Value Index Based on k-Record Values" Hindawi Journal of Probability and Statistics, Volume 2020, Article ID 5497413, 9 pages https://doi.org/10.1155/2020/5497413

Bello O. A., Adetutu O.M, Oguntolu A.F. (2016). "The Maximum Likelihood Estimation of a Longitudinal Data of Household Income in the Presence of Outlier Densities": *3rd Annual International Conference and Workshop On Mathematical Analysis And Optimization (ICAPA):* Theory And Applications At the University Of Lagos, Nigeria.

Charles I. Jones (2014)" Pareto and Piketty: The Macroeconomics Of Top Income And Wealth Inequality ", Working Paper 20742 http://www.nber.org/papers/w20742 NATIONAL BUREAU OF ECONOMIC RESEARCH 1050 Massachusetts Avenue Cambridge, MA 02138 December 2014

Christian Walck (2007), *Hand-book on Statistical Distributions for experimentalists*. Particle Physics GroupFysikum, University of Stockholm; (e-mail: *walck@physto:se*) last modification 10 September 2007

Clement, Fabio, Gallegati, Mauro (2005). *Pareto's Law of Income Distribution for Germans, the UK and US*. EconWPA

Cullen, A. and Frey, H. (1999). *Probabilistic Techniques in Exposure Assessment*. Plenum Publishing Co., 1st edition.

François Geerolf (2016) A Theory of Pareto Distributions, UCLA This version: August 2016. First version: April

KuzminV., Zaliskyi M, Odarchenko R., Polishchuk O., Ivanets O. and Shcherbyna O., "Method of Probability Distribution Fitting for Statistical Data with Small Sample Size," 2020 10th International Conference on Advanced Computer Information Technologies (ACIT), 2020, pp. 221-224, doi: 10.1109/ACIT49673.2020.9208842

Matt addy, (2019). *Business Data Science: Combining Machine Learning and Economics to Optimize, Automate, and Accelerate Business Decisions*. New York: McGraw-Hill. p. 90. ISBN 978-1-260-45277-8. The AIC is an estimate for OOS deviance.

Marie Laure Delignette-Muller and Christophe Dutang (2014); *fitdistrplus: An R Package for Fitting Distributions.*Universite de Lyon and Universite de Strasbourg, October 2014

Martorell et al., J. Martín & C.J. Pérez, C. J. Pérez (2009), "Safety, Reliability and Risk Analysis: Theory, Methods and Applications" Application of a generalized lognormal distribution to engineering data fitting Safety, Reliability and Risk Analysis (pp.869-874), Publisher: CRC Press, Taylor & Francis Group, London, ISBN 978-0-415-48513-5

Mehrotra, K. G., Kulkarni, P. M., Tripathi, R. C., &Michalek, J. E. (2000). "Maximum likelihood estimation for longitudinal data with truncated observations". Statistics in Medicine, 19(21), 2975–2988. doi:10.1002/1097-0258(20001115)19:21<2975: aid-sim598>3.0.co;2-w

Onotu S.I., Sule I.G., Adetutu M.O., Bello O. A., Oguntolu F.A. (2017). "Modelling Economic Growth in Sub-Saharan Africa: A Panel Data Approach": School of Physical Sciences (SPSBIC) Biennial International Conference, Federal University of Technology, Minna; Book of Proceeding: pp. 434-441

Ritzema (E.D), H.P(1994). Frequency and Regression Analysis Publication 16. International Institute for land Reclamation and improvement (ILRI), the Netherlands pp 175-224 ISBN 90-70754-33-9

Vito Ricci (2005). *Fitting Distribution With R*; *vitoricci@yahoo:com*

Wataru Souma (2002). *Physics of Personal income*. airxiv.ond.mat/0202388

Zaven A. Karian, Edward J. Dudewicz (2011). Handbook of Fitting Statistical Distributions ISBN 978-1-58488-711-9 Chapman & Hall/CRC Taylor & Francis Group 6000 Broken Sound Parkway NW, Suite 300 Boca Raton, FL 33487-2742

Modeling the Control of Carriers Receiving Treatment and Exposed Receiving Treatment for the Spread of Amoebiasis (Amoebic Dysentery)

[1]SULEIMAN,A. S. ,[2] ENAGI, A. I. ,[3] MUHAMMED, U. &[4] ADABARA, N. U.
[1,234]Department of Mathematics, Federal University of Technology, Minna, 23401, Nigeria
[1]suleimanaminashafii@gmail.com

Abstract

A mathematical model of Amoebiasis (Amoebic Dysentery) is formulated incorporating the effects of carriers receiving treatment and exposed receiving treatment. In this work, the basic reproduction number is computed using the next generation method. The disease free equilibrium (DFE) point of the model is obtained. The local stability of the disease-free equilibrium point of the model is established. The result show that the DFE is locally asymptotically stable if the basic reproduction number is less than one

Keywords: Amoebic Dysentery; Basic reproduction number; Disease-Free equilibrium.

INTRODUCTION

Amoebic Dysentery is an infection caused by any of the amoebas of the Entamoeba histolytica also called intestinal amebiasis and ameobic colitis, it is caused by a protozoon.Entamoeba histolytica whose scientific name means “tissue-dissolving” is second only to the organism that causes malaria as a protozoa cause of death, Free living amoebas (Visvesvara *et al.,* 2007) and (orphanet, 2009),–these species are often described as “opportunistic free-living amoebas”as human infection is not an obligate part of their life cycle.

Most infected people, about 90% are asymptomaSSStic (Haque *et al.*,2003) but this disease has the potential to make the sufferer dangerously ill. Infections can sometimes last for year. Symptoms take from a few weeks to develop and manifest themselves, but usually it is about two to four weeks. Symptoms can range from mild diarrhea to severe dysentery with blood and mucus. The blood comes from lesions formed by the amoebae invading the lining of the large intestine. In about 10% of the invasive cases the amoebae enter the bloodstream and may travel to other organs in the body. Most commonly this means the liver, as this is where blood from the intestine reaches first, but they can end up almost anywhere in the body (Nespola*et al.*, 2015). About 480 million people are infected with amoebiasis and this result in the death of between 40,000 -110,000 people a year, (Farrar *et al.*, 2013) Most infected people, about 90%, are asymptomatic (Beeching et al., 2014) but this disease has the potential to make the sufferer dangerously ill.lt is estimated that about 40,000 to 100,000 people worldwide die annually due to amoebiasis (Atlas of human infection diseases 2012) Asymptomatic carriers are the main source of transmission, infection spreads when the stool infected with cyst contaminates fresh food and water. Oral-anal sexual contact is the other

mode of transmission of infection. Amoebiasis is usually transmitted by the fecal-oral route. But it can also be transmitted indirectly through contact with dirty hands or objects as well as by anal-oral contact. Infection is spread through ingestion of the cyst form of the parasite, a semi-dormant and hardy structure found in feces. Any non-encysted amoebae, or trophozoites, die quickly after leaving the body but may also be present in stool: these are rarely the source of new infections. Since amoebiasis is transmitted through contaminated food and water, it is often endemic in regions of the world with limited modern sanitation systems, including Mexico, Central America, Western South America, South Asia, and western and southern Africa (Ryan *et al.,* 2004) Amoebic dysentery is often confused with "traveler's diarrhea" because of its prevalence in developing nations. In fact, most traveler's diarrhea is bacterial or viral in origin.

(Jinlong *et al*., 2020) propose a compartmental model for asymptomatic transmission shifts epidemic dynamics for waterborne infectious diseases, (Hailay *et al*.,2019) developed a model dynamics of direct and pathogens induced dysentery diarrhea epidemic with controls, (Sobin *et al.,* 2016) developed an Amoebiasis inspried model for Epidemic message propagation in DTN.

MATERIALS AND METHODS

Model Formulation:

we divided the population into eight classes; S(t) is used to represent susceptible, E(t) is used to represent infected Exposed, I(t) is used to represent the infected T_I (t) is used to represent Infective individuals receiving Treatment, C(t) is use to represent carrier, T_C (t)is use to represent Infected carriers receiving Treatment, T_E (t) is use to represent Infected Exposed receiving Treatment and R(t) is the recovered. This can be shown as a flow diagram in which the circle represents the different compartments and the arrows represent the transition between the compartments. The population of the susceptible class S increases through constant recruitment $\wedge$ and it will also increases as individuals move from the recovered class R into the susceptible class S at the rate ω as a result of waning off partial immunity. The population of the class will decrease when people move into the infected expose class E from the susceptible class via interaction between individuals that are prone to the infection and individuals that are expose to the infection at a rate λ and natural death at the rate μ ,the population of the infected expose class E will increase when individuals move into the vulnerable class S into the infected expose class E with contact of the susceptible individuals and the infected expose into the infected expose receiving treatment due to treatment at a rate α_1 , and progresses into the infected class I at the rate σ since some of the individuals are still exposed to the infection and natural death at the rate μ ,the infected class I population will increases when the infected expose progresses from the infected expose class to the infected class at the rate α_2 and decreases due to the death of the infection at the rate δ and natural death at the rate μ ,the population of the infected treatment class T_I will increases when the infected move to the infected treatment at the rate α_2 and decreases when they progresses to

the carrier class at the fraction rate $\rho\gamma$ and natural death at the rate μ ,the carrier class C population will increases when the infected receiving treatments progresses from the infected receiving treatments to the carrier at a fraction rate $\rho\gamma$ and decreases when the members of the carrier class move into the treatment of the carriers receiving treatment via treatment at the rate α_3 and natural death at μ ,the populations of the infected expose treatment T_E class will increase when individuals move from the expose class at the rate α_1 and decreases when individuals move from infected expose receiving treatment to the recovered at the rate θ via treatment and natural death at the rate μ ,the population of the carrier receiving treatment T_C will increases as individuals from the carrier class C move into the carrier receiving treatment via treatment at the rate α_3 and decreases as the carrier receiving treatment recovered via treatment at the rate τ and natural death at the rate μ ,the recovered class R population will increase when the infected receiving treatment at a fraction rate $(1-\rho)\gamma$, and carriers receiving treatment at the rate τ and infected expose receiving treatment at the rate θ , population will decreases as individuals of the recovered class get into the prone section , consequence to waning off of the partial immunity and due to natural death at a rate μ .

Assumptions of the Model: The population is homogeneous and transmission of amoebiasis is being horizontal not vertical while natural death rate is time constant, the recovered individuals after treatment can still develop the infection again, Both Infected Exposed and Infected Carriers spread the disease but at lower rate than the infective hence the introduction of the parameter $\in$ as the reducing factor of β .

With the assumptions, the model is given below as:

$$\frac{dS}{dt} = \wedge + \omega R - \beta\left[1+\varepsilon(E+C)\right]S - \mu S \qquad (1)$$

$$\frac{dE}{dt} = \beta\left[1+\varepsilon(E+C)\right]S - (\alpha_1 + \sigma + \mu)E \qquad (2)$$

$$\frac{dT_E}{dt} = \alpha_1 E - (\theta + \mu)T_E \qquad (3)$$

$$\frac{dI}{dt} = \sigma E - (\mu + \delta + \alpha_2)I \qquad (4)$$

$$\frac{dT_I}{dt} = \alpha_2 I - (\gamma + \mu)T_I \qquad (5)$$

$$\frac{dC}{dt} = \rho\gamma - (\mu + \alpha_3)C \qquad (6)$$

$$\frac{dT_C}{dt} = \alpha_3 C - (\mu + \tau)T_C \qquad (7)$$

$$\frac{dR}{dt} = [(1-\rho)\gamma)]T_I + \theta T_E + \tau T_C - (\mu + \omega)R \qquad (8)$$

Where $\lambda = \beta[1 + \varepsilon(E + C)]$ it's the reduction factor among the infected exposed and infected carriers

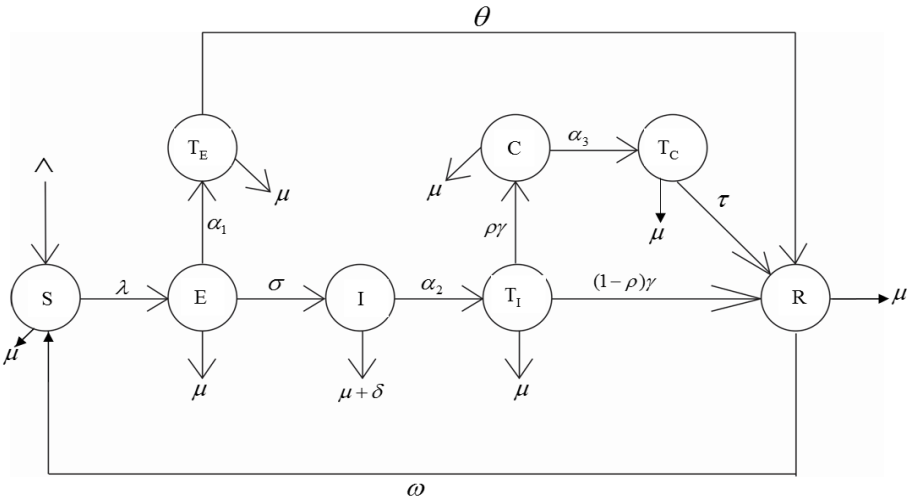

Figure 1: Schematic Representation of the Model

Table1: Variables of the model

S (t)	susceptible individuals at time t.
E (t)	Infected Exposed individuals at time t.
$T_E(t)$	Infected Exposed receiving treatment individuals
$T_I(t)$	Infective individuals receiving treatment
$T_C(t)$	Infected carriers receiving treatment
I (t)	Infective individuals at time t
C (t)	Carrier individuals at time t
R (t)	Recovered individual at time t.

Table 2: Parameters of the model

$\wedge$	constant Recruitment rate.
β	probability of susceptible individuals been infected.
N	Total population.
μ	Natural death rate.
δ	Death rate due to infection.
σ	The rate at whichInfected Exposed becomes infective.
α_1	The rate at which infected Exposed move to Treated Exposed class.
α_2	The rate at which Infective moves to Treatment infective class
α_3	The rate at which infected carriers moves to Treatment carrier class
τ	The rate at which the Treatment carrier moves to recovered class.
ω	The rate at which recovered moves to the susceptible class.
θ	The rate of recovery of infected Exposed.
$(1-\rho)\gamma$	Fraction of infective that recovered.
$\rho\gamma$	Fraction of Infective that moves to infected carrier class.

Disease-Free Equilibrium (DFE) Point: At the disease free equilibrium state there is absence of infection, In this case all the infected class will be zero expect the susceptible class.

A disease free equilibrium state of the model (1) to (8) exist at the point

$$\begin{pmatrix} S \\ E \\ T_E \\ I \\ T_I \\ C \\ T_C \\ R \end{pmatrix} = \begin{pmatrix} \frac{\wedge}{\mu} \\ 0 \\ 0 \\ 0 \\ 0 \\ 0 \\ 0 \\ 0 \end{pmatrix} \qquad (5)$$

Basic Reproduction Number: The basic reproduction number is defined as the number of secondary illness produced if any ill person is brought into a population in which everybody is prone to the disease. For this research, the basic reproduction number is defined as the number of secondary amoebiasis infections due to single amoebic dysentery individual. Applying the next generation method, the basic reproduction number is the spectral radius of the matrix FV^{-1} where F and V are transmission and transition matrices.

F is the rate of arrival of new infection into the class that is infected and V is the transmission of person out of the compartment that is infected.

From our equation

$$F = \begin{bmatrix} \beta\varepsilon S & 0 & \beta S & 0 & \beta\varepsilon S & 0 \\ \alpha_1 & 0 & 0 & 0 & 0 & 0 \\ \sigma & 0 & 0 & 0 & 0 & 0 \\ 0 & 0 & \alpha_2 & 0 & 0 & 0 \\ 0 & 0 & 0 & \rho\gamma & 0 & 0 \\ 0 & 0 & 0 & 0 & \alpha_3 & 0 \end{bmatrix} \quad (8)$$

And

$$V = \begin{bmatrix} (\alpha_1 + \delta + \mu) & 0 & 0 & 0 & 0 & 0 \\ 0 & (\theta + \mu) & 0 & 0 & 0 & 0 \\ 0 & 0 & (\mu + \delta + \alpha_3) & 0 & 0 & 0 \\ 0 & 0 & 0 & (\gamma + \mu) & 0 & 0 \\ 0 & 0 & 0 & 0 & (\mu + \alpha_3) & 0 \\ 0 & 0 & 0 & 0 & 0 & (\mu + \tau) \end{bmatrix} \quad (9)$$

The basic reproduction number R_0 is given as

$$R_0 - \frac{\beta\varepsilon \wedge}{\mu(\alpha_1 + \delta + \mu)} \quad (10)$$

RESULT AND DISCUSSION

Local Stability of the Disease-Free Equilibrium:

Theorem: The Disease-Free Equilibrium of the model Equation (1) –(8) is locally asymptotically stable if $R_0 < 1$ and unstable if otherwise.

Proof: the system (1) –(8) at DFE is given as

$J = (\mathrm{AB})$

$$\begin{bmatrix} \beta[\mathrm{I}+\varepsilon(\mathrm{E}+\mathrm{C})]-\mu & \beta[\mathrm{I}+\varepsilon]\mathrm{s} & 0 & \beta S & 0 & \beta[\mathrm{I}+\varepsilon]\mathrm{S} & 0 & \omega \\ \beta[\mathrm{I}+\varepsilon(\mathrm{E}+\mathrm{C})] & -(\alpha_1+\sigma+\mu) & 0 & 0 & 0 & \beta[\mathrm{I}+\varepsilon]\mathrm{S} & 0 & 0 \\ 0 & \alpha_1 & -(\theta+\mu) & 0 & 0 & 0 & 0 & 0 \\ 0 & \sigma & 0 & -(\mu+\delta+\alpha_2) & 0 & 0 & 0 & 0 \\ 0 & 0 & 0 & \alpha_2 & -(\gamma+\mu) & 0 & 0 & 0 \\ 0 & 0 & 0 & 0 & 0 & \alpha_3 & 0 & 0 \\ 0 & 0 & 0 & 0 & 0 & 0 & -(\mu+\mathrm{I}) & 0 \\ 0 & 0 & \theta & 0 & [(1-\rho)\tau] & 0 & \tau & -(\mu+\omega) \end{bmatrix} \quad (11)$$

$| J - \lambda I |$ *is*

and

$$\begin{bmatrix} \beta[\mathrm{I}+\varepsilon(\mathrm{E}+\mathrm{C})]-\lambda & \beta(\mathrm{I}+\varepsilon)\mathrm{S} & 0 & \beta S & 0 & \beta(\mathrm{I}+\varepsilon) & 0 & \omega \\ 0 & -(\alpha_1+\sigma+\mu)-\lambda & 0 & 0 & 0 & \beta(\mathrm{I}+\varepsilon)\mathrm{S} & 0 & 0 \\ 0 & \alpha_1 & -(\theta+\mu)-\lambda & 0 & 0 & 0 & 0 & 0 \\ 0 & \sigma & 0 & -(\mu+\delta+\alpha_2)-\lambda & 0 & 0 & 0 & 0 \\ 0 & 0 & 0 & \alpha_2 & -(\gamma+\mu)-\lambda & 0 & 0 & 0 \\ 0 & 0 & 0 & 0 & 0 & (\mu+\alpha_3)-\lambda & 0 & 0 \\ 0 & 0 & 0 & 0 & 0 & \alpha_3 & -(\mu+\mathrm{I})-\lambda & 0 \\ 0 & 0 & 0 & 0 & [(1-\rho)\gamma] & 0 & \tau & -(\mu+\omega)-\lambda \end{bmatrix} \quad (12)$$

Applying Gauss Jordan elimination method we have the following from the characteristic equation:

Therefore

$\lambda_1 = \beta[\mathrm{I}+\varepsilon]$

$\lambda_2 = \beta[\mathrm{I}+\varepsilon]\frac{\wedge}{\mu} - (\alpha_1+\sigma+\mu)$

$\lambda_3 = -(\theta+\mu)$

$$\lambda_4 = -(\mu + \delta + \alpha_3)$$

$$\lambda_5 = -(\gamma + \mu)$$

$$\lambda_6 = -(\mu + \alpha_3)$$

$$\lambda_7 = -\mu$$

$$\lambda_8 = -(\mu + \omega)$$

REFERNCES

Atlas of human Infectious Diseases, First Edition.Heiman F. L. Wertheim, Peyer Horby and John P. Woodall., (2012), Blackwell Publishing Ltd.

Beeching, Nick;Gill,Geoff (2014). "19". Lecture Notes: Tropical Medicine. John Wiley & Sons.pp. 177-182. ISBN 978118734568.

Farrar, Jeremy; Hotez, Peter; Junghanss, Thomas; Kang, Gagandeep; Lalloo, David; White, Nicholas J. (2013). Manson's Tropical Diseases. Elsevier Health Sciences. PP. 664-671. ISBN 9780702053061.

Haque, Rashidul; Huston, Christopher D.; Hughes, Molly; Houpt, Eric; Petri, William A. (2003). "Amebiasis". NEJM. 348 (16): 1565-1573. Doi: 10.1056\NEJMra022710. Archived from theboriginal on 2015-05-02 Retrieved 2012-04-12.

Nespola,Benoit; Betz, Valerie; Brunet, Julie; Gagnard,Jean-Charles; Krummel, Yves; Hansmann, Yves; Pesson, Bernard; Abou-bacar, Ahmed; Candolfi, Ermanno (2015)." First case of amebic liver abscess 22 years after the first occurrence". Parasite. 22:20 doi:10.1051\parasite\2015020. ISSN 1776-1042. PMC 4472968. PMID 26088504. Archived from the original on 2015-09-24.

Orphanet: Amoebiasis due to free living amoebae".(2009) Archived from the original on 2008-11-18. Retrieved 2009-01-17. At Orphanet.

Sobin C., V. Raychoudhury, G. Marfia, and A. Singla, (2016) "A survey of routing and data dissemination in delay tolerant network," journal of Network and Computer Application,

Ryan KJ, Ray CG, eds. (2004). Sherries Medical Microbiology (4th ed.). McGraw Hill. Ppp. 733-8. ISBN 0-8385-8529-9.

Visvesvara GS, Moura H, Schuster FL (2007). "Pathogenic and opportunistic free-living amoebae: Acanthamoeba spp., Balamuthia mandrillaris, Naegleria fowleri, and sappinia diploid". FEMS Immunol. Med. Microbiol. 50 (1) : 1-26. Doi: 10.1111\j.1574-695X.2007.00232.x. PMID 17428307.

NON-LOCAL VIBRATION OF DOUBLE – WALLED CARBON NANO-TUBE USING FINITE ELEMENT METHOD

Shaba, Abel Idrisu[1*]Jiya, Mohammed[2],Aiyesimi,Yomi Monday[3],Mohammed, Abdullahi A.[4]
[1,2,3,4]Department of Mathematics, Federal university of Technology, Minna,
* Corresponding author:proabelshaba@yahoo.com

Abstract
In this study, based on non-local elasticity theory and Euler – Bernoulli Beam theory, vibration equation of double – walled carbon nano-tube is established on simply supported system. The effects of both inner and outer surface layer on the nano-tube are taken into consideration. Finite element method is used to discretize the equation of motion to obtain the natural frequency. Detailed parametric analysis is conducted focusing on small scale, elastic medium, velocity on the stability of the pipe. Result of this research can be applied in design and improvement of fluid conveying application embedded in elastic medium

Keywords: Nano, Carbon, Vibration, Beam, Elastic, Velocity, Tube, Local

1. Introduction

The technology of conveying fluid, such as petroleum liquids and waters through long or slender pipelines, which cover different types of foundation, has evolved over the years. The speed of this liquid or fluid in the pipeline has impart energy to the pipeline making it to vibrate. The vibration of the conveying pipe can put pressures on the walls of the pipe resulting on the pipe to deflect. This deflection of the conveying pipe as a result of the moving fluid may lead to structural instability of the structure.

For any vibrating system, the analysis of such structure can be done either in domain of time or frequency. In the time domain, the independent variable of a vibration signal is time. In this case, the system itself can be model as a set of differential equation with respect to time. A model of a vibrating system can be formulated by applying either force – momentum rate relation (Newton's Second Law) or the concept of Kinetic and potential energy (Lagrangian approach). In the frequency domain, the independent variable of a vibration signal is frequency. In this case, the system can be modeled by input – output transfer function which is algebraic rather than differential model

Foundation protects and gives supports to buried pipes, this minimize the possible risk hazard that could lead to malfunctioning of structures. Therefore, having understanding knowledge of fluid conveying pipe on a Pasternak elastic foundation, enable engineers and designers to have insight in the strait of foundation of the conveying pipes. This will enable them to have conveying pipes on same type of foundation that can handle certain type of displacement and load.

In order to design a new efficient vibrating nano-scale device, researchers need detailed information about dynamic properties of the device. In contrast to macro scale structures, atomic forces play an important role in defining the mechanical characteristics of nano-structures. Hence, a clear understanding of atomic interactions is required. Furthermore, producing prototypes without having clear image of the structural properties can be very time consuming, misleading and sometimes impossible. Therefore, having a good insight of the Dynamic behavior is important for the practical development of the Nano machines. Experiments can be used to analyze the behavior of nanostructures. In recent years, elastic beam models as (Yonn *et al*., 2003), (Ke *et al* ., 2009), (Fekrmandi and Rezaee, 2011), (Asari *et al.,* 2011) and Simsek (2010)and elastic shell models in (Wang *et al.,* 2006) have been effectively used to predict resonant frequencies of CNTs. Using simple equations of motions offered by the continuum models, key parameters that affect the free vibration of CNTs can be easily studied. These studies show that, compared to MD simulations, continuum modeling is more practical and useful in the analysis of CNTs in terms of computational efforts

Sobamowu *et al* (2017) used non local elasticity theory to model dynamics behaviour of fluid

conveying structures subjected to different boundary condition using Galerkin Newton Harmonic Balancing Method. He considers three different governing equations with different boundary conditions. In case one, fluid induced vibration in pipe using non local elasticity theory and Hamilton's principle., fluid induced vibration in functionally graded micro pipe under external applied tension and global pressure and fluid induced vibration on nano tube resting on linear and nonlinear elastic foundation under external applied tension and global pressure. The result obtained shows that alteration of nonlinear induced frequency from linear frequency is tied to increasing amplitude of oscillation, flow velocity and thermal parameters.

Wu *et al* (2018) examined Dynamics analysis of the S-type fluid conveying steel pipe for Tseng weng reservoir using finite element method. They used Euler- Bernoulli theory to model the equation and finite element method to solve the equation of motion. The results obtain shows that s-pipe will be safe if it is subjected to the constant impulse and centrifugal forces.

3. Methodology

The problem under consideration is the Double- walled Carbon Nanotube (DWCNT) fluid conveying system on a visco-elastic medium

The following assumptions are taken into accounts:

The pipe is considered inextensible.

The lateral displacement $w(x,t)$ is small compared with the diameter of the pipe, so that Theory of Euler – Bernoulli is applicable.

The cross – section of the pipe is uniform and linearly elastic

Visco-elastic foundation is considered

Simply – supported boundary condition is considered.

The material of the pipe is homogenous

Stress – strain relation in one dimensional

$$\left.\begin{aligned}&(EI+h)\frac{\partial^4 w}{\partial x^4}+\left[m_f(V)^2-\Pi_0+PA\right]\frac{\partial^2 w}{\partial x^2}+(2m_fV)\frac{\partial^2 w}{\partial x\partial t}+(m_f+m_p)\frac{\partial^2 w}{\partial x^2}+kw+c\frac{\partial w}{\partial t}-\\&(e_0a)^2\frac{\partial^2}{\partial x^2}\left[\begin{aligned}&\left[m_f(V)^2-\Pi_0\right]\frac{\partial^2 w}{\partial x^2}+(2m_fV)\frac{\partial^2 w}{\partial x\partial t}+\\&+PA\\&(m_f+m_p)\frac{\partial^2 w}{\partial x^2}+kw+c\frac{\partial w}{\partial t}\end{aligned}\right]=0\end{aligned}\right\} \quad (1)$$

$$h=\frac{1}{8}\pi E_0 t_0\left(d_0{}^3+d_i{}^3\right) \quad (2)$$

$$\Pi_0=2\tau_0(d_i+d_0) \quad (3)$$

Initial condition

$$w(x,0)=\frac{\partial w(x,0)}{\partial t}=0 \quad (4)$$

Boundary condition

$$w(0,t)=w(L,t)=0 \quad (5)$$

$$w''(0,t)=w''(L,t)=0$$

The above equation eq 1 to 5 are solve using Galerkin Decomposition procedure and we have

$$[M]\ddot{U}(t)+[C]\dot{U}(t)+[K]U(t)=0 \quad (6)$$

Where M is the Mass matrix, C is the damping matrix and K is the Stiffness matrix

4. Results and Discussion

Matlab software is used to obtain the Eigen value of the characteristic equation and effects of various parameters are observed. Since the Eigen value problem yield a complex root. The imaginary part of these roots represents the natural frequency of the damped system. The real part indicates the rate of the decay of the free vibration.

5. Conclusion

The effect of foundation and non local parameter were analyzed numerically using finite element method. Some interesting conclusions were drawn.

Foundation damping decrease the critical velocity

Increase in fluid pressure increase slightly its natural frequency

References

Wu,J, Huang, C and Shaw, H (2018) Dynamic Analysis of the S-Type of fluid conveying steel pipe for Tsen-WengReservior using Finite Element Method. International Journal of Civil Engineering, 7(1): 9 – 30.

Sobamowo, M.G, Ogunmola, B.Y and Osheku, C.A (2017) thermo – mechanical nonlinear vibration analysis of fluid conveying structures subjected to different boundary condition suing Galarkin newton Harmonic balancing method. *Journal of Applied and computational mechanics,* 3(1): 60 – 79

Yoon, J.,Ru,C.QandMioduchowski, A(2003)Vibration of an embedded multiwall carbon Nanotube.*Compos SciTechnol,* 63:1533-1542

Ke, L.L,Xiang Y.,Yang,J andKitipornchai,S(2009) nonlinear free vibration of embedded Double-walled carbon nanotubes based on nonlocal Timoshenko beam theory. *ComputationalMaterials Science,* 47: 409-417.

Ansari, R.Sahmani,Sand Rouhi,H(2011) Axial buckling analysis of single-walled carbon nanotubes in thermal environments via the Rayleigh–Ritz technique.*Computational Materials Science,* 50:3050-3055.

Şimşek,M(2010) Vibration analysis of a single-walled carbon nanotube under action of a moving harmonic load based on nonlocal elasticity theory. *Physica E: Low-dimensional Systems and Nanostructures,* 43:182-191

Wang X.S., Li, Q.,Xie,Q J,Jin Z.,Wang,J.Y.,LiY., Jiang,K.L. . Fan,S.S(2006) Fabrication Of Ultralong and Electrically Uniform Single-Walled Carbon Nanotubes on Clean Substrates. *Nano Letter,*9 :3137-3141.

Fekrmandi, H andRezaee,M(2011) A Theoretical and Experimental Investigation on Free Vibration Behavior of a Cantilever Beam with a Breathing Crack.*Shock and Vibration,*19:175-186.

Analysis of T_1 and T_2 Relaxation Times from Bloch Equation for the Estimation of Age of Human Organs

*Olaoye D. O., Yusuf S. I. and Abdulraheem O. J.
Department of Mathematics, Federal University of Technology Minna, Nigeria.
*Metric60@gmail.com, si.yusuf@futminna.edu.ng
*Correspondence Author

Abstract
As one of the preferred diagnostic imaging tools, Magnetic Resonance Imaging (MRI) has become a diagnostic modality which has made an in-road into age estimation. However, many works in this area were carried out using observed statistical data to classify and analyze findings. In this research work, a time-independent non-homogenous linear differential equation from the Bloch Nuclear Magnetic Resonance (NMR) equations is evolved. The equation is solved under the influence of radio frequency magnetic field [$rfB_1(x,t) \neq 0$] and in the absence of radio frequency magnetic field [$rfB_1(x,t) = 0$]. T_1 and T_2 relaxation times were varied with a view to analyze the signals as it relates to the age of any human organ.

Keywords: T_1 relaxation time, T_2 relaxation time, radio frequency field, Magnetic resonance fingerprinting, magnetization.

1.0 Introduction

Relaxation usually means the return of a perturbed system into equilibrium. Tissue can be characterized by two different relaxation times – T_1 and T_2 . T_1(Longitudinal relaxation time) is the time constant which determines the rate at which excited protons return to equilibrium. It is a measure of the time taken for spinning protons to realign with the external magnetic field. The T_1 relaxation time, also known as the spin-lattice relaxation time, is a measure of how quickly the net magnetization vector (NMV) recovers to its ground state. The return of excited nuclei from the high energy state to the low energy or ground state is associated with loss of energy to the surrounding nuclei. Nuclear magnetic resonance (NMR) was originally used to examine solids in the form of lattices, hence the name "spin-lattice" relaxation. Two other forms of relaxation are the T_2relaxation time (spin-spin relaxation) and T_2* relaxation (Rock, 2021).

These two tissue parameters, T_1 and T_2 represent different tissue information that is largely independent of each other. Nevertheless, T_1 and T_2information is not fully independent of each other because all spin–lattice interactions that cause T_1 recovery also contribute to T_2decay (Suzuki *et al.*, 2006). In a study carried out by Yusuf (2010), the two different relaxation times – T_1 and T_2were used to carry out the general analysis of physiological flow in human body. The results show that the two relaxation parameters are very vital in describing and analyzing the flow of fluids in human body and the surrounding tissues.

Magnetic resonance fingerprinting (MRF) is a method that simultaneously and rapidly measures multiple tissue properties, with initial application in measuring T_1 and T_2. This

technique is based on the premise that acquisition parameters can be varied in a pseudorandom manner such that each combination of tissue properties will have a unique signal evolution. Using the Bloch equations, a dictionary of all possible signal evolutions can be created that includes all known acquisition parameters and all possible range of values and combination of the properties of interest (Badve *et al.*, 2015).

Badve *et al.* (2015) presented simultaneous quantification of regional brain T_1*and* T_2 relaxation times in healthy volunteers using MRF and assess differences in tissue properties resulting from age, sex, and laterality of hemispheres. They further compare different best-fit options for regression analysis of age and brain relaxometry and assess how age-sex interactions affect these findings in the context of the known literature on relaxometry measurements with aging.

The study of the living human brain has shown that at low nuclear MR frequencies, age-related factors constitute an important influence on the T_1relaxation time. The findings demonstrate the importance of understanding the variation of T_1*and* T_2 in relation to age and to the localization in the brain. For instance, in the investigation of disease, the contrast resolution between the tissues changed by disease and the normal tissue might be different, depending on the normal tissue variation in relaxation times (Agartz *et al.*, 1991).

It is in line with these that this research work is aim at investigating further the effects of $T_1$and T_2 on the estimation of age of human organs.

2.0 Mathematical Formulation

Bloch equations explain the magnetization properties of matters using relaxation times. They are given as:

$$\frac{dM_x}{dt} = -\frac{M_x}{T_2} \qquad 2.1$$

$$\frac{dM_y}{dt} = \gamma M_z B_1(t) - \frac{M_y}{T_2} \qquad 2.2$$

$$\frac{dM_z}{dt} = -\gamma M_y B_1(t) - \frac{M_z - M_o}{T_1} \qquad 2.3$$

where M_o = equilibrium magnetization

M_x = component of transverse magnetization along the x-axis

M_y = component of transverse magnetization along y-axis

M_z = component of magnetization along the field (z -axis)

γ = gyro-magnetic ratio of fluid spins

$B_1(t)$ = radio-frequency (RF) magnetic field

T_1 = Longitudinal or spin lattice relaxation time

T_2 = Transverse or spin-spin relaxation time

From the kinetic theory of moving fluids, given a property M of fluid then the rate at which this property changes with respect to a point moving along with the fluid be total derivative

$$\frac{dM}{dt} = \frac{\partial M}{\partial t} + \frac{\partial M}{\partial x}v_x + \frac{\partial M}{\partial y}v_y + \frac{\partial M}{\partial z}v_z \qquad 2.4$$

$$\frac{dM}{dt} = \frac{\partial M}{\partial t} + v.\nabla M \qquad 2.5$$

Therefore, from Yusuf *et al. (2019)* the three Bloch equations become:

$$\frac{dM_x}{dt} = \frac{\partial M_x}{\partial t} + v.\nabla M_x = -\frac{M_x}{T_2} \qquad 2.6$$

$$\frac{dM_y}{dt} = \frac{\partial M_y}{\partial t} + v.\nabla M_y = \gamma M_z \beta_1 - \frac{M_y}{T_2} \qquad 2.7$$

$$\frac{dM_x}{dt} = \frac{\partial M_x}{\partial t} + v.\nabla M_x = -\gamma M_y \beta_1 - \frac{(M_z - M_o)}{T_1} \qquad 2.8$$

If the flow is considered only along x-direction. The partial derivative along y and z direction is zero. This implies that the flow is constant along y and z directions. Therefore,

$$v.\nabla M_x = [v_i].\left[\frac{\partial}{\partial x}i\right]M = v\frac{\partial M_x}{\partial x} \qquad 2.9$$

Equations 2.6 to 2.8 become

$$\frac{dM_x}{dt} = \frac{\partial M_x}{\partial t} + v\frac{\partial M_x}{\partial x} = -\frac{M_x}{T_2} \qquad 2.10$$

$$\frac{dM_y}{dt} = \frac{\partial M_y}{\partial t} + v\frac{\partial M_y}{\partial x} = \gamma M_z \beta_1 - \frac{M_y}{T_2} \qquad 2.11$$

$$\frac{dM_z}{dt} = \frac{\partial M_z}{\partial t} + v\frac{\partial M_z}{\partial x} = -\gamma M_y \beta_1 - \frac{(M_z - M_o)}{T_1} \qquad 2.12$$

By making M_z the subject from *2.12* and simplifying the terms, we have

$$v^2\frac{\partial^2 M_y}{\partial x^2} + \frac{\partial^2 M_y}{\partial t^2} + 2v\frac{\partial^2 M_y}{\partial x \partial t} + \left[\frac{1}{T_1} + \frac{1}{T_2}\right]\frac{\partial M_y}{\partial t} + v\left[\frac{1}{T_1} + \frac{1}{T_2}\right]\frac{\partial M_y}{\partial x} + \left[\frac{1}{T_1 T_2} + \gamma^2\beta_1^2\right]M_y = \frac{\gamma\beta_1 M_o}{T_1}$$

- Awojoyogbe *et al.* (2009)

2.13

2.1 Time-independent Bloch-flow equation

For time-independent Bloch-flow equation, we have.

$$v^2\frac{\partial^2 M_y}{\partial x^2} + v\left[\frac{1}{T_1} + \frac{1}{T_2}\right]\frac{\partial M_y}{\partial x} + \left[\frac{1}{T_1 T_2} + \gamma^2\beta_1^2\right]M_y = \frac{\gamma\beta_1 M_o}{T_1} \qquad 2.14$$

Let $\left[\frac{1}{T_1}+\frac{1}{T_2}\right]=T_o$ and $\frac{1}{T_1T_2}=k$ *2.15*

$$\frac{\partial^2 M_y}{\partial x^2}+\frac{1}{v}T_o\frac{\partial M_y}{\partial x}+\frac{1}{v^2}[k+\gamma^2\beta_1^2]M_y=\frac{\gamma\beta_1 M_o}{T_1 v^2} \quad 2.16$$

Solving *2.16*,

The homogeneous part implies that $\frac{\gamma\beta_1 M_o}{T_1 V^2}=0$ *2.17*

Assuming$M_y=y;\quad \frac{1}{V}T_o=p;\quad \frac{1}{V^2}[k+\gamma^2\beta_1^2]=q$ then *2.18*

$$\frac{d^2y}{dx^2}+p\frac{dy}{dx}+qy=0 \quad 2.19$$

It can be seen that *2.16* has been changed to *2.19* which is a system of second order Ordinary Differential Equation (ODE).

The complementary solutions with the different cases are given as:

Case 1: $\frac{\sqrt{b^2-4ac}}{2}>0;\quad y_c=c_1e^{m_1x}+c_2e^{m_2x}$ where $c_1,c_2$are constants *2.20*

Case 2: $\frac{\sqrt{b^2-4ac}}{2}=0;\quad y_c=A(1+x)e^{mx}$where $A=$ constant *2.21*

Case 3: $\frac{\sqrt{b^2-4ac}}{2}<0;\quad y_c=c_1e^{(a+ib)x}+c_2e^{(a-ib)x}$ where c_1,c_2 are constants *2.22*

$$m_1=-\frac{p}{2}+\frac{\sqrt{p^2-4q}}{2} \quad 2.23$$

Recall we set $\frac{1}{v}T_o=p,\frac{1}{v^2}[k+\gamma^2\beta_1^2]=qm_1=-\frac{\frac{1}{v}T_o}{2}+\frac{1}{2}\sqrt{\frac{1}{v^2}T_o{}^2-\frac{4}{v^2}[k+\gamma^2\beta_1^2]}$ *2.24*

Simplifying

$$m_1=-\frac{1}{2v}(T_o-\sqrt{T_o{}^2-4[k+\gamma^2\beta_1^2]}) \quad 2.25$$

Such that

$$m_2=-\frac{1}{2v}(T_o+\sqrt{T_o{}^2-4[k+\gamma^2\beta_1^2]}) \quad 2.26$$

2.1.1 Case 1

For case 1:$\frac{\sqrt{b^2-4ac}}{2}>0;$ *2.27*

$$y_c=c_1e^{-\frac{1}{2v}\left(T_o-\sqrt{T_o{}^2-[k+\gamma^2B_1^2]}\right)x}+c_2e^{-\frac{1}{2v}\left(T_o+\sqrt{T_o{}^2-[k+\gamma^2B_1^2]}\right)x} \quad 2.28$$

Solving for the particular solution, using the technique of variation of parameters.

$$y_p = u_1 y_1 + u_2 y_2 \qquad 2.29$$

From *2.28* we have the identifiers as y_1 and y_2 respectively given as;

$$y_1 = e^{-\frac{x}{2v}\left(T_o - \sqrt{T_o{}^2 - [k+\gamma^2\beta_1^2]}\right)} \qquad 2.30$$

$$y_2 = e^{-\frac{x}{2v}\left(T_o + \sqrt{T_o{}^2 - [k+\gamma^2\beta_1^2]}\right)} \qquad 2.31$$

$$y_1' = -\frac{1}{2v}\left(T_o - \sqrt{T_o{}^2 - [k+\gamma^2\beta_1^2]}\right) e^{-\frac{x}{2v}\left(T_o - \sqrt{T_o{}^2 - [k+\gamma^2\beta_1^2]}\right)} \qquad 2.32$$

$$y_2' = -\frac{1}{2v}\left(T_o + \sqrt{T_o{}^2 - [k+\gamma^2\beta_1^2]}\right) e^{-\frac{x}{2v}\left(T_o + \sqrt{T_o{}^2 - [k+\gamma^2\beta_1^2]}\right)} \qquad 2.33$$

Computing the Wrouskian matrix for y_1 and y_2, we have;

$$W(y_1 y_2) = \begin{vmatrix} y_1 & y_2 \\ y_1' & y_2' \end{vmatrix} \qquad 2.34$$

$$W(y_1 y_2) = \begin{vmatrix} e^{-\frac{x}{2v}\left(T_o - \sqrt{T_o{}^2 - [k+\gamma^2\beta_1^2]}\right)} & e^{-\frac{x}{2v}\left(T_o + \sqrt{T_o{}^2 - [k+\gamma^2\beta_1^2]}\right)} \\ -\frac{1}{2v}\left(T_o - \sqrt{T_o{}^2 - [k+\gamma^2\beta_1^2]}\right) y_1 & -\frac{1}{2v}\left(T_o + \sqrt{T_o{}^2 - [k+\gamma^2\beta_1^2]}\right) y_2 \end{vmatrix}$$

2.35

$$W(y_1, y_2) = -\frac{1}{2v}\left(T_o + \sqrt{T_o{}^2 - [k+\gamma^2\beta_1^2]}\right) e^{-\frac{T_o}{v}x} + \frac{1}{2v}\left(T_o - \sqrt{T_o{}^2 - [k+\gamma^2\beta_1^2]}\right) e^{-\frac{T_o}{v}x}$$

2.36

$$W(y_1, y_2) = -\frac{\left(\sqrt{T_o{}^2 - 4[k+\gamma^2\beta_1^2]}\right)}{v} e^{-\frac{T_o}{v}x} \qquad 2.37$$

Computing the Wrouskian matrix for f_x and y_2, we have;

$$W_1(f_x, y_2) = \begin{vmatrix} 0 & e^{-\frac{x}{2v}\left(T_o + \sqrt{T_o{}^2 - [k+\gamma^2\beta_1^2]}\right)} \\ \frac{\gamma\beta_1^2 M_o}{T_1 v^2} & -\frac{1}{2v}\left(T_o + \sqrt{T_o{}^2 - [k+\gamma^2\beta_1^2]}\right) e^{-\frac{x}{2v}\left(T_o + \sqrt{T_o{}^2 - [k+\gamma^2\beta_1^2]}\right)} \end{vmatrix} \qquad 2.38$$

$$W_1 = -\frac{\gamma\beta_1^2 M_o}{T_1 v^2} e^{-\frac{x}{2v}\left(T_o + \sqrt{T_o{}^2 - 4[k+\gamma^2\beta_1^2]}\right)} \qquad 2.39$$

Computing the Wrouskian matrix for y_1 and f_x, we have;

$$W_2 = \begin{vmatrix} e^{-\frac{x}{2v}\left(T_o-\sqrt{T_o{}^2-[k+\gamma^2\beta_1^2]}\right)} & 0 \\ -\frac{1}{2v}\{T_o-\sqrt{T_o{}^2-[k+\gamma^2\beta_1^2]}\}e^{-\frac{x}{2v}\left(T_o-\sqrt{T_o{}^2-[k+\gamma^2\beta_1^2]}\right)} & \frac{\gamma\beta_1^2 M_o}{T_1 v^2} \end{vmatrix} \quad 2.40$$

$$W_2 = \frac{\gamma\beta_1^2 M_o}{T_1 v^2} \mathrm{e}^{-\frac{x}{2v}\left(T_o-\sqrt{T_o{}^2-4[k+\gamma^2\beta_1^2]}\right)} \quad 2.41$$

Dividing equation *2.39* with equation *2.37* and then integrate -

$$\mathrm{u}_1 = \int \frac{W_1}{W} dx = \int \frac{-\frac{\gamma\beta_1^2 M_o}{T_1 v^2}\mathrm{e}^{-\frac{x}{2v}\left(T_o+\sqrt{T_o{}^2-[k+\gamma^2\beta_1^2]}\right)}}{-\frac{\left(\sqrt{\mathrm{T_o}{}^2-4[\mathrm{k}+\gamma^2\beta_1^2]}\right)}{v}e^{-\frac{T_o}{v}x}} dx \quad 2.42$$

Simplifying;

$$\mathrm{u}_1 = \frac{\gamma\beta_1^2 M_o}{T_1 v\sqrt{T_o{}^2-[k+\gamma^2\beta_1^2]}} \int \mathrm{e}^{\frac{x}{2v}\left(T_o-\sqrt{T_o{}^2-[k+\gamma^2\beta_1^2]}\right)} dx \quad 2.43$$

Integrating with respect to x

$$\mathrm{u}_1 = \frac{\gamma\beta_1^2 M_o}{T_1 v\sqrt{T_o{}^2-[k+\gamma^2\beta_1^2]}} \cdot \frac{2v}{\left(T_o+\sqrt{T_o{}^2-[k+\gamma^2\beta_1^2]}\right)} \mathrm{e}^{\frac{x}{2v}\left(T_o-\sqrt{T_o{}^2-[k+\gamma^2\beta_1^2]}\right)} \quad 2.44$$

Simplifying

$$\mathrm{u}_1 = \frac{2\gamma\beta_1^2 M_o}{T_o T_1\sqrt{T_o{}^2-[k+\gamma^2\beta_1^2]}+T_1(T_o{}^2-[k+\gamma^2\beta_1^2])} \mathrm{e}^{\frac{x}{2v}\left(T_o-\sqrt{T_o{}^2-[k+\gamma^2\beta_1^2]}\right)} \quad 2.45$$

$$\mathrm{u}_1\mathrm{y}_1 = \frac{2\gamma\beta_1^2 M_o}{T_o T_1\sqrt{T_o{}^2-[k+\gamma^2\beta_1^2]}+T_1(T_o{}^2-[k+\gamma^2\beta_1^2])} \mathrm{e}^{\frac{x}{2v}\left(T_o-\sqrt{T_o{}^2-[k+\gamma^2\beta_1^2]}\right)} e^{-\frac{x}{2v}\left(T_o-\sqrt{T_o{}^2-[k+\gamma^2\beta_1^2]}\right)}$$

2.46

$$\mathrm{u}_1\mathrm{y}_1 = \frac{2\gamma\beta_1^2 M_o}{T_o T_1\sqrt{T_o{}^2-[k+\gamma^2\beta_1^2]}+T_1(T_o{}^2-[k+\gamma^2\beta_1^2])} \quad 2.47$$

Also, dividing the Wrouskian,W_2 with the Wrouskian, W and then integrate.

$$\mathrm{u}_2 = \int \frac{W_2}{w} dx = \int \frac{\frac{\gamma\beta_1^2 M_o}{T_1 v^2}\mathrm{e}^{-\frac{x}{2v}\left(T_o-\sqrt{T_o{}^2-[k+\gamma^2\beta_1^2]}\right)}}{-\frac{\left(\sqrt{T_o{}^2-[k+\gamma^2\beta_1^2]}\right)}{v}\mathrm{e}^{-2\frac{\mathrm{T_o}}{v}x}} dx$$

2.48

Simplifying

$$u_2 = -\frac{\gamma\beta_1^2 M_o}{T_1 v\sqrt{T_o{}^2-[k+\gamma^2\beta_1^2]}}\int e^{\frac{x}{2v}\left(T_o+\sqrt{T_o{}^2-[k+\gamma^2\beta_1^2]}\right)}dx \qquad 2.49$$

Integrating with respect to x

$$u_2 = -\frac{\gamma\beta_1^2 M_o}{T_1 v\sqrt{T_o{}^2-[k+\gamma^2\beta_1^2]}}\cdot\frac{2v}{\left(T_o-\sqrt{T_o{}^2-[k+\gamma^2\beta_1^2]}\right)}e^{\frac{x}{2v}\left(T_o+\sqrt{T_o{}^2-[k+\gamma^2\beta_1^2]}\right)} \qquad 2.50$$

Simplifying

$$u_2 = -\frac{2\gamma\beta_1^2 M_o}{T_o T_1\sqrt{T_o{}^2-[k+\gamma^2\beta_1^2]}-T_1(T_o{}^2-[k+\gamma^2\beta_1^2])}e^{\frac{x}{2v}\left(T_o+\sqrt{T_o{}^2-[k+\gamma^2\beta_1^2]}\right)} \qquad 2.51$$

$$u_2y_2 = -\frac{\gamma\beta_1^2 M_o}{T_o T_1\sqrt{T_o{}^2-[k+\gamma^2\beta_1^2]}-T_1(T_o{}^2-[k+\gamma^2\beta_1^2])}e^{\frac{x}{2v}\left(T_o+\sqrt{T_o{}^2-[k+\gamma^2\beta_1^2]}\right)}.e^{-\frac{x}{2v}\left(T_o+\sqrt{T_o{}^2-[k+\gamma^2\beta_1^2]}\right)}$$

2.52

$$u_2y_2 = -\frac{\gamma\beta_1^2 M_o}{T_o T_1\sqrt{T_o{}^2-[k+\gamma^2\beta_1^2]}-T_1(T_o{}^2-[k+\gamma^2\beta_1^2])} \qquad 2.53$$

Recall $y_p = u_1y_1 + u_2y_2$ *2.54*

$$y_p = \frac{\gamma\beta_1^2 M_o}{2T_o T_1\sqrt{T_o{}^2-[k+\gamma^2\beta_1^2]}+2T_1(T_o{}^2-[k+\gamma^2\beta_1^2])} - \frac{\gamma\beta_1^2 M_o}{2T_o T_1\sqrt{T_o{}^2-[k+\gamma^2\beta_1^2]}-2T_1(T_o{}^2-[k+\gamma^2\beta_1^2])}$$

2.55

Simplifying

$$y_p = \gamma\beta_1^2 M_o\left(\frac{1}{2T_o T_1\sqrt{T_o{}^2-[k+\gamma^2\beta_1^2]}+2T_1(T_o{}^2-4[k+\gamma^2\beta_1^2])} - \frac{1}{2T_o T_1\sqrt{T_o{}^2-[k+\gamma^2\beta_1^2]}-2T_1(T_o{}^2-[k+\gamma^2\beta_1^2])}\right) \qquad 2.56$$

$$y_p = \gamma\beta_1^2\, M_o\left(\frac{T_o T_1\sqrt{T_o{}^2-[k+\gamma^2\beta_1^2]}-T_1(T_o{}^2-4[k+\gamma^2\beta_1^2])-\left(T_o T_1\sqrt{T_o{}^2-[k+\gamma^2\beta_1^2]}+T_1(T_o{}^2-[k+\gamma^2\beta_1^2])\right)}{\left(T_o T_1\sqrt{T_o{}^2-[k+\gamma^2\beta_1^2]}+T_1(T_o{}^2-[k+\gamma^2\beta_1^2])\right)\left(T_o T_1\sqrt{T_o{}^2-[k+\gamma^2\beta_1^2]}-T_1(T_o{}^2-[k+\gamma^2\beta_1^2])\right)}\right) \qquad 2.57$$

$$y_p = \gamma\beta_1^2 M_o\left(\frac{-2T_1(T_o{}^2-[k+\gamma^2\beta_1^2])}{\left(T_1{}^2T_0{}^2(T_o{}^2-[k+\gamma^2\beta_1^2])-T_1{}^2(T_o{}^2-[k+\gamma^2\beta_1^2])\right)}\right) \qquad 2.58$$

Comparing common factors in numerator with denominator, we have.

$$y_p = -\frac{2\gamma\beta_1^2 M_o}{(T_1T_o{}^2-T_1)} \qquad 2.59$$

Hence the general solution to Case 1: $\frac{\sqrt{b^2-4ac}}{2} > 0$; *2.60*

$$y = y_p + y_c \qquad 2.61$$

$$y = c_1 e^{-\frac{1}{2v}\left(T_o - \sqrt{T_o{}^2 - [k+\gamma^2\beta_1^2]}\right)x} + c_2 e^{-\frac{1}{2v}\left(T_o + \sqrt{T_o{}^2 - [k+\gamma^2\beta_1^2]}\right)x} - \frac{2\gamma\beta_1^2 M_o}{(T_1 T_o{}^2 - T_1)} \qquad 2.62$$

2.1.2 Case 2

Similarly, for Case 2: $\frac{\sqrt{b^2-4ac}}{2} = 0$, the general solution is

$$y = A(1+x)e^{-\frac{T_o}{v}x} + \frac{4\gamma\beta_1 M_o}{T_0{}^2 T_1} \qquad 2.63$$

2.1.3 Case 3

For case 3: $\frac{\sqrt{b^2-4ac}}{2} < 0$;we have the general solution as $y = y_c + y_p$

$$y = e^{-\frac{T_o x}{2v}}\left(c_1 \cos\frac{x\sqrt{T_o{}^2 - [k+\gamma^2\beta_1^2]}}{2v} + c_2 \sin\frac{x\sqrt{T_o{}^2 - [k+\gamma^2\beta_1^2]}}{2v}\right) + \frac{4\gamma\beta_1 M_o}{T_1(4v^2h^2 + T_o{}^2)} \qquad 2.64$$

$$\text{Recall } \frac{\sqrt{T_o{}^2 - [k+\gamma^2\beta_1^2]}}{2v} = h \qquad 2.65$$

$$y = e^{-\frac{T_o x}{2v}}\left(c_1 \cos\frac{x\sqrt{T_o{}^2 - [k+\gamma^2\beta_1^2]}}{2v} + c_2 \sin\frac{x\sqrt{T_o{}^2 - [k+\gamma^2\beta_1^2]}}{2v}\right) + \frac{4\gamma\beta_1 M_o}{T_1(2T_o{}^2 - [k+\gamma^2\beta_1^2])} \qquad 2.66$$

3.0 Results and Discussion

The graphs displayed in figures 3.1 – 3.10 show the plots for case 1, for $h > 0$; when radiofrequency $[\gamma^2\beta^2 \ll k]$ is negligible and T_2 varied while keeping T_1constant. It can be seen that before the magnetization relaxes, it is able to detect signals between when T_2 is 0.002 and 0.027. This implies that different organs in human body can be distinguished and in turn be related to their length of time (age).

Similarly, the graphs displayed in figures 3.11 – 3.20 show the plots for case 1, for $h > 0$; when radiofrequency $[\gamma^2\beta^2 \gg k]$ is greater than k and T_2 varied while keeping T_1constant. It can be seen that before the magnetization relaxes, it is able to detect signals between when T_2 is 0.002 and 0.047. This implies that different organs in human body can be distinguished and in turn be related to their length of time (age).

Case 1: For $h > 0$; when radiofrequency $[\gamma^2\beta^2 \ll k]$ is negligible.

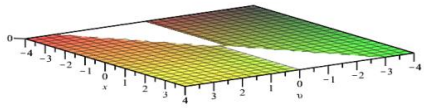

Figure 3.1 shows the plot of magnetization against velocity and distance when $T_1 = 1$ *and* $T_2 = 0.002$

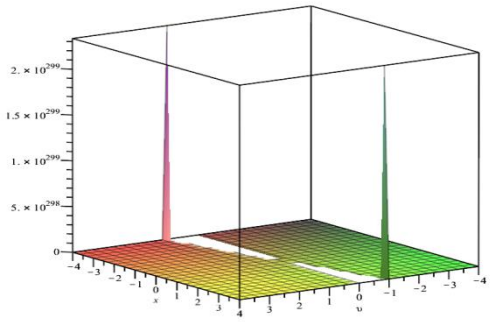

Figure 3.2 shows the plot of magnetization against velocity and distance when $T_1 = 1$ *and* $T_2 = 0.007$

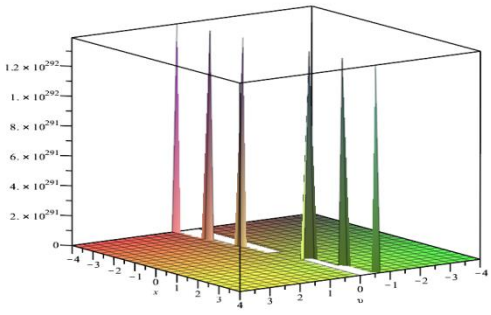

Figure 3.3 shows the plot of magnetization against velocity and distance when $T_1 = 1$ *and* $T_2 = 0.012$

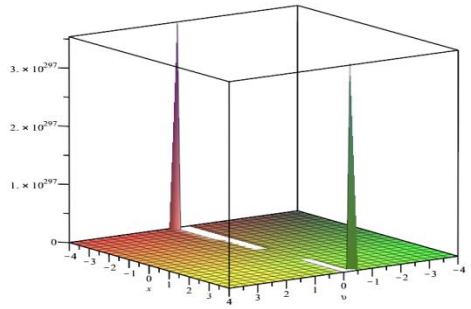

Figure 3.4 shows the plot of magnetization against velocity and distance when $T_1 = 1$ *and* $T_2 = 0.017$

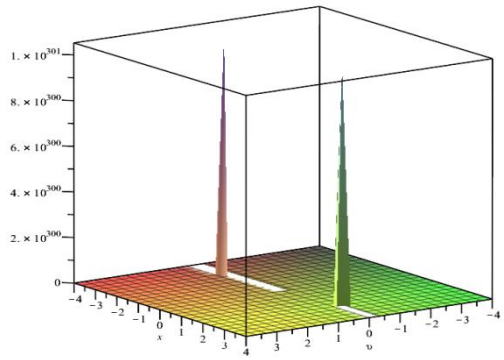

Figure 3.5 shows the plot of magnetization against velocity and distance when $T_1 = 1$ *and* $T_2 = 0.022$

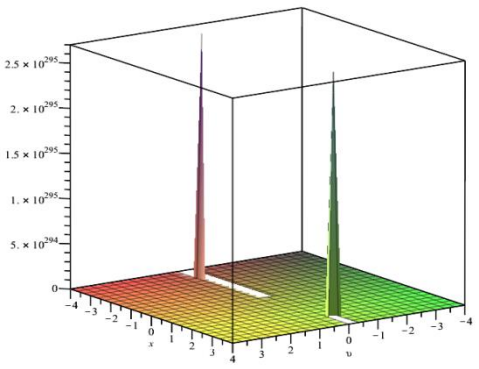

Figure 3.6 shows the plot of magnetization against velocity and distance when $T_1 = 1$ *and* $T_2 = 0.027$

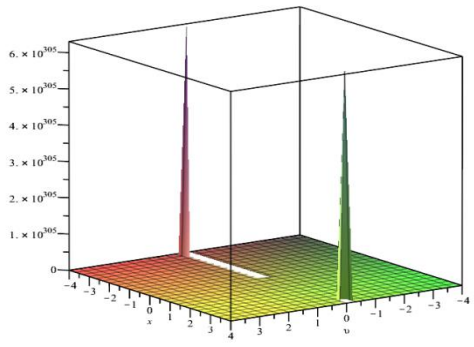

Figure 3.7 shows the plot of magnetization against velocity and distance when $T_1 = 1$ *and* $T_2 = 0.032$

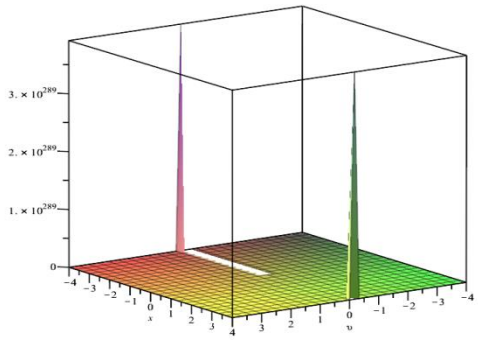

Figure 3.8 shows the plot of magnetization against velocity and distance when $T_1 = 1$ *and* $T_2 = 0.037$

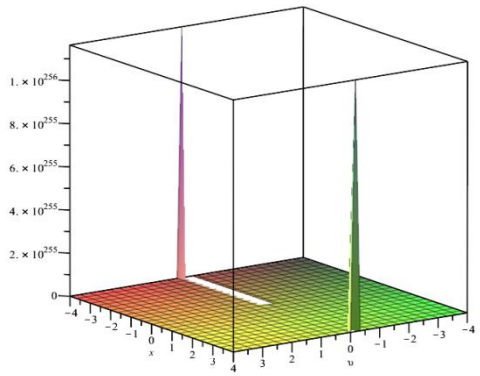

Figure 3.9 shows the plot of magnetization against velocity and distance when $T_1 = 1$ *and* $T_2 = 0.042$

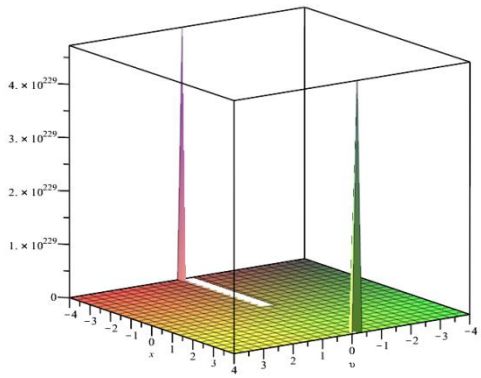

Figure 3.10 shows the plot of magnetization against velocity and distance when $T_1 = 1$ *and* $T_2 = 0.047$

Case 1: For $h > 0$; *w*hen radiofrequency $[\gamma^2\beta^2 \gg k]$ is greater than k.

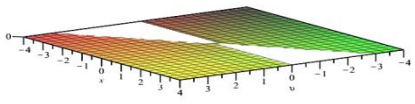

Figure 3.11 shows the plot of magnetization against velocity and distance when $T_1 = 1$ *and* $T_2 = 0.002$

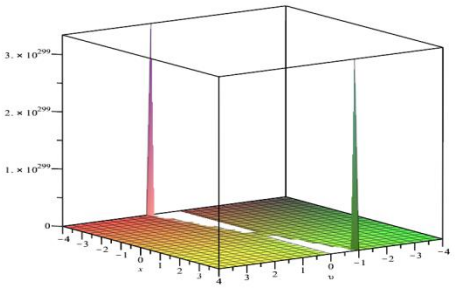

Figure 3.12 shows the plot of magnetization against velocity and distance when $T_1 = 1$ *and* $T_2 = 0.007$

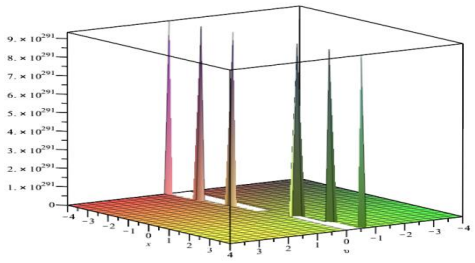

Figure 3.13 shows the plot of magnetization against velocity and distance when $T_1 = 1$ *and* $T_2 = 0.012$

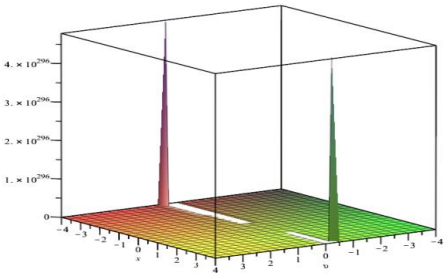

Figure 3.14 shows the plot of magnetization against velocity and distance when $T_1 = 1$ *and* $T_2 = 0.017$

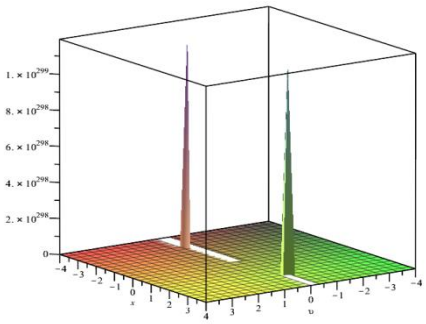

Figure 3.15 shows the plot of magnetization against velocity and distance when $T_1 = 1$ *and* $T_2 = 0.022$

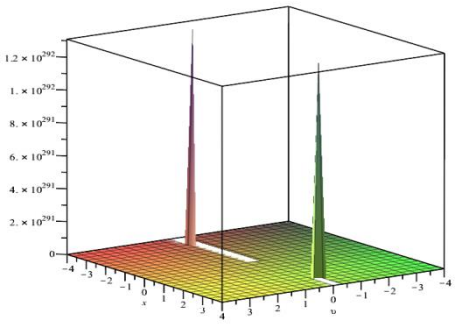

Figure 3.16 shows the plot of magnetization against velocity and distance when $T_1 = 1$ *and* $T_2 = 0.027$

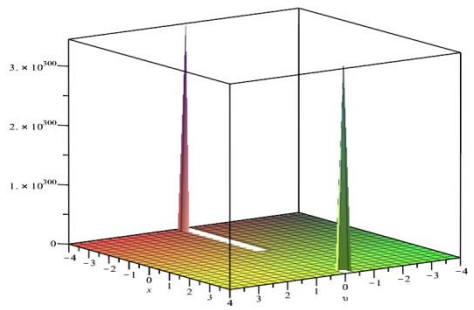

Figure 3.17 shows the plot of magnetization against velocity and distance when $T_1 = 1$ *and* $T_2 = 0.032$

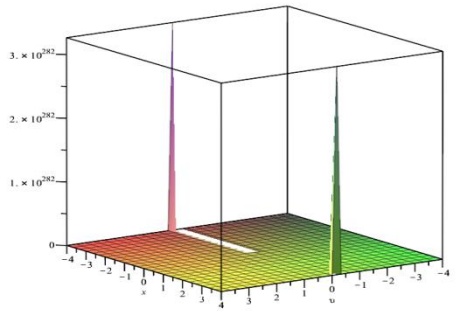

Figure 3.18 shows the plot of magnetization against velocity and distance when $T_1 = 1$ *and* $T_2 = 0.037$

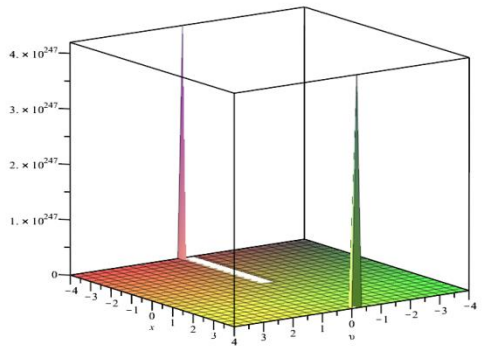

Figure 3.19 shows the plot of magnetization against velocity and distance when $T_1 = 1$ *and* $T_2 = 0.042$

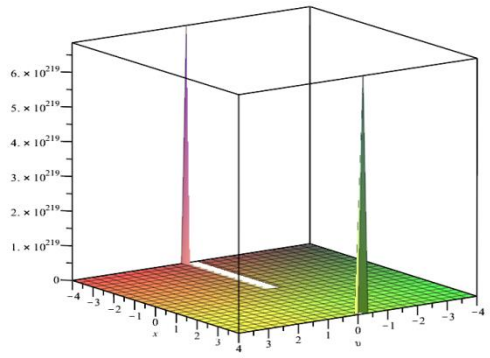

Figure 3.20 shows the plot of magnetization against velocity and distance when $T_1 = 1$ *and* $T_2 = 0.047$

4.0 Conclusion

This research work is still on-going. Hence only a part of the results has been generated and presented. So far, preliminary results generated from the work have shown the possibility of determining age of human organs from the $T_1 and\ T_2$relaxation parameters as obtained from the Bloch NMR equations. The remaining cases ($h = 0\ and\ when\ h < 0$) will eventually be examined and results generated compared and analyzed in relation to how relaxation rates could be used to estimate or determine the length of time of existence (age) of the human organ under consideration.

References

Awojoyogbe, O. B. (2009). Analytical solution of the time – dependent Bloch NMR flow equations: A Translational Mechanical Analysis. *Physica A*, 339, 437-460.

AgartzI., Saaf J., Wahlund L. and Wetterberg L.(1991). T1 and T2 Relaxation Time Estimates in the Normal Human Brain.

Badve C., Yu A.,Rogers M., Ma D., Liu Y., Schluchter M., Sunshine J., Griswold M. and Gulani V.,(2015). Simultaneous T1 and T2 Brain Relaxometry in Asymptomatic Volunteers Using MagneticResonance Fingerprinting.

Rock P. J.(2021) *https://radiopaedia.org/articles/t1-relaxation-time*.

Suzuki S.,Sakai O. and Jara4 H., (2006). Combined volumetric T1, T2 and secular-T2 quantitative MRI of the brain: age-related global changes.

Yusuf, S. I. (2010). A Study of Longitudinal and Transverse Relaxation Rates in Magnetic Resonance Imaging – MRI. A paper presented at the 4th National Conference of School of Science and Science Education, Federal University of Technology, Minna, Page 136 -151, November, 2010.

Yusuf, S. I., Aiyesimi, Y. M., Jiya M., Awojoyogbe, O. B. and Dada, M. (2019). Magnetic Resonance
Imaging of Plaques in a Cylindrical Channel. *Journal of Science, Technology, Mathematics and Education.* 15(2), 71 – 78.

A Grey-Markov Model for the Prediction of Vehicular Accident's Human Casualties along Lokoja-Abuja-Kaduna Express Way, Nigeria

*O.B. Saeed [1], Abubakar U.Y[1], Lawal Adamu[1], Usman Abubakar[2]
[1]Department of Mathematics, Federal University of Technology Minna, Nigeria
[2]Department of Statistics, Federal University of Technology Minna, Nigeria
[1]belaneetech@yahoo.com and [1]lawal.adamu@futminna.edu.ng

Abstract
Providing government of Nigeria with reliable and dependable information for road safety policy formulation to reduce loss of lives and properties along Lokoja-Abuja-Kaduna Express way is the thrust of this research. The World Health Organization (WHO) reported that road traffic accident claims roughly 1.3 million lives annually which make it one of the top causes of death worldwide. A Grey-Markov model that predicts yearly number of human casualties recorded in Vehicular accidents has been developed and implemented on Lokoja-Abuja-Kaduna express way in Nigeria. The data used in the research were collected from the archive of federal Road Safety Corps of Nigeria for a period of ten years (2010-2019). The fitted model recorded excellent performance of 95.012% *accuracy; this shows the model is reliable and dependable. Therefore, results from this model could serves as source of information for road safety policy formulation.*

Keywords: Road, Crashes, Casualty, Accident, Lokoja-Abuja-Kaduna, Express Way, Nigeria, Markov Chain and Grey-Markov

Introduction
Lokoja-Abuja-Kaduna express way is one of the major roads that connects the southern and northern parts of Nigeria. As a result of high volume of vehicular movements on this road, hundreds of road accidents that mostly result to thousands of human causalities and loss of properties are recorded every year, most of which results in deaths and disabilities (FRSCN, 2020). Due to complex factors associated with road traffic accident, its occurrence is not easily predictable and its impact has over the years affected economic and social activities of the country. This has consequently reduced Gross Domestic Product (GDP) of the country. In view of the above mentioned problems, the research is aimed at providing some quantitative information to government of Nigeria for road safety policy formulation to mitigate the loss of lives and properties. Nigeria has roughly 195,000 km of surfaced road, making it the country with largest road network in West Africa and the second largest in south of the Sahara, out of which a proportion of about 32,000 km are federal roads while 31,000km are state roads.

Road traffic crashes have been found to be influenced by many complex factors such as weather, driver factor, speed, rear by vehicular density, risk location, driver consciousness, driver fatigue nature of the rode and so on. Since Road Traffic Crash is generally a random occurrence it is therefore, quite important to select an appropriate forecasting model that will fully capture the behaviour of the system. Grey-Markov stochastic model has been selected for this purpose. Successful studies of accident occurrence have been reported in the following works: Li Qingfu *et.al* (2007) has applied Grey-Markov Model in predicting traffic volume in Manjing City, China. They concluded that the model has higher accuracy, reliability and precision in the traffic volume prediction. Presented in (Jian-Yi and Ying, 2014) is a modified Grey-Markov Model, the model was used to forecast the mine safety

accident deaths from 1990 to 2010 in China and 2001 to 2014 for coal accidents death were predicted accordingly. The result shows that the new model not only discovered the trend of the mine human error accident death toll but also overcomes the random fluctuation of data affecting precision. It was concluded that the model possesses stronger engineering application. Reported in (Xiaxia, *et.al*, 2018) is a driving risk status prediction algorithm base on Markov Chain. In the study, driving risk states were classified using clustering techniques base on feature variables describing instantaneous risk levels within time windows, were instantaneous risk levels are determined in time-to-collision and time-to-headway two-dimensional plane. Multinomial logistic models with recursive feature variable estimation method were developed to improve the traditional state transition probability estimation, which also takes into account the comprehensive effect of driving behaviour, traffic and road environment factors on the evolution of driving risk status. A "100-car" natural driving data from Virginia technology was employed for the training and validation of the prediction model. The results show that under the 5% false positive rate, the prediction algorithm could have high prediction accuracy for future medium-to-high driving risks and could meet the time line requirement of collision avoidance warning. The algorithm could contribute to timely warning or auxiliary correction to drivers in the approaching-danger state. Successful studies of vehicular accidents occurrence have also been reported in (Bamidele, 2006; John *et.al*, 2007; Nyothiri *et.al*, 2018)

Materials and Method

The Grey-Markov model consist of GM(1,1) model and Markov chain model. The Grey model deals with an uncertain system of small sample size and poor information involving both known and unknown information. The goal of Grey prediction is to whitening the system and reveals the unknown. However, in Grey model problem of poor fitting degree and low prediction accuracy may emerge when the change rate of the original data is too large. The Grey –Markov Model (GMM) is an extension of Grey Model (GM) to further reduce the prediction error. The Grey-Markov Model is made up of two components namely Grey and Markov chain model; Markov chain model can handle a situation where the change rate of the original data is too large. Hence, Markov Chain Model makes it possible to solve the problems mentioned in Grey Model. The Grey-Markov Model was established base on the advantage of both methods which adopt GM(1,1) Model to study development regulation of data sequence and uses Markov Models to study vibrating irregularities of data sequence. In general, the combination of the two models have been found to improve the prediction accuracy (Mao and Sun, 2011). As earlier mentioned we shall begin our prediction with GM(1,1) model after which we shall improve the prediction accuracy using Grey-Markov model.

The Grey-System Model GM(1,1)

The raw data series in grey GM(1,1) model is represented by $x^{(0)}(k), k = 1,2,3,..., n, x^{(0)}(k) \geq 0$ and it can also be represented as:

$$X^{(0)}(k) = \left(x^{(0)}(1), x^{(0)}(2), x^{(0)}(3),..., x^{(0)}(n)\right) \quad (1)$$

The accumulated generating sequence is given as:

$$X^{(1)}(k) = \left(x^{(1)}(1), x^{(1)}(2), x^{(1)}(3),..., x^{(1)}(n)\right) \quad (2)$$

Where $X^{(0)}(k) = \sum_{i=1}^{k} x^{(0)}(i), k = 1,2,..., n$ (3)

$$x^{(0)}(k) + ax^{(1)}(k) = b \quad (4)$$

Equation (4) represents the original form of the GM(1,1) model, is a difference equation. The symbol GM(1,1) stands for first order Grey Model in one variable.

Equation (4) is also represented as equation (5)

$$\frac{dx^{(1)}}{dt} + ax^{(1)} = b \quad (5)$$

Equation (5) is a differential equation, where a and b are parameters to be identified. a is called developing coefficient and b is grey input.

Equation (6) is the solution of equation (5)

$$\hat{x}^{(1)}(k+1) = \left(x^{(1)}(0) - \frac{b}{a} \right) e^{-ak} + \frac{b}{a} \quad (6)$$

Equation (6) is the time response function while parameters a and b are estimated using Least Square Method as follows:

$$\begin{bmatrix} a \\ b \end{bmatrix} = \left[B^T B \right]^{-1} B^T Y \quad (7)$$

Where, $B = \begin{bmatrix} \frac{-[x^{(1)}(1) + x^{(1)}(2)]}{2} & 1 \\ \frac{-[x^{(1)}(2) + x^{(1)}(3)]}{2} & 1 \\ \frac{-[x^{(1)}(3) + x^{(1)}(4)]}{2} & 1 \\ \frac{-[x^{(1)}(4) + x^{(1)}(5)]}{2} & 1 \\ \frac{-[x^{(1)}(5) + x^{(1)}(6)]}{2} & 1 \\ \vdots & \vdots \\ \frac{-[x^{(1)}(n-1) + x^{(1)}(n]}{2} & 1 \end{bmatrix}$ (8)

$$Y = \left[x^{(0)}(2), x^{(0)}(3), x^{(0)}(4),..., x^{(0)}(n) \right]^T \quad (9)$$

The reduction value of equation (6) is given below:

$$\hat{x}^{(0)}(k+1) = \hat{x}^{(1)}(k+1) - \hat{x}^{(1)}(k) = \left(1 - e^{a}\right) \left(x^{(0)}(1) - \frac{b}{a} \right) e^{-ak} \quad (10)$$

Prediction Accuracy Test

To determine the accuracy of our prediction, we shall adopt mean absolute percentage error (MAPE).

This tool is often used for determining prediction accuracy showing the same characteristics i.e. the smaller the value, the higher the prediction accuracy.

MAPE

$$MAPE = \frac{1}{n}\sum_{i=1}^{n}\left|\frac{y_i - \hat{y}_i}{y_i}\right| \times 100\% \qquad (11)$$

Where;

$\hat{y}_i$ is the Grey Model predicted value.

y_i is the Grey-Model actual value.

n is the number of prediction samples.

Lewis (1982) divided the prediction accuracy of models into four grades and the division of prediction accuracy grades is shown in the table below:

Table 1: Prediction Accuracy Test

MAPE	Prediction Accuracy
$<10\%$	High
$10\%-20\%$	Good
$20\%-50\%$	Feasible
$>50\%$	Low

The Grey- Markov Model

The Grey-Markov model (GMM) is an extension of Grey Model (GM) to further reduce prediction errors. In Grey model, the problems of poor fitting degree and low prediction accuracy may emerge when the change range of original data is too large. However, these problems can be well resolved by adopting Markov chain which can narrow down the prediction interval and improve the prediction accuracy. Markov stochastic process improves these limitations of Grey model because it reflects the stochastic volatility impact on elements by determining the transfer law of states (Ducan *et.al*, 1998).

Building the Grey-Markov Model

First step in building the GMM is to divide the residual errors into q states where each state satisfies the equi-probability principle and is defined as $R_{1,}R_{2,}\cdots,R_q$. Next, the construction of the transition matrix is done by determining the probability from state R_i to state R_j which results in the transition matrix P.

$$P^{(1)} = \begin{bmatrix} p_{(11)}^{(1)} & p_{(12)}^{(1)} & \cdots & p_{(1q)}^{(1)} \\ p_{(21)}^{(1)} & p_{(22)}^{(1)} & \cdots & p_{(2q)}^{(1)} \\ \vdots & \vdots & \cdots & \vdots \\ p_{(q1)}^{(1)} & p_{(q2)}^{(1)} & \cdots & p_{(qq)}^{(1)} \end{bmatrix} \quad (12)$$

$$P^{(m)} = \begin{bmatrix} p_{(11)}^{(m)} & p_{(12)}^{(m)} & \cdots & p_{(1q)}^{(m)} \\ p_{(21)}^{(m)} & p_{(22)}^{(m)} & \cdots & p_{(2q)}^{(m)} \\ \vdots & \vdots & \cdots & \vdots \\ p_{(q1)}^{(m)} & p_{(q2)}^{(m)} & \cdots & p_{(qq)}^{(m)} \end{bmatrix} \quad (13)$$

Where $P_{ij}^{(m)} = \dfrac{M_{ij}^{(m)}}{m_i}, (i, j = 1,2,3,..., L)$, $M_{ij}^{(m)}$ stands for the transition from R_i to R_j in m steps and m_i is the number of state R_i.

Next, the residual error must be confirmed.

Let the interval median in $[R_{i-}, R_{i+}]$ be residual error forecasting value as follows:

$$\hat{e} = \tfrac{1}{2}[R_{i-} + R_{i+}] \quad (14)$$

Hence, the Grey-Markov model is obtained as:

$$\hat{Y}(k+1) = [1+\hat{e}]\hat{x}^{(0)}(k+1) \quad (15)$$

Where, $\hat{x}^{(0)}(k+1) = \hat{x}^{(1)}(k+1) - \hat{x}^{(1)}(k)$

Hence:

$$\hat{Y}(k+1) = \left[1 + \tfrac{1}{2}(R_{i-} + R_{i+})\right]\hat{x}^{(0)}(k+1) \quad (16)$$

Application of Grey System Model for Prediction of Vehicular Accident's Human Casualties along Lokoja-Abuja-Kaduna Expressway

The data used in this research were collected from the archive of Federal Road Safety of Nigeria for the period of ten years (2010-2019).

The summary of the data is presented in table 2 below:

Table 2: Summary of Number of Vehicular Accident's Human Casualties for Period of Ten Years

S/N	YEAR	ACTUAL NUMBER OF HUMAN CASUALITIES WITHIN THE YEAR
1	2010	2883
2	2011	3629
3	2012	2623
4	2013	4273
5	2014	3200
6	2015	2913
7	2016	2822
8	2017	3044
9	2018	3131
10	2019	2790

Using equation (1) and table (2), we obtain equation 17 below

$$X^{(0)} = (2883, 3629, 2623, 4273, 3200, 2913, 2822, 3044, 3131, 2790) \quad (17)$$

From equation (2) we obtain the accumulated generating sequence as given below:

$$X^{(1)} = (2883, 6512, 9135, 13408, 16608, 19521, 22343, 25387, 28518, 31308) \quad (18)$$

Equation (19) below is obtained using equation (7)

$$\hat{a} = \begin{bmatrix} 0.02463 \\ 3592.26 \end{bmatrix} = \begin{bmatrix} a \\ b \end{bmatrix} \quad (19)$$

Where $a = 0.02463,\ b = 3592.26$

Substituting for a and b in equation (6), we obtained equation (20) below:

$$\hat{x}^{(1)}(k+1) = 14584.896 - 14296.596e^{-0.02463k} \quad (20)$$

Evaluating equation (20) for $k = 0,1,...,9$ we obtained the following values below:

$$\hat{X}^{(1)} = (2883, 6361, 9755, 13066, 16296, 19448, 22524, 25524, 28451, 31308) \quad (21)$$

We compute the simulated value using equation (22) below:

$$\hat{x}^{(0)}(k) = \hat{x}^{(1)}(k) - \hat{x}^{(1)}(k-1) \quad (22)$$

$$\hat{X}^{(0)} = (2883, 3478, 3394, 3311, 3230, 3152, 3076, 3000, 2927, 2857) \quad (23)$$

Equation (23) is the simulated values from 2010-2019

Table 3: Comparison of Actual and Grey simulated Value for Vehicular Accident's Human Casualties along Lokoja-Abuja-Kaduna Express Way from Year 2010-2019.

YEAR OF CRASH	ACTUAL NUMBER OF CRASH WITHIN THE YEAR	GREY-MODEL PREDICTION VALUES	RESIDUAL ERROR	RELATIVE ERROR (%)
2010	2883	2883	0	0
2011	3629	3478	151	4.16
2012	2623	3394	-771	-29.39
2013	4273	3311	962	22.51
2014	3200	3230	-30	-0.94
2015	2913	3152	-239	-8.20
2016	2822	3076	-254	-9.00
2017	3044	3000	44	1.45
2018	3131	2927	204	6.52
2019	2790	2857	-67	-2.40

Using equation (11), we observed from table (3) that:

$MAPE = 8.457\%$

$ACCURACY = 100\% - 8.457\% = 91.543\%$

The above figure indicates that the prediction accuracy is good; however, this prediction accuracy level can be improved using Grey-Markov Model.

Application of Grey-Markov Model for Prediction of Vehicular Accident's Human Casualties along Lokoja-Abuja-Kaduna Express Way

The prediction accuracy of the GM(1,1) can be improve by apply the Grey-Markov model. We begin by finding error state of each year. To achieve this, the error is partitioned into states. Due to the small sample size in this study, the error can be divided into three states respectively, using E_1, E_2, E_3 as shown in the table below:

Table 4: Error Partition

State	$E_1(\%)$	$E_2(\%)$	$E_3(\%)$
Error Range	$-29.39 \sim -12.09$	$-12.09 \sim 5.21$	$5.21 \sim 22.51$

From Table (4), we obtained the error states in Table (5)

Table 5: State Division for Actual Vehicular Accident's Human Casualties along Lokoja-Abuja-Kaduna Express Way

S/N	Year	Actual Number Of Human Casualties Within The Year	Grey Model Simulated Values	Relative Error (%)	Error States
1	2010	2883	2883	0	E_2
2	2011	3629	3478	4.16	E_2

3	2012	2623	3394	-29.39	E_1
4	2013	4273	3311	22.51	E_3
5	2014	3200	3230	-0.94	E_2
6	2015	2913	3152	-8.20	E_2
7	2016	2822	3076	-9.00	E_2
8	2017	3044	3000	1.45	E_2
9	2018	3131	2927	6.52	E_3
10	2019	2790	2857	-2.40	E_2

Grey Forecasting for Vehicular Accident's Human Casualties from Year 2020-2023

Evaluating equation (20) for $k = 9,10,11,12,13$

The predicted values are computed using equation (22) and the results are presented in table 8.

Table 6: Grey-Model Predicted Values from Year 2020-2023

Year	Grey Model Prediction Value
2020	2719
2021	2653
2022	2588
2023	2525

From Table (5), we construct transition probability matrix using equation (12)

$$P^{(1)} = \begin{bmatrix} 0 & 0 & 1 \\ 0.17 & 0.67 & 0.17 \\ 0 & 1 & 0 \end{bmatrix} \quad (24)$$

The two steps, three steps and four steps transition probability matrix is calculated using equation (13), hence we have them respectively:

$$P^{(2)} = \begin{bmatrix} 0 & 1 & 0 \\ 0.114 & 0.619 & 0.284 \\ 0.17 & 0.67 & 0.17 \end{bmatrix} \quad (25)$$

$$P^{(3)} = \begin{bmatrix} 0.17 & 0.67 & 0.17 \\ 0.105 & 0.699 & 0.219 \\ 0.114 & 0.619 & 0.284 \end{bmatrix} \quad (26)$$

$$P^{(4)} = \begin{bmatrix} 0.114 & 0.619 & 0.284 \\ 0.119 & 0.687 & 0.223 \\ 0.105 & 0.699 & 0.219 \end{bmatrix} \quad (27)$$

Evaluating equation (16) for $k = 0,1,2,3,...,9$

$$\hat{Y}_1 = \left[1 + \tfrac{1}{2}(-12.09\% + 5.21\%)\right] * 2883 = 2784$$
$$\hat{Y}_2 = \left[1 + \tfrac{1}{2}(-12.09\% + 5.21\%)\right] * 3478 = 3358$$
$$\hat{Y}_3 = \left[1 + \tfrac{1}{2}(-29.39\% - 12.09\%)\right] * 3394 = 2690$$
$$\hat{Y}_4 = \left[1 + \tfrac{1}{2}(5.21\% + 22.51\%)\right] * 3311 = 3770$$
$$\hat{Y}_5 = \left[1 + \tfrac{1}{2}(-12.09\% + 5.21\%)\right] * 3230 = 3119$$
$$\hat{Y}_6 = \left[1 + \tfrac{1}{2}(-12.09\% + 5.21\%)\right] * 3152 = 3044$$
$$\hat{Y}_7 = \left[1 + \tfrac{1}{2}(-12.09\% + 5.21\%)\right] * 3076 = 2970$$
$$\hat{Y}_8 = \left[1 + \tfrac{1}{2}(-12.09\% + 5.21\%)\right] * 3000 = 2897$$
$$\hat{Y}_9 = \left[1 + \tfrac{1}{2}(5.21\% + 22.51\%)\right] * 2927 = 3333$$
$$\hat{Y}_{10} = \left[1 + \tfrac{1}{2}(-12.09\% + 5.21)\right] * 2857 = 2759$$

We obtained the Grey-Markov Simulated Values presented in Table (6)

Table 7: Comparison of Actual and Grey-Markov Simulated Value for Vehicular Accident's Human Casualties along Lokoja-Abuja-Kaduna Expressway for the Period of 2010-2019

YEAR	ACTUAL NUMBER OF HUMAN CASUALTY WITHIN THE YEAR	GREY-MARKOV MODEL PREDICTION VALUES	RESIDUAL ERROR	Relative Error (%)
2010	2883	2784	-346	-15.2
2011	3629	3358	454	14.8
2012	2623	2690	237	12.6
2013	4273	3770	840	19.8
2014	3200	3119	-171	-5.3
2015	2913	3044	260	9.7
2016	2822	2970	-424	-15.0
2017	3044	2897	-173	-5.7
2018	3131	3333	-176	-5.8
2019	2790	2759	-290	-10.4

Using equation (11), we observed from Table (6) that,

$$MAPE = \frac{1}{n}\sum_{i=1}^{n}\left|\frac{y_i - \hat{y}_i}{y_i}\right| \times 100\% = 4.988\%$$

$ACCURACY = 100\% - 4.988\% = 95.012\%$. This implies that, the prediction accuracy has been improved from 91.543% to 95.012%

The above figure also indicates high accuracy level.

Table 8: Comparison of Actual Value, Grey Model and Grey-Markov Model Simulated Values for Road Accident's Human Casualties along Lokoja-Abuja-Kaduna Express high way

Year	Actual Number Of Human Casualties Within The Year	Grey Model Simulated Values	Grey-Markov Model Simulated Values
2010	2883	2883	2784
2011	3629	3478	3358
2012	2623	3394	2690
2013	4273	3311	3770
2014	3200	3230	3119
2015	2913	3152	3044
2016	2822	3076	2970
2017	3044	3000	2897
2018	3131	2927	3333
2019	2790	2857	2759

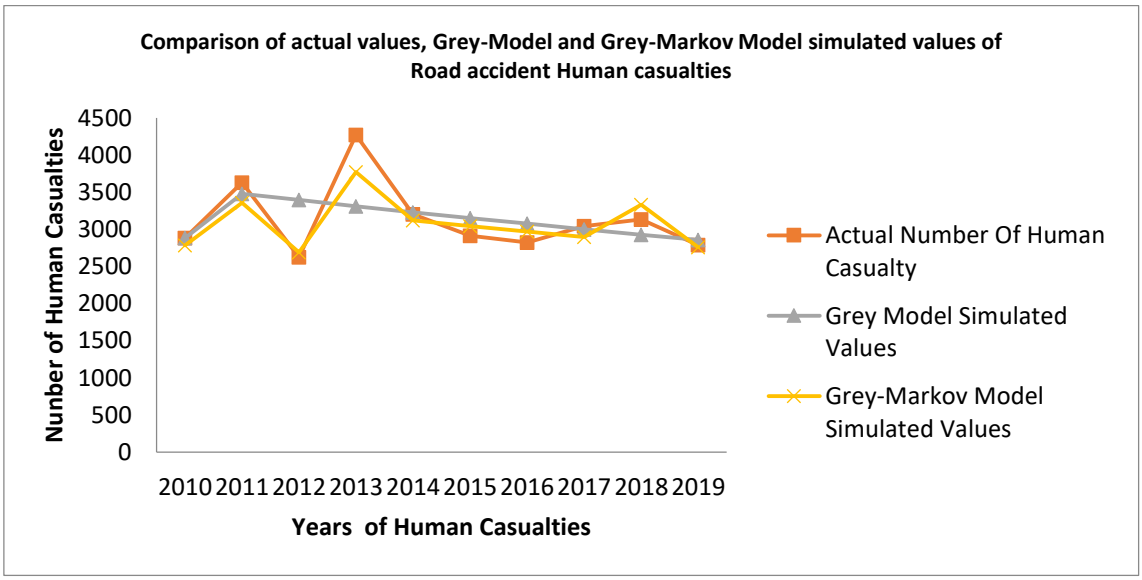

Graph 1: Comparison of Actual Value, Grey Model and Grey-Markov Model Simulated Values for Vehicular Accident's Human along Lokoja-Abuja-Kaduna Express way.

Grey-Markov Model Prediction from 2020-2023

To achieve this, we obtained the error state for year 2020 to 2023 through the use of equation (25) to (27) and the information in table (5) after which we use equation (16) and the error states to make prediction from 2020 to 2023. The results are presented in table 9.

Table 9: Grey-Markov prediction value from 2020-2023.

Year	Grey-Markov Model Prediction Value
2020	2625
2021	2562
2022	2499
2023	2438

Table 10: Comparison of Grey and Grey-Markov model predicted values from year 2020-2-23

Year	Grey-Model Prediction Values	Grey-Markov Model Prediction Values
2020	2719	2625
2021	2653	2562
2022	2588	2499
2023	2525	2438

5. Conclusion

The G,M(1,1) system model has been used to simulate the number of human casualties recorded in vehicular accidents along Lokoja-Abuja-Kaduna express way. After which a Grey-Markov model was used to improve the accuracy of the simulated values. The performance of the Grey-Markov model was impressive as it recorded 95.012% accuracy when fitted. This shows that the model is reliable and dependable; therefore the prediction made for the future years should be adopted by Nigeria government as source of information for road safety policy formulation on the express way.

REFERENCE

Bamidele M., Ifeoluwa H. (2016). Modelling of Road Traffic Accidents: A multistate Markov Approach.*Sri Lankan Journal of Applied Statistics Vol. 17(2).*

Duncan, T.E, Hu Y, Pasik-Duncan B. (1998). Stochastic calculus for fractional Brownian motion I, theory. Preprint.

F.R.S.N (2020). Archives of Federal Road Safety of Nigeria, https://www.frsc.gov.ng

Jian-Yi L., Ying Z. (2014). Application of Grey Markov SCGM $(1,1)_c$ Model to prediction of Accidents Death in Coal Mining. Hindawi Publishing Corporation International Scholarly Research Notices Vol.2014, Article ID 632804, 7 Pages http://dxidoi.org/10.1155/2014/632804

John C., Darwin J., Noime B.,Vensurmar C., (2017). Analysis of Vehicule Crash Injury-Severity in a Super High Way: A Markovian Approach. Industrial Engineering Department Publishing, Adamson University, Manila, Philippines 1000

Lewis J. (1982). "Beta-Blockade after Myocardial infarction View" Imperial Chemical Industries PLC, Pharmaceuticals Division, Macclesfield SK10 4TF

Li Q., Hu Q., Zangh P., (2007). Application of Grey-Markov Model in Predicting Traffic Volume.Preceeding of 2007 IEEE International Conference on Grey System and Intelligent Services, November 18-2-, 2007, Nianjin, China

Mao Z., Sun J., (2011). Application of Grey-Markov Model in Forecasting Fire Accidents. The Fifth Conference on Performance-based Fire Protection Engineering, ELSEVIER

Nyothiri A., Weidong Z., Sahraoui D., Yibo A., (2018). Accident Prediction System Based on Hidden Markov Model for Vehicular Ad-Hoc Network in Urban Environments .*www.mdpi.com/Journal /Information 2018, 9,311;doi:10.3390/info9120311*

Xiaoxia X., Long C., Jun L., (2018). Vehicular Driving Risk Prediction Based on Markov Chain Model.Hindawi Discrete Dynamics in Nature and Society, Vol. 2018, Article ID 4954621, 12 Pages http://doi.org/10.1155/2018/4954621.

MATHEMATICAL MODELING OF BLOOD FLOW IN THE STENOSED ARTERY

Salihu Omeiza Nasiru
Department of Mathematics, Federal University of Technology, Minna, Nigeria
so.nasiru@futminna.edu.ng

Abstract
In this paper, an analytical study of effects of blood flow in the blood vessels has been investigated. The viscosity of the blood is assumed to be varying radially with hematocrit throughout the region of the artery. The blood flow is assumed to be Newtonian fluid, incompressible, laminar, and steady. In order to model this problem, Navier-Stokes equations was used to derive the governing equations that represent this problem. We simplified the governing equations by linearizing the equations and solved by finite different method. We observed that the size of the blood vessel influenced the blood flow. A little change on the cross-sectional value makes a very significant change on the blood flow rate.

Keywords: Blood flow, Newtonian, Navier-Stokes, Artery, Density, Finite difference method.

1.0 Introduction

In the human circulatory system, artery delivers oxygenated rich blood with nutrients from the heart to each cell of the body. The study of the behaviour of blood flow in the blood vessels provides an understanding of the connection between flow and the development of diseases such as atherosclerosis, aneurysms and thrombosis. The abnormal elongation of arterial thickness is the first step in the formation of atherosclerosis disease. The accumulation of substances in the artery along the wall is known as stenosis, the presence of which changes the flow behavior and hemodynamic conditions of the artery. Coronary artery disease is caused by atherosclerosis that occurred due to stenosis which formed by fatty substances, cholesterol, cellular waste products, and smooth muscle cells accumulation on the arterial wall Akhbar *et al.* (2019). Stenosis is a localize plaque that cause the narrowing on the vessel wall and causing an alternation in the flow structure which consequently reduced the fluid flow passing to the other organs and tissues Chinyoka and Makinde (2014). As the plaque tends to rupture, an individual may suffered to the risk of cardiovascular disease such as heart attack and stroke.

The study of blood flow in the human pulmonary system is consequential for human health as a result of the fact that it deals with measuring the blood pressure and finding the flow via the blood vessel. Many researchers have studied the blood flow in the arteries and veins. Taura *et al.* (2019) worked on physiological fluid by presenting a model for possible pathways of interaction between the cardiovascular and respiratory control systems. He presents a model equation that explains the Frank-Starling mechanism, which plays an important role in the maintenance of the stability of the distribution of blood in the system. As hemodynamics is directly related to overall human health, recently it has gained a serious attention of researchers, physiologists and clinical persons to study the blood flow through

arteries. A body of work in this context of arterial blood flow in the presence of stenosis has been reported by David (2020) in his paper.

The bioheat transport phenomena in hemodynamics influence more on the growth of atherogenetic processes however offer a significant insight in fruitful experimental and theoretical investigation. The understanding of the perturbation of the temperature distribution as a function of the vessel diameter is critically important to the development of appropriate models of bioheat transport. In physiological situations, the temperature distributions perturbed when the diameter of the blood vessel is large Rabby *et al.* (2014).

According to previous study, it is interesting to note that the localized cooling regions are present within heated tissues during hyperthermia treatment when the vessel blood is large in size Santabrata and Subir (2005). The normal temperature of the human blood is about 37°C. Thus, irreversible ill effects will occur in the proteins of blood which is the cause of death after such high fever Srinivasacharya *et al.* (2017). Moreover, hypothermia or hyperthermia is widely used for many purposes such as open heart surgeries and cancer treatment, the temperature is substantially important. Temperature magnitude in hyperthermia treatment are important by raising the temperature of cancerous tissue above a therapeutic value 42°C, while maintaining the surrounding normal tissue at sub lethal temperature value. In the past, there has been a number of studies to examine heat transfer in blood vessels. Jahangiri *et al.* (2015) investigate the influence heating protocol on temperature distribution in a single channel vessel and tumor tissue considering hyperthermia treatment. They concluded that large vessel has effect on the heat transfer characteristics in tissues receiving hyperthermia treatment. The effect of heat transfer considering stenosed artery under assumption of the optically thin fluid has been presented by Sharma *et al*. (2016). The heat transfer coefficient considerably effected when the channel size, shape and cross section of channel, fluid properties, and fluid flow arrangement are varying Zain *et al.* (2017). The influence of Reynold number on heat transfer in catheterizes multiple stenosis artery and in nano fluid mini channel has been investigated by Zaman *et al*. (2016). They concluded that there would be a significant influence of Reynolds number on heat transfer enhancement along the geometry and fluid properties. Jahangiri *et al.* (2015) studied mathematical model of the heat and mass transfer through bifurcated arteries with stenosis in mother and daughter artery. They reported that at the throat of the constricted daughter artery, in particular, give appreciable influences on temperature profile.

2.0 Materials and Methods

We have adopted Taura *et al*. (2019) local arterial flow model. This includes the assumptions that the arterial vessel is incompressible material with circular section and without longitudinal movements. Therefore, blood is considered as an incompressible Newtonian fluid and the flow is axially symmetric. The model approach is to use the two-dimensional Navier-Stokes equations and continuity equation for a Newtonian and incompressible fluid in cylindrical coordinate (r, z, t):

$$\frac{\partial u}{\partial t} + w\frac{\partial u}{\partial r} + u\frac{\partial u}{\partial z} = -\frac{1}{\rho}\frac{\partial p}{\partial z} + v\left(\frac{\partial^2 u}{\partial r^2} + \frac{1}{r}\frac{\partial u}{\partial r} + \frac{\partial^2 u}{\partial z^2}\right) \tag{3.1}$$

$$\frac{\partial w}{\partial t}+w\frac{\partial w}{\partial r}+u\frac{\partial w}{\partial z}=-\frac{1}{\rho}\frac{\partial p}{\partial z}+v\left(\frac{\partial^2 w}{\partial r^2}+\frac{1}{r}\frac{\partial w}{\partial r}+\frac{\partial^2 w}{\partial z^2}+\frac{w}{r^2}\right) \tag{3.2}$$

$$\frac{1}{r}\frac{\partial}{\partial r}(rw)+\frac{\partial u}{\partial z}=0 \tag{3.3}$$

To make our work easier, we now introduce a new variable η to be the radial coordinate, which is define as:

$$\eta=\frac{r}{R(z,t)} \tag{3.4}$$

We assume that P is independent of the radial coordinate η, then the pressure P is uniformly distributed within the cross section $[P=P(z,t)]$

Therefore,

$$\frac{\partial^2 u}{\partial z^2}\le 1, \qquad \frac{\partial^2 w}{\partial z^2}\le 1, \qquad \frac{\partial P}{\partial r}\le 1,$$

We can now use simple algebra to change the variable as

$$\frac{\partial u(r,z,t)}{\partial t}=\frac{\partial u(\eta,t)}{\partial t}\cdot\frac{\partial \eta}{\partial t}+\frac{\partial u(\eta,t)}{\partial t}\cdot\frac{\partial t}{\partial t}$$

$$=-\frac{\eta}{R}\frac{\partial u(\eta,t)}{\partial t}\cdot\frac{\partial R}{\partial t}+\frac{\partial u(\eta,t)}{\partial t}$$

Equations (3.1), (3.2) and (3.3) can be re-written in the new coordinate (η,z,t) as:

$$\frac{\partial u}{\partial t}+\frac{1}{R}\left[\eta\left(\frac{\partial R}{\partial z}+\frac{\partial R}{\partial t}\right)-w\right]\frac{\partial u}{\partial \eta}+u\frac{\partial u}{\partial z}=-\frac{1}{\rho}\frac{\partial P}{\partial z}+\frac{v}{R^2}\left(\frac{\partial^2 u}{\partial \eta^2}+\frac{1}{\eta}\frac{\partial u}{\partial \eta}\right) \tag{3.5}$$

$$\frac{\partial w}{\partial t}+\frac{1}{R}\left[\eta\left(\frac{\partial R}{\partial z}+\frac{\partial R}{\partial t}\right)-w\right]\frac{\partial w}{\partial \eta}+u\frac{\partial w}{\partial z}=\frac{v}{R^2}\left(\frac{\partial^2 w}{\partial \eta^2}+\frac{1}{\eta}\frac{\partial w}{\partial \eta}+\frac{w}{\eta^2}\right) \tag{3.6}$$

$$\frac{1}{R}\frac{\partial w}{\partial \eta}+\frac{w}{\eta R}+\frac{\partial u}{\partial z}-\frac{\eta}{R}\frac{\partial R}{\partial z}\frac{\partial u}{\partial \eta}=0 \tag{3.7}$$

We now assumed that the velocity profile in the axial direction $u(\eta,z,t)$ to be expressed in the polynomial form as:

$$u(\eta,z,t)=\sum_{k=1}^{N}q_k\left(\eta^{2k}-1\right) \tag{3.8}$$

Also, the velocity profile in the radial direction is

$$w(\eta,z,t)=\frac{\partial R}{\partial z}\eta w+\frac{\partial R}{\partial t}\eta-\frac{\partial R}{\partial t}\frac{1}{N}\eta\sum_{k=1}^{N}\frac{1}{k}\left(\eta^{2k}-1\right) \tag{3.9}$$

Let $N=1$, simplifying equations (3.8) and (3.9) gives

$$u(\eta,z,t)=q(z,t)\left(\eta^2-1\right) \tag{3.10}$$

$$w(\eta,z,t)=\frac{\partial R}{\partial z}\eta w+\frac{\partial R}{\partial t}\eta\left(\eta^2-1\right) \tag{3.11}$$

Substituting equations (3.10) and (3.11) into equations (3.5) and (3.7) gives the dynamic equations of $q(z,t)$ and $R(z,t)$ given below:

$$\frac{\partial q}{\partial t}-\frac{4q}{R}\frac{\partial R}{\partial t}-\frac{2q^2}{R}\frac{\partial R}{\partial z}+\frac{4\nu}{R^2}q+\frac{1}{\rho}\frac{\partial P}{\partial z}=0 \tag{3.12}$$

$$2R\frac{\partial R}{\partial t}+\frac{R^2}{2}\frac{\partial q}{\partial z}+q\frac{\partial R}{\partial z}=0 \tag{3.13}$$

We now define the cross-sectional area $S(z,t)$ and the flow $Q(z,t)$ as:

$$S=\pi R^2, \qquad Q=\iint_s u\partial\eta = R\pi R^2$$

Expressing equations (3.12) and (3.13) in terms of $Q(z,t)$ and $S(z,t)$ from the above definitions gives:

$$\frac{\partial Q}{\partial t}-\frac{3Q}{S}\frac{\partial S}{\partial t}-\frac{2Q^2}{S^2}\frac{\partial S}{\partial z}+\frac{4\pi\nu}{S}Q+\frac{S}{2\rho}\frac{\partial P}{\partial z}=0 \tag{3.14}$$

$$\frac{\partial S}{\partial t}+\frac{\partial Q}{\partial z}=0 \tag{3.15}$$

The systems of equations (3.14) and (3.15) are the governing equation. We used the Finite difference method to solve the non-linear partial differential equations (3.14) and (3.15) by discretizing the equations using the following first order accuracy difference formula:

$$\frac{\partial Q_i}{\partial z}=\frac{Q_i-Q_{i-1}}{\Delta z} \tag{3.16}$$

And

$$\frac{\partial S_i}{\partial z}=\frac{S_i-S_i}{\Delta z} \tag{3.17}$$

Therefore,

Equations (3.14) and (3.15) becomes,

$$\frac{\partial Q_i}{\partial t}-\frac{3Q_i}{S_i}\frac{Q_i-Q_{i-1}}{\Delta z}-\frac{2Q_i^2}{S^2}\frac{S_{i+1}-S_i}{\Delta z}+\frac{4\pi\nu}{S_i}Q_i+\frac{S_i}{2\rho}\frac{\partial P}{\partial z}=0 \tag{3.18}$$

$$\frac{\partial S_i}{\partial t}=\frac{Q_i-Q_{i-1}}{\Delta z} \tag{3.19}$$

Where $i=1,2,3,...M$, the pressure gradient $\frac{\partial P}{\partial z}$ is constant all through.

We can simplify governing equations by linearizing equation (3.18) as follows:

$$\frac{\partial Q_i}{\partial t}-\frac{4\pi\nu}{S_0}Q_i+\frac{S_0}{2\rho}\frac{\partial\rho}{\partial z}+\frac{S_i}{2\rho}\frac{\partial P}{\partial z}=0 \tag{3.20}$$

The difference equations (3.19) – (3.20) can be written in the form of $\frac{\partial y}{\partial t}=f(y)$

Where,

$$y = \left(Q_1, Q_2, ..., Q_M, S_1, S_2, ...S_M\right) \tag{3.21}$$

And

$$f(y) = \begin{bmatrix} -\left(\frac{4\pi v}{S_0} y(1) + \frac{S_0}{2\rho}\frac{\partial P}{\partial z} + \frac{y(M+1)}{2\rho}\frac{\partial P}{\partial z}\right) - \\ \left(\frac{4\pi v}{S_0} y(2) + \frac{S_0}{2\rho}\frac{\partial P}{\partial z} + \frac{y(2+N)}{2\rho}\frac{\partial P}{\partial z}\right) - \\ \left(\frac{4\pi v}{S_0} y(N-1) + \frac{S_0}{2\rho}\frac{\partial P}{\partial z} + \frac{y(2N-1)}{2\rho}\frac{\partial P}{\partial z}\right) - \\ \left(\frac{4\pi v}{S_0} y(N) + \frac{S_0}{2\rho}\frac{\partial P}{\partial z} + \frac{y(2N)}{2\rho}\frac{\partial P}{\partial z}\right) - \\ \left(\frac{y(1)-Q_0}{\Delta z} - \frac{y(2)-y(0)}{\Delta z}\right) - \\ \left(\frac{y(N-1)-y(N-2)}{\Delta z} - \frac{y(N)-y(N-1)}{\Delta z}\right) \end{bmatrix} \tag{3.22}$$

The easiest way to solve (3.19) – (3.22) is by using MatLab buid in function ODE45 embedded with Runge-Kutta method. The necessary parameters for varying are: $Q_0, S_0, \frac{\partial P}{\partial z}, v, \rho$. The other values in normal condition can be obtained from the past works in this field. For example:

Initial value of Q and $Q_0 = 1 - 5.4$ liter/minute Taura *et al.* (2019)

Initial value of S and $S_0 = 1.5 - 2.0 cm^3$ Taura *et al.* (2019)

$\frac{\partial P}{\partial z} = 100 - 40 mmHg$ Sharma *et al*. (2016)

$v = 0.035 cm^2/s$ David (2020)

$\rho = 1.05 g/cm^3$ David (2020)

3.0 Results and Discussion

For us to simulate how the cross-sectional area of the artery affects the blood flow in the artery, the values of the parameters mentioned above are considered as: $\rho = 1.05 g/cm^3, v = 0.035 cm^2/\sec, Q_0 = 16.7 cm^3/\sec$ and $S_0 = 1.5 cm^2$. We chose the length of the artery model $L = 15 cm$ and the number of nodes of the system $N = 3$ and time $t = 0.2\sec$.

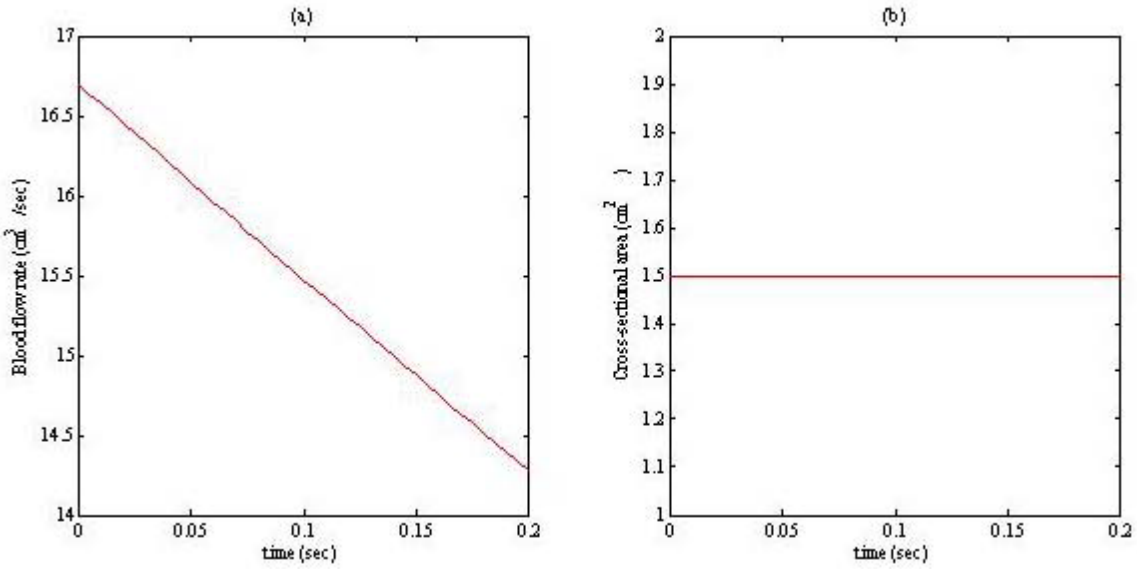

Figure 1: This shows the blood flow rate and cross-sectional areas for each node.

It is observed that the results for $Q_1, Q_2,$ and Q_3 are almost the same as depicted in Figure 1(a). Similarly, the values of $S_1, S_2,$ and S_3 in Figure 1(b) are very close and it is almost a constant. This shows that the values of the blood flow rate and the cross-sectional area are almost the same throughout in the small section of arteries. This could be due to the absence of viscoelastic effect in the model. Now since there is not much difference in the blood flow rate between the sections, we will consider only one section which is S_2 to make the comparison of the different values of the cross-sectional area. As we can see, the value for the blood flow is decreasing from its initial value.

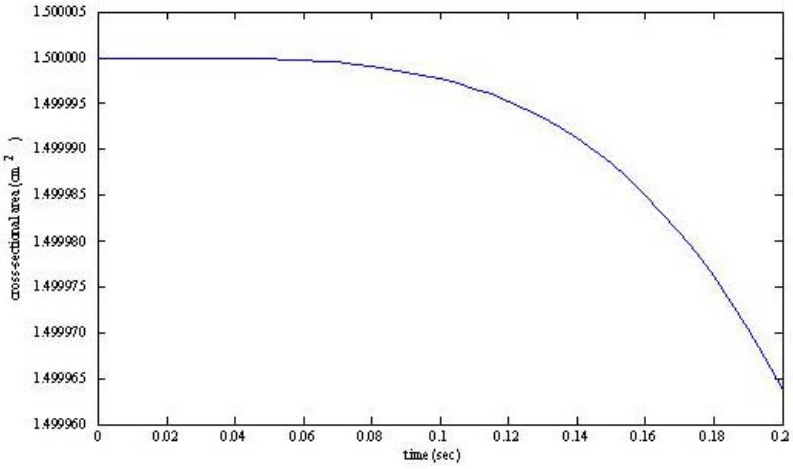

Figure 2: The cross-sectional area against time

This shows that without changing the value of the pressure gradient and the cross-sectional area of the arteries, the blood flow rate through the arteries is decreasing significantly as time increasing. It also shows that the blood flow is linearly decreasing. We assume this condition is valid in the diastole condition only. Next, we compare this result with smaller cross-sectional area.

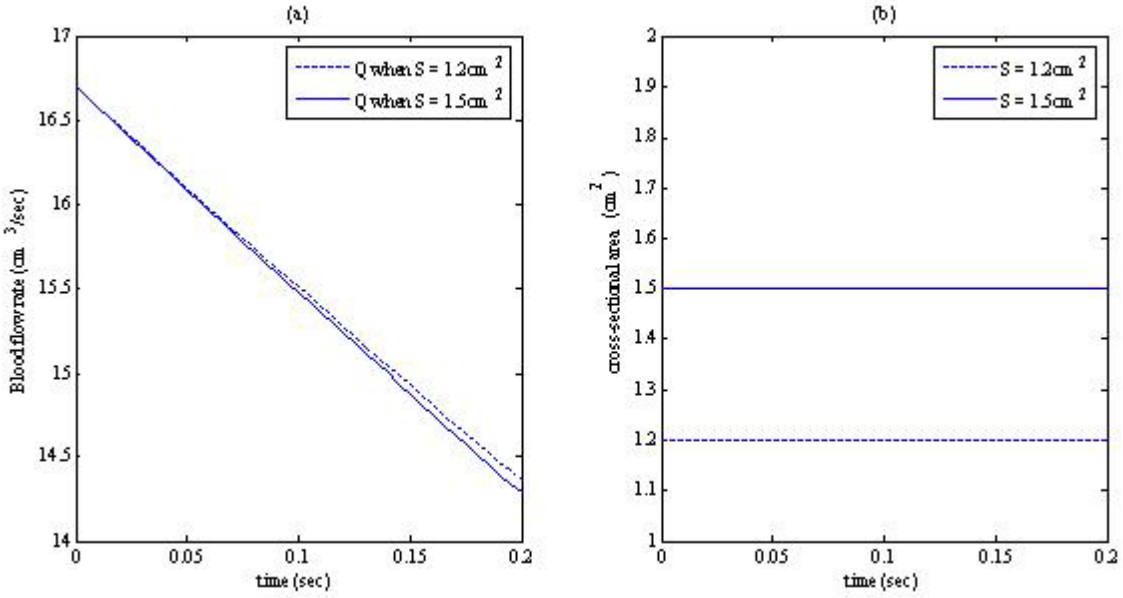

Figure 3: Comparison graph for blood flow with different value of cross-sectional area.

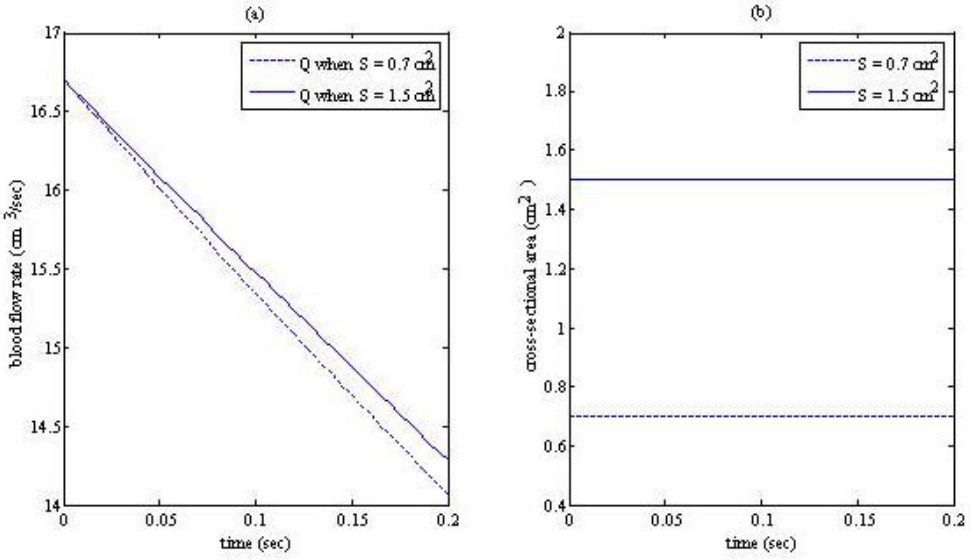

Figure 4: Comparison of *Q* at normal cross-sectional area and much smaller cross-sectional area.

As shown in Figure 5 above, when the value of cross-sectional area is below $0.8cm^2$, the blood flow rate decreases faster than the normal rate. Figure 6 shows the value of blood flow rate when the cross-sectional area is in range of between $0.1cm^2 - 0.8cm^2$. Clearly, if the cross-sectional area continues to decrease below $0.8cm^2$, the blood flow rate also decreased drastically. From this observation, we can say that this condition occur because the cross-sectional area is too small for the blood to get through it. This is also a dangerous condition for human.

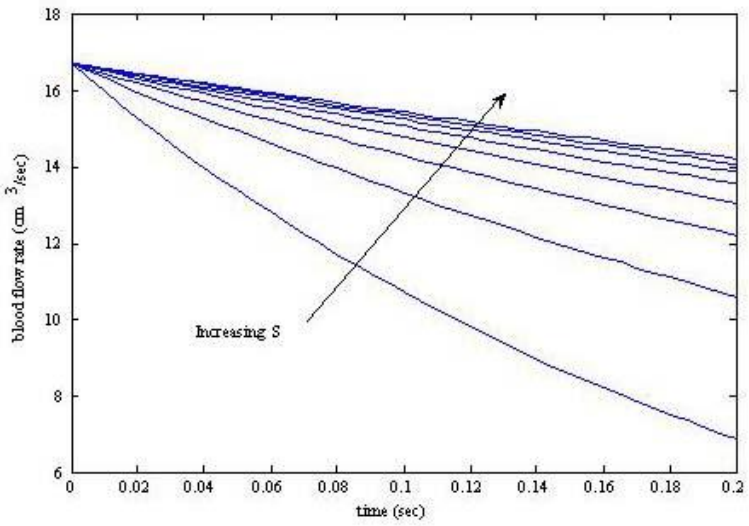

Figure 5: when cross-sectional area is in range between $0.1cm^2 - 0.8cm^2$

From the results obtained, we can conclude that cross-sectional area plays an important part in order for the blood to flow smoothly through the blood vessel. A small change in the value for the cross sectional area may affect the amount of blood flow rate through the arteries which also may affect the blood pressure. In other words, smaller cross-sectional area from normal size may contribute to hypertension or high blood pressure. When a large amount of fluid flows through a small vessel, it may cause the pressure in the vessel to increase.

References

Akhbar Zaman, Nasir Ali, Muhammad Bilal Sajid, and Tasawar Hayat. "Effects of unsteadiness and non-Newtonian rheology on blood flow through a tapered time-variant stenotic artery." *AIP advances*5, no. 3 (2019): 037129.

Chinyoka, T., and O. D. Makinde. "Computational dynamics of arterial blood flow in the presence of magnetic field and thermal radiation therapy." *Advances in Mathematical Physics*2014 (2014).

David Chato. "Heat transfer to blood vessels." Journal of biomechanical engineering 102, no. 2 (2020): 110-118.

Jahangiri, Mehdi, Mohsen Saghafian, and Mahmood Reza Sadeghi. "Numerical simulation of hemodynamic parameters of turbulent and pulsatile blood flow in flexible

artery with single and double stenoses." *Journal of Mechanical Science and Technology* 29, no. 8 (2015): 3549-3560.

Rabby, Mir Golam, Sumaia Parveen Shupti, and Md Molla. "Pulsatile non-newtonian laminar blood flows through arterial double stenoses." *Journal of Fluids* 2014 (2014).

Santabrata Chakravarty and Subir Sen. "Dynamic response of heat and mass transfer in blood flow through stenosed bifurcated arteries." *Korea-Australia Rheology Journal* 17, no. 2 (2005): 47-62.

Srinivasacharya, Darbhasayanam, and Gade Madhava Rao. "Micropolar fluid flow through a stenosed bifurcated artery." *Nonlinear Analysis-Modelling and Control* 22, no. 2 (2017): 147-159.

Sharma, Mukesh Kumar, Vinay Nasha, and P. R. Sharma. "A Study for Analyzing the Effect of Overlapping Stenosis and Dilatation on Non-Newtonian Blood Flow in an Inclined Artery." *Journal of Biomedical Science and Engineering* 9, no. 12 (2016): 576.

Taura, L. S. (2019). The use of a continuity equation of fluid mechanics to reduce the abnormality of the cardiovascular system: A control mechanics of the human heart. *Journal of Biophysics and Structural Biology Vol. 4(1), pp. 1-12, March 2012. Available online at http://www.academicjournals.org/jbsb*. DOI: 10.5897/JBSB11.010. ISSN-2141-2200 ©2012.

Zain, Norliza Mohd, and Zuhaila Ismail. "Modelling of Newtonian blood flow through a bifurcated artery with the presence of an overlapping stenosis." *Malaysian Journal of Fundamental and Applied Sciences* 13, no. 4-1 (2017): 304-309.

Zaman, A., N. Ali, O. Anwar Bég, and M. Sajid. "Heat and mass transfer to blood flowing through a tapered overlapping stenosed artery." *International Journal of Heat and Mass*

APPLICATION OF QUEUING THEORY MODEL IN EVALUATING THE EFFICIENCY OF SERVICE IN STUDENTS' ACADEMIC AFFAIRS, NIGER STATE POLYTECHNIC ZUNGERU.

Imam Muhammad Bello[1], Audu Makada[2], Ibrahim Sani Ango[3] and Ahmed Rufai Tete[4]
[1,2,3,4]Department of Mathematics and Statistics, Niger State Polytechnic, Zungeru.
Email: imammuhammad57@gmail.com
Contact: +2348037775951.

ABSTRACT

This study investigated the application of queuing theory model in evaluating the efficiency of service in students' academic affairs, Niger State Polytechnic Zungeru. The data used were primarily collected through the mean of direct observation at the office of students' academic affair, Niger State polytechnic Zungeru from 9.00am to 2.00pm for a period of 10 days. The data collected were subjected to a single queuing model. The result of the study demonstrated that the arrival rate when the service point is 1 was 0.344 *and the average time a student stays in the student's affair was* 27.97 *minutes. The study revealed furthered that the probability of the system is busy was 0.7367 (* 73.67%,*) the probability that there was no students in the system was 0.26 (26%), and average of number of students in the system is 2.8 while the average time spent in the system is 0.14. the study therefore recommended that school management students' should provide more server or staffs in support of the existing one to the office of academic affairs, Niger State polytechnic Zungeru so as to improve the service render to the students.*

Keywords: Academic Affairs, Analysis, Applications, Efficiency of Service, Queuing Model.

INTRODUCTION

Waiting for service has become part of our daily life. It happens in every corner of our society. We queue at banks, we queue at filling stations, police check points, traffic points to receive service, we line up for service in post office and we queue at school while doing registration. And the waiting phenomenon is not an experience limited to human beings only. Jobs wait to be processed on a machine, planes circle in stack before getting permission to land at an airport and cars stop at traffic lights. Waiting cannot be eliminated completely without incurring inordinate expenses and the goal is to reduce its adverse impact to tolerable levels. In our society today it is very uncommon to visits an organization be it private of public without queuing or waiting before being attended to.

In general, a queue simply implies a lineup of people or item. Thus, queuing theory is a form of operations research that uses mathematical formulas and/or computer simulation to study wait and congestion within a system. The purpose of the theory is to study the queues that result from such congestion and, through the study of these visible phenomena, discover malfunctions within the system that are transparent to the decision maker. Although queuing theory was originally applied to telephone trafficking problems, today it is being adopted by many different fields and adapted to their needs. Queuing theory has been proven to be effective in almost all areas of business and formal courses on the subject are being taught in higher institution (Ogunsakin, et al, 2013). Queuing theory is an analytical method that

models a system allowing queue, calculates it's performances and determine its' properties in other to help managers in decision making.

System performance may include mean waiting time, percentile of the waiting time, utilization of the server, throughput (i.e number of customers served per unit time), average number of customers waiting etc. Queues can be refer to as items, customers, a signal in a line awaiting some kind of service. Queuing time is the amount of time a vehicle, customer or a thing spends before being attended to for some kind of service. Queues may be finite or infinite. (Acheampong, 2013).Basically, a queuing model is characterized by; arrival process of customers, the behavior of customers, the service time, discipline capacity, waiting room or a lane. A queuing system consists of a server, a number of customers who demand service and a queue of customers waiting to be served.
Queuing models provide the analyst with a powerful tool for designing and evaluating the performance of queuing systems. A queuing system is basically made up of arrival or inputs to the system, queuing discipline and the service facility. Whenever customers arrive at a service facility, some of them have to wait before they receive the desire. It means that the customer has to wait for his/her turn, may be in a line. This situation can be frustrating when customers has to wait very long before they are served in a queue and bring dissatisfaction to them. These waiting times waste the time of customers that could have used been used in productive activities. Long waiting can reduce revenue collected at pay points. (Barak, 2012). Anyone who has gone shopping or to a movie has experienced the inconvenience of waiting in line to make purchase or buy a ticket. Not only do people spend a significant portion of their time waiting in lines, but products queue up in production plants, machinery waits in line to be served, planes wait to take off and land, and so on. Since time is a valuable resource, the reduction of waiting time becomes an important topic of analysis. Today, businesses and other organizations adopt the queuing concept because of its positive impact on efficiency and economic use of resources. Higher institutions employ queuing theory to reduce average time spent by a student to receive service. This usually leads to customers‟ satisfaction and increased patronage which automatically result to increased productivity. The arrival of customers creates opportunity for the delivery of goods and services which completes the process of production. Before the arrival of customers, it is expected that the instrument of service such as personnel, machines, goods etc. have been put in place. If these facilities are in place and customers arrive at a uniform rate, there may be no need for queues. Unfortunately, this is not always the case and so queues arise.

Significance of the Study

This study focuses on application of queuing theory on the number of students being attended to the office of academic student affair Niger State Polytechnic Zungeru during school registration. However, the outcome of this study will not only improve student's service satisfaction but will help the school management to gather enough information about waiting lines at the student affair and be able to determine the number of staffs appropriate for this office to reduce waiting times. Determining the optimal number of appropriate staffs from the findings of this study, will minimize waiting times which will affect the academic performance of the students since students can use their times in other academic activities like reading.

The Scope of the Study

This study focused on application of queuing theory to optimize the performance of staffs in Niger State Polytechnic Zungeru. To reduce the time spent by the students. The scope of this study covers number of students being attended to at the office of students' academic affair Niger State Polytechnic, Zungeru for the period of 10 days.

LITERATURE REVIEW

This chapter emphasizes on the review of related literatures on applications of queuing theory. It covers two sections including conceptual and empirical review. Queuing theory is applied in studying wait and congestion within a system. Wait happens whenever a unit must wait for service and if more than one unit is forced to wait congestion results. The problem of congestion increases proportionally with the randomness of arrivals and the variation of service times. The queues that result from this congestion are often symptomatic of other, more severe, system problems including problems with staffing, scheduling, and /or material allocation.

According to Taylor, (I996) waiting in queues or waiting lines is one of the most common occurrences in every one's life. In management science terminology, a waiting line is referred to as a queue, and the body of knowledge dealing with waiting line is known as queuing theory. Talia (2007) is of the view that the study of queues deals with quantifying the phenomenon of waiting in lines using representative measure of performance, such as average queue length, average waiting time in queue, and average facility utilization. The result of queuing analysis can be used in the context of a cost optimization model, where we seek the minimization of the sum of two costs: the cost of offering the service and the cost of waiting. The main obstacle in implementing cost models is the difficulty of obtaining reliable estimates of the cost of waiting, particularly when human behaviour is an integral part of the operation.

According to Okeke (I995), queue is defined as a collection of objects awaiting service. It is usual to think of objects in the queue as human beings only. In studying queuing systems, we need to broaden our thought of the objects involved to include for example cars awaiting routine service, or stopping to buy fuel at a filling station, machines awaiting repairs, files, in fact any discrete object which needs one type of function or the other to be performed on it. Queues are in fact about delays. Whether the actual queue is observed or not, queues form because it is not at all impossible to organize the supplies to be exactly equal to the demand.

Basic Structure and Components of a Queuing System

Dannenbring and Stair (I981) perceived that a queuing system essentially consists of the following four components;

i. An input source or calling population that generates customer.
ii. A service system that consists of one of more service facilities.
iii. A queue that indicates the number of customers waiting for (the queue does not include customers being served). When the customers arrive at the service facilities, they examine the queue conditions and then decide whether or not to join the queue. Some customers are discouraged by the length of the queue and therefore do not join the line some customers after waiting in the queue for some time become impatient and drop out of the queue.

iv. A queue discipline or service discipline according to which the customers are selected for service. The queue discipline indicates the decision rate for service. For example, in the campus refectories, students are usually served on a "first-come, first-served" basis.

According to Talia (1982), the characteristics of the input source are given by;
Size of the Calling Population; The size of the calling population is *FINITE* if the number currently in the system (customers being served plus those in the queue) is a significant portion of the number of potential arrivals.

Arrival Size: In his view, Taha (1982), an arrival can be single or batch.

Arrival Control: Most of the arrivals are subject to some degree of influence and control for example, cinema houses influence, to varying degrees the arrivals of their customers by charging discriminatory rates for films shown on weekends and weekdays. In his view Taha (1982), the queuing literature classifies control in the categories of controllable (ie registration days for college students) and uncontrollable (i.e. emergency room of a hospital)

Arrival Distribution (pattern of arrivals); According to Loomba (1978), the pattern of arrival is usually given by:

i. The distribution of times between successive arrival (i.e. inter arrival times) or
ii. ii. The distribution of the number of arrivals per unit of time (i.e. arrival rate distribution).

The pattern or distribution of arrivals can be constant or random. A constant distribution means that the time intervals between arrivals (inter arrival times) are constant. Constant distributions are common in automated assembly line operations where parts, subassemblies, and finished goods arrive after predetermined time intervals. A random distribution means that the inter arrival times cannot be predicted with certainty, and hence their pattern is given by actual empirical data or can be approximated by theoretical probability, such as the exponential distribution. The inter arrival times of many real-life phenomena (arrival at banks, gasoline station) can often be approximated by exponential distributions. The distribution of the arrival rates (i.e. the number of arrivals per unit of time) of many real-life phenomena can often be approximately by the Poisson distribution. The means of the Poisson and exponential distributions are inversely related as follows: Poisson arrival rate Mean arrival rate = λ Exponential inter arrival Times Mean inter arrival time = $1/\lambda$
The Attitude of Customers: The attitude of customers is important because it affects the length of the queue. The attitude is a reflection of different types of customers such as;

i. Impatient customers (Balking or reneging),
ii. ii. Patient customer (voluntary or involuntary).

When the customers arrive for service, they can either be immediately served (if the service facility is free) or they have to stand in the queue (if they wish to receive service). The customers who either do not join the queue (balking) or leave the queue before receiving service (reneging) are called impatient customers. The customers who either voluntarily (e.g. patients in physician"s office) voluntary (eg. Prisoners or physical entities) remain in the queue until they are called patient customers (Bose, 2001). The purpose of recognizing the attitude of the customers is that, if a waiting time of extraordinary length produces a substantial number of impatient customers, then there is the potential of lost sales.

The Service System

According to Lipsky(1992), the service system is characterized by the configuration (structure) of the service facilities and the service distribution. Configuration (structure) of the service facilities: Depending upon the nature of the service process, service facilities can be classified in terms of their configuration of channels (single or multiple) and phases (single or multiple). The term channel refers to the number of points of entry to the service system (Lipsky (1992). A single channel means that there is only one point of entry. Multiple channels refer to the parallel arrangement of service facilities ie. Two or more points of entry exist so that two or more service stations can simultaneously begin the service process.

The term phase refers to the number of service stations through which the customer must pass before the service is considered complete. A single phase implies that there exists only one service station. Multiple phase refer to the service arrangement of service facilities that is, customer must go through two or more service stations in sequence before the service is considered complete (lipsky, 1992).

Service distribution (Pattern of service): The pattern of service can be recorded by:

i. The distribution of service times.
ii. The distribution of the number of customers served per unit time (i.e. service rate).

As in the case of arrival, the distribution of service time can be constant or random. The constant service time occurs mostly in mechanized operations. In most real-life situations service times are random and can often be approximated by the exponential probability distribution. If the service is random but is specified in terms of service rates, it can often be approximated by the Poisson distribution (Loomba, 1978). Note that exponential service-time distribution gives rise to Poisson service rate (and vice -versa). The means of the two distributions are inversely related.

The queue

According to Morse (I958). The number of waiting lines and their respective lengths are the two basic aspects of the "Queue". The number of waiting lines is essentially a function of the configuration of the service facilities. (That is, one waiting line for each different point of entry into the service system. Therefore, it could form a single queue or multiple queues. In his view Lee (I966), the length or size of the queue is influenced by such factors as;

i. Physical space,
ii. Legal restrictions example, city ordinance against forming queues on specified city streets.
iii. Attitude of the customers example, long lines discourage some customers from joining the queue.
iv. The relationship of the capacity of the input source to the capacity of the service facilities.

The length of the queue can be finite or infinite. The queue is finite (truncated) when there is a limit beyond which it cannot increase, example, the queue at a gas station). The queue is infinite when there is no limit on its size example, the number of mail orders for development of photos, (Lee, I966).

The Queue Discipline

Saaty (I983) views that the queue discipline indicates the decision rule by which the customers are selected from the queue for service. In most queuing systems, the queue discipline is the first-come first-served (FCFS) or first in, first out (FIFO). However, other types of queue disciplines can be provided on the basis of assigned priorities. Some examples in the category of assigned priorities are given by the following decision rules for selecting the customer;

i. Emergency first, example, in a hospital emergency room.
ii. Reservation first, example, in a restaurant.
iii. Shortest processing time first, example, in a job shop.
iv. Preemptive priority example, when service to one customer is interrupted to provide service to another.

Another type is the random queue disciple that reflects a service system not operated in a well-organized manner example, service in a higher store with several salesmen. The specification and analysis of the queue discipline is important because it affects the operating characteristics of the queuing system.

Types of Queues

According to Egbo (2019), there are three main varieties of queuing situations commonly found in many places and circumstances around us. These include;

i. Single queue with single service print.

ii. Multiple queues with multiple service point.

Single queue with single service point: In this type of queue, only one line is formed and only one facility gives service.

Single Queue with several service points: In this type, the queue elements can go to any available service point and receive service. This is the system of queuing adopted most petrol filling stations in this era of fuel scarcity.

Multiple queues with multiple service points: in this case according to Egbo, there are several queues and several service facilities. This type of' queue reduces average time a customer or element in a queue spends, all things being equal

Elements of A Queue

According to Bose, (2011), the principal customers in a queuing situation are the customer and the server. Customers are generated from a source. On arrival at a service facility, they can start service immediately or wait in a queue if the facility is busy. When a facility completes a service, it automatically “pulls” a waiting customer, if any from the queue. if the queue is empty, the facility becomes idle until a new customer arrives. From the standpoint of analyzing queues, the arrival of customers is represented by the inter arrival time between successive customers and the service is described by the service time per time customer. Generally, the inter arrival and service times can be probabilistic as in the operation of a post office, or deterministic as in the arrival of applicants for job interviews. In his view Egbo (2017), the elements of a queue are;

a) Arrivals

b) Queue

c) Service

d) Exit/Departure.

Arrivals: This represents the people or jobs coming into the system to receive service. The arrival pattern of these objects affects the way of ordering queues. The arrival may be systematic or it may be random or systematic random. The arrival rate is a measure of the time an object takes to join a queue.

Queue: This represents the actual time spent in waiting, for service as the objects arrival there is the likelihood that they will wait or queue for their turn.
Service: This represent receiving attention. The purpose of coming to the system is to receive service. The service rate describes the time spent in actually receiving the service attention. Like the arrival rate, the service rate may be random or systematic or both.

Exit/Departure: After receiving service, the object will leave the system. Exiting from the system is also referred to as departure. This departure completes the cycle.

Queuing Structures
The basic structure of a queuing system is defined in terms of the number of service channels and the number of service stages. Anytime unit is waiting for service, it is in a queue.
The first structure in (single-channel, single stage), is the simplest of all queuing systems. In such c. system, there is only one server and consequently only one line is formed. The second structure (single-channel, multi-stage) is one in which there is only one line, but the unit must pass through several stages before service is complete. In the next queuing structure (multi-channel, single-stage), there are several lines but the unit must pass through only onstage. The final diagram represents a system in which there is more than one stage and there are several servers at each stage (multi- channel, multi-stage).

Characteristics of Queuing Systems
According to queuing theory, there are six major components of a queuing system that may determine the way in which a queue is formed:

i. Arrival Pattern: average number of arrivals per unit of time (e.g., the average number of students that need the teacher's individual attention during one class period).
ii. Service pattern: average time required to service a unit (e.g., the average amount of time it takes to complete an instructional packet).
iii. Queue discipline: manner by which units are selected for service;
i. FIFO -- first in, first out
ii. LIFO- last in, first out
iii. SIRO -- service in random order
iv. RIO -- service by priority

4. Number of service channels: number of parallel service stations that can service units simultaneously (e.g., number of IBM computers in an instructional lap).
5. Number of service stages: number of stages a unit must proceed through before the service procedure is completed (e.g.,: necking in with lab attendant, doing work at computer, checking out with lab attendant).
6. System capacity: The number of units allowed in the system at any one time (e.g., number of students allowed to enroll in a graduate class).

Basic Assumptions of the Theory
Queuing theory can only be applied to systems in which the following assumptions are met:

i. Both arrival rates and/or service rates involve a degree of uncertainty or randomness if this were not true, each event could be scheduled to the exact moment and there would never be a queue
ii. Average service rate is greater than average arrival rate - if this assumption is not met, then there would always be queue;
iii. The probability distribution of both arrival and service rates can be determined.

The Empirical Studies

Nafees (2007), analyzed queuing systems for an empirical data of supermarket checkout service unit as an example. The model designed for this example is a multiple queues multiple-server model. The study required an empirical data which included arrival time in the queue of checkout operating unit (server), departure time and service time.

In Sharma et al. (2013), queuing theory is the mathematical study of waiting lines and it is very useful to define modern information technologies requiring innovations that are based on modeling, analyzing to deals as well as the procedure of traffic control of daily life of human like telecommunications, reservation counter, supquer market, big bazaar, picture cinema, hall ticket window and also to determine the sequence of computer operations, computer performance, health services, airport traffic, airline ticket sales. Duder and Rosenwein (2001), used queuing based 'rule-of-thumb' formulas to estimate the cost of abandonment and to determine the optimum number of operators.

Whitt (2005) also used queuing analysis for staffing a call center, considering the proportion of servers present as a random variable. Cugnasca (2007), provided useful information to build availability models for computer systems used in airspace control centers based on analytical models provided by queuing theories. The researchers used queuing models to establish availability parameters related to a data center operation and its management issues.

May (2012), analyzed data from a large open pit gold mine and applied to a multichannel queuing model representative of the loading process of the haul cycle. She stated that, one method of feet selection involves the application of queuing theory to the haul cycle and most mining haul routes consist of four main components; loading, loading hauling, dumping and unloaded hauling to return to the loader. The outputs of the model was compared against the actual truck data to evaluate the validity of the queuing model developed.

Woensel and Vandaele (2007), presented an overview of different analytic queuing models for traffic on road networks. They shown that queuing models can be used to adequately model uninterrupted traffic flows. An analytical application tool to facilitate the optimal positioning of the counting points on a highway was also presented in the paper.

Brown (2012), aimed at increasing understanding of system variables on the accuracy of simple queuing models. A queuing model was proposed that combines G/G/1 modeling techniques for rework with effective processing time techniques for machine availability and the accuracy of this model was tested under varying levels of rework, external arrival variability and machine variability. The research shown that the model performed best under exponential arrival patterns and can perform well even under high rework conditions. Generalization was made with regards to the use of this tool for allocation of jobs to specific workers and/or machines based on known rework rates with the ultimate aim of queue time minimization.

Lakshmi and Lyer (2013), reviewed the contributions and applications of queuing theory in the field of health care management problems. They proposed a system of classification of health care areas which are examined with the assistance of queuing models. Their goal was to provide sufficient information to analysis who are interested in using queuing theory to model a health care process and who want to locate the details of relevant models.

Alfares (2009), presented the modeling and solution of a real-life operator scheduling problem at a call center. Queuing and integer programming models were combined to minimize the total weekly labor cost while providing an acceptable service level for each hour of each day of the week. The models determined optimum staffing levels and employee weekly work schedules for meeting a varying workload for each hour of the week. Queuing analysis was applied to data on the number and duration of calls in order to estimate minimum hourly labor demand.

Ogunsakin et al (2013) did a comparative analysis of Service Delivery by ATM in Two Banks with the application of Queuing Theory. From the empirical analysis, the study found that the average arrival rate, average service rate, average time spent in the queue for Access bank as 2.01, 1.65, 0.5 respectively and UBA as 3.28, 1.75, 1.67minutes, respectively. The study concluded that the average number of idle time obtained for the two banks were 3minutes and 7minutes respectively.

In examining the queuing process and its application to customer service delivery in Fidelity Bank Plc, Maiduguri by Bakari, (2014), the study obtained the value of the traffic intensity, otherwise known as the utilization factor to be less the one (i.e. $\rho<1$). The study concluded that the system operates under steady-state condition. Thus, the value of the traffic intensity, which is the probability that the system is busy, implies that 95% of the time period considered during data collection the system was busy as against 4% idle time. This indicates high utilization of the system.

In offering the Queuing model as a Technique of Queue solution in Nigeria Banking Industry, Anichebe (2013) found that, using a three-server system was better than a 2-server or 4-server systems in terms of the performance criteria. The study recommended that the management should adopt a three-server model to reduce total expected costs and increase customer satisfaction.

Ogbadu and Usman (2012**)** studied the Imperatives of Customer Relationship Management in Nigerian Banking Industry**.** Findings from the study revealed that there is a direct relationship between customer relationship management and customer loyalty as well as banks profitability.

Forbes (2008) analyzed the impact of airline delays on customer complaints, showing that customer expectations play an important role mediating this effect. Campbell and Frei (2010) studied multiple branches of bank, provided empirical evidence that teller waiting times affect customer satisfaction and retention. Their study revealed significant heterogeneity in customer sensitivity to waiting time, some of which could be explained through demographics and the intensity of competition faced by the branch.

Despite these studies, there is still a gap in the literature as regards studies that empirically investigate queue theory parameters in the area of study selected. Therefore, as a contribution to the existing literature on queue theory and service delivery, the present study makes use of a mathematical model to harness the complexities of queuing situations in the learning institution like Niger state polytechnic Zungeru, Niger sate Nigeria.

RESEARCH METHODOLOGY

This chapter gives a brief description of method of data collection and method of data analysis to the appopriate tools of single queueing model are clearly discussed.

Method of Data Collection

Basically, the data used for this study were obtained from primary sources. The method of data collection is through direct observation. A wrist watch, a pen and a notepad were requirements needed for the recording of relevant information such as; number of students, the arrival times of students, waiting time, and service time. The observation was made during the working hours (8am – 9pm). The recorded information was used to calculate average waiting time, average service time and the utilization factor.

Method of Data Analysis

In statistics, a research can not be completed without specifying method adopted in collecting data. Although there are two main method of data collection when a resarch is been embacked upon. The method include primary and seconday. While primary method is the technique used by the ressaerch in which data ara collected by the ressarcher himself. The secondary method are techniques used in which datata are collected via record or documenet. The method of analysis for this study is the single-server queuing modeling system which follows (M/M/S): (∞/FCFS) specification. In the case, the performance measure analysis including, the arrival time, waiting time service time, priority level, for average customers and the number of servers available were computed using the appropriate tools.

Model Formulation

The parameter that relates to probabilities in a single channel queue is;

λ / μ is the traffic intensity: This is the probability that an object arriving at the service points has to wait for some time before being attended to. An object arriving for service has to wait for service if on arrival it finds one or more objects already at the service point. This probability denoted by „rho" is given by the ratio of the arrival rate to the service rate which in obedience to the probability theory lies between zero and one.

ℓ^n is the probability that there are at least „n" items in the system is given by. It is necessary to observe that being in the system implies all the objects in the queue together with the object that is receiving service.

ns = $\frac{\lambda}{\mu - \lambda}$ **is t**he average number of objects in the system is given by

nq = $\frac{\lambda^2}{\mu\,(\mu - \lambda)}$ **is t**he average length of the queue, which is the same as the average number of object in the queue i.e. excluding the objects that is receiving attention is given by;

n-o = $\frac{\mu}{\mu - \lambda}$ **is the** average length of the queue excluding zero queuing is given by

A.S.P.T = $\frac{1}{\mu - \lambda}$ **is t**he average number of time an object is in the system which is also known as the average system process time; (A.S.P.T) is given by

A.Q.T. =$\frac{\lambda}{\mu(\mu - \lambda)}$ is the average number of time units that an object stays in the queue i.e. the average queuing time is given by

DATA ANALYSIS, RESULT AND DISCUSSION

Data Analysis

Presentation of Students Arrival time and service time for 10 days of registration in Niger State Polytechnic Zungeru, shown in the tables below

Table 4.1 Day One

Time	Arriva	Service
9-9.59am	65	55
10-10.59am	56	43
11-11.59am	64	47
12-12-59pm	54	53
1-2pm	53	42
total	292	240

Table 4.2 Day Two

Time	Arriva	Service
9-9.59am	58	39
10.10.59am	56	38
11-11.59am	61	47
12-12-59pm	43	42
1-2pm	47	32
Total	265	198

Table 4.3 Day Three

Time	Arriva	Service
9-9.59am	34	27
10.10.59am	55	39
11-11.59am	52	37
12-12-59pm	43	22
1-2pm	41	28
Total	225	153

Table 4.4 Day Four

Time	Arriva	Service
9-9.59am	24	16

10.10.59am	31	17
11-11.59am	23	14
12-12-59pm	18	14
1-2pm	20	11
Total	116	72

Table 4.5 Day Five

Time	Arriva	Service
9-9.59am	17	4
10.10.59am	35	25
11-11.59am	23	21
12-12-59pm	32	19
1-2pm	20	12
Total	127	81

Table 4.6 Day Six

Time	Arriva	Service
9-9.59am	17	12
10.10.59am	32	29
11-11.59am	23	20
12-12-59pm	36	28
1-2pm	25	21
Total	133	110

Table 4.7 Day Seven

Time	Arriva	Service
9-9.59am	5	1
10.10.59am	43	31
11-11.59am	27	22
12-12-59pm	36	31
1-2pm	25	21
Total	136	106

Table 4.8 Day Eight

Time	Arriva	Service
9-9.59am	14	9
10.10.59am	43	31
11-11.59am	42	31
12-12-59pm	39	31
1-2pm	31	25
Total	169	127

Table 4.9 Day Nine

Time	Arriva	Service
9-9.59am	10	9

10.10.59am	21	12
11-11.59am	30	22
12-12-59pm	22	18
1-2pm	19	11
Total	102	72

Table 4.10 Day Ten

Time	**Arriva**	**Service**
9-9.59am	34	19
10.10.59am	32	27
11-11.59am	46	29
12-12-59pm	33	23
1-2pm	43	30
Total	188	128

Table 4.11 Summary of Students Arrival time and service time from day 1 to day 10 during school registration in Niger state Polytechnic Zungeru,

Day	**Time**	**Arrival time**	**Service time**
1	9-2pm	292	240
2	9-2pm	265	198
3	9-2pm	225	153
4	9-2pm	116	72
5	9-2pm	127	81
6	9-2pm	133	110
7	9-2pm	136	106
8	9-2pm	169	127
9	9-2pm	102	72
10	9-2pm	188	128
Total		**1744**	**1287**

Source: Students Affairs, Niger State Polytechnic, Zungeru (2020)

Queening Theory Analysis

Average number of customers that arrive

$$\frac{1744}{10} = 174.4$$

Average number of customer that was served

$$\frac{1287}{10} = 128.7$$

:- $\lambda = \frac{60}{174.4} = 0.344\ per\ hours$

: - $\mu = \frac{60}{128.7} = 0.466\ per\ hours$

Convert to minutes

0.344 x 60 =20.60 min

0.466 x 60 = 27.96min

Utilization Factor

$$\rho = \frac{20.69}{27.96} = 0.7368$$

the average number of students in the system

$$\text{ns} = \frac{\boldsymbol{\lambda}}{\boldsymbol{\mu} - \boldsymbol{\lambda}} = \frac{20.60}{27.96-20.60} = \frac{20.60}{7.36} = 2.7989$$

Average length of the queue

$$\text{nq} = \frac{\boldsymbol{\lambda^2}}{\boldsymbol{\mu}\,(\boldsymbol{\mu} - \boldsymbol{\lambda})} = \frac{20.60^2}{27.96(27.96-20.60)} = \frac{424.36}{27.96(7.38)} = 2.06$$

Average waiting time of

$$\text{ws} = \frac{\mathbf{l}}{\boldsymbol{\mu} - \boldsymbol{\lambda}} = \frac{1}{27.96-20.60} = \frac{1}{7.36} = 0.14$$

Average waiting time of an arrival in the queuing

$$\text{wq} = \text{ws} - \frac{\mathbf{l}}{\boldsymbol{\mu}} = \frac{\text{nq}}{\boldsymbol{\lambda}} = \frac{\mathbf{2.06}}{\mathbf{20.60}} = 0.1$$

Probability that the system is busy

$$\frac{\lambda}{\mu} \times 100 = \frac{20.60}{27.96} \times 100 = 73.67$$

Probability of zero unit in the queuing

$$\text{P} = 1 - \frac{\boldsymbol{\lambda}}{\boldsymbol{\mu}} = 1 - \frac{\mathbf{20.60}}{\mathbf{27.96}} = 1 - 0.74 = 0.26$$

Discussion of Result

From the single channel queue situation, it was observed from the findings of that the arrival rate when the service point is 1 is 0.344 and the average time a student stays in the student's affair is 27.97 minutes. It was also observed that the probability that the system is busy is 73.67%, the probability that there was no students in the system is 0.26 (26%), and average of number of students in the system is 2.8 while the average time spent in the system is 0.14. By implication, it can be deduced that the queuing at students' academic affair is still very long, thus, the student that come to the office of students affair for one problem of the other

would have to wait for long before being attended to. This may be attributed to network complexities and influx of student and insufficient of service providers thus, making the service to be relatively slow

CONCLUSION AND RECOMMENDATION

Summary of findings

S/N	Services	Dataset
1	Service point	1
2	Arrival rate	174.4
3	Service rate	0.344
4	Utilization factor	0.7367
5	Probability that there is no customer in the system	0.26
6	Number of customer in the system	2.8
7	Arrival time spent in the system	0.14

This study is based on the queuing theory model in evaluating the efficiency of service in students' academic affair, Niger State polytechnic Zungeru. The type of data used for this study work is primary data, it was obtained through direct observation on the arrival and service rate of students at students' academic affair Niger State polytechnic Zungeru from 9.00am to 2.00pm for the period of 10 day. A single queuing model was applied in evaluating the pattern of the data. The result obtained shows that the arrival rate when the service point is 1 is 174.4 and the average time a student stays in the student's affair is 27.97 minutes. It was also observed that the probability that the system is busy is 73.67%, the probability that there was no students in the system is 0.26 (26%), and average of number of students in the system is 2.8 while the average time spent in the system is 0.14.

Conclusion

In conclusion, based on the above finding, it can be seen that the queuing system operated at the office of students' academic affair Niger State polytechnic Zungeru is insufficient enough. This could be as a result of the fact that the servers are not that fast by the service provider.

Recommendation

Based on the finding it can be recommended that the school management students' should provide more server or staffs in support of the existing one to the office of academic students affair Niger State polytechnic Zungeru so as to improve the service render to the students.

REFERENCE

Alfares P., (2009) Performance characterization of complex manufacturing systems with general distributions and job failures, European Journal of Operational Research 197: 588-598

Anichebe, H., (2013), Capacity planning with congestion effects, European Journal of Operational Research 134: 365-377

Acheampong Y., (2013). Structural Estimation of Callers Delay Sensitivity in Call Centers. *International Journal Service & Industrial. Management.* 6 (1), 42 -53

Aksin-Karaesmen (2011) A mathematical model of computerized manufacturing systems, roceedings of the 4th International Conference on Production Research, Tokyo, Japan: 1265-1275

Bakari B., (2009), A review of decomposition methods for open queuing methods in Rapid Modeling for Increased Competitiveness: Tools and Mindset, G Reiner, Ed., New York: Springer 67

Brown T., (2012), Motivation: New Directions for Theory, Research, and Practice. The Academy of Management Review 7(1): 80-88

Barak C. (2012). Queuing Process and its Application to Customer Service Delivery: A Case study of Fidelity Bank Plc, Maiduguri. *International Journal of Mathematics and Statistics Invention*, 2(1), 14-21.

Banks R, Campbell, D. and Frei, F. (2011). Market Heterogeneity and Local Capacity Decisions in Services. *Manufacturing & Service Operations Management Research*, 5 (1),31-41.

Cugnasca S. (2007), Approximate analysis of general queuing networks by decomposition, IEEE Transaction on Communications 27(1): 113-126

Duder R. and Rosenwein E. (2001), Employee scheduling and makespan minimization in a flow shop with multi-processor work stations: a case study, Omega 32: 121-129

Hillier J. and Lieberman M.M (2007) How disconfirmation, perception and actual waiting times impact customer satisfaction. *Int.. Serv. Ind. Manage.* 9 (1), 64 -73.

Lakshmi R. and Lyer O. (2013), Assignment problems: A golden anniversary survey, European Journal of Operational Research (176): 774-793

May T., (2012),, Optimization of mixed-skill multi-line operator allocation problem, Computers & Industrial Engineering 53: 386-393

Nafees Y. (2007) A method for planning analysis and design simulation of CIM systems, Proceedings of the 1987 Winter Simulation Conference

Olaniyi, J.K. (2004). Queuing theory and Patient Satisfaction: An overview of terminology & application in Ante-Natal care unit. http://www.upg-bulletin-se.ro. *Marketing Science*, 23(2), 38-48.

Ogbadu R. and Usman A. (2012) Waiting line model applications in manufacturing, International Journal of Production Economics 54: 1-28

Forbes E., (2008), Cross-training in a cellular manufacturing environment, Computers & Industrial Engineering 48: 609-624

Odirichukwu Suri, R., Diehl, G., de Treville, S., Tomsicek, M., (2014), From CAN-Q to MPX: Evolution of queuing software for manufacturing

Odunukwe W., (2013), The deployment of temporary production workers in assembly operations: a case study of the hidden costs of learning and forgetting, Journal of Operations Management 21: 689-707

Sharma T. Hopp, J., Spearman, M., (2013), Factory physics: foundation of manufacturing management, 2nd Edition, McGraw-Hill, New York, NY.

Suri, R., 1998, Quick response manufacturing: a companywide approach to reducing lead times. Productivity Press, Portland, OR.

Whitt D. (2005) Queuing Systems with phase type service, Operational Research Society 5(4): 109-120

Woensel R. and Vandaele S. (2007), Performance implications of assembly work teams, Journal of Operations Management 22: 387-412

Zeng, S. (2007). Waiting for Service: The Relationship between Delays and Evaluation of Service. *Journal of Marketing*, 58(2): 56-69.

SECOND REFINEMENT OF PRECONDITIONED ACCELERATED OVERRELAXATION METHOD FOR SOLUTION OF LINEAR ALGEBRAIC SYSTEMS

[1]Chuks Joseph Obed, [2]Abdulrahman Ndanusa
[1,2]*Department of Mathematics, Federal University of Technology, Minna, Nigeria*
Obedchuks74@gmail.com, as.ndanusa@futminna.edu.ng

Abstract
This present work concerns the numerical solution of linear system of algebraic equation $Ax = b$ by second refinement of accelerated overrelaxation (AOR) method. This technique is especially useful in solving linear systems arising from discretisation of ordinary differential equations or partial differential equations where the coefficient matrix is an irreducibly diagonally dominant $L - matrix$. A suitable preconditioner is applied to the linear system before a second refinement algorithm is processed. As in all iterative methods for linear systems, this is aimed at minimizing the spectral radius in order to reduce the number of iterations needed for convergence. Numerical examples proved the efficiency of second refinement of preconditioned AOR over the AOR, preconditioned AOR and first refinement of AOR methods.

Keywords: AOR, Preconditioned AOR, First-degree refinement, Second-degree refinement, Irreducible, Weak diagonal dominance.

INTRODUCTION

In order to solve the system of n linear equations in n unknowns expressed in matrix form

$$Hx = c \tag{1}$$

where H is a nonsingular square matrix of size $n \times n$ with nonvanishing diagonal entries, x and c are unknown and known vectors respectively, we consider a usual splitting of H into its diagonal, strictly lower and strictly upper parts thus,

$$H = I - E - F \tag{2}$$

where $-E$ and $-F$ are the strictly lower and strictly upper parts of H respectively. It is assumed, for simplicity, that every diagonal entry of H is unity. The Jacobi, Gauss-Seidel and successive overrelaxation (SOR) are some of the basic iterative methods for solving (1). They are defined respectively by the relations

$$x^{(n+1)} = \mathcal{L}_J x^{(n)} + k_J \qquad n = 0,1,2,\cdots \tag{3}$$

$$x^{(n+1)} = \mathcal{L}_G x^{(n)} + k_G \qquad n = 0,1,2,\cdots \tag{4}$$

and

$$x^{(n+1)} = \mathcal{L}_\omega x^{(n)} + k_\omega \qquad n = 0,1,2,\cdots \tag{5}$$

where $\mathcal{L}_J = (L + U), k_J = c,\ \mathcal{L}_G = (I - L)^{-1}, k_G = (I - L)^{-1}c,\ \mathcal{L}_\omega = (I - \omega E)^{-1}\{(1 - \omega)I + \omega F\}, k_\omega = (I - \omega E)^{-1}\omega c,$ for $0 < \omega < 2$. The accelerated overrelaxation (AOR) method introduced by Hadjidimos (1978) is a two-parameter generalization of the SOR method. Judicious exploitation of the two parameters involved leads to methods that will converge in minimal number of iterations than other methods of the same type. It has the representation

$$x^{(n+1)} = \mathcal{L}_{r,\omega} x^{(n)} + k_{r,\omega} \qquad n = 0,1,2,\cdots \tag{6}$$

where $\mathcal{L}_{r,\omega} = (I - rE)^{-1}[(1-\omega)I + (\omega - r)E + \omega F], k_{r,\omega} = (I - rE)^{-1}\omega b$, for $0 \leq r \leq \omega < 1$. The matrix $\mathcal{L}_J = (L + U)$ is known as the Jacobi iteration matrix and its spectral radius is defined by

$$\rho(\mathcal{L}_J) = \bar{\mu} \tag{7}$$

For the Gauss-Seidel iteration matrix $\mathcal{L}_G = (I - L)^{-1}$, its spectral radius is found to be the square of spectral radius of Jacobi iteration matrix, that is,

$$\rho(\mathcal{L}_G) = \bar{\mu}^2 \tag{8}$$

For matrices with certain properties, an optimum value for the relaxation parameter ω that appears in the SOR iteration matrix $\mathcal{L}_\omega = (I - \omega E)^{-1}\{(1-\omega)I + \omega F\}$ is governed by the relation

$$\omega = \frac{2}{1+\sqrt{1-\bar{\mu}^2}} \tag{9}$$

And for this choice of ω the spectral radius of the SOR iteration matrix is obtained as

$$\rho(\mathcal{L}_\omega) = \omega - 1 = \frac{1-\sqrt{1-\bar{\mu}^2}}{1+\sqrt{1-\bar{\mu}^2}} \tag{10}$$

The matrix defined by $\mathcal{L}_{r,\omega} = (I - rE)^{-1}[(1-\omega)I + (\omega - r)E + \omega F]$ is the AOR iteration matrix whose spectral radius can be computed from the formula

$$\rho(\mathcal{L}_{r,\omega}) = \frac{\underline{\mu}\sqrt{\bar{\mu}^2 - \underline{\mu}^2}}{\sqrt{1-\underline{\mu}^2}(1+\sqrt{1-\bar{\mu}^2})} \tag{11}$$

provided

$$0 < \underline{\mu} < \bar{\mu} \text{ and } 1 - \underline{\mu}^2 < \sqrt{1-\bar{\mu}^2} \tag{12}$$

for the optimum values of ω and r

$$\omega = \frac{2}{1+\sqrt{1-\bar{\mu}^2}} \text{ and } r = \frac{\left(1-\underline{\mu}^2\right) - \sqrt{1-\bar{\mu}^2}}{\left(1-\underline{\mu}^2\right)(1+\sqrt{1-\bar{\mu}^2})} \tag{13}$$

respectively; where $\underline{\mu} = \min_i|\mu_i|, = \bar{\mu} = \max_i|\mu_i|$ and $\mu_i|i = 1(1)n$ define the eigenvalues of Jacobi iteration matrix $\mathcal{L}_J = (L + U)$.

When large sparse linear systems are involved, the method of choice is obviously iterative methods. However, the number of iterations needed for such methods to attain convergence could be relatively large. When such is the case, the need arises to remodel or redesign the existing methods so as to obtain approximate solutions that attain fast convergence. This paper investigates the successive application of two acceleration techniques, preconditioning and second refinement, to the solution of linear system with coefficient matrix that is irreducibly diagonally dominant, with the aim of reducing the spectral radius to the barest minimum so as to attain convergence in a few number of iterations.

Preconditioning entails the application of a preconditioner P, a nonsingular transformation matrix, to the linear system (1) resulting in an equivalent system

$$PHx = Pc \tag{14}$$

The resulting system (7) which has the same solution as system (1) is expected to converge faster than the original system (1). Some recent developments in preconditioning techniques include the works of Li and Sun (2000), Kotakemori *et al.* (2002), Morimoto *et al.* (2004),

Ndanusa and Adeboye (2012), Mayaki and Ndanusa (2019), Faruk and Ndanusa (2019), Abdullahi and Ndanusa (2020), Ndanusa (2020), Ndanusa *et al.* (2020) and Ndanusa and Al-Mustapha (2021).

Refinement of iterative methods entail performing iterations on the linear system whose right-hand side is the residual vector for successive approximations until satisfactory accuracy results. Refinement of AOR method, introduced by Vatti *et al.* (2018) is described by the relation

$$x^{(n+1)} = \mathcal{L}_{r,\omega}{}^{2} x^{(n)} + d \tag{15}$$

where $\mathcal{L}_{r,\omega}{}^{2} = [(I - rE)^{-1}\{(1-\omega)I + (\omega - r)E + \omega F\}]^2$, $d = \omega\left[I + \mathcal{L}_{r,\omega}\right](I - rE)^{-1}c$. This paper discusses a refinement of refined accelerated overrelaxation method for solving the linear system (1), which is named second refinement of accelerated overrelaxation method. some pioneering studies in this field include the works of Kebede (2017), who proposed a new method for solving the linear system $Ax = b$ that often arise in engineering and scientific applications; this method, which is known as second-degree refinement of Jacobi iterative method, is based on the second-degree Jacobi stationary iterative method. The relationships between the spectral radius of second-degree refinement of Jacobi method and spectral radii of first-degree Jacobi, first-degree refinement of Jacobi and second-degree Jacobi methods were established. Numerical results demonstrated that for a coefficient matrix that is strictly diagonally dominant and positive definite, the second-degree refinement of Jacobi iterative method proved to be very effective and efficient as it converges faster than the existing first-degree Jacobi, first-degree refinement of Jacobi and second-degree Jacobi methods. Eneyew *et al.* (2019) focused on a second refinement of Jacobi (SRJ) method for the solution of system of linear equations obtained from ordinary differential equation and partial differential equation problems, where the coefficient matrix is strictly diagonally dominant or symmetric positive definite or $M-$matrix. In such cases, there occurs a significant reduction in spectral radius of iteration matrix of the proposed method, with attendant reduction in number of iterations, which translates to increased convergence. Some numerical examples were presented to validate the theoretical analysis which further established the superiority of the second refinement of Jacobi method over Jacobi and refinement of Jacobi methods.

Eneyew *et al.* (2020) modified the Gauss-Seidel method to obtain a second-refinement of Gauss-Seidel method for solution of system of linear equations, in order to enhance convergence rate, minimize the spectral radius, and by implication, reduce the number of iterations needed for convergence. This method is equally applicable to solution of differential equations that are transformed into linear systems by application of finite differences. Such systems are characterized by coefficient matrices that are strictly diagonally dominant, symmetric positive definite, or M-matrices. Theoretical analysis established that the method converges for these types of matrices. Results of numerical experiments further demonstrated the efficiency of second-refinement of Gauss-Seidel method over the Gauss-Seidel and refinement of Gauss-Seidel methods.

In Assefa and Teklehaymanot (2021), a second refinement of accelerated over relaxation method was introduced; which is just a refinement of first-degree refinement of accelerated over relaxation method, whereby the spectral radius of iteration matrix of the method was observed to be significantly reduced in comparison to the spectral radii of accelerated over relaxation (AOR) method and first-degree refinement of accelerated over relaxation methods. In addition, the optimal value of each parameter involved in the method was derived.

Derivation of the third-degree, fourth-degree and in general the $kth-$ degree refinement of accelerated methods were also obtained. The spectral radius of the iteration matrix and convergence criteria of the second refinement of accelerated over relaxation (SRAOR) are discussed.

Finally, a numerical experiment was undertaken to demonstrate the efficiency of the proposed method over other existing methods. Eneyew *et al.* (2021) proposed a second refinement of generalized Jacobi method for solution of linear systems. This method proved to be the fastest method to converge to the exact solution when compared to Jacobi, refinement of Jacobi, generalized Jacobi and refinement of generalized Jacobi methods for strictly diagonally dominant, symmetric positive definite and M-matrices.

MATERIALS AND METHODS

Preconditioning of Linear System

Consider a linear system of the form

$$Ax = b \tag{16}$$

where $A = (a_{ii})$ is an irreducibly diagonally dominant $L-$ matrix of order n, b is a given $n-$ dimensional vector and x is an $n-$ dimensional vector to be determined. Consider the usual splitting of A as,

$$A = D_A - E_A - F_A$$

where $D_A, -E_A$ and $-F_A$ are the diagonal, strictly lower and strictly upper triangular parts of A respectively. equation (16) is further expressed as

$$D_A{}^{-1}Ax = D_A{}^{-1}b$$
$$D_A{}^{-1}(D_A - E_A - F_A)x = D_A{}^{-1}b$$
$$\left(I - D_A{}^{-1}E_A - D_A{}^{-1}F_A\right)x = D_A{}^{-1}b$$

Thus, we have obtained the equivalent system

$$Bx = f \tag{17}$$

with the corresponding splitting

$$(I - E_B - F_B)x = f$$

Where I is the identity matrix of order n, $-E_B$ and $-F_B$ being the strictly lower and strictly upper triangular parts of B respectively. A transformation matrix P is then applied to system (17) as

$$PBx = Pf$$

which results in the preconditioned system

$$Tx = k \tag{18}$$

The matrix T of (18) has the splitting $T = D_T - E_T - F_T$. This is further transformed into

$$D_T{}^{-1}(D_T - E_T - F_T)x = D_T{}^{-1}k$$

That is,

$$Hx = c \tag{19}$$

Derivation of Second Refinement of AOR

Following Vatti *et al.* (2018) and Assefa and Teklehaymanot (2021), a reformulation of second refinement of AOR method is derived from (19) thus,

$$(I - E - F)x = c$$
$$Ix - rEx + \omega(I - E - F)x = Ix - rEx + \omega c$$
$$(I - rE)x = (I - rE)x - \omega(I - E - F)x + \omega c$$
$$(I - rE)x = (I - rE)x + \omega(c - Hx)$$
$$x = x + \omega(I - rE)^{-1}(c - Hx)$$

Consequently, the second refinement of AOR is defined as

$$x^{(n+1)} = x^{(n+1)} + \omega(I - rE)^{-1}\left(c - Hx^{(n+1)}\right) \tag{20}$$

where $x^{(n+1)}$ that appeared in the $(n+1)th$ approximation of refinement of AOR given by (15). Substituting (15) in (16),

$$x^{(n+1)} = \mathcal{L}_{r,\omega}{}^2 x^{(n)} + \omega\left[I + \mathcal{L}_{r,\omega}\right](I - rE)^{-1}c + \omega(I - rE)^{-1}(c - (I - E - F)\{\mathcal{L}_{r,\omega}{}^2 x^{(n)} + \omega\left[I + \mathcal{L}_{r,\omega}\right](I - rE)^{-1}c\})$$

$$x^{(n+1)} = \mathcal{L}_{r,\omega}{}^2 x^{(n)} + \omega\left[I + \mathcal{L}_{r,\omega}\right](I - rE)^{-1}c + \omega(I - rE)^{-1}c - \omega(I - rE)^{-1}(I - E - F)\{\mathcal{L}_{r,\omega}{}^2 x^{(n)} + \omega\left[I + \mathcal{L}_{r,\omega}\right](I - rE)^{-1}c\}$$

$$x^{(n+1)} = \mathcal{L}_{r,\omega}{}^2 x^{(n)} - (I - rE)^{-1}(\omega I - \omega E - \omega F)\mathcal{L}_{r,\omega}{}^2 x^{(n)} + \omega(I + \mathcal{L}_{r,\omega})(I - rE)^{-1}c + \omega(I - rE)^{-1}c - (I - rE)^{-1}(\omega I - \omega E - \omega F)\omega(I + \mathcal{L}_{r,\omega})(I - rE)^{-1}c$$

$$x^{(n+1)} = \mathcal{L}_{r,\omega}{}^2[I - (I - rE)^{-1}(\omega I - \omega E - \omega F)]x^{(n)} + \omega[I + \mathcal{L}_{r,\omega} + I - (I - rE)^{-1}(\omega I - \omega E - \omega F)(I + \mathcal{L}_{r,\omega})](I - rE)^{-1}c$$

$$x^{(n+1)} = \mathcal{L}_{r,\omega}{}^2[I - (I - rE)^{-1}(\omega I - \omega E - \omega F)]x^{(n)} + \omega[I + (I + \mathcal{L}_{r,\omega})(I - (I - rE)^{-1}(\omega I - \omega E - \omega F)(I + \mathcal{L}_{r,\omega}))](I - rE)^{-1}c$$

Note that,

$$I - (I - rE)^{-1}(\omega I - \omega E - \omega F) = (I - rE)(I - rE)^{-1} - (I - rE)^{-1}\omega I + (I - rE)^{-1}\omega E + (I - rE)^{-1}\omega F = (I - rE)^{-1}\{(1 - \omega)I + (\omega - r)E + \omega F\} = \mathcal{L}_{r,\omega}$$

$$x^{(n+1)} = \mathcal{L}_{r,\omega}{}^2\left[\mathcal{L}_{r,\omega}\right]x^{(n)} + \omega[I + (I + \mathcal{L}_{r,\omega})\mathcal{L}_{r,\omega}](I - rE)^{-1}c$$

$$x^{(n+1)} = \mathcal{L}_{r,\omega}{}^3 x^{(n)} + \omega\left[I + \mathcal{L}_{r,\omega} + \mathcal{L}_{r,\omega}{}^2\right](I - rE)^{-1}c \tag{21}$$

Or more compactly,

$$x^{(n+1)} = \mathcal{L}_{r,\omega}{}^3 x^{(n)} + d$$

where $\mathcal{L}_{r,\omega}{}^3 = [(I - rE)^{-1}\{(1 - \omega)I + (\omega - r)E + \omega F\}]^3, d = \omega\left[I + \mathcal{L}_{r,\omega} + \mathcal{L}_{r,\omega}{}^2\right](I - rE)^{-1}c$.

Numerical Example

Consider the matrix

$$A = \begin{pmatrix} 4 & -1 & 0 & -1 & 0 & 0 \\ -1 & 4 & -1 & 0 & -1 & 0 \\ 0 & -1 & 4 & 0 & 0 & -1 \\ -1 & 0 & 0 & 4 & -1 & 0 \\ 0 & -1 & 0 & -1 & 4 & -1 \\ 0 & 0 & -1 & 0 & -1 & 4 \end{pmatrix}$$

The various iteration matrices for the accelerated overrelaxation (AOR), refinement of accelerated overrelaxation (RAOR), preconditioned accelerated overrelaxation (PAOR), refinement of accelerated overrelaxation (RPAOR) and second refinement of accelerated overrelaxation (SRPAOR) methods obtained. The eigenvalues, parameters and spectral radii of AOR, PAOR, RPAOR and SRPAOR are computed and presented in Table 1. The rate of convergence of an iterative method $x^{(n+1)} = \mathcal{L}x^{(n)} + k$, defined by $R(\mathcal{L}) = -\log\rho(\mathcal{L})$, where $\rho(\mathcal{L})$ is the spectral radius for that iterative method, is a measure of how fast it converges. Convergence rates of the various iteration processes are also computed and compared in Table 2.

RESULTS AND DISCUSSION

Table 1 Spectral radii of AOR, PAOR, RAOR, RPAOR and SRPAOR for $\underline{\mu} = 0.1035533905$, $\bar{\mu} = 0.6035533905$, $r = 0.1940348044$ and $\omega = 1.112766298$

AOR	PAOR	RAOR	RPAOR	SRPAOR
0.03444347059	0.01577699105	0.001186352666	0.0002489134466	$6.195790390 \times 10^{-8}$

Table 2 Rates of convergence of AOR, PAOR, RAOR, RPAOR and SRPAOR for $\underline{\mu} = 0.1035533905$, $\bar{\mu} = 0.6035533905$, $r = 0.1940348044$ and $\omega = 1.112766298$

AOR	PAOR	RAOR	RPAOR	SRPAOR
3.368435832	4.149202663	6.736871665	8.298405326	16.59681065

In Table 1, the spectral radii of iteration matrices of AOR, PAOR, RAOR, RPAOR and SRPAOR are displayed, with the least value being that of SRPAOR and the highest being for AOR. This indicates that the SRPAOR converges faster than all the other methods considered in the order SPAOR > RPAOR>RAOR>PAOR>AOR. Table 2 compares the rates of convergence of the various iteration techniques. It indicates that the SRPAOR converges approximately five times as fast as the AOR.

CONCLUSION

The spectral radius of an iterative method for solution of linear algebraic systems is sufficient for convergence of the method, and the smaller it is the faster the convergence. The main goal of any new iterative method is to improve upon the convergence of existing methods. In this research, we employed the techniques of preconditioning and refinement to introduce a second refinement of preconditioned AOR method for the solution of linear systems. Numerical experiments confirmed the superiority of second SRPAOR over the AOR, PAOR, RAOR and RPAOR methods.

REFERENCES

Abdullahi, I. and Ndanusa, A. (2020). A new modified preconditioned accelerated overrelaxation (AOR) iterative method for $L-$matrix linear algebraic systems. Science World Journal, 15(2): 45 – 50.

Assefa, W. L. and Teklehaymanot, A. W. (2021). Second refinement of accelerated over relaxation method for the Solution of Linear System. *Pure and Applied Mathematics Journal*, 10(1): 32-37. doi: 10.11648/j.pamj.20211001.13

Eneyew, T. K., Awgichew, G., Haile, E. and Abie, G. D. (2019). Second refinement of Jacobi iterative method for solving linear system of equations. *International Journal of Computing Science and Applied Mathematics*, 5(2): 41-47.

Eneyew, T. K., Awgichew, G., Haile, E. and Abie, G. D. (2020). Second refinement of Gauss-Seidel iterative method for solving linear system of equations. *Ethiopian Journal of Science and Technology*, 13(1): 1-15.

Faruk, A. I. and Ndanusa, A. (2019). Improvements of successive overrelaxation iterative (SOR) method for *L*-Matrices. Savanna Journal of Basic and Applied Sciences (SJBAS), 1(2): 218 – 223.

Hadjidimos, A. (1978). Accelerated overrelaxation method. *Mathematics of Computation*, (32) 141: 149-157.

Kebede, T. (2017). Second degree refinement Jacobi iteration method for solving system of linear equation. *International Journal of Computing Science and Applied Mathematics*, 3(1): 5-10.

Kotakemori, H., Harada, K., Morimoto, M. and Niki, H. (2002). A comparison theorem for the iterative method with the preconditioner $(I + S_{max})$. Journal of Computational and Applied Mathematics, 145: 373-378.

Li, W. and Sun, W. (2000). Modified Gauss–Seidel type methods and Jacobi type methods for $Z-$ matrices. Linear Algebra and its Applications, 317: 227-240.

Mayaki, Z. and Ndanusa, A. (2019). Modified successive overrelaxation (SOR) type methods for M-matrices. Science World Journal, 14, 4, pp. 1-5.

Morimoto, M., Harada, K., Sakakihara, M. and Sawami, H. (2004). The Gauss–Seidel iterative method with the preconditioning matrix $(I + S_{max} + S_m)$. Japan J. Indust. Appl. Math., 21: 25-34.

Ndanusa, A. (2020). Convergence of preconditioned Gauss-Seidel iterative method for $L-$matrices. Communication in Physical Sciences, 6(1): 803 – 808.

Ndanusa, A. and Adeboye, K. R. (2012). Preconditioned SOR iterative methods for $L-$matrices. American Journal of Computational and Applied Mathematics, 2(6): 300-305.

Ndanusa, A. & Al-Mustapha, K. A. (2021, August 29 – September 3). *A modified SOR iterative scheme for systems of linear algebraic equations with M-matrices* [Paper presentation]. 57th Annual National Conference of Mathematical Association of Nigeria (MAN), BUK, Kano, Nigeria.

Ndanusa, A., David, B. E., Ayantola, B. B. and Abubakar, A. W. (2020). Improving preconditioned Gauss-Seidel iterative method for $L-$matrices. FUDMA Journal of Science (FJS), 4(1): 453 – 459.

Vatti, V. B. K. Sri, R. and Mylapalli, M. S. K. (2018). A refinement of accelerated over relaxation method for the solution of linear systems. *International Journal of Pure and Applied Mathematics,* 118(18): 1571-1577.

Application of Queuing Theory to an ATM Gallery of a Bank

Ngutor Nyor And Abdulateef Adekola Adeleke
Department of Mathematics, Federal University of Technology Minna, Niger State

ABSTRACT

Queues are common occurrences in life. Queues are seen in places such as Banks, Supermarket or Grocery Stores, Clinics, Petrol Filling Stations, Hospitals, Automated Teller Machine (ATM) Service Points, Motor Parks, Food Service points and so on. Queuing theory is the recognized study of waiting line and it is an entire discipline in Operations Research. The study identified that it would interest the Bank to know the optimum service rate of customers at its Automated Teller Machine (ATM) gallery. The research aimed to determine the operating characteristics of the service points with multiple server system. Data was collected from the ATM gallery of the Guarantee Trust Bank Tunga, Minna Niger State through primary source by direct observations for arrival rate, service rate and departure rate per hour for a period of one week. The Kendell-Lee Model M/M/s (∞FIFO) where L_s, L_q, W_s, and W_q were computed.

Key Words: Reneging, Jockeying, Queuing Disciplines, Queue behavior, Service Mechanism

INTRODUCTION

Analytically understanding the operating characteristics of a queue at the Automated Teller Machine (ATM) gallery of a Bank in a State Capital when there are no festivals in order to determine its traffic intensity was the trust of this study. Queuing or queue is a general aspect or phenomenon of life and it occurs in our day to day activities. Examples of queuing systems include Customers waiting for service in post-office, banks, ATM service points, supermarket, restaurants, hair-saloons; Machinery waiting for repairs or maintenance; Employees in an organization waiting to enter into an elevator; Passenger waiting at a bus stop to enter a bus; Customers waiting at an automated teller machine service point to be served; Telephone calls into a call center waiting to be answered.

Waiting and queuing problems are most normal attributes not only in our daily-life condition as listed above but also in more technical circumstances, such as in manufacturing, computer networking and telecommunications. “Queuing models provide the analyst with a powerful tool for designing and evaluating the performance of queuing system.” Queuing theory has to do with customer waiting in the line in a particular manner for their turn to receive service. It is a discipline in the field of Operation Research Management. Customer satisfaction has been declared as one of the most distinguishing features of making competitive advantage in service industries. The Automated Teller Machine (ATM) is one of the several electronic banking channels used in the banking industry. Automated Teller Machines are among the most important service facilities used by customers in the banking industry. In Nigeria, ATM as a banking instrument has enjoyed widespread acceptance and usage. In a particular survey, more than half of respondents revealed their preference for ATM as a conduit to conducting transactions.

ATMs particularly when installed off-site serve to keep customers away from bank halls. Unfortunately, most ATMs in Nigeria are on-site operating very much as another department of the bank. The issue of queue control in bank halls via ATM is essentially defeated because ultimately access to these facilities is limited to customers going to the bank. ATMs have become subjects of large service demands which directly translate to queues for services when these demands cannot be quickly satisfied. This situation becomes compounded and more evident during festive periods and month endings, around which time demand for cash is high. Banking industries can increase their profit through satisfying their customers. For instance, an ATM that receives and accommodates huge inflow of customers can be detrimental to its smooth running and response time. A slow response would greatly affect the speed at which service is provided to customers. As a result, service providers may lose customers who grow impatient and leave the system. The business order now is the ability to acquire and retain customers. This centrally lies in the ability of firms to satisfy and provide better service experiences. As such managers of service systems need to design apt strategies to tackle challenges brought about as a result of lengthy queues. Speed service and therefore queue length can be considered as the most dominant factor on customer satisfaction and applicably the revenue. (Egwe et al., 2014; Al-Mater, 2016; Kahraman & Gosavi; 2011).

Queuing model vary from single to multiple channel systems. Most at times the rate of customer arrival requiring service is greater than the service rate, this imbalance might be temporal but during this period of imbalance, a queue is always found. According to Obamiro (2014), for many customers, waiting in line or queuing is annoying or have negative experience.

This research aimed at determining the operating characteristics of the queues at an ATM Gallery of Guarantee Trust Bank (GTB) PLC Tunga in Minna, Niger State with multiple servers and multiple queues as a case study. This branch of the Bank was established on the 10th March, 2008 with the aim of reducing the stress their customers in Niger State (Minna in particular) would be encountering while trying to make transactions. It is expected to run 9 hours per day from Mondays to Fridays, while the bank ATM service point is expected to run 24hours per day and 7 days a week. GTBANK Tunga Minna is located next to Niger State Transport Authority, Plot No. 4936, Paiko Road, Minna.

Queuing Theory has terminologies such as Balking - when a customer decides not to join the queue because it is too long; Reneging - a situation where a customer leaves a queue if they have waited for a long period of time for a particular service; Jockeying - a customer switching from one queue to another, thinking he may be served faster or quicker at this new line; Service Mechanism - describes how the customers are served. It comprises of the number of servers and the duration of the service, both of which may vary in a random fashion structures, which are: single-server, single-queue; multi-server, single-queue and multi-server, multi-queue; Departure and Exist - occurs after the customer has been served; Population Source - this serves as where the arrivals are generated which could be a Finite Population Source or Infinite Population Source and Queuing Disciplines - the technique used to determine the order in which customers are attended to which may be either First-come-first-serve (FCFS)/ First-In-First-Out (FIFO); or Last-Come-First-Serve (LCFS)/ Last-In-First-Out (LIFO); or Service in Random Order (SIRO); or Service according to Priority (PR) (Priyangika & Cooray 2016).

MATERIALS AND METHODS

Consider S number of Automated Teller Machine in the banking system and the customer arrival rate is λ and the service rate of each Teller Machine is μ, using the values of Lq, Ls, Wq and Ws in two cases and comparing all these four characteristics in each case. If there are S servers then the system considered as M/M/s queuing system, in this case we will use multi server queuing model to find Lq, Ls, Wq and Ws (Vijay et al., 2015; Vijay & Badshah 2014).

Mathematical Model

For the analysis of the ATM Service Point the M/M/S queuing model will be investigated. The M/M/S model states that the arrival and service time are exponentially distributed (Poisson process). Operating characteristics in a multiple-server queuing system that has Poisson arrivals and exponential service times (M/M/S) analysis the following variables:
λ : The average customer arrival rate

μ : The average service rate

ρ = $\frac{\lambda}{s\mu}$: Utilization factor; where s= number of servers or teller machines

Probability of zero customers in the ATM gallery:

$$\rho_0 = \frac{1}{\left[\sum_{n=0}^{n=s-1} \frac{1}{n!}\left(\frac{\lambda}{\mu}\right)^n\right] + \frac{1}{s!}\left(\frac{\lambda}{\mu}\right)^s \frac{s\mu}{(s\mu-\lambda)}}$$

The average number of customers in the system:

$$L_s = \frac{\left(\frac{\lambda}{\mu}\right)^s \lambda\mu}{(s-1)!(s\mu-\lambda)}\rho_0 + \frac{\lambda}{\mu}$$

The average number of customers in the queue: $L_q = L - \frac{\lambda}{\mu}$

The average waiting time of customers in the queue: $W_q = \frac{L_q}{\lambda}$

The average waiting time customers spend in the system: $W_s = \frac{L_s}{\lambda}$

Queuing Capacity = W_S × Service rate (μ) × Total No of servers in the ATM gallery

(Inria, 2004; Forundam & Herrmann, 2007).

Data collection

The data collected for this study was Primary data through the method of direct observations and personal interview. The arrival pattern of customers in to the gallery and their service pattern were collected using the using four persons through direct observation where the pattern of arrival of customers was observed and counting was made of each customer who arrived the ATM Service Point (gallery). Also, observation was done at the service point to study the time required by a customer to be served. Data for this study was collected from Guarantee Trust Bank PLC (GTBank) Tunga Minna, Niger state. The bank has 9 Automated Teller Machines at the ATM service point. The data was collected through method of primary data collection, personal interview of some customers and direct observation in the GTBank ATM gallery for a period of one week (7 days), from Monday to Sunday. The data is divided into two different sessions; the weekday session which starts from Monday till Thursday, and the weekend session which starts from Friday till Sunday.

The data was collected three different periods for each day; which is morning, afternoon and evening. On Monday data was collected between the hour of 7am to 8am, 11am to 12noon, and 3pm to 4pm. On Tuesday data was collected between the hour of 8am to 9am, 12noon to 1pm, and 4pm to 5pm. Wednesday data was collected between the hour of 9am to 10am, 1pm to 2pm, 5pm to 6pm. Also, data was collected on Thursday between the hour of 10am to 11am, 2pm to 3pm, and 6pm to 7pm. For the weekend, data was collected on Friday between 7am to 8am, 12noon to 1pm, and 4pm to 5pm. On Saturday, data was collected from 8am to 9am, 1pm to 2pm, and 5pm to 6pm. On Sunday, data was collected between the hour of 9am to 10am, 2pm to 3pm, and 6pm to 7pm. At every hour in a day, five customers were picked at random on a particular teller machine so as to know the rate of service of each customer. At each hour of data collection there is always a queue and at least one machine will be available to serve them. Customers join the queue one by one and they are served one by one on a First-Come, First-Served (FCFC) basis. Customers have the chance to make different transactions on the teller machine before leaving the queue. For instance, a customer might decide to check account balance, withdraw a certain amount of money, transfer money to a beneficiary, buy airtime and lot more. All these could be done at a go before the customer leave the queue. It was also observed that when a customer spends more than expected service time, jockeying and reneging occurs. There is no limit on customers joining the queue. The primary data collected shows that there was complete randomness in arrival as well as service patterns. An M/M/s queuing model has been proposed for each queue, which is based on the following assumptions:

(i) The customers arrive at a particular queue one by one and follow Poisson distribution with parameter λ, where λ is the mean arrival rate.

(ii) There are nine Automated Teller Machines (servers) seen at the gallery to serve customers and they are served on FCFS basis. When a particular machine is out of service, the customers have to wait for the next free machine. The service time is independently, identically and exponentially distributed with mean rate μ.

Table 1: Frequency Table of Arrival of Customers into the ATM Gallery During Weekday (Monday to Thursday)

DAY	TIME DURATION	FREQUENCY	NO OF ACTIVE MACHINES
Mon	7:00am to 8:00am	86	3
Tues	8:00am to 9:00am	107	7
Wed	9:00am to 10:00am	163	6
Thurs	10:00am to 11:00am	139	4
Mon	11:00am to 12:00pm	131	5
Tues	12:00pm to 1:00pm	102	3
Wed	1:00pm to 2:00pm	158	4
Thurs	2:00pm to 3:00pm	125	5
Mon	3:00pm to 4:00pm	102	4
Tues	4:00pm to 5:00pm	113	5
Wed	5:00pm to 6:00pm	92	2
Thurs	6:00pm to 7:00pm	104	4

Table 2: Frequency Table of Departure of Customers from the ATM Gallery During Weekday (Monday to Thursday)

DAY	TIME DURATION	FREQUENCY
Mon	7:00am to 8:00am	79
Tues	8:00am to 9:00am	103
Wed	9:00am to 10:00am	168
Thurs	10:00am to 11:00am	149
Mon	11:00am to 12:00pm	136
Tues	12:00pm to 1:00pm	105
Wed	1:00pm to 2:00pm	150
Thurs	2:00pm to 3:00pm	130
Mon	3:00pm to 4:00pm	111
Tues	4:00pm to 5:00pm	119
Wed	5:00pm to 6:00pm	84
Thurs	6:00pm to 7:00pm	99

Table 3: Frequency Table of Arrival of Customers into the ATM Gallery During Weekend (Friday to Sunday)

DAY	TIME DURATION	FREQUENCY	NO OF ACTIVE MACHINES
Fri	7:00am to 8:00am	102	2
Sat	8:00am to 9:00am	59	4
Sun	9:00am to 10:00am	61	5
Fri	12:00Pm to 1:00Pm	158	7
Sat	1:00Pm to 2:00pm	63	5
Sun	2:00pm to 3:00pm	44	3
Fri	4:00pm to 5:00pm	122	4
Sat	5:00pm to 6:00pm	72	3
Sun	6:00pm to 7:00pm	33	3

Table 4: Frequency Table of Departure of Customers from the ATM Gallery During Weekend (Friday to Sunday)

DAY	TIME DURATION	FREQUENCY
Fri	7:00am to 8:00am	99
Sat	8:00am to 9:00am	51
Sun	9:00am to 10:00am	68
Fri	12:00Pm to 1:00Pm	145
Sat	1:00Pm to 2:00pm	60
Sun	2:00pm to 3:00pm	39
Fri	4:00pm to 5:00pm	108
Sat	5:00pm to 6:00pm	61
Sun	6:00pm to 7:00pm	29

Table 5: Duration of Service of Customers on Monday

CUSTOMERS	A.T	W.T	S.S.T	T.S.S	T.T.S.S	D.T
1st	7:02AM	90	7:03AM	132	222	7:06AM
2nd	7:02AM	225	7:06AM	172	397	7:09AM
3rd	7:03AM	340	7:09AM	110	451	7:11AM
4th	7:03AM	456	7:11AM	70	526	7:12AM
5th	7:04AM	530	7:13AM	100	632	7:15AM
6th	11:15AM	33	11:16AM	182	215	11:19AM
7th	11:16AM	100	11:18AM	134	234	11:20AM
8th	11:16AM	230	11:20AM	105	335	11:22AM
9th	11:16AM	337	11:22AM	90	427	11:24AM
10th	11:18AM	10	11:18AM	122	132	11:26AM
11th	3:30PM	76	3:31PM	108	154	3:33PM
12th	3:31PM	102	3:33PM	140	242	3:35PM
13th	3:31PM	243	3:35PM	116	359	3:37PM
14th	3:33PM	230	3:37PM	88	318	3:38PM
15th	3:34PM	243	3:38PM	196	439	3:41PM

Table 6: Duration of Service of Customers on Tuesday

CUSTOMERS	A.T	W.T	S.S.T	T.S.S	T.T.S.S	D.T
1st	8:30AM	25	8:31AM	158	183	8:33AM
2nd	8:30AM	165	8:33AM	195	360	8:36AM
3rd	8:31AM	303	8:37AM	145	448	8:39AM
4th	8:32AM	412	8:39AM	163	575	8:42AM
5th	8:32AM	575	8:42AM	99	674	8:44AM
6th	12:05PM	102	12:07PM	124	226	12:09PM
7th	12:06PM	131	12:09PM	121	252	12:11PM
8th	12:07PM	205	12:11PM	152	357	12:13PM
9th	12:07PM	350	12:13PM	102	452	12:15PM
10th	12:07PM	452	12:15PM	177	629	12:18PM
11th	4:20PM	85	4:20PM	102	197	4:23PM
12th	4:20PM	198	4:23PM	179	377	4:27PM
13th	4:22PM	302	4:27PM	199	501	4:31PM
14th	4:22PM	500	4:31PM	123	623	433PM
15th	4:23PM	498	4:33PM	143	641	4:35PM

Table 7: Duration of Service of Customers on Wednesday

CUSTOMERS	A.T	W.T	S.S.T	T.S.S	T.T.S.S	D.T
1st	9:00AM	67	9:01AM	132	199	9:03AM
2nd	9:00AM	201	9:03AM	145	346	9:06AM
3rd	9:01PM	351	9:06AM	87	438	9:08AM
4th	9:02PM	440	9:09AM	187	627	9:12AM
5th	9:03PM	564	9:12AM	93	657	9:14AM
6th	2:35PM	125	2:37PM	101	226	2:39PM
7th	2:35PM	227	2:39PM	125	352	2:41PM
8th	2:35PM	353	2:41PM	165	518	2:44PM

9th	2:36PM	454	2:44PM	134	588	2:46PM
10th	2:36PM	589	2:46PM	177	766	2:49PM
11th	6:25PM	00	6:25PM	121	121	6:27PM
12th	6:26PM	60	6:27PM	98	132	6:28PM
13th	6:26PM	135	6:28PM	145	280	6:31PM
14th	6:26PM	282	6:31PM	165	447	6:33PM
15th	6:27PM	343	6:33PM	127	470	6:35PM

Table 8: Duration of Service of Customers on Thursday

CUSTOMERS	A.T	W.T	S.S.T	T.S.S	T.T.S.S	D.T
1st	10:15AM	05	10:15AM	128	133	10:17AM
2nd	10:15AM	134	10:17AM	98	232	10:19AM
3rd	10:16AM	230	10:20AM	165	395	10:23AM
4th	10:16AM	397	10:23AM	122	519	10:25AM
5th	10:16AM	520	10:25AM	89	609	10:26AM
6th	1:30PM	16	1:30PM	91	107	1:32PM
7th	1:32PM	07	1:32PM	143	150	1:35PM
8th	1:32PM	152	1:35PM	118	270	1:37PM
9th	1:33PM	227	1:37PM	132	359	1:39PM
10th	1:33PM	361	1:39PM	128	489	1:41PM
11th	5:10PM	34	5:10PM	132	166	5:13PM
12th	5:11PM	102	5:13PM	98	200	5:14PM
13th	5:12PM	138	5:14PM	123	261	5:16PM
14th	5:12PM	262	5:16PM	114	378	5:18PM
15th	5:12PM	380	5:18PM	88	468	5:21PM

Table 9: Duration of Service of Customers on Friday

CUSTOMERS	A.T	W.T	S.S.T	T.S.S	T.T.S.S	D.T
1st	7:30AM	23	7:3OAM	98	121	7:32AM
2nd	7:31AM	86	7:31AM	123	209	7:34AM
3rd	7:32AM	146	7:34AM	165	311	7:37AM
4th	7:32AM	313	7:37AM	111	424	7:39AM
5th	7:32AM	425	7:39AM	104	529	7:41AM
6th	12:15PM	08	12:15PM	97	105	12:17PM
7th	12:15PM	108	12:17PM	127	235	12:19PM
8th	12:17PM	00	12:17PM	178	178	12:20PM
9th	12:18PM	145	12:20PM	105	250	12:22PM
10th	12:19PM	209	12:22PM	87	296	12:24PM
11th	4:00PM	56	4:01PM	143	199	4:03PM
12th	4:00PM	202	4:03PM	114	316	4:05PM
13th	4:02PM	217	4:05PM	166	383	4:08PM
14th	4:02PM	390	4:09PM	104	494	4:10PM
15th	4:03PM	435	4:10PM	113	548	4:12PM

Table 10: Duration of Service of Customers on Saturday

CUSTOMERS	A.T	W.T	S.S.T	T.S.S	T.T.S.S	D.T

1st	8:00AM	02	8:00AM	125	127	8:02AM
2nd	8:01AM	81	8:02AM	176	257	8:05AM
3rd	8:03AM	138	8:05AM	95	233	8:07AM
4th	8:03AM	235	8:07AM	134	369	8:09AM
5th	8:04AM	338	8:09AM	120	458	8:12AM
6th	1:20PM	14	1:20PM	114	128	1:22PM
7th	1:21PM	69	1:22PM	178	247	1:25PM
8th	1:21PM	248	1:25PM	99	347	1:27PM
9th	1:22PM	288	1:27PM	119	407	1:29PM
10th	1:23PM	347	1:29PM	124	471	1:31PM
11th	5:35PM	24	5:35PM	108	132	5:37PM
12th	5:37PM	12	5:37PM	124	136	5:39PM
13th	5:38PM	76	5:39PM	127	203	5:41PM
14th	5:38PM	204	5:41PM	143	347	5:44PM
15th	5:40PM	227	5:44PM	137	364	5:46PM

Table 11: Duration of Service of Customers on Sunday

CUSTOMERS	A.T	W.T	S.S.T	T.S.S	T.T.S.S	D.T
1st	9:15AM	62	9:16AM	100	162	9:18PM
2nd	9:15AM	163	9:18AM	114	277	9:20AM
3rd	9:15AM	279	9:20AM	119	398	9:22AM
4th	9:16AM	339	9:22AM	98	437	9:23AM
5th	9:16AM	438	9:23AM	121	559	9:25AM
6th	2:30PM	23	2:30PM	99	122	2:32PM
7th	2:31PM	62	2:32PM	115	177	2:34PM
8th	2:32PM	117	2:24PM	121	238	2:36PM
9th	2:32PM	239	2:24PM	118	357	2:38PM
10th	2:32PM	358	2:38PM	99	457	2:40PM
11th	6:00PM	02	6:00PM	123	125	6:02PM
12th	6:01PM	67	6:02PM	113	180	6:04PM
13th	6:02PM	121	6:04PM	102	223	6:06PM
14th	6:03PM	165	6:06PM	103	268	6:07PM
15th	6:04PM	208	6:07PM	127	335	6:10PM

NOTE
A.T: Arrival Time
W.T: Waiting Time of Customers in the Queue (per seconds)
S.S.T: Service Start Time
T.S.S: Time spent in Service (per seconds)
T.T.S.S: Total Time Spent in the System, which is Waiting Time (per seconds) + Service Time (per seconds)
D.T: Departure Time

RESULTS AND CONCLUSIONS
From Table 1, we have the average arrival rate of customers per hour during weekday as

$$= \frac{86+107+163+139+131+102+158+125+102+113+92+104}{12} = \frac{1422}{12}$$

= 118.5 ≈ 119 customers per hour

Also, from Table 1, the average active machines during Weekday are

$$= \frac{3+7+6+4+5+3+4+5+4+5+2+4}{12} = \frac{52}{12}$$ = 4.33 ≈ 4 Machines

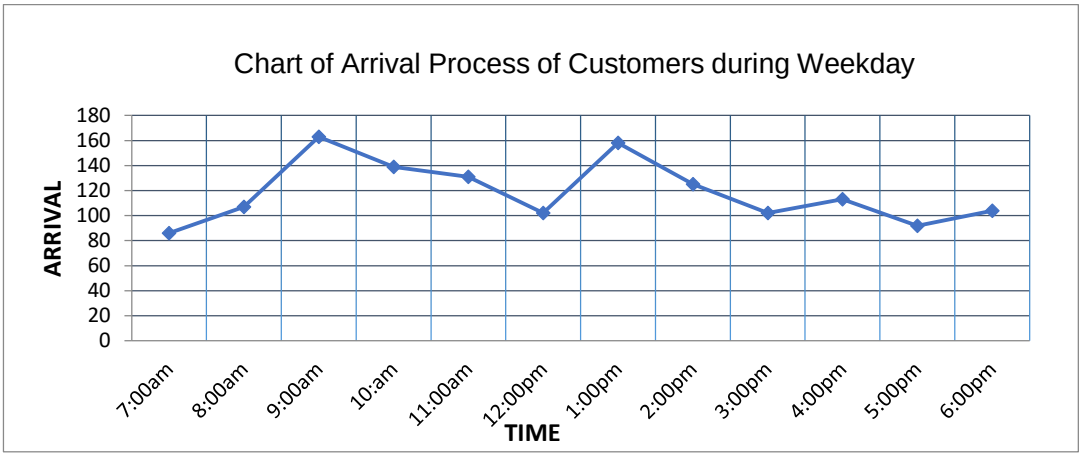

Figure 1: Chart of Arrival Process of Customers during Weekday (Monday to Thursday)

From Table 3, the average arrival rate of customers per hour during the weekend (Friday to Sunday)

$$= \frac{102+59+61+158+63+44+122+72+33}{9} = \frac{714}{9}$$

= 79.33 ≈ 79 Customers per hour

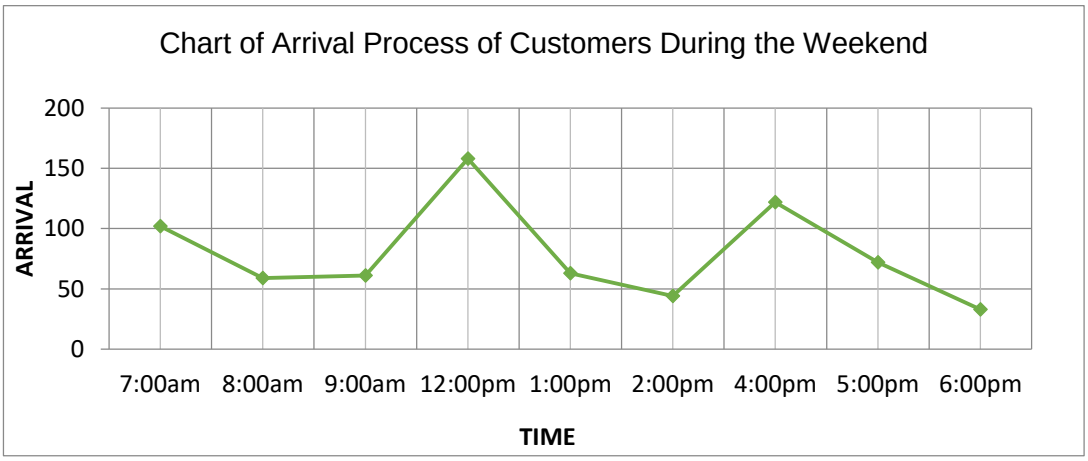

Figure 2: Chart of Arrival Process of Customers during Weekend (Friday to Sunday)

From Table 2, the average departure rate of customers per hour during weekday

$$\frac{79+103+168+149+136+105+130+111+119+84+99}{12} = \frac{1433}{12} \approx 119.42$$

Customers per hour

Also, from Table 3, the average active Machines during weekend is

$$= \frac{2+4+5+7+5+3+4+3+3}{9} = \frac{36}{9} \approx 4 \text{ Machines per hour}$$

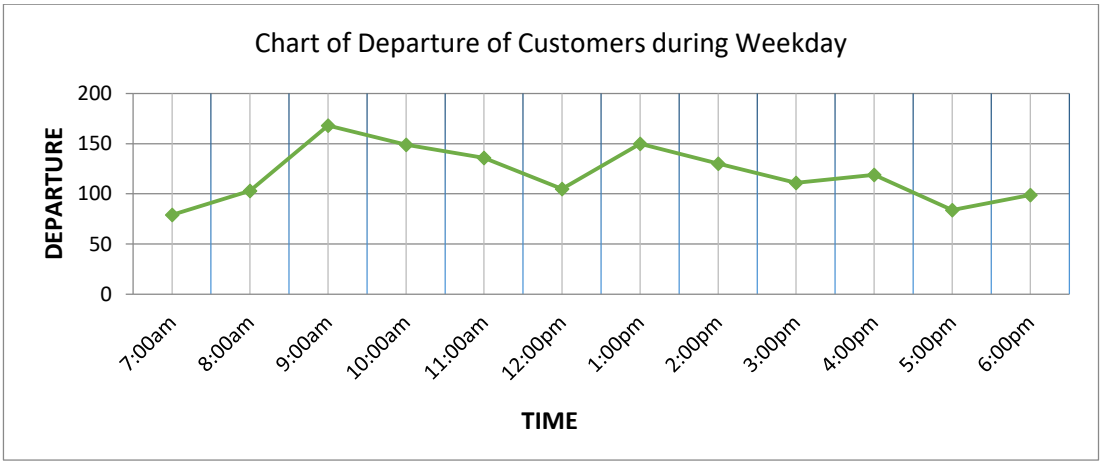

Figure 3: Chart of Departure of Customers during Weekday (Monday to Thursday)

From Table 4 the average departure rate of customers per hour during the weekend is

$$= \frac{99+51+68+145+60+39+108+61+29}{9} = \frac{660}{9} = 73.33 \approx 73 \text{ Customers per hour}$$

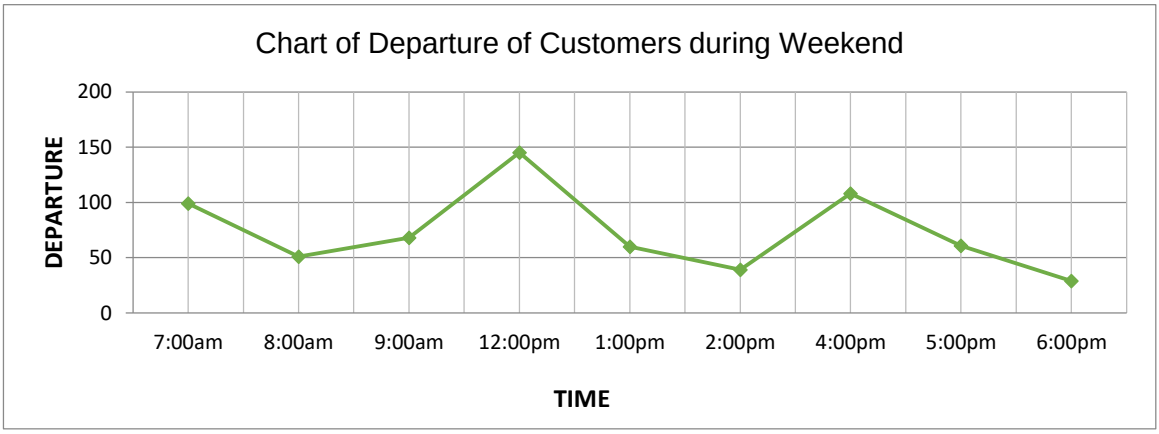

Figure 4: Chart of Departure of Customers during Weekend (Friday to Sunday)

Table 12: Summary of the Duration of Service of Customers during Weekday

Day	Average Waiting Time of Customers	Average Service Rate	Average Time Spent in the System
Monday	216.33	124.33	316.53

Tuesday	280.2	145.47	433
Wednesday	279.4	134.13	384.47
Thursday	197.67	117.63	315.73
TOTAL	**973.6**	**521.56**	**1449.73**
AVERAGE	**243.4**	**130.39**	**362.24**

Table 13: Summary of the Duration of Service of Customers during Weekend

Day	Average Waiting Time of Customers	Average Service Rate	Average Time Spent in the System
Friday	184	122.33	306.5
Saturday	153.53	128.2	281.73
Sunday	176.2	111.47	287.67
TOTAL	**513.73**	**326**	**875.9**
AVERAGE	**171.2**	**108.67**	**291.98**

From Table 12, we have that average service rate of customers during weekday is 130.39

Also from Table 13, the average service rate of customers during weekend is 108.67

Table 14: Arrival and Service rate with No of Active Machines (per hour)

Day	Arrival rate λ (per hours)	Service rate μ (per hour)	No of active machines
weekday	119	130.4	4.
Weekend	79	108.7	4.

Model Computations for Weekday (Monday to Thursday)

If customers arrive GTBank ATM gallery during weekday using a single and simple queue at a mean rate of 119 per hour and service rate of 130 per hour, if the average of 4 machines are working at their full capacity. Then we have the following results using the given formulae:

a) The average utilization factor of the system, $\rho = 0.2289$

b) The probability of no customer in the system, $\rho_0 = 0.40$

c) The average number of customers in the system, $L_s = 2.72 \approx 3$ Customers

d) The average number of customers in the queue, $L_q = 1.81 \approx 2$ Customers

e) The average waiting time of a customer in the system, $W_s = 1.37 \,\text{minutes}$

f) The average waiting time of a customer in the queue, $W_q = 0.0152\ hrs = 0.91\ Minutes$

g) The Queuing Capacity of the ATM Service Point, $C = 1602.9$

Model Computations for Weekend (Friday to Sunday)

If customers arrive GTBank ATM gallery during the weekend using a single and simple queue at a mean rate of 79 per hour and service rate of 109 per hour, if the average of 4 machines are working at their full capacity. Then we have the following computations;

a) The average utilization factor of the system, $\rho = 0.1812 \approx 0.2$
b) The probability of no customer in the system, $\rho_0 = 0.305 \approx 0.3$
c) The average number of customers in the system, $L_s = 4.75 \approx 5\ Customers$
d) The average number of customers in the queue, $L_q = 4.03 \approx 4\ Customers$
e) The average waiting time of a customer in the system, $W_s = 3.61\text{min}utes$
f) The average waiting time of a customer in the queue, $W_q = 0.051\ hrs = 3.06\ Minutes$
g) The Queuing Capacity of the ATM Service Point, $C = 3541.41$

From the results gotten, the traffic intensity (ρ) for weekday and weekend are 0.23 and 0.18 respectively, this implies that the system is stable. For a stable system, traffic intensity or Utilization factor must be less than 1 ($\rho < 1$). The lesser it becomes, the more stable the system.

The probability that there is no customer in the system during weekday and weekend (ρ_0) is 0.4 and 0.3 respectively. This implies that there is about 40% and 30% possibility that the system could be empty either during weekday or weekend respectively.

The average number of customers found in the system under study at the ATM gallery for weekend and weekday is 3 and 5 customers respectively. This implies that for every hour at least 3 customers will be seen at the GTB Minna ATM gallery during weekday and 5 customers during weekend.

The average number of customers waiting on queue for service during weekday and weekend is 2 and 4 customers respectively. This implies that there is an average of 2 to 4 customers waiting to be served by a particular server and since we have an average of 4 active servers, then there is an average of 8 to 16 customers waiting on the queue to be served by these servers.

The average time a customer spends at the ATM gallery (waiting time + service time) during weekday and weekend is 1.37minuts and 3.61minutes respectively.

The average time a customer spends on the queue waiting to be served during the weekend and weekday is 0.91minutes and 3.06minutes respectively.
The queuing capacity of the ATM gallery during weekday and weekend is 1603 and 3541 customers per day respectively.

CONCLUSION AND RECOMMENDATIONS

The result of this study has clearly shown that the ATM gallery of GTB Minna experience more customers during the weekends than the weekdays. This is obviously true because the

bank opens for service during the weekdays so some customers have their transactions carried out in the banking hall rather than visit the gallery.

It is recommended that further research can be made in this same Bank during festive periods and when salaries are paid. It would also be good to carry out a similar study on other Banks in Minna to compare their queuing characteristics with that which is studied here.

REFERENCES

Al-Mater N. (2016). Theories and Application Related to Queuing System. *Proceedings of Academics World 54th International Conference, Malacca, Malaysia,* 2nd-3rd December 2016, ISBN 978-93-86291-48-610.

Egwe A., Onwumere J.U.J. & Obiamaka P E. (2014). Efficient Queue Management in Supermarkets: A Case Study of Makurdi Town, Nigena, *European Journal of Business and Management.* Vol.6. No.39. pp.185-192.

Forundam, S. & Herrmann, J. (2007). A Survey of Fundamentals of Queuing Theory. ICR Technical Report.

Inria, P. (2004). Basic Elements of Queuing Theory: *Application to the Modeling of Computer Systems.*

Kahraman A. & Gosavi A. (2011). On the distribution of the number stranded in bulk-arrival, bulk-service queues of the M/G/1 form. *European Journal of Operational Research*. Vol. 212. No.2. pp. 352-360.

Obamiro J.K. (2014). Application of Queuing Model in Ordering the Optimal Number of Service Facility in Nigena Hospital, MSc. *Project submitted to the Department of Business Administration, University of Ilorin*.

Priyangika J.S. & Cooray T.M. (2016). Analysis of the Sales Checkout Operation in Supermarket Using Queuing Theory, *Universal Journal of Management* Vol. 4. Issue 7. pp.393-396.

Vijay P. S., Badshah V.H. & Tariq A. K. (2015). Mathematical Analysis of Single Queue Multi Server and Multi Queue Multi Server Queuing Models: Comparison Study, *Global Journal of Mathematical Analysis*. Vol 3. No. 3. pp. 97-104.

Vijay P. S. & Badshah. V.H. (2014). Mathematical Analysis of Single Queue Multi Server and Multi Queue Multi Server Queuing Model, *International Journal of Engineering Trends and Technology (UETT).* Vol. 5 No. 6. pp. 264 273.

PHYSICAL/CLIMATE SCIENCES

Trend Analysis of Temperature and Relative Humidity across the Climatic Zones of Nigeria

O. E. Agidi*, J. O. Eichie and O. D. Oyedum
Department of Physics, Federal University of Technology, Minna, Niger State, Nigeria
*Corresponding Author: agidimystic@gmail.com

Abstract
This paper presents the trend analysis of temperature and relative humidity in the climatic zones of Nigeria using Mann-Kendall trend test. The daily Temperature and relative humidity data were obtained from Nigerian Meteorological Agency (NIMET) via the data bank of the West African Science Service Center on Climate Change and Adaptive Land Use (WASCAL) of the Federal University of Technology Minna for the period of Thirty-three years (1981-2014). In order to determine the nature of the trend and significance level, Mann-Kendall trend test and Sen's estimate were employed. From this study, it was observed that temperature shows a positive Kendall's Z value which indicates an upward trend and also, implies increasing trend over time. The result also indicates that there is a significant increase in the trend at 5% level of significance since (p-values (0.0001) <0.05). The results of the relative humidity also indicate that there is an increase in the trend at 5% level of significance since (p-values (0.0001) <0.05). It can also be seen from both the Mann-Kendall and Sen's Slope that there is a possibility of an increment in temperature and relative humidity. This could be due to the impacts of climate change and this leads to devastating unfavorable changing in conditions in the study area. It is therefore recommended that the variability of temperature and relative humidity should be monitored in order to reduce its effects on human activities

Keywords: Variation, trend, temperature, relative humidity

1. INTRODUCTION

Temperature and relative humidity are very important elements that determine the weather condition of a particular area as asserted by National Centre for Environmental Information. These elements are not constant and as such they keep on changing from time to time due to human interference and this uncertainty can cause havoc to the environment (Abraham *et. al*., 2002). To forestall these devastating effects of unfavourable changing in weather conditions due to changing temperature and relative humidity, there is need for scientific prediction (Kumar *et al*., 2012). Temperature and relative humidity play an important role in the forming of natural life. It is not just significant to humans alone but also to animals, plants and all living things. It also plays a unique role in agriculture.

Climate change has been confirmed following the release of the 4th Intergovernmental Panel on Climate Change (IPPC) assessment report. Africa, of which Nigeria is a part, will be worst hit by the effect of climate change. The change in climatic conditions due to the increasing greenhouse emission has made human beings and the planet earth to experience negative impact such as persistent drought flooding, off season's rains and dry spells therefore having great impact on the growth seasons of a country dependent on agriculture (Olaniyi, 2014). According to the World Meteorological Organization (WMO), 30 years is the classical period for performing the statistics used to define climate (Goosse *et. al*., 2010).

Change in climate alters temperature regimes in most parts of the world. Temperature is one of the basic climatic parameters and changes in its pattern can affect the living components of the earth (Onoz and Bayazit, 2003). An increase in temperature can result in heat wave incidents and cause illness and death in less resilient populations. In addition, temperature changes can cause a shift in

animal and plant species (Mishra and Herath, 2012). An increase in Earth's temperature causes convectional current and increase the rate of evaporation thereby leading to cloud formation, which in turn, increases precipitation (Salami *et. al*., 2016). Increase in precipitation trend can also result to increase in the frequency of floods and could thereby affect water quality.

Trend analysis can better be used to depict and predict the changing pattern and variability of climatic parameters (such as temperature and precipitation). This analysis gives knowledge about the changing condition of the climate. Various studies were done using Mann Kendall test. Olaniran and Sumner (2001) used Mann Kendall trend test to study variables such as rainfall, relative humidity, wind speed and sea level rise in Lagos, the result showed positive Kendall's (S) values, indicating upward trend and implying increase in the parameters over time. However, temperature showed negative Kendall's (S), which indicates downward trend and implies decrease over time. Sea level rise, rainfall, relative humidity and wind speed had mean statistics of 3.99, 1.97, 3.09 and 2.26 respectively which are more than 1.96 (test statistics for a significant level of 5% (Z =1.96), this implies that the upward trend is significance and there is tendency for continuity. Temperature had statistic of 0.03 which is less than 1.96 and implies no significance, thus the reduction may not be noticed.

Dammo *et. al.* (2016) used same test to study observed trend of changes in relative humidity across North-East Nigeria (1981-2010). Results indicated consistent increase in relative humidity over the years and across location with a stable increase in relative humidity at all locations. Mann–Kendall test was also applied for detecting monthly and annual trends in the relative humidity in Iraq for the Period 1951-2010 (Abdulwahab and Alobaidi, 2015). The monthly time series showed that relative humidity decreases during winter, spring and autumn months.

This study is aimed at using Mann Kendall non-parametric test to analyse the trend in temperature and relative humidity for a 33-years period (1981-2014). Mann-Kendall non-parametric test was used for the analysis because of its applicability for a time series distribution, which does not follow a typical statistical distribution.

2. 0 MATERIALS AND METHOD

2.1 Data Acquisition

The study area is Nigeria located at the extreme inner corner of the Gulf of Guinea on the west coast of Africa. She occupies an area of 923,768 km². 910,768 km² of the area is land, while water takes up the remaining 13,000 km². Nigeria can be divided into five climatic zones namely Sahel, tropical rainforest, Guinea savannah, Sudan savannah and Coastal zones (Olaniran and Sumner, 2001). Two weather stations were selected for each of the 5 climatic zones as shown in figure 1. Table 1 shows the coordinates and elevation of the selected weather stations.

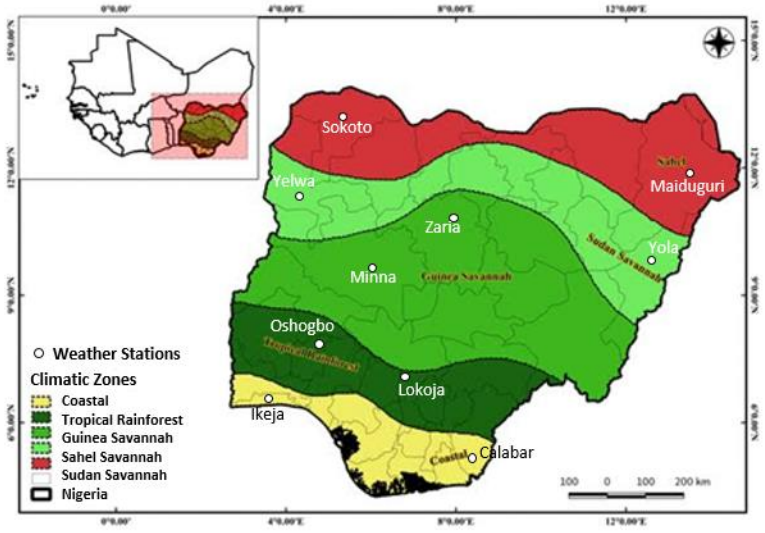

Figure 1: The selected weather stations within the climatic zones of Nigeria

Table 1: The geographical coordinates of selected weather stations.

Climatic Zone	Station	Latitude (^{o}N)	Longitude (^{o}E)	Elevation (m)
Coastal	Calabar	4.97	8.35	63
	Ikeja	6.59	3.34	36
Tropical Rainforest	Lokoja	7.81	6.74	44
	Oshogbo	7.78	4.54	304
Guinea savannah	Minna	9.60	6.55	260
	Zaria	11.09	7.72	640
Sudan savannah	Sokoto	13.02	5.25	302
	Maiduguri	11.83	13.15	354
Sahel savannah	Yelwa	10.88	4.75	243
	Yola	9.23	12.47	174

Thirty-three (33)-year period (1981-2014) data were obtained from the Nigerian Meteorological Agency (NIMET) via the data bank of the West African Science Service Centre on Climate Change and Adaptive Land Use (WASCAL) of the Federal University of Technology Minna.

2.2 Data Analysis

The mean monthly values of relative humidity and temperature were respectively computed and shown in plots and tables. Trend Analysis of the climatic zones in Nigeria was carried out using Mann-Kendall and Sen's Slope Estimator. The statistical significance of trends is indicated by p value. The significance level (the alpha value) was taken to be 0.05 for a significant trend to occur the p-value must be less than the alpha value. Mann– Kendall trend test was used to see whether there is a decreasing or increasing trend. Mann–Kendall statistics (S) is one of the nonparametric statistical tests used for detecting trends of climatic elements. Mann–Kendall trend test is also the most widely used methods since it is less sensitive to outliers (extraordinary high values within time series data) and it is the most robust as well as suitable for detecting trends (Allan *et. al.*,2013).

4.0Results and Discussion

4.1 Mean Monthly Variation of Relative Humidity and Temperature

Plot of the mean monthly relative humidity for each station in the climatic zone is shown in the plot in figure 2.

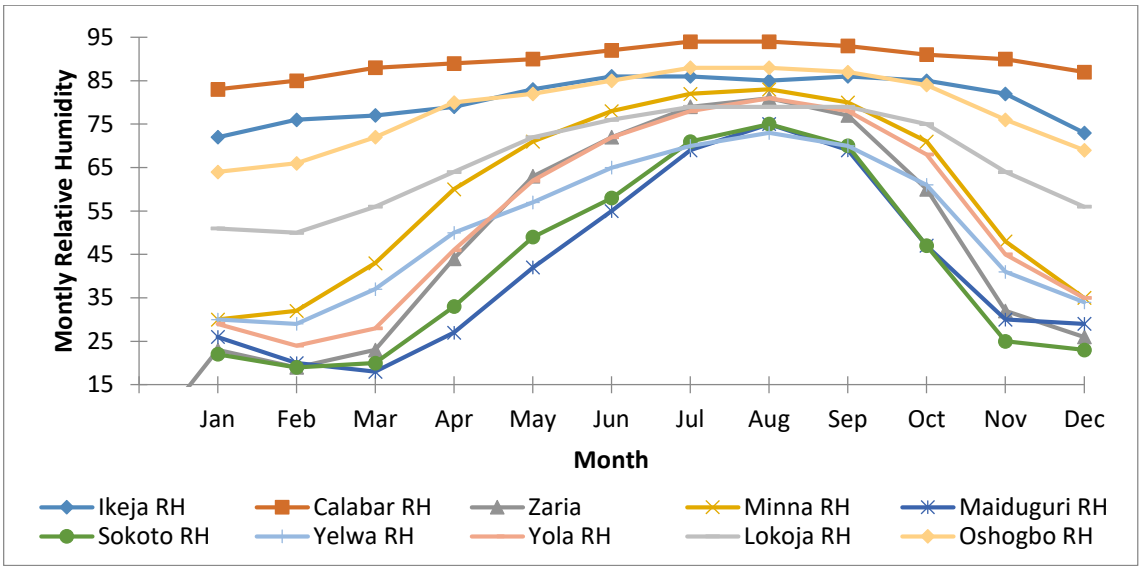

Figure 2: Mean monthly relative humidity for each station in the climatic zone

The coastal climatic zone had higher relative humidity with Calabar the highest in the zone. Calabar experiences more rainfall than Ikeja, and this makes Calabar to be cool all through the year than Ikeja, in the tropical climatic zone, Oshogbo had a higher relative humidity than Lokoja, In the Guinea savannah climatic zone the trend of Zaria is a little superimposed with that of Yola that is, they tend to have the same mean monthly variation in relative humidity this is because relative humidity increases with altitude. Zaria, though located in the guinea savannah climatic zone, tends to have the same relative humidity with the Sudan savannah climatic zone. Minna had a higher relative humidity than Zaria.

In the Sudan savannah climatic zone, Yola had a higher relative humidity than Yelwa this is because Yola is located in a mountainous area and experiences extreme seasonal variation in monthly rainfall. In the Sahel savannah climatic zone, which is the least climatic zone in the plot, Sokoto from January had higher trend than Maiduguri but in the month of August Maiduguri and Sokoto had the same peak relative humidity while in the month of October they tend to have the same mean monthly variation.

The mean monthly temperature for each station in the climatic zone is shown in figure 3.

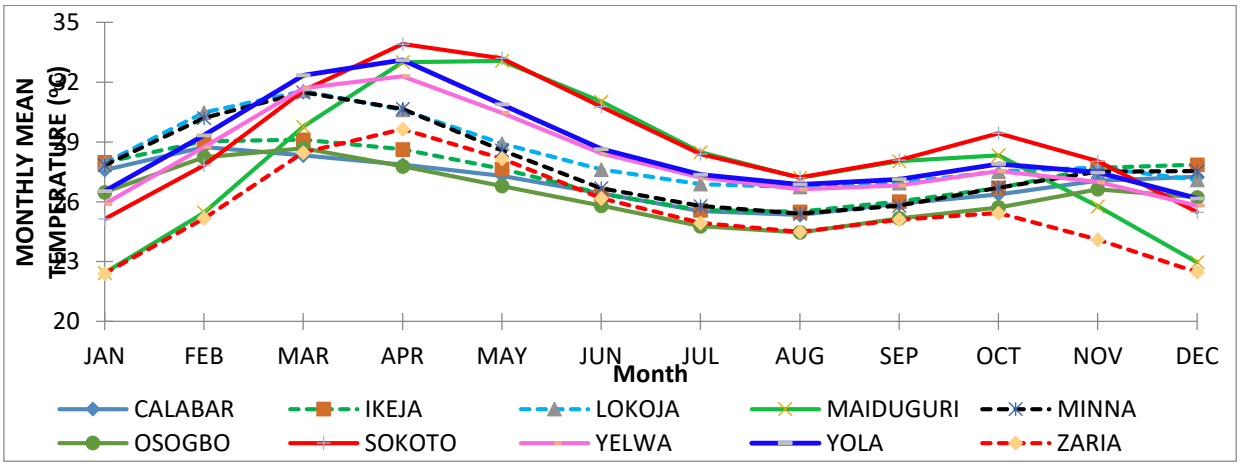

Figure 3: Mean monthly plot of temperature for each station in the climatic zone

As shown in figure 3, the coastal climatic zone had low temperature and Calabar had the lowest in the zone and Calabar experiences more rainfall than Ikeja due to high relative humidity, and these makes Calabar to be cool all through the year than Ikeja, in the Tropical climatic zone, Oshogbo had a low temperature than Lokoja, In the Guinea savannah climatic zone Minna had a higher temperature than Zaria.

In the Sudan savannah climatic zone, Yola had a low temperature than Yelwa this is because Yola is located in a mountainous land and Yola experiences extreme seasonal variation in monthly rainfall. The Sahel savannah climatic zone, which is the least climatic zone and which has the highest temperature and lowest humidity and they tend to have the lowest rainfall throughout the year.

4.2 Mann Kendall Trend (M-K) Test

The M-K test results for relative humidity and temperature, comparing with significant level of 5% (0.05), shows that the p-value of all the regions is less than the alpha value which implies that there is trend. Tables 3 and 4 show the Mann Kendall non-parametric test on relative humidity and temperature data set respectively.

Results of the Mann-Kendall test for relative humidity shown in table 3 shows four stations (Calabar, Yelwa, Lokoja and Oshogbo) having negative Z-values and Q values, which signifies a decreasing trend (downward trend) in relative humidity. The Kendall Tau (τ) values for these 3 stations indicate negative correlation and statistical dependence of the variables (time series data). The other 7 stations (Ikeja, Minna, Zaria, Sokoto, Yola and Maiduguri) had positive Z-values and Q values, which signifies an increasing trend (upward trend). The Kendall Tau (τ) values for these 7 stations indicate positive correlation. In a similar study, Ogolo (2011) showed a decreasing trend for relative humidity in the tropical rainforest region of Nigeria. According to Amadi *et. al.* (2015), trend and variation of relative humidity in Nigeria is usually affected by latitudinal variation therefore the general trend of humidity in Nigeria must be considered over various ecological zones of the country, varying from the Savannah in the North to the tropical/coastal regions of the South.

The Mann-Kendall test for temperature shown in table 4, shows all the stations (Calabar, Ikeja, Yelwa, Yola, Lokoja, Oshogbo, Minna, Zaria, Sokoto, and Maiduguri) having positive Z and Q values, which signifies an increasing trend (upward trend) in temperature. The Kendall Tau (τ) values for these 10 stations indicate positive correlation. A rise in temperature is among the indicators of climate change (Asfaw *et. al.,* 2018). Onyeneke *et. al*. (2020) reported that temperature increased substantially over time across all main agro-ecological regions in Nigeria. The rise in temperature can cause scorching of crops as well as reduced crop yield. Research conducted by Freduah *et. al.*, (2019) shows an increase in temperatures of the Savannah areas of Guinea and Sudan. These agro meteorological areas equally showed evidence of decreasing precipitation, which, along with rising temperatures. This implies that there has been a steady increase on local scale for the period 1981 – 2014 which conforms to the 3rd Assessment Report of the IPCC that showed an increase in global temperature during the twentieth century Freduah *et. al.*, (2019). The positive trends observed are in agreement with the results obtained by Freduah *et. al.*, (2019). Based on the above results, it is of great importance to consider the future effect of increasing temperatures on the environment, agriculture and health if the present trend is continuous.

5.0 CONCLUSION

It can be concluded from both Mann- Kendall and Sen's Slope that there is a possibility of increment in temperature and relative humidity. This could be due to impact of climate change. However, if caution is not taken, it may lead to devastating unfavourable changing in weather conditions in the study area. It is therefore recommended that the variability of temperature should be monitored in order to minimize its effects on human activities.

Table 3: Results of the Mann-Kendall test for Relative Humidity Data.

Climatic Zones	Stations	Kendall's Tau	Var(S)	Test Statistic (S)	Test Statistic (Z)	p-Value (two test)	Alpha	Sen's Slope (Q)	Test Interpretation
Costal	Calabar	-0.052	212143545556.667	-394757	-8.57	< 0.0001	0.05	-9.355E-5	H_1
	Ikeja	0.073	212322348090	5600220	12.15	< 0.0001	0.05	1.904E-4	H_1
Guinea	Minna	0.026	212378068391	1967333	4.26	< 0.0001	0.05	1.9384E-4	H_1
	Zaria	0.031	212380131400.667	2352806	5.1	< 0.0001	0.05	2.569E-4	H_1
Sahel	Sokoto	0.014	212380391760	1093532	2.37	0.018	0.05	2.037E-4	H_1
	Maiduguri	0.041	212380356852.667	3185102	6.91	< 0.0001	0.05	4.468E-4	H_1
Sudan	Yelwa	-0.018	212371883680.333	-1344283	-2.91	0.004	0.05	-5.570E-4	H_1
	Yola	0.016	212380996305.333	1192426	2.58	0.010	0.05	3.070E-4	H_1
Tropic	Lokoja	-0.017	212369241260	-1304752	-2.83	0.005	0.05	-1.109E-5	H_1
	Oshogbo	-0.028	212357092601	-2151759	-4.66	< 0.0001	0.05	-2.137E-4	H_1

Table 4; Results of the Mann-Kendall test for temperature data

Climatic Zones	Stations	Kendall's Tau	Var (S)	Test Statistic (S)	Test Statistic (Z)	p-Value (two test)	Alpha	Sen's Slope (Q)	Test Interpretation
Costal	Calabar	0.030	211369377937.333	2253098.000	4.9	< 0.0001	0.05	1.848E-5	H_1
	Ikeja	0.077	211845015112.667	5826080.000	12.65	< 0.0001	0.05	5.746E-5	H_1
Guinea	Minna	0.023	211920296153.667	1710687.000	3.71	0.000	0.05	0	H_1
	Zaria	0.048	212031132017.667	3634425.000	7.89	< 0.0001	0.05	3.650E-5	H_1
Sahel	Sokoto	0.024	212184607918.000	1804642.000	3.91	< 0.0001	0.05	0	H_1
	Maiduguri	0.025	212238783014.000	1866650.000	4.05	< 0.0001	0.05	1.291E-5	H_1
Sudan	Yelwa	0.047	212121336802.667	3578186.000	7.76	< 0.0001	0.05	7.493E-5	H_1
	Yola	0.033	212136144025.667	2537257.000	5.50	< 0.0001	0.05	1.754E-5	H_1
Tropic	Lokoja	0.057	212002870315.667	4313925.000	9.36	< 0.0001	0.05	5.502E-5	H_1
	Oshogbo	0.062	211662388664.333	4675299.000	10.16	< 0.0001	0.05	2.479E-4	H_1

Reference

Abraham, A, Ninan, S. P., Baikunth, N. and Saratchandran, P. (2002): Second Internaltional Workshop on intelligent Systems Design and applications computational intelligence and applications, pp. 181-186.

Kumar, A., Yang, F., Goddard, L. and Schubert, S. (2012): Differing trends in the tropical surface temperatures and precipitation over land and oceans. *Journal of Climate*, 17(3), pp. 653-664.

Olaniyi, O. A., Fumilayo, O. A. and Olutimehin, I, O. (2014): Review of Climate Change and its Effect on Nigeria Ecosystem. *International Journal of Environment and Pollution Research* 2(3), pp.70-81.

Goosse, H., Barriat, P. Y., Loutre, M.F. and Zunz, V. (2010): Introduction to climate dynamics and climate modeling.

Onoz, B. and Bayazit, M. (2003): The power of statistical tests for trend detection. *Turkish Journal of Engineering & Environmental Sciences* 2012(27) pp. 247–251.

Mishra, B. K. and Herath, S. (2012). An investigation on climate change risk for run-of-river hydropower schemes: A case study of Sunkoshi river basin. Nepal;

Salami, W., Ikpee, D., Ibitoye, B. and Oritola, F. (2016): Trend analysis of hydro-meteorological variables in the coastal area of Lagos using Mann-Kendall trend and standard anomaly index methods. *J. Appl. Sci. Environ.* Manage; 20(3): pp.797-808.

Olaniran, O. J. and Sumner, G. N. (2001): A study of climatic variability in Nigeria based on the onset, retreat, and length of the rainy season. *International Journal of Climatology*, 9(3), pp. 253-269.

Dammo, N., Yadima, G. and Sangodoyin, Y. (2016): Observed trend of changes in relative humidity across north-east Nigeria. Civil and Environmental Research; 8(3). (ISSN 2224-5790) (ISSN 2225-0514)

Abdulwahab, H. and Alobaidi (2015): Analysis of relative humidity in Iraq for the period 1951-2010. *International Journal of Scientific and Research Publications*; 5

Allan, C., Xia, J. and Pahl-Wostl, C. (2013): Climate change and water security: challenges for adaptive water management. Current Opinion in Environmental Sustainability 5(6): pp. 625–632.http://dx.doi.org/10.1016/j.cosust.2013 .09.004**.**

Ogolo, E. O. (2011): Regional trend analysis of pan evaporation in Nigeria (1970 to 2000). *J. of Geog and Reg Plan* 4(10) pp. 556 – 577

Amadi, S.O., Udo, S. O and Udoimuk, A. B. (2015): An examination of trends and variation of monthly mean relative humidity data in Nigeria from 1950 – 2012. *Int. J. Pure Appl. Sci. Technol*., 28(2) pp. 63-76

Asfaw, A., Simane, B., Hassen, A., and Bantider, A. (2018): Variability and time series trend analysis of rainfall and temperature in northcentral Ethiopia: A case study in Woleka sub-basin. Weather and climate extremes, 19, 29-41.

Onyeneke, R. U., Emenekwe, C. C., Munonye, J. O., Nwajiuba, C. A., Uwazie, U. I., Amadi, M. U., and Onyeneke, L. U. (2020): Progress in Climate–Agricultural Vulnerability Assessment in Nigeria. Atmosphere, 11(2), 190.

Freduah, B. S., MacCarthy, D. S., Adam, M., Ly, M., Ruane, A. C., Timpong-Jones, E. C. and Adiku, S. G. (2019): Sensitivity of maize yield in smallholder systems to climate

scenarios in semi-arid regions of West Africa: Accounting for variability in farm management practices. Agronomy, 9(10), 639.

Climate Variability and Its Effects on Malaria Prevalence in Kuje Area Council, Federal Capital Territory, Nigeria.

Ibrahim Arome Ahmed[1*] Prof. A. Abdulkadir[2]
[1]Department of Geography, Federal University of Technology, Minna, Nigeria
[2] Department of Geography, Federal University of Technology, Minna, Nigeria
[1]arome.pg207363@st.futminna.edu.ng
[2]abuzaishatu@futminna.edu.ng
*Corresponding author

Abstract

Malaria is on the increase in the world at large, particularly in Africa, where climate has a strong and direct influence on the development, reproduction and survival of tropical insects such as mosquitoes. This study investigated the climate variability and its effects on malaria prevalence in Kuje area council, Federal Capital Territory. The study used secondary data of rainfall, temperature and relative humidity obtained from the Nigerian Meteorological Agency, Abuja and the recorded malaria morbidity cases from Kuje General hospital in Kuje Area Council from 2006-2015. Descriptive and inferential statistics were used to analyze the data, Pearson moment correlation was used to determine the strength of the relationship between the recorded malaria morbidity cases and the selected climatic elements. Also, trend analysis was used to study the variation of malaria morbidity cases and rainfall, temperature, relative humidity within and over the years for the period under study. It was observed that malaria morbidity cases, rainfall, temperature, and relative humidity, had a positive trend except temperature which showed a slightly positive trend over the period under study, it was also shows that malaria morbidity cases had a significant trend. This indicates that the recorded malaria morbidity cases in the area council will continue at an increasing rate as the year advances, if no efficient mitigation measures are implemented. However, the selected climatic elements of rainfall, temperature, relative humidity and recorded malaria morbidity cases did not show clear patterns over the years during the study period (2006-2015). The observed results reveals that the malaria morbidity cases tend to increase during the peak of rainfall and relative humidity and then varies afterwards. This concludes that the varying wet and dry seasons creates a conducive habitat for malaria prevalence in the area council. Thus, it recommends that mitigation measures should be put in place to minimize the occurrences of malaria.

Keywords: climate variability, malaria, malaria prevalence.

1. Introduction

Malaria is alleged to be the most common serious infections disease worldwide. It is predominantly a disease of warm climates, but 41% of the world's population live in endemic areas, (WMO, 1995). Malaria is on the increase in world at large, but particularly in Africa, where climate, has a strong

and direct influence on development, reproduction and survival of tropical insects such as mosquitoes, (Okorie *et al.,* 2012). The Intergovernmental Panel on Climate Change contends that there is proof that much of the warming observed over the last 50 years has led to the emergence of large-scale environmental hazards affecting human health such as the global spread of infectious diseases (IPCC, 2007). Beginning in the mid- 1970s, there has been an emergence, resurgence and escalation of infectious diseases arising from global warming (De Savigny *et al.,* 2002). Vector-borne diseases are a major cause of illnesses and deaths in tropical countries (AMR, 2003). One of the most important vector-borne diseases in the world is malaria transmitted by the mosquito vector of the genus Anopheles most abundant in tropical/subtropical regions (WHO, 2003), hence malaria is one of the killer diseases especially in the tropics.

Climatic variations directly influence mosquito development, feeding-frequency and longevity, as well as the time in which the parasite develops inside the mosquito (Patz *et al.,* 2003; Suthersts, 2004). The optimal temperature (15^0C - 30^0C) associated with the incubation rate of the pathogen within vectors leads to the differential risks of outbreaks by regions (Campbell-Lendrum *et al.,* 2003). Increased precipitation can increase mosquito population indirectly by expanding the larval habitat and food supply. A relative humidity of below 55% and above 80% shortens the lifespan of a mosquito so much that the scope of malaria transmission diminishes as there is no time for a complete development of Plasmodium (Bhattacharya *et al.,* 2006).

Malaria continues to be a major cause of death among people living in the tropics, in spite of recent gains in the fight against the disease. In Africa, it accounts for over five hundred thousand deaths annually, which is about 90% of the worldwide annual mortality (WHO, 2013). Malaria contributes significantly to the high rates of child and maternal mortality, maternal anemia, low birth-weight, miscarriage and stillbirth. It also creates significant economic burden on families due to household expenditure on malaria treatment and reduced productivity, thereby intensifying poverty and making populations more vulnerable to malaria transmission (WHO 2013; Sachs *et al.,* 2002).

The situation could be exacerbated by the challenges posed by climate variability. Although the impact of the climate on human health is uncertain, an increase in the incidence of malaria has been identified as a potential impact of climate change in South America (Vanlieshout *et al.,* 2004) and in Africa (Ebi *et al.,* 2005). Climatic factors that feed into the phenomenon could have a direct bearing on the number of malaria cases. A number of studies have reported association between malaria cases, rainfall and temperature (Bhattarai *et al.,* 2007; Bouma *et al.,* 1996). For example, a study carried out in Ethiopia revealed an association of malaria with rainfall and minimum temperature, the strength of which varied with altitude (Teklehaimonot *et al.,* 2004). In South Africa, variations in annual cases of malaria were shown to be related to patterns of rainfall and temperature (Craig *et al.,*2004).

Indeed, the abundance of Anopheles gambiae *s.s.* in most malaria endemic regions has been shown to be at its peak during the wetter parts of the year (Bhattarai *et al.,* 2007). This could be explained by the biology of the vector where the availability of pools of water provides breeding sites and subsistence, hence directly influencing vector numbers. Anopheles gambiae *s.s.* prefers to breed in

temporary pools of clean water such as potholes, foot and hoof prints and puddles that become plentiful in the rainy seasons. Immature stages of the Anopheles gambiae *s.s.,* i.e., Eggs, larvae and pupae are aquatic forms and require suitable aquatic environments in which they develop prior to the emergence of adults from the pupae. Additionally, when water availability to the adult mosquitoes is limited, they become predisposed to dehydration leading to a direct negative effect on their population (Abagye-Antwi *et al.,* 2010).

Temperature has also been reported to correlate positively with malaria cases. For example, combinations of maximum and minimum temperatures in association with rainfall have been used to successfully fit a biological transmission model to malaria case data in Zimbabwe (Teklehaimonot *et al.,* 2004). Apart from the effect of rainfall and temperature on adult mosquito longevity, these climate parameters also influence development of the parasites within the vector. For instance, at 26˚C ambient temperature, 6˚C drops can double the development time of Plasmodium falciparum within the vector (Macdonald, 1975; Paaijamans, 2008). At relatively higher temperatures both vector and parasite development accelerate. However, the efficiency of malaria transmission varies widely and is influenced by several factors including the type of vertebrate host, parasite and vector factors (Moreira, 2004). Generally human ecology and activities that affect the environment, such as land use and urbanization have also been linked to malaria transmission.

2. Study Area

Kuje Area Council is situated in the federal capital territory of Nigeria. Kuje, the study area lies between latitude 80 27'43'' to 80 89'39'' North of the equator and longitude 70 14'35'' to 70 24'30'' East. It is bounded by Gwagwalada Area Council to the West, Eastward by Abuja Municipal Area Council, and Abaji Area Council to the South-West. Its location lies about 40km southwest of the capital city. Kuje Area Council is one of the six Area Councils in the administration of the Federal Capital Territory (FCT).

It is one of the rapid growing urban centres in the FCT with a population of about 97, 233 people (NPC, 2006) with a population projection set at 154,000 people as at 2011 (NPC 2011) and occupies an area of approximately 1,800 square kilometre (km2) and boast as one of the fertile lands in the country for agriculture. It is strategically located about 10 km to the Nnamdi Azikiwe International Airport Abuja, and experiencing rapid expansion of settlements.

The climate of Kuje Area council is not quite different from that of the Federal Capital Territory (FCT). Kuje Area council is dominated by two main seasons; rainy season, which starts from the month of April to October and the dry season occurs between the month of November and March (Balogun, 2001). The maximum temperature occurs in the month of March with temperature varying from 30^0C to 37^0C in the Northeast. Essentially this is also the period of high diurnal ranges of temperature when drops of as low as 17^0C are recorded. By July to August diurnal range exceed 70C accordingly (Adakayi, 2000). The relative humidity in Kuje Area Council rises everywhere during the rainy season and falls considerably during the dry season; In the afternoon, relative humidity could rise to about 50% during the rainy season and falls as low as 30% during the dry season. (Adakayi, 2000).

Kuje Area council is characterized by two prevailing winds, the Tropical continental (TC) air

masses or the harmattan winds is driven by the Northeast trade (NET) winds and Tropical maritime air masses is driven by the Southwest monsoon (SWM) winds. The prevailing winds south of Kuje Area council are mainly southerly which is warm and moist whilst the Northeast winds which is developed in the Sahara Desert is mainly northerly is warm and dry. The oscillation between these two air masses produces the highly seasonal characteristics of weather condition in Kuje Area Council (Adakayi, 2000; Balogun, 2001).

Rainfall is moderate with annual totals ranging approximately between 1,100mm to 1,308mm. About 60 percent of the annual rainfall occurs in the months of July, August and September. One climatic characteristics of this area is the frequent occurrence of squall lines heralded by thunderstorms, lightening and strong wind due to its physical relief. (FCDA, 1979 and Balogun 2001).

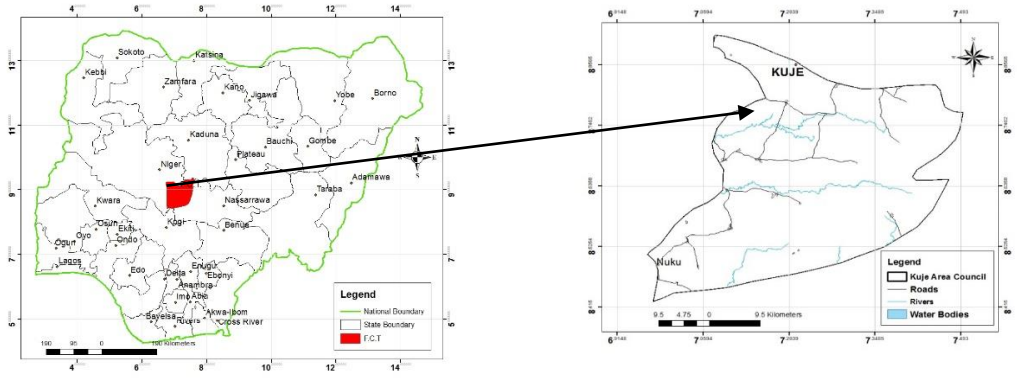

Figure 3: Map Nigeria Showing of Kuje Area Council.

Source: Remote sensing lab, Geography Department, Futminna (2017).

3. Methodology

Nature, Types And Sources Of Data

The data used in this study were purely secondary data and was acquired from the Nigerian Meteorological Agency, National Weather Forecasting and Climate Research Centre, Abuja due to its proximity to the study area, and Kuje General Hospital, Kuje Area Council Abuja. The data was acquired in both in hard and soft copies, and all adjustments (e.g., averaging) was carried out. The type of climatic data collected included Rainfall, Maximum Temperature, Minimum Temperature, Relative Humidity, and health data (Recorded malaria cases Morbidity) from Kuje General Hospital, Kuje area council. The data was on a monthly and annual basis. The length of data was for 10 years (2006-2015)

Research Design

The study investigates the relationship between climate variability and malaria prevalence in Kuje area council. Recorded malaria cases data were obtained from the general health facility in the area council while climatic data, rainfall, temperature and relative humidity records were obtained from the Nigerian Meteorological Agency Abuja. The data were subjected to both descriptive and inferential statistics. Descriptive statistics comprises of means such as the mean monthly rainfall, temperature and relative humidity (%). The descriptive statistical results were presented in graphs (lines and bars) and tables. Inferential statistics was used such as correlation to determine the variation of malaria morbidity within and over the years. Regression was used to give the various

trends while Pearson's product - moment correlation coefficient was used to test the strength of the relationship or association between malaria morbidity and the selected climatic elements. All the data were analysed using the Microsoft excel and SPSS.

4. Results and Discussion

Patterns of Rainfall, Temperature, Relative Humidity and Malaria Morbidity.

The general pattern of rainfall in the study area shows a variation over the past 10 years (2006-2015) during the study period, annual average rainfall was about 1410.37mm and a monthly average rainfall of about 117mm, with rainfall reaching its peak in the month of august with average rainfall of 319.56mm.

Annual Patterns of Rainfall and Malaria Morbidity Cases.

For the period under study (2006-2015), the annual rainfall recorded was plotted to determine the pattern, the Figure 1 shows that there was no uniformity in the temporal pattern of rainfall during the period under study. There was relatively high annual rainfall in the year 2014, this was followed by the year 2010 and 2012. The year 2013 had the least amount of annual rainfall during the period under study, The highest malaria morbidity cases was recorded in the year 2009 (286 cases), year 2012 (279 cases), year 2014 (276 cases). Also, the lowest malaria morbidity cases were recorded in the year 2013 (197 cases), as shown in the Figure 1 below.

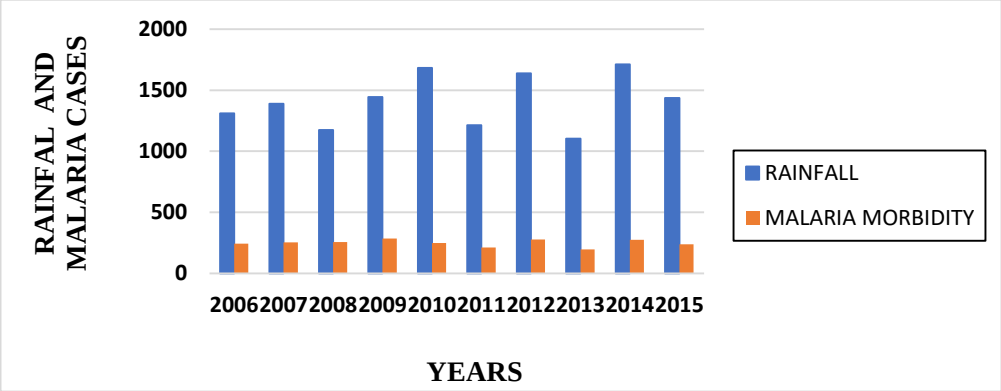

Figure 1: Patterns of annual rainfall and malaria morbidity (2006- 2015).

Seasonal Patterns of Rainfall and Malaria Morbidity

During the period under study (2006-2015), the pattern of mean monthly rainfall was established as in Figure 2. Rainfall was experienced more in the months of July, August, and September. Rainfall starts to decline from the month of September, October before the dry season sets in from November to March. Based on the 10 years study period, the mean monthly results showed that there was no month without malaria morbidity cases, the months of June, July, August recorded higher cases than the rest of the months. The results showed that malaria morbidity cases rose steadily from the month of March to August after which it declined steadily towards December, which can be observed in the Figure 2 below.

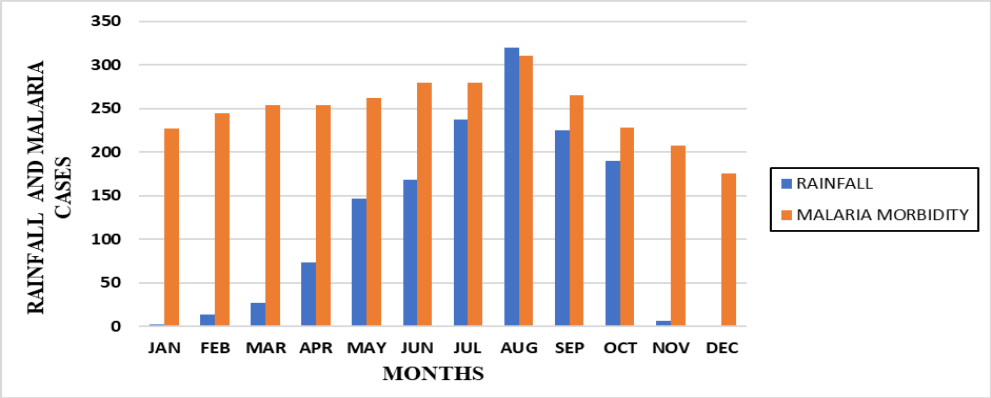

Figure 2: Patterns of mean monthly rainfall and malaria morbidity (2006- 2015).

Annual Patterns of Temperature and Malaria Morbidity

The mean annual temperature for the period under study (2006 – 2015) as shown in figure 3 below, showed that the temperature was highest in the year 2013 (29 ^{0}C), 2014 (28 ^{0}C). The lowest temperature was recorded in the year 2015 (26.9 ^{0}C), followed by the year 2007 (27.0 ^{0}C), Temperature and malaria morbidity cases were inconsistent during the period under study. High malaria morbidity cases were recorded in the year 2009 (286 cases), 2012 (279 cases), 2014 (276 cases). The lowest malaria morbidity cases were recorded in the year 2013 (197 cases), 2011 (212 cases) and 2015 (238 cases). A striking relationship was observed with the year 2009 and 2014 which had some of the highest recorded annual temperature of 27.45 ^{0}C and 28.20 ^{0}C recorded high amount of malaria morbidity cases in the study area.

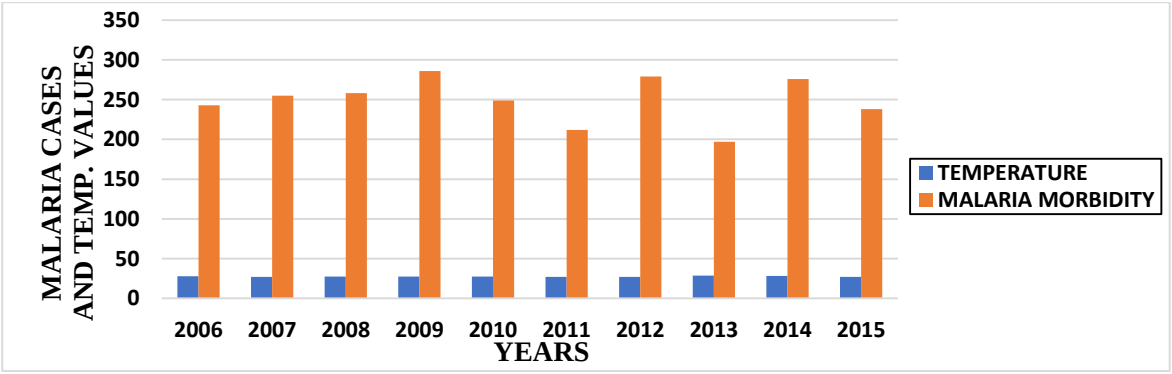

Figure 3: Patterns of mean annual temperatures and malaria morbidity (2006-2015).

Seasonal Patterns of Temperature and Malaria Morbidity

From the Figure 4 below shows the monthly mean temperature for the period under study, it was observed that the month of August registered the lowest temperature (25.3^{0}C) followed by September (26.0^{0}C). Temperature was highest in the month of March (30.9 ^{0}C), April (30.1^{0}C), as opposed to the case of rainfall and malaria morbidity cases, the periodicity of temperature over the study area does not compare well with malaria morbidity cases.

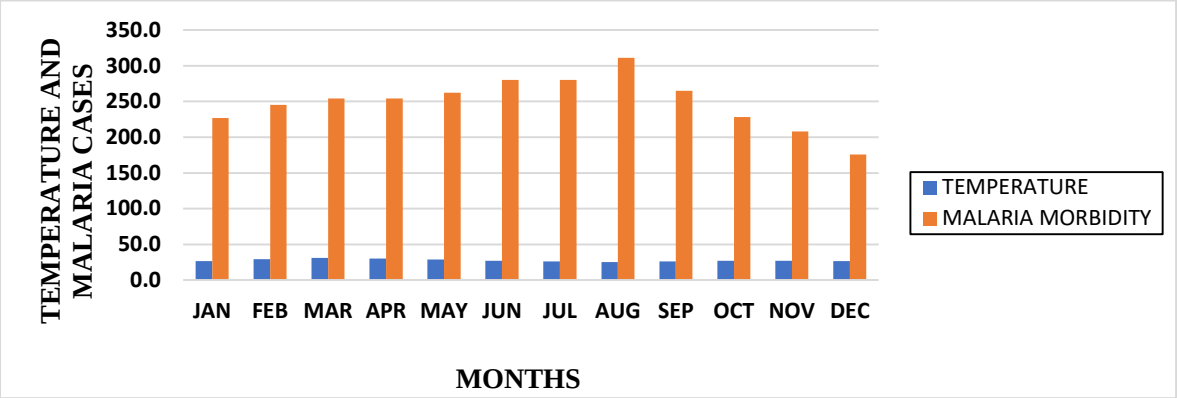

Figure 4: Patterns of mean monthly temperature and malaria morbidity (2006-2015).

Annual Patterns of Relative Humidity and Malaria Morbidity

Pattern of annual relative humidity in (%) for the period under study (2006 – 2015) showed that the relative humidity was highest in the year 2009 (70.18%), 2006 (67.76%). The lowest was recorded in the year 2008 (48.94%). The highest malaria morbidity cases were recorded in the year 2009 (286 cases), 2012 (279 cases), 2014 (276 cases), the lowest malaria morbidity cases were recorded in the year 2013 (197 cases), 2011 (212 cases) as seen in the Figure 5 below.

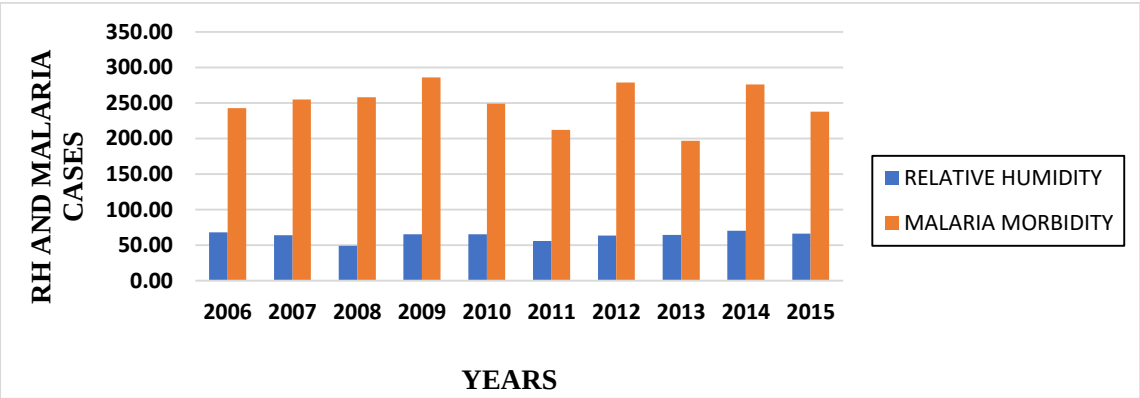

Figure 5: Patterns of mean annual relative humidity and malaria morbidity (2006- 2015).

Seasonal Patterns of Relative Humidity and Malaria Morbidity

From the Figure 6 below, relative humidity was recorded highest in the month of August (85.0%), followed by July (83.2%), September (82.3%). The lowest recorded relative humidity occurred in February (38.0%) which is during the dry season. This confirms that rainfall and temperature divide the year into two seasons with relative humidity being highest during the rainy season than during the dry season. The recorded malaria morbidity cases showed that during the period under study, it rose steadily from the month of march with it peak at the month of August and declined towards the month of December.

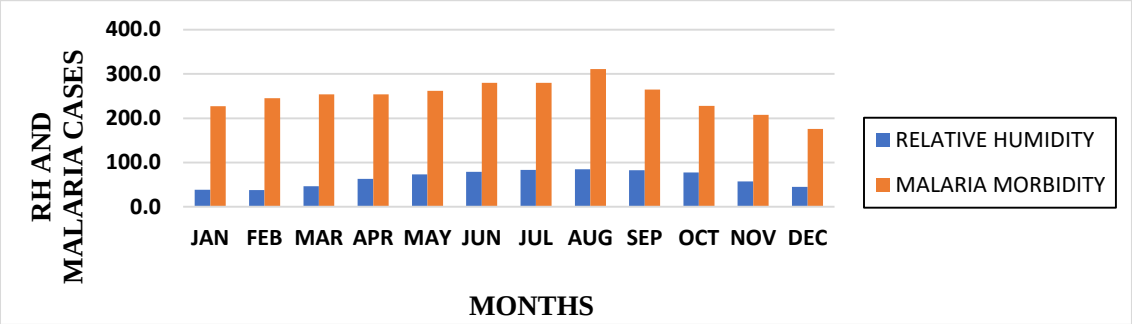

Figure 6: Patterns of mean monthly relative humidity and malaria morbidity (2006- 2015).

Trends of Rainfall, Temperature, Relative Humidity and Malaria Morbidity

Annual Trends of Rainfall and Malaria Morbidity Cases

From the Figure 7, the annual rainfall trend for the ten-year period under study was positive Y=19.014x + 1305.8. This means annual rainfall increased in the study area at the rate of 19.014% per annum during the period under study with the coefficient of determination (R^2) =0.0714, this accounted for 7.14% of the changes in the temporal rainfall occurrence observed in the study area, at a P value of 0.455, this trend is not significant. Also, during the period of 10 years under study, the recorded mean monthly malaria morbidity in the study area showed a steady trend at the rate of 1.5818% per annum. The coefficient of determination R^2 = 0.0281 implies that for the period under study (2006-2015) accounted for 2.81% of the temporal variation in malaria morbidity cases observed. In correlating malaria morbidity cases against the years, an R-value of 0.1676 and a P value of 0.6433 was observed. From that observation, malaria morbidity cases had no significant trend.

Seasonal Trends of Rainfall and Malaria Morbidity

The recorded mean monthly rainfall trend during the period under study (2006-2015) showed a positive trend as shown in Figure 7 below at Y= 8.3936x+62.947, rainfall increased at the rate of 8.3936% per month within the years with a coefficient of determination of R^2 = 0.0742, which implies that on the average of a year accounted for 7.42% of the changes observed, the seasonal trend of rainfall was insignificant at a P value of 0.3915. The trend of malaria morbidity cases within a year showed that malaria cases decreased with a negative trend insignificantly P=0.3321 towards the end of the year at the rate of -3.0557% per month during the period under study Y= -3.0557x + 269.03 with a coefficient of determination R^2 = 0.0941, which implies that for the period of twelve months every year during the period under study (2006-2015) accounted for 9.41% of the temporal variations observed.

Annual Trends of Temperature and Malaria Morbidity

The recorded temperature during the period under study (2006-2015) was established to have a positive trend. A regression of Y=0.0271x + 27.416 means that annual temperature increased at the rate of 0.0271% per annum during the period under study with a coefficient of determination R^2 = 0.0186, which implies that the period under study accounted for 1.86% of the temporal changes observed. However, at a P value of 0.7072, this trend was not significant. During the study period, the overall mean monthly malaria morbidity cases also showed a negative trend. It decreases at the rate of 1.581% per annum. The coefficient of determination of R^2 = 0.0281 which implies that for the period under study, accounted for 2.81% of the temporal in mean monthly malaria morbidity cases, with a r value of 0.1676 and a P value of 0.6433, the trend was insignificant.

Seasonal Trends of Temperature and Malaria Morbidity

The recorded mean monthly temperature trend during the period under study was negative. Temperature reduced as the months progressed from January to December. The equation Y = -0.2794x + 29.424 implies that temperature decreased at the rate of 0.2794% per month. A coefficient of determination R^2 = 0.3227 means that one year accounted for 32.27% of the temperature variations observed during the period under study, at a P value of 0.0539, this trend was not significant. The malaria morbidity cases decreased towards the end of the year at the rate of -3.0559% per month in a year during the period under study (Y = -3.0559x + 269.03), a coefficient of determination R^2 = 0.0941, implies that for the period of twelve months every year for the period under study accounted for 9.41% of the temporal variations observed. Both temperature and malaria morbidity cases had negative trends within the years, the rate which reduced towards the end of the year and can be observed that a very small decrease in temperature can greatly decrease malaria occurrence in the study area.

Annual Trends of Relative Humidity and Malaria Morbidity

The recorded Relative humidity trend for the period under study (2006-2015) showed a positive trend. During the period, Relative humidity increased at the rate of 0.5606% per annum (Y= 0.5606x + 60.046). The coefficient of determination R^2 = 0.0746 meaning the period under study accounted for 7.46% of the temporal variations observed. Malaria morbidity cases had a negative trend of 1.5818% per annum. The coefficient of determination R^2 = 0.0281, that implies that the period under study accounted for 2.81% of the temporal variations in malaria morbidity cases observed. Given that relative humidity is optimal for malaria transmission between 55% - 80%, any increase above that equally impact on malaria morbidity by decreasing the transmission.

Seasonal Trends of Relative Humidity and Malaria Morbidity

The recorded monthly relative humidity trend showed an increase from January to December with slight increase from the months of April to October (Rainy season) and decline afterwards (Dry season). In general, there was a positive trend (Y = 2.0789x + 50.523) means that Relative humidity at the rate of 2.0789% per month as it declined towards the end of the year and a coefficient of determination R^2 = 0.1674, which means that a year was accountable for 16.7% temporal variations observed. The trend of malaria morbidity cases showed that malaria morbidity cases increase from the start of the year and steadily declines at the height of the rainy season months towards the end of the year at the rate of -3.0559% per month in a year for the period under study (Y= -3.0559x + 269.03) with the coefficient of determination R^2 = 0.0941, which implies that for the period of twelve months every year accounted for 9.41% of the variations observed.

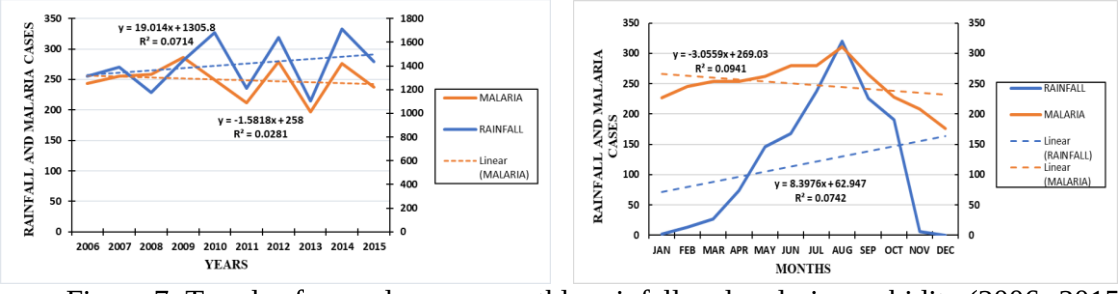

Figure 7: Trends of annual, mean monthly rainfall and malaria morbidity (2006- 2015).

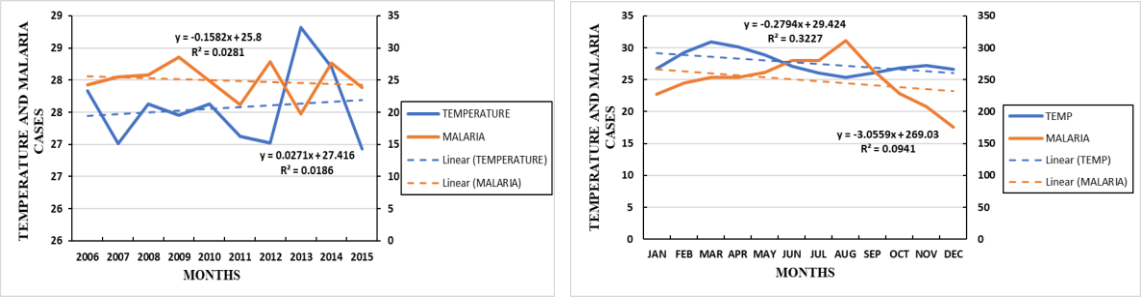

Figure 8: Trends of annual, mean monthly temperature and malaria morbidity (2006- 2015).

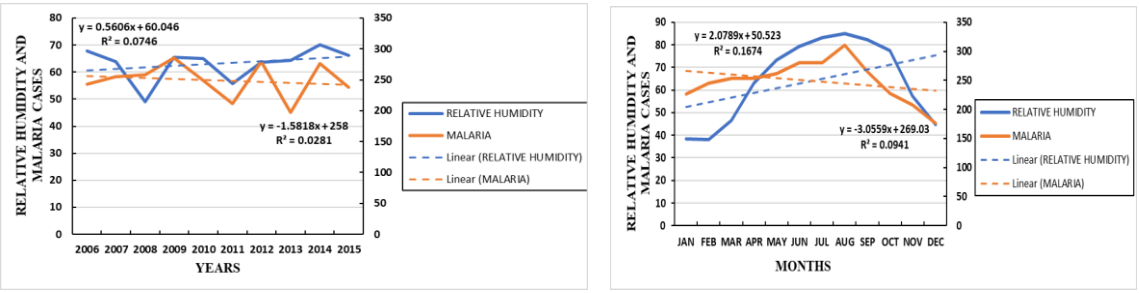

Figure 9: Trends of annual, mean monthly relative humidity and malaria morbidity (2006- 2015).

Relationship Between the Variability of Rainfall, Temperature, Relative Humidity and Malaria Morbidity.

Over the period under study (2006 – 2015) the study established an increase in the amount of rainfall and an increase in malaria morbidity cases. A year with high rainfall recorded a high morbidity. The overall relationship of the annual rainfall and malaria morbidity cases was a strong positive (r=0.6787) relationship. This relationship was significant (P= 0.030). Recorded monthly rainfall and malaria morbidity cases trend within the years positively correlated in the study area (r=0.7697) and the relationship was significant at (P= 0.0034). Months having high rainfall had significantly high malaria morbidity cases recorded. According to IISD (2013) rainfall increases vector population by creating new breeding sites, however too much rainfall will wash away breeding habitat and kill the mosquito larvae.

Relationship Between Temperature and Malaria Morbidity Cases

During the period under study (2006-2015), the study established a steady increase in temperature as well as the malaria morbidity cases. Although most of the years with high temperature recorded low malaria morbidity cases. The overall relationship between temperature and malaria morbidity cases was a weak positive (r= 0.3203) but not significant (P=0.3668). Relationship between mean monthly recorded temperature and monthly recorded malaria morbidity cases for the period under study (2006-2015) showed a weak positive correlation (r = 0.1011). Months with high temperature recorded low malaria morbidity cases while months with high morbidity had low temperature. Campbell *et al* (2003) stated that optimum temperature associated with the pathogen within the vector has to be with in 15^0C to 30^0C. Temperature is very important in determining the development rate of the mosquitoes. As temperature decreases or increases, so does the development of mosquito's parasites which according to Ting and Ming (2005) is 26 days at 20^0C and only 13 days at 25^0C.

Relationship Between Relative Humidity and Malaria Morbidity Cases

During the period under study (2006-2015), it was observed that there was an increase in relative humidity with an increase in malaria morbidity cases. Most years for the period under study having high relative humidity recorded high malaria morbidity cases. The overall relationship between

relative humidity and malaria morbidity cases was a weak positive (r=0.1933) but is not significant (P=0.5925).
For the period of twelve months during the period under study, it was established that there was a decrease in relative humidity as the months advanced from the rainy season, recording a decrease in malaria morbidity cases. The relationship between monthly recorded relative humidity and malaria morbidity cases was strong positive (r=0.6568) relationship and the relationship was significant (P=0.0203). A relative humidity value below 55% and above 80% shortens the life span of the mosquito and reduces the transmission, this means that Kuje area council with a mean relative humidity value of 63% over the period under study would be conductive for mosquito development.

Hypothesis Testing
The hypothesis was tested with the aid of regression and the Pearson product moment correlation coefficient (PPMC). By regressing annual rainfall (R2 = 0.0714), temperature (R2 = 0.0816), relative humidity (R2 = 0.0746) showed positive trends for the period under study (2006-2015), but none of the selected climatic variables were significant, malaria morbidity cases had a fairly positive trend (R2 = 0.0281).
From the observations above, the null hypothesis was rejected (H0- There was no significant trends in the selected climatic elements for the period under study) and adopted the alternative (H1- There were insignificant trends in the selected climatic elements during the period under study). He also rejected the null hypothesis (H0- There were insignificant trends in malaria morbidity cases during the period under study) and adopted the alternative (H1- There were insignificant trends in malaria morbidity cases during the period under study).
The relationship between monthly rainfall and monthly recorded malaria morbidity cases was significantly positive (r = 0.769, P = 0.003), Monthly temperature had a negative correlation with malaria morbidity cases, monthly relative humidity values had a significantly positive correlation (r=0.656, P=0.020). From the observations above, the null hypothesis was rejected (H0- There was no significant correlation between the variation of the selected climatic elements and malaria morbidity cases in Kuje area council), and adopted the alternative (H1- There is a significant correlation between the variation of the selected climatic elements and malaria morbidity cases in Kuje area council). Hence the seasonality of malaria morbidity cases in the study area could be a factor of rainfall and relative humidity variability.

5. Conclusion

Based on the above results, it was concluded that the selected climatic elements of rainfall, temperature and relative humidity and recorded malaria morbidity cases did not show clear patterns over the years during the study period (2006-2015). Rainfall and temperature showed positive, significant trends during the period under study, and also the recorded malaria morbidity cases had a significant positive trend during the study period. Rainfall and relative humidity significantly correlated positively with malaria morbidity cases and should be blamed for the prevalence of malaria cases in the study area.

The observed results reveals that the malaria morbidity cases tend to increase during the peak of rainfall and relative humidity and then varies afterwards. This concludes that the varying wet and dry seasons creates a conducive habitat for mosquito development in the area council. Since the study showed a relationship between malaria morbidity cases and rainfall, relative humidity, temperature, in Kuje area council over the period under study (2006-2015), the health service providers in the study area are recommended to be aware with the impact of the rainy season on

the occurrences of malaria and prepare enough medicines and education to people on how to control malaria.

References

Aboagye-Antwi, F. and Tripet, F. (2010) Effects of Larval Growth Condition and Water Availability on Desiccation Resistance and Its Physiological Basis in Adult Anopheles gambiae Sensus Tricto. *Malaria Journal*, 9, 225. http://dx.doi.org/10.1186/1475-2875 9-225.

Adakayi P.E. (2000) Climate Change in Dawan P.D. cedis Geography of Federal Capital Territory. Asanlu Publication, Minna.

AMR, (2003). The importance and future of malaria research in Africa. Med. Biotech Laboratories, Kampala, Uganda.

Balogun, (2001) The Federal Capital Territory of Nigeria. A Geography of its Development, University of Abuja.

Bhattacharya, S., Sharma, C. and Dhiman, R.C. (2006). Climate change and malaria in India. Current Science, Vol. 90, No. 3, 10 February 2006.

Craig, M.H., Kleinschmidt, I., Le Sueur, D. and Sharp, B.L. (2004) Exploring 30 Years of Malaria Case Data in Kwa- Zulu-Natal, South Africa: Part II. The Impact of Non-Climatic Factors. *Tropical Medicine and International Health*, 9, 1258-1266. http://dx.doi.org/10.1111/j.1365-3156.2004.01341.x

De Savigny, D.E., Mewageni, C.C., Mayombona, H., Masanja, A., Minhaji, D., Momburi, Y., Mkilindi, C., Mbuya, H., Kasale, H., Reid, and H. Mushinda (2004b). Highland malaria in Uganda: Prospective analysis of an epidemic associated with El Niño, Trans. R. Soc. Trop. Med. Hyg. 93:480–487.

Ebi, K.L., Hartman, J., Chan, N., McConnell, K.J., Schlesinger, M. and Weyant, J. (2005) Climate Suitability for Stable Malaria Transmission in Zimbabwe under Different Climate Change Scenarios. Climate Change, 73, 375-393. http://dx.doi.org/10.1007/s10584-005-68752.

Intergovernmental Panel on Climate (IPCC). (2007). Climate change 2007: Synthesis Report. Summary for policy makers. pp. 1-22. Retrieved from November 19, 2016,

Intergovernmental Panel on Climate Cange. (2007). Climate change: Impacts, adaptation and vulnerability, McCarthy. J., Canziani. O. F., Leary. N., Dokken. D., and White, K.S. (eds.). Contribution of Working Group II to the Third Assessment Report, Cambridge University Press, UK.

International Institute for Sustainable Development, (2013). Climate risk management for malaria control in Kenya: The case of the Western Highlands, UNDP. New York, USA.

MacDonald, G. (1957) The Epidemiology and Control of Malaria. Oxford University Press, London.

Moreira, L.A., Wang, J., Collins, F.H. and Jacobs-Lorena, M. (2004) Fitness of Anopheline Mosquitoes Expressing Transgenes That Inhibit Plasmodium Development. Genetics, 166, 1337-1341.http://dx.doi.org/10.1534/genetics.166.3.1337

NPC, (2006) Detail of the Breakdown of the National and State Provisional totals 2006 Census. The Federal Government Printer, FCT. Nigeria.

NPC, (2011) Detail of the Breakdown of the National and State Provisional totals 2006 Census. The Federal Government Printer, FCT. Nigeria.

Okorie F.C., Okeke, I.C., Njoku J.D., Duru, P.N. [2012], Climate variability and malaria incidence: Impact and Adaptation in Owerri Municipal of Imo State Nigeria, Advances in Education Research. November 2012, San Degio, CA, USA, pp 98-104.

Paaijmans, K.P., Jacobs, A.F.G., Takken, W., Heusinkveld, B.G., Githeko, A.K., Dicke, M. and Holtslag, A.A.M.(2008) Observations and Model Estimates of Diurnal Water Temperature Dynamics in Mosquito Breeding Sites in Western Kenya. Hydrological Processes, 22, 4789-4801. http://dx.doi.org/10.1002/hyp.7099

Patz, J., Githeko, A.K., McCarty, J.P., Hussein, S., Confalonieri, U., and de Wet. N. (2003). Chapter 6: Climate change and infectious diseases in McMichael, A., Campbell- Lendrum, D., Corvalan, C., Ebi, K., Githeko, A., Scheraga, J., & Woodward, A. (Eds.). Climate change and human health: risks and responses. Geneva: World Health Organization.

Sachs, J. and Malaney, P. (2002) The Economic and Social Burden of Malaria. Nature, 415, 680-685.http://dx.doi.org/10.1038/415680a.

Sutherst, R. W. (2004). Global change and human vulnerability to vector-borne diseases. Clinical Microbiology Reviews. 17.1.13 173.

WHO, (2013) WHO Global Malaria Programme, World Malaria Report. WHO Press, World Health Organization, Geneva.

WMO, [1995]. Climate change and health: global to local influences on disease risk; Ann Trop Med Parasitol, 100; 535-549.

Construction and Comparative Study of a Savonius and Darrieus Vertical Axis Wind Turbine

[1]M. Musa., [2]Ibrahim [1]A. G., [1]G. M Argungu., [3]C. Mohammad & [*2]Ibrahim H. I.
[1]Department of Physics, Usmanu Danfodiyo University Sokoto, Nigeria
[2]Department of Physics, Federal University of Technology Minna, Nigeria
[3]Department of Pure and Applied Chemistry, Usmanu Danfodiyo University Sokoto, Nigeria
[*]Correspondence: Email address: habson4ya@gmail.com: Tel: +234(0)8036806528

Abstract

In a previous work, a Savonius vertical axis wind turbine was designed and simulated. In this current work, the designed Savonius and Darrieus vertical axis wind turbines were constructed using wood and metals and the resulting blades were field tested under various wind speeds. The results of this test showed that under standard wind conditions the Savonius rotor will always respond to wind flow before the Darrieus VAWT. More so, the Darrieus VAWT has a higher rotational speed than the Savonius rotor. It was also observed that though it takes the Darrieus VAWT a longer time to start rotation, it also takes it a longer time to stop even when the wind speed is lowered. The Savonius rotor proves to self-start at a wind speed of 2m/s with a maximum RPM of 84rpm and minimum of 45rpm at a wind speed of 3m/s and 7.5m/s respectively. Moreso, the Darrieus blade proves to self-start at a wind speed of 5-6m/s with a maximum RPM of 88rpm and a minimum of 48rpm at a wind speed of 3.5m/s and 7.5m/s respectively under the same atmospheric conditions.

1.0 INTRODUCTION

Nigeria is well equipped with various sources of renewable energy such as solar, wind, biomass, hydropower, and ocean waves in addition to fossil fuel sources. Despite all the numerous available energy sources, their resultant contribution is yet to significantly impact and address the massive shortage of power supply (Sambo, 2012). Wind is the thermal movement of air particles and it is environmentally friendly source of energy that when properly harnessed, has the potential of satisfying the energy needs of people living around areas with high wind potential. It can also serve as a means for mitigating earth from climate change primarily caused by the emission of greenhouse gases. It has been estimated that around 10 million megawatts of energy are available in the earth's wind (GWEC, 2006). But the potential of wind energy can only be reflected in the increase of capacity of wind turbines. As of 2010, the installed capacity of wind energy system in the world is around 194,390 MW (GWEC, 2010).

It is found that although, Nigeria is blessed with reasonable wind energy resources for power generation, the country is still suffering from high level of epileptic power supply which have directly affected development and impinged negatively on economic growth with some parts of the country especially the rural areas lacking access to modern resources which come with availability of electric power.

Basically, a wind turbine is made up of rotor blades that are installed at the top of high towers, they harvest the energy of the wind by allowing the wind to attack and rotate them, which in turn

produces electricity with the help of a generator. Wind technology is improving by the day and this turbine blades are getting larger and more efficient (Greenage, 2013). The reason for maximizing the length of the blades is that, the larger the swept area of the turbine (this is the circle that the turbine produces while spinning) the more wind it will catch and therefore, this increases the energy it can generate. The reason for situating the turbines atop high towers is that, wind speeds tend to be higher at altitude and the power contained in the wind is proportional to the cube of the wind speed (Greenage, 2013).

Wind can be tapped by wind turbines that convert its kinetic energy into mechanical power, which will be in turn converted into electricity by a generator connected to the wind turbine. These turbines are of two types, Horizontal Axis Wind Turbine (HAWT) and Vertical Axis Wind Turbine (VAWT).

There is significant evidence on the environmental impact of chloro-flouro carbon (CFC's) gases to climate change and is gaining momentum, so its reduction is of paramount importance. Also, wind power has expanded rapidly to make a significant contribution to global electricity generation. The World Wind Energy Association has reported a promising yearly growth rates in global wind energy generation but despite these initiatives, in 2009, wind power still only contributes about 1.5% of the global energy generation (WWEA, 2009) and after nine years, the center for climate and energy solutions stated that, wind power has contributed more than 5% of global energy (C2ES, 2018) this shows the rapid growth of wind power

Owing to acute energy crisis that most developing countries including Nigeria are facing today, the interest in alternative energy sources has increased manifolds in the recent past. And the potential of wind energy as a source of alternative energy perhaps cannot be underestimated.

Wind energy can be utilized on a wind turbine, which in turn drives a generator to produce electricity. Thus, it is expected that wind being a non-polluting and non-toxic energy source, will go a long way in solving our energy requirements.

However, in Nigeria, the interest in windmills started in the fifties and early sixties. Few designs were developed but could not yield expected results. This could be due to intermittency in wind speed around potential localities (Ogbonaiya *et al*., 2007). However, if the challenges in design of a VAWT's could be improved, they should be able to represent suitable alternative for harnessing wind power because they accept wind from any direction and can function at a very low wind speed (Akwa *et al*., 2012).

Despite all the advantages possessed by vertical axis wind turbine, it is still not gaining popularity because of low efficiency of the Savonius rotor and low starting torque of the Darrieus type wind machines.

So, due to this reason, this research aims to compare the performance of a standalone Savonius with a standalone Darrieus vertical axis wind turbines so as to know which performed better under the same atmospheric conditions.

2.0 REVIEW OF THE PAST RESEACH ON VAWTs

Vertical axis wind turbines were first used long time ago in ancient Persia and were only used to grind grain (Cheremisinoff, 1978). A scientist and engineer in person of S. J. Savonius invented

the Savonius turbine in 1922 (Eriksson *et al* 2008) and Johnson, (1985) writes that this Savonius rotors are drag turbines since their tip speed ratio is always less than 1.

The concept of Savonius rotor was based on cutting a cylindrical drum vertically from the top to the bottom into two equal halves and then placing the two semi-cylindrical surfaces sideways along the cutting plane (Bachu, 2012). Recently, vertical axis wind turbines are always connected to a generator in order to generate electricity from it. So, its design has improved with time and the main shaft is set perpendicular to the direction of wind flow, while the generator is placed at the base of the turbine. This arrangement allows the generator and gear system to be located close to the ground, facilitating service and repair (A. R. 2010).

Vertical axis wind turbines are now applied in offshore wind farms (Holinka and Stephaine 2012), due to installation and operational challenges, they offer two major advantages which are: lower turbine centre of gravity to improve stability and reduced machine complexity in order to reduce the cost of installing a wind turbine, (Sandia, 2011). In order to improve the performance of Savonius rotor, it is important to pay more attention to some of the geometrical factors like overlap ratio and blade gap (Swirydczuk *et el*., 2012)

Jean Marie Darrieus invented and patented the Darrieus vertical axis wind turbine in 1925 and 1931 respectively. His work was re-invented in the late 1960s (Mittal, 2001), But until in late 1960s that attention was drowned to his work, and the aftermath was the invention of the a Straight Bladed VAWT or H-Rotor (Eriksson *et al*., 2008) which got its name due to the single horizontal arm supporting its two or more blades (Berg, 1996).

Traditionally, Darrieus blades with two or more blades are always having an airfoil design unlike the Savonius but its disadvantage is on the starting torque coefficient which is very low when compared to the Savonius. Which means that, a special motor will be required to start or put the blades in motion (Kragten, 2004) since it cannot self-start on its own at a lower wind speed. This is a setback of Darrieus turbine where the Savonius turbine is of obvious advantage.

Darrieus rotor is usually a non-self-starting wind turbine but it provides good power coefficient after its cut-in wind speed has been reached.

The vertical axis wind turbines are mostly feasible for places with low wind speed whereas the horizontal axis wind turbines are highly uneconomical. Furthermore, vertical axis wind turbines do not require any yawing device that brings the blades to the direction of the incoming wind, as required in case of horizontal axis wind turbines. However, the major drawback of vertical axis wind turbines are their low performance coefficients. That is why there are many research on vertical axis wind turbines in order to improve their performance. The present work is based on VAWT rotor. The VAWT rotors are of different types, like the Savonius, Helical Savonius, Eggbeater Darrieus, H-Darrieus, combined configurations of Savonius and Darrieus rotors etc.

Fagberile and Karayiannis (1994) specifically mentioned that the average wind speed in Nigeria range from 2m/s to about 4m/s with the highest average speeds of about 3.5m/s and 7.5m/s in the Southern and Northern part of the country respectively. So, on a nationwide scale, the harnessing and electrification of wind energy can only be adequately achieved in few locations such as Gusau, Jos, Kano and Sokoto. Other potential areas for electricity generation are some of the North eastern and North central states with average annual wind speeds in the range of 5-6m/s. it was on this note that, the country was rated between 1 to 3 in the Southern state and between 3 to 4 in the Northern state (IJATER, 2014) on a Beaufort scale. There is a positive prospect for utilization of wind energy

in Nigeria depending on the end use (Adaramola and Oyewola, 2011). Meaning that, there is huge prospect within the country for power generation through wind if associated challenges hindering wind energy technology (WET) advancement are overcome (Ajayi, 2010).

Based on the literature review, it has been decided to fabricate Savonius and Darrieus wind machine and to experimentally investigate their performances. The purpose of the present study is to investigate the performance of a Savonius and a Darrieus vertical wind turbines and compare their performance in various wind speed.

3.0 MATERIALS AND METHODS

METHODOLOGY

The goal of this research is to develop a combine vertical axis wind turbine (VAWT). The VAWT was designed to operate in conditions with wind patterns found in rural area of Usmanu Danfodiyo University Sokoto settings, and needed to be sufficiently mechanically efficient to be able to rotate the generator. While optimizing the VAWT for rural settings, special attention was paid to the type of turbine used and then to the design of the blades for that turbine. In order to accomplish this goal, the following objectives were addressed:

1. Analyze wind patterns characteristics in a rural environment. By gathering data from anemometers at three different locations around the campus.
2. Evaluate various turbine designs to predict which would be best for rural households based largely on efficiency but also on the following factors: vibrations, noise, aesthetics, reliability, manufacturability and cost to build.
3. Determine the efficiency of the best turbine design by manufacturing it, creating an experimental setup, and performing testing.

STUDY AREA

The Energy Research Center, Usmanu Danfodiyo University Sokoto is located at the North Western part of Nigeria, Sokoto State with Latitude 13^0 1'N and Longitude 5^0 13'E, 350m above sea level with a yearly average wind speed of 7m/s. Sokoto State shares a border with Niger Republic and is among the 5 states in Nigeria that enjoys a lot of average wind speed ranging from 2.5m/s to 7.5m/s.

To know the wind conditions, wind data were collected at Usmanu Danfodiyo University, Permanent Site Sokoto State. Wind data were collected with the help of a thermo anemometer. Data were recorded for one week in three different locations at the university permanent site and from the data it is observed that wind speed is quite low compared to the average wind data analysis of Sokoto State collected for a period of one year.

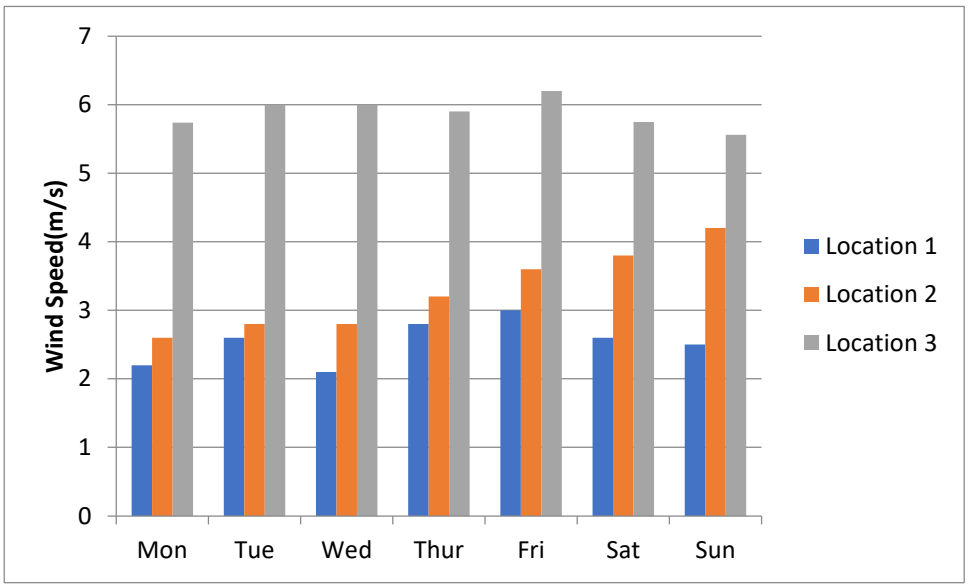

Fig 1: showing the average wind speed in three different locations for one week in the study area, Usmanu Danfodiyo University Permanent Site, Sokoto State.

Based on the data collected for the wind speed in three different locations around the main campus of the University, Location 3 was chosen for the research since it has the highest wind speed.

ANALYZING WIND PATTERNS

For this project, data were collected from anemometers at three different locations around the main campus, one on the ground at a height of 1.75m high, while the second location was at the same height (1.75m) with location one above the ground level. The third location was on the roof top of a building at a height of 4m above the ground, which were analyzed using Microsoft Excel and Qblade. Excel was used to analyze basic data such as wind speed averages, time graphs, and Reynolds numbers. The Qblade software provided information on variation of wind with direction and it provided basic wind information over different types of areas. These data were also used to more accurately to predict how different Airfoil would perform in the chosen area, thereby increasing the odds of coming up with an efficient turbine and blade design.

Power in the wind

The Kinetic power of the wind is described by:

$P_{kin} = ½ * m * v^2$ [1]

Where:

P_{kin} = kinetics power [W];

m = mass flow = ρ*A*v [kg/s];

ρ = density [kg/m^3];

A = area [m^2];

v = speed [m/s];

For a VAWT, the swept area is described by:

$A = d * h$ [2]

Where:

d = diameter of the rotor [m];
h = length of the blades [m];
The formula of the power in the wind can be written also as:

$$P_{kin} = ½ * \rho * A * V^3 \quad [3]$$

The density of the air varies with the height above sea level and temperature. The standard value used for the density of air at sea level is 1.2 kg/m^3. According to Dahmouni et al cited in Ohunakin (2011), wind power density of a location is the most important parameter to be considered in citing a wind energy conversion system (WECS) as it takes into consideration the wind speed, wind speed distribution and air density. Since the period of high wind speed coincides with dry season when the northern part of the country was usually dry and the use of wind energy for electricity generation would help alleviate the shortage of hydroelectricity that results from the low level of water in the Niger River. (Momoh *et el*., 2013).

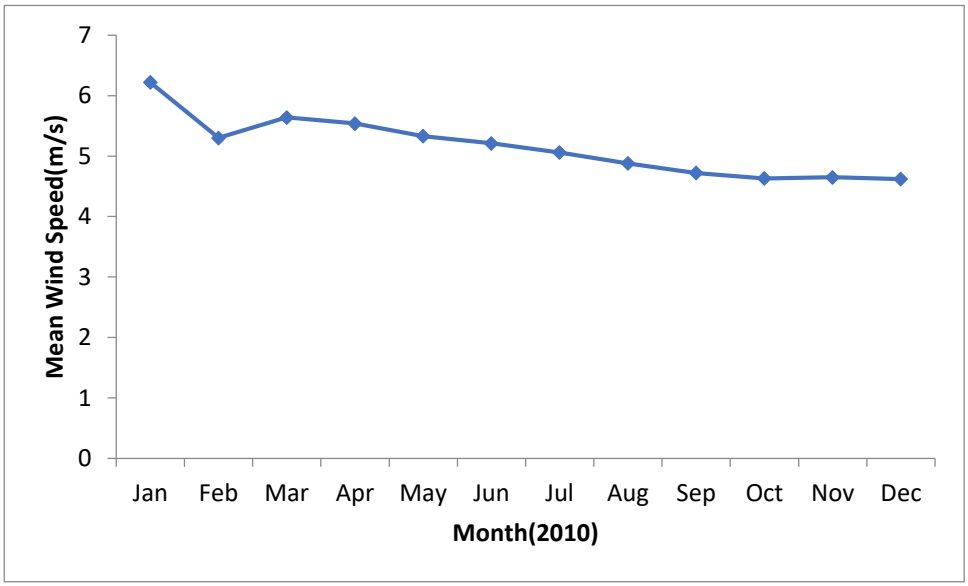

Fig 2: showing the average wind speed for one year in Sokoto State (Momoh *et el*., 2013).

CONSTRUCTING THE TURBINE

Since this turbine was a custom design, the major parts were built from raw materials found within the environment. For the VAWTs to have the right specification for easy construction and stand the test of time it must be well designed using the appropriate materials and software.

The assembly of the Darrieus which was made up of a straight wood 3m in length and a drum for the Savonius rotor. To minimize friction the rotor shaft (power shaft) was supported with two roller bearings, the stand (base) carrying the rotor blades approximately 1.2m high structure was made from 2inch angle iron, and finally the Darrieus blade were supported by galvanized pipes and three-quarter pipes.

The final design was difficult to explain so several models were constructed to help Visualize the idea. The first model was constructing the Darrieus blade. A second Model was to build the Savonius rotor. Third model was constructing the stand and finally, the fourth show the general arrangement of the whole turbine.

DARRIEUS BLADE

The Darrieus Blade was carved out from wood 3m long which was refined and accurately measured to ensure that the chord length of the airfoil shape is distributed evenly throughout the length (height of the blade). A small piece of tin was placed on the airfoil shape, traced and cut out which was placed on the wood to make the leading Edge of the airfoil while two larger, straight pieces were cut for the sides; all three pieces were then duct taped at the hinged portion to create the entire airfoil. Precautions were taking to avoid eating of the wood by termites or shrinking of the blade by painting and putting a weighted object on top of the blade to ensure the blade does not bend. The blade is 2.5m long with a chord radius of 0.26m. Since NACA 0012-34 airfoil was adopted, to enable efficiency of operation of the blade, the pitch was reduced to 0%, radius 0mm, thickness 0.04m (150%) and the origin as 0%. After properly and carefully carved with all measurement intact, the blade was preserved

SAVONIUS ROTOR

The Savonius blade was built out of a metal (drum) of diameter 0.5m and height 0.9m. The drum was cut into two equal half and welded to a shaft of 2.9m long. Another metal was welded round the diameter and length of the Savonius blade to ensure stability of the blade during rotation. The two half drums cut to make the Savonius blade were joined together by placing the half drums side by side, back and front to one another and then welded to the shaft and finally, the blades were painted to prevent corrosion or rusting of any kind.

THE ROTOR

The rotor is made up of a thick iron rod which is 3.2m long, 4.0cm in diameter and was connected to two ball bearings which were placed at the opposite ends of the rod.

THE SHAFT

The shaft is made up of 2.9m long and 5.0cm in diameter iron pipe, strong enough to hold both the Savonius and the Darrius blade. The rotor was placed inside the shaft and holes were drilled through the shaft for the in order to knot the shaft and the rotor together to enable the rotor to rotate as the shaft is rotating.

BALL BEARINGS

The ball bearings were properly greased to reduce friction and the rotor was connected to them to ensure easy and higher rotational efficiency of the turbine.

SHROUD

The shroud was made from wood; a board with a diameter of 1.2m almost the same diameter of the Savonius rotor which was knotted to the both ends of the Savonius blade to enable enclosure of the blades for safety measures and other necessary applications.

THE BASE

The base was constructed and built out of 2-inch angle iron; it was built to ensure that it can stand the weight of the turbine and speed of the wind from any direction to avoid vibration and noise from the turbine. The base or stand is 1.17m high and 2m wide which is constructed only with a cast or angle iron, strong enough to stand any resistance at any wind speed in Nigeria (Sokoto).

POWER

The maximum power of the turbine is calculated from the equation below

$P_{max} = ½ C_p \rho A V^3$ [4]

A = length x diameter

Where

P_{max} = maximum power of the turbine (W)

ρ = density of air ($1.23 kgm^{-3}$)

A = swept area of the blades of the turbine (m^2)

V = speed of the wind (m/s)

Length and diameter are all measured in (m) (Eriksson *et el*., 2008)

RESULTS AND ANALYSIS

WIND

The wind analysis was an important part of this research because it allowed for perspective time at the same location where the turbine was installed at a height of 8.17m above the ground level. Through data collected using thermo anemometer, tachometer and multimeter all the data can be combined to see what potential lies around the area. Using Xcel, a large amount of data was able to be looked at in an organized manner.

Figure 4 helps to show the average wind potential directly surrounding the area where the turbine was installed at 15min intervals at three different locations for one week each.

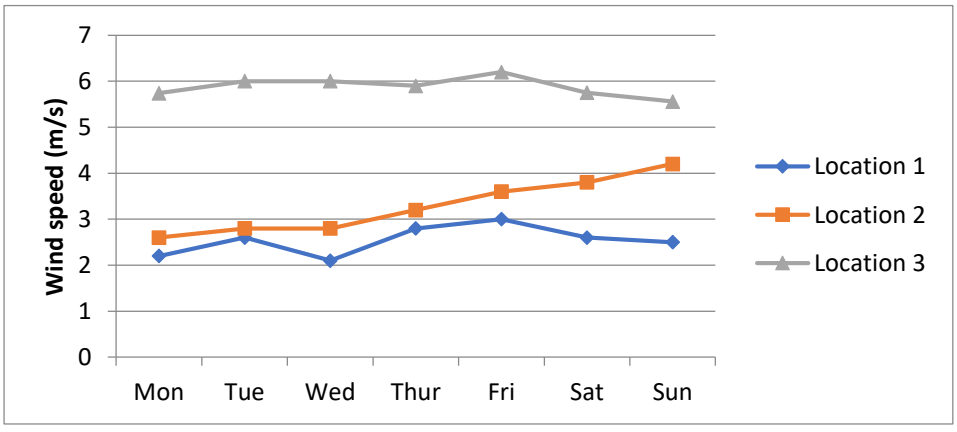

Fig. 3: Wind variation for three different locations in the University permanent site area

It was observed from the figure above that the wind potential of location 1, which was 1.8m above the ground level, has the least wind speed because wind speed increases with an increase with

altitude. So, this location does not provide the calculated wind speed require for the turbine to function efficiently.

Location 2 was approached and analyzed, the wind speed reached a maximum of 4.2ms^{-1} on Sunday at a height of 1.8m above the ground level, this is because the area was open and there were no trees to disturb the flow of the wind.

Although, the speed of the wind on this location is large enough to start up the turbine and also enable the turbine to rotate, but the number of revolutions per minute will be too small, small enough for the generator specification used during this research.

However, based on the result collected from three different locations, the third location which was at a height of 5.8m above the ground level was chosen because the speed of the wind reaches a maximum average of about 6.2ms^{-1} on Friday which is best for the turbine specification and the turbine was installed here.

More so, the wind increases and decreases at any time, so there is no certainty that the wind speed will remain constant for even a minute.

AIRFOIL ANALYSIS

In order to choose which of the turbine will work best at this wind speed, the airfoil for the Darrieus blade was taken into consideration, so the best was chosen among others; NACA 0012 was chosen but because of manufacturability complex in bringing out all the trailing edges of the blade perfectly without the use of some complex machines, a modification of NACA0012 was necessary, so it was modified to NACA 0012-34.

More so, NACA0012 was modified to NACA0012-34 because it cannot operate at a transonic speed since they were only designed with thickness location for lift in mind and not high- or low-pressure regions (Abbot, 2014), so supercritical airfoils are better to reduce wave drag and perform better in high/low pressure regions.

SAVONIUS ROTOR ANALYSIS

The Savonius rotor was tested and the observation were as follows

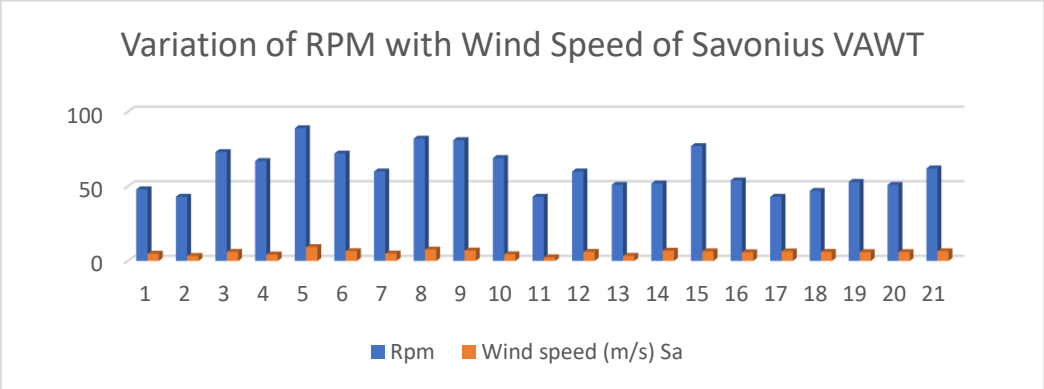

Fig. 4: Variation of Wind Speed and Rev. per minute of the Savonius Rotor

From figure 4 above, it shows that, the highest rotational speed per minute of the Savonius rotor was 89rpm at a wind speed of 9.28ms^{-1} and the lowest of 43rpm at a wind speed of 2.46ms^{-1} a cut-

in wind speed of 2.5ms^{-1} and cut-out wind speed is 12ms^{-1}. At this wind speed (9.28ms^{-1}), the turbine functions as expected

DARRIEUS BLADE

The Darrieus blade was constructed and tested, and the following result were obtained

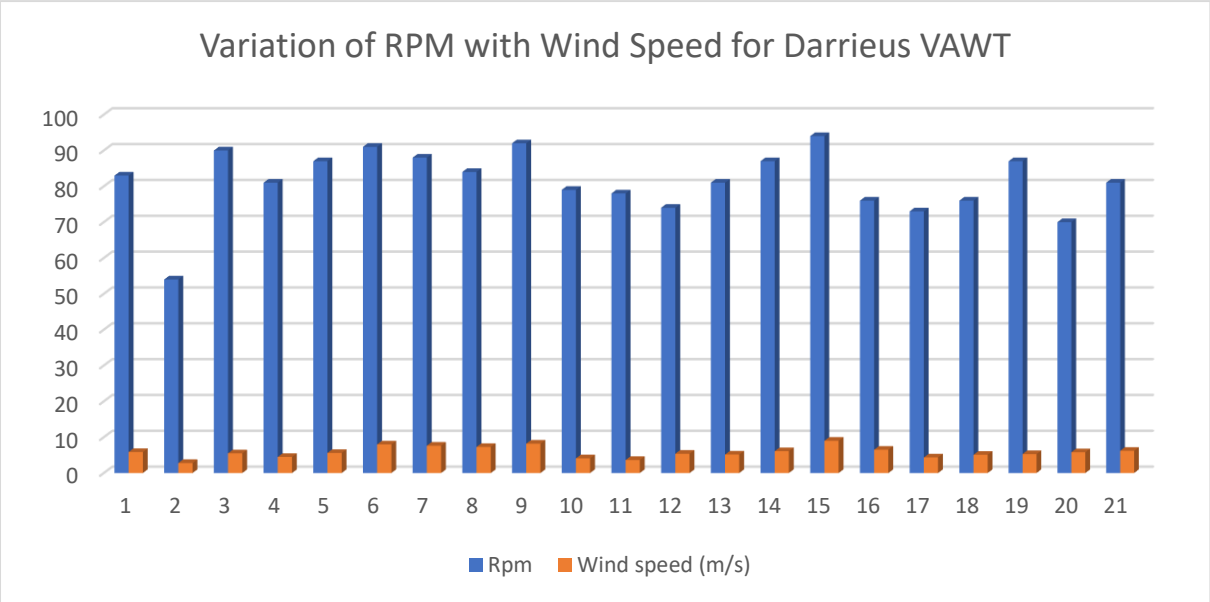

Fig. 5: Showing the variation of the wind speed and the RPM of the Darrieus turbine

From the figure above, it was observed that the combined turbine reached a maximum of 91 revolutions per minute at a wind speed of 7.9m/s and a minimum of 54 revolutions per minute at a wind speed of 3.8m/s.

From the figure below, it is observed that the Darrieus wind turbine performed better and has a higher rotational efficiency than the Savonius wind turbine. The Darrieus and Savonius both produced a maximum of 88 RPM and 84 RPM respectively when subjected to the same wind speed of 7.5m/s under the same atmospheric conditions

However, the Darrieus wind turbine did not pick up at a wind speed of 3m/s until at a speed above latter, yet, the Savonius rotor performed better than the Darrieus at a wind speed of 3.5m/s. Both Turbines produce more noise at a wind speed between 6.0 - 7.5m/s. This noise was reduced by adding more lubricants to the ball bearings and also making sure that the vibration made by the turbine is drastically reduced by holding the turbine firmly to the ground with stay wires.

Comparing the Savonius and the Darrieus vertical axis wind turbines

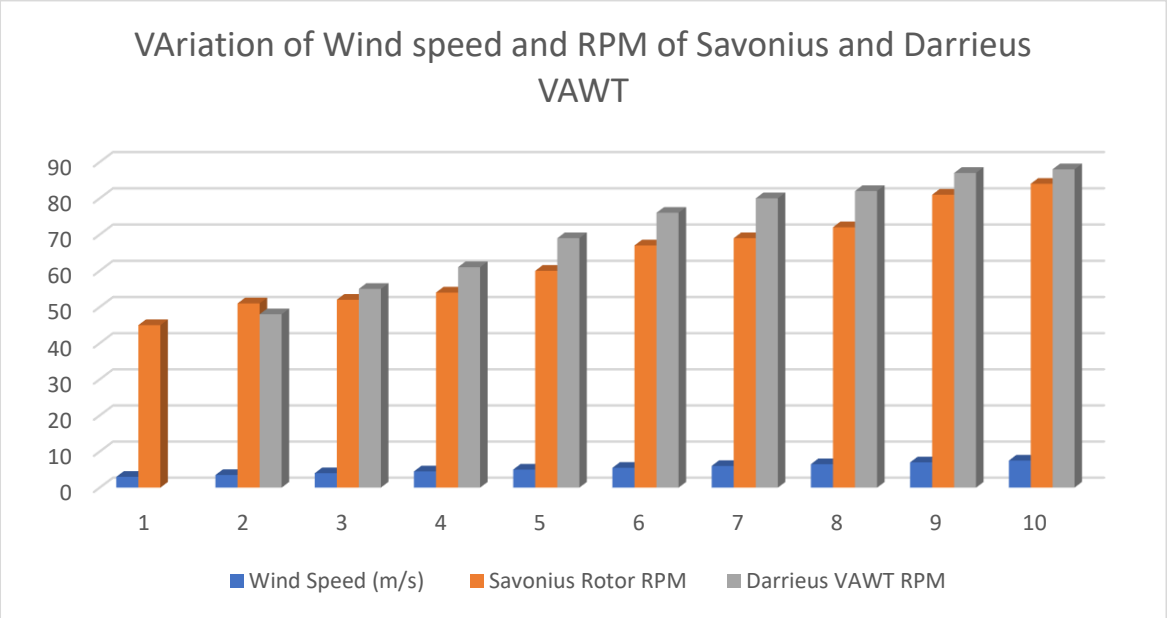

Fig 6: Showing how both the RPM of Savonius and Darrieus Wind Turbine Varies with Speed

CONCLUSION

The Darrieus VAWT, fabricated and tested proved to function as a self-starter but at a wind speed of 5.0 – 5.5 m/s while the Savonius VAWT starts at a wind speed of 2.5 m/s. The use of an asymmetric airfoil (NACA 0012-34) provided the Darrieus blade with high thickness which resulted in an increase in the efficiency of the turbine and provided the functions required for a starting mechanism for the Darrieus vertical axis wind turbine.

Blades were manufactured using Wood and Metal and the resulting airfoil was field tested under various wind speeds. The results of this test showed that under standard wind conditions the Savonius VAWT has a higher starting torque than the Darrieus VAWT but when the Darrieus blade starts it takes a lot of time for it to stop, given it its higher rotational speed even at a lower wind speed. From the results obtained during the field test of both the Darrieus and Savonius vertical axis wind turbine, under the same wind speed and atmospheric conditions, it was observed that, the Darrieus VAWT performed better than the Savonius in terms of RPM, reaching a maximum RPM of 88 while the Savonius 84

The superior capabilities of Darrieus VAWTs described have shown the need for additional applied research in the design characteristics in order to improve the starting torque of a stand-alone Darrieus VAWT.

REFERNCES

Adaramola M. S. and Oyewola O. M. (2011). Wind Speed Distribution and Characteristics in Nigeria". *ARPN Journal of Engineering and Applied Sciences*, Vol. 6, No. 2, pp. 82-86.

Ajayi O. O. (2010). *The Potential for Wind Energy in Nigeria.* Wind Engineering Volume 34, No. 3; Multi-Science Publishing Company, pp. 303 and 310.

Akwa, J. V., Vielmo, H. A. and Petry, A. P. (2012). *A Review on the Performance of Savonius Wind Turbines*, Ren and Sus Energy Rev., 16, pp 3054-3064.

Alé J. A. M. R. Petry, S. B. Garcia, G.C. Simioni, and G. Konzen (2007). *"Performance Evaluation of the Next Generation of Small Vertical Axis Wind Turbine."* European Wind Energy Conference & Exhibition, May 7-10, MIC Milano Convention Centre, Milan, Italy.

Berg, D. (1996). *Vertical Axis Wind Turbines; the Current Status of an Old Technology.* Retrieved June 22, 2010 from http://www.osti.gov/bridge/purl.cover.jsp;jsessionid=164BD5A4808122A70CCA59FCA46F984D?purl=/432928xZkiEJ/webviewable

Bachu Deb and Rajat Gupta (2012). *Fluid Flow Analysis of Savonius Rotor at Different Rotor Angle Using CFD*, volume 8 (14), 35-42

Cheremisinoff, N. P. (1978). *Fundamentals of Wind Energy.* Ann Arbor, MI: Ann Arbor Science.

Gupta R, Biswas, A and Sharma, K. K. (2008). *Comparative Study of Three-Bucket Savonius Turbine with Combined Three-Bucket-Savonius-Three-Bladed-Darrieus Turbine.* Renewable Energy 2008; 33: 1974-1981.

GWEC (2006). *Global Wind Energy Market*. Press release of Global Wind Energy Council, www.gwec.net/publications/global-wind-report-2 (2010 accessed 9 July 2006).

GWEC (2010). *Global Wind Energy Market.* Press release of Global Wind Energy Council, www.gwec.net/publications/global-wind-report-2 (2010 accessed 10 July 2010).

IJATER (2014). *International Journal of Advanced Technology & Engineering Research* www.ijater.com ISSN No: 2250-3536 Volume 4, Issue 1, Jan. 2014 55

Johnson, G. L. (1985). *Wind Energy Systems*. Upper Saddle River, NJ: Prentice Hall.

Kragten I. A. (2004). *The Darrieus Rotor, a Vertical Axis Wind Turbine with only few Advantages and many Disadvantages.* Report KD215, Populierenlaan 51, pp.3-4.

Mittal N. (2001) *Investigation of Performance Characteristics of a Novel VAWT*. Thesis Publication of Department of Mechanical Engineering, University of Strathcyclyde, pp. 10-16.

Ogbonaiya I. Okoro, E. Chikuni and P. Gvender, (2007). Prospect of Wind Energy in Nigeria *"The Installation of Wind Energy Conversion System"* June 13.

R. Gupta, A. Biswas, and K. K. Sharma (2008). *"Comparative study of a three bucket Savonius rotor with a combined three-bucket Savonius-three-bladed Darrieus rotor."* Renewable Energy, Vol. 33, pp. 1974-1981.

SAMBO A. S. (2012). Renewable Energy: *Current Situation and Future Prospects in Nigeria.* Presented at the German-African Energy Forum, Hamburg Germany.

Swirydczuk, J., and Kludzinska, K. (2012). *Improving Savonius Rotor Performance by Shaping its Blade Edges*

WWEA (2007). *"New World Record in Wind Power Capacity"* 14.9 GW added in 2006 Worldwide Capacity at 73.9 GW World Wind Energy Association, Charles-de-Gaulle-Str. 5, 53113 Bonn, Germany.

WWEA (2009). *"World Wind Energy Report."* Wind Energy Association, Charles-de-Gaulle-Str. 5, 53113 Bonn, Germany.

Holinka, Stephaine (2012). "Offshore Use of vertical axis Wind Turbines Gets Closer Look" Renewable Energy World. Retrieved 18 Sep. 2015

Biswas A., R. Gupta, and K.K. Sharma (2007). *"Experimental Investigation of Overlap and Blockage Effects on Three-Bucket Savonius Rotors."* Wind Engineering, Vol. 31, No. 5, pp. 313-368.

Argungu, G. M., Bala, E. J., Momoh, M., Musa, M. & Dabai, K. A. (2013) Analysis of Wind Energy Resource Potentials and Cost of Wind Power Generation in Sokoto: Sokoto Energy Research Centre. Northern Nigeria. *International Journal of Engineering Research & Technology (IJERT)* Vol. 2; May-2013

Eriksson, S., Hans Bernhoff, and Mats leijon, (2008), "Evaluation of different turbine concepts for wind power"

Ph.D., A.R. (2010). Wind Turbine Technology. Boca Raton, FL: CRC Press

https://www.c2es.org/content/renewable-energy/

URBAN FOREST DEGRADATION AND VULNERABILITY TO PANDEMIC NEXUS IN MINNA TOWN, NIGER STATE, NIGERIA

[1] Jibrin Abdullahi & [2]Saba Alhaji Liman

[1]Department of Geography & Environmental Mgt., Ahmadu Bello University, Zaria, Nigeria

[2]Department of Architectural Technology, Federal Polytechnic, Bida, Niger State, Nigeria

Correspondence: Abdullahi Jibrin ; +234-803-697-8420; E-mail: ajibrin@abu.edu.ng

Abstract

Most efforts to stem the tide of pandemics tend to focus on vaccine development, early diagnosis and containment, which is akin to treating the symptoms without addressing the underlying cause(s), As humans degrade urban forest structure and composition, there is likelihood for increasing the risk of disease pandemics such as COVID-19. This study is aimed at examining the effect of urban forest degradation on vulnerability to pandemic outbreak and incidence in Minna town. The study employed field survey method based on qualitative and quantitative analysis of 8 indicators of urban forest (structure and composition) degradation; 18 indicators of ecosystem services degradation and 5 indicators of vulnerability to pandemic incidence. Relative Importance Index (RII) and Ecological Risk Index (ERI) were used to analyze the data collected. Findings from the study revealed that virtually all the parameters of structure and composition of urban forest have undergone significant degradation. It was also found that ecosystem services have declined considerably over the 30 years covered. Consequent upon the current status of urban forest ecosystem degradation, ERI was generally found to be high (ranging from 0.383 to 0.764.). The study thus conclude that urban environment in Minna is conducive to host potentially dangerous conditions and pathogens that can trigger or escalate some poor human health conditions. The study hereby recommends strengthening and sustaining regulations on urban land use, urban trees, green areas and pollution. Thus, conserving urban forest is vital for avoiding the next pandemic in Minna.

Key words: Pandemic, Urban forest, Ecosystem services, Degradation, Vulnerability.

Introduction

Current rate of urbanization is quite alarming, as urban areas are projected to accommodate 68% of the world's population by 2050 (United Nations 2018). By 2050, three billion additional people will live in cities; while urbanization is frequently linked to environmental problems. Ecological systems provide humans with products and services essential for good health and survival. However, ecosystem degradation by humans has increased the risks and threats to human health (MA, 2005). In recent years, there has been a growing interest by the scientific community with regard to the potential links between the degradation of an ecological system and its impacts on human health.

Urban forests play a crucial role in improving the environmental quality of cities and urban dwellers (Roy et al. 2012; Shwartz et al. 2014). The urban forest is defined as all the trees in the urban areas including individual trees and shrubs, parks and forests in public and private spaces, along linear routes and waterways and in amenity areas. It contributes to green infrastructure and the wider urban ecosystem (Urban Forestry and Woodlands Advisory Committees Network - UFWACN, 2016). The urban forest consists of all of the trees growing on public and private lands, including trees in the downtown, old and new neighborhoods, commercial and institutional lands, city parks, and natural areas.

Urban forests, and the ecosystem services they provide, are necessary for healthy living conditions. Quantifying the status and the vulnerability of this resource are essential for maintaining a consistent and equitable supply of these ecosystem services. While the integral parts of broader landscapes of urban forests trees contribute to the stability and vitality of ecosystems and to meeting societal needs, the devastating effects of the pandemic on human health, the economy and society are undeniable (Jones et al, 2008).

Zoonotic diseases are diseases that pass from an animal to a human. Many ecologists have long suspected this, but a study now helps to reveal why. When some species are going extinct, those that tend to survive and thrive, for instance, rats and bats, are more likely to host potentially dangerous pathogens that can make the jump to humans. The analysis of around 6,800 ecological communities on 6 continents adds to a growing body of evidence that connects trends in human development and biodiversity loss to disease outbreaks — but stops short of projecting where new disease outbreaks might occur (Tollefson, 2020). Studies have long been delving into relationships between biodiversity, land use and emerging infectious diseases (Jones et al, 2008). As the world contends with the COVID-19 pandemic, efforts to map risks in communities around the globe and to project where diseases are most likely to emerge are taking center stage.

The urban forest structure, composition and function in Minna town is not insulated from the alteration and degradation occasioned by increasing rate of urbanization in the last three decades; which could have created conditions that favors emergence of pandemic diseases such as COVID-19. This study is aimed at assessing the link between urban forest ecosystem services degradation and likelihood of emergence of pandemic diseases in Minna town. The specific objectives were to evaluate the current status of urban tree structure and composition; examine the condition of urban forest ecosystem services; and assess the indicators of vulnerability to pandemic diseases in Minna town.

Conceptual Framework

This study is based on the conceptual framework of social–ecological systems which depicts relationships between Society, Ecosystem Services, and Human health (See Figure 1). The study of social–ecological systems often entails direct focus on linkages between social and ecological processes, the supply of natural resources and ecosystem services, and complex environmental problems (Grove 2009; Binder et al. 2013). There are functional and complex relationships between ecological systems, their services, human society, and infectious diseases. The primary drivers of ecosystem changes are linked to population growth and economic development. These changes trigger several ecological mechanisms that can often increase the risk of infectious disease

transmission or can change conditions of vulnerability, such as malnutrition, stress and trauma (in floods and storms, for example), immunosuppression, and respiratory ailments associated with poor air quality.

There is a wide spectrum of human disturbances to ecosystems and their services that may change disease risk via biological mechanisms. Most emerging diseases are driven by human activities that modify the environment or otherwise spread pathogens into new ecological niches (Taylor et al. 2001). These anthropogenic drivers of ecosystem disturbance can lead to specific changes in ecosystems that may or may not lead to disease emergence via mechanisms that are more directly relevant to life cycles or transmission of infectious diseases. There is concern that the extent of ecosystem changes in recent decades and the multiple ways in which habitats and biodiversity are being altered are increasing the odds that infectious diseases will be affected at some level. The specific biological mechanisms altering disease incidence, emergence, or reemergence are described here and, by way of illustration, disease case studies in this chapter are organized according to these biological mechanisms.

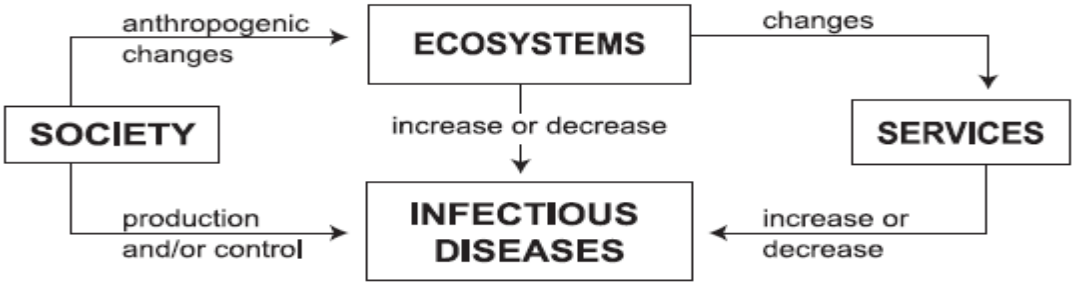

Fig. 1: Relationships between Society, Ecosystem Services, and Human Infectious Diseases
Source: Jonathan, et al, (2005)

Intact ecosystems maintain a diversity of species in equilibrium and can often provide a disease-regulating effect if any of these species are either directly or indirectly involved in the life cycle of an infectious disease and occupy an ecological niche that prevents the invasion of a species involved in infectious disease transmission or maintenance. Disease agents with much of their life cycle occurring external to the human host, such as water- and vector-borne diseases, are subjected to environmental conditions, and it is these diseases for which most linkages to ecosystem conditions have been found (Patz et al. 2000).

Materials and Methods

Study Area

Minna being the capital of Niger state is found in the North central region of Nigeria. It is located on Latitude 9°37′ 55″ North and Longitude 6°33′ 24″ East. It occupies a land area of about 884 hectares. The population of the Minna town is estimated at 304,113 (National Population Census 2006). The study area has a sub-humid tropical continental climate characterised by alternating wet and dry season; coded as 'Aw' by Koppen's classification. The mean annual rainfall is about 1,284 mm. The wet season begins in May and ends October, while the months of November to April are dry season. The mean annual temperature is about 32^{o}C. Physiographically, Minna consist of gently undulating high plains developed on basement complex rocks made up of granites,

migmatites, gneisses and schists. Inselbergs of "Older Granites" and low hills of schists rise conspicuously above the plains. Beneath the plains, bedrock is deeply weathered and constitutes the major soil parent material (saprolites) (Ojanuga, 2006). The study aare is found in Southern guinea savanna ecosystem, characterized of typical woodland plant deciduous communities trees species such as *Khaya spp., Parkia biglobosa, Delonix regia, Eucalyptus spp., Azadirachta indica and Gmelina arborea*.

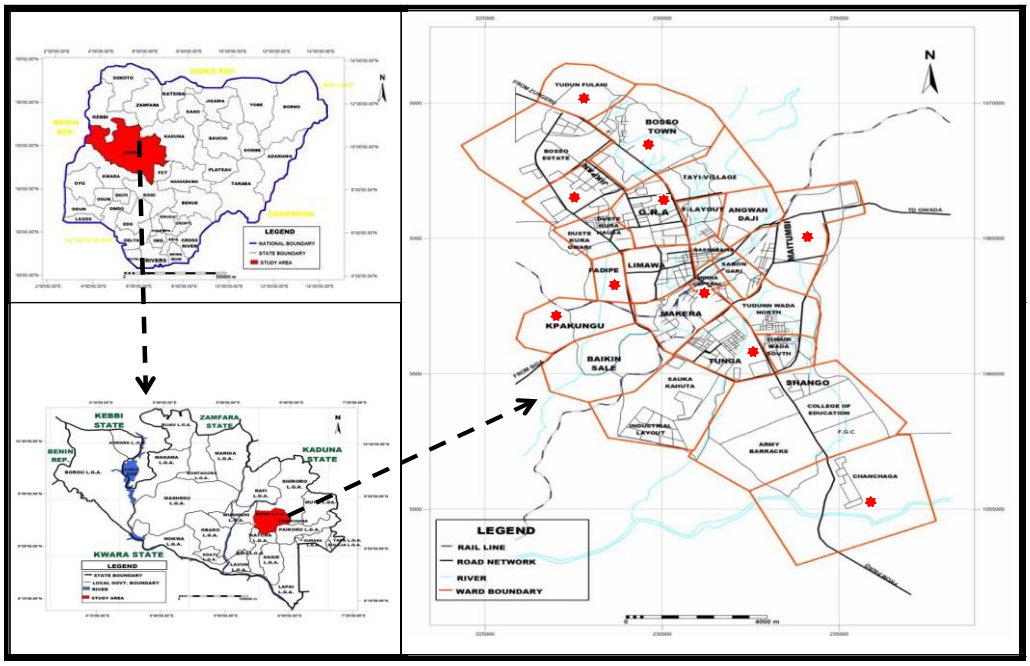

Figure 1: Geographical location of study area

Methods

The study commenced with a reconnaissance survey which was made in order to familiarise with the area and to plan for field data collection. The research made use of Field survey and qualitative method to collect data. Considering the estimated total population of Minna, the sample size was determined based on the formula of Yamane, (1967).

$$n = \frac{N}{1 + N(e)^2}$$

Where:

n = Sample Size; N = Population size; 1 = Constant e = The level of precision

A 95% confidence level and P = 0.5 yielded a sample size of 397. Equal number of 40 copies of questionnaire were administered to randomly selected household heads in all the ten wards including Bosso, Chanchaga, Fadikpe, G.R.A., Jikpan, Kpakungu, Maitumbi, Minna Central, Tunga, and Tudun Fulani.

Relative Importance Index (RII) was used to assess the perceived condition, status, severity and frequency based on Weighted five point Likert scale as follows: *Severity* (Very High=5, High=4, Moderate=3, Low=2, Very Low=1) *Frequency* (Very High (1-5 Years)=5 High (6-10 years)=4 Moderate (11-15 Years)=3 Low (16-20 Years)=2 Very Low (21-25 Years)=1). RII sum of weight is presented in the formula:

$$\frac{x_1w_1 + x_2w_2 + x_3w_3 \ldots x_nw_n}{N}$$

Where:
w = weight of answer choice
x = response count for answer choice
N = No of respondents

Assessment of the degree of risk took in to account the severity of a given stressor and the degree of alteration or potential and the frequency with which a given stressor causes alteration or disturbance in functional aspects. Based on this theoretical framework, Mattson & Angermeier (2007) proposed the Ecological Risk Index (ERI), which is used to assess the stress to which a particular ecosystem or area is subjected. Its mathematical representation can be expressed as follows:

$$\mathbf{ERI_{(i)} = F_{(i)} \times S_{(i)}}$$

Where:
F (i) = frequency of stressor 'i' considered.
S (i) = severity of stressor 'i' considered.

The classification of level of ecological risks is as presented in Table 1.

Table 1 Classification of Level of Ecological Risks

ERI score	**Level**
>0.76	Very high
0.67 – 0.75	High
0.45 – 0.66	Moderate
0.23 – 0.44	Low
<0.22	Very Low

Results and Discussion

Socio-Demographic Attributes of Respondents:

The analysis of socio-demographic attributes of the respondents (see Table 2) indicates that majority of the respondents, about 70% were males. The dominance of the male respondents can be attributed to the socio-cultural norms and values of the communities in Minna where headship

of households are exclusive reserve of the males, except in some few cases where the husband is deceased.

Table 2 Socio-Demographic Characteristics of Respondents

Variable & Categories	Frequency	Percentage (%)
Sex		
Male	279	69.75
Female	121	30.25
Age (Years)		
< 30	84	21
30 - 40	94	23.5
41 – 50	143	35.75
> 50	79	19.75
Level of Formal Education		
None	0	0
Primary	33	8.25
Secondary	164	41
Tertiary	203	50.75
Experience in Urban tree Mgt. (Years)		
5 - 10	118	29.5
11 - 20	143	35.75
21 - 30	108	27
>30	31	7.75

Source: Author's Fieldwork, 2021

As indicated in Table 2, most of the respondents were found to be over 40 years old; which implies they could be conversant about changes in the urban trees structure and composition over the last 30 years. Virtually all of the respondents were literate; with an overwhelming majority (over 91%) having attained at least secondary school level education; which implies that they are quite educated about the nature of their environment. With regards to experience on urban forest management, about 70% of respondents were found to be involved in managing urban trees (planting, nurturing and caring) for at least over 10 years. However, only about 8% of the respondents have at least over 30 years' experience in urban forest management, which implies that not many people are involved in long time management of urban trees. This weak attitude towards urban forestry might have largely contributed to degradation in the structure and composition of tree species found in Minna town over the years.

Common Urban Trees Species in Minna

A survey of common urban trees species in Minna (see Table 3) revealed there are about 23 tree species that are commonly planted either as single tree, line of trees or tree cluster, including trees in the downtown, old and new neighborhoods, commercial and institutional lands, and parks.

Table 3: List of Common Urban Trees Species in Minna

S/N	Species Scientific Name	Family	Common Name	Main Use(s)
1	*Acacia albida*	*Fabaceae*	*Acacia*	Shade, Landscaping

2	*Adansonia digitata*	*Bombacaceae*	*Baobab*	Fruit, Spiritual
3	*Anogeissus sp*	*Combretaceae*	*African Birch*	Spot, Shade
4	*Azadirachta indica*	*Meliaceae*	*Neem Tree*	Sahde, Hedge
5	*Cocos nucifera*	*Arecaceae*	*Coconut Palm*	Landscaping, Fruit
6	*Daniella oliveri*	*Fabaceae*	*Ilorin Balsam*	Hedge, Shade
7	*Delonix regia*	*Fabaceae*	*Sekeseke*	Shade, Landscaping
8	*Elaeis guineensis*	*Arecaceae*	*Palm Tree*	Heddge, Landscaping
9	*Eucalyptus camaldulensis*	*Myrtaceae*	*Blue gum tree*	Hedge, Landscaping
10	*Ficus goliath*	*Moraceae*	*Odan*	Landscaping
11	*Gmelina arborea*	*Lamiaceae*	*Gmelina*	Landscaping, Sade
12	*Hyphaene thebaica*	*Arecaceae*	*Dum Palm*	Landscaping, Fruit
13	*Irvingia gabonensis*	*Irvingiacea*	*Bush mango*	Medicinal, Landscaping
14	*Khaya senegalensis*	*Meliaceae*	*Dry Zone Mahogany*	Shade, Landscaping
15	*Mangifera indica*	*Anacardiaceae*	*Mango*	Shade, Fruit
16	*Parkia biglobosa*	*Fabaceae*	*Locust Bean*	Shade, Fruit
17	*Prosopis africana*	*Fabaceae*	*African mesquite*	Shade, Landscaping
18	*Sterculia setigera*	*Malvaceae*	*Tropical Chestnut*	Shade, Hedge
19	*Tectona grandis*	*Verbenaceae*	*Teak*	Shade, Hedge
20	*Terminalia avicennoides*	*Combretaceae*	*Idi*	Shade, Hedge
21	*Terminalia catappa*	*Combretaceae*	*Umbrella tree*	Shade,
22	*Vitellaria paradoxa*	*Sapotaceae*	*Shea butter tree*	Sade, Fruit
23	*Vitex doniana*	*Verbenaceae*	*Black Plum*	Landscaping

Source: Author's Fieldwork, 2021

Some of these tree species are planted in combination of two or three in the surroundings or inside compound. The main uses or purpose of planting such tree species include landscaping, shade, hedge, fruit and Vegetables, spiritual, spot location, and medicinal. The respondents' use or benefits from these trees points to their awareness about the importance of urban trees in providing ecosystem goods and services for their survival and healthy living. Likewise, Onyekwelu and Olaniyi (2012) observed that Urban trees species have products that are suitable for food, medicine and nutrition supplements for healthy life. Examples include edible fruits, nuts, vegetables, and medicinal substances. City trees also help to improve energy efficiency by shading buildings (Sawka et al. 2013),

Status of Urban Forest Structure and Composition

Structure refers to the physical arrangement of various physical and biological components of an ecological system. Urban forest structure is the spatial arrangement and characteristics of vegetation in relation to other objects (e.g., buildings) within urban areas (Nowak 1994). The results from the Ecological Risk Index (ERI) analysis of Urban Forest Structure in Minna revealed that tree ground cover has the highest risk index followed by reduction in tree density; deterioration in tree health and vigor; and decrease in volume of trees. Composition refers to the biodiversity of an ecological system, including the variety of genes, species, communities, and ecosystems. Among the tree composition attributes assessed, decline in tree species diversity was found to be of highest

ERI, followed by decrease in native tree species; loss of beneficial tree species and; and increase in allien tree species.

Table 4: Status of Urban Forest Structure and Composition in Minna

Component	Parameter	Severity	Frequency	ERI	Rank
Structure	Decline in tree ground cover	0.81	0.85	0.689	3
	Decrease in volume of trees	0.69	0.45	0.311	8
	Reduction in tree density	0.87	0.73	0.635	5
	Deterioration in tree health and vigor	0.72	0.66	0.475	7
Composition	Decline in tree species diversity	0.91	0.82	0.746	1
	Loss of beneficial tree species	0.76	0.86	0.654	4
	Increase in allien tree species	0.74	0.73	0.540	6
	Decrease in native tree species	0.89	0.78	0.694	2

Source: Author's Fieldwork, 2021

Overall, in terms of ERI level classification, The attributes within the high level class were decline in tree species diversity; decrease in native tree species and decline in tree ground cover. Those in the moderate level class were loss of beneficial tree species; Reduction in tree density; Increase in allien tree species and deterioration in tree health and vigor. Whereas, decrease in volume of trees recorded low level class of ERI. The implication is that most of the urban forest structure and composition attributes have undergone significant changes by being degraded over the years. This would have inhibited their ability to provide ecosystem services as they yielded previously. A healthy ecosystem is a sustainable component of the biosphere that has the ability to maintain its structure (organization), composition and function (vigor) through time and in the face of external stresses (resilience) (Mageau et al., 1995). Several studies have established relationships between different urban forest structures and specific functions such as visual quality (Schroeder, 1986), energy savings (McPherson, 1993), removal of atmospheric carbon dioxide (Rowntree and Nowak, 1991), urban heat island mitigation (Huang et al., 1987; Oke, 1989; McPherson, 1994), sound reduction (Cook and Van Haverbeke, 1977), wildlife habitat (DeGraaf and Wentworth, 1986), and personal safety (Schroeder and Anderson, 1984). Healthy ecosystems provide support to the human community, such as food, shelter, the capacity to assimilate and recycle wastes, clean air and water. Consequently, degradation in the face of poor resilience would have resulted in poor ecosystem services in Minna urban area.

Condition of Ecosystem Services

Ecosystem services can be defined as the benefits that people derive from nature. The Millennium Ecosystem Assessment (MA, 2005). Ecosystem services are fundamental to the wellbeing of man. An analysis of the urban tree ecosystem services degradation status in Minna revealed the result presented in Table 4.

Table 4: Urban Tree Ecosystem Services Degradation Status in Minna

Component	Parameter	Severity	Frequency	ERI	Rank

Provisioning Services	Food (Fruit and Vegetables)	0.85	0.84	0.714	2
	Shade	0.88	0.78	0.686	4
	Fresh air	0.83	0.92	0.764	1
	Clean water	0.65	0.77	0.501	13
Supporting Services	Habitat for animals	0.92	0.64	0.589	7
	Biodiversity	0.83	0.65	0.540	10
	Infiltration	0.79	0.87	0.687	3
	Wind break	0.67	0.81	0.543	9
Regulating Services	Reducing air temperature	0.83	0.75	0.623	5
	Air purification	0.76	0.78	0.593	6
	Noise reduction	0.59	0.72	0.425	16
	Erosion control	0.79	0.62	0.490	14
	Flood control	0.59	0.87	0.513	12
	Carbon Sequestration	0.66	0.58	0.383	18
Cultural Services	Recreational	0.86	0.66	0.568	8
	Aesthetics and Beauty	0.58	0.73	0.423	17
	Spiritual values	0.61	0.85	0.519	11
	Traditional values	0.63	0.73	0.460	15

Source: Author's Fieldwork, 2021

Table 4 shows that the ERI rage from lowest value of 0.383 to highest values of 0.764. Key ecosystem services with highest ERI values were fresh air, food, infiltration and shade while those with lowest values were carbon sequestration, aesthetics and beauty, and noise reduction. The impoverishment of human health due to the degradation of the ecosystems may be described as an "illness resulting from disrupted internal balances due to external stresses" (Odum, 1995). It is becoming obvious that degradation of ecosystems is increasingly the root cause of many of the disease infections within the human community (Rapport, 1998). Ecosystems that are sufficiently stable and biologically diverse tend to maintain the quality of human health. Degraded or collapsed ecosystems seem to have a significant impact on human health. An analysis of the literature on environmental health shows that there are many attempts to connect human health and the changing environmental conditions. Degradation of ecosystem services beyond natural thresholds, especially where these have been converted by human activities into disservices, potentially heightens risks of zoonotic diseases.

Vulnerability Indicators

Disturbance or degradation of ecosystems can have biological effects that are highly relevant to infectious disease transmission (MA, 2005). Considering the current status of urban tree forest structure, composition and ecosystem services in Minna town, specific indicators of vulnerability to pandemic diseases have been identified as follows:

i. Altered habitat leading to changes in the number of vector breeding sites or reservoir host distribution. Many ecosystem changes can alter the habitats, and hence populations, of

disease-transmitting vectors. Disturbance of habitats due to alterations in land cover or climatic change is considered to be the largest factor altering the risk of infectious diseases

ii. Niche invasions or transfer of interspecies hosts. The emergence of many diseases has been linked to the interface between tropical forest communities, with their high levels of biodiversity, and agricultural communities, with their relatively homogenous genetic makeup but high population densities of humans, domestic animals, and crops.

iii. Biodiversity change Biodiversity change includes issues of species replacement, loss of key predator species, and variation in species population density.

iv. Human-induced genetic changes in disease vectors or pathogens (such as mosquito resistance to pesticides or the emergence of antibiotic-resistant bacteria); and

v. Environmental contamination by infectious disease agents; such as faecal contamination of source waters.

An analysis of the literature on environmental health shows that there are many attempts to connect human health and the changing environmental conditions. Khabbaz et al. (2015) recognized 25 emerging or re-emerging infectious disease threats linked to wildlife between 2000 and 2013. According to these analyses, a key contributory factor in the increase in number and diversity of zoonotic diseases has been the extent to which humans are increasingly interacting with, and impacting upon, ecosystems, given the close relationships between human, animal and environmental health. For example, land use change has been estimated by the EcoHealth Alliance (2019) to be linked to 31% of outbreaks of emerging infectious diseases (EIDs), including HIV, Ebola, and Zika virus, which are considered connected to anthropogenic changes in tropical rainforests, with 15% of these EIDs linked to agricultural changes.2 Virus transmission risk has been recognised as highest from animal species that have increased in abundance and/or expanded in range by adapting to human-dominated landscapes, with domesticated species, primates and bats identified as carrying the greatest risk of zoonotic virus transmission (Kreuder Johnson et al., 2020).

Conclusion and Recommendation

The relationships between ecological systems, their services, human society, and infectious diseases have been analyzed in this study. Urban forest degradation has continued to advance alarmingly in Minna town, contributing to increased exposure to zoonoses. As humans diminish biodiversity by cutting down forests and building more infrastructure, they're increasing the risk of pandemics of diseases such as COVID-19. This study thus recommends urban forest ecosystem restoration. Restored ecosystems and nature-based methods emulating natural functions can enhance disease regulation as part of a linked set of societally co-beneficial ecosystem services. By reinstating lost ecosystem processes, these nature and nature-based solutions may potentially rebuild barriers to disease organisms transferring from animals to humans. In addition, these forms of regeneration of ecosystem functions could, if combined with sustainable management of human activities and infrastructure, enhance benefits such as access to adequate supplies of clean water, which have significant roles to play in the management of disease outbreaks.

References

Binder, C.R., Hinkel, J., Bots, P.W.G., and Pahl-Wostl, C. 2013. Comparison of frameworks for analyzing social-ecological systems. *Eco. Soc*. 18(4): 26–44. doi:10.5751/ES-05551-180426.

Cook, D. I., and Van Haverbeke, D. F. (1977) Suburban Noise Control with Plant Materials and Solid Barriers, *Research Bulletin* EM 100, U.S. Department of Agriculture, Forest Service, Rocky Mountain Forest and Range Experiment Station, Fort Collins, CO.

DeGraaf, R. M., and Wentworth, J. M. (1986) Avian guild structure and habitat associations in suburban bird communities. *Urban Ecol.* 9, 399-412.

Eakin, H., and Luers, A.L. (2006). Assessing the vulnerability of social– environmental systems. *Annu. Rev. Environ. Resour*. 31: 365–394. doi:10. 1146/annurev.energy.30.050504.144352.

EcoHealth Alliance, (2019). *Infectious Disease Emergence and Economics of Altered Landscapes* - IDEEAL. EcoHealth Alliance, New York accessed 10th April 2020.). https://www.ecohealthalliance.org/wp-content/uploads/2019/09/IDEEAL_report_ final.pdf.

Grove, J.M. (2009). Cities: Managing densely settled social–ecological systems. In *Principles of Ecosystem Stewardship*. Edited by C. Folke, G.P. Kofinas, and F.S. Chapin. Springer, New York. pp. 281–294.

Jeff Tollefson (2020) Why Deforestation and Extinctions Make Pandemics More Likely

Jonathan A. Patz, Ulisses E.C. Confalonieri (2005) Human Health: Ecosystem Regulation of Infectious In: *Millemium Ecosystem Assessment: Diseases Ecosystems and Human Well-being: Current State and Trends*, Island Press, Washington D.C. USA.

Jones, K., Patel, N., Levy, M. (2008) Global trends in emerging infectious diseases. *Nature* 451, 990–993. https://doi.org/10.1038/nature06536

Khabbaz et al. (2015) recognised 25 emerging or re-emerging infectious disease threats linked to wildlife between 2000 and 2013.

Khabbaz, R., Bell, B.P., Schuchat, A., Ostroff, S.M., Moseley, R., Levitt, A., Hughes, J.M., (2015). Emerging and re-emerging infectious disease threats. In: Mandell, J.E., Dolin, R., Blaser, M.J. (Eds.), *Principles and Practice of Infectious Diseases* Vol. 1. Saunders, pp. 158–177. https://doi.org/10.1016/B978-1-4557-4801-3.00014-X.

Kreuder Johnson, C., Hitchens, P.L., Pandit, P.S., Rushmore, J., Evans, T.S., Young, C.C.W., Doyle, M.M., (2020). Global shifts in mammalian population trends reveal key predictors of virus spillover risk. *Proc. R. Soc*. B 287, 20192736. https://doi.org/10. 1098/rspb.2019.2736.

Lindner, M., Maroschek, M., Netherer, S., Kremer, A., Barbati, A., Garcia-Gonzalo, J., et al. (2010). Climate change impacts, adaptive capacity, and vulnerability of European forest ecosystems. For. Ecol. Manage. 259(4): 698– 709. doi:10.1016/j.foreco.2009.09.023.

MA (2005). Ecosystems and Human Well-Being: Health Synthesis. Geneva, WHO: 64.

Mageau, Michael T., Costanza, Robert, and Ulanowicz, Robert E., (1995). The Development and Initial Testing of a Quantitative Assessment of Ecosystem Health. *Ecosystem Health*, Vol. 1, pp. 201-213.

Mattson, K. M., & Angermeier, P. L. (2006). Integrating Human Impacts and Ecological Integrity into a Risk-Based Protocol for Conservation Planning. *Springer Sience*+Business Media.

McPherson, E. G. (1993) Evaluating the cost effectiveness of shade trees for demand-side management. *Electricity J*. 6, 57-65.

McPherson, E. G. (1994) Cooling urban heat islands with sustainable landscapes. In *The Ecological City, Preserving and Restoring Urban Biodiversity* (R. H. Platt, R. A. Rowntree, and P. C. Muick, ed~.), pp. 151-71. University of Massachusetts Press, Boston, MA.

Millemium Ecosystem Assessment MA (2005). *Ecosystems and Human Well-Being: Health* Synthesis. Geneva, WHO: 64.

Nature Vol 584 175 The world this week News in focus © 2020 Springer Nature Limited.

Nowak, F. (1994). Understanding the structure of urban forests. *Journal of Forestry* 92:42–46.

Odum, Eugene P., (1995). Profile Analysis and Some Thoughts on the Development of the Interface Area of Environmental Health. *Ecosystem Health*, Vol. 1, pp. 41-45

Ojanuga, A.G. (2006). Agroecological Zones of Nigeria Manual. FAO/NSPFS, Federal Ministry of Agriculture and Rural Development, Abuja, Nigeria, 124 pp.

Onyekwelu, J.C. and Olaniyi, D.B. (2012). Socioeconomic importance of Urban and peri-urban forests in Nigeria. In: Research and Capacity building for agricultural transformation in Nigeria (Adebayo et al. (eds)). *Proceeding of 6th Annual conference of SAAT*, FUTA, 7-9th Nov., 2012; pp 200 – 210.

Patz, J.A., T.K. Graczyk, N. Geller, and A.Y. Vittor. (2000): Effects of environmental change on emerging parasitic diseases. Int J Parasitol, 30, 1395–1405.

Rapport, David J., Christensen, Norman, Karr, James R., and Patil, G.P., (1998). Sustainable Health of Humans and Ecosystems, unpublished report.

Rowntree, R., and Nowak, D. J. (1991) Quantifying the role of urban forests in removing atmospheric carbon dioxide. *J. Arboricult.* 17, 269-75.

Roy S, Byrne J, Pickering C (2012) A systematic quantitative review of urban tree benefits, costs, and assessment methods across cities in different climatic zones. *Urban For Urban Green* 11:351–363

Sawka M, Millward AA, McKay J et al. (2013) Growing summer energy conservation through residential tree planting. *Landscape Urban Plan* 113:1–9

Schroeder, H. W. (1986) Estimating park tree density to maximize landscape aesthetics. *J. Environ. Manage.* 23, 325-33.

Schroeder, H. W., and Anderson, L. M. (1984) Perception of personal safety in urban recreation sites. *J. Leisure Res*. 16, 178-94.

Shwartz A, Turbe´ A, Simon L, Julliard R (2014) Enhancing urban biodiversity and its influence on city-dwellers: an experiment. *Biol Conserv* 171:82–90

Taylor, L.H., S.M. Latham, and M.E.J. Woolhouse, (2001): Risk factors for human disease emergence. Phil. Trans. Soc. Lond. B., 356, 983–989.

Turner, B.L, Kasperson, R.E., Matson, P.A., McCarthy, J.J., Corell, R.W., Christensen, L., et al. (2003). A framework for vulnerability analysis in sustainability science. *Proc. Natl. Acad. Sci.* 100(14): 8074–8079. doi:10.1073/pnas. 1231335100. PMID:12792023.

UFWACN (2016). Introducing England's urban forests: Definition, distribution, composition and benefits. *Urban Forestry and Woodlands Advisory Committees Network*, England.

United Nations (2018) World urbanization prospects: the 2018 revision. Economic and social affairs. https://population.un.org/ wup/Publications/Files/WUP2018-KeyFacts.pdf. Accessed 17 Oct 2018

Building Density and Housing Submarket: A Historico-geographic Approach on Urban Morphology

Mohammed J. K.[1*], Aliyu A. A.[2] and Saidu U. A.[3]
[1&3]Department of Estate Management and Valuation, Fed. Poly. Bida, Nigeria
[2]Department of Urban and Regional Planning, Federal Polytechnic, Bida, Nigeria
[1]muhammad.jibrinkatun@fedpolybida.edu.ng, [2]aliyuabdul777@gmail.com
[3]saidumadakikamala@gmail.com
* Corresponding author

ABSTRACT

An increase in building density as a result of urban densification has become a global trend as it changes the urban forms of many cities of the developing world. This study investigates spatial changes in the building density of housing submarkets of Bida, Nigeria from 2008 to 2018. Data collected for the study includes satellite images and base maps of demarcated areas, which were georeferenced and the buildings were digitised using point features and vector approach in ArcGIS environment to achieve the area coverage, number of buildings, and buildings per hectare (ha) in the housing submarkets. The finding of the study reveals that from 2008 – 2018 the Town housing submarket had the highest number of buildings per area coverage with >10 building units/ha. The study further reveals that in the year 2018, the Gbazhi housing submarket had its highest number of buildings per area coverage with >10 building units/ha. It was concluded that the housing submarkets had a high number of buildings in the total area coverage which indicates that larger parts of the area coverage of these submarkets have already been exhausted. It was therefore recommended that there is the need for rational densification (planned densification) for urban development to check the increasing uncontrolled building density.

Keywords: Building density, housing submarket, urban morphology, urban densification

1. Introduction

Urban densification is the increase in the urbanisation level of a limited area, which could have an adverse effect on the biodiversity of its green spaces by destroying the habitats and soil temperature increase or pollutions (Vergnes et al., 2014). Urban densification causes a lot of challenges to cities ranging from a decline in housing affordability, pressure on infrastructure and difficulties of city management. Urban densification has a consequential effect on affordable housing and may cause a change in the housing market. As a result of a change in the housing market, the entire city or national economy would experience a shift either negatively or positively (Gulyani et al., 2018).

The housing market is very imperative because of the place it holds in the economy (Seo, 2008). Housing construction easily contributes to gross domestic product and its market has a direct impact on the national economy (Hu et al., 2013). Housing is a special kind of commodity that is fixed (Renigier-Biłozor et al., 2017). Consequently, the location of the house is very imperative, since

this feature is unchangeable (Cichociński & Dąbrowski, 2013). Housing has demonstrated its importance to the broader economy during the global financial crisis of 2007 – 2011, which has its roots in the United States housing market as its contribution to the national GDP fall during the period. Information on trends in housing prices is therefore essential to the governments, market participants and central banks (Hill & Scholz, 2017).

However, there is a large body of literature on the housing market (Leung, 2004; Wu et al., 2014; Muehlenbachs et al., 2015; Yang et al., 2017; Tupenaite et al., 2017; Zhou, 2018; Cameron, 2018; Cheung et al., 2018; Wang et al., 2018). For example, Xiao (2012) studied urban morphology and housing market with emphasis on street network pattern, where the street pattern is a fundamental determinant of house prices and street network pattern influences accessibility. Wang et al. (2018) analyse the spatial patterns and driving forces of Chinese housing prices where various theoretical dimensions on housing supply, demand and market, are viewed as determinants of a housing price model to examine the effect of prices of land on housing prices. These authors did not consider housing submarket in their respective studies.

The available literature on housing submarkets (for example, Royuela & Vargas, 2007; Park, 2013; Manganelli et al., 2014), very little is written on the delineation of the housing market (for example, Wu & Sharma, 2012; Manganelli et al., 2014). Studies on urban densification of housing submarkets are rare in the literature (J. K. Mohammed, Sulyman, & Alhaji, 2021). Bida is experiencing urban densification which has attracted people from different parts of the country which has consequently led to an increase in housing demand. The intensity of housing demand in the city has also resulted in increased house rents. Therefore, this study examines the pattern of spatial changes in the building density of housing submarkets of Bida, Nigeria from 2008 to 2018.

2. Literature Review

2.1. Housing Submarket

Housing submarkets are typically defined as geographic areas where the price per unit of housing quantity (defined using some index of housing characteristics) is constant (Goodman & Thibodeau, 1998). Although as an urban economic, land use and residential location model – the residential location theory (Alonso, Muth, Mills) is also applicable to housing market segmentation. Even without certain factors, segmentation of an urban area can still be carried out, if there is a disparity in households' preferences and/or income concerning accessibility and space (Kauko *et al*., 2002).

Although, there is an agreement by several researchers on using locational and structure features to define a submarket, identifying a submarket and approach to be adopted have little consensus (Xiao, 2012). Usually, spatial and non-spatial specifications for housing submarkets are the main two methods(Islam & Asami, 2009; Xiao, 2017).

2.2 Spatial Approach to Housing Submarket

People's housing choice of homogenous preferences based on geographic predefined areas are emphasised by spatial specifications which is the main index (e.g. political districts, north/south, inner/outer city, and postcode districts) (Xiao, 2012).

Hitherto, several studies have formed housing segmentation based on spatial specification For example, McCluskey & Borst (2011) utilises Geographically Weighted Regression (GWR), a geostatistical modelling method to identify and demarcate the housing submarkets. The procedure effectiveness was established by improving the accuracy of the predictive model for housing market segmentation as compared to the standard universal unsegmented model for the study areas. Goodman & Thibodeau (1998) described housing submarkets as a geographical area where housing price per service unit is constant and characteristics of individual housing are available for purchase. They argue that hierarchical models offer a suitable framework for housing submarkets delineation. Wu & Sharma (2012) develop a methodology for submarket classification based on spatially constrained data-driven to achieve spatially integrated housing market segments. Precisely, a data-driven model on cluster analysis and principal component analysis was built for housing submarkets delineation. Their findings show that spatially contiguous submarkets can be obtained without compromising housing hedonic model accuracy and attribute homogeneity.

Park (2013) recommends spatial housing submarkets division basis in enhancing the housing market understanding. The division's theoretical background is built upon the nexus between the structure of house prices and commuting patterns. An assessment of the process of 'expansion-overlap-merging' between residential spheres, defined as a unit containing a centre of employment and the surrounding residential area, provides an overview of a probable form of merged residential spheres in big cities. An empirical study of the Seoul spatial housing submarkets was identified based on the hierarchies between the local authorities from commuting patterns. Manganelli *et al*. (2014) adopted Geographically Weighted Regression (GWR) in housing market analysis, in the identification of the homogeneous areas and defining a single location marginal contribution to the property's value at the housing market. Their results of territory zone the housing market into homogeneous market areas, they conclude that the findings have useful implications in terms of taxation, programming territorial transformations, and checking ongoing or post planning decisions.

2.3. Criticisms of Spatial Approach

Both spatial and non-spatial approaches to housing market segmentation have received a wide range of criticism. Spatial-based determinations have been reprimanded for their error. Because of fast urbanization and the rise of polycentricity, the urban framework has turned out to be more intricate and thus the social-spatial structure is changing and social-spatial isolation has been upgraded. The main spatial models adopted to characterise the preferences spatial divisions appears to be less effective in peoples preference reflection and each characteristic choice in these type of cities. The traditional approaches risk is that it underestimates the amount in the submarkets. More so, the spatially based specification often looks like an *ad hoc* reason be that the use of geographical boundaries that are pre-identified. The requirements also include a prior acknowledgement of the local context and consequently make scientific research complex and not simply replicated (Xiao, 2012).

As being arbitrary is the criticism of the spatial approach, the criticism of the non-spatial specification being unstable over time. Being of non-spatial nature is another criticism of the

approach and its ambiguities in presentation for interventions of policy (Xiao, 2017).

This indicates that both spatial and non-spatial approaches of housing submarket delineation cannot effectively represent the true nature of the submarket. However, the spatial approach to the housing submarket was proven to be better in terms of physical policy and assessment. It is, therefore, better to employ a spatial method in delineating housing submarkets. It is on this background that this study intends to adopt spatial approaches to delineate the housing submarkets.

2.4. Urban Morphology, Density and Densification

There are three basic concepts used by the built environment experts to address the issue of how density affects people's lives; density, perceived density and crowding (Alexander, 1993). Density described the relationship between a given physical area and the number of objects in that area (Medayese *et al*., 2015). Density has an intrinsic relationship with urban morphology; it plays an important role in the shaping of urban forms. One of the pioneer planners Ebenezer Howard pointed out that the countryside has less density and a greener environment compared to the growing industrial city (Medayese *et al*., 2015). Alonso suggests that moving closer to the city centre the density increases and distance away from the city centre causes a decrease in density (Alonso, 1964). Density refers to by the two authors is both population density and housing density which result from rapid urbanisation.

More recently, studies show that compact development provides solutions to many urban problems such as reducing urban sprawl and infrastructure provision (Broitman & Koomen, 2015; Chhipi-Shrestha *et al*., 2017; Vergnes *et al*., 2014). However, considering Howard's and Alonso's thoughts and the recent compact development that changes urban morphology, urban densification can be referred to as planned urban densification (deliberate) and unplanned urban densification (not deliberate). Therefore urban densification can be divided into two categories; planned urban densification and unplanned urban densification (J. K. Mohammed, Sulyman, & Alhaji, 2021).

Amer *et al*. (2017) examine urban densification through roof stacking where three consecutive levels (urban, social and engineering) systematic approach was considered. Chandrabose (2019) conducted a study on urban densification and 12-year changes in cardiovascular risk markers. In a different perspective, Delmelle *et al*. (2014) assesses urban densification without growth management where it focused on local land development and housing trends in Charlotte, North Carolina, USA. Ghadami and Newman (2019) investigate the effect of the urban densification policies made after the Islamic Revolution on the urban spatial structure of Tehran as the most important metropolis in Iran. Urban densification is conceived as an urban regeneration method. For example, Treija *et al*. (2018) examine the existing approaches focused on densification in large housing estates to define the typical challenges of this process, the examples of infill developments in large housing area Imanta in Riga was analysed. Vuckovic *et al*. (2019) investigate urban densification potential in the effects of heat island mitigation and outdoor thermal conditions improvement in Vienna, Austria.

Measuring urban density has been a problem of many researchers (Ståhle *et al*., 2008). Broitman and Koomen (2015) measured residential densification using a high level of detailed spatial data that covers the whole of the Netherland. They describe land use by employing 100-metre resolution

rasterised data, residential density and local explanatory variables of a wide range. Wang et. al. (2019) generate a land-use transition of the 2001 to 2011 matrix using land-use maps with the aid of ArcGIS and examine the spatial and temporal urban density changes. In contrast, Jiao (2015)acquired high-quality Landsat TM/ETM+ images, where the images were classified using the Maximum Likelihood Classification method in ENVI 4.5. The results from image classification were processed using a non-linear least squares method to fit the proposed urban land density functions to fit a nonlinear function to the observed data by refining the parameters in successive iterations. They employed a Trust-region algorithm in their study. They fit the urban land density functions with Matlab. Urban densification was also measured using microclimate simulations with different models. The results are compared, and uncertainty ranges are documented by testing the impact of urban fabric on the current climate (Loibl, 2019). Shahtahmassebi (2016) developed a framework for measuring urban densification using time series of impervious surface fractions (ISFs) derived from remotely sensed imagery.

3. Methodology

3.1 Study Area

Bida town in the north central geopolitical region of Nigeria is the study area which is an ancient and typical traditional settlement located on latitude 9.083N and longitude 6.017E (see Figure 1). The town is the head quarter of Nupe ethnic group in Nigeria with mostly traditional buildings and a total built-up area of 67.45km2. According to the last national population census, the town has about 255,008 inhabitants (J. K. Mohammed & Sulyman, 2019).

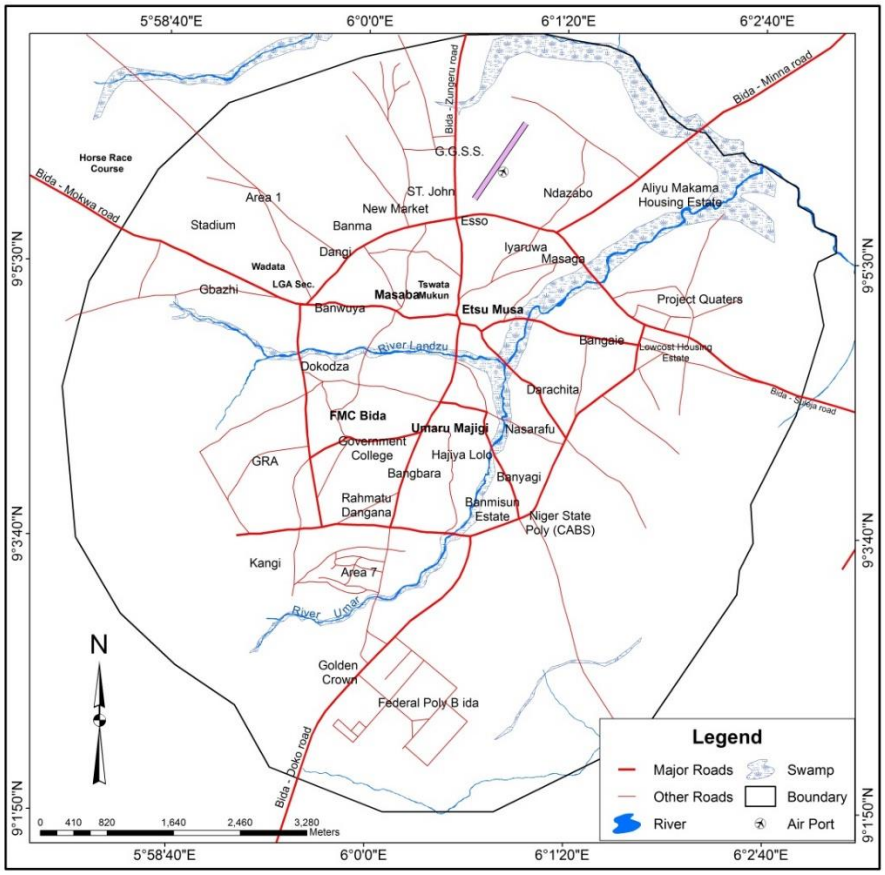

Figure 1. Bida, the Study Area

3.2 Data and Analysis

Satellite imageries were captured for the housing submarkets using the area demarcations. For each demarcated area, three satellite imageries were captured for three different periods, i.e. 2008, 2013 and 2018 using maximum resolutions on the Google Earth application. Images captured using area demarcation gives better resolution. The choice of Google Earth is due to its user-friendly and historical images available.

Satellite images captured based on the demarcated areas were georeferenced where a vector approach was adopted in digitising all the buildings using point features in the ArcGIS environment. The entire buildings for each year under study were represented by points. This research adopted residential density measurements by Niger State Urban Development Board (2015). Using this, residential density is measured using the occupancy rates of buildings and the number of buildings in a given location to give a level of density. The cartographic approach is employed in presenting residential density levels across the housing submarkets and study periods in the study area.

4. Results and Discussion

It was found out in Table 1 that in the year 2008, the Town housing submarket being the largest had the highest number of buildings with a total of 25,945. This is followed by Wadata with 1,020 buildings, Poly area with 787 and GRA with 773. The study shows that Rahmatu Dangana being

the smallest housing submarket also recorded the lowest number of buildings in that year. The result also shows that the Town with the largest area coverage and highest number of building units had the highest number of buildings to area ratio with 21.35 this is followed by Rahmatu Dangana with 5.72, Wadata 2.56 and Gbazhi 2.27. The lowest buildings to area ratio are recorded for Eyagi with 0.23.

In the year 2013 Town housing submarket had the highest number of building units with 34,242. This is followed by Gbazhi with 2,077, Ndazabo 1,758, Wadata 1,707 building units respectively. During this period, the study shows that Rahmatu Dangana had the smallest number of building units. The result also shows that the Town submarket recorded the highest number of building to area ratio with 28.18, followed by Gbazhi with 9.62, Rahmatu Dangana 9.10 and Wadata 4.28 respectively. The lowest building to area ratio is recorded for Eyagi with 0.42.

Consequently, this result shows a tremendous transition in the housing submarket of the study area where all the housing submarkets had the number of their housing units increased at different rates. The results also imply that Gbazhi had very high residential development where the number of housing units recorded for the year 2008 was 489 with the building to area ratio of 2.27 and increases to 2,077 with the building to area ratio of 9.62 in the year 2013.

In the year 2018 Town submarket had the highest number of buildings with 29,985 followed by Poly Area with 2,450, Ndazabo 2,346, Gbazhi 2,331, Wadata 2,300 and Kangi 2,134 building units respectively. The lowest number of building units recorded was in Rahmatu Dangana with 124. The Table also revealed that the Town submarket had the highest building to area ratio with 24.68. This is followed by Gbazhi with 10.80 and Rahmatu Dangana with 8.55. The lowest building to area ratio was recorded for Eyagi with 0.54 (Table 1).

Table 1: Building Units Per Hectares by Housing Submarkets 2008 - 2018

	Year 2008				Year 2013				Year 2018			
Submarket	**Area Coverage (Ha)**	**Building Units**	**Ratio**	**Building Units/Ha**	**Area Coverage (Ha)**	**Building Units**	**Ratio**	**Building Units/Ha**	**Area Coverage (Ha)**	**Building Units**	**Ratio**	**Building Units/Ha**
Kangi	457.52	661	1.44	<2	457.52	1103	2.41	2-4	457.52	2134	4.66	2-4
Rahmatu Dangana	14.5	83	5.72	5-6	14.5	132	9.10	9-10	14.5	124	8.55	7-8
Town	1214.97	25945	21.35	>10	1214.97	34242	28.18	>10	1214.97	29985	24.68	>10
Poly Area	823.13	787	0.96	<2	823.13	1648	2.00	2-4	823.13	2450	2.98	2-4
Eyagi	725.34	165	0.23	<2	725.34	304	0.42	<2	725.34	393	0.54	<2
Gbazhi	215.81	489	2.27	2-4	215.81	2077	9.62	9-10	215.81	2331	10.80	>10
Wadata	398.51	1020	2.56	2-4	398.51	1707	4.28	2-4	398.51	2300	5.77	5-6
Avenue	417.08	524	1.26	<2	417.08	1283	3.08	2-4	417.08	1976	4.74	2-4
Ndazabo	692.99	605	0.87	<2	692.99	1758	2.54	2-4	692.99	2346	3.39	2-4
Project Qtrs	984.31	358	0.36	<2	984.31	793	0.81	<2	984.31	1466	1.49	<2
GRA	800.08	773	0.97	<2	800.08	1442	1.80	<2	800.08	1889	2.36	2-4

In an attempt to explain variation in densification in housing submarkets of the study area in terms of the number of buildings per hectares as presented in Figures 2, 3 and 4. The study attempts to explain densification based on the number of buildings per hectares, but it does not directly highlight the factors responsible for the high or a low number of buildings in the housing submarket.

The study shows in Figure 2 that in the year 2008, the Town housing submarket had the highest number of buildings per area coverage with >10 building units/ha. This is followed by Rahmatu Dangana with 5-6 number of building units/ha, Gbazhi and Wadata had 2-4 number of building units/ha each. All other submarkets had <2 building units/ha in that year.

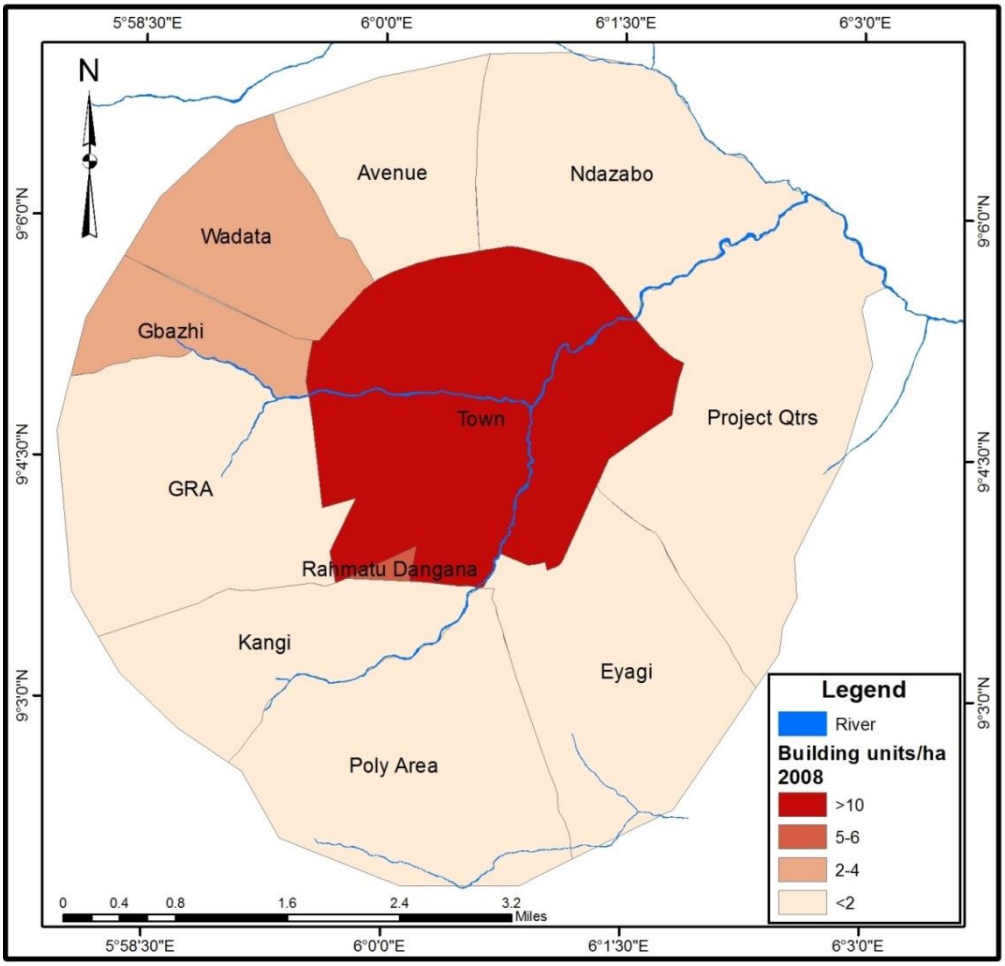

Figure 2: Number of Building Units/Ha by Housing Submarkets in the Year 2008

This implies that the Town submarket with the largest area coverage and highest number of buildings also had the highest number of buildings per area coverage. The consequence of this is that density in Town submarket cannot easily be controlled as the residential density has reached a level that if there is any disaster such as fire outbreak or epidemics, it will hardly be curtailed due to the pattern of residential development. The result also implies that during these years it is only Gbazhi and Wadata that had more than two number of building units/ha among submarkets in the urban fringe.

Residential density within the urban area of Bida considering the number of building units in the housing submarket is presented in Figure 3. Findings of the study in this section show that the Town housing submarket has the highest with >10 number of building units/ha in the year 2013. This is followed by Rahmatu Dangana and Gbazhi with 9-10 number of building units/ha, and Kangi, Poly Area, Wadata, Avenue and Ndazabo had 2-4 number of building units/ha. Housing submarkets that recorded the lowest number of buildings per area coverage are Eyagi, Project Quarters and GRA with <2 number of building units/ha.

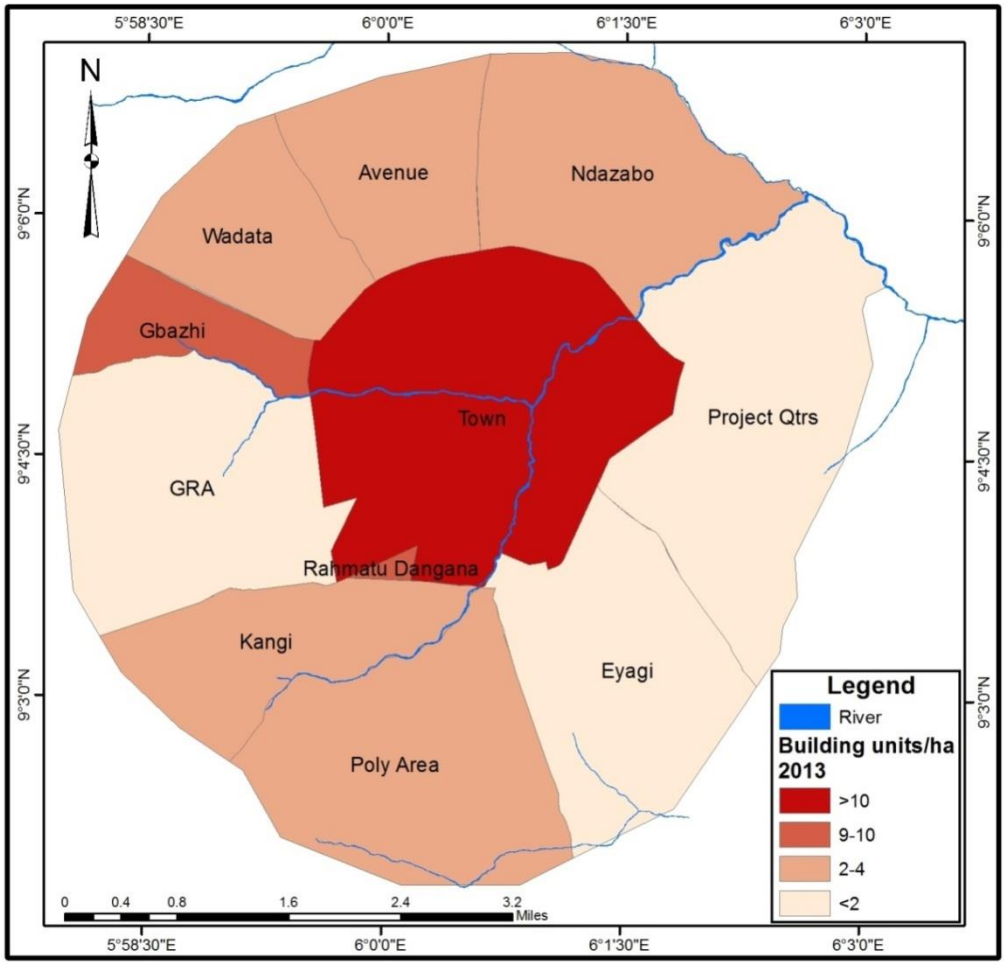

Figure 3: Number of Building Units/Ha by Housing Submarkets in the Year 2013

This result implies that a large amount of variation and tremendous transition in housing development in the housing submarket occurred during this period. The research, therefore, observed that there was a high level of urban morphological transformation resulting from the increasing level of urbanisation that leads to a high number of housing units in the housing market, which contributed to how the urban area looks like and shapes the future of urban development and the overall image of the town. This could one way or the other has an impact on several aspects of housing economics such as housing affordability, housing supply, housing demand and the housing market which includes the rental value of residential apartments.

Urban densification in Bida proceeds in an unstructured manner in the year 2018. The study shows in Figure 4 that the Town and Gbazhi housing submarkets record the highest number of buildings per area coverage with >10 building units/ha each. The study also reveals that Rahmatu Dangana and Wadata had 7-8 and 5-6 number of building units/ha each respectively in that year, and by implication made us understand that Eyagi and Project Quarters had the lowest number of buildings per area coverage with <2 building units/ha each.

The pattern of residential development demonstrates an urbanisation level that could make it difficult for any urban upgrading that may be needed later or increase the level of informality in the urban fabric. This result indicates that the housing submarkets had a high number of buildings in the total area coverage which indicates that larger parts of the area coverage of these submarkets have already been exhausted.

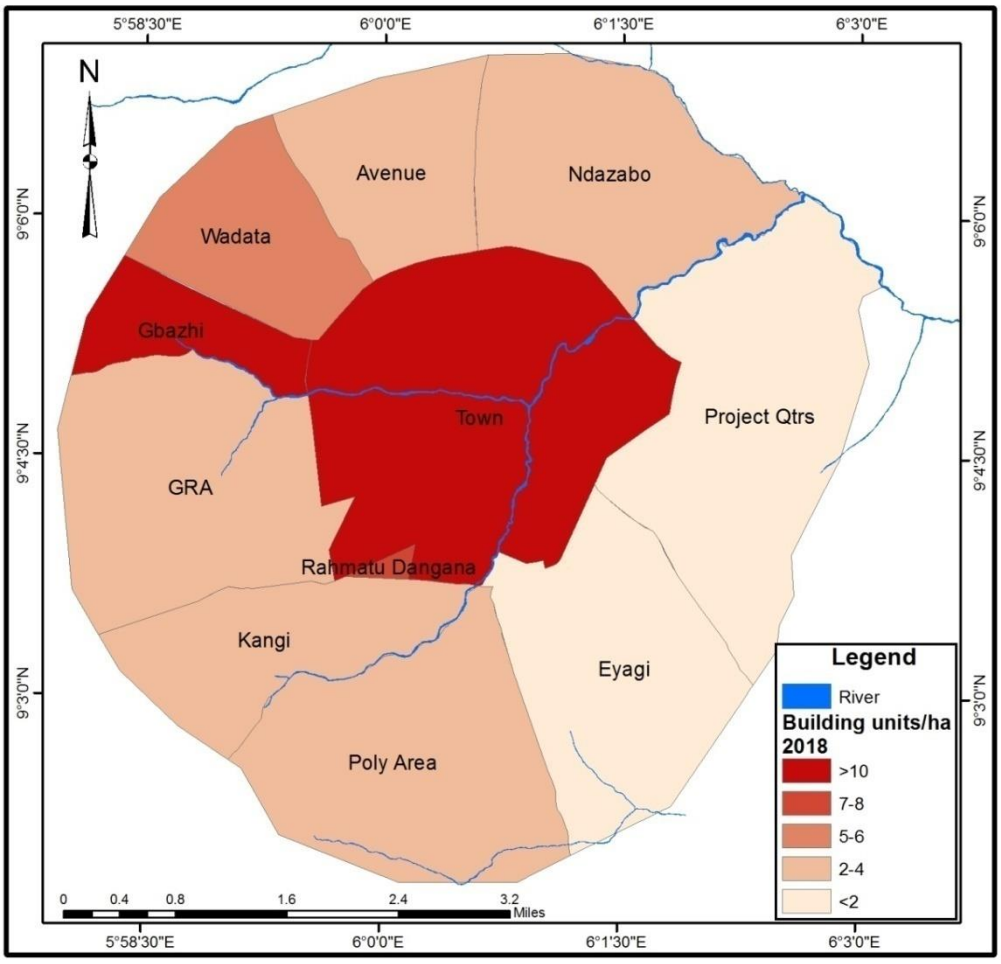

Figure 4: Number of Building Units/Ha by Housing Submarkets in the Year 2018

The results in this study revealed that Rahmatu Dangana with the smallest area coverage is highly developed in the year 2013. The implication of this result is that transition in the urban morphology experienced tremendous changes where the number of buildings in the Town submarket reduced from 34,242 in the year 2013 to 29,985 in the year 2018. This could be attributed to Bida old market razed by fire in early 2018. The result also implies that there was high residential development in Poly Area, Ndazabo and Gbazhi submarkets during this period which may have occasioned the sudden reduction. This confirms Broitman and Koomen (2015) findings where wide variation in residential density among neighbourhoods was observed.

The implication of the above is that this pattern would one way or the other has an impact on the rental value of residential apartments in the study area. Similar patterns were observed in Bida by Mohammed et al. (2021) where it was found that there has been a consistent residential development from the Town submarket in the year 2008 towards the north and south in the year 2013 with additional high density housing submarkets due to rapid urbanisation and increasing built-up areas. Similarly, Mohammed et al. (2021) found that the residential densities in Bida increase along the urban-rural gradient with clear evidence for unplanned urban densification as a result of the organic growth. Also, Mohammed & Sulyman (2021) suggest that residential densities increase shall continue along the urban-rural gradient thereby causing a transition of open spaces and low density areas into medium and high density areas in the coming years maintaining its monocentricity.

5. Conclusion

The study revealed an increasing building density in the housing submarkets of Bida. It can be concluded that the inner part of the city has a higher number of buildings throughout the study period and it is the region where commercial and cultural activities are carried out. The city centre maintains a consistently high number of buildings units/ha and high residential density through the years under review. The structure of the town shows that areas around the Central Business District (CBD) are of high density while locations within the urban fringe tend to have lower residential densities. As a result of building density changes, the urban morphology of the study area experienced a transformation during the study period. The study will help urban planners and urban managers differentiate between economic and social classes and respond to affordable housing. It will also help urban planners and authorities to efficiently solve the problem of spatial growth and management and assist in the assessment of housing values to evaluate planning regulations and urban land-use policies. The study, therefore, recommends planned densification to achieve sustainable residential density control. GIS application should be given priority in the assessment of residential density and housing market issues, particularly, the housing submarkets.

References

Alexander, E. R. (1993). Density Measures: A Review and Analysis. *Journal of Architectural and Planning Research*, *10*(3), 181–202.

Alonso, W. (1964). *Location and land use: Toward a general theory of land rent. Publication of the Joint Center for Urban Studies*. Harvard University Press.

Amer, M., Mustafa, A., Teller, J., Attia, S., & Reiter, S. (2017). A methodology to determine the potential of urban densification through roof stacking. *Sustainable Cities and Society*, *35*, 677–691. https://doi.org/10.1016/j.scs.2017.09.021

Broitman, D., & Koomen, E. (2015). Residential density change: Densification and urban expansion. *Computers, Environment and Urban Systems*, *54*, 32–46. https://doi.org/10.1016/j.compenvurbsys.2015.05.006

Cameron, T. (2018). *The House Rules: Housing Market Responses to Oil Price Shocks in Canada* [Masters Dissertation]. University of Ottawa.

Chandrabose, M., Owen, N., Giles-Corti, B., Turrell, G., Carver, A., & Sugiyama, T. (2019). Urban Densification and 12-Year Changes in Cardiovascular Risk Markers. *Journal of the American Heart Association*, *8*(15). https://doi.org/10.1161/JAHA.119.013199

Cheung, R., Wetherell, D., & Whitaker, S. (2018). Induced earthquakes and housing markets: Evidence from Oklahoma. *Regional Science and Urban Economics*, *69*, 153–166. https://doi.org/10.1016/j.regsciurbeco.2018.01.004

Chhipi-Shrestha, G., Hewage, K., & Sadiq, R. (2017). Impacts of neighborhood densification on water-energy-carbon nexus: Investigating water distribution and residential landscaping system. *Journal of Cleaner Production*, *156*, 786–795. https://doi.org/10.1016/j.jclepro.2017.04.113

Cichociński, P., & Dąbrowski, J. (2013). Spatio-Temporal Analysis of the Real Estate Market Using Geographic Information Systems. *Real Estate Management and Valuation*, *21*(2), 73–82. https://doi.org/10.2478/remav-2013-0019

Delmelle, E., Zhou, Y., & Thill, J.-C. (2014). Densification without Growth Management? Evidence from Local Land Development and Housing Trends in Charlotte, North Carolina, USA. *Sustainability*, *6*(6), 3975–3990. https://doi.org/10.3390/su6063975

Ghadami, M., & Newman, P. (2019). Spatial consequences of urban densification policy: Floor-to-area ratio policy in Tehran, Iran. *Environment and Planning B: Urban Analytics and City Science*, *46*(4), 626–647. https://doi.org/10.1177/2399808317722168

Goodman, A. C., & Thibodeau, T. G. (1998). Housing market segmentation. *Journal of Housing Economics*, *7*(2), 121–143.

Gulyani, S., Talukdar, D., & Bassett, E. M. (2018). A sharing economy? Unpacking demand and living conditions in the urban housing market in Kenya. *World Development*, *109*, 57–72.

https://doi.org/10.1016/j.worlddev.2018.04.007

Hill, R. J., & Scholz, M. (2017). Can Geospatial Data Improve House Price Indexes? A Hedonic Imputation Approach with Splines. *Review of Income and Wealth*. https://doi.org/10.1111/roiw.12303

Hu, S., Cheng, Q., Wang, L., & Xu, D. (2013). Modeling land price distribution using multifractal IDW interpolation and fractal filtering method. *Landscape and Urban Planning*, *110*, 25–35. https://doi.org/10.1016/j.landurbplan.2012.09.008

Islam, K. S., & Asami, Y. (2009). HOUSING MARKET SEGMENTATION: A REVIEW. *Review of Urban & Regional Development Studies*, *21*(2–3), 93–109. https://doi.org/10.1111/j.1467-940X.2009.00161.x

Jiao, L. (2015). Urban land density function: A new method to characterize urban expansion. *Landscape and Urban Planning*, *139*, 26–39. http://dx.doi.org/10.1016/j.landurbplan.2015.02.017

Kauko, T., Hooimeijer, P., & Hakfoort, J. (2002). Capturing Housing Market Segmentation: An Alternative Approach based on Neural Network Modelling. *Housing Studies*, *17*(6), 875–894. https://doi.org/10.1080/02673030215999

Leung, C. (2004). Macroeconomics and housing: A review of the literature. *Journal of Housing Economics*, *13*(4), 249–267. https://doi.org/10.1016/j.jhe.2004.09.002

Manganelli, B., Pontrandolfi, P., Azzato, A., & Murgante, B. (2014). Using geographically weighted regression for housing market segmentation. *International Journal of Business Intelligence and Data Mining 13*, *9*(2), 161–177.

McCluskey, W. J., & Borst, R. A. (2011). Detecting and validating residential housing submarkets: A geostatistical approach for use in mass appraisal. *International Journal of Housing Markets and Analysis*, *4*(3), 290–318. https://doi.org/10.1108/17538271111153040

Medayese, M., Martins, V. E., & Abdrazack, N. T. (2015). Density. In L. Egunjobi (Ed.), *Contemporary Concepts in Physical Planning* (First Edition, Vol. 1, pp. 263–290). University of Ibadan.

Mohammed, J. K., & Sulyman, A. O. (2019). Spatio-temporal Analysis of Bida Housing Market using Geographic Information System. In L. T. Ajibade, N. B. Tanimowo, G. Amuda-Yusuf, & N. A. Bello (Eds.), *The Proceedings of International Conference of Environmental Sciences* (pp. 306–316).

Mohammed, J. K., Sulyman, A. O., & Alhaji, A. A. (2021). Spatial Pattern of Residential Densification in Housing Submarket of a Traditional Urban Area. *Baltic Surveying*, *14*, 25–33. https://doi.org/10.22616/j.balticsurveying.2021.14.003

Mohammed, J. K., Sulyman, A. O., & Aliyu, A. A. (2021). A Spatiotemporal Analysis of Urban Densification in an Organically Growing Urban Area. *Baltic Journal of Real Estate Economics and Construction Management*, *9*(1), 94–111.

Mohammed, J., & Sulyman, A. (2021). Analysis of Urban Densification and Housing Market in Bida, Niger State, Nigeria. *Sustainable Housing and Land Management*, 60–69.

Muehlenbachs, L., Spiller, E., & Timmins, C. (2015). The housing market impacts of shale gas development. *The American Economic Review*, *105*(12), 3633–3659.

Park, J. (2013). The Division of Spatial Housing Submarkets: A Theory and the Case of Seoul. *Environment and Planning A*, *45*(3), 668–690. https://doi.org/10.1068/a45337

Renigier-Biłozor, M., Biłozor, A., & Wisniewski, R. (2017). Rating engineering of real estate markets as the condition of urban areas assessment. *Land Use Policy*, *61*, 511–525. https://doi.org/10.1016/j.landusepol.2016.11.040

Royuela, V., & Vargas, M. (2007). Defining housing market areas using commuting and migration algorithms. Catalonia (Spain) as an applied case study. *IREA–Working Papers, 2007, IR07/07*.

Seo, W. (2008). *Spatial impacts of micro neighborhood environments on residential real estate resale values: The importance of physical disorder* [The Ohio State University]. http://rave.ohiolink.edu/etdc/view?acc_num=osu1228281862

Ståhle, A. (2008). *Compact sprawl: Exploring public open space and contradictions in urban density*. School of Architecture, KTH.

Treija, S., Bratuškins, U., & Koroļova, A. (2018). Urban Densification of Large Housing Estates in the Context of Privatisation of Public Open Space: The Case of Imanta, Riga. *Architecture and Urban Planning*, *14*(1), 105–110. https://doi.org/10.2478/aup-2018-0014

Tupenaite, L., Kanapeckiene, L., & Naimaviciene, J. (2017). Determinants of Housing Market Fluctuations: Case Study of Lithuania. *Procedia Engineering*, *172*, 1169–1175. https://doi.org/10.1016/j.proeng.2017.02.136

Vergnes, A., Pellissier, V., Lemperiere, G., Rollard, C., & Clergeau, P. (2014). Urban densification causes the decline of ground-dwelling arthropods. *Biodiversity and Conservation*, *23*(8), 1859–1877. https://doi.org/10.1007/s10531-014-0689-3

Vuckovic, Loibl, Tötzer, & Stollnberger. (2019). Potential of Urban Densification to Mitigate the Effects of Heat Island in Vienna, Austria. *Environments*, *6*(7), 82. https://doi.org/10.3390/environments6070082

Wang, L., Omrani, H., Zhao, Z., Francomano, D., Li, K., & Pijanowski, B. (2019). Analysis on urban densification dynamics and future modes in southeastern Wisconsin, USA. *PLOS ONE*, *14*(3), 1–22. https://doi.org/10.1371/journal.pone.0211964

Wang, S., Wang, J., & Wang, Y. (2018). Effect of land prices on the spatial differentiation of housing prices: Evidence from cross-county analyses in China. *Journal of Geographical Sciences*, *28*(6), 725–740. https://doi.org/10.1007/s11442-018-1501-1

Wu, C., & Sharma, R. (2012). Housing submarket classification: The role of spatial contiguity. *Applied Geography*, *32*(2), 746–756. https://doi.org/10.1016/j.apgeog.2011.08.011

Wu, J., Deng, Y., & Liu, H. (2014). House price index construction in the nascent housing market: The case of China. *The Journal of Real Estate Finance and Economics*, *48*(3), 522–545.

Xiao, Y. (2012). *Urban morphology and housing market* [PhD Thesis]. Cardiff University.

Xiao, Y. (2017). *Urban Morphology and Housing Market*. Springer Singapore. https://doi.org/10.1007/978-981-10-2762-8

Yang, S., Hu, S., Li, W., Zhang, C., & Torres, J. (2017). Spatiotemporal Effects of Main Impact Factors on Residential Land Price in Major Cities of China. *Sustainability*, *9*(11), 2050. https://doi.org/10.3390/su9112050

Zhou, Z. (2018). Housing market sentiment and intervention effectiveness: Evidence from China. *Emerging Markets Review*. https://doi.org/10.1016/j.ememar.2017.12.005

Impact of Rainfall on Flood Episodes at River Niger at Lokoja, Kogi state, Nigeria

Ogungbe S.[1] Ojoye S.[2*]
[1,2]Department of Geography, Federal University of Technology, Minna, Nigeria
[1]samuelpg209284@st.futminna.edu.ng

Abstract

Rainfall is one of the factors that triggers flood occurrence. This study analysed the impact of rainfall on flood event at River Niger at Lokoja, Kogi state. The data used for this study were annual rainfall and water level data of River Niger at Lokoja from 1986-2020 (35years) from the Nigeria Meteorological Agency (NiMET) and the National Inland waterways Authority (NIWA) Headquarters Lokoja, Kogi state respectively. The study adopted the least square regression analysis, the mean and standard deviations which were used to achieve the results of this study. This study found out that rainfall fluctuates by 2.98% from 1986-2020, also about 69% of flood episodes are explained by the rainfall in the study area and 864mm of rainfall is required to trigger the water to the warning level.

Keywords: Flood, Rainfall, River Niger.

1.0 Introduction

Flood is not a recent phenomenon. The first flood event was traced backed to the mythology of Noah (Nuh) (Genesis 7:17, Quran: 71). It was believed that the flood inundates the surface of the earth and destroys man. Hitherto, the world has suffered many flood events, notably was the China floods of 1931, Eastern Guatemalan floods 1949, Yangtze river floods of 1954 and many others (Agujiobi-Odo and Ekwen n.d).

Flood is one of the prominent hydrological disasters in Nigeria. Most recently, the flood episode of 2012 which took place in most part of the country, it's began in July and ceased in November 2012 (Agujiobi-Odo and Ekwe, n.d). It claimed about 363 lives and more than 2.1million of people were displaced (NEMA, 2012). Lokoja was severely affected by the flood event of 2012. It was described as the most severe flood in 40years. Aderoju *et al* (2014) explained that the Kogi state was the most affected state in Nigeria during the flood episode of 2012. Several hundreds of kilometres of land surface were inundated by the flood water.

Rainfall is one of the imperative factors that trigger flood. Increased in rainfall intensity and prolonged torrent caused the surface of the earth to be covered by flooded water. The first mythology of flood event was believed to has occurred by prolonged rainfall (Genesis 7:14). It will be almost impossible to forecasts flood event without recourse to rainfall that undergirds it.

Climate change has triggers extreme climatic events. The change in the mean state of the earth's climate over the past decades has attenuated the usual global weather system. Flood was believed to be induced by the influence of climate change (Buba *et al*, 2021). The increased in the surface temperature of Lokoja has aided evaporation over River Niger surface and convection over the lands which are instrumental for cloud formation.The hydrological cycle is assumed to be aggravated by the rise in global warming which is expected to induced heavy rainfall and consequently results into flooding. The high surface temperature intensifies evaporations and deep convections which enhanced cloud formations (cumulus, cumulonimbus and stratocumulus) which result into moderate-heavy downpour. Heavy rainfall and rapid shrinking of snow and ice caps during the summer period caused frequent flooding (Khan, 2011). Flood can be caused by various factors such as discharge of water from the upstream dams, blockage of channel and rivers

overflowing their banks. Rainfall is the primary source of earth's water. All other factors that could cause flood are dependent on rainfall.

The confluence of River Niger and Benue Benue at Lokoja makes it more vulnerable to flooding or other severe hydrological catastrophe (Po *et al*, 2017). The topography, land configuration and terrain, rainfall intensity and distribution were responsible for flood episodes in Lokoja most especially in the year 2012. It was found that due to the variability in rainfall and water released from upstream dams raised the regime of River Niger to 12.85m and discharge was 30676cummecs (NIWA, 2018). The topography aided the flood event, the steep slope from the west to the east of Lokoja, influences the runoff to recharge the River Niger regime. The presence of Mount Patti at the western part of the area to the lowlands that surrounds River Niger to the east enhance the draining of the surface runoff to empties into the river.

The popular Lokoja flood event of 2012 was claimed to have killed about 8 persons, hundreds of houses were destroyed and several hundreds of people were displaced (NEMA, 2012). It was believed that high rainfall and release of water from the upstream dams raised the River Niger surface water. The 2018 flood event in city was said to have been triggered by high rainfall intensity with shorter period and rainstorms which makes surface water of River Niger at Lokoja to go beyond average.

Earlier studies like; Yussuf *et al* (2017) gave an overview of heavy rainfall as one of the factors that triggers flood occurrence in Lokoja but it emphasized at the municipal drainage capacity as the prominent factor of flood, this study does not well analysed the effects of rainfall on River Niger which its overflowing water submerged the adjacent land surface. Also, Audu (2012) descriptively analysed rainfall of Lokoja using the descriptive statistics. The descriptive approach only gave a summation of rainfall in which inference cannot be drawn.

In an attempt to provide solution to the limitation of the earlier studies; this study attempted to analyze the relationship between rainfall and flood episodes at River Niger at Lokoja in which inference could be drawn.This study analysed the impact of rainfall on flood events at River Niger at Lokoja, Kogi state, Nigeria. The scope of this study was restricted to rainfall trends, effects of rainfall on water level and the amount of rainfall required for River Niger to reach its warning level. The temporal scope of this study was from 1986-2020.The increasing global warming has risen the surface temperature globally, and consequently enhanced rainfall through deep convection and evaporation. It was ostensible that floods resulting from heavy rainfalls were responsible for the recurrent natural catastrophe.This study was imperative because it provides a basis for flood forecasting.

In achieving the aim of this study, the following objectives were used;

i. To examine rainfall variability of Lokoja from 1986-2020.
ii. To analyse the effects of rainfall on River Niger.
iii. To examine the amount of rainfall required for River Niger to reach its warning gauge at Lokoja.

1.2 *Study Area*

Lokoja is situated between latitudes 7°46'N-7°52' and longitudes 6°38'E-6°48'. It is the capital of Kogi state otherwise known as the "Confluence state".It is located at the confluence of River Niger and Benue. The confluence of the two Rivers covers most of its lands to the west and it swept across the city. The River Niger swept into the study area right from its entry point at "up Natako" and merged with River Benue along Ganaja village. River Niger is the major source of flood water in the study area.

The climate of the study area is marked by two distinctive seasons; dry and wet seasons. It has a similar climate as other state within the guinea savannah ecological zone in Nigeria, the annual rainfall of 1000mm-15000mm and annual average temperature of 27.8°c.

Its topography is characterized by a steep slope and a gentle slope from the east to the west. The presence of Mount Patti at the west of the study area orchestrated the steep-gentle slope to the east where River Niger is located.

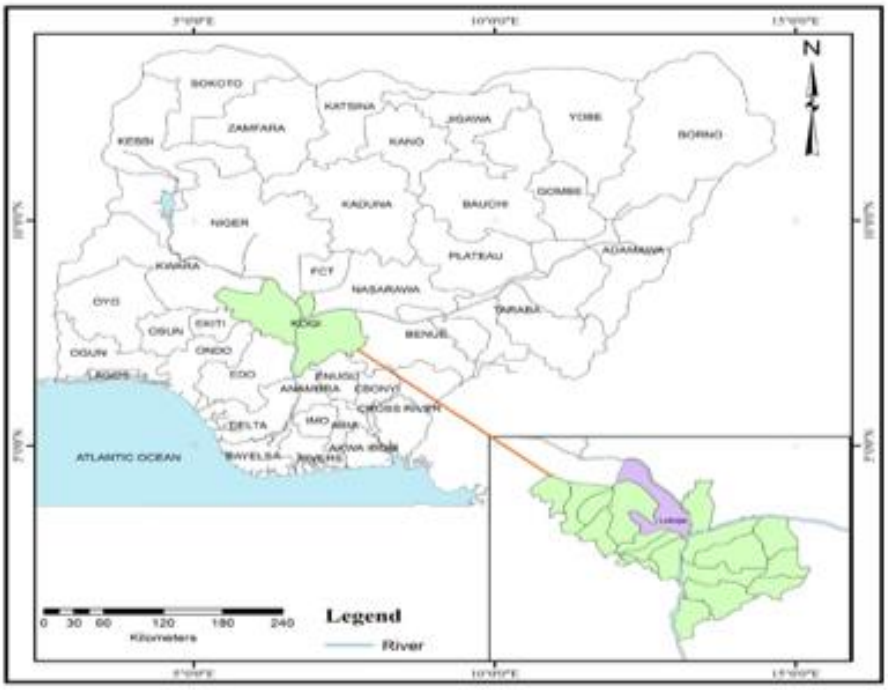

Figure 1.1 The study area

2.0 Methodology

Meteorological data for this study were obtained from the Nigeria Meteorological Agency (Nimet). One climate year (35years) data was obtained from 1986-2020. And also the hydro-meteorological from 1986-2020 were obtained from the National Inland Waterways Authority (NIWA) Headquarters, Lokoja, Kogi state.

To examine the trend of rainfall in the study area from 1986-2020, the mean Deviation was used to examine the extent of variation of rainfall annually.

It is expressed as;

$$MD = \sum f \frac{(\bar{x}-x)}{N} \quad (1)$$

Where

MD = Mean deviation

x = annual rainfall

$\bar{x}$ = mean of annual rainfalls

N = Number of years

Also the standard deviation was used to examine the variability of annual rainfall. And it is expressed as;

$SD = \sum_{i=1}^{n}(x - \overline{x}/n - 1)$ (2)

SD = Standard deviation
$\sum$ = Summation
X = Annual water level
$\bar{x}$ = mean of annual water levels
N = Number of years

The least square regression analysis was used to analyse the relationship between rainfall and water level. The least square regression analysis is expressed as;

$y = a + bx + e$ (3)

Where;
y = Water level as the dependent variable
a = the intercept of the relationship
b = Slope of the line
x = Rainfall as the independent variable
e = error

Finally, the study modifies the equation of least square to predict the amount of rainfall required for River Niger to reach its warning water level. It is expressed as;

$y = a + bx + e$ (3)

Where;
y = Water level as the dependent variable
a = The intercept of rainfall and water level
b = Slope of the relationship
x = Rainfall as the independent variable
e = error

3.1 RESULT

Figure 4.1 represents the mean annual rainfall trend over River Niger at Lokoja. The statistical analysis indicated an increase and decrease trend with an annual increase trend of ±36.6mm, which translates to fluctuations of about 2.98%. The peak rainfall was observed in the study area in 1999 with about 1767mm and the lowest rainfall was recorded in 2003 with an annual rainfall of approximately 924mm.

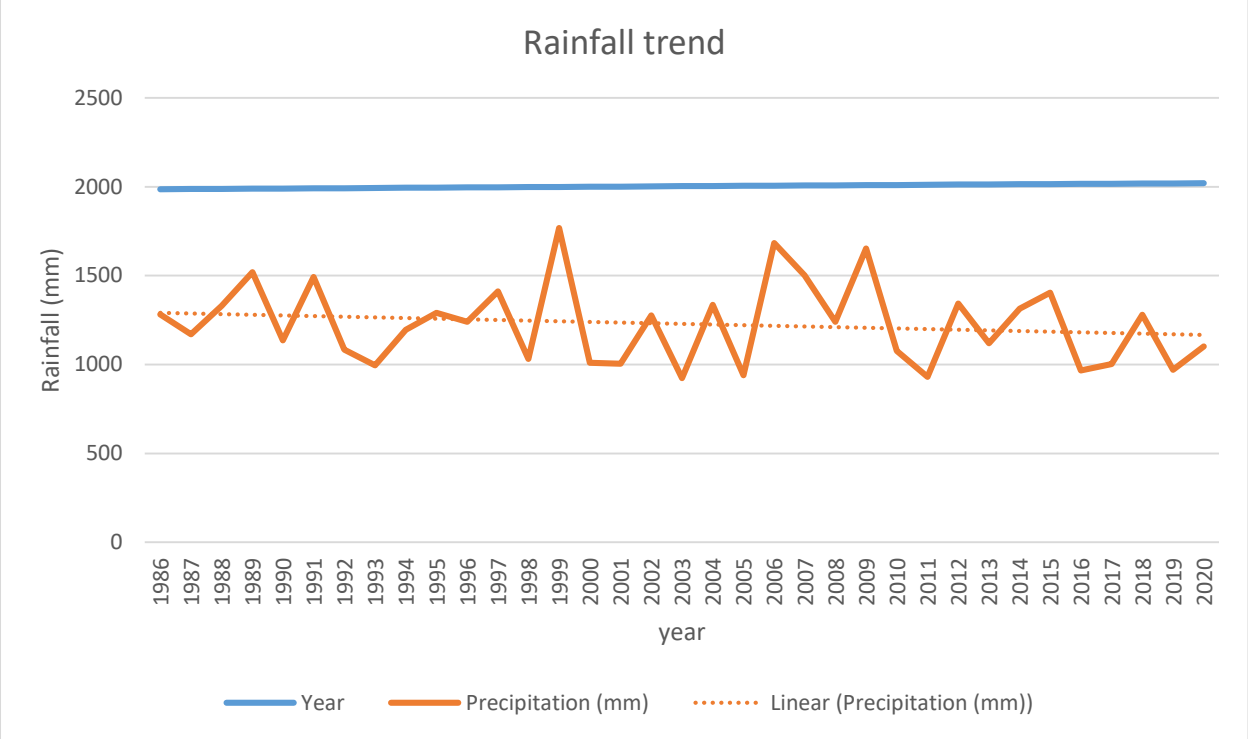

Figure 4.1 Mean Annual rainfall trends over River Niger in Lokoja

Effects of rainfall on water levels from 1986-2020

The statistical table below showed that rainfall can be relied on to explain about 69% of the water level at the study area. There was a positive relationship between rainfall and water level which implies that an increase in rainfall will raise the water level and vice versa. The analysis also showed that about 0.41 (41%) of variation can be explained by the annual rainfall that truly affects the water level of River Niger.

Table 4.1 showing the relationship between rainfall and water level

Regression Statistics	
Multiple R	0.411301
R Square	0.691684
Adjusted R Square	0.143992
Standard Error	1.389052
Observations	35

Source: Author's data analysis (2021)

Examination of amount of rainfall required to make River Niger Lokoja water level to reach its warning gauge.

Figure 4.2 showed the linear regression model of rainfall and River Niger level at Lokoja which was expressed as;

$Y = -2.6429x + 2294.8$

The warming level of 8metres was benched by the National Emergency Management Agency (NEMA). The amount of rainfall required to raise the surface water of River Niger to this height

was postulated by this study using the linear regression model as 864mm. Therefore about 864mm of rainfall would raise the surface water to the warning level.

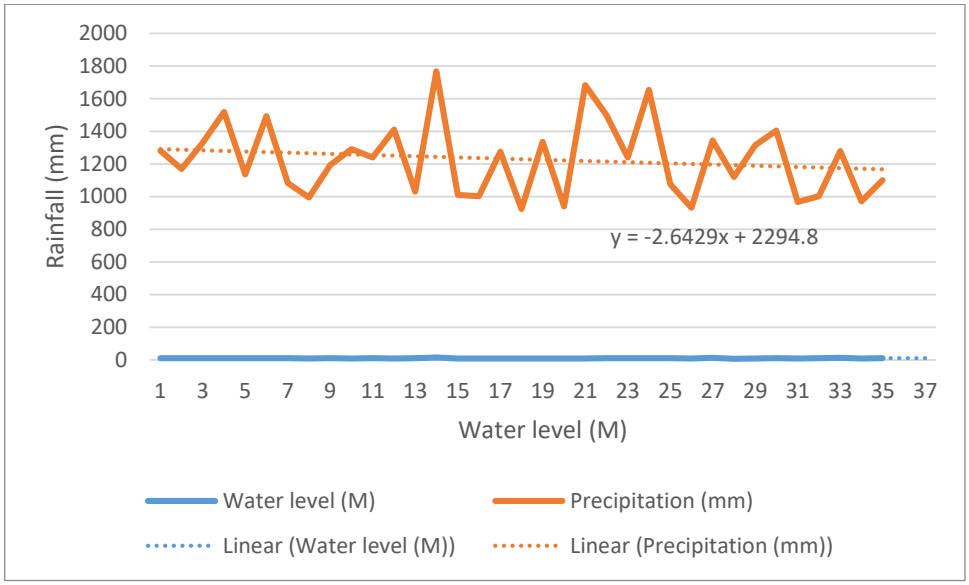

Figure 4.2 showing rainfall and water level Model.

Conclusion

This study has shown that rainfall has a positive impact on flood episodes in the study area. It can be relied on to forecast potential flood events. This study therefore suggested that further studies should investigate the impact of temperature, water discharged from the upstream dams and other large tributaries of River Niger basin as factors that triggers flood events in the study area.

References

Aich, V., Kone, B., Hattermann, F. F., and Paton, E. N. (2016). Time series analysis of floods across the Niger river Basin.Water, 8(4), 165.

Ajujiobi-Odo, N., and Ekwe, O. The Role of the Media in Managing Flood Disaster: An Audience Assement.

Audu, E. B. (2012). An analytical view of temperature in Lokoja, Kogi State, Nigeria. *International Journal of Science and Technology, 2(12), 856-859.*

Booij, M. J. (2005). Impact of climate change on 1 flooding assessed with different spatial model resolutions. Journal of hydrology, 303(1-4), 176-198.

Buba, F. N., Obaguo, S., Ogar, O., and Ajayi, F. O. (2021). A Participatory Assessment of the Impact of Flooding in Some Communities in Lokoja, Kogi State, Nigeria. *American Journal of Climate Change*, 10(1), 12-31.

Berghuijs, W. R., Harrigan, S., Molnar, P., Slater, L. J., and Kirchner, J. W. (2019). The relative importance of different flood-generating mechanisms across Europe. *Water Resources Research*, 55(6), 4582-4593.

Christensen, J. H., and Christensen, O. B. (2003). Severe summertime flooding in Europe.*Nature*, 421(6925), 805-806..

English Standard Version Bible (2001). ESV Online.https://esv.literalword.co.

English Translation: Mohammed MarmadukePickthall. The Holy Quran. Islamabad: Shalimar Recording Co. Ltd., 1975.

Jimoh, U. U., and Salami, H. (2020). Spatio-Temporal Analysis of Flooding In Lokoja (1999-2018), Kogi State Nigeria. *Int. J. Sci. Res. in Multidisciplinary Studies* Vol, 6(2).

Keef, C., Svensson, C., and Tawn, J. A. (2009). Spatial dependence in extreme River flows and rainfall for Great Britain.*Journal of Hydrology*, 378(3-4), 240-252.

Khan, A. N. (2011). Analysis of flood causes and associated socio-economic damages in the Hindukush region. *Natural hazards*, 59(3), 1239.

Ralph, F. M., Dettinger, M., White, A., Reynolds, D., Cayan, D., Schneider, T., ... and Wick, G. (2014). A vision for future observations for western US extreme rainfall and flooding.*Journal of Contemporary Water Research and Education*, 153(1), 16-32

Tabari, H. (2020). Climate change impact on flood and extreme rainfall increases with water availability.*Scientific reports*, 10(1), 1-10.

Whitcomb, J. C., and Morris, H. M. (1961). The genesis flood. SPONS AGENCY PUB DATE, 60, 60.

Yussuf, M. J., Sanni, J. E., Alabi, J. O., Onyowoicho, C. O., and Amanda, U. E. (2017). Evaluation of Drainage System in Part of Lokoja Town in Kogi State, Nigeria. *International Journal of Engineering and Modern Technology*, 3(5), 39-48.

Nuclear Data Evaluation for the Production of Technetium-99^{m} for Medical Diagnosis.

Y. M. Ahijjo
Department of Physics, Usmanu Danfodiyo University Sokoto, Nigeria
yahijjomusa@gmail.com
* Corresponding author

ABSTRACT

This study delved on the theoretical evaluation for the production of ^{99m}Tc radioisotope found as a good candidate in diagnostic imaging in the field of nuclear medicine. (p,n) and the EXFOR Data base which contains data from 21710 experiments compiled by the NRDC under the auspices of the IAEA were utilized. The nuclear data in EXFOR were found with essential information on the meaning and the quality of the data including summaries on measurement techniques, corrections and error analysis, standard reference values etc. Also obtained were digitized data from results in graphical form, and original tabulated data. The input of ^{99m}Tc specific parameters such as nuclear target, reaction type, quantity, energy range and product on EXFOR database for theoretical proton induce reaction on ^{100}Mo(p,2n)^{99m}Tc and ^{92}Mo(p,g)^{99m}Tc were carried out with energy up to 18 MeV and 4 MeV respectively using EXFOR data code to provide estimated uncertainties of energy and cross sections. The results shows that ^{100}Mo(p,2n)^{99m}Tc reaction exhibits smaller cross section than ^{92}Mo(p,g)^{99m}Tc reaction. The recommended nuclear reaction for the routine ^{99m}Tc production is ^{92}Mo(p,g)^{99m}Tc reaction due to the observed larger cross section when compared with different nuclear data. This study hence provides overview on the applications and as a precursor to the production rout of ^{99m}Tc and other popular medical radioisotopes before practical experimental endeavors. It offers immense alternatives and advantages to practical utilities of reactors and cyclotrons given as an overview of recent developments and prospects in worldwide radioisotopes production.

INTRODUCTION

Nuclear medicine is a medical specialty that involves the application of radioactive substances in the diagnosis and treatment of diseases. Nuclear medicine, in a sense, is "radiology done inside out" or "endoradiology". Nuclear medicine scans differ from radiology as the emphasis is not on imaging anatomy but the function and for such reason, it is called a physiological imaging modality (Donarl, 2009).

Radioisotopes used in nuclear medicine imaging are typically isotopes with short half-lives. Gallium-68 (^{68}Ga) has been used experimentally in the staging of lymphoma and shows a great deal of promise in bone scanning. SPECT isotopes, such as technetium-99 (^{99m}Tc) and iodine-123 (^{123}I) are more common for use in cancer imaging. Other isotopes used in cancer imaging are: chromium-51 (^{51}Cr), gold- 198 (^{198}Au), indium-113m (^{113}mIn), iodine-125 (^{125}I), iodine-131 (^{131}I), mercury-197 (^{197}Hg), mercury-203 (^{203}Hg), selenium-75 (^{75}Se), and Ytterbium-169 (^{169}Yb). Except ^{123}I, all of these radioisotopes are currently produced by research reactors (IAEA, 2009).

Due to the short half-lives of most positron- emitting radioisotopes, the radiotracers have traditionally been produced using a cyclotron in close proximity to the PET imaging facility (IAEA, 2009).Technetium-99m can be readily detected in the body by medical equipment because it emits 140.5 KeV gamma rays and its half-life for gamma emission is six hours (meaning 94% of it decays to ^{99}Tc in 24 hours). The "short" physical half-life of the isotope and its biological half-life of 1 day (in terms of human activity and metabolism) allows for scanning procedures which collect data rapidly, but keep total patient radiation exposure low. ^{99}Tc have been found in applicability to bone SPECT scanning, Mycocardial perfusion imaging (MPI), Cardiac ventriculography, evaluation of

coronary artery disease, valcular heart disease, congenital heart disease, cardiomyopathy, functional brain imaging (dementia causes), immunoscintigraphy (detection of difficult cancers), and blood pool labeling to map circulatory system disorders (Bockisch, 2009). Since this study must be utilized to give an overview on production of ^{99m}Tc isotope in nuclear medicine (n,p), by enhancing the projectiles on the target (^{99}Tc), hence, the following set of reactions will be considered for the production of ^{99m}TC only in nuclear medicine; while EXFOR code data will be employed to evaluate important production parameters viz; ^{100}Mo(p,2n)^{99m}Tc and ^{92}Mo(p,g)^{99m}TC respectively.

For most accelerator production routes they are based on the ^{100}Mo(p,2n)^{99m}Tc reaction. The cross section of this nuclear reaction was studied by several laboratories earlier but the available data are not in good agreement which suggests theoretical accounts of this sorts. For large scale accelerator production of ^{99m}Tc based on the ^{100}Mo(p,2n)^{99m}Tc reaction, a well-defined excitation function is required to optimize the production process effectively. One of the recent studies pointed out that most of the available experimental excitation functions for the ^{100}Mo(p,2n)^{99m}Tc reaction have the same general shape while their amplitudes are different. To confirm the proper amplitude of the excitation function, results of three independent experiments were compared to that of TakÃ¡cs *et al*. (2015). This study therefore presents results of a thick target count rate measurement of the E_{γ} = 140.5 keV gamma-line from molybdenum irradiated by E_p = 17.9 MeV proton beam, as an integral benchmark experiment from both Nudat and Exfore data to prove the cross section data reported for the ^{100}Mo(p,2n)^{99m}Tc and ^{100}Mo(p,pn)^{99}Mo reactions in (TakÃ¡cs *et al*., 2015).

NUCLEAR REACTIONS

Neutron activation is the most common way production of isotopes by neutron activation in a nuclear reactor, which means that radioactive isotopes are bombarded with neutrons. This method involves the capture of a neutron by the nucleus of an atom resulting in an excess of neutrons. Fission is when the nucleus splits into two or more small nuclei and free neutrons and photons (usually gamma rays). Uranium is the main fuel and it easily splits by thermal neutrons diffusing into the nucleus. The most common radioisotopes produced by fission are molybdenum-99(^{99}Mo) [which decays to technetium- 99m (^{99m}Tc)]. Thermal neutrons have special features that make them suitable for radioisotope production. They have no charge and diffuses freely into the nucleus. Large cross-sections for thermal neutron absorption and high fluxes with thermal neutrons means production on a relatively large scale (Abbas, 2014). Equation (1) & (2) shows the production of Technetium 99^m from Molybdenum-99 decay;

$$^{100}\text{Mo} + {}^{1}\text{p} \rightarrow {}^{99m}\text{Tc} + 2\text{n} \quad (1)$$

Tc-99^m decays mainly by gamma emission, slightly less than 88% of the time.

$$^{92}\text{Mo} + {}^{1}\text{p} \rightarrow {}^{99m}\text{Tc} + \gamma \quad (2)$$

MASS DEFECT

Mass defect is defined as the difference between the mass of a nucleus, and the sum of the masses of the nucleons of which it is composed. It is also the difference between the mass of a composite particle and the sum of the masses of its parts. The mass defect is determined by calculating three quantities viz: the actual mass of the nucleus, the composition of the nucleus (number of protons and of neutrons), and the masses of proton and neutron. This is then followed by converting the mass defect into energy. This quantity is the nuclear binding energy; however, it must be expressed as energy per mole of atoms or as energy per nucleon. The mass defect can be explained using Albert Einstein's formula;

$$E = mc^2 \quad (3)$$

Which is an expression of the equivalence of energy and mass. By this formula, adding energy also increases mass (both weight and inertia), whereas removing energy decreases mass. If one must inject energy to separate a system of particles into its components, then the initial mass is less than that of the components after they are separated. The energy injected is "stored" as potential energy, which shows as the increased mass of the components that store it. This is an example of the fact that energy of all types is seen in systems as mass, since mass and energy are equivalent, and each is a "property" of the other (Rod, 2010).

BINDING ENERGY

The binding energy may refer to the energy balance in processes in which the nucleus splits into fragments composed of more than one nucleon. Nuclear binding energy is the energy that would be required to disassemble the nucleus of an atom into its component parts. These component parts are neutrons and protons, which are collectively called nucleons. The binding energy of nuclei is due to the attractive forces that hold these nucleons together, and it is always a positive number, since all nuclei would require the expenditure of energy to separate them into individual protons and neutrons. If new binding energy is available when light nuclei fuse, or when heavy nuclei split, either of the processes can result in the release of this binding energy. This energy may be made available as nuclear energy and can be used to produce electricity as in (nuclear power) or in a nuclear weapon. When a large nucleus splits into pieces, excess energy is emitted as photons (gamma rays) and as the kinetic energy of a number of different ejected particles (nuclear fission products). The nuclear binding energies and forces are on the order of a million times greater than the electron binding energies of light atoms like hydrogen (Rod, 2010).

Nuclear binding energy is explained by the basic principles involved in nuclear physics. Nuclear energy is released by the splitting (fission) or merging (fusion) of the nuclei of atom(s). The conversion of nuclear mass - energy to a form of energy, which can remove some mass when the energy is removed, is consistent with the mass-energy equivalence formula:

$$\Delta E = \Delta m c^2 \quad (4)$$

Where ΔE = energy release,

Δm = mass defect, and

c = the speed of light in a vacuum (a physical constant).

Nuclear binding energy can be computed from the difference in mass of a nucleus, and the sum of the masses of the number of free neutrons and protons that make up the nucleus. Once this mass difference, called the mass defect or mass deficiency, is known, Einstein's mass-energy equivalence formula $E = mc^2$ can be used to compute the binding energy of any nucleus. Early nuclear physicists used to refer to computing this value as a "packing fraction" calculation. For example, the atomic mass unit (1 u) is equal to 1/12 of the mass of a 12 C atom—but the atomic mass of a 1 H atom (which is a proton plus electron) is 1.007825 u, so each nucleon in 12 C has lost, on average, about 0.8% of its mass in the form of binding energy. The Semi-empirical formula for nuclear binding energy masses: 1 u = (931.494028 ± 0.000023) MeV. To calculate the binding energy, we use the formula: Z (m p + m e) + N m n – m nuclide;

where Z denotes the number of protons in the nuclides and N their number of neutrons. We take: m p = 938.2723 MeV, m e = 0.5110 MeV and m n = 939.5656 MeV.

The letter A denotes the sum of Z and N (number of nucleons in the nuclide). If we assume the reference nucleon has the mass of a neutron (so that all "total" binding energies calculated are maximal) we could define the total binding energy as the difference from the mass of the nucleus, and the mass of a collection of A free neutrons. In other words, it would be (Z + N) mn – m nuclide. The "total binding energy per nucleon" would be this value divided. (Rod, 2010).

COULOMB EXCITATION

Coulomb excitation is a technique in experimental nuclear physics to probe the electromagnetic aspect of nuclear structure. In coulomb excitation, a nucleus is excited by an inelastic collision with another nucleus through the electromagnetic interaction, a type of physical interaction that occurs between electrically charged particles. In order to ensure that the interaction is electromagnetic in nature — and not nuclear — a "safe" scattering angle is chosen. This method is particularly useful for investigating collectivity in nuclei, as collective excitations are often connected by electric quadrupole transitions (Ravaioli *et al*., 2010).

As in Rutherford scattering, deep inelastic scattering of electrons by proton targets revealed that most of the incident electrons interact very little and pass straight through, with only a small number bouncing back. This indicates that the charge in the proton is concentrated in small lumps, reminiscent of Rutherford's discovery that the positive charge in an atom is concentrated at the nucleus. However, in the case of the proton, the evidence suggested three distinct concentrations of charge (quarks) and not one (Ravaioli *et al*., 2010).

Q-VALUE AND THRESHOLD FOR REACTION

In nuclear science, Q-value of a reaction is the amount of energy released by that reaction. The value relates to the enthalpy of a chemical reaction or the energy of radioactive decay products. It can be determined from the masses of reactants and products. Q values affect reaction rates. In general, the larger the positive Q value for the reaction, the faster the reaction proceeds, and the more likely the reaction is to "favor" the products. A reaction with a positive Q value is exothermic, i.e. has a net release of energy, since the kinetic energy of the final state is greater than the kinetic energy of the initial state. A reaction with a negative Q value is endothermic, i.e. requires a net energy input, since the kinetic energy of the final state is less than the kinetic energy of the initial state (Krane, 1998).

Chemical Q values are measurement in calorimetry. Exothermic chemical reactions tend to be more spontaneous and can emit light or heat, resulting in runaway feedback (i.e. explosions). Q values are also featured in particle physics. For example, Sargent's rule states that weak reaction rates are proportional to Q5. The Q value is the kinetic energy released in the decay at rest. (Martin and Shaw, 2007).

MATERIAL

The under listed materials below were employed in a bid to evaluate the nuclear data of Technetium-99^{m} production for medical diagnosis purposes for the application in nuclear medicine.

Personal computer; Internet for access to I.A.E.A experimental data, EXFOR code, Proton, Neutron and Molebdenum-99m

EXPERIMENTAL NUCLEAR REACTION DATA (EXFOR) CODE

Experimental Nuclear Reaction Data (EXFOR) Database Version of 2017-06-09 (Software Version of 2017-05-15). The EXFOR contains an extensive compilation of experimental nuclear reaction data. Neutron reactions have been compiled systematically since the discovery of the neutron, while charged particle and photon reactions have been covered less extensively. The EXFOR contains data from 21710 experiments. EXFOR is compiled by the Nuclear Reaction Data Centres Network (NRDC) under the auspices of the International Atomic Energy Agency (IAEA). JENDL, ENDF, JEFF, BROND and CENDL are produced based on EXFOR by JAEA Nuclear Data Center and Japanese. Nuclear Data Committee (JAEA-NDC+JNDC), Cross Section Evaluation Working Group (CSWEG), NEA Joint Evaluation Project, Russian Nuclear Data Center (CJD) and Chinese Nuclear Data Center and Nuclear Data Committee of China, respectively.

SIGNIFICANCE OF EXFOR DATA CODE

EXFOR contains many data that have never been published in numerical form. It is therefore a publication medium supplementary to conventional formal publication. EFOR data are currently updated. When authors revise their data after publication, EXFOR files are kept up-to-date accordingly. The numerical data in EXFOR are supplemented by explanatory text giving essential information on meaning and quality of the data including summaries on measurement techniques, corrections and error analysis, standard reference values used etc. EXFOR also contains numerical data which were digitized from results published only in graphical form, and where the original tabulated data could not be obtained from the authors. EXFOR is designed for flexibility, to meet the diverse needs of the nuclear reaction data centers and to allow the compilation of every diverse type of quantities while making computerized processing of the data possible. EXFOR is a compilation of the Authors original published experimental data. While format allows the inclusion of data renormalized to up-to-date standard values (with proper documentation), this task is normally left to data evaluators who systematically review the experimental works.

METHOD

EXCITATION FUNCTION

The cross section for incident energy to excite an atom to a particular excited state expressed as a function of incident energy. It was found to describes a graphical plot of the cross section of a radionuclide or reaction channel as a function of the bombarding projectile energy. A nuclear reaction was utilized to demonstration a complete set of study of the exit channel (1n, 2n & 3n) for the excitation function in order to allow a determination of the optimum energy used to maximize the yield.

NUCLEAR REACTION

The method used in EXFOR to obtain data using the following nuclear reaction could be seen below as an illustration.

$$^{100}\text{Mo(p,2n)}^{99m}\text{Tc} \quad (5)$$

$$^{92}\text{Mo(p,g)}^{99m}\text{Tc} \quad (6)$$

TARGET

The target is the radionuclide chosen in making the nuclear reaction. In the EXFOR database, space is giving to select the target nuclide of choice for a particular reaction we want to run, once the target is selected EXFOR will load it and let you go to the next step.

Reaction Type

Reaction type is the projectiles and the ejectiles of a particular reaction. Projectile is the bombarding particle or radiation (in this case gamma rays) to induce the target nuclide to undergoes nuclear reaction and ejectiles are the emitted particles or radiation after the target is being transformed into daughter nuclide. The EXFOR, allow to select the reaction type in the form (projectiles, ejectiles), it then load and go to the next step.

Quantity

The quantity is the function that was requested from EXFOR to evaluate cross section, CST temperature dependent cross section, kinetic energy e.t.c). In this paradigm, interested in the reaction cross section.

Energy Range

Energy range was used to enhance the range at which the reaction must proceed. In choosing the energy range it was not necessarily restricted to start from zero (ground state) it was made to choose at any point of choice. But an interval was maintained throughout theoretical reaction interval that were chosen.

Product

The product is the residual nuclide or daughter nuclide produced. After strictly following all the necessary steps observed above, EXFOR therefor automatically gave the product a sustained reaction. Upon all this processes, it was mandated that any given reaction must be a balanced one; meaning the mass of reactants must be equal to the mass of products otherwise the reaction will not proceed.

RESULT AND DISCUSSION

The proceeding theories of Technetium-99^{m} production for medical imaging is that ^{99m}Tc is the most used tracer nuclide in nuclear medicine. The metastable state ^{99m}Tc is radioactive with a half-life of 6.007 hours considerably longer (by 14 orders of magnitude, at least) than most nuclear isomers, though not unique. Which offers it a short half-life relative to many other known modes of radioactive decay and it is in the middle of the range of half-lives of other radiopharmaceuticals. By gamma emission or internal conversion, the resulting ground-state technetium-99 resulted in decays with a half-life of 211,000 years to stable ruthenium-99. This process emits soft beta radiation without a gamma. This outcome of low radioactivity from the daughter product suggests a good feature for radiopharmaceuticals applicability.

Theoretical proton induce reaction on ^{100}Mo(p,2n)^{99m}Tc and ^{92}Mo(p,g)^{99m}Tc were found with energy up to 18 MeV and 4 MeV respectively using EXFOR data code to provide estimated uncertainties of energy and cross sectional values. Excitation function which is a measure of Cross section data versus incident particles or radiation energy was found enhancing as well.

Table 4.1: Cross section and proton incident energy data for ^{100}Mo(p,2n)^{99m}Tc

proton energy (MeV)	Cross section (barns)
8.5±0.05	0.092±0.014
10±0.05	0.317±0.046
11.3 ±0.05	0.536±0.079
12.5±0.05	0.681±0.092
13.5±0.1	0.63±0.09
14.6±0.1	0.689±0.097
15.6±0.1	0.749±0.107
16.6±0.1	0.807±0.112
17.5±0.1	0.812±0.112

Table 4.2: Cross section and incident energy data for ^{92}Mo(p,g)^{99m}Tc

Proton energy (MeV)	Cross section (barns)
1.725±0.025	3.94e-7±1.5e-8
1.775±0.025	6.99e-7±2.1e-8
1.825±0.025	9.32e-7±3e-8
1.875±0.025	1.25e-6±3e-8
1.925±0.025	1.85e-6±4e-8
1.975±0.025	2.62e-6±7e-8
2.025±0.025	4.24e-6±1.6e-7
2.075±0.025	4.78e-6±2.1e-7
2.125±0.025	6.67e-6±1.9e-7
2.175±0.025	9.11e-6±2.4e-7
2.225±0.025	1.19e-5±3e-7
2.275±0.025	1.47e-5±4e-7
2.325±0.025	2.03e-5±5e-7
2.375±0.025	2.49e-5±5e-7
2.425±0.025	3.02e-5±7e-7
2.475±0.025	3.78e-5±1.1e-6
2.525±0.025	4.92e-5±1.3e-6
2.575±0.025	5.9e-5±1.5e-6
2.625±0.025	3.46e-5±1.6e-6
2.675±0.025	2.74e-5±1.8e-6
2.725±0.025	1.42e-5±1.5e-6
2.775±0.025	1.1e-5±1e-6
2.825±0.025	1.06e-5±1.2e-6
2.875±0.025	9.06e-6±1.48e-6
2.925±0.025	7.95e-6±1.54e-6
2.975±0.025	6.86e-6±1.51e-6
3.025±0.025	9.94e-6±1.57e-6
3.075±0.025	1.02e-5±1.4e-6

^{100}Mo(p,2n)^{99m}Tc Reaction

It can be seen that from the figure 4.1 below which is a function of ^{100}Mo(p,2n)^{99m}Tc reaction data code from about 8.5±0.05 – 17.5±0.1 MeV of proton energy is presented in table 4.1. From 8 up to 8.4 MeV the cross section is not observed since the energy there is not presented, from energy around 8.5±0.05 MeV small cross section is first observed at 0.092±0.014 barns, apparently the cross section increases gradually as the proton energy increases of about 8.5±0.05 MeV – 12.5±0.05 MeV at 0.092±0.014 barns – 0.681±0.092 barns, then the value of cross section begins to decrease down to about 0.63±0.09 barns at energy of 13.5±0.1 MeV, hence it increases gradually. The maximum cross section is around 0.812±0.112 barns at proton energy of about 17.5±0.1 MeV which is clearly observed from the table 4.1 above.

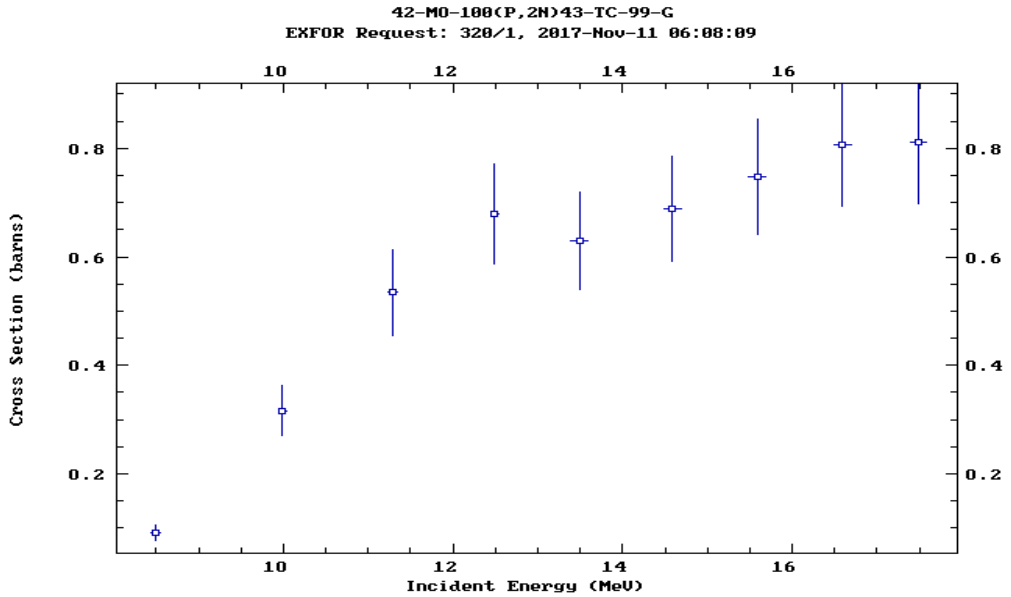

Figure 4.1: Excitation function of proton reaction on ^{100}Mo(p,2n)^{99m}Tc

^{92}Mo(p,g)^{99m}Tc Reaction

It can also be seen that from the table 4.2 above which is the function of ^{92}Mo(p,g)^{99m}Tc reaction data code from about 1.725±0.025 MeV – 3.075±0.025 MeV a proton energy was presented, which is the relationship between proton induce reaction and reaction cross section. It is clearly shows that around 3.94e-7±1.5e-8 barns a small cross section is observed at proton energy of 1.725±0.025 MeV, obviously as the energy increases gradually to 1.875±0.025 MeV from where the cross section decreases to 1.25e-6±3e-8 barns, also as the energy increases continuously the cross section increases from about 1.25e-6±3e-8 barns – 9.11e-6±2.4e-7 barns and then slow down to 1.19e-5±3e-7 barns at 2.225±0.025 MeV which is increasing, from where it increase a bit at 1.47e-5±4e-7 barns and then decreases down to 3.46e-5±1.6e-6 barns at the energies of 2.275±0.025 MeV and 2.625±0.025 MeV. The maximum cross section is around 9.94e-6±1.57e-6 barns at the energy of around 3.025±0.025 MeV which is the main target.

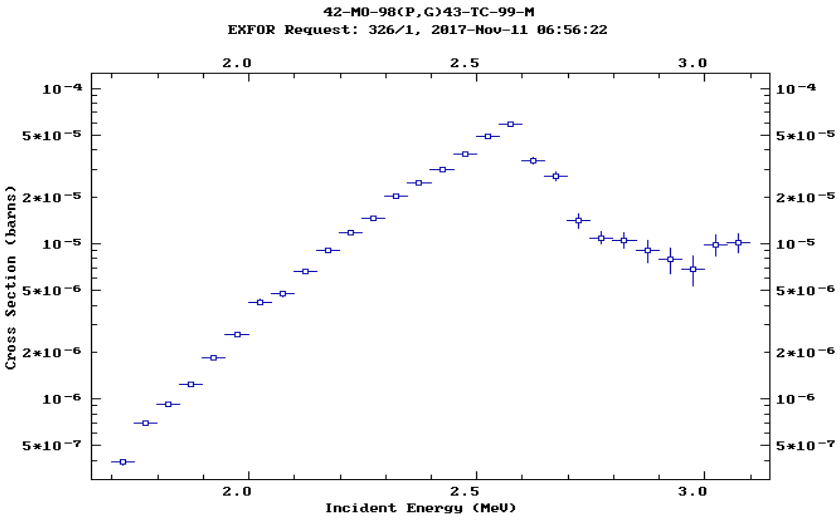

Figure 4.2: Excitation function of proton induced reaction on ^{92}Mo(p,g)^{99m}Tc

CONCLUSON AND RECOMMENDATION

The theoretical evaluation of nuclear reactions for the production of ^{99m}Tc radionuclide have been ascertained with proton reactions on ^{100}Mo(p,2n)^{99m}Tc and ^{92}Mo(p,g)^{99m}Tc respectively. The maximum cross section obtained from proton induced reaction on ^{100}Mo(p,2n)^{99m}Tc was approximately 0.812±0.112 barns at proton energy of about 17.5±0.1MeV which suggests a smooth nuclear reaction. Also the maximum cross section obtained from the other proton reaction on ^{92}Mo(p,g)^{99m}Tc was approximately 9.94e-6±1.57e-6 barns at the energy of around 3.025±0.025 MeV which was found satisfactory in comparison with related studies.

The decay of Technetium reactions could be adapted as an elegant and practical tool for nuclear medicine data for the production of diagnostic radioisotope for gamma camera imaging techniques.

RECOMMENDATION

From the nuclear data code obtained from EXFOR on ^{100}Mo(p,2n)^{99m}Tc and ^{92}Mo(p,g)^{99m}Tc reactions respectively, ^{100}Mo(p,2n)^{99m}Tc reaction is having the smaller cross section than ^{92}Mo(p,g)^{99m}Tc reaction. The recommended nuclear reaction for the routine ^{99m}Tc production is ^{92}Mo(p,g)^{99m}Tc reaction because of it larger cross section when compared with different nuclear data.

As described in this paper, one of the eight most popular reactor-based medical isotopes molybdenum-99 (^{99}Mo) (or direct production of ^{99m}Tc) can be easily made in substantial amount with particle accelerators after ascertaining the theoretical details. Thus, this save cost of subjecting practical samples into test that accounts to physical nuclear reactions in reactors or cyclotrons.

REFERENCES

Abbas, K. (2014). Medical Isotope Production and Use. Retrieved from http://www.isotopeworld.com/filestore/Medical Isotope Production and Use. pdf

Bailey, D.L., Townsend, D.W., Valk, P.E. and Maisey, M.N. (2005). *Positron Emission Tomography*: Basic Sciences.

Bartlett, K. and Christopher, A. (2014). EMI and the CT scanner [A] and [B]. Retrieved from www.blackwellpublishing.com/grant/docs/10EMI.pdf

Bockisch, A. (2009). Hybrid Imaging by SPECT/CT and PET/CT: Proven Outcomes in Cancer Imaging. *Semin Nucl Med*: **39** (4) 276-289.

Cho, A. (2010). Mass of the Common Quark Finally Nailed Down. Science Magazine. American Association for the Advancement of Science.

Donarl, M.K. (2009). Nuclear medicine. Tumor localizing radionuclides in retrospect and prospect. *Semin Nucl Med*: (3) 186–189.

Earth Times, (2010). Research and Markets. Europe Nuclear Imaging Equipment. Market Analysis and Opportunity Assessment Report. Retrieved from http://www.earthtimes.org/articles/SPECT/CT.

EXFOR. (2016). Experimental Nuclear Reaction Data "Interactive decay scheme for ^{99m}Tc. Retrieved from http://www-nds.indcentre.org.in/exfor/exfor.htm .

Fletcher, B. and James, W. (2008). Recommendations on the Use of 18F-FDG PET in Oncology. *Journal of Nuclear Medicine:* **49**(3) 480-508. Retrieved from http://www.ncbi.nlm.nih.gov/pubmed/18287273

Gelbart, W.Z. (1993). High Current Radioisotope Production with Solid Target Systems. Production of the Particle Accelerator Conference: pp -309.

Henkin, R. (1996). The Nuclear Medicine. Retrieved from www.nucbooks.n

IAEA. (2009). International Atomic Energy Agency. Nuclear Technology Review. IAEA: pp -45 Retrieved from http://wwwnaweb.iaea.org

IAEA. (2015).International Atomic Energy Agency "Nuclear Reactors Technology. Retrieved from http://wwwnaweb.iaea.org/research_reactors/isotope_prod

Jennifer, P. (2012). Nuclear Medicine Instrumentation. Jones & Bartlett Publishers: pp -189

Kerry, M. (2016). Nuclear Medicine. Retrieved from http://www.molecularimaging .net/index.php?option=com_articles&view

Krane, K.S. (1988). Introductory Nuclear Physics: pp -381

Luig, H., Kellerer, A.M. and Griebel, J. R. (2011). Radionuclides Introduction. Ullmann's Encyclopedia of Industrial Chemistry.

Martin, B. and James, D. (2006). Radioisotopes in Industry. *World Nuclear Association. Physics of Radiation Protection*: pp -130.

Martin, B.R. and Shaw, G. (2007). Particle Physics: P -34

Milton, B.F. and Stevenson, N.R (1995). Cyclotrons for Isotope Production. *Particle Accel. Conf*: pp 95-39.

Mohr, P.J., Taylor, B.N. and Newell, D.B. (2015). The 2014 CODATA Recommended Values of the Fundamental Physical Constants. National Institute of Standards and Technology.

NIBIB: National Institute of Biomedical Imaging and Bioengineering. (2016). The physics of Medical Imaging. Retrieved from https://www. nibib.nih.gov/.../fy- 2016

O'Leary, D. (2012). The deeds to deuterium. Nature Chemistry: pp -236. Bibcode: 2012NatCh...4.236O. doi: 10.1038/nchem.1273

Olive, K.A. (2014). Review of Particle Physics. Chin. Phys. C. 38: 090001. Bibcode: 2014ChPhC.38i0001O. doi: 10.1088/1674-1137/38/9/090001

Petrucci, R.H., Harwood, W.S. and Herring, F.G. (2002). *General Chemistry*: pp -1025–26

Prigent, A. and Piepsz, A. (2005). Functional Imaging in Nephro-Urology.

Ravaioli, F.T., Ulaby, E.M. and Umberto, G. (2010). Fundamentals of applied electromagnetics. pp -13

Rozovsky, C. and Katia, M. (2008). Value of SPECT/CT for Correlation of MIBG Scintigraphy and Diagnostic CT in Neuroblastoma and Pheochromocytoma: **190** 1085-1090.

Rod, N. (2010). Nuclear Binding Energy. The Department of Physics and Astronomy Hyperphysics. Retrieved from www.gsu.org

Smirnov, V. and Vorozhtsov, S. (2015). Modern Compact Accelerators of Cyclotron Type for Medical Applications. Joint Institute for Nuclear Research. Joliot-Curie 6, Dubna, Moscow region, 141980 Russia

TakÃ¡cs, S.F., DitrÃ³i, M., Aikawa, H. and Haba, N. (2016). *Nucl. Instrum. Meth.* **375** pp 60-66. Doi: 10.1016/j.nimb.2016.03.040. Retrieved from https://www-nds.iaea.org/publications/staff_pub.php

Wilson, C. (2012). The Technetium-99m Generator. Retrieved from http://www.bnl.gov/bnlweb/history/tc-99m.asp

WNA, World Nuclear Association. (2017). Public Health Radioisotopes for Medical Imaging. Retrieved from http://ec.europa.
eu/health/radioisotopes_en.htm

Theoretical Nuclear Data Evaluation for the Production of ^{64}CU, A Tool in PET & SPECT

Y. M. Ahijjo[1*] A. N. Baba-Kutigi[2]

[1]*Department of Physics, Usmanu Danfodiyo University Sokoto, Nigeria*

[2]*Department of Physics, Federal university Dutsinma, Katsina, Nigeria*

[1]*yahijjomusa@gmail.com*

* *Corresponding author*

ABSTRACT

Radioisotopes of copper have received considerable research effort because they offer a varying range of half-lives and positron energies, making them useful for diagnostic imaging and / or targeted radiotherapy. Among the isotopes of copper, copper -64 was more suitable for therapeutic purposes. Copper -64 ($T_{1/2}$ = 12.7 hrs), β^+ 0.653MeV (17.8%) β^- 0.578MeV (38.4%) EC (43.8%) has decay characteristics that allow for positron emission tomography (PET) imaging and targeted radiotherapy of cancer. The 12.7hours half-life of ^{64}Cu provide the flexibility to image both smaller molecules, larger and slower clearing proteins. Copper-64 was produced in large scale using cyclotrons based on the reaction of ^{64}Ni (p,n) ^{64}Cu. Also the half live of 12.7hrs is ideal for the purposes of nuclear medicine, as it allows for experiments extending over several days, yet is short enough to limit the patient's exposure. Nuclear model calculation was performed for the reactions of ^{64}Zn (n,p) ^{64}Cu within the energy range of 0-20MeV , ^{64}Ni (p,n) ^{64}Cu within the energy range of 1-25MeV and ^{66}Zn (d,α) ^{64}Cu within the energy range of 1-200MeV using EXFOR code and compared it with ENDF/B-VIII. ^{64}Cu provide higher image quality than other isotopes of copper hence it is more suitable in PET.

Keywords: ^{64}Cu, positron emitters, nuclear model calculations

Introduction

The Nuclear medicine is the use of radioactive materials in diagnostic or therapeutic procedures, most notably treatments for various forms of cancer, heart disease, gastrointestinal, endocrine, neurological disorders and other abnormalities within the body. Because nuclear medicine procedures are able to pinpoint molecular activity within the body, they offer the potential to identify disease in its earliest stages as well as a patient's immediate response to therapeutic interventions (Geiger *et al., 1909).* Diagnostic procedures generally involve the use of relatively small amounts of radioactive materials to facilitate imaging of certain organs to help physicians locate and identify tumors, size anomalies, or other physiological or functional organ problems. Therapeutic uses of radioactive materials typically are intended to kill cancerous tissue, reduce the size of a tumor, or reduce pain.

Nuclear medicine is a medical specialty that uses radioactive tracers (radiopharmaceuticals) to assess bodily functions and to diagnose and treat disease. Specially designed cameras allow doctors to track the path of these radioactive tracers. Single Photon Emission Computed Tomography or SPECT and Positron Emission Tomography or PET scans are the two most common imaging modalities in nuclear medicine (*Chadwick, 1932).* The beta emission which is positively charged could be shown as below.

$$ {}_{1}^{1}p \rightarrow {}_{o}^{1}n + {}_{1}^{0}\beta \quad (1) $$

$$ {}_{Z}^{A}X_{parent} \rightarrow {}_{Z-1}^{A}X_{daughter} + {}_{1}^{0}\beta_{positron}^{+} \quad (2) $$

The history of nuclear medicine is rich with contributions from gifted scientists across different disciplines in physics, chemistry, engineering, and medicine. The multidisciplinary nature of nuclear medicine makes it difficult for medical historians to determine the birth date of nuclear medicine. This can probably be best placed between the discovery of artificial radioactivity in 1934 and the production of radionuclides by Oak Ridge National Laboratory for medicine related use, in 1946 (Edward, 1979).

The origins of this medical idea date back as far as the mid-1920s in Freiburg, Germany, when George de Hevesy made experiments with radionuclides administered to rats, thus displaying metabolic pathways of these substances and establishing the tracer principle. Possibly, the genesis of this medical field took place in 1936, when John Lawrence, known as "the father of nuclear medicine", took a leave of absence from his faculty position at Yale Medical School, to visit his brother Ernest Lawrence at his new radiation laboratory (now known as the Lawrence Berkeley National Laboratory) in Berkeley, California. Later on, John Lawrence made the first application in patients of an artificial radionuclide when he used phosphorus-32 to treat leukemia (*Chadwick, 1932).* More recent developments in nuclear medicine include the invention of the first positron emission tomography scanner (PET).

Specifically, PET studies evaluate the metabolism of a particular organ or tissue, so that information about the physiology (functionality) and anatomy (structure) of the organ or tissue is evaluated, as well as its biochemical properties (*Hilgers et al., 2010).*

Figure 1: PET machine (*Hilgers et al., 2010).*

The concept of emission and transmission tomography, later developed into single photon emission computed tomography (SPECT), was introduced by David E. Kuhl and Roy Edwards in the late 1950s (Geiger *et al., 1909).* Hence, this study is in a bid to determine baseline date of ^{64}Cu used in PET as well as SPECT imaging exploring the nuclear data code in EXFOR.

THEORETICAL BACKGROUND

According to Laforest (2005), the excitation function of the reaction ^{64}Zn (n,p) ^{64}Cu was measured within the energy range of 13.63MeV to 14.73MeV using neutron generator reactor of the institute of experimental physics. In his finding he used NUDAT code to evaluate the theoretical data of ^{64}Cu, he concluded that among all the isotopes of copper, ^{64}Cu was best used in PET.

According to Calson (2001), he also did simplier work with Laforest (2005) where he bombarded neutron with Nickel-64 yielding copper-64 as product and proton within the energy range of 3-10MeV using ALICE-IPP. In his finding, he compared the theoretical data ^{64}Cu and the measured data from ENDF.

The table below shows various isotopes of copper with their half-life, beta decay, electron capture, positron emission.

Table 2.1: Showing different isotopes of copper

Isotope	Half life	β^- (MeV)	β^+ (MeV)	β^+ intensity (MeV)	EC(%)	γ(MeV)	γ intensity (%)
^{60}Cu	23.7 min		1.91 1.98 2.95 3.77 (2.94)	11.6 49 15 5	7.2	0.511 0.826 1.33 1.79 3.12	185 21.7 88 45.4 4.8
^{61}Cu	3.3 h		0.93 1.22 (1.16)	5.5 5.1	36	0.283 0.373 0.511 0.656 1.19	12.2 2.1 123 10.8 3.7
^{62}Cu	9.67 min		2.93	97.2	2	0.511 0.511	195 35.2
^{64}Cu	12.7h	0.579	0.65	17.6	40	1.35	0.5

According to Lewis *et al*., 1999 Copper-64 is potentially useful for not only tumor imaging but also tumor therapeutics. In these radiotracers, the amount of annihilation γ- rays following to β^+ decay yields higher image quality in Cu PET imaging unless saturation of the detector occurs. Lewis et al., 2008 reported that ^{64}Cu-ATSM appeared to have a higher image quality than ^{60}Cu-ATSM in cancer of the uterine cervix. However, the high-energy positron and gamma emissions of ^{60}Cu, compared to ^{64}Cu, are the greatest disadvantages of using ^{60}Cu as a PET imaging agent. In addition, they did not consider that true coincidence events between ^{60}Cu- and ^{64}Cu-ATSM imaging should be adjusted, although the radiation doses of the two radiotracers were the similar in whole body imaging. Instead of ^{60}Cu, ^{62}Cu-ATSM has been utilized because ^{62}Cu-ATSM generates ^{62}Zn/^{62}Cu and it is less expensive.

Laforest, 2005 compared ^{18}F and ^{64}Cu, he made a conclusion that the two radiotracers of tumour hypoxia may be obtained with an easy and safe radiolabelling procedure in sufficient amount for clinical practice. In terms of isotope physical properties, fluorine-18 and copper-64 present the same maximal positron energy, which results in similar close intrinsic image resolution. However, copper-64 presents a longer half-life, which permits easier logistics for PET centres distant from the production cyclotron. Copper-64 production is accessible to a large number of medical

cyclotrons that have the possibility to irradiate solid targets. The major drawback of copper-64 is the associated emission of β^- (38.5%), which associates ^{64}Cu-ATSM with a less favourable dosimetry in comparison to ^{18}F-FMISO.

Copper-64 is the only copper isotope that possesses all three decay modalities, and it has a half-life (12.7 h) favorable for biological studies. The detailed decay scheme of copper-64 is shown in Fig. 2.1 it can undergo electron capture (EC) and β+ emission to nickel-64, and β– emission to zinc-64. Both daughter nuclides are stable.

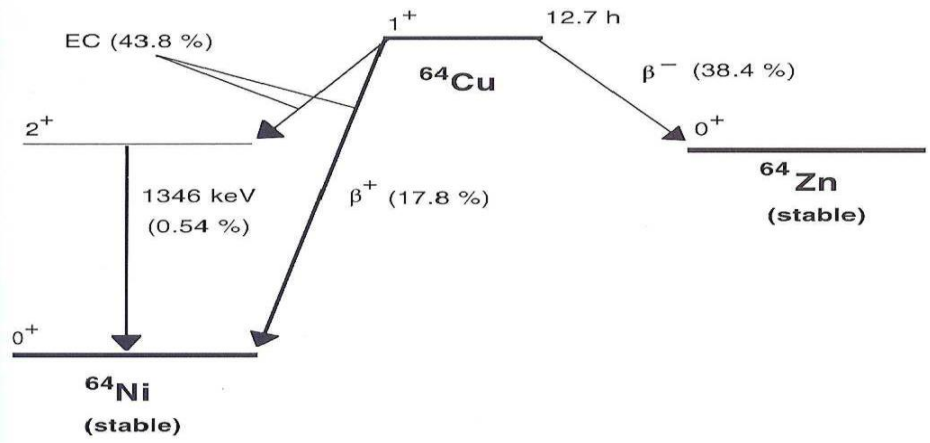

Fig 2.1 : Decay scheme of copper-64 (Qaim *et al*., 2007).

Copper-64 ($T_{1/2}$ = 12.7 hours; β^+, 0.653 MeV [17.8 %]; β^-, 0.579 MeV [38.4 %]) has decay characteristics that allow for positron emission tomography (PET) imaging and targeted radiotherapy of cancer. The well-established coordination chemistry of copper allows for its reaction with a wide variety of chelator systems that can potentially be linked to peptides and other biologically relevant small molecules, antibodies, proteins, and nanoparticles. The 12.7-hours half-life of ^{64}Cu provides the flexibility to image both smaller molecules and larger, slower clearing proteins and nanoparticles (Kalka *et al.*,1990*)*. In a practical sense, the radionuclide or the ^{64}Cu-radiopharmaceuticals can be easily shipped for PET imaging studies at sites remote to the production facility. Due to the versatility of ^{64}Cu, there has been an abundance of novel research in this area over the past 20 years, primarily in the area of PET imaging, but also for the targeted radiotherapy of cancer. The biologic activity of the hypoxia imaging agent, $^{60/64}$Cu-ATSM, has been described in great detail in animal models and in clinical PET studies. An investigational new drug application for ^{64}Cu-ATSM was recently approved by the U.S. Food and Drug Administration (FDA) in the United States, paving the way for a multicenter trial to validate the utility of this agent, with the hopeful result being FDA approval for routine clinical use (Calson,2001*)*. Nuclear data is information describing the properties of atomic nuclei and the fundamental physical relationships governing their interaction (Kalka *et al*.,1990*)*. It is also referred to as the quantitative results of any scientific investigation of nuclear properties of matter, nuclear physical data, or nuclear constants (Edward, 1979). These data is characterized by fundamental physical processes which underline all nuclear technologies (Jonah, 2004).

SIGNIFICANCE OF NUCLEAR DATA

Nuclear data play an important role in the production and the application of medical and industrial radioisotopes (ANISTA, 2014). Out of the basic nuclear data, the activation cross sections and the related production yields are also requested (Friedman, 1980). These data can be obtained

experimentally and/or by using nuclear reaction computer codes like NUDAT, Tally's but we are restricted to EXFOR computer code (IAEA, 2004). The significance of the experimental data is to give direct information for the production of radionuclide and their contribution to the development of nuclear reaction model code (Herman, 1993).

BINDING ENERGY

Binding energy is the amount of energy essential to separate a particle from a system of particles or to scatter all the particles of the system. **Binding energy** is particularly appropriate to subatomic particles in atomic nuclei, to electrons bound to nuclei in atoms, and to atoms and ions bound together in crystals (*Jonah, 2004).*

When two nucleons are bound together into a nucleus and a certain mass disappears, it is converted into energy which is known as Nuclear binding energy. In order to break the nucleus into its constituent particles, the same amount of energy is required for this purpose. Nuclei are made up of protons and neutron, but the mass of a nucleus is usually less than the sum of the individual masses of the protons and neutrons which makes it up (*Talou et al., 2004)*. The difference is a measure of the nuclear **binding energy** which holds the nucleus jointly. This **binding energy** can be determined from the Einstein relationship: **Nuclear binding energy**$= \Delta mc^2$**.** Nuclear **binding energy** is the energy needed to separate an atomic nucleus totally into its constituent protons and neutrons, or, consistently, the energy that would be liberated by combining individual protons and neutrons into a single nucleus. For example, the hydrogen-2 nucleus, which is made up of one proton and one neutron, can be alienated entirely by providing 2.23 million electron volts (MeV) of energy. On the other hand, when a slowly moving neutron and proton coalesce to form a hydrogen-2 nucleus, 2.23 MeV are released in the form of gamma radiation (*Jonah, 2004)*.

At the atomic level, the *atomic binding energy* of the atom derives from electromagnetic interaction, mediated by photons. It is the energy required to disassemble an atom into free electrons and a nucleus. Electron binding energy is a measure of the energy required to free electrons from their atomic orbits. This is more commonly known as ionization energy. Among the chemical elements, the range of ionization energies is from 3.8939 eV for the first electron in an atom of cesium to 11.567617 keV for the 29th electron in an atom of copper (*Hilgers et al., 2010)*.

At the nuclear level, nuclear binding energy is the energy required to disassemble a nucleus into the free, unbound neutrons and protons it is composed of. It is the energy equivalent of the mass defect, the difference between the mass number of a nucleus and its true measured mass. Nuclear binding energy derives from the nuclear force or residual strong force, which is mediated by three types of mesons. The average nuclear binding energy per nucleon ranges from 2.22452 MeV for hydrogen-2 to 8.7945 MeV for nickel-62 (*Talou et al., 2004)*.

MASS DEFECT

Binding energy is the energy that is lost when a nucleus is created from protons and neutrons. If the total mass of the nucleons (protons and neutrons) that compose an atom is added up, this sum is less than the actual mass of the atom. This missing mass, called the mass defect, which is a measure of the atom's binding energy. It is denoted by 'ΔM'. Mass defect can be determined with the following formula: Mass defect = (unbound system calculated mass) - (measured mass of nucleus), that is (sum of masses of protons and neutrons) - (measured mass of nucleus). As soon as the nucleons are combined together to form a nucleus, there will be a mass defect as they lose a minute amount of mass (Kalka *et al.*,1990*)*.

The mass of the nucleus is always different from the sum of the masses of its constituent. The difference in measured mass M and the mass number is called mass defect.

$$\text{Mass defect } \Delta M = (M - A) \quad (9)$$

Q – VALUE

In nuclear physics , the *Q* value for a reaction is the amount of energy released by that reaction. The value relates to the enthalpy of a chemical reaction or the energy of radioactive decay products. It can be determined from the masses of reactants and products *(Balogun et al., 2003)*. Q values affect reaction rates. Considering the energy conservation of the simple reaction, enables the general definition of *Q* based on mass-energy equivalence, where *K* is kinetic energy, m_i is initial mass and m_f is the final mass:

$$Q = K_f - K_i = (m_i - m_f)c^2 \quad (10)$$

Q-value =mass of the reactant – mass of the product

This can be denoted as

$$\text{Q- value} = (M_A + M_x - M_B - M_y)c^2 \quad (11)$$

A reaction with a positive *Q* value is exothermic, i.e. has a net release of energy, since the kinetic energy of the final state is greater than the kinetic energy of the initial state. A reaction with a negative *Q* value is endothermic, i.e. requires a net energy input, since the kinetic energy of the final state is less than the kinetic energy of the initial state (Kalka *et al*.,1990*)*.

THRESHOLD IN RADIOACTIVITY

In particle physics, the threshold energy for production of a particle is the minimum kinetic energy a pair of traveling particles must have when they collide. The threshold energy is always greater than or equal to the rest energy of the desired particle. In most cases, since momentum is also conserved, the threshold energy is significantly greater than the rest energy of the desired particle and thus there will still be considerable kinetic energy in the final particles (Kalka *et al.*,1990*)*.
Consider particle "a" moving with velocity V toward particle "A" which is at rest.

Particle's "B", "C", "D", etc. emerge.

$$E_{thres} = Q\times\left(1 + \frac{M_x}{M_A}\right) \quad (12)$$

CROSS SECTION

Cross section is the quantitative measure of the probability with which nucleus and other collision processes occur (Hilgers *et al*., 2010). The probability of a particular nuclear reaction occurring is determined by measuring the cross section σ.

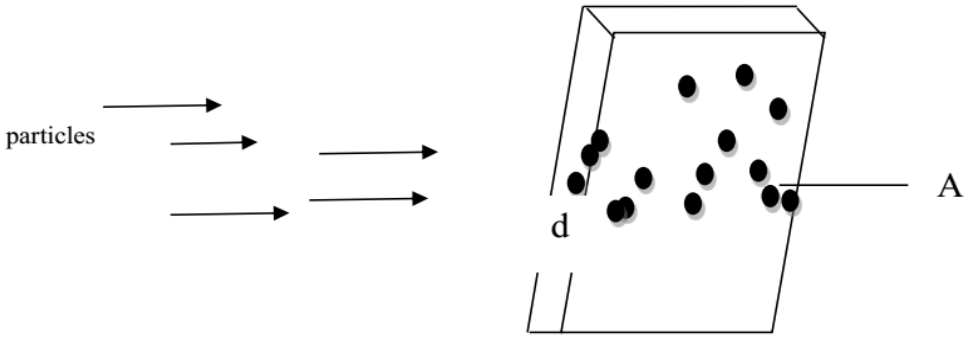

Figure 2.2: Illustration of cross section

$$A_{1=}\, n(Ad)\sigma \tag{13}$$

$$R = R_o \frac{A_1}{A} = R_o \frac{n(Ad)\sigma}{A} \tag{14}$$

$$\sigma = \frac{R}{R_o nd} \tag{15}$$

$$\sigma = \frac{R}{I} \quad \text{(barn or m}^2\text{)} \tag{16}$$

Where σ is cross section

R is the number of reactions per unit time per nucleus

I is the number incident particles per unit time per unit area

A_1 is the total cross-sectional area of all the nuclei of the slab

R_o is the number of particles that strike the slab every second

n is number of nuclei per volume

Materials

The under listed materials below were employed in order to ascertain the nuclear code of Copper-64 for the benefit of nuclear medicine.

a. Proton ^1_1H used in bombarding the projectile (target) and also as product yield.
b. Deuterium ^2_1H used in bombarding the projectile.
c. Neutron ^1_0n used in bombarding the projectile (target) and also as product yield.
d. Alpha particle $^4_2\alpha$ as product yield.
e. Zinc -64 as projectile.
f. Nickel -64 as projectile.
g. Zinc -66 as projectile.
h. EXFOR code

Methodology

The (n,p) Reaction

The cross section of each impurity nuclides with neutron was calculated in (n,p) reaction channel. The (n,p) reaction is an example of a nuclear reaction, it occurs when a neutron enters a nucleus and a proton leaves the nucleus i.e. Zn-64 undergoes an (n,p) nuclear reaction when bombarded with neutron forming Cu-64 and a proton.

Zn-64(n,p) ^{64}Cu

The (d,α) Reaction

The (d,α) reaction is an example of a nuclear reaction, it occur when a deuterium enters a nucleus and an alpha particles leaves the nucleus.

Zn-66(d,α) ^{64}Cu

The (p,n) Reaction

The cross section of each impurity nuclides with proton was calculated in (p,n) reaction channel. The (p,n) reaction is an example of proton induced reaction, it occur when a proton enters a nucleus and a neutron leaves the nucleus.

Ni-64(p,n) ^{64}Cu

EXPERIMENTAL NUCLEAR REACTION DATA (EXFOR) CODE

EXFOR is the library and format for the collection, storage, exchange and retrieval of experimental nuclear reaction data. For an interpretation and validation of our data, nuclear model calculation using EXFOR code was performed.

The EXFOR Data Library is a unified computerized system (Library format) by which International, Regional and National data analysis centers exchange experimental nuclear reaction data. Compilation and exchange of experimental Nuclear reaction data is coordinated by the International Atomic energy Agency (IAEA, 2012). The U.S. version of EXFOR is CSISRS (cross section information storage and retrieval system) also known as exchange formats. EXFOR is online software which can be accessed by any one [user friendly], exchange format for experimental numerical nuclear reaction data presents in a convenient compact form numerical data as well as physical information necessary to understand the experiment and interpret the data. http://www-nds.iaea.org/exfor/

COMPILED PHYSICAL QUANTITIES IN EXFOR:

The compile physical quantities that make EXFOR useful are as follows:
Cross Sections (CS) for (n.X), (p,X), (n, p, X), (N,G)

Resonance Parameters (RP): Energy (EN), Spin/Parity (±J)

Cross Sections Partial (CSP) for (N,P, X)

Fission Yields (FY) for (N,F)

Fission product yields (F,Y)

Double differential Angular-Energy

Thick/Thin Targets, Partial, Differential, Saturated Yields

Outgoing Particles Multiplicity (MLT) for induced (N,F), and spontaneous, (0,F) fission

Cross sections Averaged over incident energy.

Protons (P), Deuterons (D), Alphas (A), 3He (HE3), 3H (T40% (increasing)

Spontaneous Fissions (02%)

neutron-induced reaction (up to 1 GeV)

gamma-induced reaction (up to 1 GeV)

Electrons (E) Energies from Ultra-cold Neutrons (UN) to Protons Energies

RESULTS AND DISCUSSION

The theoretical model code EXFOR was used to determine the excitation function (a graph of cross section against incident energy). The cross section for the Zn-64(n,p) Cu-64 reaction are given in table 4.1, the cross section for the Ni-64(p,n) Cu-64 in table 4.2 and the cross section for the Zn-66(d,α) ^{64}Cu in table 4.3. The investigated reactions are discussed below:

Zn -64(n,p)Cu-64

The excitation function for the Zn-64(n,p)Cu-64 nuclear reaction is shown by closed circles in figure 4.1. Table 4.1 contains the numerical values of the measured cross section and their uncertainties. The result of the excitation function calculation of Zn-64(n,p)Cu-64 is plotted together with experimental data taken from EXFOR data code and evaluated data files ENDF/B-VIII, The value has also been compared with ENDF/B-VIII evaluated library. A reasonable agreement of theoretical excitation function was obtained with an energy range of 0-20MeV.

Table 4.1: Cross section of the Zn-64(n,p)Cu-64 reaction

Projectile energy (MeV)	Cross section (mb)
0.0±0	15±1.60
2.3 ±0	17.34±0.76
2.5 ± 0	30.90±1.30
2.92 ±0	67.30±2.60
3.01± 0	75.90±2.90
3.57 ± 0.1	136±8.4320
4.00±0.08	132.9±3.80
4.28± 0.1	156±9.6720
4.59 ±0.1	154±9.8560
4.7 ±0.1	160±11.36
4.9±0.05	181.6±6.3
5.16±0.1	166±9.296
5.26 ±0.1	165±8.415
5.48±0.1	151±34.73
6±0.065	205.2±7.9
7±0.075	219.5±8.4
8.37± 0.29	23±12
9.37±0.23	251±14
9.9±0.25	249±13
10.4±0.165	249±13

11±0.5	275±17
11.4±0.175	243±12
13.04 ±0.4	218±24
13.32±0	192±12
13.56 ±0	175±11
13.77±0.13	232±9
13.9 ±0.3	190±11
14.11 ±0.13	209±90
14.3± 0.14	200±80
14.5 ±0.3	171±10
14.73 ±0.23	185±80
14.9 ±0	127.4±8.3
15±0.3	159±10
15.4±0.2	138±80
15.9± 0.5	141±18
16.6 ±0.1	148±18
17.99±0.075	61± 8
19.02±0.11	57±5
20±0.5	45±89

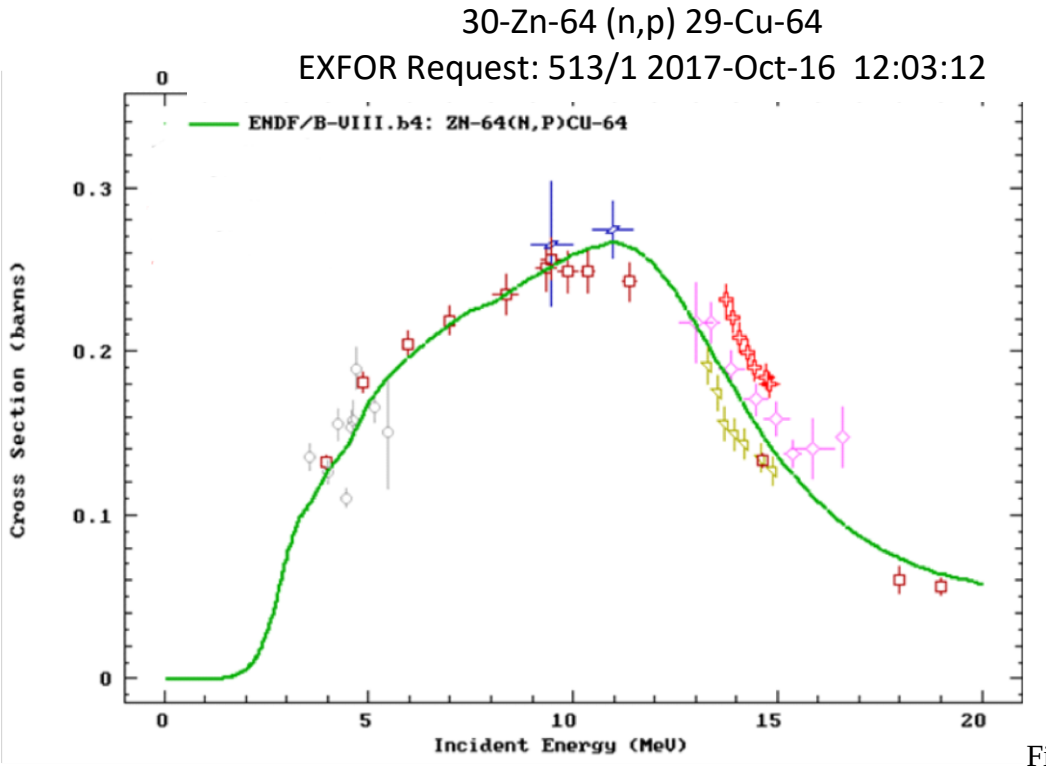

Figure 4.1: Showing the graph of cross section against incident energy of the reaction Zn-64(n,p)Cu-64 using EXFOR, Experimental Nuclear Reaction Data (EXFOR/CSISRS, 2012).

Ni-64(p,n) Cu-64

The excitation function for the Ni-64(p,n) Cu-64 nuclear reaction is shown by closed circles in figure 4.2. Table 4.2 contains the numerical values of the measured cross section and their uncertainties. The result of the excitation function calculation of Ni-64(p,n) Cu-64 is plotted

together with experimental data taken from EXFOR data code and evaluated data files ENDF/B-VIII(no data found), The value has also been compared with ENDF/B-VIII evaluated library and they are not in good agreement with EXFOR code. A reasonable agreement of theoretical excitation function was obtained with an energy range of 1-25MeV.

Table 4.2: Cross section of the Ni-64(p,n) Cu-64

Projectile energy (MeV)	**Cross section (mb)**
1±2.2	2.7±3
3.3±0.3	38±9
3.4±0.7	32±4
3.5±1.8	69±6.9
3.8±0.6	65±8
3.9±0.3	1±14
4.2±0.3	186±22
4.5±0.3	141±17
4.7±1.3	242.3±24.2
5±0.3	198±24
5±0.6	214±27
5.15±0	375±50
5.4±0.6	230±29
5.5±0.3	311±35
5.8±0.3	281±31
6.02±0	275±35
6.2±0.3	360±38
6.2±0.9	397±39.7
6.6±0.3	435±44
6.6±0.6	359±46
6.9±2	529.1±52.9
7.1±0.8	569.3±69
7.2±0.2	473±49
7.6±0.2	520±54
7.8±0.5	475±6
8±0.2	531±54
8.2±0.2	505±52
8.2±0.7	624.9±62.5

8.4±0.2	521±54
8.4±0.5	521±66
8.8±0.2	554±56
8.8±1.6	668.3±66.8
9±0.6	752.5±75.2
9.1±0.2	581±62
9.3±0.5	592±75
9.5±0.2	573±59
9.6±0.5	655±83
9.8±0.2	659±62
10±0.5	792±79.2
10.2±0.2	645±60
10.4±0.4	650±82
10.4±1.3	769±76.9
10.5±0.2	66±68
10.6±0.4	836.7±83.7
10.7±0.4	738±94
10.8±0.2	662±67
11±0.1	657±62
11.3±0.1	661±62
11.3±0.4	656±83
11.5±0.4	712±71.2
11.8±0.4	655±83
11.9±1.1	676.5±67.7
12.1±0.3	610.7±61.1
12.3±0.4	523±67
12.7±0.4	489±62
12.9±0.3	462±46.2
13.2±0.4	365±46
13.3±0.9	454.7±45.5
13.5±0.2	391.8±39.2
14.1±0.3	260±33

14.2±0.2	277.8±27.8
14.3±0.3	263±33
14.5±0.8	276±27.6
14.8±0.2	249.2±24.9
15.3±0.3	180±23
15.5±0.3	182±23
15.5±0.1	191.5±19.2
15.7±0.7	191.5±19.2
16.5±0.3	152±19
16.9±0.6	131.6±13.2
17.6±0.2	145±19
18±0.5	101.4±10.1
18.6±0.2	150±19
19±0.4	81.3±8.1
20±0.4	701±7
21±0.3	604±6
21.9±0.3	56.5±5.6
22.8±0.2	51.7±5.2
23.7±0.2	44±4.4
24.6±0.1	40.5±4.1

Experimental Nuclear Reaction Data (EXFOR/CSISRS, 2012).

EXFOR Request: 513/1 2017-Oct-16 12:53:43

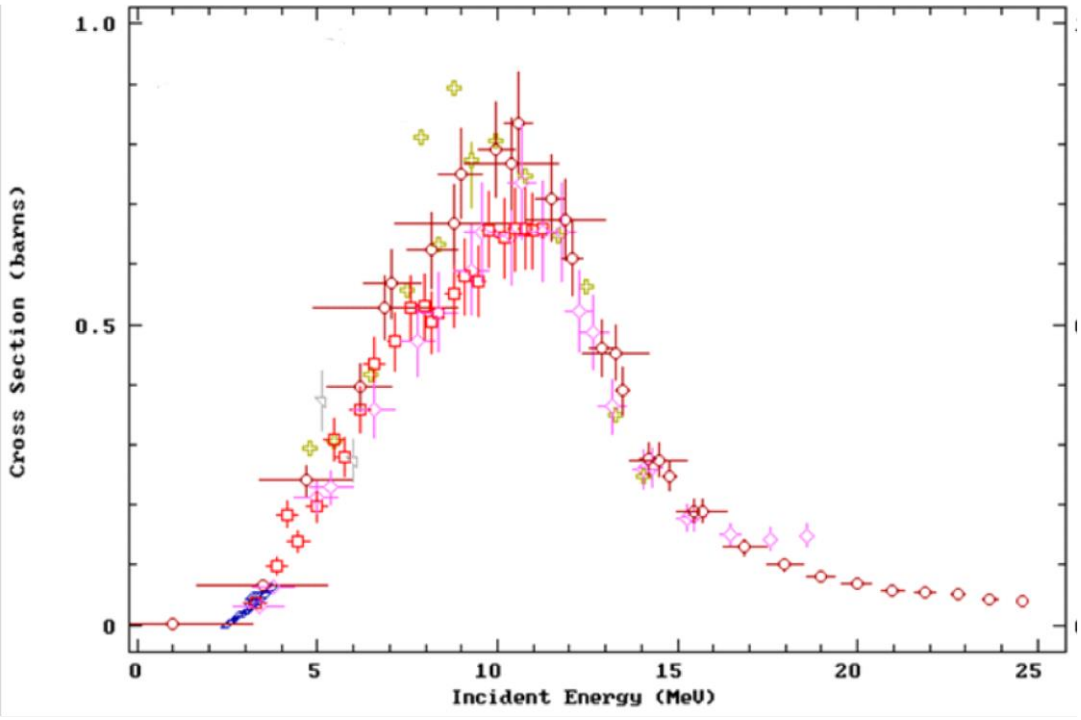

Figure 4.2: Graph of cross section against incident energy of the reaction Ni-64(p,n) Cu-64 using EXFOR code 28-Ni-64 (p,n) 29-Cu-64 Figure 4.2: Graph of cross section against incident energy of the reaction Ni-64(p,n) Cu-64 using EXFOR code 28-Ni-64 (p,n) 29-Cu-64 Experimental Nuclear Reaction Data (EXFOR/CSISRS, 2012).

Zn-66(d,α) ^{64}Cu

The excitation function for the Zn-66(d,α) ^{64}Cu nuclear reaction is shown by closed circles in figure 4.3. Table 4.3 contains the numerical values of the measured cross section and their uncertainties. The result of the excitation function calculation of Zn-66(D,α) ^{64}Cu is plotted together with experimental data taken from EXFOR data code and evaluated data files ENDF/B-VIII, The value has also been compared with ENDF/B-VIII evaluated library and they are in good agreement with EXFOR code. A reasonable agreement of theoretical excitation function was obtained with an energy range of 1-200MeV, at 30MeV-200MeV the cross section remains uniform.

Table 4.3: Cross section of Zn-66(d,α) ^{64}Cu

Projectile energy (MeV)	**Cross section (mb)**
1e-11	0
1	4.79519×10^{-28}
2	5.27005×10^{-28}
3	0.572629
4	1.79826
5	12.665
6	23.8334
7	31.4115
8	35.9548
9	37.7375
10	36.0587
11	31.6341
12	27.1121
13	22.0779

14	18.3896
15	15.6493
16	13.3174
18	10.4506
19	9.55371
20	8.58136
22	7.35237
24	6.37516
26	5.47511
28	4.82227
30	4.19699
30	
	0
200	0

30-Zn-66 (d,α) 29-Cu-64
EXFOR Request: 513/1 2017-Oct-16 01:03:12

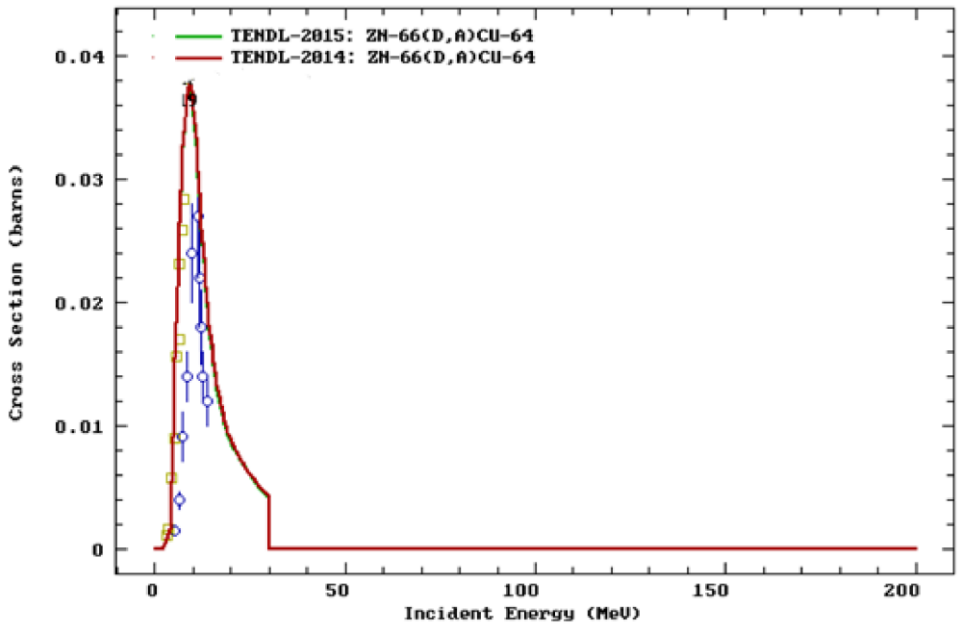

Figure 4.3: Graph of cross section against incident energy of the reaction of Zn-66(d,α) ^{64}Cu using EXFOR
Experimental Nuclear Reaction Data (EXFOR/CSISRS, 2012).
The calculated Q-value and threshold energy for the following equations above are as follows

Q- value of Ni-64(p,n) ^{64}Cu= $(M_A + M_x - M_B - M_y)c^2$

= (63.9298 +1.0073-63.9298-1.0087) × 931Mev

= -0.0014× 931 Mev

= -1.30Mev

This shows the reaction is an endoergic i.e. energy was absorbed in the reaction.

Q-value of ^{64}Zn (n,p) ^{64}Cu = $(M_A + M_x - M_B - M_y)c^2$

= (63.9291 +1.0087-63.9298-1.0073) × 931Mev

=0.0007× 931 Mev

=0.6517Mev

This shows the reaction is an exoergic i.e. energy was released in the reaction.

Q-value of ^{66}Zn (d,α) ^{64}Cu = $(M_A + M_x - M_B - M_y)c^2$

= (65.9260 +2.014-63.9298-4.0026) × 931Mev

=0.0076× 931 Mev

=7.08Mev

This shows the reaction is an exoergic i.e. energy was released in the reaction.

Therefore threshold energy for Ni-64(p,n) Cu-64 was calculated as

E_{thres} = -1.30×$\left(1 + \frac{1.0073}{63.9298}\right)$Mev

= -1.32Mev

E_{thres} for Zn-64(n, p) Cu-64 =0.6517×$\left(1 + \frac{1.0087}{63.9291}\right)$Mev

=0.662Mev

E_{thres} for Zn-66(d, α) Cu-64 = 7.08×$\left(1 + \frac{2.014}{63.9291}\right)$Mev

=7.30Mev

Conclusion

^{64}Cu has decay characteristics that allow for positron emission tomography (PET) imaging and targeted radiotherapy of cancer. Positron emission tomography (PET) is a valuable technique for some diseases and disorder, because it is possible to target the radiochemical used for particular bodily function. It is also a nuclear medicine functional imaging technique that is used to observe metabolic process in the body, tumor is an abnormal growth of cells that serves no purpose in the human body.^{64}Cu can be technically reproduced by several different reaction with the most common method using either reactor or an accelerator. ^{64}Cu is used in medical application in the study of Wilson disease (it is genetic disorder in which copper builds up in the body) and in brain scans for tumor.

The nuclear model calculation of excitation function were performed with EXFOR, data of the excitation function was compared with data from ENDF/B-VIII with the following reactions ^{64}Zn (n,p) ^{64}Cu within energy range of 0-20MeV, ^{64}Ni (p,n) ^{64}Cu within the energy range of 1-25MeV and ^{66}Zn (D,α) ^{64}Cu within the energy range of 1-200MeV. From this study it may be concluded that copper-64 provide higher image quality than the other isotopes of copper which is best used in PET imaging.

References

Anista, D.A. (2012). Australian nuclear science research and technology. Agency Health implication of radioisotope and prospect for the uses of nuclear energy.pp3-4.

Balogun G.I.,Garba, H.B., Umar, I.M., Oladipo, O.A., Egun, P.M., and Ewa, I.O.(2003) "Nuclear model calculation on the excitation function of neutron induced reaction". *Journal of nuclear physics*, 7(13).97-100.

Balraj , M.S. (2012). Nuclear Instruments & Methods in Physics Research Report of IAEA. pp 171.

Bernard, L.C (1971). Concept of Nuclear Physics. Tata.McGraw-Hill.New Delhi pp. 57- 105.

Bisinger , S.M., Hilgers, K.T., Nayak, D.G. and Coenen, H.H. (2007) .Positron emission intensities in the decay of 64Cu, 7Br and 124I, Radiochim. pp 67–69.

Bromley, N.B. (2012). "Copper -64 radiopharmaceuticals for Pet imaging of cancer". *International nuclear physics journal*, 3(2). 11-16.

Calson, B.V. (2001). "A brief over few of models of nucleon induced reaction". *Journal of work shop on Nuclear Data Science and Technology*, 6(1). 44-56.

Chadwick, W.A. (1932). "Introduction to PET and SPECT". *Journal of nuclear physics*, 1(2). 12-14.

Coppellaro P.T (2012). "Introduction to applied nuclear physics spring". *Journal of science and engineering department MIT*, 2(1) .43-98.

Dale, T.Z. (1985). "Comparison of image quality with 64Cu and 62Cu labeled radiotracters in PET". Nuclear medicine journal, 5(4). 45-74.

Dehdashi, T.R, Krane, M.O., David, R.S., and Friday, R.E. (2003). "Medical radioisotopes production without a nuclear reactor". *Phy Med Biol*, 4(3). 112-115.

Edward, Y. (1979). "Neutron induced reaction on 64Cu". *International journal of nuclear medicine*, 3(1).1-2.

EXFOR/CSISRS. (2012). Experimental Nuclear Reaction Data http://www-nds.iaea.org/exfor/

Fowler, D.A. (1991). "Radionuclide production". *Phy Med Biol*, *3*(2). 14-17.

Friedman, F.G. (1980). "Production and clinical application of radiopharmaceutical and medical radioisotopes". *Phy Med Biol*, 25(1). 103-115.

Friobrich, P.K. and Lipperheide,R.B.(2001) Theory of Nuclear Reactions,Oxford University Press, Oxford.pp 21-65.

Fujibayashi, R.A., Bonte, Y.T., Roland, C.Z., Bailey, R.F., Qaim, G.H. and Roderson, J.K. (2006). Nuclear physics and radioactivity. University press. pp 45-64.

Gaur, R.K. and Gupta, S.L. (2005). Engineering physics university publisher. pp 13-20.

Geiger, T.U., Shedrack, R.E., Francis, J.K., and Anthony, G.R. (1909). Nuclear physics. University press. pp 56-72.

Green, H.K., Roland, T.D., Edward, G.C. and Roderson, Z.A. (1988). A personal history of nuclear medicine. University press. pp 45-53.

Hassan, R.E., Francis, B.C., Johnson, H.Y. and David, P.G. (2010). Introduction to radioactivity. *International press.* pp 11-34.

Hende, R. A. and Edwad, J.K. (1996). *Charged-Particle Cross Section Database for Medical Radioisotope Production.* http://www-nds.iaea.or.at/ndspub/rnal/www/

Herman, F.L. (1993). Theoretical Nuclear Physics, Nuclear Reactions New York Publishers. pp 54.

Hilgers, K.Y., Stoll, T.D., Skakun, Y.P, Coenen, H. H. and Qaim, S.M. (2010).Cross-section measurements of the nuclear reactions. University press publishers. pp 5-12.

Hughes, D.J. (1957). Nuclear Energy Oxford University Press London.pp 22-56.

Hughes,D.J. (1978). Neutron Cross Sections International Series of Monographs on Nuclear Physics Perganon Press New York.pp 80-110.

Inguar, K.L., Davidson, R.E., Edward, C.S., Michael, D.J. and Richard, L.H. (1974). "Application of radioactive isotopes in industry, science and agriculture". *Atomic energy journal*,7 (1). 9-15.

International atomic energy agency (IAEA,2004).

International atomic energy agency (IAEA,2012).

Jonah, S.A. (2004). "Shell Structure Effect in Neutron Cross Section Calculation by theoretical Model Code", *Nigerian journal of Physics* 16 (2). 8-10.

Jonah, S.A. (2005) Fission Neutron-induced analytical Sensitivities and Interference factors in N.A.A. with MNSR Reactors C.E.R.T. Abu. Zaria.pp 29-40.

Jonah, S.A., Liaw, J.R., and Matos, J.E. (2007). Monte Carlos simulation of Core PhysicsParameters of the Nigeria. Research Reactor – 1 (NIRR 1) SCIENCE Direct Annuals of Nuclear energy. pp 34

Kalka, H.T., Torgman, J.L., Lien, H.N., Lopezs, R.K. and Seegler, D. (1990). "Description of (n p) and (n 2n) Activation Cross Section for Medium Mass Nuclei within Statistical Multi Theory". *Journal of International atomic energy agency,* 1(4) 163 – 171.

Laforest, K.P. (2005). "A glance at the history of nuclear medicine". *Phy Med Biol*, 4(3). 111-116.

Lawson, E.T. (1999). A textbook of radiology and industrial radiography. University press. pp 23-27.

Lewis, F.D., Itogo, E.W., Edward,C.Z., Lilley, B.C., Richard, G.J. and Ramson, Z.Y. (1999). Nuclear medicine physics. A handbook for teachers and student. pp 23-67.

Meshik, D.K. (2005). "The working of an ancient nuclear reactor". *Scientific American journal,2*(1). 13-25.

Okazawa, L.M., Stern, N.B., Henderson, T.E. and David, R.S. (2008). Fully three- dimensional positron emission tomography. American publishers. pp 43-55.

Pierre, M. W and Sheldon, E.Y (1971) .Physics of Nuclei and Particles. Academic Press Inc. London. pp 56-70.

Qaim, S.M. (2005). Nuclear data for the production of therapeutic radionuclide. International atomic energy agency (IAEA) press. pp 45-51

Schwerer, O.E. and Lemmel H. D. (1996) Co-ordination of the nuclear reaction data centers. INDC(NDS)-360 Distr. G, NC., IAEA, Vienna, Austria. pp 31.

Svoboda, O.D. (2011). Experimental Study of Neutron Production and Transport Faculty of Nuclear Sciences and Physical Engineering press. pp 44.

Talou, P.G., Chadwick, M.B., Dictrech, F.M., Herman,T.A. and Kawanu, A. K. (2004) "Sub Group A Nuclear Model Codes". *Report of the Sixteenth Meeting of the WPEC,* 1(2) 26 – 28.

Uhl, M.E. and Strohmaier, B.F. (1976) Computer code for particle induced activation cross section and related quantities. *IRK Report,* Vienna, Austria.9(3). 23-31.

Measurement of Signal Powers and Path Loss Predictions of Ibrahim Badamasi Babangida University Lapai Click FM (89.9 MHz) Within the Main Campus

Jibrin, A.Y[1*]., Ndanusa, B[1]., Muhammad, A.B[1]., Dauda, S. U[2]., Muhammad, B.L[1]., Mohammed, I. K[3]., and Danjuma, A.B[4].

[1]Department of Physics, Ibrahim Badamasi Babangida University, Lapai, Niger State, Nigeria

[2]Department of Electrical Engineering, Federal University of Technology, Minna, Nigeria

[3]Department of Physics Federal University of Technology, Minna, Nigeria

[4]Department of Physics, College of Education Minna, Niger State, Nigeria

* Corresponding author: jibrinyabagi@ibbu.edu.ng jibrinbida@yahoo.com alajbm222@gmail.com

ABSTRACT

Several factors affect radio propagation. These factors are determined by its path from point of propagation to the point of reception. Therefore, there arises the need to measure the received signal power at points away from the transmitter base in order to reduce these effects. The measurements of the signal power of 89.9 MHz Ibrahim Badamasi Babangida University Campus Click FM Radio was conducted along four profiles, namely Profile A (along 250 Hall), Profile B (along ICT Centre), Profile C (towards Entrepreneurship Centre) and Profile D (towards the Senate Building). Five measurements were considered with intervals of 50m away from the base station successively for each profile. An Agilent handheld spectrum analyzer, GPS receiver tape rule and a mobile receiving antenna were used for the measurements. It was observed that the signal strength – Line of Sight distance (LOS) characteristics were very similar in each of the four routes and that the little variation among them was due to environmental factors such as vegetation and buildings. In most cases, the signal power reduces with an increase in distance, and therefore, the path loss prediction was made using the Free Space Path Loss Model, Ericsson Model and Lee's Model. The highest losses were 237.5 dB, 265.5 and 214.00 dB for Free Space Path Loss Model, Ericsson Model and Lee's Model respectively while the lowest losses were 225.5 dB, 224.1 dB and 189.8 dB respectively. The contour map was also developed. The studies recommend that the radio frequency of the station and the transmitting antenna height should be increased.

Keywords: contour map, line of sight, path loss, signal power

1. Introduction

A radio wave is an electromagnetic wave which emanates from a radiating source (Bakare *et al.*, 2019). Radio waves propagating through space undergo loss of power or path loss. There is usually a reduction in the quality of wireless signal when there are blockages or obstacles like buildings within their line of sight. This is because the signal line of sight is being obstructed by these obstacles. As such, some of the signal quality will be lost because of these obstacles (Elechi,2016). These radio waves travel from transmitter to receiver in three types of modes known as radio propagation modes namely; Ground Surface wave, Tropospheric or Space wave and Ionospheric or sky wave (Lodro, 2016). The space wave that travels on the line of sight from the transmitter

through the troposphere transmits signal on the Ultra High Frequency broadcast band (Akinbolati *et al.,* 2018). The direct transmitted, reflected or refracted waves are the signal that would be received at some locations away from the transmitter (Ugweje, 2017). Path loss or path attenuation is the reduction in power density (attenuation) of an electromagnetic wave as it propagates through space (Akpaida, *et al.,* 2018.). Path loss in wireless communication is the unwanted reduction in signal power that occurred between the transmitter and receiver. This path loss can be measured in different areas such as urban, suburban and rural areas by using suitable propagation path loss models. These propagation models can generally be classified into three main types; the empirical, deterministic and stochastic (Crane, 1980). Path loss normally includes propagation losses, absorption losses and diffraction losses. Propagation losses are caused by the natural expansion of the radio wave front in free space which usually takes the shape of an ever-increasing sphere. Absorption losses (sometimes called penetration losses) are caused when the signal passes through media not transparent to electromagnetic waves. Diffraction losses are caused when part of the radio wave front is obstructed by an opaque obstacle (Sahoo *et al.,* 2011).

Path Loss Models

Different propagation models have been developed to predict the propagation of radio signals in the atmosphere (Klima *et al.*, 2005). The semodels considered factors affecting the propagation of radio waves and are significant in the determination of the primary and secondary coverage areas for Broadcasting Stations (Groskopf, 1991). For this application, the Free Space Path Loss Model, Ericsson Model and Lee's Model were used comparatively.

Free Space Path Loss (FSPL) Model

This model determines the signal attenuation that would result if all absorbing, diffracting, obstructing, refracting, scattering and reflecting influences are well eliminated in order not to have effect on the propagation. The FSPL Model is given by

$$L = 20\log_{10} d + 20\log_{10} f + 32.45 \quad (1)$$

where, d is the line of sight (LOS) distance away from the transmitter in meters (m), f is the frequency of the wave in Giga Hertz (GHz) and L is the path loss in decibel (dB).

Ericsson Model

This model was provided by Ericsson company and used by network planning engineers. It is the modified form of Okumura – Hata model that allows the changing of parameters according to the environment. Path loss can be calculated using the Ericsson model provided in equation 2 (Milanovic *et al*., 2007).

$$L = a_0 + a_1 \log_{10}(d) + a_2 \log_{10}(h_b) + a_3 \log_{10}(h_b)\log_{10}(d) - 3.2[\log_{10}(11.75h_r)^2] + g(f) \quad (2)$$

where; f is the frequency in MHz, h_r is the Height of the receiving antenna (m), h_b is the Height of the transmitting antenna (m).

$g(f)$ is given by the following in equation 3 (Milanovic *et al*., 2017).

$$(f) = 44.49\log_{10}(f) - 4.78[\log_{10}(f)]^2 \quad (3)$$

The parameters a_o, a_1, a_2 and a_3 for their respective terrains are given in Table1 (Milanovic *et al.*, 2017).

Table 1: Parameters Values for Ericsson Model

Environment	a_o	a_1	a_2	a_3
Rural	45.95	100.6	12	0.1
Suburban	43.90	68.63	12	0.1
Urban	36.20	30.20	12	0.1

Lee's Model

Lee proposed a path loss equation for the radio frequency propagation channel (Bejide *et al.*, 2017). This model is given equation 4.

$$L = 40\log_{10} d - 20\log_{10} h_r h_t \quad (4)$$

where, d is distance (km), h_r and h_t are receiving and transmitting antenna heights respectively.

This paper, therefore, measures the signal powers and predicts the path loss of radio frequency signal of IBB Click FM (89.9MHz) at different locations.

2. Methodology

2.1 Materials

The instruments and materials used in the course of this research were N9342C Handheld Spectrum Analyzer made by Agilent Technologies with a frequency range of 100 kHz –7.0 GHz, Garmin eTrex 10 GPS receiver, Century TV Receiving Antenna with model number WA - 5020TG-C of AC 16 V, 50 Hz, 3 W and TapeRule.

2.2 Methods

Four profiles were chosen around the Radio Station; Profile A (towards 250 Hall), Profile B (along School ICT Center), Profile C (towards Entrepreneurship Centre) and Profile D (towards the Senate Building). Five points of measurements were marked with a separation of 50 m along each of these four profiles.

2.3 Collection of Radio Station's Information

Relevant information was collected from the radio station under study and tabulated in Table 2.

Table 2: Important Parameters

Parameter	Value
Name	IBBU Click FM
Frequency	89.9 MHz
Transmitting Power	150 W
Height of transmitting antenna	50 m
Height of receiving antenna	1.45 m

2.4 Measurement of the Signal Power

The signal powers were measured along each of the selected profiles from point to point. At each point, the latitude, longitude and elevation above the sea level were also measured.

2.5 Development of Contour Map

The station's contour map was developed from the Latitude, Longitude and Signal power values at the various points of measurements.

3. Results and Discussion

Table 3 shows readings for signal powers received at different points within the school's main campus. The measurements were taken twice only in free space at various points, the two values' average was calculated to obtain higher accuracy. A tabular representation of values was made for line of sight distance and measured signal powers along the four profiles. Graphical representation was also made.

Table 3: Received Signal Powers

S/N	LOS Distance (m)	Received Signal Power (dBm)			
		Profile A	Profile B	Profile C	Profile D
1	0	- 21.64	-21.64	-21.64	-21.64
2	50	- 33.54	-52.02	-72.84	-65.87
3	100	- 36.36	-61.37	-66.31	-64.37
4	150	- 51.35	-65.81	-66.40	-71.75
5	200	- 63.33	-64.66	-74.84	-72.43

Table 3 shows the overall results for the received signal powers whose measurements were taken for five points with 50 m intervals between them along the four profiles, namely Profile A, Profile B, Profile C and Profile D with their corresponding line of sight distances away from transmitting antenna. Table 3 is represented graphically below.

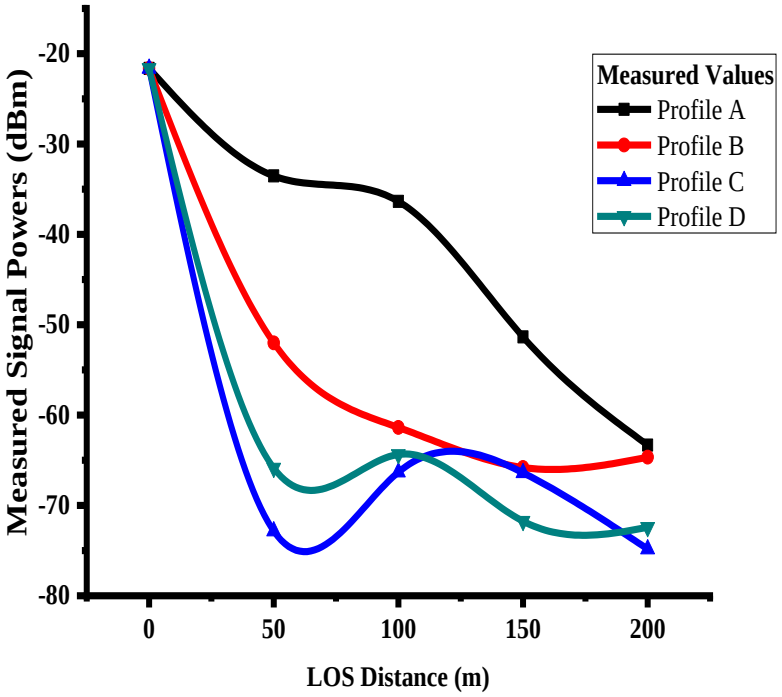

Figure 1. Graphical Illustration of the Measured Signals

From the above, the signals were seen to vary with distances and do not follow a regular pattern of variation; meaning that, factors such as vegetation and wave properties might have affected the effective transmission of the radio signals and led to variations signal reception at each point. At some instance and in most cases, the signal varies with distance. Close to the base station, the signal powers which are negative values (in dBm) were seen to be closer to zero which means that the signal strength is higher at those points. Moving away from the base station, the signal loss rises, meaning that less signals were received there. The overall signal power received have been illustrated graphically in the above Figure 1.

3.1 Contour Map of the Location

The contour map generated from the Latitude, Longitude and Signal power values at the various points of measurement is shown in Figure 2.

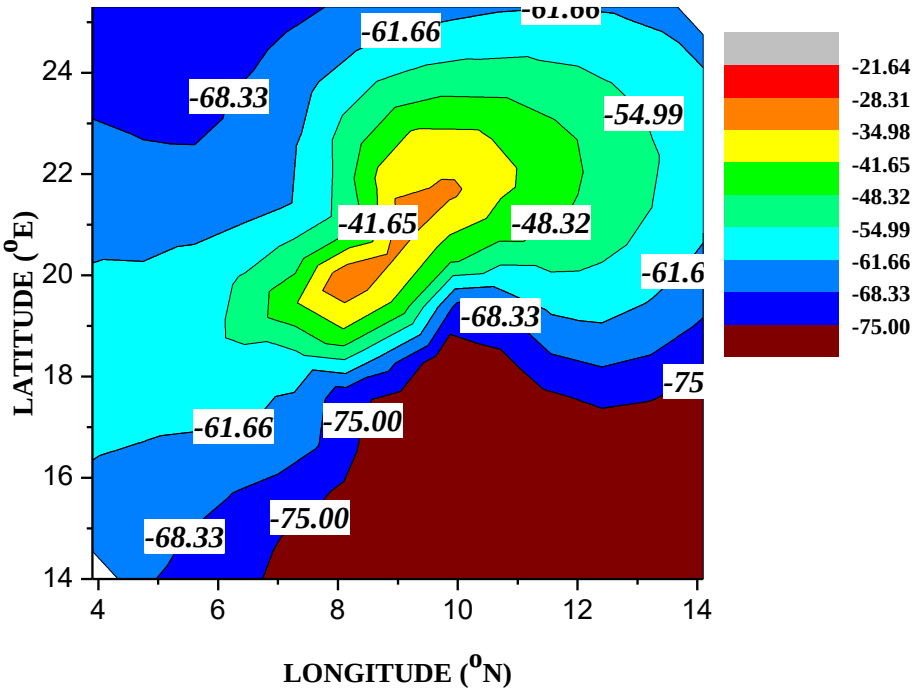

Figure 2. Contour Map of the Location

3.2 Path Loss Predictions

The path losses of the radio frequency signals were calculated using the FSPL Model, Ericsson Model and Lee's Model by equations 1, 2 and 4, respectively. The calculated path losses are shown in Table 4. Consequently, the values are illustrated graphically in Figure 3.

Table 4: Path Losses Predictions

LOS Distance	Path Loss Predictions		
	FSPL Model (dB)	Ericsson Model (dB)	Lee's Model (dB)
0	-	-	-
50	225.5	224.1	189.8
100	231.5	244.8	201.8
150	235.0	256.9	208.9
200	237.5	265.5	214.0

Table 4 shows path losses at each point away from the transmitting antenna for each of the two selected models.

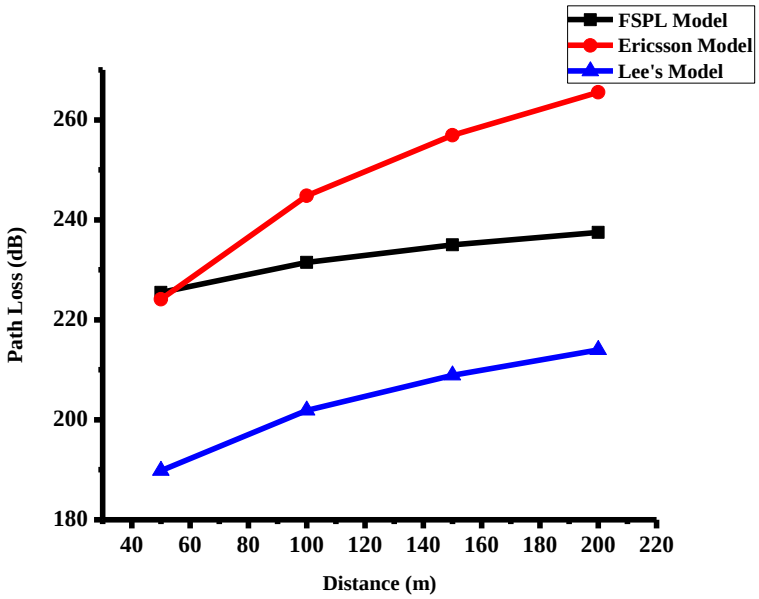

Figure 3. Path loss – LOS Graph

3.3 General Discussion

Table 3 and Figure 1 show readings for signal powers received at different points within the school's main campus. The measurements were taken only in free space.

It can be seen from the results of the signal power measurements along the four profiles that in most cases, the signal powers received by the receiving antenna decreases with an increase in distance away from the transmitting antenna. However, in all cases, the decrease was not equal and, in some cases, do not depend on the distance. Factors such as elevation above the sea level, building obstructions, vegetation and other environmental factors influence the signal receptions and cause signal loss too. However, the effect of distance seems to be more. Thus, this justifies the use of FSPL Model, Ericsson Model and Lee's comparatively. The highest and lowest path losses were recorded from Ericsson and Lee's model respectively. FSPL Model is more suitable for a very clear LOS scenario.

4. Conclusion

This research work was to determine the path loss of 89.9MHz IBB University Click FM and to examine the amount of signal reception at points away from the signal transmitting antenna. The research was carried out as expected, and it was observed that Profile C and D recorded the highest signal losses while Profile A and B recorded lower signal losses. With the analysis of readings obtained, the chosen models for study of the radio station's path-loss were comparatively, the FSPL Model, Ericsson Model and Lee's Model. The path losses were also illustrated graphically for better understanding which is, of course, the goal of the research.

Acknowledgements

The authors gratefully acknowledge Department of Physics Ibrahim Badamasi Babangida University, Lapai, Click FM IBBUL and Department of Telecommunication Engineering Federal University of Technology Minna, Nigeria for the logistic support of this research work.

References

Akinbolati, A., Femi-jemilohun, O. J., & Tikyaa, E. V. (2018). *Path Loss Modeling Suitable for Macro Cell Prediction for Analogue Decimetric Waves in Ekiti State, Nigeria.*FUDMA Journal of Sciences (FJS), 2(3), 250–255.

Akpaida,V.O., Anyasi, F.I., Uzairue, S.I, & Idim, A.I. (2018). *Determination of an Outdoor Path Loss Model and Signal Penetration Level in Some Selected Modern Residential and Office Apartments in Ogbomosho, Oyo State, Nigeria.* Journal of Engineering Research and Reports, 1(2): 1 – 25.

Bakare, B.I., Nwakpang, F.M. & Desire, A.E. (2019). *Propagation Analysis of Radio Frequency (RF) Signal of Love FM Transmitter in Port Harcourt, Nigeria.* IOSR Journal of Electronics and Communication Engineering, vol.14(2), pp. 05 – 12.

Bejide, O.V., Onumanyi, A.J., & Onwuka, E.N. (2017). *Empirical Pathloss Models for the 802.11a/b/g Propagation Channel at the Bosso Campus of the Federal University of Technology, Minna.* International Engineering Conference (IEC).

Crane, R.K. (1980). *Prediction of Attenuation by Rain.* IEEE Transactions on Communications, Vol.28, pp.1727-1732.

Elechi, P. (2016). *Investigation of GSM Signal Loss in Multi-Storey Building.* Proceedings of International Conference and Exhibition on ICT & Telecommunication, December.

Grosskopf, R.(1991). *Field Strength Prediction in the VHF and UHF Range Including Multipath.* Propagation, Proc. 7th International Conference on Antennas and Propagation (ICAP 1991), York Conference Publication, 333, vol 2,pp. 965-967,London.

Klima, J., & Mozucha, M. (2005). *Influence of Terrain in Multipath Propagation of FM.* Journal of Electrical Engineering, 56(5), 113–120.

Lodro, M. (2016). *Antennas and Wave Propagation*.

Milanovic, J., Rimac-Drlje, S., &Bejuk, K. (2007). *Comparison of Propagation Model Accuracy for WiMAX on 3.5GHz.* Proceedings of the 14thIEEE International Conference on Electronic Circuits and Systems, Dec. 11 - 14, IEEE Xplore Press, Morocco, pp: 111 - 114. DOI: 10.1109/ICECS.2007.4510943.

Sahoo, S.K. & Behere, P.K (2011). *Path Loss – A Parameter that Affects Channel Performance in Mobile Communication.* National Journal of Computer Science and Technology, 3(2)

Ugweje, O. (2017). *Radio Frequency and Wireless Communications.* https://doi.org/10.1002/047148296X.tie151

Spatial Distribution of Healthcare Facilities and Workforce in Wushishi Local Government Area of Niger State, Nigeria.

Ishaq, A.B[1] Adamu, Y.M[2]
[1]Department of Geography, Federal University of Technology Minna, Niger State, Nigeria
[2]Department of Geography, Bayero University Kano, Nigeria
aishaq@futminna.edu.ng
ymadamu.geog@buk.edu.ng

Abstract

This study examined the spatial distribution of healthcare facilities and workforce in Wushishi Local Government Area of Niger State. The objectives of the study are to assess the healthcare facilities and workforce available, the spatial pattern of the facilities, distribution of the workforce and the relationship between population and the available healthcare facilities and workforce. Primary data was collected using a handheld GPS to obtained Coordinates (Longitude and latitude) of the individual health care facility; the secondary data were collected from Niger State Ministry of Health and National Population Commission. The two sets of data were merged together to produce map and nearest neighbor analysis results using ArcGIS 10.4.1 software interface. The population from National Population Commission was projected to 2021. Tables were also used to show the ratio of population to the healthcare facilities and workforce. The result of the nearest neighbor analysis shows that the spatial pattern is clustered with Z-score of (2.737318) at (0.006194) level of significance (P value). The distribution of health facilities and workforce were uneven as they are concentrated around 4 wards of Akare, Sabon Gari, Tukunji/Yamigi and Zungeru leaving the remaining 7 wards at advantage regarding access to healthcare services. Interms of workforce the study area is lacking Doctors and Nurses/Midwives as there are only 5 Doctors and 18 Nurses/Midwives available to carter for the entire study area. For Health facilities, Beds and Community Health Extension Worker, the study area meet the State, Country and World Health Organization target interms of population ratio, however they are also unevenly distributed across the L.G.A. The Study therefore recommends that the government should employ more doctors and nurses and also distribute the healthcare facilities and workforce equitably to every member of the society according to need.

Keywords: spatial distribution, health facilities, workforce, healthcare services

1. Introduction

Health is a crucial component of human well-being. It is a concept that relates to and describes a person's state of well-being and not simply absence of disease. Ogundare (1982) linked health to food in importance to individual existence, and opined that the concern and attention that any government pays to health could well determine the wellbeing of the people. The World Health Organization (1978), defines health as the complete physical, mental and social well-being and not merely the absence of disease or infirmity. It is the journey towards the highest levels of mental, emotional and physical stability. According to Awoyemi *et al.* (2011), improvement in health leads to improvement in life expectancy, which serves as a robust indicator of human development. Evidence has shown that among poor countries, increase in life expectancy is strongly correlated with increase in productivity and income. Increased productivity by individual or group of people in all sectors depends on the health conditions of the labour force, while improved health and quality of life depends to a great extent on the availability of, and accessibility to health care services at affordable cost Deaton (2003).

Healthy population and access to healthcare services are significant factors influencing economic development and prosperity. Thus, accessibility to healthcare facilities describes people's ability to use health services when and where they are needed. Healthcare decisions are strongly influenced by the type and quality of services available in the local area and the distance, time, cost, and ease of traveling to reach those services (Haynes *et al.*, 2005). Health care services in Nigeria are provided by a multiplicity of health care providers in the public and private sectors. As at December 2020, Nigeria has a total of 40,399 health facilities across the 36 states and the Federal Capital Territory. Of this number, 34,383 (85%) are PHC facilities, 5858 (14%) are secondary-level facilities, while 158 (1%) are tertiary-level facilities. More than 66% of the facilities are public (government) owned (Federal Ministry of Health, 2020). According Millennium Development Goals performance tracking survey of (2015), most primary health facilities across the country are poorly equipped, with only a quarter of health facilities having more than 25% of the minimum equipment package. The availability of basic amenities to support an enabling working environment and quality services (for example electricity or generator, emergency transportation system, and good sanitary and waste management practices) is poor in many of the Healthcare (MDG, 2015). Health outcomes and utilization of healthcare Services in Nigeria have been found to be low but vary across regions with the Northeast, Northwest regions and rural areas faring considerably worse off than the rest of the country, a pattern largely attributed to the high levels of poverty in the North (WHO, 2010).

2. Literature Review

Healthy population and access to healthcare services are significant factors influencing economic development and prosperity. Healthcare, like many public services are not equally available. This is because it is not 'pure' public good (Cox and Reynolds 1974). Thus, accessibility to healthcare facilities describes people's ability to use health services when and where they are needed. Healthcare decisions are strongly influenced by the type and quality of services available in the local area and the distance, time, cost, and ease of traveling to reach those services. A number of studies have attempt to determine the spatial distribution and accessibility to Health Care facilities in various part of the world. Owoyele *et al.* (2015) for example conducted a study on the service radii and accessibility of health facilities in suleja Niger State, Nigeria. This was an attempt to see the radius covered by the health facilities to the neighboring communities. Questionnaire and Lorenz curve were used to collect data and show the level of inequalities between the population and available healthcare facilities. Findings shows that there are inequalities in the spatial distribution of health facilities (hospitals and clinics) within the study area. In terms of distance travel, 34.5% of the respondent travel less than 1km while 11% travel more than 4km before accessing healthcare facilities. The study therefore recommend that the minimum distances for health facility should not be more than 1km for health clinic, 2km for maternity homes and 3-4km for a General hospital. Omotayo (2018) examine the spatial distribution and accessibility to healthcare facilities in Akure South local government area of Ondo State, Nigeria. GPS was used to gather the coordinate of each of the existing healthcare facilities in the 11 political wards of the study area.

Nearest Neighbour Analysis was used to establish the distribution pattern of public and private healthcare facilities. 551 questionnaires were randomly administered to the respondents in the 11 political ward of the study area. The result revealed that the distribution of healthcare facilities were random rather than being clustered or dispersed and that commuting distance to the healthcare facilities is within the WHO recommended distance. The study therefore recommend that stakeholders in the health sector and Town Planners should ensure equity in the distribution of public healthcare facilities across the Local Government Area of the State. This study is similar to that of Owoyele *et al.* (2015), however the findings is in contrast to each other. Abdulkarim *et al.*, (2017), examine the spatial distribution in terms of physical access and man power ratio to the population in Bichi LGA of Kano, State. The result found out that the healthcare facilities is unevenly distributed and the man power ratio to the population such as doctors, nurses and

midwives among others are not evenly distributed as well. The study therefore recommend that government should distribute health care facilities equitably to every member of the society according to need. The aim of these study therefore was to examine the spatial distribution of healthcare facilities and workforce in Wushishi Local Government Area of Niger State. To achieve this aim, the study assess the healthcare facilities and workforce available, the spatial pattern of the facilities, distribution of the workforce and the relationship between population and the available healthcare facilities and workforce

3. Methodology

3.1 Study Area

The study was conducted in Wushishi L.G.A of Niger State, located in the North-central geopolitical division of Nigeria. Its administration headquarters is situated in Wushishi town. It is located close to the middle of Niger state. The local government area shares borders with Mashegu, Rafi, Lavun, Gbako, and Bosso local government area. Wushishi is located between Longitude 9°43'N and Latitude 6°04'E (Niger State Government, 2015). The 2006 Population and housing Census put Wushishi population at 81,783. However, as at 2021 the population of Wushishi is put at 128,688 (Author's Projected Population, 2021).

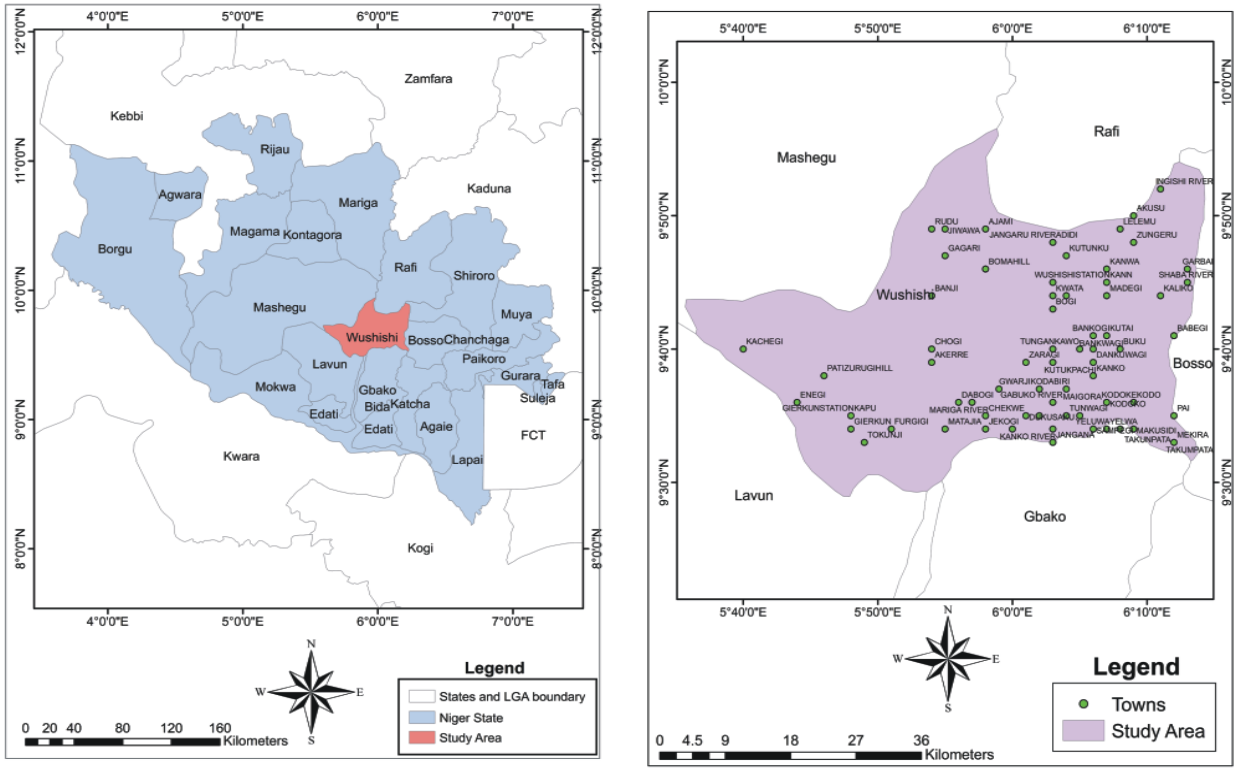

Figure 1: Map of Niger State Showing Study Area
Source: Department of Geography, Federal University of Technology, Minna

Primary Data and Sources: Coordinates (Longitude and latitude) of the individual healthcare facilities were collected using a handheld GPS (Global positioning system). The map of Niger State from which the map of Wushishi is extracted was scanned and saved as a Jpeg file.

Secondary Data and Sources: Map of Wushishi was extracted from topographic map of Niger State. Information from the Ministry of Health (Niger State) about the address, location, Ward, beds, doctors, nurses, name and types of healthcare facilities was collected. Population data was obtained from the National Population Commission.

The population for Wushishi L.G.A area were projected to 2021 using exponential growth model at a growing rate of 3% per annum. The following formula were used to determine the population.

$$\text{Growth Rate} = \frac{P_1 - P_0}{P_0} \times 100$$

$$PP = P_0 (1 + r/100)t$$

Where PP = Projected Population
P_1 = Population at present time
P_0 = Initial Population
r = Annual rate of growth
t = Difference between the projection year and previous census
Source: Adopted from the work of Adamu (2017).
Nearest Neighbor Analysis was used to show the spatial pattern of the healthcare facilities in the study area.
In addition, tables were also used to present the ratio of population to the healthcare facilities and workforce available. The following formulas were used to determine the ratio of the population to the health facilities and workforce.

A. $\frac{\text{Number of health Facilities}}{\text{Total population}} \times \frac{10,000}{1}$

B. $\frac{\text{Number of Beds}}{\text{Total population}} \times \frac{10,000}{1}$

C. $\frac{\text{Number of Health Workers}}{\text{Total population}} \times \frac{100,000}{1}$

4. Result and Discussion

4.1 Distribution of Healthcare Facilities in Wushishi

Distribution of healthcare facilities is important because it provides us with information regarding the numbers and types of health facilities that are available at different location within the study area. This will be able to show the availability and accessibility of healthcare services available to the people so as to be able to identify the underserved areas in order to improve the healthcare service delivery. Wushishi L.G.A has a total of 42 healthcare facilities comprising both primary and secondary health facilities. Out of these, 33 (79%) are public health facilities while 9 (21%) are private health facilities (Table 1). Primary health facilities which are provided by the local government and form the entry point of communities into the health care system constitute the highest with a total number of 41 (98%), followed by Secondary health facilities with 1 (2%). It is important to note that Wushishi L.G.A does not have a single tertiary health facilities. These health facilities are also distributed among the 11 wards in Wushishi with Zungeru having the highest with 8 (19%), followed by Tukunji/Yamigi with 7 (17%), Akare with 5 (12%) with the remaining 22 (52%) distributed among the 8 wards (Table 4). It is also important to note that the only general hospital is situated in sabon gari ward. When the health facilities to population ratio is considered, Wushishi health facilities ratio stand at 3.3: to 10000 population for the entire L.G.A (Table 2). This is higher than Niger State and WHO global average of 2.5: to 10000 and 2: to 10000 population respectively. However, it should be noted that having enough health facilities without the appropriate corresponding manpower to mount it those not necessary translate to the provision of efficient and good healthcare services.

Table 1. Distribution of Healthcare Facilities in Wushishi by Wards

S/N	Ward	Facility Name	Facility Level	Facility Type	Lon	Lat	Ownership
1	Akare	Akare Primary Health Care Centre	Primary	Health Centre	5.91384	9.6714	Public
2	Akare	Cheji Health Post	Primary	Health Post	5.90778	9.67638	Public
3	Akare	Girin Health Post	Primary	Health Post	5.88418	9.64839	Public

4	Akare	Pakara Primary Health Clinic	Primary	Health Centre	5.98593	9.71912	Public
5	Akare	Victory Maternity Home	Primary	Maternity Home	5.90523	9.67484	Private
6	Barwa	Barwa Primary Health Care Centre	Primary	Health Centre	6.07326	9.72666	Public
7	Gwarjiko	Dabogi Primary Health Clinic	Primary	Health Clinic	5.94592	9.59419	Public
8	Gwarjiko	Ebosoko Dabiri Primary Health Clinic	Primary	Health Clinic	6.02131	9.59784	Private
9	Gwarjiko	Ekangi Primary Health Clinic	Primary	Health Clinic	5.96564	9.56405	Public
10	Gwarjiko	Gwarjiko Primary Health Clinic	Primary	Health Clinic	5.98935	9.62134	Public
11	Kanwuri	Al-Barka Clinic And Maternity Home	Primary	Maternity Home	6.07138	9.73379	Private
12	Kodo	Kanko Primary Health Clinic	Primary	Health Clinic	6.10393	9.62475	Public
13	Kodo	Kodo Primary Health Clinic	Primary	Health Clinic	6.11678	9.60429	Public
14	Kodo	Makusidi Primary Health Centre	Primary	Health Centre	6.11678	9.57491	Public
15	Kodo	Yelwa Health Post	Primary	Health Post	6.11048	9.56711	Public
16	Kwata	Madegi Primary Health Clinic	Primary	Health Clinic	6.12295	9.7348	Public
17	Kwata	Tashen Jirgi Primary Health Clinic	Primary	Health Clinic	6.08324	9.7201	Public
18	Kwata	Wadata Maternity Home	Primary	Maternity Home	6.04504	9.74743	Private
19	Lokogoma	Lokogoma Primary Health Clinic	Primary	Health Clinic	6.04824	9.56759	Public
20	Lokogoma	Nagenu Primary Health Clinic	Primary	Health Clinic	6.05431	9.59871	Public
21	Lokogoma	Ndace Mamman Health Post	Primary	Health Post	6.08008	9.58412	Public
22	Maito	Maito Primary Health Clinic	Primary	Health Clinic	6.04075	9.65148	Public
23	Maito	Tungan Kawo Health Post	Primary	Health Post	6.05229	9.66941	Public
24	Sabon Gari	Al-Nur Nursing Home	Primary	Health Clinic	6.07951	9.72357	Private
25	Sabon Gari	Bankogi Primary Health Clinic	Primary	Health Clinic	6.09201	9.69251	Public
26	Sabon Gari	Wushishi Primary Hcc	Primary	Health Centre	6.07689	9.72996	Public
27	Sabon Gari	Wushishi General Hospital	Secondary	General Hospital	6.07946	9.72968	Public
28	Tukunji/Yamigi	Alheri Primary Health Clinic	Primary	Health Clinic	5.66	9.75768	Private
29	Tukunji/Yamigi	Enagi Health Post	Primary	Health Post	5.72543	9.58929	Public
30	Tukunji/Yamigi	Gbayafu Primary Health Clinic	Primary	Health Clinic	5.75783	9.53997	Public
31	Tukunji/Yamigi	Saminaka Health Post	Primary	Health Post	5.65909	9.72765	Public
32	Tukunji/Yamigi	Tungan Sayyadi Primary Hcc	Primary	Health Centre	5.65909	9.74907	Public
33	Tukunji/Yamigi	Yelwa Tukunji Primary Health Clinic	Primary	Health Clinic	5.82912	9.53572	Public
34	Tukunji/Yamigi	Yemigi Primary Health Clinic	Primary	Health Centre	5.94592	9.48723	Public
35	Zungeru	Erena Health Post	Primary	Health Centre	6.21161	9.74039	Public
36	Zungeru	Idp Plc Primary Health Clinic	Primary	Health Clinic	6.26598	9.87635	Public
37	Zungeru	Immani Primary Health Clinic	Primary	Health Centre	6.19461	9.73653	Private
38	Zungeru	Kaliko Model Primary Health Centre	Primary	Health Centre	6.20271	9.72696	Public
39	Zungeru	Kankare Dano Primary Health Clinic	Primary	Health Clinic	6.173	9.81316	Public
40	Zungeru	Maàji Primary Health Clinic Katuna	Primary	Health Centre	6.19482	9.68737	Private
41	Zungeru	Nomau Maternity Home	Primary	Maternity Home	6.15174	9.8061	Private
42	Zungeru	Zungeru Primary Health Care Center	Primary	Health Centre	6.15078	9.79751	Public

Source: Niger State Ministry of Health (2021)

Table 2. Healthcare Facilities to Population Ratio in Wushishi

L.G.A	Population	Health Facilities	Ratio Per 10,000
Wushishi	128688	42	3.3

Source: Niger State Ministry of Health (2021)

4.2 Spatial Pattern of Healthcare Facilities in Wushishi

The distribution pattern of health care facilities in Wushishi was determined by average nearest neighbor in ArcGIS 10.4.1 software interface. The nearest neighbor analysis for healthcare facilities in the study area shows that the pattern of healthcare facilities is clustered. This is because nearest neighbor statistical analysis showed that the observed mean distance of (2961.8264 meters) is lower than the expected mean distance of (3801.0393 meters) with a nearest neighbor ratio of (0.779151). Similarly, the z-score (critical value) of -2.737318 at 0.006194 level of significance (p-value) shows that there are less than 1% likelihood that this clustered pattern could be the result of random chance. However, the spatial distribution of HCF in Wushishi LGA shows that the concentration of HCF especially around Zungeru, Tukunji, Akare and Sabon-Gari wards in the East and also the Southern part of the LGA is due to the presence of the administrative headquarter located in Sabon Gari ward, high population density and settlement that are located their compare to the Northern and Western part of the LGA which are mostly low populated areas (Table 4 and Figure 2). This result is also similar to that of Kibon and Ahmed (2012) and Musa *at el.*, (2012) who discovered that the spatial pattern of health care facilities in Kano metropolis and Jigawa State Nigeria are clustered in nature.

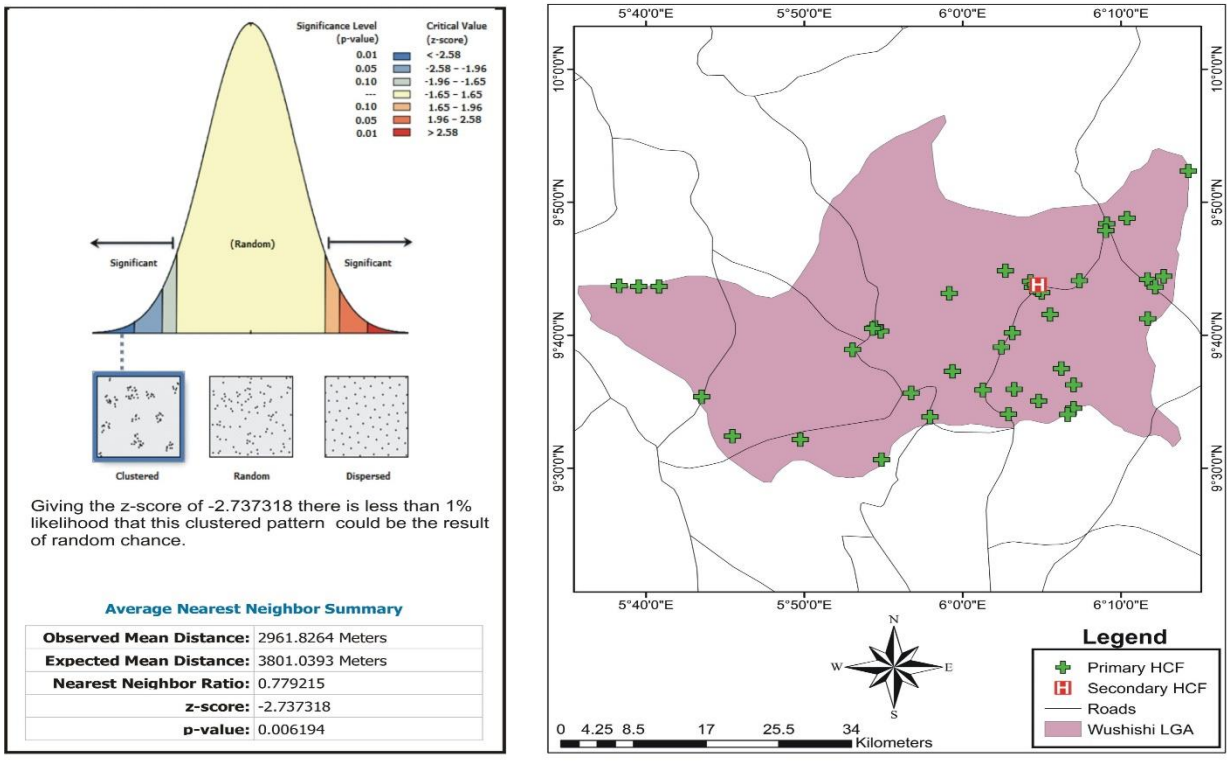

Figure 2. Nearest Neighbor Analysis and Spatial Distribution of HCF in Wushishi LGA as at 2021

4.3 Distribution of Hospital Beds in Healthcare Facilities in Wushishi

The importance of beds in any healthcare facilities cannot be overemphasize, this is because it serve as a platform in which patients are kept for proper diagnosis, observation and treatment; it also serve as a symbol of improvement of healthcare facilities and yardstick for measuring the level of accessibility and utilization of health services for maintaining a healthy population (Adamu and Sani, 2017). Wushishi has a total hospital beds capacity of 275, (Table 3 and 4). The distribution of beds across the ward shows that Zungeru has the highest with 66 (24%), followed by Sabon Gari with 65 (23.6%), Akare with 33 (12%), Tukunji/Yamiji with 23 (8.3%) and the remaining beds 88 (32%) were distributed among the remaining 7 wards. This figure is for both Public and Private Health facilities. The bed population ratio of Wushishi stood at 21.4: to 10000 population. This figure is higher than the State average and WHO global target of 12.9: to 10000 and 27: to 10000 population respectively. This shows that the number of bed spaces per population in Wushishi is adequate, however it is not evenly distributed across the L.G.A. This corresponds with the assertion by Adamu *et al.*, (2017) that inadequate and unequal distribution of beds spaces led to large number of the population to lack access to the basic platform for being diagnosed, observed and treated for maintaining their health status.

Table 3. Hospital Beds to Population Ration in Wushishi

L.G.A	Population	Beds	Ratio Per 10,000
Wushishi	128688	275	21.4

Source: Niger State Ministry of Health (2021)

Table 4. Distribution of Health Workforce (Doctor, Nurses/Midwives and CHEW) in Wushishi

Ward	Health Facilities	Beds	Doctors	Nurses/Midwives	Chew
Akare	5	33	0	1	6
Barwa	1	8	0	1	3
Gwarjiko	4	16	0	0	5
Kanwuri	1	9	0	0	5
Kodo	4	18	0	1	5
Kwata	3	13	0	0	4
Lokogoma	3	14	0	0	4
Maito	2	10	0	0	2
Sabon Gari	4	65	5	8	18
Tukunji/Yamigi	7	23	0	0	11
Zungeru	8	66	0	7	21
Total	**42**	**275**	**5**	**18**	**75**

Source: Niger State Ministry of Health (2021)

4.4 Distribution of Doctors in Wushishi

Wushishi L.G.A has a total number of 5 medical doctors as at 2021, giving a doctor population density of 3.9: to 100,000 (Table 4). This figure is below the WHO global target of 230 doctors per 100,000 population. It is also lower than the State, Country and Sub-Saharan Africa average of 6 doctors to 100,000, 38: to 100,000 and 15: to 100,000 respectively (National Health and Development Survey, 2012). However, it is interesting to note that all the 5 medical doctor works

at the Wushishi general hospital which is located at Sabon Gari ward. The implication of this is that Wushishi L.G.A will be grossly underserved in terms of doctors as any patient seeking the medical attention of a doctor will have to travel all the way to Wushishi General Hospital irrespective of cost and distance, thereby limiting their chances of getting a good healthcare services that will cater for their health needs. This assertion is the same with that of Adamu *et al.* (2017) and Niger State Government (2015) that state that only people living in urban areas of the state were privileged to have good health care services because of the presence of general hospitals.

Table 5. Doctors to Population Ratio in Wushishi

L.G.A	Population	Doctors	Ratio Per 100,000
Wushishi	128688	5	3.9

Source: Niger State Ministry of Health (2021)

4.5 Distribution of Nurses/Midwives in Wushishi

Wushishi L.G.A has a total of 18 Nurses and Midwives distributed across 5 wards leaving the 6 remaining wards without the presence of Nurses and Midwives. Among these 5 wards Sabon Gari have the highest number of Nurses and Midwives with 8 (44%), followed by Zungeru with 7 (39%), the remaining 3 (17%) where distributed between Akare, Barwa and Kodo with one each. The concentration of Nurses and Midwives within Sabon Gari and Zungeru is due to the fact that there is the presence of general hospital and 3 private clinics in Zungeru and the Nurses and Midwives usually work closely together with medical doctors. However, the population ratio of Nurses and Midwives in Wushishi is 14: to 100000 across population the L.G.A (Table 6 and Figure 3). This figure is lower than the State, Country and Sub-Sahara Africa average of 19: to 100000, 148: to 100000 and 72: to 100000 respectively (NHDS, 2012).

Table 6. Nurses/Midwives Population Ratio in Wushishi

L.G.A	Population	Nurses/Midwives	Ratio Per 100,000
Wushishi	128688	18	14

Source: Niger State Ministry of Health (2021)

4.6 Distribution of Community Health Extension Worker in Wushishi

Unlike the doctors and Nurses/Midwives that were concentrated in general hospital and some few private clinics. The Community Health Extension Workers were dispersed across the various wards in the L.G.A. It is also important to note that the CHEW are more visible and are the engine block that mount the primary healthcare facilities especially in rural areas of the State. Wushishi has a total number of 75 CHEW, this number is 3 times higher than the combine figures of Doctor and Nurses/Midwives which stand at 23. Out of these numbers, Zungeru Ward has the highest with a total of 21 (28%), followed by Sabon Gari with 18 (24%), Tukunji/Yamigi with 11 (15%), Akare with 6 (8%) and the remaining 19 (25%) is distributed among the remaining 7 wards. It is important to note that majority of the CHEW 56 (75%) were distributed among 4 ward (Table 4 and Figure 3). However, Wushishi L.G.A has a CHEW population ratio of 58.2: to 100000. This figure is higher than the State and Country average of 53: to 100000 and 25.3: to 100000 population respectively (Nigeria Health Policy 2019). It is also interesting to note that for the first time Wushishi L.G.A have a population ratio that is higher than that of the State and Country Level.

Table 7. CHEW Population Ratio in Wushishi

L.G.A	Population	Doctors	Ratio Per 100,000
Wushishi	128688	75	58.2

Source: Niger State Ministry of Health (2021)

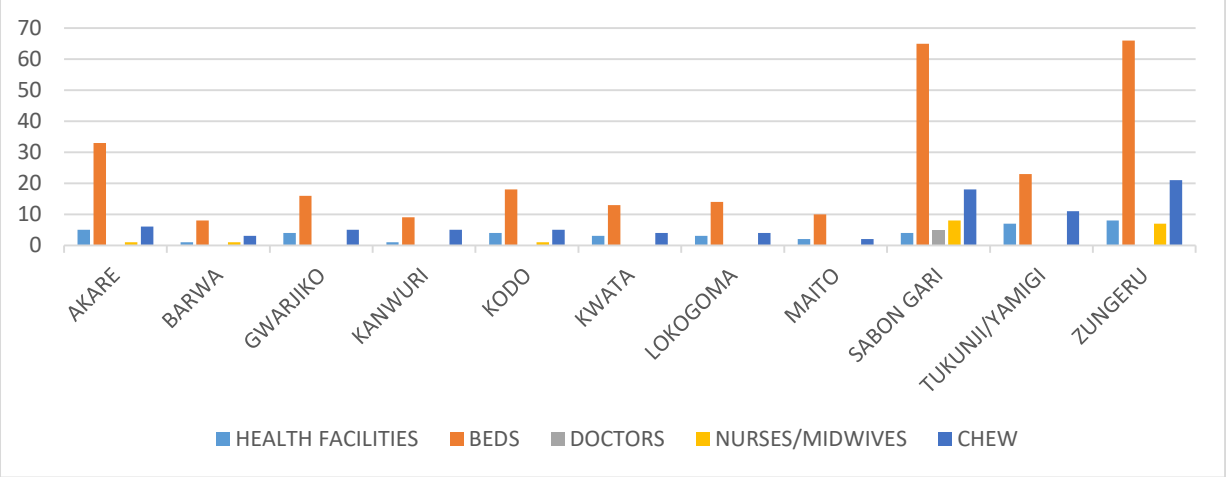

Figure 3. Distribution of Health Facilities and Workforce in Wushishi

5. CONCLUSION

There is no equity in the distribution of healthcare facilities and workforce in Wushishi Local Government Areas. The distribution of health facilities and workforce follows a similar pattern of the nearest neigbour analysis results which shows that most of the healthcare facilities are clustered around 4 wards out of the 11 existing wards in the study area. These 4 wards are Zungeru, Tukunji/Yamigi, Sabon Gari and Akare. For example, 24 (57%) of the health facilities, 187 (68%) of hospital beds, 5 (100%) of doctors, 16 (89%) of Nurses/Midwives and 56 (75%) of CHEW were all concentrated within these 4 wards. However, when we look at the disparity in the distribution of healthcare facilities and workforce between the remaining 7 wards, the difference is much, thereby denying access to good and adequate healthcare services to them. Interms of the relationship between population and number of healthcare facilities, beds and CHEW, the result shows that the study area have adequate man power in that respect and also meet the minimum requirement of country and global target, however they are not equitably distributed across the L.G.A. For doctors and Nurses/Midwives population ratio wushishi fall short in this regards with only 5 doctors and 18 Nurses/Midwives attending to the entire L.G.A. population. Consequently it is pertinent to note that, health is a right not a privilege, for every individual in the society to realize his potentials within his community there is need to have access to good healthcare services. Therefore, healthcare facilities and workforce should be shared equitably by every member of the society according to need. However, further study need to be done to understand the choice of utilization and factors affecting utilization in the study area.

References

Abdulkarim I.A., Danbuzu L.A.S., Dardau H., and Umar A. A. (2017). Spatial Distribution of Healthcare Facilities in Bichi Local Government Area, Kano State Nigeria. Katsina Journal of Natural and Applied Sciences V. 6 P. 1.

Adamu, Y., M. and Sani M. (2017). Healthcare Services Provision, Challenges and Prospects for Sustainable Development in Nigeria: A Case Study of Sokoto State.

Awoyemi, T.T, Obayelu, O. A., and Opaluwa, H. I. (2011). Effect of Distance on Utilization of Health Care Services in Rural Kogi State, Nigeria. Journal of Human Ecology, 35(1): 1-9.

Cox and Reyhold (2004). Maternal healthcare among adolescent. http://info.k4health.org/youthwg/PDFs/YouthLens/YL11e.pdf

Deaton, A. (2003). Health, inequality, and economic development. Journal of Economic Literature XLI: 113-58.

Federal Ministry of Health (2020). Nigeria Health Facility Registry. https://hfr.health.gov.ng/download/facility-list

Millennium Development Goals performance tracking survey report (2015). Federal Republic of Nigeria, National Bureau of Statistics.

Musa I.J and Abdulhamed, I. (2012). The accessibility problems of primary Health Care to rural people in Jigawa state, Nigeria. Department of Geography Ahmadu Bello University Zaria, Nigeria. *Global Advance Research Journal of Social Science. Vol. (4) Pp.3-22*

Niger State Government (2015). Niger State, Facts and Figures 2015.

National Population Commission and National Bureau of Statistics Estimate (2016). National Population Estimate.

National Health and Development Survey (2012) Nigeria Health Indicators. Federal Ministry of Health.

Owoyele, G.S., Ajobiewe, T.O., Idowu, O.O, Shuaibu, S.I., and Martins, V.I. (2015). Spatial Analysis of Health Facilities in Suleja, Niger State, Nigeria. Ethiopian Journal of Environmental Studies & Management V. 8(3) P. 264 – 271, 2015

Ogundare, E.I. (1982). Healthcare Delivery is a success in Oyo State. Daily Sketch October 27, P.7.

Omotayo, B., O. (2018) Spatial Distribution and Accessibility to Healthcare Facilities in Akure South Local Government Area of Ondo State, Nigeria. Anallelle Uniiversiităţiiii diin Oradea,, Seriia Geografiie Anallelle Uniiversiităţiiii diin Oradea,, Seriia Geografiie, Article no. 281101-750.

Usman A, K., and Ahmed M. (2013). Distribution of Primary Health Care Facilities in Kano Metropolis Using GIS (Geographic Information System). Research Journal of Environmental and Earth Sciences V. 5(4). P. 167-176, 2013.

World Health Organization (2010). Global Health Observatory country views: Nigeria statistics summary (2002–present). Geneva. http://apps.who.int/gho/data/node.country.country-NGA.

World Health Organization (1978) Primary Health Care: Report of the International Conference on Primary Health Care. WHO, Alma Ata, Geneva.

Health Implication of Dam in Some Parts of Tafa Local Government Area of Niger State, Nigeria

Ishaq, A.B[1] Ahmed, Y[2] Waziri, A.M[3] Odekunle, M.O[4]
[1,2,3,4]Department of Geography, Federal University of Technology Minna, Niger State, Nigeria
aishaq@futminna.edu.ng
odemary@futminna.edu.ng

Abstract
Although dams have beneficial effects, they are also acknowledged as having serious environmental repercussions if they are not properly managed. The aim of this research was to examine the impact of Kofa dam in Niger State on the health status of a riparian community downstream (Kofa) against a control community (Karfe). The objectives of the study are to assess the health implications of proximity to Kofa dam and to investigate the perception of the community members located near the dam on its health implication. A convenient 3% sample size was adopted resulting to 130 respondents and questionnaires, focus group discussion and personal observation were used to elicit data. The result unveiled that communicable water-related diseases are more common in the catchment area, which were identified as malaria, water related diseases (bilharzias, diarrhea, rashes measles) and cholera among others which are mostly associated with water. Case-control study was then conducted in one community (Karfe) which is about 5km away from the experimental community in other to ascertain the health status of the communities with regards to the function of the dam. Most of the diseases identified in the control community are conventional diseases in Nigeria such as: Malaria, Ulcer, Diabetes, which invariably signifies that the diseases identified there has no correlation what so ever with the waterborne diseases found in the experimental community. The study therefore shows some degree of association between the presence of the dam and poor health status of the downstream community in close proximity to it. However, it was recommended that Government should assist in providing the community with safe drinking water so as to prevent the community from using the untreated dam water for their domestic use and provide the community with health education, mosquito netting, medical facilities and drugs to promptly diagnose and treat infected persons in the communities particularly Kofa as it is the community located in close proximity to the dam and is mostly affected by waterborne disease.

Keywords: dam, health, waterborne disease, conventional disease, riparian

1. Introduction

Throughout the world, especially the developing world, dams and related water infrastructure projects continue to be planned, constructed and operated to meet human needs through energy generation, agricultural production and the supply of drinking water. For most countries, dams are a crucial part of economic and social development and, as such, they aim to achieve important socio-economic development objectives. Through their potential to alleviate poverty, they can contribute significantly to the enhancement of human health. Large dams became a prominent instrument for economic development in the past century. Worldwide, the number of large dams stood at 5000 in 1950 (International Commission on Large Dams, 1998); three quarters of these were in North America, Europe, and other industrial regions. By 2000, the number of large dams had climbed to over 45,000, and these were spread among more than 140 countries (ICOLD, 1998). On average, two large dams were built per day for half a century (World Commission on Dam, 2000). Today, the number of large dams exceeds 50,000 (WCD, 2006).

A dam, as the name implies, is the structural damming, locking, or controlling the flow of river water through the construction of barrier across the river channel (Ahmed, 2002). Dams provide water storage that has enabled large cities like Phoenix, Arizona, to grow in desert regions. About

half of the world's large dams were built primarily for irrigation, many of them in Asia as the Green Revolution spread (WCD, 2000). Undeniably, large dams have played an important role in economic development. However, large dams have also brought serious environmental and social consequences. Whereas the benefits have generally been delivered to urban centre's or industrial-scale agricultural developments, river-dependent populations located downstream of dams have commonly experienced a difficult upheaval of their livelihoods, health problems, loss of food security, and other impacts to their physical, cultural and spiritual well-being. While downstream river-dependent communities may benefit from some degree of flood protection and enhanced irrigation opportunities provided by dams, adverse impacts are far more common and usually outweigh the benefits to downstream people, resulting in reduction of their incomes, livelihood and increase in environmental problem (Anul *et al.*, 2007). Today, 200 million people are affected, the equivalent of the entire population of the United States of America. Disease is widespread in Africa, Japan, the Philippines, Thailand, Laos and other parts of Asia, the Middle East, the West Indies and parts of South America. In all, 71 countries are affected (WCD, 2000).

Empirically researches unveiled that dams are associated with socio-economic and health consequences. For example Yamana (2004) noticed that tropical diseases such as malaria, schistosomiasis, river blindness and rift valley fever are mostly cause as a result of consuming water contaminated by human, animal, or chemical wastes, and parasites that spend at least part of their life cycles in water. Epidemic of malaria disease is more prevalent around dams. River blindness found in the river basins of central and South America and Tropical Africa bring untold hardship to the people. In the same vein, Hunter (2009) also found out that there was a strong relationship between dam construction and health status of riparian community within the dam vicinity. Goldsmith *et al*. (1984) in the book "Dam and Disease" talk about the Social and Environmental Effect of Large Dams, in which they identified Malaria, Schistosomiasis, Filariasis, and Onchorcerciasis (River blindness) as some of the major disease found in dam situated areas. Malaria, schistosomiasis, lymphatic filariasis and onchorcerciasis were found but not limited to diseases concern in water resource projects. Water resource projects lead to the aggregation of people; the ensuing health consequences include sexually transmitted diseases, accidental injuries, acute respiratory infections, diarrhea and tuberculosis. In 1977, prior to the construction of Jebba dam (which was completed in 1982, creating a reservoir about 100km long), it was predicted that onchocerciasis, trypasonomiasis would be important public health problems around this impoundment. Nigeria is not left out in terms of dam construction; several dams have been constructed all over the states in an attempt to generate hydropower e.g. Kainji dam which is the largest hydroelectricity project in the country, Jebba (on the Niger) and Shiroro (on the Kaduna tributary). In Kano state for example, we have Saint Thomas dam, Tiga dam, Kusalla dam, Challawa dam and the Bakolori dam in Zamfara state among others, all constructed for the purpose of generating hydroelectricity, supply of water for domestic use and for Agricultural purposes (irrigation).

The problems related to Dam are numerous based on their nature and magnitude. For the purpose of this study, the research concentrate more on the problems related to the health implication of the people. The health issue associated with Dams can be represented into two categories depending on the nature of the problem involved, namely;

1. **Communicable diseases** e.g. Vector borne (Malaria), water-born (Diarrhea, cholera, Typhoid, Schistosomiasis or Bilharzias, Guinea worm, River blindness or (Onchocerciasis), sexually transmitted, and zoo nose
2. **Non - communicable disease** e.g. poisoning by minerals, biological toxins, pesticide residues and industrial effluent

The aim of the study was to ascertain the health implication of dam in some part of Tafa L.G.A, in Niger State. To achieve this aim, the study assess the health implication of proximity to Kofa dam

and also investigate the perception of the community members located near the dam on its health implication.

2. Methodology

2.1 Study Area

Kofa and Karfe which are the two study areas are located between Lat 9°14'35" N and Lon 7°14'15" E, and between Lat 9°13'2" N and Lon 7°12'58" E respectively. The two communities are located in Tafa Local Government Area of Niger State, Nigeria. Tafa has an area of 222 km² and a population of 83,544 according to the 2006 census. The inhabitants of the village live in mud-brick houses with thatched roofs, although there are some few modern houses. The most common occupation is farming and other menial economic activities. Most of the inhabitants come into contact with the Kofa dam at least once a day for various reasons, including fishing, bathing, washing, and collecting water for domestic use as there is no supply of tap water in the village. Children also play barefoot along the dam-shore and in the water. A common problem in this village is the lack of basic health and sanitary amenities, such as a clean water supply, combined with a low economic level. The dam is located in between the two communities with the closest to it been the experimental communities (Kofa) with a distance of about 0.43km to the dam. The source of the river is river Iku and it direction of flow is from East to West, the company that construct the dam are CIBAS (Imperisit Bakolori). The construction started in 1990 and was commission in 1997 by General Sani Abacha. The sole purpose of the dam was to supply water for domestic use in the catchment areas which is about 144 square kilometers and has a capacity of about 30 million cubic meter of water.

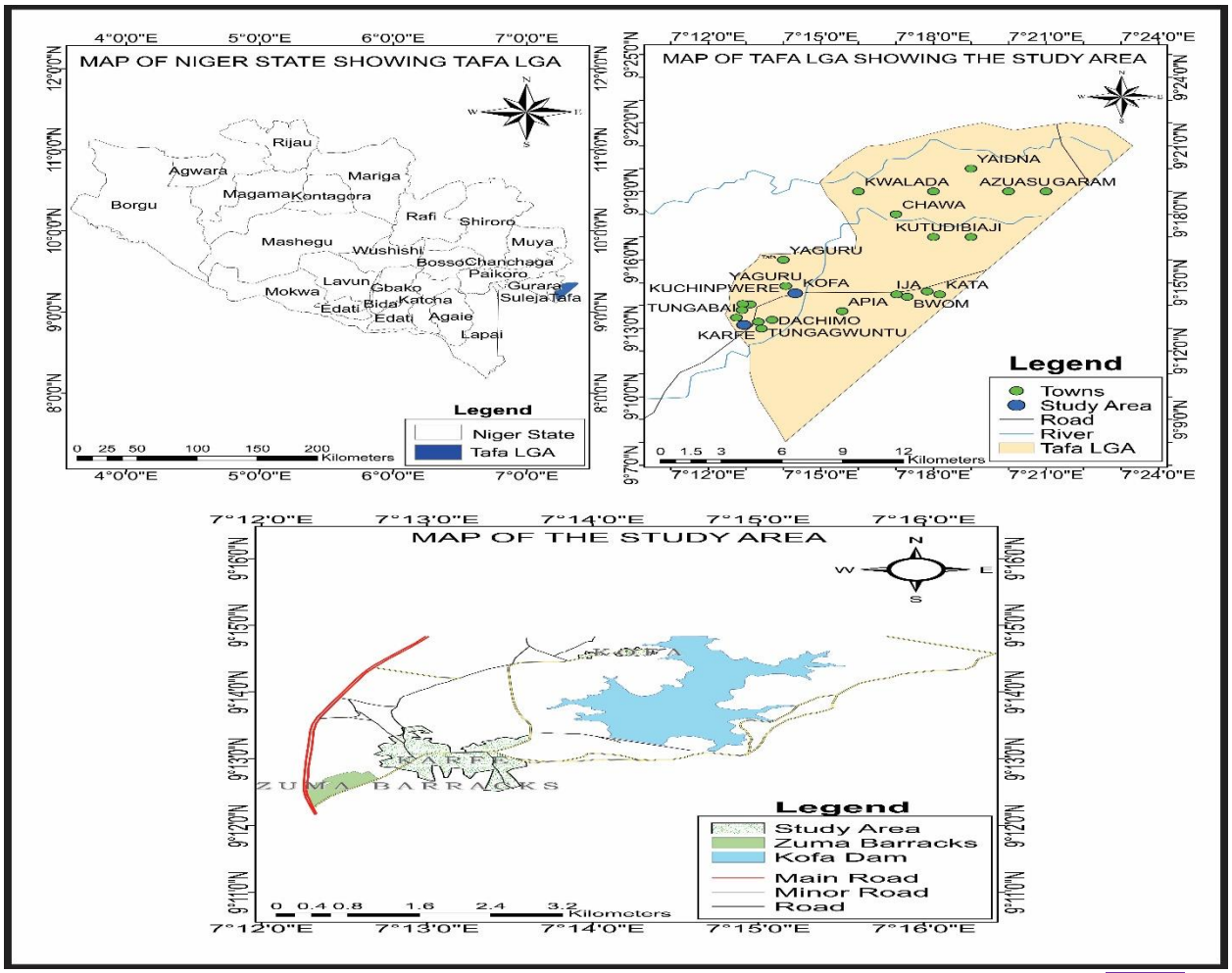

Figure 1: Map of Niger State Showing Study Area
Source: Department of Geography, Federal University of Technology, Minna

2:2 Method of Data Collection and Analysis

This study was conducted using descriptive survey research design. Probability sampling method served as the techniques in which random sampling were used to administered the questionnaires to the respondents. Primary data were acquired with the use of questionnaires, Focus Group Discussion and personal observation. Data for this study were collected using both closed and open ended questionnaire to generate information for the study. The sampling population for the two study areas was 4324. A convenient 3% sample size for the two study areas totaling 130 respondents participated in the study. 65 questionnaires each were administered to the study areas of Kofa and Karfe respectively. Focus Group Discussion was also conducted in the two study areas in four phases; two groups for each area were used with a population of twelve persons per group. Educational background and Age of the respondents were employed as the criteria to determine the sample size of the Focus Group Discussion. The secondary data used were from both publish and unpublished information obtain from books, journals, seminar papers, encyclopedias, student's project, magazines and online materials among others.

Data for this study were analyzed using descriptive statistical analysis. Data gathered were edited, coded and analyzed using SPSS and presented in charts and tables.

3 Data Analysis and Presentation

3.1 Demographic characteristics of Respondents

Sex of Respondents
The result presented in table 1 below indicates that the male respondents are more than the female respondent in the proportion of 78.2% to 21.8% respectively. This is because the male respondents are more readily available than the females who are mostly housewives and are usually indoors except for the few who were seen coincidentally working outside their household.

Table 1: Sex of Respondents

	Frequency	Percent	Valid Percent	Cumulative Percent
male	97	78.2	78.2	78.2
female	27	21.8	21.8	100.0
Total	124	100.0	100.0	

Source: Field work, (2018)

Age of Respondents

The result in figure 2 indicates that respondents from age 26-30 for Kofa and Karfe have the highest percentage with 12. 1% and 9.9%, followed by 31-35 with 8.1% and 8.9%, 36-40 with 5.6% and 7.3%, 21-25 with 5.6% and 4.8%, 41-45 with 4.0% and 1.6%, 46-50 with 4.0% and 2.4%, 51-55 with 2.4% and 8.1%, 56-60 with 2.4% and 5.6%, 16-20 with 2.4% and 1.6%, 61-65 with 1.6% and 2.0%, and lastly 66-70 with 1.6% and 2.4% respectively.

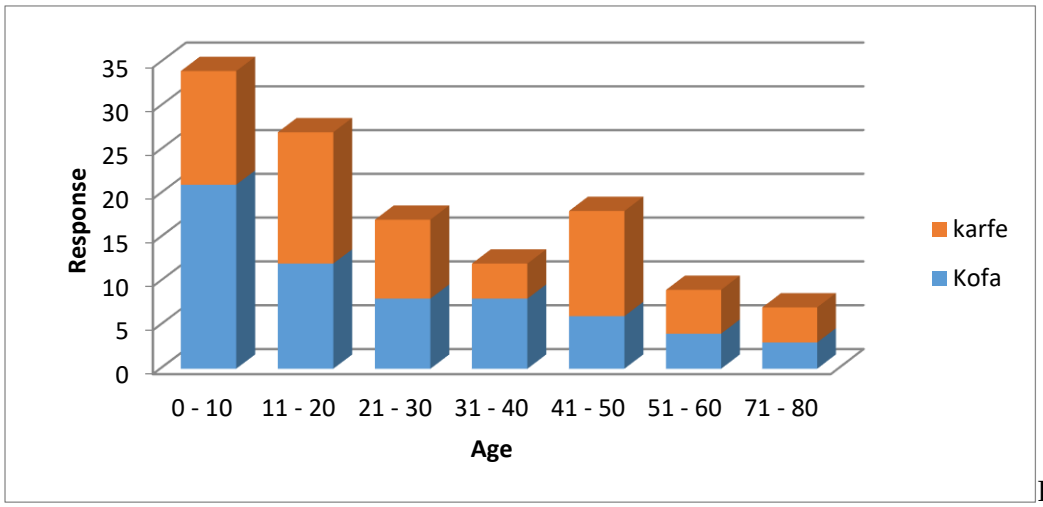

Figure 2. Age of Respondents

3.2 Sources of Water in the Study Areas

The Source of water plays a major role in determining the health status of the study areas. The research identified three sources of water as indicated in Table 2.

Table 2: Table Showing Different Sources of Water

	Kofa		Karfe	
	No.	%	No.	%
Dam	10	8.1	0	0.0
Borehole	3	2.4	0	0.0
both dam and borehole	49	39.5	0	0.0
Tap	0	0.0	62	0.0

Source: Field Work (2018)

3.3 Common Diseases in the Study Areas

Another factor that was considered to be important in determining the health status of the study areas is the type of diseases prevalent in the area. This research identified that there is an overlap between the diseases found in both communities. Thus, some diseases are more common in one community than the other. Some of the diseases identified are water-related, airborne while some are vector borne (Malaria fever) and other conventional diseases found irrespective of the environment. The results of the common diseases for the two communities are shown in the Table 3.

Table 3. Common Disease in the Study Area

		Kofa		Karfe	
		NO.	%	NO.	%
Malaria	Yes	60	48.4	62	50.0
	No	2	1.6	0	0.0
Bilharzia	Yes	30	24.2	8	6.5
	No	32	25.8	54	43.5

Typhoid	Yes	49	39.5	17	13.7
	No	13	10.5	45	36.3
Diarrhea	Yes	29	23.4	15	12.1
	No	33	26.6	47	37.9
Measles	Yes	13	10.5	0	0.0
	No	49	39.5	62	50.0
Rashes	Yes	16	12.9	0	0.0
	No	46	37.1	62	50.0
Pile	Yes	18	14.5	29	23.4
	No	44	35.5	33	26.6
Swollen Stomach	Yes	21	16.9	0	0.0
	No	41	33.1	62	50.0
Eye Problem	Yes	20	16.1	0	0.0
	No	42	33.9	62	50.0
Cholera	Yes	15	12.1	3	2.4
	No	47	37.9	59	47.6
Hypertensive	Yes	0	0.0	10	8.1
	No	62	50.0	52	41.9
Ulcer	Yes	0	0.0	9	7.3
	No	62	50.0	53	42.7
Diabetes	Yes	0	0.0	7	5.6
	No	62	50.0	55	44.4
Others	Yes	44	35.5	13	10.5
	No	18	14.5	49	39.5

Source: Field Work (2018)

On the health implication of proximity to kofa dam, the result in Table 3 show a high rate of disease occurrence in kofa against Karfe. Waterborne diseases are the major diseases prevalent in Kofa except for Malaria fever which is more frequent in Karfe than in the former. Proximity to Kofa dam has a serious health implication to the inhabitants as illustrated from the research findings. Prior to the construction of the dam, disease occurrence and most especially disease outbreak are very limited in Kofa, this is because the dam was initially a flowing river which make it difficult for new breed of mosquito, snail and other disease carriers to reproduce younger breeds. However, after the construction of the dam the pattern of disease occurrence change as the community began to notice few disease outbreaks such as bilharzias, typhoid, cholera and other water related diseases. Human contact with the river also increases exponentially as the dam became their major source of water for domestic and agricultural use. The only alternative source of water in the community is a single borehole which was not functional at the time of carrying out this research. This however exposes the inhabitant to have direct physical contact with the dam water frequently which makes them vulnerable to most of the waterborne diseases. Apart from the diseases, several death cases were also recorded. These results are similar to those of Yamana (2004) and Anul *et al.* (2007) who also found out that waterborne and malaria are more frequent in areas with dams and water body.

However the situation in Karfe is the opposite in terms of disease occurrence, this can be explained as shown Table 3 that most of the disease in Karfe are more of conventional diseases that is more attributed to lifestyle habit than the environment except for malaria fever which is one of the predominant disease in Karfe. These disparities may be attributed to the fact that malaria fever is a vector borne disease that travel long distance by it host (mosquito) before receding in a particular area depending on some factors such as cleanliness of the environment and the type of water people use for their day to day activities. It should be noted that unlike in Kofa, Karfe has a good water supply system (tap) which the inhabitant use for all their domestic activities. This may explain to some extent the minimal presence of waterborne disease.

3.4 Perception of Community Members Located near the Dam on its Health Implication

The people of Kofa community are fully aware of the health implication of the dam. Most of the respondents from the Focus Group Discussion argue that prior to the construction of the dam there were little presence of diseases, most especially waterborne diseases. However, after the construction of the dam in 1997 there was a change in the pattern of disease occurrence as some diseases such as bilharzias, cholera, diarrhea, eye problem and rashes become more frequent in the area. Within this time frame some few disease outbreak occurred most especially cholera and bilharzias. The dam also poses a great danger to the life of the people as about 95 deaths were recorded since the construction of the dam to date, this causes so much psychological problem as their love ones are lost while trying to cross the dam to their farm land and neighboring villages. Injury became more prominent in the community as several children are drowned on a day to day basis while swimming in the river. The water became a breeding ground for mosquito and other host and agent of diseases as the water became polluted and stagnant, children are mostly affected with the diseases as they are one of the group that come in contact with the contaminated water most often. Adult are not left out as some of them are affected with various eye problem and rashes. Swollen stomach is another major disease that surface mostly on children after the construction of the dam. In terms of the culture of the people, they try as much as possible to purify the water by boiling it before use as prescribe by medical health practitioners after preliminary lap test of the water. In general, the health status of the inhabitant living in Kofa community is on a positive note compare to when the dam was constructed, this is because many type of health educational program have been conducted to the people on how to use the water and take precautionary measures. Government have also been supportive on their part by providing them with some drugs most especially for bilharzias and cholera.

4. Conclusion

Health implications of dam are influence by numerous factors including the environment, culture and source of water among others. Source of water is the most influential factor in determining the types of diseases found in the two communities. However, there are differences between the type of diseases found in both the study areas as waterborne and malaria fever are prevalent in Kofa, there is minimum presence of waterborne disease in the other community without the dam (Karfe). There is also an overlap between some of the diseases in both areas as malaria and conventional diseases (typhoid, hypertensive, ulcer etc), whereas cultural and environmental factor plays more prominent role in their occurrence than the presence of dam and water body. The control community (Karfe) consistently had a much better health status than the riparian community which is closer to the dam. However, the study therefore showed that there was a strong association between the presence of the dam and poorer health status of the downstream community in close proximity to it and more specifically waterborne diseases.

4.1 Recommendations

Water development projects should only be undertaken if they can be shown to benefit large sectors of the population instead of the urban elite. Dam should not be built if they displace indigenous peoples from their homes and destroy their culture unless compensation is provided to ensure that the affected people are made no worse off, and preferably better off than before the project. However, this research recommends the followings:

1. Government should assist in providing the community with safe drinking water so as to prevent the community from using the untreated dam water for their domestic use.

2. Government should also assist in providing the community with health education, mosquito netting, medical facilities and drugs to promptly diagnose and treat infected persons in the communities particularly Kofa as it is the community located in close proximity to the dam and is mostly affected by waterborne disease.

Although, no one solution will solve all of the health problems associated with dam, however well-integrated strategies chosen according to local characteristics and requirement can reduce the health problem to a minimal level.

REFERENCE

Ahmed, M.I. (2002). Introduction to Environmental Problems and Management Kano: Wadec publishers. Page 168.

Anul, N., and Durmus, N. (2007). Positive and Negative Impact of Dams on the Environment. A paper Publish by Department of Investigation Planning, Yucetepe/ Ankara.

Goldsmith, E. and Hildyard, N. (1984). "Dam and Disease". UK, Publisher.

Hunter (1993). Parasitic Diseases in Water Resources Development: The need for intersectoral negotiation. World Health Organization, Geneva 1993.

International Commission on Large Dams (1998). "World Register of Dams".

Tetteh, I.K., and Frempong, E. (2001). An Analysis of the Barekese Dam in Kumasi, Ghana. Unpublished Dissertation. Department of Biological Science, Kwame Nkrumah University of Science and Technology, Kumasi, Ghana.

World Commission on Dams (2000), (2006). "Dams and development: A new framework for decision-making" The report of the World Commission on Dams, Earthscan, London.

Yamana, T. (2004). The Impacts of Dams and Reservoirs on Public Health. A publication of Merowe Dam Group, London.

ASSESSING THE ENVIRONMENTAL IMPACT OF P00R DRAINAGE IN BOSSO TOWN, NIGER STATE, NIGERIA

Ahmed Y[1], Ishaq, A.B[2], Waziri, A.M[3] and Odekunle, M.O[4]
[1,2,3,4]Department of Geography, Federal University of Technology Minna, Niger State. Nigeria
yusuf.ahmed@futminna.edu.ng,
aishaq@futminna.edu.ng,
a.waziri@futminna.edu.ng
odemary@futminna.edu.ng

Abstract

The research is to examine the environmental impacts of poor urban drainage system in Bosso town. Poor drainage system have become a problem which lead to soil erosion, flooding and other land degradation processes of the ground surface, gully erosion and excess surface water to the infrastructure and settlement which also lead to flooding. The research is also to locate the erosion prone areas and examine the drainage pattern within the study area, to identify and analyze the major environmental impacts of poor drainage in the study area. The data for the analyses was collected through terrain analysis on the study area with the aid of digital elevation model (DEM) from shuttle radar topographic mission (SRTM) and the drainage network of the study area was extracted through the interpolation of flow accumulation and flow direction from the SRTM data (DEM) using ArcGIS 10.3 software, the digital elevation model was further classified using image classification scheme feature in Idrisi software and an overlay of the DEM and google earth image of the study area to generate the risk map of the study area and Questionnaire was used which frequency-percentage technique was adopted as one of the techniques for the analysis. The analysis of frequency percentage is one of the first techniques used in the analysis of research data that were collected through the use of questionnaire. The frequency-percentage technique is relatively easy to analyze, present and interpret. Frequency percentage= $\frac{number\ of\ observed}{total\ number} \times \frac{100}{1}$ *. there are a lot of poor drainage system in the study area which have result to very high erosion risk zone attributed to low slope and high surface soil moisture while the very low risk zones can be attributed to factor such as high slope and low run-off respectively which the drainage should be linked to solve the problem of erosion and other land degradation processes.*

Keywords: drainage, flooding, land degradation, impact, digital elevation model (DEM), shuttle radar topographic mission (SRTM)

1.0 Introduction

Drainage systems are pathways created naturally or constructed to address the increasing problems of diffuse sewage and run-off over an area. The run-off whether deliberate or accidental can be a major cause of flooding and polluted stagnant water in urban environment. Water is very essential for so many purposes such as for human consumption, plants use and other various purposes, but can also cause devastation through erosion and flooding when it's not properly controlled on the earth's surface.

Due to the development of infrastructures as a result of urbanization, the surface runoff water is drastically increasing in the urban area damaging infrastructures, displacing people from the affected area and sometimes leads to loss of lives (Udosen, 2011). The contributed runoff water therefore needs to be safely disposed or evacuated to the rivers/outlets channels so that the functional utility of the infrastructure is maintained and therefore avoid the damages. Adequate drainage is very essential in the design of an urban area since it affects the town serviceability and

usable life. If ponding on the traveled way occurs, aquaplaning becomes an important safety measure.

Drainage systems are of advantageous towards various environmental sectors such as buildings, agricultural sectors, landscape and among others. These advantages includes; water accumulation prevention, it reduces the occurrence of soil erosion, it guarantees a healthy living if properly managed, it reduces flooding and other environmental-related problems.

Drainage design involves providing facilities that collect, transport and remove storm runoff from the town or city. Flood which is another output of inadequate drainage system is also discussed as follows. Flood is the overflow of water into an environment that is normally dry thereby causing inundation and harm to plants and animals including man. Its harm can be extended to man's buildings and infrastructures (Udosen, 2011).

This study tends to describe the two kinds of drainages that are available in the entire Bosso town, their dimensions and also their effects on the environment. These kind of drainages which are available in the study area includes the artificial drainage system (constructed drainage system) and the natural drainage system (originated through occurrence of erosion or flooding). There are poor nature of urban drainages in most parts of Bosso town and which are not efficient enough to channel the stagnant water that flows on the earth surface for hours or even days after a heavy down pour. This surface flow is however what often leads to the occurrence of the natural drainages which on the other hand disorganizes and disintegrates the landscape of the area. As a result therefore, the study tends to look at all these geographical/environmental problems which are viable in Bosso town, Niger state with a view to finding a lasting solutions to these environmental problems.

Bosso is a local government area in Niger State, Bosso local government has an area of 1,592km² and a population of 147,359 at the 2006 census, the postal code of Bosso is 920 (Nipost, 2010). Bosso is a commercial urban area or more of a central place in Niger state. Bosso lies between Latitude 9º 33'N and 9º 40'N, and Longitude 6º 29'E and 6º 35'E on a geological base of undifferentiated basement complex of mainly gneiss and magnetite. At the North corridor of the town lays a continuous steep out crop of granite, which form a limitation towards physical development in that axis. In the present political zoning system, it is within the north central zone (Niger state ministry of environment, 2013).

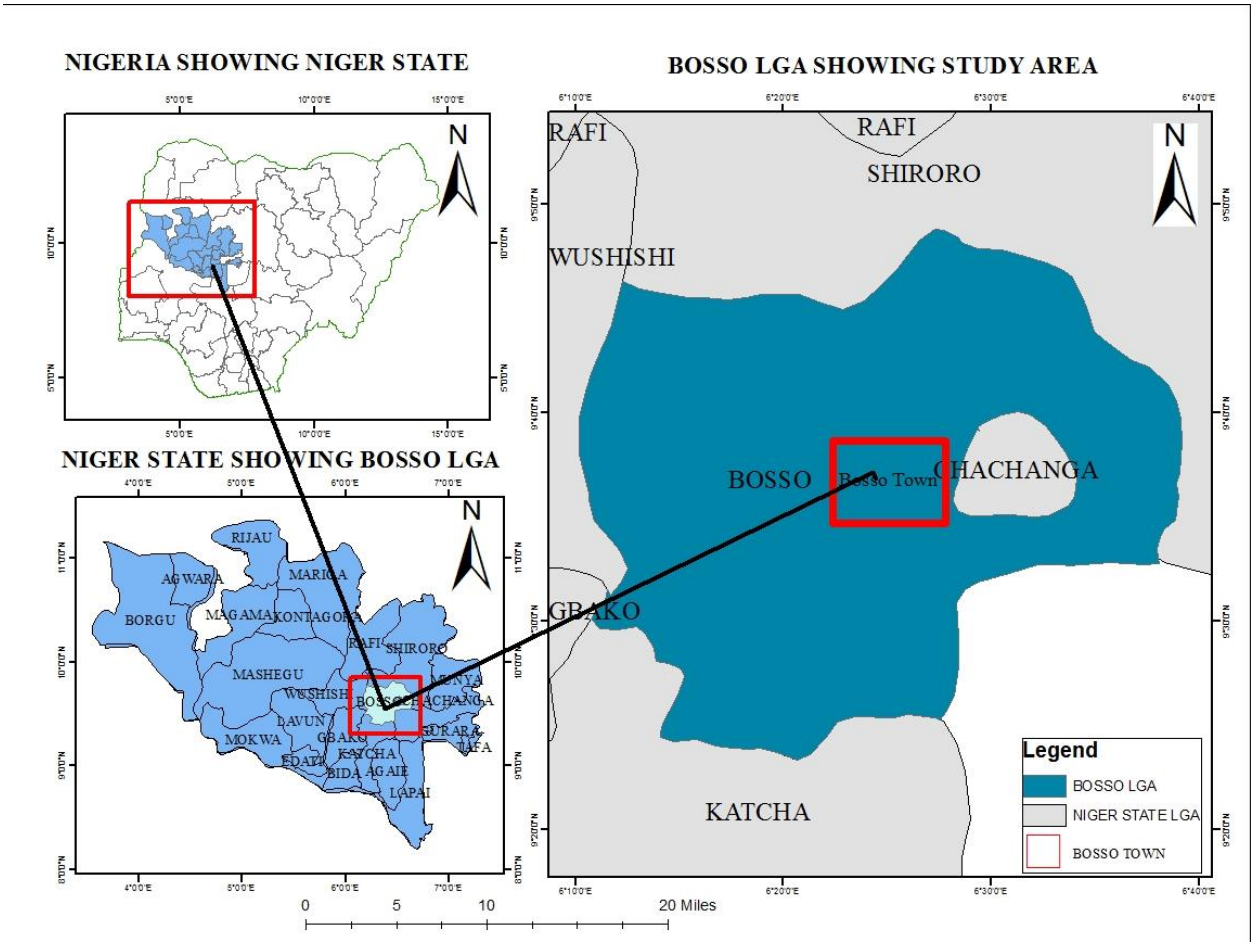

Figure 1.1: Map of the study area

Source: Author' analysis, 2018

1.0 Literature Review

A drainage has in it stream flow and channel characteristics that are in certain equilibrium in three stream regimes which are the upstream, the middle stream and the downstream. When any of the either upstream, middle stream and downstream is tempered with in any way either through human activities or natural cause, the impacts goes directly to the environment thereby causing environmental pollution, Mrokwa (2014).

Consequently, under the scenario, the drainage system upstream affects the downstream due to the induced high speed of the water from the upstream to the downstream location of the channel which has resulted in the distortion of the ecological balance. In the control of the effects, there are local efforts by the dwellers downstream of the channel to reduce the effect by using large stones and concrete reinforced materials to cover some of the areas affected by the artificial erosion activities (Blackham, 2006).

Other additional informal changes in the drainage such as soil excavation from the river bank during the dry season for use in the house construction, cause destruction of the environment with negative effect on the drainage system. On causes of the serious environmental degradation, there is a grievous effect on the drainage system that aggravates solution to erosion and flooding (Blackham, 2006).

Remote sensing and geospatial techniques can be applied in drainage studies through various means such as digital elevation model in determining the flow path/direction, processing of satellite images in the analysis of land use change, terrain analysis, delineation of watershed and among others. Solomon *et al* (2012) use Geographic Information System (GIS) and Remote Sensing Data

for extracting the river drainage pattern. The areas of basins studied using GIS and Remote Sensing Techniques in similar studies are of the range of a few hundreds to a little over thousand sq.km, whereas the study area considered here is 81,155 km². Accuracy of the morphometric properties (based on shape of the basin) depends on the accuracy in delineation of the watershed which is governed by the resolution of the satellite imagery available.

A new approach was developed by Li, Wang, & Hao (2008), in which the river system in digital maps was considered as the correct river network (CRN) while that extracted from DEM was called the digital river network (DRN).Morphometric parameters of a watershed can be studied from the digital network extracted from using GIS.

3.0 Methodology

This include various ways and stages of data collection and how each data was analyse. From primary data source to the secondary data and how it was analyzed.

3.1 Sources of Data

The sources of data for this research includes primary and secondary data sources. Primary source of data for this study include GPS coordinates of gully sites, field survey, questionnaire and oral interview, these four primary sources of data were used to achieve some of the objectives of this study. Secondary data source such as satellite images, drainage map of the study area, internet, journals, text books and related research works were also used to achieve the objectives of this research.

3.2 Data Collection

This is the extensive personal observation carried out by visiting the study area to get the first-hand details on the nature of the drainages such as their capability and efficiency of evacuating surface runoff during rainy season and also the impact of human activities on the existing drainages within the study area.

3.2.1 Oral Interview

An oral interview is an effective research technique which help the interviewer access his or her information needed to carry out his research effectively and efficiently. This method involved personal meetings with designated affected people as result human activities on the drainage channels within the study area.

3.2.2 Questionnaire

Structured questionnaire was designed to collect useful data and information from the respondents. The questionnaire contained multiple choice questions that respondents required to select the option that appealed to them. The areas covered by the questionnaire include causes of the environmental effects poor drainage in the study area, and mitigation and adaptation to cope with the environmental effects.

3.2.3 Sample Size and Technique

Random sampling size technique was adopted in this research. Using this technique, 250 structured questionnaires was distributed randomly across the study area in order to acquire the necessary field data needed to accomplish some of the objectives of this research. Out of the 250 questionnaires administered, 233 questionnaires containing the necessary information were returned while 17 were omitted due to incompleteness and uncoordinated response.

3.1.4 Satellite-Based Data

Digital elevation model (DEM) from shuttle radar topographic mission (SRTM) which has spatial resolution of 30m is acquired in respect to the study area. Digital elevation model is used in this research to delineate the drainage network and to locate the upstream and downstream areas which enables the location of areas that are more vulnerable to surface erosion and flooding. Thus DEM from SRTM data covers objective one of this thesis.

3.3 Method of Data Analysis

3.3.1 Locating the erosion prone areas and examine the drainage pattern within the study area

This objective was carried out through the terrain analysis on the study area with the aid of digital elevation model (DEM) from shuttle radar topographic mission (SRTM) and the drainage network of the study area was extracted through the interpolation of flow accumulation and flow direction from the SRTM data (DEM) using ArcGIS 10.3 software.. The digital elevation model was further classified using image classification scheme feature in Idrisi software and an overlay of the DEM and google earth image of the study area was done to generate the risk map of the study area (Bosso Town)

3.3.2 Identify and analyze the major environmental impacts of poor urban drainage within Bosso town

A frequency-percentage technique was adopted as one of the techniques for the analysis. The analysis of frequency percentage is one of the first techniques used in the analysis of research data that were collected through the use of questionnaire. The frequency-percentage technique is relatively easy to analyze, present and interpret. Frequency-percentage was used to achieve objective two, three and four of this research.

$$\text{Frequency percentage} = \frac{number\ of\ observed}{total\ number} \times \frac{100}{1}$$

4.0 Result/Discussion

This chapter presents the results and discussion based on the earlier stated objectives in the previous chapter. It was analysed using descriptive statistics and remote sensing techniques.

4.1 Analysis of erosion prone areas and drainage pattern within the study area

4.1.1 Digital Elevation Model (DEM)

Elevation and slope play an important role in governing the stability of a terrain. Slope has a dominant effect on the contribution of rainfall to stream flow. It controls the duration of overland flow, infiltration and subsurface flow. Combination of the slope angles basically defines the form of the slope and its relationship with the lithology, structure, type of soil, and the drainage.

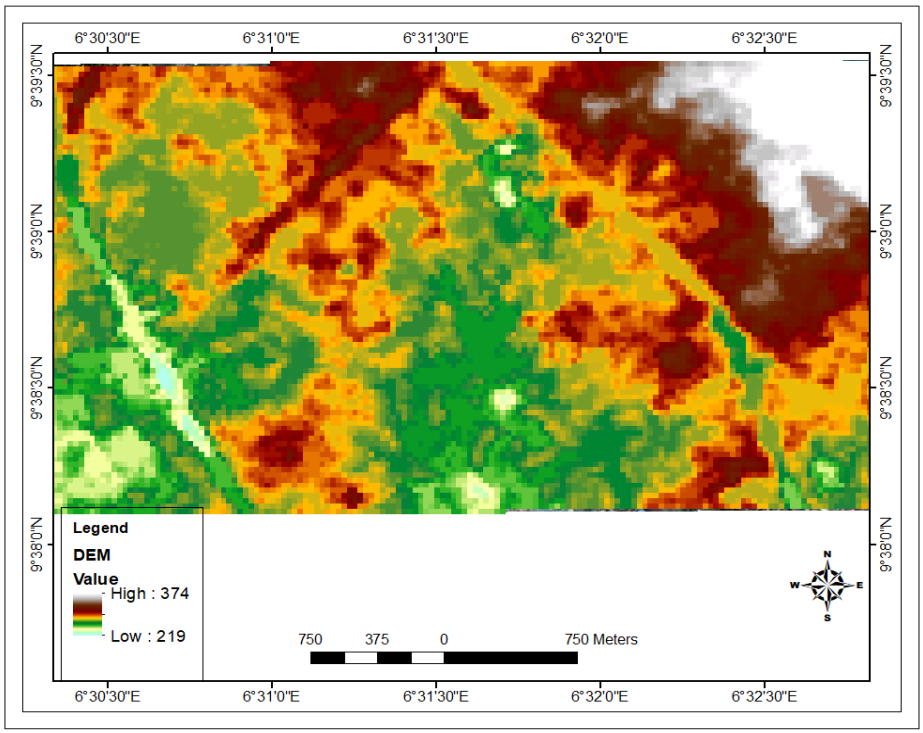

Figure 4.1: Digital Elevation Model of the Study Area
Source: Data Analysis, 2018

Digital Elevation Model (DEM) of the study area was derived from Shuttle Radar Topographic Mission (SRTM) data and the spot heights collected from field survey was used to update the elevations data. The DEM of the study area has elevation ranging from 219 m to 374 m as presented in figure 4.1.

4.1.2 Drainage Patterns of the Study Area

Figure 4.2 portrays the drainage network over the study area, as the areas with unconstructed drainages and abused constructed drainages as a result of human activities are more vulnerable to erosion, flood and other environmental problems such as pollution and landscape degradation during wet season. Areas with more channelized drainages are definitely less vulnerable to erosion and other environmental-related problems but if the constructed drainage channels are not well maintained, the area may fall into environmental danger as that of the areas with no good drainage network.

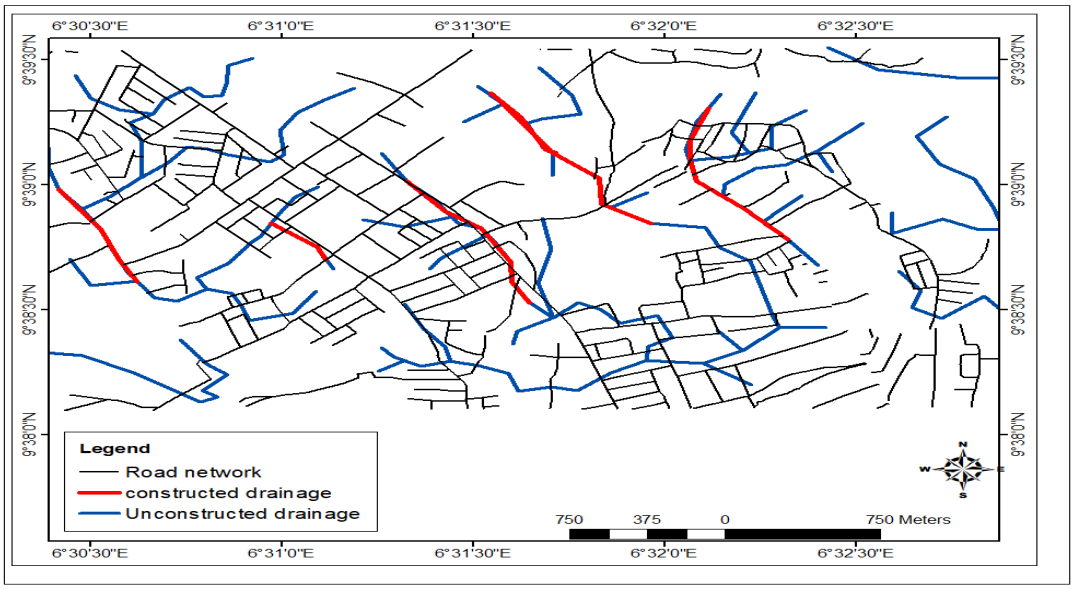

Figure 4.2: Drainage Map of the Study Area
Source: Data Analysis, 2018

4.1.3 Erosion Prone Sites

Erosion and environmental pollution are the major hazard faced by the settlement at the study area. The study showed that the study area lacks efficient drainage system and this is attributed to human activities and attitude towards the environment as buildings and other structures are indiscriminately erected very close to the drainage lines. The study shows that some of the residential buildings were built on floodable terrain as well as wastes from various homes are being dumped indiscriminately on the water ways across the study area. Water run-off during rainfall is usually through the street, this situation aggravate the settlement vulnerability and incidence of flood as shown in the figure 4.3. These communities include Hayan-gwari, tudun-fulani, church villa, Behind Futminna staff quarters, okada road, Bosso estate (From Left-Right respectively).

Figure 4.3: Erosion Prone area over the Study Area
Source: Data Analysis, 2018

4.1.4 Erosion Risk Map of the Study Area

Figure 4.4 presents the erosion risk map of the study area which illustrates how various parts are susceptible to erosion risk. Generally, the erosion risk map over the study is categorized as High, Moderate and Low risk zones covering 2.18 Km^2 (17.59%), 6.26 Km^2 (50.52%), and 3.95 Km^2 (31.88%), of the total area respectively. The very high erosion risk zone can be attributed to low slope and high surface soil moisture while the very low risk zones can be attributed to factor such as high slope and low run-off respectively. So therefore, the drainage network between upland and low land area should be well linked and a regular maintenance should be encouraged to address drainage issues especially in the highly risk zone (low-lying areas)

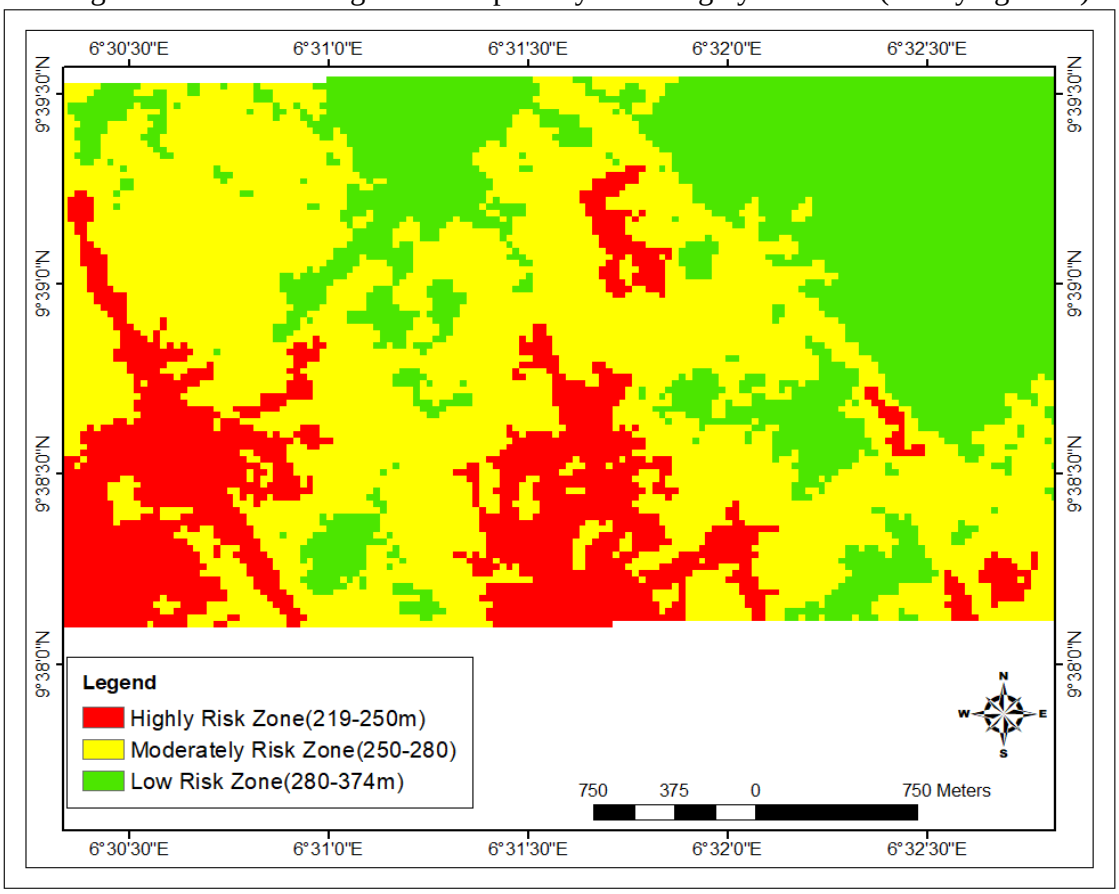

Figure 4.4: Erosion Risk Map over the Study Area
Source: Data Analysis, 2018

4.2 Analysis of the major environmental impacts of poor drainage in the study area

This section presents the major environmental impacts of poor drainages over the study area derived from the analysis of questionnaire.

4.2.1 Demographic Analysis of the Respondents

Figure 4.5, showed that about 54.08% of the respondents are male whereas 45.92% are female. The higher percentage of male respondent is an attention that men are mostly involved in activities that have bearing on the environment.

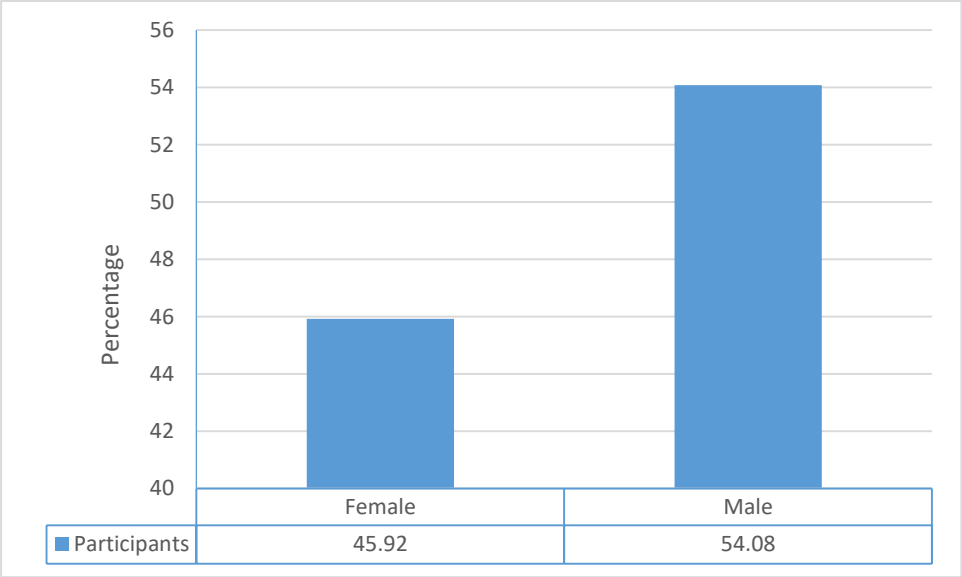

Fig 4.5: Gender Distribution of the Respondents
Source: Field Survey, 2018

Similarly, information on educational qualification of the respondents are presented in Figure 4.6. These shows that about 60.52% of the respondents had attained higher level of education while primary, secondary and no formal education representing 10.30%, 22.75% and 6.44% respectively.

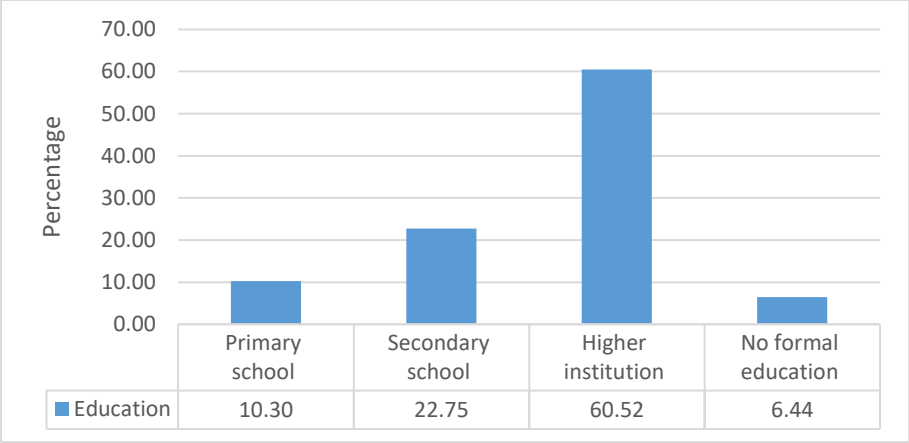

Figure 4.6: Educational Qualification of the Respondents
Source: Field Survey, 2018

Furthermore, information on the range of years by which the various respondents has settled in the study area is presented in figure 4.7. The results showed that (8.15%) has been living there for less than 5years, (17.60%) for 5-9years, (18.88%) for 10-14years, (20.60%) for 15-20years and (34.76%) for over 20years. These implies that the majority of the respondents are familiar with the study area as they have lived over 20years.

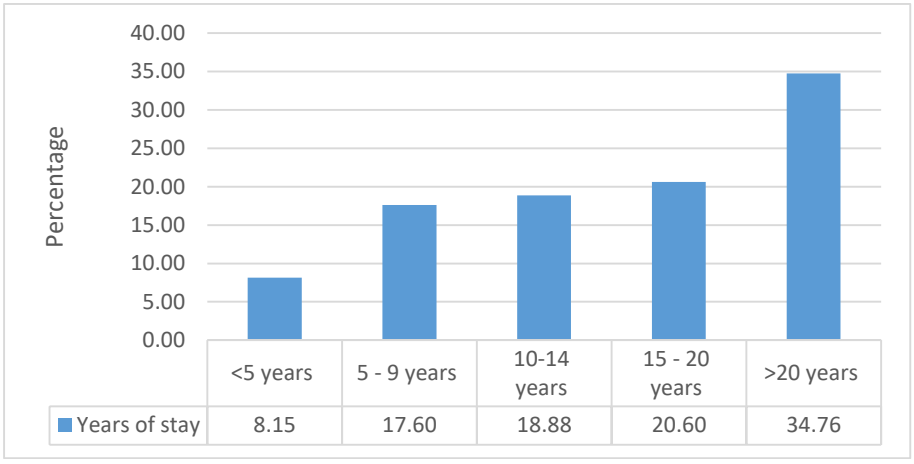

Fig 4.7: Respondents years of stay
Source: Field survey, 2018

4.2.2 Major environmental impacts of poor drainage in the study area

The major environmental impacts of poor drainage in the study area was assessed through the use of questionnaire on current environmental condition which revealed that the study area is currently degraded or seriously degraded as shown in figure 4.8 that degraded ranked the highest with (44.20%), followed by seriously degraded ranked (31.47%) and moderate ranked lowest with n=59 (25.32%). This implies that the study area is under treat of erosion as most of the area along the unconstructed channel are degrading.

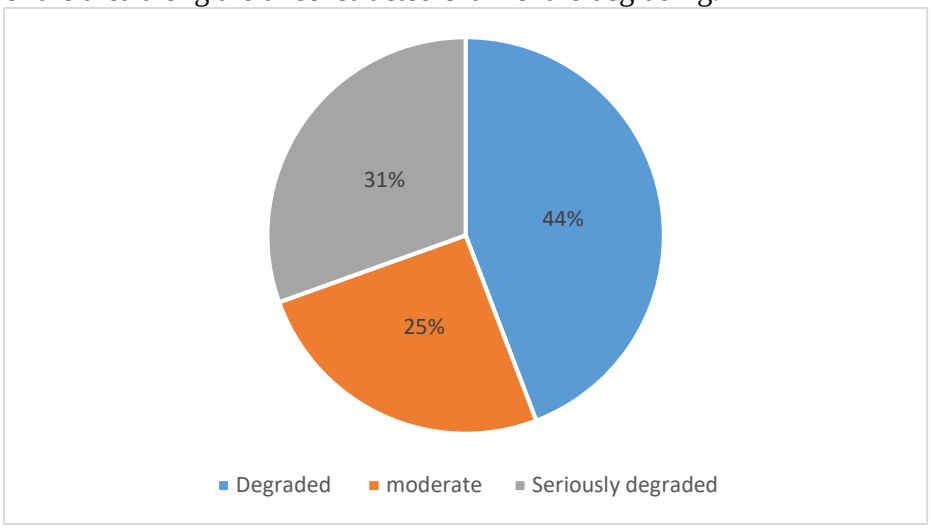

Fig 4.8: Current Environmental Condition over the Study Area
Source: field survey, 2018

5.0 Conclusion and Recommendation

Bosso and its environs are expanding rapidly both in area and population, with a corresponding increase in the urban poor population in slum settlements. The study shows that erosion, flood and environmental pollution are the major hazard faced by the settlements. This is as a result of non-functional drainage system as the little available drainage are being converted to refuse dump sites and also, indiscriminate human activities on available space especially on flood prone locations. Water run-off during rainfall is usually through the street, this situation aggravate the settlement vulnerability and incidence of flood. Most of the flood and erosion

sites identified are usually located at a low land area of the settlement, declaring that low lying areas are prone to flooding.
The following recommendations are as follows;

1. Residential buildings shouldn't be erected very close to drainage lines and other high risk zones.
2. Areas of high hazard need immediate attention, hence appropriate protection measures should be taken earlier.
3. Regular environmental sanitation should be implemented within the local government area to ensure that the existing drainages are well maintained and cleared of blockages by sediments, refuse and other solid materials.
4. Unconstructed drainages should be channelized to effectively evacuate storm run-off within the study area to a larger river outlet during wet season.
5. Embankments and other structural flood control measures should be constructed at areas of high risk.

References

Blackham, D. (2006). The resistance of herbaceous vegetation to erosion: implications for stream form. PhD, University of Melbourne.

Mrowka, J. P. (2014). Man's impact on stream regime quality: Manners and Mikesell (Eds), Perspectives on Environment, pp. 79-104.

Udosen, C. (2011). "Flood Problems in Uyo Local Government Area" Eroflod Consulting service. Uyo.

Solomon *et al*, (2012). Extraction of drainage pattern from ASTER and SRTM Data for river basin. *International Conference on Environment, Energy and Biotechnology*.

Li, L., J. Wang, and Z. Hao. 2008. Appropriate contributing area threshold of a digital river network extracted from DEM for hydrological simulation. IAHS-AISH Publication (322): 80-7.

SPATIAL DISTRIBUTION OF HOTELS IN MINNA: A GIS CLOUD MAPPING TECHNOLOGY MODEL

Odekunle, M.O[1] Adebona, A. O[2] Ahmed, Y[3] Acha, S. & Waziri, A.M[3]
[1,2,3,4]Department of Geography, Federal University of Technology Minna, Niger State. Nigeria
Corresponding email: odemary@futminna.edu.ng yusuf.ahmed@futminna.edu.ng
a.waziri@futminna.edu.ng

Abstract
Hotels are important to every society. This is because they create lodging facilities for businesses people and tourists. Hotels commonly provide a number of different services within the same or different building which are often available for the use of both residents and non-residents of the hotel. This study evaluates spatial distribution of hotels in Minna metropolis using Geographic information techniques and creating a mobile application of the hotels using GIS cloud. Coordinates and information about each hotel used in this study was collected. The points were analyzed in ArcGIS 10.2 environment to depict each hotel's geographical location on the map. A total of 46 hotels were surveyed. 6 Guest inns, 5 lodges, 1 motel, 2 Suites and 32 Hotels were surveyed. A cursory look at the map of the metropolis shows that hotels are found almost throughout the metropolis. It can also be seen that most of these hotels are situated along major roads for easy access. The hotels data were imported into the GIS cloud engine in csv. Format. A database was created on the GIS cloud engine anchoring the data using javascript. GIS cloud Mobile Data Collection was obtained from iOperating System Appstore to anchor the data on mobile phone. It is recommended that hoteliers who already have hotels should endeavor to upgrade their services so that they can compete with other international brands.

Keywords-Hotels; Geographic Information Systems; GIS Cloud; Mobile Data Collection.

1.0 Introduction

Hotel is an establishment that provides paid lodging on a short term basis. A hotel provides different services which may range from lodging, restaurant etc. It can be said to be a business enterprise having a building for public accommodation and furnishes lodging and usually provides meals, beverages and personal services, usually regarded as home away from home. Mapping hotels and developing a mobile map with the GIS cloud technology is essential in the modern era as paper maps are gradually becoming obsolete (Baba, 2016).

Hotels have long been a significant constituent in the economies of many nations. Hotels are directly linked to the economy and are an integral part of many other economic activities (Mohanty, 2008). A hotel as a service commerce are keen on locations that are accessible to their potential market because they seek for increased demand from potential guests. Hotels in urban areas are usually highly clustered, because agglomeration results in hotels enjoying benefits from clustering. Generally, one incentive for choosing to locate close to other hotels is to gain a significant positive influence in hotel efficiency (Barros, 2005; Urtasun and Guiterriez, 2006).

Internationally, hotels can be classified based on different criteria. They may be classified based on the location, range of property, the amenities and the kind of service they render. The length of stay of customers, theme, as well as the target market may also be used as a basis for classification (Omogunloye and Ayeni, 2012). The most common method used in classifying hotels is the use of rating (star rating) based on the services rendered. High number of stars indicates more luxury. The most rated star is the 5-star hotel.

The use of service-oriented architecture in Geographic Information Systems (GIS) is becoming progressively more prevalent. This approach helps to hide the technical information of the datasets in question by revealing them through standard, implementation neutral web interfaces, potentially making them presented to wider audiences. The recent emergence of cloud computing conveys new possibilities in service deployment. In the modern societies, Geodata sets are crucial, especially following the near explosive growth in the use and importance of location-aware devices. The most efficient way to convey data geodata to, and between humans is by the use of maps.

Cloud has demonstrated a potential to fulfill a demand that brings about the way IT (Information Technology) is devised, developed, implemented, extended, enhanced, maintained and sold. Cloud computing has been used for different purposes like tourism management. Cloud computing can also be employed in the spatial distribution of some phenomenon's, in this case, it's the spatial distribution of hotels in a particular place. This research shows the spatial distribution of hotels operating in the cloud, in relation with their location, working hours, the kind of the hotel.

Minna is a city in Middle Belt Nigeria, with an estimated population of 304,113 in 2007. Minna is the capital of Niger state. This is largely responsible for the concentration of hotels in the area and as therefore, given birth to the need to map the distribution of hotels using GIS cloud technology. It is located between latitude 9º41'6.3''N, 6º30'0''E and longitude 9º35'7.7''N, 6º36'34''E and it is situated at elevation 243 meters above sea level. Minna is estimated to occupy a land mass of about 6,784SqKm (Simon, Duntoye, & Oyewole, 2018). Minna is the home of Nigeria's former Head of State Abdulsalami Abubakar and former Military President Gen. Ibrahim B. Babangida, Presently Abubakar Sani Bello is the governor of Niger State (Encyclopedia Britannica, 2009).

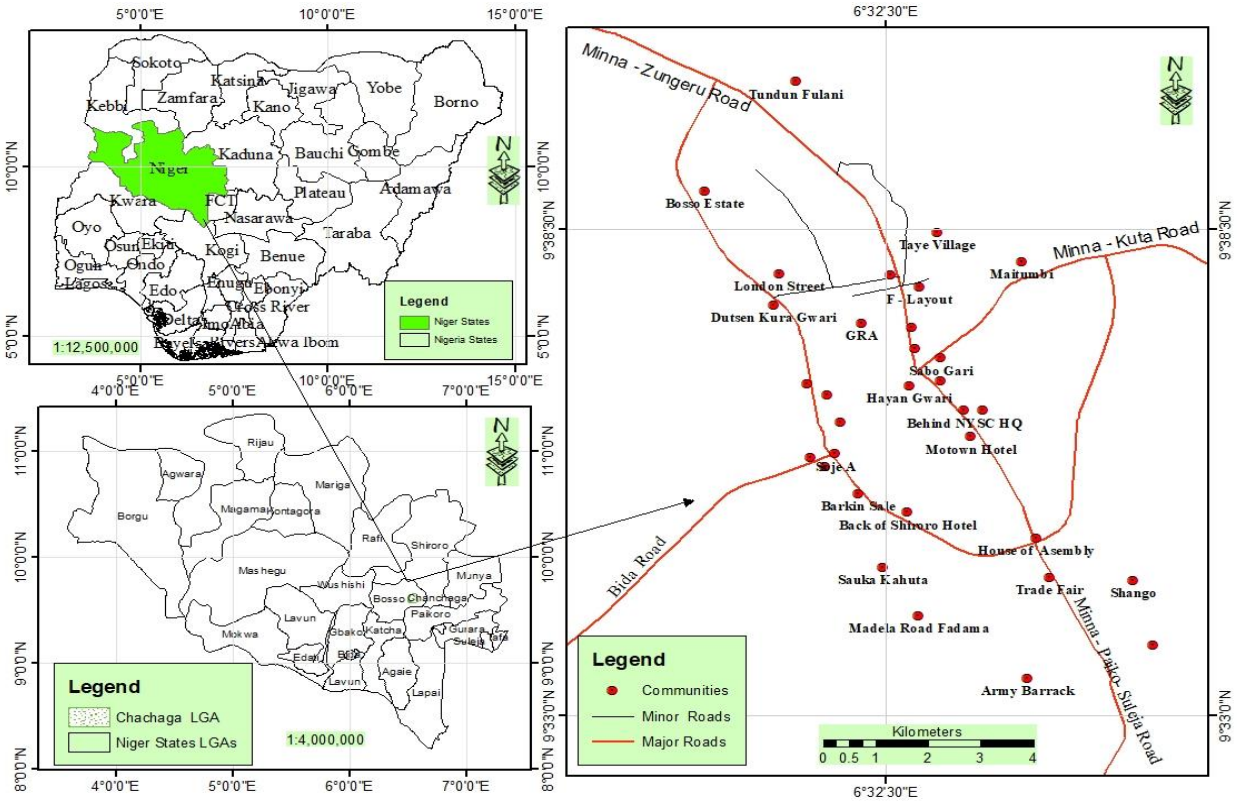

Figure 1: The Study Area

Technology is advancing all over the world and the use of manual maps, that is, paper maps is becoming obsolete. This sole reason prompts the use of Geographic Information System and Remote Sensing techniques in gathering information and to understand our immediate

environment. Therefore, there is need to create a mobile map of hotels in Minna metropolis which can be used by individuals.

2.0 Literature Review

(Scott, 2008) defines a hotel as a wide spectrum of property types from larger units having up to or maybe in excess of 1000 letting bedrooms, to smaller units maybe having as few as 10 or even less. Hotels commonly provide a number of different services within the same or different building which are often available for the use of both residents and non-residents of the hotel. These include the provision of letting bedroom, food and beverage services in restaurants, bars and banqueting rooms, conference/mailing rooms and leisure facilities (Otegbulu and Tenigbade, 2011).

Hotels are important to every society. This is because they create lodging facilities for business people and tourists (Omoguloye and Ayeni, 2012). Hotel investments hold vast potentials for job creation and economic stimulus. They create jobs, generate foreign exchange, purchase goods and services locally, and also pay taxes. Visitors in the hotels spend outside the hotel and help to improve the socio-economic status of the area (International Finance Corporation, 2012).

Cloud computing is a technology that allows the provision and utilization of resources over the internet in lieu of installations on a desktop computer (Cecowski, M. 2007). Information Systems (IS) can be consumed as utilities like water and electricity through cloud computing (Carr, N.G. 2008). Four deployment models are specified in the National Institute of Standards and Technology (NIST) cloud computing definition: Private, Public, Community and Hybrid clouds. Adoption of cloud computing brings about technological, economical and environmental benefits to an organization, which is also the case for hospitality industry. New technologies and competitive marketing strategies available through the cloud such as the use of social media, channel management, online reservation streams, hotel review portals and increased use of mobile technology for improved customer service have significantly changed the way hotels interact with their customers and will still change for a long time to come (Protel hotelsoftware GmbH. 2012).

GIS Cloud is an Integrated System of Hardware, Software and Spatial Data to produce maps and reports which simplifies the analysis and the informed decision making. It is a type of virtualized computing resources that are provisioned based on service-level agreements. ESRI and GIS Cloud Ltd are among the global organizations that are already using cloud computing to provide on-demand services to users (Rajkumar Buyya, 2008). GIS Cloud main characteristic is its unique vector visualization engine which improve the way we can use and present maps. It also allows the integration to any other GIS solutions. The GIS CLOUD solutions include: Mobile Data Collecting, Map viewer, Map portal, Map editor. Customers focus more on their applications and the development team manages and supervises the security and reliability of the GIS Cloud solution. GIS Cloud is the solution for increased GIS applications in optimized planning, informed decision making and emergencies at reasonable cost in no time and efforts. It allows in site mobile data collection, editing and publishing in real time using another programmer or application. Also, it gives the opportunity to develop, edit, and publish on the map from the field using the internet and simple gadgets (Omar Al-Bayari, 2018).

In 2013, Adeyemi mapped the locational patterns of hotels in Akure, Ondo State, Nigeria. In order to make this possible, a record of hotels in the area, their addresses, as well as an analogue map of Akure were obtained from the Ondo State Tourism Board. Coordinates of the hotels were captured (64 out of 65) using a hand held GPS. The study records that hotels are found all over the town but are concentrated outside the central business district. It further revealed that Oke-Ijebu/ Ijapo axis located in the North Eastern part of the town is were the highest number of hotels in the area are found representing 31.3%. It is so because this axis is majorly the residential area in Akure and has an express road linking it to the CBD (Central Business District) which allows patrons easy access. The study further showed that most of the hotels with higher ratings cluster around the Government Residential Area of the state.

Similarly, Shunopaul Baba (2016), investigate the spatial distribution and service delivery of hotels in Kaduna metropolis. Where research questions were formulated to guide the study among which is where the hotels are located, what the pattern of distribution is and what are the services provided by these hotels and the proximity of the hotels to banks, offices. Findings reveals that the number of hotels in one area differs from that of other areas. It is worthy of note that the metropolis does not have a single hotel in the 4 and 5star categories. This means they do not provide the services that guest require and they do not meet the international standards for hotels.

3.0 Methodology

This includes the various stages involved in acquiring the desired result. It also involves the steps employed in digital mapping and includes all activities carried out from planning to actual data acquisition and refinement.

3.1 Sources of Data

- Primary data: this is the data collected by the researcher himself for the purpose of the research. Coordinate points of various hotels within the study area were collected using hand held GPS.
- Secondary data: these are the data being utilized by the researcher that was provided by other people. These include shapefiles (LGA, minor roads shp, major roads shp), journals, materials obtained from the internet and others.

3.2 Data Collection

Coordinates of hotels across the study area was collected with parameters which include name of the hotels, working hours, address, district, road name and pictures were taken. The hotel coordinates obtained from the field was input into excel in csv. Format. The georeferenced shape files of the study area was used in the ArcGIS 10.1 environment.

3.3 Methods of Data Analysis

The hotels in the study area were identified using hand held GPS and then mapped. This was achieved by computing the coordinate points into excel and saved on the local disk. Thereafter, the coordinates were added to the shape files (LGA, minor road shp, major road shp) in the ArcGIS environment were the point location of various hotels in the study area was displayed with their attributes.

Mobile map of Hotels

To fulfil the objectives, a relational database of the hotels in the study area was created. The hotel was associated with a set of attributes:

- Coordinates.
- Name of hotels.
- Address.
- District.
- Road name.
- Contact.
- Working hour.
- Picture.
- Distance to city center (Mobil).
- Cost of transport.
- Hotel facilities.

Importing data to GIS cloud

It is important to import data into GIS cloud to create a mobile map. The data could be csv. Or xls. Format. In this case, csv. Format was adopted. The steps used in importing the data are;

- On the later Tab or open Database Manager.
- Select Import CSV or XLS function
- Browse for the uploaded XLS or CSV in File Manager
- Set the table parameters, select the coordinate fields and click import.

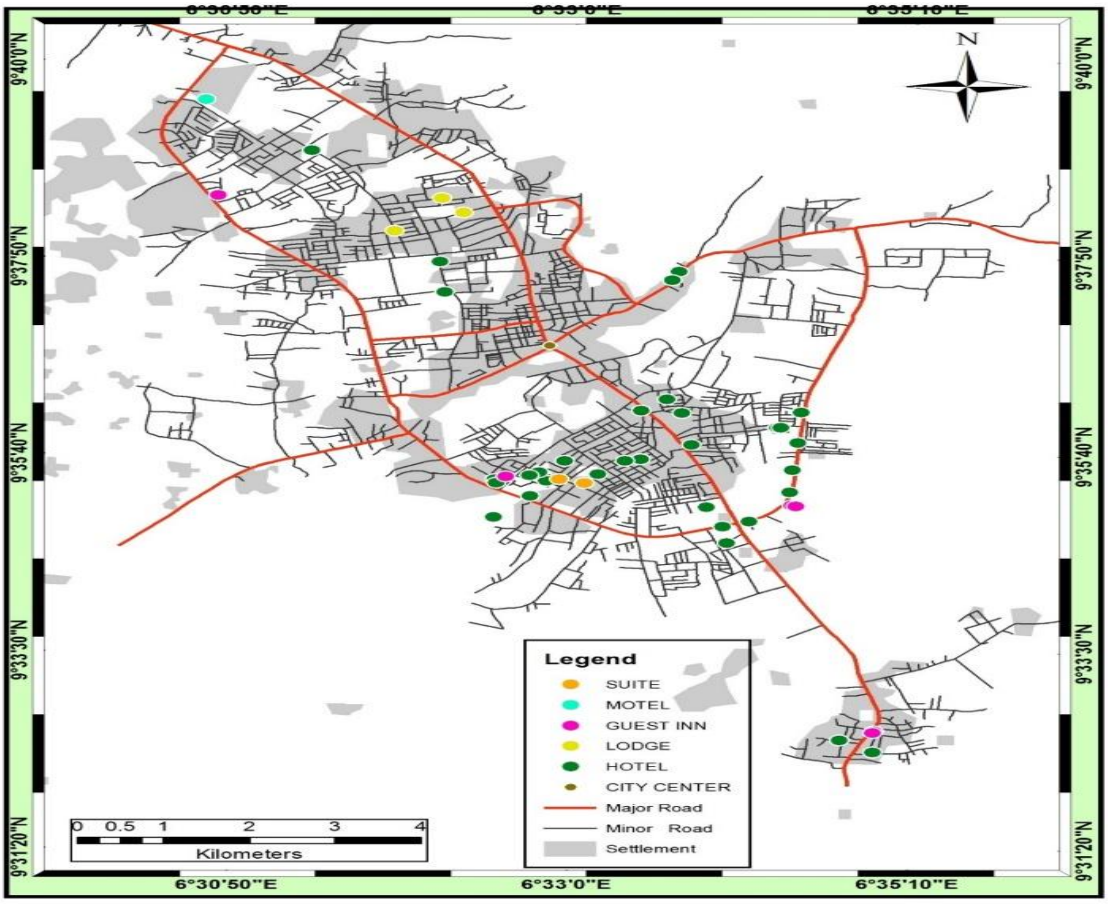

Figure 2: Distribution of different categories of hotels in Minna metropolis.

Steps in creating mobile map on GIS cloud

The steps involved in creating a data base with GIS cloud to synchronizing it with mobile data collector includes:

1. Import csv. or xls. data into GIS cloud.
2. Edit the data structure using variables, strings or reals.
3. Name the fields starting with letters or an underscore(_)
4. Overlay the data with an open street map.
5. Synchronize the data with mobile data collector on a mobile phone.

Features of mobile map of hotels in Minna metropolis.

- It will give users information about the hotels in Minna metropolis.
- It will give a friendly user interface.
- It will provide a navigation option where users can get direction.

4.0 Result/Discussion

GIS cloud for mobile app is synchronized with mobile data collector which enables users to interact with the app with a friendly user interface. Data collected and analyzed with ArcMap can be turned into mobile map using the GIS cloud model. Figure 3 on the last page of this paper gives an outlook of mobile map of hotels in Minna. When running the app, the data integrated with GIS cloud synchronized with mobile data collector will be displayed which is on the main screen. There is also splash screen that comes up linked with the main screen that display the information of each hotels on the app. This information linked with the main screen includes:

- Coordinates.
- Name of hotels.
- Address.
- District.
- Road name.
- Contact.
- Working hour.
- Picture.
- Distance to city center (Mobil).
- Cost of transport.
- Hotel facilities.

There is also a navigation option that allow the users to access locations. Each hotel on the map is depicted as a point and when clicked on displays the information about the hotel.

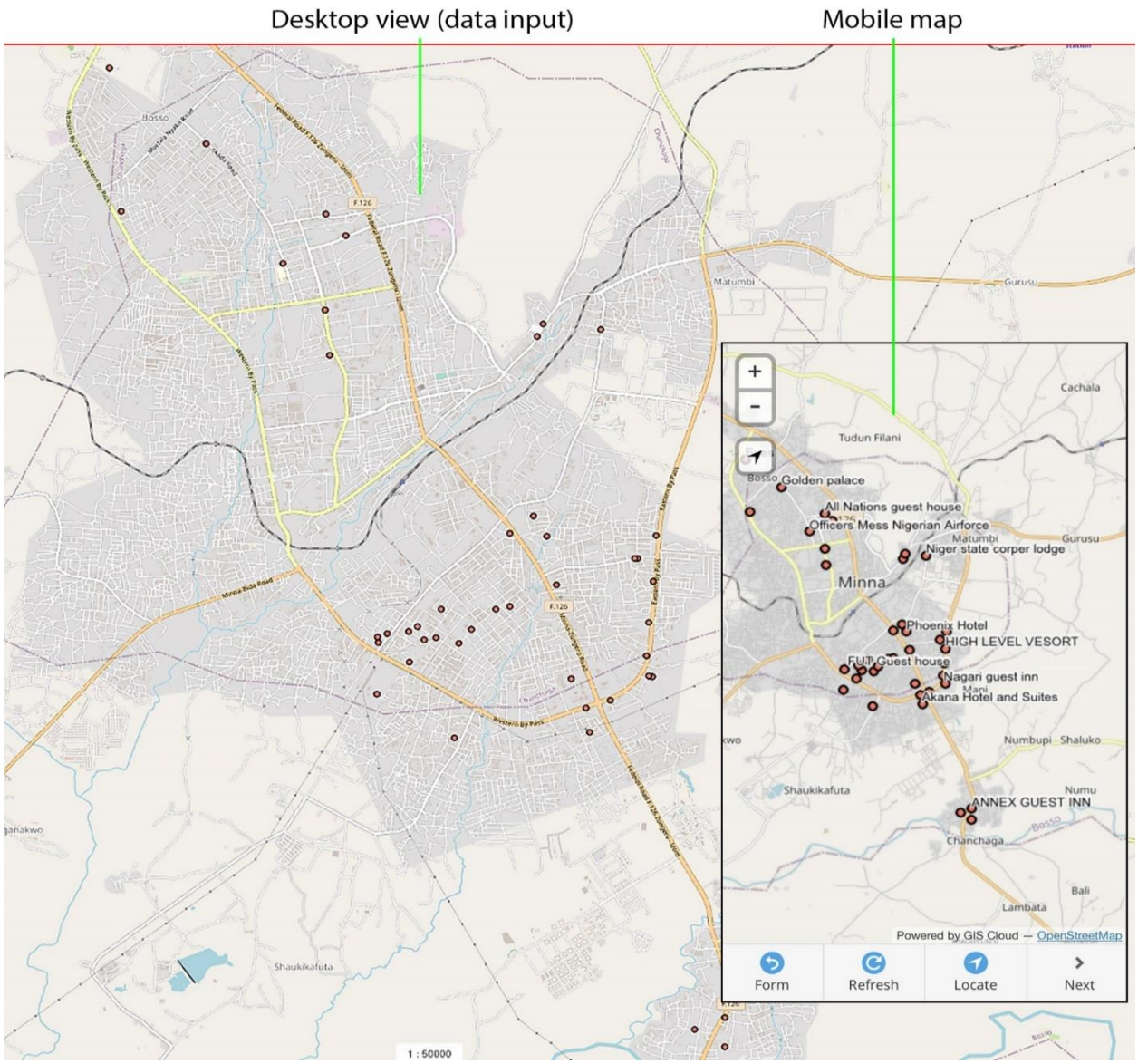

Figure 3: Hotels in Minna metropolis showing on desktop and mobile

5.0 Conclusion and Recommendation

This study was based on the spatial distribution of hotels in Minna metropolis. Three research questions were formulated to aid the study which are where are the locations of the hotels are and how it can be mapped out? What is the pattern of distribution of hotels in Minna? How can mobile app of hotels in Minna be developed? After the analysis, it was revealed that hotels in the metropolis cluster in areas that have easy access to the central business district of the city. Also, the nearest neighbor ratio is 0.629090. Mobile app of Minna was developed using GIS cloud engine which will help visitors and inhabitants to access information about hotels in Minna metropolis.

This study recommends possible methods that would aid hotels in Minna metropolis to manage their data and create a friendly database for records and for their customers.

1. Hoteliers who already have hotels should endeavor to upgrade their services so that they can compete with other international brands.
2. Hotels should have a detailed geodatabase that will help their customers in surfing the services they render.

3. Hotels in the metropolis should have a collective mobile app that would aid customers in navigation and other services.
4. Map produced in this research work should be implemented for use in other places other than hotels.

References

Adeyemi, B.A. (2013). Mapping the Locational Pattern of Hotels in Akure, Ondo State.Journal of Humanities and Social Sciences.

Barros, C.P (2005). Measuring Efficiency in the Hotel Sector. Annals Tourism of Tourism Research 32(2)456-477

Baba, S. (2016). Spatial distribution and service delivery of hotels in Kaduna metropolis, Nigeria.

Carr, N.G.: The big switch: Rewiring the world, from Edison to Google. WW Norton & Company (2008)

Cecowski, M., Becker, S., Lehrig, S. (2017): Cloud Computing Applications, pp.47 {60. Springer International Publishing, Cham (2017) Encyclopedia Britannica, (1964).London: William Benton.esri. (n.d.). Retrieved from https://www.esri.com

Encyclopedia Britannica, (1964).London: William Benton.

International Finance Corporation (2012) Annual Report. http//:www.ifc.org

Mohanty, P. (2008). *Hotel Industry and Tourism in India*.New Delhi: APH Publishing.

Omar Al-Bayari. (2018). GIS Cloud Computing; Aplication. 1-4.

Omogunloye, O.G. &Ayeni, O.O. (2012). Analysis of Hotels in Lagos State with Reference to Other Spatial Data.*Research Journal in Engineering and Applied Sciences*, 1(6), 393-403

Otegbulu, A.C&Tenigbade, O. (2011).An Assessment of Lodger‟s Value Perception of Hotel Facilities and Services. *Journal of Sustainable Development*, 4(4), 91-100

Protel hotelsoftware GmbH: Top Four Indicators it's Time to Change a Running [Property Management] System (2012)

Rajkumar Buyya, Chee Shin Yeo, and Srikumar Venugopal. (2008) “Market-Oriented Cloud Computing: Vision, Hype, and Reality for Delivering IT Services as Computing Utilities,” Keynote Paper, Proceedings of the 10th IEEE International Conference on High Performance Computing and Communications (HPCC 2008, IEEE CS Press, LosAlamitos, CA, USA), Sept. 25-27, 2008, China.

R. Funsho, Simon, Duntoye Dorcas Busayo, and Oyewole Kehinde(2018).The Effects of Urbanization on Micro-Climate of Minna Urban Area. *Journal of Geography, Environment and Earth Science International 15*

Scott, B. (2008). Hotels in the Edited Book Valuation: Principles into Practice 6 th ed. London: EG books.

Shunopaul Baba. (2016). Spatial Distribution and Service Delivery of Hotels in Kaduna Metropolis, Nigeria. 55-56.

Analysis of Drought and Flood Occurrence Using Markov Chain

[1]Musa, Oziohu Khadijat; [1]Lawal, Adamu
[1]Department of Mathematics Federal University of Technology, Minna.

Abstract
Flood and drought are among the most common natural disasters affecting the world. In this paper, Markov model has been used to analyse and predict flood and drought occurrences in Birnin Kebbi Nigeria. The Standardized Precipitation index (SPI) was used to classify the annual rainfall of Birnin Kebbi into three states (flood, normal and drought). After some successful iterations of the model, the model stabilized to equilibrium probabilities, revealing that in the long-run 20% of the years in Birnin Kebbi will experience flood, 60% will experience normal rainfall and 20% will experience drought. It was also observed that, a drought year cannot be followed by a flood year and the probability of a drought year to be followed by a normal year is high while the probability of a normal year to be followed by a drought year and a drought year to be followed by another drought year is extremely small. Results from this research is an important information to the government and people of Kebbi state for better understanding of rainfall dynamics in their locality.

Keyword: Markov model, Annual Rainfall, Standardized Precipitation Index, Transition Probability, Equilibrium Probabilities.

Introduction

Floods and droughts are among the most disastrous natural hazards in the world (Bates, *et al.*, 2008; IPCC, 2007b, 2012). Drought occurs when there is significant rainfall deficit that causes hydrological imbalances and affects the land productive systems. Drought practically occurs in all climatic regions with both high and low mean rainfalls (Um *et al*. 2017). It can result in damaging agricultural production and the natural environment (Gidey*et al*. 2018). Drought is often seen as a "creeping" phenomenon with slow onset and cessation. As a result, an effective drought monitoring system is the most important tool for developing and implementing efficient mitigation strategies. However, not only can the onset of drought conditions be rapid, an indication of how long drought conditions may continue will enable improved planning and resource allocation. For this reason, a capability to accurately forecast the onset, persistence and cessation of drought conditions will enable more effective drought mitigation strategies to be developed (Singleton, 2012). Guha-sapir *et al* (2012) defines flood as significant rise of water level in a stream, lake, reservoir or coastal region. Also, (Nelson, 2007) defined flood as excessive water run-off or the rise in water level in a particular area which is more than what the particular environment can absorb. Flood and drought are one of the most devastating natural disasters in the world.

In Nigeria, the story is not different as these has caused serious havoc to our environment and the economy. However, little or nothing can be done to avoid its occurrence but prior information such as prediction of flood and drought can assist the farmers, stakeholders and the general public to take adequate proactive measure in order to mitigate their effects. Hence, the result from this model will provide adequate information about flood and drought in some upcoming years for the studied areas. According to NEMA, in 2012 alone, floods caused more than N2.6 trillion in economic damage, much of which could be attributed to large-scale trans boundary floods (from rivers Niger and Benue). In 2019, about 126 deaths were recorded, over 48,000 people were displaced and property worth millions of Naira destroyed across the country (Nigeria Hydrological Services Agency, 2020).The Standard Precipitation Index (SPI) was introduced by McKee *et al*. (1993) as measure of the precipitation deficit that is uniquely related to probability. It can be calculated for any accumulation timescale, usually from monthly precipitation observations, and is typically expressed

as SPI-n, where n is the number of months of accumulation. The time series is analogous to a moving average in the sense that a new value is calculated each month and is auto-correlated to previous months depending on the accumulation timescale (Singleton, 2012).

Materials and Method

Birnin Kebbi is the capital city of Kebbi state, is located in north-western Nigeria on (12˚ 27′ N and 4˚ 11′ E).The data used for this research work were obtained from the National Oceanic and Atmospheric Administration (NOAA) for the period of thirty years (1991 to 2020). After which the SPI was used to classify the rainfall into states

Model Formulation

Suppose that the SPI rainfall classification for a year is considered as a random variable x, the collection of these random variables over the years constitute a stochastic process χ_n, n=0,1,2,3,…, we assume that this stochastic process satisfies Markov property.

Let the annual rainfall be modelled by a three-state Markov model based on the SPI classification
State 1: Flood (SPI Value ≥1)
State 2: Normal (-0.99≤SPI Value ≤0.99)
S**tate 3**: Drought (SPI Value ≤ -1)
The transition probability matrix is represented by

$$P=\begin{bmatrix} P_{11} & P_{12} & P_{13} \\ P_{21} & P_{22} & P_{23} \\ p_{31} & P_{32} & P_{33} \end{bmatrix} \quad (1)$$

Following (Lawal, 2017), let $P^{(n)}$ be the probability state vectors of the Markov chain, where n=0,1,2,3,… and let $P_i^{(n)}$ be the probability that the annual rainfall is in the ithstate at the nth year. $P^{(0)}$ is the initial state vector of the Markov chain and p$^{(n)}$ is the state vector at the nth year. Then, by induction we have that

$$P^{(n)} = P^{(n-1+1)} = P^{(n-1)}.P = P^n \quad (2)$$

On iteration we have,

$$P^{(n)} = P^{(0)}P^n \quad (3)$$

That is, the initial state vector $P^{(0)}$ and the transition matrix P determine the state vector $P^{(n)}$ at the nth year. If we now let

$$P^{(n)} = \begin{bmatrix} P_1^n & P_2^n & P_3^n \end{bmatrix} \quad (4)$$

Denote the probabilities of finding the annual rainfall in any of the three states at the nth year and also let

$$P^{(0)} = \begin{bmatrix} P_1^n & P_2^n & P_3^n \end{bmatrix} \quad (5)$$

Denote the initial state vector and its elements, the Markov chain model for annual rainfall based on SPI classification in the study area can be represented by

$$\begin{bmatrix} P_1^n & P_2^n & P_3^n \end{bmatrix} = \begin{bmatrix} P_1^0 & P_2^0 & P_3^0 \end{bmatrix} \begin{bmatrix} P_{11} & P_{12} & P_{13} \\ P_{21} & P_{22} & P_{23} \\ P_{31} & P_{32} & P_{33} \end{bmatrix}^n \quad (6)$$

Limiting State Probability

The limiting state probability is represented by equation (7) below and is obtained when n → ∞ in equation (3).

$$\pi = \pi P \quad (7)$$

where $\pi = \begin{bmatrix} \pi_1 & \pi_2 & \pi_3 \end{bmatrix}$

$$\pi = \sum_{i=1}^{3} \pi_i = 1 \quad (8)$$

These equations will be use to find the limiting state probabilities for our model.

Results and Discussion

Table 1: A Summary of SPI Annual Rainfall Classification of Bernin Kebbi.

SPI classification	frequency	State
SPI value ≥ 1	6	Flood
-0.99≤ SPI value≤ 0.99	18	Near normal
SPI value ≤ -1	6	Drought

From Table 1, we obtained the transition count presented in equation (9)

$$C = \begin{bmatrix} 2 & 2 & 2 \\ 4 & 10 & 3 \\ 0 & 5 & 1 \end{bmatrix} \quad (9)$$

The probability transition matrix obtained from equation (9) is presented below

$$P = \begin{bmatrix} 0.333 & 0.333 & 0.333 \\ 0.235 & 0.588 & 0.176 \\ 0 & 0.833 & 0.167 \end{bmatrix} \quad (10)$$

Calculating P^n , on iteration we have

$$P^2 = \begin{bmatrix} 0.189 & 0.584 & 0.225 \\ 0.216 & 0.571 & 0.211 \\ 0.196 & 0.629 & 0.174 \end{bmatrix} (11)$$

$$P^4 = \begin{bmatrix} 0.206 & 0.585 & 0.205 \\ 0.205 & 0.584 & 0.206 \\ 0.207 & 0.582 & 0.207 \end{bmatrix} (12)$$

$$P^{8} = \begin{bmatrix} 0.206 & 0.583 & 0.205 \\ 0.205 & 0.583 & 0.205 \\ 0.206 & 0.583 & 0.206 \end{bmatrix} (13)$$

$$P^{20} = \begin{bmatrix} 0.204 & 0.577 & 0.204 \\ 0.204 & 0.577 & 0.203 \\ 0.203 & 0.578 & 0.203 \end{bmatrix} (14)$$

$$P^{30} = \begin{bmatrix} 0.202 & 0.573 & 0.202 \\ 0.202 & 0.572 & 0.202 \\ 0.202 & 0.573 & 0.202 \end{bmatrix} (15)$$

$$P^{50} = \begin{bmatrix} 0.199 & 0.563 & 0.199 \\ 0.199 & 0.563 & 0.199 \\ 0.199 & 0.563 & 0.199 \end{bmatrix} (16)$$

Limiting State Probabilities

As n increases, p^{n} gets closer to equation (16) that is, n≥50 the transition probabilities stabilise to equation (16), and from equation (3) with the initial state probability vector

$$P^{0} = [1 \quad 0 \quad 0]$$

$$P^{(n)} = P^{0}P^{n} = [1 \quad 0 \quad 0] \begin{bmatrix} 0.199 & 0.563 & 0.199 \\ 0.199 & 0.563 & 0.199 \\ 0.199 & 0.563 & 0.199 \end{bmatrix}$$

$$P^{(n)} = [0.199 \quad 0.563 \quad 0.199] \qquad (16)$$

Correcting to one decimal place, we have:

$$P^{(n)} = [0.2 \quad 0.6 \quad 0.2]$$

This is the probability of finding the annual rainfall based on SPI classification fall in any of three states for large n (1.e n ≥ 50)

From equation (3), we obtained the limiting state probability vector that is equation (7).

Thus: $\pi = \pi P$ (0.2 0.6 0.2)

The interpretation of this result is that, in the long-run 20% of the years during rainy season in Birnin Kebbi will experience flood, 60% will experience normal rainfall while 20% will experience drought. As it can be seen from equation (10) (transition probability matrix) a drought year cannot be followed by a flood year and the probability of a drought to be followed by a normal year is high while the probability of a normal year to be followed by a drought and a drought year to be followed by another drought year is extremely small.

Conclusion

The rainfall pattern of Birnin Kebbi, Kebbi state has been analysed using Markov Chain with the help of Standardized Precipitation Index (SPI). Results from the research is an important information to the government and people of Kebbi state for better understanding of rainfall dynamics and viable agricultural production.

References

Bates D, Maechler M, Bolker B, Walker S (2014) lme4: linear mixed-effects models using Eigen and S4. R Package Version 1:1–23

Gidey, E., O. Dikinya, R. Sebego, E. Segosebe, and A. Zenebe. 2018. Analysis of the long-term agricultural drought onset, cessation, duration, frequency, severity and spatial extent using vegetation health index (VHI) in Raya and its environs, northern Ethiopia. *Environmental Research System* 7 (13). https://doi.org/10.1186/s40068-018-0115-z.

Guha-Sapir, D., Vos, F., Below, R., &Ponserre, S. (2012). Annual Disaster Statistical Review 2011: The numbers and trends. Brussels*: Centre for Research on the Epidemiology of Disasters, Institute of Health and Society (IRSS), and Université catholique de Louvain.*

IPCC. 2007. Summary for Policymakers. In: Climate Change 2007: Impacts, Adaptation and Vulnerability. Contribution of Working Group II to the Fourth Assessment Report of the Inter-governmental Panel on Climate Change, M.L. Parry, O.F. Canziani, J.P. Palutikof, P.J. van der Linden and C.E. Hanson, Eds., Cambridge University Press, Cambridge, UK, 7-22.

Lawal, A; Abubakar, U.Y; Danladi, H; Andrew, S. G.(2016) Markovian Approach for the Analysis and Prediction of Weekly Rainfall Pattern in Makurdi, Benue State, Nigeria*J. Appl. Sci. Environ. Manage* Vol. 20 (4) 965-971.

Lawal A.(2017).*Stochastic model of rainfall precipitations for crop production in some selected states of north central Nigeria*. Unpublised Phd thesis, Department of Mathematics Federal University Technology Minna.

McKee, T. B., Doesken, N. J., Kliest, J. (1993). The relationship of drought frequency and duration to time scales. In: Proceedings of the 8th *Conference on Applied Climatology, Anaheim, CA, America. Meteorol. Soc. Boston*, pp. 179–184.

Nelson, D. R., Adger, W. N., & Brown, K. (2007). Adaptation to Environmental Change: Contributions of a Resilience Framework. *Annual Review of Environment and Resources, 32*(1), 395-419.

Singleton, A. (2012). Forecasting Drought in Europe with the Standardized Precipitation Index: An assessment of the performance of the European Centre for Medium Range Weather Forecasts Variable Resolution Ensemble Prediction System. *Journal of the International Society for the Prevention and Mitigation of Natural Hazards*, DOI 10.1007/s11069-019-03665-6.

The Nigeria Hydrological Services Agency, (2020). Annual Flood Outlook. https://www.google.com/url?sa=t&source=web&rct=j&url=https://nihsa.gov.ng/wp-content/uploads/2020/06/2020-NIHSA-Annual-Flood-Outlook-AFO-5-2.pdf&ved=2ahUKEwiS7rSEx6LzAhWsDmMBHV82DVQQFnoECBUQAQ&usg=AOvVaw1JaPlygzezDG70hkgW0tXJ

Um, M., Y. Kim, D. Park, and J. Kim. 2017. Effects of different reference periods on drought index estimations from 1901 to 2014. *Hydrology and Earth System Sciences* 21: 4989–5007.

Empirical Electric Field Strength Models for Digital Terrestrial Television Signals in Minna, Niger State, Nigeria

M. K. Abdullahi*, A. S. Moses and O. D. Oyedum,
Department of Physics, Federal University of Technology, Minna, Niger State, Nigeria.
*Corresponding Author:
E-mail: kassimmamunetu@gmail.com

ABSTRACT

Propagation models play vital roles in planning network coverage, the interference estimations and analyzing radio communication networks. This work adapted some existing empirical field strength models that are best suitable for Minna, Niger State, Nigeria, using the Ultra High Frequency (UHF) signal of StarTimes Terrestrial Television, Minna. The models used are: free space, Hata, International Telecommunication Union-Recommendation (ITU-R P. 529-3) and Energy Regulatory Commission (ERC) Report 68 models. The television station transmits at a frequency of 642 MHz. The signal levels of the transmitted signal were measured radially along four radial routes using Digital Signal Level Meter (GE-5499) and the corresponding distances were also measured using Global Positioning System (GPS). Data processing and computation were carried out using Microsoft Excel spread sheet. The results show that the free space model gives a better prediction for signal field strength in Minna after the general modification with the correction factor of -27.88 and Root Mean Square Error of 7.21 dBμV/m.

Keywords: Coverage area, empirical propagation model, field strength, signal level, UHF

1. Introduction

In a broadcasting system, propagation models are main prediction tools used for designing, planning and analysing wireless communication networks. It is important to point out that there are no general method or algorithms that is universally accepted as the best propagation models. Therefore, each model can be useful for some specific environment and accuracy of any particular technique depends on the fit between the parameters available for the area concerned and the parameters required by the model (Moses *et al*., 2015).

Electric field strength curves or propagation curves are essential parameters neccessary for the planning of VHF and UHF transmission especially for the determination of the coverage areas and the field strength signal levels desired (Moses *et al*., 2015). The field strength of an antenna's radiation at a given point in space, is equal to the amount of voltage induced in a wire antenna located at that given point (Kennedy and Bernand, 1992). This field strength is affected by a number of conditions such as time of day, atmospheric conditions, transmitter-receiver distance, transmitter power and others like, terrain effect, transmitting and receiving antenna heights, and the gain of the transmitting antenna (Bothias, 1987). The present trend in broadcasting is to use widespread broadcast transmitter of VHF or UHF range of frequencies to serve areas not far away from the transmitter (Barclay, 1991).

Propagation models can be divided into three main groups, namely: empirical, deterministic and semi-deterministic models (Abhayawardhana *et al*., 2005). The aim of this work is to adapt some existing empirical field strength models in UHF to suit Minna in Niger State.

2. Field strength models

Field strength models are radio signal propagation models which present the electric field strength as a function of the signal distance from the point of transmission. There are various empirical field

strength models for broadcasting services, but attention will be given to free space model, Hata model, International Telecommunication Union Radio (ITU-R P.529-3) model and European Radio Communications Committee (ERC Report 68) model because they are widely accepted (Faruk *et al*., 2013; Moses *et al*., 2015).

2.1. Free space model

Free-space propagation model is used to predict received signal strength when the path between the transmitter and receiver is a clear and unobstructed line-of-sight (Obiyemi *et al*., 2012). The ideal propagation radiates in all directions from transmitting source and propagating to an infinite distance with no degradation. Attenuation occurs due to spreading of power over greater areas (Nadir *et al*., 2008).

$$S = \frac{P_T}{4\pi d^2} \quad (1)$$

$$S = P_T - 20\log d - 41 \quad (2)$$

where:

S = power flux density in decibels relative to 1 W.m^{-2}

P_T = power in decibels (dB) relative to 1 kW

d = distance (km)

The equivalent field strength, E is given as:

$$E = \sqrt{S.120\pi} \quad (3)$$

$$= \frac{\sqrt{30P_T}}{d} \quad (4)$$

$$\text{or } E\ (mV/m) = \frac{173\sqrt{P_T(KW)}}{d\ (km)} \quad (5)$$

$$E = P_T - 20\ \log d + 104.8 \quad \text{in dB}\mu V/m \quad (6)$$

2.2. Hata model

The model is based on an empirical relation derived from Okumura's report on signal strength variability measurements (Okumura *et al*., 1968). The original Hata equation is given in terms of a path loss in dB.

$$E = 69.82 - 6.16 \log f + 13.82 \log h_b + a\ (h_m) - (44.9 - 6.66 \log(h_b)) \times \log d\ (dB\mu V/m) \quad (7)$$

where:

E = Field strength at a distance from a 1 kW ERP transmitter in $dB\mu V/m$.

f = Frequency of the transmission (MHz)

h_b = Height of the base station or transmitter (m)

h_m = Height of the mobile or receiver (m)

d = Distance between the receiver and transmitter (km)

2.3. ITU-R P.529-3 model

The ITU-R determines the analytical expressions that are suitable for same frequency ranges and correspond approximately to some of its propagation curves. The equation is given by (Recommendation, ITU-R P.529-3, 1999).

$$E = 69.82 - 6.16 \log(f) + 13.82 \log h_b + a\ (h_m) - (44.9 - 6.55\log(h_b)(\log d)^b \quad (8)$$

where:

E = Field strength for 1 kW ERP

f = Frequency (MHz)

h_b = Base station antenna height in the range of 30-200 m.

h_m = Mobile station antenna height in the range 1-10 m.

d = Distance (km)

$$a(h_m) = (1.1\log f - 0.7)\, h_m - (1.56 \log f - 0.8) \quad (9)$$

b = 1 for d ≤ 20 km (10)

$$b = 1 + (0.14 + 1.87 \times 10^{-14} f + 1.07 \times 10^{-3}\, h_b) \left(\log \frac{d}{20}\right)^{0.8}$$

for 20 km $< d <$ 100 km (11)

where:

$$h_b = \frac{h_b}{\sqrt{1+7\times10^{-8} h_b^2}} \quad (12)$$

This model is suitable for use over the ranges:
Frequency range, 150-1500 MHz
Base station height, 30-200 m
Mobile height, 1-10 m
Distance range, 1-100 km

2. 4 ERC report 68 model
In this model, the equation covers the same frequency range as the original Hata equation. This equation has only the distance term raised to the power b and the equation equates approximately to the original Hata equation for distances less than 20 km. The equation is given by (Spectrum Planning Report, 2001):

$$E = 69.75 - 6.16 \log(f) + 13.82 \log(h_b) + \alpha \times (44.9 - 6.55\log(h_b)) \times (\log(d)) + a(h_m) + b(h_b) \quad (13)$$

where:

α = 1 if d < = 20 km
(14)

$$\alpha = 1 + (0.14 + 1.87 \times 10^{-4} \times f + 1.07 \times 10^{-3} \times h_m) \times (\log(d/20))^{0.8}$$

if d > 20 km

$$a(h_m) = (1.1\log(f) - 0.7) \times \text{minimum}(10, h_m) - (1.56 \log(f) - 0.8) + \text{maximum}(0, 20\log(h_m/20)) \quad (15)$$

$$b(h_b) = \text{minimum}(0,\ 20 \log(\ h_b/30) \quad (16)$$

This model is suitable for the ranges:
Frequency range 150 – 1500 MHz
Base station height 1-200 m
Mobile height 1-200 m
Distance range 1-100 km

3. Data collection and analysis
This work was carryout in Minna, Niger State, Nigeria, using the StarTimes Terrestrial UHF television signal. The television station transmits signal at frequency of 642 MHz and the output

power of the transmitter was 1.95 kW while the transmitting antenna was mounted on a mast of 150 m above the ground level.

Data processing and computation were carried out using Microsoft office excel application software. From the measured signal levels, the field strength values in dBµV/m were calculated for a 1 kW Effective Radiated Power (ERP) transmitter to aid comparison with other models. The field strength for each route was obtained and the corresponding field strength as predicted by the free space, Hata, ITU-R.P529-3 and ERC Report 68 models were also evaluated.

For each model, the Root Mean Square Error (RMSE) was determined along the four routes and the Mean Prediction Error (MPE) was also determined and used as a correction factor to modify each model to get the least RMSE. As a result of different routes considered, there are a number of correction factors for each model for the city. So, to generalise each model for all routes in Ekiti State, the average values of the MPE of the four radial routes considered were estimated and used as the correction factors to generalised the field strength models.

4. Results and discussion

4.1. Electric Field Strength

The comparison of the field strength models with the measured field strength for four routes considered are shown in the Figures 1 to 4. The models have the same trend for all the routes considered. From the Figures shown, the free space model has the highest field strength prediction while the ERC Report 68 model has the lowest field strength prediction. The RMSE of the field strength models for each route is shown in the Table 1. For routes A, B, C and D, Hata model has the least RMSE of 9.06 dBµV/m

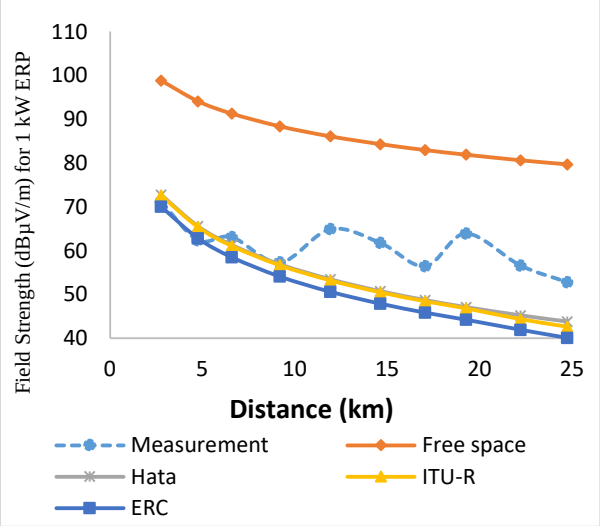

Figure 1: Field strength models for route A

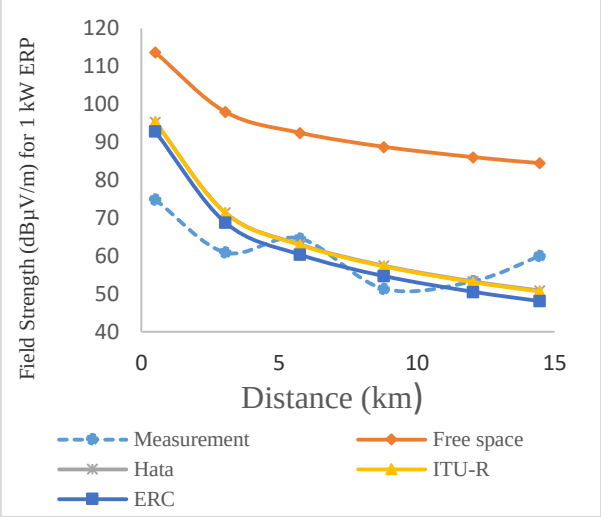

Figure 2: Field strength models for route B

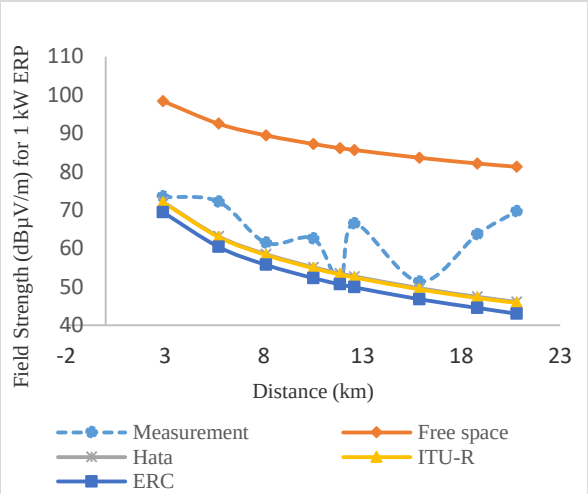

Figure 3: Field strength models for route C

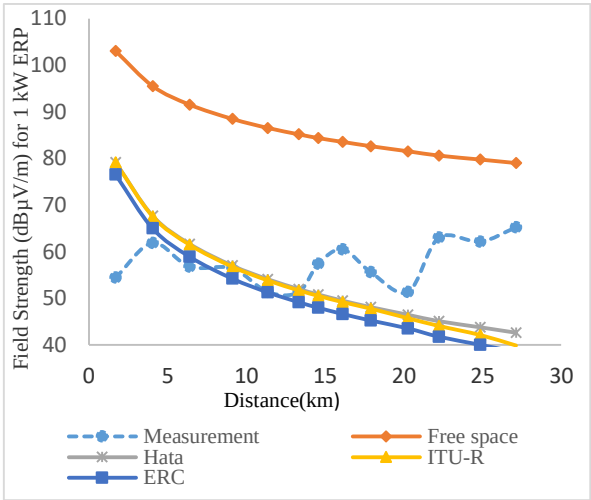

Figure 4: Field strength models for route D

Table 1: Root mean square error of the field strength models

ROUTE	Free Space	Hata	ITU-R	ERC
A	26.10	9.06	9.45	11.43
B	33.48	10.43	10.47	9.70
C	24.75	11.39	11.64	13.62
D	30.14	12.58	13.58	14.19

4.2. Modified field strength models

Figure 5 to 8 show the modified field strength models for all the routes taken. Table 2 shows the correction factors used for modified field strength models, while Table 3 gives the RMSE of the modified field strength models for each route. From the Figures shown, free space model has the lowest field strength prediction with all the models following the same trend.

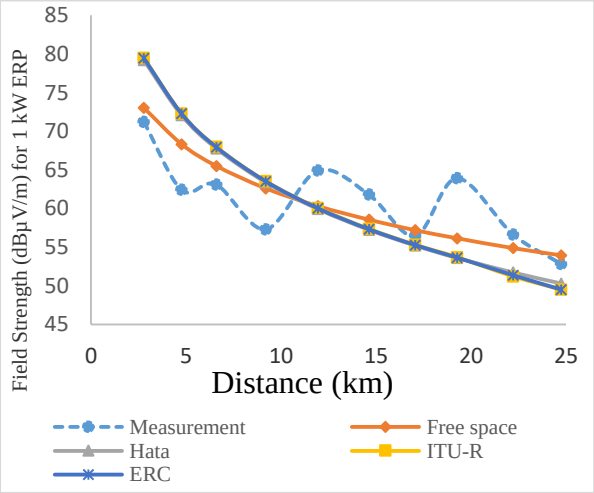

Figure 5: Modified field strength models for route A

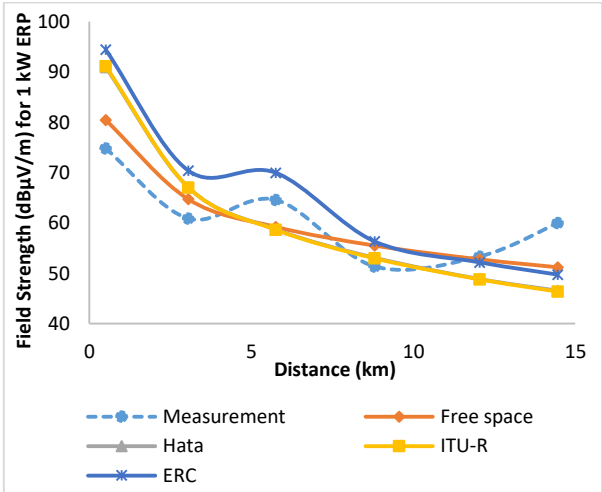

Figure 6: Modified field strength models for route B

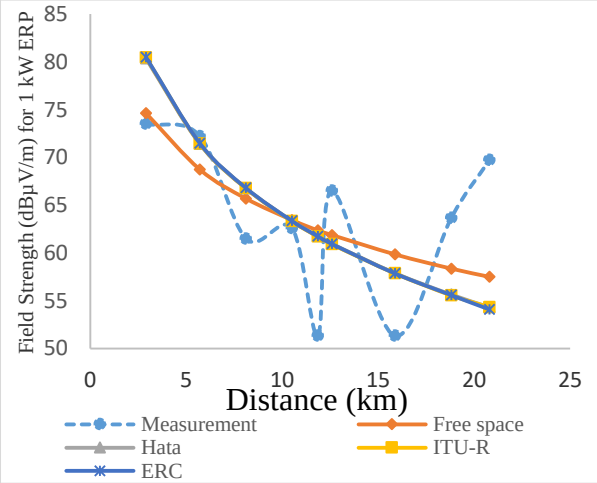

Figure 7: Modified field strength models for route C

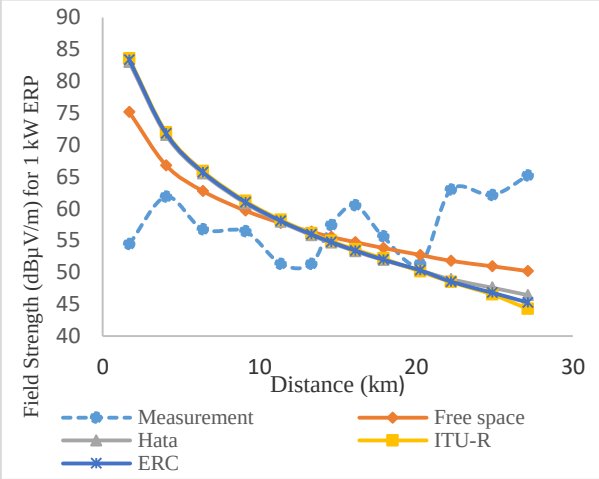

Figure 8: Modified field strength models for route D

Table 2: Correction factors used for the modified and Generalised field strength models

ROUTE	Free Space	Hata	ITU-R	ERC
A	-25.78	6.50	6.89	9.43
B	-33.22	-4.34	-4.26	1.68
C	23.78	8.23	8.46	11.06
D	28.77	3.87	4.43	6.83
Average	**-27.88**	**3.56**	**3.88**	**7.25**

Table 3: Root mean square error of the modified field strength models

ROUTE	Free Space	Hata	ITU-R	ERC
A	4.08	6.32	6.46	6.44
B	5.32	9.46	9.56	10.31
C	6.87	7.88	7.90	7.95
D	9.12	12.10	12.65	12.44
Average	**6.34**	**8.94**	**9.14**	**9.28**

4.3. Generalised field strength models

The generalised field strength models are shown in Figures 9 to 12. The free space has the lowest field strength prediction. The correction factors used to generalise the field strength models for Minna are the average values of the Mean Prediction Error (MPE) of all the four routes. Table 4 show the RMSE values of the generalised field strength models for each route and the RMSE values for Minna are the average values of the RMSE of the generalised field strength models for all the routes. It is observed from the results that, free space model has the average least RMSE of 7.21 dBμV/m for all the routes considered.

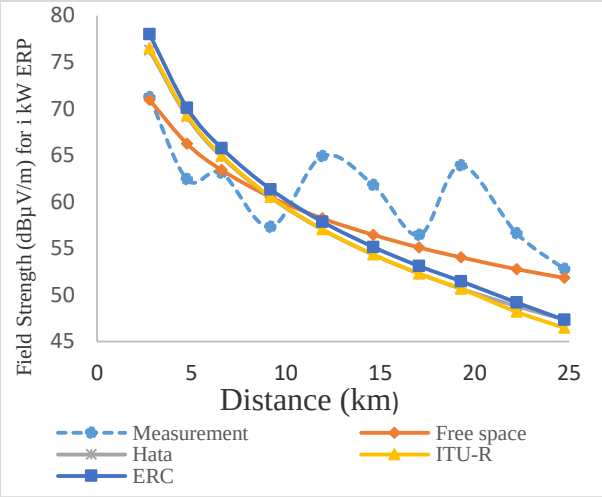

Figure 9: Generalised field strength models for route A

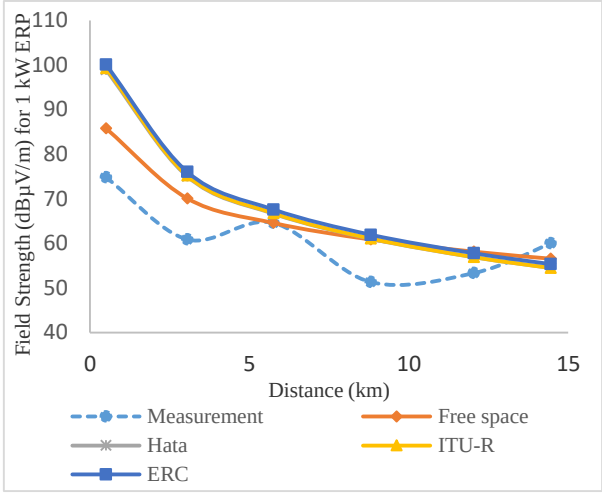

Figure 10: Generalised field strength models for route B

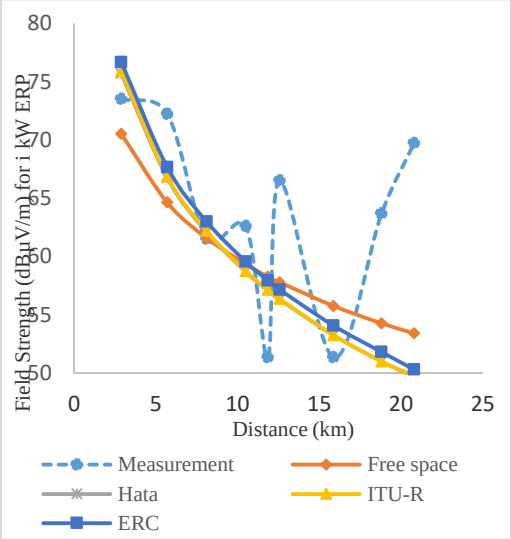

Figure 11: Generalised field strength models for route C

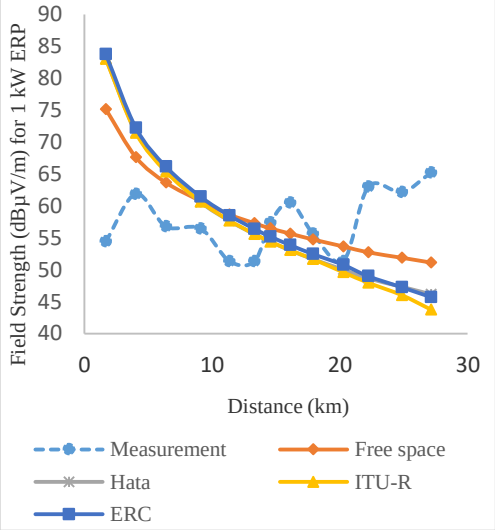

Figure 12: Generalised field strength models for route D

Table 4: Root mean square error of the generalised field strength models

ROUTE	Free Space	Hata	ITU-R	ERC
A	4.51	6.97	7.13	6.87
B	7.32	12.37	12.56	13.08
C	8.01	9.16	9.13	8.82
D	9.02	12.20	12.66	12.46
Average	**7.21**	**10.17**	**10.37**	**10.30**

5. Conclusion

The generalised field strength models for the StarTimes Terrestrial Television, Minna were obtained by using the average of the RMSE of the four routes as the correction factor for each models. The average values of RMSE of the generalised field strength models for the four routes are taken as the RMSE value for Minna. The correction factors used for all the field strength models are as follows: -27.88 for free space, 3.56 for Hata, 3.88 for ITU-R P and 7.25 for ERC Report 68 models with average RMSE of 7.21dBµV/m for free space, 10.17 dBµV/m for Hata, 10.37 dBµV/m for ITU-R and 10.30 dBµV/m for ERC Report 68 models respectively. Hence, the generalised free space field strength model gives more accurate prediction for field strength in Minna as compared to other models used.

References

Abhayawardhana, V. S., Wassell, I. J., Crosby, D., Sellars, M. P. and Brown, M. G. (2005) Comparison of empirical propagation path loss models for fixed wireless access systems. 61th IEEE Technology Conference, Stockholm, 1(1), 73-77.

Barclay, L. W. (1991). Basic Radio System Parameters. In Hall, M. (Ed); Radio Wave Propagation Institute of Electrical and Electronics Engineers (IEEE) Electromagnetic Wave Series. *Peter Peregrinus Limited, London, United Kingdom*, 43-44.

Bothias, L. (1987). Radio wave propagation, *McGraw-Hill Inc. New York, St. Louis San Francisca Montreal Toronto.*144-175.

Faruk, N., Ayeni, A., and Adediran, Y. A. (2013). On the study of empirical path loss models for accurate prediction of TV signal for secondary users. *Progress In Electromagnetics Research, 49*, 155-176.

Kennedy, G and Bernand, D.(1992). *Electronic Communication Systems*, McGraw Hill/Macmillan

Moses, A. S., Oyedum, O. D. and Ajewole, M. O. (2015). Empirical Field Strength Model for Terrestrial Broadcast in VHF Band in Makurdi City, Benue State, Nigeria. *International Research Journal of Enginnering and Technology*, 2(1), 23-27.

Nadir, Z., Elfadhil, N. and Touati, F. (2008). Path loss determination using Okumura-Hata model and spline interpolation for missing data for Oman. *Proceedings of the world congress on Engineering* Vol.1, 2-4.

Obiyemi, O. O., Ibiyemi, T. S., Gbenga-Ilori, A. O. and Ojo, J. S. (2012). Path loss model for radio wave propagation at VHF/UHF Bands using electric field strength measurement over Ilorin Middle-belt, Nigeria. *2nd International Conference on Advances in Computational Tools for Engineering Applications (ACTEA)*, 43-46.

Okumura, Y., Ohmori, E., Kwano, T. and Fakuda, K.(1968). Field strength and variability in UHF/VHF Land Mobile Radio Service. *Review of Electronic Communication Laboratory*. 16(1), 9-10.

Recommendation, ITU-R P.529-3(1999). Prediction Methods for the Terrestrial Land Mobile Service in the VHF and UHF Bands, pp. 6-7 Singapore. 80-150.

Spectrum Planning Report. (2001). Investigation of Modified Hata Propagation Models. Spectrum Planning Team, Radiofrequency Planning Group, Australian Communications Authority.

Determination of Uranium, Thorium and potassium Concentration in Building Materials in Minna, Niger State.

Muhammad Y. U, Olarinoye I.O., M.T. Kolo
Department of Physics, Federal University of Technology Minna, Niger State, Nigeria

Abstract

The present research was conducted to measure the concentration of the natural radionuclides in building materials and associated radiological risk parameters. Three samples of concrete blocks, burnt clay and mud blocks each were collected in Minna area of Nigeria. The samples were collected locally and analysed for ^{238}U, ^{232}Th, and ^{40}K concentrations by gamma spectrometric using high purity germanium detector. The specific activity of ^{238}U, ^{232}Th, and ^{40}K had mean value of 30.649± 4.6 Bqkg^{-1}, 36.717 ± 5.508 Bqkg^{-1} and 420.98± 63.147 Bqkg^{-1} in the concrete blocks while the mean activity concentrations of 23.285 ± 3.492 Bqkg^{-1} 100.639 ± 15.095 Bqkg^{-1} and 707.869 ± 106.180 Bqkg^{-1}obtained in brick blocks and the value 10.691 ± 1.603 Bqkg^{-1}, 91.590 ± 13.738 Bqkg^{-1} and 759.189 ± 113.878 Bqkg^{-1}obtained in mud blocks. The average values of the calculated absorbed dose rate (91.8964 nGy h^{-1}, 53.83047 nGy h^{-1}, 101.0152 nGy h^{-1}) in mud blocks concrete blocks and brick blocks, respectively, was higher than the world average value of 59 nGy h^{-1}, average annual effective dose (indoor) of 0.45 mSv y^{-1}, 0.26 mSv y^{-1} and 0.49 mSv y^{-1} in mud blocks, concrete blocks and brick blocks, respectively, and annual effective dose (outdoor) of 0.11 mSv y^{-1}, 0.07 mSv y^{-1} and 0.12 mSv y^{-1} in mud blocks, concrete blocks and brick blocks, respectively was lower than the recommended limit of 1 mSv y^{-1} for public exposure. Our study shows that the different types of building materials analyzed do not pose any significant radiation risks. They are therefore safe for construction purposes.

INTRODUCTION

Radioactivity is the spontaneous emission of energy in form of particles or photons by an atomic nucleus that is unstable (Turhan *et al.,* 2008). Radioactivity thus helps a nucleus to attain stability. It could be natural or artificially induced. When it occurs naturally, it is called natural radioactivity and the nuclides are called naturally occurring radionuclides. The earth crust is a major source of naturally occurring radionuclides. Man and his environment are continuously exposed to this source of ionising radiation. It has been reported that the largest source of external radiation exposure to man comes from natural sources (Lyngkhoi *et al.,* 2020). Natural sources of external radiation include primordial radionuclides from the earth crust and cosmic radiation. Radiation from terrestrial sources presents the largest source of natural radiation. One major source of natural radionuclide to man is building materials.

The fact that many building materials are derived from natural rocks, sand and other geological formations bearing minerals that are rich in diverse radionuclides suggest they could be a source of radiations. Research has shown that ^{238}U, ^{232}Th, and ^{40}K are the major sources of natural radioactivity in building materials (Celestine *et al.,* 2018). These radionuclides emit gamma rays and they have been found to occur naturally in building materials (Kumara *et al.,* 2018). The presence of these radionuclides in building materials necessitate the need to measure the level of natural background radiation that humans are exposed to, and to develop standards as regard the use of building materials (Asgharizadeh et al., 2012). In Nigeria however, there is no regulations for radiological content of building materials. From the perspective of radiological safety, it is important for radionuclide content of building materials to be evaluated. This will reveal the safety of such building materials when used for building construction. Consequently, many previous

researches within and outside Nigeria have been conducted to assess the radiological safety of common materials used for construction of homes, offices and other structures for human habitation (Dainius et al., 2021). This work is thus aimed at evaluating the specific activity of ^{238}U, ^{232}Th and ^{40}K in common building block such as concrete blocks, local mud bricks, and burnt brick blocks used within Nigeria with the view to ascertain their safety as construction/building materials.

MATERIALS AND METHODS

The materials used for this research are: Hand trowel, Hand glove, Masking tape, Polythene bags, Marker, Sieve (500 µm mesh size), and Marinell beakers (500g).

Gamma Spectrometric Analysis

Gamma spectrometer is used to determine the number and energy of photons being emitted by radionuclides within the samples. This information was used to identify the radionuclides present in the samples and to determine the activities of each radionuclide. These number and energies of photon are represented by discrete lines known as photon spectrum or spectral. The spectrum is a plot of total collected counts in a channel versus the channel number (L'Annunziata, 2012). In gamma ray spectrometry, the net area under the photopeak of associated energy is a direct measure of the activity of the radionuclide. The first step of identifying and determining the activity of natural radionuclides in the samples is to collect the spectral data of photons emitted by radionuclides performed by multichannel analyser (MCA).

Sample Collection

Samples of concrete, burnt clay, and mud blocks were collected from block industries in Minna. The samples were transported to the laboratory for further preparation and analysis.

Sample Preparation

The collected samples were dried, pulverised, and 200 g of each sample was measured in transparent self-adhesive packaging nylon bag (10 cm height and 50 mm diameter) and sealed. The equipment was calibrated against the reference sample with known activity concentrations of ^{238}U, ^{232}Th, and ^{40}K. The following gamma transitions were used: ^{238}U, 351 KeV (^{214}Bi); ^{232}Th, 582 KeV (^{208}Tl); and ^{40}K, 1461 KeV. Plate I shows Solid concrete Block, Mud clay block, and Common Solid Burnt clay Bricks and Plate II shows Brick dust, Concrete dust and Mud dust. Plate III shows samples of brick dust packed, Mud dust packed and Concrete dust packed and their label for identification. The samples were transported to the laboratory for further preparation and analysis.

Plate I: (a) Solid concrete Block **(c)** Mud clay block and **(c)** Common Solid Burnt clay Bricks

Plate II: (a) Brick dust **(b)** Concrete dust and **(c)** Mud dust

Plate III: (a) Brick dust packed **(b)** Mud dust packed and **(c)** Concrete dust packed and label for identification

Estimation of Absorbed Dose Rate (ADR) and Annual Effective Dose (AED)

The measured activity of ^{238}U, ^{232}Th and ^{40}K were converted into doses ($nGyh^{-1}Bq^{-1}kg^{-1}$) by applying the factors 0.462, 0.604, and 0.0417 for ^{238}U, ^{232}Th, and ^{40}K respectively (UNSCEAR, 2000, Gupta *et al.*, 2011). These factors were used to calculate the total absorbed gamma dose rate in air using the Equation 2. Where; A_U, A_{Th} and A_k are the activity ($Bq\ kg^{-1}$) of uranium, thorium and potassium in the samples respectively. To estimate annual effective doses, account must be taken of (i) the conversion coefficient from absorbed dose in air to effective dose and (ii) the indoor occupancy factor. Annual estimated average effective dose equivalent received by a member is calculated using a conversion factor of 0.7 $SvGy^{-1}$, which is used to convert the absorbed rate to annual effective dose with an outdoor occupancy of 20% and 80% for indoors (Zastawny *et al.*, 1979; Gupta *et al.*, 2011). The annual effective doses are determined as follows (equations 3 and 4)

$$\mathrm{ADR(nGyh^{-1})} = q_u A_U + q_{Th} A_{Th} + q_K A_K \quad (1)$$

$$\mathrm{ADR(nGyh^{-1})} = 0.462 A_U + 0.604 A_{Th} + 0.0417 A_K \quad (2)$$

$$\text{Indoor AED (mSy)} = \mathrm{ADR(nGyh^{-1})} \times 8760\mathrm{h} \times 0.8 \times 0.7\mathrm{SvGy^{-1}10^{-6}} \quad (3)$$

$$\text{Outdoor AED (mSv)} = (\text{Absorbed dose})\mathrm{nGyh^{-1}} \times 8760\mathrm{h} \times 0.2 \times 0.7\mathrm{SvGy^{-1}10^{-6}} \quad (4)$$

The Radium equivalent activity (Ra_{eq}) was used to represent the specific activities of ^{226}Ra, ^{232}Th and ^{40}K contained in the samples by a single quantity. It was determined that 10 pCi/g (370 Bq kg^{-1}) ^{226}Ra or 7 pCi/g (259 Bq kg^{-1}) ^{232}Th or 130 pCi/g (4810 Bq kg^{-1}) ^{40}K produces the same gamma-ray dose rate. The Ra_{eq} was then calculated using the equation:

$$Ra_{eq} = A_{Ra} + 1.43A_{Th} + 0.077A_k \quad (5)$$

where, A_{Ra}, A_{Th}, and A_k are the concentrations in ($Bq\ kg^{-1}$) of ^{238}U, ^{232}Th, and ^{40}K in the samples respectively.

RESULTS AND DISCUSSION

Activity Concentrations of Natural Radionuclides in Concrete Blocks, Clay Bricks and Mud blocks

Table 1 represents the activity concentrations obtained by direct gamma-ray spectrometry measurements of the building material samples. Activity of ^{238}U, ^{232}Th and ^{40}K is reported throughout this paper in Bq kg^{-1} dry weight. The mean activity concentration of ^{238}U in concrete blocks was found to be 30.649± 4.6 Bq kg^{-1}, while for ^{232}Th and ^{40}K was found to be 36.717 ± 5.508 Bq kg^{-1} and 420.98± 63.147 Bq kg^{-1} respectively. In mud clay blocks, the activity concentration of ^{238}U was found to be 10.691 ± 1.603 Bq kg^{-1}, while for ^{232}Th and ^{40}K it was found to be 91.590 ± 13.738 Bq kg^{-1} and 759.189 ± 113.878 Bq kg^{-1} respectively. In burnt clay bricks, the activity concentration of ^{238}U was found to be 23.285 ± 3.492 Bq kg^{-1}, while for ^{232}Th and ^{40}K

it was found to be 100.639 ± 15.095 Bq kg^{-1} and 707.869 ± 106.180 Bq kg^{-1} respectively. The results show a high activity of ^{40}K in mud clay blocks and burnt clay bricks. The obtained results are comparable to the world average concentration of these radionuclide in building materials reports by the UNSCEAR (UNSCEAR, 2000), which are 35 Bq kg^{-1} for ^{238}U, 30 ^{232}Th and 400 Bq kg^{-1} for ^{40}K. The small variation between the mean activity concentration obtained for ^{238}U and ^{232}Th in the three samples is ascribed to the fine particle nature of the soils.

Table 1: Activity concentration for each sample

Activity concentration (Bq kg^{-1})			
Sample	**^{238}U**	**^{232}Th**	**^{40}K**
MB	10.691 ± 1.603	91.590 ± 13.738	759.189 ± 113.878
CB	30.649± 4.600	36.717 ± 5.508	420.98± 63.147
BBB	23.285 ± 3.492	100.639 ± 15.095	707.869 ± 106.180

Equation 2 was used to calculate the average absorbed dose rate values for each of the samples shown in Table 2. Equation 3 and 4 was used to calculate indoor/outdoor annual effective dose values for each of the samples shown in Table 3.

Table 2: The average absorbed dose rate

	The average absorbed dose rate			
Samples	**^{238}U (**Bq/kg)	**^{232}Th**(Bq/kg)	**^{40}K**(Bq/kg)	**Dose Rate (nGy h^{-1})**
MB	10.691	91.59	759.189	91.8964
CB	30.649	36.717	420.98	53.83047
BBB	23.285	100.639	707.869	101.0152

Table 3: Annual Effective dose for Indoor and outdoor

Sample	Indoor AED (mSv/y)	Outdoor AED (mSv/y)
MB	0.45	0.11
CB	0.26	0.07
BB	0.49	0.12

Equation 5 was used to calculate radium equivalent activity for mud blocks, concrete blocks and brick blocks as shown in Table 4.

Table 4: Radium equivalent activity (Ra_{eq})

Sample	Ra_{eq} ($Bqkg^{-1}$)
MB	200.122
CB	115.569
BBB	221.704

The mean concentrations of ^{238}U, ^{232}Th and ^{40}K in the samples collected in Minna and other studies conducted internationally are shown in Table 5. The comparison demonstrate that the average activity concentrations obtained in this study are lower than other studies. The higher activity concentration of ^{40}K obtained for Mud clay blocks, 759.189 Bq kg^{-1}, is within the range of UNSCEAR report (UNSCEAR, 2000) which is 140–850 Bq kg^{-1}.

Table 5: Reported values of gamma activity in building material (Bq kg^{-1}), from work conducted worldwide and results obtained in this study

Region	**^{238}U**	**^{232}Th**	**^{40}K**	**References**
Meghalaya, India	3.8 – 92.7	14.2 – 112.2	40.9- 777.1	Lyngkhoi *et al.*, 2020
Agaba-Amman highway	44.4	36.3	208	Al-Jundi *et al.*, 2003
Rajasthan, India	30.0–78.0	43–106	50.0–137	Nageswara *et al.*, 1996
Turhan, Turkey	144.9	169.9	1792.3	Turhan1 *et al.*, 2008
Araba valley: surface samples	21.0–38.7	15.1–35.0	96.0–762	Abusini *et al.*, 2008
Minna, Niger state, MB, CB and BBB	10.691-30.649	91.59-100.639	420.98-759.189	This work

CONCLUSION

The results obtained from this work is within the world average concentration of radionuclide in building materials reported by UNSCEAR. The highest activity was found in mud blocks and burnt clay bricks. The radiological parameters like radium equivalent activity (Ra_{eq}), absorbed dose rate (ADR), indoor/outdoor annual effective dose (AED), were determined. The calculated values of Ra_{eq} for all the building materials analyzed ranged from 115.569 to 221.704 Bq kg^{-1}, which is lower than the recommended maximum value of 370 Bq kg^{-1}. The average annual effective dose (indoor) of 0.45 mSv y^{-1}, 0.26 mSv y^{-1} and 0.49 mSv y^{-1} in mud blocks, concrete blocks and brick blocks, respectively, and annual effective dose (outdoor) of 0.11 mSv y^{-1}, 0.07 mSv y^{-1} and 0.12 mSv y^{-1} in mud blocks, concrete blocks and brick blocks, respectively obtained were lower than the recommended limit of 1 mSv y^{-1} for public exposure. The study, therefore, shows that the commonly used building materials analysed do not pose any significant radiation risk and hence, the use of these materials for construction purposes is safe without any radiological threat to the dwellers. The results set a baseline data for significant standards on radiation exposure of the measured radionuclides in the selected building materials used in Nigeria.

REFERENCES

Aboubakar Mohamed. 2018. Natural radionuclides in building constructing materials and assessment of indoor radon concentration. University of Rome Tor vergata. Pg. 4 -27

Asgharizadeh, F., Abbasi, A., Hochaghani, O., & Gooya, E. S. (2012). Natural radioactivity in granite stones used as building materials in Iran. *Radiation protection dosimetry*, *149*(3), 321-326.

Ademola, J. A. and Farai, I. P. (2005). Annual effective dose due to natural radionuclides in building blocks in eight cities of southwestern Nigeria. Radiat. Prot. Dosim. 114, 524–526

Ahmad, N. and Matiullah Khatibeh, A. Indoor radon levels and natural radioactivity in Jordanian soil. Radiat. Project. Dosim. 71(3), 231–233 (1997).

Al-Jundi, J., Al-Bataina, B. A., Abu-Rukah, Y. and Shehadeh, H. M. Natural radioactivity concentration in soil samples along the Amman Aqaba Highway, Jordan. Radiat. Meas. 36, 555–560 (2003).

Al-Zoughool, M. and Krewski, D. (2009). Health effects of radon: a review of the literature. Int. J. Radiat. Biol. 85, 57–69

Barnard Smit, Arnaud Faanhof. (2006). Nuclear Chemistry, NWU-NC-TH-05, Theme 5, Measurement of Radioactivity, Part 3: g-Spectrometry, Adapted for use NWU, NECSA, South Africa.

Celestine Okogbue, Mathias N. 2018. The 226Ra 232Th and 40K contents in the Abakaliki baked shale construction materials and their potential radiological risk to public health, southeastern Nigeria.

Chen, C., Jiang, Weng, P. and Chu, T. Evaluation of natural radiation in houses built with black schist. Health Phys. 64(1), 74–78 (1993).

Dainius J and Milda P. 2021. Natural Radioactivity and Radon Exhalation from Building Materials in Underground Parking Lots. Department of Physics, Vilnius Gediminas Technical University, Sauletekio Ave. 11, LT-10223 Vilnius, Lithuania

EC (European Commission) 1999 Radiation Protection 112: Radiological protection principles concerning the natural radioactivity of building materials Directorate-General Environment, Nuclear Safety and Civil Protection

Faten Adel Ismael C., Amera G. B, Najeba F.S. (2017),Comparison of Various Plastics 2007;

Wastes Using X-ray Fluorescence. American Journal of Materials Synthesis and Processing 5(2): 24-27

Hassan, N. S. (2012). Assessment and GIS mapping of terrestrial Gamma radiation in Elfao area in Elgedaref states.

Gregory Choppin (2013). Radiochemistry and Nuclear Chemistry; Elsevier; 4th Edition. pg;

88 – 99
Karahan, G. and Bayulken, A. Assessment of gamma dose rates around Istanbul (Turkey). J. Environ. Radioact. 47, 231–221 (2000).
Knoll, G. F. (2010). Radiation detection and measurement. Unites States of America: John Wiley & Sons. Inc.
Koblinger, L. Mathematical models of external gamma radiation and congruence of measurements. Radiat. Prot. Dosim. 7, 227–234 (1984).
Kumara PARP, Mhakumara P, Jayalath A. 2018. Estimating natural radiation exposure from building materials used in Sri Lanka. J Rad Res App Sci. ;11:350–354.
L'Annunziata, M. F. (2012). Handbook of radioactivity analysis. San Diego, California: Academic Press.
Lyngkhoi B, Nongkynrih P. 2020. Radioactivity in building materials and assessment of risk of human exposure in the East Khasi Hills District, Meghalaya, India. Doi.org/1080/ 23144808X2020.
Mustonen, R. Methods for evaluation of radiation from building materials. Radiat. Prot. Dosim. 7, 235–238 (1984)
Nafaa Reguigui, 2014 gamma ray spectrometry, Centre for national nuclear Sciences and Technologies Tunisia. pp 106- 120
Nageswara, M. V., Bhati, S. S., Rama Seshu, P. and Reddy, A. R. Natural radioactivity in soil and radiation levels of Rajasthan. Radiat. Protect. Dosim. 63(3), 207–216 (1996)
Orabi, M. Estimation of the radon surface exhalation rate from a wall as related to that from its building material sample. Can. J. Phys. 96, 353–357 (2018).
Orabi, M. Development of a simulation model for estimating the indoor gamma radiation dose. Radiat. Phys. Chem. 147, 114–117 (2018)
Orabi, M. (2018). Multi-layer description model for radon concentration in soil. Eur. Phys. J. Plus 133, 135
Raymond L. Murray, Keith E. Hobbert, (2015). An introduction to the concepts, systems and applications of nuclear processes: Nuclear Energy. 4th edition; pg; 31 – 46
Sahoo, B., Sapra, B., Gaware, J., Kanse, S., Mayya, Y., 2011. A model to predict radon exhalation from walls to indoor air based on the exhalation from building material samples. Sci. Total Environ. 409, 2635–2641.
Stranden, E. Radioactivity of building materials and the gamma radiation in dwellings. Phys. Med. Biol. 24, 921–930 (1979).
Turhan S, U N Baykan and K Sen . 2008. Measurement of the natural radioactivity in building materials used in Ankara and assessment of external doses. Saraykoy Nuclear Research and Training Centre, Istanbul Road30km,06983 Saray, Ankara, Turkey
UNSCEAR (2000). "Effects of Atomic Radiation to the General Assembly" in United Nations Scientific Committee on the Effect of Atomic Radiation. (UNSCEAR, 2000) United Nations: New York.
Yu-Ming, L., Pei-Huo, L., Ching-Jiang, C. and Chig- Chung, H. Measurement of terrestrial gamma radiation in Taiwan, Republic of China. Health Phys. 52, 805–811 (1987).

A review on CZTS (Cu_2ZnSnS_4) synthesis methods and characterisation

T. Yahaya, K. I. Mohammed, A. A. Abubakar and K. U. Isah
School of Physical Sciences, Physics Department, Federal University of Technology, Minna, Nigeria
yahayatitus250@gmail.com

Abstract
Cu_2ZnSnS_4, copper, zinc, tin, sulphide (CZTS) is a p-type semiconductor with high absorption coefficient and a low cost promising absorber material, having a direct band gap from 1 to 1.5 eV, which is ideal for making absorber layer for solar cell. Owing to the cost effective noble metal, less abundance and industrial large scale application purpose, an effective replacement of indium and gallium in $CuInxGa_{1-x}S(Se)_2$ (CIGS) is highly demanded. There are several approaches to improving the performance of as solar cell by enhancing the power conversion efficiency with a less costly and facile device. In this work we present a brief review on different synthesis methods and characterisation of CZTS material. It is therefore, essential for engineering of CZTS material and the optimisation of the fabrication method for the improvement of solar cell.

Keywords-- Cu_2ZnSnS_4, Optimisation, Fabrication.

1.0 INTRODUCTION

Lately, it is feasible to take the resources and natural elements into accounts because of the emergence of solar cells (Huang *et al.,* 2016). Aside from silicon-based solar cell, the $CuInxGa_{1-x}S(Se)_2$ (CIGS) thin film solar based cell has drawn in much consideration since its fine steadiness and potential power conversion(Huang *et al.,* 2016). In any case, the use of costly materials like indium and additionally gallium expands the manufacturing. Lately, Cu_2ZnSnS_4 (CZTS) was seriously examined and expected to be the most encouraging contender to replace $Cu(In,Ga)Se_2$ (CIGS) (Camara *et al.,* 2013), in which raw materials utilized have minimal expenses, less toxic, and earth abundant. Besides, CZTS likewise has an immediate band gap of 1.4–1.5 eV with high absorption coefficient in the visible rannge (>104 cm−1) (Khare *et al.,* 2011).

The Cu_2ZnSnS_4 (CZTS) compound, non-toxic and abundant, can be a potential alternative for the light absorbing layer in the thin film devices of solar cells to replace conventional absorbent layers, such as CdTe and Cu.In; Ga/Se_2 (CIGS) (Li *et al.,* 2012). Shockley–Queisser balance calculations also show that the photon theoretical limit efficiency of CZTS thin film solar cells is 32.2% (Zhou *et al.,* 2011). CZTS has an absorption coefficient of over 10^4 cm^{-1} with band gap of about 1.5 eV (Leitao *et al.,* 2011). It is a semiconductor material of p-type, I2-II-IV-VI4 quaternary compound by substitution of selenium with sulfur, indium with zinc and gallium with tin in the $CuInGaSe_2$ (CIGS) compound (Mali *et al.,* 2012). Each component of CZTS is easily available and abundant in the Earth's crust: copper (Cu) 50 ppm, zinc (Zn) 75 ppm, tin (Sn) 2.2 ppm and sulfur (S) 260 ppm. These characteristics in combination make it suitable to have exciting findings, ensuring widespread and low cost applications in thin film solar cells. Moreover these properties are the key factors needed to make solar technology competitive with carbon based fuels (Mali *et al.,* 2012).

Therefore, synthesis of CZTS micro- or nanocrystallines has attracted much attention, and then, many solution-based processes have been proposed, such as hot-injection method, hydrothermal method, solvothermal method, and microwaveirradiated method, Sol gel method, Electrospining (Liu *et al.,* 2013) and several others. Generally, there are two principal crystallographic phase structures of CZTS, which are the so-called stannite (space group I42m) and kesterite (space group I4) (Chen *et al.,* 2009). The only difference between the two structures is the arrangement of Cu

and Zn atoms. It has been experimentally confirmed that CZTS usually crystallizes in kesterite phase as it is thermodynamically more stable than the stannite (Schorr, 2007).

2.0 DIFFERENT METHODS OF SYNTHESIS

2.1 Electrochemical deposition method

Electrochemical deposition is a coating method to reduce the cations in the aqueous solution, organic solution, or hot-dip fluid in the cathode by supplying potential difference with external circuit power. In the 1970s, people began to try the electrochemical deposition of semiconductor materials (Lincot, 2005). Nowadays, the electrodeposition technique has been widely employed in the fabrication of solar cells, such as the CIGS solar cells research (Lincot, 2004) and the CdTe cells produced. Although CdS in the electrodeposition had used the thiourea as precursors (McCandless *et al.,* 1995), it was very difficult to find such a stable sulfur source in the electrodeposition CZTS.

Scragg *et al.* (2008), the Bath University in Britain employed the method of laminating and vulcanizing electrodeposition Cu/Sn/Zn to obtain the CZTS solar cells with a conversion efficiency of 0.8% (Scragg *et al.,* 2008). In 2010, by annealing for 2 hours at 575^{o}C in an atmosphere of N_2 carrier gas containing S powder and 10% H_2, they obtained the cells device with a conversion efficiency of 3.2% through improved technology (Scragg *et al.*, 2010).

Shinde *et al.* (2012) reported a novel chemical successive ionic layer adsorption and reaction (SILAR) technique for CZTS thin films formation by sequential reaction on solar lime glass (SLG) substrate surface. CZTS thin films were formed by sequential immersion of the substrate into the beakers containing the cationic precursor solutions of 0.1M $CuSO_4$, 0.05M $ZnSO_4$, and 0.05M $SnSO_4$ (1:1:1) and the anionic precursor solution of 0.2M thioacetamide. The films obtained were then annealed at 400 ^{o}C for 4h.The photoelectrochemical solar cell (PEC) cell was constructed using the annealed CZTS thin film and exhibited an efficiency of 0.12%.

2.2 Vacuum deposition method.

Vacuum deposition method is a physical deposition method that puts the film raw material into the vacuum chamber and heats it to high temperature to make the atoms or molecules escape from the surface then form a vapor stream entering the surface of the plated substrate; due to the low temperature of substrate, it condenses to form a solid film. Katagiri *et al*. (1997), in Nagaoka University of Technology utilized the electron beam evaporation to fabricate the Cu_2ZnSnS_4 thin film solar cells with an efficiency of 0.66% for the first time. Later, through improving technology with employing ZnS as evaporation source, they obtained the photoelectric conversion efficiency of 2.62% Katagiri *et al*. (2001). Also through adding NaS and improving the vacuum background of annealing with a stainless steel chamber, they and obtained an efficiency of 5.45% Katagiri *et al*. (2003).

Wang *et al*. (2010) obtained the CZTS solar cell with an efficiency of 6.8% by co-evaporation, they further improved equipment and craft, employing the Cu, Zn, and Sn evaporation source of Knudsen type and Veeco S source box in metal tantalum with valves; the substrate temperature increased from110 ^{o}C to 150 ^{o}C, and the annealing temperature increased from 540 ^{o}C to 570 ^{o}C, the annealing time was also 5 minutes. Although the film was only 600 nm, they still obtained the CZTS solar cells with an efficiency of 8.4%, which is currently the highest CZTS cells efficiency without Se (Shin *et al*., 2011).

2.3 Electron beam evaporation method

Electron beam evaporation method is to employ electric field to make electron getting kinetic energy to bombard the evaporation material of anode, which can make the material vaporize to achieve evaporation coating. Nagaoka *et al.* (1996) National College of Technology Research Group, used the electron beam evaporation and curing method to fabricate the solar cells of ZnO: Al/CdS/ CZTS/Mo/SLG structure with the open circuit voltage of 400 mV, short circuit current of

6.0 mA/cm^2, and fill factor of 0.277, and the conversion efficiency was only 0.66%. Yan *et al.* (2011) improved the conversion efficiency, employed Cu, Sn (or SnS2), and ZnS as vapor deposition material by electron beam evaporation method, changing the order of deposition from an evaporation to multiple cycles evaporation, using soda lime glass instead of the ordinary glass, using ZnO:Al instead of ZnO as a window layer, and finally the cells efficiency was increased to 5.45%.

Electron beam evaporation method overcomes many defects of the resistance heating evaporation, especially suitable for the production of high-melting point material and high purity thin film material. At present, preparation of the CZTS thin film with electron beam evaporation method is the most widely study in the laboratory, and the surface morphology, phase matching, and optical performance of thin film are better Yan *et al.* (2011).

2.4 Magnetron sputtering method

Magnetron sputtering is that the electrons crash with Argon (Ar) atom in the electric field with ionizing abundant argon ions and electrons, and the electrons fly to the substrate. The Ar ions are accelerated in the electric field to bombard the target with sputtering a lot of target atoms, and the neutral target atoms (or molecules) are deposited on the substrate to form film.

Tanaka *et al.* (2005) for the first time used vacuum based hybrid sputtering to deposit CZTS thin films on a quart glass substrate. Films were fabricated by the sequential deposition of metal elements and annealing in 'S' flux, varying the substrate temperature from 300 °C to 500 °C. Film thickness decreased with increase in substrate temperature. Single phase, stoichiometric CZTS film with stannite structure was obtained at 400 ^oC. However, composition of the thin films became Zn-poor at and above 450 ^oC, Resistivity, carrier concentration and Hall mobility of the films at 400 °C were 0.130 Ωcm, 8×10^{-18} cm^{-3} and 6 cm^2 V^{-1}s^{-1} respectively.

Yeon *et al.* (2015) successfully prepared CZTS thin films through sulphurisation of ion beam sputtered precursors. Their results show that electrical and optical properties of the prepared films have strong dependence on atomic ratio of the constituents. By optimizing the precursor preparation conditions they obtained low resistivity of -0.1562 cm.

2.5 Spray pyrolysis method

Spray pyrolysis method is to heat the surface of substrate to about 600 ^oC and then spray one or more metal salt solutions onto the substrate surface; high temperature will cause pyrolysis of the spray coating, which will form a coat on substrate surface. The quality and performance of thin film fabricated by spray pyrolysis relate to substrate temperature. If the substrate temperature is too high, it will be uneasy for the film to be adsorbed on the substrate; when the substrate temperature is too low, the crystallization of film will be deteriorated. According to experiment results, the CZTS thin film will have better optical property if the substrate temperature is controlled within the range of 500 ^oC – 650 ^oC in pyrolysis.

Zhang *et al.* (2010) made a reaction in CuCl2, ZnCl2, and SnCl2 and vulcanized them in SC $(NH_2)_2$ solution by spray pyrolysis method. The substances reacted for 1 hour at the substrate temperature of 340 ^oC and were annealed for 120 minutes at 550 ^oC. Finally, the CZTS thin films with a band gap of 1.5 eV were fabricated. The spray pyrolysis device is simple and easy to operate; the experimental procedure is simple, and no vacuum and gas protection devices are needed, so the cost is low, and the thin-film materials have good performance (Zhang *et al.*, 2010).

2.6 Pulsed laser deposition method

Pulsed laser deposition method is a physical vacuum deposition process that makes the high-power pulsed laser focus on the target surface to produce high temperature and cauterization and then produce high pressure and high temperature plasma; the plasma emission expands in directional

local area and deposits the substrate to form a thin film. (Washio *et al.*, 2012) deposited CZTS thin films epitaxially on GaP substrates using pulsed laser deposition PLD. The band gap of the films was found to be 1.5 eV and films were nearly stoichiometric. (Wadia *et al.*, 2009) prepared CZTS thin films using PLD. Film was Sn-rich and the band gap was 1.5 eV. In another report, (Vigil *et al.*, 2015) prepared CZTS precursor using PLD and then annealed in N_2+H_2S (5 %) atmosphere.

Sugimoto *et al.* (2011) prepared polycrystalline CZTS thin films through PLD at room temperature. Study of laser incident energy revealed that structural, morphological and optical properties were improved up to incident energy of 2.5 J/cm. Shin *et al.* (2013) deposited CZTS thin films on heated Mo-coated glass substrates using PLD. Band gap of the films varied from 1.53 to 1.98 eV depending on substrate temperature From EDAX results, all the films were Cu rich and S-deficient.

2.7 Screen Printing

Zhou et al. (2010) reported a simple and low cost screen printing approach for the preparation of CZTS absorber layers. Microparticles of CZTS prepared using wet ball milling and sintering methods, were dispersed in isopropanol. Separately, ethyl cellulose was dissolved in isopropanol. The screen printable paste was then made by mixing both solutions with small quantity of terpinol and deposited onto 'Mo' coated polyimide substrates. Band gap, sheet resistance, carrier concentration, and Hall mobility of the screen printed CZTS layers were 1.49 eV, 2.42×10^3 Ω/cm, 3.81×10^{18} cm^{-3}, and 12.61 cm^2 $V^{-1}s^{-1}$ respectively.

2.8 Chemical Bath Deposition

Chalapathi *et al.* (2015) deposited SnS and ZnS on 'Mo' coated SLG substrates through chemical bath deposition (CBD) in which 'Cu' ions were incorporated into the precursor films via ion exchange technique. These CZTS precursor films were then annealed in H_2S atmosphere at 500 "C. They could produce compositionally uniform microcrystalline CZTS with kesterite structure and band gap of 1.45 eV.

2.9 Successive Ionic Layer Adsorption and Reaction (SILAR) Deposition

Sugimoto *et al.* (2011) reported fabrication of CZTS thin film based solar cells using similar approach. CZTS thin films were formed by sequential immersion of substrate into the solutions of cationic and anionic precursors, as deposited films were dried in oven at 60 °C for 30 min and reported an efficiency of 1.85 % on a solar cell based on CZTS prepared from SILAR technique.

Bag *et al.* (2012) reported a novel chemical successive ionic layer adsorption and reaction (SILAR) technique for CZTS thin film formation by sequential reaction on SLG substrate surface. Films were then annealed in vacuum at 400 "C. X-ray diffraction studies showed formation of kesterite structure of CZTS films.

2.10 Sol-Gel Deposition

Sol-gel is one of the catalysts preparation methods of CZTS thin films; it is a homogeneous process resulting in continuous transformation of a solution into hydrated solid precursor. This method has several promising advantages over the conventional techniques. It offers better control of the texture, composition, homogeneity and structural properties of the final solids.

Tanaka *et al.* (2009) reported fabrication of CZTS-based thin film solar cell using sol-gel method. They used CZTS films prepared over 'Mo' coated glass substrates by sulphurising precursors deposited by sol-gel technique as the absorber layer. Zhang *et al.* (2009) prepared CZTS films by sol-gel spin coating deposition. They avoided usual sulphurisation process Film with a nearly stoichiometric composition was prepared at synthesizing temperature of 280 ^oC. Absorption coefficient and the optical energy gap of the deposited films were 2.9 x 10^4 cm^{-1} and 1.5 eV respectively.

Wang *et al.* (2011) prepared CZTS thin films by spin-coating the sol-gel precursor followed by annealing in a nitrogen atmosphere. Band gap and absorption coefficient of the films were 1.51 eV and 10^4 cm^{-1} respectively. Zhou *et al.* (2010) deposited sol-gel processed CZTS thin films without sulphurisation. The grain size was up to 1 µm and the Cu/(Zn+Sn) and Zn/Sn ratios were 0.93 and 1.07 respectively.

2.11 Hydrothermal deposition

Hydrothermal method is the methods that does not require any expensive precursors or equipment and can be readily adopted for industrial production processes. It possesses remarkable reliability and selectivity as well as high efficiency at low temperature (Habib, 2012).

Hydrothermal and solvothermal methods have been developed to prepare CZTS nanoparticles. The hydrothermal method is defined as a method that uses water as a solvent in a sealed reaction container when the temperature is raised above 100 ^{0}C, while a solvothermal method uses an organic solvent in the precursor solution (Habib, 2012).

The organic solvents such as ethylene glycol and oleylamine used in the solvothermal method are toxic and harmful to the environment. Thus, it is desirable to develop suitable hydrothermal method for fabrication of CZTS material, because of its low environmental impact (Habib, 2012).

Chopra *et al*. (2004) synthesized nanocrystalline CZTS powder through hydrothermal process using thiourea as sulphur precursor. They got kesterite CZTS of particle size 4-5 nm High temperature thermal annealing treatments are, needed for the an-deposited nanocrystal films to form large grains, which are crucial for high performance thin film solar s Based on the experience with CIGS and CIS film deposition for solar cells, films with micrometer sized grains in the absorber layer can produce cells with high power conversion efficiencies The current progresses in CZTS nanocrystal based solar cells have demonstrated that without stain growing thermal treatment process, solar cells are generally unable to generate 1% efficiency

Weber *et al*. (2010) reported that even when kesterite crystal structure nanocrystals have been formed in deposited films, thermal annealing cannot be omitted. To make CZTS thin films from the nanocrystals, CZTS nanocrystals are generally dispersed in a solvent or a mixture of solvent and binder before being subjected to film deposition. The CZTS slurry or paste with suitable rheological properties must be prepared to create a uniform layer with homogenous film thickness. The nanocrystal coatings are normally accomplished by either repeating spin coating or doctor-blading to achieve 1 to 2 µm of film thickness, which is mostly reported as the absorber layer thickness for thin film solar cells. The as-deposited film is usually subjected to soft baking at a temperature around 300 ^{0}C followed by a high temperature annealing 500 to 580 ^{0}C for a designed duration. Although CZTE crystal ready tam the ocean amount of chalogen (sulphur in most cases)the thermal annealing process of the nanocrystal films still requires the presence of chalogen vapour Under high vacuum conditions, the CZES phase decomposes at temperature above 550 °C (Weber *et al*., 2010). The decomposition rate largely varies depending on the temperature, total pressure of the annealing chamber, and the partial pressure of the volatile products. Therefore in order to prevent the loss of CZTS phase and the formation of undesired phases an atmospheric base pressure and a chalcogen source are normally applied in the thermal annealing process, sulphur (sulphurisation) or selenium (selenisation) is a reasonable option to prevent the decomposition of CZTS and CZTSe.

3.0 CHARATERISATION

3.1 Visible ultraviolet spectroscopy (UV-VIS)

UV-VIS spectrophotometry is a quantitative strategy used to quantify how much a compound substance ingests light. This is finished by estimating the power of light that goes through an

example (as an element of frequency) regarding the force of light through a reference test or clear with a gadget called spectrophotometer.

UV spectrophotometer principle follows the Beer-Lambert Law. This law states that whenever a beam of monochromatic light is passed through a solution with an absorbing substance, the decreasing rate of the radiation intensity along with the thickness of the absorbing solution is actually proportional to the concentration of the solution and the incident radiation.

This law is expressed through this equation:

$$A = \log (I0/I) = ECI \quad (1)$$

A stands for the absorbance, I0 refers to the intensity of light upon a sample cell, l refers to the intensity of light departing the sample cell, C stands for the concentration of the solute, L stands for the length of the sample cell and E refers to the molar absorptivity.

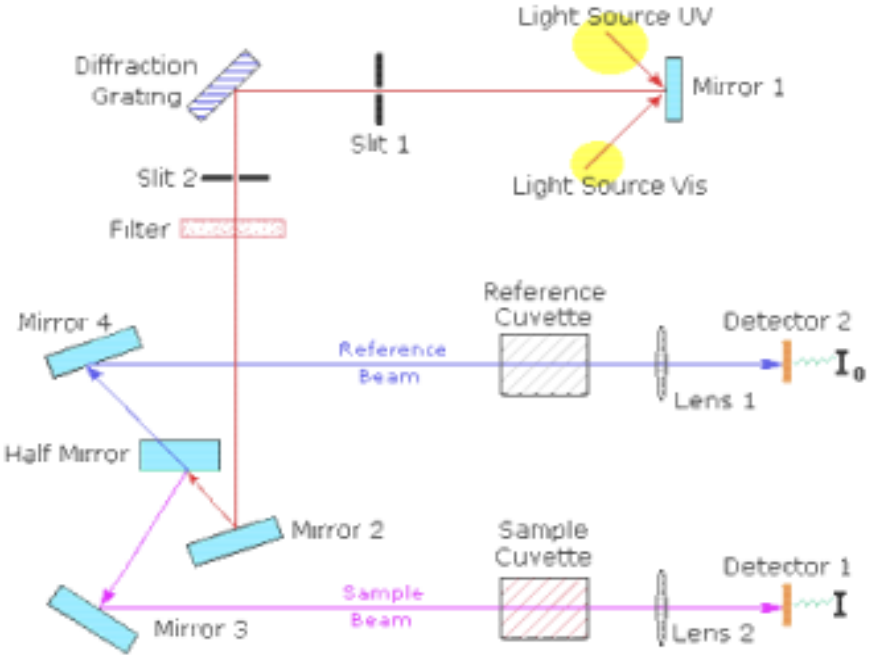

Figure 1: diagram of the components of a typical spectrophotometer (Fox, 2006).

Cho *et al.* (2013) Synthesised Cu_2ZnSnS_4 thin films by a precursor solution paste, The results show that CZTS materials have low transmittance levels, indicating that the solids promote adequate absorption conditions mainly concentrated in the region of 2.0-1.54 eV, which evidence media values associated to an appropriate behavior in terms of UV absorption coefficients. The results also show a direct relationship between the synthesis temperature and the optical properties of the materials. It was observed that the energy gap decreases as the treatment temperature increases. This behavior suggests effective electronic transitions in the valence band, so that at higher temperatures a better consolidation of the Kesterite phase was achieved, decreasing the percentage of secondary phases in the CZTS materials.

Khalate *et al.* (2017), who sythesised CZTS by chemical treatment showed similar behavior and found that the optical properties of CZTS are influenced by the temperature in processes that are clearly dependent of synthesis conditions. In effect, the synthesized materials exhibit characteristic band-gap values for each system, in which the CZTS material show a remarkable result, reaching Eg values around 1.54 eV.

3.2 X-ray diffraction analyses

X-Ray diffraction (XRD) is an incredible procedure for assurance of precious stone design and cross section boundaries. An essential instrument for such investigation is the Bragg spectrometer as shown in fig. 3 below.

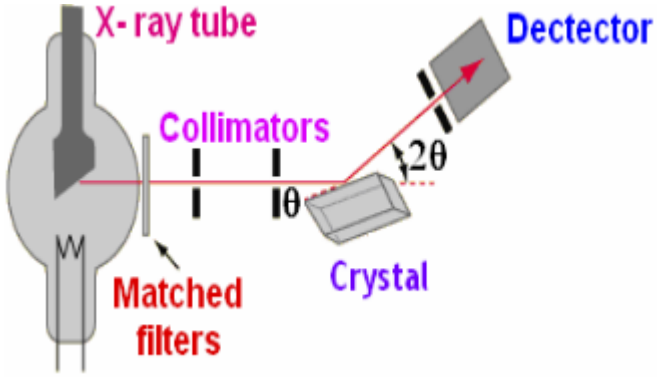

Figure 2: Schematics of X-ray diffractometer (Guinier, 1963)

Fig. 3 shows the schematics of X-ray diffractometer. Diffraction in general occurs only when the wavelength of the wave motion is of the same order of magnitude as the repeat distance between scattering centers. This condition of diffraction is nothing but Bragg's law and is given as,

$$2d \sin\theta = n\lambda \quad (2)$$

where d is inter-planer spacing, θ is diffraction angle, λ is wavelength of x-ray and n is order of diffraction.

For slight movies, the powder procedure related to diffractometer is most regularly utilized. In this procedure the diffracted radiation is recognized by the counter cylinder, which moves along the rakish scope of reflections. The forces are recorded on a PC framework. The 'd' values are determined utilizing connection (2.5) for known upsides of θ, λ and n. The X-beam diffraction information in this manner got is imprinted in even structure on paper and is contrasted and Joint Committee Power Diffraction Standards (JCPDS) information to recognize the obscure material. The example utilized might be powder, single gem or slim film. The crystallite size of the stores is assessed from the full width at half greatest (FWHM) of the most exceptional diffraction line by Scherrer's equation as follows (Barrett and Massalski, 1966);

$$D = \frac{0.9\lambda}{\beta \cos\theta}$$

Where, D is crystallite size, λ is wavelength of X-ray used, β is full width at half maxima of the peak (FWHM) in radians, θ is Bragg's angle. The X- ray diffraction data can also be used to determine the dimension of the unit cell.

According to the collection code ICDD: 00-001-1281. The presence of this phase in the solids is related to the synthesis temperature established in current work and becomes more evident in those materials that were synthesized at low temperatures. This relationship has been reported by Pinzón *et al.* (2021), observing that the intermediate phases of covallite, could be attributed to the incomplete transformation of sulphides at low temperatures. Moreover, non-stoichiometric relations of Zn, Sn and Cu can lead to formation of inhomogeneous materials Rajesh *et al.* (2013).

3.3 Scanning electron microscopy (SEM)

It can give significant data about the surface provisions of an item, its surface, the shape, size and plan of the particles making up the article that are lying on the outer layer of the example or have been uncovered by crushing or synthetic drawing, the components and mixtures the example is made out of and their relative proportions in regions around 1 μm in measurement. Filtering electron microscopy (SEM) is a fundamental instrument for material portrayal particularly microstructural/morphological properties. Moreover, it can show the plan of particles in the example and their level of request. Filtering electron magnifying lens goals are at present restricted to around 25 Angstroms. The figure underneath shows a schematic outline of examining electron microscopy (Weber *et al*., 2010).

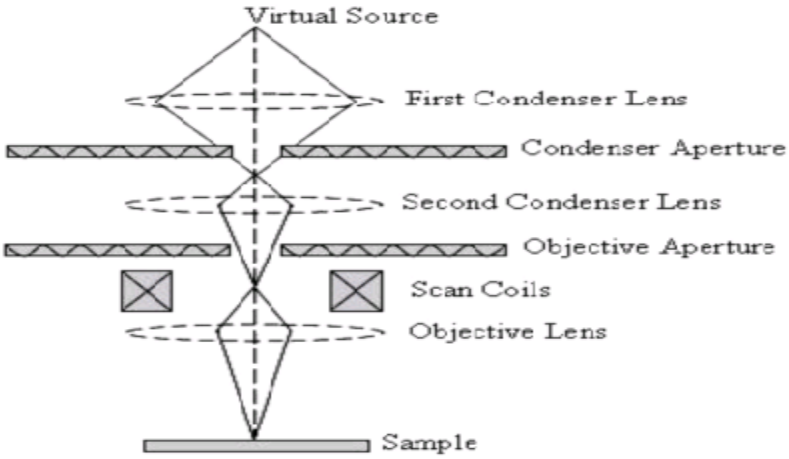

Figure 3: A schematic diagram of scanning electron microscopy

The examining electron magnifying lens produces a light emission in a vacuum. That shaft is collimated by electromagnetic condenser focal points, centered by a goal focal point, and checked across the outer layer of the example by electromagnetic redirection loops. The essential imaging strategy is by gathering optional electrons that are delivered by the example. The optional electrons are distinguished by a glimmer material that produces blazes of light from the electrons. The light glimmers are then distinguished and enhanced by a photomultiplier tube. By relating the example examine position with the subsequent sign, a picture can be shaped that is strikingly like what might be seen through an optical magnifying lens, the light and the shadowing show very normal looking surface geology (Habib, 2012).

Zhou *et al.* (2015), Reported a work via a facile liquid reflux method and the morphology of these materials was improved with increasing synthesis temperature, since the concentration of agglomerates decreased noticeably. Elemental composition analyzes performed on the CZTS samples, using X-ray dispersive energy spectroscopy (EDX), revealed that the experimental compositions differ about 1% with the theoretically calculated compositions. This difference can be caused by the tendency of zinc and tin towards the formation of sulfides at low temperatures; however, based on the properties identified up to this point and by effect of the low synthesis temperatures, it is expected that these products could be reduced in posterior thermal treatments to help to consolidate the main phase of Cu_2ZnSnS_4 (Zhou *et al.*, 2015).

3.4 Raman spectroscopy analyses

The Raman microscopy analyzes carry out on the CZTS solids show that in addition to the characteristic signals of the CZTS material secondary phases of Cu_2SnS_3, Sn_2S_3, SnS_2, are observed along CZTS1-CZTS5 materials, mainly in the case of $Cu_{2-x}S$ and ZnS phases, being clear a notable

evolution in terms of synthesis temperature Pinzón *et al.* (2017). The consolidation of a Kesterite phase is more evident in CZTS5 sample, with a strong signal around 287 cm^{-1}, as indicated in Figure 4a.

The signals of magnified Raman spectrum of CZTS5 sample is shown in Figure 4b, and exhibit a more detailed evidence of secondary phases with the main peak related with the Cu2ZnSnS4 system in the Kesterite phase. The figure shows a signal at 338 cm^{-1} related to the A-asymmetric vibrational mode of the Kesterite. This mode linked to the vibrations of the sulfur atoms in the crystal lattice is associated with the main signal of the CZTS molecule Pinzón *et al.* (2017). Likewise, the intense signal found at 287 cm^{-1} is related to the characteristic phononic frequencies of CZTS. The signals at 243, 255 and 257 cm^{-1} are also associated with the CZTS material.

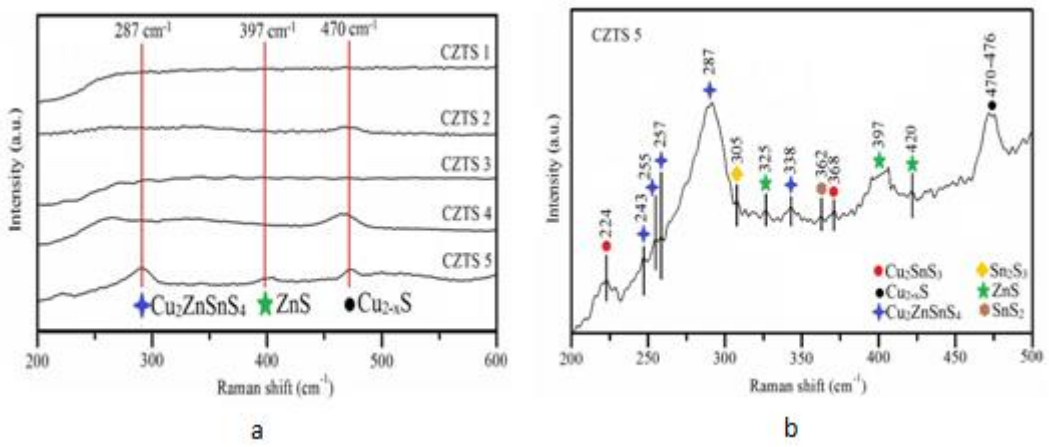

Figure 4: (a) Evolution of main vibrational Raman signals along CZTS1- CZTS5 samples with presence of secondary phases of ZnS and Cu_2S and **(b)** Raman magnified spectrum for the CZTS5 system showing the signals associated with the vibration band Pinzón *et al.* (2017).

3.5 Fourier transformation ifrared spectroscopy (FTIR)

FTIR spectroscopy offers both qualitative and quantitative analysis for organic or inorganic samples. The basic principle of FTIR spectroscopy is to identify chemical bonds in a molecule by producing an infrared absorption spectrum. The infrared spectra then produce a profile of the sample, a distinctive molecular fingerprint as well as scan samples for different components. No two unique molecular structures can produce the same infrared spectrum, similar like a fingerprint concept. Hence, this makes infrared spectroscopy becoming very useful for many analysis categories Bag *et al.* (2012)

4.0 Conclusion

This review summarises resent advances of CZTS and their performance as an alternative material for costly materials like indium and gallium, this include different synthesis and characterisation method. With the further development of the preparation technology and equipment, as well as the mature theoretical research about basic features and crystallisation condition of CZTS thin film, with its environmentally friendly features, rich content in the earth crust, and good photoelectric performance, CZTS thin film will certainly become a promising photovoltaic material after CIGS thin film.

References

Bags, S., Gunawan, O., Gokmen, T., Zhu, Y., Todora, T.K. & Mitzi, D. B. (2012). Low band gap liquid-processed CZTS solar cell with 10.1% efficiency. *Energy Environmental Sciences*, (5): 7060-7065

Camara, S. M., Wang, L., & Zhang, X. (2013). Easy hydrothermal preparation of Cu2ZnSnS4 (CZTS) nanoparticles for solar cell application. *Nanotechnology*, *24*(49), 495401.

Chalapathi, U., Uthanna, S. & Raja, S. (2015). Growth of Cu_2ZnSnS_4 thin films by a two stage process-Efect of incorporating of sulfur at the stage precursor. *Solar Energy materials and solar cells*, (132): 127-133

Chen, S., Gong, X. G., Walsh, A., & Wei, S. H. (2009). Crystal and electronic band structure of Cu 2 ZnSn X 4 (X= S and Se) photovoltaic absorbers: First-principles insights. *Applied Physics Letters*, *94*(4), 041903.

Cho, J. W., Ismail, A., Park, S. J., Kim, W., Yoon, S., & Min, B. K. (2013). Synthesis of Cu2ZnSnS4 thin films by a precursor solution paste for thin film solar cell applications. *ACS applied materials & interfaces*, *5*(10), 4162-4165.

Chopra, K. L, Paulson, P D & Dutta, V. (2004). Thin film solar cell: an overview Programmed Photovolt: *Research Application*, (12): 69.92

Habib, S. L., Idris, N. A., Ladan, M. J. & Mohammed, A. G. (2012) Unlocking Nigeria's solar PV and CSP potentials for sustainable electricity development *International Journal of Scientific and Engineering Research* (5): 2010-2012

Huang, Y., Li, G., Fan, Q., Zhang, M., Lan, Q., Fan, X. & Zhang, C. (2016). Facile solution deposition of Cu2ZnSnS4 (CZTS) nano-worm films on FTO substrates and its photoelectrochemical property. *Applied Surface Science*, *364*, 148-155.

Katagiri, H., Jimbo, K., Moriya, K., & Tsuchida, K. (2003, May). Solar cell without environmental pollution by using CZTS thin film. In *3rd World Conference onPhotovoltaic Energy Conversion, 2003. Proceedings of* (Vol. 3, pp. 2874-2879). IEEE.

Katagiri, H., Nishimura, M., Onozawa, T., Maruyama, S., Fujita, M., Sega, T., & Watanabe, T. (1997, August). Rare-metal free thin film solar cell. In *Proceedings of Power Conversion Conference-PCC'97* (Vol. 2, pp. 1003-1006). IEEE.

Katagiri, H., Saitoh, K., Washio, T., Shinohara, H., Kurumadani, T., & Miyajima, S. (2001). Development of thin film solar cell based on Cu2ZnSnS4 thin films. *Solar Energy Materials and Solar Cells*, *65*(1-4), 141-148.

Khalate, S. A., Kate, R. S., Kim, J. H., Pawar, S. M., & Deokate, R. J. (2017). Effect of deposition temperature on the properties of Cu2ZnSnS4 (CZTS) thin films. *Superlattices and Microstructures*, *103*, 335-342.

Khare, A., Himmetoglu, B., Johnson, M., Norris, D. J., Cococcioni, M., & Aydil, E. S. (2012). Calculation of the lattice dynamics and Raman spectra of copper zinc tin chalcogenides and comparison to experiments. *Journal of Applied Physics*, *111*(8), 083707.

Khare, A., Wills, A. W., Ammerman, L. M., Norris, D. J., & Aydil, E. S. (2011). Size control and quantum confinement in Cu 2 ZnSnS 4 nanocrystals. *Chemical communications*, *47*(42), 11721-11723.

Leitao, J. P., Santos, N. M., Fernandes, P. A., Salomé, P. M. P., Da Cunha, A. F., González, J. C., ... & Matinaga, F. M. (2011). Photoluminescence and electrical study of fluctuating potentials in Cu 2 ZnSnS 4-based thin films. *Physical Review B*, *84*(2), 024120.

Li, J., Du, H., Yarbrough, J., Norman, A., Jones, K., Teeter, G., ... & Levi, D. (2012). Spectral optical properties of Cu 2 ZnSnS 4 thin film between 0.73 and 6.5 eV. *Optics express*, *20*(102), A327-A332.

Lincot, D. (2005). Electrodeposition of semiconductors. *Thin solid films*, *487*(1-2), 40-48.

Liu, W. C., Guo, B. L., Wu, X. S., Zhang, F. M., Mak, C. L., & Wong, K. H. (2013). Facile hydrothermal synthesis of hydrotropic Cu_2ZnSnS_4 nanocrystal quantum dots: band-gap engineering and phonon confinement effect. *Journal of materials chemistry A*.

Mali, S. S., Patil, B. M., Betty, C. A., Bhosale, P. N., Oh, Y. W., Jadkar, S. R., ... & Patil, P. S. (2012). Novel synthesis of kesterite Cu2ZnSnS4 nanoflakes by successive ionic layer adsorption and reaction technique: characterization and application. *Electrochimica Acta*, *66*, 216-221.

McCandless, B. E., Mondal, A., & Birkmire, R. W. (1995). Galvanic deposition of cadmium sulfide thin films. *Solar energy materials and solar cells*, *36*(4), 369-379.

Pinzón, D. L., Cuaspud, J. A., Vera López, E., & Schmal, M. (2021). Hydrothermal Synthesis and Evaluation of the Cu2ZnSnS4 for Photovoltaic Applications. *Materials Research*, *24*.

Pinzón, D. S., Perez, G. S., Cuaspud, J. G., & López, E. V. (2017). Synthesis and characterization of the Cu2ZnSnS4 system for photovoltaic applications. In *Journal of Physics: Conference Series* (Vol. 786, No. 1, p. 012027). IOP Publishing.

Rajesh, G., Muthukumarasamy, N., Subramaniam, E. P., Agilan, S., & Velauthapillai, D. (2013). Synthesis of Cu 2 ZnSnS 4 thin films by dip-coating method without sulphurization. *Journal of sol-gel science and technology*, *66*(2), 288-292.

Schorr, S. (2007). Structural aspects of adamantine like multinary chalcogenides. *Thin Solid Films*, *515*(15), 5985-5991.

Scragg, J. J., Dale, P. J., Peter, L. M., Zoppi, G., & Forbes, I. (2008). New routes to sustainable photovoltaics: evaluation of Cu2ZnSnS4 as an alternative absorber material. *physica status solidi (b)*, *245*(9), 1772-1778.

Shin, B., Gunawa, O., Zhu, Y., Bajarczuk, N. A. Chey, S. J. & Guha, S. (2013). Thin film solar cell with 8.4 % power conversion efficiency using an earth-abundant Cu_2ZnSnS_4 absorber. *Programmed Photovoltaic Research Application*, (21): 72-76

Shin, B., Gunawan, O., Zhu, Y., Bojarczuk, N. A., Chey, S. J., & Guha, S. (2013). Thin film solar cell with 8.4% power conversion efficiency using an earth-abundant Cu2ZnSnS4 absorber. *Progress in Photovoltaics: Research and Applications*, *21*(1), 72-76.

Shinde, N. M., Dubal, D. P., Dhawale, D. S., Lokhande, C. D., Kim, J. H., & Moon, J. H. (2012). Room temperature novel chemical synthesis of Cu2ZnSnS4 (CZTS) absorbing layer for photovoltaic application. *Materials Research Bulletin*, *47*(2), 302-307.

Sugimoto, H., Hiroi, H., Sakai, N., Muraoka, S. & Katou, T. (2011). Over 8% efficiency Cu_2ZnSnS_4 submodules with ultra-thin absorber. *IEEE photovoltaic Specialist conference* 2997

Tanaka, K., Kasaki, D., Nishio, M. & Ogawa, H. (2009). Pnuematically sprayed CZTS films under Ar and Ar-H_2 atmosphere. *Journal of physics D: Applied Physics*, (47): 24:29

Tanaka, K., Livreri, P. & Sunseri, C. (2005). A review of CZTS thin film deposition methods. *Energy Procedia*, (43): 104-109

Vigil, G. O. Courel, M. Rodrignez, E M. Olarte D. Frutis. A M. & Sancedo, E (2015). Electrical properties of sprayed CZTS thin film and its relation with secondary phase formation and solar cell performance. *Solar Energy Materials and Solar Cells*, (132); 476-484

Wadia, C. Alivisatos, A. P. & Kammen, D. (2009). CZTS-based solar cell from sol-gel pin Coating and its characterization. *Environment Science and Technology*, (43). 2072-2077

Wang, K., Gunawan, O., Todorov, T., Shin, B., Chey, S. J., Bojarczuk, N. A., ... & Guha, S. (2010). Thermally evaporated Cu 2 ZnSnS 4 solar cells. *Applied Physics Letters*, *97*(14), 143508.

Wang, K., Mitzi, D. B., Barkhouse, R. & Aaron, D. (2011). Prospects and performance limitations for Cu-Zn-Sn-S-Se photovoltaic technology. *Philadelvia Transnational Royal Society*, (371): 1-22

Washio,T., Shinj., T., Tajima, S., Fukano, T., Motohiro, T., Jumbo, K. & Katagari, H. (2015). Study of optical and structural properties of CZTS thin films grown by co-evapouration and spray pyrolsis. *Iopscience*,(65): 141-145

Weber, R., Ishino, K., Moritake, R & Minemoto, T (2010) Improvement of CZTS thin film morphology using Cu-Zn-Sn-O precursor grown from sputtering. *Current Applied Physics.* (13) 1861-1870

Yang, Z. (2011). Research on one-step Preparation of CZTS films and electrochemical optical properties [MS thesis]. *Dalian University of Technology*.

Yeon, H. J., Mohauty, B. C., Denk, H.Y., Lee, S. M. & Yong, S. C. (2015). Single elementary target-sputtered Cu_2ZnSnS_4 thin film solar cells. *Solar Energy Materials and solar cells*, (132): 136-141

Zhang, S. (2010). CZTS thin film and its research progress of solar cell. *Engineering and Technology*, (8), 67-69.

Zhang, X. G. & Shae, A. (2009). Defect physics of kesterite thin film cell absorber Cu_2ZnSnS_4. *Applied Physics Letters*, (96): 23-28

Zhou, J., Ye, Z., Wang, Y., Yi, Q., & Wen, J. (2015). Solar cell material Cu2FeSnS4 nanoparticles synthesized via a facile liquid reflux method. *Materials Letters*, *140*, 119-122.

Zhou, Y. L., Zhou, W. H., Du, Y. F., Li, M., & Wu, S. X. (2011). Sphere-like kesterite Cu2ZnSnS4 nanoparticles synthesized by a facile solvothermal method. *Materials Letters*, *65*(11), 1535-1537.

Zhou, Z., Wang, Y., Xu, D. & Zhang, Y. (2010). Fabrication of Cu_2ZnSnS_4 screen printed layers for solar cells. Solar Energy Materials and Solar Cells, (94): 2025-2042

Estimation of Depth to Structures Associated with Gold Mineralisation Potential over Southern Part of Kebbi State using Aeromagnetic Data

*[1]Augie A.I., [2]Salako K.A., [2]Rafiu A.A. and [3]Jimoh M.O.
[1]Department of Applied Geophysics, Federal University Birnin Kebbi, Nigeria.
[2]Department of Geophysics, Federal University of Science and Technology Minna, Nigeria.
[3]Department of Geology, Federal University of Technology Minna, Nigeria.
*Corresponding Author: email; ai.augie@fubk.edu.ng, Phone; +2348137330559

Abstract

In this study, magnetic signatures together with the geological settings of the area were employed in estimating the depth to structures that may host gold mineral over southern part of Kebbi State and its environs. Acquired aeromagnetic grids data covering the study area was processed, analyzed and interpreted using the following techniques; IGRF computation, Reduction to Equator (RTE), First Vertical Derivatives (FVD) and Euler Deconvolution. Results from these techniques have revealed the alteration zones and depth to the structures that could be host to gold mineralisation. These regions were corresponded to the following areas; Fakai, SE parts of Yauri and Shanga, Ngaski, Zuru, Magama, Rijau, Eastern part of Wasagu/Danko and Bukkuyum. FVD technique revealed the spatial and structural resolution in imagery thereby showing major structures which normally play an important role in determining the gold mineral. The structures found within the aforementioned areas are the architecture of a mineralized body as compared with the geology of the area, which falls under the following earth materials; quarzt-mica schist, granite, biotite, gneiss, diorite, medium coarse grained and biotite homblende granite. Estimated depth to magnetic sources (anomalies)/ or structures that could be host to gold mineralisation was found to be from 81.616 m to 181.171 m using algorithms Euler Deconvolution.

Keyword: Depth to Structures, Gold Mineralization, Yauri-Zuru Schist Belt, FVD and Euler Deconvolution.

INTRODUCTION

Structures in the Nigerian basement complex usually control the mineralisation and may be deep-seated and therefore require a geophysical approach that will delineate the possible pathways for gold exploration and exploitation (Ejepu *et al.,* 2018). The gold mineralisation is found through structurally controlled and spatially associated with shear zones and hydrothermal veins formed in response to the regional stress field (Sani *et al.*, 2017).

Structures such as fractures in gold mineralisation act as conduits for the mineralisation solution and second, as loci of deposition of mineralisation fluid (Adetona *et al.*, 2018). Faults and shear zones are potential pathways of fluids (Sani *et al.*, 2019) and thus, knowledge of the structural architecture of a mineralised area, the distribution and orientation of faults and shear zones, their formation and possible reactivation during the structural evolution and the tectonic conditions is a key to understand the formation, origin and location of mineral deposits as well as for exploration and findings of new targets as suggested in Adewumi and Salako (2018).

Historically, recorded gold production in Nigeria started by 1913 and peaked in the period of 1933 (Garba, 2000 & 2003). The gold production declined during the Second World War period and never recovered as mines were abandoned by mostly colonial companies (Danbatta, 2005). In Northern Nigeria, the most prominent occurrences are found at Maru, Anka, Malele, Tsohon-Birnin Gwari, Kwaga and Gurmana (Danbatta, 2008).

The discovery of petroleum led to a subsequent shift of the Nigerian economy, leading to a lack of attention to gold exploration, despite the widespread potentials. This development has prompted a need to map out regional structural features as well as its depth which might serve as conduits for the mineralizing fluids in areas where such mines were abandoned (Augie & Sani, 2020).

In this study, acquired aeromagnetic data was used with the view to determine the depth to the structures that could be host to gold mineralisation using the algorithms Euler deconvolution method. The method makes use of a structural index in addition to producing depth estimates. In combination, the structural index (SI) and the depth estimates have the potential to identify and calculate depth estimates for a variety of geologic structures such as faults, magnetic contacts, dikes, sills, etc (Daniel *et al.*, 2019).

LOCATION AND GEOLOGICAL SETTINGS OF THE STUDY AREA

The study area lies within the southern part of Kebbi state and, some part of Zamfara and Niger States between latitudes 10°30′0″N and 12°0′0″N, and longitudes 4°0′0″E and 5°30′0″E. The area covers the following local government areas (LGAs); Yauri, Zuru, Ngaski, Shanga, Fakai, Danko/Wasagu, Sakaba, Koko Besse, Maiyama, Bagudo and Suru in Kebbi State, Kebbe, Gummi and Bukkuyum LGAs in Zamfara State and, Rijau, Agwara, Borgu and Magama LGAs of Niger State (Figure 1).

Geologically, the study area falls under the Basement Complex rocks and some part of sedimentary basin. These comprise of; granite, rhyolite, biotite-granite, meta-conglomerate, quartz-mica schist, migmatite, varieties of schists, sandstones, ironstones and laterites (Figure 1). The metasediments in these areas also comprise of quartzites, schists and phyllites; whereas the Older Granites consist of granodiorites/ or diorites. Furthermore, dacites/rhyolites are overlain and intrude the basement gneisses, metasediments and granitic rocks of the southern (Anka-Yauri schist) part Kebbi (Bashar *et al.*, 2017).

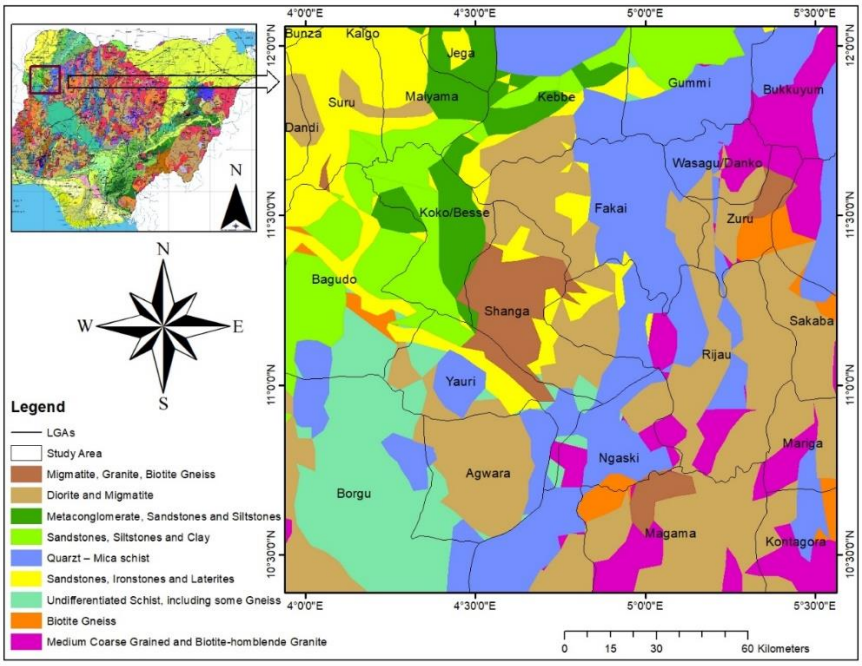

Figure 1: Location and Geological Map of the Study (Olugbenga & Augie, 2020).

METHODOLOGY

Aeromagnetic surveys over parts of the country were carried out by Fugro airborne surveys between 2005 and 2010 on behalf of the Federal Government of Nigeria. The data are under the custody of the Nigeria Geological Survey Agency (NGSA). In this study, nine (9) aeromagnetic data were used covering southern part of Kebbi and its environs of Basement Complex of northern Nigeria. These aeromagnetic datasets consist of sheets; 72 Giru, 73 Eokku, 74 Donko, 95 Kaoje, 96 Shanga, 97 Zuru, 117 Konkwesso, 118 Yelwa and 119 Chifu. The data were established under the following high-resolution survey conditions; Flight line spacing (500 m), Terrain clearance (80 m), Tie line spacing (2000 m), Flight direction is NW-SE and the Tie line direction is NE-SW.

The acquired data were corrected by removing geomagnetic gradient using the main/core field (International Geomagnetic Reference Field, IGRF). The data was collected in grid form which was further converted it in digitized form (X, Y and Z). The X and Y represents longitude and latitude respectively measured in metres (m), and Z represent the magnetic intensity measured in nano Tesla (nT). The acquired corrected aeromagnetic dataset was subjected to the minimum curvature gridding method to produce the Total Magnetic Intensity (TMI) map.

DATA PROCESSING

In this study, different processing techniques were employed to processed, enhanced, and interpreted magnetic data with aid of Geosoft (Oasis Montaj) and Surfer software. These techniques include: reduction of magnetic equator (RTE), first vertical derivative (FVD) and Euler Deconvolution. The Total Magnetic Field Intensity (TMI) value acquired from NGSA which was short-up 33,000 nT for the convenience of contouring or imaging. For these reasons, the value (33,000 nT) must be added back to give the TMI grids for the area (Augie & Ologe, 2020; Augie & Ridwan, 2021). The generated core fields (DGRF for the epoch period) are subtracted from the grid values (TMI) to give the magnetic anomaly (TMI anomaly) as shown in Fig. 2.

(a) Reduction to Magnetic Equator (RTE) Technique

The study area falls within magnetic equatorial zones of low inclination (low latitudes) where reduction to pole technique cannot be applied; because the North to South bodies have no detectable induced magnetic anomaly at zero geomagnetic inclination. This technique can make the data easier to interpret without losing any geophysical meaning. At low latitudes, a separate amplitude correction is usually required so as to prevent North-South signal in the data from dominating the results. As a result, reduced to the pole data may present a less 'honest' view of the data.

RTE techniques usually has an amplitude component [*sin(I)*] and a phase component [*i.cos(I) cos(D-θ)*]. The field strength is only required for apparent susceptibility calculation, but is re-calculated along with the inclination and declination in the other controls, so the values are always synchronized (Reid *et al*, 1990), as given in equation (1).

$$L(\theta) = \frac{[\sin(I) - i.\cos(D-\theta)]^2 \times (-cos^2(D-\theta)}{[sin^2(Ia) + cos^2(Ia).cos^2(D-\theta] \times [sin^2(I) + cos^2(D-\theta)]}, if\ (Ia| < I), Ia = I \quad (1)$$

where,

I is Geomagnetic inclination in ^{o}, D is Geomagnetic declination in ^{o} azimuth and Ia is inclination for amplitude correction (never less than I).

(b) First Vertical Derivatives (FVD) Technique

FVD was applied to TMI anomaly (RTE) in order to quantify the spatial rate of change of the magnetic field in horizontal, or vertical directions. Derivatives essentially enhance high frequency anomalies (that is shallow features) relative to low frequencies anomalies (that is deep features) and sharpen the edges of anomalies (Adewumi & Salako, 2018).

Vertical derivatives are a measure of curvature, and large curvatures are associated with shallow anomalies. Thus, it enhances near-surface features at the expense of deeper anomalies. The

anomaly in FVD is considerably narrow and more closely reflects the width of the magnetic rock body causing it and the derivatives are given in equation (2):

$$\mathbf{FVD} = \frac{\partial M}{\partial z} \tag{2}$$

(a) Euler Deconvolution Technique

Euler deconvolution is a useful tool for providing initial estimates of the locations and depths of magnetic sources (Adetona *et al.,* 2018). Euler deconvolution is a method to estimate the depth of subsurface magnetic anomalies and can be applied to any homogeneous field, such as the analytical signal of magnetic data. It is particularly good at delineating the subsurface contacts (Ajala *et al*, 2021). It is based on the fact that the potential field produced by many simple sources obeys Euler's homogeneity equation (Holden *et al.,* 2008). If a given component of the magnetic anomalous field ΔT (x, y, z) satisfies the following equation:

$$\Delta T(x, y, z) = tn\Delta T(x, y, z) \tag{3}$$

where n is the degree of homogeneity, then differentiating Equation 3 with respect to t gives Equation 4:

$$X\frac{\partial \Delta T}{\partial x} + X\frac{\partial \Delta T}{\partial y} + X\frac{\partial \Delta T}{\partial z} = n\Delta T \tag{4}$$

where x, y, and z are the coordinates of the field observation points and assumed to be at the origin.

According to Thompson, (1982), considering the potential field data, Euler's deconvolution equation can be expressed as

$$(x - x_0)\frac{\partial \Delta T}{\partial x} + (y - y_0)\frac{\partial \Delta T}{\partial y} + (z - z_0)\frac{\partial \Delta T}{\partial z} = N(B - T) \tag{5}$$

where (x_0, y_0, z_0) is the position of a magnetic source whose total magnetic field T is measured at (x, y, z). The total field has a regional value B, and N is the degree of homogeneity (structural index), which is equivalent to n in Equation (5). The unknown coordinates (x_0, y_0, z_0) are estimated by solving a determined system of linear equations using a prescribed value for N with the least squares method.

RESULTS AND DISCUSSION

TMI and RTE Maps

Figure 2 is the colour image of the IGRF corrected total magnetic intensity (TMI). The map gives the vector sum of all components of the magnetic field. It primarily used in this study to reveal the magnetic characteristic of the various lithological units in the area. The magnetic signatures range from a low of 32951.0 nT (minimum) along NW region of the study area, to a high of 33114.0 nT (maximum) in the SE parts of the region.

TMI anomalies were further reduced to magnetic equator in order to produce anomalies which depend on the inclination and declination of magnetized body, the local earth's field and orientation of the body with respect to the magnetic north. With application of reduced to the equator (RTE), the regional magnetic field align horizontally and most of the source magnetizations are horizontal. The resultant composite color depicting reduced-to-equator magnetic anomalies are given in Figure 3. The distinct pattern in Figure 3 of highs and lows and, the steep gradients between them at places that describe prominent magnetic linears are attributable to the complex assemblage of features of varied dimensions and direction.

The high magnetic trend lies under the following areas; Bagudo, Koko/Besse, Suru, Shanga, Northern part of Zuru, Yauri, Southern part of Ngaski, Wasagu/Danko, Northern part Borgu and Magama. While the areas of low magnetic anomalies are; Southern part of Zuru, Sakaba, Northern

part of Ngaski, Rijau, Mariga and Northern parts of Gummi & Bukkuyum. The areas with moderate magnetic trend are; Fakai, Kebbe, Southern part of Gummi, Agwaru and Northern part of Borgu (see Figure 3).

Thus, lows and high regions were characterized in difference rock formations that lead to difference in the magnetic susceptibility of the rocks within the area and usually the susceptible rocks occur at depths shallower than the curie points isotherm.

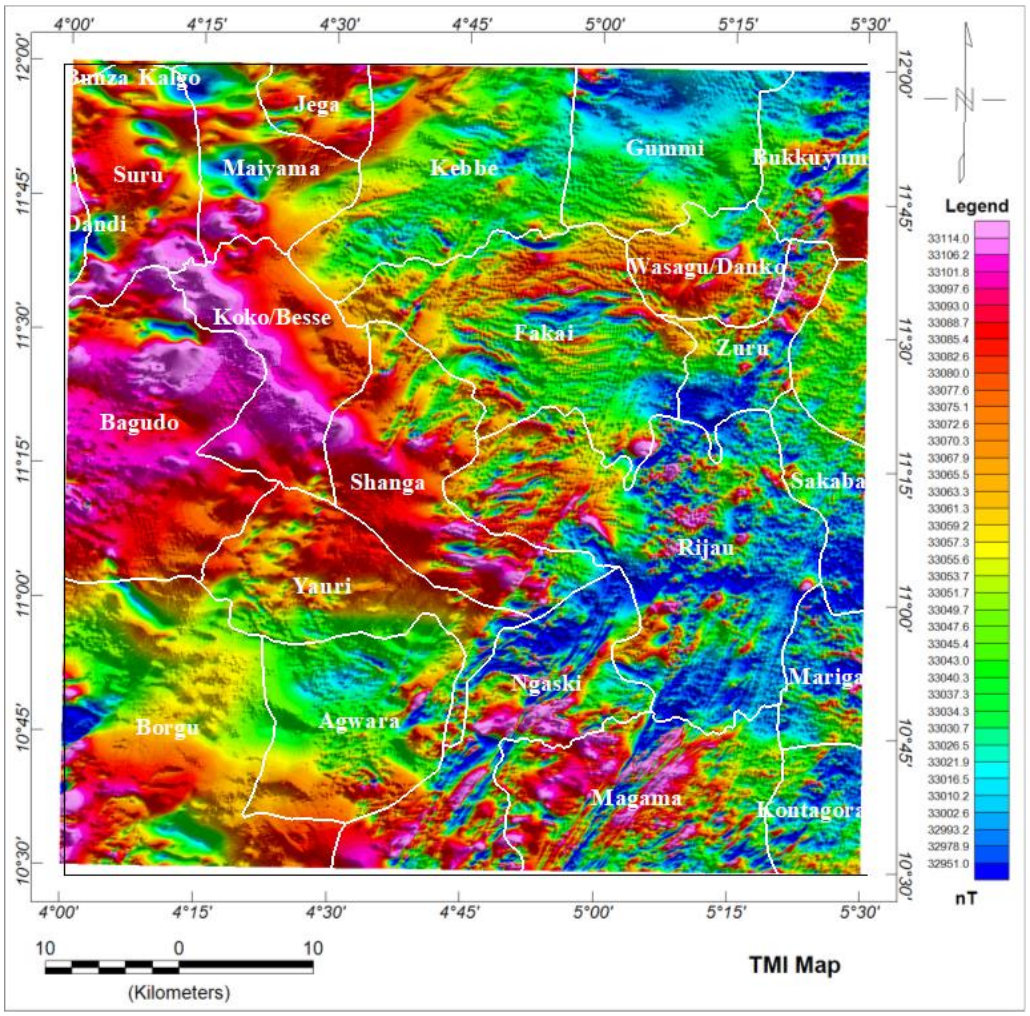

Figure 2: Total Magnetic Intensity (TMI) Map of the Study

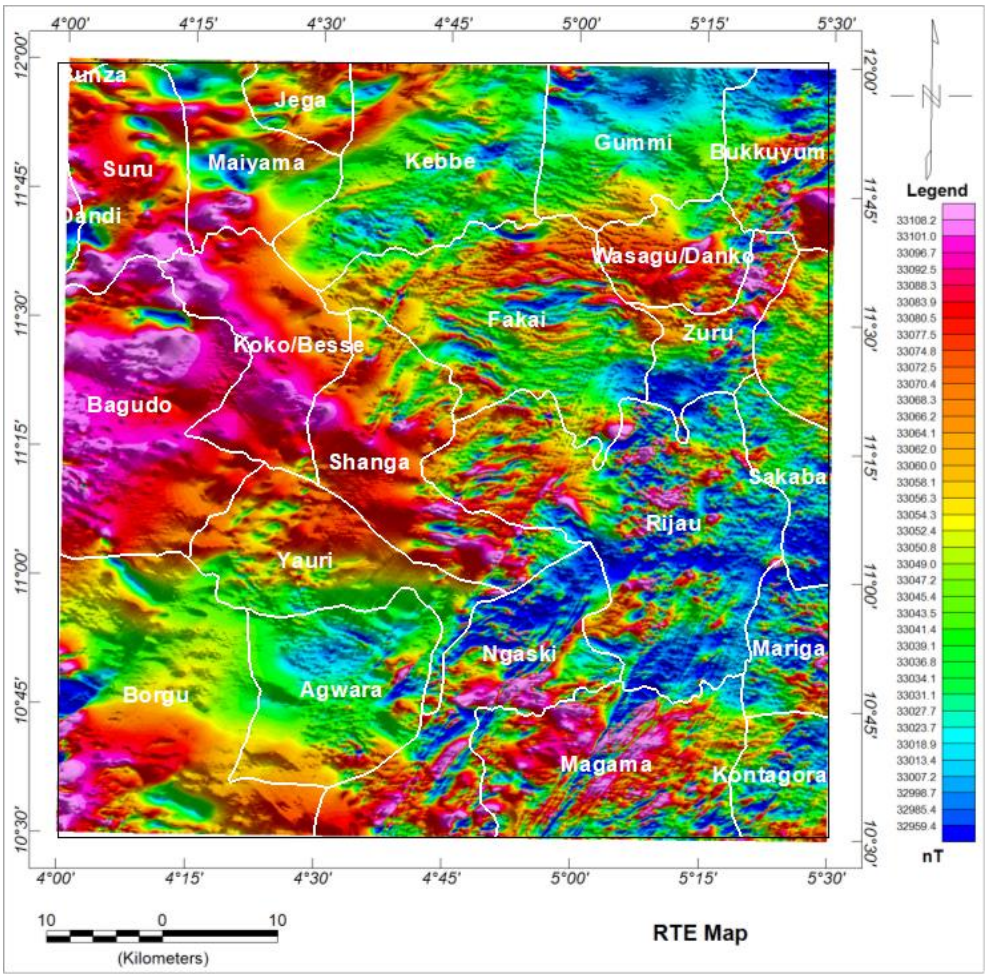

Figure 3: Reduction to Magnetic Equator (RTE) Map of the Study Area

FVD Map

FVD map (Figure 4) enhanced the spatial and structural resolution in imagery thereby showing major structural and lithological detail which were not previous appear in TMI and RTE maps (Figures 2 & 3). Looking at Figure 4 carefully, most of the structures delineated are found within SE and NE part of the study area. These areas were corresponding to; Fakai, SE parts of Yauri and Shanga, Ngaski, Zuru, Magama, Eastern part of Wasagu/Danko and Bukkuyum.

These structures found within the aforementioned areas are the architecture of a mineralized body and, according to the geological setting (see Figure 1) of the area, the regions comprise of the following rock materials; quarzt-mica schist, granite, biotite, gneiss, diorite, medium coarse grained and biotite homblende granite. Most of these structures found in the area has underlain on basement complex as compared with the geological map of the study area (Figure 1).

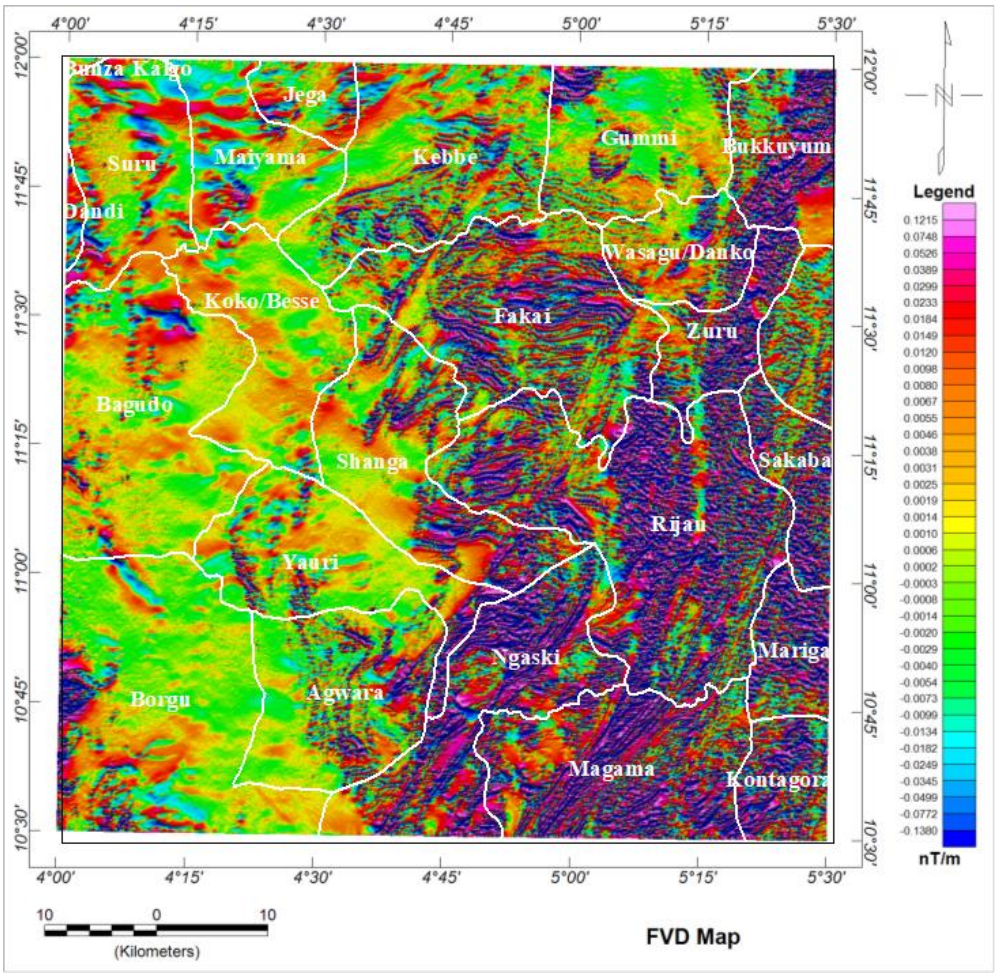

Figure 4: First Vertical Derivative (FVD) Map of the Study Area

Euler Deconvolution Map

Figure 5 presents the result of the Euler deconvolution map produced from the study area. The Euler Depth map shows that the depth to magnetic sources (anomalies)/ or structures that could be host to gold mineralisation. Shallow and deeper depths were obtained from these results which were ranges from 81.616 m to 544.740 m. shallow depths ranging from 81.616 m to 181.171 m at the areas corresponds to; Fakai, SE parts of Yauri and Shanga, Ngaski, Zuru, Magama, Eastern part of Wasagu/Danko and Bukkuyum. These regions have falls under Nigerian basement complex which usually control the mineralisation as compared with the results from FVD map and the geological setting of the area (Figure 1).

The regions of deeper depths on the Euler depth map corresponds to the regions of thick sediments on the Figure 5. These zones have lies under the following areas; Bunza, Bagudo, Dandi, Jega, Suru, Koko/Besse, Western parts of Yauri and Shanga, and Southern parts of Borgu. The maximum depth of 544.744 m was obtained and this may be sufficient for hydrocarbon as compared with the geology of the area.

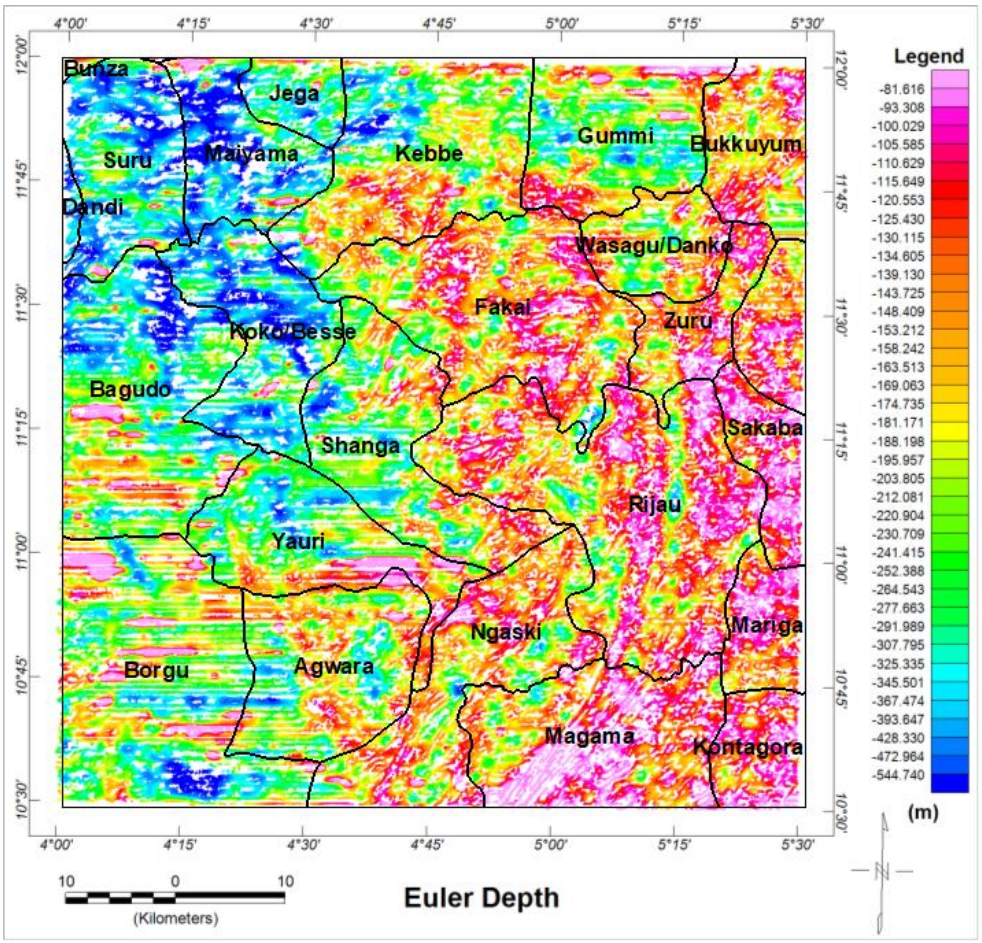

Figure 5: Euler Deconvolution Map of the Study Area

CONCLUSION

The acquired aeromagnetic data of southern parts of Kebbi State and its environs has been analysed and interpreted qualitative and quantitatively using three processing techniques; Reduction to Magnetic Equator (RTE), First Vertical Derivatives (FVD) and Euler deconvolution. The result obtained from these techniques have revealed the structures and also depth to that structures that may host gold mineral. These areas were corresponding to; Fakai, SE parts of Yauri and Shanga, Ngaski, Zuru, Magama, Eastern part of Wasagu/Danko and Bukkuyum. The depth to magnetic sources (anomalies)/ or structures that could be host to gold mineralisation was found to be from 81.616 m to 181.171 m.

REFERENCES

Adetona, A. A., Salako, K. A. & Rafiu, A. A. (2018). Delineating the Lineaments Within the Major Structures around Eastern Part of lower Benue Trough from 2009 Aeromagnetic Data, *FUW Trends in Science & Technology Journal*, Vol. 3 No. 1, pp. 175–179 e-ISSN: 24085162; p-ISSN: 20485170.

Adewumi, T. & Salako, K.A. (2018). Delineation of Mineral Potential Zone using High Resolution Aeromagnetic Data over Part of Nasarawa State, North Central, Nigeria, *Egyptian Journal of Petroleum*, https://doi.org/10.1016/j.ejpe.2017.11.002

Ajala, S.A. Salako, K. A. Rafiu, A. A, Alahassan, U. D. Adewumi, T. & Sanusi, Y.A. (2021). Estimation of Sedimentary Thickness for Hydrocarbon Potential over Part of Adamawa

Trough, Nigeria Using Magnetic Method, *Earth Sciences Pakistan (ESP)*, 5(1), 07-11, DOI: http://doi.org/10.26480/esp.01.2021.07.11

Augie, A.I. & Ologe, O. (2020). Analysis of Aeromagnetic Data for Coal Deposit Potential over Birnin Kebbi and its Environs Northwestern Nigeria, *Nigerian Journal of Science and Environment,* Vol.18 (1), pp. 145 – 153.

Augie, A.I. & Ridwan, M.M. (2021). Delineation of Potential Mineral Zones from Aeromagnetic Data over Eastern Part of Zamfara, *Savanna Journal of Basic and Applied Sciences,* Vol. 3(1), pp. 60-66.

Augie, A.I. & Sani A.A. (2020). Interpretation of Aeromagnetic Data for Gold Mineralisation Potential over Kabo and its Environs NW Nigeria, *Savanna Journal of Basic and Applied Sciences,* Volume 2, No. 2, pp. 116-123.

Bashar, M. G. Sanusi, Y. A. & Udensi, E. E. (2017). Interpretation of Aeromagnetic Data Over Birnin-Kebbi and Its Adjoining Areas Using First Vertical Derivative and Local Wavenumber Methods, *IOSR Journal of Applied Geology and Geophysics*, Vol. 5(5), pp. 44-53.

Danbatta, U. A. (2005). Precambrian Crustal Development of The Northwestern Part of Zuru Schist Belt, NW Nigeria. A paper presented at the 41st Annual Conference of Nigerian Mining, and Geos. Soc. (NMGS).

Danbatta, U.A. Abubakar, Y. I. & Ibrahim A. A. (2008). Geochemistry of Gold Deposits in Anka Schist Belt, Northwestern, Nigeria, *Nigerian Journal of Chemical Research*, Volume 13, pp. 19-29.

Daniel, E. Jimoh, R & Lawal, K. (2019). Delineation of Gold Mineral Potential Zone Using High Resolution Aeromagnetic Data Over Part of Kano State, Nigeria, *Journal of Geology Geophysics* 8:464. 10.35248/2381-8719.464

Daniel, E. Jimoh, R & Lawal, K. (2019). Delineation of Gold Mineral Potential Zone Using High Resolution Aeromagnetic Data Over Part of Kano State, Nigeria, *Journal of Geology Geophysics* 8:464. 10.35248/2381-8719.464

Ejepu J. S. Unuevho, C. I. Ako, T. A. & Abdullahi S. (2018). Integrated Geosciences Prospecting for Gold Mineralization in Kwakuti, North-Central Nigeria, *Journal of Geology and Mining,* Vol. 10(7), pp. 81-94, DOI: 10.5897/JGMR2018.0296.

Holden, E.J., Dentith, M., and Kavesi, P. (2008). Towords the Automatic Analysis of Regional Aeromagnetic Data to Identify Regions Prospectives for Gold Deposits, *Computer Geosciences,* 34, 1505 – 1513

Olugbenga, T. T. & Augie, A. I. (2020). Estimation of Crustal Thickness within the Sokoto Basin North-Western Nigeria Using Bouguer Gravity Anomaly Data, WASET, *International Journal of Geological and Environmental Engineering*, Vol. 14, No. 9, pp. 247–252.

Reid, A.B. Allsop, J.M. Granser H, Millet A.J. & Somerton, I.W. (1990). Magnetic interpretation in three dimensions using Euler deconvolution. *Geophysics*, Vol.55, pp.80-91

Sani, A.A. Augie, A.I. & Aku, M.O. (2019): Analysis of Gold Mineral Potentials in Anka Schist Belt North Western Nigeria using Aeromagnetic Data Interpretation, *Journal of the Nigerian Association of Mathematical Physics,* Volume 52, pp 291-298.

Sani, M.A. Raimi, J. Elatikpo, S.M. & Lawal, K.M. (2017). Magnetic Interpretation of Structures Associated with Gold Mineralisation Around Kundila and Ginzo Area, Northwestern Nigeria, *Nigerian Journal of Scientific Research*, 16(2): 240 – 246. njsr.abu.edu.ng

Thompson, D.T. (1982). A New Technique for Making Computer-Assisted Depth Estimates from Magnetic Data, *Geophysics*, Vol.47, pp.31–37.

IMPACT OF WASTE DISPOSAL SITE ON GROUNDWATER QUALITY AT RAFIN-TOFA SOLID WASTE DUMPSITE, KAMPALA, NIGER STATE, NIGERIA

Atabo, S.I., Alhassan, U. D. and Rafiu, A. A.
Department of Geophysics, Federal University of Technology, Minna, Nigeria

Abstract

A massive solid waste dumpsite at the outskirt of Minna metropolis was investigated using 2D electrical resistivity imaging (ERI), with the aims of determining the impact of the dumpsite on groundwater quality. By visual observation of solid waste dumpsite, it is found that it consists of various constituents such as paper, organic matter, metals, glass, ceramics, plastics, textiles, dirt, and wood among others. Resistivity data were collected from parallel survey profile lines using a Wenner-Alpha array configuration. Inversion of the data was carried out using 2D regularized least-squares optimization methods with robust (L1-norm) model constraints. Potential zone of leachate infiltration into the subsurface from the dumpsite was identified from the electrical imaging. A synthetic resistivity inverse model was used to discuss and validate the field results. The 2D ERI sections of the model resolve clearly the subsurface lithological variations. Interpretation of the field data showed that 2D ERI technique was effective in delineating groundwater contaminated zones. The vertical and horizontal sensitivity of the 2D Wenner-Alpha array for sub- surface resistivity variations made it possible to determine the position and extent of leachate infiltration into groundwater. The current work demonstrates the usefulness of the ERI technique as a complementary tool for environmental site investigation.

Keywords: *2D, waste, dumpsite, resistivity, leachate, infiltration, Wenner-Alpha, groundwater*

Introduction

The Earth's surface which is the troposphere, sits at the interfaces of the solid lithosphere, the gaseous atmosphere, and the watery hydrosphere. Gases, liquids, and solids are exchanged between these spheres in three grand cycles. These cycles include the water or hydrological cycle, the rock cycle and the biogeochemical cycle. The Earth crust is also constantly being altered by geogenic and anthropogenic processes at extremely slow rates in human terms.

Geophysical principles have been used to unravel the dynamic nature of the earth (Rein hard, 2006). Various geophysical exploration methods have been and are used on land surface and beyond to solve a variety of subsurface detection problems (Ameh *et al.*, 2020). Each of these methods measures properties that are related to subsurface lithology and their geologic configurations (Gadallah & Fisher, 2009). The subsurface properties of the earth vary in diverse ways. These include; density, propagation velocity, magnetic susceptibility, electromagnetic wave reflectivity and transmissivity, self-potential, resistivity and induced polarization. These properties are measured using diverse formats. There are three basic ways in which the electrical current can be conducted within the earth, these includes Electrolytic, Ohmic and Dielectric conductions (Lowrie, 2007). In the electrolytic conduction (ionic conduction), the electrical current is propagated through the pores of the rocks or soil saturated with water, containing ions of minerals and dissolved salts. In the Ohmic conduction (electronic conduction), the electrical current is propagated via the crystalline structure of some materials in the rocks, mainly metals. Dielectric conduction has to do with the existence of an alternating electrical field which can cause ions in the structure of insulating materials to have a cyclic change in their positions. Geoelectrical properties are utilized in geophysics to exploit for materials in the subsurface which may be located by their anomalous electrical conductivities (Slater *et al.*, 2010). Resistivity method involves the introduction of

electrical current into the ground and the resultant measured potential differences at the surface give an indirect indication of the subsurface resistivity distribution.

Any material that is discarded after its primary use is termed waste. Society produces different types of waste; domestic waste, industrial wastes, mining wastes and radioactive wastes (Ranke, 2001). Liquid or solid wastes, hazardous or non-hazardous wastes infiltrating into groundwater can cause some chemical reactions which may produce substances dangerous to environment & health (Ige, 2013). In the last decade the study area has witness a major increase in waste disposal on uncontrolled disposal sites. Waste disposal is an expensive urban environmental problem. The degradation of water quality is undesirable irrespective of whether it results directly from leachate escaping from the landfill or from geogenic processes (Rowe, 2011; Amadi *et al*.,2017). Leachate is formed when rainwater and runoff percolate through solid waste, leaching out soluble salts and biodegraded organic products. Due to downward Darcy velocity and diffusion, contaminants will migrate from the landfill through soil into the groundwater system (Franz, 1993).

Study Description

This study site is located on the SE of Zungeru sheet 163 which is NW of Minna metropolis (Figure 1.5). It lies within latitude 9°40′22.0″North and 9°41′01.9″North and longitude 6°26′6.7″East and 6°25′53.2″East, it occupies a total area of about 5.3 km^2. The site is located along Maikunkele-Zungeru road. A portion of this site is already been utilized for engineered open waste dumpsites serving the Southwestern part of Minna city. On a general note, all the sites under study are at the outskirt of Minna metropolis with good road network which allow for easy access to the sites.

Topographically the dumpsite area is mostly flat lying, with moderately undulating ridges within the vicinity of Maikunkele urban sprawls of Minna (Figure 1.1). The altitude of the area is about 280 meters above sea level. All streams around the area drain into the River Chanchaga catchment basin. Most tributaries of the River Chanchaga are ephemeral and dry up during the zenith of dry season. The drainage system of the study area is structurally controlled. The drainage pattern of the study area is characterized as dendritic in nature.

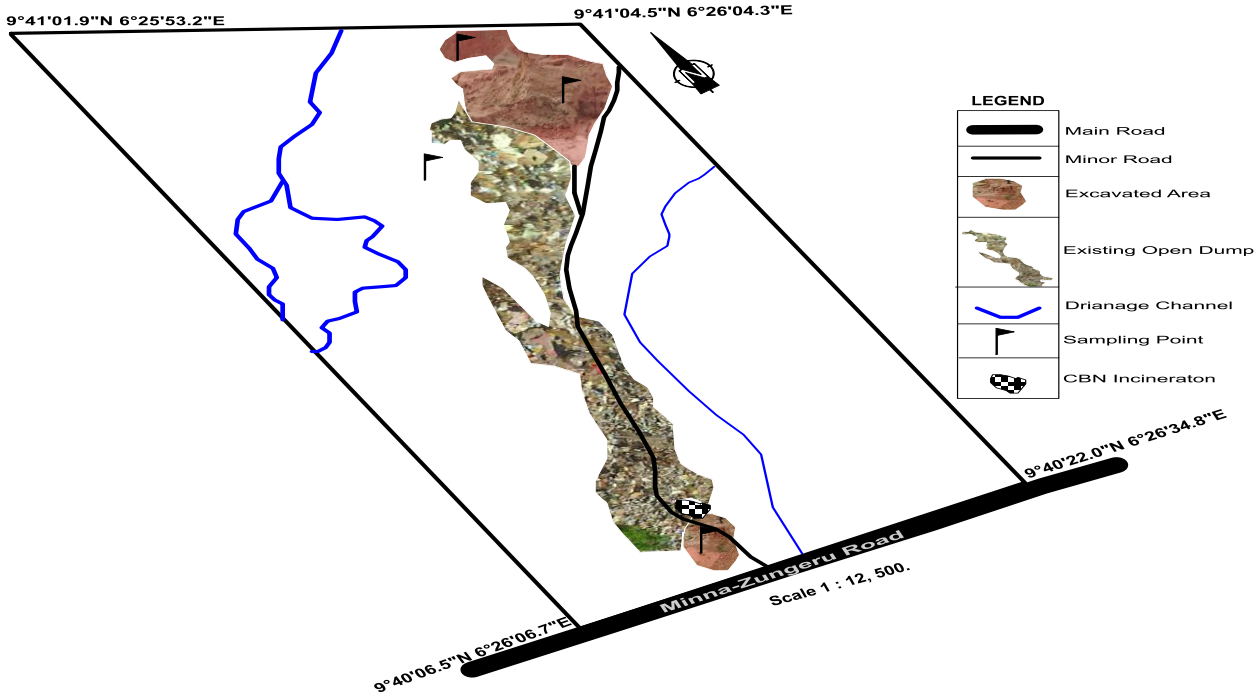

Figure 1.1: Study Area Location

Materials and Method

2D Electrical Resistivity Imaging (ERI) survey using a Wenner-Alpha array as outlined by Loke (1999) was conducted along six parallel profiles within the vicinity of the dumpsite. The selection of the ERI locations was dependent on the availability of areas free of heap of waste as an obstacle. When the conditions to enable the electrodes penetrate the natural soil was allowed, the roll-along technique was applied for getting continuous profile. The apparent resistivity measurements were acquired using ABEM SAS 4000 Terameter equipment. A pre-defined sequence of combinations of four stainless steel electrodes with current electrodes ($C_1 and\ C_2$) and potential electrodes ($P_1 and\ P_2$) for different electrode spacing (a) and data acquisition levels (n) was adopted.

The profile length (L) of the electrical cable spread was restricted 100m with a total of 21 electrodes on a profile line. At the initial series of measurement transverse the spacing in the middle of nearby electrodes (a) at 1a was set at 5m. For the initial measurement, electrodes numerals 1, 2, 3 and 4 represents C_1, P_1, P_2 and C_2. For the following measurement, numbers electrodes 2, 3, 4, and 5 represents C_1, P_1, P_2 and C_2 in that order. This arrangement was sustained till electrodes numbers 18, 19, 20 and 21 represents C_1, P_1, P_2 and C_2 in turn. Eighteen mid-points were established for the first measurement sequence. The entire measurement technique was replicated for 2a, 3a, 4a, 5a, 6a etcetera. Beginning at the first series of measurement 1a, a total number of 18 mid-points were established, and the mid-point decreases by three in successively sequences measured. For a profile of 100m, at 2a, mid-points =15, at 3a=12, 4a =9, 5a=6 and 6a=3 (Figure 1.2). The subsurface resistivity values acquired are arranged in apparent resistivity pseudo-sections which give a qualitative approximation of the subsurface resistivity distribution. An inversion procedure using the RES2DINV software ver. 3.71 (Loke, 2012) was used to generate 2D ERI sections from the apparent resistivity data. RES2DINV uses finite difference method based on the regularized least squares optimization procedure to produce a true 2D synthetic resistivity model is designed to discuss and validate the interpretation of the field data. The software iteratively determines the model blocks (Figure 1.3) resistivity that will closely produce the measured apparent resistivity data (Loke, 1997).

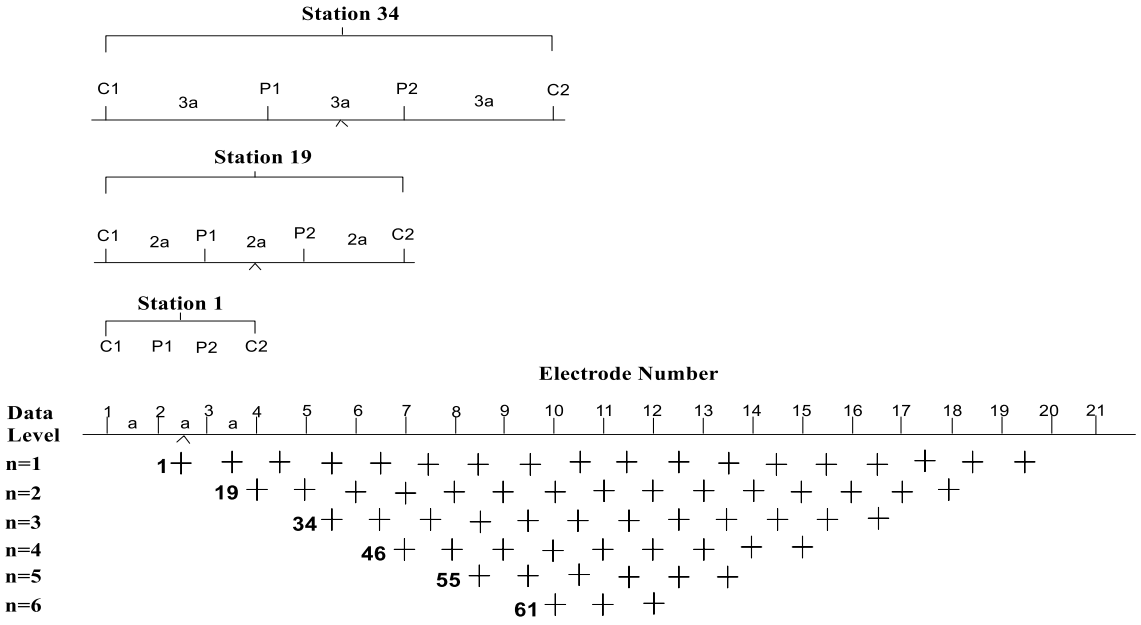

Figure 1.2 Sequence of 2D Wenner resistivity measurement to build a pseudosection (After Loke, 1999).

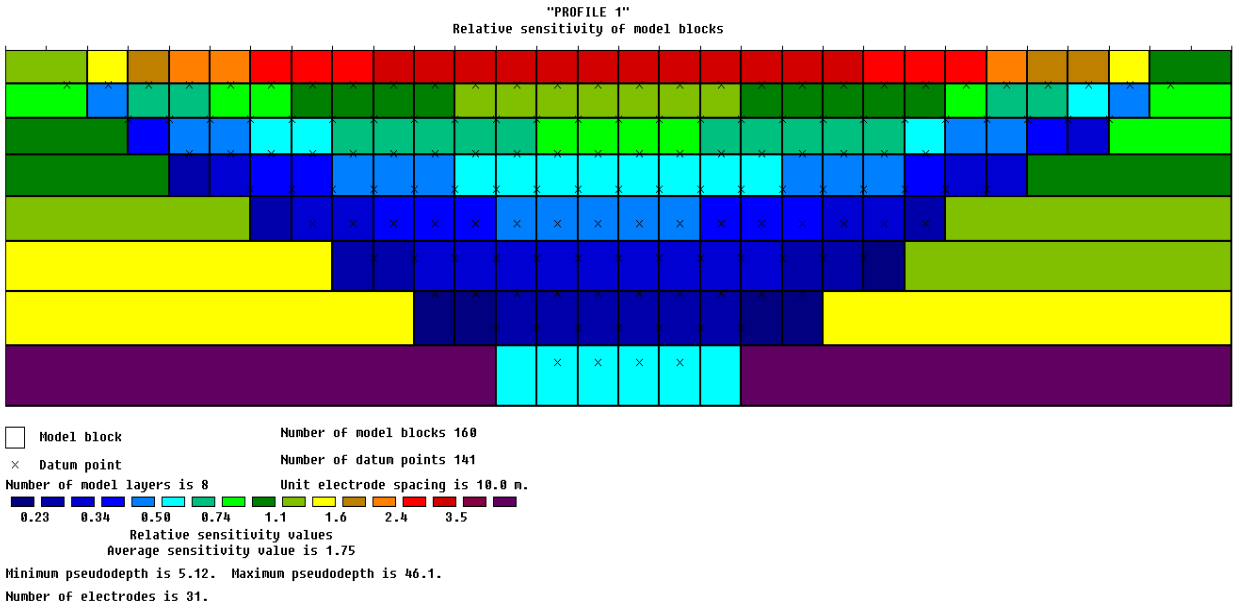

Figure 1.3: Relative sensitivity of the apparent resistivity model block

Results and Discussion

The 2D Earth resistivity imaging obtained along profile 01 is shown in Figure 1.4. The inverse model of this profile shows a clear disparity between low, moderate and large conductive zone within the subsurface. From the surface to about 6 m depth on the profile, the resistivity response is of a moderate range between 13 ohm-m to 41 ohm-m. This is interpreted as unpolluted lateritic soil with a minimal leachate contamination zone observed at 65 m to 70 m on the surface profile distance to the depth of about 6 m. From 0.0 m to 40.0 m distance on the surface profile line, the profile is characterized by low resistivity value range of 2 ohm-m to about 8 ohm-m. This is interpreted as possible polluted zone due to leachate infiltration from the dumpsite. From about 45 m to 100 m on the profile, from the depth of 12.0 m to 19.8 m, the profile is characterized with high resistivity value range of about 70 ohm-m to above 131 ohm-m. This zone is interpreted as unsaturated and unpolluted fresh basement rock.

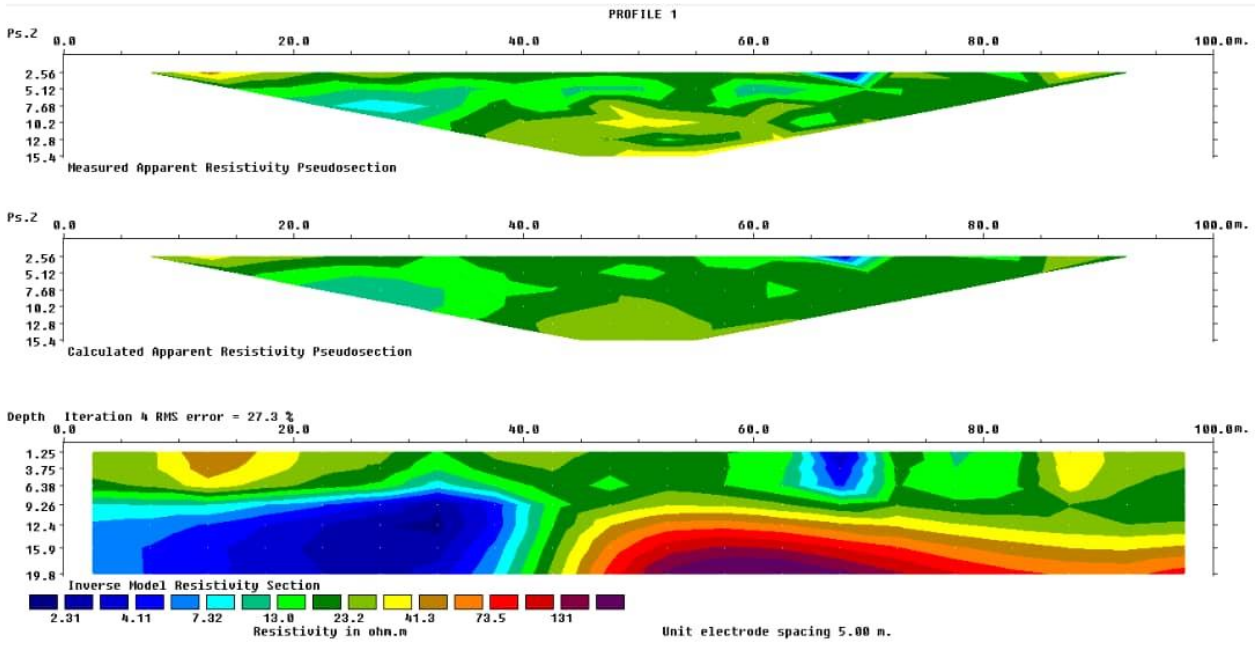

Figure 1.4: 2D Inverse ERI Plot for Profile 01

A more resistive zone representing the fresh basement rock zone with unsaturated waste underlain a much conductive leachate saturated top layer (Figure 1.5). Unfractured basement rock are often less infiltrated due to the competent nature of the materials that defined the rock. Irrespective of the disposal of a range of waste types with differing resistivity were at the site, the 2D ERT model shows relatively little variation within the area of the landfill. It is likely that this may be due to mixing of leachate within the landfill, which has led to the homogenization of saturated waste resistivity.

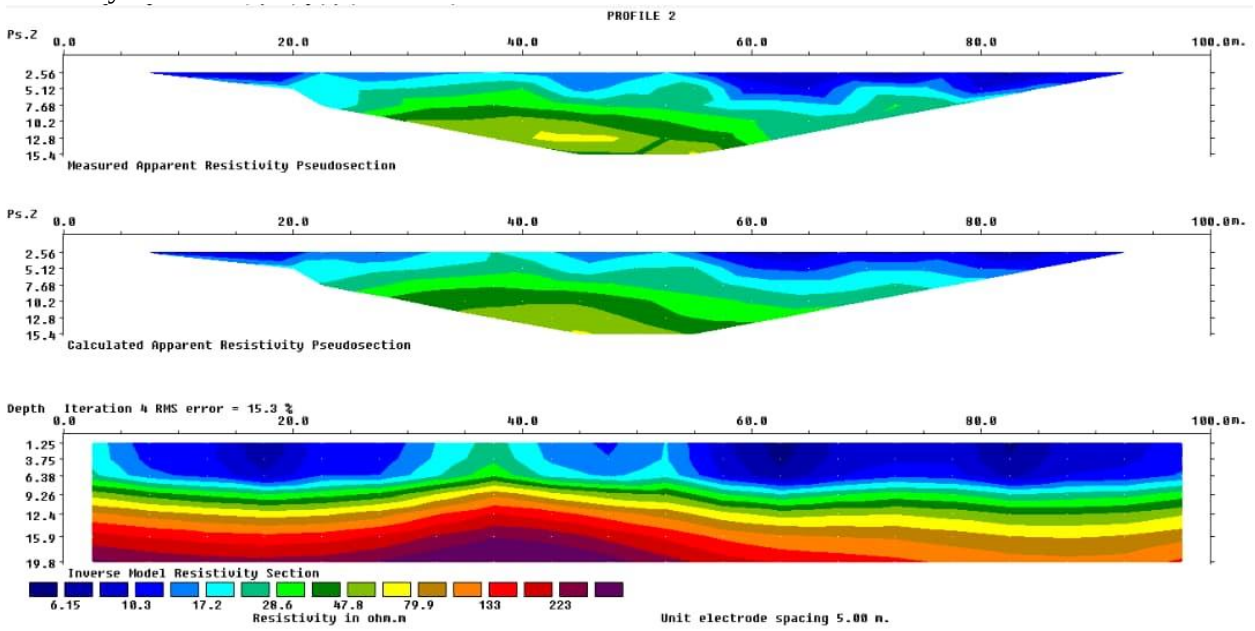

Figure 1.5: 2D Inverse ERI Plot for Profile 02

The model reveals homogenous low electrical resistive zone (< 8.0 Ohm-m to 17.8 Ohm-m) at depth ranging from 1.25-19.8 m across the model (Figure 1.6). This reflects a leachate infested shallow subsurface. From the depth of 12.4 m - 19.8 m across the profile the moderately high resistivity response (87.9 Ohm-m to >131.0 Ohm-m) of this zone on the profile is observed reflects an unsaturated subsurface lithology. It is evident that this area is free from leachate contaminations.

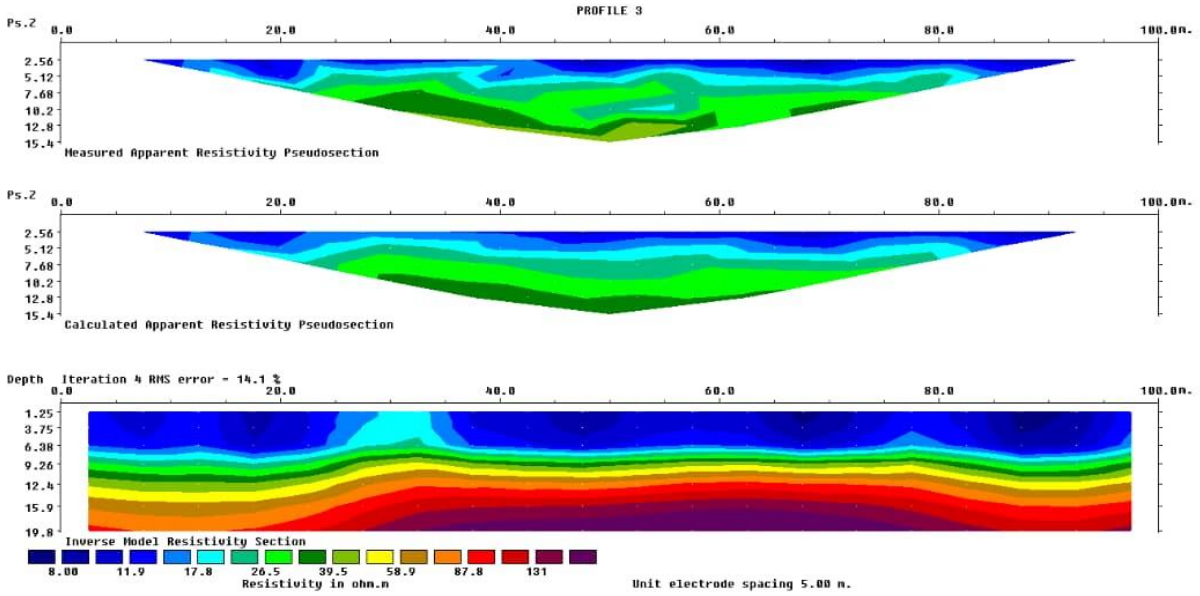

Figure 1.6: 2D Inverse ERI Plot for Profile 03

The ERI generally shows lower resistivity zones from about 6 m to 16 m depth of the profile (Figure 1.7). This area on the profile is characterized with low resistivity value range of less than 4 ohm-m to about 15 ohm-m indicating that this zone is highly conductive. The zones of low resistivity as expressed in the middle layer extend to both end sections of the profile; this zone is identified as anomalous zone with the greatest potential for association with leachate infiltration. The shallowest exposed bedrock is found around 25 m to 40 m, 50 m to 55 m and 85 m to 90 m on the surface of the profile, with resistivity values ranging between 88 ohm-m to above 204 ohm-m. This layer represents weathered to moderately weathered basement rock, as observed on the surface.

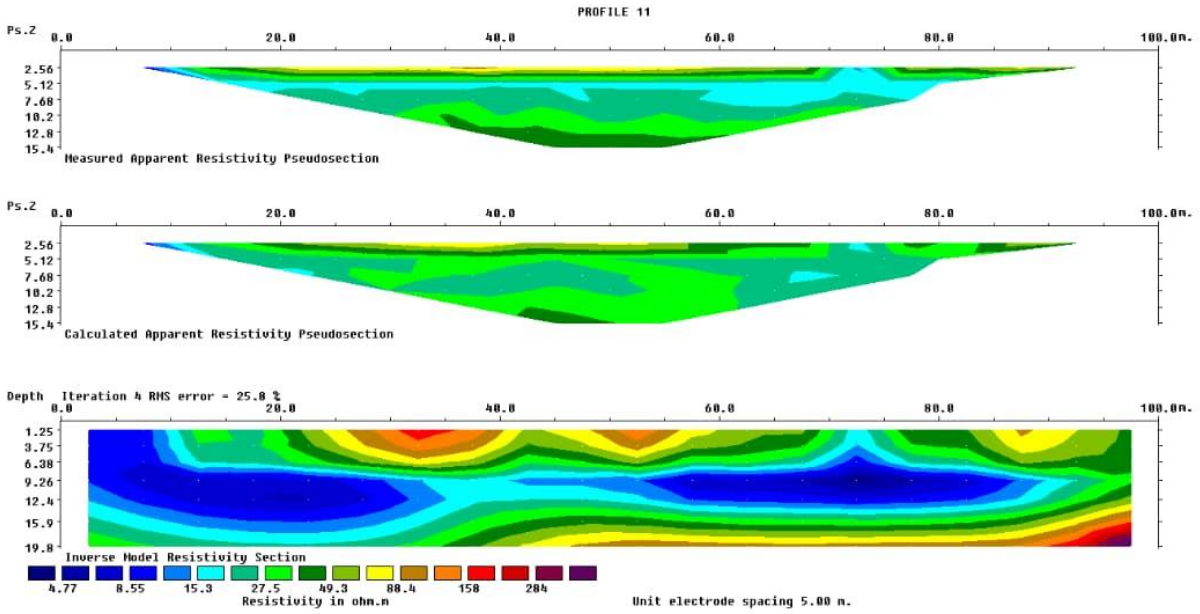

Figure 1.7: 2D Inverse ERI Plot for Profile 04

Conclusion

Electrical resistivity imaging surveys have been undertaken at an un-engineered waste dumpsite. Data from these surveys have been modeled using 2D inversion algorithms. By visual observation of the solid waste dumpsite, it is found that it consists of various constituents such as paper, organic matter, metals, glass, ceramics, plastics, textiles, dirt, and wood among others. The ERI results provide 2D subsurface images with good spatial resolution along the survey profile. From the interpretation of the 2D inverse models, it was established that low resistivity zones below the waste dumpsite are indicative of leachate migration into the groundwater that is contained in the bedrock. The disposal of waste on the dumpsite is a potential threat to the contamination and pollution of groundwater resources within the vicinity of the dumpsite and beyond.

Reference

Amadi, A. N., Olasehinde, P. I., Obaje, N.O., Unuevho, C.I., Yunusa, M.B., Keke, U., & Ameh, I. M. (2017). Investigating the Quality of Groundwater from Hand-dug Wells in Lapai, Niger State, North-central Nigeria using Physico-chemical and Bacteriological Parameters. *Minna Journal of Geoscience*, 1(1), 77 – 92.

Ameh, I. M. Amadi, A. N. Unuevho, C. I. and Ejepu, J. S. (2020). Hydrogeophysical Investigation of Groundwater Systems in Otukpo, Benue State, North-Central Nigeria. J. Chem. Soc. Nigeria, Vol. 45, No.5, pp 897 – 905.

Franz, T. (1993). Hydrogeological computer model used in evaluating contaminant transport. Geotechnical News, 11(4), pp. 50-52

Gadallah, M.R. and Fisher, R. (2009). *Exploration Geophysics*. Springer-Verlag Berlin Heidelberg.

Ige, O. O. (2013). Geological and Geotechnical Evaluation of an Open Landfill for Sanitary Landfill Construction in Ilorin, South-western Nigeria. *Journal of Environment and Earth Science*, 3 (3), 9-17.

Loke, M. H. (1997). Res2DINV software user's manual. *University Sains Malaysia, Penang*.

Loke, M. H. (1999). Electrical imaging survey for environmental and engineering studies. (A practical guide to 2-D and 3-D surveys). Retrieved from http://www.abem.se/files/res/2dnotes.pdf.

Loke, M. H. (2012). Res2dinv ver. 3.71: Rapid 2-d resistivity & ip inversion using the least-squares method. geotomo software.

Lowrie, W. (2007). Fundamentals of Geophysics (Second Edition). Cambridge University Press, New York.

Ranke, H. G. (2001). Appropriate Design and Operation of Sanitary Landfill in Sustainable Economic Development and Sound Resource Management in Central Asia. Proceedings of an International Conference, Nottingham, United Kingdom.

Rein hard, K. (2006). *Groundwater Geophysics*. Springer-Verlag Berlin Heidelberg Press London, 92.

Slater, L. D., Ntarlagiannis, D., Day-Lewis, F. D., Mwakanyamale, K.., Versteeg, R. J., Ward, A., Strickland, C., Johnson, C. D., & Lane Jr., J.W. (2010). Use of electrical imaging and distributed temperature sensing methods to characterize surface water-groundwater exchange regulating uranium transport at the Hanford 300 Area, Washington: *Water Resources Research*, 46 (10).

INVESTIGATION OF THE EFFECT OF HIGH CONCENTRATION OF RADIOACTIVE ELEMENTS ON GEOTHERMAL PARAMETERS WITHIN PARTS OF KADUNA AND PLATEAU STATE, NIGERIA

John K. Moses, Adetona A. Abbass, Mufutau O. Jimoh, Aliyu B. Shakirat
Department of Physics, Federal University of Technology Minna, Niger State.
Email: kanamoses12@gmail.com, a.abbass@futminna.edu.ng, mo.jimoh@futminna.edu.ng, shakirat@futminna.edu.ng

Abstract
The study focuses on both quantitative and qualitative analysis of high resolution aeromagnetic data for the determination of geothermal parameters within Naraguta and Maijuju, Plateau State. The result is correlated with the analysis of radiometry concentration data of the study area. The study area covers a total of 6,050 km^2. Two aeromagnetic data sheets were used which cover the major towns Naraguta and Maijuju. The study area is bounded by latitude 9°30' to 10°00' and longitude 8°30' to 9°30'. The aeromagnetic data was divided into sixteen blocks. Each of the blocks was subjected to Fast Fourier Transform analysis and then spectral analysis to determine the Curie depth within the study area. The modified Curie depth method was then used in evaluating the geothermal parameters. The region was found to have a shallow Curie point depth of 2km which occurs at Western and Southern edge of the study area. The heat flow of the study areas has values ranging from 20 to 305 mW/m^2 with an average heat flow of 111.00 mW/m^2. The regions with anomalous high heat flow ranging from 110 to 305 mW/m^2 was obtained around Bowon Dodo, Dan Tsofo, Kadunu, Gimi, Kaura and Zankan of the study areas. The geothermal gradients also has a value ranging from 5 to 125 °C/Km with an average of 44.40 °C/Km. Correlating this result with analysis of the radiometric data, regions of high radioelement concentration did not correspond to region of high heat flow as expected. The high concentration of uranium, thorium and potassium measured within the study area must have arisen from the weathered in-situ basement rocks that give rise to the high geothermal gradient.

Key words: Curie point depth, heat flow, geothermal gradient, radiometric data.

Introduction

Geothermal energy is natural energy generated and stored in the Earth. Earth's geothermal energy originates from the formation of the planet, radioactive disintegration of minerals, volcanic activity and solar energy absorbed at the surface.

The study of subsurface temperature, geothermal gradients and heat flow in association to the curie-point depth (CPD) is crucial in understanding the thermal maturation of sediments and the past thermal regimes in a basin. CPD estimation have been published for various tectonic settings by several authors such as Tanaka *et al*., (1999); Nuri *et al*., (2005); Trifonova *et al*., (2009); Okobo *et al*., (1985); Raj *et al*., (2020); Adetona *et al*., (2017); Maden (2010).

The CPD is known as the depth at which the dominant magnetic mineral in the crust passes from a ferromagnetic state to a paramagnetic state under the effect of increasing temperature (Nagata 1961). Shallower CPD usually corresponds to higher heat flow in a given region. The Curie temperature of titano-magnetite which is the magnetic mineral that is very common in igneous rocks is within the range of a few hundreds to 580 °C. It is expected that geothermically active areas would be associated with shallow Curie point depth (Nuri *et al.*, 2005). The geothermal gradient which is the difference in temperature between the core of the planet and its surface drives a continuous conduction of thermal energy in the form of heat from the core to the surface and is about is about 1 °C km^{-1} on average (Lowrie W, 1997).

In thermally normal continental regions, the average heat flow is about 60 mWm$^{-2.}$ Values between 80-100 mWm^{-2} are good geothermal source, while values greater than 100 mWm^{-2} indicate

anomalous conditions (Cull and Conley, 1983; Jessop *et al.*, 1976). This research analyses an aeromagnetic data using spectral analysis. The result from the heat flow and geothermal gradient is then correlated with the Ternary map from the analysis of the radiometric data of the concentration of uranium, thorium and potassium.

Location of the study area

Naraguta sheet area comprises the following towns; Jos, Bukuru, Vom, Barkin Ladi, Rukuba, Foron, Miango, Kigom, Ganawuri located in Plateau state, North Central Nigeria. It is bounded by longitude 8°30′ to 9°00′ and latitude 9°30′ to 10°00′and covering an area of about 2970 sqkm. The study area has high relief features with elevation range between 1800 m to 5300 m above sea level. Maijuju lie between longitude 9º 00′ E to 9º 30′ E and latitude 9^0 30′ N to 10^0 00′ N. The study area covers approximately 2970 km^2 and covers Jarawa, shere, shona, jimjim, Wai, bijim, Gohzi, Lere, Girim, Langai, Maijuja, Fedaki, Maigemu, Gora and accessible through road and several footpath and river channel connect to the study area. It is shown in Figure 1.

Geology of the study area

The Jos-Plateau owes its preservation largely to the close concentration of resistant Younger Granites and Older, and indeed almost all the upland areas coincide with outcrops of one of these two rocks (Macleod *et al.*, 1971). The Jos-Plateau is dominated by three rock types: Basement Rocks, Younger Granite Rocks and Basalts or Basaltic Rocks. The study area is an area of Younger Granite Complexes, forming distinctive groups of intrusive and volcanic rocks bounded by ring dykes or faults (Macleod *et al*., 1971). Volcanic activities which occurred several years ago, created vast basaltic plateau and volcanoes, producing regions of mainly narrow and deep valleys, and sediments from the middle of rounded hills with shear facies. Other rocks found in the area are Basic rocks (Gabbro and Dolerite) and Basement rocks such as Migmatite which are resistant to erosion. Figure 2 is the geological map of Naraguta(sheet 168) and Maijuju(sheet 169) respectievly. The most common mineral in the area is Cassiterite. Other minerals in the area include columbite, wolfram, pyrochlore, fergosonite, thorite, zircon, monazite, xenotime, beryllium minerals, molybdenite, cryolite and other minor minerals such as topaz, gelana, pyrite, arsenopyrite, bismuthinite, and chalcopyrite.

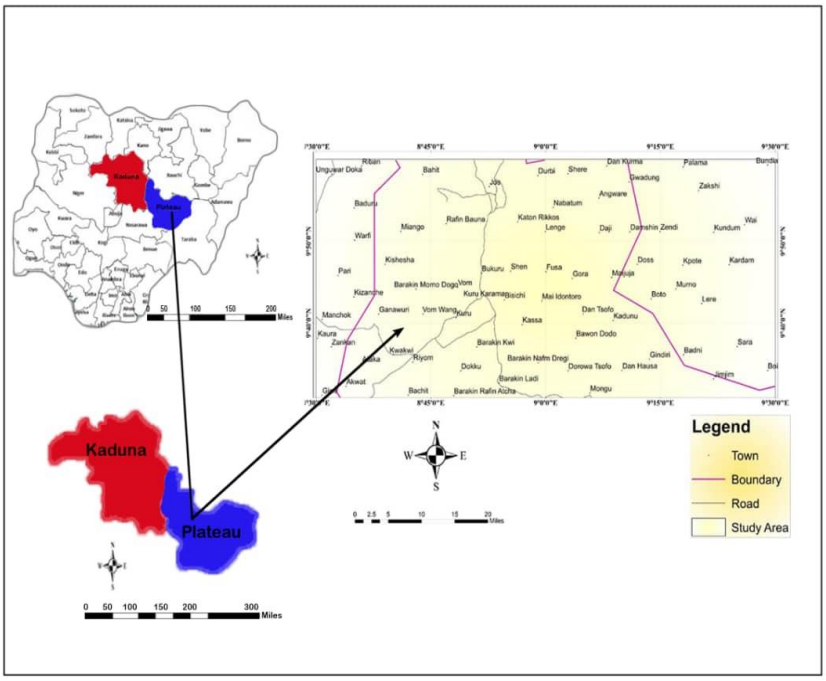

Figure 1: Location map projected from the administrative map of Nigeria.

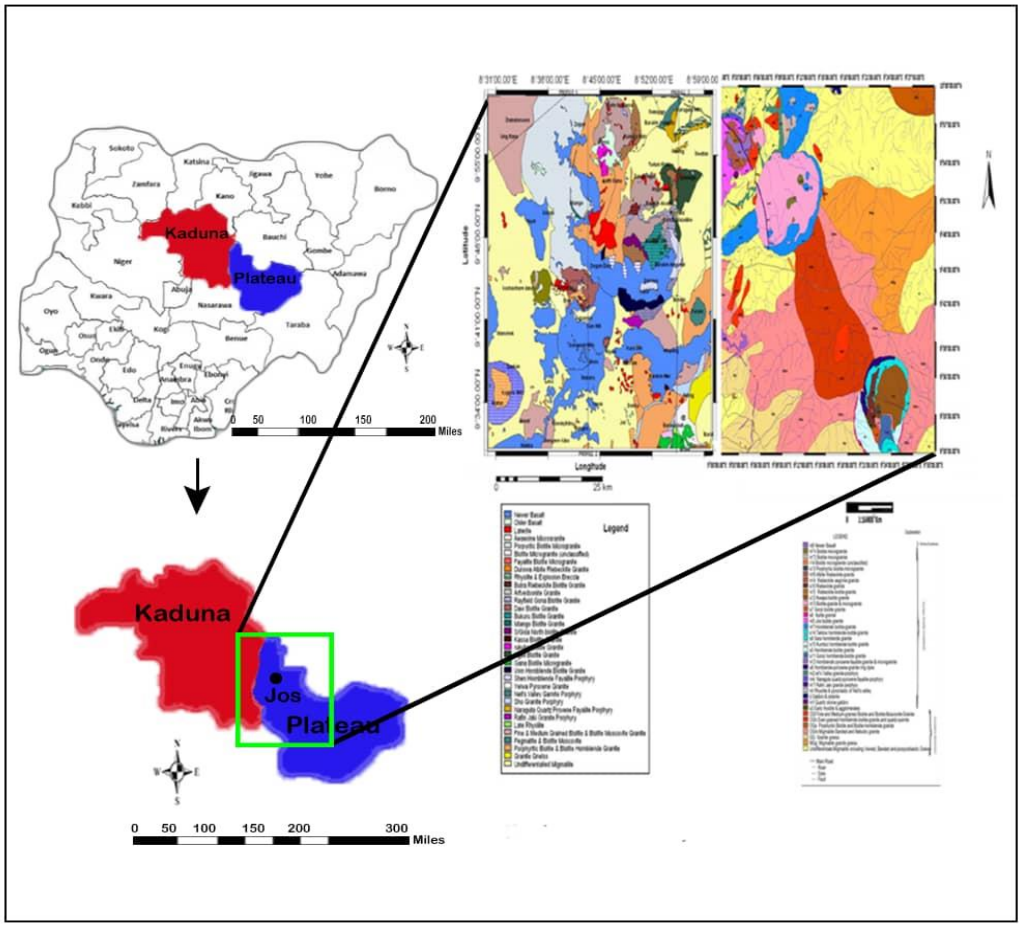

Figure 2: Geological map of the study area; Naraguta sheet 168 and Maijuju Sheet 169 (Adapted from NGSA, 2009).

Methodology

The method used to estimate Curie point depth is based on the spectral analysis of magnetic anomaly data. The basic 2-D spectral analysis method was described by Spector, and Grant **(**1970). They estimated the depth to the top of magnetized rectangular prisms (Z_t) from the slope of the log power spectrum. Bhattacharyya and Leu (1975a, 1975b, and 1977) further calculated the depth of the centroid of the magnetic source bodies (Z_0). Okubo *et al.* (1985) developed the method to estimate the bottom depth of the magnetic bodies ((Z_b) using the spectral analysis method of Spector and Grant **(**1970). Following the method presented by Tanaka *et al.* (1999), it was assumed that the layer extends infinitely in all horizontal directions. The depth to a magnetic source's upper bound is much smaller than the magnetic source's horizontal scale, and the magnetisation M(x, y) is a random function of x and y (Blakely, 1995) introduced the power-density spectra of the total-field anomaly $\rho_{\nabla T}$

$$\rho_{AT}|\mathrm{k}| = \boldsymbol{A}e^{-2|\mathrm{k}|Z_t}\left(\left[1 - e^{-|\mathrm{k}|(Z_b - Z_t)}\right]^2\right) \quad (1)$$

K is wave number and

A is a constant, if k is less than the thickness of layer we can approximate to

$$ln\rho_{AT}\left(|\mathrm{K}|^{\frac{1}{2}}\right) = ln\boldsymbol{B} - |\mathrm{K}|Z_t \quad (2)$$

B is a constant.

From the slope of the power spectrum, the upper bound and the centroid of a magnetic body can be estimated. The lower bound of the magnetic source can be derived (Okubo *et al.*, 1985) and (Tanaka *et al.*, 1999) as

$$Z_b = 2Z_0 - Z_t \quad (3)$$

Z_b is the Curie point depth, ferromagnetic minerals are converted to paramagnetic minerals due to temperature of approximately 580℃.
Summarily, the depth to the base of the magnetic source (the Curie point depth) is calculated in four procedures (Tanaka et al., 1999) as follows:

1. Calculate the radially averaged power spectrum of the magnetic data in each window;
2. Estimate the depth to the top of the magnetic source (Z_t) using the high wave number portion of the magnetic anomaly power spectra;
3. Estimate the depth to the centroid of the magnetic source (Z_0) using a lower wave number portion of the magnetic anomaly power spectra
4. Calculate the depth to the base of the magnetic source (Z_b) using $Z_b = 2Z_0 - Z_t$ The value of Z_b is the Curie point depth/DBMS.

Also the heat flow of the study area which has an assumption that the direction of the temperature variation is vertical and the temperature gradient $\frac{\Delta T}{\Delta Z}$ is constant; Fourier's law takes the form:

$$q = -k\frac{\Delta T}{\Delta Z} \quad (4)$$

where, q is heat flow and k is thermal conductivity. The Curie temperature can also be defined as:

$$\Theta^0 C = \left(\frac{\Delta T}{\Delta Z}\right) Z_b \quad (5)$$

$$q = k\left(\frac{\theta ℃}{Z_b}\right) \quad (6)$$

Geothermal gradient ($\frac{\Delta T}{\Delta Z}$) of the study area was further estimated using curie point temperature of 580°C and thermal conductivity of 2.5 $Wm^{-1}°C^{-1}$ which is the average thermal conductivity for igneous rocks is used in the study as standard (Nwankwo et al., 2009).

$$\frac{\Delta T}{\Delta Z} = \frac{580℃}{Z_b} \quad (7)$$

Radiometric data processing

Radiometric heat production (H) is related to the decay of primarily, the radioactive isotopes 232Th, 238U and 40K and can be estimated based on the concentration (C) of the respective elements through the expression;

$$H(\mu W/m^3) = p\,(9.52C_U + 2.56\,C_{Th} + 3.48C_K)\,10^{-5} \quad (8)$$

Where;

H= radioactive heat production

P= density of rock adapted from (Telford et al., 1990). C_U, C_{Th}, C_K are concentrations of uranium, thorium and potassium respectively. The concentration of the three radiometric elements is read from the radiometric map covering the study area.

Results and interpretation

The result from the Total magnetic intensity- reduce to equator map shows that the Biotite Granite at the almost mid portion of the study area shows low susceptibility ranging from -138.9 to -70.0 nT which might be as a result of overlying sedimentation of Porphyry Quartz Prophry. The Migmatitic Gneisis, and porphyritic granite situated at the Northern, Eastern and Western edge of the study area shows appreciable high susceptibility ranging from 69.3 to 102.4 nT as a result of intrusive activities associated with the listed granite rocks as shown in Figure 3.

The total magnetic intensity data of the study area was divided into 16 square overlapping blocks each of an area of 22.5 km^2. The fast Fourier transform was performed on each section using oasis montaj and the data was extracted using Microsoft Excel. A plot of graph of energy against wave number in cycle/km for each window was done. A straight line is then fit to the energy spectrum both for the higher and lower portion in an effort to determine the slope as well as determine the depth to the bottom and top of the magnetic source. This implies that the depth to the top and bottom of magnetic source was evaluated for every window 22.5 km^2 apart. Figure 4 shows sample graph of the logarithms of spectral energies for the Blocks of the study area. The derived values of the depth to top and bottom of the magnetic source were used in the estimation of the Curie-point depth, heat flow and the geothermal gradient of the study area using equation 9 – 12. The result of the determined values of Z_o, Z_t and Z_b for the sixteen blocks are shown in Table 1.

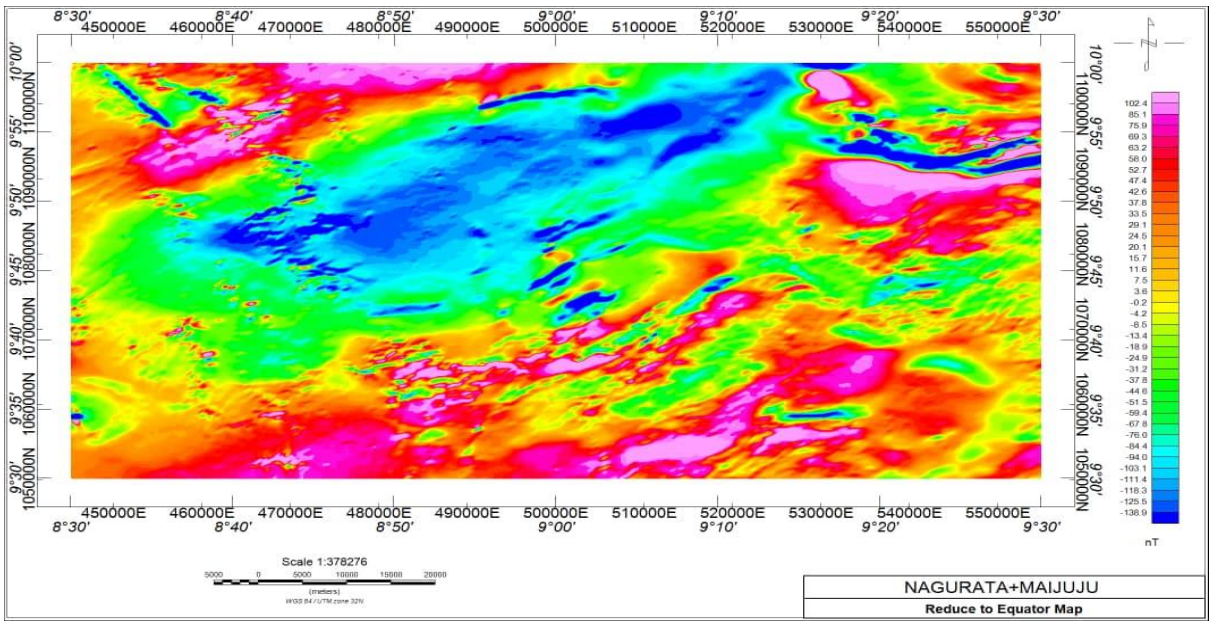

Figure 3: TMI Reduce to Equator Map (RTE) of Naraguta and Maijuju

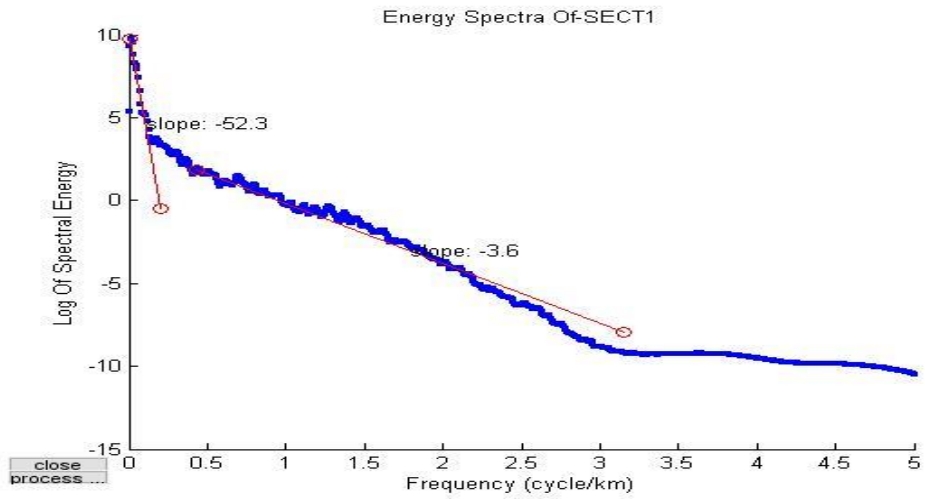

Figure 4: The matlab plot of the log of spectral energy against frequency.

The Curie point depth map of the study area is shown in the figure 5. The Curie depth varies from 2 km to 44 km. High depth up to 44 km where recorded at the northern part of the study area, descending to 2 km at western and south eastern edge of the study area. The prominent areas which recorded high depth is situated at the North Eastern edge of the study area corresponding to Durbi, Shere, Nabatum, Daji and Katon Rikkos towns respectively. Also, shallow Curie point depths were observed at the western edge and south eastern edge. These regions correspond to Pari, Manchok, Ataka, Gimi, Mongu, Kadunu and Jimjim town respectively.

The heat flow map figure 6 depicts that heat flow varies from 20 mW/m^2 to 305 mW/m^2. High anomalous heat flow ranging from 110 mW/m^2 to 305 mW/m^2 is recorded in the study area. The most prominent high heat flow is situated at South Eastern and Western edge of the study area. These regions correspond to Bawon Dodo, Gimi and Kaura town, and this might occur as a result of high Uranium concentration which was observed on composite map of Figure 7. While the lowest heat flow were observed at the North Eastern edge of the study area corresponding to Durbi, Shere, Dan kurma and Angware towns respectively. The geothermal gradient map in figure 4.6 shows the variation of temperature with increase in depth. The geothermal gradient varies from $5\,℃/Km$ to $125\,℃/Km$ with an average value of $44.40\,℃/Km$. High anomalous geothermal gradient up to $125\,℃/Km$ was observed in the study area. The regions with high geothermal gradient are situated at Southern and Western edge of the study area. These regions correspond to Bawon Dodo, Gimi and Kaura town, and this may have occur as a result of high Uranium concentration which was observed on composite map in Figure 7. While the lowest geothermal gradient were observed at the North central and Eastern edge of the study area corresponding to Durbi, Shere, Dan kurma and Angware towns respectively.

Table 1: Estimated values of the Curie point depth, geothermal gradient and heat flow

S/N	LON °E	LAT °N	Grad 1	Grad 2	Depth to Centroid Z_0 (km)	Depth to top Zt (Km)	Curie Point Depth Z_b(km)	Geothermal Gradient (°C/km)	Heat Flow mW/m^2
1	8.62	9.875	52.3	3.6	4.16136	0.2864	8.0362	72.17267	180.431
2	8.87	9.875	159	4.42	12.6511	0.3516	24.9506	23.24587	58.114
3	9.12	9.875	266	5.75	21.1648	0.4575	41.8722	13.85166	34.629
4	9.37	9.875	127	2.95	10.1050	0.2347	19.9753	29.03580	72.589
5	8.62	9.625	41.3	2.17	3.28612	0.1726	6.3995	90.63085	226.577
6	8.87	9.625	132	2.41	10.5028	0.1917	20.8139	27.86589	69.664
7	9.12	9.625	30.1	2.41	2.3949	0.1917	4.5981	126.13670	315.341
8	9.37	9.625	91.4	4.72	7.2724	0.3755	14.1693	40.93351	102.333
9	8.75	9.875	124	1.37	9.8663	0.1090	19.6236	29.55617	73.890
10	9.25	9.875	251	5.29	19.9713	0.4209	39.5218	14.67544	36.688
11	8.75	9.625	115	2.31	9.1502	0.1838	18.1166	32.01475	80.036
12	9.25	9.625	122	2.9	9.70719	0.2307	19.1836	30.23409	75.585
13	8.75	9.75	153	3.85	12.1737	0.3063	24.0412	24.12523	60.313
14	9	9.75	156	4.66	12.4124	0.3707	24.4541	23.71783	59.294
15	9.25	9.75	53.4	4.33	4.2488	0.3445	8.15324	71.13730	177.843
16	9	9.75	61.8	4.27	4.9172	0.3397	9.4947	61.08639	152.716

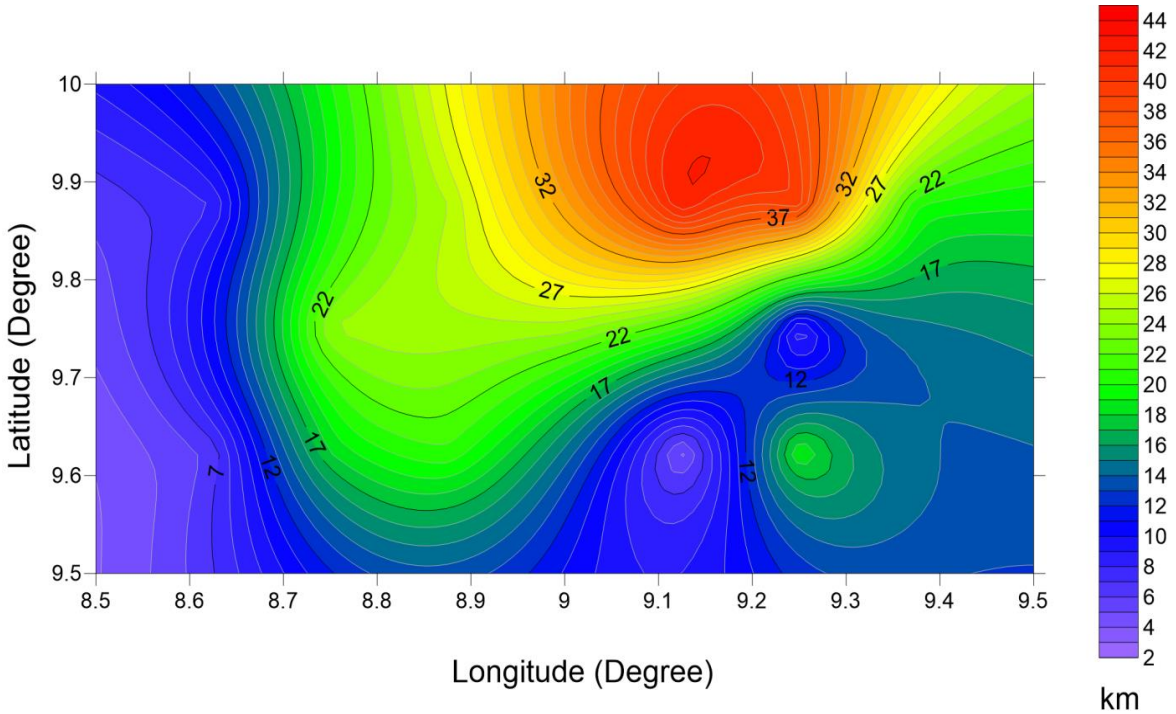

Figure 5: Curie point depth contour map of Naraguta and Maijuju

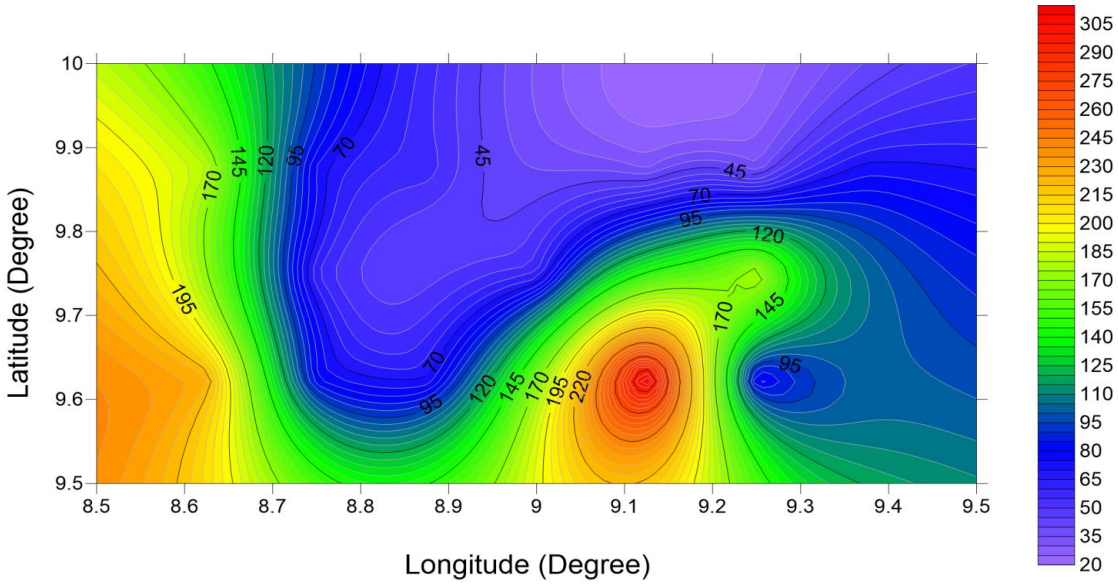

Figure 6: Heat flow contour map of Naraguta and Maijuju

The correlation of ternary map and geothermal gradient

The Ternary map is also known as the composite map. This map was produced by combination of the three concentration maps namely; potassium, uranium and thorium maps representing red, blue and green coloration respectively. It revealed the slight variations in their relative concentration. In Figure 7, the white regions in the composite map are indications of strong contents in potassium, uranium and thorium. The cyanide indicates strong content in thorium and uranium but weak potassium content. It is also observed that regions containing Granite and Biotite show red coloration indicating strong content in potassium but weak in uranium and thorium. While the blue and dark blue regions marked within the study areas depicts strong content in uranium and it is located at the south east, south west and north western edge of the study area.

The regions depicting strong content in Uranium correspond to where high heat flow and geothermal gradient were situated.

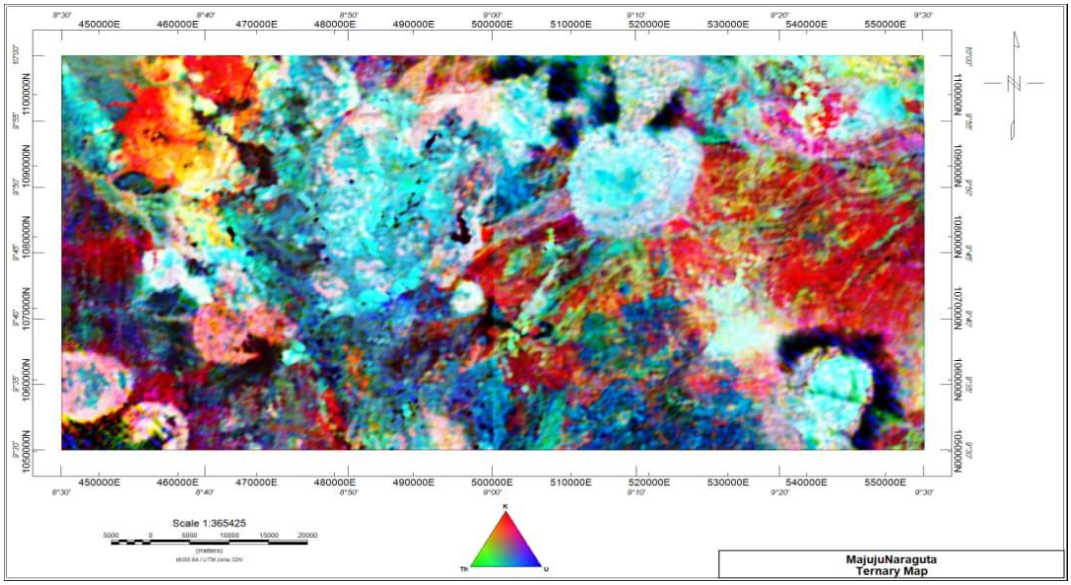

Figure 7: Ternary map of the study area

Conclusion

Curie-point depth contour map of the study area shows a range depth of 2 km to 44 km. High depth up to 44 km were recorded at the northern part of the study area, descending to 2 km at western and south eastern edge of the study area. Anomalous heat flow obtained within this study area ranges from 110 to 305 mW/m^2. This region also corresponds to the shallowest Curie point depths range of 2 to 7 km. The most prominent high heat flow is situated at South Eastern and Western edge of the study area. These regions correspond to Pari, Manchok, Ataka, Gimi, Mongu, Kadunu, Dorowa Tsofo and Bawon Dodo towns. The towns with 80 to 100 mW/m^2 which are considered moderate for geothermal energy exploration were recorded at Vom,Wai, Kardam, Rafin Bauna, Badni, Boi, Mumo, Barkin Kwi, Kuru, Lere, Bundia, and Bukuru.

Also, a correlation of delineated geothermal parameters and concentration of radionuclides across the study area can be clearly established. The result of the heat flow does not conform when correlated to the result of the Ternary map. Spots where high concentrations of the three radioelements were observed are Daji, Badni and Jimjim. They are dominated with the following rock types that host the radioelements; Prophyry Quartz prophry and Migmatic Gneisis. These areas are not where the high heat flow and high geothermal gradient are obtained as expected. The high concentration of radio nuclei elements are measurement at the shallow depth, since gamma rays penetration through materials (rocks and air) are usually below 1 m (0-0.5 m) (Alistaiv *et al*., 2014). This can be explained from the history of the study area known for mining of Tin, columbite and gold for a very long time in the early 50s, 60s and 70s. The high concentration observed at this spots can be trace to human interference during mining and processing of mineral ores. But noteworthy is the fact that these minerals occur within the bedrock in situ which is where the high heat and geothermal emanates from (Lowrie, 2007).

CONFLICT OF INTERESTS

The authors have not declared any conflict of interests.

REFERENCES

Abraham, M. E., Lawal, K.M., Ahmed, L.A. (2014). Spectral analysis of aeromagnetic data for geothermal investigation of Wikki Warm Spring, north-east Nigeria. *Geothermics* 50: pp85–90.

Adetona, A. A., Salako, K. A., Rafiu A. A. (2017). Curie Depth and Geothermal Gradient from spectral analysis of aeromagnetic data over upper Anambra and lower Benue Basin, Nigeria**.** *Nigeria Journal of Technological Research (NJTR)* 12(2) pp 20-26 DOI:https://dx.doi.org/10.4314/njtr.v12i2.4

Alistair, T. M., Thomas., L. H., Paul., L. Y., David., C. W., Alan, J. C. (2014). Gamma-ray Spectrometry in Geothermal exploration: State of the Art Techniques. *Energies* 7: 4757–4780; doi: 10.3390/en7084757

Bansal, A. R., Gabriel, G., Dimri, V. P. and Krawczyk, C. M. (2011). Estimation of depth to the bottom of magnetic sources by a modified centroid method for fractal distribution of sources: An application to aeromagnetic data in Germany, *Geophysics*, 76(3), L11–L22, 10.1190/1.356001.

Bhattacharyya, B. K., and Leu, L. K. (1975a). Analysis of magnetic anomalies over Yellowstone Park: mapping of Curie point isothermal surface for geothermal reconnaissance. *Journal of Geophysical research* 80(32), 4461-4465

Bhattacharryya, B. K., and Leu, L. K. (1975b). Spectral analysis of gravity and Magnetic anomalies due two dimensional structures, *Geophysics*, Vol. 40, pp. 993-1031

Blakely, R. J. (1995). Potential theory in gravity and magnetic applications. Cambridge University Press, Cambridge

Cull, J. P., and Conley, D. (1983). Geothermal gradients and heat flow in Australian sedimentary basins. *Geoscience Australia, Canberra*. Record 8:4:329-337. http://pid.geoscience.gov.au/dataset/ga/81160

Jessop, A. M., Habart, M. A., Sclater, J. G. (1976). The world heat flow data collection 1975. Geothermal services of Canada. Geothermal Series 50:55-77.

Lowrie, W. (2007). Sources of heat in the Earth. In Lowrie, W (2nd ed.), *Fundamentals of Geophysics* (pp. 227). Cambridge, Cambridge University Press.

Macleod, W. N., Turner, D. C., Wright, E. P. (1971). The Geology of Jos Plateau, *Geological Survey of Nigeria*. Issue 32, Vol. 1-2.

Maden, N. (2010). Curie-point depth from spectral analysis of magnetic data in Erciyes stratovolcano (Central TURKEY). *Pure Applied Geophysphysics* 167:349–358.

Nagata, T. (1961). *Rock magnetism*. Tokyo, Maruzen Company Tokyo.

Nuri, D. M., Timur, U. Z., Mumtaz, H., Naci, O. (2005). Curie Point Depth variations to infer thermal structure of the crust at the African- Eurasian convergence zone, SW Turkey. *Journal of Earth planets Space*. 57: pp373-383

Nwankwo, L. I., Olasehinde, P. I., Akoshile, C. O. (2009). An attempt to estimate the Curie-point isotherm depths in the Nupe Basin, West Central Nigeria. Global Journal of Pure and Applied Science 15:427433.

Obaje, N. G. (2009). Geology and Mineral Resources of Nigeria, London: *Springer Dordrecht Heidelberg*, pp. 5-14.

Okubo, Y., Graff, R. G., Hansen, R. O., Ogawa, K., Tsu, H. (1985). Curie point depths of the Island of Kyushu and surrounding areas, *Geophysics*, Vol.53, 481–494.

Raj, K., Bansal, A., Abdolreza, G. (2020). Estimation of Depth to Bottom of Magnetic Sources Using Spectral Methods: Application on Iran's Aeromagnetic Data. *Journal of Geophysical Research: Solid Earth*, volume 125 issue3

Ross, H. E., Blakely, R. J., Zoback, M. D. (2006). Testing the use of aeromagnetic data for the determination of Curie depth in California: *Geophysics*, 71, no. 5, L51–L59, doi:10.1190/1.2335572.

Spector, A., and Grant, F. S. (1970). Statistical models for interpreting aeromagnetic data, *Geophysics*. Vol.35, pp. 293- 302.

Tanaka, A. Y., Okubo, Y., Matsubayashi, O. (1999). Curie point depth based on spectrum analysis of the magnetic anomaly data in East and Southeast Asia, *Tectonophysics*, 306, 461–470.

Telford, W. M., Geldart, L. P., Sherif, R. E., Keys, D. A. (1990). Applied Geophysics. Cambridge: Cambridge University Press

Trifonova, P., Zhelev, Z., Petrova, T., Bojadgieva, K. (2009). Curie point depth of Bulgarian territory inferred from geomagnetic observations and its correlation with regional thermal structure and seismicity, *Tectonophysics*, 473, 362–374.

Characterization of TiO_2-ZnO composite

* Sherifat ibrahim O. * Muhammad Bakeko M.
*Department of Physics, The Federal University of Technology, minna.
*Department of Physics, The Federal Polytechnic Bida

Abstract

The impact of calcination temperature on TiO_2, ZnO and TiO_2/ZnO composite thin film synthesis using Aerosol assisted chemical vapor deposition was investigated. XRD pattern show crystalline TiO_2, ZnO but amorphous TiO_2/ZnO composite , bandgap energy from optical characterization shows TiO_2, ZnO to be 3.35eV , 3.27eV and composite TiO_2/ZnO at 3.25eV, 3.18eV and 3.14eV as it varied, SEM morphology shows proper distribution of particles with spherical shape for titanium oxide and zinc oxide but agglomerated particles for the composite material. The EDX shows presence of Zn, Ti and O and their percentage composition. The bandgap energy and crystalline show they are good materials for optoelectronic and photovoltaic application.

Introduction

The semiconductor metal Oxide (SMO) has been studied separately and attempts have been made to synthesize nano-composite of these semiconductor metal oxides as well for use in various applications(Dubey et al., 2021). TiO_2 nanoparticle is the most efficient SMO and typical forms the photoanode in Dye Sensitized Solar Cell (DSSC) and electron transport layer for perovskite solar cell(PSC) application, and so its nano-composite have been found to have improved unique physical/chemical, structural and optical properties (Firdaus *et* al, 2012).

TiO_2 nanoparticles has bandgap energy between 3.0-3.2eV(Hou & Lund, 2021) as a photoanode , they offer fast electron transfer and a large number of contact sites, that is a high specific surface area to adsorb dye. TiO_2 is cheap(Bera et al., 2021), has low sheet resistance, suitable for high temperature treatment, good flexibility and nontoxic nature(Nanomaterials et al., 2021). Going by these properties its nano-composite is synthesize with the purpose to reducing its optical bandgap by introducing an intermediate energy levels in the host TiO_2 so that lower energy light spectrum may be captured in the solar cell.

ZnO nanoparticle, is typical an n-type semiconductor, its bandgap energy is ~3.3 eV(Özgür, 2005 and Stefańska et al., 2018) compared to that of the TiO_2, ZnO possess high anisotropic growth, it has good intrinsic electrical and optical properties, better electron mobility, high electron diffusion coefficient and an easy separation of photogenerated electrons(Angaiah et al., 2019). In addition, it has a higher energy bandgap and it has high distribution of electron accepting states in the conduction bands. ZnO has lower isoelectric point (IEP~9) compared to TiO_2 (IEP~6-7) meaning is less acidic and can achieve diverse morphology mantaining crystallinity and so it is said to achieve diverse morphologies with high crystalline structure making it a suitable candidate for a composite mixture with TiO_2 for solar cell application.

TiO_2 is characterized with low electron mobility (~0.1-1cm^2/Vs) and the photocatalytic activity under UV radiation restrict further efficiency improvement and long term stability of the device. In composite photoanode system, it is believed that a proper combination of the electronic structure of constituent's e.g the conduction bandedge and distribution of the electron-acceping states in the conduction band is a critical factor for good device performance.

Improvement of the efficiency of ZnO and TiO_2 thin film materials can be achieved by doping/mixing them together. This has been observed to modify and correct the draw backs of these materials in their pure forms hence resulting in better performance (Firdaus *et al.* 2012).

Also, the characteristics of thin films are greatly influenced by the methods used in depositing them; another factor that affects the quality of deposited thin films is temperature. This study has taken into consideration these factors by the use of proven good quality film deposition method,

annealing and doping) which are promising to yield improved thin films for applications in different areas that they can suitably be applied.

Titanium dioxide and zinc oxide share common properties: these include nontoxicity, thermal and chemical stability, and insolubility in water, resistance to chemical breakdown and photo corrosion, and mechanical strength. Among the methods proposed for the synthesis of TiO_2-ZnO oxide are electrospinning technique, a chemical co-precipitation method, the sol-gel technique, or solvothermal and hydrothermal methods, such factors as temperature variation, type of reagent used, rate of stirring, pH, the ratio of water to precursors, and calcination conditions enable precise control of the synthesis to obtain better materials, in terms of their morphology, crystallites size, and the crystallographic structure. Moreover, ZnO has a band gap of 3.37 eV, which is slightly more negative than that of TiO2. Therefore, the synthesis of TiO2-ZnO oxide systems can result in the injection of conduction band electrons from ZnO to TiO2, which is favorable to electron-hole separation. Therefore, the incorporation of these two materials into an integrated structure is of great significance because the resulting products may possess improved specific and well-defined physical and chemical properties, which were determined during their synthesis.

This work is targeted at investigating the optical and structural properties of Zinc Oxide, Titanium dioxides, and their Nano-composite thin films. The deposition method adopted for this study is Aerosol Assisted Chemical Vapour Deposition. The method is chosen because of certain advantages which include (i) flexibility (ii) good quality film yield and (iii) availability of experimental equipment and facilities.

Method

Materials used for the deposition

The materials used for depositing of the pure samples of TiO_2 and ZnO and the nanocomposite ZnO/ TiO_2 thin films are listed below. Zinc Acetate, Titanium Isopropoxide, Substrate, and Methanol, all the chemical were used without further modifications. Other equipments include the Magnetic stirrer, 3D printer coupled with accessories such as (atomizer) die – head and substrate heater, Electrical weighing balance, 1ml and 2ml syringes and needles and Beakers.

Procedure

The deposition method used in this study for depositing TiO_2, ZnO and nanocomposite ZnO/ TiO_2 thin Films is Aerosol Assisted Chemical Vapour Deposition (AACVD).

First 0.2 molar masses of Zinc Acetate and Titanium Isopropoxide were measured, weighed by means of electrical weighing balance, and then dissolved in 50ml of methanol in separate containers and properly stirred using a magnetic stirrer. The solutions were fed into the atomizer (die – head), maintaining substrate temperature at 300^{o}C, at nozzle to substrate distance of 5mm, pure samples of ZnO and TiO_2 thin films were deposited respectively while maintaining a constant total spray volume of 0.4ml for each sample. The next three samples are the nanocomposite (ZnO / TiO_2) thin films deposited in the ratio of 1.9: 0.1, 1.8: 0.2 and 1.7: 0.3 respectively.

The samples were each annealed at 400^{o}C temperatures and in total five (5) thin film samples were deposited. Table 3.1 gives a clearer view of the experimental design.

Table 1: Experimental design of deposited thin films using AACVD method

Sample Code	*Volume of 0.2M ZnO*	*Volume of 0.2M TiO_2*	*Deposition time*	*Total volume sprayed (ml)*	*Flow rate (ml/hr)*	*Substrate temperature (°C)*	*Substrate to nozzle distance (mm)*
AG	0	4	300	0.20	2.77	400	5
BG	4	0	300	0.20	2.77	400	5
CG	3	1	300	0.20	2.77	400	5
DG	2	2	300	0.20	2.77	400	5
EG	1	3	300	0.20	2.77	400	5

3.2 Film Characterization

At the end of the experiment, samples were characterized in order to determine their optical properties using UV spectroscopy, from which deduction of band gap energy of deposited films were made using modified version of Tauc's plot of $(\alpha hv)^2$ and the photon energy by extrapolation. To determine the structural properties and morphology, x-ray diffraction and scanning electron microscopy were used to investigate the crystalline phases of the prepared films respectively.

RESULT and DISCUSSION

Optical Properties

The optical characteristics of the thin films were investigated by the use of UV-Vis spectroscopy (Axiom Medicals Model UV750). The corresponding band gap energy of the deposited thin films were estimated by the extrapolation of the linear relationship between $(\alpha hv)^2$ and the photon energy (hv) according to Tauc's equation which is given by: $\alpha hv = A(hv - Eg)^n$

Where α is the coefficient absorption, h is the Planck's constant, υ is the photon frequency, E_g is the band-gap and A is a constant of proportionality. n depends on the nature of transition and is given as n = ½ for direct allowed band-gap(Cu & Czts, 2017) . The optical band gap energies are determined by extrapolation of the linear portion of $(\alpha hv)^2$ versus hv curve to $(\alpha hv)^2 = 0$. The band-gaps of the ZnO nanoparticles specimen TiO_2 and ZnO/TiO_2 are 3.27, 3.25 and the ZnO/TiO_2 composite bandgap energy are CG 3.18, DG 3.14, EG 3.34, the value shows increment with increase in composition of TiO_2 except for the EG which shows complete deviation. These values are appropriate band-gap energy for Dye and perovskite solar cell photo anode and electron transport layer to deliver high solar to electrical output as they can absorb photons consisting of visible and infrared rays.

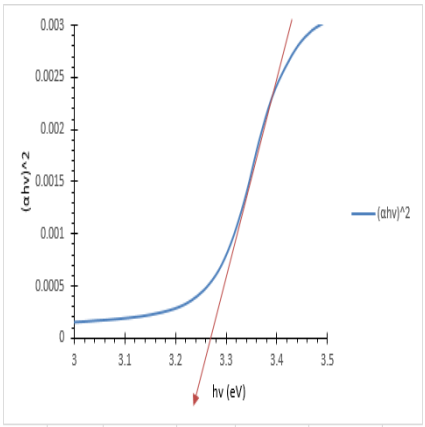

Figure 4.: Tauc's plot of sample AG at 400°C

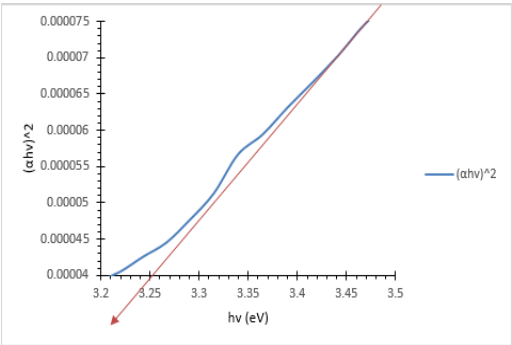

Figure 4.1.2: Tauc's plot of sample BG at 400°C

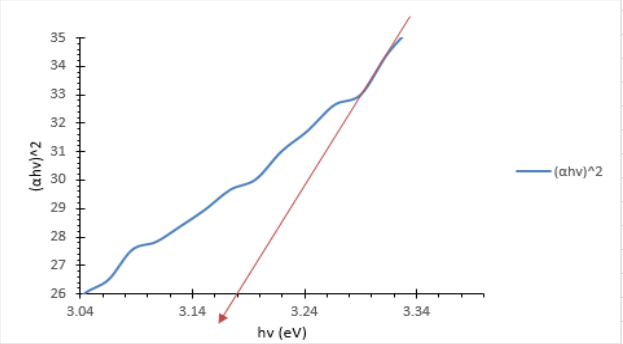

Figure 4.1.3: Tauc' plot of sample CG at 400°C

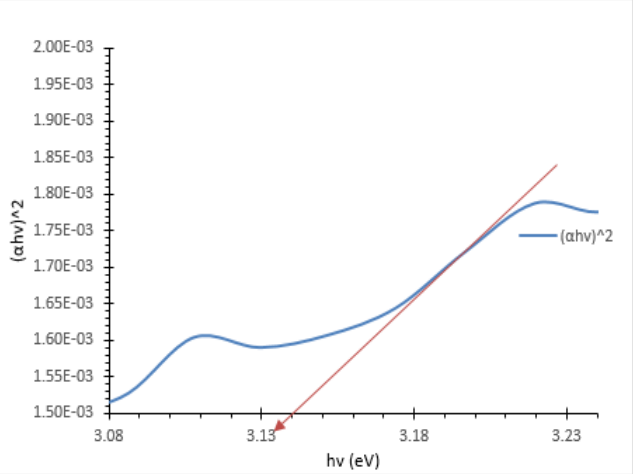

Figure 4.1.4: Tauc's plot of sample DG at 400°C

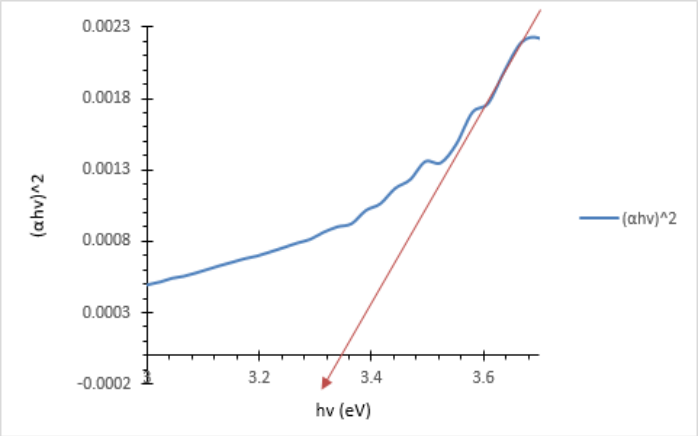

Figure 4.1.5: Tauc's plot of sample EG at 400°C

TABLE 4.1: Estimated band gap energies for the deposited thin films using Tauc's model

Sample ID	Temperature °C	Doping concentration ZnO/TiO_2	Band Gap Energy (eV)
AG	400	0:4	3.35
BG	400	4:0	3.27
CG	400	3:1	3.25
DG	400	2:2	3.18
EG	400	1:3	3.14

Table 4.1 shows the band gap energy for pure samples of ZnO (AG), TiO_2 (EG) and ZnO/TiO_2 composites (BG, CG, DG) annealed at 400°C temperature with varied compositions of zinc oxide, titanium oxide. Band gap energy is an important property in semiconductor materials that determine to an extent the performance of the semiconductor material. This is because the smaller the band gap energy the better the conductivity due to ease of electron transport to the conduction band from the valence band.

The change in the band gap energies of ZnO and TiO_2 is detectable with the impacts of annealing temperature and doping. It is observed that the band gap energy increases as the temperature increases leading to the increasing crystallite size (Shujah et al., 2016).

4.2 Structural Analysis

The crystal structure of TiO_2, ZnO, and TiO_2/ZnO composite thin films were analyzed using X-Ray Diffraction (XRD) in order to ascrtain the crystalline nature and phases of the thin films deposited on the substrate. Figure 4.2 shows the diffraction patterns of samples AG, BG, CG, DG, and EG which were annealed at 400°C temperature.

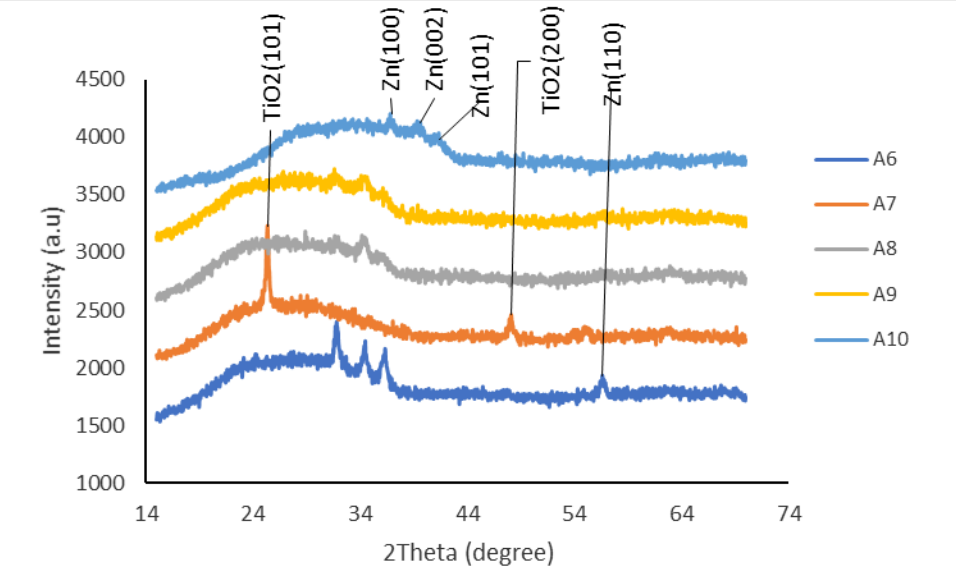

Figure 4.2: X-Ray Diffraction (XRD) Patterns for Samples AG, BG, CG, DG, and EG.

The XRD pattern for TiO_2 coinside with the wide angle XRD pattern assigned to the anatase phase structure(Dai et al., 2010), it appears to have a dominant peak at the diffraction angle of 2θ = 25.36° and another smaller peak 48.07° corresponding to the (hkl) (1 0 1) and (2 0 0) and is in agreement with data base file (JCP2 file_21-1272).

The diffraction pattern for pure ZnO revealed the formation of hexagonal zincite phase at 2θ = 31.77°, 34.42°, 36.25° and 56.60° which correspond to the (hkl) (100), (002), (101) and (110) planes The XRD measurement of ZnO zincite phase structure is in agreement with the data base file (JCP2 file_36-1451) .

Sample ZnO/ TiO_2 composite seem not to show peak corresponding to TiO_2, a possibility demonstrating that titanium ion were dispersed uniformly onto ZnO nanoparticles. As evident from the table 4.2, the crystallite size of ZnO nanoparticles increases with change in composition ratio of ZnO/TiO_2. As shown on table 2. shows a negligible shift in (110) Brag reflection for the samples with a different amount of the ZnO composition, This shift could be attributed to the strain in the lattice of compounds.

The crystallite sizes were calculated by the use of the Debye Scherrer (Patterson, 1993; Coutanceau *et al*., 2012) formula which is given by:

$$D = \frac{\lambda k}{\beta cos\theta}$$

Where D is the crystallite diameter, λ is the x-ray wavelength with a value of 1.54060nm, β is the the full wide at half maximum, k is the scherrer's constant which is given as 0.94 and θ is the Bragg's angle.

Table 4.2: Crystallite sizes obtained by the Debye Scherrer's formula and d-spacing obtained using Bragg's law.

Samples	Samples Ratio	2-Theta (°)	Crystallite size D	d-spacing (m)	LITERATURE VALUE d-spacing (m)
ZnO	4:0	31.81 34.48 36.34 56.61	3.02559 5.57816 5.48763 2.65498	2.81067 2.59848 2.47015 1.62437	2.8141 2.6019 2.4753 1.6247 (Kihara and Donnay, 1985).

ZnO/TiO_2	3:1	31.82 34.32	2.77232 2.21434	2.80998 2.61048	
ZnO/TiO_2	2:2	31.60	3.25700	2.82851	
ZnO/TiO_2	1:3	28.89	2.14348	3.08735	
TiO_2	0:4	25.36 48.10	10.98552 1.93954	3.50890 1.88985	3.5165 1.8921(Preeti,&Sunil R., 2020) (Howard *et al*., 1991).

It can be seen that the values presented for the d-spacing agrees well with the literature values of the structural parameters for Zincite (Kihara and Donnay, 1985) and for Anatase (Howard *et al*.,1991). Crystallite size and d-spacing play a fundamental role in the performance of DSSC. For example, the smaller the crystallite size is, the larger the surface area will be, which entails that when using ZnO, TiO_2 or its composite as photoanode or ETM in solar cell, large surface area is to the advantage to produce a high output power. Table 1 shows the average crystallite diameter, of TiO_2 , ZnO and ZnO/TiO_2 composite samples synthesise and annealed at 400°C

4.3 SEM Morphological

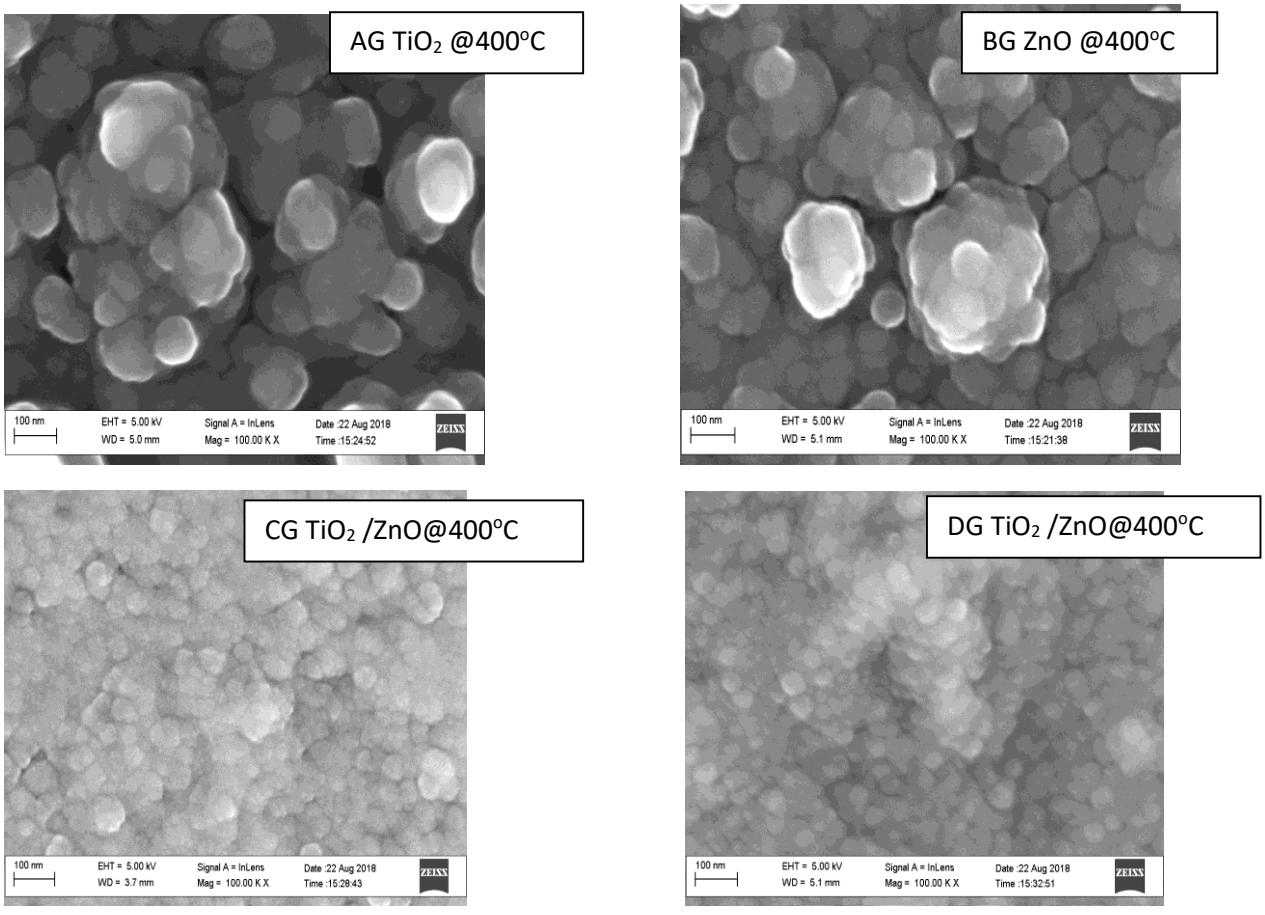

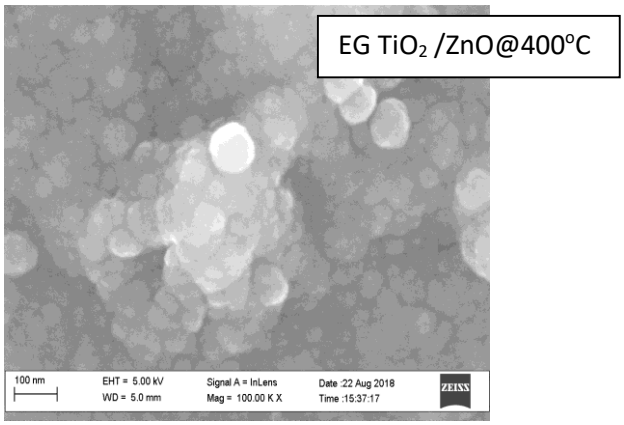

Figure 4.3: Scanning Electron Microscopy (SEM) Images of Samples AG, BG, CG, DG, and EG.

SEM images shows the morphology of ZnO, TiO_2 and composite ZnO/TiO_2 thin films. Figure 4.3 is the ZnO sample (BG) with doping ratio of 4:0, TiO_2 sample (AG) with doping ratio of 0:4 and three ZnO/TiO_2 composite samples (CG, DG and EG) with ratios of 3:1, 2:2, 1:3 separately. All the sample thin films were annealed at 400°C temperature. SEM morphology indicates that calcination aid proper TiO_2 and ZnO particle size distribution which appears in spherical shape with high homogeneity. The images shows that AG and BG particle tends to be densely packed together, like clustering of smaller particles which brings about the development of larger grains with better crystallinity which is connected to the increased crystallite sizes. SEM analysis of the synthesize TiO_2-ZnO oxide composite showed that the molar ratio of the precursors has no significant effect on the SEM morphology of the resulting materials, all the composite look similar in form and the composite samples appear to form agglomeration which explains their amorphous structure as observed in the XRD analysis.

The samples CG ,DG and EG form agglomeration armorphous compound.

4.4 EDX Analysis

EDX result typically reveals the elemental compositions of the deposited thin films and the percentage weight of each of the constituent elements in the thin film. Figure 4.4.1, confirms the amount of Ti and oxygen present in the nanomaterial, and the distribution of Ti in TiO_2 is found to be uniform, it also appears uniform for Zn distribution in the ZnO precursor. The inset shows the percentage weight of each element present.

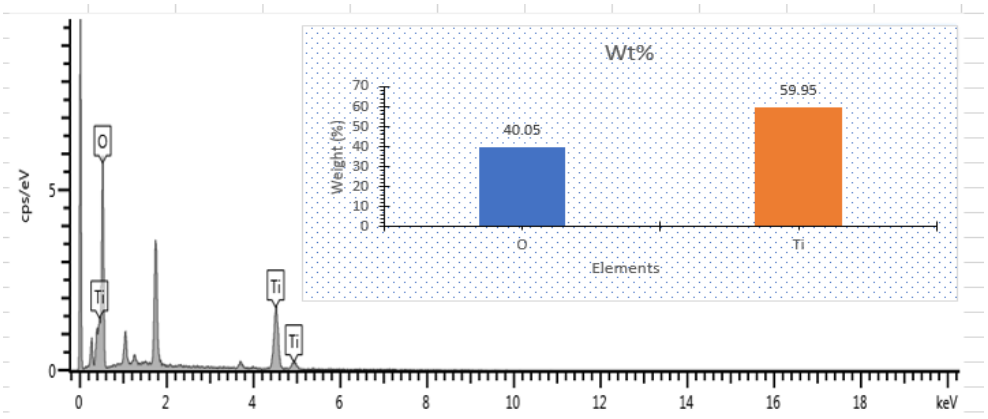

Figure 4.4.1: Elemental composition of sample AG

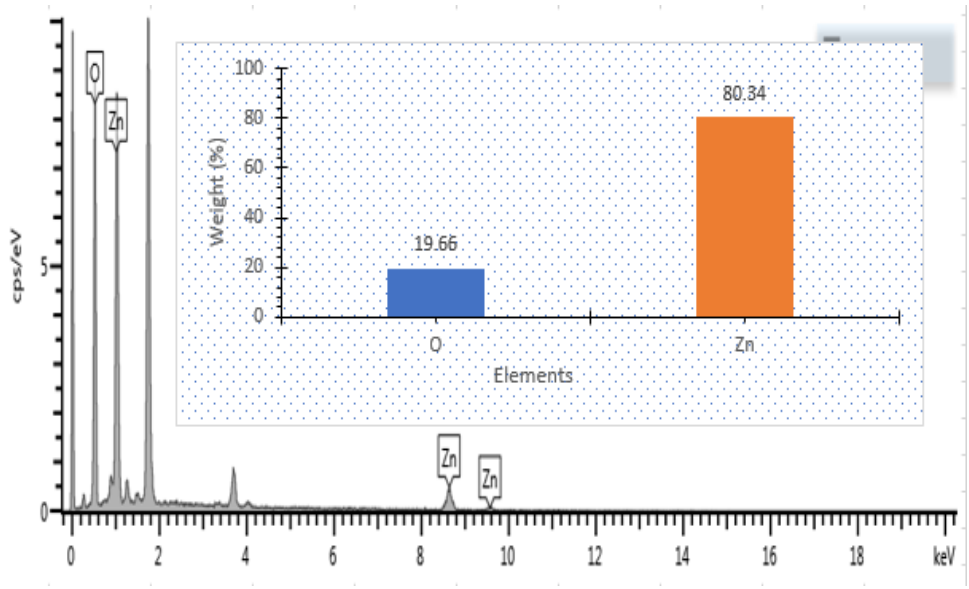

Figure 4.4.2: Elemental composition of sample BG

The composition of in TiO_2/ZnO appears to show zinc at higher energy compared to titanium for all the composite sample a possible indication why zinc appear faintly on the composite XRD analysis. No other element appeared show all samples where purely ZnO and TiO_2

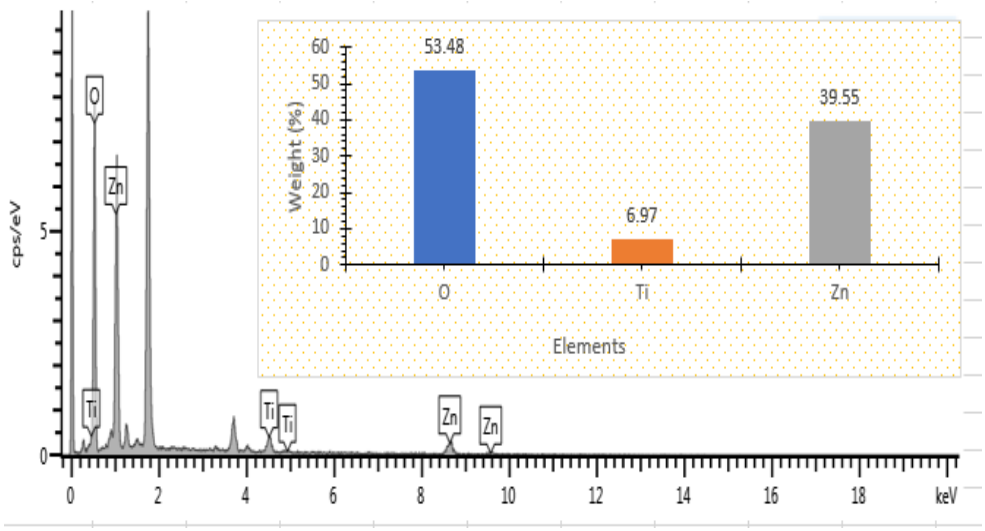

Figure 4.4.3: Elemental composition of sample CG

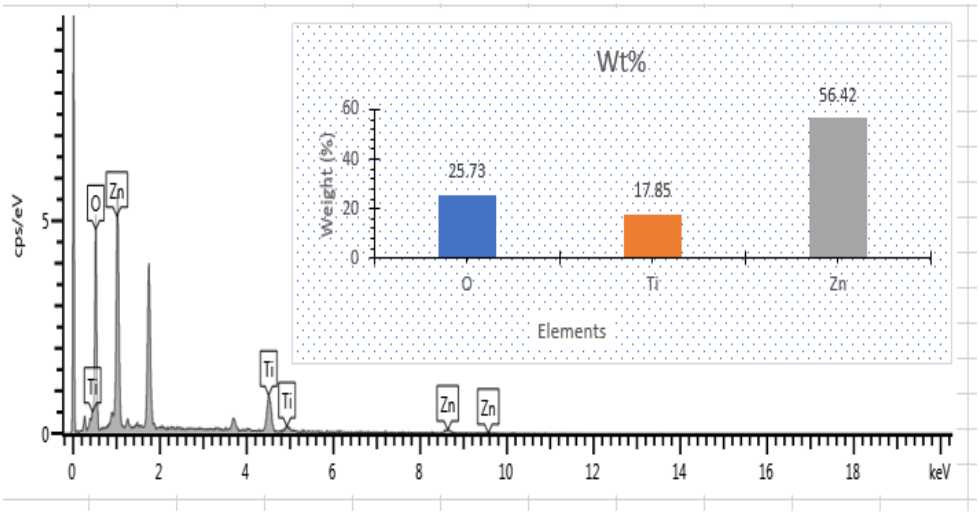

Figure 4.4.4: Elemental composition of sample DG

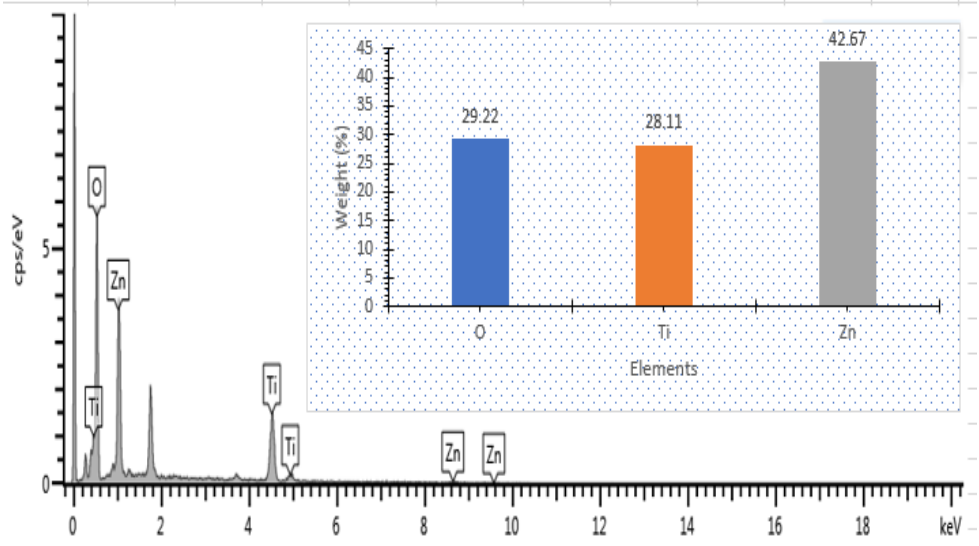

Figure 4.4.5: Elemental composition of sample EG

5.1 CONCLUSION

This research work investigated the impact of calcination temperature on the semiconductor metal oxide (SMO) typically TiO_2 , ZnO and TiO_2/ZnO composite thin film deposited using ESD method, the optical characteristics and the bandgap energy of pure ZnO, TiO_2 and ZnO/TiO_2 nanocomposite where calculated.The XRD reveals a well crystallized nanoparticle with projection indicating the anatase TiO_2 structure and a crystalline ZnO. For the composite only CG appears to show slight projection for ZnO otherwise the other samples appear to be poor crystals. The crystal structure parameter such as, the crystallite size (D) and the d-spacing were determine using the Debye Scherrer's formular and the Bragg`s law separately

The SEM image morphological analysis showed particle uniformly distributed for titanium oxide and zinc oxide precursors with spherical shape but very good homogeniuty, SEM image for the composites show possible agglomeration and appear to be amorphous. EDX analysis showed the element Zn, Ti and O which form the compositions. The investigation reveals that ESD synthesis method can be used for deposition of crystalline SMO for the applications in optoelectronics, and photovoltaic materials.

REFERENCES

Angaiah, S., Arunachalam, S., Murugadoss, V., & Vijayakumar, G. (2019). *A Facile Polyvinylpyrrolidone Assisted Solvothermal Synthesis of Zinc Oxide Nanowires and Nanoparticles and Their Influence on the Photovoltaic Performance of Dye Sensitized Solar Cell*. 59–65. https://doi.org/10.30919/esee8c280

Bera, S., Sengupta, D., Roy, S., & Mukherjee, K. (2021). *Research into dye-sensitized solar cells : a review highlighting progress in India Journal of Physics : Energy OPEN ACCESS Research into dye-sensitized solar cells : a review highlighting progress in India*.

Cu, S., & Czts, Z. (2017). *Structural and Optical Properties of Chemically*. *5*(2), 1–7.

Dai, S., Wu, Y., Sakai, T., Du, Z., Sakai, H., & Abe, M. (2010). *Preparation of Highly Crystalline TiO 2 Nanostructures by Acid-assisted Hydrothermal Treatment of Hexagonal-structured Nanocrystalline Titania / Cetyltrimethyammonium Bromide Nanoskeleton*. 1829–1835. https://doi.org/10.1007/s11671-010-9720-0

Dubey, R. S., Jadkar, S. R., & Bhorde, A. B. (2021). *Synthesis and Characterization of Various Doped TiO 2 Nanocrystals for Dye-Sensitized Solar Cells*. https://doi.org/10.1021/acsomega.0c01614

Hou, X., & Lund, P. D. (2021). *TiO 2 nanotubes for dye-sensitized solar cells — A review*. *August 2020*, 921–937. https://doi.org/10.1002/ese3.831

Nanomaterials, T., Yohi, S., Velauthapillai, D., Ravirajan, P., & Senthilnanthanan, M. (2021). *Cost Effective Solvothermal Method to Synthesize Zn-Doped*.

Preeti, and Sunil R. (2020). *Rietveld refinement and structural characterization of Rietveld refinement and structural characterization of*. https://doi.org/10.1088/1757-899X/872/1/012171

Özgür, Ü. (2005). *A comprehensive review of ZnO materials and devices*. *041301*.

Stefańska, K. S., Kubiaka, A., Piasecki, A., Goscianska, J., Nowaczyk, G., Jurga, S., & Jesionowski, T. (2018). *TiO 2 -ZnO Binary Oxide Systems : Comprehensive Characterization and Tests of Photocatalytic Activity*. 1–19. https://doi.org/10.3390/ma11050841

Firdaus C. M., M. S. B. Shah Rizam, Rusop M., Rahmatul Hidayah S., (2012). Proceedia Engineering, 41, 1367-1373.

Fujishima, A., Rao, T. N. & Tryk, D. A., (1972). Titanium dioxide photocatalysis. *J. Photochem. Photobiol.*, C **1,** 1-21.

Hou X., Choy K. L., (2006). Processing and application of Aerosol Assisted Chemical Vapor Deposition. 12(10), 583-596.

Geology, Geochemistry and Mineralogy of Tajimi Iron Ore Resources in Part of Koton-Karfe, Sheet 227SW, North–Central Nigeria

Mubaraq Olayiwola Adewole[1] and Usman Shehu Onoduku[2]
Department of Geology, Federal University of Technology, Minna [1,2]
almubaraqadewole.f@gmail.com +2348066500877[1]
onoduku.usman@futminna.edu.ng +2348035904399[2]

ABSTRACT

*The geology, mineralogy and geochemistry of Tajimi iron ore resources in part of Koton- karfe, sheet 227SW, North–Central Nigeria was studied with the aim of ascertain the geology and provide compressive data on the geochemistry, mineralogical composition and grade determination. Twelve iron ore samples were analysed for mineralogical characteristics using X-Ray Diffraction (XRD). Ten representative iron ore samples were also analysed for multi-elemental concentration using X-ray Fluorescence (XRF), INAA, TO-ICP, TO-MS and TD-ICP. The geology of the studied area comprises of gneiss, granite, ferruginized sandstone/siltstone, quartzite, an intrusion of aplite, pegmatite and iron mineralization. XRD result revealed four iron facies hematite, goethite, ilmenite and magnetite, other minerals are quartz, garnet, corundum and Illite. Geochemical result shows that Fe_2O_3 content ranges from 29.78 to 69.52% and average of 51.05. SiO_2 and Al_2O_3 with average content 17.71% and 14. 88% respectively. MnO with average content of 5.34%. MgO and TiO_2 have average concentration 2.87% and 2.13% respectively. The average concentrations of Na_2O, K_2O, CaO, are 1.19%, 1.74%, 0.67%, respectively while Phosphorus and Sulphur with average concentration of 0.536% and 0.445% respectively. The grade is 35.71% of Fe content. Binary plot of TiO_2-SiO_2 discrimination diagram and petrogenesis ternary plot of Fe vs (Co + Ni + Cu + Zn) *10 vs Mn of the Tajimi iron ore, combine with field evidence suggested Tajimi iron ore to be of sedimentary origin. A ternary plot of FeO + MnO vs SiO_2 vs Fe_2O_3 of Tajimi iron ore shown is magnetite silicate facies and hematite facies, this suggested Tajimi is oxide facie type form under oxidizing condition, this also agreed with X Ray Diffractive result. The comparison of the Tajimi iron ore shows that it is of low grade with 35.71% of Fe content and contain high percentage of gauge (silicate 17.71%. and alumina 14. 88%) and contaminant (Phosphorus 0.536% and Sulphur 0.445%) which are above the generalized permissible limit for steel production.*

Keywords: Tajimi, Iron ore, Gneiss, Hematite, Grade.

Introduction

Nigeria is vast country blessed with abundant of natural mineral resource. For any nation to be industrialization its iron and steel industry most developed. Nigeria as a nation hoping to join the Steel Producing Countries and currently owns two steel Companies; Delta steel company and the Ajaokuta Steel company and two are non-functional partly due to shortage of the raw materials and other factors. The Aladja was designed to process iron ore by Direct Reduction method to give 68% iron concentrate and Ajaokuta Steel Company designed to use blast furnace to give 64% iron concentrate. The steel industries are desirous of exploring and exploiting iron ore deposits that can be as sources of raw materials to the steel industries.

Iron ores are rocks from which iron elements can be extracted. The ores are usually containing iron oxides and vary in color from dark grey, bright yellow, or deep purple to rusty red. Iron ore defined by Gross, (1993) as raw material of suitable grade of iron composition and physical quality that can be mined and processed for profit or economic benefit. Iron is estimated to make up 32.07% of the Earth's mass and its elemental abundance varies between 5% of the Earth's crust and as much as 80% of the planet's core (Ferenczi, 2001)

Many scholars have reported the occurrence of iron formations in the Nigerian. Two broad groups are identified: the metamorphosed iron formations that are mostly Precambrian and the Sedimentary (oolitic) iron ore deposits that are Cretaceous. The Precambrian iron-formations are

named differently by different workers. Some named them ferruginous quartzites (e.g. Truswell and Cope, 1963; Olade, 1978): and others simply called them `ironstones' (e.g. McCurry, 1976; Ajibade, 1976; Holt *et al*., 1978). In addition, banded iron formation (BIF) has been used by Adekoya (1996), Mucke *et al*., (1996) Ibrahim, (2008) describe those banded and chert-bearing iron deposits in the metasedimentary belts of northwestern Nigeria with a high silica-iron minerals ratio. The employed term has genetic importance because it indicates the nature of the primary silicate minerals.

Oyelowo *et. al., (*2016), Interpreted occurrence of iron ore at Tajimi stated that residual magnetic map revealed numerous prominent positive anomalies mostly trending N-S, characterized by relative higher magnetic intensity values. Spectral analysis of the magnetic data suggests the existence of two main source depths which range from 6 m to 20 m. He further interpreted VES data characterized the area into three subsurface layers: top soil, anomalous low resistivity layer (iron ore zone) and weathered/fractured bedrock. However, he suggested coring, chemical analysis and complimentary geophysical prospecting to deduce the iron ore type and estimate the proven tonnage of the iron ore formation in Tajimi village.

Nigeria as a nation has many undeveloped iron ore deposits which Tajimi iron resource is among, meanwhile this present research work is intend to ascertain the geology and provide compressive data on mineralogy and geochemistry of Tajimi iron resource and infer its possibility of economic viable deposit.

Study Area

The study area is bounded by Latitude: 08° 2' 30"N, to 08° 4' 00"N and Longitude: 006° 36' 00"E to 006° 37' 30"E (Figure 1.1) The area is located within the Koto-karfe Sheet 227SW, Central Nigeria and it is easily accessible through Lokoja –Okene road via untarred road which is about 34km to the iron location. It also accessible through Jakura – Obajana Road.

Materials and Methods

Desk Study

This stage involved preparation of topographical map of the area by extraction of location from topo- map of Koto –Karfe Sheet 227 SW obtained from Nigeria Geological Survey Agency (NGSA). This was followed by literature review of the Tajimi area at every stages of the research.

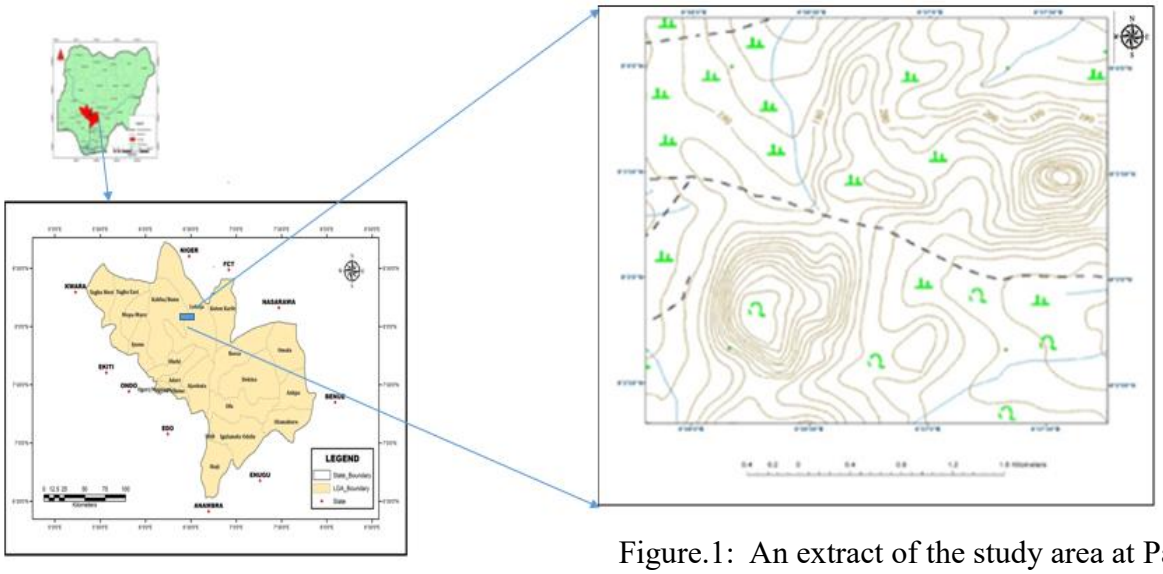

Map of Nigeria and Kogi State showing project location

Figure.1: An extract of the study area at Part of Koto –Karfe Sheet 227 SW

Geological Mapping

Geological mapping on a scale of 1:10,000 of the study area was carried out by adopted grids and traverse method. The rock types were carefully studied and sampled with the aid of geological hammer and well labelled using designated code to avoid mix up. Sample points and features photograph were located using the Global position system (GPS). Hand specimens of the rock samples from field were studied based on the colour, mineralogy, texture, physical properties and structural feature were carefully studied and documented.

Laboratory Analyses

Twelve iron ore samples were analysed at National Steel Raw Materials Exploration Agency (NSRMEA) laboratory in Kaduna for mineralogical characteristics using X-Ray Diffraction (XRD) also another ten representative iron ore samples were analysed at Activation laboratory, Ontario, Canada, for multi-elemental concentration using various geochemical methods.

Results and discussion

Geology of the Study Area

Geology of Tajimi area and its environs comprises of; gneiss, granite, ferruginized sandstone/siltstone, iron ore and quartzite, intrusions of aplite, pegmatite with distinctive mineralogical, petrological and textural characteristic.

Gneisses are sandwiched the iron ore around the studied area which occupied central portion account for about 37%. Four different types of gneisses were encountered within the area based of the structure, these are banded gneiss, coarse grain gneiss, granite gneiss and phylitic gneiss. Iron ore occupied NNW and SSW trending N-S direction account for about 8%. Granite occur as outcropping and low-level exposure in western portion of the area account for about 30% have boundary with gneiss at east part. Aplite-pegmatite this occur as intrusions in almost all the rock types found within the area account for about 3%. Quartzite occur as ridges, fragment and quartz vein within gneiss, aplite, pegmatite and granite in study area it accounts for about 2%. Ferruginized sandstone/siltstone found at eastern flank of the investigated area account for about 20% has boundary with gneiss at western end. **(**Figure: 2)

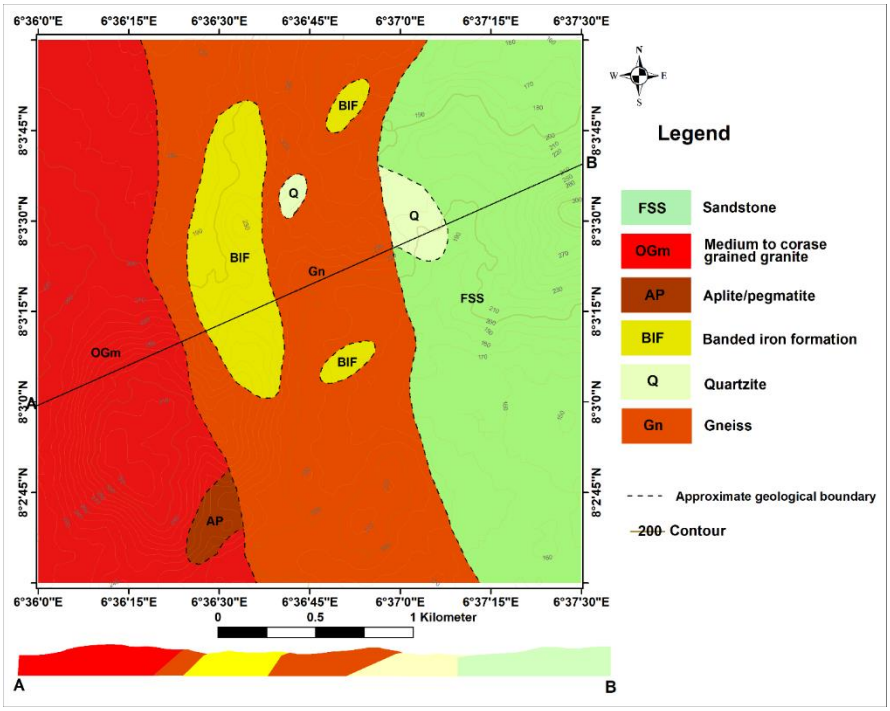

Figure 2: Geological map of Tajimi Iron ore

Gneiss

Different types of gneisses were encountered within the study area based of the structure. They occurred as massive covered wide range area. These rocks have conspicuous alternating bands of leucosome and melanosome minerals. The leucosome is dominated by quartz approximately to 60% or feldspar in some place, while the melanosome is dominated mainly by biotite. The bands have thickness that is milli-metric in thickness and generally traceable for relatively long distance. Gneiss with well aligned minerals which is pronounced foliation on the surface. It is occurred as massive. Biotite and feldspar are well foliated from field observation. Plate I: the minerals are well aligned along the foliation plane in the fresh samples**.** Plate II. Weathered felsic granite gneiss, highly fractured and with weak foliation and presence of quartz intrusion.

Granites

The rocks were found in the western part of the mapped area and covers about 30% of the region. They are divided into two, based on the colour. These are the leucocratic granite and the melanocratic granite. The leucocratic granite has fine to medium grained textures. Mineralogically, the leucogranite are composed essentially of quartz, feldspar, and biotite.

The melanocratic granite referred as biotite granite is composed of quartz, biotite and feldspar. The biotite granite has mafic segregations that dotted most of the surface. The two granites have an intrusion that occupied the void within the rock such vein and dyke. These veins are mostly quartz and feldspar. Plate III

Aplite/Pegmatite

This rock found as an intrusion in almost all rock types within study area like gneiss, granite and ferruginized sandstone/siltstone. This rock can also be referred to as aplitic pegmatite, consists of both the pegmatite (coarse-grained) and fine-grained aplite. The coarse-grained pegmatite covers a wider area relative to the aplitic pegmatite. Mineralogically, this rock composed of quartz, plagioclase feldspar, muscovite and other accessory minerals. Plate IV and V

Iron Ore

From field observation the Iron Ore aligned in N-S direction. The iron ridge occurs as conically shaped bodies in three conical hills. These bodies are described as northern, central and southern ore bodies based on their geographical position within the study area for easy description. On the surface, the ores occur as cobbles, boulders and massive. The southern portion iron ridge was trending north-south precisely 025° covered by very thick overburden which gives rise to obscured outcropping of the host rock. The rocks disposition was fractured into blocks by tangential fault as observed on the displaced block. The iron has tin band alternation of iron and quartz as observed. In hand specimen rocks are foliated, fine to medium grained and weathered in some place. It is brownish in colour. **(**Plate: VI**)** some of *insitu* ore body trending N180°S with dip 43°W, 50°W at difference position. The central ore ridge occurs as scattered boulders and highly fractured with glassy luster. Fine to medium grained, dark in colour. At northern ridge, the iron ore occurs as breccia's, they are angular to sub-angular all over the area, it also occurs as boulders and massive. The area has undergone episode of tectonic activities. **(**Plate VII & VIII). It has glassy luster, fine to coarse grained. Bands of iron and silica are more pronounced. These bands are in millimetric thickness. The quartz is more resistant to weathering than iron ore as observed on the field.

Ferruginized Sandstone/Siltstone

The sandstone/siltstone are found at the eastern part of the study area covered about 30%. These rocks are part of the sandstone/siltstone member of Southern Bida Basin. The colour of these varies yellowish, brownish to dark brown and darkish. Sandstone has texture fine to medium to coarse grains. These rocks have been ferruginized and intruded by pegmatite in some area.

Quartzite

The quartzites occur as quartz veins in gneisses, aplite, granite and iron ore bodies. It was liberated from pegmatite in some places to form orthoquartzite. It is also occurred as ridge in some area. They are intrusions and can be referred to as fault rocks.

Laterite

Laterite is found in at the central ore body occur as impregnation on iron cobbles and pebbles. This laterite is formed in-situ and is thought to be the products of chemical weathering of the ore body developed mostly along joints and cracks. This laterite has magnetic properties it was attracted with magnetic pen. It is mostly brown in colour.

Plate II: Gneiss with minerals aligned along the foliation plane
(08º0 3' 29.5"N, 006º 36' 45.5"E)

Laboratory Results

Mineralogical Analysis of the Tajimi Iron

The analysis revealed minerals that are present in the iron ore and provide the quantitative for all minerals. The typical result of X-ray diffraction analysis of the iron ore deposit is shown in appendix.

From the analysis result, it is clear that the predominant minerals in Tajimi iron ore are quartz, followed by Hematite, goethite, ilmenite and magnetite, iron ore facies are suggested to be oxide types. Other minerals are Illite, garnet and corundum have lowest peak also indicate in the figure :3

Geochemistry

Ten representative iron ore samples were analyzed for multi-elemental analyses using various geochemical methods (XRF, ICPMS, INAA, TO-ICP, TO-MS and TD-ICP).). Major oxides and trace elements were determined.

Major element composition

The result of geochemistry of analysed samples, table 1: revealed the major oxides composition of SiO_2 with values ranging between 6.75 and 23.75% and average value of 17.71%. The Fe_2O_3 have value range between 29.78 and 69.52% with average of 51.05 and corresponding computed Fe contents which varies between 20.83 and 48.69% with mean of 35.71%. Al_2O_3 have value varying

between 5.07 and 27.65% with average of 14. 88%, these values are relatively high compared with other iron formation in Nigeria such as Muro with 0.1 to 0.45%, (Adekoya, 2012) Birnin Gwari with 3.78% (Adekoya, 1998) and Wanako with value ranging between 5.29 and 6.11%. (Muhammad, 2014) Al_2O_3 content of the present study can be compared with that of Agbaja plateau with 14.76% of Al_2O_3, Konto Karfe Ironstone with value of 12.60% Al_2O_3 (Imurana & Harana, 2017) and Kazaure iron deposit with 11.3% of Al_2O_3. (Ibrahim, 2018) Table 3. The higher in alumina may be as result of adjacent ferruginised sandstone. Initially the area belief to be sedimentary basin that later metamorphosed to form metasediment and deposit was later enrich in aluminum. MnO have concentration value varying between 1.19 and 9.89% with average 5.34%, these values can be compared with Maru Iron Formation whose MnO ranges between 2.29 and 9.37% with average 7.60% according to Adekoya (1998) and MnO of Kazaure Iron Formation varying between 0.007 and 17.83% according to Ibrahim, (2018) MgO and TiO_2 have concentration values varying between (0.98 and 5.96% with average 2.87%) and 1.05 to 4.99% with average of 2.13% respectively. The average concentrations of Na_2O, K_2O, CaO, are 1.19%, 1.74%, 0.67%, respectively while Phosphorus (P) and Sulphur (S) with average concentration of 0.536% and 0.445% respectively. From figure 4 average concentration of major oxide (%) shown that Fe_2O_3 have the highest peak with 51.052% while SiO_2 have 17.708% followed Al_2O_3 with 14.88% and CaO has least of 0.677%.

Trace element (TE)

Table 4.8 presented chemical data of trace element of Tajimi iron ore. The result of the Trace elements is containing low and high values compared with other BIF in Nigeria (Adekoya, 1998; Muhammed & Ibrahim, 2017 and Ibrahim, 2018) and Precambrian Iron Formation in different part of the world (James, 1966; Barbosa and Gross, 1973; Gole, 1981). Table 4.9 shown comparison of concentration of trace elements of the study area with other iron ore deposits. Concentrations of V (4-20) 11.7ppm, Co (10- 21) 14.71ppm, Zn (2-8) 5.4ppm and Ni (2-12) 6.7ppm are low. Co, V, Zn and Ni, the concentrations of elements are significant low compared with other BIF in the Nigeria as shown in the table 4.9. The sources of these ferromagnesian elements are generally mafic to ultra-mafic rocks. Ba (388-1023) 851.1ppm and Cr (77-132)107.6ppm these elements concentrations are higher compared with that of Algoma- type BIF 170ppm and 78ppm, Lake Superior BIF 180ppm and 122ppm, Orissa BIF 70ppm and 30ppm, Manas Garais Itabirite 179ppm and 28.5ppm, Maru BIF 293ppm and 23ppm respectively but this similar with Wonaka BIF 1103ppm and 140.5ppm. Ba and Cr show appreciable concentration which could be use as pathfinder element of BIF. The enrichment of these ferromagnesium elements (Co, Ni, Zn and Cr) in the BIF as pathfinder of the possible origin of the BIF (Ibrahim, 2018). Cu (2-21)9.7ppm this has similar concentration value with all the deposits considered for comparison except that of Kazaure FMP with 316ppm, Wonaka BIF with 261.5ppm and Algoma- type BIF with 96ppm which are relatively high concentration. Elements such as Cu, Co, Ni and Zn are used as pathfinder of origin of the BIF in the area (Bonatti et al., 1972). The appreciable concentrations of Ba and Cr elements may suggest that the protolith of the BIF is mafic to ultramafic rock.

Figure 5: shown the average concentration of trace elements in ppm Ba indicate highest peak with average value of 851.1ppm, Cr with concentration of 107.6ppm, Ag with 84.7ppm, Sr with concentration of 30.4ppm Ni with 6.7 Zn with 5.4, Bi with value 29.8ppm and W with concentration of 5.38ppm.

Determination of Grade of Tajimi Iron Ore

The quality of raw material for steel production (iron ore) and its viability for commercial exploitation is mainly determined by its chemical composition (Abraham *et al.*, 2012). The certain generalisation are set to known the quality of iron ore. If the Fe contents (wt %) of ore is greater than 65% referred as high grade (H), ore with Fe contents varied between 62 to 64% the ore termed as medium or average grade donated by (M) , while ore with Fe contents below 58% categorised

as low grade ore (L) as shown in table 4: (Abraham *et al.*, 2012 Ahmed *et al.*, 2017**).** Table 1: shown the average concentration of SiO_2, Al_2O_3, phosphorous P and Sulphur S are 17.708%, 14.88%, 0.536% and 0.445% respectively, these values are higher than the generalized standard for steel production.
Conversion factor is calculated to be 0.6994

Figure 5: Average Concentration (ppm)
Trace Elements of Tajimi Iron ore

Grade =Average Con. of Fe_2O_3 X Conversion Factor
= 51.052 X 0.6994

=35.71% Grade of Fe content

Base on the grade calculation, Tajimi Iron Ore is classified as low grade.

Provenance of Tajimi Iron Ore
The process of ore formation is relatively complex. The processes generally range from magmatic/ hydrothermal to metamorphic/ metasomatism and sedimentary. The Tajimi area is underlain by metasedimentary and metavolcanic rocks of Igarra, Kabba and Jakura regions (Oyelowo *et al.*, 2016). The field evidences revealed the Tajimi Iron Formation is emancipated from sedimentary source. (Figure 6 and 7)
Petrogenesis ternary plot of Fe vs (Co + Ni + Cu + Zn)10 vs Mn was plotted for the BIF of the study area (Figure 6) which shows that the Tajimi iron ore fall within the field of submarine-hydrothermal source, suggesting that the iron ore is of sedimentary origin.

TiO_2 and SiO_2 composition of the Tajimi iron ore was plotted in discrimination diagram as modified after Tarney, 1977 which was used to determine to the iron ore protolith(s) (Figure 7). The plot of TiO_2 and SiO_2 discrimination plot also confirmed the petrogenesis of Tajimi Iron ore to be of sedimentary origin (Figure 6).

An attempt to unravel the ore facies type of the Tajimi iron ore (Figure 8), the chemical compositional ternary plot of FeO + MnO vs SiO_2 vs Fe_2O_3 shows the Tajimi iron plotted within magnetite silicate facies and hematite facies suggesting the BIF in the study area to be predominantly of magnetite silicate facie and hematite facies type respectively. This is an indication that magnetite and hematite form under oxidation condition in the basin and minerals are oxide facies type.

Conclusion
Geology of the Tajimi Iron ore area revealed the following rock types; gneiss, granite, ferruginized sandstone and quartzite. Intrusion of aplite, pegmatite and iron mineralization. XRD results shows that Tajimi iron ore contains hematite, goethite, ilmenite and magnetite which suggested to be oxide iron facies type. Other minerals include quartz, illite, garnet and corundum. The result from geochemical has shown Fe_2O_3 have average of 51.05%. The grade of the iron ore calculated to be 35.71% grade of Fe content which suggested that Tajimi ore is of low grade. Binary plot of TiO_2-SiO_2 discrimination diagram and petrogenesis ternary plot of Fe vs (Co + Ni + Cu + Zn) *10 vs Mn of the Tajimi iron ore, combine with field evidence suggested Tajimi iron ore to be of sedimentary origin. A ternary plot of FeO + MnO vs SiO_2 vs Fe_2O_3 of Tajimi iron ore shown is magnetite silicate facies and hematite facies, this suggested Tajimi is oxide facie type form under oxidizing condition, this also agreed with X Ray Diffractive result.

The comparison of the Tajimi iron ore shows that it is of low grade with 35.71% of Fe content and contain high percentage of gauge (silicate 17.71% and alumina 14.88%) and contaminant (Phosphorus 0.536%and Sulphur 0.445%) which are above the generalized permissible limit for steel production.

Table 1 Concentration of major oxides of the iron ore from the study area (in %) and trace elements in (ppm).

S/No	AMO01	AMO02	AMO03	AMO04	AMO05	AMO06	AMO07	AMO08	AMO09	AMO010	**MIN**	**MAX**	**AVERAGE**
SiO_2	23.34	23.75	19.72	14.99	22.94	13.96	6.79	21.86	14.74	14.99	**6.79**	**23.75**	**17.708**
Fe_2O_3	43.88	55.88	59.54	41.84	29.78	69.52	63.43	41.76	65.21	39.68	**29.78**	**69.52**	**51.052**
Al2O3	15.22	9.13	8.83	27.65	21.61	5.07	14.31	12.78	8.38	25.82	**5.07**	**27.65**	**14.88**
Na_2O	1.14	1.09	1.38	1.45	0.13	1.09	1.18	1.89	1.19	1.36	**0.13**	**1.89**	**1.19**
K_2O	1.13	0.46	1.88	1.69	6.53	0.22	0.44	1.8	0.47	2.87	**0.22**	**6.53**	**1.749**
CaO	0.34	0.76	0.52	0.54	0.11	0.58	0.24	2.4	0.89	0.39	**0.11**	**2.4**	**0.677**
MnO	4.73	1.19	1.9	6.33	9.89	3.21	4.5	8.31	5.58	7.73	**1.19**	**9.89**	**5.337**
MgO	3.61	2.21	2.25	1.89	1.57	0.98	3.56	5.96	1.93	4.76	**0.98**	**5.96**	**2.872**
TiO_2	2.19	1.6	1.92	1.05	2.49	4.99	2.74	1.34	1.34	1.65	**1.05**	**4.99**	**2.131**
P_2O_5	2.55	1.74	0.99	1.45	2.05	0.28	1.54	1.02	0.11	0.55	**0.11**	**2.55**	**1.228**
SO_2	1.95	1.4	1.2	1.35	2.45	0.17	1.35	0.85	0.22	0.12	**0.12**	**2.45**	**1.106**
TOTAL	**100.08**	**99.21**	**100.13**	**100.23**	**99.55**	**100.07**	**100.08**	**99.97**	**100.06**	**99.92**	**99.21**	**100.23**	**99.93**
Fe	30.69	39.08	41.64	29.26	20.83	48.69	44.36	29.2	45.6	27.75	**20.83**	**48.69**	**35.71**
Mn	3.67	0.92	1.47	4.91	7.67	2.49	3.49	6.44	4.32	5.55	**0.92**	**7.67**	**4.093**
P	1.11	0.76	0.43	0.63	0.89	0.12	0.67	0.46	0.05	0.24	**0.05**	**1.11**	**0.536**
S	0.78	0.56	0.48	0.54	0.98	0.07	0.54	0.34	0.09	0.1	**0.07**	**0.98**	**0.448**
FeO	35.09	42.42	46.26	32.51	23.14	54.09	49.29	32.45	50.67	30.83	**23.14**	**54.09**	**39.675**
FeO+MnO	39.82	43.61	48.16	38.84	33.03	57.3	53.79	40.76	56.25	38.56	**33.03**	**57.3**	**45.012**
Ba	1020	988	890	1022	982	680	789	1008	744	388	388	1022	851.1
Rb	15	16	20	15	21	18	17	19	15	22	15	22	17.8
Sr	33	48	26	21	27	19	23	29	44	34	19	48	30.4
Pb	4	5	4	8	10	7	6	7	5	12	4	12	6.8
W	2	6	3	4	2.8	7	6	5	10	8	2	10	5.38
Zn	5	7	6	6	3	3	2	8	8	6	2	8	5.4
Ni	5	7	4	2	2	8	12	10	8	9	2	12	6.7

Cr	111	122	130	109	98	77	80	123	132	94	77	132	107.6
Co	10	12	11	15	21	12.8	15	18.3	14	18	10	21	14.71
V	4	8	8	9	12	11	14	15	20	16	4	20	11.7
Bi	12	24	36	31	37	28	29	44	31	26	12	44	29.8
Se	11	15	11	17	15	16	12	10	9	25	9	25	14.1
Cu	2	21	10	7	13	7	6	12	15	4	2	21	9.7
Hg	23	12	54	43	60	103	111	76	43	33	12	111	55.8
Hf	2	3	15	4	3	8	12	9	6	10	1.5	12	7.2
Ag	100	87	66	78	79	88	108	111	97	33	33	111	84.7
As	22	17	24	8	14	12	22	19	13	11	8	24	16.2

Table 2: Comparison of average concentration (ppm) of Trace Element of Tajimi BIF, other BIF in Nigeria and other part of the world

Elements	Tajimi BIF Present study	Maru BIF	Wonaka BIF	Kazaure FMP	Algoma-type BIF	Lake Superior BIF	Orissa BIF	Manas Garais Itabirite
Ba	(388-1023) 851.1	293	1103	4651.3	170	180	70	179
Rb	(15-22) 17.8	20	8	71.74	ND	ND	ND	ND
Sr	(19-48) 30.4	51	25.9	183	ND	ND	ND	ND
Pb	(4-12) 6.8	<10	ND		ND	ND	ND	ND
Zn	(2-8) 5.4	26	204	558.9	33	2	ND	ND
Ni	(2-12) 6.7	<10	456.75	440	83	32	15	20.3
Cr	(77-132) 107.6	23	140.5	354	78	122	30	28.5
Co	(10-21) 14.71	100	15	427.7	38	27	36	69
V	(4-20) 11.7	44	145.6	816.4	97	30	30	35
Cu	(2-21) 9.7	<10	261.75	316.	96	10	10	22
Mn	40930	37408	35175	2635	1400	4600	120	1785
Ti	8544	959	3158	7538	860	160	40	216.6

Source: Adekoya, 1998, Muhammed, 2014, Ibrahim, 20118

Table 3: Comparison of Tajimi Iron ore with some other Nigeria Iron Ore Formation

S/No	Author/year	Deposits	Fe	Fe_2O_3	SiO_2	Al_2O_3	TiO_2	MnO	MgO	CaO	Na_2O	K_2O	P_2O_5	SO_2
1	Muhammad, 2014	Wonaka	29.17	41.67	50.75	5.29	0.87	4.37		0.48	0.02	0.03		
2	Adekoya, 2012	Muro	33.58	47.98	50.33	0.1	0.01	0.06-	0.01	0.01	0.01	0.01	0.15	---
3	Adekoya, 1998	Birnin Gwari	40.42	57.75	30.55	3.78	0.12	5.63	0.01	0.50	0.01	0.13	0.07	---
4	Adekoya, 1998	Maru	40.88	58.41	26.21	3.69	0.20	7.60	0.01	0.16	0.05	0.01	0.13	---
5	Ibrahim, 2018	Kazaure	39.47	56.39	25.55	11.3	1.88	0.34	2.14	0.86	0.86	1.22	0.09	---
6	Imurana & Harana, 2017	Konto Karfe	47.43	67.81	16.98	12.49	0.125	0.2	0.34	0.178	---	---	0.98	0.15
7	The present Study	Tajimi Iron Ore	35.71	51.05	17.71	14.88	2.13	5.34	2.88	0.68	1.19	1.75	1.22	1.10

Table 4: Major Elements and minerals of Interest in Assessing Iron Ore Quality for Steel Production (After Abraham J. B *et al.,* 2012 Ahmed *et al.,* 2017**)**

Components	Fe			SiO_2	Al_2O_3	P	S
Content (%)	< 58	62 - 64	> 65	< 6	3 - 4	0.05 - 0.07	0.1
Tajimi iron ore	35.71			17.71	14.88	0.536	0.448
Grade	Low	Medium	High				

Reference

Abraham, J. B., Andrey, V. K., Joseph, K. B., & Par, G. J. (2012). "Characterization of Chemical Composition and Microstructure of Natural Iron Ore from Muko Deposits" *International Scholarly Research Network ISRN Materials Science Volume* 2012, Article ID 174803, 9 pages doi:10.5402/2012/174803. 2012.

Adekoya, J. A., Okonkwo, C. T., & Adepoju, M. O. (2012). Geochemistry of Muro Banded Iron- Formation, Central Nigeria. *International Journal of Geosciences*, 3, 1074-1083.

Adekoya, J. A. (1998). The geology and geochemistry of the Maru Banded Iron Formation, northwestern Nigeria. *Journal of African Earth Sciences 241*

Adekoya, J. A. (1996). The Nigerian Schist belts: Age and depositional environment implications from associated banded iron-formations. *Journal Mining and Geology*, 32: 27–46.

Ajibade, A.C. (1976). Provisional classification and correlation of the schist belts of northwestern Nigeria. In: Geology of Nigeria, C.A. Kogbe (Ed.). Elizabethan Publishing Co., Lagos, pp. 85-90.

Ahmad, I. H., Umar, S. U., Abdullahi, A. M., & Maude, K. A. (2017). "Geochemistry and Economic Potential of Jaruwa Iron Ore, NW- Nigeria*", Imperial Journal of Interdisciplinary Research*. Vol. 3, Number 3, 2017, pp 1067

Barbosa, A. L. M. and Gross Sad, J. H. (1973). Tectonic control of sedimentation and trace element distribution in Ores of Central Minas Gerais (Brazil). In: Genesis of Precambrian iron and manganese deposits, Proceedings of Kiev Symposium, 1970. Earth Sciences, 9, 1 25-1 31 .Unesco, Paris

Bonatti, E., Kraemer, T., Rydell, H. 1972. Classification and genesis of submarine iron manganese deposits In Horn, D.R. (E.d.), Conference of Ferromanganese Deposit on the Ocean Floor. Harriman New York, Anden House. Pp. 149-166

Ferenczi P. (2001). Iron ore, manganese and bauxite deposits of the Northern Territory. Report - Northern Territory Geological Survey.

Gole, M. J. (1981) . Archean banded iron-formations, Yilgarn Block, Western Australia. Economic Geology 76, 1 9541 974 Gross G.A, (1993). Industrial and genetic models for iron ore in iron-formations: in Kirkham RV, Sinclair WD, Thorpe RI and Duke JM (editors) *'Mineral Deposit Modelling.' Geological Association of Canada*, *Special Paper* 40. 151-170.

Holt, R., Egbuniwe, I. G., Fitches, W. R. and Wright, J. B. (1978). The relationships between low-grade metasedimentary belts, calc-alkaline volcanism and the Pan African orogeny in NW Nigeria. *Geological Rundsh*, 67(2): 631-646.

Ibrahim, A. A (2018). "Ferruginised Metapelites of The Kazaure Schist Belt, Northwestern Nigeria " *Nigerian Journal of Basic and Applied Science* (June, 2018), 26(1): 106-114

Ibrahim, A. A. (2008). Petrography, geochemistry and origin of iron formations of the Kazaure Schist belt. NW Nigeria. *Journal Mining and Geology*, 44(1): 13–20.

Ibrahim, A. A. (2003). The geology and geochemistry of Kazaure Banded Iron Formation. NW Nigeria. *Unpubl. M.Sc. Thesis, A.B.U. Zaria*, p.89 Nigeria. *Journal of Mining and Geology*, 29: 63-76.

Imrana, A. & Haruna., I.V (2017). Geology, Mineralogy and Geochemistry of Koton-Karfe Oolitic Iron Ore Deposit, Bida Basin. Kogi State, Nigeria. *International Journal of Scientific & Technology* Research Volume 6, Issue 08, August 2017

James, H. L. (1966). Data of Geochemistry, 6th Edition, Chemistry of the iron-rich sedimentary rocks. U. S. Geological Survey Professional Paper 440-W, 61 p. Washington DC, USA.

Mucke, A., (2005). The Nigeria manganese rich iron –formation and their host rocks from sedimentation to metamorphism. *Journal of Africa Earth Science 41*

Mucke, A., Annor, A. & Numann, U., (1996). The Algoma-type iron formation of the Nigerian metavolcano-sedimentary schist belts. *Mineral. Deposita*, 28, pp. 136-145

Muhammad A. U., (2014). Geology and Geochemistry of Rocks and Banded Iron Formation of Northern Part of Wonaka Schist Belt, Northwestern Nigeria. Unpublished Msc thesis. A B U Zaria

Olade, M. A. (1978). General Features of a Precambrian Iron Deposit and its Environment at Itakpe Ridge Okene, Nigeria. *Transactions of Institution of Mining and Metallurgy, Section*, 87, pp. 8

Oyelowo, B., Gbenga, O. Razak M., & Simeon, O. *(*2016) Geophysical prospecting for iron ore deposit around Tajimi village, Lokoja, North–Central Nigeria

Truswell, J. F. & Cope, R. N. (1963). The geology of parts of Niger and Zaria Provinces, Northern Nigeria. Geological Survey, Nigeria Bull 29:1–104.

Geochemical Evaluation of Afuze Coal, Anambra Basin, Nigeria

Sylvia Emalu Alemoh[1] and Usman Shehu Onoduku[2]
Department of Geology, Federal University of Technology, Minna [1, 2]
sylvalem@yahoo.com (+2347063311055) & onoduku.usman@futminna.edu.ng
(+2348035904399)

Abstract
This research is about investigating the proximate and ultimate analyses of Afuze coal in Anambra Basin. The study area is located at Ovbiowu community in Edo State. The geochemical analysis results were achieved by Coal sampling and various laboratory methods. The proximate result reveals average moisture content of 15.20%, volatile matter of 48.42% and ash content of 19.89% with fix Carbon of 16.42%. The ultimate analysis result showed the presence of C (42.16%), H (4.44%), N (1.16%), Al (0.23%), Si (1.37%), S (1.02%), Fe (1.16%), and Ca (0.24%) as major elements while trace elements are Ti (1610ppm), V (36ppm), Cl (110ppm), Sr (20ppm), Zr (42ppm) and Cd (20ppm). The correlation of Fix Carbon and other parameters shows that Fix Carbon strongly correlates with Moisture Content, and correlates negatively with Volatile Matter and Ash. The proximate results rank the Afuze coal as sub-bituminous coal grade. The value place the Afuze coal at a disadvantage for metallurgical coking coal however; favours its usage as feed for coal power systems and possibly liquefaction. The ultimate data indicates that Cd and Ti have high concentration in the Afuze coal while the other elements are low in content.

Keywords; Afuze Coal, Anambra Basin, proximate and ultimate characteristics, Sub- bituminous

1.0 Introduction

Coal is a black or brownish-black combustible fuel found in sedimentary rock. It is composed mainly of organic elements such as Carbon, Hydrogen and Oxygen, and other constituent including Nitrogen. Globally, coal is one of the leading commodities in terms of industrial importance and monetary value, but not popularly utilized due to its low patronage occasioned by the much emphasis on petroleum.

The aim of this research is to ascertain the geochemical qualities of the Afuze Coal using Proximate and Ultimate analyses and to establish their suitability as industrial minerals.

The objectives of this research include:

i. To collect Coal samples for the study area.
ii. To conduct Geochemical analyses of the Coal samples in order to establish their Proximate and Ultimate Characteristics.
iii. To ascertain the possible uses of Afuze Coal.

2.0 Geological setting

The study area is located within Ovbiowu- Emai clan a village around Afuze in Owan-East Local Government area of Edo State. The study area lies within Latitude 07º1'0"N and 7º2'45"N and Longitude 06º1‘30"E and 6º2'45"E.

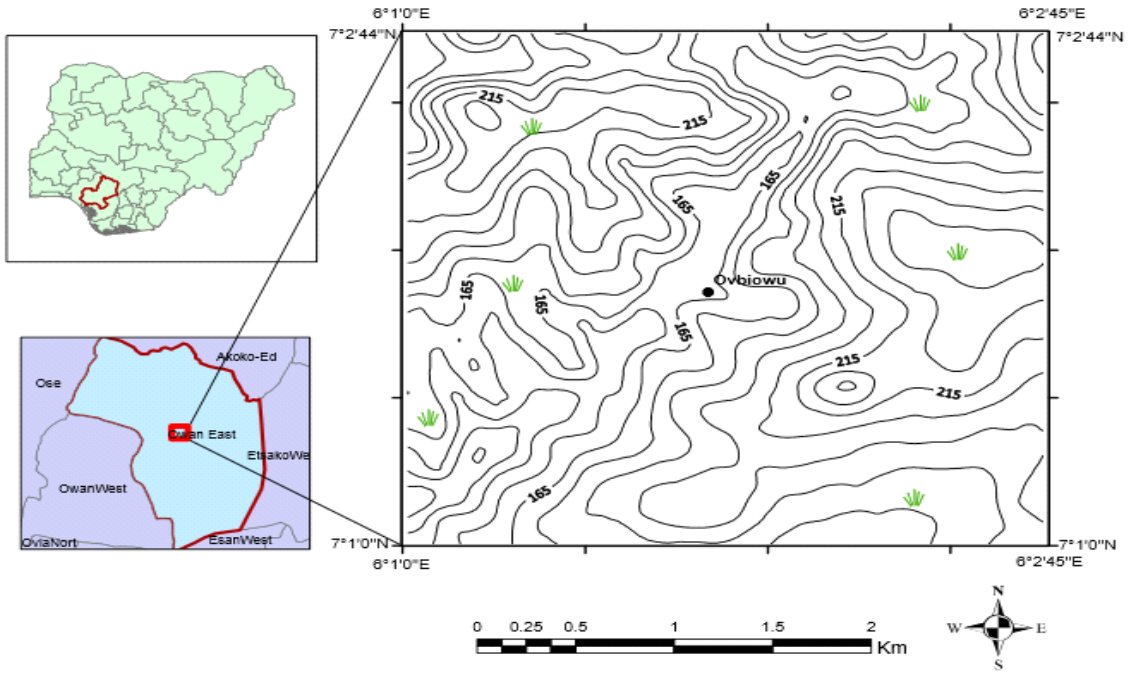

Figure 1: Topographic Map of the Study Area, Adopted from OSGoF, 2019

3.0 Research Methodology

Methods for this research include:

i. Field sampling and collection of Coal samples
ii. Laboratory analyses

3.1 Field work and sampling

The geographic coordinates were identified and marked on the base topographic map, a global positioning system (GPS) was used to take and record the spatial data of each location. Coal samples were with the aid of a hammer and chisel and prepared for laboratory analyses.

3.2 Laboratory analyses

Different methods of laboratory analyses were carried out for specific parameter depending on the nature of the analysis involved. Coal is a special geo-material whose analyses are very wide and are parameters depended.

i. Proximate analysis
ii. The Ultimate analysis

The proximate result which includes the Moisture (MC), Volatile Matter (VC), Fixed Carbon (FC) and Ash of the Afuze Coal reported on as received basis is presented in Table 1 & Figure 2.

The ultimate results which consist of the elemental characteristics such as Carbon, Hydrogen, Nitrogen and Sulphur are expressed in Table 2 and Figure 2.

4.0 Results and Discussion

4.1 Field results

The Proximate and Ultimate analyses of the Afuze (Ovbiowu) Coal samples were established as shown in Tables (1 and 2) below.

The economic potential of the Coal deposit was established based on the analyzed geochemical characteristics of the Coal.

Table 1: Proximate analysis result of Afuze (Ovbiowu) Coal

	Parameters (As received basis)			
Sample Names	MC(Wt%)	VM(Wt%)	Ash (Wt%)	FC(Wt%)
AFZC 1	14.5	47.38	19.3	18.28
AFZC 2	13.3	49.72	20.65	16.28
AFZC 3	15.6	49.27	20.12	14.85
AFZC 4	16.77	48.2	17.89	25.11
AFZC 5	15.3	48.07	21.06	15.31
Average	15.09	46.89	19.08	18.04
Minimum	13.3	47.38	17.89	14.85
Maximum	16.77	49.72	20.65	25.11

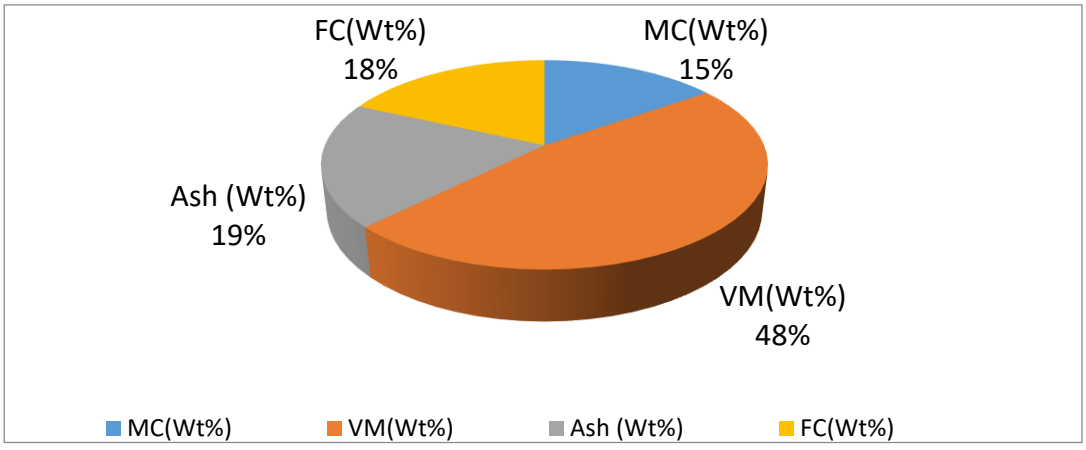

Figure 2: Pie Chart showing the concentration of the proximate parameters

The Moisture Content falls within the acceptable value range of 10% to 45% for sub-bituminous Coal. The Ash and Fixed Carbon contents are low when compared with other Nigerian coals. The moisture content of the Afuze coal is high compared to Okaba 5.99 %) and Ogboyoga (6.93 %) coal.

Table 2: Ultimate analysis result of Afuze Coal

	Parameters (Calculated)			
Sample Name (Wt%)	Carbon (Wt%)	Hydrogen (Wt%)	Nitrogen (Wt%)	Sulphur (Wt%)
AFZ C 1	41.99	3.98	1.13	1.41
AFZ C 2	42.85	4.59	0.95	1.16
AFZ C 3	39.79	3.85	1.15	1.39
AFZ C 4	43.71	3.96	0.92	1.29
AFZ C5	39.84	3.63	1.1	1.45
Average	41.63	4.43	1.05	1.34
Minimum	39.79	3.63	1.1	1.29
Maximum	41.99	4.59	1.15	1.45
Lignite- Sub- bituminous Coal rank	65-76	5	1	1

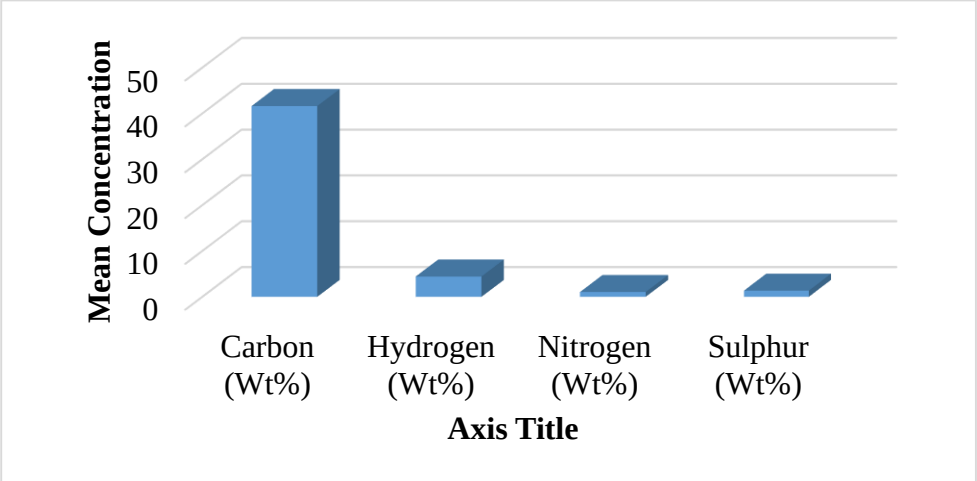

Figure 3: The distribution of the Ultimate parameters of the Afuze Coal

Carbon (C) has an average value of 41.63 % closely favours the 65-76 % range classification of the Lignite-Sub-bituminous coal rank. The hydrogen (H) content of the Afuze coal varies from 3.63 % to 4.59 % with an average content value of 4.43 % (Table 2). The Nitrogen (N) content ranges between 1.1 % and 1.15 % with an average value of 1.05 %. And Sulphur (S) has an average value of 1.34%.

Table 3: Concentration of Major (%) Elements in Afuze Coal and their Enrichment/Depletion

Sample No	Al (%)	Si (%)	S (%)	Fe (%)	K (%)	Ca (%)
AFZC 1	0.181	1.464	0.988	1.03	BDL	0.23
AFZC 2	0.183	1.51	1.025	1.024	BDL	0.24
AFZC 3	0.21	1.03	0.759	0.84	BDL	0.231
AFZC 4	0.39	1.763	1.53	1.77	0.05	0.28
AFZC 5	0.149	1.095	0.79	1.14	BDL	0.213
Average	0.223	1.372	1.0182	1.16	NC	0.238
World Coal Average	1	2.8	2	1	0.01	1
EDF	0.23	0.49	0.51	1	NC	0.24

BDL-below detection limit, NC- Not computed
World Coal Average (Ketris and Yudorich, 2002)
EDF-Enrichment/depletion factor is the relationship between the identified elements in the Coal to the World Coal Average

Table 4: Concentration Trace (ppm) Elements in Afuze Coal and their Enrichment/Depletion

Sample Number	P (ppm)	Ti(ppm)	V (ppm)	Cr (ppm)	Mn (ppm)	Cl (ppm)	Sr (ppm
AFZC 1	BDL	146	28	BDL	BDL	85	20
AFZC 2	218	164	42	BDL	198	90	15
AFZC 3	BDL	139	33	BDL	BDL	195	25
AFZC 4	487	223	45	34	BDL	125	22
AFZC 5	BDL	134	29	BDL	205	55	18
Average	NC	1611	35.4	NC	NC	110	20
World Coal Average	220	500	22	15	100	120	130
EDF	NC	3.22	1.64	NC	NC	0.92	0.15

BDL-below detection limit, NC- Not computed

World Coal Average (Ketris and Yudorich, 2002)

EDF-Enrichment/depletion factor is the relationship between the identified elements in the Coal to the World Coal Average

From Table 3, the content of Al ranges from 0.151% to 0.395% with a median value of 0.22 % for the Coal samples. The value is less than the world average limit of 1% which implies that there was a limited supply of Al source materials into the Coal environment. Also, comparison of the Al enrichment/depletion (EDF) value with the limits of Ruch *et al.* (1974) confirms that the element is low in the Afuze Coal (Table 3). The Si content of the Afuze Coal varies between 1.031% and 1.76% with average value of 1.37%. In comparison with the world Coal average of 2.8%, the element is considered to be in low concentration. The enrichment and depletion (EDF) of 0.49 further justifies the low concentration of the element in the Coal because the element falls within the depleted group of elements in Table 3 Sulphur concentration in Afuze Coal varies between 0.763% and 1.533% with a median value of 1019%, and when compared with the world Coal average of 2%, this concentration is low. Also, the enrichment and depletion (EDF) value of 0.51% when compared with the limit values in Table 3 ascertained that S is depleted in the Afuze Coal.

Table 5: Correlation of Fix Carbon against other parameters of Afuze Coal

	MC (Wt%)	VM (Wt%)	Ash (Wt%)	FC (Wt%)
MC (Wt%)	1			
VM (Wt%)	-0.3515	1		
Ash (Wt%)	-0.61731	0.392819	1	
FC (Wt%)	0.583711	-0.36367	-0.92665	1

The Fix Carbon was correlated against other parameters such as Volatile Matter, Moisture Content and Ash, it shows that Fix Carbon strongly correlates with Moisture Content, and correlates negatively with Volatile Matter and Ash.

5.1 CONCLUSIONS

The aim of this research is to ascertain the geochemical qualities of the Afuze Coal using Proximate and Ultimate analyses. The proximate result revealed that the Afuze Coal have the average Moisture content 15.09%, Volatile matter 46.89 %, Ash 19.08% and Fixed Carbon 18.04% respectively. The ultimate result showed the presence of Carbon (41.63%), Hydrogen (4.43%), Nitrogen (1.05%), and Sulphur (1.34%). These content value places Afuze Coal as sub-bituminous Coal. The percentage weight of total Carbon (C) varies from 39.79% to 41.99% with an average value of 41.63% (Table 2). The result favours the usage of the Afuze Coal as feed for power generation and domestic energy but unsuitable for metallurgical coke production.

5.2 RECOMMENDATION

Based on the outcome of the research work, it is recommended that the government should equally diversify the economy by not only relying on petroleum but investing in the solid mineral sector.
From the result of the study, it is recommended that Afuze Coal is suitable for power generation and domestic energy.
However, subsequent research should be conducted and that more evaluation indices namely ash chemistry, heating value, vitrinite reflectance, free swelling index, grindability, specific gravity, lithostratigraphy and petrographic studies be conducted through the use of advanced analytical techniques to satisfactorily rank and postulate other technological benefits of the Afuze Coal.

REFERENCES

Adedosu, T. A., Adedosu, H. O. & Adebiyi, F. M. (2007). Geochemical and mineralogical significance of trace metals in Benue Trough coals, Nigeria. *Journal of Applied sciences* 7, 3101-3105.

Adekunle, J. O., Ibrahim, J. S., & Kucha, E. I. (2015). Proximate and Ultimate analysis of biocoal briquettes of Nigeria's Ogboyoga and Okaba sub-bituminious coal. *British Journal of Applied Science and Technology*, 7,123.

Braide, S. P. (1992). Geological development, origin and energy mineral resources potential of the Lokoja formation in the Southern Bida Basin. In: Nwajide, C. S. (Ed.), *Geology of Nigeria's Sedimentary Basins. Lagos*, CSS Press.

Ezeh, E. & Okeke, O. (2016). Proximate and ultimate analysis of some Nigerian coal deposits. *British Journal of Environmental sciences*, 4, 34-38. Retrieved on April 18, 2017 from http://www.eajournals.org.

Femi, B. F., & Yomi B. G., (2013). Appraisal of the economic geology of Nigerian coal resources. *Journal of Environment and Earth Science*. 3, 25-31. Retrieved on March 05, 2021 from http:// www.iiste.org.

Goodarzi, F. (2002). Mineralogy, elemental composition and modes of occurrence of elements in Canadian feed-coals In: Vassileva, C. G., Baxter, D., and Andersen, L. K. (Eds.), *Relationships between chemical and mineral composition of coal and their potential applications as genetic indicators. Part 1. Chemical characteristics of Geological Balcanica*, 39, 21-41. Retrieved on May 20, 2021 from http://www.geology.bas.bg.

Isaiah, A. M., Seyi, A. S. &Ita, O. B. (2015). Instrumental neutron activation analysis (INAA) of high ranking Nigeria coals from Enugu and Okaba, *International Journal of Scientific Research and Innovative Technology*, 2, 60-69. Retrieved on May 13, 2021 from http://www.ijsrit.com.

Ketris, M. P. & Yudovich, Y. F. (2002). Estimations of Clarkes for carbonaceous biolithe: World averages for trace element contents in black shales and coals. *International Journal of Coal Geology*, 78, 135-148. Retrieved on April 4, 2021 from http://www.researchgate.net/ publication/222079407.

Wright, J. B., Hastings, D. A., Jones, W. B., & Williams, H. R. (1985). Geology and mineral resources of West Africa. In: Nwajide, C. S. (Ed.), *Geology of Nigeria's Sedimentary Basins*, Lagos, CSS Press

ASSESSMENT OF PARENTS PERCEPTION OF IMMUNIZATION SERVICES IN GOMBE LOCAL GOVERNMENT AREA OF GOMBE STATE, NIGERIA

Sani Dayyabu, Mohammed Isma'il, Bilkisu Yayaji Ahmed and Sunday Acha
Department of Geography, Federal University of Kashere, Gombe State, Nigeria
Department of Geography and Environmental Management, Ahmadu Bello University, Zaria
Department of Geography, Gombe State University, Gombe, Nigeria
Department of Geography, Federal University of Technology, Minna, Niger state, Nigeria
Email: sdayyabu29@gmail.com, migeogjameel@gmail.com and
bilkisuyayajiahmed68@yahoo.com

ABSTRACT

Immunization is the administration of antigen in the form of a vaccine, to produce an immune response to the body so as to protect it against future exposure to illness. Immunization is one of the most cost-effective child endurance interventions that are accomplished all over the world. All countries in the world have an immunization programme to distribute chosen vaccines to the targeted beneficiaries, particularly focusing on pregnant women, infants and children, who are at a high risk of diseases preventable by vaccines. This research provides reasonable information on the Assessment of parent's perception of immunization services in Gombe Local Government Area of Gombe state, Nigeria. 400 parents were randomly interviewed and systematic sampling technique was used to obtain streets and housing samples. Descriptive statistics of mean/standard deviation and frequency was used to analyze data obtained from the field. The Results show that the parents perception on immunization uptake in Gombe is categorized in to 6, the first category carries the highest score which shows that almost all parents perceived Immunization as a way of child development and a good service for the general health condition of children in Gombe Local Government Area with the mean score of 4.23 & 4.39 respectively. Further information on perception revealed that parents looked at immunization as the way of reducing population growth 3.48, and others does not patronizes it due to their nature of occupation (3.03), some is because it is against their culture (3.06), some believe that it reduces population growth (3.48) and others deny immunization due to religious beliefs (3.37). Regarding the level of immunization in Gombe, it was observed that about 70% of the parents of children 0-23 months of age carry their children to immunization which is more than half of the population in the study area; therefore, the level of immunization uptake in Gombe is very high. The study recommends that: Government should improve awareness campaigns and empowerment of parents especially women/caregivers of the children 0-23 months of age in the study Area. Additional Health care facilities should be constructed around some Areas of the Political wards for effective Immunizations service delivery to avoid congestion and waste of time to the mothers/caregivers, Government should also encourage formal Education to higher levels as it is one of the factors that influences immunization uptake, the masses in the local government Area should be enlightened on the present situation of immunization and to be encouraged on its compliance so that level of perception will be increased and secondary data should be made available for future investigations, Government should employ additional manpower for efficient and easy immunization services, easy networking systems should be provided for easy report of monthly, quarterly or annual immunization status to the Federal capital territory Abuja, Available power supply should be ensured to avoid vaccine spoilage in refrigerators and Lastly further researches on morbidity are encouraged in the Gombe local Government Area of Gombe state.

Key Words: Perception, Parents, Immunization and Services.

INTRODUCTION

Immunization remains one of the most successful and cost-effective public health interventions for disease prevention. It has been estimated that the Expanded Programme on Immunization (EPI) in low and middle-income countries (LMICs) has prevented more than two million child deaths since

its initiation in 1974. Although, Africa has made some progress in immunization services, large numbers of children remain unvaccinated and under-vaccinated. Only a quarter of eligible children in Nigeria receive all recommended vaccinations. This is well below the 90% level of coverage recommended by the World Health Organization (WHO) for the sustained control of vaccine-preventable diseases (VPDs) (Oku et. al, 2017). Some of the reasons for Nigeria's consistently low immunization coverage rates include mothers' poor knowledge of immunization, leading to low confidence and lack of trust concerns about immunization safety; long distances to and long waiting times at health facilities; and poor attitudes and skills of health workers (Oku et. al, 2017). Some of these problems are linked to gaps in communicating vaccination information. Several studies suggest that parents' good understanding of vaccine-preventable diseases, how vaccination works and the vaccination schedule contribute to children being vaccinated (Oku et. al, 2017).

Children are the future of any country, so their development is as significant as the development of other assets, immunization is a vital part for the proper development of the children, it plays a fundamental role in the children's lives as a protective health action because it protects them from most dangerous childhood diseases, its process will become more successful if the child receives all the required doses (Sourabh, 2016). Over two million deaths of infants below five years are averted through immunization every year (Tilottama and Madulekha, 2013). According to World Health Organization (WHO, 2010), an estimated 18.7 million infants globally are still missing out on essential vaccines. In researches from some parts of Africa, vaccine preventable diseases is still a root of childhood mortality, estimated at three million death every year (Ibnouf, Van den Borne and Maarse, 2014).

Many developing countries had difficulty in ensuring that children received prescribed course of immunizations and Nigeria inclusive, the United Nations Children's Fund (UNICEF) has regarded immunization as an important component of child survival programms (WHO Bulletin, 2018). According to Adetukunbo (2007), immunization of children is one of the most cost effective public health interventions. The ultimate goal of immunization is eradication of diseases globally. Tinashe (2015) reiterated that others refused immunization based on religious beliefs. Some groups of parents consider compulsory vaccination as undesirable act of undermining individual rights (Brown, Oluwatosin and Ogundeji, 2015). This is because of poor understanding and provision of immunization services (Regmi, 2015). Nigerian Demographic and Health Survey (NDHS, 2018) report revealed that there is very low coverage of immunization service in the country, and the poor rates recorded are due to some factors mentioned in some studies like Kabir and Ahamadu (2016) found that numerous factors like inadequate knowledge of vaccination, lack of proper locations, lengthy waiting time, conveyance problems, inadequate medical amenities and poor incentive slowed down even acknowledgement of the goals of immunization packages, also Rasheed (2017) exposed that socioeconomic aspects like income status, occupation, poor health amenities and incentives also hindered and caused variations in utilization of immunization services. Similarly, socio demographic factors like mother's age, child gender, marital and educational conditions of the mother were considered to be the factors influencing immunization services. These influences cut across all states and are mostly found in the northern region of the country (Rasheed, 2017). Data from the 2018 National Demographic and Health Survey (NDHS), revealed that children whose mothers have no education are more likely to die young (170 deaths per 1000 live births) than children whose mothers have more than secondary education (56 deaths per 1,000 live births), also under five mortality is more than 3 times higher among children in the poorest households (173 deaths per 1,000 live births) compared to children in the wealthiest households (53 deaths per 1,000 live births). As children develop they are exposed to many risks, one of these risks being infections most of these will cause mild illnesses, however, despite great medical advances, infection can still cause severe illness, disability and, at times, death (Kabir and Ahamadu 2016). Before the introduction of global immunization, out of estimated 125million children born worldwide every year, approximately 12 million or nearly 10% die before the age of one, 97% of the deaths occurring

in the developing countries and Nigeria inclusive. Also over 800,000 newborn babies died from neonatal Tetanus and over 275,000 children in the developing world were affected by paralytic polio every year in most cases before the age of 3years, tuberculosis had as many as 10million victims every year, and most of the affected children are under the age of 5 (WHO Bulletin, 2018). It is estimated that out of every 1000 Nigerian children born, 187 will die before their fifth birthday, measles alone accounting for about 50% pertussis 600,000 deaths annually, neonatal tetanus 800,000 deaths, with a case fatality rate of about 85% occurring every year with few deaths but polio is now reduced drastically (WHO Bulletin, 2018). In Nigeria, the trends in vaccination coverage revealed that children aged 12-23 months with no vaccinations from 1990 were 36%, 2003 27%, 2008 29%, 2013 21%, and in 2018 is 19%, also all basic vaccinations coverage has gradually increased from 29% in 1990 to 31% in 2018 which is inadequate (NDHS, 2018).

Gombe state is experiencing influx of people since when it was created, this leads to increase population with diverse societies especially in the Gombe Local Government Area which serve as the capital of the state (GSPHDA, 2019). It was reported by the World Health Organization (WHO,2018) that Gombe state recorded less than 50% coverage of immunization due to numerous factors which include cultural and religious beliefs, poor records keeping, poor outreaches and little awareness to the parents of the 0-23 months children. Furthermore, according to Gombe Local Government Area Primary Healthcare Department (GLGPHCD, 2019) revised report states that in 2018, out of the 506,129 0-23 month's children, more than 2/3 are not immunized in the area which is below the expected target. Among the principal causes of mortality and morbidity in Gombe Local Government Area are vaccine preventable diseases, pneumonia, tuberculosis, and neonatal tetanus (Gombe State Ministry of Health, 2010). According to Nigerian demographic and health survey (2018), north eastern part of Nigeria is one of the regions in the country with the second highest total fertility rate (TFR) with 6.1 live birth per woman, and Gombe state emerged the second highest with TFR of 6.6 live births per woman in the region, Furthermore, Verbal and Social Autopsy Study (2019) shows that north eastern region emerged second to the last with children reported to have received at least one immunization with 59.5%. Nigerian Demographic and Health Survey (2018) also shows that Gombe state emerged the least in terms of all age appropriate vaccination with just 6.1% in north east and recorded the highest with children with no vaccination of 34.4% in the region. NDHS, (2018), again proved that in the whole country Gombe state emerged the fourth least with children with no vaccination, hence, this will be one of the reasons why the state recorded the highest number of infant and child mortality in north east with 189 deaths per 1000 live births, because immunization is one of the indicators used to monitor progress towards reduction in child morbidity and mortality. Therefore what are the reasons behind high mortality rate in the area, perhaps, misperception of immunization by the parents of children contributed on the setback of full child immunization in the study area while the immunization is a key fundamental element of public health and prerequisite to social and economic development, and a crucial element that enables every child to reach his or her full physical and intellectual potential (Oyefara, 2014). Ahmed (2016) studied the spatial analysis of tuberculosis spread in Gombe Local Government Area of Gombe state, the study applied GPS in collecting the coordinates of the Health centers and used nearest neighbor analysis to examine the TB spread in the area, the study revealed that lack of access to healthcare centers, public education on TB, are the major causes of Tuberculosis disease in Gombe Local Government area. Muhammad (2016) studied spatio temporal analysis of polio cases in Kaduna central senatorial zone both primary and secondary data were used, his results shows that polio cases have been declining within the study area from 2006-2014 due to the wider immunization coverage. Osowole and Obute (2001) studied parents' awareness and perception of the polio eradication programme in Gombe Local Government Area, Gombe state they employed Focus Group Discussions in the data analysis, their result showed that lack of advocacy and reluctance in releasing children for polio immunization were the major problems causing polio outbreak in the Area. Mihigo et al., (2017), studied challenges of immunization in the African region and used both primary and secondary data, their result showed that issues of sustainable funding and resources for immunization, vaccine stock outs

and logistics, data issues and laboratory infrastructure, are the major problems of immunization in the African region.

However, most of the above reviewed literatures shows less attention was paid to Gombe and any study on population characteristics in relation to immunization in Gombe is paramount important due to the current changes that are taking place in the area. Furthermore, most of the reviewed literatures focused on either some vaccine preventable diseases like tuberculosis, polio, Measles etc, as an entity but this study looked at the perception of immunization services in general perspective in Gombe. The study further investigates the level of immunization in Gombe L.G.A. the study does not focused on salary earners only but to all parents of 0-23 month's children in the LGA. In view of the above challenges of Immunization services in Nigeria and Gombe in specific, research of this kind is very important in order to investigate the parental perception and level of immunization in \\\Gombe Local Government.

Aim and Objectives

The aim of this research is to provide empirical information on the Parental perception of immunization services in Gombe Local Government Area of Gombe state, Nigeria.

1. To assess parent's perception on immunization in Gombe Local Government Area.
2. To determine the level of Immunization in Gombe L.G.A.

THEORETICAL FRAMEWORK/IMPORTANCE OF IMMUNIZATION

The benefits or importance of child immunization can never be over emphasized as it protects children from vaccine preventable diseases and most importantly eradication of morbidity and reduction of mortality rates around the globe World Health Organization (WHO, 2010).

An overwhelming majority of health professionals, medical researchers, and professional medical organizations (such as the American Academy of pediatrics and the American Academy of family and practice Physicians) recommend immunization. Getting immunized is important for at least two reasons: To protect yourself and to protect those around you. Vaccines are the best way we have to prevent infectious disease. Successful immunization depends on the cooperation of every person World Health Organization (WHO, 2010).

According to Health Belief Model of Charles Abraham (1975) and Anti-vaccine conspiracy theory of Daniel Jolly and Karen Douglas (2014), people are motivated to take care of their health and family members before considering other material needs. They consider health as a fundamental aspect of which without it nothing can go okay in all humans' endeavors. The later theory of Douglas emphasize on the issues that may cause barriers to vaccine uptake which are detrimental to the children health conditions, while the first one of Charles Abraham shows how perception of parents or people in general influences vaccine uptake, it emphasizes that humans are to think positively before actions, meaning that people should not misrepresent immunization as a negative way of causing backwardness to population (Rosensetock, 1995).

Barriers to successful vaccination

According to Carlos Vallbona Adapted from Orenstein et, al. theory (1993), four key types of known barriers to successful vaccination can be identified: Missed opportunities for administering vaccines, shortfall in the healthcare delivery system, inadequate access and incomplete public awareness or motivation to ask for immunization. This theory is related to this research, because parents of the 0-23 month's children in Gombe are characterized with some of the stated barriers like the inaccessibility, missed opportunities of vaccination, vaccine stock outs and the rest.

Similarly, the American Academy of pediatrics suggested that the following barriers:

- ✓ Awkward and inconvenient locations and hours at clinics where vaccinations are given;
- ✓ Long waiting line at these clinics.

- ✓ Shortage of clinic personnel and resources.
- ✓ Lack of education/awareness of the importance of timely vaccinations on the part of the parents.
- ✓ Cost.
- ✓ Personal fears of inflicting or receiving "pain" and inadequate knowledge of the risks of vaccination.
- ✓ Lack of "walk-in" clinic vaccination facilities.
- ✓ Requirement of physical examination or physician referrals before vaccination
- ✓ Religious beliefs are also a potential barrier to herd immunity.

METHODOLOGY

In every study to be conducted there must be proper methods to be used in conducting it, hence this research involves the use of qualitative and quantitative techniques that were sourced from both primary and secondary data. The primary data were collected through field observations and interviews from parents of children 0-23 months of age, while the secondary data were obtained from existing literatures which include records from: Gombe state ministry of health, Gombe Local Government Primary Healthcare Development Agency (GSPHDA), Independent National Electoral Commission manual, Gombe Local Government Primary Healthcare Department, and other published and non published materials. This study also involves the use of 506,129 0-23 months children as sampling frame in the study Area according to Rew micro plan records of Gombe Local Government Area, Primary Health care Department (2018), in which 400 was used as sampling size which was derived through the use of Yamane (1967) formula. Data collection was obtained through the use of both simple random and systematic sampling techniques. Simple random was used to obtain the streets samples and the first house in each sampled street, while systematic sampling technique was used to obtain the remaining sample houses in each sampled street by the use of dice to determine the sequence of intervals of houses to be skipped in each sampled street. However, numbering was used in counting houses and streets from which the samples were derived. Lastly, this research employed the used of descriptive statistics like: Cross tabulations, frequency tables and percentages to analyzed data obtained from the field.

Study Area

Location and Ariel Extent

The Geographical coordinates of the study area ranges between Latitude $10^{\circ}14'$ 30''N and $10^{\circ}19'$ 30''N and Longitudes $11^{\circ}7'$ 0'' E and 11° 13' 30'' E (Satellite images of Gombe, 2015). It occupies an area of about $45Km^2$ (ministry of land and survey Gombe, 2008). Gombe local government area is located approximately at the center of Gombe state. It is bounded by Kwami L.G.A in the north and almost surrounded by Akko Local Government Area in the south east and south west; Gombe town is well linked by road to other regional centers like Biu/Maiduguri, Potiskum/Damaturu, Bauch/Jos, Kari/Kano, and Kumo/Yola (Adam Modu Abbas et; al 2017).

Climate

The climate of Gombe state is part of tropical continental climate characterized by distinctive rainy and dry seasons. The wet season start around April to October with an average annual rainfall of 650-1000mm, while dry season commences around November to April with the coldest months in January and February. Relative humidity in pattern has been 94% in August and drops to less than 10% during Hamatan period (Gombe state diary, 2008). The dry season become distinctly severe when the north East trade wind over the region becomes established. The wind originating from the Sahara belt that is high pressure area at that period, this dry and dust laden wind produces the harsh conditions of the season. Temperature becomes lower at 75^0F (25^0C) particularly during the period from December to February due to the harmattan. Average relative humidity is also lowest at about 15% during the harmattan period of the dry season; this shows that climatic conditions hinders most parents in Gombe local government area to engage in the immunization of their children, because of marketing in the dry season and farming in the rainy season (Abdullahi 2017).

Topography and Hydrology

Gombe town is largely at the foot of Akko escarpment in the west of the town. Developments are taking up sites on the escarpment and on Tumfure plains as well as southwards and up the higher grounds to the east beyond the newer Liji area. The highest point on the landscape is on the Liji hills, and the sandstone hills dotting the southern parts of the town site. The highest part of the buildup area of the town is located at the western gateway of about 1850ft (610.5m) above the sea level and the lowest part at the BCGA areas with about 1250ft (412.5m) above the sea level. The study area in conclusion shows low grounds in BCGA, Yelon Guruza area, and high grounds located in Tunfure and Liji hills, many rivers truncate the older part of the town with all flowing eastwards from their source at the Akko escarpment. The rivers and streams, some of which have tributaries with active gullies have truncated the town, particularly at the north east parts, creating east striations on the landscape so this also affect the immunization coverage in the area due to the high level of obstacles and flowing of rivers during the rainy season (Gombe state diary, 2018).

Soils and Vegetation type

The soil is a tropical ferruginous type, dark grey in colour and has PH value ranging from 4-6, depending on the location (Layarank, 1990). The vegetation of Gombe is typically 'a high close canopy, with sprinkling of under shrubs and a sparse growth of grass to a more open grass of less height more spreading and stunted shrubs and dense growth of grass''. It can also be described as Sudan savanna with open grassland which dries up during dry season. The anthropogenic activities affected and modified the natural vegetation through deforestation, overgrazing, bush burning, constructions and Agriculture, all these activities causes low patronage of immunization because of flooding, windstorm and other natural disasters especially in the rainy season (Abdullahi, 2017).

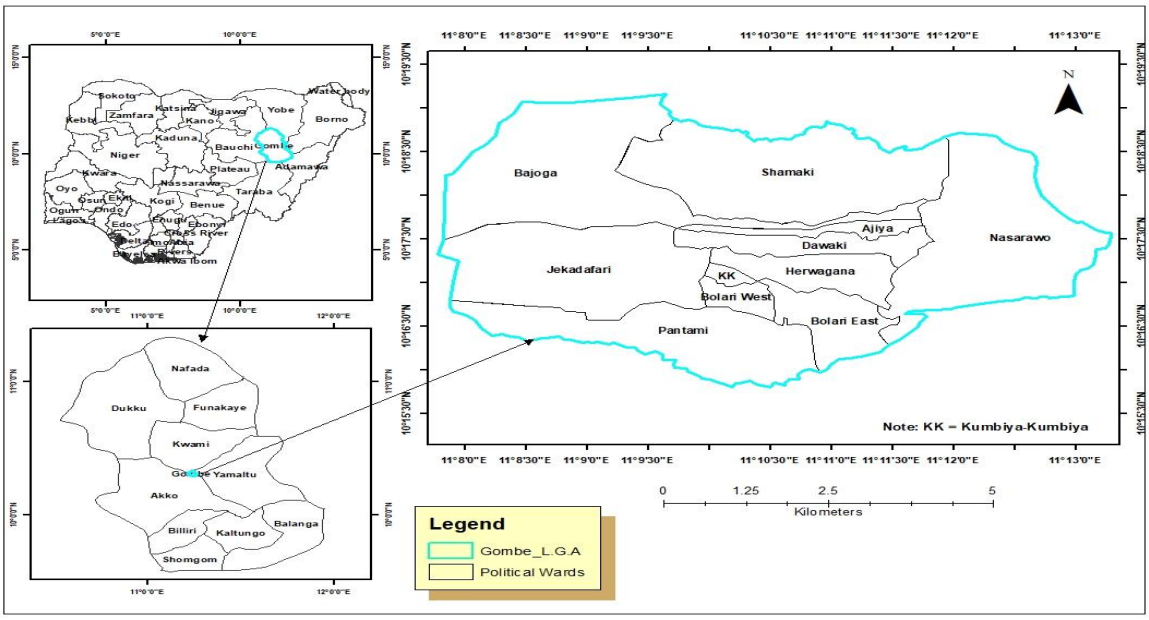

Gombe Local Government Area, Gombe State, Nigeria.
Source: ***Adapted from Administrative Map of Gombe (2021).***

Health Sector

There are 21 (9-Maternity, 12-Dispensaries) primary health care facilities, 2 secondary healthcare facilities (general hospital and specialist hospital) and 1 tertiary which is the federal teaching hospital. There are 32 Private clinics and laboratory services and 7 TB Centers, health personnel workers are 157. The L.G.A has a school of health technology, 1 school of nursing and midwifery and a proposed college of medical sciences at the Gombe state university. International development partners (IDPs) in the health sector are World Health Organization, United Nations Children Fund,

World Bank and MTN foundation. The Millennium Development Goals (MDGs) office in the presidency and the National Health Insurance Scheme (NHIS) are partnering with the Gombe L.G.A in achieving the sustainable development goals 4, 5, and 6, but still immunization is not well practiced as a result of different perception of the masses (Gombe state ministry of health, 2010).

Population and People

According to National Population and Housing Census (2006), priority table, Gombe town has population of 266,844 people with males having 146,721, and Females having 120, 123 people, (National Bureau of Statistics, 2012). While according to population projection of 2021 by the united nation world population prospect, Gombe local government area has the total projected population of 529, 000 people at 3.93% growth rate. The people of Gombe could be said to be diverse in terms of different languages spoken, the customs and the traditions being adhered to. According to Joseph Greenberg's (Undated) in Abba et al (2000), linguistic classification, the most dominant linguistic to be found in this area to the Afro-asiatic and Niger-Congo family of languages. Thus the ethno-linguistic composition of Gombe state include, among others, the Fulbe (Fulanis), Bolewa, Tera, Tangale, Tula, Waja, Wurkun, Jara, Dadiya, Cham, Awak, Pero, Kamo, Kushi and Bangunji. There are also more recent migrants such as Kanuri, the Hausa language, does serve the purposes of commerce, interaction, and of education at the lower levels of school systems. The English language remains the official language as obtains all over Nigeria and as a result of cultural diversity, immunization service in the area is affected (Abba, et al 2000).

Socio-economic Activities

Gombe state is abundant with physical, human and economic resources, it is the center of economic activities; it serves as the meeting point of investors from surrounding states which are: Borno and Yobe to the north and east, Taraba and Adamawa to the south and Bauchi to the west. This advantage triggers the state to be vibrant in all aspects. Again, the state is blessed with natural resources like coal, limestone, abundant land and so forth. There within the short period of time in existence, it encountered tremendous progress. In addition to that, the state is located in the sub-Saharan savannah thus it is a productive farming area cultivating crops like maize, millet, rice, guinea corn, sorghum, soybean, beans e.t.c, and vegetables like tomatoes, pepper, water melon, cabbage and so on. Gombe is the collection and distribution center for the cereals, which are transported by road and sold at many northern states and exported in to the Niger republic. The area is also beneficial in animal husbandry were hide and skin are produced for leather and the products are supplied to the southern states of Nigeria and Abuja, therefore these activities strengthen the economic base of Gombe. The occupational pattern of Gombe people is dominated by public service, Farming and business, and these activities tend to causes under utilization of immunization in the area because of the massive engagements day by day (Gombe state diary, 2018).

RESULTS AND DISCUSSION

This section devoted to the analysis and discussion of results from the data collected in 11 wards in the Gombe Local Government Area. All the data are formed in to tables and which shows frequencies of the variables used in the study Area.

Level of Immunization

In order to understand the parental perception of immunization services, it is very important to know the Level of Immunization which is the extent at which the immunization service is accepted or not in the study Area. Table 1 shows the level of immunization in the study area.

Table 1 Level of Immunization

	Frequency	Percentage	Valid Percentage	Cumulative Percentage
Valid Yes	272	68.0	68.0	68.0
No	128	32.0	32.0	100.0

Total	**400**	**100.0**	**100.0**

Source: Field Survey (2021)

The results of the analysis shown in Table 1 shows that about 70% of the parents of children 0-23 months of age carry their children to immunization which is more than half of the population in the study area, therefore, the level of immunization uptake in Gombe is very high, and this is true because Gombe Local Government Area is the city center that comprises People with varied social background in terms of Education, Politics, and ideology. Therefore, there is high proportion of people that carries their children to immunization which is agreed with the current situation in the Area as it is the most developed Area in the whole Gombe state (Gombe state diary, 2018).

Table 2 Perception of Parents on Immunization

Reasons	Mean	Std. Deviation
It is against my culture	3.06	1.306
My religion is against it	3.37	1.379
My husband does not like it	2.89	1.240
Nature of my occupation	3.03	1.177
Immunization consumes more time	2.97	1.166
The clinic is far	2.76	1.158
Accessibility problem	2.72	1.149
I don't have idea on it	2.81	1.053
It reduces pop. Growth	3.48	1.931
Immunization helps in my child development	4.23	3.640
It is good in the health of child	4.39	3.624
Congestion	1.73	.849

Source: Authors field Survey (2021)

As regards to the parents perception and views on immunization uptake in Gombe, Table 4.5 (mean score) categorizes parents perception on immunization in to 6 major categories, the first one carries the highest score which shows that almost all parents perceived Immunization as a way of increasing child Development in Gombe Local Government Area with the mean score of 4.39 & 4.23 respectively, this is in conformity with the findings of (Oyefara, 2014) who states that immunization is a key fundamental element of public health and prerequisite to social and economic development, and a crucial element that enables every child to reach his or her full physical and intellectual potential. On the other hand, some group of parents looked at it as the way of reducing population growth (3.48), this is in line with Ahmed (2016) that some people believe that some vaccines (especially polio vaccines) contain substances that could prevent pregnancy. Others said their religion is against it (3.37), this is in conformity with Ahmed (2016) that some group of muslim women in northern Nigeria are suspicious of vaccinations and prevents them from taking their children for vaccination, and Gombe state is no exception. Others believed that it is against their culture (3.06) and the rest is due to their nature of occupation (3.03), and this is related with the findings of Adebiyi (2013) who studied determinants of full child immunization among aged 12-23 months children and their results show that demographic and socioeconomic features like religion, culture, income, occupation, education influences immunization uptake.

Also Ahmed (2016) studied geographical analysis of maternal health care services in Gombe state and found that the factors that contribute to the problem of women utilization of immunization are: Cost, distance in terms of travel time, perceived proximity, lack of access and poor utilization of free maternal healthcare services and knowledge. It was noted again by Ahmed (2016), that the women with the least immunization rates are the ones that make decision to utilize health facilities,

while those with the highest immunization rates are those that make the decision together with their husbands. This analysis is real because Gombe Local Government Area is characterized with people of heterogeneous background, some parents misperceived immunization as a negative way of hindering population growth and others looked at it as a way of child development (Gombe State Primary Health Care Development Agency GSPHDA, 2021). Again Tinashe (2015) reiterated that others refused immunization based on religious beliefs. Some groups of parents consider compulsory vaccination as an undesirable act of undermining individual rights (Brown, Oluwatosin and Ogundeji, 2015). Also the result is in accordance with the Health belief model of Charles Abraham (1975) and Anti-vaccine conspiracy theory of Karen Douglas (2014) which states that Perception of people influences Immunization or vaccination uptake in every community.

CONCLUSION

Conclusively, this study assessed the parental perception of immunization services in Gombe Local Government Area of Gombe State, Nigeria. Descriptive statistics like Cross tabulation, mean score containing tables were employed in analyzing data on perception of parents on immunization and level of immunization in Gombe Local Government Area of Gombe state, Nigeria. The Results show that the parents perception on immunization uptake in Gombe was categorized in to 6, the first category shows that almost all parents perceived Immunization as a way of child development and a good service for the general health condition of children in Gombe Local Government Area, some group of the parents looked at immunization as the way of reducing population growth, and others does not patronizes it due to their nature of occupation, and some is because it is against their culture, some believe that it reduces population growth, Others deny immunization due to religious beliefs. Regarding the level of immunization in Gombe, it was observed that almost all of the parents of children 0-23 months of age carry their children to immunization in the study area; therefore, the level of immunization uptake in Gombe is very high.

RECOMMENDATIONS

In line with the findings of this work, the following recommendations are made:

- ✓ Government should improve awareness campaigns and empowerment of parents especially women/caregivers of the study Area.
- ✓ Additional Health care facilities should be constructed around some Areas of the Political wards like Bajoga, Pantami, Nasarawo, Jekadafari, Herwagana, and Bolari West, for effective Immunization service delivery to avoid congestion and waste of time to the mothers/caregivers.
- ✓ Government should also encourage formal education to higher levels in the study Area as higher qualification is one of the key factors that influences immunization uptake.
- ✓ Traditional and religious leaders should put hands in encouraging parents on the immunization uptake in the study Area.
- ✓ Further researches should look at the impact of other childhood diseases on the development of children in the study Area.
- ✓ Women in the study Area should be empowered to have variety of knowledge through awareness programmes.
- ✓ The masses in the local government Area should be enlightened on the present situation of immunization and to be encouraged on its compliance so that level of its uptake will be made available for future investigations.
- ✓ Further researches on Vaccine preventable diseases and other child killer diseases are encouraged so seek their impact on people of Gombe local Government Area of Gombe state.

REFERENCES

Abba, A.S., Shehu, A. and Abba A. (2000). Gombe State: *A History of the land and the people.* Ahmadu Bello University Press Limited, Zaria, Nigeria.

Abdullahi U.Y (2017), Socio-economic Determinants of House ownership in Gombe Local Government Area of Gombe State, a Published Msc. Dissertation in the Department of Geography, Bayero University Kano, Nigeria.

Adam ModuAbbas et al., (2018), Demographic and Socio Economic Determinants of House Ownership in Gombe Local Government Area, Gombe State. J. of Social Sciences and Public Policy, Vol. 10, Number 1, Pp. 1-3.

Adetukunbo (2007), Incomplete Childhood Immunization in Nigeria: a Multilevel Analysis of individual and contextual factors. *BMC Public Health Journal* 17:23 DOI 10.1186/s112889-017-4137.7.

Ahmed Mashkurah. (2016), Spatial Analysis of Tuberculosis spread in Gombe Local Government Area, Gombe State, Nigeria, an Msc. Unpublished Dissertation in the Department of Geography and Environmental Management, Ahmadu Bello University Zaria, Nigeria.

Daniels, J and Karen, D. (2014) Breast-feeding influences cognitive development in Filipino children. *Journal of Nutrition*, 135, 2589-2595.

Ibnouf, A.H., Van den Borne, H.W., Maarse, J. M. (2014). Factors Influencing Immunization Coverage among Chilgren Under Five years of age in Khartoum State, Sudan. *Journal of the South African Academy of family Practice/Primary Care. Retrieved on http://www.researchgate.net/publication/270850700. 10.04.2019*.

Miligo R., Okeibunor J., Anya B., Mkanda P., and Zawaira F., (2017),: Challenges of immunization in the African region. *The Pan African journal medical journal: http://www.panafrican-med-journa.com/content/series/27/3/12/full.*

Ministry of Health (2010). Gombe Strategic Health Development Plan (2010-2015*), Medical Journal of Health Sciences* 1 (1):11-12.

Muhammad G. S (2016), Spatio Temporal Analysis of Polio Cases in Kaduna Central Senatorial Zone, Kaduna State, Nigeria (From 2006-2014), an Msc. Dissertation in the Department of Geography and Environmental Management, Ahmadu Bello University Zaria, Nigeria.

National Population Commission (NPC) (Nigeria) and ICF. 2019. Nigerian Demographic and Health survey (2018) Abuja, Nigeria, and Rockville, Maryland, USA: NPC and ICF.

Nigeria Demographic and Health survey (2018). Key Indicators Report. Retrieved On *https://www.DHSprodramm.com.pdf 07.04.2019.*

Obasi, P.C; Henry-Ukoha, A; Ukewuihe, I.S and Chidiebere-Mark, N.M (2013) Factors affecting Agricultural Productivity among Arable crop Farmers in Imo State, Nigeria, *America Journal of Experimental Agriculture* 3(2): 443-454

Oku A, Oyo-Ita A, Glenton C, Fretheim A, Ames H, Muloliwa A, et al. (2017) Perceptions and experiences of childhood vaccination communication strategies among caregivers and health workers in Nigeria: A qualitative study. PLoS ONE 12(11): e0186733. https://doi.org/10.1371/journal.pone.0186733

Osowole & Obute (2001), Parents' Awareness and Perception of the Polio Eradication Programme in Gombe Local Government Area, Gombe State. Department of health promotion and education, faculty of public health, college of medicine, University of Ibadan, Ibadan, Nigeria.

Rasheed, K. O (2017), Beliefs knowledge and Perception of parents to Pediatrics. *Journal of Management and sustainability*, Vol. 4(12), 73-85 Retrieved on *https://www.researchgate.net/publication/121427418.* 09.06.2019.

Regmi, J. (2015) Socio-cultural influences on Vaccination-Vaccinators Perspective, Study From Nepal, Unpublished Thesis, Institute of Faculty of Health Sciences, University of Eastern Finland Retrieved on *https://www.researchgate.net/scientificcontribution/2111106703.* 05.07.2019.

Rew Micro plan Register (2020), Gombe Local government Area Primary Health Care development Agency.

Rosenstock, I. Stretcher, V., and Becker, M. (1994). The health belief Model and HIV risk behavior Change in Diclement, R.J, (eds), Preventive AIDS Theories, and Methods of behavioral interventions. New York Plnum press pp 5-24.

Sourabh, S. (2016); Child Immunization Coverage – A Critical Review, Department of Computer Science & IT, Bhaderwah Campus, University of Jammu, J&K, India.

Sani M. L. (2002): Evaluation of the National programme on Immunization (NPI) activities in Wamakko District of Wamakko Local Government Area of Sokoto State, Nigeria. An Unpublished Mph dissertation in the Department of Public Health, Faculty of Medicine, Ahmadu Bello University Zaria, Nigeria.

Tilottama and Madhulekka, (2013) Rural Health Differences, the Health of Population and Rural Culture. *American Journal of Health studies, 94(10) 1675-1679. Retrieved on https://nigeriacrvs.gov.ng.12.04.2019*.

Vallboa C. M. D. (1993), Importance of immunization in Child care and prevention. *Child and Adolescent Social work journal, Volume 10, Number 5.*

World Health Organization (2018), Bulletin, Millennium Development Goals.

Yamane, T. (1967). Statistics: An Introductory Analysis, 2nd Ed., New York: Harper and Row

Independent National electoral Commission Manual, (INEC, 2006)

Rain fade characteristics at Ku- and Ka-bands in some parts of Nigeria

M. S. Bawa* and K. C. Igwe
Department of Physics, Federal university of Technology, Minna, Nigeria
*Corresponding author, muhbawashe@gmail.com

Abstract

Rain fade characteristics at Ku- and Ka-bands in parts of North-eastern (Damaturu, Bauchi and Maiduguri) and South-western (Abeokuta, Ibadan and Ikeja) regions of Nigeria is presented in this work. 33 years (1983-2015) rainfall data were collected from the Nigerian Meteorological Agency (Nimet) for the locations. Chebil rain rate model was used to compute the point rainfall rate, while ITU-R P.618-12 model was used to compute the rain-induced attenuation at frequencies of 11 GHz, 14 GHz, 20 GHz, and 40 GHz. Point rainfall rate of 85.24 mm/h, 98.20 mm/h and 99.30 mm/h were obtained at Damaturu, Maiduguri and Bauchi respectively, while higher rainfall rate of 99.70 mm/h, 104.8 mm/h and 108.20 mm/h, were recorded at Abeokuta, Ibadan and Ikeja respectively. Three elevation angles were considered: 23^o, 42.5^o and 55^o. The results obtained show that rain-induced attenuation for the Southwestern region varied from 20.56 dB to 41.00 dB at 23^o elevation angle, 12.85 dB to 26.44 dB at 42.5^o elevation angle and 10.61 dB to 22.34 dB at 55^o elevation angle at Ku band, while the rain-induced attenuation computed for the Northeastern region varied from 18.59 dB to 37.65 dB at 23^o elevation angle, 11.61 dB to 23.46 dB at 42.5^o elevation angle and 9.59 dB to 20.52 dB at 55^o elevation angle for exceedance time percentage of 0.01% at Ku-band. For the Ka-band, the rain-induced attenuation for the Southwestern region ranged between 59.71 dB and 183.75 dB at 23^o elevation angle, 40.39 dB and 133.48 dB at 42.5^o elevation angle and 35.12 dB and 122.11 dB at 55^o elevation angle, while the rain-induced attenuation computed for the Northeastern region ranged between 54.06 dB and 168.97 dB at 23^o elevation angle, 36.50 dB and 120.79 dB at 42.5^o elevation angle and between 31.71 dB and 111.76 dB at 55^o elevation angle for same 0.01 percentage of time exceedance.

Keywords: Elevation Angle, Ka-Band, Ku-Band, Rain-Induced Attenuation, Rain Rate.

1. Introduction

Rainfall is a natural and time varying phenomenon that changes from location-to-location and from year-to-year. Above a certain threshold frequency, attenuation due to rainfall becomes one of the most important limits to the performance of line-of-sight (LOS) microwave links (Das and Maitra, 2016). In temperate climates this frequency threshold is about 10 GHz, while in the tropical and equatorial climates, the incidence of rainfall on radio links becomes serious for frequencies as low as 7 GHz since the tropical and equatorial climates experiences higher rainfall intensities of larger raindrops than the temperate climate (Rakshit *et al,.* 2017). In order to successfully estimate rain attenuation along the link path, the point rainfall rate characteristics must be available in the location of interest. For such rainfall rate characteristics, information such as integration time, average rainfall cumulative distribution, and worst-month rainfall rate distribution are all required by a radio link planner in order to estimate path loss (Sujan *et al.,* 2017).

Igwe *et al.* (2019) evaluated some rain attenuation prediction models for satellite communication at Ku and Ka bands. It was observed that rain attenuation at Ka-band (19.45GHz) was significantly higher than at Ku-band (12.675GHz) for all the elevation angles. The predicted rain attenuation by ITU-R model exceeded for 0.001 % of the time is as high as 52 dB, 54 dB and 75 dB at 55°, 42.5° and 23° respectively. Also, at 0.01 % of time, the rain attenuation predicted varies between 37 dB and 47 dB at the Ka-band frequency for the three elevation angles.

Also Igwe *et al.* (2021) obtained 5-minutes integration time rainfall data for the North central region of Nigeria from the Tropospheric Data Acquisition Network (TRODAN) Anyigba, Nigeria. One minute integration time rainfall was measured at Minna, Nigeria. To obtain the best performing rain rate model suitable for the region, two globally recognised rain rate models were evaluated and compared with the 1-minute measurements. These are the Lavergnat-Gole (L-G) and ITU-R P.837-7 models. The results obtained showed that the ITU-R P.837-7 and L-G models respectively underestimated the measured rain rate by 7.3 mm/h and 9 mm/h at time percentage exceedance of 0.1%, while they underestimated the measured rain rate by 23.4 mm/h and 13 mm/h respectively at 0.01%. At 0.001%, the measured rain rate was overestimated by the ITU-R P.837-7 and L-G models by 27.4 mm/h and 3 mm/h respectively. Further performance evaluation of the predefined models was carried out using different error metrics such as sum of absolute error (SAE), mean absolute error (MAE), root mean square error (RMSE), standard deviation (STDEV) and Spearman's rank correlation. The results obtained adjudged the Lavergnat-Gole model as the best rain rate prediction model for this region.

2. Methodology

Daily rainfall data of 33 years (January, 1983 to December, 2015) was acquired from the Nigerian Meteorological Agency (NIMET), Chebil rain rate model outlined in equation (5) was used to compute the rain rate, while ITU-R P.618-12 rain attenuation model was employed to calculate the rain-induced attenuation. Some of the input parameters needed for the ITU-R P. 618-12 model are: point rainfall rate for the location for 0.01% of an average year (mm/h), height above sea level of the Earth station (Km), elevation angle (degree), latitude of the Earth station (degree), frequency (GHz) and effective radius of the Earth (8500 Km).

2.1 Rain Rate Computation

2.2 Rain Attenuation Computation

The step by step procedure for calculating the attenuation distribution is given below:

Step 1: Determine the rain height, H_R as:

$$H_R = h_o + 0.36 \text{ (km)} \quad (1)$$

where h_o is the 0°C isotherm height above mean sea level of the location.

Step 2: Determining the slant-path length, L_S, below the freezing rain height as obtained by:

$$L_s = \frac{(h_R - h_s)}{\sin\theta} \text{(km)} \quad (2)$$

where θ is the elevation angle and h_S is the height of the location above sea level.

For $\theta < 5^{\theta}$, the following formula is used:

$$L_s = \frac{2(h_R - h_s)}{\left(\sin^2\theta + \right)\frac{2(h_R - h_s)^{1\backslash 2}}{R_e} + \sin\theta} \text{ (km)} \quad (3)$$

If h_R - h_S is less than or equal to zero, the predicted rain attenuation for any time percentage is zero and the following steps are not required.

Step 3: Calculate the horizontal projection, L_G, of the slant-path length from:

$$L_G = L_S \text{Cos } \theta \quad \text{(Km)} \quad (4)$$

Step 4: Determine the point rainfall rate $R_{0.01}$ (mm/h) exceeded for 0.01% of an average year. This is obtained using Chebil rain rate model given as:

$$R_{0.01} = \alpha M^{\beta} \quad (5)$$

where, α and β are regression coefficients defined as α = 12.2903; and β = 0.2973, while M is the annual average rainfall.

Step 5: Obtain the specific attenuation, γ_R using the frequency-dependent coefficients given in Recommendation ITU-R P.618-10 and the rainfall rate, $R_{0.01}$ determined from step 4, by using:

$$\gamma R = k(R_{0.01})^{\alpha} \text{ (dB\km)} \quad (6)$$

where Parameters k and α are determined as functions of frequency in GHz as given in ITU-R P. 618-12

Step 6: Calculate the horizontal reduction factor, $r_{0.01}$ for 0.01% of the time given as:

$$r_{0.01} = \frac{1}{1 + 0.78\sqrt{\frac{L_G \gamma R - 0.38\left(1 - e^{-2L_G}\right)}{f}}} \quad (7)$$

Where f is the frequency in GHz.

Step 7: Calculate the vertical adjustment factor, $V_{0.01}$, for 0.01% of the time given as:

$$\zeta = Tan^{-1}\left(\frac{h_R - h_S}{L_G r_{0.01}}\right) \quad \text{(degrees)} \quad (8)$$

$$For \zeta > \theta, L_R = \frac{L_G r_{0.01}}{\cos\theta} \quad \text{(km)} \quad (9)$$

else,

$$L_R = \frac{(h_R - h_S)}{\sin\theta} \quad \text{(km)} \quad (10)$$

If $|\varphi| < 36^{\circ}$, x = 36 - $|\varphi|$ (degrees)

else, x = 0 degree

$$V_{0.01} = \frac{1}{1 + \sqrt{\sin\theta\left(31\left(1 - e^{-(\theta/(1+x))}\right)\frac{\sqrt{L_R \gamma_R}}{f^2} - 0.45\right)}} \quad (11)$$

Step 8: The effective path length through rain, L_E (Km), is calculated as:

$$L_E = L_R V_{0.01} \quad (12)$$

Step 9: The predicted attenuation exceeded for 0.01% of an average year is obtained from:

$$A_{0.01} = \gamma R L_E \text{ (dB)} \quad (13)$$

Step 10: The estimated attenuation to be exceeded for the other percentages of an average year, in the range 0.001% to 10%, may be estimated from the attenuation to be exceeded for 0.01% for an average year by using:

$$A_P = A_{0.01}\left(\frac{p}{0.01}\right)^{-\left(0.655 + 0.033\ln(p) - 0.045\ln(A_{0.01}) - \beta(1-p)\sin\theta\right)} \text{ (dB)} \quad (14)$$

where p is the percentage probability of interest and β is given by:

If $P \geq 1\%$ $or |\varphi| \geq 36°$ $\beta = 0$

If $P < 1\%$ and $|\varphi| < 36°$ and $\theta \geq 25°$: $\beta = -0.005(|\varphi| - 36)$

otherwise:

$\beta = -0.005(|\varphi| - 36) + 1.8 - 4.25\ sin\theta$

where;

$$\beta = \begin{Bmatrix} 0 if \ \geq 1\% or / \varphi / \geq 36° \\ -0.005(/ \varphi / -36°) if, p < 1\% and / \varphi / < 36° and \theta \geq 25° \\ -0.005(/ \varphi / -36°) + 1.8 - 4.25 \sin \theta, otherwise \end{Bmatrix}$$

2.3 Study Locations

The study location is parts of two geographical zones of Nigeria. These include the Southwestern region and the Northeastern region of Nigeria. The Southwestern States are Abeokuta, Ibadan and Ikeja, while the Northeastern region include Damaturu, Bauchi and Maiduguri States.

3. Results

The point rainfall rate calculated using Chebil model is presented in Table 1.

Table 1: Point Rainfall Rate for the Study Locations.

Location	Damaturu	Maiduguri	Bauchi	Abeokuta	Ibadan	Ikeja
$R_{0.01}$ (mm/hr)	85.20	98.20	99.30	99.70	104.80	108.20

The results from Table 1 shows that higher rainfall rates at 0.01 percentage time exceedance was experienced in Abeokuta, Ibadan and Ikeja than in Damaturu, Bauchi and Maiduguri. Hence, higher rain-induced attenuation is expected in Southwestern part than in Northeastern part of the country. Table 2 shows the geographical and experimental parameters used for the computation of rain-induced attenuation in the study locations.

Table 2: Geographical and experimental parameters for the study locations.

Station	Damaturu	Bauchi	Maiduguri	Abeokuta	Ibadan	Ikeja
Longitude (ºN)	11.9	9.8	13.2	3.55	3.90	3.33
Latitude (ºE)	11.7	10.3	11.8	6.42	7.43	6.58
Altitude (m)	451	616	320	66	230	129
Isotherm Height (Km)	4.412	4.416	4.416	4.410	4.400	4.390
Frequency (GHz)	11, 14, 20 & 40	11, 14, 20 & 40	11, 14, 20 & 40	11, 14, 20 & 40	11, 14, 20 & 40	11, 14, 20 & 40
Elevation Angles	23º, 42.5º & 55º	23º, 42.5º & 55º	23º, 42.5º & 55º	23º, 42.5º & 55º	23º, 42.5º & 55º	23º, 42.5º & 55º
Polarisation Angles	Vertical, Circular & horizontal	Vertical, Circular & horizontal	Vertical, Circular & horizontal	Vertical, Circular & horizontal	Vertical, Circular & horizontal	Vertical, Circular & horizontal

The predicted rain-induced attenuation at 23^0 elevation angle for horizontal, circular and vertical polarisations for the study locations is presented in Tables 3-5

Table 3: The predicted rain-induced attenuation at 23^0 elevation angle for horizontal polarisation

Frequency (GHz)	Damaturu	Bauchi	Maiduguri	Abeokuta	Ibadan	Ikeja
11.00	21.22	22.74	23.45	23.45	24.88	25.58
14.00	34.14	36.45	37.65	37.66	39.88	40.99
20.00	62.94	66.96	69.30	69.56	73.52	75.58
40.00	156.66	162.57	168.97	170.56	178.91	183.75

Table 4: The predicted rain-induced attenuation at 23^0 elevation angle for circular polarisation

Frequency (GHz)	Damaturu	Bauchi	Maiduguri	Abeokuta	Ibadan	Ikeja
11.00	19.89	21.30	21.98	21.99	23.32	23.98
14.00	31.95	34.06	35.19	35.25	37.28	38.31
20.00	58.25	61.83	64.05	64.36	67.92	69.81
40.00	148.09	155.55	161.72	163.31	171.22	175.85

Table 5: The predicted rain-induced attenuation at 23^0 elevation angle for vertical polarisation

Frequency (GHz)	Damaturu	Bauchi	Maiduguri	Abeokuta	Ibadan	Ikeja
11.00	18.59	19.89	20.54	20.56	21.80	22.42
14.00	30.10	32.00	33.10	33.21	35.08	30.04
20.00	54.06	57.26	59.36	59.71	62.93	64.67
40.00	141.56	148.57	154.52	156.10	163.58	167.99

Table 3 shows that the Northeastern region (Damaturu, Bauchi and Maiduguri) recorded rain-induced attenuation values for horizontal polarisation that ranged between 21.22 dB and 23.45 dB at 11 GHz downlink frequency, while values ranged between 34.14 dB and 37.65 dB at 14 GHz uplink frequency. For the Southwestern region (Abeokuta, Ibadan and Ikeja) rain-induced attenuation values varied from 23.45 dB to 25.58 dB at 11 GHz downlink frequency, while values varied from 37.66 dB to 40.99 dB at 14 GHz uplink frequency of Ku-band. For the Ka band, the Northeastern region recorded attenuation values for the range between 62.94 dB and 69.30 dB at 20 GHz downlink frequency, while values ranged between 154.66 dB and 168.97 dB at 40 GHz uplink frequency. The Southwestern region recorded rain-induced attenuation values that ranged between 69.56 dB and 75.58 dB at 20 GHz downlink frequency, while values ranged between 170.56 dB and 183.75 dB at 40 GHz uplink frequency at 0.01% time exceedance.

As observed in Table 4, the rain-induced attenuation for circular polarisation, recorded values that varied from 19.89 dB to 21.98 dB at 11 GHz downlink frequency, while values varied from 31.95 dB to 35.19 dB at 14 GHz uplink frequency for the Northeastern region. The Southwestern region recorded attenuation values that ranged between 21.99 dB and 23.98 dB at 11 GHz downlink frequency, while values ranged between 35.25 dB and 38.31 dB at 14 GHz uplink frequency at 0.01% time exceedance at Ku band. The Northeastern region recorded rain-induced attenuation values that ranged between 58.25 dB and 64.05 dB at 20 GHz downlink frequency, while values ranged between 148.09 dB and 161.72 dB at 40 GHz uplink frequency. For the Southwestern region recorded attenuation values varied from 64.36 dB to 69.81 dB at 20 GHz downlink frequency, while values varied from 163.31 dB to 175.85 dB at 40 GHz uplink frequency at Ka-band.

From Table 5, the Northeastern region recorded attenuation values for vertical polarisation that ranged between 18.59 dB and 20.54 dB at 11 GHz downlink frequency, while values ranged between 30.10 dB and 33.10 dB at 14 GHz uplink frequency. The rain-induced attenuation values varied from 20.56 dB to 22.42 dB at 11 GHz downlink frequency, while values varied from 33.21 dB to 36.04 dB at 14 GHz uplink frequency of the Southwestern region at 0.01% time exceedance at Ku band. Rain-induced attenuation values varied from 54.06 dB to 59.36 dB at 20 GHz downlink frequency, while values varied from 141.56 dB to 154.52 dB at 40 GHz uplink frequency for the Northeastern region. The Southwestern region recorded rain-induced attenuation values that ranged between 59.71 dB and 64.67 dB at 20 GHz downlink frequency, while values ranged between 156.10 dB and 167.99 dB at 40 GHz uplink frequency at 0.01% time exceedance at Ka band.

Figures 1-4 show the graphical comparison of rain attenuation at downlink and uplink frequencies

of Ku- and Ka- bands at horizontal polarisation for the study locations at 42.5° elevation angle for different percentages of time exceedance.

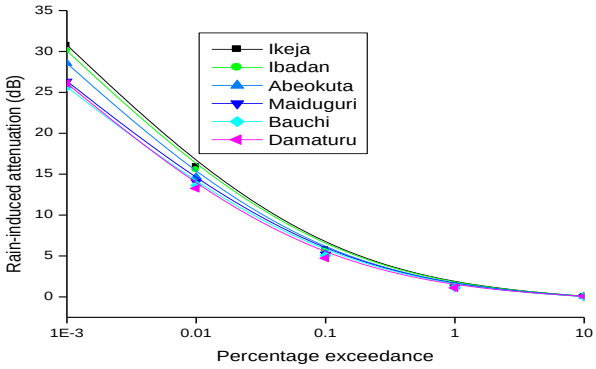

Figure 1: Rain-induced attenuation at 11 GHz downlink, horizontal polarisation

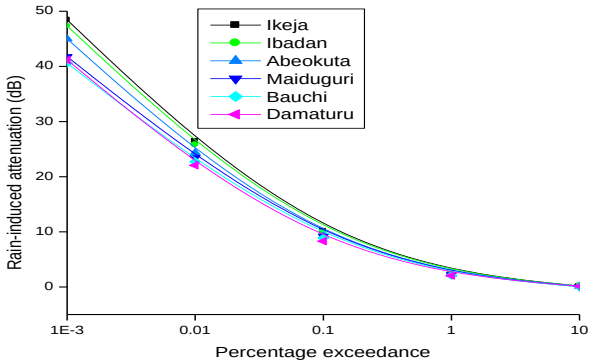

Figure 2: Rain-induced attenuation at 14 GHz uplink, horizontal polarisation

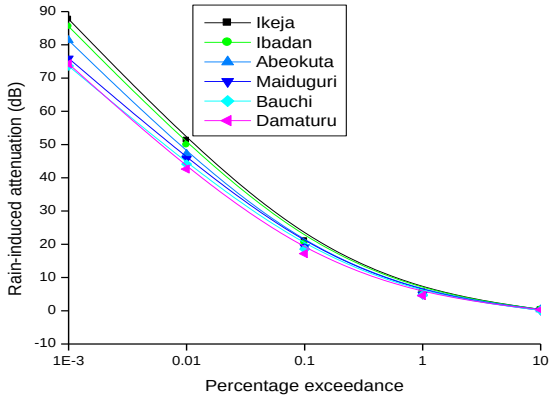

Figure 3: Rain-induced attenuation at 20 GHz downlink, horizontal polarisation

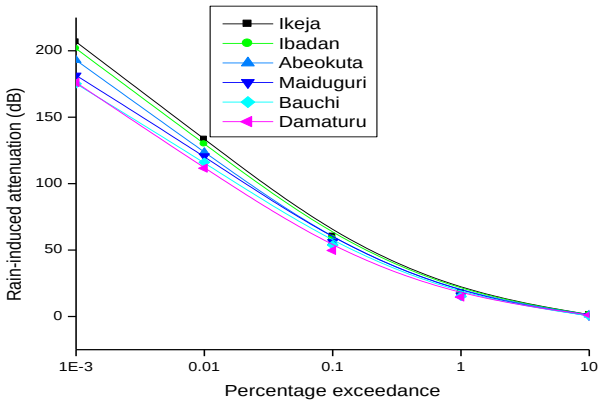

Figure 4: Rain-induced attenuation at 40 GHz uplink, horizontal polarisation

Figures 1-4 revealed that the rain-induced attenuation values for horizontal polarisation ranged between 13.26 dB and 14.04 dB at 11 GHz downlink, while values ranged between 22.07 dB and 23.46 dB at 14 GHz uplink frequency for the Northeastern region. The Southwestern region recorded rain-induced attenuation values that varied from 14.66 dB to 15.95 dB at 11 GHz downlink frequency, while values varied from 24.35 dB to 26.44 dB at 14 GHz uplink frequency of Ku-band. The Northeastern region recorded rain-induced attenuation values that varied from 42.62 dB to 45.68 dB at 20 GHz downlink frequency, while values varied from 111.63 dB to 120.79 dB at 40 GHz uplink frequency. Rain-induced attenuation for the Southwestern region recorded values that ranged between 47.17 dB and 51.30 dB at 20 GHz downlink frequency, while values ranged between 123.57 dB and 133.48 dB at 40 GHz uplink frequency at 0.01% time exceedance at Ka-band.

Figures 5-8 show the graphical comparison of rain attenuation at downlink and uplink frequencies of Ku- and Ka- bands at circular polarisation for the study locations at 42.5° elevation angle for different percentages of time exceedance.

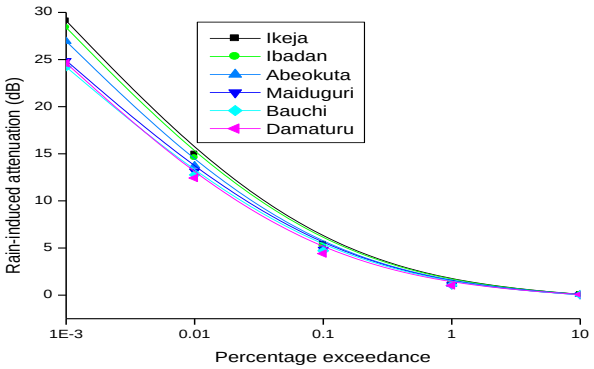

Figure 5: Rain-induced attenuation at 11 GHz downlink, circular polarisation

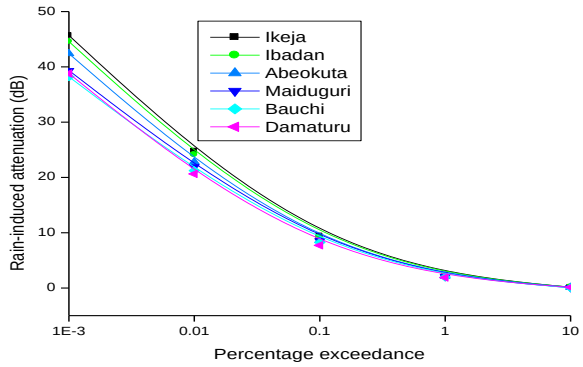

Figure 6: Rain-induced attenuation at 14 GHz uplink, circular polarisation

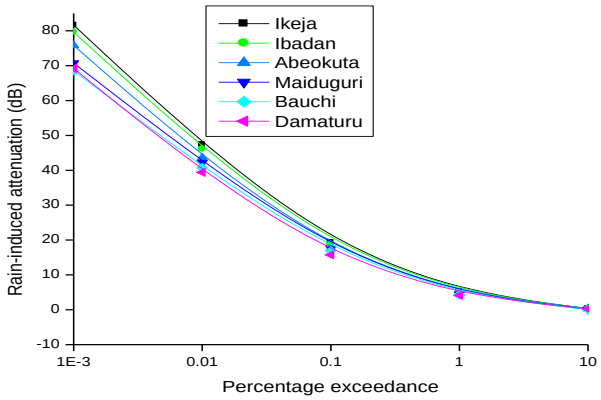

Figure 7: Rain-induced attenuation at 20 GHz downlink, circular polarisation

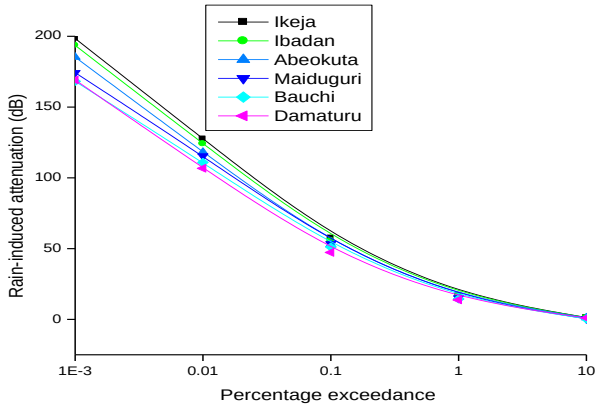

Figure 8: Rain-induced attenuation at 40 GHz uplink, circular polarisation

As observed from Figures 5-8 rain-induced attenuation computed for circular polarisation for the Northeastern region recorded values that varied from 12.43 dB to 13.17 dB at 11 GHz downlink, while values varied from 20.64 dB to 21.93 dB at 14 GHz uplink frequency. The Southwestern region recorded attenuation values that ranged between 13.74 dB and 14.99 dB at 11 GHz downlink frequency, while values ranged between 22.79 dB and 24.78 dB at 14 GHz uplink frequency at Ku-band. For Ka band, the Northeastern region recorded attenuation values that ranged between 39.39 dB and 42.21 dB at 20 GHz downlink, while values ranged between 106.70 dB and 115.45 dB at 40 GHz uplink frequency. The Southwestern region recorded attenuation values that varied from 43.59 dB to 47.34 dB at 20 GHz downlink frequency, while values varied from 118.12 dB to 127.54 dB at 40 GHz uplink frequency at 0.01% time exceedance.

Figures 9-12 show the graphical comparison of rain attenuation at downlink and uplink frequencies of Ku- and Ka- bands at vertical polarisation for the study locations at 42.5° elevation angle for different percentages of time exceedance.

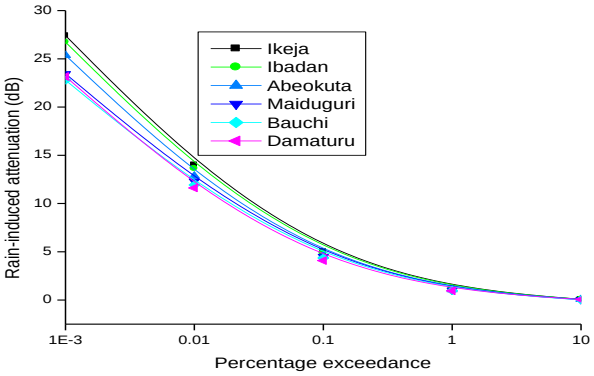

Figure 9: Rain-induced attenuation at 11 GHz downlink, vertical polarisation

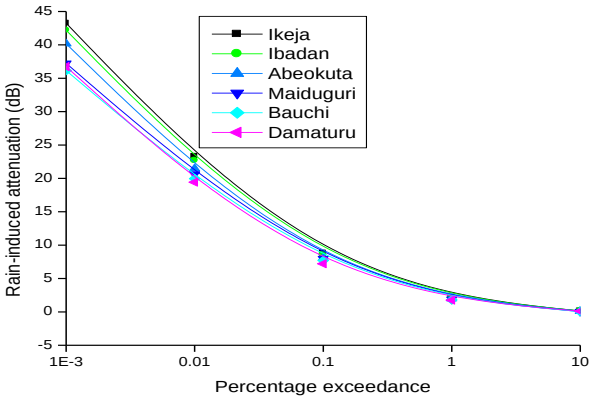

Figure 10: Rain-induced attenuation at 14 GHz uplink, vertical polarisation

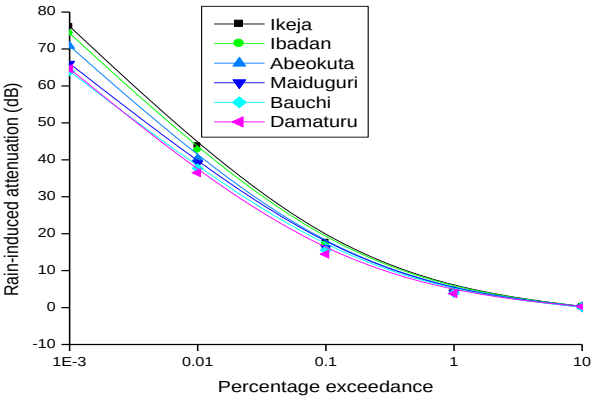

Figure 11: Rain-induced attenuation at 20 GHz downlink, vertical polarisation

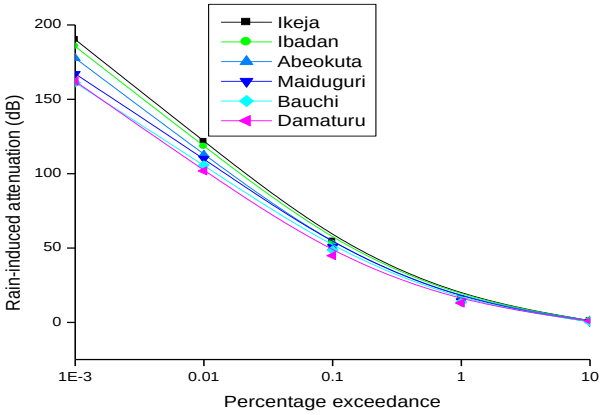

Figure 12: Rain-induced attenuation at 40 GHz uplink, vertical polarisation

It is observed from the Figures 9-12 that the Northeastern region recorded attenuation values computed for vertical polarisation that ranged between 11.61 dB and 12.31 dB for 11 GHz downlink frequency, while values ranged between 19.43 dB and 20.64 dB for 14 GHz uplink frequency. For the Southwestern region rain-induced attenuation values varied from 12.85 dB to 14.01 dB at 11 GHz downlink, while values varied from 21.47 dB to 23.31 dB at 14 GHz uplink frequency at 0.01% of time exceedance at Ku-band. The Northeastern region recorded attenuation values for vertical polarisation that varied from 36.50 dB to 39.10 dB at 20 GHz downlink, while values varied from 101.81 dB to 110.14 dB at 40 GHz uplink frequency. Rain-induced attenuation for the Southwestern region had values that ranged between 40.39 dB and 43.81 dB at 20 GHz downlink, while values ranged between 112.71 dB and 121.64 dB at 40 GHz uplink frequency at 0.01% of time exceedance at Ka-band.

The predicted rain-induced attenuation at 55^0 elevation angle for horizontal, circular and vertical polarizations for the study locations is presented in Tables 6-8

Table 6: The predicted rain-induced attenuation at 55^0 elevation angle for horizontal polarisation

Frequency (GHz)	Damaturu	Bauchi	Maiduguri	Abeokuta	Ibadan	Ikeja
11.00	10.94	11.73	12.09	12.09	12.83	13.19
14.00	18.60	19.86	20.52	20.53	21.73	22.34
20.00	37.05	39.49	40.37	41.03	43.40	44.63
40.00	101.77	107.28	111.76	112.89	118.72	122.11

Table 7: The predicted rain-induced attenuation at 55^0 elevation angle for circular polarisation

Frequency (GHz)	Damaturu	Bauchi	Maiduguri	Abeokuta	Ibadan	Ikeja
11.00	10.26	10.98	11.33	11.34	12.03	12.37
14.00	17.40	18.54	19.17	19.21	20.32	20.88
20.00	34.23	36.39	37.72	37.91	40.05	41.18
40.00	97.19	102.37	106.70	107.83	113.35	116.58

Table 8: The predicted rain-induced attenuation at 55^0 elevation angle for vertical polarisation

Frequency (GHz)	Damaturu	Bauchi	Maiduguri	Abeokuta	Ibadan	Ikeja
11.00	09.59	10.26	10.59	10.61	11.26	11.56
14.00	16.38	17.42	18.03	18.09	19.11	19.64
20.00	31.71	33.64	34.90	35.12	37.05	38.10
40.00	92.65	97.51	101.68	102.80	108.01	111.10

From Table 6, the Northeastern region recorded rain-induced attenuation values computed for horizontal polarisation that ranged between 10.94 dB and 12.09 dB at 11 GHz downlink frequency, while values ranged between 18.60 dB and 20.52 dB at 14 GHz uplink frequency. The attenuation values varied from 12.09 dB to 13.19 dB at 11 GHz downlink frequency, while values varied from 20.53 dB to 22.34 dB at 14 GHz uplink frequency for the Southwestern region at 0.01% time exceedance at Ku band. Rain-induced attenuation for horizontal polarisation, values varied from 37.05 dB to 40.37 dB at 20 GHz downlink frequency, while values varied from 101.77 dB to 111.76 dB at 40 GHz uplink frequency for the Northeastern region. The Southwestern region recorded rain-induced attenuation values ranged between 41.03 dB and 44.63 dB at 20 GHz downlink frequency, while values ranged between 112.89 dB and 122.11 dB at 40 GHz uplink frequency at 0.01% time exceedance of Ka band.

Table 7 shows that the Northeastern region recorded attenuation values for circular polarisation that ranged between 10.26 dB and 11.33 dB at 11 GHz downlink frequency, while values ranged between 17.40 dB and 19.17 dB at 14 GHz uplink frequency. For the Southwestern region attenuation values varied from 11.34 dB to 12.37 dB for 11 GHz downlink frequency, while values varied from 19.21 dB to 20.88 dB at 14 GHz uplink frequency at Ku-band. For the Ka band, the Northeastern region recorded attenuation values for ranged between 34.23 dB and 37.72 dB at 20 GHz downlink frequency, while values ranged between 97.19 dB and 106.70 dB at 40 GHz uplink frequency. The Southwestern region recorded attenuation values ranged between 37.91 dB and 41.18 dB at 20 GHz downlink frequency, while values ranged between 107.83 dB and 116.58 dB at 40 GHz uplink frequency at 0.01% time exceedance.

The results from Table 8 indicates that values of rain-induced attenuation for vertical polarisation varied from 09.59 dB to 10.59 dB at 11 GHz downlink frequency, while values varied from 16.38 dB to 18.03 dB at 14 GHz uplink frequency for the Northeastern region. The Southwestern region recorded attenuation values in the range of 10.61 dB and 11.56 dB at 11 GHz downlink frequency, while values ranged between 18.09 dB and 19.64 dB at 14 GHz uplink frequency at 0.01% time exceedance at Ku band. The Northeastern region recorded rain-induced attenuation values for circular polarisation that ranged between 31.71 dB and 34.90 dB at 20 GHz downlink frequency, while values ranged between 92.65 dB and 101.68 dB at 40 GHz uplink frequency. For the Southwestern region recorded attenuation values that varied from 35.12 dB to 38.10 dB at 20 GHz downlink frequency, while values varied from 102.80 dB to 111.10 dB at 40 GHz uplink frequency at Ka-band.

4. Conclusion

The statistics of rainfall attenuation for earth-space communication links at Ku-and Ka-bands have been investigated based on local input data. Rain-induced attenuation values were computed for 0.001%–10% time exceedance using ITU-R P.618-12 rain-induced attenuation model for locations studied. The results revealed that, for the rain-induced attenuation predicted for 0.01 percentage of time exceedance, availability of signal is possible at 42.5° and 55° elevation angle but impossible at 23° elevation angle at Ku-band.

For Ka-band, the predicted rain-induced attenuation values for 0.01 percentages of time exceedance

have shown that availability of signal is impossible at all three elevation angles. This implies total signal fade out during such rainfall events in the regions.

As observed from the computed rain-induced attenuation, the horizontal polarisation had highest amount of rain-induced attenuation followed by the circular polarisation, while the vertical polarisation had the least amount of rain-induced attenuation at all the operational frequencies of Ku- and Ka-bands and elevation angles. The Northeastern States showed a moderate rain-induced attenuation prediction due to low amount of rainfall intensity in the region. It implies that satellite communication signals will experience more rain-induced attenuation in the Southwestern region than the Northeastern region.

From the results obtained, it shows that increase in frequency leads to corresponding increase in attenuation, attenuation is also a function of frequency.

Acknowledgements
The authors are grateful to the Management of the Nigerian Meteorological Agency (NIMET), Abuja for providing the data used for this work.

References

Chebil, J., and Raihman, T. A. (1999). Rain rate statistics conversion for the prediction of rain attenuation in Malaysia. *Electronics Letters*, 35(12), 1019-1021.

Igwe, K. C., et al. "Evaluation of some rain attenuation prediction models for satellite communication at Ku and Ka bands." *Journal of Atmospheric and Solar-Terrestrial Physics* 188 (2019): 52-61.

Igwe, K. C., et al. "Performance evaluation of some rain rate conversion models for microwave propagation studies." *Advances in Space Research* (2021).

ITU-R P.618-10 (2009). Propagation data and prediction methods required for the design of earth-space telecommunication systems.

ITU-R Recommendation P.838-3 (2005). Specific attenuation model for rain for use in prediction methods.

Rakshit, Gargi, Arpita Adhikari, and Animesh Maitra. "Modelling of rain decay parameter for attenuation estimation at a tropical location." *Advances in Space Research* 59.12 (2017): 2901-2908.

Shrestha, Sujan, et al. "Rain specific attenuation and frequency scaling approach in slant-path for Ku and Ka-band experiments in South Korea."(2017): 625-628